



Invited Review

Snowballs in Africa: sectioning a long-lived Neoproterozoic carbonate platform and its bathyal foreslope (NW Namibia)



Paul F. Hoffman ^{a,b,*}, Galen P. Halverson ^c, Daniel P. Schrag ^b, John A. Higgins ^d, Eugene W. Domack ^{e,1}, Francis A. Macdonald ^f, Sara B. Pruss ^g, Clara L. Blättler ^h, Peter W. Crockford ^c, E. Blake Hodgin ^b, Eric J. Bellefroid ⁱ, Benjamin W. Johnson ^{a,j}, Malcolm S. W. Hodgeskiss ^{c,k}, Kelsey G. Lamothe ^{c,l}, Samuel J.C. LoBianco ^{b,f}, James F. Busch ^m, Bolton J. Howes ^d, J. Wilder Greenman ^c, Lyle L. Nelson ⁿ

^a School of Earth & Ocean Sciences, University of Victoria, Victoria, BC V8P 5C2, Canada^b Department of Earth & Planetary Sciences, Harvard University, Cambridge, MA 02138, USA^c Department of Earth & Planetary Sciences, McGill University, Montreal, QC H3A 0E8, Canada^d Department of Geosciences, Guyot Hall, Princeton University, Princeton, NJ 08544, USA^e Department of Geological Oceanography, University of South Florida, St. Petersburg, FL 33701, USA^f Department of Earth Science, University of California, Santa Barbara, CA 93106-9630, USA^g Department of Geosciences, Smith College, Northampton, MA 01063, USA^h Department of Geophysical Sciences, University of Chicago, Chicago, IL 60637, USAⁱ Department of Geology & Geophysics, Yale University, New Haven, CT 06520-8109, USA^j Department of Geological & Atmospheric Sciences, Iowa State University, Ames, IA 50011-1027, USA^k Department of Geological Sciences, Stanford University, Stanford, CA 94305, USA^l School of Earth Sciences, University of Melbourne, Parkville, Victoria 3010, Australia^m Department of Earth Sciences, Dartmouth College, Hanover, NH 03755, USAⁿ Department of Earth & Planetary Sciences, Johns Hopkins University, Baltimore, MD 21210, USA

ARTICLE INFO

ABSTRACT

Keywords:

Carbon isotope excursion
Carbonate platform
Congo craton
Cryogenian
Diagenesis
Glaciation
Ediacaran
Marinoan
Megakarst
Namibia
Neoproterozoic
Snowball Earth
Sturtian
Tonian

Otavi Group is a 1.5–3.5-km-thick epicontinental marine carbonate succession of Neoproterozoic age, exposed in an 800-km-long Ediacaran–Cambrian fold belt that rims the SW cape of Congo craton in northern Namibia. Along its southern margin, a contiguous distally tapered foreslope carbonate wedge of the same age is called Swakop Group. Swakop Group also occurs on the western cratonic margin, where a crustal-scale thrust cuts out the facies transition to the platformal Otavi Group.

Subsidence accommodating Otavi Group resulted from S–N crustal stretching (770–655 Ma), followed by post-rift thermal subsidence (655–600 Ma). Rifting under southern Swakop Group continued until 650–635 Ma, culminating with breakup and a S-facing continental margin. No hint of a western margin is evident in Otavi Group, suggesting a transform margin to the west, kinematically consistent with S–N plate divergence. Rift-related peralkaline igneous activity in southern Swakop Group occurred around 760 and 746 Ma, with several rift-related igneous centres undated. By comparison, western Swakop Group is impoverished in rift-related igneous rocks.

Despite low paleoelevation and paleolatitude, Otavi and Swakop groups are everywhere imprinted by early and late Cryogenian glaciations, enabling unequivocal stratigraphic division into five epochs (period divisions): (1) non-glacial late Tonian, 770–717 Ma; (2) glacial early Cryogenian/Sturtian, 717–661 Ma; (3) non-glacial middle Cryogenian, 661–646 ± 5 Ma; (4) glacial late Cryogenian/Marinoan, 646 ± 5–635 Ma; and (5) non-glacial early Ediacaran, 635–600 ± 5 Ma. Odd numbered epochs lack evident glacioeustatic fluctuation; even numbered ones were the Sturtian and Marinoan snowball Earths. This study aimed to deconstruct the carbonate succession for insights on the nature of Cryogenian glaciations. It focuses on the well-exposed southwestern apex

* Corresponding author at: 1216 Montrose Ave., Victoria, BC V8T 2K4, Canada.

E-mail address: paulhoffman@gmail.com (P.F. Hoffman).

¹ Deceased

of the arcuate fold belt, incorporating 585 measured sections (totaling >190 km of strata) and > 8764 pairs of $\delta^{13}\text{C}/\delta^{18}\text{O}_{\text{carb}}$ analyses (tabulated in Supplementary On-line Information).

Each glaciation began and ended abruptly, and each was followed by anomalously thick ‘catch-up’ depositional sequences that filled accommodation space created by synglacial tectonic subsidence accompanied by very low average rates of sediment accumulation. Net subsidence was 38% larger on average for the younger glaciation, despite its 3.5–9.3-times shorter duration. Average accumulation rates were subequal, 4.0 vs 3.3–8.8 m Myr⁻¹, despite syn-rift tectonics and topography during Sturtian glaciation, versus passive-margin subsidence during Marinoan. Sturtian deposits everywhere overlie an erosional disconformity or unconformity, with depocenters ≤ 1.6 km thick localized in subglacial rift basins, glacially carved bedrock troughs and moraine-like buildups. Sturtian deposits are dominated by massive diamictite, and the associated fine-grained laminated sediments appear to be local subglacial meltwater deposits, including a deep subglacial rift basin. No marine ice-grounding line is required in the 110 Sturtian measured sections in our survey.

In contrast, the newly-opened southern foreslope was occupied by a Marinoan marine ice grounding zone, which became the dominant repository for glacial debris eroded from the upper foreslope and broad shallow troughs on the Otavi Group platform, which was glaciated but left nearly devoid of glacial deposits. On the distal foreslope, a distinct glacioeustatic falling-stand carbonate wedge is truncated upslope by a glacial disconformity that underlies the main lowstand grounding-zone wedge, which includes a proximal 0.60-km-high grounding-line moraine. Marinoan deposits are recessional overall, since all but the most distal overlie a glacial disconformity. The Marinoan glacial record is that of an early ice maximum and subsequent slow recession and aggradation, due to tectonic subsidence. Terminal deglaciation is recorded by a ferruginous drape of stratified diamictite, choked with ice-rafterd debris, abruptly followed by a syndeglacial-postglacial cap-carbonate depositional sequence. Unlike its Sturtian counterpart, the post-Marinoan sequence has a well-developed basal transgressive (i.e., deepening-upward) cap dolomite (16.9 m regional average thickness, $n = 140$) with idiosyncratic sedimentary features including sheet-crack marine cements, tubestone stromatolites and giant wave ripples. The overlying deeper-water calci-rhythmite includes crystal-fans of former aragonite benthic cement ≤ 90 m thick, localized in areas of steep sea-floor topography. Marinoan sequence stratigraphy is laid out over ≥ 0.6 km of paleobathymetric relief.

Late Tonian shallow-neritic $\delta^{13}\text{C}_{\text{carb}}$ records were obtained from the 0.4-km-thick Devede Fm (~770–760 Ma) in Otavi Group and the 0.7-km-thick Ugab Subgroup (~737–717 Ma) in Swakop Group. Devede Fm is isotopically heavy, +4–8‰ VPDB, and could be correlative with Backlundtoppen Fm (NE Svalbard). Ugab Subgroup post-dates 746 Ma volcanics and shows two negative excursions bridged by heavy $\delta^{13}\text{C}$ values. The negative excursions could be correlative with Russøya and Garvellach CIEs (carbon isotope excursions) in NE Laurentia.

Middle Cryogenian neritic $\delta^{13}\text{C}$ records from Otavi Group inner platform feature two heavy plateaus bracketed by three negative excursions, correlated with Twitya (NW Canada), Taishir (Mongolia) and Trezona (South Australia) CIEs. The same pattern is observed in carbonate turbidites in distal Swakop Group, with the sub-Marinoan falling-stand wedge hosting the Trezona CIE recovery. Proximal Swakop Group strata equivalent to Taishir CIE and its subsequent heavy plateau are shifted bidirectionally to uniform values of +3.0–3.5‰.

Early Ediacaran neritic $\delta^{13}\text{C}$ records from Otavi Group inner platform display a deep negative excursion associated with the post-Marinoan depositional sequence and heavy values ($\leq +11\text{\textperthousand}$) with extreme point-to-point variability ($\leq 10\text{\textperthousand}$) in the youngest Otavi Group formation. Distal Swakop Group mimics older parts of the early Ediacaran inner platform $\delta^{13}\text{C}$ records, but after the post-Marinoan negative excursion, proximal Swakop Group values are shifted bidirectionally to $+0.9 \pm 1.5\text{\textperthousand}$. Destruction of positive and negative CIEs in proximal Swakop Group is tentatively attributed to early seawater-buffered diagenesis (dolomitization), driven by geothermal porewater convection that sucks seawater into the proximal foreslope of the platform. This hypothesis provocatively implies that CIEs originating in epi-platform waters and shed far downslope as turbidites are decoupled from open-ocean DIC (dissolved inorganic carbon), which is recorded by the altered proximal Swakop Group values closer to DIC of modern seawater.

Carbonate sedimentation ended when the cratonic margins collided with and were overridden by the Atlantic coast-normal Northern Damara and coast-parallel Kaoko orogens at 0.60–0.58 Ga. A forebulge disconformity separates Otavi/Swakop Group from overlying foredeep clastics. In the cratonic cusp, where the orogens meet at a right angle, the forebulge disconformity has an astounding ≥ 1.85 km of megakarstic relief, and km-thick mass slides were displaced gravitationally toward both trenches, prior to orogenic shortening responsible for the craton-rimming fold belt.

1. Introduction

Throughout geologic time, carbonate compounds have accumulated on and in the seafloor in response to alkalinity input from CO₂ outgassing and rock weathering (Garrels and Mackenzie, 1971; Holland, 1978, 1984; Zeebe and Wolf-Gladrow, 2001). The resulting carbonate rocks preserve geochemical proxy records of global change over the ages, viewed through the veil of diagenesis.

Marine carbonate accumulation is heavily biased in favor of warm shallow seas (Köppen and Wegener, 2015; Rodgers, 1957; Fairbridge, 1964; Michel et al., 2019), reflecting the temperature- and inverse pressure-dependence of carbonate saturation in seawater (Millero, 1979). Carbonate accumulation is a direct indicator of regional climate, not global climate. Whether global climate is warmer or colder,

carbonate accumulates preferentially in the warmest areas of the surface ocean.

The occurrence of glacial and periglacial deposits within marine carbonate platform successions of Cryogenian age (717–635 Ma) presents a climatic paradox (Harland, 1964; Harland and Herod, 1975; Hambrey and Harland, 1981; Fairchild, 1993; Kirschvink, 1992). It implies that glaciers reached sea level in the warmest areas, and did so in regions that lacked mountains from which glaciers could have descended from frigid heights. The paradox was underscored when reliable paleomagnetic data disclosed low paleolatitudes for South Australia during the younger Cryogenian ‘Marinoan’ glaciation of that region (Embleton and Williams, 1986; Schmidt et al., 1991; Sohl et al., 1999; Evans, 2000; Evans and Raub, 2011), and for Laurentia at the onset of the older Cryogenian ‘Sturtian’ glaciation (Macdonald et al., 2010a;

Table 1
Geologic epochs.

middle Ediacaran	ca 600 Ma ¹
early Ediacaran	635 Ma ²
late Cryogenian (Marinoan glaciation)	646 ± 5 Ma ³
middle Cryogenian (inter-snowball)	661 Ma ⁴
early Cryogenian (Sturtian glaciation)	717 Ma ⁵
late Tonian	

¹Lehmann et al. (2015); ²Rooney et al. (2015), Zhou et al. (2019); ³Kendall et al. (2006), Prave et al. (2016), Bao et al. (2018), Nelson et al. (2020); ⁴Rooney et al. (2015, 2020a); ⁵Macdonald et al. (2010a, 2018), MacLennan et al. (2018), Lan et al. (2020).

Denyszyn et al., 2009; Eyster et al., 2017, 2020). Because paleomagnetic constraints remain sparse and are subject to alternative (if radical) interpretation (Abraevitch and Van der Voo, 2010; Halls et al., 2015), temporal linkages were sought between carbonate accumulation and glaciation that rule out stratigraphic gaps across which significant paleogeographic changes could have occurred. Such linkages were found (Hoffman, 2011a; Rose et al., 2012; Benn et al., 2015; Ali et al., 2018; MacLennan et al., 2018).

The discovery of an ice-albedo threshold at which fully global glaciation becomes unavoidable was an unanticipated consequence of early attempts to model the climate system mathematically in one dimension (pole-to-equator), assuming radiative energy balance (Budyko, 1968, 1969; Eriksson, 1968; Sellers, 1969). The idea that such a ‘white-earth disaster’ could be self-reversing emerged as an after-thought, once it was realized that temperature-dependent silicate weathering self-adjusts atmospheric CO₂ so as to maintain a habitable climate in the face of solar brightening (Walker et al., 1981). The stabilizing geochemical feedback guards the ice-albedo threshold as well, but the slow geochemical response time allowed defenses to be overrun by swift events. A global glaciation, if it did occur, might not be permanent, however. Since CO₂-consuming weathering reactions would be seriously curtailed, continued CO₂ outgassing would, over millions to tens of millions of years, accumulate to a ‘greenhouse’ threshold at which sudden deglaciation would occur (Walker et al., 1981; Abbot, 2014). The cost would be prolonged and increasingly severe ocean acidification (Higgins and Schrag, 2003; Le Hir et al., 2008), in response to rising pCO₂, and an extended greenhouse aftermath combining ice-free planetary albedo and residual excess CO₂ (Mills et al., 2011).

The preceding concepts from climate physics and geochemistry were first applied in geology by Kirschvink (1992), who named the panglacial state, ‘snowball’ Earth, alluding to its appearance from space. Initially supported only by Klein and Beukes (1993), snowball Earth rose to the level of controversy after the extreme CO₂ hysteresis was advanced as explaining attendant C-isotope excursions and postglacial ‘cap’ carbonates (Hoffman et al., 1998b; Hoffman and Schrag, 2002; Halverson et al., 2002; Schrag et al., 2002; Higgins and Schrag, 2003; Tziperman et al., 2011). Cap carbonates are blankets of dolomite and/or limestone with many unusual sedimentary structures that directly overlie terminal glacial deposits or their disconformity surfaces over vast areas. Having no younger analogues of remotely comparable scale, cap carbonates had long been considered paradoxical (Norin, 1937; Harland, 1964; Dunn et al., 1971; Williams, 1979; Kennedy, 1996; Shields, 2005). Barite in Marinoan cap carbonates and carbonate-hosted sulfate in Marinoan synglacial lake deposits provided triple-O isotope evidence for atmospheric chemistry consistent with extreme CO₂ levels (Bao et al., 2008, 2009; Cao and Bao, 2013; Crockford et al., 2018). But many early attempts to test the hypothesis geologically were led astray by ignorance of surface processes on snowball Earth or failure to discriminate early (low-CO₂) from late (high-CO₂) snowball conditions (Warren et al.,

Table 2
Acronyms and abbreviations used in this paper.

aka	also known as
Bz	basin zone
ca	circa (approximately)
CA-	chemical abrasion, isotope dilution, thermal ionization, mass spectrometry
IDTIMS	
CAS	carbonate associated sulfur
CDNF	continentward-dipping normal faults
CDz	Central (Damara) or Swakop zone
CIE	carbon isotope excursion
CKz	Central Kaoko zone
Cn1, 2, etc.	Cryogenian CIE 1, 2, etc.
DIC	dissolved inorganic carbon
E	east
EBM	energy balance model
EKz	Eastern Kaoko Zone
ELA	(Ice) equilibrium-line altitude
En1, 2, etc.	Ediacaran CIE 1, 2, etc.
EPS	extracellular polymeric substances (mucilagenous cyanobacterial product)
FISC	fibrous isopachous sheet-crack cement
Fm	Formation (formally-defined stratigraphic unit)
FST	falling-stand systems tract
FSz	foreslope zone
Ga	10 ⁹ years before present
GCM	general circulation model
GE	glacio-eustasy
GI	glacio-isostasy
Gyr	10 ⁹ years
HCS	hummocky cross-stratification
HST	highstand systems tract
IDTIMS	isotope dilution, thermal ionization, mass spectrometry
IG	ice gravity
IPz	inner platform zone
IRD	ice rafted debris
IUGS	International Union of Geological Sciences
ka	10 ³ years before present
kyr	10 ³ years
LA-ICPMS	laser ablation, inductively coupled plasma, mass spectrometry
LGM	last glacial maximum (~20 ka)
LIP	large igneous province
LST	lowstand systems tract
Ma	10 ⁶ years before present
Mb	Member (formally-defined stratigraphic sub-unit)
MFS	maximum flooding stage
MSR	microbial sulfate reduction
Myr	10 ⁶ years
N	north
NDz	Northern (Damara) or Outjo zone
OML	Otavi Mountainland
PGE	platinum group element (Ru, Rh, Pd, Os, Ir, Pt)
S	south
SDz	Southern (Damara) or Khomas zone
SHRIMP	Sensitive high-resolution ion microprobe mass spectrometry
SIMS	Secondary ion mass spectrometry
SKz	Southern Kaoko zone (Zerrissen deep-sea fan)
SOI	Supplementary on-line information
SST	sea-surface temperature
Tn–1, etc.	Tonian CIE –1, –2, etc.
TOC	total organic carbon
TST	transgressive systems tract
VCDT	Vienna Canyon Diablo Troilite (analytical standard)
VPDB	Vienna Pee Dee Belemnite (analytical standard)
W	west
WKz	Western Kaoko or Coastal zone
wrt	with respect to

2002; Donnadieu et al., 2003; Goodman and Pierrehumbert, 2003; Pollard and Kasting, 2004; Pierrehumbert et al., 2011; Goddérus et al., 2011; Tziperman et al., 2012; Abbot et al., 2013; Ashkenazy et al., 2013, 2014; Ewing et al., 2014; Creveling and Mitrovica, 2014; Benn et al., 2015; Ashkenazy and Tziperman, 2016; Jansen, 2016; Hoffman et al., 2017a; Yang et al., 2017; Liu et al., 2020).

Snowball events should be long-lived because pCO₂ must be raised about 3 orders of magnitude from inception to reach the deglaciation threshold. Because of ice-albedo feedback, snowball inception should

be geologically instantaneous at low latitudes and deglaciations should be instantaneous (≤ 2 kyr) globally. These strong predictions have been increasingly borne out over the last decade with precise CA-ID-TIMS U–Pb ages for volcanic zircon and Re–Os isochron ages for organic-rich sediments (Rooney et al., 2015, 2020a; Hoffman et al., 2017a; Cox et al., 2018; MacLennan et al., 2018; Zhou et al., 2019; Nelson et al., 2020). The ages are consistent between multiple paleocontinents and within individual basins. Sturtian glaciation began in low paleolatitudes at 717 Ma (Macdonald et al., 2010a, 2018; Lan et al., 2014, 2020; Cox et al., 2015; MacLennan et al., 2018) and terminated 56 Myr later at ~ 661 Ma (Rooney et al., 2015, 2020a; Cox et al., 2018; Zhou et al., 2019). Marinoan onset is weakly constrained radiometrically at 646 ± 5 Ma (Kendall et al., 2006; Zhang et al., 2008; Liu et al., 2015; Prave et al., 2016; Nelson et al., 2020; Rooney et al., 2020a) but termination 11 ± 5 Myr later is tightly constrained at 635 Ma (Condon et al., 2005; Calver et al., 2013; Rooney et al., 2015; Prave et al., 2016; Zhou et al., 2019). Astrochronology of a basinal drillcore section in South China suggests a duration of 9.8 Myr for the complete inter-

snowball epoch (Bao et al., 2018, see discussion 4.1.12.), implying Marinoan onset ~ 651 Ma. Once the Cryogenian chronology came into focus (Table 1), it became apparent that average sediment accumulation rates for Cryogenian glaciations were an order of magnitude slower than for any younger glaciations, scaled for duration (Partin and Sadler, 2016; Pu et al., 2016). This result is well explained by the weak hydrologic cycle of a snowball Earth (Abbot et al., 2013). Resolving the Cryogenian chronology was a turning point in acceptance of the snowball hypothesis by Neoproterozoic specialists.

It is now more urgent than ever to exploit the wealth of information contained in carbonate platforms built before, between and after the tandem Cryogenian snowballs, so as to understand the circumstances that led to their rare occurrences, and their longterm consequences. Snowball events produce large sea-level falls (≥ 300 m), even in glaciated areas where bedrock was depressed by ice-sheet loading (Liu and Peltier, 2013; Creveling and Mitrovica, 2014; Benn et al., 2015). Ice grounding lines, where the bulk of glacially eroded sediment was deposited (Domack and Hoffman, 2011; Dowdeswell and Fugelli, 2012),

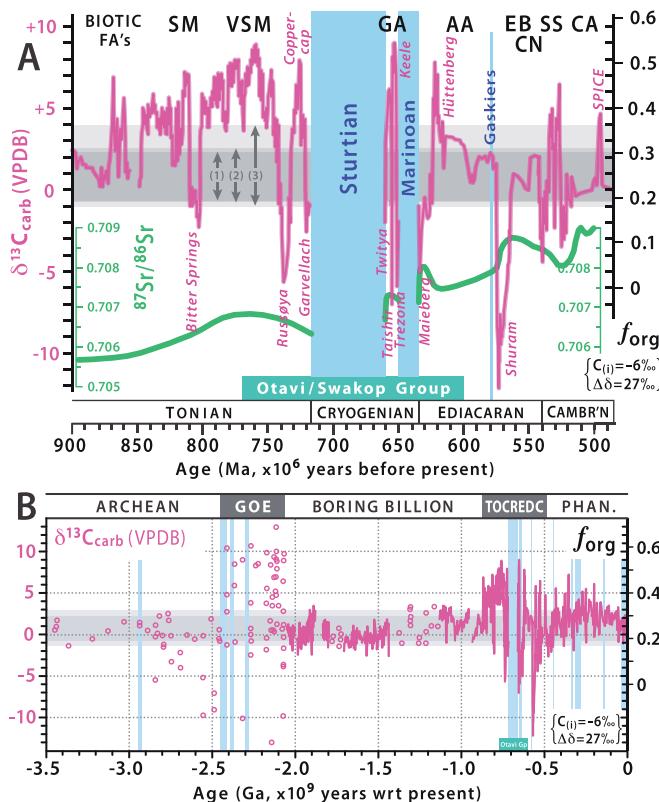


Fig. 1. (A) Composite $\delta^{13}\text{C}$ (magenta) and $^{87}\text{Sr}/^{86}\text{Sr}$ (green) records of marine carbonates deposited between 900 and 490 Ma, based on data from NW Canada (Mackenzie Mountains Supergroup), NE Svalbard (Akademikerbreen Group), NW Namibia (Otavi Group), N Ethiopia (Tambien Group), NE Oman (Huqf Supergroup), southern Morocco (Taroudant Group) and elsewhere. $\delta^{13}\text{C}$ curve is slightly modified after Halverson et al. (2018a). $^{87}\text{Sr}/^{86}\text{Sr}$ curve is from (Tonian) Park et al. (2020), (Cryogenian–Ediacaran) Zhou et al. (2020) and (Cambrian) Peng et al. (2012). Conventional interpretation of fractional organic burial (f_{org}) assumes an isotopic composition of $-6\text{\textperthousand}$ (VPDB) for C input and fractionation of $27\text{\textperthousand}$ between coexisting organic and carbonate C. Named $\delta^{13}\text{C}$ excursions in magenta italics. Aqua bar indicates estimated Otavi/Swakop Group time frame. Blue bars indicate durations of Cryogenian global glaciations (Sturtian and Marinoan) and mid-Ediacaran extra-tropical glaciation (Gaskiers). Grey bars indicate $\delta^{13}\text{C}$ ranges of (1) modern marine dissolved inorganic carbon (Kroopnick, 1985), (2) Cenozoic benthic foraminiferal aragonite (Zachos et al., 2001) and (3) post-525 Ma marine carbonate running mean (Saltzman and Thomas, 2012). Notable biotic (eukaryotic) first appearances, in stratigraphic order: SM, scale microfossils (Cohen and Knoll, 2012); VSM, vase-shaped microfossils (Porter and Knoll, 2000; Halverson et al., 2018b; Lahr et al., 2019); GA, green algal biomarker C_{29} stigmastane (Brocks et al., 2017; Hoshino et al., 2017); AA, acanthomorphic acritarchs, including *Tianshushania spinosa* phosphatized embryos (Cohen et al., 2009; Yin et al., 2011; Xiao et al., 2014; Hawkins et al., 2017); EB, Ediacara soft-bodied macrofossils (Narbonne, 2005; Xiao and Laflamme, 2008; Bobrovskiy et al., 2018); CN, *Cloudina-Naracalathus* calcified macrofossils (Wood, 2011); SS, ‘small-shelly’ microfossils (Kouchinsky et al., 2012); CA, Cambrian ‘explosion’ of arthropods and many other groups (Erwin et al., 2011; Giribet and Edgecombe, 2019). (B) Composite $\delta^{13}\text{C}$ record of marine carbonates deposited since 3.5 Ga (Hoffman and Lamothe, 2019). Data sources: 3.5–2.06 Ga (Krissansen-Totton et al., 2015); 2.041–1.43 Ga (Hodgskiss et al., 2019); 1.12–0.96 Ga (Gilleadeau and Kah, 2013); 0.92–0.52 Ga (Halverson et al., 2018b); 0.52–0.0 Ga (Saltzman and Thomas, 2012). Magenta lines represent composite high-resolution records from long-lived carbonate-rich successions. Open circles represent discontinuous or short-lived records with uncertain correlation. Grey bands as (1) and (2) in A. Variability in $\delta^{13}\text{C}$ was enhanced during GOE (Great Oxidation Event including Lomagundi CIE) and TOCREDC (Tonian-Cryogenian-Ediacaran-Cambrian, expanded in A), and muted during Boring Billion and Phanerozoic.

would have been many 100 s of m below glacial sea level, because of thick floating ice (Tziperman et al., 2012; Goodman and Strom, 2013). It is therefore optimal to study those carbonate platforms where foreslope wedges of bathyal depth (~200–3500 m wrt sea level) are preserved and exposed.

Stratigraphic correlation between carbonate platforms and their foreslopes is a challenge, even with biostratigraphic constraints (e.g., Grotzinger, 1986b; Crevello et al., 1989; Collom et al., 2009; Playton et al., 2010; Playton and Kerans, 2015a, b). The Neoproterozoic C-isotope record ($\delta^{13}\text{C}_{\text{carb}} = [\delta^{13}\text{C}_{\text{sample}} / \delta^{13}\text{C}_{\text{standard}} - 1] \times 10^3$) from marine carbonate platforms is characterized by sustained positive carbon-isotope excursions (CIEs, Table 2) punctuated by deep negative CIEs (Fig. 1A). Their magnitudes are unparalleled in the past 2.0 Ga (Fig. 1B). The CIEs hold promise for correlation because they are quantitatively reproducible at basin scale (Burns and Matter, 1993; Halverson et al., 2002; Johnston et al., 2012; Rose et al., 2012) and at least qualitatively so interregionally as demonstrated by independent radiometric dating (Swanson-Hysell et al., 2015a; MacLennan et al., 2018; Canfield et al., 2020; Rooney et al., 2020b). Some insist, however, that these CIEs are diagenetic (Knauth and Kennedy, 2009; Derry, 2010a; Swart and Kennedy, 2012; Jiang et al., 2019), unrelated to ocean chemistry, while others suggest that they record epi-platform waters decoupled from open-ocean thermocline DIC (Swart and Eberli, 2005; Geyman and Maloof, 2019; Hoffman and Lamothe, 2019; Bold et al., 2020). These concerns raise the more general question: how well do we understand carbonate sedimentation and diagenesis in Neoproterozoic oceans and epeiric seas, where carbonate chemistry operated under biological and biophysical boundary conditions distinct from younger (and older) times (e.g., Grotzinger, 1990; Grotzinger and James, 2000; Ridgwell et al., 2003; Higgins et al., 2009; Krissansen-Totton et al., 2015; Peters et al., 2017; Ison and Planavsky, 2018; Strauss and Tosca, 2020)? How well do we really understand carbonate sedimentation and diagenesis on modern marine platforms (Geyman and Maloof, 2019)?

Not all of these factors were in sharp focus when the decision was made to launch a multi-year investigation of the Otavi/Swakop Group carbonate platform in NW Namibia (Table 3). They did sharpen the motivation to continue the project as the years flew by. The Namibian succession is particularly well exposed in the western half of an 800-km-long fold belt that rims the SW promontory of Congo craton (Figs. 2–4). The platform succession (Otavi Group) has a well-defined aggradational S-facing margin, beyond which is a distally tapered foreslope (Swakop Group) (Fig. 5). Carbonate sedimentation began before 0.76 Ga (late Tonian) and ended with collisional subduction at 0.60 Ga (Figs. 1A, 5 & 6). Both Cryogenian glaciations and/or their respective cap carbonates are recognizable virtually everywhere in both groups (Figs. 5 & 6), providing a first-order basis for correlation (Table 1). Subsidence was driven by N–S crustal stretching followed by thermal contraction and flexure. The rift-to-shelf transition is middle Cryogenian on the platform and late Cryogenian in the foreslope and basin (Fig. 5). The platform–foreslope transition is fully exposed in at least one oblique unbroken cross-section. We see no evidence of a western margin, which we suspect was a transform margin kinematically consistent with N–S stretching as observed. The SW cape of the craton, where the bounding Damara and Kaoko orogens meet (Fig. 3), is exceptionally interesting in its tectono-stratigraphic development, both during Cryogenian continental breakup and middle Ediacaran collisional restructuring (Hoffman, 2021a, b).

A preliminary stratigraphic synthesis of the Otavi/Swakop Group in Kunene Region (Hoffman and Halverson, 2008), the northwesternmost of the country's thirteen political regions, appears in *The Geology of Namibia: Vol. 2* (Miller, 2008b). It was based on results through 2005, the halfway point of the project in terms of its 26 field seasons. The present paper is an expanded update of that work, building on a total of 585 measured sections totalling over 190 km of strata, and 8764 pairs of carbonate $\delta^{13}\text{C}$ and $\delta^{18}\text{O}$ measurements, all of which are tabulated in Supplementary On-line Information (SOI) S1. and S2. A select 25 of the

Table 3
Section number code and field participants in addition to PFH, 1993–2018.

Year	Section #	Field party (partial seasons in <i>italics</i> , professionals <u>underlined</u>)
1993	xx	Paul Hoffman (U. Victoria), Hu Guowei (U. Victoria), Jody Spence (U. Victoria)
1994	5xx	Hu Guowei (U. Victoria), <u>Andrey Bekker</u> , <u>Tony Prave</u> (CCNY), field excursion participants
1995	10xx	Hu Guowei (Harvard U.), <u>Nu Hongjia</u> (Harvard U.), <u>Dawn Sumner</u> (MIT), <u>Tony Prave</u> (CCNY)
1996	15xx	Galen Halverson (U. Montana), Ben Holtzman (Brown U.)
1997	20xx	Galen Halverson, Adam Maloof (Carleton Coll.), Gad Sofer (Harvard U.), <u>Jay Kaufman</u> (U. Maryland), field excursion participants
1998	25xx	Galen Halverson (Harvard U.), Cris Carman (Harvard U.)
1999	30xx	Ryan Ewing (Colorado Coll.), field excursion participants
2000	40xx	John Higgins (Harvard U.), Samantha Evans (South Florida U.), <u>Dan Schrag</u> (Harvard U.)
2001*	45xx	Galen Halverson (Harvard U.), Matt Hurtgen (Penn State U.)
2002*	50xx	Woody Fischer (Harvard U.), James Saenz (U. Mass. Boston.), IAS field excursion participants
2003*	55xx	Gabe Jostrom (Harvard U.), Hugh Daigle (Harvard U.), <u>Eugene Domack</u> (Hamilton Coll.), <u>Ricardo Trindade</u> (U. São Paulo)
2004*	60xx	Francis Macdonald (Harvard U.), David Jones (Harvard U.)
2005	65xx	Jon Husson (Harvard U.), Corey Rennell (Harvard U.), <u>Ricardo Trindade</u> (U. São Paulo), <u>Afonso Nogueira</u> (U. Amazonas), <u>Bernhard Peucker-Ehrenbrink</u> (Woods Hole Inst.)
2006	70xx	Tim Fox (Hamilton Coll.), Mary Beth Day (Hamilton Coll.), <u>Eugene Domack</u> (Hamilton Coll.)
2007	75xx	Clara Blättler (Harvard U.), Sara Pruss (Smith Coll.)
2008	80xx	Karen McKinnon (Harvard U.), Allen Pope (Harvard U.), <u>Eugene Domack</u> (Hamilton Coll.) field excursion participants
2010*	85xx	Tor O'Brien (Harvard U.), Alex Fachler (Camosun Coll.)
2011	90xx	Peter Crockford (U. Victoria), Alex de Moor (Hamilton Coll.), <u>Eugene Domack</u> (Hamilton Coll.)
2012	95xx	Marcus Kunzmann (McGill U.), <u>Justin Strauss</u> (Harvard U.), <u>Thomas McGuire</u> (U. Victoria)
2013	13xx	Blake Hodgin (U. Victoria), Glenn Jasechko (U. Victoria), <u>Pierre Sansjoüre</u> (U. Bretagne Occidentale)
2014	14xx	Eric Bellefroid (McGill U.), Ben Johnson (U. Victoria)
2015	150xx	Malcolm Hodgskiss (McGill U.), <u>Tim Gibson</u> (McGill U.), Aviv Bachan (U. California Berkeley), <u>Kelsey Lamothe</u> (McGill U.), <u>Galen Halverson</u> (McGill U.), <u>Clive Calver</u> (Mineral Res. Tasmania), Carol Dehler (Utah State U.), <u>Susannah Porter</u> (U. California Santa Barbara), Mary Hubbard (Montana St. U.)
2016	16xx	Kelsey Lamothe (McGill U.), Sam LoBianco (Harvard U.)
2017*	17xx	James Busch (Princeton U.), Bolton Howes (Princeton U.), Judy Pu (Harvard U.), Eiel Antilla (Harvard U.), <u>Zhang Shihong</u> (China U. Geosci), Ren Qiang (China U. Geosci)
2018	18xx	Kelsey Lamothe (McGill U.), Wilder Greenman (McGill U.)
2019	19xx	Lyle Nelson (Johns Hopkins U.), Emily Geyman (Princeton U.)

most informative and accessible sections are described as field guides in SOI S3.

The main text is divided in four parts. Part 1. contains: (1.1.) a brief summary of previous work (Figs. 6 & 7); (1.2.) an outline of regional Damaran (Pan-African) tectonics (Figs. 2 & 3) and structure of the Otavi/Swakop Group (Fig. 4); (1.3.) an introduction to the paleogeographic zonation used in the paper (Figs. 5, 6 & 8); (1.4.) an overview of Damara Supergroup (Neoproterozoic) stratigraphy in Kunene Region (Figs. 5, 6 & 9A–C); (1.5.) a preview of the C-isotope record and the numbering scheme used for negative and positive $\delta^{13}\text{C}$ excursions (Fig. 9D); (1.6.) a summary of radiometric age constraints on Otavi/

Swakop Group (Figs. 5, 6, 9 & 10A) and paleomagnetic constraints on paleogeography (Fig. 11); and (1.7.) a description of the classification scheme used for carbonate lithofacies (Table 4), and the graphics symbology (Fig. 12) and abbreviations of formation names (Table 5) used in columnar sections. Methods employed for geological mapping, measuring stratigraphic sections, and analytical procedures for stable-isotope measurements are described in SOI S4.

In Part 2., we describe and interpret Otavi/Swakop Group stratigraphic and lithofacies development in each of 11 transects, numbered Tr1–11 (Fig. 8B). Each transect represents a coherent structural panel in which we have measured multiple columnar sections. The transects'

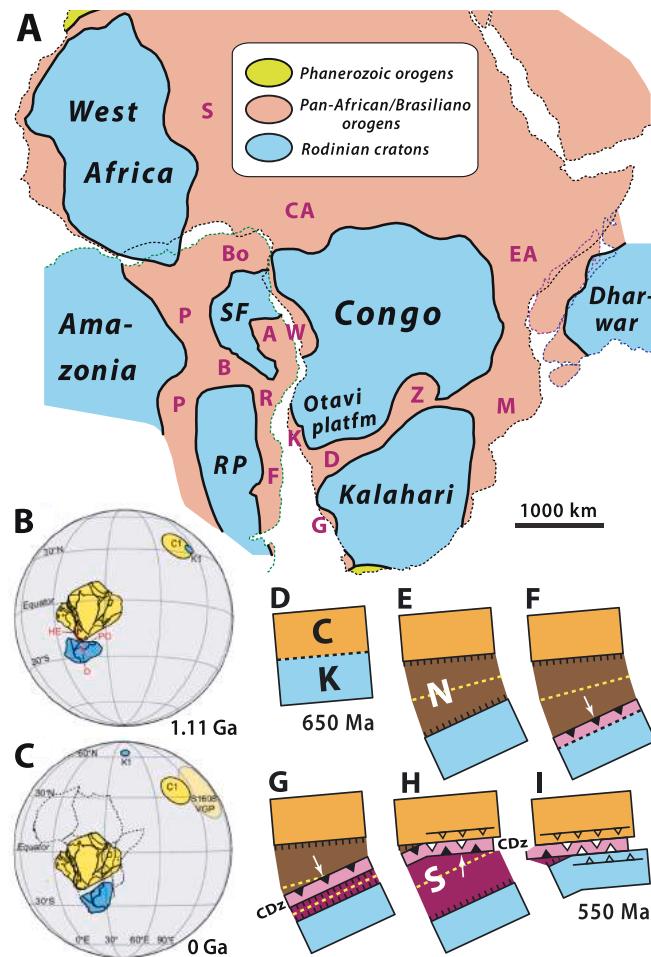


Fig. 2. (A) Tectonic elements of West Gondwana (South America–Africa–Arabia) in a pre-Atlantic, pre-Red Sea reconstruction (modified after de Wit et al. 2008). Rodinian blocks are paleocontinents and microcontinents resulting from breakup of Tonian supercontinent Rodinia and composed of crust consolidated before 1.0 Ga. Abbreviations (cratonic blocks italicized): A, Araçuaí orogen; B, Brasília orogen; Bo, Borborema orogen; CA, Central African orogen; D, Damara orogen; EA, East African orogen; F, Dom Feliciano magmatic arc; G, Gariep orogen; K, Kaoko orogen; M, Mozambique orogen; P, Paraguay orogen; R, Ribeira magmatic arc; RP, Rio Plata craton; SF, São Francisco craton; S, Saharides accretionary orogen (Sengör et al., 2020); W, West Congo orogen; Z, Zambezi orogen, including the Lufilian thrust-fold belt. Pan-African–Brasiliano orogens are Ediacaran–early Cambrian collision and accretion zones related to assembly of Gondwana. Otavi Group carbonate platform covers the SW promontory of Congo craton and its folding resulted from collisions in the bordering Kaoko and Damara orogens. Equivalents of Otavi/Swakop Group are extensively exposed on the margins of Congo craton (e.g., Delpomodor and Préat, 2013; Miller, 2013; Cailteaux and De Putter, 2019) and preserved in subsurface in the central intracratonic Congo Basin (Kadima et al., 2011). (B–C) Restoration of Kalahari craton (blue) at 1.11 Ga (B) relative to Congo craton (yellow) in its present position, based on alignment of Umkondo dyke swarms (red lines) and paleomagnetic poles C1 (Salminen et al., 2018) and K1 (Swanson-Hysell et al., 2015a) from 1.11-Ga dykes in each craton (Salminen et al., 2018). (C) Same paleomagnetic poles with cratons in their present positions. Ernst et al. (2013) give an alternative restoration. (D–I) Hypothesized short-lived (650–550 Ma) Wilson cycle in Damara belt (see text in 1.2.3.) involving two successive seaways corresponding to Northern (N) and Southern (S) zones and transfer of a continental ‘ribbon’ (CDz, Fig. 3) from the Kalahari (K) to Congo (C) margin. Black dotted lines are rifts, yellow dotted lines are spreading ridges, ticks indicate rifted margins; closed barbs indicate subduction zones and open barbs collision zones and thrust margins with barbs on the upper plates. Subduction vectors (white arrows) are orthogonal to trenches. Note subduction initiation in F and subduction-polarity flip in H in response to CDz–Congo collision. CDz–Kalahari collision in I. Damaran cycle is analogous to Mesozoic terrane transfers from Gondwana to Eurasia across Tethys paleocean (e.g., Sengör, 1984; Salminen et al., 2018). Hoffman (2021b) gives a plate model (D–I) with Kaoko and Gariep orogens included.

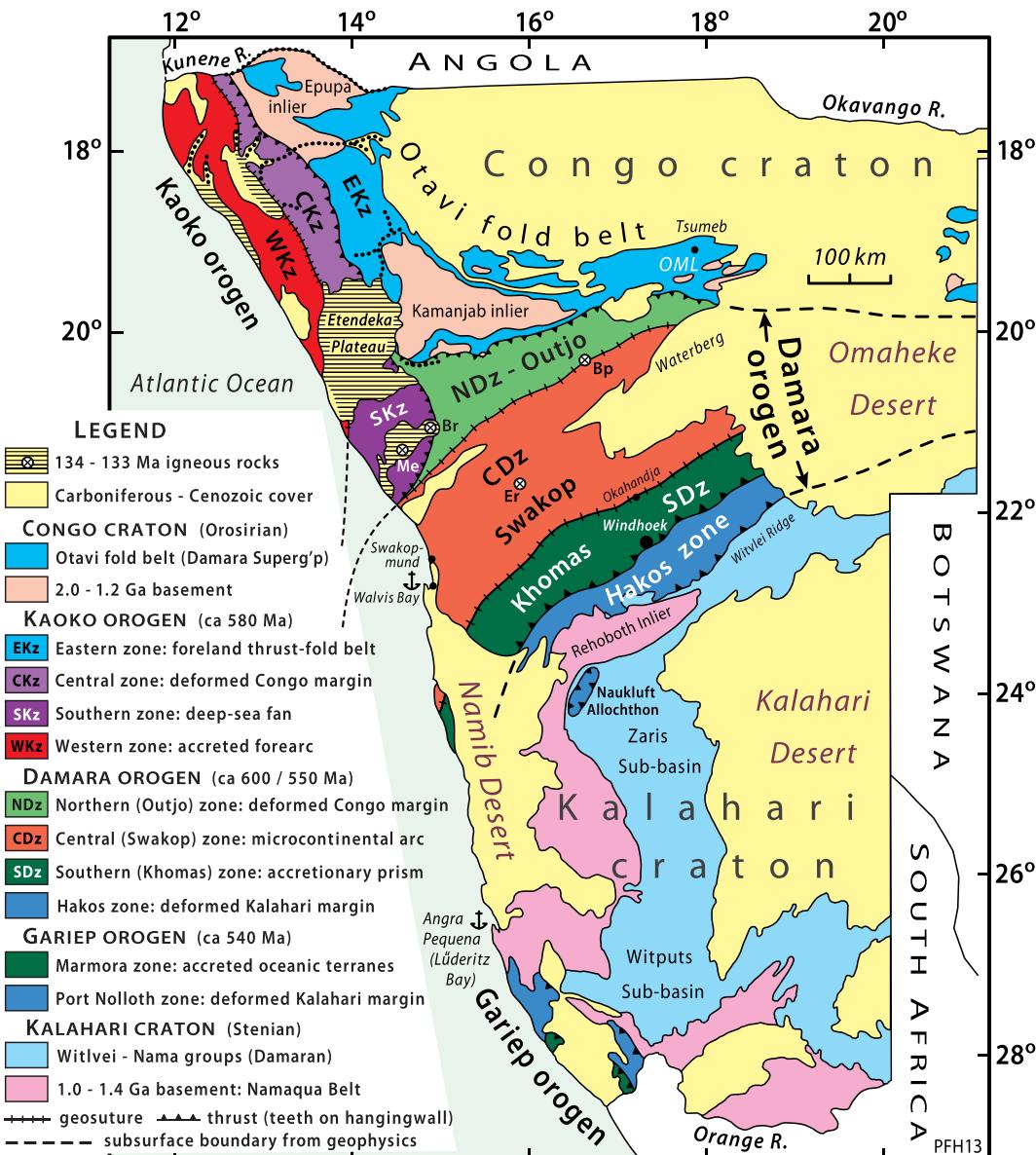


Fig. 3. Tectonic elements map of Namibia (minus Kaprivi strip). Damara orogen (Ediacaran-Cambrian) separates Congo (Orosirian) and Kalahari (Stenian) cratons, which are bordered to the W by Damara-age Kaoko and Gariep orogens, respectively. Damara is a composite orogen, in which CDz (Swakop terrane) collided first with Congo craton to form NDz (Outjo belt) with metamorphic ages ≤ 600 Ma (Lehmann et al., 2015), after which its SSE-facing accretionary prism (SDz or Khomas belt) collided with Kalahari craton at ca 550 Ma (Grotzinger et al., 1995; de Kock et al., 2000; Johnson et al., 2006) to form Hakos zone (Miller, 2008b). Since there is no magmatic arc on either cratonic margin, subduction is inferred to have been S-directed in NDz and N-directed in SDz, implying subduction flip (McKenzie, 1969) following NDz collision. Similarly lacking remnant magmatic arcs, western Congo and Kalahari margins were subducted westward, Congo colliding with WKz (Dom Feliciano) forearc to form CKz having metamorphic ages ≤ 580 Ma (Seth et al., 1998), and Kalahari with Rio Plata craton (Fig. 2) at 540 Ma. EKz is a foreland thrust-fold belt related to CKz collision and involves Damara Supergroup (Fig. 6D). Alternative plate-scale tectonic interpretations are discussed in text 1.6.2–3. SKz is a structurally rootless deep-sea fan of Cryogenian-middle Ediacaran age (Fig. 6A) and uncertain provenance, preserved in a wide belt of W-facing CKz-age folds (Miller, 1983; Swart, 1992a; Passchier et al., 2002; Foster and Goscombe, 2013; Nieminski et al., 2018). Otavi fold belt (Fig. 4) comprises basement-involved (thick-skinned) Damara Supergroup folds of Kaoko and Damara trend that meet at a cusp, aka syntaxis (Hoffman, 2021a).

spatial distribution reflects the first-order folds of the basement surface, manifest by Kamanjab and its satellite basement inliers (Figs. 4 & 8A). The transects range in length from 15 km in Tr2 (38 columnar sections) to 60 km in Tr5 (66 sections). The order in which the transects are described is arbitrary. Otavi/Swakop Group thickens northward from 0.5 km in Tr2 to 3.7 km in Tr11 (Fig. 5). We chose to start in the south (Tr1–5), in the foreslope and basin zones (FSz and Bz, Figs. 5 & 8B), and progress northward (Tr6–11) across the outer and inner platform zones (OPz and IPz, Figs. 5 & 8B). For each transect we provide a geologic map, fence diagram and images of significant sedimentary features. Columnar sections and fence diagrams employ a common legend and colour scheme wherever possible (Fig. 12). In many transects we add detailed maps and

diagrams illustrating key relationships. The text amounts to a field guide to the figures. The orientation of transects Tr7–11 (Fig. 8B), imposed by coast-parallel folds, is fortuitous. Systematic stratigraphic changes occur in the coast-parallel direction (Fig. 5); coast-normal changes are relatively feeble and unsystematic. Each transect contributes an essential brush stroke to the overall picture. For each brush stroke, there was no substitute for multiple, closely-spaced, measured sections. Each could be improved with more sections that might change the overall interpretation. The broad picture is bound to change in future with new transects and improved existing ones.

In Part 3, we integrate the litho- and chemostratigraphic ($\delta^{13}\text{C}$ and $\delta^{18}\text{O}$) records from each formation in turn, progressing from oldest to

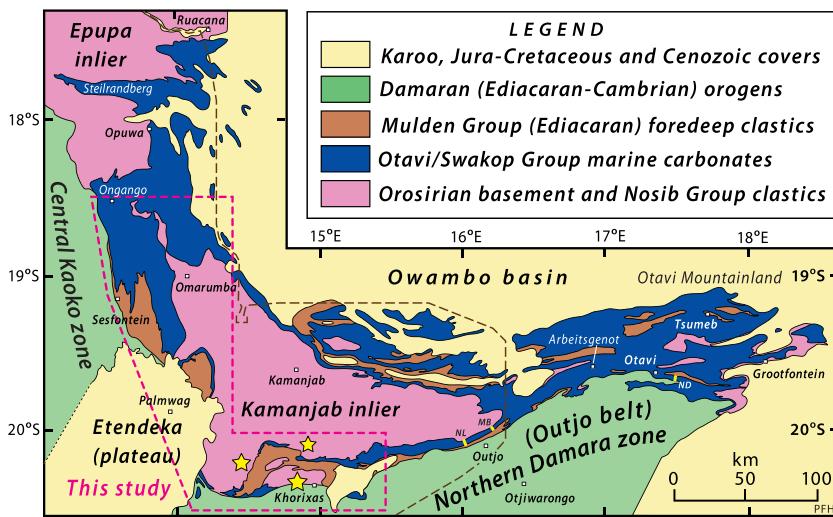


Fig. 4. Otavi fold belt bordering southwestern promontory of Congo craton (Fig. 2) in northern Namibia (Fig. 3) (simplified after Miller and Schalk, 1980). Antiformal inliers expose Orosirian (2.05–1.80 Ga) basement and autochthonous Nosib Group (Fig. 6D & E) clastics. Carbonate-dominated Otavi/Swakop Group (770–600 Ma) was folded, along with the basement surface and synorogenic (Ediacaran) foredeep clastics (Mulden Group), around axial surfaces trending parallel to CKz and NDz. Between Kamanjab and Epupa inliers, Otavi and Mulden groups were thrust ENE and tightly folded above a décollement over Nosib Group before thick-skinned folding. Yellow stars indicate Ediacaran megakarst, where Otavi/Swakop Group was erosionally removed, creating paleovalleys in which foredeep clastics (Mulden Group) directly overlie basement. Dashed magenta line shows limits of this study. Dashed brown line is Kunene Region eastern boundary. Farm names (see text 4.1.2. and 4.1.5.): MB, Mountbatten; ND, Nordland; NL, Neuland.

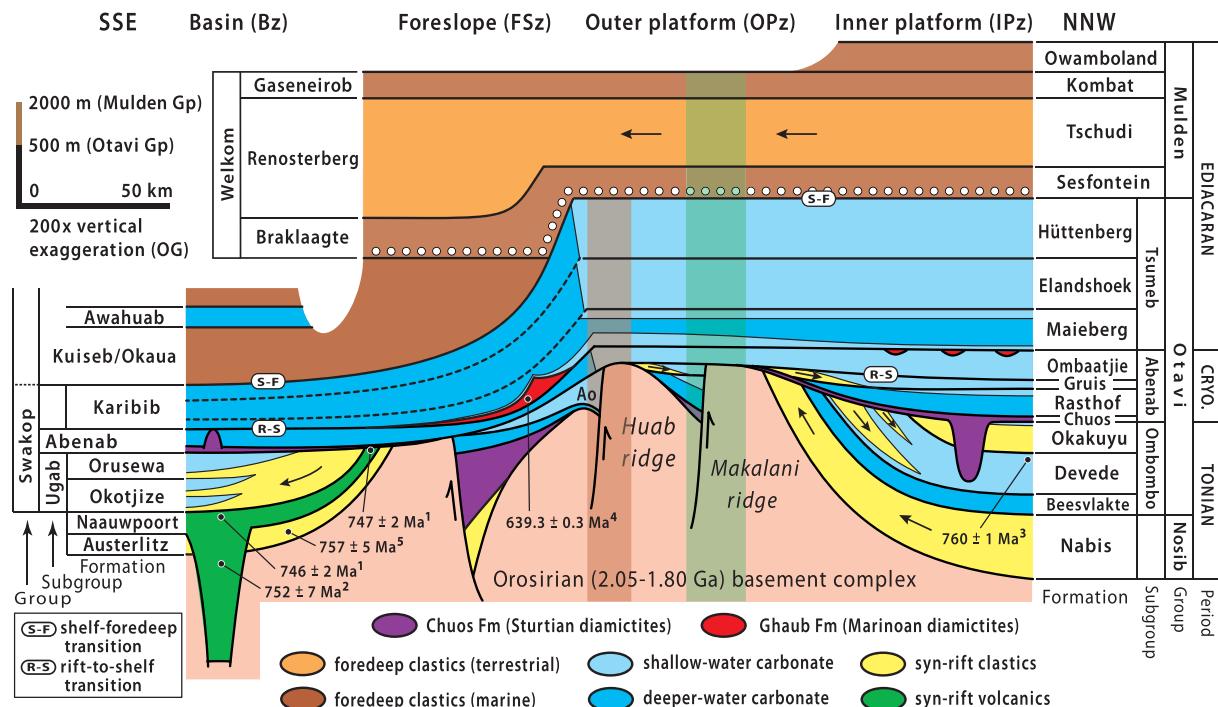


Fig. 5. Composite stratigraphic restoration of the Otavi/Swakop Group in a SSW–NNW cross-section of the study area (Fig. 4): basin and foreslope zones belong to Swakop Group; outer and inner platform zones to Otavi Group. Extreme vertical exaggeration (200×) rotates normal faults toward vertical. Key tectono-stratigraphic horizons: R–S, rift-to-shelf transition; S–F, shelf-to-foredeep transition. Huab and Makalani ridges are interpreted as rift-shoulder uplifts related to south-facing normal faults of Devede through Gruis Fm age. Pale-green screen indicates area hidden by Cretaceous onlap (Etendeka, Fig. 8). Pale-brown screen indicates area where Otavi Group was locally removed by sub-Mulden Group megakarst erosion (Fig. 4). Both areas were paleovalleys localized on buried Huab and Makalani rift-faults. Huab ridge–foreslope transition is fully exposed in transect Tr5 (Fig. 9), where the ridge is bounded basinward by a sharp flexure but no fault. Abbreviations: Ao, Okonguari Fm; OG, Otavi Group. Arrows in clastic units indicate paleocurrent directions from fluvial crossbedding. U–Pb zircon age constrains: ¹ Hoffman et al. (1996); ² de Kock et al. (2000); ³ Halverson et al. (2005); ⁴ Prave et al. (2016); ⁵ Nascimento et al. (2016). According to SACS (South African Committee for Stratigraphy) (1980), Kuiseb Fm belongs in Swakop Group, but δ¹³C data (Halverson et al., 2005; Hoffman and Halverson, 2008) imply that Karibib Fm in Swakop Group is isochronous with Tsumeb Subgroup in Otavi Group. Based on lithologic contrast, we prefer to place Kuiseb Fm outside Swakop Group (Table 5).

youngest (Figs. 6 & 10D). We relate them to the histories of subsidence and sea-level change. We identify rift-to-drift transitions by consilient structural and sedimentological criteria, and document their progression in time from platform to basin. We develop a sequence stratigraphy for the late Cryogenian (Marinoan) post-rift glaciation that includes falling-stand, low-stand, transgressive and high-stand systems tracts. We compare syn-rift Sturtian and post-rift Marinoan glacial deposits (Fig. 5),

finding far greater heterogeneity of eroded source rocks in the former, as expected, but surprisingly little difference in average accumulation rate (Table 6) considering the evident paleotopographic contrast. We document 6 positive and 7 negative CIEs (Fig. 10D), which can be correlated between the platform and the lower foreslope and basin with the aid of the Chuos and Ghaub formations (Fig. 5), representing the two snowball epochs (Table 1). Both positive and negative CIEs tend to be destroyed to

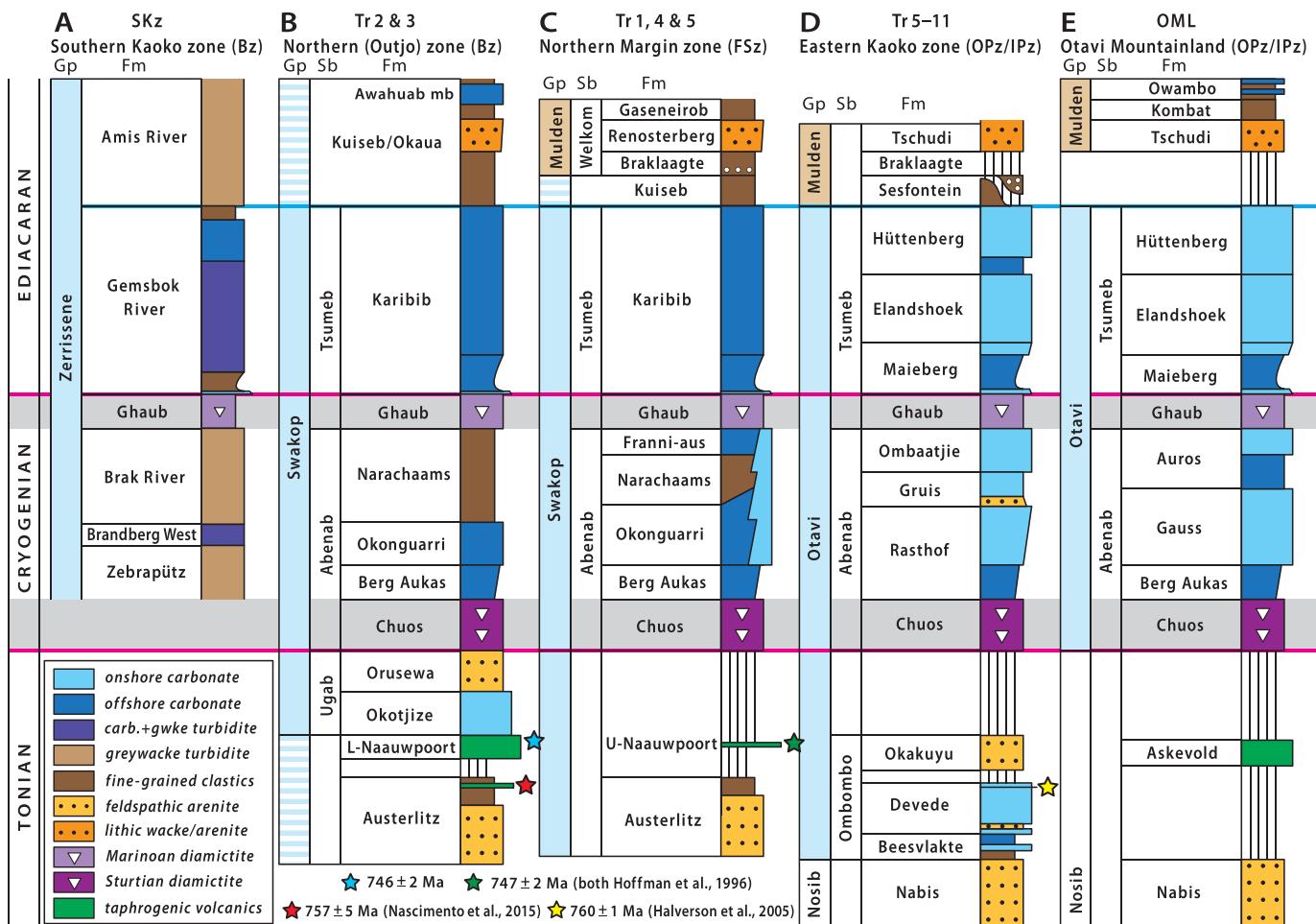


Fig. 6. Damara Supergroup stratigraphic divisions and nomenclature (SACS (South African Committee for Stratigraphy), 1980; Miller, 2008b) by tectonic zone (Fig. 3): (A) Southern Kaoko zone (Bz); (B) Northern Damara zone (Bz); (C) Northern Margin zone (FSz); (D) Eastern Kaoko zone (IPz); (E) Otavi Mountainland (IPz). Magenta correlation lines are base of Sturtian and top of Marinoan glacial deposits (Chaos and Ghaub Fms respectively), defining the Cryogenian Period (Knoll et al., 2006; Shields-Zhou et al., 2015). Grey bands are early and late Cryogenian glacial epochs (Table 1). Blue correlation line marks passive margin-to-foredeep transition, corresponding to arrival of Congo craton at trenches in front of WKZ (Dom Feliciano) and CDz (Swakop) arcs (Fig. 3). Swakop Group is the contiguous off-shelf (Bz and FSz) equivalent of Otavi Group (OPz and IPz), but limits of group (pale blue box) vary between zones. In this paper, we correlate Kuiseb/Okaua Fm in B with lower Mulden Group of C and D. Turbidite-dominated Zerrissene Group in A can be correlated with Otavi/Swakop Group by Marinoan ice-raftered debris (Fig. 210E & F) between Brak River and Germsbok River Fms (Miller, 1983, 2008a; Swart, 1992a), and chemostratigraphically by $\delta^{13}\text{C}$ records in Germsbok River and Karibib Fms (Figs. 189 & S30B) (Hoffman and Lamothe, 2019). Original contiguity of Zerrissene Group with the Congo margin remains an open question (Miller, 1983; Swart, 1992a; Passchier et al., 2002; Nieminski et al., 2018). Kuiseb Fm in C disconformably overlies Karibib Fm and unconformably (?) underlies Braklaagte Fm in Tr1 (Figs. 14 & 15). Austerlitz and Naauwpoort Fms were originally placed in Nosib Group (Hedberg, 1979; SACS (South African Committee for Stratigraphy), 1980), but radiometric ages indicate their correlation with Ombombo Subgroup of Otavi Group (Hoffmann and Prave, 1996).

varying degrees on the upper foreslope, which we attribute to seawater-buffered early diagenesis in that zone, driven by geothermal porewater convection (Higgins et al., 2018; Ahm et al., 2018, 2019; Hoffman and Lamothe, 2019; Bold et al., 2020). Ironically, these findings imply that thoroughly-altered dolomites in the upper FSz are a more reliable geochemical proxy for open-basin thermocline waters, while shallow bank-top records preserved through sediment-buffered early diagenesis are more useful for chemostratigraphic correlation. In 3.5., we briefly discuss the destruction of the carbonate platform and stratigraphic relations between Otavi/Swakop Group and overlying foredeep (aka foreland basin) clastics of Kuiseb Fm and Mulden Group (Figs. 5, 6 & 8). 3.6. is a synthesis of basin development, 3.7. a synthesis of C-isotope variability and comparison with coeval global $\delta^{13}\text{C}_{\text{carb}}$ records (Figs. 1A & 10D), and 3.8. a review of other proxy data (S, B, Ca, Mg, Sr, Zn, Cr, Os, He, N and Fe isotopes) published from the Otavi/Swakop Group.

In Part 4., we integrate the history of carbonate platform development with that of glacial erosion and rock mass redistribution, and conclude with eleven specific recommendations for future studies.

Much work remains. We made only brief forays in the Otavi/Swakop

Group N of 18.5°S and E of 16°E (Fig. 4). In the N, the Steilrand Mountains (Hedberg, 1979) offer a 100-km-long E-W structural transect in which the orientation of depositional trends is virtually unknown. In the E, the Otavi Valley syncline (Hedberg, 1979), east of Otavi town (Fig. 4), offers a possible second transect of the platform-foreslope transition after Transfontein Ridge (Tr5). We make no claim as to providing detailed sedimentological descriptions or interpretations, although we mention and illustrate what we consider to be significant sedimentological features where they occur. What we strove for is stratigraphic context—let the sedimentology begin.

Field work in Namibia benefits from a well-developed safari-tourism industry, well-maintained roads, well-stocked grocery stores, modest living and transportation costs, and political stability as a multi-racial, pan-tribal, representative democracy. It is a safe and friendly environment of relatively undisturbed natural beauty (Mendelsohn et al., 2002). High-quality 1:50 K topographic maps, satellite imagery and aerial photographs are available, as are geological maps, field guides and reports, a national geological library, and a professional geological community. As Ben Mapane, a professor of geology at the University of

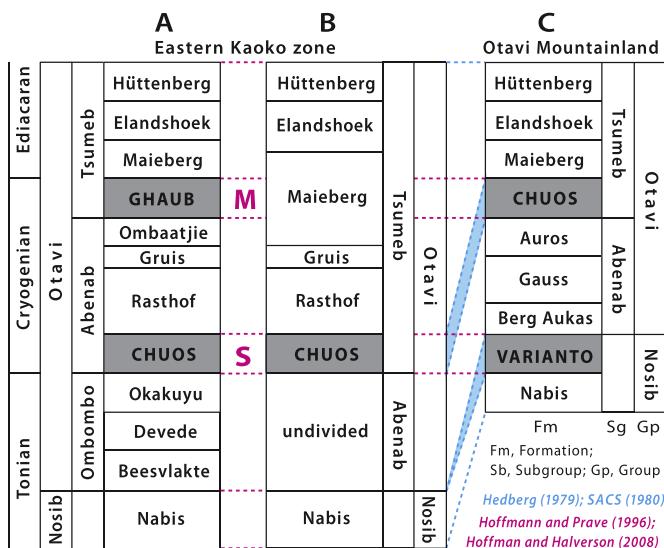


Fig. 7. Comparison of stratigraphic nomenclature for Otavi Group in Eastern Kaoko zone according to: (A) Hoffmann and Prave, 1996; Hoffman and Halverson, 2008; this study; (B) Hedberg, 1979; SACS (South African Committee for Stratigraphy), 1980; Miller, 1997; and correlations with Otavi Mountainland (C) according to A (blue) and B (magenta). Only one glaciation was recognized in B, with the result that basal Tsumeb Subgroup diamictite in OML (Le Roex, 1941) was correlated with Chuos Fm in EKz and neither Varioanto nor Ghaub Fms were recognized as glaciogenic (viz., Frets, 1969; Martin et al., 1985; Eyles and Januszczak, 2007; Nascimento et al., 2018). In B, Tonian strata (Ombombo Subgroup) in EKz were correlated with Cryogenian strata (Abenab Subgroup) in OML. Recognition of distinct Sturtian (S) and Marinoan (M) glaciations (Hoffmann and Prave, 1996) led to the new correlations (magenta). Revised definition of Maieberg Fm in A is closer to that in its type area in C (on Maieberg 790 farm, SACS (South African Committee for Stratigraphy), 1980). As defined in B, Maieberg Fm straddles the Marinoan glaciation (M) and its associated disconformity (Figs. 43, 164 & 206).

Namibia jokingly remarked, “*Namibia is Africa for beginners.*”

We dedicate this paper to Dick C. Frets, Pietro Guj, Ronald M. Hedberg, Roy McG. Miller and Hubertus R. Porada, whose accurate and insightful geological maps, produced in the 1960s and 1970s as partial fulfillment of doctoral thesis requirements, were indispensable to our project.

1.1. Previous and concurrent studies

1.1.1. Otavi Mountainland

The Otavi Group (formerly Otavi Series, see SACS (South African Committee for Stratigraphy), 1980, for historical review) was first studied in the Otavi Mountainland (OML) of north-central Namibia (Figs. 3, 4 & 6E), where carbonate-hosted Cu-Pb-Zn-Ag-V deposits were mined for Cu in pre-colonial times. The ore body at Tsumeb (Söhnge, 1964, 1967; Lombaard et al., 1986; Kamona and Günzel, 2007) was in production for most of the 20th Century (1906–33, 1937–40, 1948–96), peaking in the mid-1960s. Mineral specimens from the supergene enriched zone at Tsumeb grace museums and private collections around the world (Wilson, 1977; Cairncross, 1997).

The Otavi Group of the OML is divided into Abenab and Tsumeb subgroups (Fig. 6E), and seven lithostratigraphic formations (Martin, 1965; Hedberg, 1979; SACS (South African Committee for Stratigraphy), 1980), based on surveys to meet the needs of mineral exploration (Schneiderhöhn, 1920, 1929; Smit, 1962; Söhnge, 1957, 1964; Krüger, 1969; Lombaard et al., 1986; Hegenberger, 1987; King, 1994).

A discontinuous band of ‘tillite,’ up to ~200 m thick, was first described (Le Roex, 1941) within the Otavi Group around the east-plunging closure of Sargberg syncline (Hedberg, 1979), 30 km south of

Tsumeb. This ‘Otavi tillite’ was correlated by Hedberg (1979) with the Chuos Tillite (Gevers, 1931) in Central Damara zone (CDz, Fig. 3), but it was later renamed Ghaub Fm and correlated with the global Marinoan glaciation (Hoffmann and Prave, 1996; Prave et al., 2016). The Ghaub Fm and its distinctive cap-carbonate sequence, Maieberg Fm, were recently restudied in their type area (Bechstädt et al., 2009, 2018).

An older diamictite, the Varioanto Fm (SACS (South African Committee for Stratigraphy), 1980), occurs locally in the OML between conglomeratic sandstone of the Nabis Fm (Nosib Group) and the basal unit of the Otavi Group, Berg Aukas Fm (Söhnge, 1957; Hedberg, 1979). This older diamictite was eventually correlated with Chuos Fm (Kaufman et al., 1991; Hoffmann, 1994), which is affiliated with the global Sturtian glaciation (Hoffmann and Prave, 1996). A glaciomarine origin for Varioanto/Chuos diamictite as proposed by Martin (1965) is supported by recent sedimentological studies in OML (Le Heron et al., 2013b).

C- and O-isotope values were obtained prior to our study from a total of 40 drillcore samples from around Tsumeb as part of a pilot study of stable isotopes in Neoproterozoic carbonate successions throughout Namibia (Kaufman et al., 1991). The $\delta^{13}\text{C}_{\text{carb}}$ record inferred from this small sample set exhibits oscillations that range between -5% and $+10\%$ PDB (PeeDee Belemnite standard). It broadly anticipated our findings. Drillcores from the Tsumeb area were recently used to study the petrography and C-S stable-isotope chemostratigraphy of Hüttenberg Fm (Delpomdor et al., 2018; Cui et al., 2018), the youngest unit in the Otavi Group and host to the youngest high-amplitude positive $\delta^{13}\text{C}$ excursion of the Neoproterozoic Eon (Fig. 1A).

1.1.2. Kunene Region

In the more remote Eastern Kaoko zone (EKz, Fig. 3), glacial deposits were recognized in Otavi Group and mapped after World War II because of their association with low-grade iron-formation (Martin, 1964, 1965). These glacial deposits were also correlated, correctly as it turned out, with Chuos Fm of Central Damara zone (Gevers, 1931). Much of the Otavi/Swakop Group was systematically mapped in a series of PhD thesis projects overseen by the University of Cape Town’s Precambrian Research Unit (Frets, 1969; Guj, 1970, 1974; Miller, 1974, 1980; Porada, 1974, Hedberg, 1979). The last named provides 1:250,000-scale maps (6 sheets) and a stratigraphic synthesis of Otavi Group as a whole (Hedberg, 1979). The northern plunge of Kamanjab inlier (Fig. 3) was mapped by Killick et al. (1980) and the central segment of Northern (Outjo) zone was mapped by Clifford (2008). Otavi Group was incorporated somewhat marginally in regional tectonostratigraphic syntheses by Porada (1979, 1989), Porada et al. (1983), Coward (1983), Martin (1983), Miller (1983, 1997), Hoffmann (1989), Henry et al. (1990) and Stanstreet (1991).

When our project began, there was still some question regarding the glacial origin of the ‘tilloids’ or ‘mixtites’ of the Otavi Group and close correlatives (Schermerhorn, 1974, 1975, 1976; Martin et al., 1985), and they were generally considered to occupy a single horizon (e.g., Hedberg, 1979; SACS (South African Committee for Stratigraphy), 1980; Miller, 1997). It soon became apparent, independent of our findings, that there are in fact two discrete glacial horizons (Kaufman et al., 1991; Hoffmann, 1994; Hoffmann and Prave, 1996; Hoffman et al., 1998a) within the Otavi Group, with the result that carbonate strata (Ugab and Ombombo subgroups) stratigraphically beneath the Sturtian Chuos Fm in the west are Tonian in age and not correlative with the Cryogenian Abenab Subgroup in the east (Hoffmann and Prave, 1996; Hoffman et al., 1998a; Hoffman and Halverson, 2008). Before the recognition of two discrete glaciations in the Otavi Group, stratigraphic correlations between the Eastern Kaoko zone and Otavi Mountainland were hopelessly confused (Fig. 7B & C).

Concurrent with our work, independent and semi-independent topical studies in the western Otavi Group have appeared with increasing frequency. They have targeted the Tonian Ombombo and Ugab subgroups (Hood et al., 2015; Lamothe et al., 2019), the Sturtian

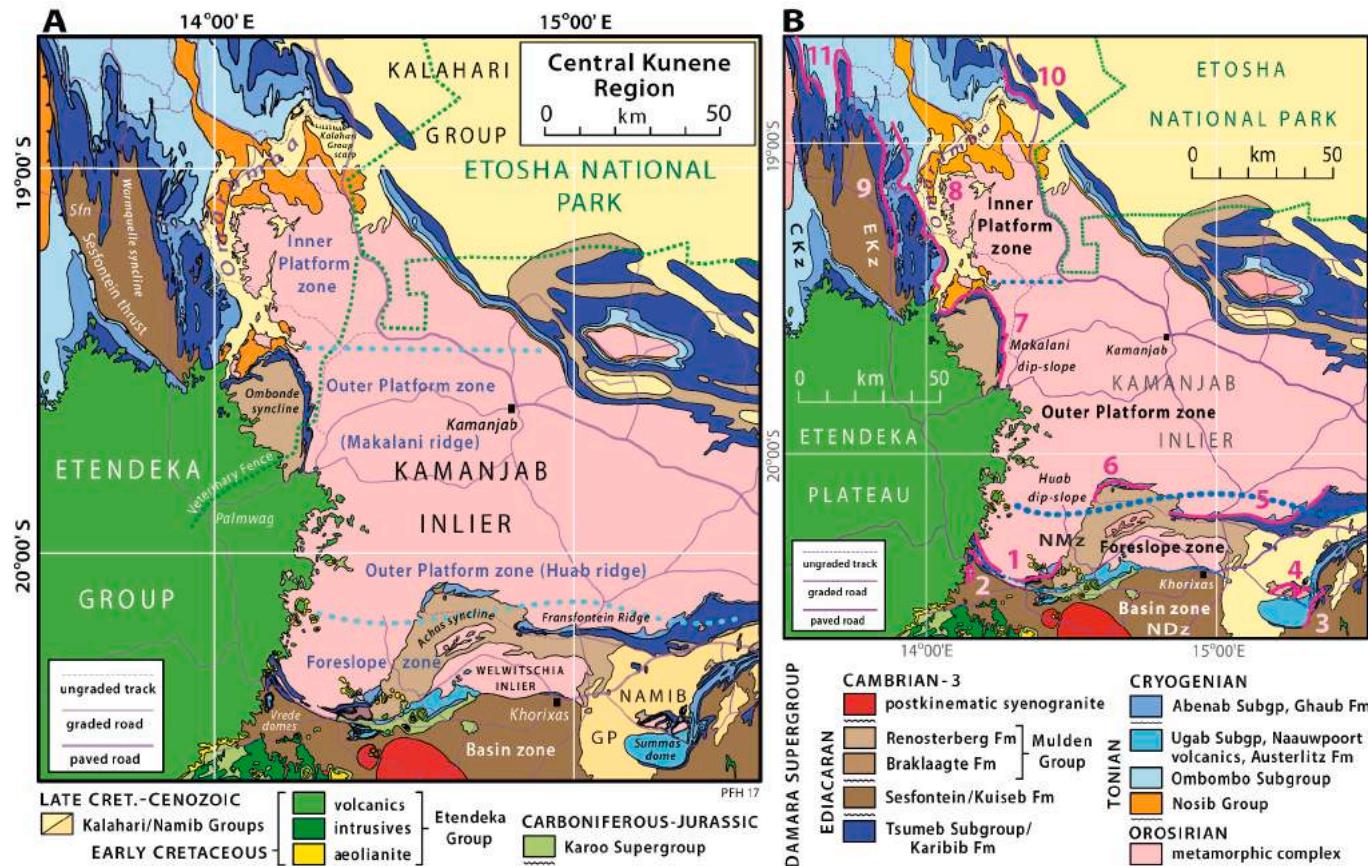


Fig. 8. (A) Simplified geological map of the western environs of Kamanjab inlier (Fig. 4), based on maps of Frets (1969), Guj (1970), Porada (1974), Hedberg (1979), Killick et al. (1980), Miller (1980a), Miller and Schalk (1980), Miller and Grote (1988), Schreiber (2006), and Clifford (2008). Otavi/Swakop Group is best exposed in this area because of low rainfall (14–28 cm average annual precipitation, decreasing toward WSW) and dissection on Southern African Coastal Escarpment. Outcrop of Otavi/Swakop Group is structurally controlled by long-wavelength basement-involved folds associated with Kamanjab inlier, and flat-lying cover of Karoo Supergroup (Carboniferous–Jurassic), Etendeka Group (Early Cretaceous), Kalahari Group (Late Cretaceous–Cenozoic) and Namib Group (Neogene, in lower right). Platform zonation indicated by aqua dots and blue lettering. (B) Same map showing locations of transects Tr1–11 investigated in this study. Basin zone (Bz) is encountered in Tr2 and 3; foreslope zone (FSz) in Tr1, 4 and part of 5; outer platform zone (OPz) in Tr5–7; and inner platform zone in Tr8–11. Otavi Group was not investigated NE of Kamanjab inlier, where recessive intervals critical for sequence stratigraphic interpretation are generally masked by calcrete. Stratigraphic fence diagrams for each transect: (Tr1) Figs. 14, 18, 22 & 27; (Tr2) Figs. 28, 30 & 32; (Tr3) Figs. 39, 40 & 152; (Tr4) Fig. 41; (Tr5) Figs. 43, 45, 46, 58, 62, 65 & 68; (Tr6) Figs. 71, 76 & 85; (Tr7) Fig. 88; (Tr8) Figs. 99, 103, 105 & 107; (Tr9) Figs. 123, 125 & 129; (Tr10) Fig. 135; (Tr11) Figs. 139, 140, 143, 144 & 145. Stratigraphic comparison of Tr10 and 11 (Figs. 196, 197, 144 & 145) supports the overall finding that N–S (or Damara-normal) stratigraphic and facies changes dominate in Otavi/Swakop Group over W–E (Kaoko-normal) changes.

Chuos Fm (McGee et al., 2012; Busfield and Le Heron, 2013, 2018; Le Heron et al., 2013a) and associated iron formation (Lechte and Wallace, 2016, Lechte et al., 2018, 2019), the Rasthof Fm cap-carbonate sequence (Yoshioka et al., 2003; Katsuta et al., 2007; Tojo et al., 2007; Pruss et al., 2010; Le Ber et al., 2013; Wallace et al., 2014; Le Heron et al., 2020) and its protistan microbiota (Bosak et al., 2011; Dalton et al., 2013; Moore et al., 2017), and the Marinoan Ghaub Fm (Condon et al., 2002; Eyles and Januszczak, 2007; Domack and Hoffman, 2011; Prave et al., 2016; Busfield and Le Heron, 2018). Millimeter-scale fossils described as ‘sponge-like’ were reported from pre-Sturtian and pre-Marinoan parts of the Otavi Group (Brain et al., 2012), but might alternatively represent macroalgal ‘warty sheets’ (Cohen et al., 2020). Chemostratigraphic studies have included carbonate-associated sulfate (CAS) S-isotopes (Hurgen et al., 2002, 2006), B-isotopes (Kasemann et al., 2005, 2010), Mg-isotopes (Kasemann et al., 2014; Ahm et al., 2019), Ca-isotopes (Kasemann et al., 2005, 2014; Ahm et al., 2019), Cr-isotopes (Rodler et al., 2016, 2017), Fe isotopes (Lechte et al., 2019), and U-isotopes (Hood et al., 2015). We review these studies in section 3.8.

Prave (1996) offered an unconventional tectono-stratigraphic interpretation of the western Otavi Group, while Maloof (2000) and Nascimento et al. (2016) arrived at different conclusions regarding Otavi Group stratigraphy and structure in the west of the Northern Damara

Zone (NDz). Detrital zircon age spectra have been obtained from Damaran (Neoproterozoic–Cambrian) units in NDz and Kaoko orogen (Foster et al., 2015; Konopásek et al., 2014, 2017; Nascimento et al., 2017; Nieminski et al., 2018), and their stratigraphic and tectonic significance has been discussed (Hoffman and Halverson, 2018; Nascimento et al., 2018).

The Geology of Namibia in 3 volumes (Miller, 2008a–c) is a monumental synthesis totalling 1533 authoritative pages and 980 colour figures. Neoproterozoic–Cambrian (Damaran) geology is described in Volume 2. The same author examined litho- and tectono-stratigraphic parallels between the Damara Supergroup in Namibia and the broadly coeval Katanga Supergroup of southern Congo and Zambia (Miller, 2013).

1.2. Regional tectonic setting and structure

Namibia is underlain by two pre-Tonian cratons, Congo and Kalahari (Fig. 2). They are separated by the 0.60–0.50-Ga Damara orogen striking normal to the Atlantic coast (Miller, 1983, 2008b). Along the coast, Congo craton is bordered by the 0.59–0.55-Ga Kaoko orogen and Kalahari craton by the 0.54–0.50-Ga Gariep orogen. Kaoko and Gariep orogens are sinistral-oblique collision zones involving the Ribeira and

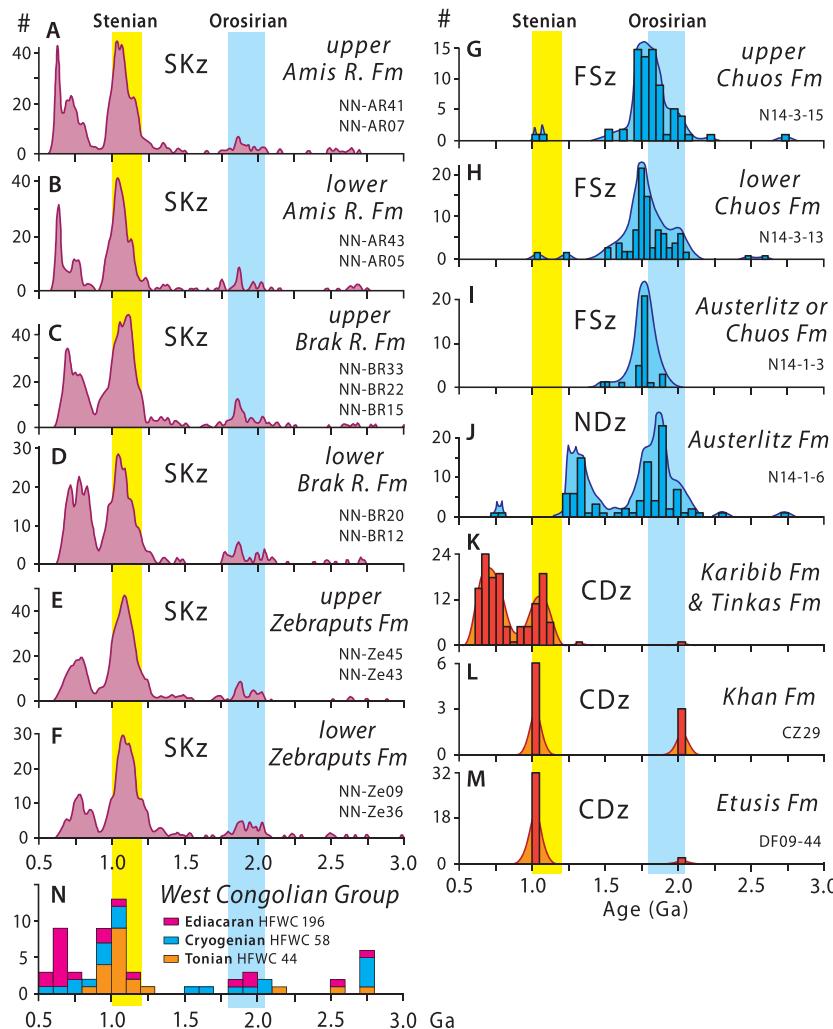


Fig. 9. Probability density plots of detrital U-Pb zircon age distributions for Damaran terrigenous formations in SKz/Zerriessene deep-sea fan (A–F) (Nieminski et al., 2018), Congo craton-derived formations in FSz (G–I) and NDz/Outjo belt (J) (Nascimento et al., 2018), CDz/Swakop terrane (K–M) (Foster et al., 2015), and (N) equatorial West Congo belt (Frimmel et al., 2006). Depositional ages: A–B, middle Ediacaran; C, middle or late Cryogenian; D–F, middle Cryogenian; G–H, early Cryogenian; I, late Tonian or early Cryogenian; J, late Tonian; K, middle Cryogenian and early Ediacaran; L–M, late Tonian. Synorogenic (middle Ediacaran) formations from Congo craton (Kuiseb Fm and Mulden Group) are not shown since their sources were not limited to Congo craton. Stenian (1.0–1.2 Ga) age mode distinguishes SKz and CDz formations from those derived from SW Congo craton (G–J), but dominates Congo craton-derived late Tonian (upper Sansikwa Subgroup) and middle Cryogenian (Haut Shiloango Subgroup) detritus (N) in equatorial West Congo belt (Frimmel et al., 2006; Affaton et al., 2016).

Dom Feliciano composite magmatic arcs of South America (Fig. 2A), which had earlier been accreted to the São Francisco and Rio de la Plata cratons, respectively (de Wit et al., 2008; Siegesmund et al., 2018).

The Otavi Group (Hedberg, 1979; Hoffmann and Prave, 1996; Miller, 2008b) belongs with the folded Neoproterozoic cover (Damara Supergroup) of the SW promontory of Congo craton (Fig. 2A). As a carbonate platform, the Otavi Group is connected to a distally-tapered foreslope wedge, named Swakop Group (Fig. 5), along the southern margin of Congo craton and the adjacent Northern or Outjo zone of Damara orogen (Figs. 3, 8A & B). Swakop Group also occurs in the Central Kaoko zone (CKz, Fig. 3) (Guj, 1970; Henry et al., 1992/93; Stanistreet and Charlsworth, 1999), but a lateral transition with the Otavi Group of Eastern Kaoko zone has yet to be demonstrated. If the western margin of Congo craton originated as a transform margin (Hoffman, 2021b), Swakop Group in Central Damara zone should represent deformed rhombochasm (Carey, 1958), imprecisely termed ‘pull-apart’ basins in North America.

Thick-skinned (i.e., basement-involved) folds involving Damara Supergroup trend parallel to Damara and Kaoko orogens. Structural culminations of which Kamanjab basement inlier is the largest (Figs. 3 & 4) manifest local constructive interference folding and proximity to the Kaoko–Damara syntaxis or cusp (Goscombe et al., 2017; Hoffman, 2021a). In the Eastern Kaoko zone (EKz, Fig. 3), thick-skinned folding was preceded by eastward-directed thin-skinned thrusting and short-wavelength (≤ 4 km) folding, related to collision at ~ 0.59 Ga of the western Congo margin with the Ribeira–Dom Feliciano magmatic arcs and their cratonic backstops (Goscombe et al., 2003a, 2005, 2018;

Goscombe and Gray, 2007). The geosuture is inferred to lie between the Central and Western Kaoko zones (Fig. 3) (Will et al., 2004; Goscombe and Gray, 2007; Konopásek et al., 2005, 2016). Recently, it has been suggested that no Neoproterozoic oceanic lithosphere ever existed between São Francisco and Congo cratons (Konopásek et al., 2020; Percival et al., 2021). This model provides no physical mechanism (e.g., subduction) for the orogenic transpression observed in Kaoko orogen (Goscombe & Gray, 2008; Jung et al., 2014a).

1.2.1. Congo craton

In Namibia, crystalline basement of Congo craton is exposed in Kamanjab, Epupa and smaller inliers within the Otavi belt (Fig. 4). The inliers are oblate antiformal structures and their existence shows that basement temperatures reached the field of quartz dislocation creep, consistent with pervasive greenschist-grade retrograde metamorphism of basement rocks and prograde metamorphism of Neoproterozoic cover.

Where exposed, the basement is a compositionally heterogeneous complex of ortho- and paragneisses of mainly Orosirian (2.05–1.80 Ga) age (Tegtmeyer and Kröner, 1985; Miller, 2008a; Kröner et al., 2010, 2015). The northern Kamanjab inlier includes a tightly infolded succession of intermediate and felsic metavolcanics, clastic metasediments, iron formation and marble named Khoabendus Group (Porada, 1974), which is broadly coeval with older phases of the gneissic complex (Miller, 2008a). Eastern Epupa inlier hosts the southern end of a 400-km-long Ectasian (1.40–1.20 Ga) intrusive complex composed of anorthosite, layered gabbro and anorogenic granitoid rocks (Ashwal and

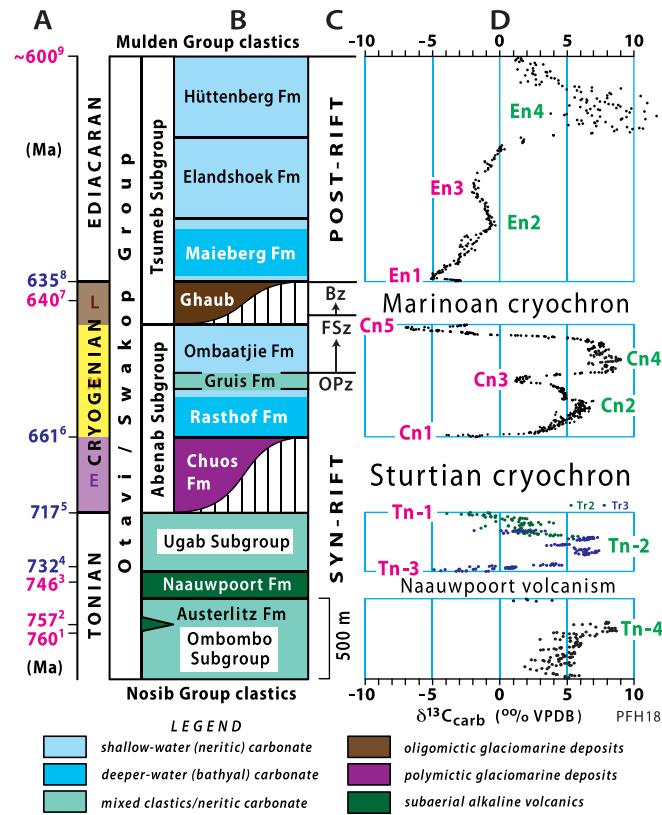


Fig. 10. Unscaled radiometric age constraints (A) for Otavi/Swakop Group stratigraphy (B), tectonostratigraphic transitions (C), and $\delta^{13}\text{C}$ records (D). Ages coloured magenta were obtained from Otavi/Swakop Group directly; those coloured blue were obtained elsewhere for events recognized in Otavi/Swakop Group. Age sources: 760 ± 1 Ma (Halverson et al., 2005), zircon U–Pb ID-TIMS age from tuff in upper Devede Fm (Ombombo Subgroup); 757 ± 5 Ma (Nascimento et al., 2016), zircon SHRIMP ion probe age from crystal-rich ash-flow tuff in Austerlitz Fm (Tr1); 746 ± 2 Ma (Hoffman et al., 1996) zircon U–Pb ID-TIMS age from crystal-rich ash-flow tuff in upper part of Lower Naauwpoort Fm (Miller, 1980) in Tr3; 732.2 ± 4.7 Ma (Rooney et al., 2014) Re–Os isochron age from organic-lean carbonate in Coppercap Fm (Coates Lake Group, Windermere Supergroup, NW Canada), recording recovery from Tn-3 (Russøya CIE, Fig. 1); 717.4 ± 0.2 and 716.9 ± 0.4 Ma (Macdonald et al., 2010a, 2018), zircon U–Pb CA-ID-TIMS ages from rhyolite lava (uppermost Mount Harper Group) and tuffaceous diamictite (basal Eagle Creek Fm, Rapitan Group), respectively, at low paleolatitude in NW Canada; 700 Ma Sturtian glacial onset between 717.4 ± 0.2 and 716.9 ± 0.4 Ma (Macdonald et al., 2010a, 2018), zircon U–Pb CA-ID-TIMS age of tuff in lowermost postglacial Datangpo Fm in SE Guizhou, plus consilient U–Pb and Re–Os ages from postglacial cap carbonates and underlying deglacial deposits in Mongolia, NW Canada, South Australia and other areas of South China; 639.3 ± 0.3 Ma (Prave et al., 2016) zircon U–Pb CA-ID-TIMS age for tuff in middle Ghaub Fm of Tr5 (section 5–8, Figs. 43 & 58); 635.5 – 635.0 Ma, constrained by consilient zircon U–Pb ID-TIMS and CA-ID-TIMS ages from tuffs in postglacial cap dolomites and underlying deglacial deposits in CdZ (Hoffmann et al., 2004), South China (Condon et al., 2005; Zhou et al., 2019) and Tasmania (Calver et al., 2013); 580 – 550 Ma $^{39}\text{Ar}/^{40}\text{Ar}$ age spectra for metamorphic micas associated with D1 deformation in NDz (Lehmann et al., 2015), and 580 – 550 Ma U–Pb (zircon and monazite) and Sm–Nd (garnet) ages for early synkinematic metamorphism and anatexis in CKz (Seth et al., 1998; Goscombe et al., 2005). Syn- to post-rift (right-to-shelf) transition in C is diachronous, younging basinward in late Cryogenian time. C-isotope excursions (CIEs) are numbered by Period with negative excursions (odd numbers) in magenta and positive ones (even numbers) in green. Tonian CIEs have negative numbers ordered from top downward. Cryogenian and Ediacaran CIEs are numbered positively from base upward. Numbered CIEs provisionally correlate with informally named CIEs (Fig. 1): Tn-4, Draken; Tn-3, Russøya; Tn-2, Coppercap; Tn-1, Garvellach; Cn1, Twitya; Cn2, Gauss; Cn3, Taishir; Cn4, Keele; Cn5, Trezona; En1, Maieberg; En4, Hüttenberg. $\delta^{13}\text{C}$ records (this study): Ombombo Subgroup from Tr8 (section 8–9, Fig. 148); Ugab Subgroup from Tr2 and 3 (green and blue dots, respectively) (Fig. 153); Abenab Subgroup from Tr9 (9–3, Fig. 133); Tsumeb Subgroup from Tr10 (10–1 and OML, Fig. 185). Cryogenian Period is divided informally in this paper into early (purple), middle (yellow) and late (brown) epochs with boundaries at 661 Ma (end-Sturtian, Rooney et al., 2020a) and 646 ± 5 Ma (Marinoan onset, Kendall et al., 2006; Prave et al., 2016; Bao et al., 2018).

Twist, 1994; Mayer et al., 2004; Drüppel et al., 2007; McCourt et al., 2013; Maier et al., 2013; Kröner and Rojas-Agramonte, 2017; Lehmann et al., 2020).

The basement of Epupa inlier in Namibia and SW Angola is cut by N–NNW-trending gabbro-norite dykes that are indistinguishable in age, 1110 ± 3 Ma (Ernst et al., 2013), from the NW/SE Umkondo swarm of Kalahari craton (de Kock et al., 2014; Swanson-Hysell et al., 2015b). The respective dyke-swarm azimuths and paleomagnetic poles can be reconciled if the cratons were in mutual contact but Kalahari was rotated $\sim 45^\circ$ clockwise wrt Congo, and the centre of its buried NW margin was moved out to the SW tip, or cape of Congo craton (Fig. 2B) (Salminen et al., 2018). An alternative less conservative anticlockwise rotation was also proposed (Ernst et al., 2013). Neither model requires that the cratons remained together during the Neoproterozoic Rodinia-to-Gondwana transformation (Fig. 2D–I). Like Arabia, India, Southeast

Asia and Australia over the Tethyan cycle, they could have been reunited after separate travels in a new neighbourhood (Swanson-Hysell et al., 2015b; Salminen et al., 2018).

As exposed in the Otavi belt (Fig. 4), the Neoproterozoic Damara Supergroup consists of three broadly conformable groups (Figs. 5 & 6). The carbonate-dominated Otavi/Swakop Group is underlain by the terrestrial siliciclastic Nosib Group and overlain by the marine and terrestrial synorogenic clastics of Mulden Group. Otavi/Swakop Group and its Sturtian and Marinoan glacial deposits have correlatives in distant parts of Congo craton (Cahen, 1963; Trompette, 1994). These include the 1000-km-long West Congo foreland belt (Cahen, 1950, 1978; Schermerhorn, 1961; Schermerhorn and Stanton, 1963; Stanton et al., 1963; Kröner and Correia, 1973; Cahen and Lerpersonne, 1981; Trompette, 1994; Frimmel et al., 2006; Tait et al., 2011; Delpomdor and Préat, 2013; Mickala et al., 2014; Ackouala Mfere et al., 2020), a

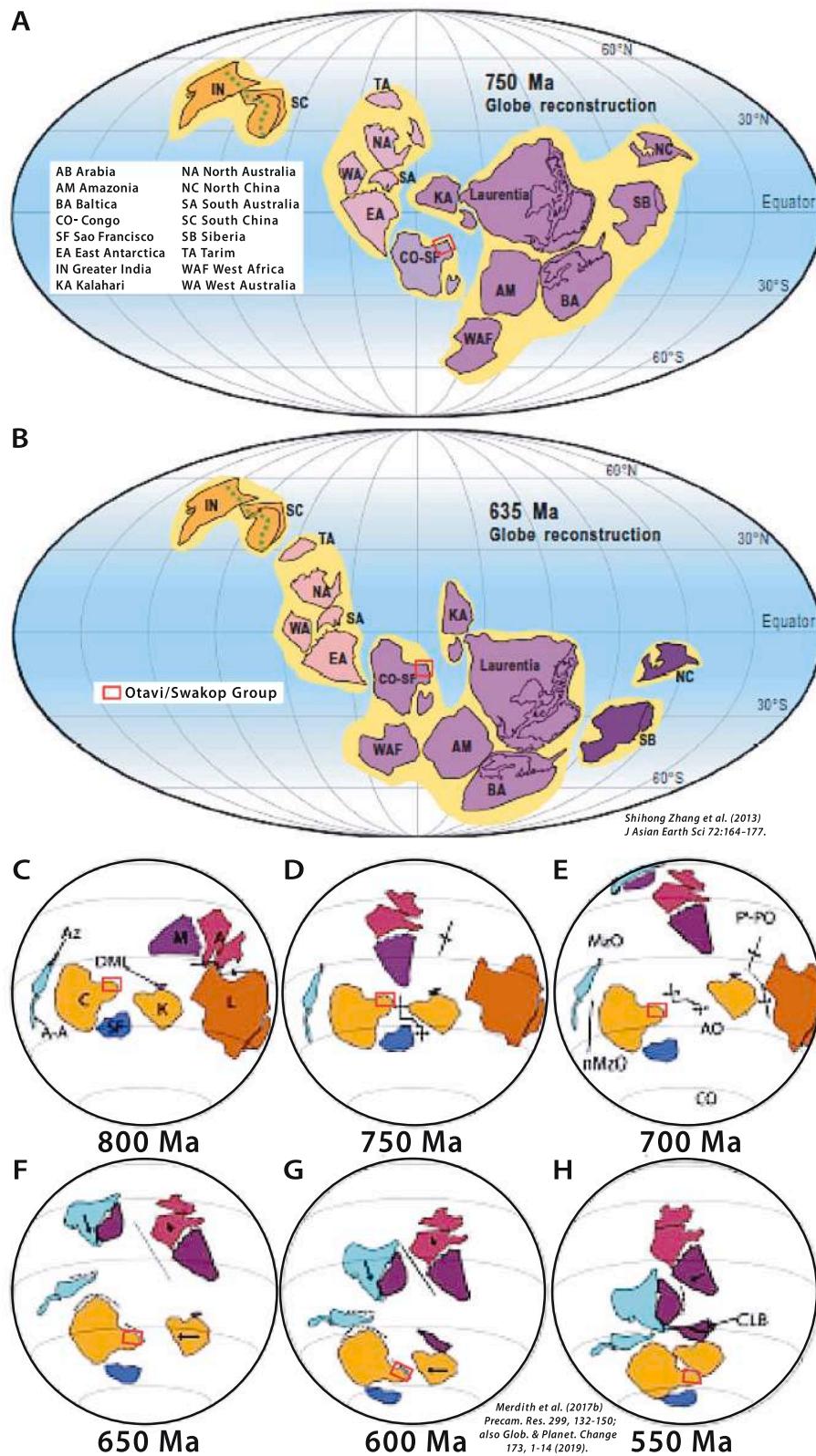


Fig. 11. Paleomagnetically and geologically constrained global paleogeographic maps for (A) 750 Ma and (B) 635 Ma according to Zhang et al. (2013). Red rectangle indicates area of Otavi/Swakop Group carbonate platform. Position of Congo craton in A is constrained by paleomagnetic pole (Meert et al., 1995) at 46°N, 325°E ($\alpha_{95} = 0^{\circ}$) from 748 ± 6 Ma syenitic phase of Mbizi igneous complex (Mbende et al., 2004) in southern Tanzania. Southern hemisphere location is consistent with westward-directed (present coordinates) contourites in FSz of Otavi/Swakop Group (Figs. 47E & 54F), consistent with left-turning of upwelling bottom currents. No Cryogenian rift-margin conjugate to SW Congo is evident in B, suggesting a kinematically conservative scenario in which Dom Feliciano (WKz) and Swakop (CDz) arcs (not shown) were the Cryogenian conjugates, separated from Congo by short-lived (≤ 50 Myr) marginal seas (Konopásek et al., 2018). However, our study revealed little evidence for Cryogenian rifting or passive-margin subsidence on Congo western (Kaoko) margin (Figs. 196 & 197), in contrast to its southern (Damara) margin, where Cryogenian rifting and early Ediacaran passive-margin subsidence are clearly manifest. Our finding is more compatible with scenario (C–H) of Merdith et al., 2017b, in which the Kaoko margin opened earlier, ~0.90 Ga (Merdith et al., 2019), due to clockwise rotation of São Francisco (dark blue) relative to Congo (ochre). Passive-margin subsidence related to opening of the resulting wedge-shaped basin (sphenochasm of Carey, 1958) would have already run its course before Otavi/Swakop time. Nosib Group (Figs. 5, 6D–E & 8A), the age of which is poorly constrained, could manifest erosion of an early Tonian rift shoulder on the western Congo margin. Alternatively, Kaoko margin opened as a transform margin simultaneous with southern-margin opening. Cratons: A, Australia; A, Afif–Abas; Az, Azania; C, Congo; CLB, Coats Land Block (East Antarctica); DML, Dronning Maud Land (East Antarctica); K, Kalahari; L, Laurentia; M, Mawsonland (East Antarctica); SF, São Francisco. Paleogeceans: AO, Adamastor; CO, Clymene; MzO, Mozambique; nMzO, Neo-Mozambique; P-PO, Panthalassa.

Table 4
Carbonate lithofacies.

Lithofacies	Description	Depositional environments
Microbialaminite	Undulose microbialaminite; associated fenestrate fabrics, tepees and tepee breccia, grainstone lenses, intraclast conglomerate, cm-scale channels	Intertidal–supratidal flats
Grainstone	Well-sorted calc–dolarenite; generally oolitic or intraclastic; with or without large-scale crossbedding; associated intraclast breccia; beds ≥ 0.2 m thick	Wave-dominated shoreface, off-shore bars, tidal channels
Stromatolite	Discrete columnar, branching, domal, or mounded microbial buildups; typically associated with grainstone	Shallow sublittoral: lower wave-dominated shoreface, tidal channel
Ribbonite	Wavy laminated calci–/ dololutite; with or without wave or current ripples, or low-angle cross-lamination; beds ≤ 0.2 m	Shallow neritic/shelf (above storm wave base)
Rhythmite	Flat parallel-laminated calci–/ dololutite; with or without turbidites or debrites	Deeper shelf, bathyal/slope-rise (below storm wave base)

segmented North Congo (Ubangui–Lindi) foreland belt (Verbeek, 1970; Poidevin, 2007; Tait et al., 2011), the intracratonic subsurface Congo basin (Kadima et al., 2011), non-calcareous East Congo outliers (Cahen and Lerpersonne, 1967; Bjørlykke, 1973), and the Cu ore-bearing Katangan salient of the SE Congo foreland (Cahen and Lerpersonne,

1981; Jackson et al., 2003; Master and Wendorff, 2011; Miller, 2013; Cailteaux and De Putter, 2019). Conceivably, a Neoproterozoic carbonate platform once covered the entire Congo craton, or roughly the area of the conterminous United States of America.

1.2.2. Kaoko orogen

Kaoko orogen (Fig. 3) is a sinistral-oblique collision zone between the western margin of the Congo craton and the Ribeira and Dom Feliciano magmatic arcs (Fig. 2a) and their cratonic backstops (Goscombe et al., 2003a; Goscombe and Gray, 2008). North of the Cretaceous Etendeka outlier, Kaoko orogen is divided into three coast-parallel zones (Miller, 2008b).

Western Kaoko zone (WKz, Fig. 3), or Coastal terrane, is a Buchan-type metamorphic belt with a Cryogenian–early Ediacaran magmatic history that distinguishes it as the preserved leading edge of the Ribeira–Dom Feliciano magmatic arc (Will et al., 2004; Goscombe and Gray, 2007; Heilbron et al., 2008, 2013; Konopásek et al., 2008, 2016; Oyhantçabal et al., 2009, 2011; Faleiros et al., 2011; Tupinambá et al., 2012; Basei et al., 2018; Hueck et al., 2018). A cluster of igneous crystallization ages ~ 590 Ma in the Ribeira arc has been attributed to slab-failure magmatism (Bercovici et al., 2015; Whalen and Hildebrand, 2019), consequent to arc-continent collision (Alves et al., 2013).

Central Kaoko zone (CKz, Fig. 3) consists of Congo basement and Damara Supergroup (Guj, 1970; Dürr and Dingeldey, 1996; Stanistreet and Charlesworth, 1999) that underwent deep (30 km) burial, basement anatexis, inverted Barrovian-type metamorphism in a sinistral transpressive regime undergoing rapid exhumation (Goscombe et al., 2003b, 2005; Will et al., 2004; Jung et al., 2014a), creating a system of E-vergent, basement-cored, thrust nappes with NW-plunging stretching lineations and left-slip kinematic indicators in the map plane (Stanistreet

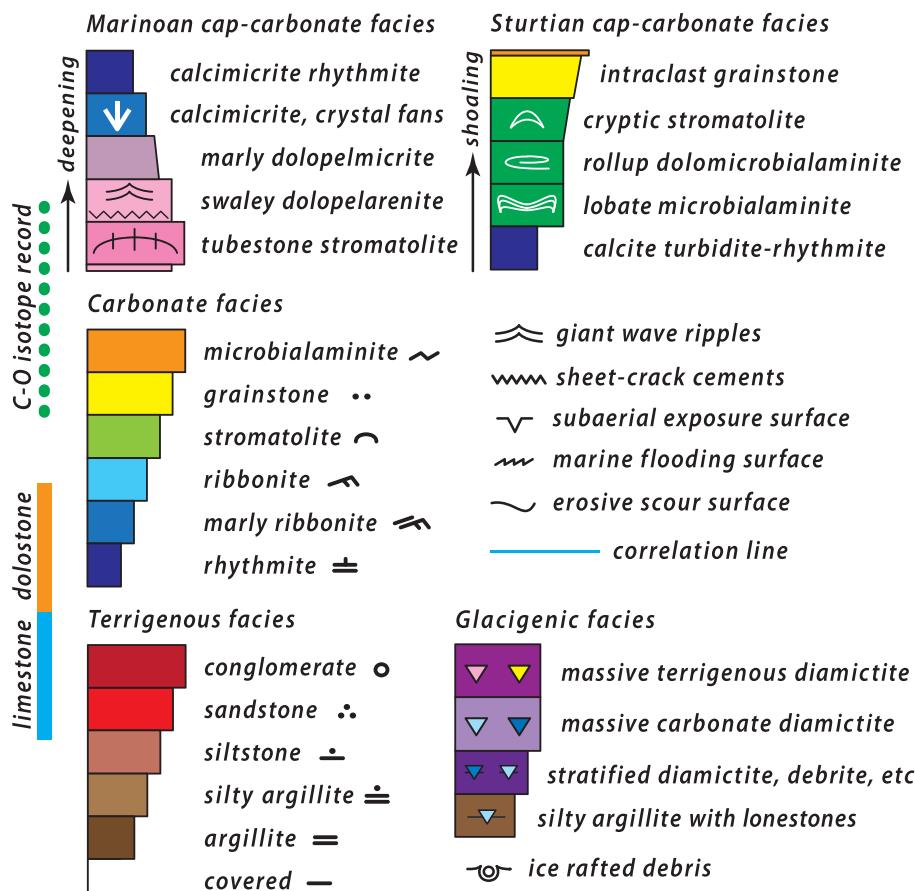


Fig. 12. Generalized legend and colour scheme used for columnar sections and fence diagrams in this paper, with additions and modifications where needed. Colour-coded carbonate facies in legend are described in Table 4. Reduced legend reappears for reference in Figures containing columnar sections.

Table 5Table of formations and members¹ with abbreviations for maps and figures.

MULDEN GROUP					
Welkom Subgroup					
Middle Ediacaran	Gaseneirob Fm		Wa		
	Renosterberg Fm		Wr		
	Braklaagte Fm		Wb		
	Soutrivier Mb (↓)		Ws		
	Sesfontein Fm		Ms		
	Okaua Fm		Mo		
	Kuiseb Fm				
	Awahuab Mb (↑)		Ka		
	Kuiseb schist		Ks		
SWAKOP GROUP			OTAVI GROUP		
Tsumeb Subgroup					
Early Ediacaran	Karibib Fm	Tkb	Hüttenberg Fm	Th	
			Elandschoek Fm	Te	
	Keilberg Mb (↓)	Tk	Maieberg Fm	Tm	
			Keilberg Mb (↓)	Tk	
Late Cryogenian	Bethanis Mb (↑)	Tb			
	Ghaub Fm	Tg	Ghaub Fm	Tg	
Abenab Subgroup					
Middle Cryogenian	Franni-aus Fm	Af	Oombaatjie Fm	Ab	
	Narachaams Fm	An	Gruis Fm	Ag	
	Okonguarri Fm	Ao	Rasthof Fm	Ar	
Early Cryogenian	Chuos Fm	Ac	Chuos Fm	Ac	
Ombombo Subgroup					
Late Tonian	Ugab Subgroup				
	Orusewa Fm	Us			
	Okotjize Fm	Ut			
	Upper Naauwpoort Fm	Nvu			
	Lower Naauwpoort Fm	Nvl	Okakuyu Fm	Ok	
	Austerlitz Fm	Ua	Devede Fm	Od	
			Beesvlakte Fm	Ob	
			NOSIB GROUP		
			Nabis Fm	Nn	

¹(↓) member at base of formation; (↑) member at top of formation; names italicized.

Table 6

Stratigraphic thickness data and average accumulation rates for Cryogenian glacial–periglacial formations in this study. Incomplete and zero-thickness sections are excluded. Accumulation rates are averaged over entire glacial stages.

Glacial epoch	Sections	Median	Average	Maximum	Average accumulation rate ¹
² Marinoan	157	32.3 m	52.9 m	602.0 m	3.3 m Myr ⁻¹
³ Marinoan	"	"	"	"	4.8 m Myr ⁻¹
⁴ Marinoan	"	"	"	"	8.8 m Myr ⁻¹
⁵ Sturtian	110	76.0 m	227.0 m	1660.1 m	4.0 m Myr ⁻¹

¹ Assuming Marinoan duration of ²16 Myr, ³11 Myr or ⁴6 Myr; and ⁵56-Myr for Sturtian.

and Charlesworth, 1999; Goscombe et al., 2003a; Konopásek et al., 2005; Goscombe and Gray, 2008). Basement anatexis began by 580 Ma (Seth et al., 1998) and synkinematic granite emplacement persisted for another 30 Myr (Goscombe et al., 2005). Diachronous collision between Congo craton and Ribeira–Dom Feliciano composite magmatic arc and its cratonic backstop is inferred at ~590–585 Ma, and a final cluster of cooling ages ~530–520 Ma (Goscombe et al., 2017, 2018) suggest reactivation in response to a remote collision possibly involving Amazonia (Fuck et al., 2008; Schmitt et al., 2008; Bandeira et al., 2012;

McGee et al., 2015a, b).

Eastern Kaoko zone (EKz, Fig. 3) is synonymous with the northern branch of Otavi fold belt (Fig. 4). EKz is characterised by tight folds and eastward translation of Otavi and Mulden groups above a detachment zone (thrust duplex) in the basal Otavi Group (Beesvlakte Fm). The detachment zone was re-deformed by thick-skinned folds of the basement and autochthonous Nosib Group (e.g., Killick et al., 1980). The Otavi–Mulden group transition marks abrupt drowning of the long-lived carbonate platform and burial by thick synorogenic clastics, beginning with deepwater marine deposits (Sesfontein Fm) in more internal areas (CKz and western EKz). Basal Mulden Group clastics are shallower and younger eastward, culminating in >3.0 km of sandstone (Renosterberg Fm) deposited by a southeastward flowing alluvial system (Hoffman and Halverson, 2008). We interpret Mulden Group as a foredeep sequence related to southward younging collision on Congo craton's western margin (Stanistreet et al., 1991) and/or collision on its northern margin (Kamguia Kamani et al., 2021).

South of Etendeka Plateau (SKz, Fig. 3), a deep-sea fan of middle Cryogenian–early Ediacaran age (Zerrissene Group) appears on strike with CKz (Miller et al., 1983; Swart, 1990, 1992a, b; Paciullo et al., 2007; Nieminski et al., 2018). The fan is estimated to be 1.62 km thick (Miller et al., 1983; Swart, 1992a), but no floor or roof is exposed in a 100-km-wide train of mainly westward vergent, chevron-type, doubly-plunging folds. Axial planes of N/S oriented chevron-type D1 folds fan across the belt. Plunge reversals are attributed to sinistral shear (D2) and transpression (D3) (Passchier et al., 2002), or alternatively to N/S shortening related to terminal collision in Damara orogen (SDz) (Hälbich and Freyer, 1985). SKz was intruded at 0.53 Ga by metaluminous quartz-poor granites that are synkinematic with D2 (Seth et al., 2000; Schmitt et al., 2012). A Marinoan synglacial horizon, a few decameters thick, in the middle of the turbidite succession contains ice rafted limestones (Miller et al., 1983; Swart, 1992a; Miller, 2008b). The directly overlying carbonate-dominated turbidites (Gemsbok River Fm, Fig. 6A) match δ¹³C profiles of the early Ediacaran Karibib Fm (Fig. 6B–C) of Swakop Group (Hoffman and Lamothe, 2019).

Zerrissene Group deep-sea fan was initially inferred to be indigenous to Congo craton (Miller et al., 1983; Porada et al., 1983), but displaced laterally since continental promontories do not normally host major rivers. Limited paleocurrent data, mainly from climbing ripples, indicate southerly-directed flows with skewness favouring either a western (Swart, 1992a) or eastern (Congo) source (Passchier et al., 2002). Detrital-zircon age spectra (Nieminski et al., 2018) are remarkably unchanging except for the late appearance of young grains (630–625 Ma) in Amis River Fm (Fig. 6A). The primary mode is Stenian (1.2–1.0 Ga) in all samples (Fig. 9A–F), with smaller late Tonian and Orosirian modes. The Stenian peak is weak or absent in clastics derived from SW Congo craton (Fig. 9G–J) (Nascimento et al., 2017), but is prominent in Damaran sediments of CDz (Fig. 9K–M) (Foster et al., 2015). A potential source for Stenian-age detritus is NW Kalahari craton (e.g., Gamsberg and related granites, Miller, 2008a). Detrital age spectra (Blanco et al., 2011) from northern Nama Group (N of Osis ridge) on Kalahari craton more closely resemble those from Zerrissene deep-sea fan (Nieminski et al., 2018) than those derived from SW Congo craton (Fig. 9G–J), although the latter remain badly undersampled (see 4.1.10.). However, Stenian detrital age peaks are observed in Tonian and middle Cryogenian clastics of the equatorial West Congo belt (Fig. 9N) (Frimmel et al., 2006; Affaton et al., 2016), 1760 km N of where Zerrissene deep-sea fan now resides. Southward tectonic translation of the Zerrissene deep-sea fan and even Central Damara zone might conceivably have resulted from transform opening of the western Congo margin (Hoffman, 2021b).

Subduction polarity for the Kaoko orogen has been inferred as westward dipping (Stanistreet et al., 1991; Oyhantçabal et al., 2009, 2011; Chemale Jr. et al., 2012; Nieminski et al., 2018) or eastward dipping (Goscombe and Gray, 2007, 2008; Konopásek et al., 2014, 2018; Goscombe et al., 2018). Eastward-dipping subduction implies that the

western Congo margin faced a back-arc basin (e.g., Konopásek et al., 2018). When back-arc basins open, part of the pre-existing arc is generally stranded as a remnant arc on the margin opposite the active arc (Karig, 1974). Since no remnant magmatic arc is known in Central Kaoko zone, we infer westward-dipping subduction to account for 0.66–5.90-Ga arc magmatism in Western Kaoko zone (Coastal terrane) and the South American magmatic arcs (Fig. 2a). Accordingly, death by drowning and burial of Otavi Group in Eastern Kaoko zone was a direct consequence of abortive subduction of Congo margin beneath an accretionary prism (orogen) in front of the Ribeira–Dom Feliciano composite magmatic arcs.

1.2.3. Damara orogen

Damara orogen separates the Kalahari and Congo cratons (Figs. 2a & 3) and includes three internal zones—Southern (Khomas), Central (Swakop) and Northern (Outjo) zones—in addition to external thrust and fold belts (Martin, 1983; Miller, 1983, 2008b; Hegenberger, 1993; Goscombe et al., 2018, 2020). Southern zone (SDz, Fig. 3) is a SE-facing accretionary prism (Khomas schist) that is dominated by semi-pelite but encloses many serpentinite bodies (Barnes, 1983) and a narrow strike-parallel belt of mafic igneous rocks (Matchless amphibolite), attributed to ridge subduction (Hoffmann, 1991; Meneghini et al., 2014). Central zone (CDz, Fig. 3) is a 160-km-wide ‘ribbon’ continent with strongly-deformed Neoproterozoic sedimentary cover (Lehtonen et al., 1996; de Kock, 2001), intruded by arc-type granitoids of intermediate composition (de Kock et al., 2000; Jacob et al., 2000) and a plethora of post-kinematic syenogranite bodies as occur in all three Damara internal zones (Miller, 2008b). Northern zone (NDz, Fig. 3) contains attenuated Congo basement and basinal Neoproterozoic cover (Swakop Group) that were folded and thrust NNW toward Congo craton (Clifford, 2008; Miller, 2008b).

The standard tectonic model for Damara orogen (Barnes and Sawyer, 1980; Kasch, 1983b; Kukla, 1992; Johnson et al., 2006; Gray et al., 2008; Miller, 2008b Fig. 13 .291; Foster and Goscombe, 2013; Goscombe et al., 2018) holds that an oceanic seaway (Khomas sea) closed at 0.55 Ga in Southern zone as a result of NW-dipping subduction, manifested by 0.56-Ga arc magmatism in Central zone (de Kock et al., 2000; Jacob et al., 2000). Collision of the Kalahari margin with the Khomas accretionary prism caused SE-directed crustal-scale thrust-imbrication in the southern external (Hakos) zone (Fig. 3) (Kasch, 1983a; Martin et al., 1983; Kukla and Stanistreet, 1991; Kukla 1992; Miller, 2008b). Flexural subsidence of the northern Nama Group foredeep occurred in response to the collision in Southern zone (Germs and Gresse, 1991; Gresse and Germs, 1993; Grotzinger et al., 1995; Saylor et al., 1998; Blanco, et al., 2009, 2011). Central zone is inferred to be leading edge of Congo craton in the standard model and Northern zone was an intracontinental rift basin (Outjo basin) that contracted in response to collision in Southern zone (Miller, 2008b, 2013; Goscombe et al., 2018). If rifting in Northern and Southern zones were broadly coeval, Outjo basin (Fig. 3) did not originate as a back-arc basin because subduction in Southern zone had yet to begin (Miller, 2008b Fig. 13.291). Testable predictions of the standard model are broadly coeval orogenesis in Northern and Southern zones, and broadly correlative development of their respective foredeeps, Mulden and northern Nama Groups.

Certain observations call for early stages in the standard model to be revised. First, contraction of Northern zone preceded collision in Southern zone by 50 Myr. Early deformation in widely spaced areas of Northern zone was accompanied by phengite growth yielding $^{40}\text{Ar}/^{39}\text{Ar}$ laser-ablation age spectra of 598 ± 4 , 594 ± 7 and 584 ± 4 Ma (Lehmann et al., 2015). The resulting fabrics were refolded by coast-parallel Kaoko D1 structures, related to crustal anatexis in Central Kaoko zone at 580 ± 3 Ma (Seth et al., 1998). In contrast, collision in Southern zone should be younger than arc magmatism in Central zone at 563 ± 4 Ma (Jacob et al., 2000) and 558 ± 5 Ma (de Kock et al., 2000). It should be synchronous with foredeep subsidence in the northern Nama Group at

548.8 ± 1 Ma (Grotzinger et al., 1995) and older than post-tectonic granite emplacement in Southern zone at 549 ± 11 Ma (Johnson et al., 2006).

If the foredeeps bordering Northern and Southern zones were broadly coeval, we should expect to find Ediacara-type fauna (EB & CN, Fig. 1A) in marine strata of Mulden Group since they are so well developed in Nama Group (Grotzinger et al., 2005; Grotzinger and Miller, 2008). None has been found. If Mulden Group formed ~550 Ma like Nama Group (Grotzinger et al., 1995), we might expect to see the 574–567-Ma Shuram CIE (Fig. 1A) (Grotzinger et al., 2011; Rooney et al., 2020b) in the underlying Otavi Group. There is no Shuram (aka Wonoka) CIE in Otavi Group (Halverson et al., 2005). The simplest explanation is that Mulden Group predates Ediacara-type fauna and Otavi Group ended before the Shuram CIE (Fig. 1A). Even if Mulden Group detritus was derived from the western or northern Congo margins (discussed in 1.2.2. above under Eastern Kaoko zone), the subsidence to accommodate it must have had a more local origin since Mulden Group extends eastward along the southern Congo margin beyond Otavi Mountainland (Figs. 4 & 6E). The origin of sub-Mulden Group subsidence along the southern Congo margin can be found in early independent closure of Outjo basin by ~600 Ma, producing the orogenic Northern zone (Lehmann et al., 2015). We infer that the crust of Outjo basin was sufficiently thin and the lithosphere sufficiently old for buoyancy-powered subduction. Otherwise, there is no engine for early contraction and orogenesis in Northern zone. Independent evidence for subduction is one of the most prominent geophysical anomalies in southern Africa (Corner, 2000, 2008; Khoza et al., 2013; Corner and Durrheim, 2018), which tracks the Northern–Central boundary zone for 1000 km from the Atlantic rifted margin into Botswana. This long-wavelength (i.e., deep-seated) negative anomaly in total magnetic intensity is comparable in scale and character to anomalies in the Canadian Precambrian Shield associated with plate-scale boundaries like the Grenville Front tectonic zone (Rivers et al., 2012; Miles and Oneschuk, 2016).

The Damaran Wilson cycle lasted only 85–100 Myr from opening of the Northern (Outjo) basin at 650–635 Ma to closure of the Southern (Khomas) basin at 550 Ma. If we assume that Congo and Kalahari cratons separated and were later reunited (1.2.1., Ernst et al., 2013; Salminen et al., 2018), a basin or pair of basin 2125–2500 km wide could have opened and closed in that time-frame, assuming average spreading and closure rates of 5 cm yr^{-1} . A simple scenario that accounts for two basins with different histories is shown schematically in Fig. 2D–I. Separation of Kalahari and Congo cratons opens Outjo (N) basin (Fig. 2E). A crustal ribbon (Central zone, CDz) separates from Kalahari craton in response to subduction initiation at the southern margin of Outjo basin (Fig. 2F–G). Slab rollback pulls Central zone northward, closing Outjo basin and opening Khomas basin (S) in its wake (Fig. 2G–H). Central zone collides with the Congo passive margin (Fig. 2H), creating the Northern zone orogen (600–590 Ma). Subduction polarity-flip as a consequence of collision (McKenzie, 1969; Suppe, 1981, 1984) initiates subduction at the northern margin of Khomas basin (Fig. 2H). Closure of Khomas basin leads to collision of the Kalahari passive margin with Central zone (Fig. 2I), which is backstopped by Northern zone and Congo craton, all of which absorb the effects of terminal collision in Southern zone. The cycle is consistent with the relative age of rift basins on the northern (older) and southern (younger) margins of Central zone (de Kock, 2001). It rationalizes the co-occurrences of Stenian intrusive and detrital ages in Central zone (Fig. 9K–M) (Kröner et al., 1991; Foster et al., 2015) and the Kalahari margin (Miller, 2008a; Blanco et al., 2011). A critical turning point in the Wilson cycle is subduction initiation in Outjo basin (Fig. 2F). Subduction initiation at passive margins is rare and can only occur in a limited time-window (Cloetingh et al., 1982). The oceanic plate must be sufficiently old (cold) to sink but sufficiently young (warm) to rupture.

The remaining challenge (e.g., Passchier et al., 2016) is to kinematically couple the inferred Damara collisions at ca 600 and 550 Ma

with the coastal ones at ca 590 and 540 Ma, utilizing offshore geophysical data (Corner, 2000, 2008; Corner and Durrheim, 2018).

1.2.4. Post-orogenic cover

Flat-lying cover rocks are divisible into four systems (Miller, 2008c), Karoo Supergroup (Carboniferous–Jurassic), Etendeka Group (Early Cretaceous), Kalahari Group (Late Cretaceous–Pliocene) and Namib Group (Miocene) (Fig. 8A).

The Karoo Supergroup is floored by a Carboniferous glacial erosion surface and vestigial lodgement tillite of the Dwyka Fm. U-shaped valleys cut by Carboniferous ice streams are currently occupied by the first-order Kunene, Hoaruseb and Hoanib rivers, and their main tributaries (Martin, 1961, 1981; Miller, 2008c). Oddly, the Atlantic Coast of Southern Africa is one of the few rifted margins within former Gondwana where Carboniferous ice flowed toward the present ocean (Du Toit, 1937, his Fig. 9). The bulk of the Karoo Supergroup consists of Permian and early Mesozoic terrestrial deposits, culminating in aeolian sandstone of an erg, present also with the same paleo-wind direction in conjugate eastern Brazil, active at the onset of Paraná–Etendeka flood-basalt volcanism (Jerram et al., 1999, 2000a, b).

The Etendeka Group is a 0.9-km-thick succession of basalt lava flows and subordinate latite and quartz-latite ash-flow tuffs (Marsh et al., 2001; Miller, 2008c). It was co-extensive with the Paraná flood-basalt province of southern Brazil before Atlantic opening (Peate, 1997). Both are connected by seafloor volcanic lines ('hotspot' tracks) to the mantle double-plume presently situated under the South Atlantic islands of Tristan and Gough (Rohde et al., 2013; Hoernle et al., 2015). Corrected $^{40}\text{Ar}/^{39}\text{Ar}$ ages imply that flood basalt eruptions began at 134.7 ± 1.0 Ma and lasted for <1.0 Myr as in other large flood-basalt provinces (Thiede and Vasconcelos, 2010). New magnetostratigraphic data from the Etendeka Supergroup, however, suggest a more extended and steady eruptive timescale of >4 Myr (Dodd et al., 2015), with ages of 135.5–131.5 or 139.5–135.5 Ma according to the geomagnetic polarity timescales of Gee and Kent (2007) and Ogg et al. (2012), respectively. The latter timescale appears to be inconsistent with the Paraná–Etendeka radiometric chronology. The Etendeka volcanics are broadly coeval with a cluster of large peralkaline granitic ring-complexes (e.g., Erongo, Messum, Brandberg, etc.) in Namibia between 20° and 22°S latitudes (Fig. 3), but these have yet to be precisely dated. Mafic volcanism was fed by coast-parallel and coast-normal dyke swarms. The dykes and lavas are structurally tilted only at the coast and offshore. The cessation of Etendeka volcanism (Dodd et al., 2015) preceded the onset of South Atlantic seafloor spreading in offshore Namibia (Collier et al., 2017) by 1.9 Myr (Gee and Kent, 2007) or 1.2 Myr (Ogg et al., 2012), and by 5.8 or 6.3 Myr, respectively, north of the Rio Grande Fracture Zone, which meets the African continent at latitude 18.4°S (Fig. 3).

A continent-wide composite erosion surface (King, 1962, p. 265–272) separates the Etendeka Group and older rocks from semi-lithified terrestrial deposits of the Late Cretaceous–Cenozoic Kalahari Group (Miller, 2008c). These deposits, up to 0.6 km thick, form an enormous internal segmented basin covering much of the elevated interior of central and southern Africa. The development of the Kalahari Group was long and complex. The long arm of Cenozoic deposits that wrap around the northern plunge of Kamanjab inlier (Fig. 8A), for example, repose in a Carboniferous subglacial valley and are 200 m lower in elevation than deposits of the Owambo Basin on the high plateau under Etosha National Park (Miller et al., 2010). The Kalahari Group is undergoing erosion at the top of the coastal escarpment but the offshore depositional record indicates that sediment delivery peaked in the Late Cretaceous, 80–66 Ma (Guillocheau et al., 2012), after which drainage in Namibia was mainly directed internally. Miocene–Pliocene uplift of Southern Africa is inferred from climatic cooling and strengthening of the Benguela Current and coastal upwelling (Jung et al., 2014b).

Outliers of Namib Group occur in the southeast of the Kamanjab area (Fig. 8A). They belong to a dissected terrace composed of Miocene

conglomerate (Bertram Fm) deposited by the proto-Ugab River (Mabbutt, 1950; Miller, 2008c).

1.3. Paleogeographic zones

Four paleogeographic zones are distinguished, two each in the Otavi and Swakop Groups (Figs. 5, 8A & B). Distinctions are based on stratigraphic relations and sedimentary facies, but we stress that the facies zonation was progressive with platform development. The names are descriptive of what each zone would become by ca 550 until 600 Ma, not what it was during early stages of development. Since zones are specified 565 times in the text, we often substitute the acronyms Bz (basin zone), FSz (foreslope zone), OPz (outer platform zone) and IPz (inner platform zone) (Table 2). Bz and FSz are Swakop Group; OPz and IPz are Otavi Group (Figs. 5 & 6).

Bz (basin zone) corresponds to the Northern (Outjo) zone in the tectonic zonation scheme (NDz, Fig. 3). It includes transects Tr2 and Tr3 (Fig. 8B). It is distinguished by the presence of the Tonian Ugab Subgroup and by basinal facies of the Cryogenian Abenab Subgroup and Ediacaran Karibib Fm (Figs. 5 & 6B).

FSz (foreslope zone) corresponds to the Northern Margin zone of Miller (2008b) and includes transects Tr1, Tr4 and the western two-thirds of Tr5 (Fig. 8B). Tonian strata are absent in Tr5, but Austerlitz and/or Naauwpoort formations (Fig. 6C) occur in Tr1 and Tr4. Foreslope sedimentary facies developed progressively in the Cryogenian Abenab Subgroup and Ediacaran Karibib Fm (Fig. 5). For the Cryogenian, we distinguish proximal (upslope) and distal foreslope sub-zones, reflecting changes in lithofacies and Marinoan glacial erosion and sedimentation.

OPz (outer platform zone) includes the northeastern arm of transect Tr5 and all of Tr6 and Tr7 (Fig. 8B). It corresponds to the southern part of Miller's (2008b) Northern Platform. Tonian strata are absent, and upper Abenab and Tsumeb subgroups are neritic (water depths ≤ 200 m) in facies (Fig. 5). Marinoan syn-glacial Ghaub Fm is virtually absent in the FSz, but the postglacial cap dolomite (basal Maieberg Fm, Fig. 5) is expanded in thickness (60–160 m).

IPz (inner platform zone) includes transects Tr8 through Tr11 (Fig. 8B). The Tonian Nosib Group and Ombombo Subgroup are present in the Eastern Kaoko zone (Figs. 3 & 6D). Abenab and Tsumeb subgroups are platformal in facies, deeply drowned only in the two glacial aftermaths (Fig. 5). The Marinoan Ghaub Fm is thin and discontinuous, but the subglacial surface has ≤ 150 m of relief relative to the directly underlying Ombaatjie Fm. The basal Maieberg Fm cap dolomite (Keilberg Mb) is thinner (10–33 m) than in the OPz, and thinnest (≤ 16 m) where the subglacial surface is most deeply eroded.

The paleogeographic zones (Fig. 8A) parallel the southern (Damara) margin of SW Congo craton (Figs. 2A & 3). Crustal stretching responsible for platform subsidence was oriented parallel to the Atlantic coast and to Kaoko orogen (Hoffman and Halverson, 2008). Stretching is manifested by Damara-parallel synsedimentary growth faults and rift-shoulder uplifts (Fig. 5), giving rise to alluvial aprons shed northward off rift-shoulder dip-slopes into the Tonian–middle Cryogenian neritic carbonate succession (Fig. 5). In contrast, W/E changes in Otavi Group stratigraphy, thickness or facies across Eastern Kaoko zone (Figs. 3 & 4) are small, or stratigraphically confined (e.g., Ombaatjie Fm, Fig. 6D).

Swakop Group is preserved at higher grades of metamorphism and tectonic strain as recumbent synclinal enclaves between the basement-cored nappes of Central Kaoko zone (CKz, Fig. 3) (Guj, 1970; Henry et al., 1992/93; Stanistreet and Charlesworth, 1999; Konopásek et al., 2017). This area of limited vehicle access and unlimited bedrock exposure will require some changes in methods relative to our study. One motivation is to test and refine the hypothesis that the western margin of Congo craton originated as a transform margin (Passchier et al., 2016; Hoffman, 2021b).

1.4. Stratigraphic overview

The table of formations (Table 5) gives abbreviations used on maps and figures. Only two letters are needed in most cases: the first letter of the Subgroup name in upper case followed by the first letter of the formation name in lower case. Three letters are used for members (Nvu) or to avoid ambiguity (Tkb). Abenab and Tsumeb subgroups are extended to their age-equivalents in Swakop Group, since correlations are not in doubt at the subgroup level in our transects. Where no subgroup exists, the first letter of the Group name is used (Nn, Ms). Where group affiliation is in question, the formation name is put in upper case (Ks).

By established precedent (Martin, 1965; Frets, 1969; SACS (South African Committee for Stratigraphy), 1980), Swakop Group (Bz & FSz) and Otavi Group (OPz & IPz) refer to different facies of the same succession. Distinct Sturtian (Chuos Fm) and Marinoan (Ghaub Fm) glacial–periglacial units occur in both groups. The names Swakop Group and Kuiseb Fm (Table 5) are not local. Swakop River drains the Central zone of Damara orogen (CDz, Fig. 3), and Kuiseb River drains the Southern zone (SDz). Certain names have long been applied to analogous formations in different tectonic zones of the orogen. This simplified nomenclature and description, but was risky for correlation. Damara orogen is 2.5 times wider than the Western Alps of Europe, consistent with a composite origin at the plate scale (Figs. 2D–I & 3).

Within our study area (Fig. 4), the late Tonian Okotjize and Devede formations of Ugab and Ombombo subgroup, respectively, are lithologically similar but differ in age (Fig. 6B & D). Okotjize Fm overlies 747 ± 2 Ma Naauwpoort volcanics (Hoffman et al., 1996), whereas uppermost Devede Fm holds a tuff yielding igneous zircons dated at 759.95 ± 0.86 Ma (Halverson et al., 2005). Okotjize Fm must accordingly be ≥ 10 Myr younger than Devede Fm.

The middle Cryogenian (Table 1) is represented by different formations in Swakop and Otavi groups (Fig. 6B–E). This is necessitated by major facies changes from basin to platform. Berg Aukas, Okonguarri, Narachaams and Frannis-aus formations of Swakop Group (Fig. 6B & C) are collectively correlative with Rasthof, Gruis and Ombaatjie formations of Otavi Group (Fig. 6D). Differences in middle Cryogenian nomenclature between Eastern Kaoko zone (Fig. 6D) and Otavi Mountainland (Fig. 6E) stem from early miscorrelation (Fig. 7B & C), real stratigraphic differences (Hedberg, 1979), and sequence-stratigraphic (Fig. 6D) versus purely lithologic (Fig. 6E) definitions of formations. We prefer the sequence-stratigraphic approach so long as it is compatible with mappability as the primary criterion. Formations as here defined are indicated by blue correlation lines between lithology-based columnar sections (Fig. 12).

The early Ediacaran Karibib Fm of Swakop Group (Fig. 6B & C) is time-equivalent to the Maieberg, Elandschoek and Hüttenberg formations of Otavi Group (Fig. 6D). The basal Ediacaran Keilberg Mb, the Marinoan ‘cap’ dolomite, is recognizable in both groups as is the succeeding post-snowball maximum flooding stage. Kuiseb (Schist) Fm (Fig. 6B & C) is an assemblage of semi-pelitic schist, quartzite and marble stratigraphically overlying Karibib Fm that has long been assigned to Swakop Group (SACS (South African Committee for Stratigraphy), 1980). In our view, it has more in common lithologically and genetically with Mulden Group (Fig. 6C & D). But since the Otavi/Swakop-to-Mulden transition deserves further study, we leave Kuiseb Fm ungrouped (Table 5) for now.

1.4.1. Nosib Group

In the IPz (Fig. 5), Otavi Group is conformably underlain by Nosib Group (Hedberg, 1979; Kröner and Correia, 1980; SACS (South African Committee for Stratigraphy), 1980), a km-thick southeastward-tapered sheet-like succession of subfeldspathic arenite and conglomerate unconformably overlying the Orosirian basement complex. It is well exposed around the northern plunge of Kamanjab inlier (Fig. 8A), where crossbedding orientations indicate southward-directed fluvial transport.

In the OPz, Nosib Group is absent on Huab ridge (Tr5 & 6) and in Tr7 it is progressively truncated by Abenab Subgroup from N to S in an offlap associated with Makalani dip-slope (Fig. 5). We infer that Nosib Group was deposited before Huab and Makalani rift-shoulders formed, and is not related to rifting on the southern margin of Congo craton.

In the distal FSz and Bz (Fig. 5), coarse-grained clastics of Austerlitz Fm overlying basement were logically included in Nosib Group (Hedberg, 1979). However, Austerlitz Fm in its type area (Austerlitz 515 farm, see ahead Fig. 15) contains a crystal-rich dacite ash-flow tuff (Fig. 6B) dated at 757 ± 5 Ma (Nascimento et al., 2016). The age is indistinguishable from a tuff dated at 759.95 ± 0.86 Ma (Halverson et al., 2005) in uppermost Devede Fm of Ombombo Subgroup (Fig. 6D) in Tr11 (IPz). Likewise, Naauwpoort Fm volcanics in Tr3 and 4 (Fig. 6B & C) were included in Nosib Group (SACS (South African Committee for Stratigraphy), 1980), but were later found to be 11–16 Myr younger (746 ± 2 and 747 ± 2 Ma, Hoffman et al., 1996) than the Devede Fm tuff (Fig. 6D). Thus, we limit Nosib Group to IPz (Fig. 6D & E), where it must be significantly older than 760 Ma. However, we cannot rule out a Nosib age for undated Austerlitz Fm in Tr1 and 4. In the sections that follow (1.4.2.–1.4.6.), formation names are italicized for easy reference the first time they are used and described.

1.4.2. Ombombo Subgroup

The recognition of two discrete glaciations in northern Namibia (Hoffmann and Prave, 1996) led to division of the Otavi Group into three subgroups (Table 5, Fig. 7A). In IPz, the pre-Sturtian Ombombo Subgroup conformably overlies Nosib Group and consists of three formations, Beesvlakte, Devede and Okakuyu (Hoffman and Halverson, 2008; Hood et al., 2015) in ascending order (Figs. 5 & 6D). *Beesvlakte Fm* is a recessive argillaceous and marly unit containing the sole-thrust or thrust duplex of the E-directed thin-skinned thrust-fold belt of Eastern Kaoko zone (EKz, Fig. 3). *Devede Fm* (Fig. 6D) is a resistant 0.3–0.4-km-thick stack of peritidal dolomite cycles. The lower part of the formation contains a northward-tapered set of cycles that begin with quartz-chert conglomerate, sandstone or mudcracked siltstone. The upper part of the formation features massive pink-dolomite biostromes up to 65 m thick. They are constructed of *Tungussia*-type columnar stromatolites typified by extreme-divergent branching (Hofmann, 1969). *Okakuyu Fm* (Fig. 6D) is a stack of coarsening-upward clastic cycles, composed of siltstone, sandstone and quartz-chert-dolomite conglomerate. A cycle capped by stromatolitic dolomite with coarse-grained ooids (≤ 2 mm diameter) is locally preserved in Tr11 beneath the Sturtian glaciogenic Chuos Fm. Giant ooids before Sturtian glaciation are observed elsewhere (Trower, 2020) and before Marinoan glaciation in Swakop Group (Hoffman, 2011a). Falling sea level raises carbonate saturation (Berger, 1982) and phosphorus in runoff that favours low-density ikaite ($\text{CaCO}_3\cdot 6\text{H}_2\text{O}$) precursor, both recipes for giant ooid formation (Trower, 2020). Okakuyu Fm was cannibalized from Devede Fm, Nosib Group and locally from basement. A conglomerate high in the Okakuyu Fm in Tr8 contains pebbles of undeformed amygdoidal ‘dacite’ (field term) lithologically resembling Upper Naauwpoort volcanics in Tr4. Offlap of Ombombo Subgroup beneath Chuos Fm north of Makalani ridge (Fig. 5) suggests that rift-shoulder uplift and dip-slope denudation sourced the clastic wedges in Ombombo Subgroup (Hoffman and Halverson, 2008). Southward-directed paleocurrents in Nabis Fm (Nosib Group) in the same area indicate that Makalani ridge only came into existence in post-Nosib time.

1.4.3. Ugab Subgroup

In transect Tr3 (Bz, Northern zone), ≤ 0.74 km of shallow-water carbonate admixed with clastics conformably overlie 746-Ma Lower Naauwpoort Fm volcanics and disconformably underlie Sturtian Chuos Fm diamictite. Miller (1974, 1980) divided the pre-Sturtian sedimentary sequence into a lower carbonate-dominated *Okotjize Fm* and an upper siliciclastic-dominated *Orusewa Fm* (Fig. 6B). In Tr2, 120 km to the West (Fig. 8B), a lithologically similar sequence of mixed shallow-water carbonates and clastics is exposed at the foot of Etendeka Plateau (Malof,

2000). C-isotope chemostratigraphic correlation with Tr3 (Lamothe et al., 2019) suggests that Tr2 preserves upper Okotjize Fm and an upward extended section of Orusewa Fm. Chemostratigraphic correlation between Tr2 and Tr3 is supported by an age of 743 ± 10 Ma (LA-ICPMS) for the youngest detrital zircon grain in a sample of Ugab Subgroup from Tr2 (Nascimento et al., 2017, 2018; Hoffman and Halverson, 2018).

1.4.4. Abenab Subgroup

The middle division of the Otavi Group, Abenab Subgroup (Miller, 2008b), begins and ends at glacial disconformities beneath Sturtian Chuos Fm and Marinoan Ghaub Fm, respectively (Fig. 6). As originally defined in Otavi Mountainland (Fig. 7C), ‘Abenab Stage’ did not include Chuos (then Varianto) Fm, which was placed in Nosib Group (SACS (South African Committee for Stratigraphy), 1980). In ascending order, it consisted of thin-bedded dark-grey dolomite of *Berg Aukas Fm*, massive pale-grey partly-oolitic dolomite of *Gauss Fm*, and decametric alternation of the above lithologies in *Auros Fm* (Hedberg, 1979; King, 1994; Miller, 2008b).

In the Otavi Group west of 15.5°E (Fig. 4), Abenab Subgroup (Fig. 6D & 7A) consists of Chuos, Rasthof, Gruis and Ombaatjie formations (Hedberg, 1979; Hoffmann and Prave, 1996; Hoffman and Halverson, 2008). Rasthof and Gruis formations were named by Hedberg (1979); Ombaatjie Fm was named by Hoffmann and Prave (1996). Hoffman and Halverson (2008) defined these same formations more precisely, and such that formations defined major depositional sequences or sequence sets, while still being amenable to lithological mapping on the ground and/or by air-photo interpretation. Consequently, the post-Chuos formations in Kunene Region (Fig. 6D) are not exactly equivalent to those in Otavi Mountainland (OML) (Fig. 6E), which were defined by lithofacies. For example, the highstand dolomite grainstone at the top of the Rasthof Fm (Fig. 6D) would be mapped as Gauss Fm in OML (Fig. 6E). In Kunene Region, the transition from Berg Aukas to Gauss lithology is gradational over 100 m or more. In the absence of chemostratigraphic data in OML, we do not know to what extent Gauss Fm in OML includes equivalents of Gruis and lower Ombaatjie formations in the western region (Fig. 6D).

In Kunene Region, the Sturtian *Chuos Fm* consists of polymictic diamictite and associated glacial-periglacial deposits of highly variable thickness (Martin, 1965; Hoffman and Halverson, 2008; McGee et al., 2012; Le Heron et al., 2013a; Lechte and Wallace, 2016; Hoffman et al., 2017b; Lechte et al., 2018, 2019). Median, average and maximum thicknesses of 110 measured sections (Table 6) are 76, 227 and 1660 m, respectively, excluding incomplete and zero-thickness sections. Considering the 56-Myr duration of Sturtian glaciation (Rooney et al., 2020a), the average rate of net accumulation was a paltry 4.0 m Myr^{-1} (0.004 mm yr^{-1}), an order of magnitude less than for Phanerozoic glaciations of comparable duration and similar to rates for non-carbonate shelf mud accumulation (Partin and Sadler, 2016). Chuos Fm is regionally thin but locally thick—only 27% of the sections are above average. The local thickenings have different origins (Hoffman et al., 2017b): a subglacial rift-basin in Tr1, a moraine-like buildup in Tr2, and an overdeepened bedrock trough in Tr8.

Rasthof Fm (Hedberg, 1979; Yoshioka et al., 2003; Katsuta et al., 2007; Tojo et al., 2007; Hoffman and Halverson, 2008; Pruss et al., 2010; Le Ber et al., 2013; Wallace et al., 2014) is the post-Sturtian ‘cap-carbonate sequence’ (Hoffman and Schrag, 2002). It is 130–450 m thick on the platform and it begins at a knife-sharp contact overlain by its deepest water facies, a finely laminated dark-grey dolomite rhythmite hosting cm-scale limestone turbidites. The turbidite-rhythmite member (Ar1) is overlain by a bizarre succession of sublittoral microbialaminites and stromatolites (Ar2), characterized by void-filling cements, neptunian dykes, lobate stromatolites interpreted as expansion folds, and mat-rollup structures. These unusual neritic microbialites supported protistan heterotrophs whose globular agglutinated tests are found in high concentrations and modest spatial diversity (Bosak et al., 2011; Dalton et al., 2013; Moore et al., 2017). These microbial facies are gradationally

overlain by high-energy dolomite grainstone (Ar3), typically 50–200 m thick, ending at a mappable subaerial exposure surface marked by supratidal tepees (Kendall and Warren, 1987). The absent transgressive systems tract (TST) and overthick highstand systems tract (HST) imply that Chuos Fm constitutes lowstand deposits of a deeply-subsided basin. The rise in relative sea level accompanying deglaciation must have been swift and profound, given the observed sharp basal contact of Rasthof Fm without reworking of Chuos Fm diamictite. In outcrop, the ridge-forming Rasthof Fm produces a mesokarst unfriendly to ruminants, creating a feedback of grazing avoidance, tall grass and treacherous footing.

In contrast, the recessive trail-laden *Gruis Fm* (Hedberg, 1979; Hoffman and Halverson, 2008) is a 90–140-m-thick stack of sub-meter-scale peritidal cycles (parasequences) riddled with subaerial exposure surfaces. It weathers to fine gravel as its name implies in Afrikaans. Most cycles are couplets of marly dolomite ribbonite (Table 4) overlain by beige or pinkish dolomite microbialaminite with supratidal tepees. On Huab and Makalani dip-slopes (Fig. 5), interpreted as rift-shoulder uplifts (Hoffman and Halverson 2008), Gruis Fm oversteps the offlapping Rasthof Fm and directly onlaps crystalline basement. In both areas, Gruis Fm changes in facies from coastal-marine carbonate to alluvial conglomerate and sandstone, with decameters of buried relief on the basement erosion surface. These dramatic facies changes take place within ~15 km across depositional strike in Tr6 (Huab ridge) and Tr7 (Makalani ridge). Gruis Fm records the last episode of rift-shoulder uplift in the platform area of Kunene Region (Hoffman and Halverson, 2008). Crustal stretching may have continued longer in OML (Bechstädt et al., 2018), although $\delta^{13}\text{C}$ data are needed to test the correlation of “Auros shale” units on which their interpretation hinges. In Kunene Region, crustal stretching and block rotations continued into Marinoan time in the distal FSz (Soutput subbasin of Tr1, Hoffman et al., 2017b) and Bz (Tr3, Hoffman et al., 2018).

Ombaatjie Fm (Hoffmann and Prave, 1996; Halverson et al., 2002; Hurtgen et al., 2002; Hoffman and Halverson, 2008) is a cliff-forming 100–300-m-thick aggradational stack of shoaling-upward carbonate-dominated cycles. The cycles are >20x thicker (10–40 m) than those in Gruis Fm. The lower half of the formation (cycles b1–3) is dominated by cliff-forming ooid-intraclast limestone grainstone with patchy secondary dolomite. The upper, more-dolomitized half of the formation (cycles b4–8) has thinner (10–20 m) cycles, more commonly capped by intertidal microbialaminite. Argillite occurs at the bases of many cycles throughout the formation, and mature marine quartzarenite beds occur locally, notably at the base of cycle b4 suggesting minor reactivation of Makalani ridge. Mounded *Tungussia*-type stromatolites and enigmatic beds of Fe-rich carbonate intraclast-packstone (Dunham, 1962) occur widely in the two youngest cycles (b7 & 8), which correspond to the descending and ascending legs respectively of the Trezona CIE Cn5 (Figs. 1A & 10D) (Halverson et al., 2002, 2005; Tziperman et al., 2011). A Marinoan glacial trough cuts out cycle b8 and part of b7 in Tr8 and the south end of Tr9. A possible carbonate aeolianite forms the top of Ombaatjie Fm locally near the platform edge in Tr6.

Swakop Group is the off-shelf equivalent of Otavi Group and the distinction increases up-section. This necessitates independent stratigraphic nomenclatures for post-Chuos formations (Fig. 6B–C). Directly overlying Chuos Fm in Swakop Group are dark-grey dolomite rhythmite and microbialaminite, locally with rollups and stromatolites, lithologically similar to lower Rasthof Fm (Ar1 & 2) of Otavi Group. The upper Rasthof Fm grainstone (Ar3) becomes indistinct down-slope and the terminal sequence boundary disappears. The lower-Rasthof-type facies in Swakop Group are similar to those that define Berg Aukas Fm in OML (Fig. 6E). Rather than define a new formation, we extend Berg Aukas Fm to include its 2–200-m-thick stratigraphic and lithological correlatives in Tr1–5 (Fig. 6B–C). It is there overlain by a distally-tapered carbonate wedge named *Okonguari Fm* in Northern (Outjo) zone NE of Tr3 (Clifford, 1967, his Table 2, see also Miller, 2008b, p. 13–145–148). The wedge grades from dolomite grainstone with stromatolites proximally, to limestone turbidites distally. Its maximum thickness is 1320 m in Tr5.

Most proximally, Okonguarri Fm underlies Ombaatjie Fm, which is cut out basinward by lowstand Marinoan glacial erosion. Distally, Okonguarri Fm is conformably overlain by *Narachaams Fm* (Fig. 6B–C), which consists of argillite with siltstone- and dolomite turbidites. Formerly defined as a member of Ombaatjie Fm (Hoffman and Halverson, 2008), it is here promoted to formation rank as an easily mappable unit. Also promoted in rank is the overlying *Franni-aus Fm* (Hoffman and Halverson, 2008), a coarsening-upward turbidite-debrete sequence that is interpreted as a glacioeustatic falling-stand wedge and harbinger of Marinoan glaciation (Hoffman, 1999, 2011a). It preserves the ascending arm of the Trezona CIE Cn5 (Figs. 1A & 10D), which is physically linked to Marinoan glaciation in the type Trezona Fm of South Australia by ice rafted debris (Rose et al., 2012, 2013). Tr5 (Transfontein Ridge) receives twice the rainfall of Tr2, with the result that recessive units like Narachaams Fm tend to be armoured by calcrete, as well as by calcrete-loving thorn bushes (*Acacia mellifera*), whose delicate foliage hides razor-sharp bidirectional ‘claws’.

1.4.5. Tsumeb Subgroup

Tsumeb Subgroup (Hedberg, 1979; SACS (South African Committee for Stratigraphy), 1980; King, 1994; Miller, 2008b) begins at the sub-Ghaub Fm Marinoan glacial disconformity, and ends at the disconformity beneath Kuiseb Fm (Fig. 6B) or Mulden Group (Fig. 6C–E). Marinoan glaciomarine deposits of *Ghaub Fm* form an ice grounding-zone wedge in the upper FSz (Domack and Hoffman, 2011) and taper downslope into Outjo basin (Bz). The grounding-zone wedge consists of intertongued massive (ice proximal) and stratified (ice distal) carbonate diamictites with a peak thickness of 0.60 km. Ghaub Fm is absent from OPz but reappear as discontinuous lodgement tillites in IPz. The Marinoan glacial surface is easily recognized everywhere across the platform because it is directly overlain by a syndeglacial ‘cap’ dolomite, the distinctive Keilberg Mb in Maieberg Fm (Hoffmann and Prave, 1996; Hoffman et al., 2007; Hoffman and Halverson, 2008; Hoffman, 2011a). *Keilberg Mb*, a pale buff-weathering, pinkish-tinted, laminated doloparenite (Folk, 1959), is recognizable in all zones and has shallow-water features (sorted peloids, giant wave ripples, swaley crossbedding) in FSz as well as on the platform, implying diachroneity on the time scale of post-Marinoan sea-level rise (Hoffman et al., 2007; Yang et al., 2017).

The Ediacaran Otavi Group consists of Maieberg, Elandschoek and Hüttenberg formations (Fig. 6D–E). Collectively, they are 0.75 km thick in Tr8–9, 1.61 km in Tr10, and 2.02 km thick in Tr11 and OML. The 0.2–0.4-km-thick *Maieberg Fm* is a single depositional sequence, while the younger and thicker *Elandschoek* and *Hüttenberg* formations are stacks of m-scale peritidal cycles (parasequences). Relative to background tectonic subsidence, Maieberg and Elandschoek–Hüttenberg formations represent “catch-up” and “keep-up” stages, respectively. The “catch-up” reflects sudden deep flooding of the platform during Marinoan deglaciation, following a prolonged glacial period of post-rift thermal subsidence without compensatory sediment accumulation (Hoffman et al., 1998a, b). Keilberg Mb is the TST of the post-Marinoan depositional sequence (Maieberg Fm). It has a sharp base and a gradational top, passing upward into deeper-water lithofacies (rhythmite, Table 4) of middle Maieberg Fm member Tm2. Keilberg Mb is thickest (≤ 130 m) in OPz and thinner in glacial troughs in IPz and in Swakop Group. It hosts unusual sedimentary structures, including ‘tubestone’ stromatolite (Cloud et al., 1974; Hegenberger, 1987; Corsetti and Grotzinger, 2005; Santos et al., 2021), giant wave ripples (Allen and Hoffman, 2005a; Hoffman and Li, 2009) and cymbal-shaped sedimentary volcanoes. The overlying, deeper-water, maximum-flooding stage of Maieberg Fm is notable for proliferation of sea-floor cement (pseudomorphosed-aragonite crystal fans), which is localized on paleobathymetric highs on the upper FSz, outermost OPz and the rims of glacial troughs in IPz. This points to enhanced vertical mixing in the water column as favouring benthic carbonate production.

In Swakop Group, the Maieberg–Elandschoek–Hüttenberg division of Ediacaran strata can only be recognized chemostratigraphically

(Halverson et al., 2005; Hoffman, 2011a). Combined in *Karibib Fm* (Fig. 6B–C), they form a distally tapered wedge of carbonate rhythmite and rhythmite-clast debrite (Table 4). Karibib Fm is generally dolomitized, but in Tr3 and to the NE in Northern zone (Clifford, 2008) it is preserved as limestone. A basal dolomite equivalent to Keilberg Mb is generally present, as is a directly overlying marly interval corresponding to the maximum flooding stage of Maieberg Fm. The Keilberg Mb in Swakop Group is characterized by crumpled sheet cracks filled by fibrous-isopachous dolomite cement (Kennedy et al., 2001b; Hoffman et al., 2002; Hoffman and Macdonald, 2010). Locally in Tr5, Keilberg Mb contains giant wave ripples (Hoffman et al., 2007), the only wave-generated structures in distal FSz at any stratigraphic level and a testament to the magnitude of net Marinoan sea-level fall, even at the glacial termination when global ice volume was smallest in the snowball state (Abbot et al., 2013; Benn et al., 2015). In Karibib Fm as a whole, intraclast debrite coarsens stratigraphically upward, apparently in response to aggradational steepening rather than progradation of the foreslope, for which there is little evidence (e.g., upper Otavi Group overlying lower Swakop Group).

1.4.6. Kuiseb Fm and Mulden Group

Destruction of Otavi/Swakop Group carbonate platform was unanticipated and irreversible. The platform was briefly raised above sea level before collapsing southward and westward into deep troughs (foredeeps). The troughs filled up with great thicknesses of synorogenic clastic deposits (Kuiseb Fm and Mulden Group) as the trough axes progressed onto Congo craton in advance of the Northern zone (Fig. 2H) and Kaoko orogenic belts. Thrust sheet by thrust sheet, mass was transferred kinematically from the lower (Congo) plate to the overriding orogenic plate(s).

Although Otavi Group and clastics of Mulden Group (Fig. 6C–E) are structurally conformable at map scale (Hedberg, 1979; Miller 1997), they are sharply separated by a karstic disconformity. The disconformity is most simply explained as a migrating flexural forebulge (Parsons and Molnar, 1976). Over most of Otavi fold belt (Fig. 4), this disconformity appears to have < 200 m of total stratigraphic relief (Hedberg, 1979). However, in the syntaxis or cusp where Northern zone and Central Kaoko zone intersect (Fig. 8A), karstic relief exceeds total Otavi Group thickness and basal Mulden Group clastics depositionally overlie the Orosirian (1.80–2.05 Ga) basement complex (yellow stars, Fig. 4). Megakarst paleochannels, some reoccupied by modern rivers (e.g., upper Huab River), have long been recognized in the area of Tr6 (Frets, 1969; Guj, 1974; Miller, 2008b), but the full depth (> 1.85 km) and grandeur of this Ediacaran megakarst landscape (Hoffman, 2021a) has perhaps been underestimated. In its day, it resembled the castellated topography at the dissected edge of the Miocene (Bertram Fm) gravel terrace around the famous Fingerklip (Rock Finger) NE of Tr4 (Fig. 8B), but 20-times higher. The inferred depth of the sub-Mulden Group karst valley system (Hoffman, 2021a) equals the maximum depth of the present Grand Canyon of Arizona (USA).

Stratigraphically coeval with megakarst development (i.e., post-Otavi and pre-Mulden), a coherent map-scale mass slide in Tr7 (Fig. 8B) moved 20 km westward (downslope) on a brittle detachment surface, later broadly folded, that ramps stratigraphically down-section westward from the top of Otavi Group in the hangingwall to the top of the basement in the footwall (Hoffman and Hartz, 1999; Hoffman et al., 2016b). The detachment is recognizable by 0.4 km of missing stratigraphy, at whatever level. It defines a series of ramps and flats with an overall average cut-off angle of 1.1° relative to the stratigraphic plane. A paleovalley filled by Mulden Group conglomerate, gently tilted by thick-skinned Kaoko-related folding, is cleanly incised across the detachment surface at a steep angle, demonstrating a pre-Mulden age for the detachment. In Tr4 and the Swakop Group belt extending NE (Fig. 8B), early (pre-folding) detachment surfaces with both normal (missing stratigraphy) and thrust (repeated stratigraphy) kinematics were directed southeastward (Clifford, 1962, 2008) toward the advancing Northern zone

orogenic belt. These structures postdate the local post-Karibib Fm clastics (Okaua Fm, Fig. 6B), which are deeper-water and likely older than the Mulden Group conglomerate in Tr7 (Braklaagte Fm, Fig. 6D) due to their more internal location and potential asynchronicity of the Outjo and Kaoko-related foredeeps. In both Tr4 and Tr7, early mass slides are associated with flexure of Congo lithosphere beneath advancing orogenic wedges (Northern zone and Kaoko belt). Heightened forebulge relief giving rise to coeval megakarst was imposed by the cusp geometry, assuming synchronous subduction in both belts (Hoffman, 2021a).

The oldest post-Karibib Fm clastics in Northern zone (Tr2-3) are *Kuiseb* and *Okaua* formations (Figs. 5 & 6B), which are deepwater quartz-mica schists with arenaceous turbidites, coarsening-upward deltaic(?) bodies of quartz-arenite, and local dolomite-chert olistostromes and olistoliths (Frets, 1969; Hedberg, 1979; Miller, 1980, 2008b; Clifford, 2008; Nascimento et al., 2016). Kuiseb Fm of Northern zone has long been placed in Swakop Group (SACS (South African Committee for Stratigraphy), 1980; Miller 2008b), originally because it was correlated with parts of upper Tsumeb Subgroup. However, $\delta^{13}\text{C}$ chemostratigraphy suggests that Karibib Fm is correlative with the entire Tsumeb Subgroup (Halverson et al., 2005; Hoffman and Halverson, 2008; Hoffman and Lamothe, 2019), implying a post-Otavi Group age for Kuiseb Fm (Table 4).

A map-scale band of calcite marble in Kuiseb Fm, unit D₂C (Frets, 1969), was named *Awahuab Mb* (Fig. 5) by Miller (2008b, p. 13–166). However, Nascimento et al. (2016) correlated this unit with Karibib Fm and inferred that the depositionally underlying Kuiseb schist was Cryogenian in age (their ‘Brak River Fm’). Consequently, Nascimento et al. (2016) were obliged to infer a thrust fault beneath the schist wherever it overlies Karibib Fm (e.g., Tr2, Fig. 8B), which it does nearly everywhere. We examined the depositional base of Awahuab Mb in separate areas where the contact is well exposed (on farms Driekrone 516 and Twyfelfontein 534), and found no diamictite (Ghaub Fm) or cap dolomite (Keilberg Mb), which serve to identify the base of Karibib Fm in Northern zone (Fig. 6B). Nor is there any negative $\delta^{13}\text{C}$ anomaly as normally occurs in basal Karibib Fm (CIE En1, Fig. 10D). Values of $\delta^{13}\text{C}$ are +2.6–5.4‰ (VPDB) in lower Awahuab Mb and decline up-section (SOI S2., samples P1600-01), opposite to the overall Karibib Fm trend. Therefore, we agree with Frets (1969) and Miller (2008b) that Awahuab Mb is post-Karibib in age, and that the depositionally underlying schist is Kuiseb Fm, not Cryogenian. Accordingly, there is no need (or evidence) for large-scale thrusting as postulated (Nascimento et al., 2016) where Kuiseb schist (depositionally) overlies Karibib Fm in Northern zone (Fig. 6B).

In the most distal FSz (Tr1), Kuiseb Fm is overlain unconformably (Frets, 1969) by Welkom Subgroup (Fig. 6C), which directly onlaps Otavi/Swakop Group northward (Fig. 5). Three formations make up Welkom Subgroup (Miller, 2008b, pp. 13-224–226). *Braklaagte Fm* consists of tabular-bedded greenish siltstone and fine-grained sandstone with wedges of dolomite-chert conglomerate and debrite derived from Karibib Fm, and more rarely conglomerate derived from basement and/or pre-Ediacaran Swakop Group. Braklaagte Fm occupies paleovalleys in the megakarst of Tr6, where conglomerate and debrite that buttress Otavi Group are named *Soutrivier Mb* (Miller, 2008b). Dolomite-clast conglomerate correlated with Braklaagte Fm fills a paleovalley incised across Ombonde detachment in Tr7 (Fig. 6D). *Renosterberg Fm* conformably overlies Braklaagte Fm in Tr1 and 6, and onlaps Otavi Group directly on megakarst highs and in Tr5 and 7 generally. It consists of reddish-brown weathering felspathic-lithic sandstone of fluvial origin. Large-scale crossbedding indicates SE-directed paleoflow (Hoffman and Halverson, 2008). Renosterberg Fm is 3.0 km thick in Tr7 with no top exposed (Fig. 8B). In Tr6, it is overlain by greenish thin-bedded siltstone of *Gaseneirob Fm*. In Tr10 and OML, fluvial sandstone of Mulden Group is named *Tschudi Fm* (Fig. 6D-E). The source of Renosterberg/Tschudi sandstone is uncertain. One possibility is southward-younging collisional orogeny in West Congo and Kaoko belts (e.g., Stanistreet et al. 1991). Another is collisional orogeny on the northern margin of Congo craton, which was underway in Cameroon by 0.62 Ga (Kamguia

Kamani et al., 2021).

In Eastern Kaoko zone (Tr9), Hüttenberg Fm is overlain disconformably by *Sesfontein Fm* (Fig. 6D), which consists of greenish-grey phyllite with arenaceous turbidites and local dolomite-chert olistostromes and olistoliths. This assemblage attains great thickness in Warmquelle syncline (Fig. 8A), where it lithologically resembles Kuiseb Fm but overlies Otavi Group rather than Swakop Group. Sesfontein Fm could be younger than Kuiseb Fm (Fig. 5), depending on the relative age of Kaoko- and Outjo-related foredeeps. Sesfontein Fm is included in Mulden Group (SACS (South African Committee for Stratigraphy), 1980).

1.5. C-isotope record

The composite carbonate C-isotope record for Otavi Group (Fig. 10D) is broadly similar to correlative Neoproterozoic platformal successions in northwestern Canada, Arctic Europe, South Australia and western Mongolia (Fig. 1A). Broad positive anomalies ($\delta^{13}\text{C} \geq +5\text{‰ VPDB}$) are punctuated by relatively sharp negative excursions (e.g., Halverson and Shields-Zhou, 2011; Bold et al., 2016; Halverson et al., 2018b). In this work, we will demonstrate that these features are regionally reproducible. We will document isotopic gradients across the platform, both positive and negative, and will suggest that certain gradients result from diachroneity, some reflect synoptic paleoenvironmental variability, and others are products of spatially variable modes of porewater-controlled diagenesis. We will elaborate on the inference that seawater-buffered dolomitization tends to destroy CIEs and not produce them (Hoffman and Lamothe, 2019; Bold et al., 2020).

For brevity and simplicity, we number the $\delta^{13}\text{C}$ excursions (CIEs) according to geologic Period, with odd numbers for negative excursions and even numbers for positive anomalies (Fig. 10D). We number the Cryogenian (Cn1, Cn2, etc.) and Ediacaran (En1, En2, etc.) CIEs from the base of the respective cap-carbonate sequence—there is no $\delta^{13}\text{C}$ record of seawater during Cryogenian glaciations on account of progressive ocean acidification and resulting absence of marine carbonate production (Higgins and Schrag, 2003; Le Hir et al., 2008; see section 2.5.3. for discussion of purported synglacial carbonate cement in Ghaub Fm). Since the base of the Tonian is absent, we number the Tonian CIEs (Tn1–1, Tn2–2, etc.) downward from the base of the Chuos Fm in Tr2 (Fig. 10D).

In total, there are 6 positive and 7 negative CIEs in Otavi Group. Certain of them have been named and correlated globally (Fig. 1A): Tn-5, Bitter Springs CIE (Halverson et al., 2007); Tn-3, Russoya CIE (Halverson et al., 2018a); Tn-2, Coppercap CIE (Strauss et al., 2015; Crockford et al., 2021); Tn-1, Garvellach CIE (Fairchild et al., 2018); Cn1, Twitya CIE (Kaufman et al., 1997); Cn3, Taishir CIE (Johnston et al., 2012); Cn4, Keele CIE (Kaufman et al., 1997); Cn5, Trezona CIE (McKirdy et al., 2001); En1, Maieberg CIE (Halverson et al., 2005); En4, Hüttenberg CIE (Cui et al., 2018).

Organic contents of Otavi Group carbonate rocks are low, generally $\leq 0.2\text{ wt\% TOC}$ (Cui et al., 2018). The $\delta^{13}\text{C}_{\text{org}}$ of outcrop samples shows little variation or covariation with $\delta^{13}\text{C}_{\text{carb}}$ (unpublished data), suggesting contaminant organic matter. We therefore present no organic C isotope data. Organic matter may have been destroyed by topographically driven groundwater flow during late Ediacaran-Cambrian orogeny, responsible for virtually complete destruction of primary remanent magnetization in Damaran sedimentary rocks (Evans, 2000).

1.6. Radiometric and paleomagnetic constraints

1.6.1. U-Pb chronostratigraphy

We calibrate the depositional chronology of the Otavi Group (Fig. 10A-B) with internal U-Pb zircon ages (Fig. 5) from associated igneous rocks (Hoffman et al., 1996; Halverson et al., 2005; Nascimento et al., 2016; Prave et al., 2016), and from external age constraints from low paleolatitudes on Sturtian (717–661 Ma) and Marinoan

(645 ± 5 –635 Ma) glaciations (Rooney et al., 2015, 2020a; Macdonald et al., 2018; Zhou et al., 2019; Lan et al., 2020; Nelson et al., 2020). Synchronicity of Cryogenian glaciation and deglaciation at low paleo-latitudes is an empirically supported consequence of planetary ice-albedo bifurcation (Hoffman et al., 2017a, and references therein). We take 600 Ma as the age of Otavi/Swakop Group destruction by foredeep flexure and burial, based on earliest dynamo-thermal metamorphism in Northern (Outjo) and Central Kaoko zones of 600–590 Ma (Lehmann et al., 2015) and ~ 580 Ma (Seth et al., 1998; Goscombe et al., 2005), respectively.

An upper intercept age of 759.3 ± 1.3 Ma (Halverson et al., 2005) was calculated from U–Pb (IDTIMS) analyses of eight zircon grains selected from a 15-cm-thick volcanic ash (bentonite) layer in upper Devede Fm (Ombombo Subgroup), 16 m below the base of the Okakuyu Fm (Fig. 6D). The weighted mean $^{207}\text{Pb}/^{206}\text{Pb}$ age of the grains is 759.95 ± 0.86 Ma, which is considered the best estimate of the age of the zircons and inferentially the ash bed (Halverson et al., 2005). The sample was collected in the IPz at $-18.8836^\circ/13.7967^\circ$, between the N end of Tr9 and SE end of Tr11 (Fig. 8B). A second 10-cm-thick bentonite, 1.5 m stratigraphically higher at the same location, was sampled but has not been processed.

In the allochthonous Summas Mountains inlier of Tr3 (Fig. 8B), a U–Pb (IDTIMS) upper intercept age of 746 ± 2 Ma (Hoffman et al., 1996) was obtained from three concordant and one discordant zircon fractions separated from a welded ash-flow tuff in the middle part of the ≥ 6.6 -km-thick Lower Naauwpoort Fm (Miller, 1980), sampled at $-20.492^\circ/15.292^\circ$ on farm Renosterkop 389. The date provides a maximum constraint on the depositionally overlying Okotjize Fm (Ugab Subgroup, Fig. 6B).

In Tr4 directly north of the Summas Mountains (Fig. 8B), a U–Pb (IDTIMS) upper intercept age of 747 ± 2 Ma (Hoffman et al., 1996) was obtained for five zircon fractions, one concordant, that were selected from a spherulitic, feldspar-phyric, massive to flow-banded, rhyolite lava in Upper Naauwpoort Fm (Miller, 1980). The lava is downward facing at the sample site ($-20.4771^\circ/15.2904^\circ$ on farm Renosterkop 389), but is depositionally overlain by downward-facing basement-clast diamictite of Chuos Fm (Hoffman and Halverson, 2008). The age provides a minimum constraint on the age of the underlying Austerlitz Fm (Fig. 6B).

The Oas peralkaline quartz-syenite is a rift-related stock in the southwest of Welwitschia inlier in the FSz (Fig. 8A). It intrudes both crystalline basement and feldspathic arenite of Austerlitz Fm (Fig. 6B), and is overlain nonconformably by lower Swakop Group (Frets, 1969). One multi-grain and three single-grain fractions of zircon were analyzed by IDTIMS from a sample collected at $-20.3621^\circ/14.7257^\circ$ on farm Oas 486. All grains were concordant with a weighted mean $^{207}\text{Pb}/^{206}\text{Pb}$ age of 756 ± 2 Ma (Hoffman et al., 1996), providing a minimum age constraint for Austerlitz Fm in that area.

An indistinguishable U–Pb (SHRIMP) zircon age of 757 ± 5 Ma (Nascimento et al., 2016) was obtained for a “dacite sill from the Naauwpoort Formation intercalated at the base of the Chuos Formation” on farm Austerlitz 515 in the NDz south of Tr1 (Fig. 8B). They describe the age as a “minimum age for deposition of the base of the Chuos Formation” (Nascimento et al., 2016). It should be borne in mind that those authors do not accept a glacial or periglacial origin for either Chuos or Ghaub formations (Nascimento et al., 2018). Their stratigraphic limits for those formations are therefore bound to differ from ours, and from those recommended by SACS (South African Committee for Stratigraphy) (1980). As a minimum constraint on glacial onset, the 757 ± 5 Ma age (Nascimento et al., 2016) would conflict with the 746 ± 2 and 747 ± 2 Ma maximum age constraints from Lower and Upper Naauwpoort formations (Hoffman et al., 1996), and with the 759.95 ± 0.86 Ma maximum constraint from upper Devede Fm (Halverson et al., 2005). We remapped the area around the dacite dated by Nascimento et al. (2016)—near $-20.4573^\circ/14.4561^\circ$ on farm Austerlitz 515—which we interpret to be a crystal-rich welded ash-flow tuff with associated

chlorite schist. In a set of ENE-plunging folds, these volcanic rocks are overlain with apparent disconformity by a ≥ 75 -m-thick sequence of quartz-pebble conglomerate, orange and grey dolomite, and oligomictic carbonate-clast debrites. This latter sequence is disconformably overlain in turn by poorly stratified diamictite, in which subrounded clasts of dolomite and basement-derived granodiorite are dispersed in a matrix of schistose metagreywacke. We interpret the polymictic diamictite as the Chuos Fm (SACS (South African Committee for Stratigraphy), 1980) and the 757 ± 5 Ma dacite age as a maximum (not minimum) constraint on glacial onset, consistent with other chronometric constraints from Kunene Region (Fig. 10A) and globally (Macdonald et al., 2010a, 2018; Lan et al., 2014, 2020; Cox et al., 2015; Song et al., 2017; MacLennan et al., 2018). Importantly, the 757 ± 5 Ma age (Nascimento et al., 2016) shows that volcanism in allochthonous Northern zone on Austerlitz farm was indistinguishable in age from the autochthonous Oas quartz-syenite in Welwitschia inlier, and significantly older than the peralkaline Summas Mountains volcanic centre (Naauwpoort Fm) in Tr3-4, 90 km to the East.

1.6.2. Paleomagnetic constraints

There are few reliable paleomagnetic constraints for the Congo craton during Otavi Group time (Evans and Raub, 2011). Meert et al. (1995) obtained paleomagnetic poles at $46^\circ\text{N}/325^\circ\text{E}$ ($\alpha_{95} = 09^\circ$) from the 748 ± 6 Ma (Mbede et al., 2004) syenitic phase of the Mbozi igneous complex in southern Tanzania, and $29^\circ\text{S}/319^\circ\text{E}$ ($\alpha_{95} = 05^\circ$) from the 547 ± 4 Ma Sinyai dolerite in NW Tanzania. The late Tonian (Mbozi) pole places the present south-facing margin of the Otavi Group carbonate platform at $\sim 10^\circ$ paleolatitude, facing the paleoequator (Fig. 11). It is generally assumed to have lain in the southern hemisphere (Evans, 2000; Trindade and Macouin, 2007; Pisarevsky et al., 2008; Li et al., 2013; Zhang et al., 2013; Merdith et al., 2017a, b, 2019) and this is supported in Otavi Group by persistent westward-directed (left-turning) contourites (e.g., starved current ripples) in Rasthof and Ghaub (Bethanis Mb) formations in FSz (Hoffman and Halverson, 2008; Hoffman, 2011a). A subequatorial location is consistent with the carbonate-rich facies, given that a continental promontory (Fig. 2A) would be relatively free from direct riverine input.

The Sinyai dolerite paleopole suggests that the Otavi platform rotated $\sim 50^\circ$ clockwise and retreated to the southern mid-latitudes by late Ediacaran time. Strict application in Namibia of the Tanzanian paleomagnetic constraint depends on a torsionally rigid Congo craton, which is somewhat questionable for the Sinyai dolerite pole, since Pan-African orogenesis was underway by 547 ± 4 Ma. Poleward migration of Otavi platform to $\sim 55^\circ\text{S}$ by 600 Ma (Fig. 11G) (Merdith et al., 2017a, b, 2019) is questionable considering that carbonate production continued unabated until that time (Fig. 10A).

1.7. Carbonate rock classification and presentation in columnar sections

Our field classification scheme for neritic (0–200 m paleowater depth) carbonate lithofacies (Table 4) was adapted for use in naturally weathered outcrops. It is not well suited for drill-core or unweathered quarries and roadcuts. In the text, grain-scale characteristics are described using a terminology that is an amalgam of Folk (1959) and Dunham (1962), the former for grain types and the latter for texture and inferred depositional regime. We use ‘grainstone’ (Dunham, 1962) rather than ‘arenite’ (Folk, 1959) for thick-bedded, well-sorted, sand-to granule-size sediment when referring strictly to carbonate (Table 4). ‘Microbialaminite’ is modified after ‘cryptalgalaminite’ (Aitken, 1967) and refers to low-relief microbial mat-mediated laminated deposits with inter- or supratidal indicators (e.g., ‘tepees,’ Kendall and Warren, 1987). ‘Stromatolite’ (Kalkowski, 1908) refers to microbially laminated structures with synoptic relief ≥ 5 cm, typically columnar, branching or mounded. Stromatolite and grainstone commonly co-occur. ‘Ribbonite’ (Halverson et al., 2002) is a wavy thin-bedded (≤ 0.2 m) lutite (mudrock) or fine grainstone with low-angle cross-strata or bedforms

such as wave ripples or starved ripples indicating wave action or traction currents. ‘Rhythmite’ (Bramlette, 1946) refers to parallel-laminated micrite or marlstone (argillaceous carbonate) in which wave or traction-current bedforms are absent, but gravitationally emplaced turbidites or debrites may or may not be present.

These five lithofacies classes (Table 4) are typically intergradational when juxtaposed as shown in the Table (e.g., ribbonite over rhythmite or rhythmite over ribbonite). The vertical sequence (Table 4) is one in which relative water depth increases downward. The Tonian of Swakop Group and all of Otavi Group are built of stacked regressive (shoaling-upward) subcycles bounded by disconformities or marine flooding surfaces, overlain by condensed transgressive (deepening-upward) subcycles. The middle Cryogenian and Ediacaran of Swakop Group on the growing bathyal (200–3500 m paleowater depth) foreslope, consist of rhythmite with upward-coarsening sets of turbidites and debrites, suggestive of stochastic sediment lobe dynamics.

We present our measured sections graphically as columnar sections using a consistent colour scheme and symbology, wherever possible, as illustrated in Fig. 12. Calcite or dolomite mineralogy is indicated as blue or orange vertical bars. Sections from which $\delta^{13}\text{C}/\delta^{18}\text{O}$ records were obtained (SOI S1. & S2.) are indicated by green dotted lines. Distinct colours and symbols are used for Sturtian and Marinoan cap-carbonate sequences (Fig. 12) because of their uniqueness and unusual structures. The facies tabs project widthwise according to relative water depth (carbonates) or grain size (terrigenous). The uneven edge faces seaward or downslope. Subaerial exposure and flooding surfaces are indicated by symbols (Fig. 12) on the even side of stratigraphic columns.

Glacigenic facies are classed as massive (including sheared) diamictite, stratified diamictite, or rhythmite and ribbonite with ice-rafterd limestones. Most (but not all) ‘massive’ diamictites are ice-contact deposits. ‘Stratified’ diamictites accumulated under an intervening water column. They are heterogeneous assemblages including laminated suspension-plume fall-out rich in ice-rafterd debris (IRD), grainstone and/or ribbonite with limestones, and turbidites and/or debrites lacking unworked IRD. Primary division into ‘massive’ and ‘stratified’ deposits goes back to the earliest studies of glacial sediments (Smith, 1839; Lyell, 1840; de Charpentier, 1841). Marinoan ice grounding-zone deposits are crudely cyclic. Stratified diamictites grade upward into massive diamictite, representing ice grounding-line advances. Massive-to-stratified transitions are usually more condensed and locally associated soft-sediment disturbance suggests abrupt grounding-line retreats. More proximal massive diamictites have erosive bases and amalgamate, with channels of sorted meltwater-flow deposits. Successive diamictite bodies commonly differ in clast type, implying an ice sheet composed of multiple tributaries draining different bedrocks that respond non-uniformly to orbital or other forcing (Benn et al., 2015).

Columnar sections are aligned according to specified datums and arranged in lateral sequence along each transect or subtransect. Background colour shades indicate correlation of formations and members from section to section. Vertical scale bars are numbered in meters relative to the datum, and section locations are given in inset maps and/or separation distances in kilometres. Each fence diagram includes a lithofacies legend. Coordinates for sections with $\delta^{13}\text{C}/\delta^{18}\text{O}$ data are given in SOI S2. For want of space, formation and member names may be abbreviated according to the scheme in Table 5.

2. Eleven transects

The layout of transects (Fig. 8B) is dictated by Kamanjab inlier, a composite structural antiform produced by crustal shortening and lithospheric flexure related to the orthogonal Kaoko and Damara orogens (Goscombe et al., 2017). Transects are onlapped by Early Cretaceous cover of the Etendeka Group volcanic plateau (Fig. 4). Calcrete covers

recessive units in Damara Supergroup on the NE flank of Kamanjab inlier except in Tr10, which is erosionally dissected at the lip of the coastal escarpment by headwall erosion of Cenozoic Kalahari Group (Miller, 2008c) from within the U-shaped Omarumba (Carboniferous) glacial valley (Fig. 8A) (Martin, 1961, 1968).

Both the early Cryogenian (Sturtian) and late Cryogenian (Marinoan) glaciations—i.e., glacial-periglacial deposits, glacial disconformity and/or cap carbonate—can be clearly distinguished and mapped in all transects. Therefore, Otavi Group can be consistently divided into three periods and five epochs: (1) late Tonian, (2) early Cryogenian (=Sturtian), (3) middle Cryogenian (inter-snowball), (4) late Cryogenian (=Marinoan) and (5) early Ediacaran. The Cryogenian (Shields-Zhou et al., 2015) begins at the base of Chuos Fm and the Ediacaran (Knoll et al., 2006; Narbonne et al., 2012) at the base of Keilberg Mb in Maieberg Fm (Fig. 6). Because ice-albedo feedback is powerful at low latitudes, it is implausible that glaciations and deglaciations in Otavi/Swakop Group were not synchronous on a geological time scale with tropical coasts elsewhere. If a glacial origin for Chuos or Ghaub formations is rejected (Eyles and Januszczak, 2007; Nascimento et al., 2016, 2018), the age division (Table 1) falls apart. The fence diagrams in each transect remain, however, since their datums are locally defined.

Transects Tr1–6 border Damara orogen (Figs. 3 & 8B). Tr2 and 3 are within the Northern zone (NDz) and are structurally allochthonous, having been thrust NNW relative to Kamanjab inlier. Tr1, 4 and 5 are autochthonous and represent the FSz (Northern Margin zone of Miller, 2008b). Tr6 is also autochthonous and, along with the northeastern segment of Tr5, represents the OPz (Fig. 5).

Transects Tr7–11 border Kaoko orogen (Figs. 3 & 8B). Tr7 represents OPz and is autochthonous with respect to Kamanjab inlier. Tr8–11 represent IPz and all but Tr10 have been thrust eastward, relative to Kamanjab inlier, on a thin-skinned sole thrust at the base of Otavi Group. Tr10 could be the autochthonous backthrust in a frontal triangle structure of the eastward vergent thin-skinned thrust-fold belt, but Cenozoic (Kalahari Group) cover to the east prevents verification that Tr10 is autochthonous.

Certain of the larger thrust ramps in Tr9 are oblique, trending SSW–NNE, suggesting a resolved component of sinistral shear in the foreland thrust-fold belt. On the other hand, finite strain indicators in the sole-thrust zone are stretched W–E, nearly normal to strike. The magnitudes of thin-skinned displacement should increase from east to west, reaching ~65 km in Tr11 assuming 50% thin-skinned shortening. This shortening estimate is reasonable given tight folding and thrusting of Otavi Group, in which Nosib Group does not participate. Parts of Tr7 and Tr11 were displaced ~20 km westward on brittle, low-angle, normal-sense detachments interpreted as mass slides (mass transport complexes). Their timing associates sliding with lithospheric flexure (foredeep), just prior to tectonic shortening (Hoffman and Hartz, 1999; Hoffman et al., 2016b; Hoffman, 2021a).

2.1. Transect Tr1 – Aba-Huab autochthon

At the southwestern promontory or ‘heel’ of Kamanjab inlier (Fig. 8A), an arcuate panel of autochthonous Swakop Group carbonate links the Kaoko and Damara forelands (Frets, 1969). Nearly 40 km in length, the steeply dipping panel emerges from beneath the Etendeka volcanic onlap to the NW and disappears beneath synorogenic foredeep deposits of Welkom Subgroup to the E (Fig. 13). The panel (Fig. 14) is principally exposed on three farms, Opdraend 718, Bethanis 514 and Toekoms 508 from W to E. There is a 5-km-wide gap in the panel (Fig. 14) where the Swakop Group is cut out beneath a basement thrust at the Northern (Outjo) zone boundary. East of the gap, the picturesque Camp Xaragu, one of several restcamps in the immediate area, is conveniently located near the western closure of Bethanis synclinorium (Fig. 15). The E-plunging synclinorium is cut by three N-directed thrust-

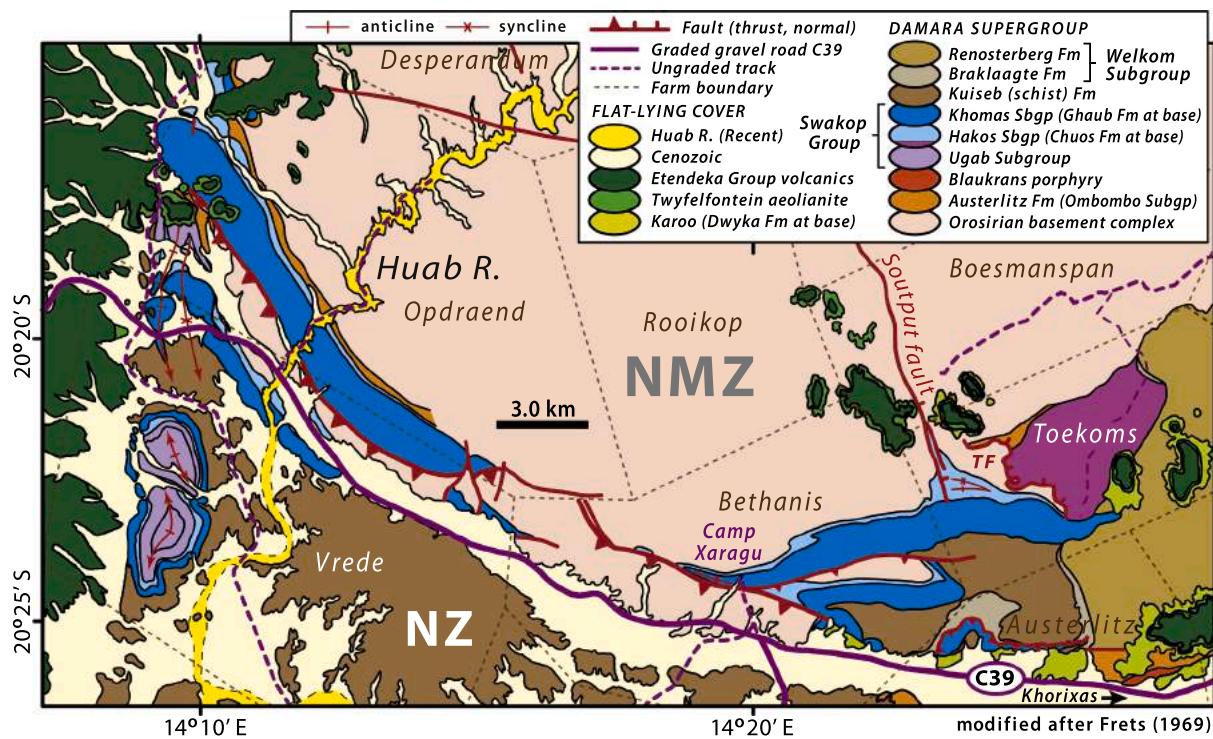


Fig. 13. Geology around southwestern lobe of Kamanjab inlier (Fig. 8A), modified after Frets (1969). Tilted and broadly folded Neoproterozoic rocks of Tr1 (Fig. 8B) are autochthonous or paraautochthonous with respect to Congo craton and belong to Northern Margin zone of Miller (2008b) and distal FSz in the Otavi/Swakop Group facies zonation. SW-dipping thrust (heavy bars) separates NMz from Northern Damara zone (NDz) of Miller (2008b). Structural domes exposing Swakop Group on Vrede farm at foot of Etendeka (plateau) in NDz make up Tr2 (Fig. 29). TBF, Toekoms border fault.

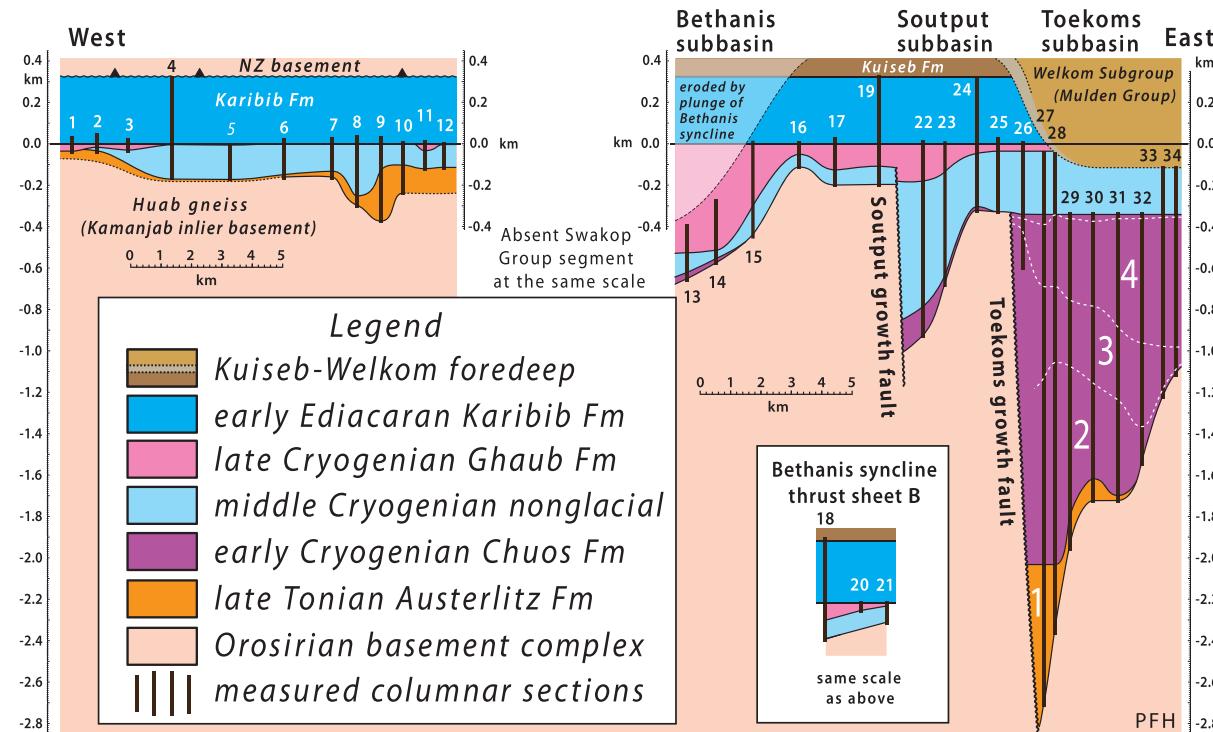


Fig. 14. Summary of Swakop Group stratigraphy and measured sections 1–1–34 in Tr1. See Figs. 15 & 27 (inset) for section locations. Datum (0.0 m) is basal Karibib Fm, which is also the base of Ediacaran Period. Note progressive westward younging of Toekoms, Soutput and Bethanis subbasins—early, middle and late Cryogenian respectively.

sheets, labelled B, C and D (Fig. 15), with A being autochthonous Kamanjab inlier. We interpret Kuiseb Fm and Welkom Subgroup as foredeep deposits (Hoffman, 2021a) of a diachronous trough that migrated cratonward, as it progressively filled, in front of the advancing thrust front (Fig. 16). The informal transect name Aba-Huab (Little Huab) derives from the westward-draining tributary to Huab River that

flows along the Karoo-age paleovalley directly S of Bethanis synclinorium (Fig. 16).

There are abrupt stratigraphic changes along strike in the eastern half of transect Tr1 (Fig. 14). Three subbasins formed progressively from E to W over time. Toekoms subbasin (sections 1–26–34) developed in late Tonian and early Cryogenian, Soutput subbasin (sections 1–22–25) in

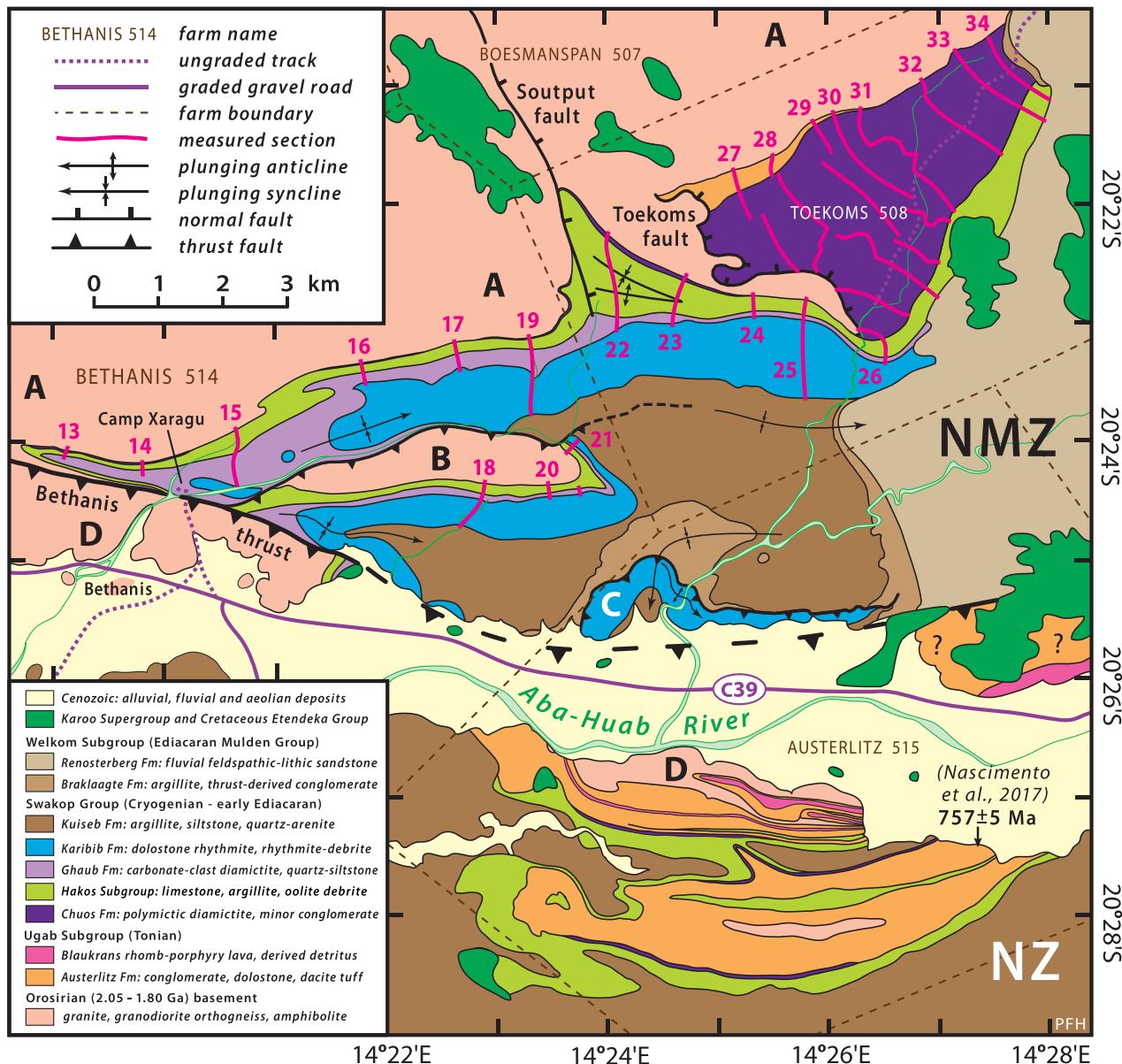


Fig. 15. Geology on parts of farms Bethanis 514, Austerlitz 515 and Toekoms 508 showing locations of sections 1–13–34 in eastern part of Tr1 (Figs. 8B & 13). Field guides are SOI S3.2., Bethanis subbasin (1–14–15); SOI S3.3., Soutput subbasin; and SOI S3.4., Toekoms subbasin. Soutput and Toekoms subbasins are bordered by middle and early Cryogenian growth faults respectively (Figs. 14, 18 & 22). Bethanis subbasin is preserved on the footwall of the Northern (Outjo) zone boundary thrust ('Bethanis Fault' of Frets, 1969), which carries basement labelled D in its hangingwall. Splay thrusts in footwall of Bethanis thrust are labelled B and C. Autochthonous (Kamanjab inlier) basement is labelled A. Swakop Group cover in A is similar to B (Fig. 14), and also to C where only Karibib (Fig. 21A & B) and Kuiseb (Fig. 21C & D) are exposed in a hangingwall anticline. Swakop cover in D is distinct from that in A–C. Braklaagte Fm (Welkom Subgroup) contains dolomite-chert conglomerate (Fig. 21E & F), apparently derived from hangingwall Karibib Fm of overriding thrust C. At E, dolomite-chert conglomerate is incised by younger orthogneiss-limestone conglomerate, apparently derived from Bethanis thrust. Braklaagte Fm is accordingly cogenetic with active thrusting at its southern preservation limit, consistent with foredeep basin model (Fig. 16). Kuiseb Fm was arguably folded before Braklaagte Fm was deposited (Frets, 1969), the resulting unconformity defining the Swakop–Mulden group boundary (SACS (South African Committee for Stratigraphy), 1980). However, multiple diachronous unconformities are expected at the active margins of collisional foredeeps. We prefer to consider Kuiseb Fm as the earliest foredeep deposits, with a forebulge disconformity between Kuiseb and Karibib Fms. This presents two alternative explanations for missing strata (i.e. Ghaub and Karibib formations) in the hangingwall anticlinorium (D) of Northern zone (NDz): (1) erosion during forebulge uplift (Fig. 16A), or (2) submarine mass-slide in response to plate flexure and seismicity on foredeep outer slope (Clifford, 2008; Hoffman and Hartz, 1999; Hoffman et al., 2016b; Ge et al., 2019).

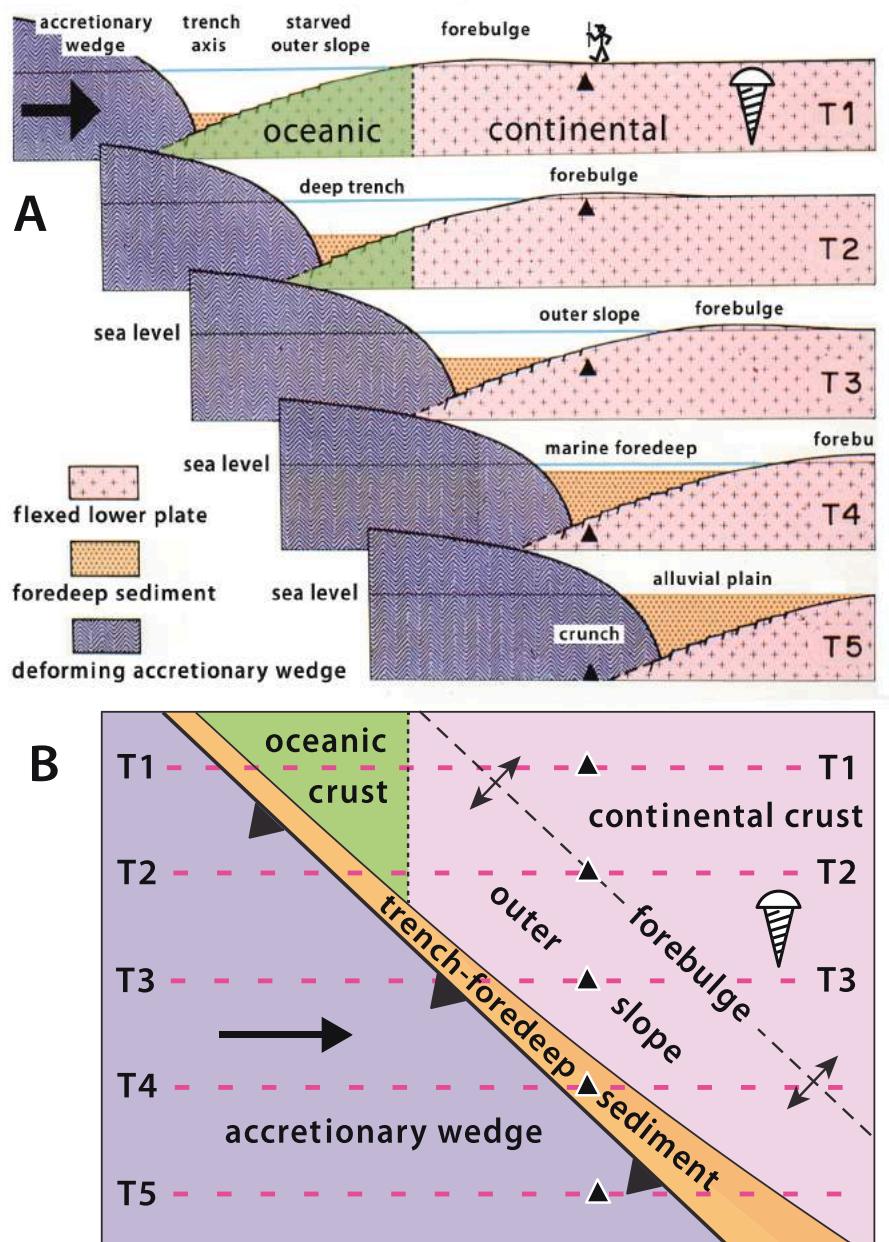


Fig. 16. Foredeep development (Hoffman, 1987) as a model for Kuiseb Fm and Mulden Group (Figs. 5 & 6) in northern Namibia: (A) Congo craton on right is fixed, while actively-accreting NDz and/or CKz on left converge with craton. Over time T1–5, foredeep fills with sediment delivered largely by axial transport with local contribution from actively deforming wedge or outer-slope normal faults in plane of section. Progression over time at any given location (e.g., black triangle) recapitulates transverse environmental zonation (Walther's law): T1, surface at sea level; T2, peripheral bulge crest; T3, starved outer slope; T4, foredeep depositional axis; T5, active tectonic shortening and thickening above a craton-directed sole thrust. Wedge deforms internally, so as to maintain critical wedge taper, and accretes through mass transfer from subducting craton. (B) Planform of oblique collision between an upper-plate accretionary wedge (brown) and a lower plate divided into continental (pink) and oceanic (green) crust and trench-foredeep sediment (orange). Forebulge and outer slope are indicated. Dashed red lines are transects at times T1–5, when black triangles correspond to situations at each time step identical to black triangles in A.

middle Cryogenian, and Bethanis subbasin (sections 1–13–19) in late Cryogenian (Table 1). The Soutput and Toekoms subbasins are localized by asynchronous, non-parallel, growth faults (Fig. 15). Soutput fault (Frets, 1969) has a strike of 345° and a straight trace, suggesting a steep dip. Toekoms fault (Fig. 15) has a strike of 300° and a sinuous trace, suggesting a shallow dip. When Swakop Group was steeply tilted during Damaran deformation, the growth faults were also rotated. The mean strike and dip ($n = 46$) of Swakop Group in the Toekoms subbasin is 040/46. If the fault planes are co-rotated by 46° around the Swakop Group strike, which restores bedding to horizontal, Toekoms fault restores to a Damara-parallel strike of ~255° and a cratonward dip of ~57° beneath Toekoms subbasin (Fig. 17). Soutput fault restores to a Kaoko-parallel strike of ~335° and a cratonward dip of ~60° beneath Soutput subbasin (Fig. 17). The significance of these and alternative fault-plane restorations is discussed near the ends of sections 2.1.3, and 3.6.4.

2.1.1. Bethanis subbasin (sections 1–13–19)

This is the most accessible of the subbasins and offers the best

introduction to the overall stratigraphy of this transect. A field guide is provided in SOI S3.2., including geologically annotated satellite images in Fig. S2. Swakop Group is preserved in a composite E-plunging synclinorium (Fig. 15). The synclinorium is truncated on the south by Bethanis thrust (D in Fig. 15), defining the northern limit of Northern zone (NDz). In the synclinorial axis, a splay thrust carries a basement-cored N-facing anticline (B in Fig. 15) of Swakop Group that closely resembles the adjacent autochthonous panel (A in Fig. 15) in stratigraphy and facies (Fig. 14). A smaller splay thrust on the south limb of the synclinorium (C in Fig. 15) carries a N-facing anticline of Karibib Fm structurally over dolomite-chert-clast conglomerate of Braklaagte Fm. Karibib Fm in thrust-sheet C is disconformably overlain by S-facing siltstone of lower Braklaagte Fm with a basal sandy dolomite-clast debrite (Fig. 20 in Frets, 1969; Hoffman and Halverson, 2018).

Cryogenian stratigraphy of Bethanis and Soutput subbasins is depicted in a W–E fence diagram (Fig. 18) and the entire Swakop Group is summarized in a composite section from Bethanis subbasin (Fig. 19). A composite section is necessitated by the plunge of the synclinorium.

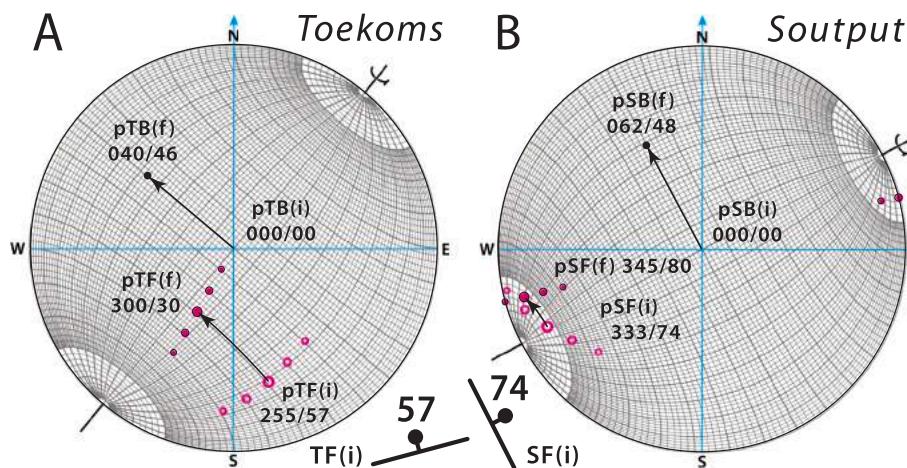


Fig. 17. Stereonets showing rotations of poles-to-bedding of originally horizontal strata to their final (present) orientations in (A) Toekoms subbasin (pTB(f)) and (B) Soutput subbasin (pSB(f)), and co-rotations of poles to the respective boundary faults (magenta) from their initial (pTF(i) and pSF(i)) to final orientations (pTF(f) and pSF(f)). Final bedding orientation of 040/46° in A is the average strike-and-dip of bedding ($n = 46$) within Toekoms subbasin. Final bedding orientation of 062/48° in B is the average strike-and-dip ($n = 13$) of basal Swakop Group strata in Bethanis and Toekoms subbasins (1–14–19 and 27–34, Fig. 15). The restored orientation of Toekoms boundary fault (pTF(i)) of 255/57°, assuming a final orientation of 300/30° (pTF(f)), is consistent with a cratonward-dipping normal fault parallel to Northern zone. The restored orientation of Soutput boundary fault (pSF(i)) of 333/74°, assuming a final orientation of 345/80° (pSF(f)), is oblique to Kaoko belt and more steeply inclined than is characteristic of normal faults. Its orientation is, however, consistent with that of splay faults at rift-transform junctions (Tibaldi et al., 2016).

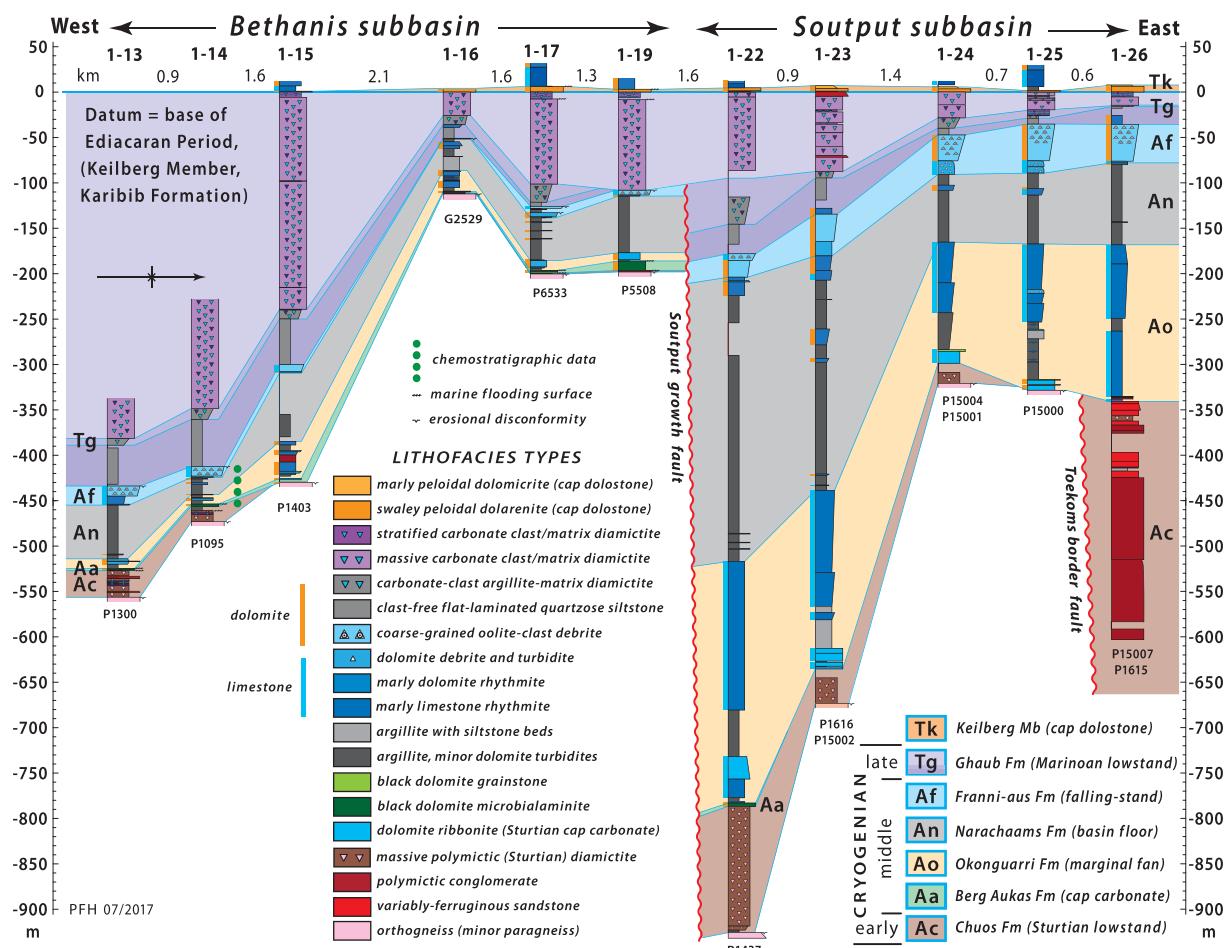


Fig. 18. Lower Swakop Group columnar sections 1–13–26 from autochthonous Bethanis and Soutput subbasins in Tr1. See Fig. 15 for section locations. Datum (0.0 m) is base of Ediacaran Karibib Fm (Keilberg Mb). Soutput growth fault was active from late Sturtian until early Marinoan, peaking in middle Cryogenian. Additional sections between 1 and 19 and 1–22 are needed to validate the stratigraphic age of fault cessation. Toekoms growth fault was most active in early Cryogenian. If a growth fault formerly bordered the Bethanis subbasin, it would have been most active in late Cryogenian (Fig. 14).

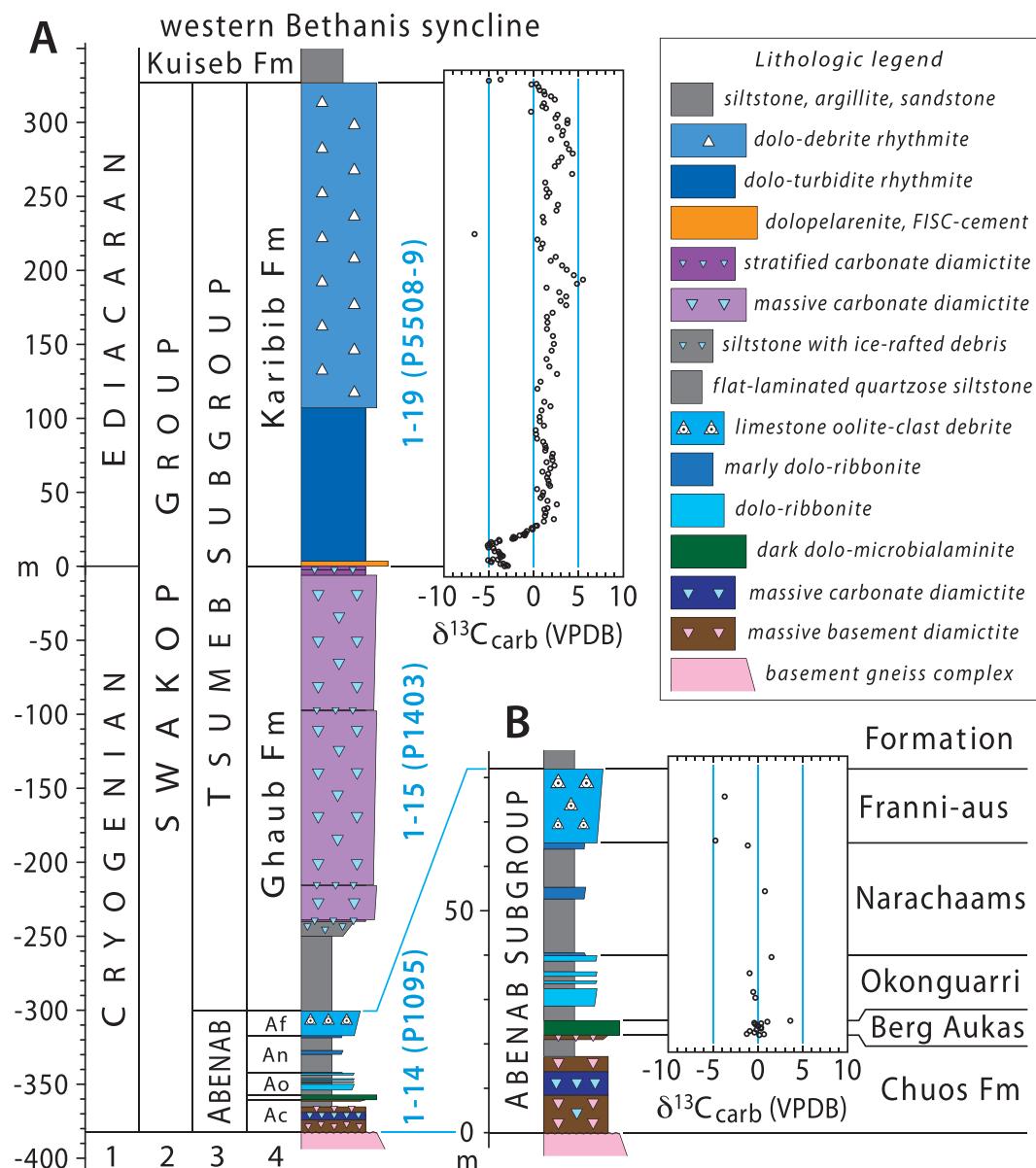


Fig. 19. (A) Swakop Group composite columnar section and $\delta^{13}\text{C}$ data from Bethanis subbasin, combining 1–14 (Abenab Subgroup), 1–15 (Ghaub Fm) and 1–19 (Karibib Fm). See Fig. 15 for section locations. Datum (0.0 m) is base of Ediacaran and Karibib Fm (Keilberg Mb). See (B) for Abenab Subgroup formation names. (B) Expanded columnar section and $\delta^{13}\text{C}$ data for Abenab Subgroup, which includes all strata between subglacial disconformities beneath early Cryogenian Chuos and late Cryogenian Ghaub formations (Figs. 6 & 10). Chuos Fm includes both basement-derived and carbonate-derived diamictites, whereas Ghaub Fm is overwhelmingly carbonate-derived above the basal quartz-siltstone member (Tg_q, Fig. 20A), with rare basement clasts in carbonate diamictite (g, Fig. 20D). Abbreviation (lithologic legend): FISC, fibrous isopachous sheet-crack cement (Fig. 34E).

Sturtian Chuos Fm is limited in Bethanis subbasin to the westernmost sections 1–13–14 (Fig. 18). The glacial deposits unconformably overlie Orosirian orthogneiss and pegmatite that underwent Damaran greenschist-grade retrograde metamorphism. Above the unconformity are $\leq 34\text{ m}$ of bouldery polymictic diamictite with minor lenses of stratified pebble conglomerate and dropstone-bearing laminated argillaceous siltstone. The debris is mainly derived from the basement but most diamictite bodies include a small fraction of sedimentary (dolomite and sandstone) material and a few are composed entirely of detrital carbonate, matrix and clasts. Since no pre-Sturtian carbonate is exposed in Tr1, or elsewhere in the FSz or OPz (Fig. 5), potential sources are limited to Ombombo Subgroup in IPz, $> 100\text{ km}$ to the north, or Ugab Subgroup of Northern zone (Tr2–3), which lay farther south before Damaran thrusting (Fig. 8A). A thin unit of stratified diamictite directly underlies the postglacial Berg Aukas Fm cap carbonate in sections 1–13

and 14 (Figs. 18 & 19B).

The non-glacial middle Cryogenian is represented by four formations (Fig. 6B–C)—Berg Aukas, Okonguarri, Narachaams and Franni-aus. The first is the post-Sturtian cap carbonate and the last is a falling-stand wedge leading into the Marinoan (Fig. 20A). Okonguarri and Narachaams formations represent ‘business as usual’ in FSz, which at that time was in the waning stages of crustal stretching in a fully marine setting.

Berg Aukas Fm, only $\leq 10.5\text{ m}$ thick in Bethanis subbasin (Figs. 18 & 19B), is lithologically distinctive, laterally continuous and has sharp lower and upper contacts. It is mostly dolomite but locally calcitic basally. It grades upward from grey-coloured rhythmite or ribbonite to charcoal-black microbialaminite with roll-ups. The basal contact, while sharp, appears conformable with stratified diamictite of the Chuos Fm where the latter is present. The top of Berg Aukas Fm is a sharp flooding

surface overlain by argillite of basal Okonguarri Fm.

Okonguarri Fm is weakly developed in Bethanis subbasin. It consists of argillite and silty argillite, like the overlying Narachaams Fm, but with coarsening upward packages of marly-dolomite and dolomite ribbonite. The argillite and silty argillite of Narachaams Fm are interrupted by spaced decimeter-scale Fe-dolomite turbidites.

Franni-aus Fm (Fig. 18 & 19B) is an overall upward-coarsening stack of carbonate turbidites and debrites, distinguished by clasts composed of unusually coarse-grained (≤ 3 mm diameter) oolite toward the top. Elsewhere, Franni-aus Fm is largely or completely neomorphosed to pale-grey dolomite, with attendant authigenic chert concentrated in

coarser debrites. In Bethanis subbasin, it is preserved as dark-grey limestone (Fig. 20A), making it more susceptible to tectonic strain. The ooids are deformed less easy to recognize in outcrop than where dolomitized. Where exposed, the basal Franni-aus Fm sharply overlies argillaceous Narachaams Fm at what appears to be a submarine scour surface. In Bethanis subbasin, the uppermost Franni-aus debrite is abruptly overlain by the quartz-siltstone basal member of Ghaub Fm (Fig. 20A).

The Marinoan Ghaub Fm (Figs. 18 & 19A) is a major ridge-forming unit in Bethanis subbasin, but it begins with 50–60 m of reddish-brown weathering, parallel-laminated, quartz-siltstone (Fig. 20A). In

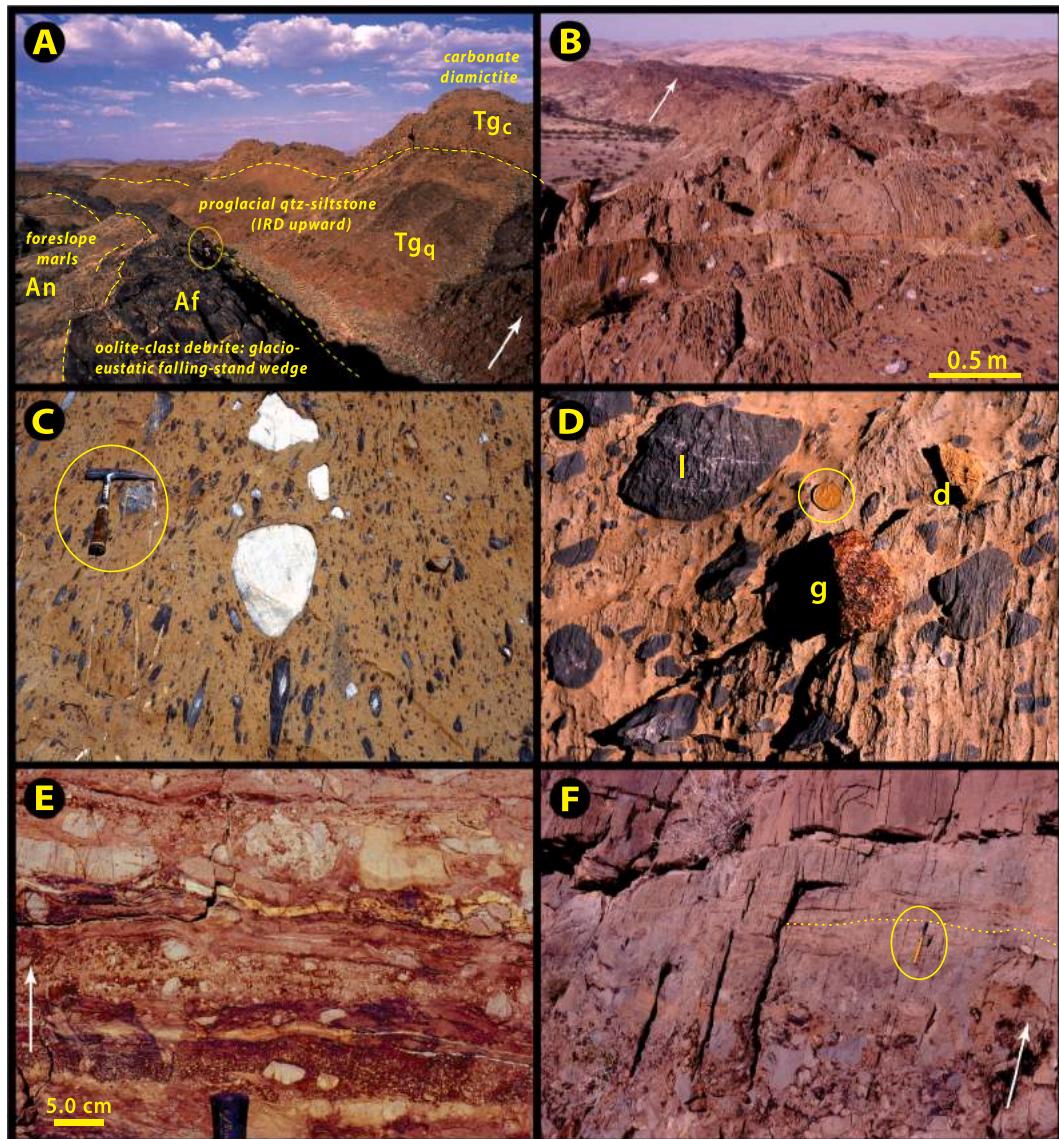


Fig. 20. Images of Marinoan glacial record in autochthonous Bethanis subbasin near Camp Xaragu (Fig. 15): white arrows indicate stratigraphic younging. (A) View looking ESE at Marinoan glacial onset from $-20.4040^\circ/14.3261^\circ$ in section 1–14 (see location Fig. 15 and columnar section Figs. 18 & 19). Person (circled) gives scale. Marinoan onset is inferred at sharp contact between limestone oolite-clast debrite (Af, Franni-aus Fm) and quartz-siltstone laminites (Tg_q member of Ghaub Fm). Franni-aus Fm falling-stand wedge sharply overlies argillite and marl of middle Cryogenian Narachaams Fm (An). IRD appears in upper Tg_q, which is sharply overlain by massive carbonate diamictite (Tg_c) in an ESE-plunging syncline in the footwall of Bethanis thrust (Fig. 15). (B) Massive limestone diamictite of Ghaub Fm at $-20.4054^\circ/14.3275^\circ$ in 1–14 (Figs. 15 & 19). (C) Dedolomitization in Ghaub Fm diamictite at $-20.4067^\circ/14.3334^\circ$ (1–14). Dark limestone clasts are flattened in the plane of tectonic foliation, but the white clasts that are not flattened were composed of dolomite at the time of tectonic flattening, and subsequently replaced (dedolomitized) by sparry calcite. Note warping of foliation around the white undeformed clasts. (D) Unflattened clasts of limestone (l), dolomite (d) and granite (g) in Ghaub Fm diamictite at $-20.4065^\circ/14.3332^\circ$ (1–14). Matrix is dolomitic-limestone wackstone. Coin (circled) is 2 cm in diameter. (E) Stratified carbonate diamictite of Ghaub Fm at $-20.2673^\circ/14.1616^\circ$ in 1–3 (Fig. 27). Small white circular grains are single ooids eroded from underlying Franni-aus debrite that was poorly lithified at the time of Marinoan glaciation. (F) Sharp contact (dashed) between stratified dolomite diamictite of Ghaub Fm and swaley dolomite ribbonite of Keilberg Mb ‘cap dolomite’ of Karibib Fm (same location as E). 15-cm-long pen (circled) gives scale. Contact marks the termination of Marinoan glaciation and start of the Ediacaran Period (Narbonne et al., 2012).

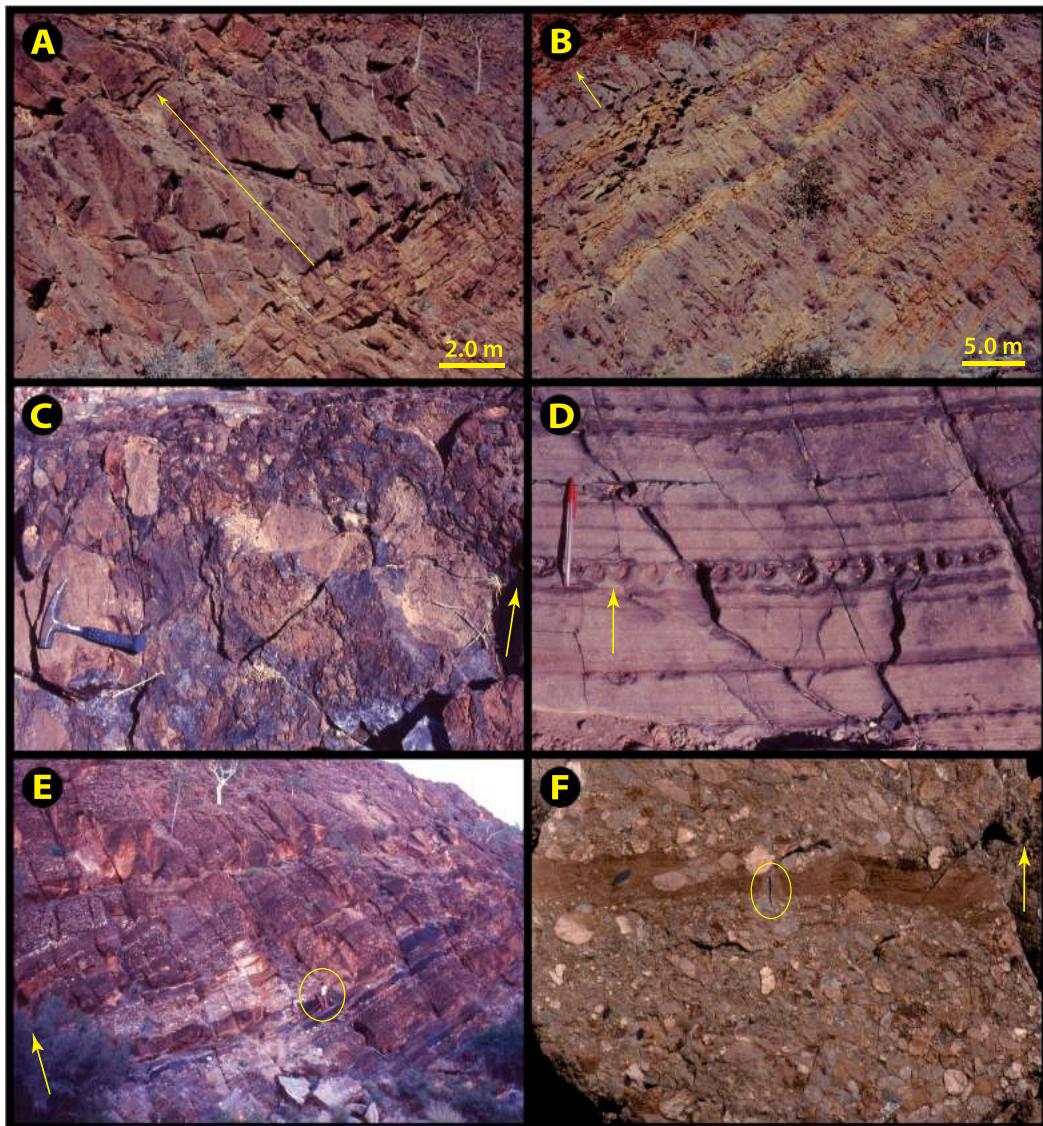


Fig. 21. Images of thrust sheet C (Fig. 15) and its immediate footwall in Bethanis syncline (Tr1). Arrows indicate stratigraphic younging. (A) Single 4.0-m-thick dolomite debrite (under arrow) within thin-bedded dolomite rhythmite of early Ediacaran Karibib Fm in hangingwall of splay thrust C (Fig. 15) at $-20.4204^{\circ}/14.4014^{\circ}$. (B) Thick debrites and thin-bedded rhythmite in Karibib Fm at $-20.4205^{\circ}/14.4007^{\circ}$. Arrow in upper left indicates the same debrite shown in A. (C) Dolomite-clast debrite with subarkosic matrix near base of Kuiseb Fm that disconformably overlies Karibib Fm in hangingwall of splay thrust C (Fig. 15) at $-20.4237^{\circ}/14.4084^{\circ}$. Debrite has a graded top (upper part of image) indicating SW-facing away from Karibib Fm. This debrite was sampled for detrital zircon geochronology (sample N-14-2-7, Nascimento et al., 2017) but mis-identified as “Ghaub Fm” (Hoffman and Halverson, 2018). (D) Load casts (Rayleigh–Taylor instabilities) in terrigenous siltstone of Kuiseb Fm indicate SW stratigraphic younging, facing away from disconformably underlying Karibib Fm, in hangingwall of splay thrust C (Fig. 15) at $-20.4243^{\circ}/14.4079^{\circ}$. Nascimento et al. (2017), following Schreiber (2006), interpret the siltstone as pre-Marinoan and the Karibib as NE-younging (discussed in Hoffman and Halverson, 2018; Nascimento et al., 2018). (E) Dolomite- and chert-clast conglomerate and sub-feldspathic sandstone displaying large-scale foreset bedding in Braklaagte Fm (Welkom Subgroup) in footwall of splay thrust C (Fig. 15) at $-20.4195^{\circ}/14.4149^{\circ}$. Person (circled) gives scale. Dolomite and chert clasts are derived from Karibib Fm in hangingwall of thrust C. (F) Dolomite- and chert-clast conglomerate in the Welkom Subgroup at same location as E. Pen (circled) is 15 cm long. Kuiseb Fm and Welkom Subgroup are interpreted alternatively as olistolith-bearing passive margin deposits (Nascimento et al., 2017, 2018) or as foredeep deposits (Fig. 16) associated with collisional orogeny (Hoffman and Halverson, 2018; this paper).

the last 10–12 m of siltstone, sparse granule- and pebble-size carbonate and basement-derived limestones appear without a perceptible break in sedimentation. These heterolithic clasts are associated with impact-related deformation of host siltstone, typical of ice-raftered debris. We could not distinguish between iceberg rafting and ice-shelf rafting, but no iceberg ploughmark structures were observed in the laminated siltstone. The arrival of ice-raftered debris signals the onset of glacial flow off Otavi platform, which requires an ice sheet thick enough to spread under its own weight. This may have lagged the snowball onset by $\geq 10^5$ years (Donnadieu et al., 2003; Pollard and Kasting, 2004).

Sharply overlying the siltstone are 240 m (section 1–15, Figs. 18 &

19A) of mainly massive, heterolithic, carbonate-clast diamictite (Fig. 20B). The clasts are supported by detrital carbonate wackestone matrix (Fig. 20C & D). Both the clasts and matrix include limestone and dolomite (Fig. 20D), the limestone clasts being selectively flattened in the cleavage plane (Fig. 20C). Certain unstrained clasts, evidently composed of dolomite at the time of bulk strain, were subsequently dedolomitized or partially dedolomitized to white calcite (Fig. 20C). Small basement granitoid clasts occur rarely (Fig. 20D). Decimeter-scale horizons of stratified diamictite (Fig. 20E) with abundant ice-raftered debris subdivide the massive diamictite into decameter-scale subunits (Fig. 19A). A thicker unit of stratified diamictite (7.6 m in 1–17) occurs

at the top of the Ghaub Fm (Fig. 18), directly beneath the basal Ediacaran cap dolomite (Fig. 20F).

Karibib Fm is the distal FSz-equivalent of ≤ 2.0 km of shallow-water Ediacaran carbonate on the platform (Fig. 5). In Tr1, it is a medium-grey and buff-coloured dolomite rhythmite (Fig. 21B, Table 4) with upward-increasing amounts of intraclast debrite (Fig. 21A). In section 1–17 (Fig. 19A), Karibib Fm is 322 m thick, but is chemostratigraphically correlative with the 3–6x thicker Tsumeb Subgroup (Fig. 10D). Karibib Fm begins with Keilberg Mb, a pale-grey laminated ‘dolopelarenite’ (peloidal dolomite grainstone) with swaley, low-angle cross-stratification, which is ≤ 6.0 m thick in the Bethanis subbasin. Crumpled sheet cracks filled by fibrous, isopachous, dolomite cement occur near but not at the base of the Keilberg Mb throughout the FSz (Hoffman and Macdonald, 2010). The base of Keilberg Mb is sharp (Fig. 20F) and its top is a flooding surface overlain by recessive marly calcite or dolomite rhythmite, representing the postglacial maximum-flooding stage. Toward the top of Karibib Fm as a whole, coarser intraclast debrites include clasts that are conspicuously dedolomitized to white calcite.

Karibib Fm is abruptly overlain by ≥ 0.3 km of greenish-grey phyllite and siltstone with cm-scale turbidites of fine-grained lithic sandstone (Fig. 21D) referred to as Kuiseb Fm (SACS (South African Committee for Stratigraphy), 1980) (Figs. 6C & 15). Within this fine-grained siliciclastic succession are local dolomite-chert olistostromes and olistoliths, evidently derived from Karibib Fm. A 7.9-m-thick, dolomite-clast debrite or conglomerate with a subarkosic matrix (Fig. 21C) occurs near the base of Kuiseb Fm in thrust-sheet C (Fig. 15). This unit, which has been inferred as Tonian (Schreiber, 2006) or late Cryogenian

(Nascimento et al., 2017) in age, is graded at the top consistent with stratigraphic younging away from the underlying Karibib Fm (Hoffman, 2021a; see also Fig. 20 in Frets, 1969). Overlying the debrite, siltstone hosts sandy turbidites with load balls (Rayleigh–Taylor instabilities, Fig. 21D) that also indicate stratigraphic facing away from the disconformably underlying Karibib Fm (Fig. 15). In Tr1, Kuiseb Fm is overlain unconformably to paraconformably by dolomite-chert conglomerate of Braklaagte Fm (Figs. 15, 21E & F) (Hoffman, 2021a).

2.1.2. Soutput subbasin (sections 1–22–25)

In a distance of just 2.3 km, Cryogenian formations nearly triple in aggregate thickness westward, toward Soutput growth fault, from 320 m in 1–24 to 930 m in 1–22 (Fig. 18). Chuos Fm grows by 117 m (6.3x) over the same stretch, Okonguarri by 94 m (1.8x) and Narachaams by a whopping 233 m (4.0x). The shortlived Berg Aukas, Franni-aus and Keilberg all get thinner, but Ghaub Fm swells by 131 m (3.7x) between the same sections (1–22–24). The thicker sections (1–22–23) cross a prominent ESE-plunging fold-pair (Fig. 15). When these sections were measured, care was taken to trace individual beds around the plunging axial closures. We are confident that columnar sections 1–22–23 (Fig. 18) reflect true stratigraphic thickening. A field guide to Soutput subbasin is given in SOI S3.4. and a geologically annotated satellite image in Fig. S3B.

The most interesting changes across Soutput growth fault are in Okonguarri Fm (Fig. 18). On the up-thrown side, Okonguarri is thin (≤ 10 m) and bedforms indicate bottom traction currents and/or storm-wave action. The down-thrown side is inflated (≤ 215 m) by decameter-

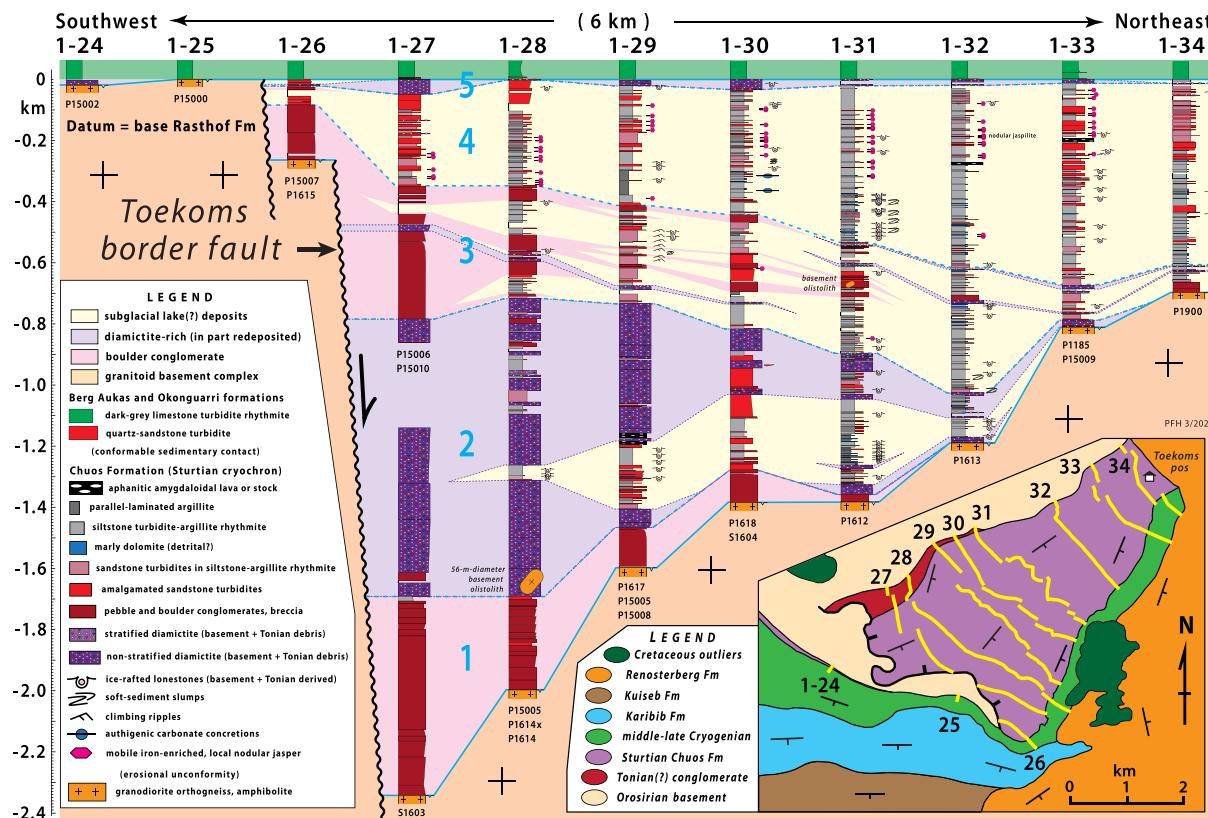


Fig. 22. Columnar sections of Sturtian Chuos Fm (Units 2–5 in blue) and pre-Sturtian (?) conglomerate (Unit 1) in Toekoms subbasin of Tr1 reveal a tilted half graben that thickens toward Toekoms border fault. The border fault was active in Sturtian and pre (?)-Sturtian (unit 1) time, but ceased before the Berg Aukas/Okonguarri limestone turbidite-rhythmite was deposited. Proximal to the border fault, the subbasin is dominated by resedimented (?) conglomerate and diamictite (including decameter-scale basement olistoliths in 1–28 & 31, Fig. 23), but distally the predominant facies are parallel-laminated silt-mudstone and sandstone turbidites, with numerous slumps and ice-raftered limestones (Figs. 24 & 25). Units 1 and 3 (in blue) are conglomerate-rich, Units 2 and 5 diamictite-rich, and Unit 4 is dominated by siltstone laminites. Aphanitic amygdaloidal lava or stocks (bostonite) occur in Unit 2 (1–29) and 4 (1–32–33). All facies become progressively more ferruginous with stratigraphic height and distance from the border fault, and evidence of fracture-related Fe mobility is ubiquitous, although the source of Fe is likely indigenous to the subbasin. Sedimentation was largely or entirely subaqueous, and ubiquitous flat lamination (Fig. 24C & D) implies quiet water (Hoffman et al., 2017b).

scale packages of decimeter-scale limestone and dolomite turbidites. The changes imply differential subsidence and seafloor topography across the fault during middle Cryogenian sedimentation.

Displacement on Soutput growth fault evidently began before Sturtian glaciation ended and continued into Marinoan glacial time. Chuos diamictite terminates against the fault and is absent on its footwall (Fig. 18). The base of Frannis-aus Fm is offset by ~100 m, accommodated mainly by 70–90 m of siltstone-dominated lower Ghaub Fm in 1–22 that is absent altogether in 1–19 (Fig. 18). The main Ghaub Fm massive carbonate diamictite complex appears not to be offset at the fault-line at all (Fig. 18). The simplest inference is that Soutput growth became inactive before the massive diamictite complex was deposited. This differs from Bethanis subbasin, in which the main Ghaub diamictite swells the most in thickness (Fig. 14).

2.1.3. Toekoms subbasin (sections 1–26–34)

Toekoms subbasin (McGee et al., 2012; Hoffman et al., 2017b) is exposed as a wedge of sedimentary and minor volcanic rocks that dip steeply (46°) southeastward and thicken southwestward toward a sinuous basement-bounding fault (Figs. 15, 22–23 & 24A). The thickness of strata that terminate sharply against the basement fault is ca 2.4 km, at least 1.6 km of which are Sturtian (Chuos Fm) in age (Figs. 22–23 & 25A). The fault is overstepped by dark-grey limestone turbidites of Okonguarri Fm (Fig. 23). Faulting began with deposition of a basal wedge-shaped mass of conglomerate (Unit 1 in Fig. 22). This conglomerate (Fig. 24B) underlies the first diamictite body (Unit 2, Fig. 22) and could therefore be pre-Sturtian in age (McGee et al., 2012). However, it is lithologically indistinguishable from conglomerate tongues in Units 2 and 3, which are intimately associated with diamictite (Fig. 22). Although the diamictite bodies appear to have been resedimented into deeper water, their ultimate glacial origin is supported by the occurrence of extrabasinal limestones (Fig. 24E), presumably ice rafted, in stratified deposits of Units 2–5 (Fig. 22). McGee et al. (2012) report that

a pegmatite dated at 763 ± 5 Ma (weighted average LA-ICPMS $^{206}\text{Pb}/^{238}\text{U}$ age of 24 concordant zircon core analyses) intrudes a basal breccia in Unit 1, but we were unable to confirm this observation, finding no pegmatite clearly intrusive into Swakop Group of Toekoms subbasin. A field guide to Toekoms subbasin is given in SOI S3.3. and a geologically annotated satellite image in Fig. S3A.

Three general features stand out concerning the sedimentary fill of the subbasin. The first is the intimate association of coarse-grained, compositionally-immature debris with delicate, parallel-laminated, mud- and silt-size sediment (Fig. 24C & D). The second is that virtually all of the coarse-grained units—conglomerates, diamictites and sandstones—thicken toward the border fault (Fig. 22). The third is the ferruginous nature of the subbasin as a whole, smeared by post-depositional Fe mobilization. Evidence of mobility includes pervasive fracture-controlled Fe mineralization (Fig. 23D), selective ferruginization of more permeable (sandstone) beds (Fig. 22), and a general increase in Fe enrichment stratigraphically upward and outward with respect to the border fault (Fig. 22). Ferric iron enrichment is so intense in the upper parts of the more distal sections that distinguishing basic lithologies is difficult.

We tentatively divide the subbasin into five stratigraphic units (Figs. 22 & 23). Unit 1 consists of grain-supported bouldery debris (Fig. 24A) differing little in bulk composition from basement source rocks—granodiorite orthogneiss, porphyritic syenogranite and chloritized amphibolite. Thick depositional units of conglomerate, both upward-coarsening and upward-fining, are locally accompanied by beds and lenses of feldspathic sandstone or pebbly sandstone. From 635 m thick in 1–27, Unit 1 tapers distally and pinches out completely between 1 and 31 and 32, a mere 3.0 km from the border fault in the line of section. The true orthogonal distance must be ≤ 3.0 km. From the sedimentology we infer that the rift basin was terrestrial at this stage of development, and we agree with McGee et al. (2012) that glacial action is not required for any feature in Unit 1.

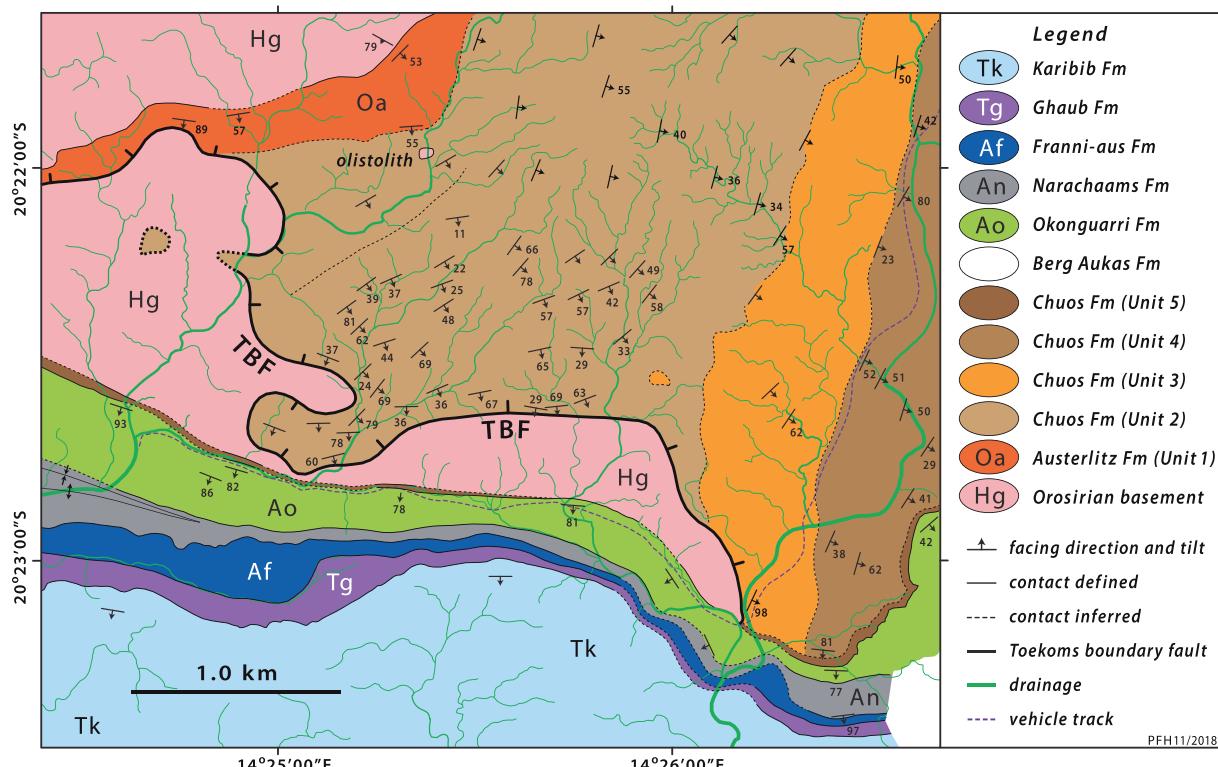


Fig. 23. Stratigraphy and structure of the tilted Toekoms subbasin at its termination against the co-rotated Toekoms border fault (TBF). The sinuous trace of the crystalline basement against which the SE-dipping strata abut (Fig. 25A) suggests a warped and gently NE-dipping fault plane ($pTF_{(p)}$ in Fig. 17). Chuos Fm Units 1–5 are as shown in Fig. 22 (in blue). Average strike/dip of beds in Toekoms subbasin ($n = 46$) is $040/46$ ($pS_{(p)}$, Fig. 17).

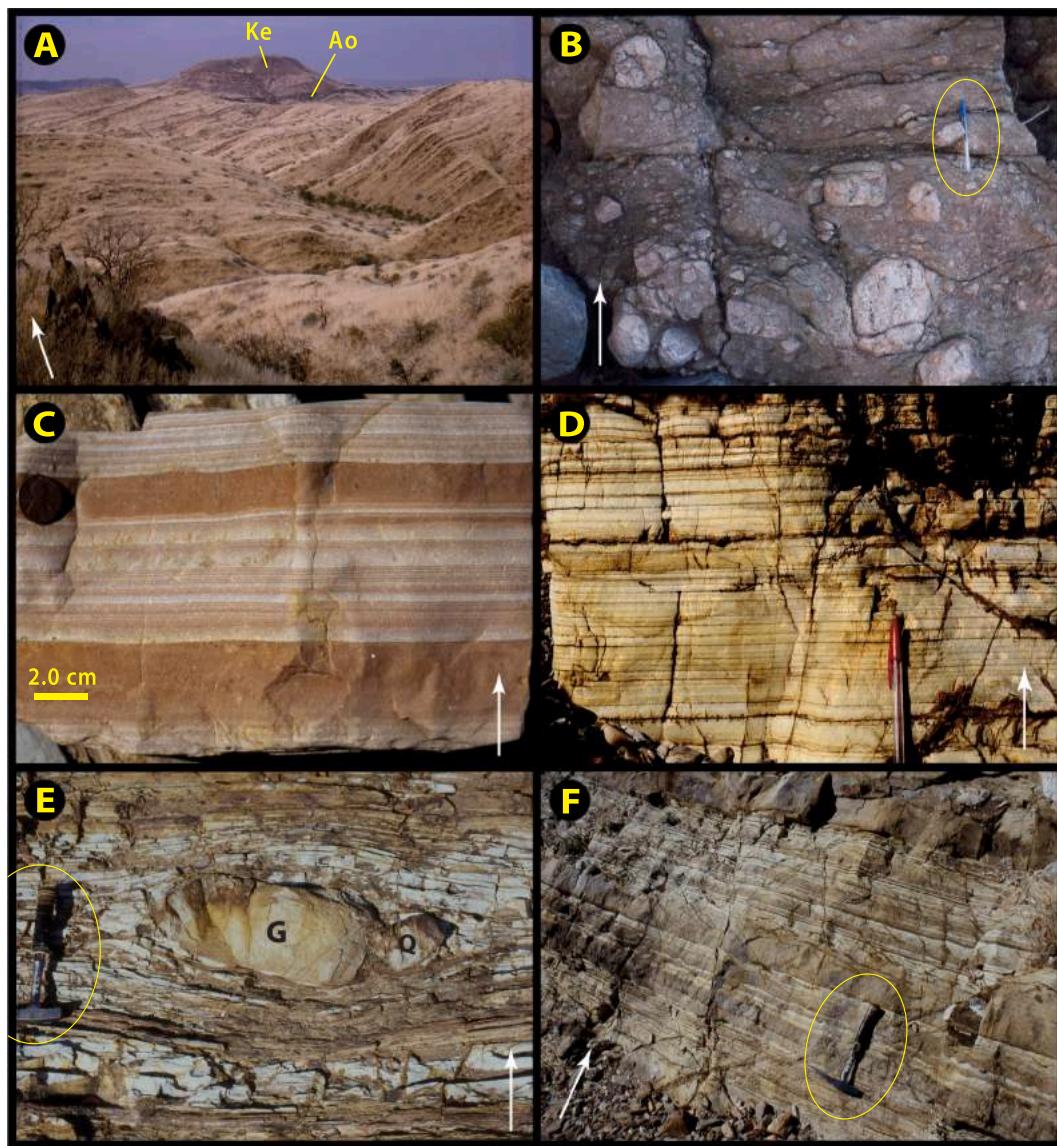


Fig. 24. Images of Toekoms subbasin in Tr1: white arrows indicate stratigraphic younging. (A) View of tilted early Cryogenian Chuos Fm looking southward from the basement (foreground) at the base of section 1–32 (Fig. 22): at $-20.3427^{\circ}/14.4553^{\circ}$. The hill on the skyline, 2.7 km distant, is an outlier of flat-lying Lower Cretaceous aeolianite and lava flows (Ke), at the foot of which is a dark band of tilted Okanguarri Fm limestone (Ao) at the top of 1–31 (Fig. 22). Tall grass indicates above-average rainfall the previous summer. (B) Poorly-sorted basement-derived conglomerate of pre-Sturtian (?) Unit 1 (Fig. 22): at $-20.3645^{\circ}/14.4129^{\circ}$. Pen (circled) is 15 cm long. (C) Siltstone turbidites (white, graded) in reddish-brown mudstone of Chuos Fm Unit 4 in 1–29 (Fig. 22): $-20.3749^{\circ}/14.4434^{\circ}$. (D) Parallel-laminated siltstone of Unit 4 in 1–29 (Fig. 22); same location as C. (E) Pair of ice-rafterd dropstones, composed of fine-grained granite (G) and quartzarenite (Q), hosted by parallel-laminated siltstone of Unit 4 in 1–29: $-20.3747^{\circ}/14.4431^{\circ}$. Hammer handle (circled) is 33 cm long. (F) Sandstone turbidites with sharp bases and graded tops in Unit 3 in 1–29 (Fig. 22): $-20.3704^{\circ}/14.4402^{\circ}$. Hammer (circled) is 33 cm long.

Unit 2 is the major (but not exclusive) diamictite-rich interval. It tapers distally from 980 m in 1–27 to just 22 m in 1–33 (Fig. 22). Diamictite bodies are mostly massive and poorly stratified. Matrix-supported bouldery debris is derived from basement and extrabasinal carbonate sources. The bodies vary in the size and density of large clasts, and the fraction of silt or sand in the generally argillaceous matrix. Minor conglomerate and sandstone beds accompany diamictite proximally (Fig. 25A), but distally the diamictite tongues are hosted by parallel-laminated argillite and siltstone (Fig. 24C & D), with or without sandy turbidites (Fig. 24F). The fine-grained laminated deposits contain ice-rafterd limestones (Fig. 24E), as indicated by symbols in the fence diagram (Fig. 22). The dropstones are mostly composed of basement-derived granodiorite, porphyritic syenogranite, metagabbro and quartzite. The millimetric lamination of the argillite and silty argillite is remarkably parallel (Fig. 24C & D): traction-current bedforms are absent

and climbing ripples are strictly associated with turbidites (Bouma C subunits). The intimate association of these fine-grained basinal deposits suggests that many if not most of the diamictite bodies were resedimented downslope from primary ice-proximal environments.

A basement olistolith, 56 m in diameter, occurs in a drainage near the base of Unit 2 in 1–28 ($-20.3662^{\circ}/14.4898^{\circ}$), ~380 m above the basement surface (Figs. 22 & 23). Two aphyric amygdaloidal igneous bodies, lavas or hypabyssal intrusives, occur in the middle of Unit 2 in 1–29 ($-20.3611^{\circ}/14.4307^{\circ}$). Both are underlain by subaqueous sediments and overlain by diamictite. The “debris flow lobe” previously reported in this unit (McGee et al., 2012) is an artifact of satellite-image interpretation, but this should not obscure the truth of the principal conclusion of those authors, which is that all but Unit 1 of the fault-bounded basin fill is Sturtian (synglacial) in age. The transition from Unit 1 to 2 appears conformable on the outcrop scale, marked by an

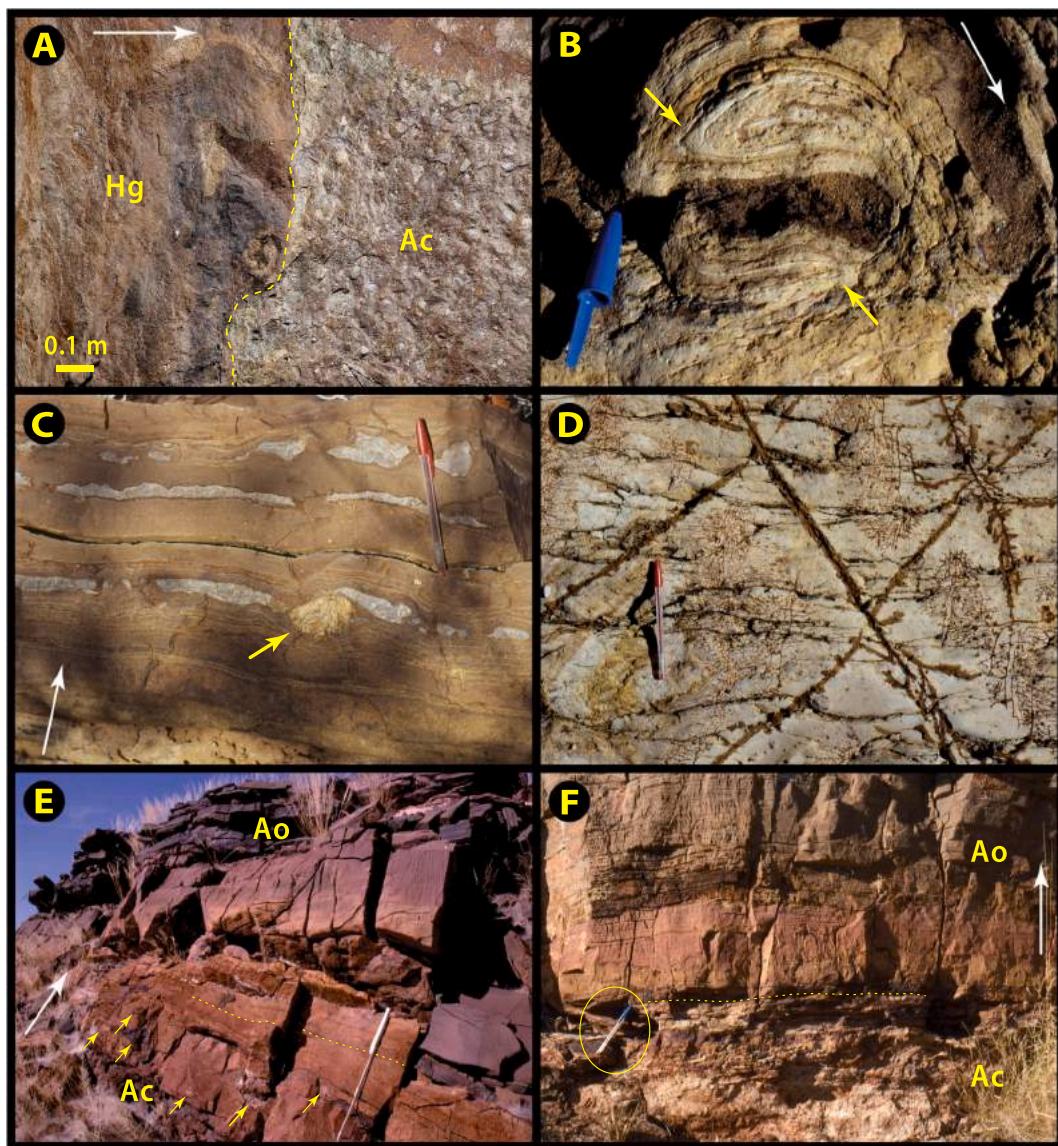


Fig. 25. More images of Toekoms subbasin: white arrows indicate stratigraphic younging. (A) Toekoms border fault as a possible sedimentary contact (dashed) between basement granodiorite (Hg) and redeposited (?) Chuos Fm diamictite (Ac) of Unit 2 in 1–27 (Fig. 22): near $-20.3770^{\circ}/14.4314^{\circ}$. (B) Refolded fold within a m-scale soft-sediment slump mass of siltstone and sandstone turbidites of Unit 4 in 1–31 (Fig. 22): at $-20.3659^{\circ}/14.4455^{\circ}$. Pen cap is 5.8 cm long. Stubby arrows indicate refolded soft-sediment folds. (C) Authigenic chert nodules (white) and ice-rafterd dropstone of granite (Stubby arrow) in thin-bedded siltstone of Unit 4 in 1–31 (Fig. 22): $-20.3624^{\circ}/14.4586^{\circ}$. (D) Fracture-controlled Fe mineralization (brown) on siltstone bedding plane of Unit 4 in 1–29 (Fig. 22): $-20.3700^{\circ}/14.4395^{\circ}$. (E) Conformable contact (dashed) between stratified diamictite of Chuos Fm Unit 5 with IRD (Stubby arrows) and dark-grey limestone turbidites (discoloured basally) of Okonguarri Fm (Ao) in 1–27: $-20.3811^{\circ}/14.4458^{\circ}$. Scale 0.65 m. Characteristic Berg Aukas Fm microbialaminite is absent in 1–23–33 (Figs. 18 & 22). (F) Sharp contact between thin ferruginous sandy diamictite (Ac, Unit 5) and discoloured limestone turbidites (Ao) between 1 and 31 and 32 (Fig. 22): $-20.3625^{\circ}/14.4588^{\circ}$.

abrupt first appearance of diamictite in all but section 1–30 (Fig. 22).

Unit 3 contains diamictite bodies also, but they are subordinate to other lithofacies (Fig. 22). Conglomerate is dominant proximally (1–27 and 28) and thin conglomerate tongues extend to 1–33, but laminated fine-grained sediments with turbidites and limestones dominate distally. The turbidites are invariably graded (Fig. 24F) and composite depositional units are common. Climbing ripples in sandy turbidites indicate eastward-directed paleoflow with wide dispersion, more consistent with fan-aprons than with axially confined flows. Soft-sediment slumps occur (1–32) but less commonly than in Unit 4. Overall, Unit 3 is tapered distally from ~490 m thick in 1–27 to ~110 m in 1–33.

Unit 4 is dominated by fine-grained laminated facies with turbidites in all but the most proximal sections (1–27–28), where sandstone is dominant. Slumps (Fig. 25B) and limestones (Figs. 24E & 25C) are widespread, and their co-occurrence suggests that some slumps were

impact induced. The largest limestones are ~1.0 m in diameter. Thin turbidites and fine-grained debrites composed of detrital dolomite occur in the more distal sections (1–30–33). Nodules of authigenic chert (Fig. 25C) and ankerite (?) occur locally in silty argillite (1–32 and 30, respectively). Sandstone appears to increase in the most distal sections (1–33 and 34), contrary to the overall distally fining trend. However, the upper part of this section is the most intensely ferruginized, masking the primary sediment type. Aphyric amygdaloidal igneous bodies occur in Unit 4 (1–32 and 33). Overall, Unit 4 thickens distally, from ~80 m (1–26) to ~670 m (1–33).

Unit 5 is defined by the final reappearance of diamictite, close to or in contact with the cap carbonate (Fig. 25E). The diamictite varies in thickness, from 2.5 m (1–28) to 47.6 m (1–27), but its presence in every section (1–26–34) implies broad conformity between Chuos and Okonguarri formations (Figs. 22 & 23).

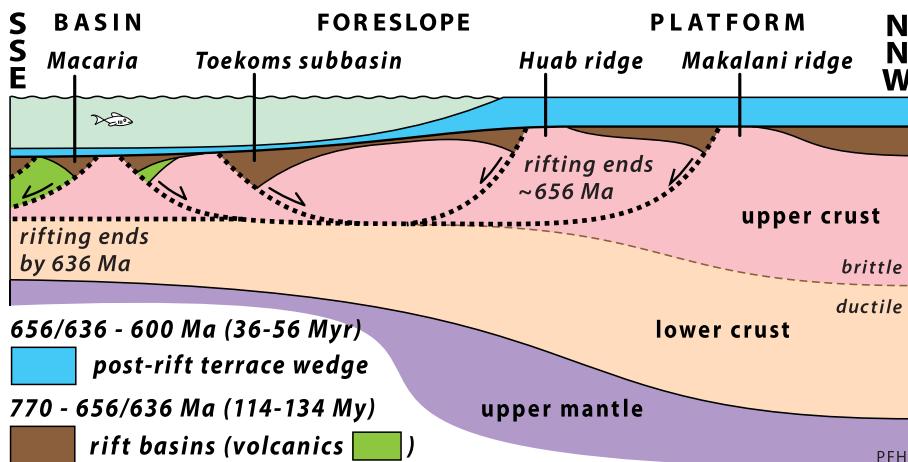


Fig. 26. Tectonic model for the southern rifted margin of Congo craton in which seaward-dipping Huab and Makalani ridge faults in OPz are mechanically linked to cratonward-dipping Toekoms and related faults in distal FSz. Seaward-dipping fault in Bz (Macaria) is geometrically consistent with pre-Karibib Fm structural tilting in Tr3 (Figs. 37 & 40). Crustal necking determines the location of the OPz–FSz transition. Compare with crustal structure on the present Austral South Atlantic conjugate margins (Chauvet et al., 2021).

The diagnostic black dolomite microbial laminitite of Berg Aukas Fm in Bethanis and western Soutput (1–22) subbasins (Fig. 18) is absent in the Toekoms subbasin. Instead, Chuos Fm is sharply overlain by black to dark grey limestone turbidites of Okonguarri Fm (Fig. 25E & F). The parallel-sided and graded limestone turbidites are interbedded southward with argillite and northward with quartz sand- and siltstone turbidites. In 1–22–26 (Fig. 18), Okonguarri Fm is overlain by Narachaams, Franni-aus and Ghaub formations. To the northeast (1–27–34), post-Okonguarri formations of Swakop Group are erosionally truncated beneath sandstone of Renosterberg Fm (Figs. 14 & 15). Where the base of the sandstone ramps across the upper Swakop Group, the relationship appears to be that of a depositional onlap across which the Swakop and Renosterberg bedding attitudes are subparallel, but critical relationships are partly covered by alluvium shed off the nearby Cretaceous outlier (Figs. 15 & 24A).

The Toekoms border fault (Fig. 25A) was rotated when the basin including the basement surface was tilted during Damaran orogenesis. The strata dip 46° on average ($n = 46$) and strike (right-hand rule) 040° (Fig. 23). The border fault strikes ~300° and its sinuous trace suggests a low dip. If we assume the fault surface dips 30° on average to NE, then rotating the fault plane around the strike of the tilted strata (040°) restores the fault plane to a 255° strike and 57° dip (right-hand rule) when the sedimentary strata were horizontal (Fig. 17A). The restored fault strike is subparallel to Damara orogen, and to Huab and Makalani rift-shoulder uplifts in OPz (Fig. 5). The restored dip of Toekoms border fault toward NNW (pTF_0 in Fig. 17) is antithetic to the inferred Huab and Makalani growth faults, and we speculate that they were part of a linked fault system (Fig. 26) that accommodated intermittent NNW/SSE crustal stretching in late Tonian and Cryogenian time. Continentward-dipping normal faults have been imaged seismically at the outer edges of both volcanic and non-volcanic South Atlantic rifted continental margins (McDermott et al., 2015; Clerc et al., 2018; Chauvet et al., 2021). A cratonward-dipping Toekoms fault could explain through footwall excision why differential subsidence producing the shelf break and FSz occurred to the north of Toekoms rift basin (Fig. 26).

The 2-D geometry of Toekoms subbasin as defined by the five lithostratigraphic units (Fig. 22) is consistent with growth faulting and synkinematic sedimentation (e.g., Purser and Bosence, 1998). The shift in locus of maximum accumulation from fault-proximal (Units 1–2) to fault-distal (Unit 4) over time is characteristic of Mesozoic half grabens

developed over listric border faults, imaged seismically on North Atlantic continental margins (Petrie et al., 1989; Driscoll et al., 1995).

The volumes of resedimented diamictite in Units 2–4, the sparse but pervasive distribution of ice-rafterd limestones in associated laminites (Fig. 22), and lack of well-sorted sand or gravel stratigraphically above Unit 1, are consistent with subaqueous deposition beneath an ice shelf (Domack and Powell, 2018). Ubiquity of parallel lamination in fine-grained units (Fig. 24C & D) and absence of traction-current bedforms suggest that Toekoms subbasin was limited in size. As discussed in section 3.3.1., Chuos Fm lithofacies are regionally more similar to glacial deposits in continental than marine environments, prompting speculation that Toekoms subbasin was a Sturtian subglacial lake (Hoffman et al., 2017b), becoming a marine basin in the Sturtian aftermath. We do not consider the ferruginous nature of Toekoms subbasin to be a marine indicator—meltwater discharge from beneath modern Taylor Glacier (McMurdo area, East Antarctica) contains 3.45 mM of total dissolved Fe (Mikucki et al., 2009), presumably sourced from subglacial weathering of Jurassic Ferrar mafic sills upstream.

Soutput fault strikes 345° (Frets, 1969) and its relatively straight linear trace (Fig. 15) implies a steep dip. Strata within Soutput subbasin do not dip uniformly because of the curved basement surface and an eastward-tapered dip reversal (Fig. 15). To restore Soutput fault, we tilt correct the basement surface (i.e., basal cover stratum) in Bethanis and Toekoms subbasins (1–14–19, 27–34, Fig. 15), which averages 062/48° ($n = 10$). This tilt correction (Fig. 17B) is more broadly based than the one described earlier using only Toekoms subbasin dips (2.1.). This preferred tilt correction (Fig. 17B) results in only a small reorientation of Soutput fault. An assumed present fault-plane orientation of 345/80° (SF(f)) restores to an initial orientation of 333/74° (SF(i)).

The restored dip of 74° is steeper than failure angles in normal faulting and the strike of 333° is oblique to Kaoko belt (345°, Fig. 4). The steep dip and oblique strike are consistent with a splay fault at a rift-transform junction (e.g., Tibaldi et al., 2016). Such a splay fault would connect a NNW-dipping normal fault in Northern zone (e.g., Toekoms border fault) with a NNW–SSE left-slip (strike-slip) fault system in Kaoko belt (Hoffman, 2021b).

2.1.4. Opdraend autochthon

The autochthonous Swakop Group panel on Opdraend farm is

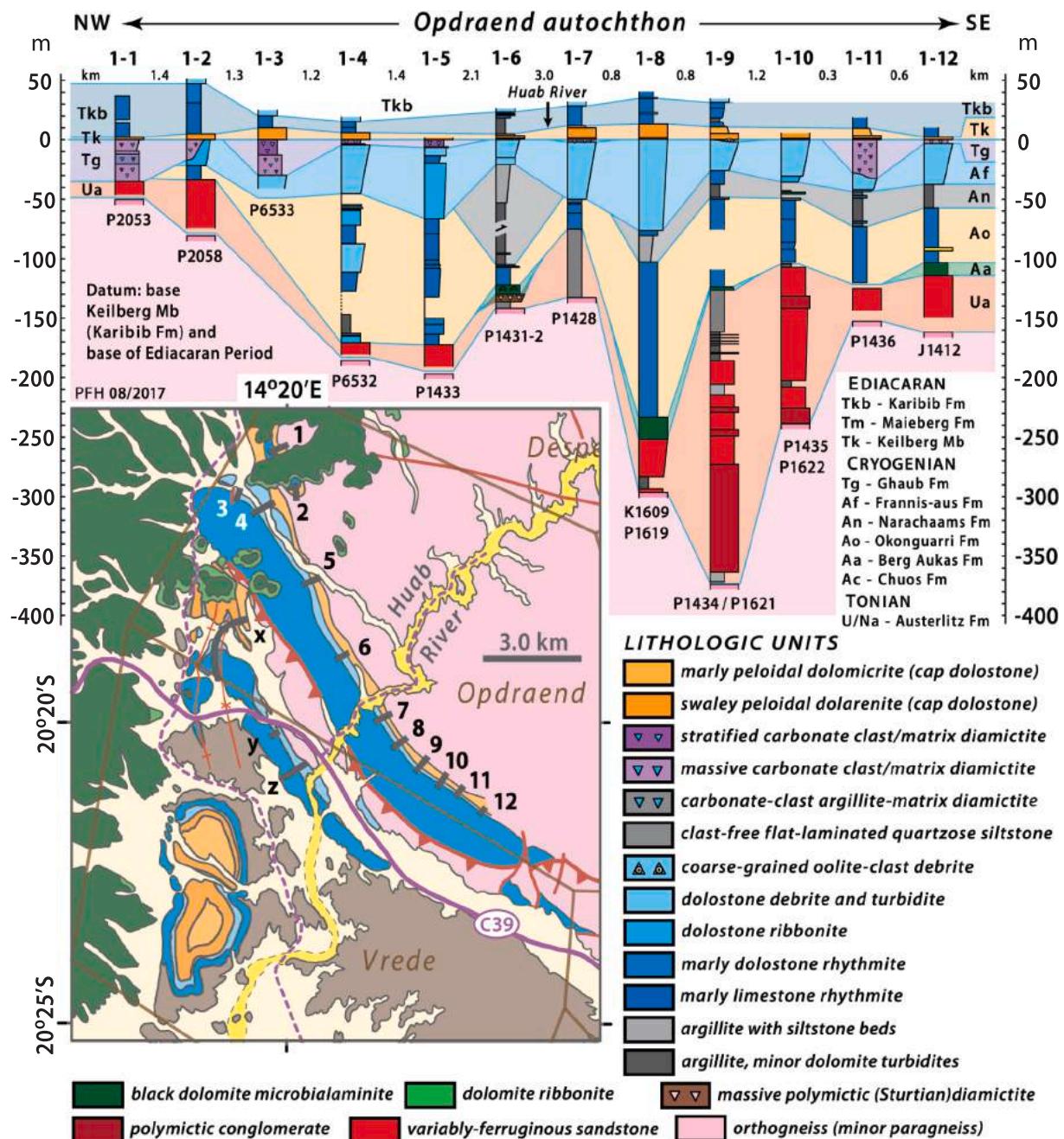


Fig. 27. Lower Swakop Group columnar sections in the Opdraend sector (Fig. 14) of Tr1: Marinoan Ghaub Fm (1–1 – 3, 11) is better developed than Sturtian Chuos Fm (1–6 only), opposite to allochthonous sections (x – z) in the adjacent Northern zone (inset map and Fig. 28).

bisected by the gorge of Huab River (Figs. 13 & 27). Alteration related to emplacement of Etendeka volcanics increases with proximity to the Cretaceous outlier. The Swakop Group exhibits less stratigraphic variability compared with the area E of the gap (Fig. 14). However, the thickness of pre-Sturtian clastics was not measured N of Huab River (1–1–5, Fig. 27) because of small-scale intrafolial folding.

With the possible exception of section 1–6, no Sturtian diamictite was observed within or above the basal clastic unit, which is a mixed assemblage of conglomerate, pebbly sandstone, siltstone and argillite (Fig. 27). A Sturtian age cannot be ruled out if these are terrestrial proglacial outwash (sandur) facies. But we have no evidence supporting such an interpretation. The search for glacially shaped clasts is thwarted

by tectonic foliation. We tentatively favour a Tonian age (Austerlitz Fm or Ugab Subgroup, Fig. 6B), analogous to but lithologically distinct from unit 1 in Toekoms subbasin (Fig. 22).

Black dolomite microbial laminitic, diagnostic of Berg Aukas Fm, occurs locally (1–6, 8–9 and 12). Elsewhere, the basal clastics are sharply overlain by nondiagnostic grey dolomite rhythmite. It remains to be determined if the inconsistency is due to facies change within Berg Aukas Fm or erosional truncation beneath Okonguarri Fm (Fig. 27).

The oolite-clast debrites of Franni-aus Fm are dolomitized and silicified, unlike their calcitic preservation in Bethanis subbasin. Marinoan Ghaub Fm varies in thickness from 0 to 33 m in sections just 0.3 m apart (1–10 and 11). Reciprocal thickness changes (Fig. 27) indicate that

Ghaub Fm thickenings coincide with paleochannels, incised into underlying strata (1–1, 3 and 11). This differs from the situation in Bethanis subbasin, where Ghaub Fm thickening is related to increased subsidence, not incision of older strata (Fig. 18). Higher rates of subsidence and sedimentation in Bethanis subbasin may have reduced the time interval in which Franni-aus Fm resided at burial depths favourable for dolomitization.

Keilberg Mb cap dolomite sharply defines the basal Ediacaran in every section. It varies in thickness from 2.0 (1–1) to 12.6 m (1–8). It is overlain by ≤ 50 m of marly calcite and/or dolomite rhythmite, equivalent to middle Maieberg Fm in Otavi Group (Fig. 6C–E), and ≤ 200 m of pure dolomite rhythmite and debrite (Karibib Fm). The Ediacaran Swakop Group (Karibib Fm) is essentially the same on Opdraend as over the Bethanis and Soutput subbasins (Fig. 14). Although Frets (1969) interpreted the autochthonous Karibib Fm (his unit D₁C) on Opdraend farm as synclinal, we observed monoclonal dips toward SW and no downward-facing beds. Cryogenian strata do not reappear on the SW side of the Karibib belt (Fig. 27). We therefore infer that basement SW of the autochthonous Swakop Group is allochthonous, and that a SW-dipping thrust occurs beneath it and constitutes the boundary fault of Northern zone (NDz).

2.1.5. Highlights from Tr1

Chief highlights are the three asynchronous Cryogenian subbasins (Fig. 14, 18 & 22). Toekoms subbasin is principally Sturtian in age, related to an originally cratonward NNW-dipping normal fault striking parallel to Northern (Outjo) zone. Soutput subbasin is principally middle Cryogenian in age, related to an originally NE-dipping splay fault at a rift-transform junction between Northern zone and Kaoko belt. Bethanis subbasin is principally of Marinoan age, and cannot be related to any known fault because of the plunge of Bethanis synclinorium and truncation by the Northern zone boundary thrust (Fig. 13). Toekoms rift-basin was filled subaqueously as a subglacial lake or fjord (McGee et al., 2012; Hoffman et al., 2017b). Bethanis subbasin was partly filled subaqueously—the basal 60-m-thick quartz-siltstone laminites—but the thicker and younger deposits are mainly massive carbonate diamictites resembling sublimation tills. The subbasins manifest Cryogenian rifting on the distal FSz at the SW cape of Congo craton (Hoffman, 2021b).

2.2. Transect Tr2 – Vrede domes

Allochthonous Swakop Group of Northern zone is exposed directly south of Opdraend on farm Vrede 719 (Figs. 13 & 27). It outcrops in a S-plunging anticline–syncline pair that straddles the Vrede–Opdraend farm boundary and is bisected by the graded gravel road C39. To the S, it is exposed in a pair of structural domes situated between Etendeka plateau and Huab River. We devoted more attention to Vrede domes, which are well exposed, less altered and offer wider areal coverage. We begin, however, with the northern area (Fig. 28) as it provides a useful stratigraphic overview and a bridge between Tr1 and Vrede domes.

2.2.1. Opdraend–Vrede allochthon

Three sections from the E limb of the plunging syncline are shown in Fig. 28. Section x (Fig. 27) was measured near the fold closure, section y near the C39 road crossing, and section z near Huab River crossing. Section x preserves ≥ 270 m of Tonian clastics and carbonates, correlative with Ugab Subgroup (Fig. 6B), that also core Vrede domes (Malooft, 2000; Lamothe et al., 2019). These are missing in section z (Fig. 28), but the nature of their disappearance is unknown due to cover (Fig. 27). Sturtian Chuos and Berg Aukas formations are well developed, but Marinoan Ghaub Fm and Keilberg Mb are quite condensed relative to Tr1 (Fig. 28).

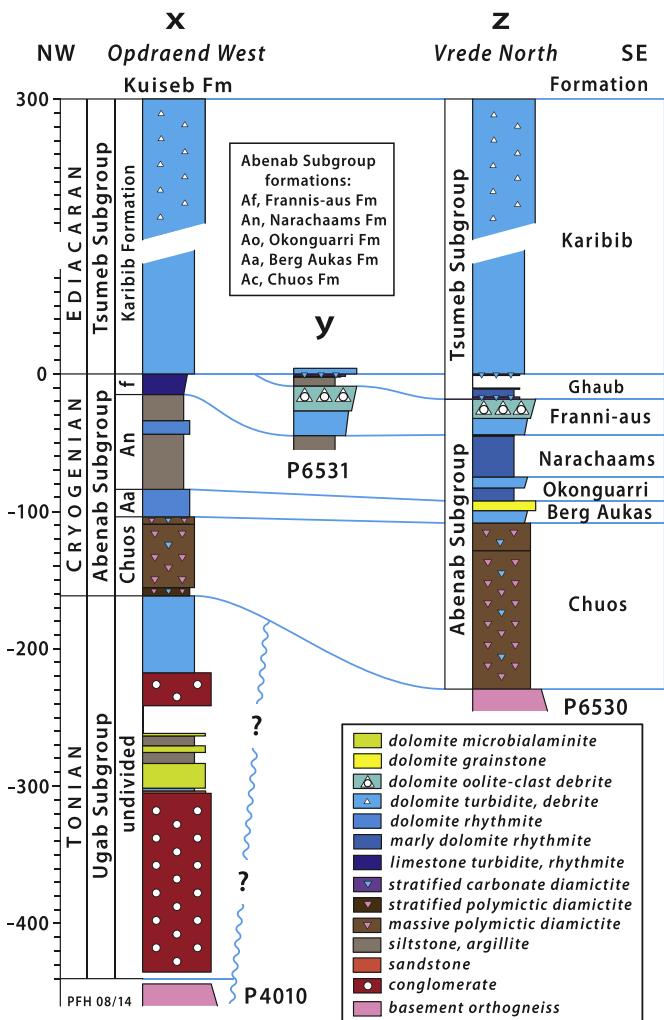


Fig. 28. Swakop Group columnar sections from the northernmost Northern zone: see inset map (Fig. 27) for locations. Thick Chuos Fm and thin Ghaub Fm are opposite to their relative thickness in adjacent autochthonous Tr1 (Fig. 27).

2.2.2. Vrede domes

Vrede domes (Figs. 29 & 13) were first mapped and described by Frets (1969). They were interpreted as interference folds by Malooft (2000), who distinguished three discrete ages of cleavage development. The first and last cleavages formed parallel to Damara orogen and the second parallel to Kaoko orogen (Fig. 33F). A simple interpretation is that the first cleavage is related to shortening across Northern zone at 0.60–0.59 Ga (Lehmann et al., 2015), the second to collision in Kaoko orogen at 0.59–0.58 Ga (Goscombe et al., 2005) and the last to collision in Southern zone at 0.55 Ga (Miller, 2008b). No basement is exposed in either dome—the structurally deepest rocks are marble tectonites in the core of the S-dome (Fig. 29). The marble tectonite is not included in the measured sections (Fig. 30), nor was it sampled for chemostratigraphy. A field guide to Vrede domes is given in SOI S3.5., with geologically annotated satellite images in Fig. S4.

A succession of pre-Sturtian (sub-Chuos Fm) mixed clastics and carbonates ≥ 0.65 km thick is exposed in the cores of Vrede domes (Figs. 29 & 30). It is tentatively correlated with the late Tonian (746–717 Ma) Ugab Subgroup of Tr3 on chemostratigraphic grounds (Lamothe et al., 2019). A line of 16 measured sections follows the

circumference of the domes in a counter-clockwise direction from left to right (Fig. 30). The southernmost and northernmost sections are 1–3 and 1–15, respectively. The sections document a remarkable facies change from basement-derived alluvial conglomerate (Fig. 31A) in the N to neritic dolomite (Fig. 31B) in the S (Fig. 30). This change takes place over a N–S distance of just 4.2 km (Fig. 29), or perhaps twice that distance before doming. In detail, the facies change consists of a back-stepping set of terrigenous clastic tongues, invasive into shallow-marine dolomite subequally composed of ribbonite (Table 4), *Tungussia*-type stromatolite and grainstone, commonly oolitic (Fig. 30). Except for the marble tectonite, the carbonate is exclusively dolomite.

A prominent mappable flooding surface near the top of the Tonian succession is overlain by ≤ 89.0 m of dolomite ribbonite (Fig. 30). We take this flooding surface as the datum (0.0 m). Since it is stratigraphically close to the base of Chuos Fm, lateral variation in thickness of ribbonite above the datum should closely mimic local paleotopographic relief on the Sturtian glacial erosion surface (Fig. 30). Accordingly, the maximum relief overall was 78 m and between adjacent sections was ≤ 30 m. Such modest relief is not unexpected for a glacial erosion surface on what was flat-lying, lithologically uniform, pre-

lithified (Fig. 31D), dolomite ribbonite (Fig. 30).

The Sturtian glacial erosion surface is exposed in 17 of 22 Cryogenian measured sections (Fig. 32), aligned in parallel with the Tonian sections (Fig. 30). Chuos Fm is thin (≤ 20 m) or missing in the NE half of S-dome and all of N-dome. Where Chuos Fm is absent (e.g., 1–33, 35 and 37), dark-grey to black dolomite microbialaminite of Berg Aukas Fm (Fig. 33A) directly overlies the glacial surface (Fig. 32). In the SW half of S-dome (Fig. 29), a NE-tapered wedge of Chuos Fm thickens to a maximum of 223 m in 1–23 (Fig. 32). The Chuos wedge is a composite mass of mainly massive polymictic diamictite (Fig. 31E & F), but which includes discrete bodies of carbonate diamictite, laminated siltstone and argillite, stratified diamictite and clast-supported conglomerate, in decreasing order of abundance (Fig. 32). Note that the lenticular form of the wedge in Fig. 32 is an artifact of curvature in the line of sections (Fig. 29). The wedge does not occupy a paleovalley because there is no incision of Tonian stratigraphy beneath it (Fig. 30). Therefore, the wedge must have been a positive paleotopographic feature when Sturtian glaciation ended, either a moraine-like buildup or an erosional outlier of an originally more tabular deposit (Hoffman et al., 2017b).

The Chuos Fm is sharply overlain by a thin (1.5–4.3 m) Berg Aukas

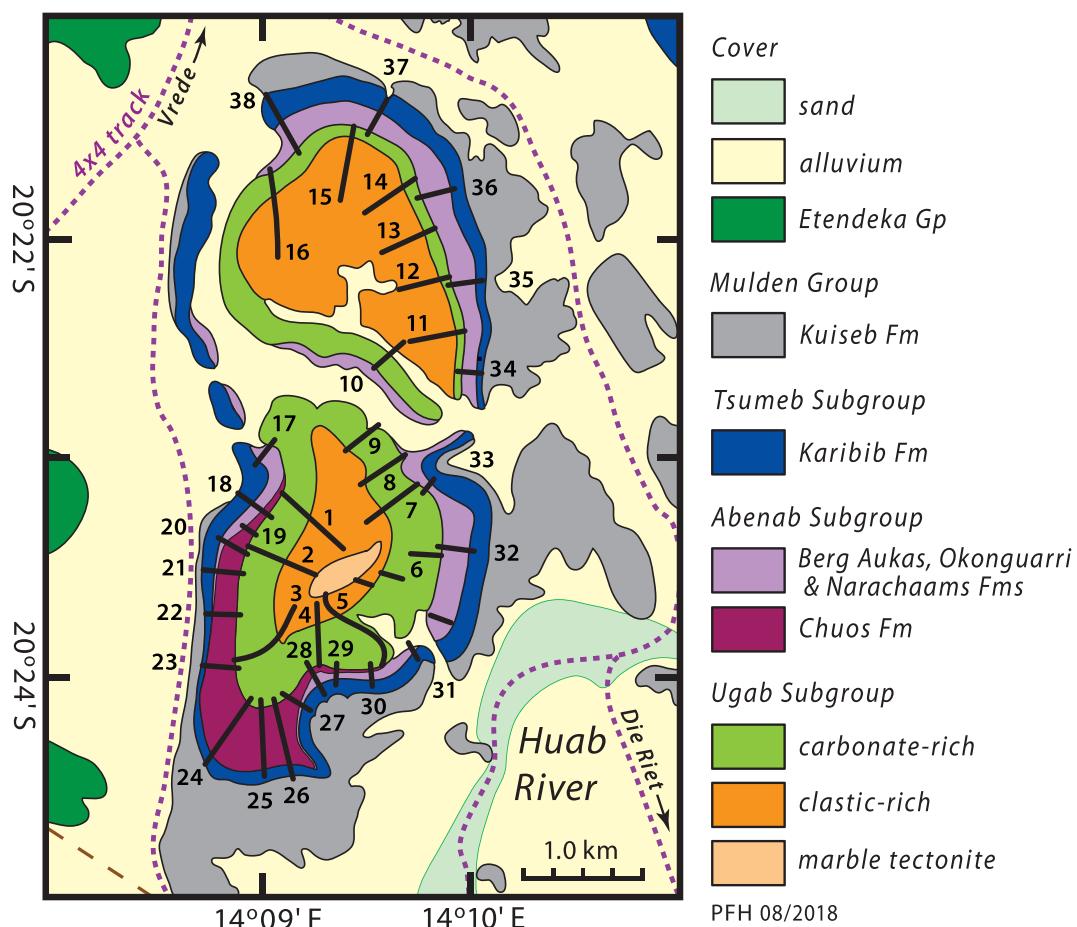


Fig. 29. Swakop Group stratigraphy exposed in structural domes on farm Vrede 719, in Northern zone at the foot of Etendeka (Early Cretaceous) volcanic outlier (Figs. 8A & 27). The domes are products of three successive shortening episodes (Malof, 2000): (D1) Damara-normal, (D2) Kaoko-normal and (D3) Damara-normal. Deformations can be related to collisions of Central zone (D1), Ribeira–Dom Feliciano–Rio de la Plata composite terrane (D2), and Kalahari craton (D3) with greater Congo craton (Figs. 2 & 3). Numbered sections 1–16 are Tonian Ugab Subgroup (Figs. 30) and 17–38 are Cryogenian Abenab Subgroup and early Ediacaran Karibib Fm (Fig. 32). Field guide (SOI S3.5.) includes geologically annotated satellite images of both domes (Fig. S4A & B).

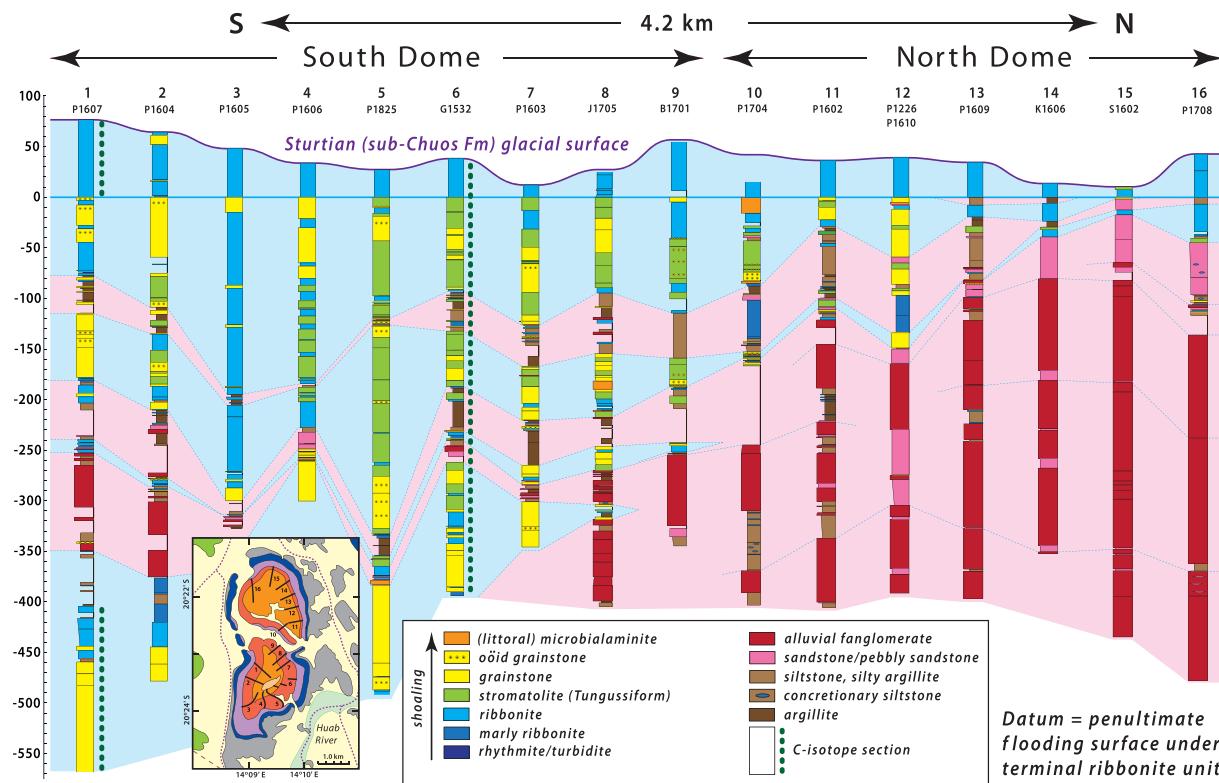


Fig. 30. Late Tonian Ugab Subgroup columnar sections from Tr2: see inset map and Fig. 29 for section locations. Sections are ordered anti-clockwise 2–1–16, with 2–3 and 2–15 being the most S and N, respectively. Datum (0.0 m) is the flooding surface that floors the uppermost dolomite ribbonite unit, selected to give a sense of paleotopographic relief on the sub-Chuos Fm (base Sturtian) erosion surface (Hoffman et al., 2017b). Sections document a facies change from alluvial fanglomerate (N) to neritic carbonate (S) in a backstepping sequence of clastic advances and retreats. Corrected for tectonic shortening (e.g., 43%), facies change occurred in a distance of 6.0 km. The facies pattern could reflect intermittent fault-related uplift and erosion in the north, in a regime of progressive crustal stretching and subsidence (e.g., Fig. 26).

Fm, composed of maroon weathering, dark-grey to black, dolomite microbialaminite (Fig. 31C), locally with roll-up structures (Fig. 33A). This Sturtian cap dolomite is sharply overlain by green argillite hosting sets of closely spaced, parallel-sided, cm-scale, dolomitic turbidites (Fig. 33B). The carbonate turbidite-bearing argillite is 14–36 m thick and represents an attenuated distal facies of Okonguarri Fm (Fig. 6B). It is followed by 37–206 m of parallel-laminated argillite and siltstone (Fig. 33C & D) of Narachaams Fm, with pyrite-rich zones but only minor amounts of carbonate, either as turbidites or authigenic nodules and layers. Bedforms related to wave action or bottom traction currents are absent, but low-angle truncation surfaces (Fig. 33E) are not uncommon. Either top-lap or down-lap truncations are observed, suggesting soft-sediment slip. We suspect a tectonic origin for the local variability in thickness of Narachaams Fm, related to disharmonic folding of the relatively stiff bounding Tonian and Ediacaran dolomites. This could be tested with fine-scale mapping and sectioning of the well-exposed E flank of S-dome between sections 1–32 and 33 (Figs. 32 & S4B). An alternative explanation for variable Narachaams thickness is differential erosion on the Marinoan (sub-Ghaub Fm) erosion surface (Fig. 32). We consider this explanation less likely because of the broadly uniform thicknesses of synglacial Ghaub Fm and its cap dolomite, Keilberg Mb (Fig. 32). In overall lithologic character, the inter-snowball deposits of

Vrede domes bear comparison with the coeval Datangpo Fm of South China (Peng et al., 2019; Wei et al., 2019) and Macdonaldryggen Fm of Arctic Laurentia (Fairchild et al., 2016).

Ghaub Fm is thin and discontinuous in Vrede domes, averaging 2.3 m ($n = 10$) where present and missing altogether in 7 of 17 exposed sections (Fig. 32). It consists of two lithotypes: carbonate-clast diamictite (Fig. 34B & D) with rare basement clasts (Fig. 34C), and terrigenous siltstone with cm-scale limestones. Consistent with a regionally observed Ghaub/Keilberg reciprocal thickness relation, the Marinoan cap dolomite (Fig. 34A) is relatively thick and omnipresent in Vrede domes, averaging 16 m in 15 exposed sections (Fig. 32). Section 1–31 has a rare example of an outsize clast within the basal Keilberg Mb (Fig. 34C & D). Overall, Keilberg Mb is a pale-grey buff-weathering stratified micro-peloidal dolomite. The lower but not basal Keilberg Mb is riddled with crumpled sheet cracks filled by isopachous fibrous dolomite cement (Fig. 34E). The isopachous axisymmetric nature of the fibrous cement indicates that the cracks opened incrementally and cementation occurred contemporaneously in crack-seal cycles. Extension was in the paleovertical direction, suggesting pore-fluid overpressuring. Hoffman and Macdonald (2010) speculated that overpressuring was caused by rapid sea-level fall in response to ice-sheet retreat and consequent loss of ice-sheet gravity (Clark, 1976; Mitrovica et al., 2009; Creveling and

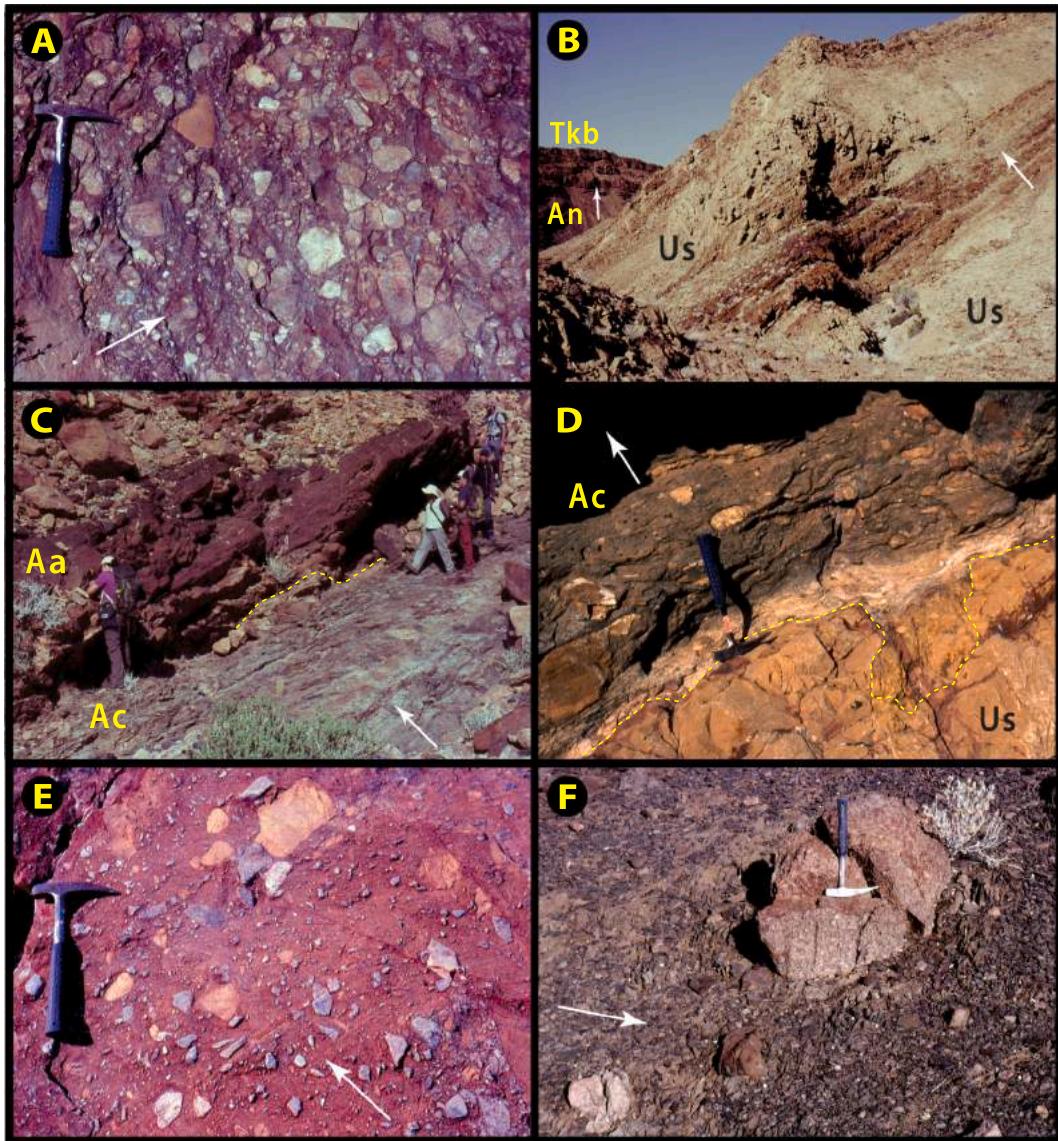


Fig. 31. Images from Vrede domes (Tr2): white arrows indicate stratigraphic younging. (A) Ugab Subgroup alluvial fanglomerate at $-20.3748^{\circ}/14.1621^{\circ}$ in 2–11 (Fig. 30), composed of basement granitoid, vein-quartz, siliciclastic and carbonate debris. Note reverse grading during fan advance in lower left. (B) Distal part of siliciclastic advance (dark brown) within pale stromatolite-dominated (*Tungussia*-type) dolomite around -120 m relative to datum at $-20.3977^{\circ}/14.1596^{\circ}$ in 2–5 (Fig. 30). Us, Orusewa Fm; An, Narachaams Fm; Tkb, Karibib Fm. Siliciclastic advance encompasses interbedded siltstone, fine-grained sandstone, oolitic dolarenite and stromatolite. (C) Berg Aukas Fm (Ar) cap dolomite overlying Sturtian Chuos Fm (Ac) diamictite in 2–30 (Fig. 32); at $-20.4003^{\circ}/14.1596^{\circ}$. Berg Aukas Fm is discoloured by Fe, possibly mobilized from overlying Etendeka flood basalt. Berg Aukas Fm cap dolomite is key to recognizing Sturtian age of diamictite (Hoffman et al., 2017b), which is overlain by Marinoan cap dolomite (Keilberg Mb) in 2–23–26 (Figs. 32 & 34A). (D) Disconformity (dashed) between Chuos diamictite (Ac) and semi-brecciated Tonian dolomite ribbonite (Us) at $-20.4000^{\circ}/14.1598^{\circ}$ in 2–30, 40 m ENE of (C). Basal diamictite is dominated by dolomite clasts but basement clasts (C) predominate overall. (E) Polymictic Chuos diamictite at $-20.4082^{\circ}/14.1492^{\circ}$ in 2–25 includes dolomite and basement debris in a matrix of similar mixed composition. (F) Boulder (beneath hammer) of porphyritic syenogranite in clast-poor argillaceous Chuos diamictite at $-20.3997^{\circ}/14.1469^{\circ}$ in 2–22.

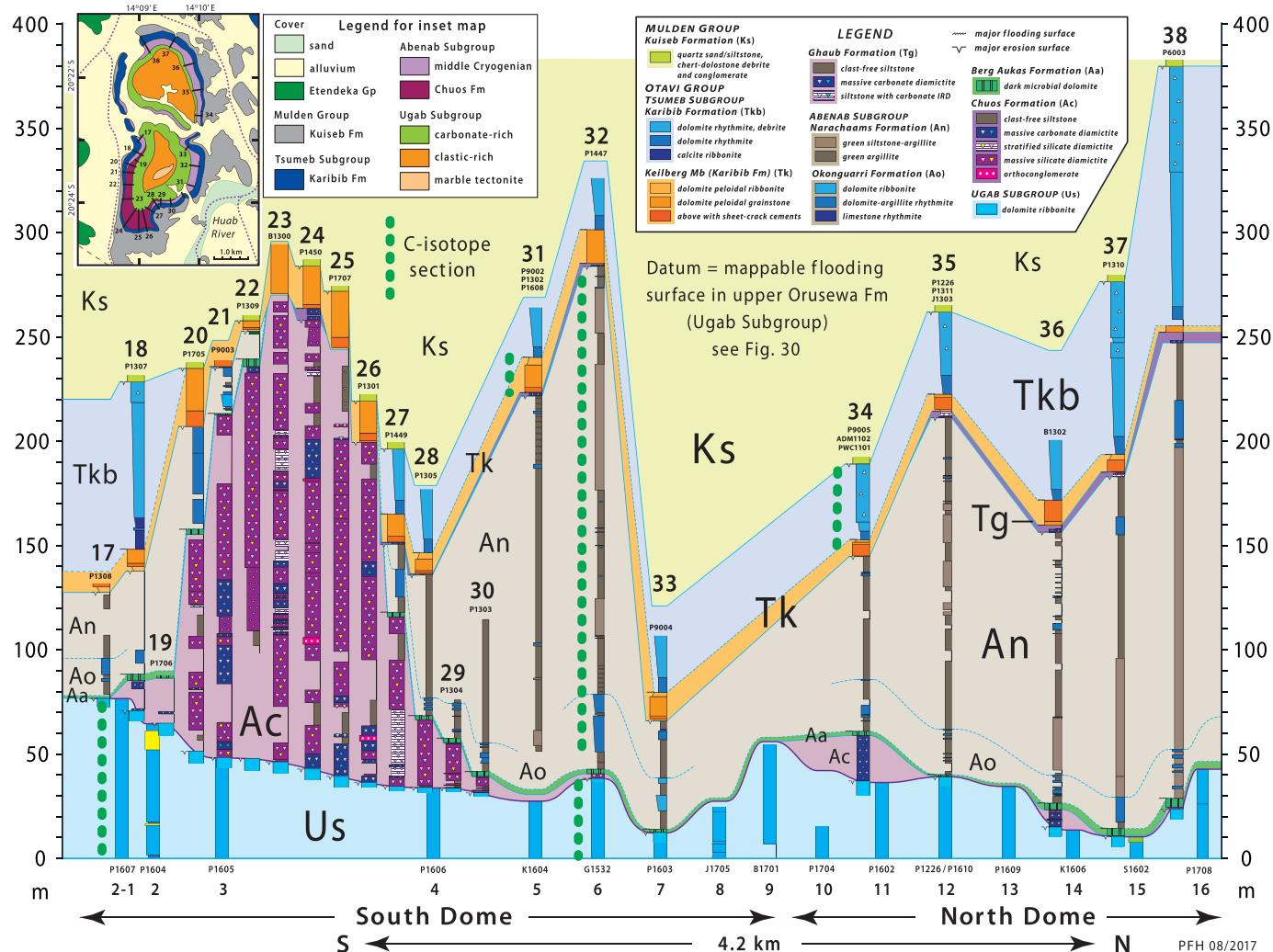


Fig. 32. Cryogenian and early Ediacaran columnar sections from Tr2: see inset map and Fig. 29 for section locations. Sections are ordered anticlockwise 2–17–38, similar to Fig. 30. Most S and N sections are 2–25 and 2–37, respectively. Datum (0.0 m) is the same upper Ugab Subgroup flooding surface as in Fig. 30. The mound-like appearance of the Chuos diamictite buildup (2–18–30) is an artifact of curved line of sections. The simplest geometry is a NE-tapered wedge (Figs. 29 & 35). The diamictite wedge has complex internal structure and could be a moraine-like build-up or an erosional remnant of a formerly more extensive deposit. It is draped by a thin Berg Aukas Fm cap dolomite (Figs. 31C & 33A) and buried by middle Cryogenian basinal deposits Ao and An (Fig. 33B–F). During Marinoan glaciation, the Sturtian diamictite wedge was erosional decapitated (2–23–26) and, upon deglaciation, covered by basal Ediacaran Keilberg Mb cap dolomite, with (2–24) or without (2–26) underlying Ghaub Fm diamictite. Juxtaposition of Marinoan cap dolomite (Fig. 34A) gave rise to misidentification of Ac diamictite wedge as Marinoan (Hoffman and Halverson, 2008), an interpretation made untenable by Berg Aukas Fm drape (2–18–22, 27–32) (Hoffman et al., 2017b).

Mitrovica, 2014).

Karibib Fm (including Keilberg Mb) is relatively thin in Vrede domes, averaging 80 m ($n = 5$) away from the Chuos Fm wedge (Fig. 32), over which it thins as discussed at the end of this section. In comparison, Karibib Fm is 327 m thick in Tr1 (Fig. 19) and 480 m in Tr5. In Vrede domes, Keilberg Mb is overlain by a 10-m-thick interval of marly dolomite rhythmite representing the post-Marinoan MFS. Intraclast debrites in the upper Karibib Fm have conspicuous dedolomitized clast-moulds filled by white sparry calcite (Fig. 34F). Similar late sparry cement (not necessarily coeval) fill leftover ‘smiley-face’ voids (Fig. 34E) in the lower Keilberg Mb sheet-cracked zone.

Karibib Fm is disconformably overlain by quartz-sandstone and

siltstone of Kuiseb Fm, locally (1–27) with a basal dolomite-chert pebble conglomerate. Karibib-derived dolomite-chert olistoliths and olistromes are prominently exposed in Kuiseb schist E of N- and S-domes (Fig. S4A & B). We see no evidence or need for a large-scale thrust contact between Karibib and Kuiseb formations in Vrede domes as previously inferred (Nascimento et al., 2016, 2017, 2018). The arenaceous Kuiseb Fm in Vrede domes (‘Brak River Fm’ of those authors) has little in common lithologically with Okonguari or Narachaams formations (Fig. 32).

Karibib Fm thins over the Chuos Fm wedge because of erosional downcutting beneath Kuiseb Fm (Fig. 32). Where the wedge is thickest, sub-Kuiseb erosion cuts down to Keilberg Mb (1–20–26). We surmise

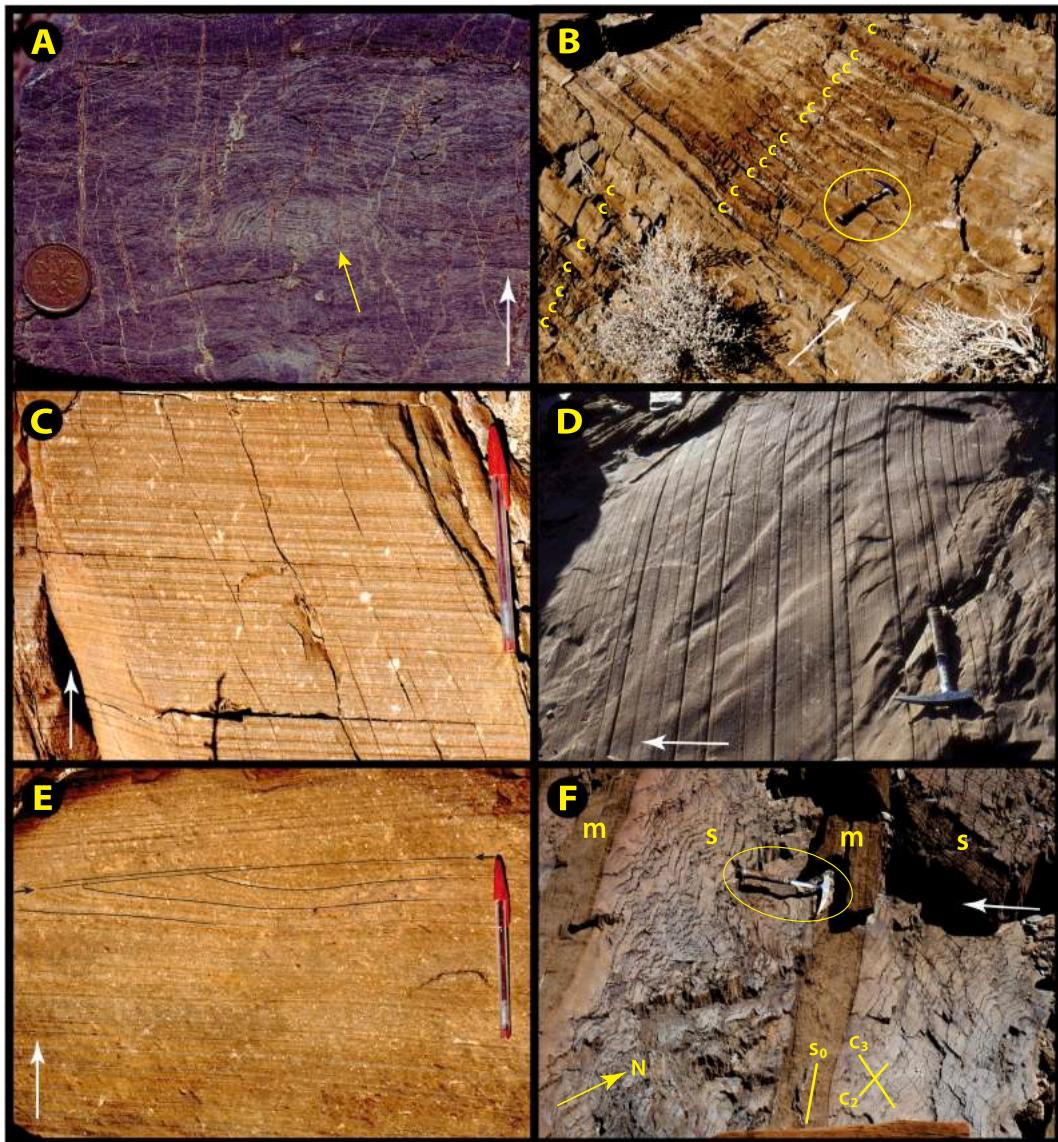


Fig. 33. More images from Vrede domes (Tr2): white (only) arrows indicate stratigraphic younging. (A) Microbialaminite with roll-up structures (oblique arrow) in Berg Aukas Fm cap dolomite in 2–38 (Fig. 32); at $-20.3629^{\circ}/14.1514^{\circ}$. Roll-up microbialaminite is an iconic facies in Berg Aukas and Rasthof formations (Hoffman et al., 1998a; Pruss et al., 2010). (B) Siltstone (brown) with regularly spaced cm-scale limestone turbidites (c) of the lower Narachaams Fm in 2–37 (Fig. 32); $-20.3590^{\circ}/14.1601^{\circ}$. Limestone turbidites represent distal equivalents of the Okonguarri Fm of Tr1 (Figs. 18 & 27) and Tr5 (Fig. 43). (C–D) Characteristic parallel laminated siltstone of Narachaams Fm in 2–36 (Fig. 32); $-20.3622^{\circ}/14.1633^{\circ}$. Evidence of wave action or bottom traction currents are absent, but soft-sediment slumps occur sparingly. (E) Synsedimentary discordance (small black arrows) in Narachaams Fm in 2–37 (Fig. 32), at $-20.3598^{\circ}/14.1597^{\circ}$, presumably the result of slumping given the absence of traction-current bedforms. (F) Two generations of tectonic cleavage in Narachaams siltstone (s) and marly limestone (m) in 2–37 (Fig. 32); $-20.3596^{\circ}/14.1597^{\circ}$. S_0 is primary layering. Arrow (lower left) indicates geographic N. Younger cleavage (C_3) parallels the Damara orogen and crenulates an older cleavage (C_2) that parallels the Kaoko orogen. An older Damara-parallel cleavage (C_1) was recognized in Tr2 by Maloof (2000). Three cleavages record successive collision events felt at the junction of two orogens (Fig. 3): C_1 , NDz collision ≥ 600 Ma; C_2 , CKz collision ≥ 580 Ma; and C_3 , SDz collision ≥ 550 Ma.

that Kuiseb downcutting over the Chuos prominence is no coincidence, despite the ≥ 60 -Myr difference in age. Consider existing (but structurally-restored) geometric relations between the wedge and enclosing formations (Fig. 35A, schematically generalized from Fig. 32). Following Sturtian glaciation, the Chuos wedge was draped by Berg Aukas and Okonguarri Formations, and buried by Narachaams Fm (Fig. 35B). Whether Narachaams Fm has a drape or onlap relationship against the wedge is unknown because internal stratigraphic control is lacking (Fig. 35B). Certainly the drape of Okonguarri Fm was

exaggerated by its early preferential compaction. During Marinoan glaciation, the wedge and its enclosing deposits were truncated (Fig. 35C). Following Marinoan glaciation, Keilberg Mb and Karibib Fm were deposited. Continued differential compaction of Okonguarri and Narachaams formations caused Keilberg Mb to sag and Karibib Fm to thicken with distance from the wedge apex (Fig. 35D). Sub-Kuiseb erosion, related to forebulge uplift (Hoffman, 2021a), truncated Karibib Fm with deepest erosion in its most elevated area at the Chuos wedge apex (Fig. 35E). Continued preferential compaction of

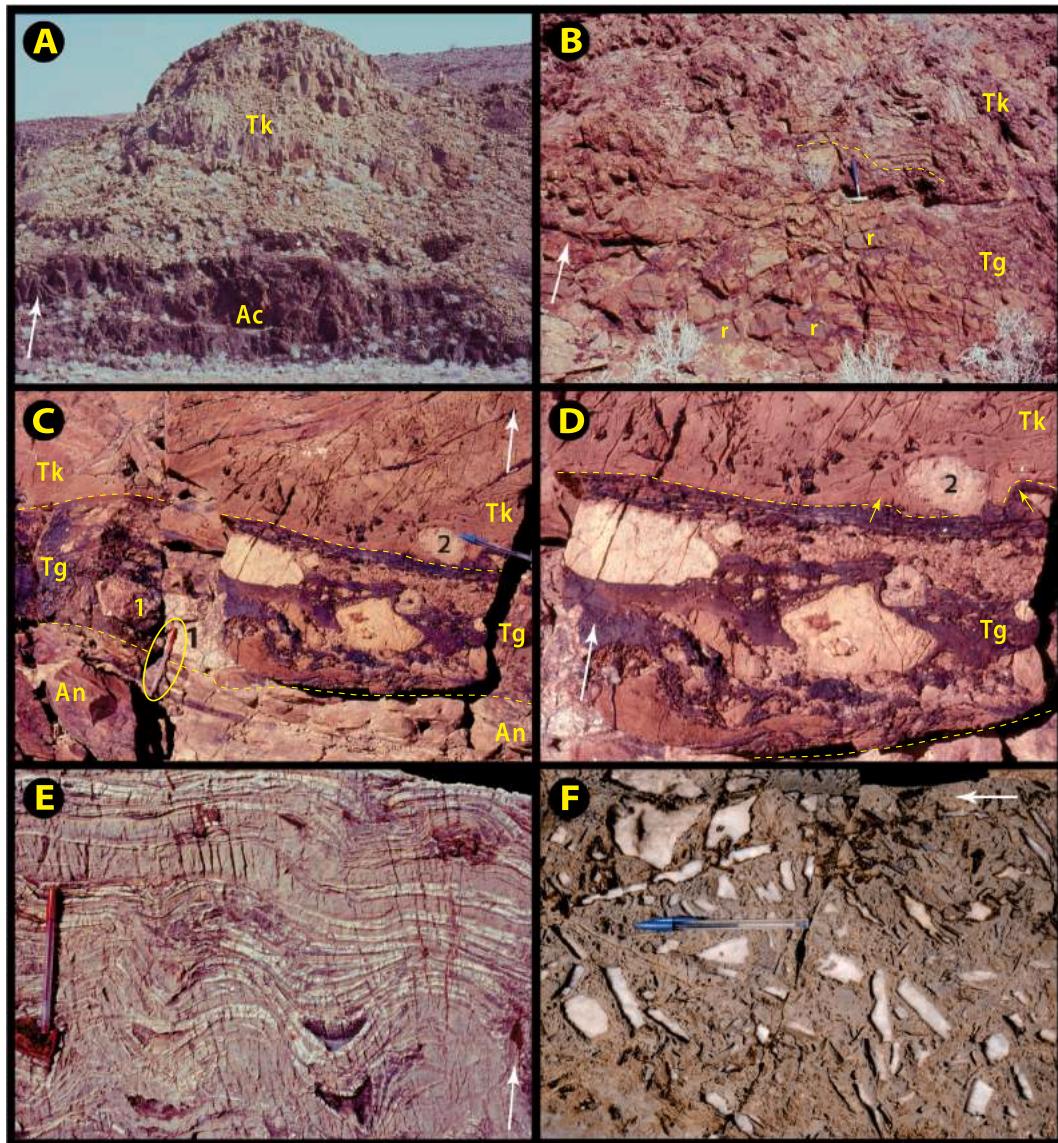


Fig. 34. More images from Vrede domes (Tr2): white (only) arrows indicate stratigraphic younging. (A) Sturtian Chuos Fm diamictite (Ac) overlain by Marinoan Keilberg cap dolomite (Tk) in 2–23 (Fig. 32): at $-20.4079^{\circ}/14.1468^{\circ}$. Contact is covered but no Ghaub diamictite was recognized in scree. (B) At $-20.4086^{\circ}/14.1470^{\circ}$ in 2–24, Keilberg cap dolomite (Tk) is separated from polymictic Chuos diamictite (not shown) by 5.5 m of carbonate-clast diamictite (Tg) tentatively correlated with Ghaub Fm. Grey dolomite clasts (r) could be derived from Berg Aukas Fm, which would exclude a Sturtian age for Tg. However, no clasts of Berg Aukas-diagnostic rollup microbial laminites (Fig. 33A) were found in Tg. (C–D) 30-cm-thick weakly stratified Ghaub Fm diamictite (Tg) in 2–31 (Fig. 32) at $-20.3983^{\circ}/14.1628^{\circ}$ sharply overlies Narachaams Fm argillite (An) with authigenic pyrite lenses (base of circled red pen). Tg underlies Keilberg Mb cap dolomite (Tk) with fibrous sheet-crack cement (upper left in C). Tg contains heterogeneous dolomite clasts and rare large basement granitoid clasts (1). Rare dolomite dropstones (2) occur in basal Tk, here with impact-related deformation (stubby arrows in D) and post-impact onlap. IRD has only been observed in Tk in NDz, consistent with diachronous (upslope-younging) Tk onset (Hoffman et al., 2007). (E) Fibrous isopachous dolomite sheet-crack cements (white) in lower (but not basal) Tk micro-peloidal ribbonite in 2–24 (Fig. 32): $-20.4086^{\circ}/14.1470^{\circ}$. Characteristic buckling intensifies with sheet-crack development. The largest buckle-related voids contain late-stage sparry calcite (recessed). Subvertical fibre growth of early dolomite cement implies hydrostatic jacking and pore-fluid overpressuring, possibly resulting from rapid regional sea-level fall in gravitational response to ice-sheet retreat and meltdown (Clark, 1976; Hoffman and Macdonald, 2010; Creveling and Mitrovica, 2014). Coexisting fibrous dolomite cement and micrite have similar C and O isotopic compositions (Figs. 174 & 176). (F) Intraclast debrite in upper Karibib Fm in 2–37 (Fig. 32): $-20.3579^{\circ}/14.1598^{\circ}$. Partial or complete neomorphic replacement of certain dolomite intraclasts by sparry calcite (white) is characteristic of the upper Karibib Fm in Tr1 and 2.

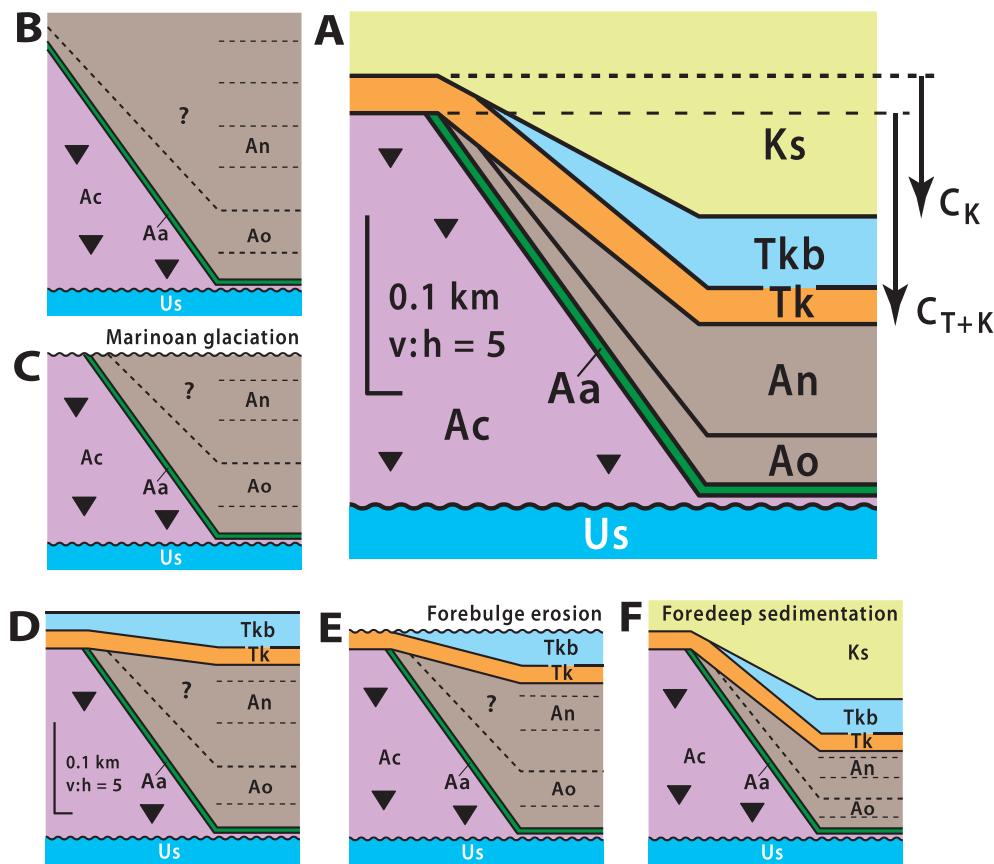


Fig. 35. Effects of progressive differential compaction of argillaceous Okonguarri (Ao) and Narachaams (An) formations relative to the Chuos Fm diamictite wedge (Ac) in Tr2, 2–18–30 (Fig. 32). (A) End-state showing compaction during Kuiseb Fm (Ks) time (C_K) and during Kuiseb Fm plus Karibib Fm ($Tk + Tkb$) time (C_{T+K}). (B) Effect of compaction during Ao and An sedimentation. (C) Erosional truncation of Chuos wedge during Marinoan glaciation. (D) Continued compaction in response to loading by Karibib Fm ($Tk + Tkb$). (E) Erosional truncation during forebulge uplift related to NDz and/or CKz collisions. (F) Compaction in response to loading by synorogenic Kuiseb Fm (Ks). Heterogeneous deformation of argillaceous Ao + An (Fig. 32) during refolding (Malooft, 2000) is not shown. Other abbreviations (Table 5): Aa, Berg Aukas Fm; Us, Orusewa Fm (Ugab Subgroup).

argillaceous Okonguarri and Narachaams formations caused Kuiseb Fm to sag (Fig. 35F) off the wedge as observed (Fig. 32). Accordingly, the stratigraphic geometry records an 80-Myr history (660–580 Ma) of differential compaction (Fig. 35).

2.2.3. Highlights from Tr2

Highlights from Vrede domes include: (1) N-to-S facies change from alluvial conglomerate to neritic carbonate in the 0.5-km-thick late Tonian Ugab Subgroup over a distance of 4.2 km (Fig. 30); (2) NE-tapered positive-relief wedge of Sturtian glacial deposits with an aspect ratio of 0.15 (0.223/1.5 km) in the SW of S-dome (Figs. 29 & 32); (3) mainly terrigenous basin-plain and distal turbidite-fan deposits of inter-snowball age (Okonguarri and Narachaams formations) that drape and bury the Sturtian glacial wedge (Figs. 32 & 35); (4) erosional decapitation of the Sturtian wedge during Marinoan glaciation, with the result that Marinoan cap dolomite (Keilberg Mb) directly overlies Sturtian glacial deposits (Chuos Fm) (Fig. 32), prompting former miscorrelation of Sturtian deposits as Marinoan in age (Malooft, 2000; Hoffman and Halverson, 2008); (5) erosional downcutting of Kuiseb clastics into Karibib dolomite over the buried Sturtian wedge, possibly reflecting prolonged differential compaction of the argillaceous inter-snowball formations (Fig. 35).

2.3. Transect Tr3 – Summas dome allochthon

Summas dome (Fig. 8A) is the northernmost in a SSW–NNE line of three structural domes crossing Northern zone cored by terrestrial peralkaline volcanic rocks of late Tonian age (Miller, 1974, 1980, 1983, 2008b; Schreiber, 2006). Most of Summas dome is allochthonous with respect to Congo craton and is carried on a thrust that is folded into the domal structure. This thrust emerges in the NE quadrant of the dome (Fig. 36), where structurally beneath the thrust is a basement-cored autochthonous (or parautochthonous) Damaran succession (Fig. 6C) described in section 2.4. (Tr4 in Fig. 8B). Allochthonous Tr3 was obtained from the monoclinal eastern flank of Summas dome (Figs. 36 & 37), plus two sections from the refolded Rondehoek anticline (Fig. 36). Field guides to both structures are provided in SOI S3.6., including annotated satellite images in Fig. S4. From a regional perspective (Fig. 8B), Tr3 is cozonial with Tr2 (Vrede domes), while Tr4 is cozonial with Tr1 (Aba-Huab autochthon).

2.3.1. Tonian in Tr3

No basement is exposed in the Summas allochthon: the oldest rocks belong to Lower Naauwpoort Fm (Miller, 1974, 1980; SACS (South African Committee for Stratigraphy), 1980), consisting of ≥ 6.6 km of alkali-rhyolite ash-flow tuff and minor lava (Miller, 1980). The ash-flow

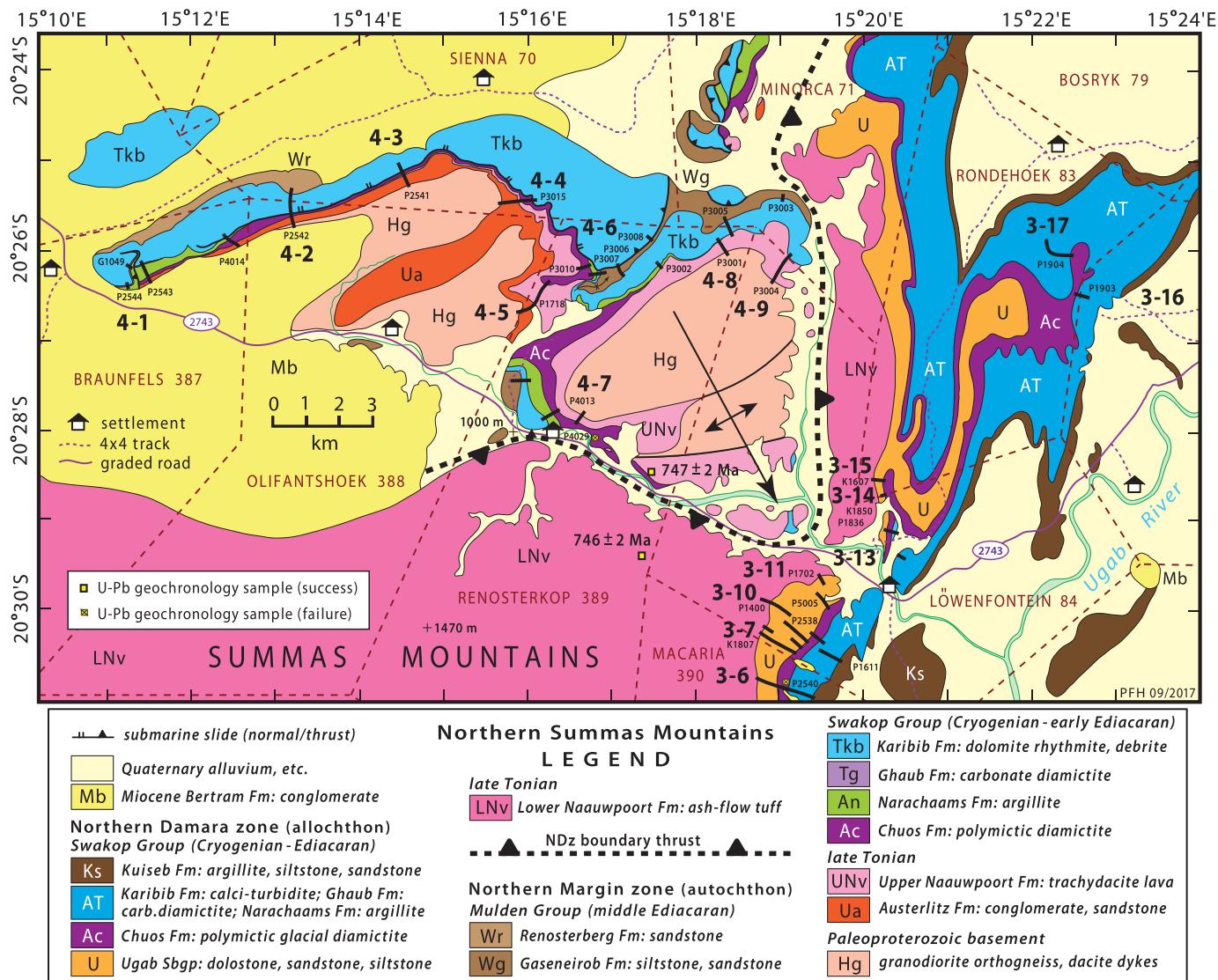


Fig. 36. Geology of Tr3 and 4 (modified after Miller, 1974, 2008a, b; Schreiber, 2006) on the E and N flanks, respectively, of Summas Mountains dome (Fig. 8A). Dome is cored by alkali-rhyolite ash-flow tuffs of Lower Naauwpoort Fm (LNV), depositionally overlain by Swakop Group of Tr3 (Fig. 39). See Fig. 37 for locations of 3–1–5. Refolded boundary thrust (inferred) separates Northern zone from (par)-autochthonous basement and distal FSz strata of Tr4, including basal coarse-grained clastics (Austerlitz Fm), trachy-dacite lava (Upper Naauwpoort Fm) and Swakop Group (Fig. 41). Lower and Upper Naauwpoort Fm volcanics have indistinguishable U–Pb zircon ages of 746 ± 2 Ma and 747 ± 2 Ma, respectively (Fig. 6B & C) (Hoffman et al., 1996). Field guides for Tr3 and 4 are SOI S3.6..

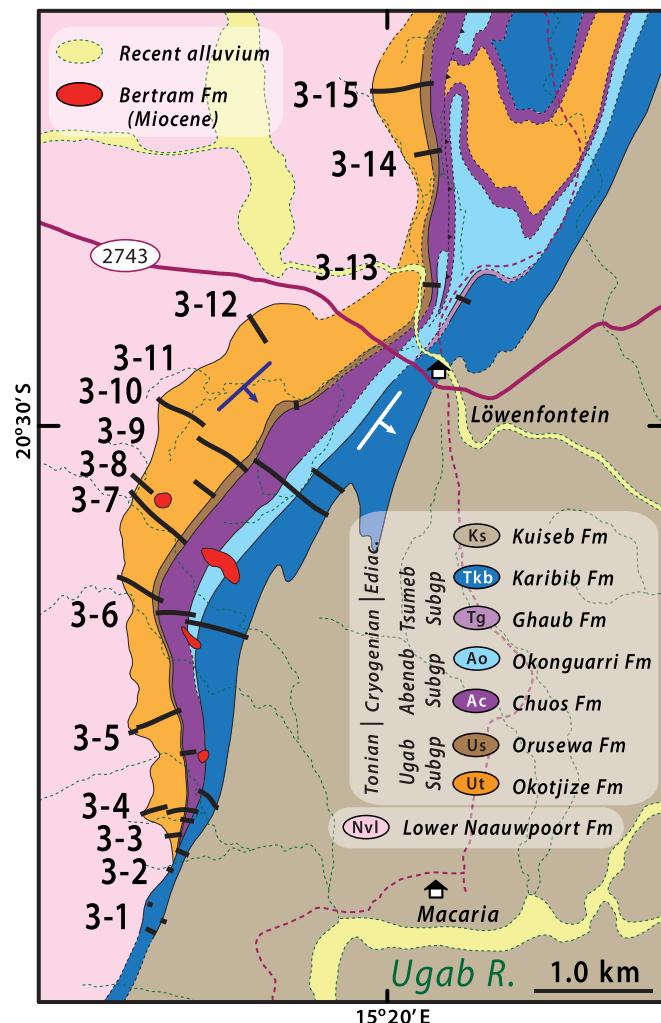


Fig. 37. Locations of columnar sections 3–1–15 (Fig. 39) on the E flank of Summas dome (Fig. 8A). Note unconformity beneath Karibib Fm that progressively truncates the Okonguarri, Berg Aukas (not shown), Chuos, Orusewa, and Okotjize formations from north to south (Fig. 40).

tuff is variably welded and eutaxitic, and most contain broken crystals as well as flattened pumice fragments in a matrix of devitrified shards (Fig. 38A). A veneer of tuffaceous siltstone and volcanic-derived sandstone overlies the volcanic pile and we include these sedimentary deposits in the basal Okotjize Fm (Figs. 6B, 37 & 39).

The most complete (and accessible) sections of Swakop Group occur on the eastern flank of Summas dome on farms Löwenfontein 84 and Macaria 390 (Figs. 36 & 37). The Tonian is represented by the 0.75-km-thick Okotjize and Orusewa formations (Fig. 6B) of Ugab Subgroup (Fig. 39). These formations are younger than 746 ± 2 Ma, the U–Pb (IDTIMS) age of igneous zircon from the stratigraphically underlying Lower Naauwpoort Fm (Hoffman et al., 1996). Okotjize Fm consists of peritidal dolomite and sandstone with subordinate siltstone and argillite (Fig. 39). Conversely, Orusewa Fm consists of siltstone and argillite with subordinate dolomite and sandstone. Since Orusewa is relatively thin, 10–140 m, its omnipresence beneath Chuos Fm (Fig. 39) indicates that Ugab and Abenab subgroups are structurally concordant.

2.3.2. Cryogenian in Tr3

Similar to Ugab Subgroup, Chuos Fm is thickest in the middle of the transect (Figs. 37 & 39). It is mainly composed of massive polymictic diamictite with subrounded boulders of basement orthogneiss up to 1.7 m in diameter (Fig. 38B). In section 3–15, massive and stratified diamictites host outsized blocks of variably oriented and folded limestone marble. One large block (B3 in Fig. 38C), 40 m from base to peak, is perched on the upper surface of a massive diamictite body. The block is nearly buried by stratified diamictite and only its peak projects into the next massive diamictite. In 3–13, stratified ferruginous diamictite contains boudinaged layers of authigenic chert (Fig. 38D). Authigenic chert suggests that geochemical cycling of Fe and Si were coupled (Fischer and Knoll, 2009) through adsorption of dissolved silica onto hydrous surfaces of ferric oxide particles in Sturtian seawater. In 3–10, massive diamictite holds subrounded clasts of porphyritic dacite (Fig. 38E) resembling Upper Naauwpoort Fm in Tr4. Chuos Fm tends to be more ferruginous toward its top (Fig. 38F), but evidence of Fe mobility causes us to doubt that this represents the original distribution of Fe in the

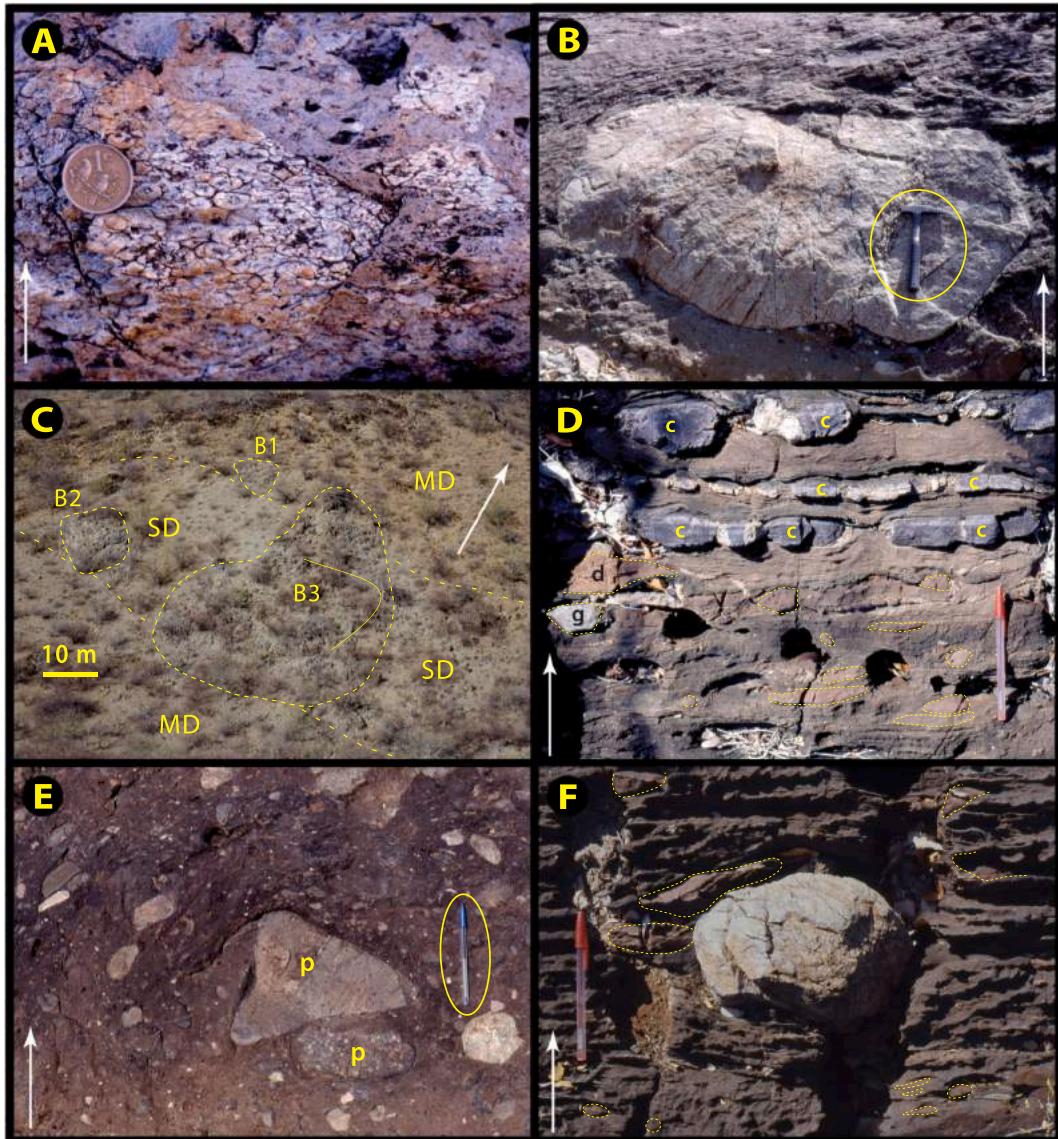


Fig. 38. Images from Summas dome allochthon (Tr3): white arrows indicate stratigraphic younging. (A) Lithic-rich ash-flow tuff (Lower Naauwpoort Fm) with large fragments of devitrified glass (2-cm-diameter coin for scale). (B) 1.75-m-long basement-derived granitoid boulder in Chuos Fm diamictite in 3–10: at $-20.5030^{\circ}/15.3237^{\circ}$. (C) Southward-looking view of 40-m-high limestone olistolith (B3) within stratified (SD) and massive (MD) diamictites of Chuos Fm in 3–15 (Figs. 36 & 37): $-20.4757^{\circ}/15.3374^{\circ}$. Stratified diamictite dips 69° SE. Bedding in limestone blocks B1 and B2 dips 78° and 31° S, respectively, and bedding in B3 is folded. Base of B3 is at $20^{\circ}28.544^{\circ}\text{S}, 15^{\circ}20.233^{\circ}\text{E}$. (D) Authigenic chert (c) in foliated diamictite with dolomite (d) and minority granitoid (g) clasts in Chuos Fm in 3–13 (Fig. 39): $-20.4900^{\circ}/15.3372^{\circ}$. (E) Porphyritic dacite clasts (p) in Chuos Fm diamictite in 3–10: near $-20.5040^{\circ}/15.3234^{\circ}$. Porphyry closely resembles Upper Naauwpoort Fm trachy-dacite lava in (par)-autochthonous Tr4 (e.g., 4–5). (F) Porphyritic granite boulder in ferruginous dolomite-clast (dashed outlines) diamictite of Chuos Fm in 3–13: $-20.4899^{\circ}/15.3371^{\circ}$. Pen is 15 cm long in all images.

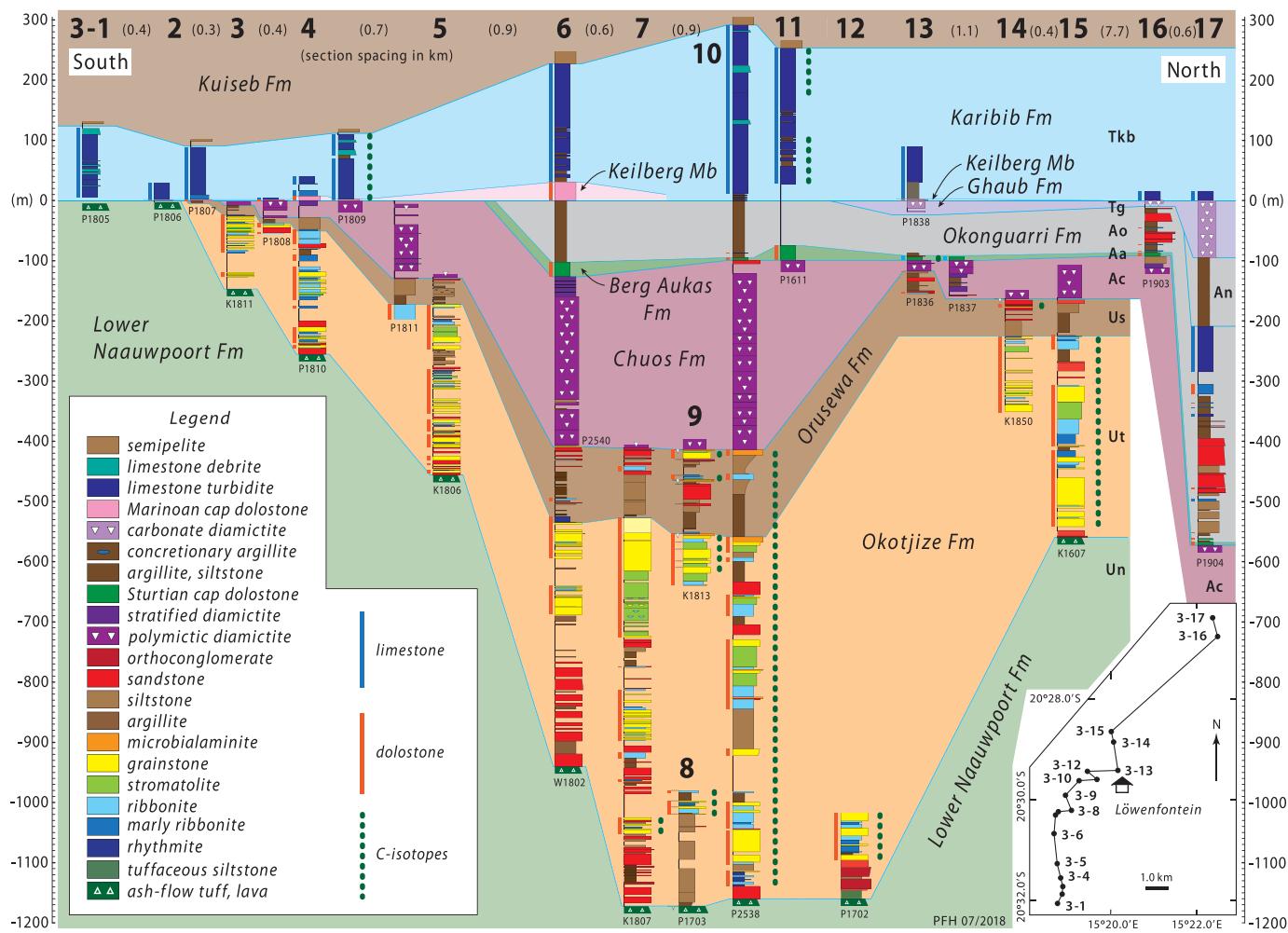


Fig. 39. Swakop Group (post- 746 ± 2 Ma) columnar sections from Tr3 on E flank of Summas dome (Figs. 36 & 37). Datum (0.0 m) is basal Ediacaran Karibib Fm. Note progressive N-to-S truncation of Berg Aukas, Chuos, Orusewa and Okotjize formations beneath Karibib Fm (Fig. 40), implying northward tilting and erosional beveling of Marinoan age. Note also continuity of Orusewa Fm beneath Chuos Fm, demonstrating that diamictite thickening (3–6–10) is not due to incision. Formation names abbreviated as in Fig. 37 legend.

formation. Chuos Fm is sharply overlain by ≤ 24 m of dark-grey calcite or dolomite rhythmite of Berg Aukas Fm, which in 3–13 includes a 0.4-m-thick lens of coarse-grained quartz sandstone. Berg Aukas is overlain by mixed argillite, siltstone, sandstone and limestone turbidites of Okonguari Fm, and greenish-grey laminated argillite of Narachaams Fm, variably truncated by the sub-Ghaub Fm (Marinoan glacial) disconformity (Figs. 37 & 39).

2.3.3. Marinoan–Ediacaran in Tr3

Between sections 3–2 and 3–6, basal Karibib Fm cuts systematically down section from N to S across Abenab and Ugab subgroups (Figs. 37 & 40). In 3–2, Karibib Fm directly overlies Lower Naauwpoort volcanics. Karibib Fm is not thickened in the area of downcutting as would be expected if downcutting resulted from erosional incision. If anything, Karibib Fm and its basal Keilberg Mb are thinner in the more deeply eroded area (Fig. 40). Structural tilting and erosional beveling of Tonian and Cryogenian strata, in response to crustal stretching and normal faulting of Marinoan age, is proposed to explain the stratal geometry (Hoffman et al., 2018). Tilt-correction of Karibib Fm yields a N–NE dip for older strata, consistent with a S–SW (seaward)-dipping normal fault as indicated beneath ‘Macaria’ basin in Fig. 26. Absence of Ghaub Fm in the area of Karibib downcutting is consistent with net Marinoan glacial erosion. Thinning of Karibib Fm in the same area suggests small-scale

positive topography due to greater erosion resistance of Lower Naauwpoort and Okotjize formations relative to Chuos and Okonguari formations (Fig. 40).

Ghaub Fm is best developed in Rondehoek fold (3–17) and 3–13, where ≥ 20 m of relatively fine-grained dolomite-clast diamictite conformably underlie a 2.8-m-thick Keilberg cap dolomite (Fig. 39). Keilberg Mb is transgressive (i.e., deepening-upward) and low-angle cross-stratification implies water depths above storm wave base for its first 1.2 m of accumulation. In section 3–4 (P1809), a 2.5-m-thick Keilberg Mb with fibrous isopachous sheet-crack cement (Fig. 34E) is separated from underlying Chuos Fm polymictic diamictite by 2 cm of laminated dololutite with cm-size dropstones of dolomite and basement granodiorite (Fig. 40). This easily overlooked IRD layer is presumed to represent Marinoan glaciation, a situation reminiscent of the glacially-decapitated Chuos wedge in Vrede south dome (e.g., 2–24 in Fig. 32). Above the cap dolomite, Karibib Fm consists of 0.1–0.3 km of limestone turbidites and fine intraclast debrites (Fig. 39). It is abruptly overlain by argillite, siltstone and sandy turbidites of Kuiseb Fm.

2.3.4. Highlights from Tr3

The chief highlight is stratigraphic evidence for collective rotation and erosional beveling of Tonian and Cryogenian formations during Marinoan glaciation, prior to basal Ediacaran deglaciation (Fig. 40). It

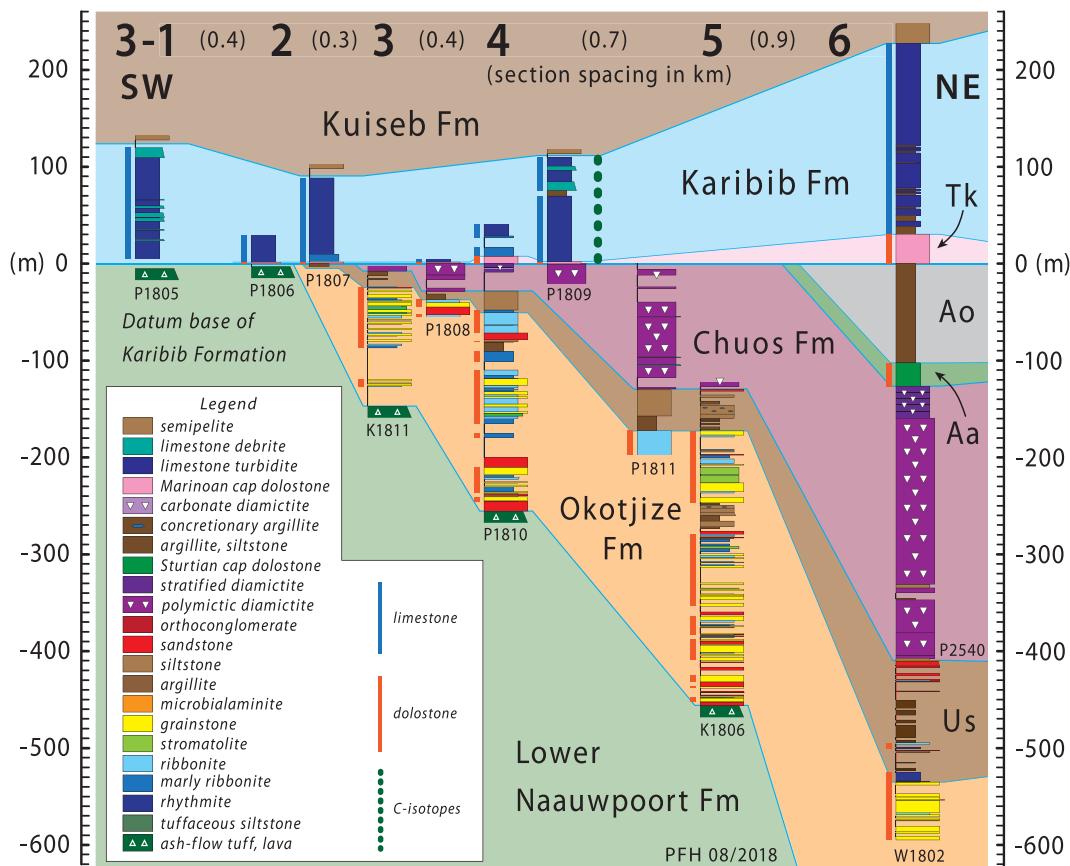


Fig. 40. Enlarged part of Fig. 39 showing critical stratigraphic relations in 3–1–6: see Fig. 39 caption. Formation names abbreviated as in Fig. 37 legend.

follows that crustal stretching in NDz occurred 5–20 Myr after the rift-to-shelf transition in OPz (Figs. 10 & 5). This accounts for the presence of basement clasts in Ghaub Fm of Tr1–3 (e.g., Figs. 20D & 34C), and with their absence in other transects.

2.4. Transect Tr4 – Summas dome autochthon

Crystalline basement of Tr4 and its autochthonous Damara Supergroup cover are exposed in a broad anticline that plunges SE beneath the allochthon of Tr3 (Fig. 36). It is onlapped from the W by a Miocene terrace (Bertram Fm) of conglomerate and silcrete (Miller, 2008c). The basement consists of orthogneiss—granitic, granodioritic and tonalitic in composition—of presumed Paleoproterozoic age (Miller, 2008a, pp. 4–9). It is intruded by a dense swarm of dykes, apparently feeders to Upper Naauwpoort Fm trachydacite lavas (Miller, 1980). The strike of the dyke swarm bends from ENE near section 4–7 to NNE near 4–9 (Fig. S7B). If the bending is a product of the SE-plunging basement anticline, then the dykes mostly likely dipped SSE before folding. Such a dip could have resulted from rotation of vertical dykes by slip on listric normal faults dipping away from the craton (e.g., Henry et al., 1990), compatible with the tilt of pre-Karibib Fm strata in Tr3 (Figs. 37, 40 & 26).

Autochthonous cover (Fig. 41) includes Tonian, Cryogenian and Ediacaran sequences: the Cryogenian beginning at the base of Chuos Fm (Shields-Zhou et al., 2015) and ending at the top of Ghaub Fm (Knoll et al., 2006; Narbonne et al., 2012). Chuos Fm occurs in all sections except 4–9, but Ghaub Fm appears in section 4–1 only (Fig. 41).

Consequently, basal Ediacaran Karibib Fm was extrapolated eastward based on mappable continuity. This is problematic across the structural break between sections 4–5–6 and 4–7–9 (Figs. 36 & 41). Miller (2008b, Fig. 13.12) interprets our ‘Karibib Fm’ in 4–7–9 (Fig. 41) as Tonian (‘Ombombo Subgroup’). While we think this is unlikely because, from 4 to 8 toward 4–7, it consistently overlies Chuos Fm, we cannot rule out the Cryogenian (Okonguari Fm?) as an alternative interpretation.

2.4.1. Tonian in Tr4

A lower sedimentary assemblage (Austerlitz Fm) and an upper volcanic assemblage (Upper Naauwpoort Fm) make up the pre-Sturtian succession in Tr4 (Fig. 41). Austerlitz Fm unconformably overlies basement orthogneiss and is an upward-fining assemblage of basement-derived boulder and cobble conglomerate, pebbly sandstone, and recessive thin-bedded siltstone and locally dolomite (Fig. 41). Ranging 0–240 m thick, it presents an alluvial to lacustrine or paralic transition. Lower units are more variable in thickness than higher ones, suggesting structural conformity with the overlying Upper Naauwpoort volcanic rocks.

Miller (1974, 1980, 2008b, SACS (South African Committee for Stratigraphy), 1980) described and named the volcanic assemblage Upper Naauwpoort Fm and placed it within Nosib Group. It consists of variably porphyritic and amygdaloidal lavas of alkali-rich (9.4% Na₂O + K₂O) intermediate (62% SiO₂) composition (Miller, 1980). The lava is dark greenish in colour and falls squarely in the trachydacite field of the IUGS volcanic rock classification. Numerous epidote-rich zones

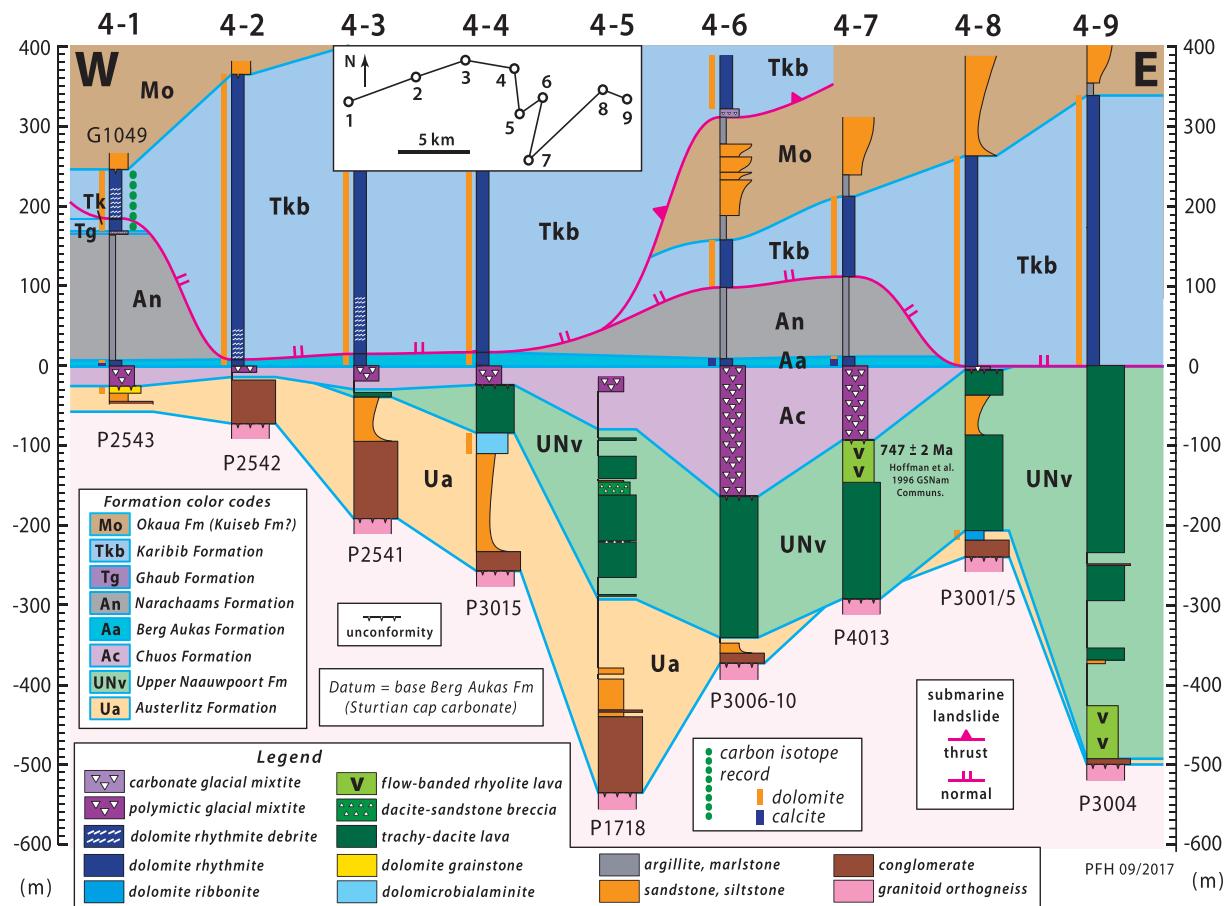


Fig. 41. Swakop Group columnar sections in Tr4, on the (par)-autochthonous distal FSz to N of and structurally below Summas dome (Fig. 8B). Fig. 36 gives section locations. Datum (0.0 m) is base of Berg Aukas Fm (post-Sturtian cap carbonate). Basal clastics (Austerlitz Fm) and overlying volcanics (Naauwpoort Fm) were included in the Nosib Group (Hedberg, 1979; Miller, 1980; Schreiber, 2006), but U–Pb zircon dating (Hoffman et al., 1996; Halverson et al., 2005) indicates that the volcanics and perhaps both formations are younger than the Devede Fm (Ombombo Subgroup), which postdates the Nosib Group in the IPz (Fig. 6B–D). Above the datum, stratigraphic omissions (e.g., Karibib Fm over Berg Aukas Fm) and duplications (e.g., Karibib Fm over Okaua Fm) are tentatively related to southeastward directed landsliding documented NE of Tr3–4 (Clifford, 1962, 2008).

and veins suggest Na metasomatism of igneous plagioclase. Breccia zones up to 17 m thick (4–5) consist of self-supporting angular blocks of porphyritic lava, engulfed by fine-grained sandstone with variably disturbed stratification (Fig. 42A). The sandstone fills narrow fractures in lava blocks and is not fused in contact with even the largest blocks. The breccias may be peperites, formed where lava flowed over moist unconsolidated sediment. The thickest volcanic section (495 m) is 4–9, and Sturtian glacial erosion beneath Chuos Fm could account for the lava pile's westward taper (Fig. 41).

A U–Pb (IDTIMS) age of 747 ± 2 Ma was determined for igneous zircon in a feldspar-phyric, flow-banded, rhyolite lava (Fig. 42B), 3 km SE of 4–7 (Fig. 36). Where dated, the rhyolite is depositionally overlain by steeply dipping, SW-facing, Chuos Fm diamictite (Fig. 41). The age is statistically indistinguishable from the allochthonous Lower Naauwpoort age of 746 ± 2 Ma in Tr3 (Hoffman et al., 1996). Allowing for analytical uncertainty, the indistinguishable ages support a model (Miller, 1980, p. 17) in which Lower Naauwpoort Fm (≥ 6.6 -km-thick, no base exposed) occupied a cauldron-subsidence structure that underwent cycles of resurgence (Smith and Bailey, 1968), when lava (Upper Naauwpoort Fm) flowed outside the subsidence structure, like a lava levées.

Miller (1974, 1980, 2008b) assigned both Lower and Upper Naauwpoort volcanics to Nosib Group but affiliated the underlying

conglomerate-dominated assemblage (Austerlitz Fm in Fig. 41) differently over time. At first he correlated it with Okotjize Fm (Miller, 1974), then included it in Upper Naauwpoort Fm (Miller, 1980), and finally placed it in Ombombo Subgroup (Hoffmann and Prave, 1996) of the IPz (Figs. 5 & 6D) (Miller, 2008b, Fig. 13.12). Correlation with Okotjize Fm is problematic because that formation postdates Naauwpoort volcanism (Fig. 39), whereas Austerlitz Fm in Tr4 precedes it (Fig. 41). Similarly, affiliation with Ombombo Subgroup is problematic since Nosib Group underlies Ombombo Subgroup in IPz (Figs. 5 & 6D) but overlies Austerlitz Fm in Tr4, so long as Naauwpoort volcanics are included in Nosib Group.

Hedberg (1979, p. 72–80) gave the name Austerlitz Fm to conglomerate and sandstone that overlie crystalline basement of SW Welwitschia inlier (Fig. 8A) and underlie Naauwpoort volcanics in their type area (farm Naauwpoort 511). Hedberg (1979) proposed extending Austerlitz Fm to Tr4 and we adopt this correlation, bearing in mind that Naauwpoort volcanism in Welwitschia inlier and Summas dome (Fig. 8A) need not be coeval. On farm Austerlitz 515 (Fig. 15), NDz basement is separated from Sturtian diamictite (Chuos Fm of Hoffman and Halverson, 2008, Fig. 13.85) by a conglomerate-bearing heterolithic succession that includes a crystal-rich dacite ash-flow tuff from which zircon was dated by SHRIMP at 757 ± 5 Ma (Nascimento et al., 2016). This age is 10 ± 7 Myr older than Upper Naauwpoort Fm volcanism in Tr4

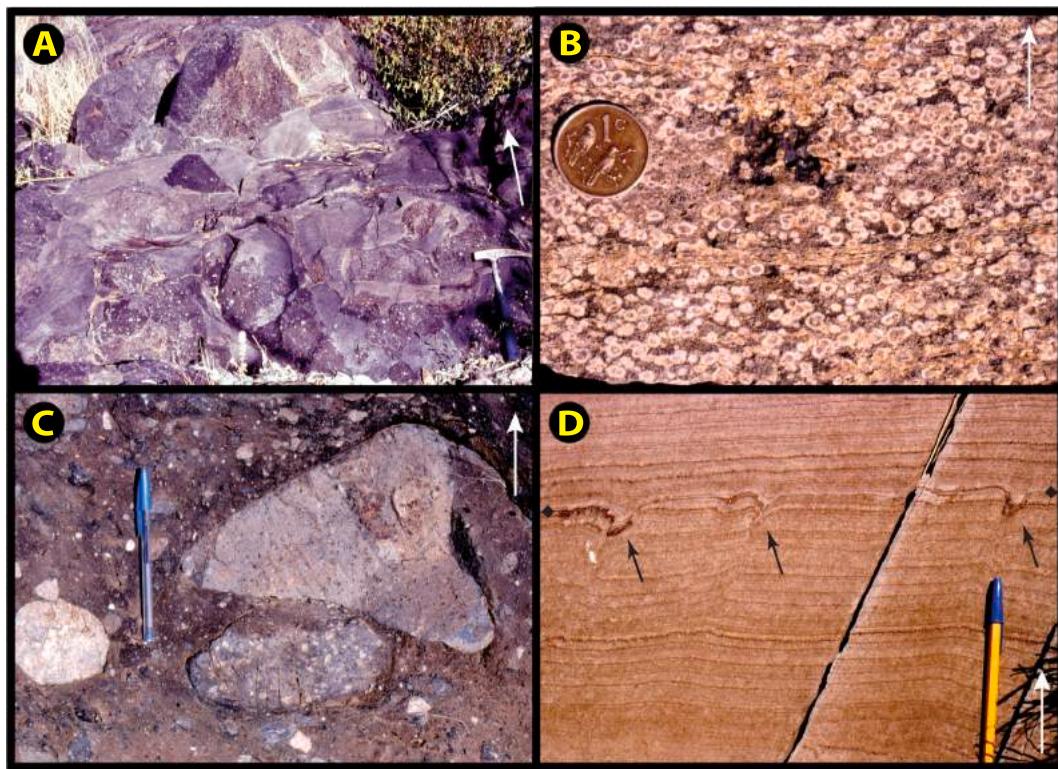


Fig. 42. Images from Tr4: white arrows indicate stratigraphic younging. (A) Peperite (?) breccia composed of blocks of feldspar-phyric trachydacite (Miller, 1980) lava in a matrix of stratified subfeldspathic sandstone in 4–5 (Figs. 36 & 41): at $-20.4421^{\circ}/15.2702^{\circ}$. (B) Flow-banded feldspar-phyric rhyolite in 4–7 (Figs. 36 & 41): $-20.4769^{\circ}/15.2904^{\circ}$. Its U–Pb zircon age at this location is 747 ± 2 Ma (Hoffman et al., 1996). The rhyolite is physically underlain (stratigraphically overlain) by downward-facing (overturned) Chuos Fm diamictite, dipping steeply NE. Coin is 2 cm in diameter. (C) Clasts of feldspar-phyric trachydacite, derived from Upper Naauwpoort Fm (Tr4), within Chuos Fm diamictite in 3–10: near $-20.5040^{\circ}/15.3234^{\circ}$. (D) Parallel-laminated siltstone of Narachaams Fm in 4–1 (Figs. 36 & 41): at $-20.4373^{\circ}/15.1889^{\circ}$. Possible fluid or gas escape pits (small black arrows) occur at a common stratigraphic horizon (black diamonds).

(747 ± 2 Ma, Hoffman et al., 1996), but indistinguishable from an IDTMS age of 756 ± 2 Ma (Hoffman et al., 1996) for Oas quartz-syenite (Frets, 1969), a large intrusive body in southern Welwitschia inlier. It should be borne in mind that in none of these areas has the duration of volcanism been determined.

2.4.2. Cryogenian in Tr4

In only one section (4–1) is the Cryogenian ‘complete’—meaning that early, middle and late Cryogenian (Table 1) deposits are all present (Fig. 41). Chuos Fm in 4–1 is a ferruginous-schist with ‘floating’ sub-rounded clasts of tonalitic orthogneiss, quartzite and buff dolomite. Maximum measured thickness of Chuos diamictite is 164 m in 4–6 (Fig. 41). In 4–1, Chuos diamictite is sharply overlain by 3.0 m of bluish-grey calcite rhythmite and 4.0 m of black dolomite rhythmite or microbialaminite, coupled as Berg Aukas Fm (Fig. 41). This Sturtian cap carbonate is continuous as far as 4–7 (Fig. 41). In 4–1, Berg Aukas Fm is overlain by 2.7 m of marly dolomite rhythmite (=Okonguari Fm?) and 154 m of greenish-grey argillite and marlstone of Narachaams Fm, characterized by flat parallel lamination without bedforms aside from small (≤ 1 cm) pits (Fig. 42D) of unknown origin (dewatering pits?). The complete absence of mudcracks and current bedforms rules out raindrop impressions. As in Tr2 (Fig. 33C & D), Narachaams Fm is worth consideration as a target for inter-snowball cyclostratigraphy (e.g., Bao et al., 2018). Eastward from 4 to 1, post-Keilberg Karibib Fm cuts steeply down-section structurally across Narachaams Fm onto the top of Berg Aukas Fm, with the result that Narachaams Fm is missing from 4 to 2 to

4–4 (Fig. 41). Back in 4–1, Marinoan glaciation is represented by 4.0 m of dolomite-clast diamictite above 2 m of cover (Fig. 41). This Ghaub Fm diamictite is sharply overlain by 14 m of Keilberg Mb pinkish to buff-coloured dolomite, its lower (but not basal) part characteristically expanded by partly-silicified, fibrous-isopachous, sheet-crack cement (e.g., Fig. 34E).

2.4.3. Ediacaran in Tr4

Karibib Fm is a 60–360-m-thick sequence of carbonate rhythmite, turbidite and intraclast debrite (Fig. 41). It is completely dolomitized and lightly silicified in Tr4, similar to Tr1 and 2 but unlike Tr3, where Karibib Fm is an undolomitized and more-distal foreslope facies (Fig. 39). In Tr4, it is disconformably overlain by quartz-sandstone and finer-grained clastics of Okaua Fm (Clifford, 2008), which appears broadly equivalent to Kuiseb Fm but placed in Mulden Group (Clifford, 2008).

As previously noted, Narachaams and Ghaub formations are missing in sections 4–2–4, where Karibib Fm rests directly on Berg Aukas Fm for 12 km parallel to strike (Fig. 36). Nearly 0.18 km of strata are missing, implying an early (pre-doming) low-angle fault of normal-sense displacement (Fig. 41). In the area of composite section 4–6, this sub-Karibib fault ramps stratigraphically up-section, resulting in duplication of Karibib and Okaua formations (Fig. 41). Accordingly, the ramp has a thrust-sense of displacement. As discussed in 2.3.1., the affiliations of units Tkb and Mo in sections 4–7–9 are uncertain. If they are Cryogenian in age, rather than Ediacaran, then the steep fault again has a

normal sense not a thrust sense of displacement. A major change in Cryogenian facies or sequence would then be required between 4 and 1 and 4–6–9. More mapping in this interesting area is needed.

Along strike from Tr3 and 4 to the NE, Clifford (1962, 2008) identified and mapped an early SE-directed thrust he named Saturn slide (Clifford, 2008). It has a strike length of ca ≥ 13 km, a thrust separation of ≥ 3 km, and it duplicates nearly the entire Swakop Group although its relationship to Okaua Fm is not exposed (Clifford, 2008). We suggested that Saturn ‘nappe’ (i.e., the displaced mass, Clifford, 2008) is a submarine mass slide by analogy with map-scale structures in Tr7 and Tr11 (Hoffman et al., 2016b; Hoffman, 2021a). Large-scale coherent mass slides (imaged seismically) in existing continental-slope sediments typically have extended zones with listric normal faults in up-slope areas, and shortened zones with imbricate thrust faults in down-slope areas (e.g., Butler and Paton, 2010). Thrusting is observed to succeed normal faulting, or vice versa, in areas where the extension–compression transition migrated up or down slope, respectively (Armandita et al., 2015). There may be no intrinsic inconsistency, therefore, in the co-occurrence of thrust- and normal-sense displacements in a slope-related mass slide as tentatively inferred in Tr4 (Figs. 36 & 41).

2.4.4. Highlights from Tr4

Highlights include major changes in Tonian stratigraphy compared with Tr3: (1) appearance of pre-Naauwpoort sediments (Austerlitz Fm); (2) disappearance of post-Naauwpoort sediments (Ugab Subgroup); and (3) change in Naauwpoort volcanism from >6.6 km of alkali-rhyolite ash-flow tuffs in Tr3 to ≤ 0.5 km of mainly trachy-dacite lava in Tr4. Cryogenian–Ediacaran highlights in Tr4 include evidence for stratigraphic omissions and duplications of ≥ 0.2 km of strata on brittle low-angle detachment surfaces, tentatively interpreted as gravitational mass slides by analogy with better-documented examples in the Otavi Group of Tr7 and 11.

2.5. Transect Tr5 – Transfontein homoclinal

Located 30 km upslope from Tr4, Transfontein Ridge is the most fascinating and challenging of all transects because it alone crosses the FSz–OPz transition from Swakop to Otavi Group (Figs. 5, 8B & 43). Tr5 has the most measured sections of any transect—66 through the entire Abenab and lower Tsumeb subgroups, and many more through the Marinoan Ghaub Fm, which attains its maximum development in the FSz of Tr5.

The name Transfontein Ridge refers to present-day topography, wherein resistant Otavi/Swakop Group carbonates are tilted homoclinally S–SE, with dips of 35–60° (Fig. 43B). They form a ridge that rises ≤ 240 m topographically above the basement gneiss complex to the N, or the foredeep clastics (Mulden Group, Fig. 6C) and Miocene terrace gravel (Bertram Fm, Fig. 43B) to the S. Locally, there are dip reversals in the form of small syncline-anticline pairs in the Cryogenian of sections 5–5–6, 47–49 and 65–66 (Fig. 43A). Dip reversals also occur in an eastward-widening belt of open folds in Ediacaran Karibib Fm E of 5–36. Minor thrusts locally duplicate the Karibib–Mulden boundary interval (e.g., 5–8 and 45), possibly owing to strong rheologic contrast across their interface.

Over the entire length of Tr5 (62 km), the ridge is breached only by the drainage channel at Transfontein itself (Fig. 43B). Easily accessible sections at Transfontein (5–7, Fig. 44) are described in SOI S3.7., with geologically annotated satellite images in Figs. S8 and S12. They are beautifully representative of the distal FSz and exemplify Marinoan snowball-related falling-stand (FST), low-stand (LST), transgressive (TST) and highstand (HST) depositional sequences (Fig. S10). A field

guide to the western termination of Transfontein Ridge (5–1) is given in SOI S3.8. with annotated satellite images in Figs. S14 and S15.

Because of its length and disparity of facies (Fig. 43), Tr5 is described here in four segments: western (5–1–15), west-central (5–15–30), east-central (5–30–49) and northeastern (5–49–66). The last segment samples OPz and is more similar in facies and sequence structure to Tr7–11 (Fig. 8B) than to other segments of Tr5 with which it is physically connected in outcrop (Fig. 43B). The transect crosses the facies zones obliquely, with the western and west-central segments running nearly parallel to the inferred depositional strike, and the east-central and northeastern segments transecting the zonation at a ca 45° angle of azimuth (Fig. 43B).

Regardless of geologic age, carbonate platform–foreslope transitions are rarely simple (e.g., Wilson, 1975; Grotzinger, 1986b; Tucker et al., 1990; Schlager, 2005; Playton and Kerans, 2015a, b). The Otavi–Swakop group facies transition is no exception. The fence diagram (Fig. 43) was constructed as a crude restoration of the Marinoan termination (within the dictates of fitting information on a page). The rules of construction were the following. The datum for sections 5–1–25 (Fig. 43A) is the base of Frannis-aus Fm (Fig. 6C), the Marinoan FST. The datum was projected across Marinoan gullies (5–20–22, 26–28), where Frannis-aus Fm has been eroded away. The datum for sections 5–49–66 (Fig. 43A) is the base of Keilberg Mb, the Marinoan TST. There is no datum for sections 5–25–49, the east-central segment which we identify as upper or proximal FSz. Sections 5–25–49 were hung so as to yield a smooth sub-Ghaub Fm glacial erosion surface while minimizing relief on Duurwater moraine (Fig. 43A) and the basement surface in Kranstoort trough (Fig. 43A).

The datum for the western and west-central segments (5–1–25) was arbitrarily set 600 m below the datum for the northeastern segment (5–49–66). By this means paleobathymetric relief between OPz and FSz is restored (Fig. 43). The 600-m offset is conservative. Two-thirds of it (0.4 km) is demonstrable from Marinoan headwall erosion of Ombaatjie Fm between 5 and 44 and 49 (Fig. 43A). 0.1–0.2 km more are accounted for by the thickness of Franni-aus and Ghaub formations in the western segments (Fig. 43A), which must be added to reach a common datum (i.e., base Keilberg Mb). Paleobathymetric relief at Marinoan termination could have been significantly greater than shown (Fig. 43), but the external dimensions of the figure would then fit less snugly on the page. As shown, the crest of Duurwater moraine projects above the top of the Ombaatjie Fm platform (Fig. 43). The crest of the moraine would be lowered by increasing the arbitrary offset of 600 m between the distal FSz and OPz datums.

As restored (Fig. 43), Tr5 invites speculation regarding Cryogenian glacial erosion. Was Marinoan erosion concentrated at a headwall of Ombaatjie Fm shelf carbonate, with the resulting debris piled up as Duurwater moraine (Fig. 43A) at an ice-shelf grounding-line ca 6 km downslope? Was Kranstoort trough (Fig. 43A) a Sturtian U-shaped paleovalley cut into basement, with relict lateral moraines of Chuos diamictite preserved bilaterally (5–23–31 and 47)? Although the reconstruction results (unavoidably) in significant local relief on the basement surface of Kranstoort trough (Fig. 43), ‘walking out’ its contact with the overlying Berg Aukas Fm cap carbonate revealed no fault intersection east of the Sturtian half graben at 5–23 (Fig. 43). We do infer, however, the existence of a SSW-side-down, Berg Aukas and Okonguari-age flexure of the basement surface between 5 and 47 and 50 (Fig. 43).

2.5.1. Western segment of Tr5 (5–1–15)

The stratigraphic sequence and facies of this segment are relatively consistent between sections (Figs. 43 & 44) and reminiscent of Bethanis subbasin in Tr1 (Figs. 18 & 19). Sections are relatively widely spaced W

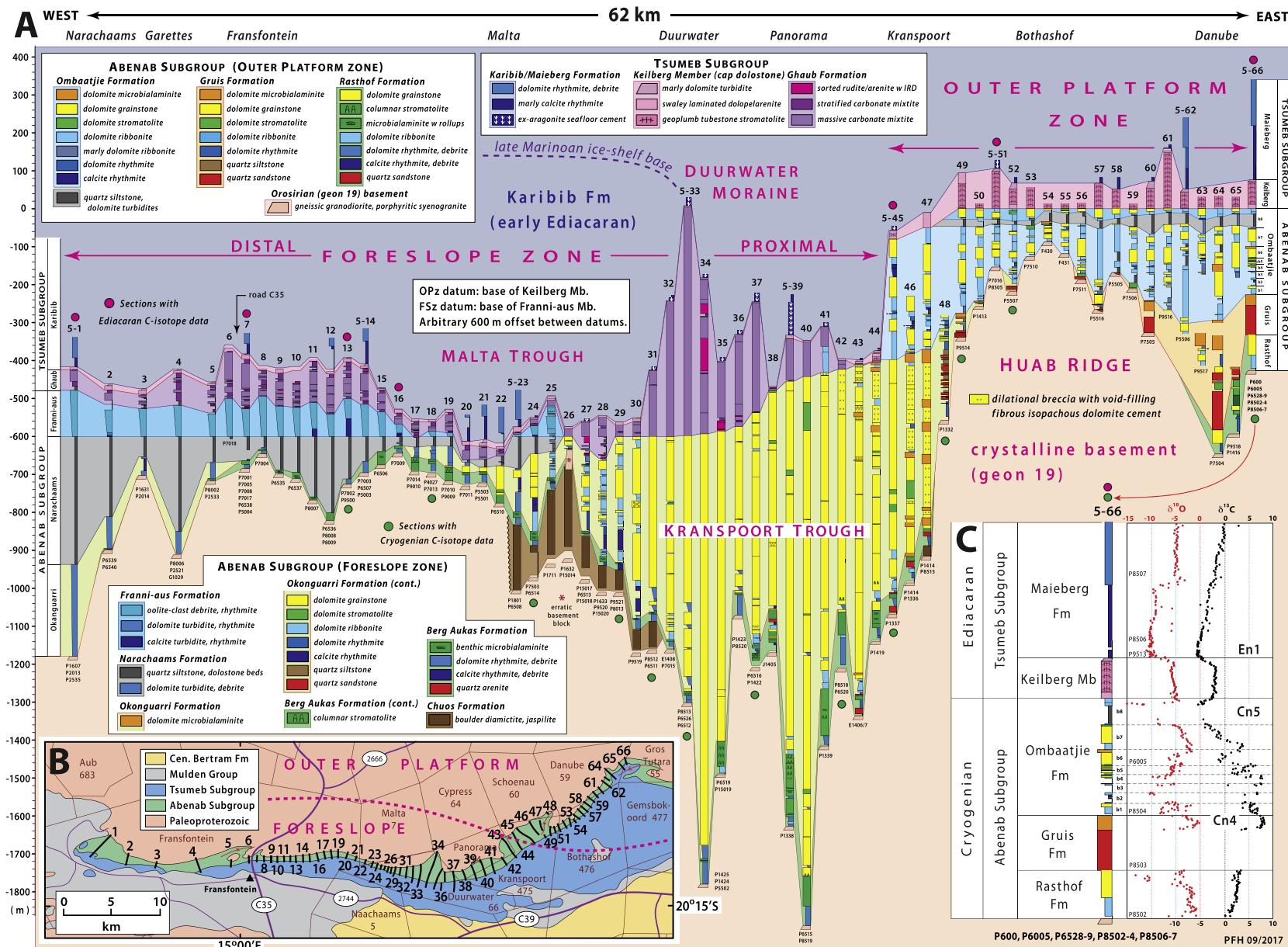


Fig. 43. (A) Cryogenian and early Ediacaran columnar sections from Tr5 (Fig. 8B), which offers an oblique unbroken section crossing the FSz–OPz transition (Fig. 5) on farm Kranstoort 475 (Fig. 64). Datum at –600 m for 5–1–25 is base of Franni-aus Fm (Fig. 44) and datum at 0.0 m for 5–49–66 is base of Keilberg Mb (Fig. 44). Datums are placed arbitrarily 600 m apart and sections 5–26–48 are interpolated. Green and red dots indicate Cryogenian and Ediacaran sections, respectively, with C-isotope data. (B) Location map for columnar sections in A showing the projected shelf break (dashed red line) at OPz–FSz boundary. (C) O- and C-isotope profiles (red and black dots, respectively) for OPz section 5–66. Field guide with annotated satellite images of sections near Transfontein (5–6 & 7) is SOI S3.7.

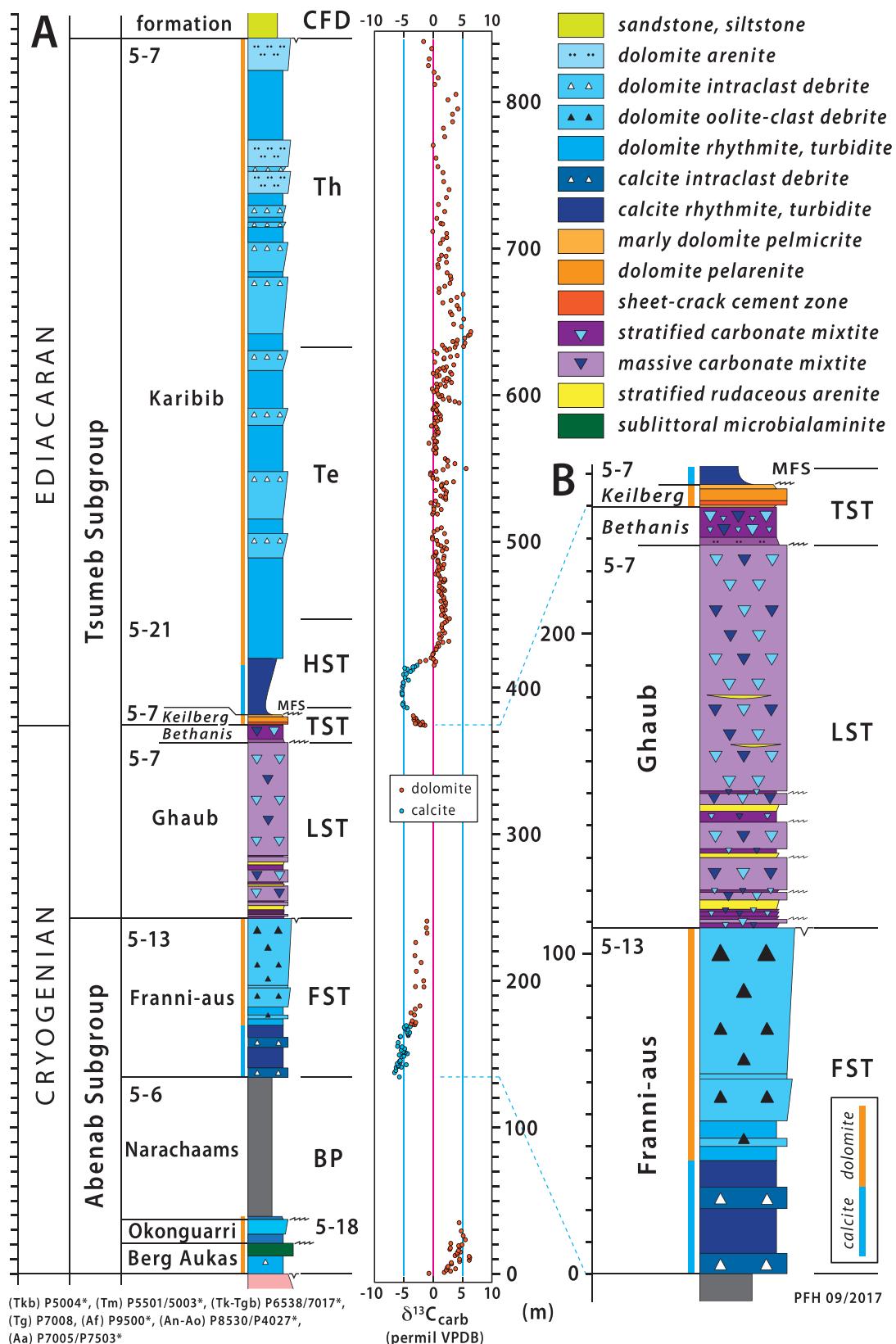


Fig. 44. (A) Composite columnar section and $\delta^{13}\text{C}_{\text{carb}}$ records of Swakop Group in distal FSz near Transfontein: section numbers (*isotopes) in lower left. (B) Expanded Marinoan section: see Fig. 43 for section locations (5–6, etc.) of each formation. Sequence stratigraphic divisions: TST, transgressive systems tract (Berg Aukas Fm); BP, basin-plain argillite (Narachaams Fm); FST, falling-stand systems tract (Fran尼-aus Fm); LST, low-stand systems tract (Ghaub Fm); TST (Bethanis and Keilberg members); MFS, maximum flooding surface; HST, highstand systems tract (Maieberg Fm equivalent); Te, chemostratigraphic Elandshoek Fm equivalent; Th, chemostratigraphic Hüttenberg Fm equivalent; CFD, collisional foredeep (Mulden Group).

of Transfontein (5–6), but we augment them with 24 additional sections of Marinoan Ghaub Fm and Keilberg Mb (Figs. 45 & 46). Fig. 46 (see also Fig. S11) covers most of the stretch studied in detail by glacial sedimentologist Eugene W. Domack (Domack and Hoffman, 2011). Figs. 5–8 and 10 in their paper correspond to sections 5–7, 12 and 14–16 here, respectively. The sections examined by Eyles and Januszczak (2007) are numbered 3 and 18 in Fig. 45. The termination of Swakop Group west of 5–1 is described and discussed in Hoffman (2021a).

Sturtian diamictite (Chuos Fm) is all but absent west of section 5–23: 0.5 m of stratified diamictite with small basement clasts occurs at the base of 5–2. Elsewhere, Berg Aukas Fm directly overlies basement (e.g., Fig. 44). E of 5–4, Berg Aukas Fm begins with grey dolomite rhythmite that coarsens upward through addition of dolomite turbidites and intraclast debrites. The top of Berg Aukas Fm is the familiar black-and-tan dolomite microbialaminite with roll-up structures. Between 5 and 7 and 16, Berg Aukas Fm is sharply overlain by argillite of Narachaams Fm (Fig. 43). West of 5–7, Berg Aukas and Narachaams formations are separated by a westward-thickening wedge of Okonguarri Fm, composed of dolomite rhythmite with turbidites and intraclast debrites (Fig. 47C & D). In 5–3, the debrites include tabular clasts of Berg Aukas-type microbialaminite (Fig. 47C), suggesting derivation, but other clasts appear to be encrusted by the same microbialaminite (Fig. 47E), implying contemporaneity. In the same section (5–3), trains of starved (isolated) current ripples (Fig. 47F) occur at some horizons. The tilt-corrected dips of their foreset laminae consistently indicate WSW-directed bottom currents, consistent with Coriolis-driven left-turning bottom currents (upwellings) and accordingly a southern-hemisphere

paleo-location (Fig. 11). The coarsening-upward debrite-rich Okonguarri Fm thickens westward to 226 m in 5–1, where m-scale blocks of dolomite stromatolite and oolite occur. Okonguarri Fm is everywhere abruptly overlain by argillaceous Narachaams Fm (Fig. 43).

The normally recessive Narachaams argillite is unusually well exposed between 5 and 2 and 3, where 0.2 km of reddish-brown argillite and silty argillite carry numerous thin turbidites composed of quartz-calcite and quartz-dolomite wackestone. A lone debrite holds clasts of limestone, dolomite and chert. Both contacts of Narachaams argillite are well defined.

Franni-aus Fm (Figs. 43 & 44) is a 60–120-m-thick, coarsening-upward sequence of carbonate rhythmite and intraclast debrite (Fig. 48A). Where exposed, the lower part of the sequence (Fig. 44) consists of limestone rhythmite and rhythmite-clast debrite (Fig. 48C & D). The coarser-grained upper part of the sequence is dolomitic and heavily silicified. The debrites are characterized by tabular clasts of well-sorted and very coarse-grained oolite (Fig. 48E & F). The ooids are up to 3 mm in diameter and their presence as independent grains and as unbroken grains at clast margins implies that the oolite source rock was not fully lithified when it was redeposited by debris flows. Although oolite is not uncommon in the lower Ombaatjie Fm of OPz (Fig. 5), there is no known external source for oolite as coarse-grained as that in Franni-aus debrites (Fig. 48F). Their $\delta^{13}\text{C}$ composition (Fig. 44, see 3.3.5.) implies that the oolite is endemic to Franni-aus Fm and records the Trezona CIE Cn5 recovery (Fig. 10D). We interpret Franni-aus Fm as a glacioeustatic falling-stand wedge (FST), related to ice-sheet growth at higher latitudes at the Marinoan glacial onset (Hoffman, 1999, 2011a).

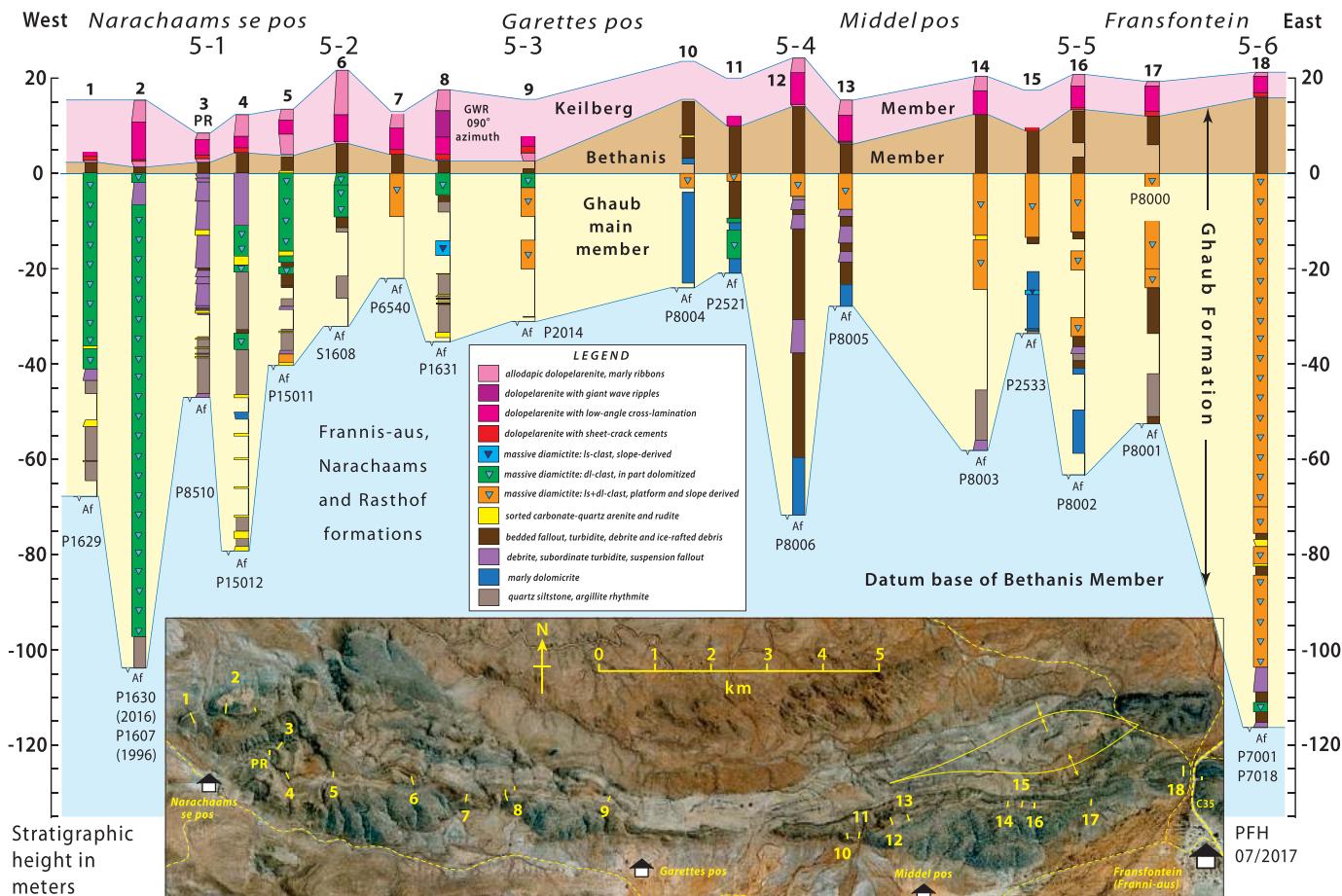


Fig. 45. Marinoan Ghaub Fm and Keilberg Mb cap dolomite in distal FSz on Transfontein Ridge (Tr5) W of Transfontein. Sections are numbered 5–1–6 as in Fig. 43 with additional Marinoan sections 1–18. For eastward continuation see Fig. 46. Note lateral lithofacies variability in the Ghaub main member. Sections 2 and 3 (5–1), just 1.2 km apart, are dominated by massive diamictite and bedded debrite, respectively. In contrast, Bethanis and Keilberg members (TST, Fig. 44) are laterally continuous (see also Fig. 46). Google Earth: Image © 2020 CNES/Airbus & Maxar Technologies.

Occurrence of extrabasinal IRD in chemostratigraphically correlative strata of Trezona Fm in South Australia (Rose et al., 2012, 2013) strengthens the glacioeustatic inference linking CIE Cn5 temporally with Marinoan glacial onset.

Marinoan lowstand deposits of Ghaub Fm (Fig. 44) rest on a laterally continuous erosion surface that is sharp, smoothly-undulating and without associated size-sorted deposits (Fig. 49A & B). Heterolithic, stratified and nonstratified, non-silicified carbonate diamictites of Ghaub Fm contrast with heavily silicified, oligomicitic, oolite-clast debrites of Franni-aus Fm (Fig. 49A & B). In 5–9, parallel grooves on the sub-Ghaub erosion surface have tilt-corrected azimuthal orientations of ca 210° (Domack and Hoffman, 2011). Clasts of Franni-aus Fm oolite and debrite, both calcitic and dolomitic, are prominent as clasts in many diamictite bodies within Ghaub Fm (Fig. 50C & D). The basal meters of the Ghaub are typically recessive, thin-bedded, brown- to tan-weathering, detrital carbonate marl and micrite (Fig. 49A–C). Heterolithic carbonate limestones (Fig. 49E) increase in abundance upward, grading into or truncated by the first massive diamictite (Fig. 49C–F). Stratified diamictites higher in the formation resemble the basal stratified interval but are less terrigenous. We infer that the sub-Ghaub surface was eroded by glacial action (Domack and Hoffman, 2011), implying that basal Ghaub Fm in Tr5 does not record the first Marinoan ice advance (Hoffman, 2005). Rather, basal Ghaub Fm records a

readvance, preceded by an earlier Marinoan glacial maximum, which is presumably represented by basal Ghaub deposits farther downslope. An overall recessional grounding line is consistent with ongoing tectonic subsidence and ice-shelf (sea-glacier) thinning (Abbot et al., 2013) over the entire Marinoan epoch (Table 1).

Ghaub Fm is 26–140 m (average 75 m) thick in the western segment (Figs. 45 & 46). Each section 5–5–15 contains more than five discrete units of massive diamictite (Fig. 50A & B), typically separated by thinner stratified intervals (Figs. 48B & 49D). In the simplest interpretation, massive tills are mainly ice-contact deposits laid down upstream from a grounding line; stratified tills are subaqueously deposited, downstream from a grounding line. In reality, some massive diamictites form from ‘rainout’ due to rapid melting of debris-laden basal ice immediately seaward of a grounding line. This should be particularly true for grounding lines attached to ice shelves, which translate more slowly than free-floating icebergs. Massive diamictites (tillites) in Ghaub Fm are somewhat variable in clast size and concentration, but more so in composition. Some are mixtures of limestone and dolomite debris (Fig. 50A), others are exclusively limestone (Fig. 50B) or dolomite. Many of the latter are products of post-depositional dolomitization, visibly discordant at the outcrop scale and generally accompanied by modest silicification. In some cases, the fine-grained carbonate-wackestone matrix is selectively dolomitized (Fig. 50C).

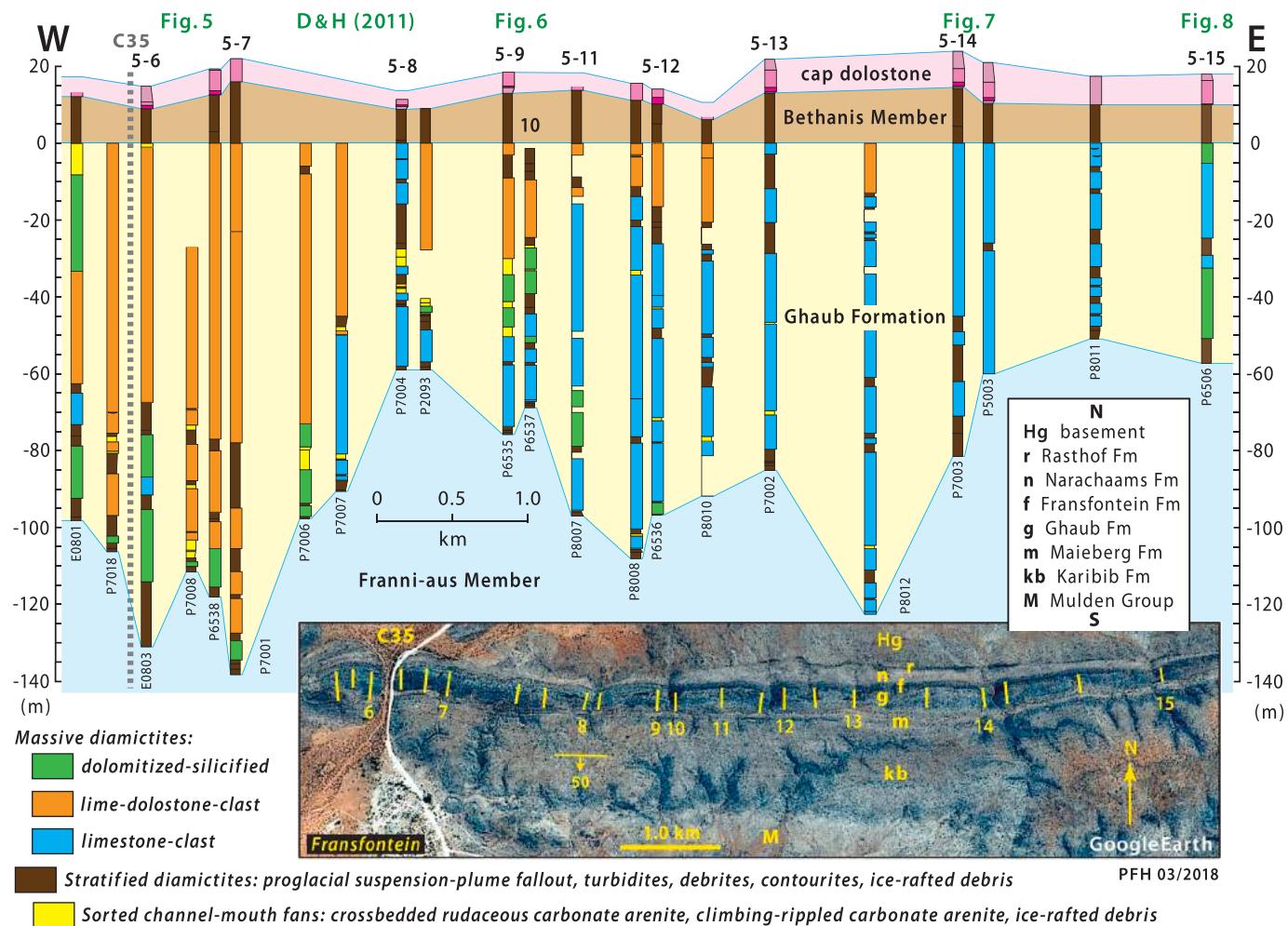


Fig. 46. Marinoan Ghaub Fm and Keilberg Mb cap dolomite in distal FSz on Transfontein Ridge (Tr5) N and E of Transfontein. Sections are numbered 5–6–15 as in Fig. 43 with additional Marinoan sections. For stratigraphic context of 5–7 see Fig. 44. Numbers in green refer to figures in Domack and Hoffman (2011), who interpreted Ghaub Fm here as part of an ice grounding-zone wedge deposited by an ice sheet flowing off the carbonate platform (Fig. 178A). Alternations of stratified and massive diamictites record small-scale grounding-line retreats and readvances. Sorted facies are localized as channel-mouth fans at subglacial meltwater discharge sites. Bethanis Mb (uppermost Ghaub Fm) is inferred to represent terminal deglaciation and TST first stage (Fig. 44). See Fig. 45 for westward continuation. Google Earth: Image © 2020 CNES/Airbus

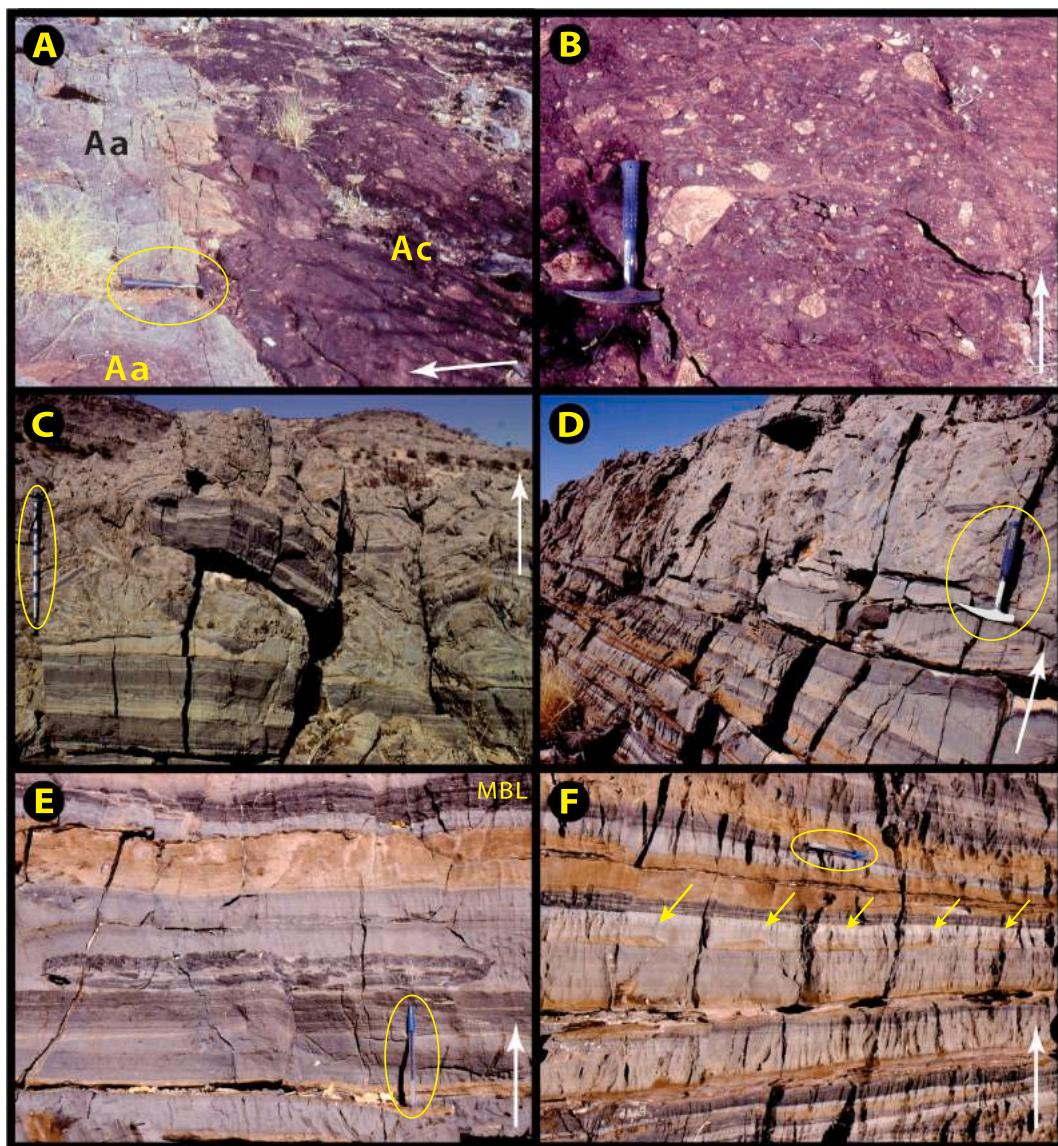


Fig. 47. Images of Sturtian Chuos, Berg Aukas and Okanguarri formations in west-central (Fig. 58) and western (Fig. 43) segments of Fransfontein Ridge (Tr5): white arrows indicate younging directions. (A) Sharp contact (hammer) in 5–25 (Fig. 58) between Berg Aukas Fm (Aa) cap dolomite and Chuos Fm (Ac) ferruginous basement-clast massive diamictite: at $-20.1974^\circ/15.1247^\circ$. Cusps of diamictite at contact result from tectonic shortening of a rheological interface. (B) Ferruginous basement-clast massive diamictite (Chuos Fm) at same location as A, showing fracture-related colour (mineralogy?) changes. Hammer handle is 33 cm long. (C–D) Intraclast debrite in Berg Aukas Fm dolomite rhythmite in 5–3 (Fig. 43): $-20.1983^\circ/14.9130^\circ$. Monopod in (C) is 55 cm long. (E) Tabular intraclast and sublittoral microbial laminites in Berg Aukas ribbonite at same location as C–D (Fig. 43). Tabular intraclast is a lithified debrite. (F) Starved current ripples (arrows) in Berg Aukas ribbonite same location as C–E (Fig. 43). Foreset laminae indicate flow from near left to far right, or E to W. Contour-current azimuth may reflect left turning of upwelling bottom water in the paleo-southern hemisphere (Fig. 11B).

Outsize clasts are generally subrounded, and whether dolomitized or not they are welded through greenschist-grade metamorphic recrystallization to their matrix. This makes it impossible to observe striations or clast shapes in 3-dimensions. The matrix is a carbonate wackestone that is texturally indistinguishable from the diamictite on a microscopic scale. Metamorphic recrystallization has likely destroyed any grain-scale glacial fabrics, and clast-scale fabric analysis is limited to dolomite clasts on account of tectonic strain (Fig. 50A). Certain massive diamictites contain wispy lenticles of fine-grained, weakly stratified diamictite (Fig. 50E & F). We attribute them to transient ice-bed separation in the presence of basal meltwater. The wispy lenticles are locally deformed or sheared-off (Fig. 51E), as are some stratified intervals (Fig. 51F). We ascribe these soft-sediment deformations to shearing of the bed by grounded glacial flow. Indications of subglacial meltwater and soft-sediment deformation imply that the Marinoan

glacial ice was sufficiently thick to reach the pressure-melting temperature basally.

There are two broad classes of stratified Ghaub deposits: stratified diamictite and sorted rudaceous arenite. Stratified diamictites are assemblages of laminated lutite, turbidite and debrite in highly variable proportions (Fig. 49C–F). All are composed exclusively of detrital carbonate. IRD is concentrated in laminated lutite, which exhibits normal and reverse grading and is interpreted as suspension-plume fallout or ‘plumite’ (Witus et al., 2014; Dowdeswell et al., 2015). IRD (Figs. 49E, 51C & 52C) is associated with impact-related deformations and post-impact drapes. We cannot distinguish between IRD delivery by shelf ice or icebergs, but high concentrations of IRD are consistent shelf-ice, which travels more slowly than free-floating icebergs and consequently discharges its basal cargo closer to a grounding line.

Well-sorted Ghaub deposits include channelized rudaceous arenites

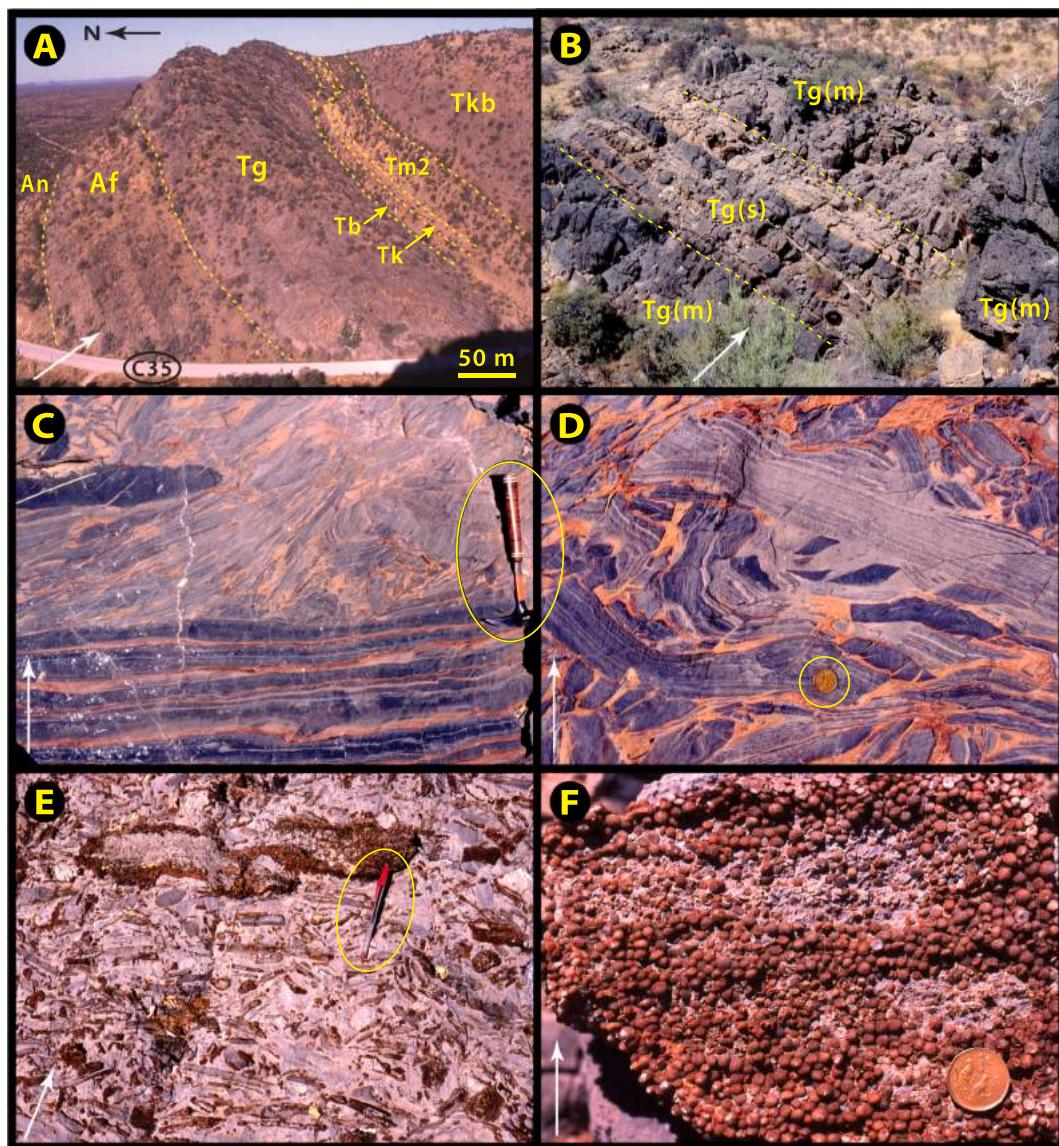


Fig. 48. Images of the Marinoan FST (Frannis-aus Fm) and LST (Ghaub Fm) in distal FSz of Transfontein Ridge near Transfontein (Tr5): white arrows indicate stratigraphic younging. (A) Overview of Marinoan sequence stratigraphy in 5–7 (Fig. 44) at $-20.1978^{\circ}/15.0164^{\circ}$, looking E across regional road C35. Abbreviations: An, Narachaaams Fm; Af, Frannis-aus Fm FST; Tg, main Ghaub Fm LST; Tb, Bethanis Mb (TST); Tk, Keilberg Mb (TST); Tm2, lower Karibib Fm marly limestone rhythmite member (MFS); Tkb, Karibib dolomite rhythmite (\pm debris) (HST). See also field guide SOI S3.7. (B) Stratified diamictite ($Tg_{(s)}$) sandwiched between massive diamictites ($Tg_{(m)}$), Ghaub Fm in 5–8: $-20.2006^{\circ}/15.0336^{\circ}$. Visible section is ~ 50 m thick. (C–D) Marly calcite rhythmite and intraclast debris, lower Franni-aus Fm in 5–12: $-20.1997^{\circ}/15.0577^{\circ}$. (E) Cherty dolomite intraclast debris with loose grains and tabular slabs of coarse-grained ooid grainstone (pen tip), upper Franni-aus Fm in 5–1: $-20.1992^{\circ}/15.0710^{\circ}$. (F) Selectively silicified dolomite ooid grainstone clast in intraclast debris, upper Franni-aus Fm at same location as E. Coin is 2 cm in diameter. Ooid grainstone originated in the surf zone of the FSz during Marinoan glacioeustatic fall, which caused it to be subaerially exposed, partially lithified and gravitationally redeposited downslope as intraclast debris (Hoffman, 1999, 2011a).

forming prograded clinoforms (Fig. 51A–D), and fine-grained arenites with aggradational climbing ripples (Fig. 52A–F). Climbing-ripple and clinoform orientations indicate SSW-directed currents (Fig. 51A) with dense suspended loads. The sorted deposits resemble grounding-line fans developed at the mouths of subglacial meltwater channels (Powell, 1990; Domack and Powell, 2018).

Stratified intervals typically begin abruptly (Fig. 53A & B). A basal sandy layer, more or less disturbed, sharply overlies massive diamictite (Fig. 53C & D), in some cases graded at the top (Fig. 49F). The basal arenite is generally overlain by the most distal facies of the stratified

interval (Fig. 53A–F). Stratified diamictites become coarser-grained and more charged with IRD upward (Fig. 53A & F), implying glacial advance, ultimately passing into massive diamictite. The observed asymmetry of stratified diamictites suggests slow grounding-line advances and rapid retreats. This is opposite to the pattern of rapid advances (surges) and slow retreats attributed to internal ice dynamics in polythermal ice sheets that terminate subaerially (Hagen, 2008; Robinson and Dowdeswell, 2011). Large grounding-line migrations (≤ 500 km) under mature snowball conditions could have been orbitally forced at low latitudes (Benn et al., 2015), but those on the Swakop

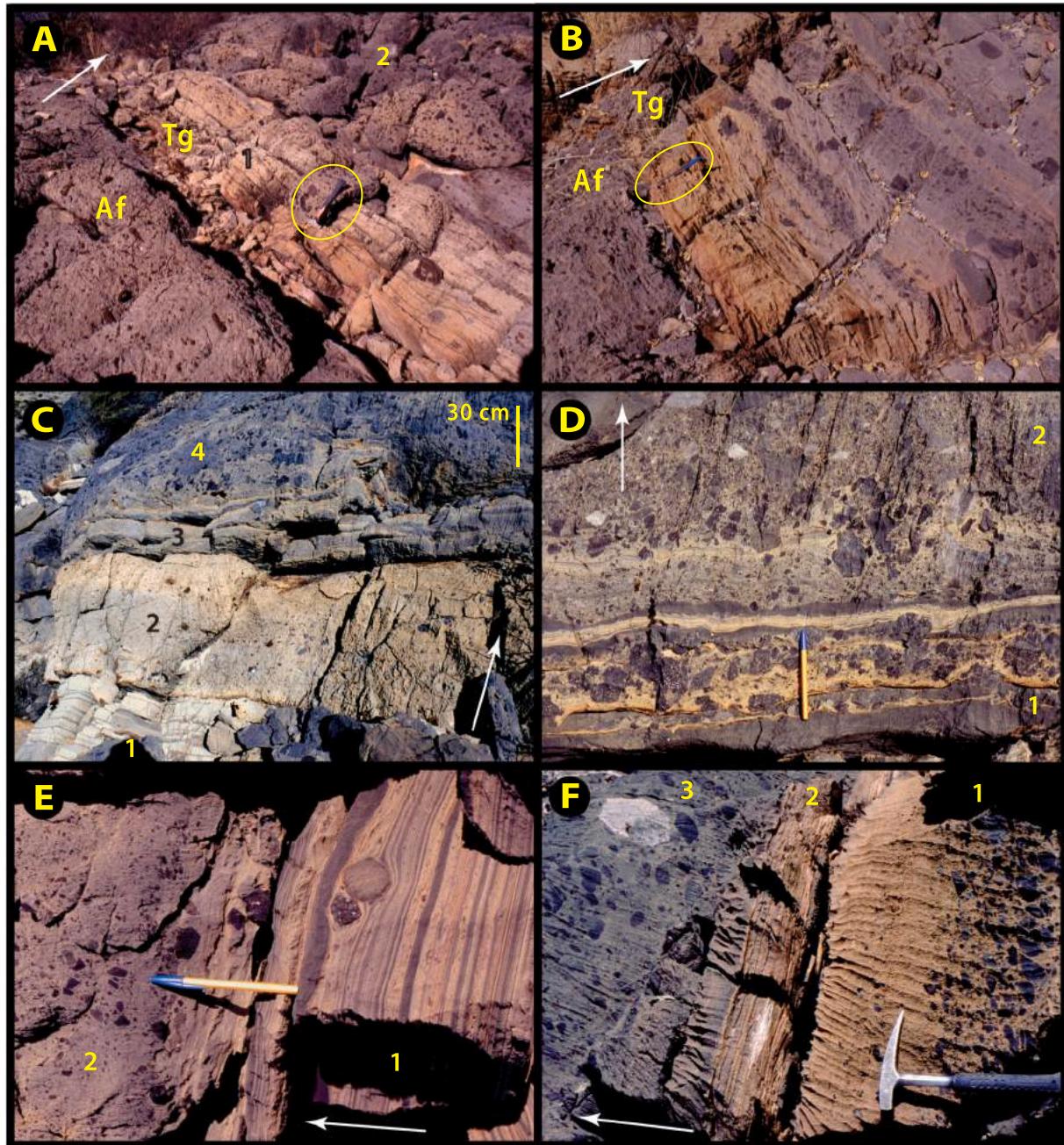


Fig. 49. Images of the Marinoan FST (Frannis-aus Fm) to LST (Ghaub (Fm) transition on distal FSz of Transfontein Ridge (Tr5): white arrows indicate stratigraphic younging. (A) Sharp (erosive?) contact at $-20.2005^{\circ}/15.0337^{\circ}$ in 5–8 between cherty intraclast debrite (Af, Frannis-aus Fm) and stratified marly dololutite (Tg, Ghaub Fm) that is increasingly IRD-rich stratigraphically upward (arrow). Basal stratified Tg (unit 1) grades upward into massive calcite diamictite (unit 2), recording the first (preserved) ice grounding-line advance in this section. Earlier advance indicated by sub-Tg erosion surface. Hammer 33 cm long circled. (B) Detail of Af/Tg contact recording Marinoan glacial onset in 5–7: near $-20.1979^{\circ}/15.0186^{\circ}$. Sharp erosive contact (base of pen, circled) is overlain by stratified marl that becomes increasingly IRD rich (polymictic limestone clasts) upward recording the first (preserved) grounding-line advance. Older advance(s) must have occurred if sub-Tg erosion surface was glacial. (C) Basal Ghaub grounding-line advance sequence in 5–9 near $-20.1998^{\circ}/15.0382^{\circ}$: 1, stratified dololutite with rare IRD; 2, composite debrite; 3, stratified diamictite, grading to 4, massive diamictite. (D) Detail of transition from (unit 1) stratified to (unit 2) massive clast-rich (“rain-out”?) diamictite in same location as C. (E) Gradational (non-erosive) transition from (unit 1) stratified basal Ghaub with IRD into (unit 2) massive limestone-clast diamictite, near $-20.1984^{\circ}/15.0776^{\circ}$ between 5 and 14 and 15. (F) Stratified intertongue in lower Ghaub between massive diamictites in 5–12 at $-20.2004^{\circ}/15.0405^{\circ}$. Overlying lower diamictite (not shown) is: 1, graded debrite; 2, dololutite ribbonite (detrital) and fine-grained debrite; and 3, massive limestone-clast diamictite.

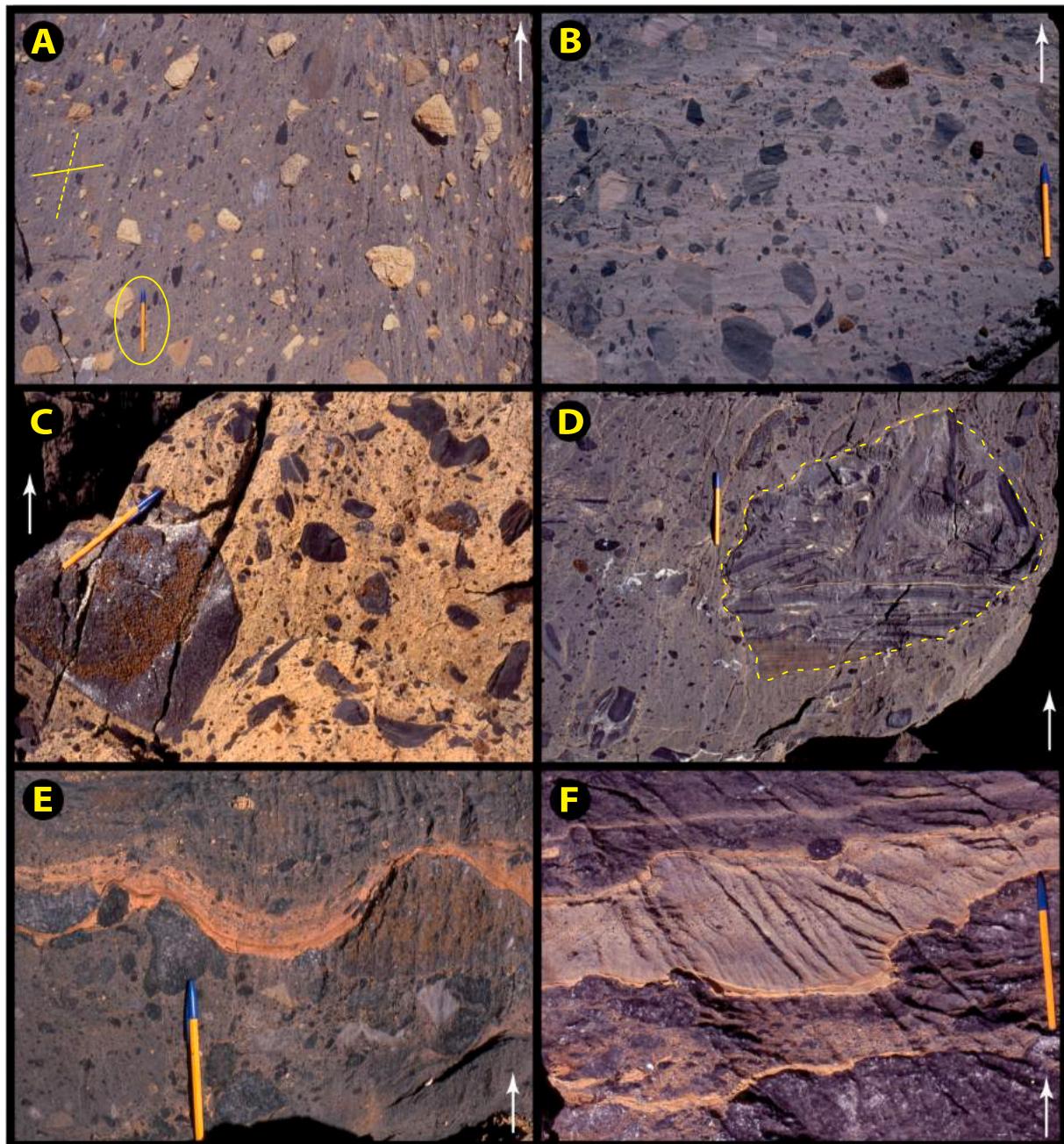


Fig. 50. Images of massive diamictites in Marinoan Ghaub Fm of distal FSz on Transfontein Ridge (Tr5): white arrows indicate stratigraphic younging. (A) Mixed dolomite-clast (buff) and limestone-clast (dark grey) diamictite in 5–7: at $-20.1982^{\circ}/15.0201^{\circ}$. Solid yellow line indicates stratigraphic layering; dashed yellow line indicates tectonic cleavage and flattening plane of limestone clasts. Wackestone matrix has the same mixed composition as the clasts. (B) Polymictic limestone clast diamictite in 5–13 near $-20.2003^{\circ}/15.0577^{\circ}$. Silicified Af-derived oolite clasts have reddish-brown coating of desert varnish. (C) Limestone-clast diamictite with dolomite-rich matrix in 5–12 near $-20.2006^{\circ}/15.0501^{\circ}$. Pen rests on Af-derived silicified oolitic limestone clast. (D) Limestone-clast diamictite with large clast (dashed outline) of Af limestone intraclast debris (compare with Fig. 48C): same location as B. (E–F) Stratified dolosiltite lenses (ice–bed separation surfaces?) within massive limestone-clast diamictite in 5–12 at $-20.1998^{\circ}/15.0502^{\circ}$. Such lenses are common in Ghaub Fm massive diamictite and are locally subject to glaciectonic deformation (Fig. 51E), suggesting that the enclosing diamictite bodies were deposited by wet-based grounded ice.

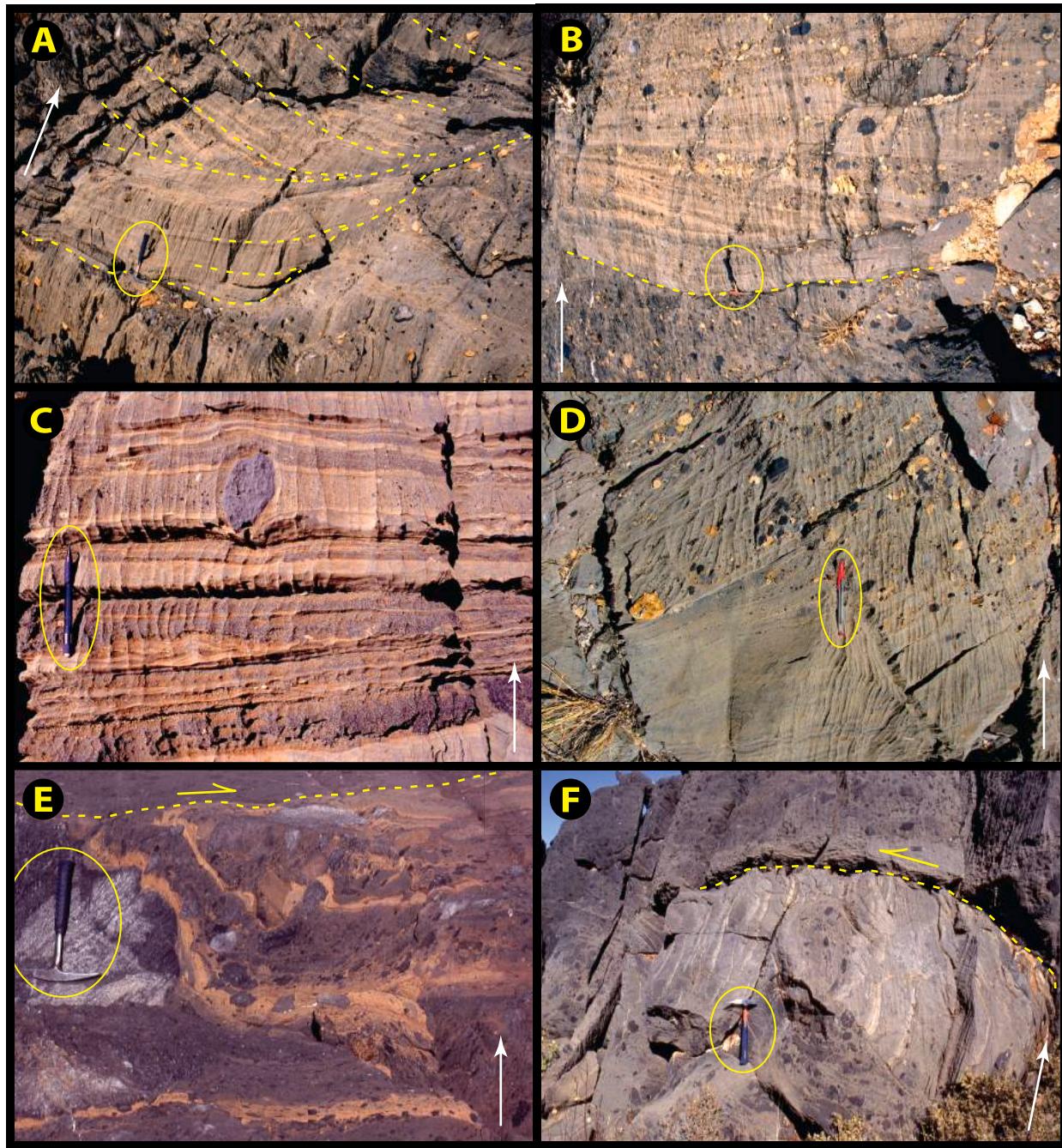


Fig. 51. Images of channelized sorted facies and glacitectonic structures in Marinoan Ghaub Fm in distal FSz of *Transfontein Ridge* (Tr5): white arrows indicate stratigraphic younging. (A) Massive diamictite (lower right) at $-20.1983^{\circ}/15.0196^{\circ}$ in 5–7 is cut by a channel (hammer-head at base of) filled by stratified and sorted arenite that onlaps the channel walls and passes upward into SSW-tilted clinoforms with basal downlaps. The channel is interpreted as a subglacial conduit for SSW-directed meltwater flow. (B) Channelized surface (base of hammer) on massive dolomite-limestone-clast diamictite in 5–7 at $-20.1981^{\circ}/15.0187^{\circ}$ is overlain by non-parallel stratified sorted detrital carbonate sand and gravel with outsize dropstones. (C) Sorted detrital carbonate sandstone beds with outsized clast at $-20.1980^{\circ}/15.0196^{\circ}$ in 5–7 indicates subglacial meltwater flow and discharge at ice grounding line. (D) Distally-fining clinorms of detrital carbonate sand and gravel of an inferred grounding-line fan where subglacial meltwater was discharged, near $-20.1980^{\circ}/15.0186^{\circ}$ in 5–7. (E) Stratified dolosiltite lenses (Fig. 50E–F) are folded and sheared off beneath a subglacial deformation surface (dashed line with half-arrow indicating inferred sense of ice motion, at $-20.2003^{\circ}/15.0502^{\circ}$ in 5–12). (F) Glacitectonic (?) thrust and related fold place massive over stratified limestone-clast diamictites in 5–12 at $-20.2003^{\circ}/15.0492^{\circ}$. Folding of stratified diamictite implies local N-directed (!) shear.

Group FSz would have been damped by the forward-dipping (relative to glacial flow) bedrock slope (Pollard and DeConto, 2007), the stabilizing effect of grounding-zone sediment buildup (Alley et al., 2007; Domack and Hoffman, 2011), and gravitationally-induced sea-level falls accompanying ice-sheet retreats (Gomez et al., 2010, 2012).

Westward from Transfontein (5–6), stratified diamictite becomes

more common at the expense of massive diamictite. Section #3 (Fig. 45), for example, contains no massive diamictite at all (Eyles and Januszczak, 2007), just a 31-m stack of polymictic carbonate debrites (Fig. 54E). This section is exceptional (Fig. 45)—just 1.1 km to the NW, a 104-m-thick Ghaub section (#2 in Fig. 45) is composed 85% of massive diamictite. Sections #1–9 and #14–17 (Fig. 45) contain quartz siltstone and

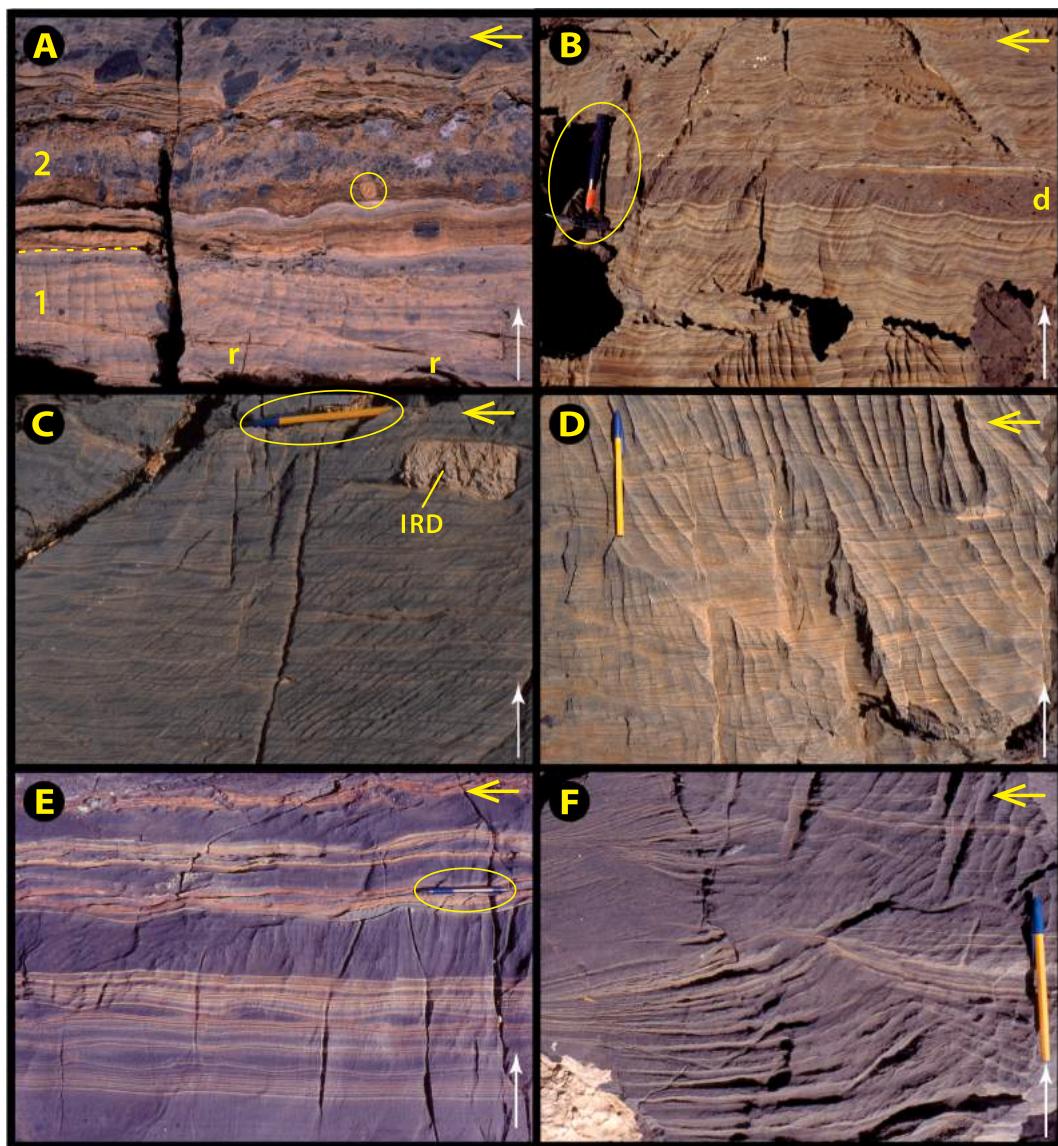


Fig. 52. Images of Marinoan Ghaub Fm in distal FSz on Transfontein Ridge (Tr5), showing bedforms produced by bottom currents charged with suspended sediment: white arrows indicate stratigraphic younging and yellow arrows right-to-left paleocurrent sense. (A) Stratified diamictite (unit 2) in 5–13 overlying detrital carbonate arenite with climbing ripples (r) and fine-grained IRD: at $-20.1993^{\circ}/15.0577^{\circ}$. Paleocurrent azimuth is 150° . (B) Fine-grained debrite (d) within stratified dololutite with highly aggradational ripple-like bedforms. (C) Multiple climbing ripple trains near $-20.2003^{\circ}/15.0399$ in 5–9 indicating consistent right-to-left bottom currents with significant suspension fallout. Paleocurrent azimuth is 190° , consistent with flow driven by hydraulic head of an ice sheet on platform. Ice-raftered limestone (IRD) is in upper right. (D) Bundled laminae within climbing ripples with abundant very fine-grained IRD (near $-20.1980^{\circ}/15.0117$ in 5–6), produced by right-to-left bottom currents with high suspended loads, characteristic of glacier-associated meltwater flows. (E) Starved ripples in stratified detrital carbonate arenite and lutite with very fine-grained IRD at $-20.1953^{\circ}/15.0988^{\circ}$ in 5–17. Starved ripples indicate bottom traction currents, not density flows. (F) Climbing ripples with ≤ 6 cm relief in detrital calcarenite at same location as E.

minor sandstone basally, similar to Bethanis subbasin in Tr1 (Fig. 18). The terrigenous detritus resembles Franni-aus Fm, from which it could have been derived by glacial erosion higher on the foreslope, as illustrated by the sub-Ghaub Fm gully between 5 and 20 and 20 and 22 (Fig. 43).

Throughout the western segment, Ghaub Fm ends with a continuous stratified diamictite that differs from all earlier ones in its chocolate-brown matrix colour and the concentration, clast-size disparity, and lithological diversity of IRD (Fig. 54A–D). This unit was defined (Hoffman and Halverson, 2008) as the Bethanis Mb in Ghaub Fm

(Figs. 45 & 46) and forms a terminal deglacial drape ranging from 1.5 to 16.0 m in thickness. Bethanis Mb commonly begins with an overthick sand-size flow unit (Fig. 54A), and invariably ends abruptly with disappearance of debrite and IRD (Fig. 55A–D). Although bed thickness in Bethanis Mb declines upward, maximum IRD size does not—meter-size dropstones (mostly stromatolite) occur sporadically throughout (Fig. 55B). Nested dropstones (Condon et al., 2002), suggestive of iceberg as opposed to ice-shelf rafting, occur sparingly in Bethanis Mb but not older parts of Ghaub Fm. Starved ripples produced by WSW-

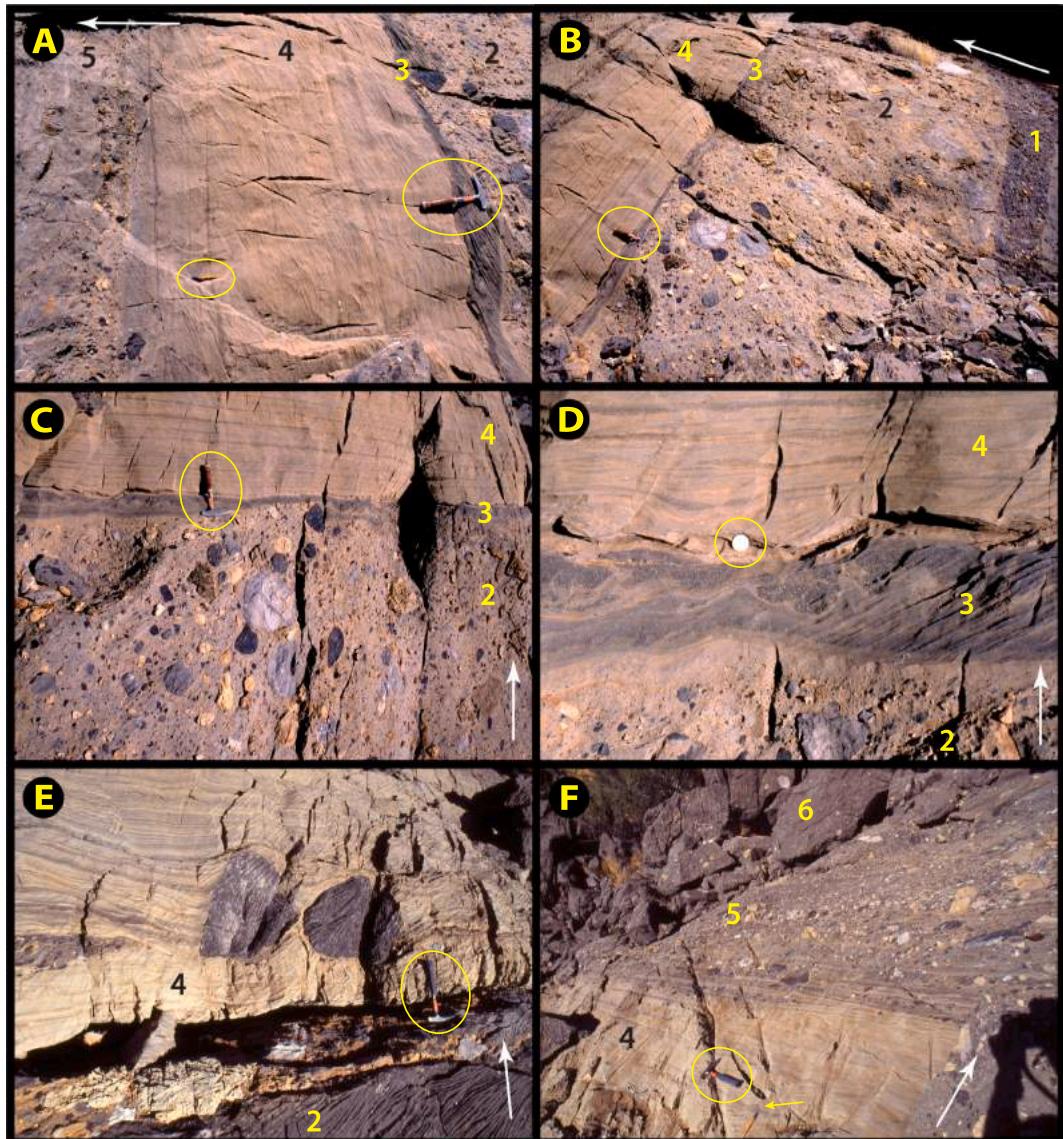


Fig. 53. Images of asymmetric ice grounding-line retreat and readvance cycles in Marinoan Ghaub Fm of distal FSz on Transfontein Ridge (Tr5); white arrows indicate stratigraphic younging. (A–D) Cycle at $-20.1978^{\circ}/15.0115^{\circ}$ in 5–6 involving: 1. carbonate-clast conglomerate; 2. massive diamictite with dolomite and limestone clasts; 3. disturbed calcarenous bed with load casts (D) possibly related to sudden flotation of ablative grounded ice during retreat; 4. stratified and current-rippled dolarenite with little or no IRD; 5. stratified diamictite with abundant IRD. Paucity of IRD in unit 4 suggests that IRD was not dispersed far from the grounding line. This is more consistent with ice-shelf rafting than iceberg rafting because an ice shelf moves seaward more slowly than free-floating icebergs. (E–F) Cycle near $-20.2000^{\circ}/15.0392^{\circ}$ in 5–9 with similar sequence as in A–D, except that unit 2 is a massive limestone diamictite and unit 4 contains a pair of limestone dropstones in E. In F, unit 5 is gradationally overlain by massive dolomite- and limestone-clast diamictite (unit 6).

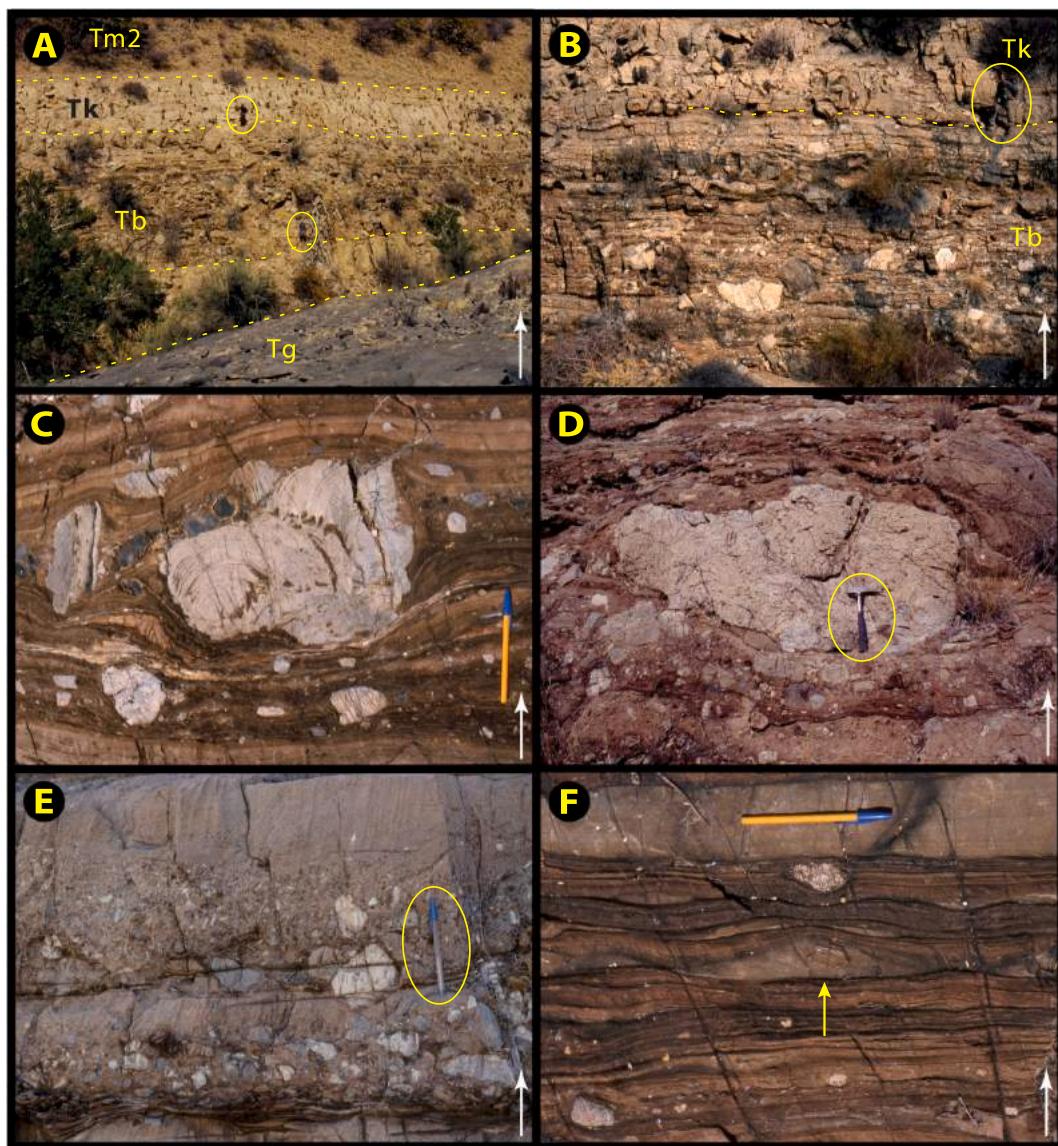


Fig. 54. Images of terminal Marinoan Bethanis Mb (Ghaub Fm) in distal FSz on Transfontein Ridge (Tr5): white arrows indicate stratigraphic younging. (A) Stratified dolomite diamictite of Bethanis Mb (Tb) at $-20.1995^{\circ}/15.0181^{\circ}$ in 5–7 (Figs. 44 & 48A) sharply overlies massive limestone diamictite of main Ghaub Fm (Tg) and sharply underlies basal Ediacaran Keilberg Mb cap dolomite (Tk). The lower of two geologists (circled) stands near the top of a thick composite debrite that commonly occurs at the base of Bethanis Mb. Tm2 is poorly-exposed MFS of postglacial marine transgression. (B) Sharp conformable contact (see Fig. 55C) at $-20.1997^{\circ}/15.0187^{\circ}$ (5–7) between Bethanis (Tb) and Keilberg (Tk) members of Ghaub and Karibib formations, marking abrupt cessation of IRD and onset of primary carbonate production. Geologist (circled) gives scale. (C) Large dropstone of stromatolitic dolomite in typical chocolate-brown coloured stratified diamictite of Bethanis Mb near $-20.2008^{\circ}/15.0574^{\circ}$ in 5–13. (D) 2.7-m-diameter dropstone in Bethanis Mb in same location as B. (E) Pair of debrites at base of Bethanis Mb at $-20.1910^{\circ}/14.8511^{\circ}$ in 5–1 (Fig. 55B). (F) Starved ripple (arrow), one in a train, in Bethanis Mb at $-20.1987^{\circ}/15.0863^{\circ}$ in 5–15. Foreset orientations indicate W-directed (present coordinates) contour currents (left to right in image), consistent with paleo-S-hemisphere (Fig. 11B) and counter-clockwise turning of upwelling bottom waters. Abundance in Bethanis Mb of IRD of all sizes and diverse sources is attributed to collapse of the tropical sea-glacier that buttressed outlet glaciers, causing accelerated ice-sheet drainage and tropical iceberg armadas. Characteristic chocolate-brown color, absent below Bethanis Mb, reflects oxidation of dissolved Fe and Mn in the snowball ocean following sea-glacier collapse (Kirschvink, 1992; Klein and Beukes, 1993).

directed contour currents are well developed in Bethanis Mb in 5–15 (Fig. 54F). Their orientation is consistent with southern hemisphere left turning of upwelling bottom waters at 635 Ma (Fig. 11B). The last Bethanis debrite is draped by ca 1.0 cm of marl (Fig. 55C), upon which micropeloidal dolomite of Keilberg Mb was deposited without a perceptible break in sedimentation.

We tentatively relate the base of Bethanis Mb to collapse of the tropical sea glacier, triggering Marinoan terminal deglaciation. The ice flux (as icebergs) from outlet glaciers would have abruptly increased due

to loss of ice-shelf buttress (De Angelis and Skvarca, 2003; Rebasco et al., 2014), and top-down oxidation of the snowball ocean would have transferred dissolved Fe and Mn into the sediment (Kirschvink, 1992), explaining the chocolate-brown colour of Bethanis Mb (Fig. 54C & F). The abrupt disappearance of IRD and debrite at the top of Bethanis Mb should date the retreat of those outlet glaciers landward of tidewater. The speed of their retreat, relative to marine strandlines, would have been accelerated by the combined effects of ice-sheet mass loss, gravitationally induced sea-level fall (Clark, 1976), and glacio-isostatic

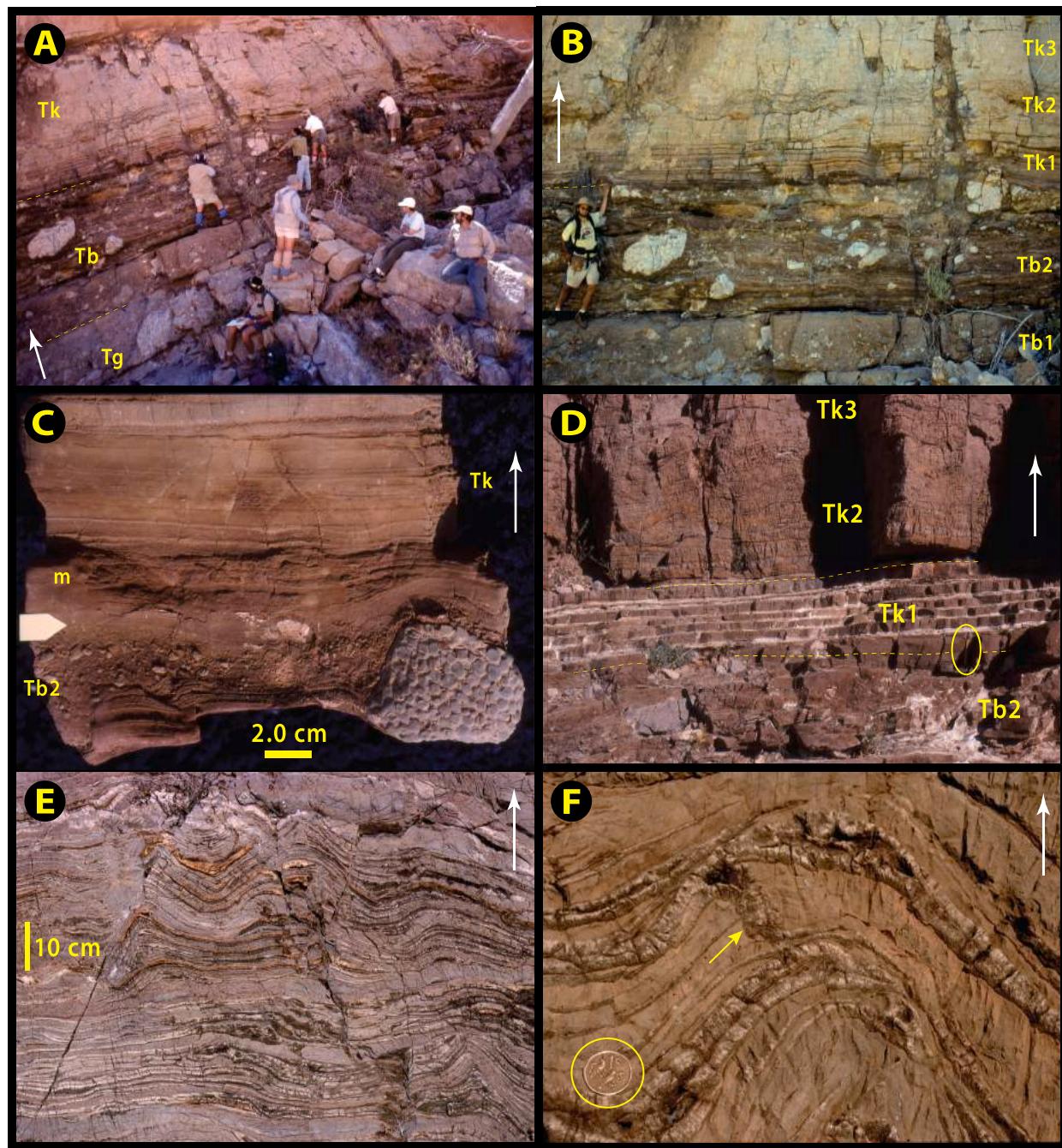


Fig. 55. Images from the Marinoan glacial termination (Bethanis and Keilberg members) in the distal FSz on Fransfontein Ridge (Tr5): white arrows indicate stratigraphic younging. (A) Participants of the 1999 field excursion at contact between Bethanis and Keilberg members at 'Pip's Rock' ($-20.1910^{\circ}/14.8511^{\circ}$) in 5–1 (section 3 in Fig. 45). Examining the contact are (left to right) Dan Schrag, Joe Kirschvink, Jay Kaufman and Galen Halverson. Sitting (left to right) are Roy Miller (taking notes), Doug Erwin and Sam Bowring. Standing center-stage providing oratory is Nick Christie-Blick. Miller is gazing at colour change from grey to brown in debrites at base of Bethanis Mb, suggesting oxidation of dissolved Fe and Mn during Marinoan deglaciation. (B) Bethanis Mb–Keilberg Mb transition at 'Pip's Rock'. Units: Tb1, basal Bethanis Mb debrites (Fig. 54E); Tb2, stratified diamictite rich in IRD; Tk1, coarsening-upward dololutite turbidites; Tk2, dolopelarenite with fibrous-isopachous sheet-crack cements and intrafolial folds (E–F); Tk3, dolopelarenite with low-angle cross-stratification. Shoaling in Tk1 is attributed to sealevel fall in response to waning ice-sheet gravity (Clark, 1976), causing pore-fluid overpressure and sheet-crack development (Hoffman and Macdonald, 2010). (C) Detail of Bethanis Mb–Keilberg Mb transition (white tab at left) at $-20.2010^{\circ}/14.8898^{\circ}$ in 5–2 (section 7–8, Fig. 45). Terminal Bethanis Mb debrite with outsize clast of giant oolite (Frannis-aus Fm derived) is conformably overlain by 2 cm of marly dololutite followed by upward-coarsening dolopelarenite. The contact is typically abrupt but apparently unbroken. (D) Same transition at $-20.1911^{\circ}/14.8507^{\circ}$ in 5–1, downstream from 'Pip's Rock,' showing basal Keilberg Mb (Tk1) turbidites and sheet-cracked interval (Tk2). (E) Sheet cracks with fibrous isopachous dolomite cement in lower (but not basal) Keilberg Mb dolopelarenite. Yellowish colour is desert varnish accumulated where fibrous dolomite cement is replaced by chert. Sheet cracks indicate vertical extension, presumably driven by pore-fluid overpressure. Cracking and cementation occurred contemporaneously and incrementally. Voids formed where cracks were buckled and were subsequently filled by sparry calcite or geodal quartz. (F) Detail of fibrous isopachous early cement (white) and late void-filling sparry calcite (dissolution cavities) in buckled dololutite. Note cement-filled crack that transects layering (arrow), resulting in layer-parallel shortening that contributes to characteristic buckling of sheet-cracks (Tk2).

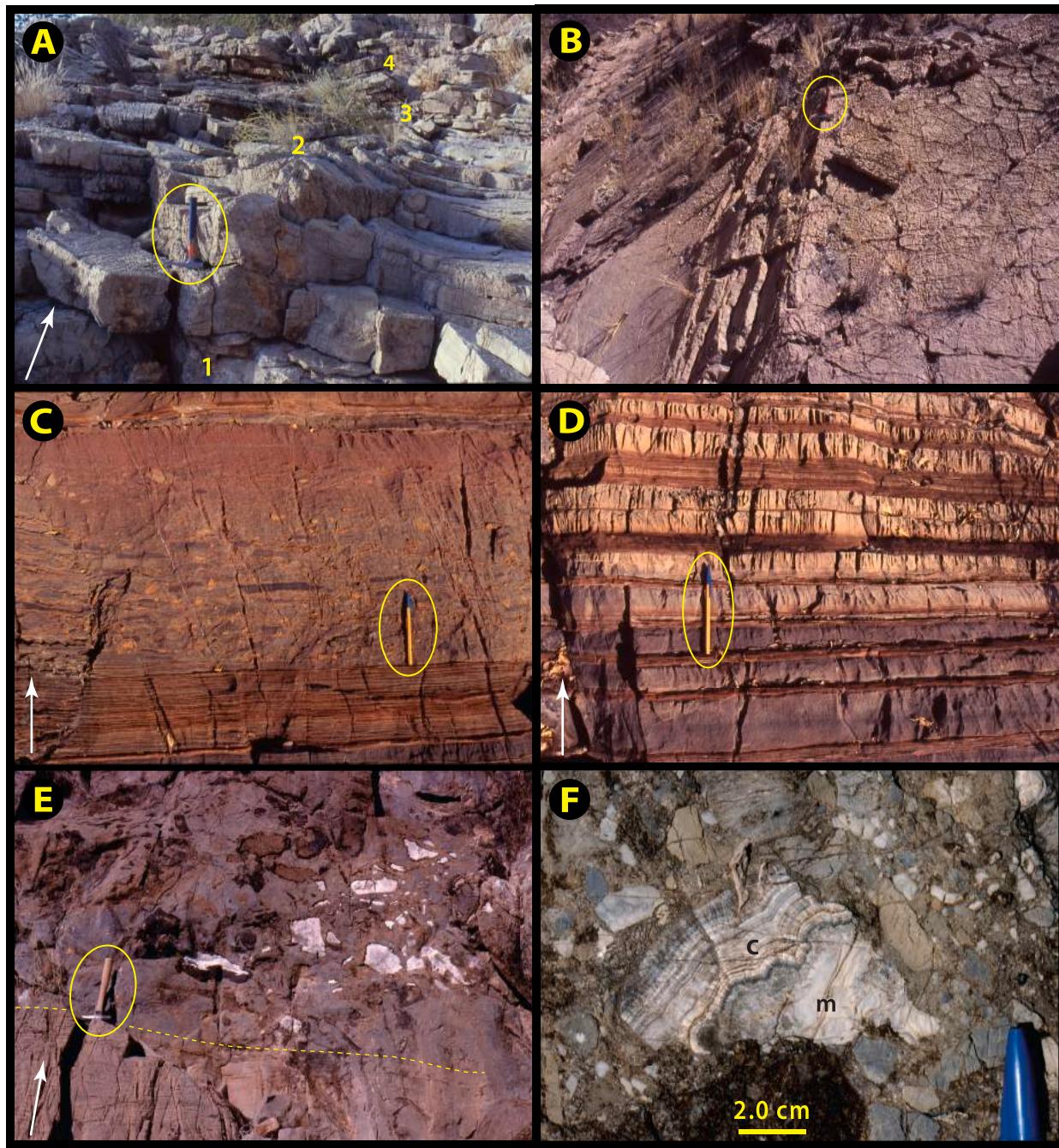


Fig. 56. Images from early Ediacaran Karibib Fm and Marinoan Ghaub Fm in distal FSz on Transfontein Ridge (Tr5): white arrows indicate stratigraphic younging. (A) Oblique cross-section of giant wave ripples in Keilberg Mb cap dolomite in 5–14. Wave ripple developed from a plane bed (1) and aggraded through a stratigraphic thickness of 2.4 m (2) before terminal onlap by a plane bed (3). Offset younger giant wave ripple in background (4) developed independently. These are the only wave-generated bedforms observed in distal FSz after the rift-to-shelf transition ca 655 Ma. (B) Oblique plan view of giant wave rippled bedding surface in Keilberg at $-20.2009^\circ/15.0721^\circ$ in 5–14. Hammer handle (circled) parallels the straight crestline which has an azimuthal orientation of 120° and synoptic relief of 0.38 cm. Giant wave ripples are not attributed to storms but to long-period (20–30 s) waves generated where wind speeds of 20-m/s ($3 \times$ normal tradewind velocity) are sustained over large areas of fetch (Allen and Hoffman, 2005a, b; Jerolmack and Mohrig, 2005). Cyclonic winds (e.g., hurricanes, typhoons) would not produce the preferred meridional orientation observed in post-Marinoan giant wave ripples (Hoffman and Li, 2009), nor the closely similar orientations of successive generations of giant wave ripples (A) at a given location (Allen and Hoffman, 2005b). (C) Tabular intraclast debrite in deepwater calcite rhythmite of Maieberg Fm member Tm2 at $-20.2017^\circ/15.0717^\circ$ in 5–14. Note clast-size gradation. (D) Change from calcite rhythmite (grey) to dolomite rhythmite (buff) in Maieberg Fm middle Tm2 member at same location as C. (E) Blocky intraclast debrite in upper Karibib Fm at $-20.2050^\circ/15.0225^\circ$ in 5–7. Base of debrite dashed. Certain blocks have been selectively replaced by void filling sparry calcite cement (white). (F) Conglomerate bed in Ghaub Fm at $-20.1916^\circ/14.8519^\circ$ in 5–1 with angular clast of fibrous isopachous dolomite cement (c), grown on dolomitic host-rock (m), of the type commonly developed in pre-Marinoan Okonguarri (Tr5) and Rasthof (Tr6) formations in Kranstoort trough and Huab ridge (Figs. 62, 66E-F, 71 & 75E-F).

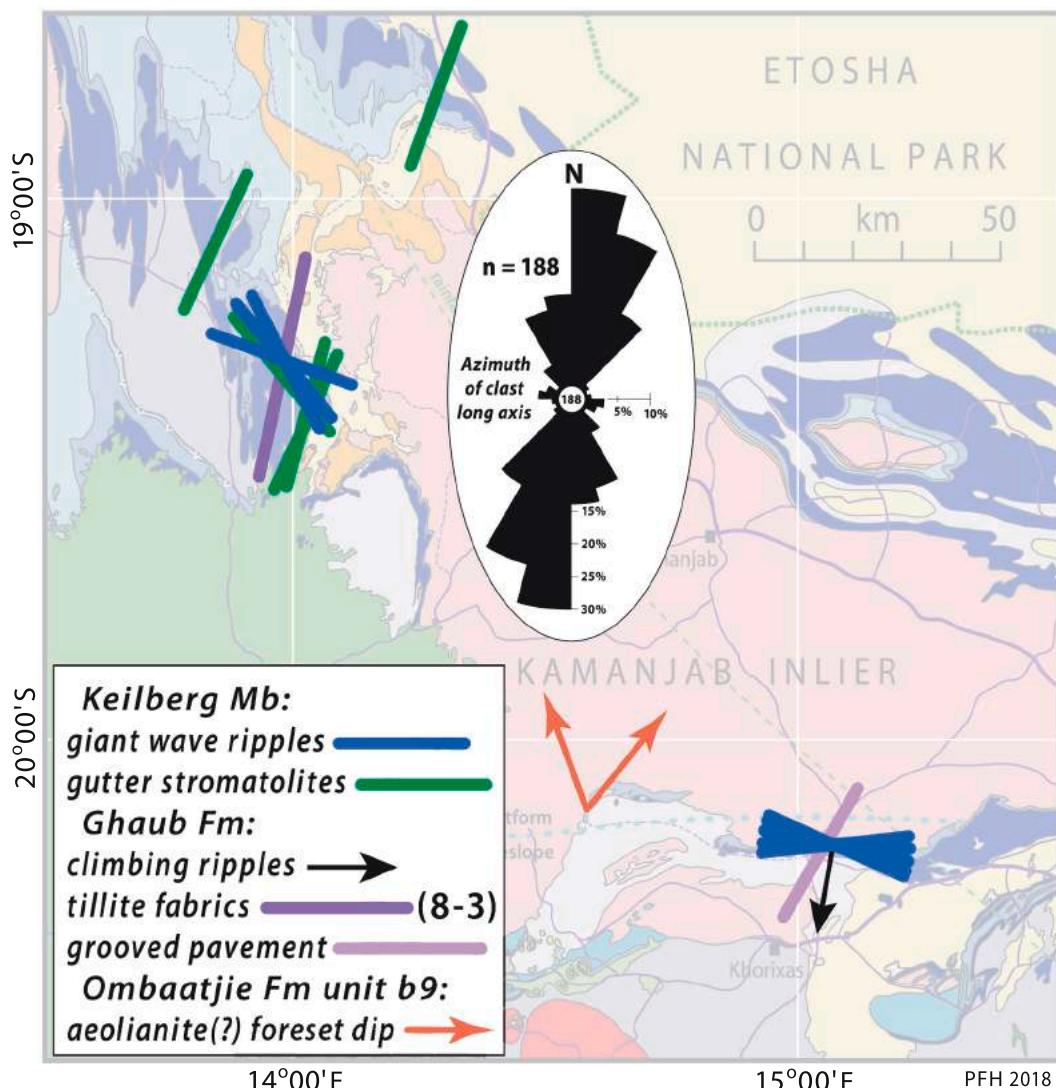


Fig. 57. Paleo-azimuths related to Marinoan glaciation in Tr5–10 (Fig. 8B). Orientations are consistent with SSW-directed glacial and subglacial meltwater flows, and NNE-directed long-period wave propagation during syndeglacial marine transgression. Ombaatjie Fm cycle b9 aeolianite (Figs. 71, 78B & 79B) may have formed when glacioeustatic fall exposed the platform before a local ice-sheet formed. Bidirectional foresets ($n = 2$) could indicate a barchan dune.

'rebound' (Creveling and Mitrovica, 2014). No anomalous amounts of Os or He, or shifts in Os-isotope composition, were observed at either the base or top of Bethanis Mb, or in the cm-thick marl beneath Keilberg Mb (Peucker-Ehrenbrink et al., 2016).

The basal Ediacaran Keilberg Mb cap dolomite is 8.1 m thick on average ($n = 10$) in the western segment (Figs. 45 & 46). It is divisible into four units, Tk1–4 (Fig. 55B). Tk1 is an upward-coarsening set of dolomite turbidites, ≤ 0.7 m thick in aggregate (Fig. 55D). Tk2 is ≤ 2.0 m thick (Fig. 55B) and consists of thin-bedded dolopelarenite that is disturbed to varying degrees by buckled sheet-cracks filled by fibrous isopachous dolomite cement (Fig. 55E & F). The fibrous dolomite cement tends to be selectively silicified (Fig. 55E). Such sheet-crack cements do not occur in Tk1 or in Bethanis Mb, contrary to expectation if they originated by destabilization of glacial-age permafrost clathrate (Kennedy et al., 2001b). Alternatively, sheet cracks were attributed to pore-fluid overpressures resulting from gravitationally induced sea-level fall (Hoffman and Macdonald, 2010), consistent with the apparent decrease in water depth between Tk1 and 2. Early deglacial regression is inferred during post-Weichselian (post-Wisconsinian)

retreat of the Greenland Ice Sheet (Clark, 1976). Even during a snowball deglaciation, rates of regional sea-level fall could have temporarily exceeded the rate of global-mean ('eustatic') sea-level rise (Creveling and Mitrovica, 2014).

Tk3 is ≤ 4.5 m thick and consists of thin-bedded dolopelarenite with low-angle swaley cross-stratification. Giant wave ripples (Fig. 56A & B) occur in sections 5–14 (Fig. 46), 5–16, 21, 26b and 30 (Fig. 43), and between 5 and 2 and 3 (#8 in Fig. 45). They are trochoidal in form, with ≤ 38 cm of relief, ≤ 4.5 m in wavelength and ≤ 2.4 m in continuous-aggradational thickness (Allen and Hoffman, 2005). Aggradation is achieved through buildup of bidirectional, crestward-coarsening, foreset laminae. Crestal orientations of giant wave ripples in the western segment fall between 085° and 120° (Fig. 57). They locally deviate significantly from the tectonic strike (e.g., bedding–cleavage intersection).

Tk4 is ≤ 6.0 m thick and consists of cm-thick tabular layers of dololite with upward-thickening inter-layers of purplish argillite. In contrast to its sharp base (Fig. 55B & C), the top of Keilberg Mb is gradational. The dolomite becomes progressively more argillaceous and

thinly bedded. The base of the first limestone layer, or its dolomitized equivalent, is taken as the top of Keilberg Mb.

Keilberg Mb is part of a deepening-upward sequence (TST) that begins at the base of Bethanis Mb and ends at the maximum flooding stage (MFS) in lower Karibib Fm (Fig. 44). Unit Tk1 records a short-lived regression superimposed on the glacioeustatic transgression. That the Tk1 regression is a gravitational effect of ice-sheet mass loss (Hoffman and Macdonald, 2010) appears plausible in principle at least, based on numerical simulations of sea-level changes during and after Marinoan deglaciation (Creveling and Mitrovica, 2014).

The best-exposed section of the maximum flooding stage of the lower Karibib Fm in the western segment is 5–14 (Figs. 43 & 46). Above a 6.0-m-thick Keilberg Tk4 are 42 m of marly calcite rhythmite, most argillaceous and reddish-coloured basally. This grades into 18 m of grey-coloured calcite turbidites, which coarsen upward with sporadic intraclast debrites (Fig. 56C). Exactly 60 m above the top of the Keilberg Member, the grey limestone turbidites change to buff-weathering dolomite turbidites (Fig. 56D). At 76 m above the Keilberg, the first ridge-forming intraclast debrites (Fig. 56E) and semi-coherent slumps appear in the Karibib Fm HST (Fig. 44).

The only complete section of Karibib Fm that we have measured in Tr5 is at Transfontein (5–7, Fig. 44). At 468 m, it is 43%, 208% and 369% thicker than Karibib Fm in Bethanis subbasin (Fig. 19), Summas allochthon (3–8, Fig. 39) and Vrede N-dome (2–38, Fig. 32), respectively. These differences reflect the southward taper of Karibib Fm. At Transfontein, Karibib Fm is composed of ~11 coarsening-upward sequences of dolomite rhythmite, turbidite, intraclastic debrite and arenite (Fig. 44). With the significant exception of the upper arenite-topped sequences, the lithologies do not change greatly with height, suggesting a more aggradational than progradational margin development. We cannot discern, without many more sections, if and how sea level forcing interacted with submarine-slope sedimentary dynamics in cyclic sequence construction (Wunsch et al., 2017).

2.5.2. West-central segment (5–15–30) of Transfontein Ridge

Like the western segment, the west-central segment of Tr5 (Fig. 58) runs subparallel to the inferred strike of the FSz (Figs. 8B & 43B), but it could be inferred from sedimentary facies that it begins to climb the foreslope at its eastern end (5–28–30). Stratigraphically, the west-central segment (Fig. 58) differs in three notable respects from the western segment. First, Sturtian ferruginous diamictite of Chuos Fm (Fig. 47A & B), ≤177 m thick, abruptly appears east of a pre-Berg Aukas border fault just west of section 5–23 (Fig. 58). Second, an eastward-thickening and coarsening wedge of Okonguarri Fm dolomite expands at the expense of Narachaams and Frannis-aus formations, which are finally cutout by the Marinoan glacial surface between 5–25a and 26 (Fig. 58). Third, the sub- Ghaub Fm disconformity defines transverse paleo-gullies, which cut through resistant Frannis-aus dolomite into soft Narachaams argillite (Fig. 58). Their depth/width dimensions in the plane of section are 0.04/0.50 km (5–17), 0.08/2.00 km (5–20–22) and 0.06/0.80 km (5–27–28). The paleo-gullies are filled by subglacial stratified diamictite of lower Ghaub Fm that are particularly well exposed in section 5–17 (Figs. 60 & 61).

Chuos Fm on the hangingwall of the pre-Berg Aukas border fault (Fig. 58) is poorly exposed compared with the overlying carbonates. Ferruginous diamictite (Fig. 47A & B), holding subrounded pebbles and boulders of basement orthogneiss (granodiorite, porphyritic monzogranite and amphibolite), forms resistant ledges. The diamictite includes both massive and stratified varieties. It is unclear if the most ferruginous zones are true jaspilites, with ice rafted debris, or simply ferruginized diamictite. The Fe doubtless originates within Chuos Fm, with which it is spatially associated, but there is much outcrop-scale

evidence of Fe remobilization. Where not strongly ferruginous, the argillaceous diamictite matrix is recessive. Where only clasts are exposed, they are distinguishable from basement in situ by their randomly oriented gneissic foliations (i.e., a ‘conglomerate’ test).

An erratic paleo-block of basement granodiorite orthogneiss, 40 × 160 m in exposed dimensions, occurs in section 5–26 (Fig. 58). The block sits atop >126 m of Chuos Fm diamictite and is onlapped by Berg Aukas Fm and covered by Okonguarri Fm into which the block projects (Fig. 58). We do not know if the basement block was glacially transported, like Sturtian olistoliths of Kingston Peak Fm in the Death Valley area of California (Macdonald et al. 2013a) or in Sturtian synglacial half grabens in Olary Region of South Australia (Conor and Preiss, 2020). Alternatively, it was part of a landslide emplaced after the glacial retreat. Either way, it stood out on a till plain that was flooded during Sturtian deglaciation and it was eventually buried by marine carbonate mud and sand of Okonguarri Fm (Fig. 58).

Berg Aukas Fm sharply overlies Chuos diamictite (Fig. 47A) and oversteps the Chuos border fault onto basement near 5–23 (Fig. 58). A younger dextral fault, ~30 m to the W, does displace Berg Aukas but its apparent slip is small compared with the Chuos boundary fault. Berg Aukas Fm is rather uniform in thickness, 20–40 m, and it begins with a coarsening-upward sequence of rhythmites and turbidites, mainly dolomitic but locally calcitic (5–25 and 30). At 5–18, two beds of laterally linked pseudo-columnar stromatolites occur low in base-covered sections, but such beds are exceptional. The rhythmite-turbidite sequence grades into black-and-tan sublittoral microbialaminite with roll-up structures, the signature Berg Aukas facies. Discrete columnar stromatolites appear within this unit in 5–17–21 and 24a (Fig. 59A–F). The columns reach ≥1.2 m in height and their smoothly arched laminations have ≤15 cm of synoptic relief (Fig. 59C). Between the columns are accumulations of abraded intraclasts of microbial roll-up (Fig. 59D). As is the case with late Holocene marine stromatolites, columnar stromatolite development appears to be a response to a more physically energetic environment (Logan et al., 1974; Dill et al., 1986; Reid et al., 1995; Playford et al., 2013). Locally (5–19–22a), shoal-water dolomite grainstone (unit Aa3, Fig. 59A) caps the microbialaminite–stromatolite unit, ending at a marine flooding surface beneath Okonguarri Fm (Fig. 58).

The Okonguarri Fm is an eastward thickening wedge of limestone and dolomite that overlies the Berg Aukas and underlies either Narachaams argillite or Ghaub diamictite (Fig. 58). The wedge continues across the east-central segment (5–30–49), filling a basement cavity (‘Kranspoort trough’ in Fig. 43). Overall, the wedge coarsens and shoals eastward, and to a lesser degree, stratigraphically upward. Its lower and westward parts are dominated by rhythmite and turbidite, much of it calcitic. Eastward and upward, the turbidites coarsen to intraclast debrites that intercalate with dolomite ribbonite and grainstone, some of it coarsely oolitic. The more shoalward parts of the wedge are described in 2.4.3. The western extremities of Okonguarri Fm are critical. Is the Okonguarri–Narachaams formation contact a facies change, a major flooding surface, or a disconformity?

The choice of datums for the west-central fence diagram (Fig. 58) was chosen to highlight the inferred geometry of the sub-Ghaub disconformity. The base of Franni-aus Fm is the datum in 5–15–25a (as in Fig. 43A), drawing attention to the incised paleo-gullies (5–17 and 20–22a). At 5–17, the gully coincides with the appearance of a 13-m-thick, coarsening-upward basal sequence of stratified carbonate diamictite (Figs. 60 & 61). Sedimentologically, the stratified diamictite consists of calcitic turbidites (Fig. 60A & E), slumps (Fig. 60B), debrites (Fig. 60A, 61C & D) and laminated lutite (plume fallout) with IRD (Figs. 60E & F, 61A & B). The larger dropstones are composed of oolitic limestone derived from Franni-aus Mb and are associated with impact-

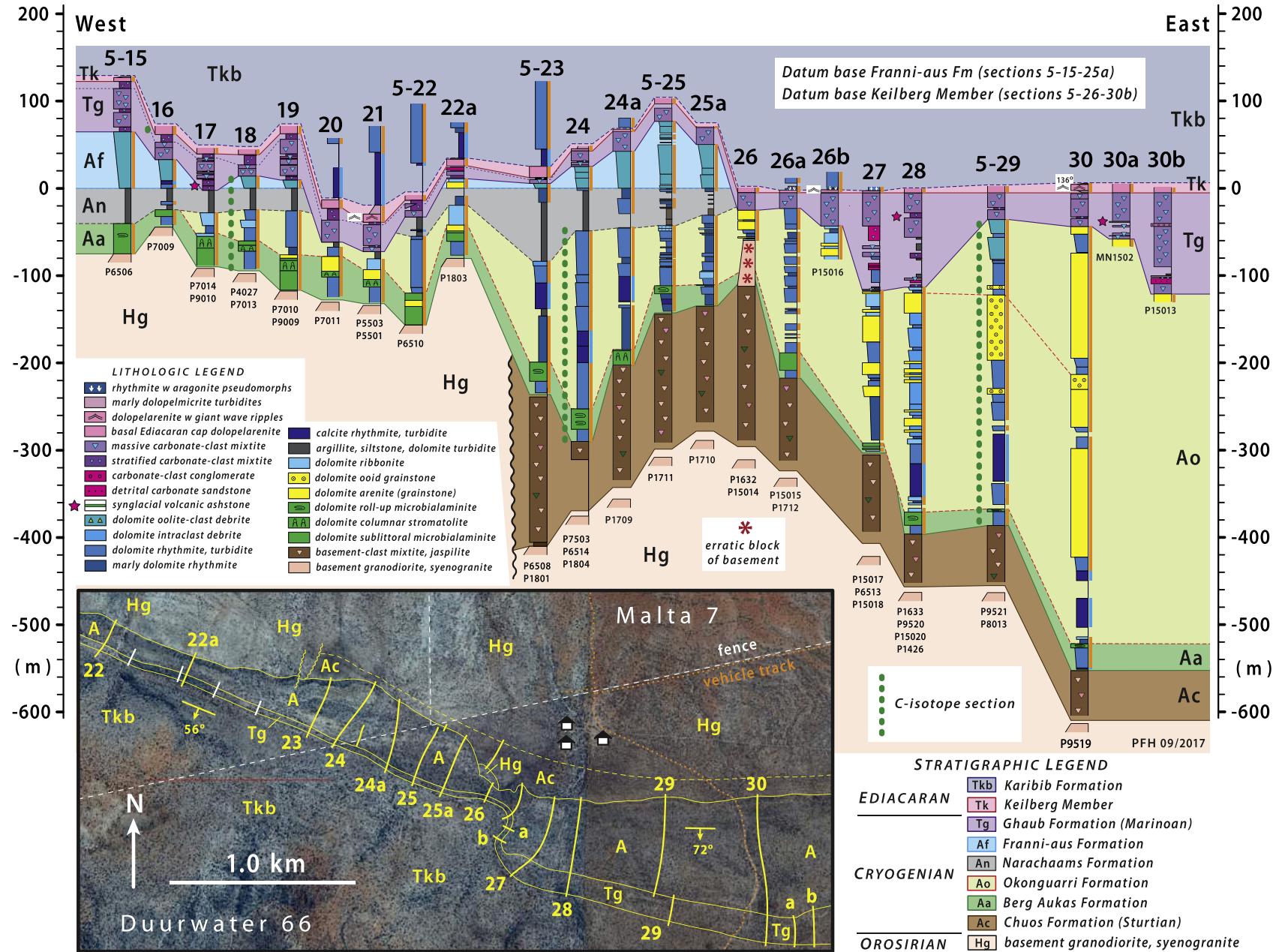


Fig. 58. Cryogenian and earliest Ediacaran columnar sections from the west-central segment of Tr5 (5-15–30) on Transfontein Ridge: datum (0.0 m) is base of Franni-aus Fm (Af) in 5-15–19 and 22a–25a; other sections are interpolated. Notable stratigraphic features include: (1) a fault-bounded subbasin (half graben) of Sturtian Chuos Fm ferruginous diamictite (5-23–31); (2) an erratic block of basement granodiorite, 40 × 160 m in exposed dimensions, perched on top of Chuos Fm in 5–26 and projecting 50 m stratigraphically upward into Okonguari Fm; (3) the distal tapered edge of Okonguari Fm (5-17–30) in Kranstoort trough (Fig. 43); (4) the eastward limits of Narachaams and Franni-aus formations (5-25a–26); (5) transverse troughs of Marinoan Ghaub Fm (5-17, 20–22 and 26–29) incised into Franni-aus, Narachaams and Okonguari formations; (6) volcanic ash layers (red stars) in Ghaub Fm (5-17, 28, 30a) including one in 5-28 dated at 639.29 ± 0.26 Ma (Prave et al., 2016); and (7) giant wave ripples in Keilberg Mb cap dolomite in 5-21, 26b and 30. Google Earth: Image © 2020 CNES/Airbus.

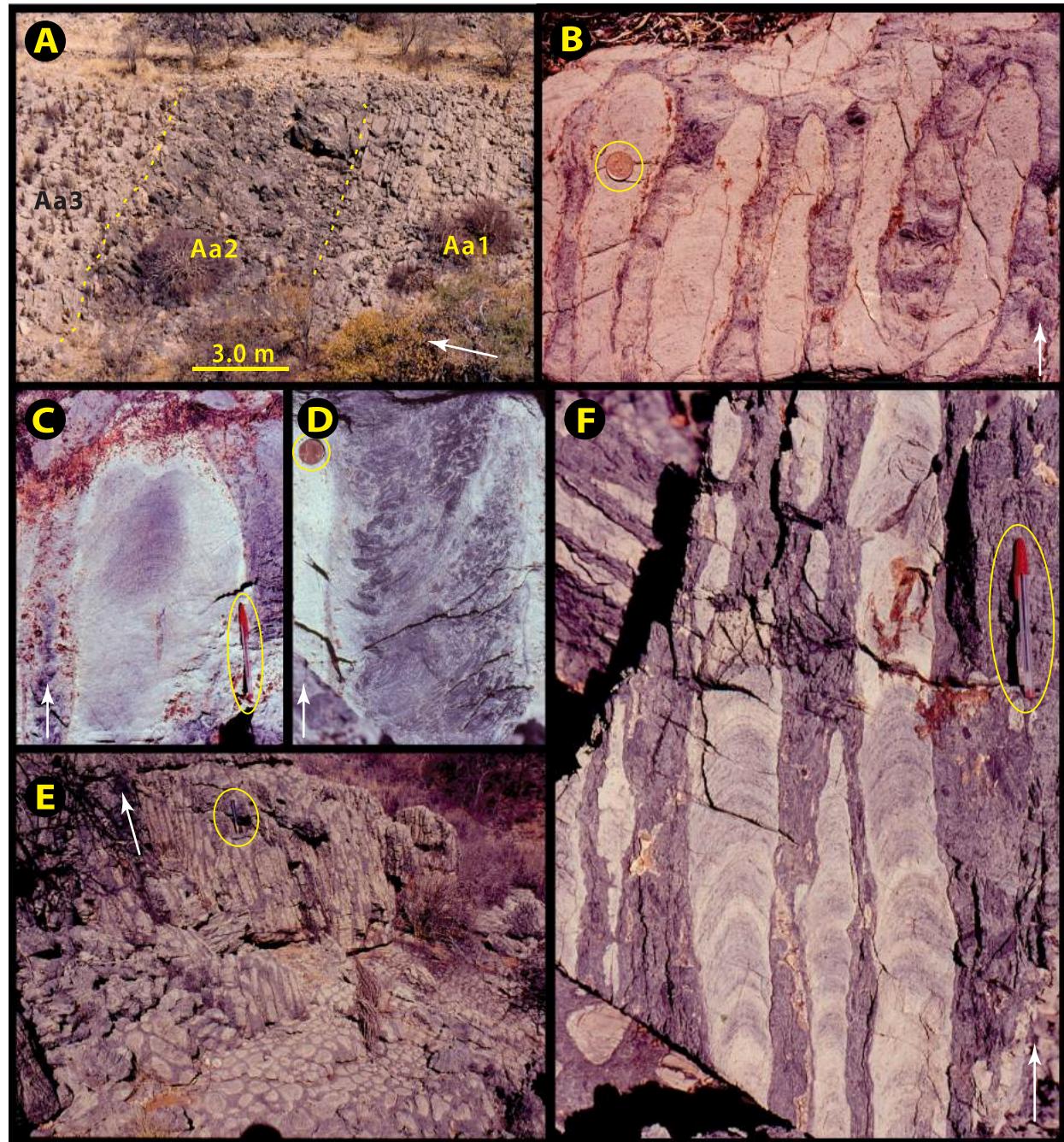


Fig. 59. Images of Sturtian cap carbonate (Berg Aukas Fm) in WC and EC segments of Tr5 on Transfontein Ridge (Figs. 58 & 62); white arrows indicate stratigraphic younging. (A) Three divisions of Berg Aukas Fm at $-20.1945^{\circ}/15.1005^{\circ}$ in 5–18: Ar1, dolomite rhythmite; Ar2, microbial intraclastite with simple columnar stromatolites; Ar3, dolomite grainstone and microbalaminite. (B) Discrete columnar stromatolites enclosed in microbial intraclastite at $-20.1995^{\circ}/15.2452^{\circ}$ in 5–40. (C) Columnar stromatolite flanked by intraclastite (D) microbial intraclastite between stromatolites at same location as A. (E–F) Discrete columnar stromatolites within microbial intraclastite at same location as B.

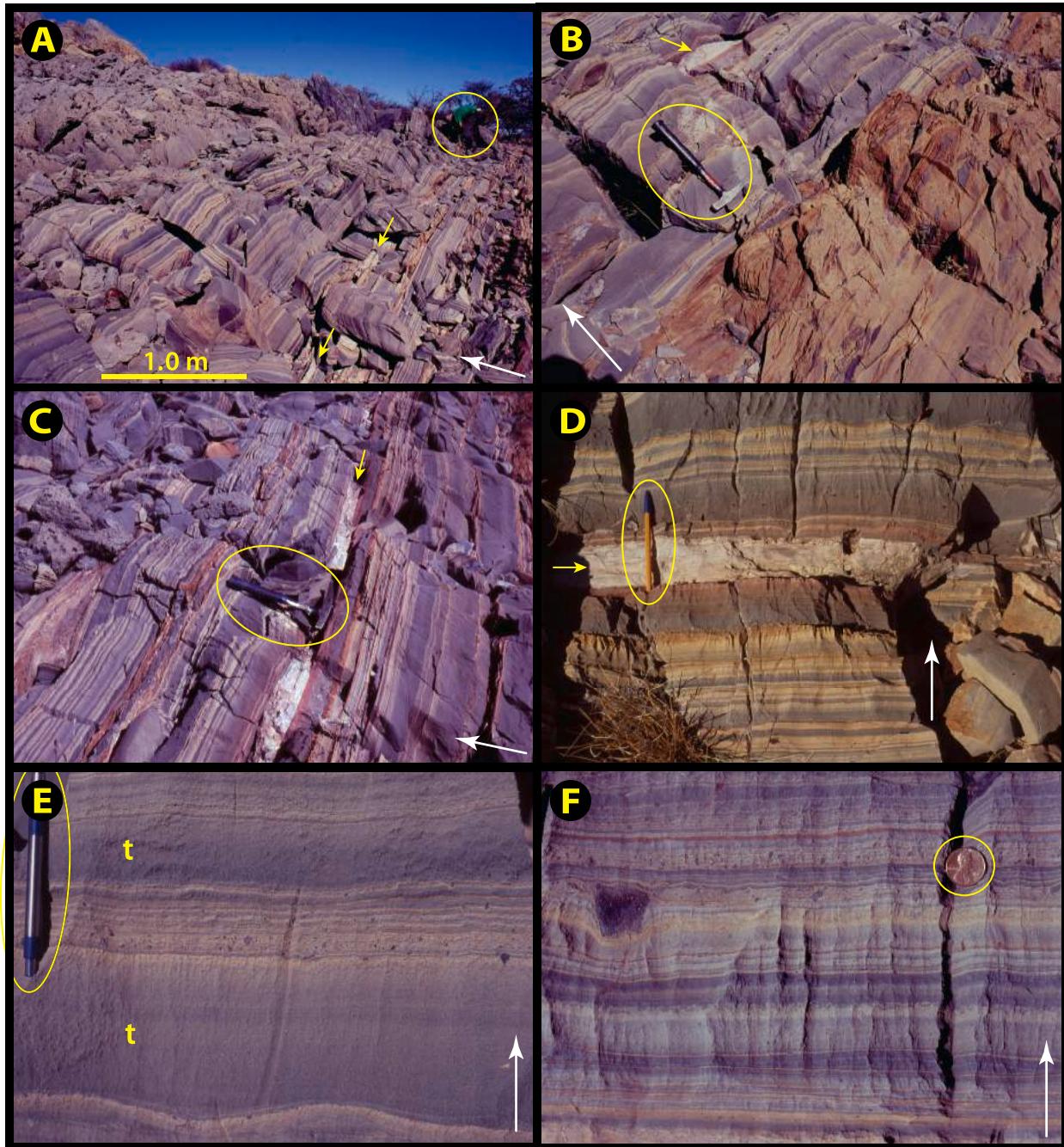


Fig. 60. Images of subglacial plume fallout and volcanic ash layer in Marinoan lower Ghaub Fm filling an incised trough in WC segment of Transfontein Ridge at $-20.1952^{\circ}/15.0993^{\circ}$ in 5-17 (Fig. 58); white arrows indicate stratigraphic younging. A 0.6-km-wide trough is incised through resistant Franni-aus Fm FST wedge into soft underlying Narachaams Fm argillite. Ghaub Fm inside trough begins with 13.0 m of delicately stratified detrital carbonate with IRD increasing in size and abundance stratigraphically upward. The stratified interval, which hosts an 8-cm-thick tuff (bentonite) layer, is overlain by 24.2 m of massive diamictite separated into four tabular bodies composed of dololutite laminites (suspension-plume fallout) with limestone turbidites. Ghaub Fm ends with 5.6 m of Bethanis Mb stratified diamictite. (A) Overview of transition from stratified (lower right) to massive (upper left) carbonate diamictite. The stratified beds abut against the trough walls, composed of Franni-aus Fm oolite-clast chert-dolomite debrite (Figs. 48E-F & 49A-B). Geologist (circled) seeks continuation of pale tuff layer (yellow arrows). (B) Slumped bed of marl with dolomite clasts, overlain by limestone turbidites in dololutite laminites. Altered tuff layer (bentonite) in upper left. (C-D) 8-cm-thick tuff layer (yellow arrow) near base of the stratified interval composed of dololutite laminites (suspension-plume fallout) with limestone turbidites. Note reddish discolouration of carbonate in contact with tuff. No igneous zircons were obtained from samples of this layer. Submarine deposition of airborne volcanic ash in the absence or presence of an ice shelf is discussed by Prave et al. (2016) and Hoffman et al. (2017a), respectively. (E-F) Limestone turbidites (t) as event beds in ambient dolosiltite laminites deposited as suspension-plume fallout, peppered with fine-grained IRD. Note absence of IRD in turbidites, consistent with a steady ‘rain’ of IRD and near-instantaneous turbidite emplacement. IRD is presumed to have melted from base of an ice shelf. These are the most ice-distal lithofacies in the distal-to-proximal trough-filling vertical sequence (A).

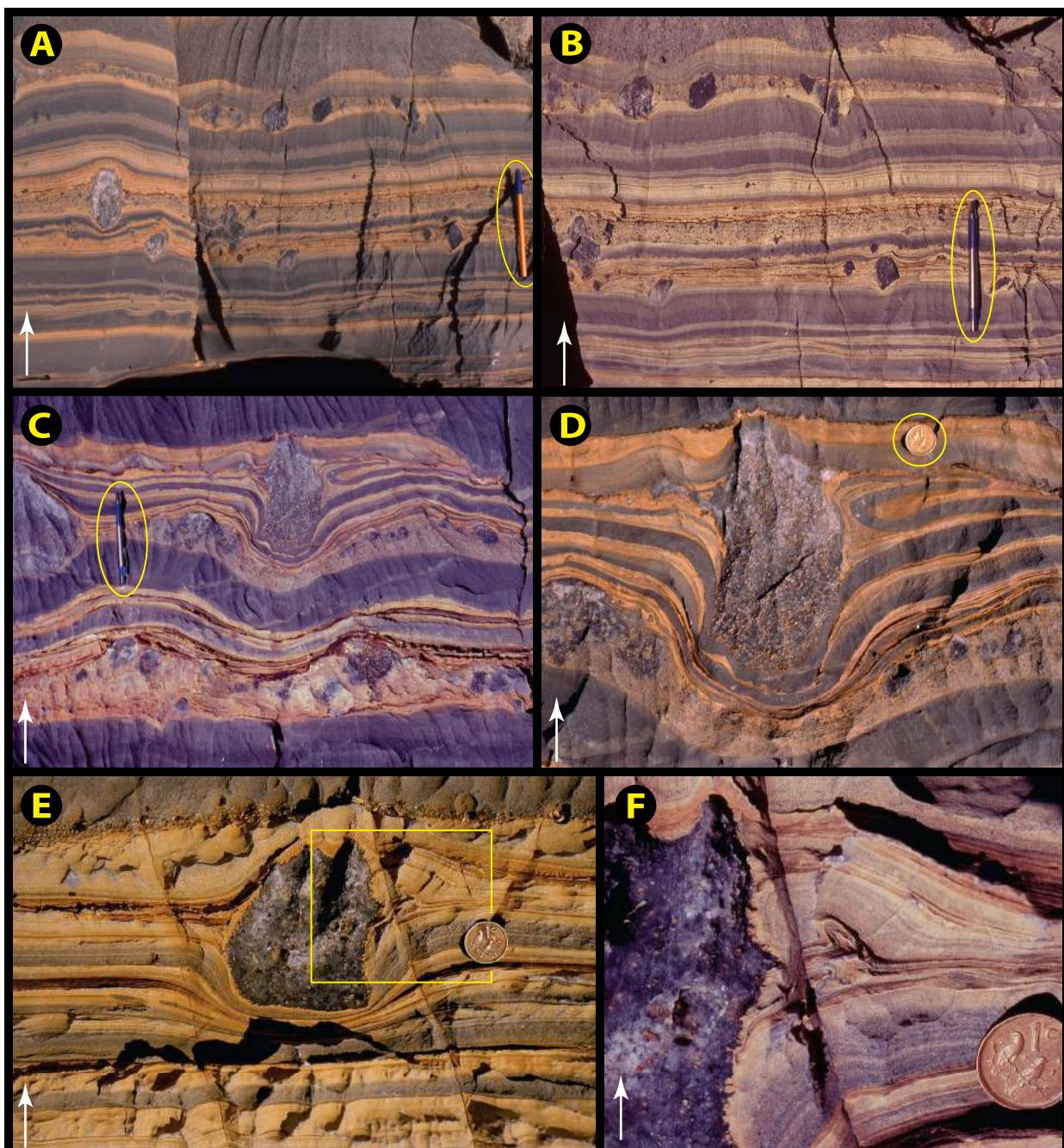


Fig. 61. Images of Ghaub Fm IRD, suspension-plume fallout and turbidites from the incised Marinoan trough at 5–17 (Fig. 58) on Transfontein Ridge, stratigraphically above images in Fig. 60: white arrows indicate stratigraphic younging. (A–B) Limestone turbidites (grey) and laminated dololutite (buff) interpreted as suspension-plume fallout with IRD: at $-20.1952^{\circ}/15.0994^{\circ}$. IRD is absent in turbidites and was inferentially dropped from the base of a marine ice shelf, rather than from icebergs for which there is no evidence (e.g., plough marks). Laminated plume fallout has normal and reverse grading, but turbidites are normally graded (fining-upward). Abundance of IRD in laminites and absence in turbidites seems contrary to the interpretation of Ghaub Fm as strictly nonglacial mass-flow deposits (Eyles and Januszczak, 2007). (C–D) Ice-raftered dropstone (Franni-aus Fm oolite-debrite derived) at $-20.1956^{\circ}/15.0985^{\circ}$, with impact-related structures including punctured layers and a doubly folded ejection flap (below the 2-cm coin in D). Lower half of coin (circled) in D rests on 1st post-impact layer. (E–F) Ice-raftered dropstone (Franni-aus oolite-debrite derived) at $-20.1952^{\circ}/15.0993^{\circ}$ with impact-related structures including a double-fold (above and to left of coins) that accommodates horizontal shortening and vertical extension (negligible lithostatic load) in response to impact.

related deformations such as ‘double-flap’ recumbent folds (Fig. 61C & D) and ‘mirror-image’ folds manifesting horizontal shortening and vertical thickening on the sea floor (Fig. 61E & F).

A discrete, parallel-sided, bentonite layer (altered volcanic ash) occurs low in the sequence at 5–17 (Fig. 60C & D), but it yielded no igneous zircons. Tuffs also occur in the middle Ghaub Fm near section 5–28 and 5–30a (Fig. 58), and the former yielded ten zircons, nine of which yielded a weighted mean $^{206}\text{Pb}/^{238}\text{U}$ date by CA-IDTIMS of $639.29 \pm 0.26 / 0.31 / 0.75$ Ma (analytical/analytical+tracer/analytical+tracer+ decay constant, 2σ errors) (Prave et al., 2016). The date implies that the middle Ghaub Fm was deposited ca 4.0 Myr before the Marinoan deglaciation (Prave et al., 2016).

The Ghaub tuffs were presumably erupted subaerially and carried from afar, since no local volcanic source of Marinoan age is known in the Otavi fold belt. Prave et al. (2016) consider that the Ghaub tuffs imply the absence of a marine ice cover. A counter scenario, consistent with a snowball state, is that sea glacier flow collects volcanic ejecta globally and sequesters it on the equatorial sublimation surface (Hoffman et al., 2017a, p. 21). It would then be further concentrated by meltwater flushing through moulin, where its passage to the sea floor would be without risk of dispersal by wave action. In this scenario, the sea glacier

contributes to the subaqueous deposition of discrete ash layers erupted subaerially at remote locations. Estimated lag times between volcanic eruptions onto ice and ultimate sedimentation onto the subglacial sea-floor are ≤ 0.5 Myr (Hoffman et al., 2017a).

Narachaams and Frannis-aus formations are cut-off between 5–25a and 26 (Fig. 58), requiring a different datum for sections 5–26–30. We substitute the base of Keilberg Mb as the datum E of 5–26. There, by definition, any local Ghaub thickening appears as a ‘gully’. A true paleo-gully is indicated by lower stratified facies in 5–27–28, analogous to but less well exposed than those in 5–17. The terminal Bethanis Mb of Ghaub Fm pinches out between 5 and 23 and 24 (Fig. 58) and does not reappear to the E.

The ever-present Keilberg Mb averages 6.85 m ($n = 18$) in thickness in the west-central segment of Tr5. Giant wave ripples occur in 5–21, 26b and 30. In most sections sheet-crack cement defines a zone close to but not at the base of the cap dolomite. In 5–26a–27, cm-scale pseudomorphs of chert and/or dolomite after upward-fanning clusters of prismatic pseudo-hexagonal aragonite appear in dull-grey coloured dolomite rhythmite, directly overlying the buff-coloured Keilberg Mb.

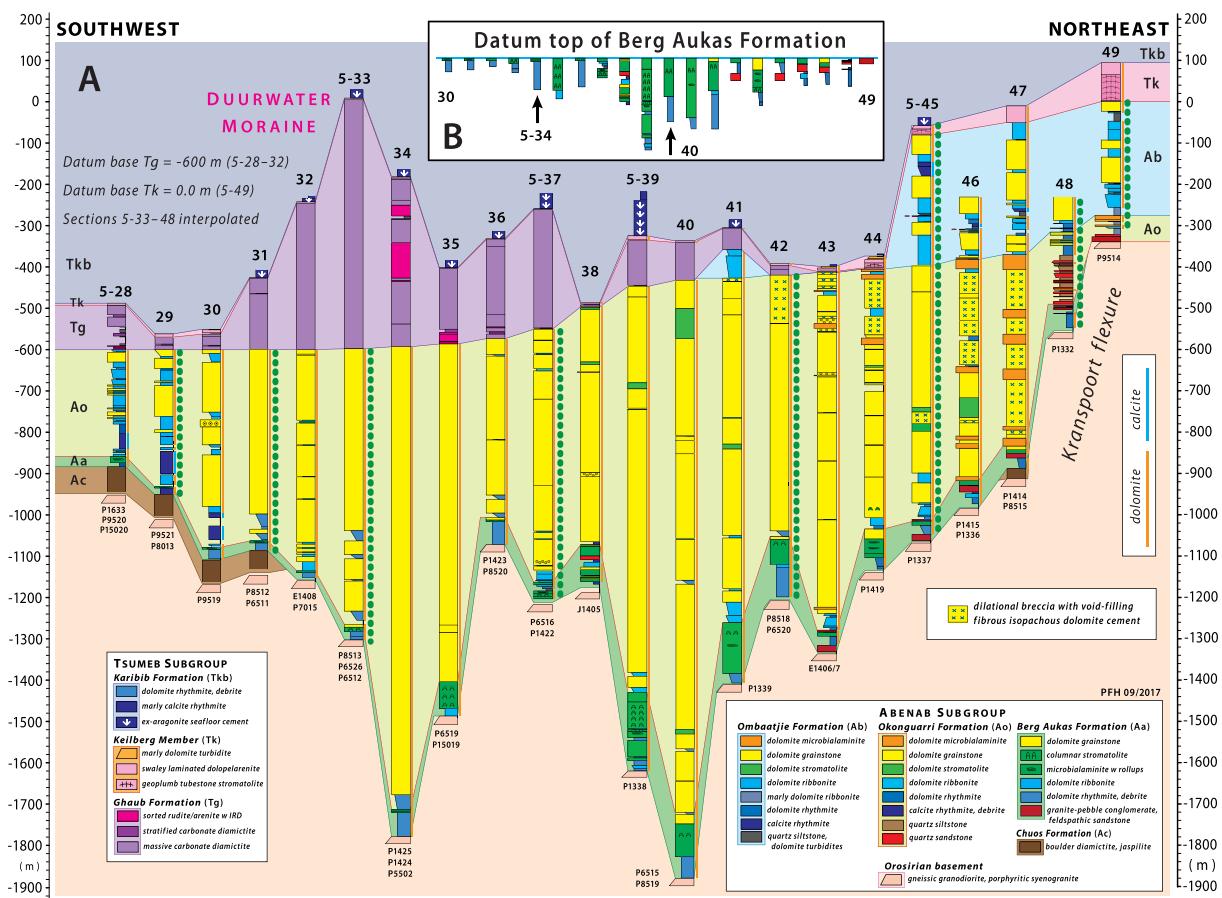


Fig. 62. (A) Cryogenian and earliest Ediacaran columnar sections from proximal FSz (EC segment, 5–28–49) on Transfontein Ridge (Tr5). Stratigraphic features include: (1) post-Sturtian Berg Aukas (Aa) cap carbonate onlapping Orosirian crystalline basement east of 5–31; (2) medial and proximal parts of Okonguarri Fm (Ao) ramp of Kranstoort trough (Fig. 43); (3) Marinoan headwall erosional truncation of Ombaatje Fm (Ab) outer shelf; (4) 600-m-thick Duurwater moraine (Fig. 43), a composite buildup of massive carbonate diamictite and conglomerate of Ghaub Fm (Tg), marking the terminal Marinoan ice grounding-line on the proximal FSz; (5) upslope pinchout of Ghaub diamictite just short of 5–45, beyond which a rapidly-thickening Keilberg cap dolomite (Tk) onlaps the upper Ombaatje shelf; (6) attenuation of Keilberg Mb as a macropeloidal lag (Fig. 67A) over Duurwater moraine; (7) localization of Duurwater moraine of macroscopic crystal fans (former aragonite neomorphosed by calcite, dolomite or chert, Fig. 67B) in lower Karibib Fm (Tkm). The basement depression occupied by Kranstoort trough (Fig. 43) may have originated as a Sturtian glacial cirque terraced by Chuos Fm diamictite (5–26–31 and 47). Basement-derived clastic tongues in proximal Berg Aukas and Okonguarri formations (Fig. 66A–D), and pervasive dilational breccia with fibrous-dolomite marine cement (Fig. 66E–F), suggest active crustal flexure (Fig. 65B) between 5 and 45 and 49 (Fig. 43) in early-middle Cryogenian time. There are two datums: base of Ghaub Fm (Tg) at -600 m from 5 to 28–32, and base of Keilberg Mb (Tk) at 0.0 m at 5–49. Sections 5–33–48 are interpolated. (B) Berg Aukas Fm at the same scale as A but with a top-Berg Aukas Fm datum.

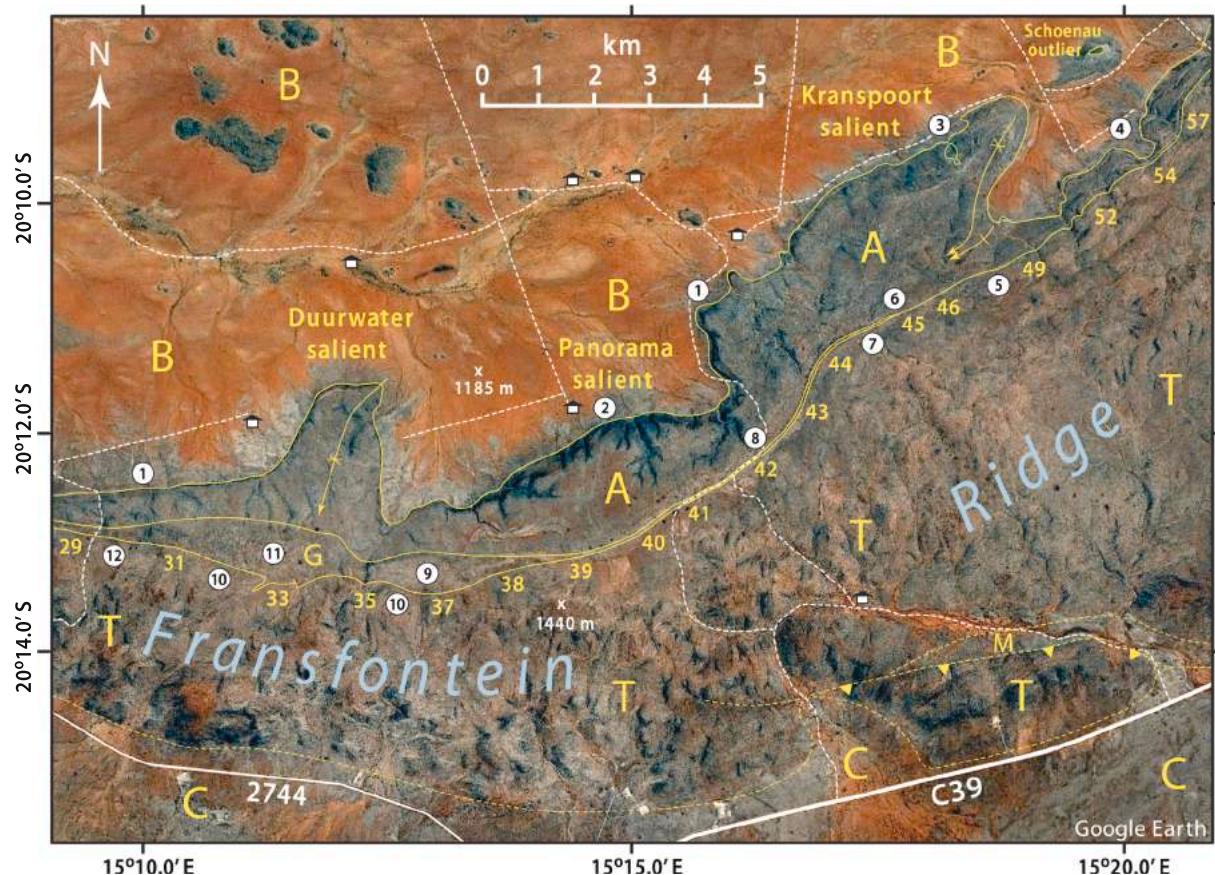


Fig. 63. Annotated satellite image of proximal FSz (EC segment of Tr5) on Transfontein Ridge, 5–29–57 (Fig. 43), showing surface expression of Duurwater, Panorama and Kranspoort salients discussed in text. Stratigraphic layering dips S and SE, with the exception of upright open folds as indicated by conventional symbols. Solid white lines are numbered graded roads and dashed white lines are vehicle tracks within farms. House symbols indicate settlements. Geologic units: B, Orosirian crystalline basement; A, Abenab Subgroup (early and middle Cryogenian); G, Ghaub Fm (Marinoan); T, Tsumeb Subgroup/Karibib Fm (early Ediacaran); M, Mulden Group (middle Ediacaran); C, flat-lying Bertram Fm (Cenozoic). Yellow numbers 29–57 indicate columnar sections (Figs. 43, 62, 65 & 68). Ridge (T) has 250 m of relief above the basement (B) sand plain. Points of geologic interest (white circles): 1, clastic tongues in Berg Aukas Fm (Fig. 66A–D); 2, columnar stromatolites in upper Berg Aukas (Fig. 59D–F); 3, inlier of monzogranite surrounded by Berg Aukas Fm, interpreted as a paleotopographic basement high reaching the top of the Berg Aukas Fm; 4, basement paleotopographic high that reaches the middle Ombaatjie Fm at its exposed crest (5–54, Fig. 58); 5, Marinoan subglacial erosion surface cuts off Ombaatjie Fm cycle b8 between 5 and 47–49 (Figs. 43 & 68); 6, pinchout of Ghaub Fm diamictite; 7, Marinoan subglacial erosion surface cuts off most of the Ombaatjie Fm between 5 and 44–45; 8, Ghaub Fm diamictite floored by Okonguarri Fm dolomite grainstone in which dilational breccia is sealed by marine fibrous-dolomite cement (Fig. 66F) that predates Marinoan glaciation (*contra* Kennedy et al., 2001a); 9, eastern lobe of Marinoan Duurwater moraine; 10, attenuated Keilberg Mb macropeloidal lag (Fig. 67A) and silicified ex-aragonite crystal fans in lower Karibib Fm; 11, western lobe of Duurwater moraine; 12, discontinuous volcanic tuff ≤ 1.1 m thick in the middle Ghaub Fm. Google Earth: Image © 2020 CNES/Airbus & Maxar Technologies.

2.5.3. East-central segment (5–30–49) of Transfontein Ridge

This key segment (Fig. 62) links the distal FSz to the OPZ (Fig. 43). The strike of beds swings from 090° in 5–30–39 to 050° in 5–39–49 (Fig. 63). The Cryogenian outcrop belt widens in three salients, centered on farms Duurwater 66, Panorama 314 and Kranspoort 475 from W to E (Fig. 63). The cuspatate Duurwater and lobate Kranspoort salients are largely structurally controlled, although important stratigraphic changes also take place in Kranspoort salient (Figs. 64 & 65). The shallow Panorama salient (Fig. 63) houses the eastern subbasin of Kranspoort trough (Figs. 43 & 62) and is mainly stratigraphic in origin.

Chuos diamictite pinches out between 5 and 31 and 32 (Fig. 62) and reappears only once, in 5–47. Conversely, Berg Aukas Fm swells to a maximum thickness (190 m) in 5–39 (Fig. 62B). Tall, slender, columnar stromatolites (Fig. 59E & F) occur within intraclastic sublittoral microbialaminite in 5–35–42. From 5 to 43 eastward, Berg Aukas Fm contains increasing amounts of locally sourced, basement-derived, clastic detritus (Fig. 66A & B) and co-occurring dolomite-clast debrite (Fig. 66C & D). The clastic influx is accompanied by direct evidence for mesoscale relief on the basement erosion surface. Between 5 and 47 and 48, a paleotopographic basement high forms a small inlier of porphyritic

monzogranite, encircled by outward-dipping sandy dolomite of Okonguarri Fm (Figs. 63 & 64). The onlapping Berg Aukas Fm pinches out near the base of the basement high. Measuring 0.24×0.3 km in size, 'Schoenau inlier' (Fig. 65) is centred geographically at $-20.1587^\circ / 15.3035^\circ$. Between section P8515 (5–47) and the crest of the basement high at section P1334, a distance of 0.48 km, there is ≥ 0.4 km of stratigraphic onlap (Fig. 65), implying an average basement surface paleo-slope of 40° .

Yet, despite this sedimentological and stratigraphic evidence for basement topography and erosion during Berg Aukas sedimentation, not a single growth fault cuts the basement surface (Figs. 64 & 65). The base of Berg Aukas or Okonguarri Fm was walked out between 5 and 46 and 51—no fault was found. This implies that if accommodation for Kranspoort trough (Figs. 43 & 62) is fault related, a blind basement-only fault would have to be invoked. Hoffman and Halverson (2008) postulated a crustal flexure (Kranspoort flexure in Fig. 65B) to reconcile evidence for basement activation without faulting (Coleman et al., 2019). They associated flexure with the tip of an inferred south-dipping normal fault responsible for Huab ridge (Figs. 5 & 26). The footwall (rift shoulder) of the fault is exposed in Tr6, and its hangingwall in the western and west-

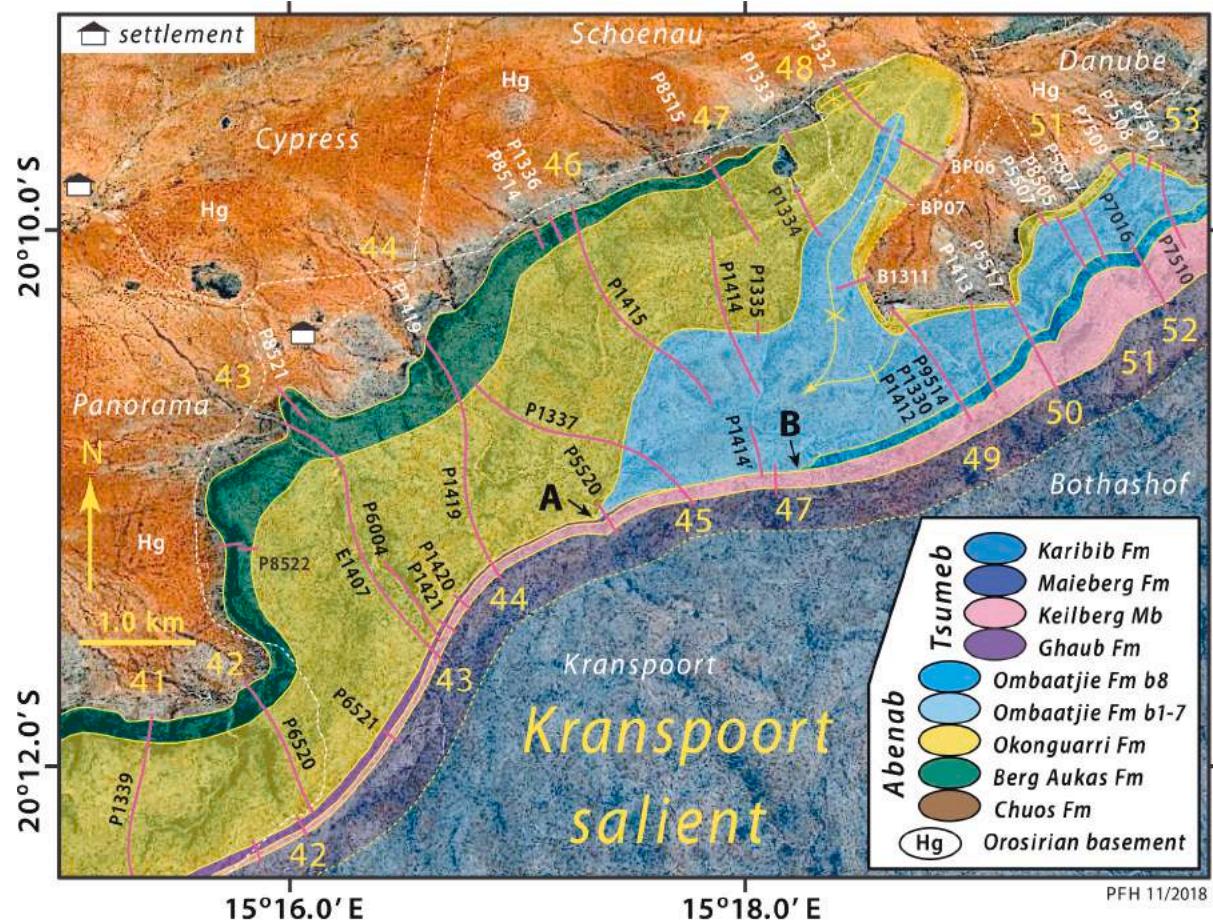


Fig. 64. Annotated satellite image of Kranspoort salient (5–41–53) on Transfontein Ridge (Tr5), showing locations of columnar sections (Figs. 43, 62, 65 & 68) numbered in yellow. Note syncline–anticline pair between 5 and 48–49. Key stratigraphic relation is the Marinoan glacial erosion surface (beneath Ghaub Fm and/or Keilberg Mb) which truncates Omboaatjie Fm outer shelf (Figs. 43 & 62) at a steep angle. Stratigraphic cutoffs: A, base of Omboaatjie Fm; B, base of Omboaatjie cycle b8 (Fig. 68). Also shown is Schoenau basement inlier, between 5 and 47 and 48, which projects as a paleotopographic high into Okonguarri Fm (P1335, Fig. 65). It possibly formed a barrier behind which fine-grained carbonates and clastics (5–48 to 49, Fig. 65) substitute for shoreface grainstone and stromatolites in front. Google Earth: Image © 2020 CNES/Airbus.

central segments of Tr5 (Fig. 8B). In Tr6, the rift shoulder was last active when Gruis Fm was deposited (Fig. 5 and 2.6.1.), broadly contemporaneous with Okonguarri Fm in Tr5 (Fig. 6C & D).

Another process unrelated to tip-line flexure may have contributed to the making of Kranspoort trough (Fig. 62). During the protracted (56 Myr) Sturtian snowball, Huab ridge was a subglacial rift shoulder, not unlike the Neogene Transantarctic Mountains (Fielding, 2018; Wannamaker et al., 2018; Goodge, 2020). If an ice sheet poured slowly across the rift shoulder into the growing Northern (Outjo) rift basin, transverse glacial valleys like those of the Transantarctic Mountains (Stump, 2011) should have been cut into Huab ridge basement. As evidence for a glacial origin is the observation that Chuos Fm diamictite is preserved at similar paleo-elevations on both sides of Kranspoort trough (5–28–31 and 5–47, Fig. 62). These could be relict lateral moraines if Kranspoort trough was incompletely ice filled during the late stages of Sturtian glaciation (Benn et al., 2015). According to the trough reconstruction (Fig. 62), the maximum ice depth at that time would have been 0.65–0.95 km in the line of Tr5. Rapid deglaciation left no other recessional debris inside the trough, where Berg Aukas Fm formed a basal sedimentary drape over a glacially-fluted basement surface.

Okonguarri Fm of Kranspoort trough is dominated by tabular bedded to massive dolarenite, intermittently oolitic and/or stromatolitic (Fig. 62). The stromatolites are ruggedly mounded, typical of high-

energy environments (Reid et al., 1995; Playford et al., 2013). Where flooding surfaces occur, the ribbonites that overlie them coarsen rapidly back to grainstone. The incidence of ribbonite increases southwestward, while that of stromatolite and microbial laminites increases northeastward (Fig. 62). Kranspoort trough is bisected into two subbasins of subequal depth (Fig. 62) by a basement ridge (5–36–38). Northeast of Schoenau inlier (5–48–52), basement-derived conglomerate, sandstone and siltstone are interfingered with dolomite rhythmite and ribbonite. As the most proximal facies of Okonguarri Fm (Fig. 65), these quieter-water facies could represent an estuary protected behind shoreface grainstone barrier facies. Alternatively (not shown), the clastic-rich rhythmite–ribbonite facies represents a thickened Berg Aukas Fm, in which case a shoreward unconformity beneath Omboaatjie Fm must be inferred to account for the abrupt disappearance of Okonguarri Fm.

Progressing NE from section 5–41 toward Huab ridge basement high, first the upper and ultimately the entire Okonguarri Fm is pervaded by dilatant oligomictic breccia (Figs. 62 & 65). The breccia cracks and voids are filled by fibrous isopachous dolomite cement (Fig. 66E & F), which may constitute 60% or more of the rock volume. If the cement was originally dolomite, it presumably precipitated from marine-derived porewaters. The breccia is selectively developed in dolomite grainstone and is spatially associated with the up-slope trough margin (5–47–49). The age of brecciation and cementation must predate

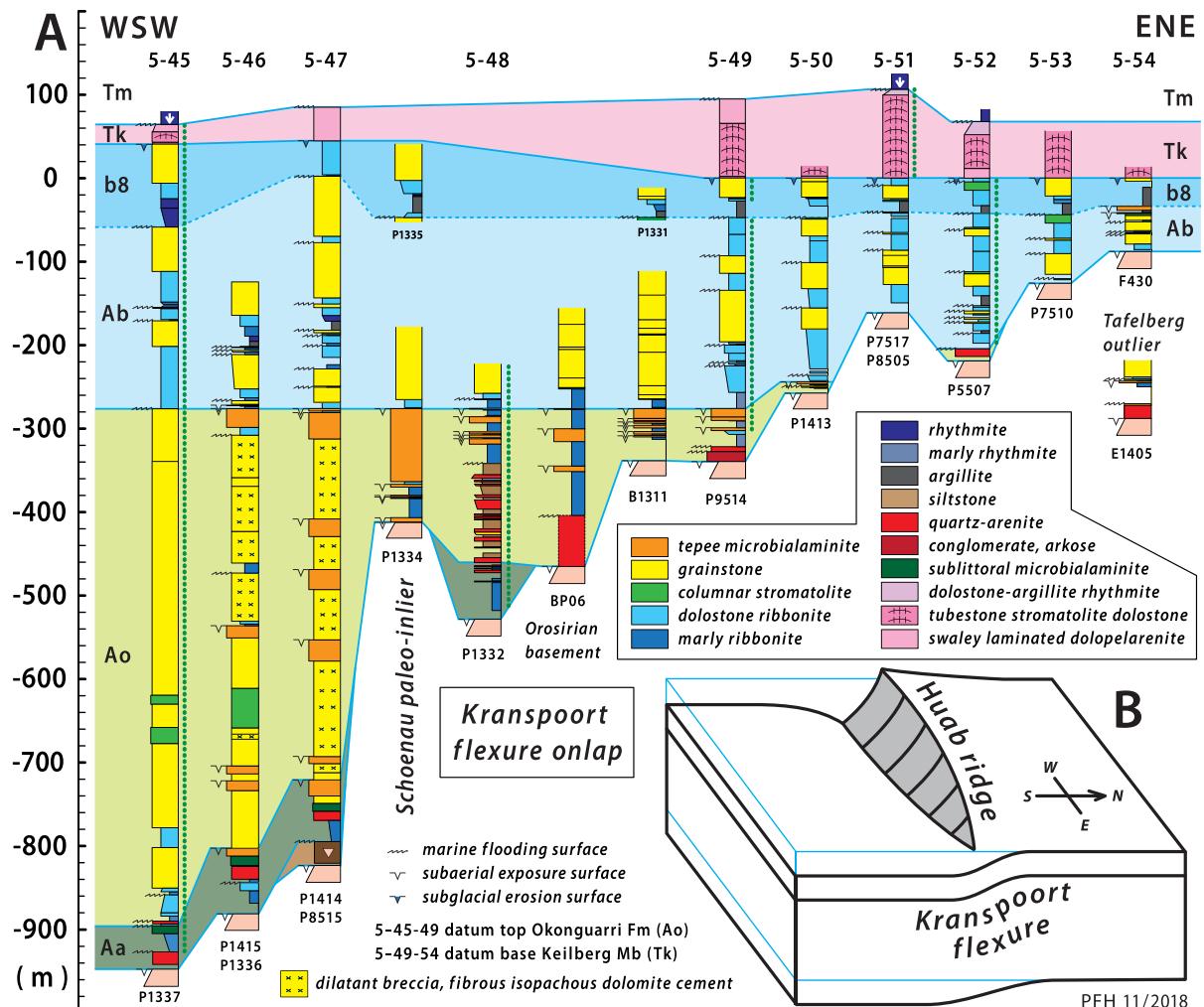


Fig. 65. (A) Cryogenian and earliest Ediacaran columnar sections showing stratigraphic onlap of Kranspoort flexure (B) between 5 and 45–54: section locations in Fig. 64. Schoenau paleo-inlier located in Fig. 68B. Datums are base of Ombaatjie Fm between 5 and 45–49 and base of Keilberg Mb between 5 and 49–54. (B) Kranspoort flexure is inferred to express Huab ridge (Fig. 5) normal-sense displacement beyond the fault tip-line.

Marinoan glaciation, since Ghaub Fm disconformably overlies cemented breccia in section 5–42 (Fig. 62), where the vehicle track crosses the Okonguari–Ghaub contact (Fig. 64). Clasts of the fibrous-isopachous dolomite cement occur in Ghaub Fm diamictite (Fig. 56F). The cements are not synglacial and have no bearing on the chemistry of the Marinoan ocean, contrary to a previous interpretation (Kennedy et al., 2001a). The spatial distribution of the Okonguari Fm dilatant breccias suggests a mechanical connection to synsedimentary flexure (Fig. 65B) of the basement surface in the area of sections 5–47–49 (Figs. 62 & 65A).

Is it possible that the pair of keel-like subbasins of Kranspoort trough, centred on 5–34 and 40 (Fig. 62), are not stratigraphic in origin? Could they reflect tectonic strain related to Duurwater and Panorama salients (Fig. 63), with which they are broadly coincident? Duurwater salient is coaxial with a SSW-plunging cuspatate syncline in the basement-cover interface. Dips of bedding along the axial trace of this structure (5–34) are consistently 21–29° (steepening rapidly on the limbs) and the stratigraphic thickness is roughly twice that of pre-Ghaub sections outside the salient (5–30–32 and 36–38). How much of the thickening results from tectonic strain associated with cuspatate basement pinching (Ramsay and Huber, 1987)? It would be tempting to attribute much of the keel-like subbasin (5–32–36) to tectonic strain, but for one observation. The Berg Aukas should be the most strained, since it lies closest to the basement interface where a cuspatate syncline should be most

pinched. In fact, there is little or no Berg Aukas thickening in the cusp (Fig. 62B), certainly far less than Okonguari thickening. The difference cannot be attributed to rheology because Berg Aukas rhythmite should have been weaker than Okonguari grainstone, and should in consequence be more strained, not less. We therefore conclude that Okonguari thickening in Duurwater salient is primarily stratigraphic, and that the tectonic cusp may have been localized where the basement surface was erosionally incised. In Panorama salient (Fig. 63), there is no cuspatate syncline. Bedding is tilted rather uniformly 35–45° toward SSE, with small-scale dip reversals in the lower Berg Aukas rhythmite.

The Marinoan Ghaub Fm averages 41.3 m in thickness ($n = 23$) in the west-central segment (5–15–30b), but eastward from 5 to 30 it thickens steeply to 602 m in 5–33, before tapering to zero-thickness between 5 and 43 and 44 (Figs. 62–64). It does not reappear up-slope in Tr5 and is generally absent from the OPz. Ghaub Fm in 5–33 is the thickest (602 m) in the region and the average of sections 5–31–37 (320 m, $n = 7$) is six times the 53-m average of all (non-zero) Ghaub sections ($n = 157$). These over-thick Ghaub sections, named Duurwater moraine (Figs. 43 & 62), are notable for their paucity of stratified diamictite. They are dominated by massive diamictite (Fig. 67A), but variable in clast lithology, size and concentration. The clasts are generally subrounded and the largest (usually dolomite stromatolite) reach 3.0 m in diameter. Large bodies of clast-supported carbonate conglomerate occur in 5–34–35, at different stratigraphic levels.

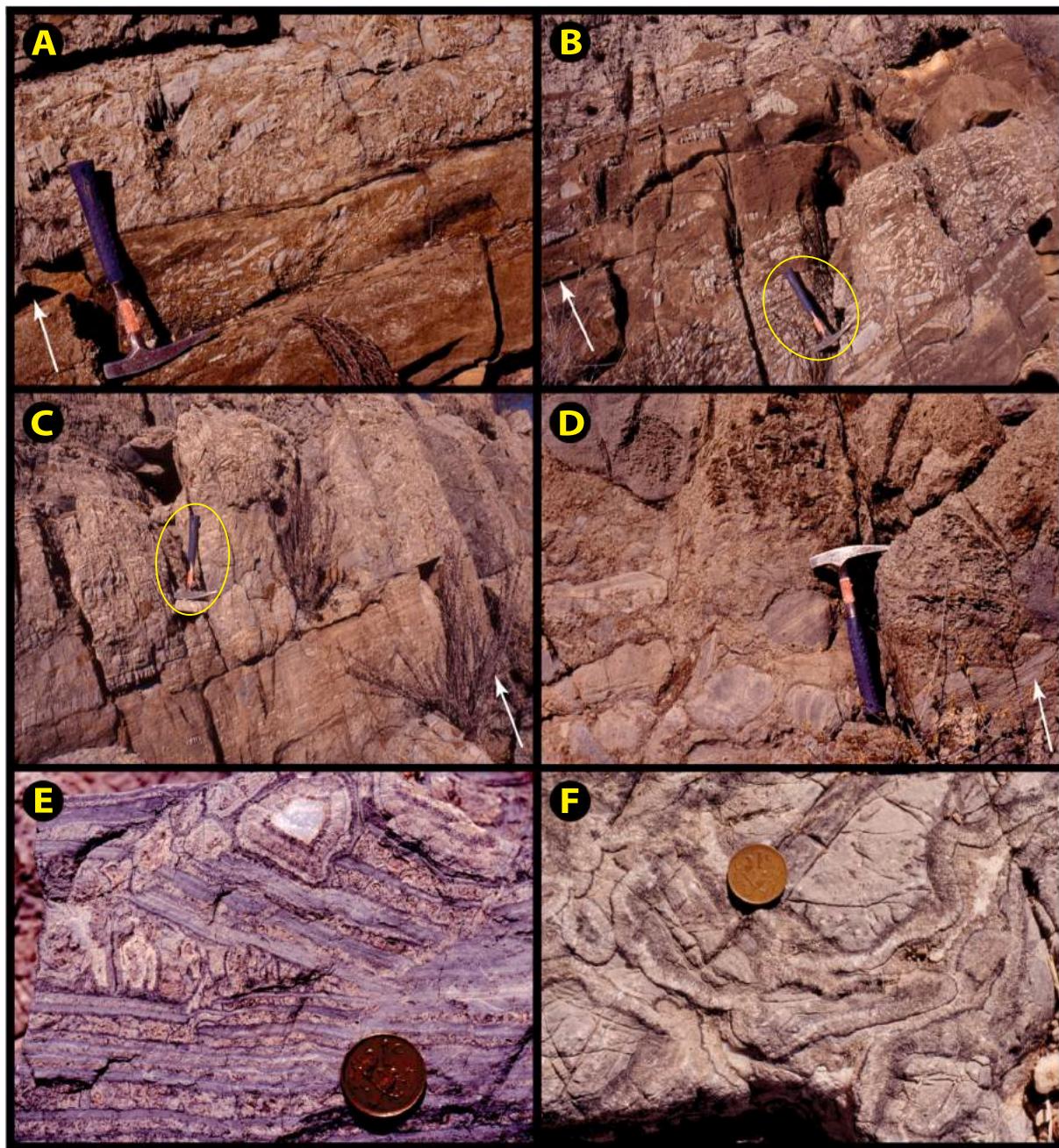


Fig. 66. Images from Kranstoort flexure (Figs. 62 & 65B) on the proximal side of Kranstoort trough (Fig. 43) on Transfontein Ridge (Tr5): white arrows indicate stratigraphic younging. (A-B) Dolomite-intraclast conglomerate and basement-derived feldspathic quartzarenite (brown-stained) in lower Berg Aukas Fm at $-20.1632^{\circ}/15.2852^{\circ}$ in 5–46 (Fig. 62). (C-D) Dolomite-intraclast conglomerate with feldspar and quartz-rich matrix: lower Berg Aukas Fm at same location as A-B (Fig. 62). Clast above hammer in D is stromatolite. (E-F) Fibrous dolomite marine cement in Okonguarri Fm dilatant breccia, spatially associated with Kranstoort flexure (Fig. 65) near $-20.1693^{\circ}/15.2914^{\circ}$ in 5–46. Flexure inferred as a synsedimentary crustal monocline forming the proximal margin of Kranstoort trough (Figs. 43 & 62). Late stage void-filling quartz (white).

The upper Okonguarri Fm provides no marker bed to serve as a datum for restoration of the sub-Ghaub Fm disconformity. We had no recourse but to fix this surface arbitrarily. We did so (Fig. 62) mindful that accommodating Ghaub thickening by incision would require an even deeper Kranstoort trough. Facies changes in the cap-carbonate sequence described in the next paragraph are consistent with positive topography for Duurwater moraine. Basically, we fitted the Marinoan disconformity to a gentle incline (5–30–43) with a step coincident with local thinning of Ghaub Fm in section 5–38. Between 5 and 44 and 49, the disconformity is controlled by step-wise truncation of platformal Ombaatjie Fm (Figs. 62 & 64).

The Marinoan cap-carbonate sequence provides independent evidence that Duurwater moraine was a positive paleotopographic feature. Keilberg Mb is unusually thin over the moraine (5–31–41), averaging just 2.9 m ($n = 11$) compared with 7.8 m ($n = 25$) in Tr5 to the W of the moraine (5–01–30), and a whopping 75.0 m ($n = 9$) in the OPz (5–45–66). Despite a modal thickness of only 2.5 m, Keilberg Mb draped on the moraine has the coarsest and best sorted macropeloidal texture observed anywhere in the region (Fig. 67B). We infer that the Keilberg is thin over the moraine because of winnowing. Finer peloids were removed, leaving a lag of macropeloids ≤ 2.5 mm in diameter (specific gravity unknown).

Silicified crystal fans, pseudomorphic after benthic aragonite (Fig. 67C), are highly localized over Duurwater moraine in marly calcite rhythmite, locally dolomitized, that conformably overlies Keilberg Mb and represents the post-glacial maximum flooding stage (MFS) of Karibib Fm (Fig. 62). Over the moraine, crystal fans are decimetric in scale and in 5–39 occur through 87 m of lower Karibib Fm MFS rhythmite. Crystal fans are nearly absent downslope from the moraine—tiny examples (≤ 1.0 cm) are known in only one small area (5-26a–27). Up-slope, crystal fans are again well developed at the outermost edge of OPz, in 5–45–51 (Fig. 68).

Why should benthic crystal fans be spatially associated with seafloor topography? In the modern ocean, vertical mixing (i.e., upward lifting of denser bottom water) is strongly enhanced over seamounts and rough topography (Ledwell et al., 2000; Mashayek et al., 2017). We speculate that topographically induced vertical mixing was important in maintaining critical oversaturation with respect to aragonite in bottom waters of the Marinoan aftermath. We think maintaining critical oversaturation is critical because crystal fans as an abiotic growth habit are favoured by ion kinetics when precipitation rates are high (Lasaga, 1998).

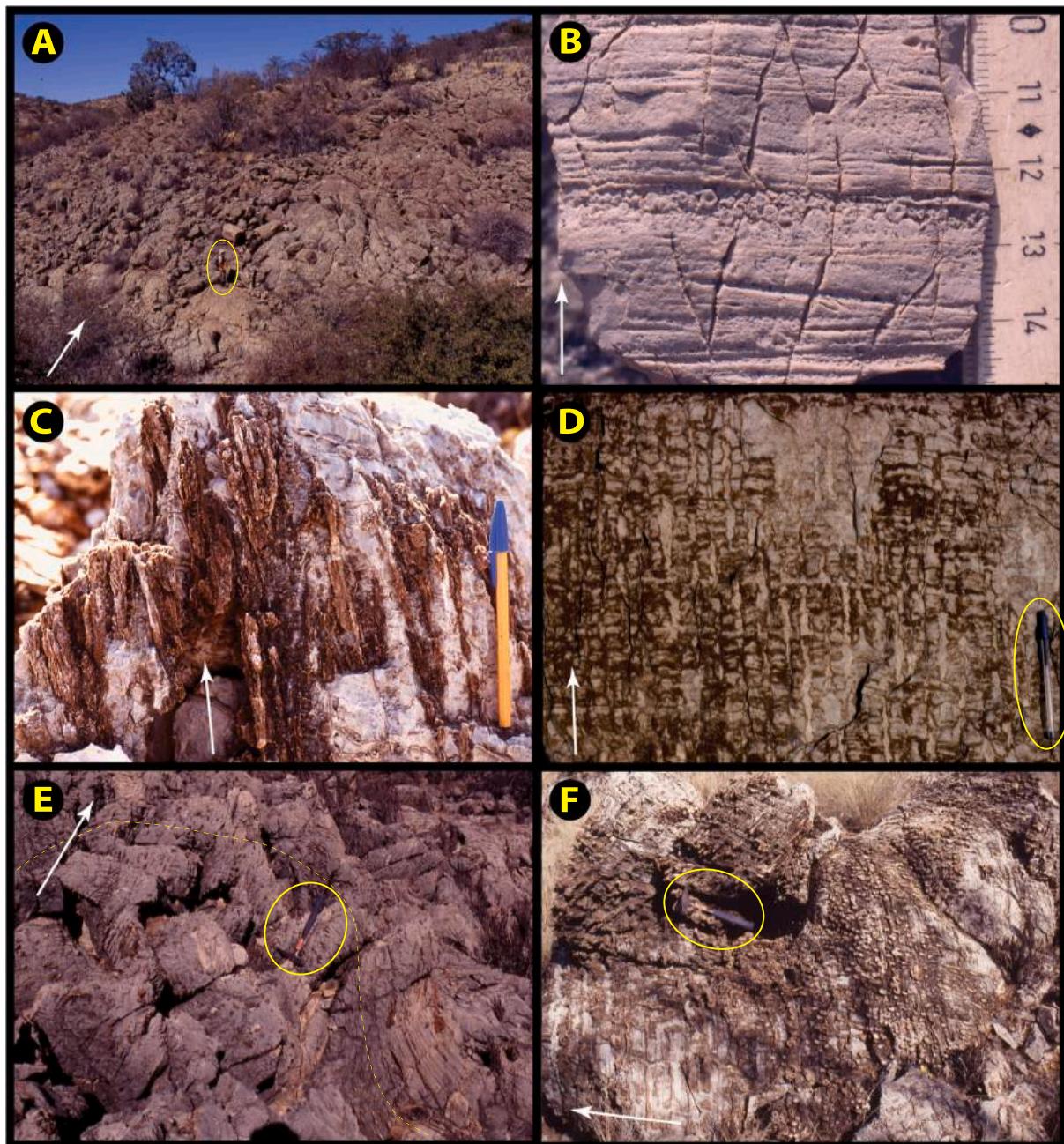


Fig. 67. Images from Marinoan Duurwater moraine (Figs. 43 & 62) and its cap carbonate in proximal FSz, and Keilberg Mb tubestone stromatolite in OPz (Fig. 68) on Fransfontein Ridge (Tr5). White arrows indicate stratigraphic younging. (A) Composite massive diamictite in Duurwater moraine $-20.2177^{\circ}/15.2145^{\circ}$ in 5–37 (Fig. 62). Geologist (circled) gives scale. (B) Macropeloidal lag with low-angle crossbedding in attenuated Keilberg cap dolomite veneer on Duurwater moraine near $-20.2232^{\circ}/15.2253^{\circ}$ between 5 and 37 and 38. (C) Selectively-silicified former-aragonite crystal fans (sea-floor cement) in lower Karibib Fm on Duurwater moraine at $-20.2254^{\circ}/15.2157^{\circ}$ in 5–37. (D–F) Tubestone stromatolites in Keilberg cap dolomite in OPz. Tubular structures are filled by pale-coloured dolomiticrite in D at $-19.6661^{\circ}/14.2593^{\circ}$ in Tr7 (7–6, Figs. 88 & 92). The same structures are selectively silicified (E) at $-20.1066^{\circ}/15.3832^{\circ}$ in 5–66 and (F) at $-20.1105^{\circ}/15.3886^{\circ}$ in 5–66 (opposite limb of syncline). Dashed line indicates (stromatolitic) stratification in E.

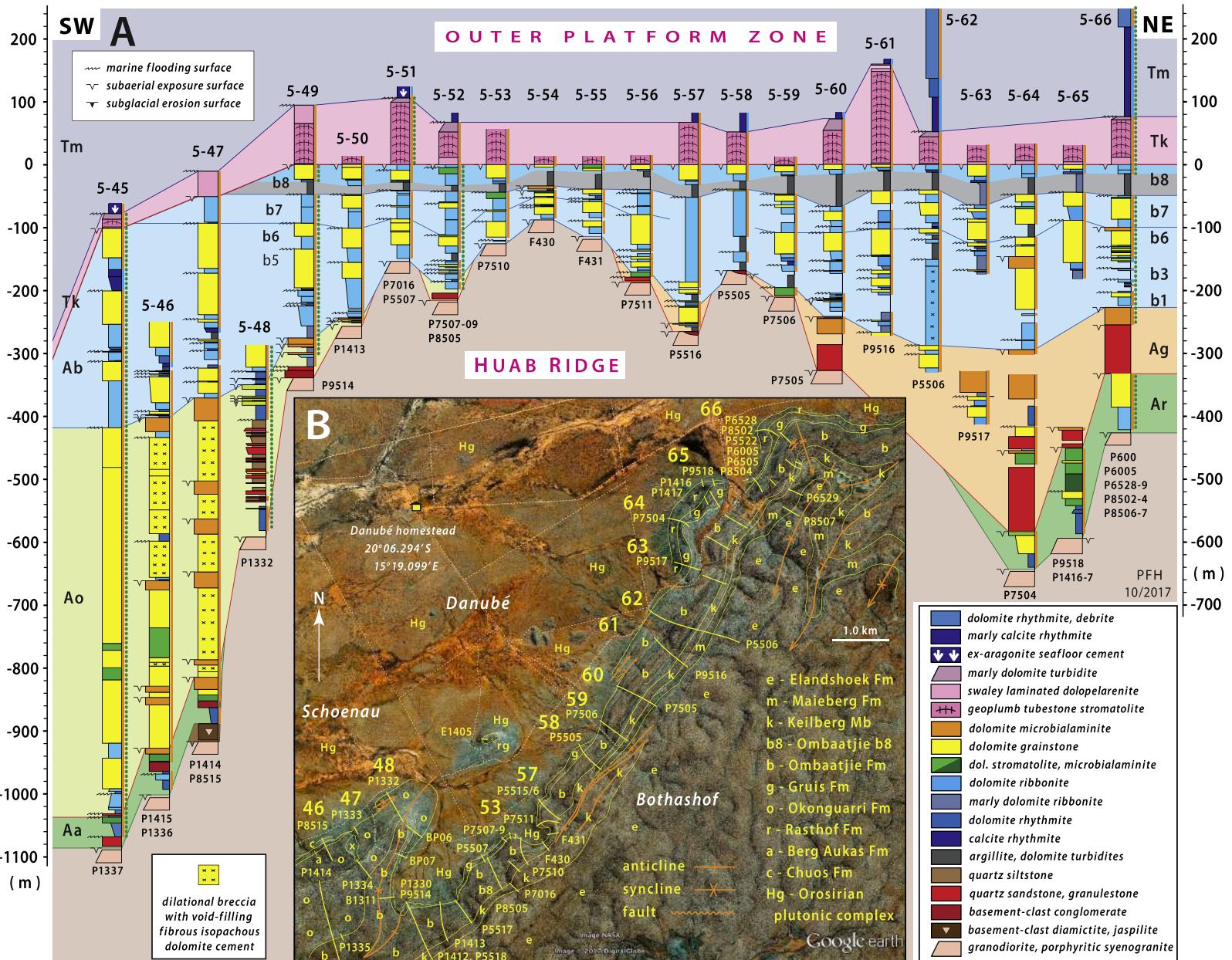


Fig. 68. (A) Cryogenian and earliest Ediacaran columnar sections from OPz (5-45–66) in NE segment of Transfontein Ridge (Tr5). Datum 0.0 m is base of Keilberg Mb (Tk) between 5 and 49–66. Successive offlaps of Rasthof Fm (5-64–66) and Gruis Fm (5-56–66) implies intermittent uplift and erosion of Huab ridge in pre-Oombaatjie Fm time. Berg Aukas and Okonguari formations onlap basement in Kraspoort flexure south of Huab ridge. Oombaatjie cycle b8 is cut-off by Marinoan erosion between 5 and 47–49 (at B in Fig. 64). Absence of distinct facies at the Oombaatjie shelf edge (5-45) indicates significant headward erosion during Marinoan glaciation. Keilberg cap dolomite thickens dramatically in OPz relative to FSz. Crystal fans (sea-floor cement) occur in post-Keilberg Mb Maieberg Fm (Tm2 member) at Marinoan shelf edge (5-45–51). (B) Annotated satellite image showing formations and sections 5–46–66 locations in OPz on Transfontein Ridge. White dashed lines are vehicle tracks on farm Danubé 59. Google Earth: Image © 2020 CNES/Airbus & Maxar Technologies.

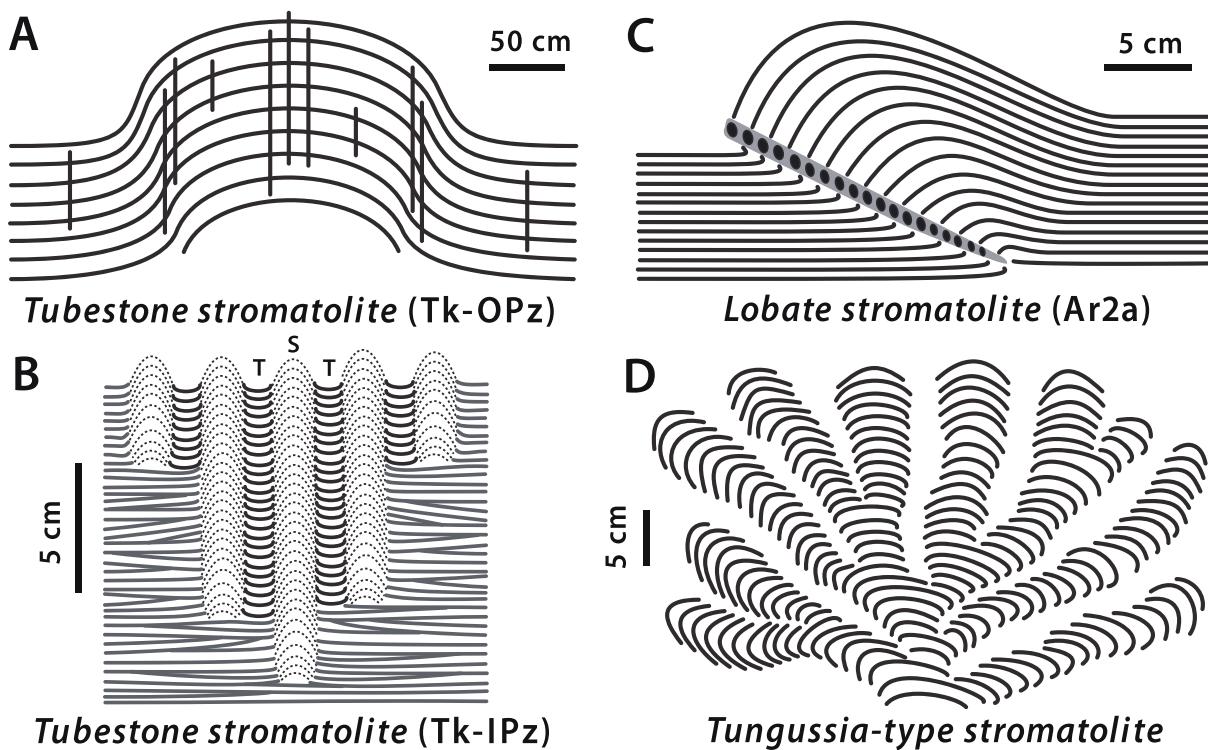


Fig. 69. Characteristic stromatolite morphotypes: note scale bar 10× smaller in A than B–D. (A) Tubestone stromatolite of Keilberg Mb in OPz (Figs. 67D–F, 68, 71, 79C–D, 81E, 82, 85, 88, 94E, 174–175, 177A & 178). Vertical (geoplumb) rods are dolomitic or void-filling dolospar or silica cement. (B) Tubestone stromatolite in IPz (Figs. 117–119, 120C–D, 136C & D). Background sediment is low-angle cross-stratified dolopelarenite. Arched stromatoids (S) are stacked to form a honeycomb in plan enclosing circular pits (T) with dolomitic fills laminated concave-up. Upward (geoplumb) perpetuation of micrite fills for ≥1.0 m (i.e., ≥50× their width) defines the ‘tube’ (T) structure. (C) Lobate stromatolite of Rasthof Fm member Ar2a in IPz (Figs. 110A–B, 111, 124E, 125, 126E–F, 135, 139, 142A & 159–160). The inclined shaded area is rich in void-filling dolomite cement and broken laminae. The structure implies horizontal compression but is self-similar in any azimuth, suggesting accommodation to laterally expansive microbial growth (e.g., Lokier et al., 2018). (D) *Tungussia*-type columnar stromatolite with highly divergent branching, characteristic of late Tonian Devet Fm (Figs. 99, 101C–F, 105, 107 & 123) and Ugab Subgroup (Figs. 30 & 39), and middle Cryogenian Omboaatjie Fm cycle b7 and 8 in IPz (Figs. 127E & 129). As drawn (from Hofmann, 1969), the structure is depicted as 2-dimensional. In 3D, many columns would project into or out of the page, appearing elliptical in section.

2.5.4. Northeastern segment (5–49–66) of Transfontein Ridge

This segment (Fig. 68) extends into the OPz (Fig. 8B) and the appropriate stratigraphic nomenclature changes to that of Otavi Group (Table 5, Fig. 6D). After describing the northeastern segment, we will return to the OPz–FSz transition and correlations between Otavi and Swakop groups (2.5.5.).

Chuos Fm does not appear in this segment of Tr5 and Rasthof Fm only in 5–64–66 (Fig. 68). Disconformably overlying Rasthof Fm and onlapping basement to the SW is a mixed assemblage of non-feldspathic quartz-arenite and m-scale peritidal cycles of dolomite ribbonite, grainstone and pinkish buff-coloured microbialaminite with tepees (Table 4). This assemblage is correlated with Gruis Fm (Figs. 5 & 6D) (Hedberg, 1979; Hoffman and Halverson, 2008). Basement-onlapping Gruis Fm is overstepped by Omboaatjie Fm, which directly overlies basement in 5–51 and 53–55 (Fig. 68).

Omboaatjie Fm (Hoffmann and Prave, 1996; Hoffman and Halverson, 2008) is the youngest formation in Abenab Subgroup on the platform (Table 3, Figs. 5 & 6D). In Tr5, it is an aggradational stack of 8 decameter-scale, shoaling-upward, ribbonite-to-grainstone cycles (b1–8), separated by flooding surfaces most of which lack evidence for subaerial exposure (Fig. 68). Argillite occurs basally in some of the older cycles and a thicker argillite with thin dolomite turbidites is omnipresent at the base of Omboaatjie cycle b8 (Fig. 68) (Hoffman and Halverson, 2008). As documented in 3.3.4., cycle b7 consistently records the descending branch of CIE Cn5 (Fig. 10D) and cycle b8 the ascending branch. The b8 argillite occupies the CIE nadir. The b8 argillite and CIE Cn5 provide independent grounds for measuring paleotopographic relief on the Marinoan glacial surface across the platform, as discussed in

3.6.3. Taking the base of cycle b8 as a datum suggests that there is ≤26 m of relief on the Marinoan glacial surface in the northeastern segment of Tr5 (Fig. 68), where it is everywhere marked by basal Keilberg Mb in the absence of Ghaub Fm.

Keilberg cap dolomite is 75.0 m thick on average ($n = 9$) in this segment (Fig. 68). With a little practice, the pale pinkish to buff-coloured Keilberg dolomite can be confidently distinguished from the duller light grey-coloured grainstone of the sharply underlying Omboaatjie Fm cycle b8 (Fig. 68). By far the dominant Keilberg lithofacies is ‘tubestone’ stromatolite (Fig. 69A & B) (Cloud et al., 1974; Hegenberger, 1987; Corsetti and Grotzinger, 2005; Santos et al., 2021). Tubestone stromatolite is distinguished by cm-diameter rod-shaped structures, oriented paleovertically (geoplumb) irrespective of the host stromatolite lamination (Figs. 67D & 59A). The rods tend to be selectively silicified (Fig. 67F), but where not silicified their ragged interiors contain cavity-filling dolomitic with concave-upward lamination and variable amounts of late void-filling sparry cement (Fig. 67D). The domical form of the stromatolite lamination (Fig. 67E) tends to be obscured by the tubes and their silicification. The domes tend to be broadly arched centrally and steepened peripherally (Fig. 69A). Tubestone stromatolite is unique to Keilberg Mb in Otavi/Swakop Group and does not occur W of 5–44 in Tr5 (Fig. 62).

As noted earlier, benthic crystal fans occur in Maieberg Fm MFS rhythmite in 5–45 and 51 (Fig. 68). In 5–66, the calcite rhythmite member of Maieberg Fm is 142 m thick, compared with 60 m for the thickest equivalent section in FSz (5–14, Fig. 43).

Because of folding, we do not have a complete Tsumeb Subgroup section (Fig. 5) from the OPz segment of Tr5. The closest monoclinal

sections of the complete Tsumeb Subgroup near the platform edge are located on the S flank of Kamanjab inlier E of longitude 16.0°E (Fig. 4).

2.5.5. Development of the FSz–OPz transition zone (5–40–51)

The critical transition zone (CTz) between Swakop (FSz) and Otavi (OPz) groups, 5–40–51, is ca 7 km wide, normal to depositional strike (Figs. 43, 62, 64–65 & 68). It bears witness to prolonged sea-level lowstands accompanied by glaciation (Fig. 1), superimposed on the tectonic transformation of an active rift zone to a subsiding passive-margin (Fig. 26). From a stratigraphic perspective, its development can be divided into 5 stages, 3 constructive and 2, wholly or partly, destructive. Since Tonian strata are absent (Fig. 5), the first stage is Sturtian.

During the 56-Myr-long Sturtian snowball, the transition zone was a structural high, a tectonically active rift shoulder (Fig. 26). There are no data on Sturtian glacial flow directions in the region. The geometry of Kranspoort trough (Fig. 43) and its relict plaster of Chuos Fm diamictite (e.g., 5–47) suggest that this major post-Sturtian sedimentary basin originated as a glacial cirque or valley.

Stage 2 encompassed post-glacial marine flooding, deposition of microbialite-rich carbonate (Berg Aukas Fm), and construction of an enormous distally tapered wedge of carbonate grainstone and associated facies (Okonguarri Fm). Accommodation for the wedge was provided by Sturtian erosion and proximally by S-side-down crustal flexure (Figs. 62 & 65B) of post-Sturtian age, manifest by proximal shedding of basement-derived detritus into the carbonate wedge, dilatant brecciation and re lithification of proximal grainstone, and absence of basement faulting indicated by physical continuity of Berg Aukas Fm. Stage 2 corresponds to Rasthof and Gruis formations in Otavi Group (5–64–66, Fig. 68).

Stage 3 involved post-rift subsidence accommodating Ombaatjie Fm, which oversteps both Gruis and Okonguarri formations onto the basement of Huab Ridge (Figs. 5, 43, 65 & 68). The base of Ombaatjie Fm marks the rift-to-shelf transition in OPz (Figs. 5 & 10), although small-scale fault reactivations are recorded as terrigenous clastic pulses in Ombaatjie Fm cycles b4 and b8. Correlations with Swakop Group depend critically on the inferred Okonguarri–Ombaatjie contact surface in sections 5–45–50 (Figs. 62, 65 & 68). Since a 6% rise in $\delta^{13}\text{C}$ from CIE Cn3 to Cn4 (Fig. 10D) ends at the base of Ombaatjie Fm, $\delta^{13}\text{C}$ records were obtained from 5 to 45, 47 and 49 (see 3.3.5.) to test the Okonguarri–Ombaatjie contact placement based on lithologic grounds (Fig. 62).

Stage 4 was the Marinoan snowball. Originally, the Ombaatjie Fm must have had a distinct shelf-edge facies—a stromatolite reef or barrier bar complex as occur on the windward margins of marine carbonate platforms (Wilson, 1975; Grotzinger, 1986a, 1989), or prograded clinoforms as underlie their leeward margins (Eberli and Ginsburg, 1987; Eberli et al., 2001). No such facies are present (Figs. 62 & 68). Instead, normal platformal facies of Ombaatjie Fm were simply truncated by Marinoan headwall erosion between sections 5–44 and 45 (Fig. 62). In Marinoan time, the platform and its upper FSz projected well above the grounding line elevation of the Otavi ice sheet (Domack and Hoffman, 2011), due to net sea-level fall (Liu and Peltier, 2013; Creveling and Mitrovica, 2014) and the thickness of the tropical sea glacier (Li and Pierrehumbert, 2011; Tziperman et al., 2012). Marine seismic-reflection profiling of the existing Antarctic continental shelf reveals numerous cross-cutting unconformities due to glacial erosion, many tens to hundreds of meters in depth and resulting in abrupt lateral truncation of units (Anderson, 1999). They are observed more frequently in strike-oriented than dip-oriented profiles (Anderson, 1999). It is possible that much of the mass eroded from the Ombaatjie Fm shelf-margin is collected in Duurwater moraine (Figs. 43 & 62), which crests 12 km WSW of the Ombaatjie headwall on Transfontein Ridge (5–33 to 45, Fig. 63), or 7 km downslope in the inferred dip direction (Fig. 43B). The contrast in $\delta^{13}\text{C}$ between CIE Cn5 at the top of Ombaatjie Fm and Cn4 through the bulk of the formation (Fig. 10D) provides a means to distinguish headwall from top-side erosion of Ombaatjie Fm as sources

of Duurwater morainal debris.

Stage 5 was aggradation of the Ediacaran Tsumeb Subgroup of Otavi Group (Fig. 5), an estimated 1.4 km thick at the shelf break (Hoffman, 2021a), and the distally-tapered Karibib Fm of Swakop Group.

According to the developmental scheme just outlined, Berg Aukas and Okonguarri formations combined are equivalent to Rasthof and Gruis formations combined (Table 5). Narachaams and Frannis aus formations combined are equivalent to Ombaatjie Fm (Table 5). Karibib Fm is equivalent to Maieberg, Elandshoek and Hüttenberg formations (Fig. 5), which will be introduced in Tr9–11. These correlations will be chemostratigraphically tested in sections 3.3. and 3.4.

2.5.6. Highlights from Tr5

The chief highlight is the transect itself—an oblique section of the lower to upper FSz and outermost OPz, continuously exposed on Transfontein Ridge (Fig. 43). Earlier iterations of the Tr5 fence diagram are given in Hoffman (2005, Fig. 9; Hoffman, 2011a, Figs. 8 & 9). The section includes: (1) a Sturtian diamictite-filled half graben and large glacial cirque (Kranspoort trough) that was carved from basement and lined by paired moraines; (2) drapes of sublittoral (disphotic?) microbialites (Berg Aukas and Rasthof Fms) recording massive post-Sturtian marine flooding and severe ocean warming, selective for bacterial primary production (Brocks et al., 2017; Brocks, 2018); (3) a distally-tapered wedge of Cryogenian synrift carbonate (Okonguarri Fm), composed of shoreface grainstone proximally and turbidites distally, accommodated by Kranspoort trough and rift-related crustal flexure in front of Huab ridge; (4) aggradation of a post-rift cyclic carbonate shelf (Ombaatjie Fm), accommodated by post-rift thermal subsidence, while fine-grained terrigenous laminites accumulated on the lower foreslope and basin; (5) frontal truncation of the Ombaatjie Fm shelf by headward Marinoan glacial erosion, and buildup of a 0.6-km-high grounding-line moraine (Duurwater moraine) on the middle foreslope, ~7 km (projected) in front of the eroded Ombaatjie Fm shelf edge; (6) post-Marinoan marine flooding (Fig. S10C–F) and warming, leaving a winnowed macropeloidal cap dolomite and prolific benthic aragonite fans over Duurwater moraine, and a tubestone stromatolite barrier rim (Keilberg Mb) on the outer shelf margin; (7) aggradation of a ≤ 2.0 -km-thick early Ediacaran carbonate platform (Tsumeb Subgroup) and its distally-tapered foreslope extension (Karibib Fm); (8) incision of sub-Mulden Group paleovalleys (section 3.5. and Figs. S12, S14 & S19–S21), recording forebulge uplift leading to flexural collapse and collisional destruction of the passive-margin carbonate platform. According to conservative stratigraphic restoration (Fig. 43A), local relief on Sturtian and Marinoan lowstand glacial erosion surfaces was 1.78 and 0.66 km, respectively, in the line of Tr5 sections (Fig. 43B).

No feature in Tr5 is more extraordinary than Duurwater moraine (Figs. 43 & 62). With a peak thickness of 602 m (5–33) of massive carbonate diamictite, inferred paleobathymetric relief of 0.56 km (Fig. 62) and basal width of 7.0 km (5–30–38) in the line of sections, Duurwater moraine was higher and steeper than any ice-shelf moraine or morainal bank in the present polar seas. For example, it was at least 3× higher and steeper than the prominent grounding-line ridge on Trinity Peninsula Shelf of Bransfield Basin, West Antarctic Peninsula (Banfield and Anderson, 1997). Despite low average rates of sediment accumulation during Cryogenian snowballs (Partin and Sadler, 2016), the growth of a tall grounding-line moraine was evidently favoured by prolonged glaciation (Prave et al., 2016), grounding-line stability imparted by a forward-dipping bedrock slope (Pollard and DeConto, 2007) and self-stabilization by sediment buildup itself (Alley et al., 2007; Domack and Hoffman, 2011; Cowan et al., 2020). These factors evidently overcame the tendency for the grounding line to migrate upslope over time in response to ice-shelf thinning (Abbot et al., 2013) and tectonic subsidence (Halverson et al., 2002). We cannot appeal to regional or global sea-level falls (Gomez et al., 2010, 2012; Benn et al., 2015) in response to ice-sheet retreat because the moraine itself implies a healthy flux of ice off the platform.

2.6. Transect Tr6 – upper Huab River paleo-outlier

West of Transfontein Ridge, a broad syncline (Achas syncline, Fig. 8A) of synorogenic foredeep clastics (Welkom Subgroup of Mulden Group, Fig. 6C) separates Kamanjab inlier from satellite basement inliers to the south (Fig. 8A). On both sides of Achas syncline (Frets, 1969), Mulden Group depositionally overlies basement directly, filling broad paleovalleys in a mid-Ediacaran megakarst landscape (Hoffman, 2021a). A 30-km-long panel of SE–S-dipping Otavi Group is exposed as a paleo-outlier on the N limb of Achas syncline (Fig. 70). This panel is Tr6 (Fig. 71).

Tr6 exposes an outer-platform facies of Otavi Group that onlaps and buries a Cryogenian rift shoulder (Huab ridge, Fig. 5). Pulsed uplift and rotation of the rift-shoulder dip-slope is inferred from successive offlap-onlap cycles—Gruis onlap over Rasthof offlap, and Ombaatjie onlap over Gruis offlap (Fig. 71). A rift-to-shelf transition is inferred at the base of Ombaatjie Fm.

The NE-striking western horn of Tr6 (Fig. 70) is excavated by the deep gorge of the upper Huab River (Fig. 72) (Frets, 1969). It was here (on farm Tweelingskop 676) that Cryogenian uplift, rotation, erosion and marine submergence of the metamorphic basement complex were first recognized and interpreted as the uplifted footwall ('rift shoulder') of a crustal-scale normal fault (Soffer, 1998). A field guide to this area is given in SOI S3.9. and geologically annotated satellite images in Figs. S16–19.

The western terminus of the Otavi Group paleo-outlier is just S of Sout River (Figs. 70 & S20) on farm Welkom 680. It results from step-wise erosional downcutting (Fig. 71) beneath foredeep clastics (Braklaagte and Renosterberg formations, Fig. 6C) of Welkom Subgroup (Miller, 2008b, p. 13–224–226; Hoffman, 2021a). Just beyond the Otavi termination, the clastics (Braklaagte Fm) are deeply incised into the basement complex. The depth of basement incision at this location compensates for the rise of the basement surface over the buried rift-shoulder, implying that the incision was graded to the broader basement plain flooring the megakarst landscape. Megakarst depth of ≥ 1.85 km was estimated from the total restored thickness of the local Otavi Group (Hoffman, 2021a), equal to the maximum depth of the Grand Canyon of Arizona (USA). A field guide to this area is given in SOI S3.9.4. and geologically annotated satellite images Fig. S20.

The eastern terminus of the Otavi panel is obliquely truncated by

Huab fault (Fig. 70) (Frets, 1969). This ENE-trending sigmoidal high-angle fault accommodates 3 km of apparent sinistral brittle displacement of Orosirian basement structure (Frets, 1969), and where it intersects the Otavi panel, the SE side of the fault is upthrown. Critically, fault displacement postdates Ombaatjie Fm (likely the entire Otavi Group) and predates Welkom Subgroup (Fig. 70). The existing fault geometry and kinematics could relate to a conjugate transcurrent fault regime (Freund, 1970, 1974) in a horizontal strain field accommodating NE–SW shortening and NW–SE extension. Such a strain field would be consistent with dextral or sinistral transpression in Kaoko orogen or Northern zone, respectively. However, the Otavi Group dips steeply southward in the area of Huab fault (Fig. 73), as does Welkom Subgroup less steeply. If faulting predates the latter, the fault plane must be tilt-corrected to restore its original orientation. If the fault plane is sub-vertical at present, as suggested by its independence of topography (Fig. 73), then its tilt-corrected dip was ca 30° SSE (Hoffman, 2021a). Such fault-plane orientation is more consistent with NNW-directed thrusting and the observed SE-side-up component of movement.

2.6.1. Cryogenian of Tr6

As with co-zonal Tr5, Sturtian glacial deposits are preserved sparingly and Tonian not at all (Figs. 70 & 71). Pockets of basement-derived diamictite a few hundred meters in strike length occur at the basement contact at longitudes 14° 35.4', 37.3' and 46.5' E (Figs. 70, 72 & 73). At the first location (P2509, Fig. 72), 36 m of massive diamictite overlies a sharp and smooth erosion surface on retrograde-metamorphosed granodiorite. The diamictite carries rounded and faceted cobbles and boulders of basement rock types dispersed in a schistose wackestone matrix (Fig. 74A & B). The massive diamictite is overlain by 12 m of stratified diamictite, in which terrigenous siltstone with lenticular beds of detrital dolomite is crowded with rounded clasts of basement and rare dolomite. Both units pinch out 0.5 km to the west (Fig. 72).

Instead of the normal sharp irreversible contact between Chuos diamictite and Rasthof cap carbonate, the contact in P2509 is gradational. Above the stratified diamictite is a sequence of channelized debrites, which basally appear to be redeposited diamictite but with increasing stratigraphic height become increasingly populated by typical Rasthof-type microbialaminite and stromatolite clasts (Fig. 74C). Debrites composed exclusively of Rasthof stromatolite appear before the sequence is truncated by sub-Gruis Fm erosion (Fig. 71). South of P2509,

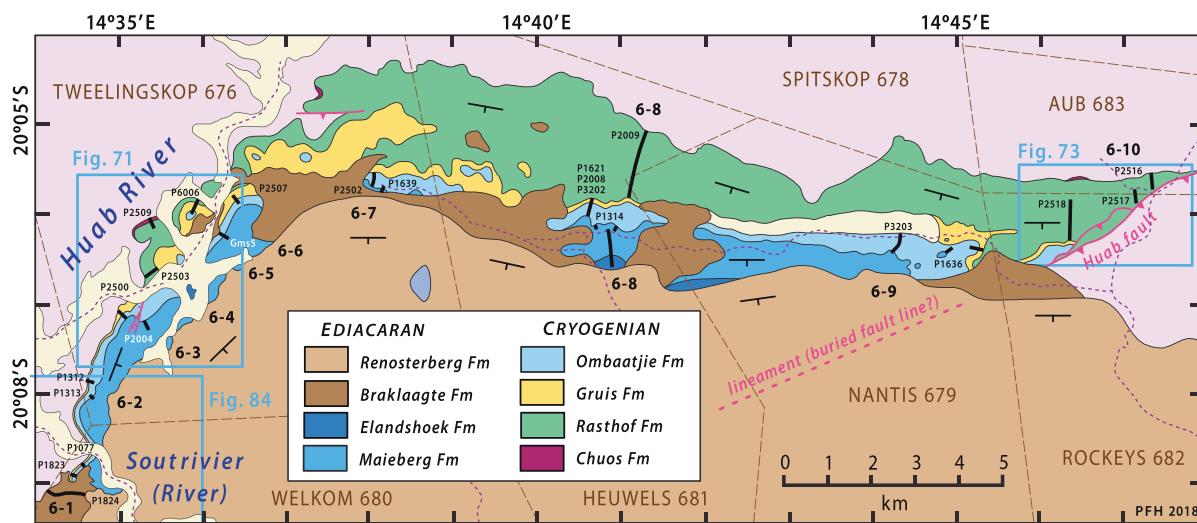


Fig. 70. Geological map of Tr6 (Fig. 8B): a S- to SE-dipping karstic paleo-outlier of OPz Otavi Group on Huab ridge (Fig. 5). Blue rectangles indicate areas of Figs. 71, 73 & 84. Sections 6–1–10 indicated in black. Farm names and boundaries in brown, vehicle tracks by purple dashed lines, basement metamorphic complex in pale pink, active flood plains and other covered areas in pale yellow.

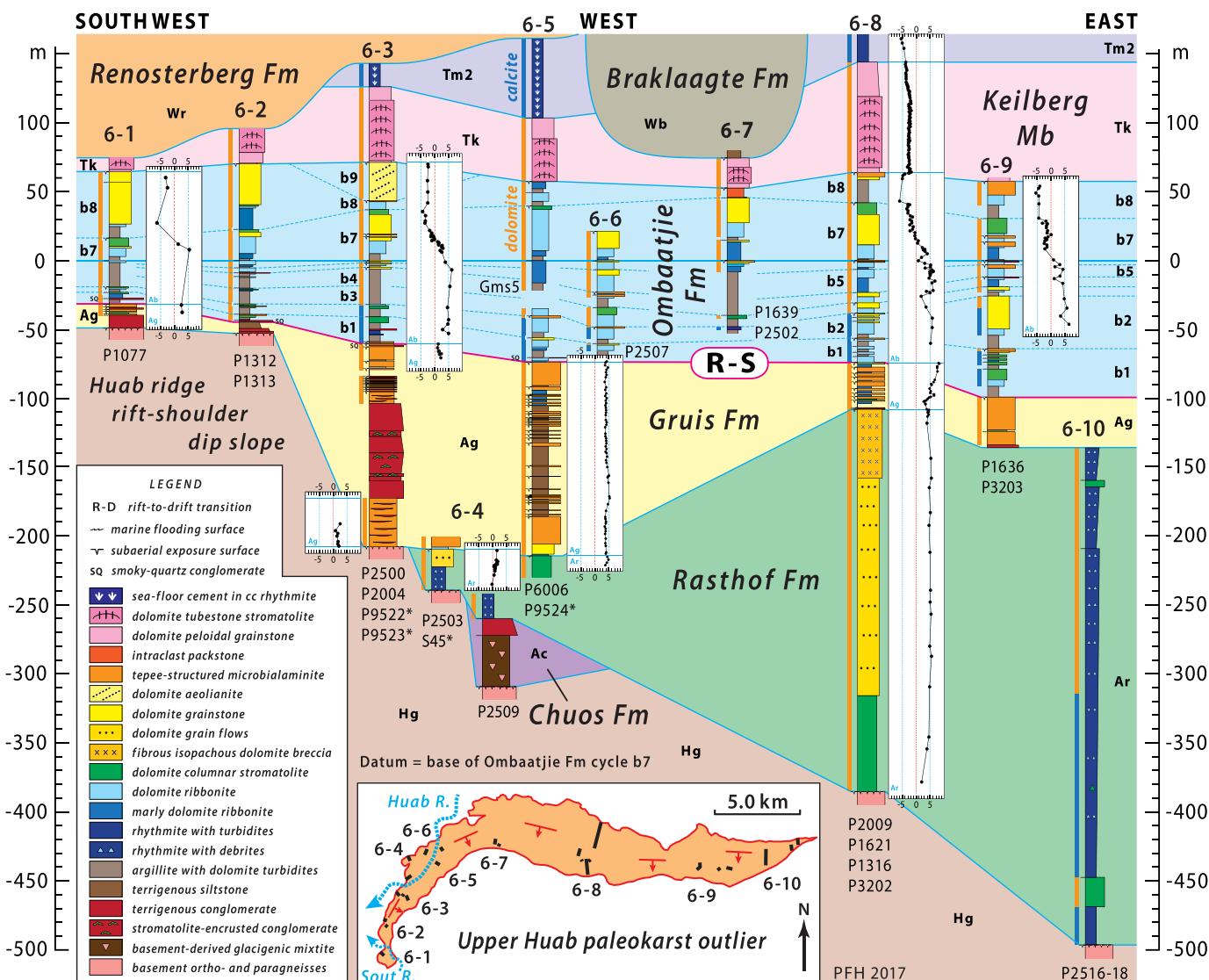


Fig. 71. Cryogenian and earliest Ediacaran columnar sections (6–1–10) and $\delta^{13}\text{C}_{\text{carb}}$ records from Huab paleo-outlier (Tr6); see inset map and Fig. 70 for section locations. Datum is base of Omboaatjie Fm cycle b7. Red correlation line (labelled R–S) is the inferred rift-to-shelf transition (base of Omboaatjie Fm) in OPz. Rasthof Fm offlap (6–3–8) is coincident with facies change in middle Gruis Fm from alluvial fanglomerate (exclusively basement-derived) to littoral carbonate in just 1.5 km (6–3–5). In contrast, Omboaatjie Fm changes little in lithofacies or cyclic structure, although it thickens by $\frac{1}{3}$ (6–1 to 9) and aeolian (?) dolomite (cycle b9) appears in 6–3 only. Offlap-onlap relations record rift-shoulder uplift (Huab ridge, Fig. 5) and erosion of Gruis Fm age. Rotation of dip-slope apparently ceased by Omboaatjie Fm time. Crystal fans (former aragonite sea-floor cement) are well developed in middle Maieberg Fm (Tm2) in 6–3–5 (Figs. 80A–F & 81A–B), but are absent in 6–8 (Figs. 81C & 82).

where Chuos diamictite is absent, Rasthof dolomite debrite and rhythmite with rare basement (schist) clasts unconformably overlie metamorphic basement (Fig. 72).

Rasthof Fm is progressively eroded by Gruis Fm west and south of section 6–7 (Figs. 70 & 71). Consequently, more complete Rasthof sections occur in the long W–E segment of Tr6, where we have few measured sections (Figs. 71 & 73). In 6–8, 70 m of stromatolitic dolomite (Fig. 75A–D) directly overlie basement quartz-sericite schist. The remainder of this 284-m-thick Rasthof section is composed of tabular-bedded dolomite grainstone, the upper 50 m of which are brecciated and cemented by fibrous isopachous dolomite (Fig. 75E & F), similar to dilational breccia in Okonguari Fm in Tr5 (5–41–47, Figs. 62 & 66F).

A major facies change occurs in Rasthof Fm between 6 and 8 and 10 (Fig. 71). Dolomite stromatolite and grainstone (6–8) are replaced 10 km to the east by argillite-hosted carbonate turbidites and debrites

with isolated outsized (2×4 m) stromatolite blocks. This facies change has been investigated by Malcolm W. Wallace (University of Melbourne) and associates, who are conducting a detailed comparison with a coeval (Cryogenian inter-snowball) Balcanoona Fm reef complex in NE Flinders Ranges of South Australia (Giddings and Wallace, 2009; Giddings et al., 2009; Hood et al., 2011, 2016; Hood and Wallace, 2012, 2015; Wallace et al., 2014).

As a contribution to their work, we measured 8 closely spaced Rasthof sections near the eastern termination of Tr6 (Figs. 73 & 76). In the more easterly sections, the basal 60–100 m of Rasthof Fm consists of dolomite rhythmite and cm-scale turbidites graded calcite-to-dolomite (Fig. 74D & E). Intrastratal ‘domino-type’ fault duplexes (Fig. 74F) are enigmatic as to age and origin. Within 0.3 km to the west (P1819, 21), the abiotic bedded facies is entangled with irregular mounds of bulbous stromatolitic dolomite (Fig. 75A–D), riddled with cm-scale cavities

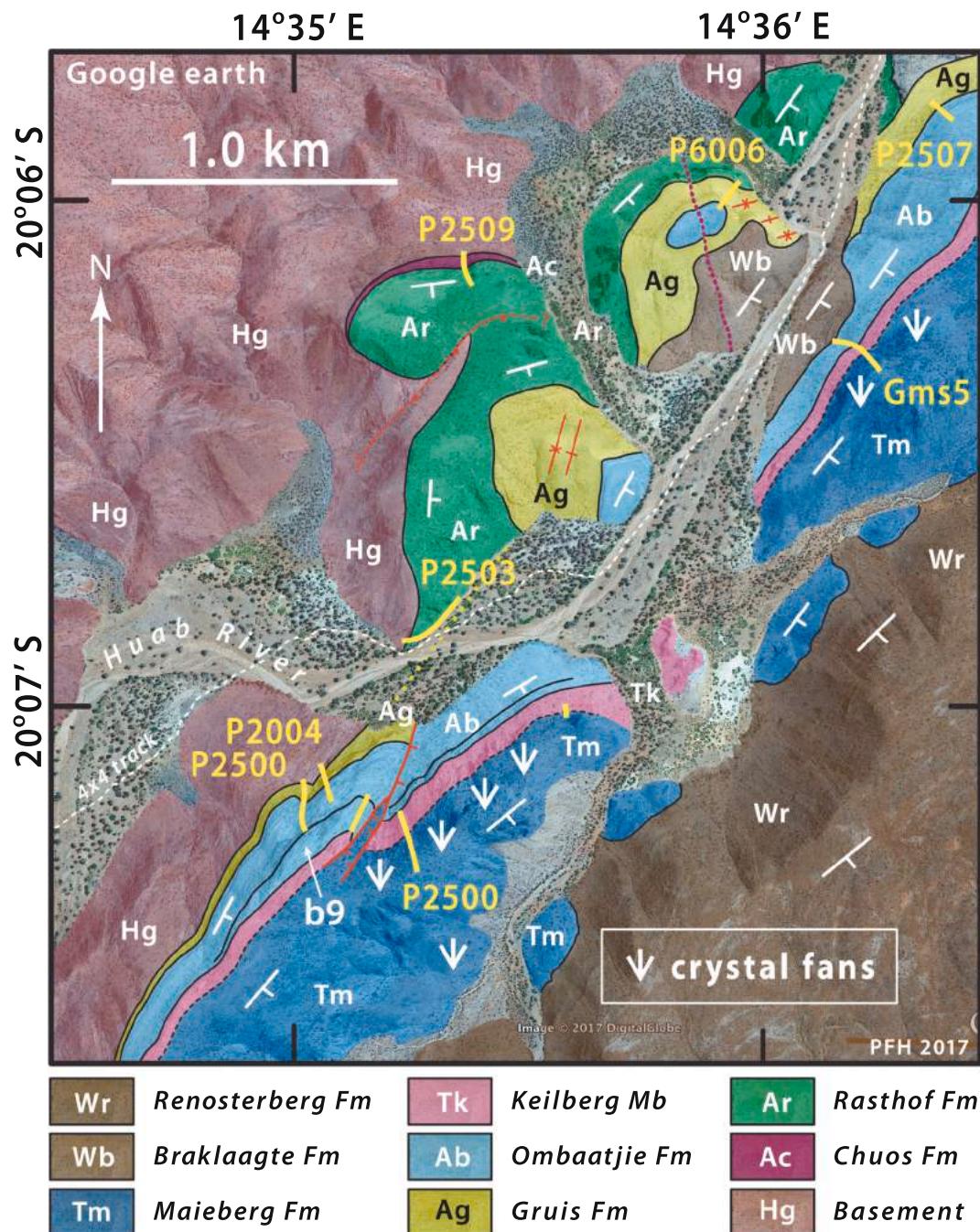


Fig. 72. Annotated satellite image of Huab River on farm Tweelingskop 676 (Fig. 70), where critical Cryogenian offlap-onlap relations (6–3–5) are inferred (Figs. 71 & 86, see also field guide, SOI S3.9.). In upper right, modern Huab River has re-incised a paleokarst canyon of pre-Braklaagte Fm age (Frets, 1969; Guj, 1974), which was incised into Otavi Group down to Gruis Fm (Figs. 85 & 193) and filled-in by Braklaagte Fm before structural tilting to make Achas syncline (Fig. 8A). Google Earth: Image © 2020 Maxar Technologies.

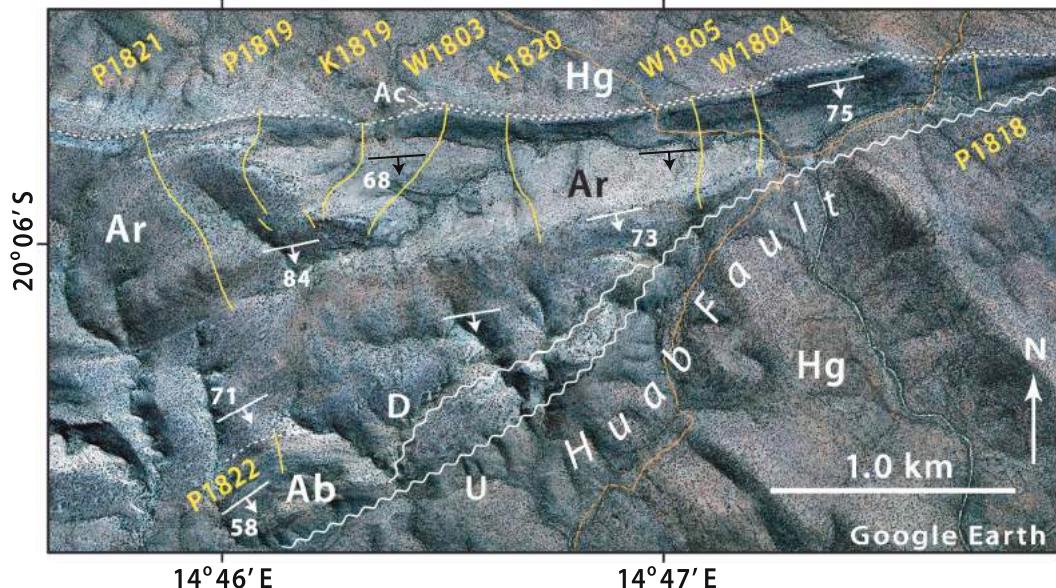


Fig. 73. Annotated satellite image of E end of Tr6 on farms Aub 683 and Rockeys 682, showing sections (yellow lines) documenting E-deepening ‘shale-out’ in lower Rasthof Fm (Fig. 76). Section dips steeply SSE, and D/U indicate down/up-thrown sides of Huab Fault (Frets, 1969). Dashed orange lines are vehicle tracks: N to Kamanjab and S to Khorixas. Google Earth: Image © 2020 Maxar Technologies.

lined by fibrous dolomite cement (Fig. 75A & B). Above this basal carbonate-rich unit, the more easterly sections present an upward-coarsening stack of argillite-hosted carbonate turbidites and debrites culminating in dolomite grainstone (Fig. 76). In the three most westerly sections, the same interval is dominated by coarse-grained debrite, ribbonite, dolarenite and bedded dolorudite composed of tabular-intraclasts. The basin-scale significance of the apparent reef–forereef facies change is unknown. This is not surprising considering that 90% of the 25-km-long Rasthof Fm outcrop belt lacks closely spaced sections.

Gruis Fm (Figs. 70 & 71) is ≤ 50 m thick in the zonal (W–E) segment of Tr6, where it consists of meter-scale couplets of marly dolomite ribbonite and pale pinkish-coloured dolomite microbialaminite with tepees. Southward (6–1–6), the formation thickens and undergoes a remarkable facies change coincident with progressive erosional truncation of the underlying Rasthof Fm (Fig. 71). In 6–5 (P6006), each marly ribbonite half-cycle becomes a thicker greenish siltstone, and the formation as a whole expands to 125 m. In 6–3, where Gruis Fm onlaps the basement metamorphic complex directly (Fig. 77A & B), it is 150 m thick and a 70-m-thick complex of alluvial fanglomerates appears in place of the siltstone-rich middle part of the formation in 6–5 (Fig. 71). The fanglomerate is exclusively derived from the basement complex (Fig. 77C), and both pebble imbrication and current ripples indicate northward-directed sediment transport. This is consistent with the observed absence of Rasthof-derived debris in the fanglomerate, because no Rasthof exists to the south of 6–3 (Fig. 71). It is compatible with the observed proximal-to-distal facies changes in Gruis Fm. Beds and lenses of basement-derived conglomerate are intimately associated with supratidal (tepeed) dolomite (Fig. 77D) beneath and above the main fanglomerate complex. Within the fanglomerate complex are numerous encrusting stromatolites composed of chemically precipitated carbonate. These non-marine stromatolites resemble active travertines associated with natural springs in the area, as well as stromatolites in a terrestrial fanglomerate in NW Canada between 1.74 and 1.84 Ga in age (Hoffman, 1976). Southward from 6 to 3, Gruis Fm thins rapidly as a result of basement onlap. It does not pinch out, however, but forms a

10–20-m-thick carapace of conglomerate and supratidal dolomite cycles (Fig. 77E & F), indicating that the tilted basement surface was eroded nearly to sea level as far south as 6–1 before the end of Gruis Fm time (Fig. 71).

The overlying Ombaatjie Fm is an aggradational stack of eight or more shoaling-upward peritidal carbonate cycles or parasequences, with a 15 m average thickness (Fig. 78A & B). The cycles are locally capped by microbialaminite with tepees, indicating subaerial exposure, but more commonly they end at marine flooding surfaces (Fig. 71). The cycles are informally numbered b1 through b8 (Fig. 71), but some of the cycles are composites (e.g., cycle b1 in 6–1, 8 and 9; cycle b2 in 6–8, and cycle b7 in 6–3, 7 and 9). We therefore cannot assume that the numbered cycles are exactly correlative between sections. Thin beds of smokey quartz-pebble conglomerate (Fig. 78C & D) in cycle b1 (labelled SQ in Fig. 71) are the last indication that basement was still locally exposed in earliest Ombaatjie time. The carbonate in cycles b1 and 2 is typically calcite, whereas the remaining cycles are generally dolomitic (Figs. 71 & 78B).

Ombaatjie Fm cycles b7 and 8 have distinctive lithologies and host the Trezona CIE Cn5 (Fig. 10D) (Halverson et al., 2002; Schrag et al., 2002; Tziperman et al., 2011). As discussed below and in 3.3.4., we infer this pair of cycles to be broadly correlative within and between all transects in OPz and IPz. Meter-scale karstic relief is conspicuously associated only with the exposure surface (b7/8) at the nadir of the CIE (Fig. 78E). As a whole, the formation changes relatively little in aggregate thickness (95–150 m) or lithology over the length of the transect (Fig. 71). The broadly uniform thickness and shallow-marine facies of the Ombaatjie Fm are consistent with a tectonic transition at its base from active crustal stretching in Gruis time to passive thermal subsidence (surface R-S in Fig. 71) (Halverson et al., 2002).

The datum for the fence diagram (Fig. 71) is the base of cycle b7. This cycle is characterized by a steady decline of $\sim 10\text{‰}$ in carbonate $\delta^{13}\text{C}$, from $\sim +5\text{‰}$ (VPDB) in cycles b1–6, to $\sim -5\text{‰}$ at the cycle b7 to 8 transition (Fig. 71). Cycle b7 is regionally associated with unusually well developed and diverse stromatolites (e.g., Fig. 79A). The time scale of

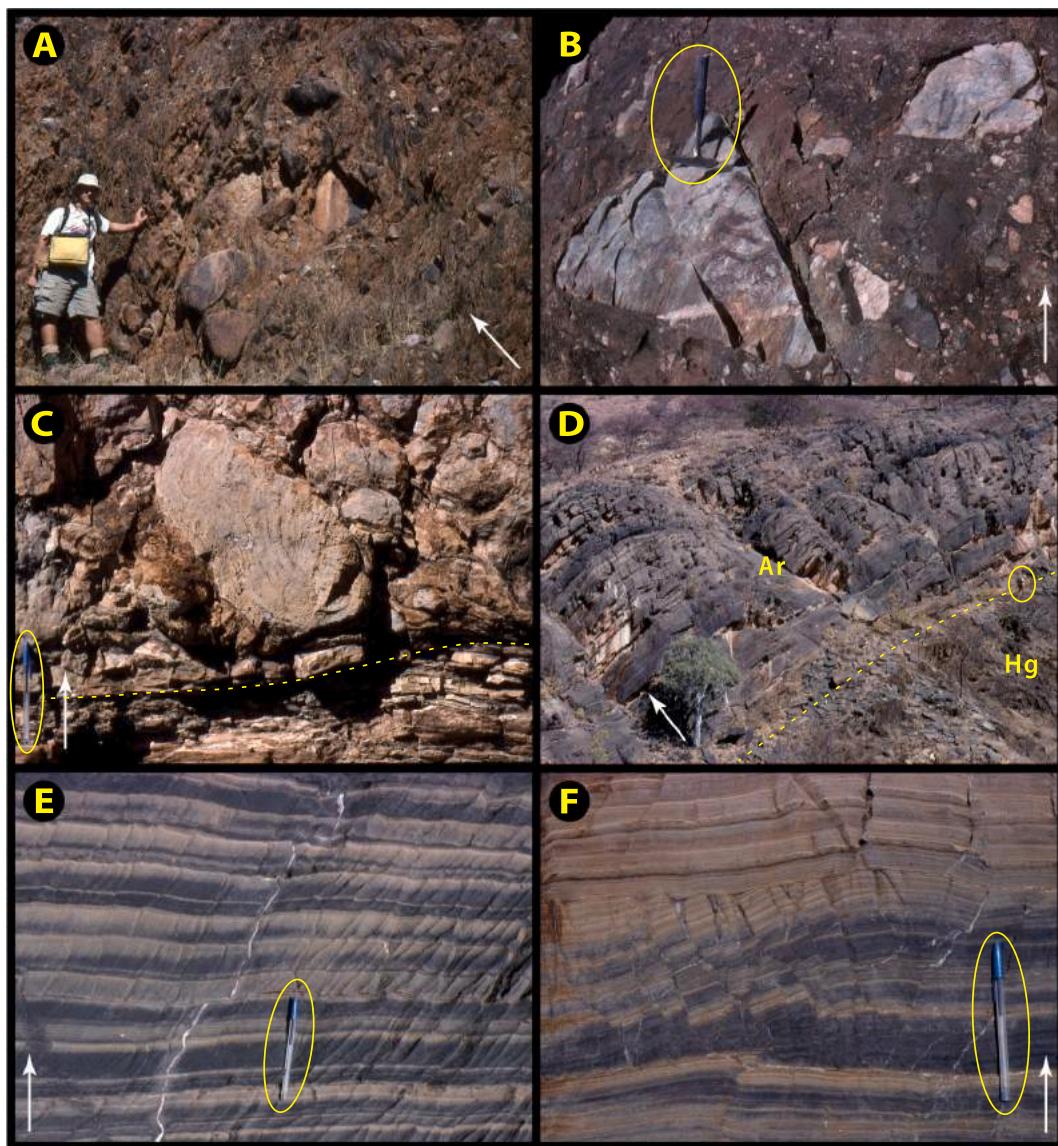


Fig. 74. Images of Sturtian Chuos Fm and lower Rasthof Fm cap carbonate in Huab paleo-outlier (Tr6): white arrows indicate stratigraphic younging. (A) Chuos Fm diamictite in which surrounded boulders of basement metamorphic or granitoid rock are suspended in a gritty phyllite matrix at $-20.1013^{\circ}/14.5906^{\circ}$ near 6–4 (P2509, Fig. 72). (B) Faceted boulder of basement gneiss in Chuos Fm diamictite at $-20.1022^{\circ}/14.5886^{\circ}$ near 6–4 (P2509). (C) Base of carbonate-clast debrite (dashed line) in an atypical gradational (resedimented) contact between Chuos and Rasthof Fm at $-20.1024^{\circ}/14.5894^{\circ}$ in 6–4 (P2509). (D) Lower Rasthof Fm at $-20.0958^{\circ}/14.7721^{\circ}$ in 6–10 (K1819, Fig. 73), where weakly dolomitic calcite rhythmite with turbidites (Fig. 76) directly overlies a great unconformity on Orosirian basement. (E) Centimetric calcite turbidites (dark grey) with authigenic dolomite (buff) developed preferentially from the tops of graded beds at $-20.0955^{\circ}/14.7804^{\circ}$ near 6–10. Cleavage is $\sim 30^{\circ}$ and karstic relief $\sim 45^{\circ}$ from vertical on the page. (F) Domino-type fault duplex in lower Rasthof Fm carbonate rhythmite at same location as E. Fault planes are nearly perpendicular to primary layering, unlike standard normal faults.

the $\delta^{13}\text{C}$ decline (i.e., cycle b7) is estimated to be ~ 0.6 Myr in a thermal subsidence model of the post-Gruis Otavi Group (Halverson et al., 2002). The excursion to mantle-like values has long been correlated with the global Trezona CIE (Cn5, Fig. 10D) (Halverson et al., 2005; Halverson and Shields-Zhou, 2011). We use the base of cycle b7 as the datum for the Tr6 fence diagram (Fig. 71) instead of the zero per mil $\delta^{13}\text{C}$ crossing (e.g., Halverson et al., 2002) because it permits alignment of sections lacking isotope data (6–2, 5 and 7).

Ombaatjie cycle b8 has an interesting sedimentological puzzle. Intercalated in the argillite or marlstone unit near the base of the cycle in 6–7 and 8 are beds of enigmatic intraclast packstone (Fig. 78F). The

intraclasts, 1–5 mm in diameter, are rounded, subequant and composed of a uniform micritic Fe-rich carbonate phase, probably ankerite or siderite. The intraclasts are grain supported, size sorted, and low-angle cross-stratified, but they are not held together by void-filling cement but by dolomicrite. The micrite presumably infiltrated after the intraclasts were deposited, and also occurs as lenses and tabular intraclasts. The packstone texture is pseudomorphed in nodules of authigenic black chert (Fig. 78F) and is characteristically spotted with cm-scale clusters of authigenic pyrite (oxidized by weathering). We speculate that the intraclasts are lags of authigenic carbonate, the origin of which could be related to enhanced anaerobic respiration (Tziperman et al., 2012).

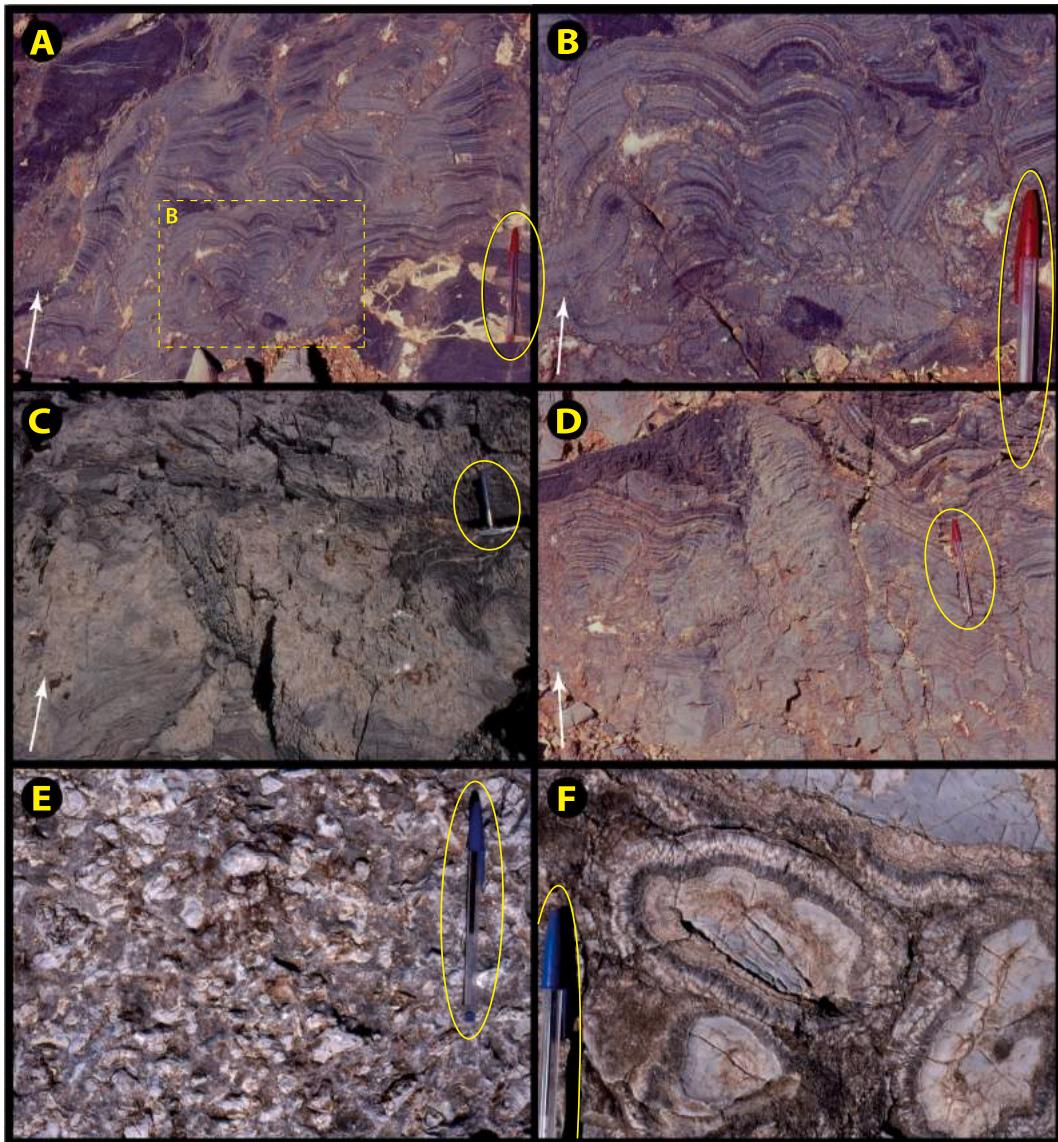


Fig. 75. Images of Rasthof Fm in Huab paleo-outlier (Tr6): white arrows indicate stratigraphic younging. (A-D) Dolomite stromatolite in lower Rasthof Fm at $-20.0957^{\circ}/14.7685^{\circ}$ in 6-10 (P1819, Fig. 73), only 300 m to west along strike from turbidite/rhythmite facies at K1819 (Figs. 73 & 76). Dashed box in A is the area of B. Stromatolites in A-B have chambered void-filling sparry cements, those in C-D have irregular nascent columns. (E-F) Dilatant discordant breccia sealed by fibrous isopachous marine (?) dolomite cement in upper Rasthof Fm at $-20.0963^{\circ}/14.6598^{\circ}$ between 6 and 7 and 6-8. This style of cemented breccia is pervasive in zones and closely resembles breccias in Okonguarri Fm in Tr5 that appear spatially associated with syndepositional Kranstoort flexure (Figs. 65 & 66E-F).

Intraclast packstone is closely associated with the nadir of the Trezona CIE all across the platform: its spotty distribution in IPz correlates with preservation of cycle b8 beneath the Marinoan disconformity (Hoffman and Halverson, 2008).

In section 6–3 (Fig. 78B), the cycle b8 is incised by a unit of limited lateral extent (b9 in Figs. 71 & 78B). Remarkably uniform in lithology and isotopic composition, unit b9 is 28 m thick and composed of medium grey-coloured, recrystallized dolomite. It is brecciated for a meter or more below a smooth and sharp contact with the overlying Keilberg Member (Fig. 79B), which is distinguishable from b9 by its paler colour (Fig. 78B) and pinkish tint, finer grain size and less-recrystallized texture. Authigenic chert in upper b9 appears to be truncated at the contact. Palimpsest ‘pinstripe’ lamination can be perceived in the upper

part of b9, as well as indistinct large-scale foreset layering (Fig. 79B) that dips 20° in a 025° direction (i.e., 20–025°). Correcting for tectonic tilt, given by primary layering in the overlying basal Keilberg Member (20–112°), restores the foreset layering to 27–340°. In an adjacent section, 0.12 km to the E, chert sheets in upper b9 dip 33–074° beneath a sub-Keilberg erosion surface dipping 20–120°. Tilt-corrected, the chert sheets (aeolian foresets?) dip 24–039°. Following Hoffman and Halverson (2008), we interpret b9 as a carbonate aeolianite and infer that it was deposited under the influence of onshore winds (south-southwestlies), producing barchan-type dunes with foresets inclined toward 340° and 039° (Fig. 57). A dune field presumably developed because of the fall in global mean sea level at the inception of Marinoan glaciation. The initial glacioeustatic fall would be large and rapid in a global

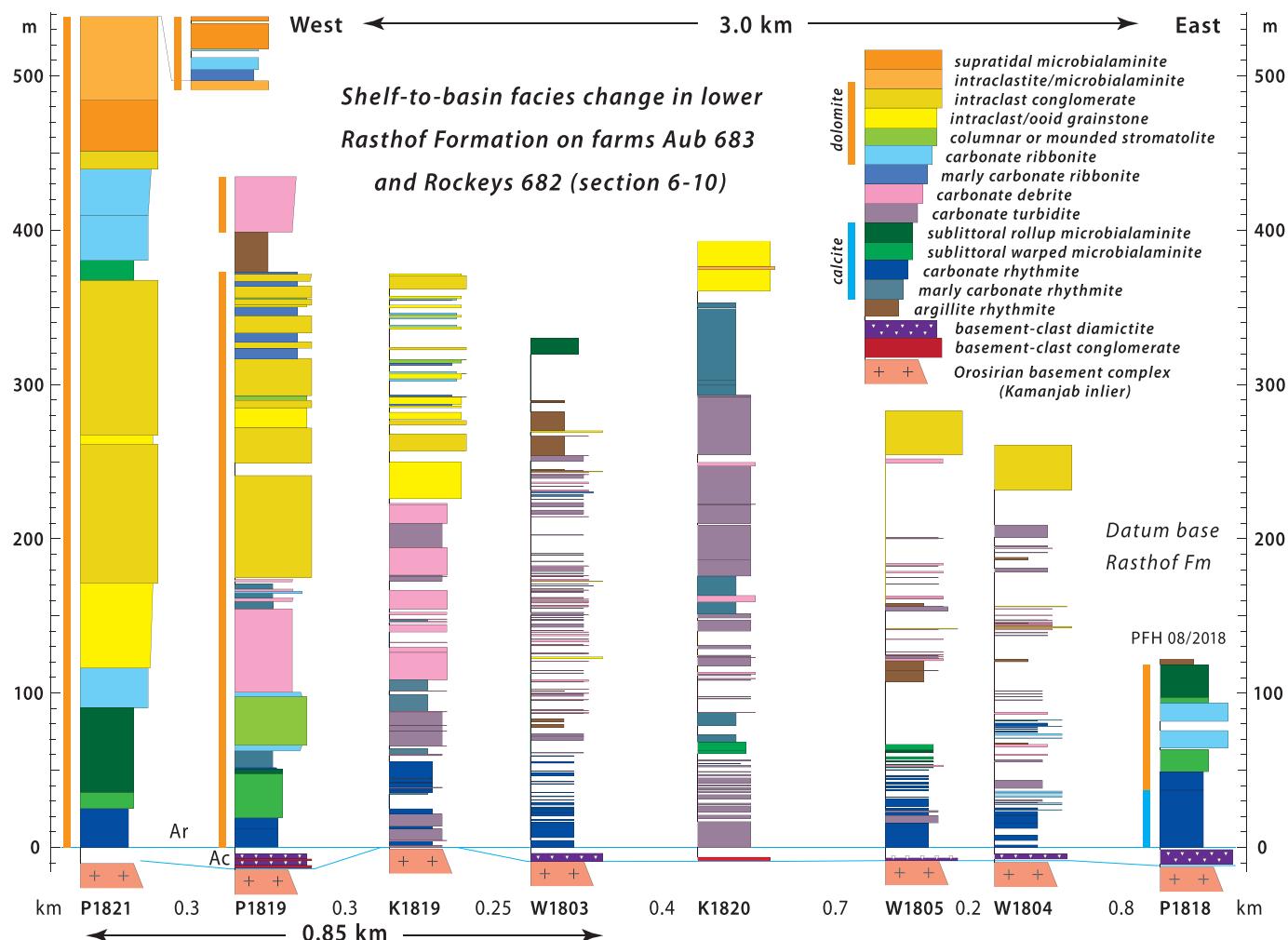


Fig. 76. Closely spaced columnar sections of lower Rasthof Fm at 6–10, documenting sudden (≤ 0.85 km) facies change from shoal-water stromatolite and grainstone (left) to deepwater turbidite and argillaceous rhythmite (right). Note thin basal Chuos Fm diamictite.

paleogeography lacking polar continents (Voigt et al., 2011). The putative b9 aeolianite should be the youngest preglacial deposit in OPz, potentially contemporaneous with Frannis-aus Mb (FST) in Tr1 and 5 (Hoffman and Halverson, 2008).

2.6.2. Early Ediacaran of Tr6

Keilberg Mb is little changed from the cozonial NE segment of Tr5 (Fig. 68). It is 50–80 m thick and tubestone stromatolite (Fig. 69A) is the dominant lithology, although mechanically bedded dolopelarenite generally forms a thin basal layer. Stromatolite synoptic morphology consists of meter-scale humps and saddles (Figs. 69A, 79C & D). The ‘tubes’ are defined by authigenic silica that selectively replaces dolomitic in cm-scale subcircular pits having convex-downward laminations and remarkable paleovertical persistence (Fig. 79F). Another zonal trait is that the Keilberg is more recrystallized and richer in authigenic silica compared with the IPz, where the nature of the tube structure is more readily apparent and where the host stromatolite is better organized on two scales, centimetric and decametric (see ahead 2.8.3.).

At $-20.1138^\circ/14.5966^\circ$ in 6–4, at the N end of the small Keilberg ‘island’ outcrop on the floodplain of Huab River (Fig. 72), meter-scale voids in Keilberg stromatolite are filled by radial prismatic silica

(Fig. 79E) that resembles void-filling botryoidal aragonite cement in Holocene reefs (Ginsburg and James, 1976). This would be interesting as evidence for aragonite precursor in a Marinoan cap dolomite (Fabre et al., 2013; Ahm et al., 2019). However, the age of the cavities is unknown and the prismatic habit could also be that of void-filling quartz.

The top of Keilberg Mb is gradational but well-defined (Fig. 79F). The very pale-coloured, blocky Keilberg Mb contrasts with the sombre-coloured, tabular-bedded, dolomitic limestone of the Tm2 member of Maieberg Fm (Fig. 82). Whereas the upper Keilberg is a low-angle cross-stratified dolopelarenite (Fig. 71), lower Tm2 consists of marly limestone rhythmite and nodular rhythmite with dolomitic turbidites and no wave-generated bedforms. In 6–3 and 5 (Figs. 70–72), pseudomorphed crystal fans aggregated in a variety of forms pervade Tm2 rhythmites directly above Keilberg Mb (Figs. 80, 81A & B). The crystal fans are pseudomorphed by calcite, chert or dolomite, of which the last are best preserved (Fig. 81B) and display the characteristic hollow, prismatic, pseudo-hexagonal habit of aragonite (Soffer, 1998). Although the prisms are millimetric in scale (as microcrystalline aggregates), they are arranged in three-dimensional fractal constructions (Fig. 80A) that locally determined seafloor topography on the scale of decameters (Fig. 80B). The crystal fans were not growing in a sediment-free

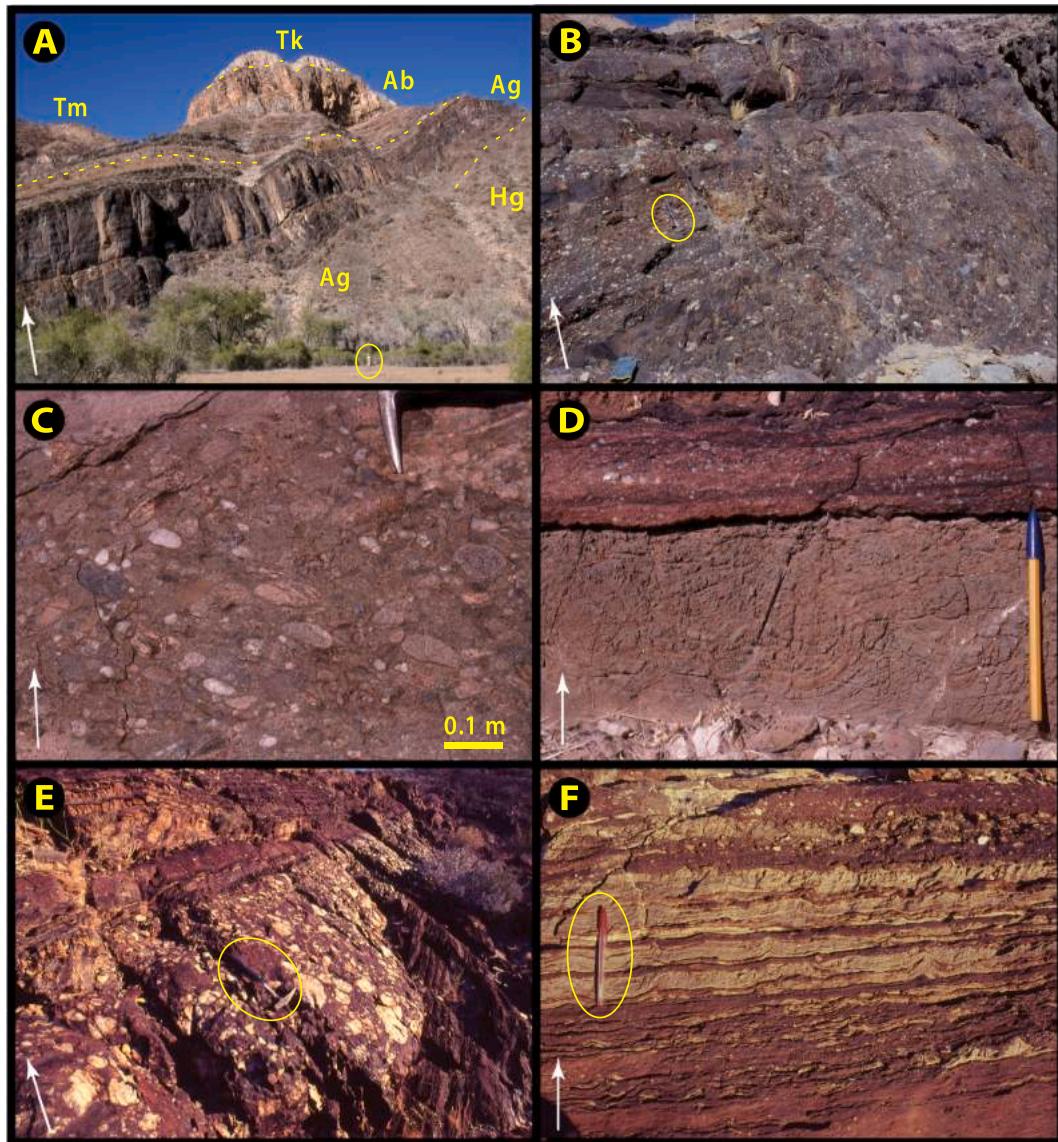


Fig. 77. Images of middle Cryogenian Gruis Fm on rift-shoulder dip-slope in western Huab paleo-outlier (Tr6): white arrows indicate stratigraphic younging. (A) Section 6–3 (Fig. 71) as viewed from N in Huab River. Geologist (circled in foreground at $-20.1158^{\circ}/14.5859^{\circ}$) gives scale. Ridge rises 270 m above the river-bed. Units: Hg, Huab gneiss (basement); Ag, Gruis Fm, alluvial fanglomerate; Ab, Ombaatjie Fm, peritidal cycles; Tk, Keilberg Mb, basal Ediacaran cap dolomite; Tm, middle Maieberg Fm calcite rhythmite with mounded crystal fans (pale). Basal Rasthof Fm cutoff (Fig. 71) is behind photographer. Gruis Fm fanglomerate is exclusively basement derived. (B–C) Basement-derived alluvial fanglomerate in middle Gruis Fm at $-20.1177^{\circ}/14.5868^{\circ}$ near 6–3. (D–F) Interstratified quartz-pebble conglomerate and tepee-structured dolomite microbial laminites of Gruis Fm in 6–1; at $-20.1477^{\circ}/14.5737^{\circ}$ (P1077, Figs. 71 & 85).

environment. Their growth was repeatedly interrupted or snuffed out by turbidites or other sedimentation events (Fig. 81A), but a new population of crystal fans soon replaced them (Fig. 80E).

In 6–3, non-silicified fractal arrays (Fig. 80A) are well exposed in the central down-dropped block of the forked normal fault (Fig. 72) at $-20.1207^{\circ}/14.5858^{\circ}$. On the ridge directly above, fractal arrays cluster to form decameter-scale mounds separated by troughs in which crystal fans are rare or absent (Fig. 80B). Selectively silicified fan arrays (Fig. 80C & D) are accessibly exposed on the ridge to the northeast at $-20.1183^{\circ}/14.5915^{\circ}$. Low on the dip-slope of the same ridge at $-20.1250^{\circ}/14.5888^{\circ}$, prismatic pseudomorphs are selectively dolomitized (Fig. 81B), making their acicular, commonly hollow and sediment-

filled, pseudo-hexagonal habit (due to polysynthetic twinning) visible with a hand lens (Soffer, 1998). In 6–3, seafloor cements pervade the first 90 m of M2 (Fig. 82), limited by the sub-Renosterberg Fm disconformity (Figs. 70 & 71).

In 6–5, the aragonite pseudomorphs are preserved as pinkish-coloured calcite that contrasts with the host blue-grey calcite rhythmite and buff-coloured dolomite turbidite (Fig. 80E & F). The pseudomorphs are bunched in upward-flaring bundles or sheaves, against which the host layering abuts or truncates (Fig. 81A). The bundles are up to 0.7 m wide and 1.7 m tall (Fig. 80F), although their synoptic relief on the ancient sea floor was only a few centimeters. Where not dolomitized or silicified, the aragonite pseudomorphs are composed of void-filling

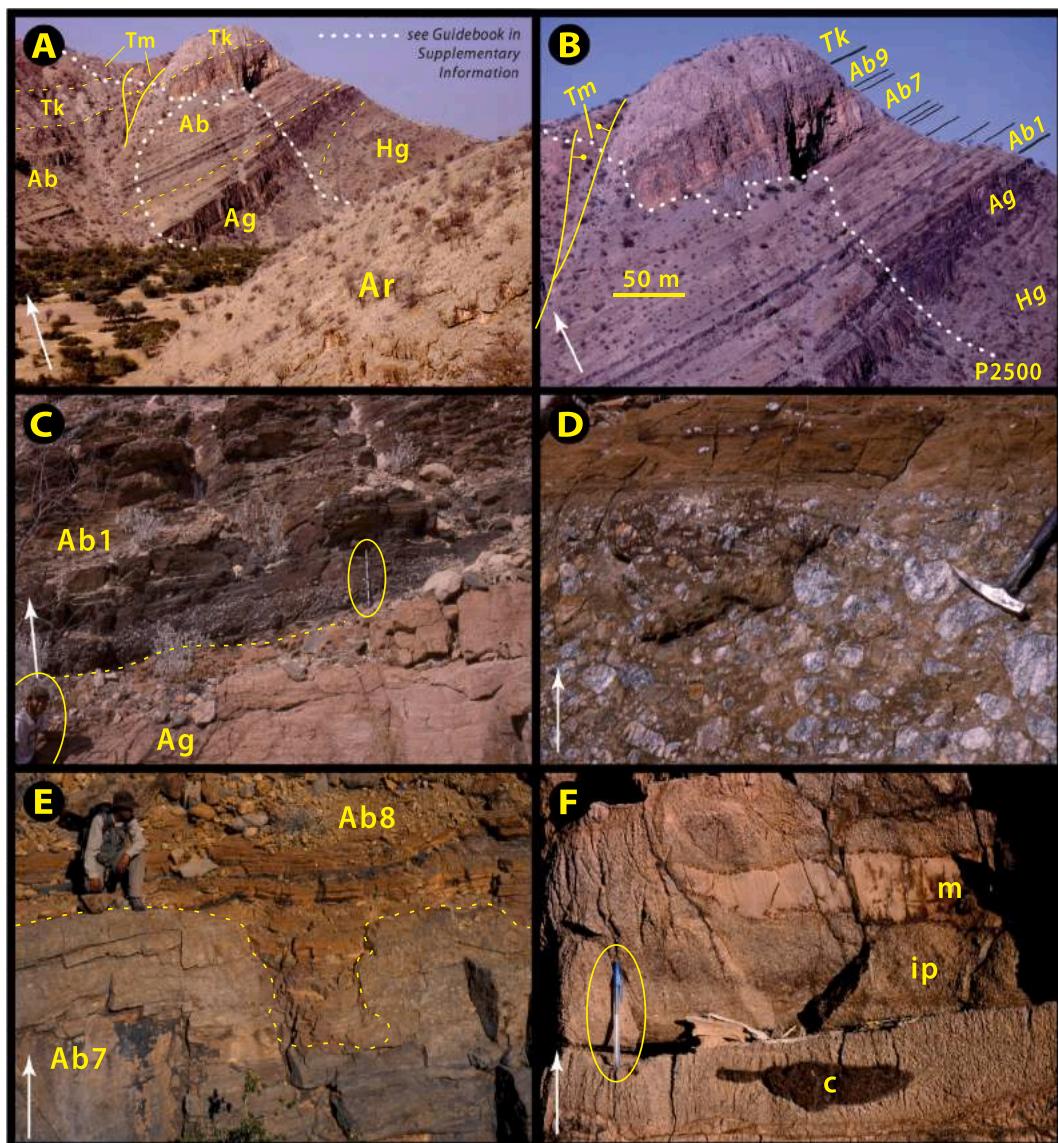


Fig. 78. Images of post-rift Ombaatjie Fm on rift-shoulder dip slope in western Huab paleo-outlier (Tr6): white arrows indicate stratigraphic younging. (A) View looking SW toward basement (Hg) onlapped by Gruis Fm (Ag) conglomerate in 6–3 (Fig. 77), from Gruis Fm spur at $-20.1078^{\circ}/14.5925^{\circ}$ in 6–4 (Figs. 70–72). Rasthof Fm (Ar) dip-slope (near right) is truncated at sub-Gruis Fm disconformity between 6 and 3 and 4 (Fig. 71). Post-rift sequence: Ab, Ombaatjie Fm; Tk, Keilberg Mb; Tm, middle Maieberg Fm (Tm2). Note down-dropped Maieberg Fm fault wedge. (B) Detail of 6–3 (P2500, Fig. 71), base of dotted line at $-20.1190^{\circ}/14.5841^{\circ}$ with 9 cycles in Ombaatjie Fm (Ab1–9) indicated on sky line. Colour contrast between Ab9 dolomite aeolianite (?) and Keilberg Mb (Tk) is less apparent on outcrop (Fig. 79B). (C) Disconformity at $-20.1197^{\circ}/14.5841^{\circ}$ in 6–3 between Gruis Fm (Ag) dolomite microbialaminite and Ombaatjie Fm (Ab1) argillite with basal smoky quartz-pebble conglomerate. Gad Soffer (lower-left) for scale. (D) Near-basal Ombaatjie Fm smoky quartz-pebble conglomerate near $-20.1186^{\circ}/14.5855^{\circ}$ in 6–3, overlain by sandy authigenic (?) dolomite with outsized quartz granules. (E) Disconformity (dashed line) at $-20.1304^{\circ}/14.5780^{\circ}$ in 6–2 (Fig. 71) between Ombaatjie Fm cycle b7 Tungussia-type stromatolite (Ab7) and cycle b8 marly dolomite ribbonite (Ab8). (F) Ankerite (Fe-dolomite) intraclast packstone (ip) in cycle b8 at $0968^{\circ}/14.6373^{\circ}$ in 6–7 with dolomitic clast (m) and authigenic chert nodule (c). Intraclast packstone is regionally extensive in cycle b8 (Fig. 127F) but its origin is a mystery.

sparry calcite with relatively low Sr contents of 150–600 ppm (Soffer, 1998).

Maieberg Fm seafloor cements encompass the MFS of the cap-carbonate depositional sequence (Fig. 82), so the problem they pose is how alkalinity is pumped into this environment in order to maintain critical oversaturation with respect to aragonite, despite evident high rates of precipitation. The crystal-fan motif itself indicates rapid growth, whereby a (negative) ionic concentration gradient is maintained at the crystallizing surface. Consequently, crystals that project higher grow

faster, with the result that a small number of crystals come to dominate the overall structure (Lasaga, 1998).

Maieberg sea-floor cements are localized in the southern horn of Tr6, in 6–3 and 5. In 6–1 and 2, Maieberg Fm is cut out beneath Renosterberg Fm (Figs. 71 & 9C). In 6–8 (Fig. 70), a well-exposed complete Maieberg section has no macroscopic sea-floor cement at all (Figs. 81C & 82). Seafloor cement is co-located with the dip-slope of the buried Cryogenian rift shoulder (Huab ridge, Fig. 5). It is analogous to their association with Huab ridge in Tr5 (5–45 and 51, Fig. 68), except that in Tr6 they are on

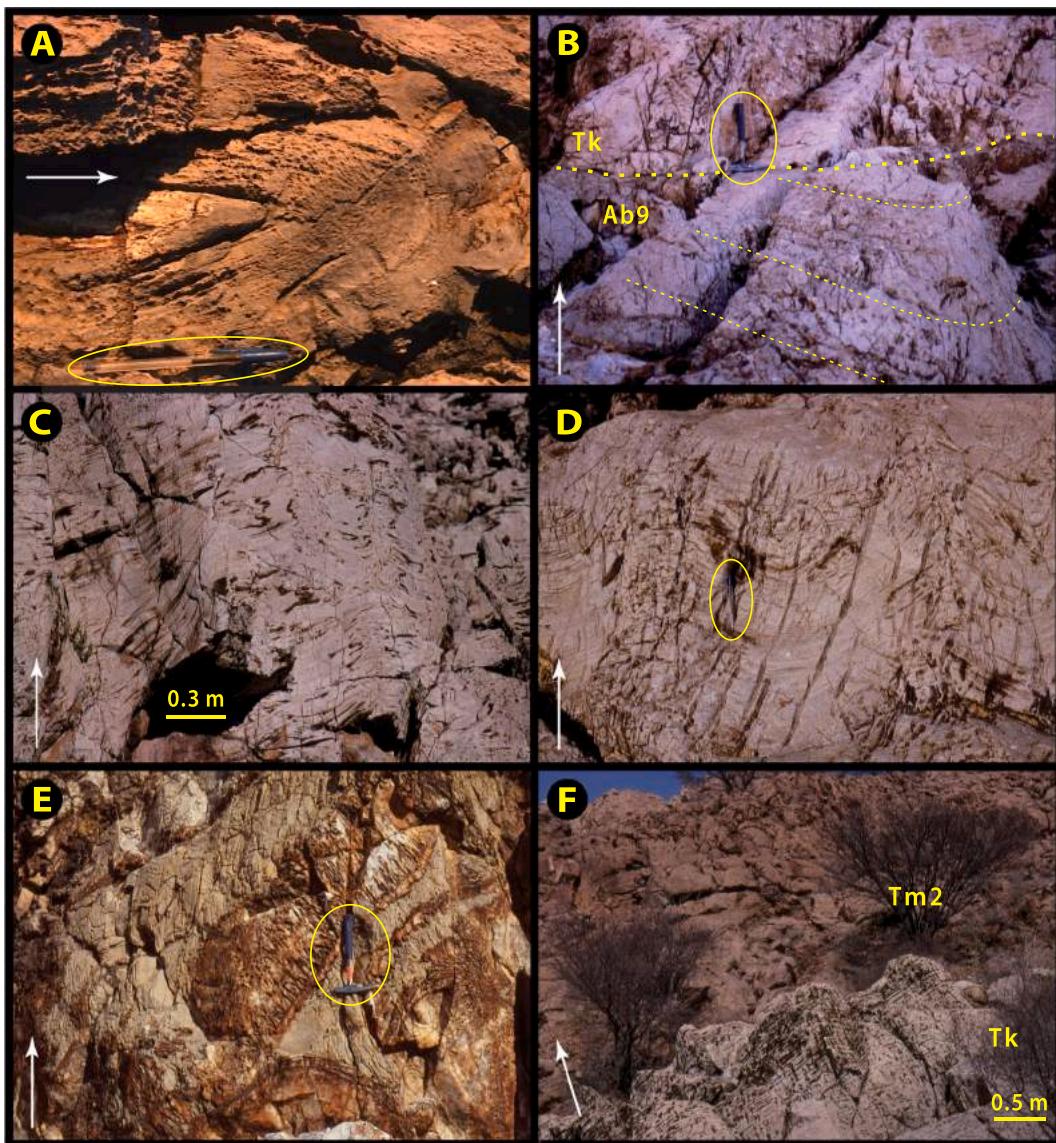


Fig. 79. Images from the Marinoan prelude and aftermath in Huab paleo-outlier (Tr6): white arrows indicate stratigraphic younging. (A) Conical (*Conophyton*-like) stromatolite in Omabaatjie Fm cycle b7 at $-20.1062^{\circ}/14.7379^{\circ}$ in 6–9 (Fig. 71). Stromatolites are unusually diverse and well developed across the Otavi platform coincident with Cn5 (Trezena) CIE, encompassed by cycles b7 and 8. This coincidence supports a sedimentary origin for the CIE and has been attributed to enhanced anaerobic respiration preceding Marinoan glaciation (Tziperman et al., 2011). (B) Marinoan subglacial erosion surface (heavy dashed line) at $-20.1203^{\circ}/14.5853^{\circ}$ in 6–3 (Fig. 78A–B). Below the surface is dolomite aeolianite (?) with NNW-dipping (tilt-corrected) foresets (light dashed lines) of Omabaatjie Fm cycle Ab9 (Figs. 57 & 71). Above the surface is dolopelarenite ribbonite of the basal Keilberg Mb cap dolomite (Tk), which is distinguished from Ab9 by slightly paler colour and faint pinkish tint. (C–D) Tubestone stromatolites in basal Ediacaran Keilberg Mb cap dolomite in 6–4: at $-20.1151^{\circ}/14.5973^{\circ}$ on the Keilberg inselberg (rock island) in the Huab River floodplain (Fig. 72). Short, stacked, tubular structures infilled by dolomicrite or void-filling non-fibrous cement are localized in stromatolite crests and may have influenced their development. (E) Botryoidal prismatic cement, dolomitized and selectively silicified, filling meter-scale cavities in Keilberg Mb cap dolomite at $-20.1139^{\circ}/14.5967^{\circ}$ in 6–4. Cement morphologically resembles botryoidal aragonite cement filling cavities in a Holocene reef limestone in Belize (Ginsburg and James, 1976). (F) Tubestone stromatolite of Keilberg Mb (Tk) in foreground at $-20.1201^{\circ}/14.5860^{\circ}$ in 5–3, overlain by sombre rhythmite with former-aragonite sea-floor cement (Figs. 80A–B) of middle Maieberg Fm (Tm2 member).

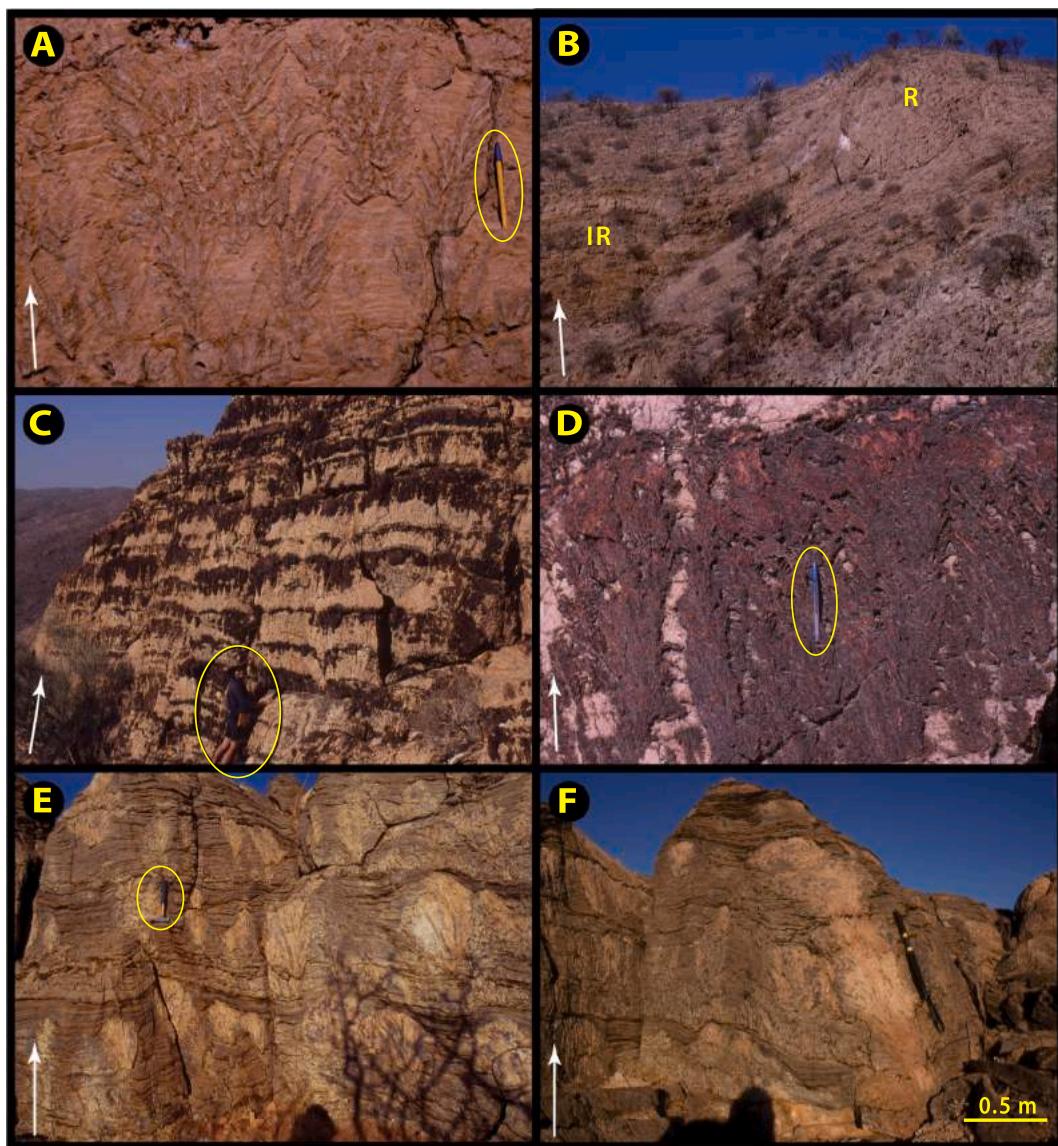


Fig. 80. Images of former aragonite sea-floor cements in Tm2 member of Maieberg Fm in western Huab paleo-outlier (Tr6): white arrows indicate stratigraphic younging. (A) Dendritic aragonite pseudomorphs in dolomitized Tm2 in 6–3: at $-20.1207^\circ/14.5857^\circ$. (B) Reef-like mound (R) rich in former aragonite sea-floor cement and inter-reef (IR) turbidite rhythmite lacking sea-floor cement in Tm2: $-20.1212^\circ/14.5870^\circ$ in 6–3. (C–D) Partial silicification (brown desert varnish) of crystal fans in dolomitized Tm2 rhythmite in 6–4: $-20.1183^\circ/14.5914^\circ$. (E–F) Plumose calcitized-aragonite sea-floor cement ‘bouquets’ in marly limestone rhythmite of Tm2 in 6–5: $-20.1059^\circ/14.6028^\circ$. Benthic crystal fans record anomalous carbonate oversaturation of bottom waters at intermediate-depth.

the landward rather than the seaward side of the buried ridge as in Tr5. In both cases, they occur close to the shelf break in earliest Ediacaran (Tm2) time. Like Duurwater moraine, where Tm2 crystal fans are also well developed (Fig. 62), the top of the foreslope would have been a zone of enhanced vertical mixing (Fig. 5).

Unlike Karibib Fm in FSz, Maieberg Fm in Tr6 shoals to a subaerial exposure surface marked by microbial laminites with tepees (Fig. 82). The Maieberg depositional sequence is 398 m thick in 6–8 and the TST (Keilberg Mb) is expanded (≥ 100 m) compared with other depositional sequences of the Otavi Group. Even more striking is the absence of higher-order cycles (parasequences) within the sequence as a whole. As a single TST-HST, Maieberg Fm is 33× thicker than the 12-m average thickness of depositional cycles in the underlying Ombaatjie Fm

(Fig. 71), and 145× thicker than the 2.75-m average thickness of cycles in the overlying lower Elandshoek Fm (Fig. 82). According to the thermal subsidence model (Halverson et al., 2002) referred to in 2.6.1., accommodation for Maieberg Fm could have been created during Marinoan glaciation if its duration was ≥ 6 Myr, assuming (for simplicity) no net erosion, sediment accumulation or sea-level change (i.e., pre- and post-glacial sea levels were similar). If glaciation had been short-lived, no net accommodation would remain after complete glacio-isostatic adjustment. If accommodation had been created slowly, after glaciation, Maieberg Fm would have been deposited incrementally as small-scale cycles, like Elandshoek and Hüttenberg formations (Hoffman and Halverson, 2008), not as a single 0.3-km-thick HST (Fig. 82). Historically, Maieberg Fm provided the first indication that Marinoan

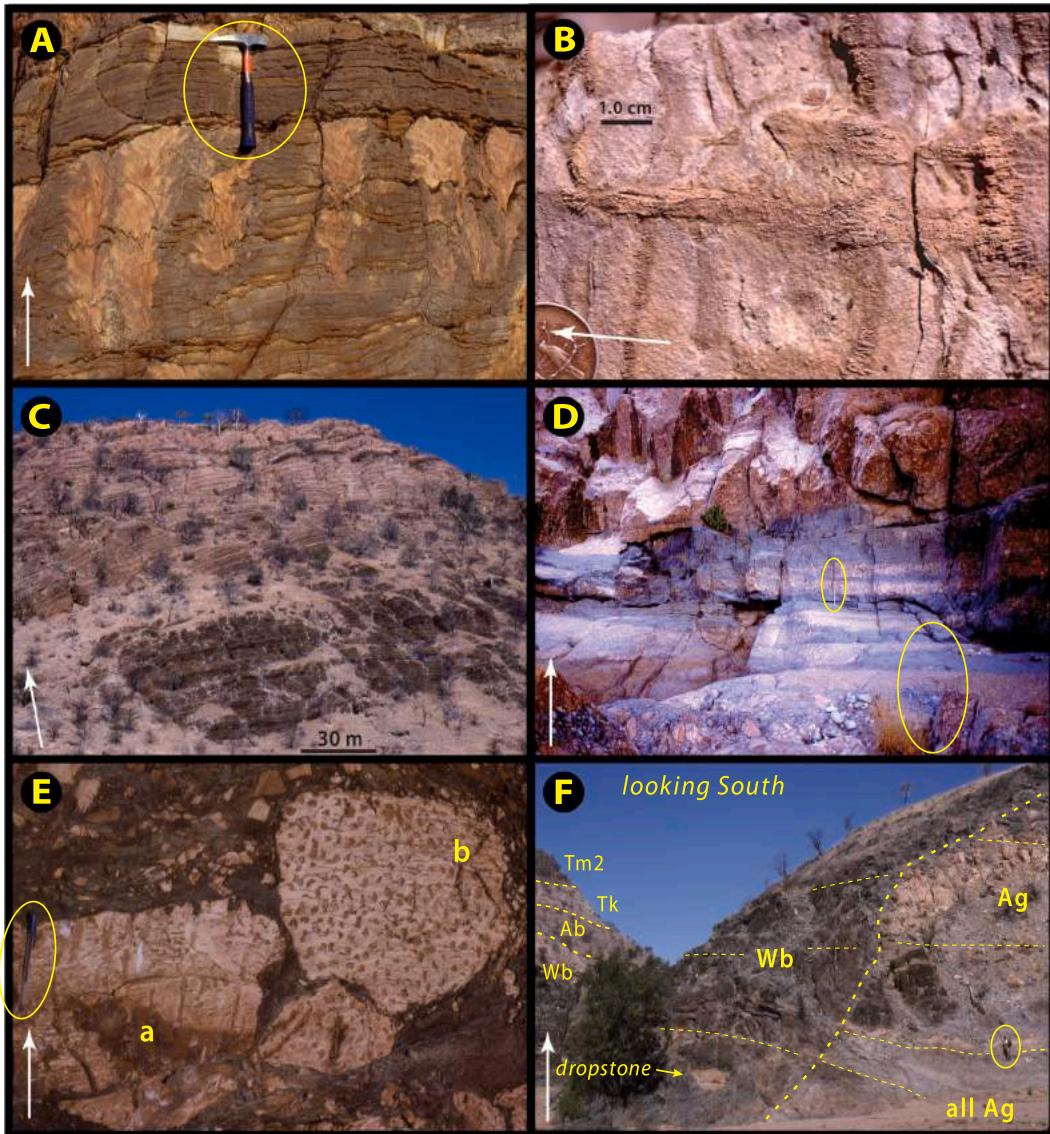


Fig. 81. Images of Maieberg Fm (Marinoan cap-carbonate sequence) and paleokarst-filling Braklaagte Fm (Welkom Subgroup, Table 5, Fig. 6D) in Huab paleo-outlier (Tr6): white arrows indicate stratigraphic younging. (A) Erosionally truncated plumose sea-floor cement 'bouquets' in marly limestone rhythmite of middle Maieberg Fm (Tm2 member) at $-20.1062^{\circ}/14.6026^{\circ}$ in 6–5. Note layer-parallel cm-scale stylolites. (B) Prismatic pseudomorphs of dolomite after square-tipped, polysynthetically twinned, pseudo-hexagonal aragonite crystals (top to the left) in Tm2 at $-20.1250^{\circ}/14.5887^{\circ}$ in 6–3 (documented in Soffer, 1998). (C) Greenish marly limestone rhythmite (dark) and pinkish-buff limestone rhythmite in Tm2, the lower highstand tract of the Maieberg cap-carbonate sequence at $-20.1048^{\circ}/14.6812^{\circ}$ in 6–8 (P1314) (Fig. 82). Sea-floor cement is absent here, suggesting that cement development in western Tr6 is spatially related to buried Huab rift-shoulder (Fig. 71) and earliest Ediacaran platform rim (Fig. 5). (D) Paleokarst-filling argillaceous siltstone (dark) and dolomite-clast breccia, conglomerate, debris and (non-glacial) dropstones in Braklaagte Fm near $-20.1021^{\circ}/14.6017^{\circ}$ in 6–6 (Figs. 70 & 72). Braklaagte Fm is at stratigraphic level of Gruis Fm (with which it is structurally conformable), 600 m below the top of Otavi Group in 6–8 (Figs. 85 & 193). Scale (circled) is 1.0 m. (E) Sedimentary breccia in Braklaagte Fm at $-20.1043^{\circ}/14.6018^{\circ}$ in 6–5 (Gms5) holding blocks of Keilberg Mb tubestone stromatolite. In blocks a and b, the 'tubes' are oriented parallel and perpendicular to outcrop surface, respectively. However, stromatolitic lamination is steeply inclined in both blocks, showing that tubes are oriented at high and low angles to lamination in blocks a and b, respectively. This suggests that blocks a and b are derived from central and marginal parts of arched stromatolites, respectively (Fig. 69A). (F) Steep sub-Mulden paleokarst valley walls cutting Gruis Fm (Ag) in foreground at $-20.1007^{\circ}/14.6013^{\circ}$ in 6–5 (P6006) and Oombaattjie Fm (Ab) on opposite bank of Huab River (Gms5, Fig. 72). Geologist (circled) gives scale. Paleovalley is filled by Braklaagte Fm (Wb): argillaceous siltstone holding a large dolomite block (arrow, lower left) dropped from paleokarst wall. Other units: Tk, Keilberg Mb; Tm2, middle Maieberg Fm. Paleokarst is described in Frets (1969), Guj (1974), Miller (2008b) and Hoffman (2021a).

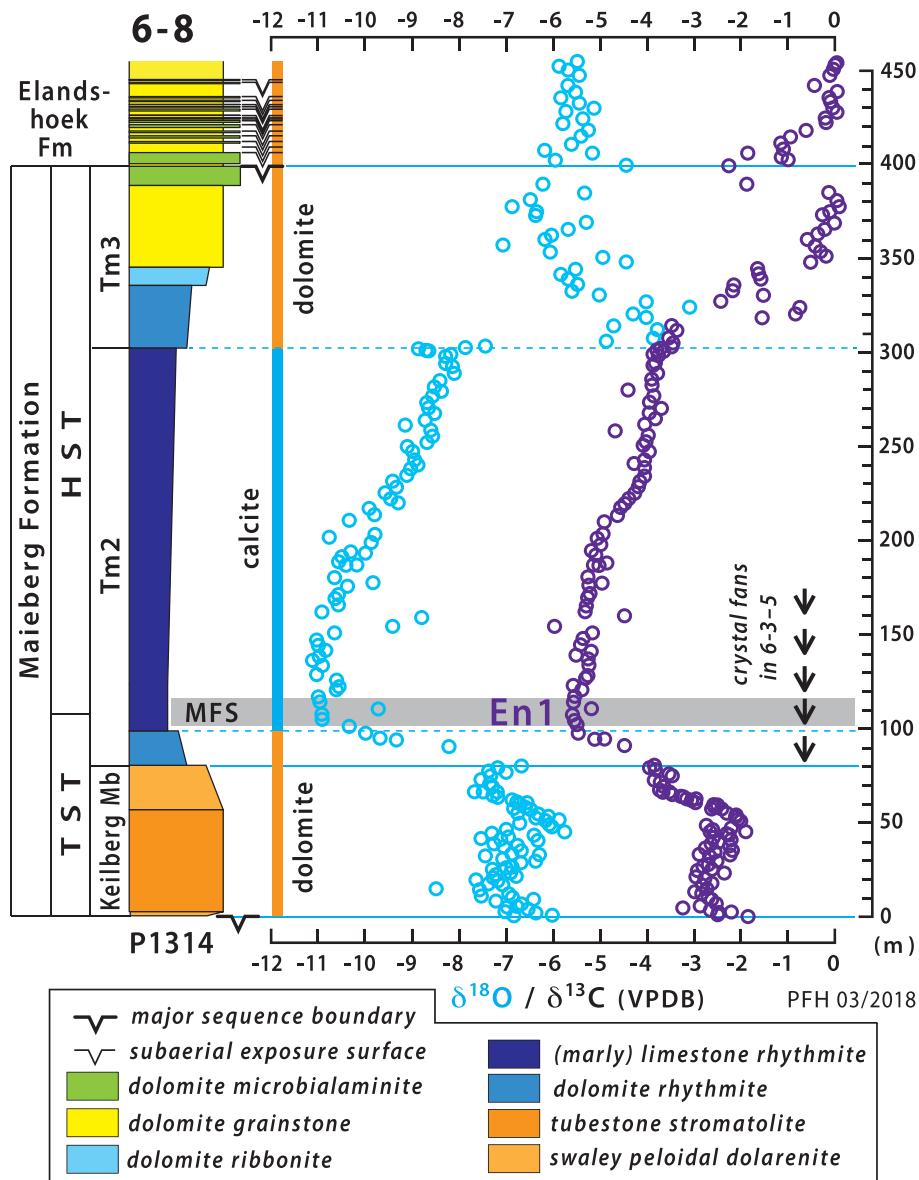


Fig. 82. Columnar section 6–8 (Figs. 70 & 81C) with $\delta^{18}\text{O}$ and $\delta^{13}\text{C}_{\text{carb}}$ data for Maieberg Fm and lower Elands-hoek Fm. Note co-variation in O- and C-isotope records and mantle-like $\delta^{13}\text{C}$ values at nadir of CIE En1 (Fig. 10), coincident with MFS (maximum flooding stage) in lower Tm2. Abbreviations: TST, transgressive systems tract; HST, highstand systems tract; Tm2, Maieberg Fm middle member; Tm3, upper member.

glaciation was long-lived, consistent with a snowball CO_2 hysteresis (Walker et al., 1981; Hoffman et al., 1998a, b; Hoffman and Schrag, 2002).

Frets (1969) and Guj (1974) described deep karstic relief on the disconformity surface between the Otavi and Mulden groups in Tr6 (Fig. 70). Deeper parts of the paleokarst are filled by subaqueously deposited siltstone, fine-grained sandstone and carbonate-clast debrite of Braklaagte Fm (Fig. 81D & E), while in more elevated areas the same disconformity is overlain by fluvial lithic sandstone of Renosterberg Fm (Fig. 83E & F). Frets (1969, Fig. 4) noted that the modern Huab River locally reoccupies a Mulden-age paleovalley on farm Tweelingskop (Fig. 72). On both walls of the modern gorge, steeply inclined disconformity surfaces separate gently co-tilted Abenab Subgroup and Braklaagte Fm (Fig. 81F). The latter consists of karst-filling greenish argillaceous siltstone (Fig. 81D) with carbonate-clast debrite (Fig. 81E),

talus and limestones (Fig. 81F). Clasts of Keilberg Mb tubestone stromatolite are locally prominent (Fig. 81E). In 5–5 (Gms5), these Keilberg-derived clasts lie ≥ 100 m stratigraphically below their source horizon.

The SW termination of Tr6 (Fig. 84) is described in Miller (2008b, p. 13–224) and Hoffman (2021a), and a field guide to the area is given in SOI S3.9.4. with geologically annotated satellite images in Fig. S20. At the map-scale, the Otavi and Mulden groups are structurally subparallel, but structural discordance at the outcrop scale is common because of different deformation mechanisms due to rheological contrast between dolomite and semipelitic. From 6 to 8 to 6–1 (Fig. 70), the sub-Mulden Group disconformity cuts stepwise down-section across Otavi Group (Fig. 85), finally reaching its base 0.6 km S of Sout River (Fig. 84). The final steeply inclined disconformity surface is buttressed by dolomite-clast debrite (Fig. 83A), conglomerate (Fig. 83B) and terrigenous silt- and sandstone (Fig. 83C) of Braklaagte Fm (Figs. 84 & 85). The

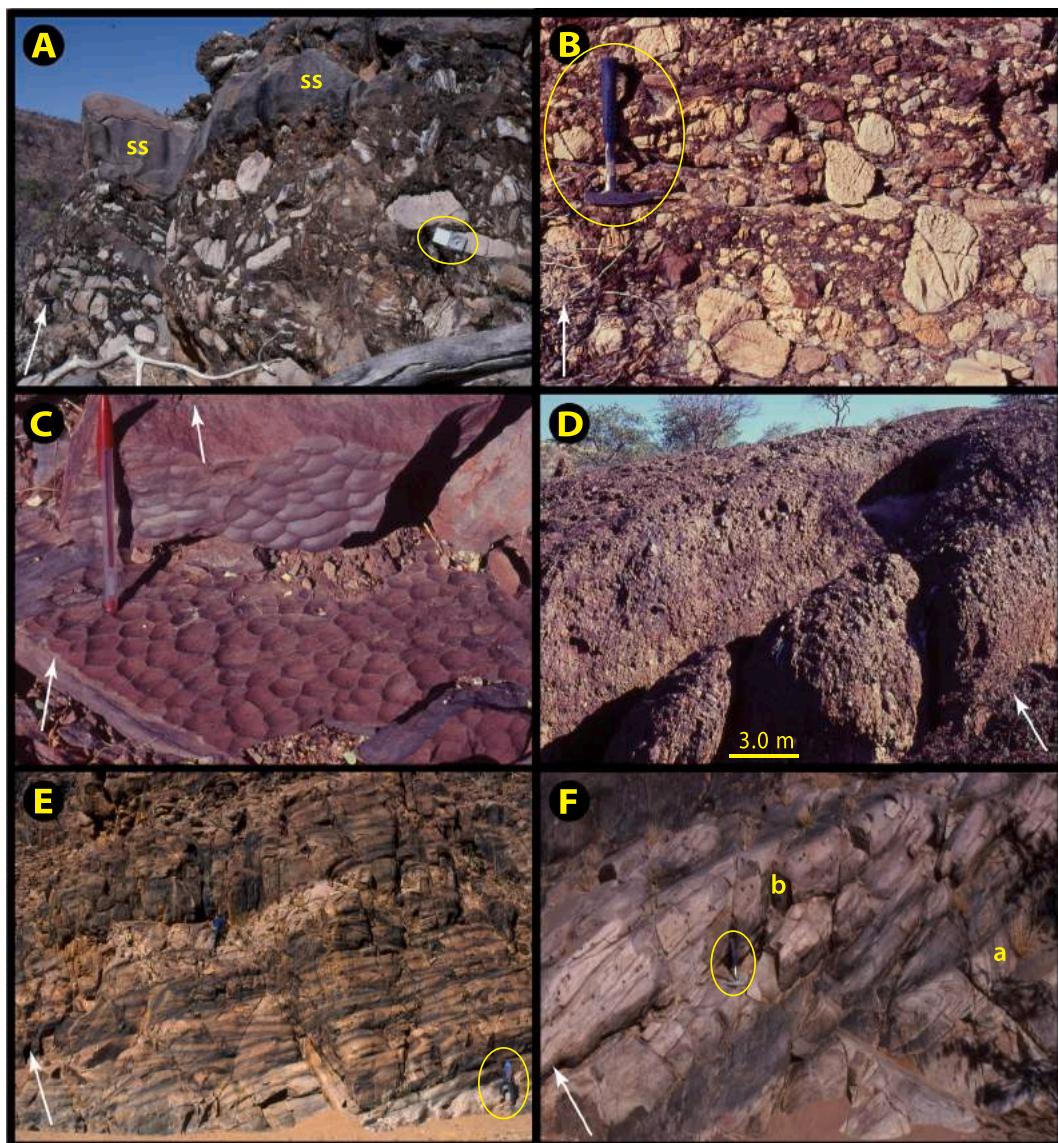


Fig. 83. Images of Welkom Subgroup (Fig. 6C) in western Huab paleo-outlier (Tr6): white arrows indicate stratigraphic younging. (A) Angular dolomite clasts, mostly Keilberg-derived, and sandstone (ss) in Braklaagte Fm at 6–1. Unfolded 16 cm Breithaupt transit (circled) gives scale. (B) Dolomite roundstone-clast conglomerate with red siltstone matrix in Braklaagte Fm at $-20.1507^{\circ}/14.5712^{\circ}$ in 6–1 (P1823, Fig. 85). (C) Small-scale desiccation (?) cracks in Braklaagte Fm argillaceous sandstone at $-20.1506^{\circ}/14.5714^{\circ}$ in 6–1. (D) Basement-clast conglomerate in Braklaagte Fm filling basement incision at $-20.1564^{\circ}/14.5634^{\circ}$ in 6–1 south of P1824 (Fig. 84). (E–F) Meter-scale trough crossbedding in fluvial lithic sandstone of Renosterberg Fm along Sout River at $-20.1601^{\circ}/14.5941^{\circ}$ on farm Welkom 680 (Fig. 70). Geologist (circled) for scale in E. Tilt-corrected foreset azimuths record SE-directed paleoflow (Fig. 85). Note overturned foresets in bed a, and Fe-carbonate concretions (dark spots) in bed b.

terrigenous component is a finer-grained, paralic precursor of the conformably overlying fluvial Renosterberg Fm (Fig. 83E & F), and Braklaagte Fm expands beneath Renosterberg as the disconformity they rest upon cuts down-section (Fig. 85). Hoffman (2020) interprets Braklaagte Fm as the initial foredeep sediments that partially infilled an ancient landscape where karst-mountains of subhorizontal to gently deformed Otavi Group stood above valleys floored by crystalline basement (Huab gneiss). This mid-Ediacaran megakarst landscape, attributed to forebulge uplift, was finally buried by Renosterberg Fm sandstone (Figs. 85 & 70). Together, Otavi and Mulden groups were subsequently tilted 20–50° SE during folding of Achas syncline (Fig. 8A).

South of the Otavi Group cut-off, Braklaagte Fm continues to thicken,

implying basement incision (Figs. 84 & 85). In section P1824, basal Braklaagte Fm is a 9-m-thick debris composed of Keilberg Mb dolomite blocks ≤ 4 m in diameter (Fig. 85). These blocks rest 420 m stratigraphically below their horizon of origin (Fig. 85). Farther S, Braklaagte Fm begins with basement-clast conglomerate (Fig. 83D). The depth of basement incision of ≥ 0.3 km compensates for uplift of the basement surface over the buried rift shoulder (Fig. 85), suggesting that the basement incision may have been graded to the basement surface beyond the rift shoulder.

2.6.3. Huab dip-slope development

From the absence of Tonian strata (Fig. 5), and from offlap–onlap

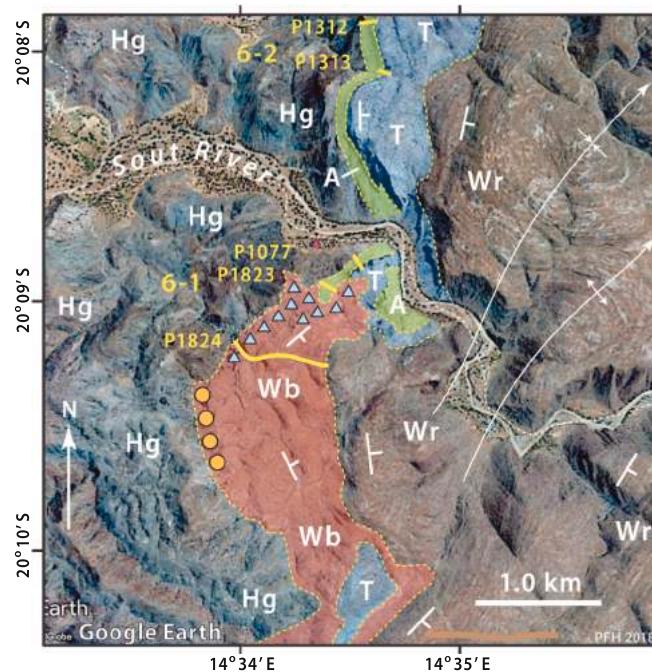


Fig. 84. Annotated satellite image of southwestern terminus of Otavi Group paleo-outlier (Fig. 70) in Tr6, showing locations of columnar sections (Fig. 85). Renosterberg (Mr) and Braklaagte (Mb) formations (Welkom Subgroup) truncate the Abenab (A) and lower Tsumeb (T) subgroups (Otavi Group) at a buttress unconformity incised an additional 0.3 km into Orosirian metamorphic basement (Hg). Blue triangles indicate dolomite-clast breccia (Fig. 83A) and conglomerate (Fig. 83B), derived mainly from the Keilberg Mb. Orange circles indicate basement-clast roundstone conglomerate (Fig. 83D). Small red triangle is a perfect campsite (see field guide SOI S3.9.). Google Earth: Image © 2020 Maxar Technologies.

relations and associated facies changes in the Cryogenian (Fig. 71), we infer the rise and fall of Huab ridge as a paleo-cuesta (Fig. 86A). It was last active in Gruis Fm time, when basement and cover were raised and tilted northward, producing an actively-eroding subaerial dip-slope. We postulate that Huab ridge was the rift shoulder of a S-side-down normal fault (Figs. 86 & 65B) that was part of a regional rift system (Fig. 26), active outboard until Marinoan time (Fig. 40). The stratigraphic geology of Tr6 allows us to suggest the following developmental history of the ridge.

During late Tonian and Sturtian time, the basement of Huab ridge underwent net erosion, resulting in the near absence of pre-Rasthof strata (Fig. 71). The basement was deeply flooded in the Sturtian aftermath, providing accommodation for ≤ 0.35 km of sublittoral Rasthof carbonate aggraded to sea level. The paucity (not absence) of basement detritus in Rasthof Fm is consistent with rapid deglacial inundation and the great thickness of the HST as a consequence of tectonic subsidence accumulation during the 56-Myr-long Sturtian glaciation (Rooney et al., 2015, 2020a).

The basement was then raised in the south and the northward-tilted Rasthof blanket was erosional bevelled by the sub-Gruis Fm disconformity (Figs. 71 & 86). At the foot of the tilted basement surface, physically weak lower Rasthof rhythmite was preferentially eroded, producing a Gruis Fm depocenter near the basement–Rasthof contact (Fig. 71). The planation surface and its Gruis Fm mantle were then lowered evenly along the transect, accommodating the aggradational Omaatjie Fm cycles (Figs. 71 & 86). Omaatjie Fm accommodation (subsidence) is attributable to lithospheric cooling following the cessation of active rifting (R–S, Fig. 71). The youngest preserved Omaatjie cycle (b9) is tentatively interpreted as a carbonate aeolianite associated with glacioeustatic fall at the inception of Marinoan glaciation (Fig. 57).

Due to lowered sea level (Liu and Peltier, 2013) and a thick sea glacier (Tziperman et al., 2012), the OPz including the subcropping Huab ridge was an area of net erosion during the Marinoan snowball. However, the depth of glacial erosion was shallow due to the weak hydrologic cycle (Partin and Sadler, 2016), enabling extensive preservation of cycle b8 (CIE Cn5 recovery leg, Fig. 10D), which is linked in time with Marinoan glacial onset in South Australia (Rose et al., 2012).

OPz was deeply drowned once again in the Marinoan aftermath, creating accommodation for the 0.4-km-thick Maieberg depositional sequence (Fig. 82). An extraordinary degree of carbonate oversaturation is implied by the expanded TST (Keilberg Member) and profuse sea-floor cement in the deepest-water facies (Fig. 82). Anomalous Maieberg accommodation is attributable to thermal subsidence accumulation during prolonged Marinoan glaciation (Hoffman et al., 1998a; Halverson et al., 2002; Prave et al., 2016). Localization of seafloor cement, by analogy with Duurwater moraine and Huab ridge in Tr5 (Fig. 43), may correlate spatially with enhanced vertical mixing at the edge of the platform (Wunsch, 1970).

2.6.4. Highlights from Tr6

Chief highlights are: (1) middle Cryogenian offlap–onlap relations related to Huab rift-shoulder rise and fall; (2) prolific production of aragonite sea-floor cement during the maximum post-Marinoan flooding stage; (3) forebulge-related megakarst landscape formation and burial by foredeep clastics of Welkom Subgroup. Megakarst uplift of Otavi Group was ≥ 1.85 km relative to sea level (Hoffman, 2021a) and was spatially localized at the cusp (syntaxis) where the forelands of Kaoko belt and Northern (Outjo) zone meet at a right angle.

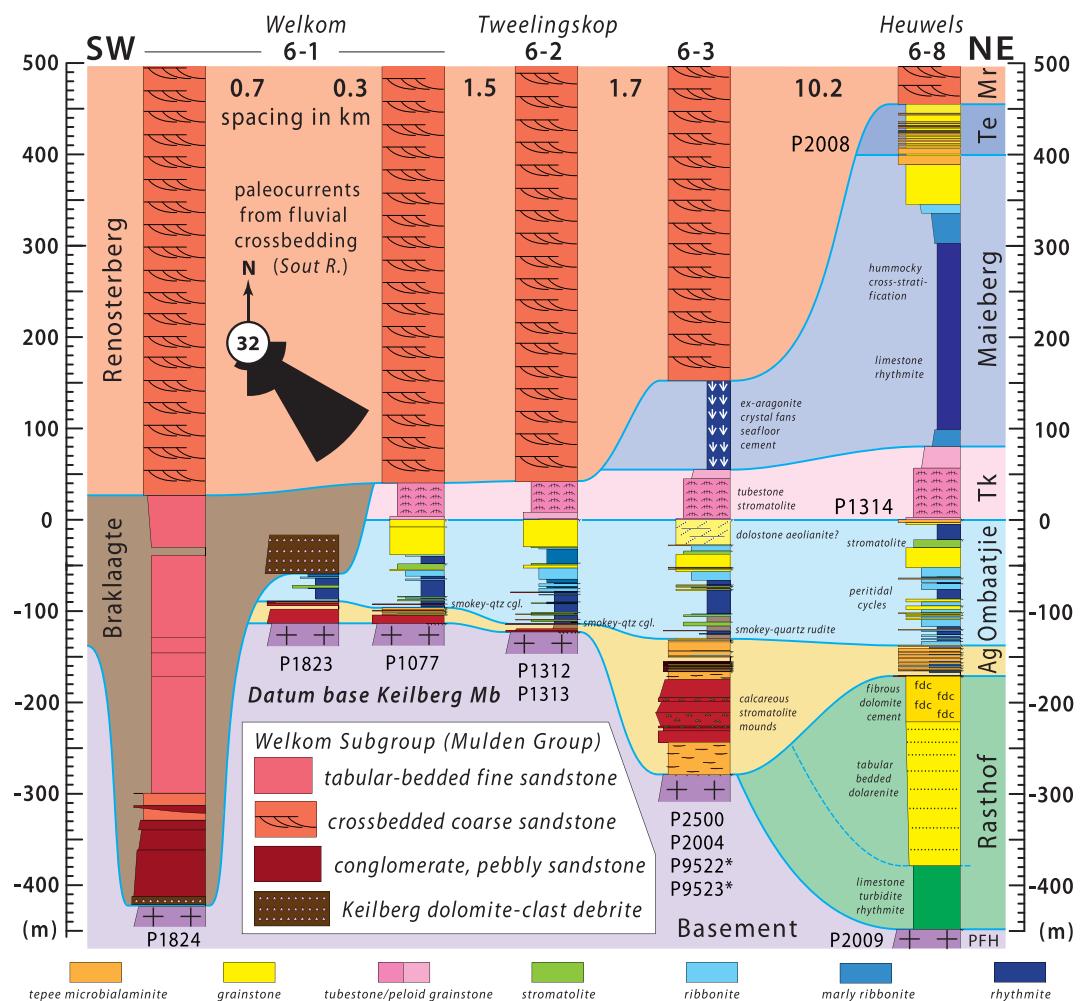


Fig. 85. Cryogenian–Ediacaran columnar sections near southwestern terminus of Otavi Group paleo-outlier in Tr6, where Otavi Group thins from below due to onlap of buried rift-shoulder (Fig. 86) and from above by paleokarst erosion beneath foredeep clastics of Welkom Subgroup (Hoffman, 2021a). Paleokarst valley was progressively infilled by Braklaagte and Renosterberg formations. Basal debris of Braklaagte Fm in P1824 (far left) contains angular blocks derived from Keilberg Mb, which is 420 m higher in the stratigraphic sequence and therefore is the height from which the blocks fell into the paleovalley, assuming little axial transport.

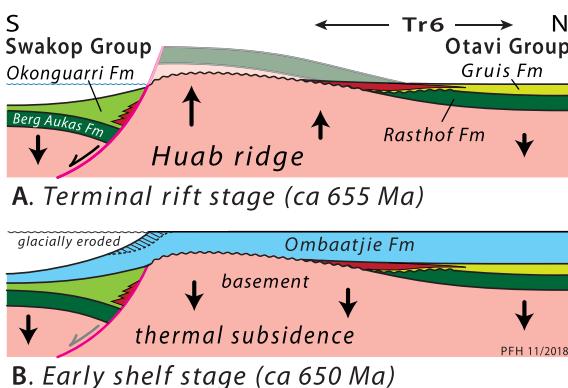


Fig. 86. Schematic development of Huab ridge as (A) an active rift-shoulder uplift eroded to provide (red) proximal Gruis Fm clastics (Figs. 71 & 77), and (B) passively buried by Oombaattjie Fm shallow-marine carbonate cycles (Fig. 71) during post-rift thermal subsidence. Huab paleokarst (Tr6) preserves most of the rift-shoulder dip slope.

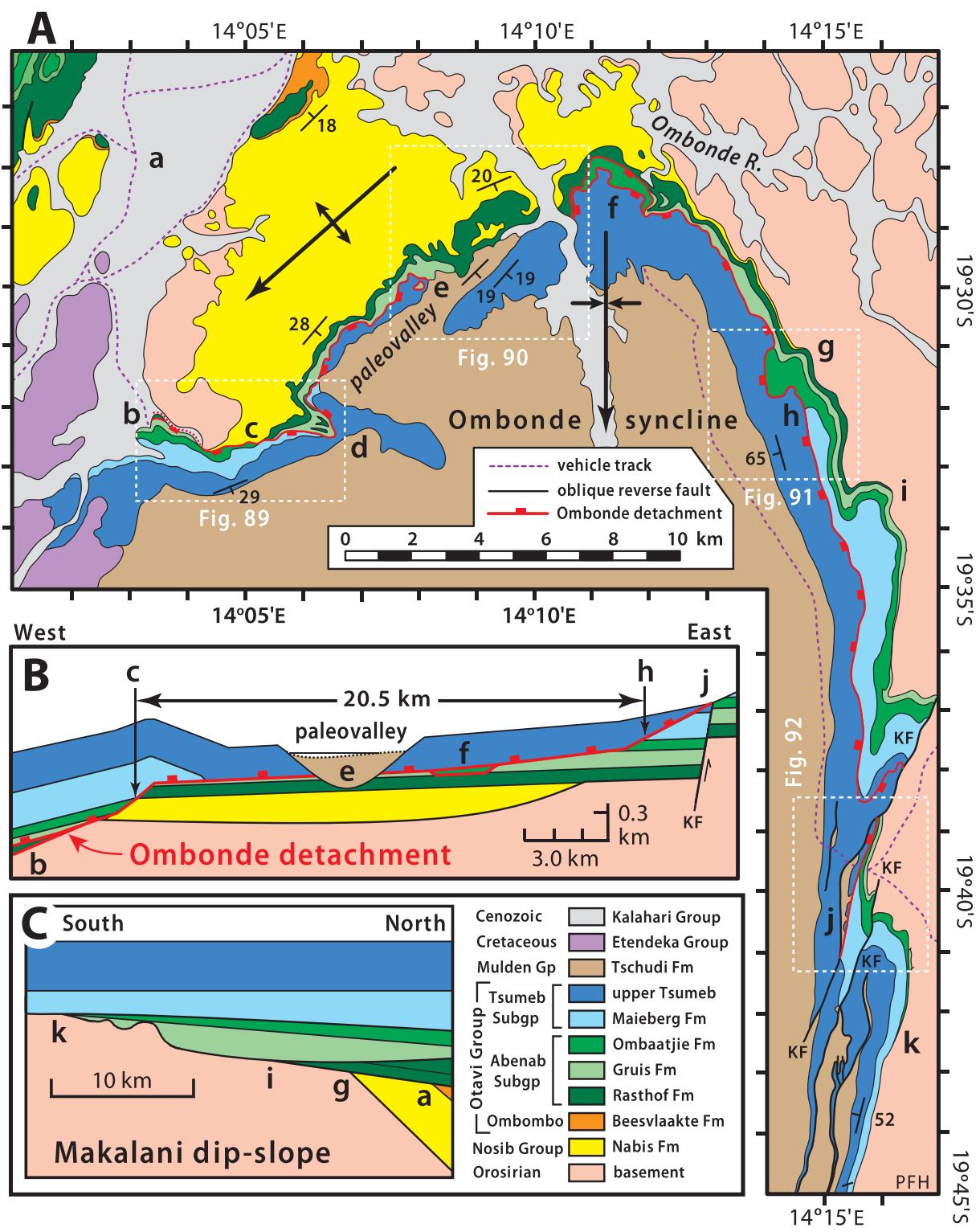
2.7. Transect Tr7 – Omonde (Grootberg) syncline

Between Tr6 and 7, there is a 40 km gap imposed by Early Cretaceous onlap of Kamanjab inlier (Fig. 8B). The separation is not so grave as

might be feared—Otavi Group of Omonde syncline (Fig. 87) is virtually a repetition of stratigraphic and facies relations in Tr6, but associated with a more northerly basement uplift named Makalani ridge (Fig. 5). In addition to S–N offlaps and onlaps of Cryogenian age related to Makalani ridge (Fig. 87C) (Hoffman and Halverson, 2008), Omonde syncline features a map-scale, low-angle, normal-sense, W-directed, detachment fault of Ediacaran age (Fig. 87B) (Hoffman and Hartz, 1999; Hoffman et al., 2016b; Hoffman, 2021a). Omonde detachment is folded along with autochthonous cover and basement in a S-plunging V-shaped syncline (Fig. 87A).

Omonde syncline (Miller, 2008b, p. 13–226, formerly ‘Grootberg syncline’ of Hedberg, 1979) is a thick-skinned structure with a steeply-dipping ($50\text{--}70^\circ$) E limb and a more gentle W limb that crests in a broad SW-plunging anticline before disappearing beneath Etendeka flood basalt (Fig. 8A). At the southern limit of exposure, again defined by Cretaceous onlap, the syncline holds ~5 km of Tschudi Fm (Fig. 6D) subfeldspathic arenite with basal siltstone. Orientations of meter-scale crossbeds ($n = 64$) in these compositionally immature fluvial arenites indicate SE-directed transport (Hoffman and Halverson, 2008), similar to Renosterberg Fm in Tr6, with which Tsudi Fm in Tr7 is easily correlated.

Omonde detachment (Hoffman and Hartz, 1999) is a brittle, low-angle, normal-sense (i.e. younger over older) fault that angles down across the entire Otavi Group in its footwall from E to W across the



(caption on next page)

Fig. 87. Ombonde syncline (Grootberg syncline of Frets, 1969), an upright S-plunging thick-skinned structure in Tr7 (Fig. 8B), which exposes the folded Ombonde detachment (red line with teeth on hangingwall), a brittle low-angle normal fault that ramps stratigraphically downward from E to W in both its footwall and hangingwall (Hoffman and Hartz, 1999; Hoffman et al., 2016b; Hoffman, 2021a). 20 km of westward displacement of detachment hangingwall occurred after the upper Tsumeb Subgroup and before the basal Mulden Group were deposited. (A) Geological map showing vehicle tracks (dashed purple lines), areas of Figs. 89–92 (dashed white rectangles) and locations noted in the text (a–k). Abbreviation: KF, *en echelon* set of dextral-oblique subvertical reverse faults. (B) Projected W–E cross-section, restored prior to folding, showing Ombonde detachment in the plane of slip. Minimum age of detachment is constrained by sub-Mulden Group incision at e, and its maximum age by hangingwall strata at j. (C) Projected S–N stratigraphic section showing progressive N-to-S onlap of Makalani dip-slope (Figs. 5 & 26). Erosional cut-offs a, h, j and l are located on map (A) and document intermittent uplift, dip-slope rotation and erosion inferentially related to intermittent rift-shoulder uplift analogous to and synchronous with Huab ridge (Fig. 86). In B, matching footwall and hangingwall stratigraphic cut-offs against Ombonde detachment (e.g., c and h) provide mutually-consistent estimates of W-directed slip of ~20.5 km on detachment surface prior to folding, assuming that the observed 16.4 km of slip was shortened 20% by folding. Locations: a, erosional cut-off of basal Beesvlakte Fm; b, Rasthof Fm horse within Ombonde detachment; c, basal Maieberg Fm hanging-wall cut-off against detachment; d, paired hanging-wall cut-offs of basal Elandshoek Fm against antiformally-folded detachment surface, indicating a S–N cut-off line and primary W dip of detachment surface relative to undeformed strata; e, erosional truncation of detachment by lower Mulden Group paleovalley as shown in B, constraining the age of slip on detachment. Paleovalley at e is filled by dolomite+chert-clast conglomerate (Fig. 210B), derived from Tsumeb Subgroup with which Mulden Group conglomerate was co-rotated during folding; f, Ombaatjie Fm horse within Ombonde detachment; g, erosional cut-off of basal Nabis Fm; h, basal Maieberg Fm footwall cut-off against detachment, contiguous with c before slip on detachment surface as shown in B; i, erosional cut-off of basal Rasthof Fm; j, paleo-outcrop of detachment surface at top of Tsumeb Subgroup, including small-scale paleovalleys incised across the detachment surface and filled by lower Mulden Group clastics (Fig. 92); k, erosional cut-off of basal Ombaatjie Fm across a set of small-scale paleo-troughs of possible Marinoan subglacial origin (Fig. 88).

syncline (Fig. 87A & B). The fault is a brittle surface, recrystallized under metamorphic conditions during thick-skinned folding, where 0.4 km of Otavi or Nosib group strata are missing, at whatever stratigraphic level (Fig. 87B). The fault has an exposed strike length of 51 km (Fig. 87A), or 22 km in the direction of tectonic transport (Fig. 87B). The fault surface

is divided into ramps and flats—ramps where crossing rheologically strong layers (Hüttenberg, Ombaatjie and Rasthof formations) and flats within weak ones (Maieberg and Gruis formations). The average cutoff angle of the fault relative to stratigraphic layering is 1.1°. The relative westward displacement of the hangingwall, based on multiple matching

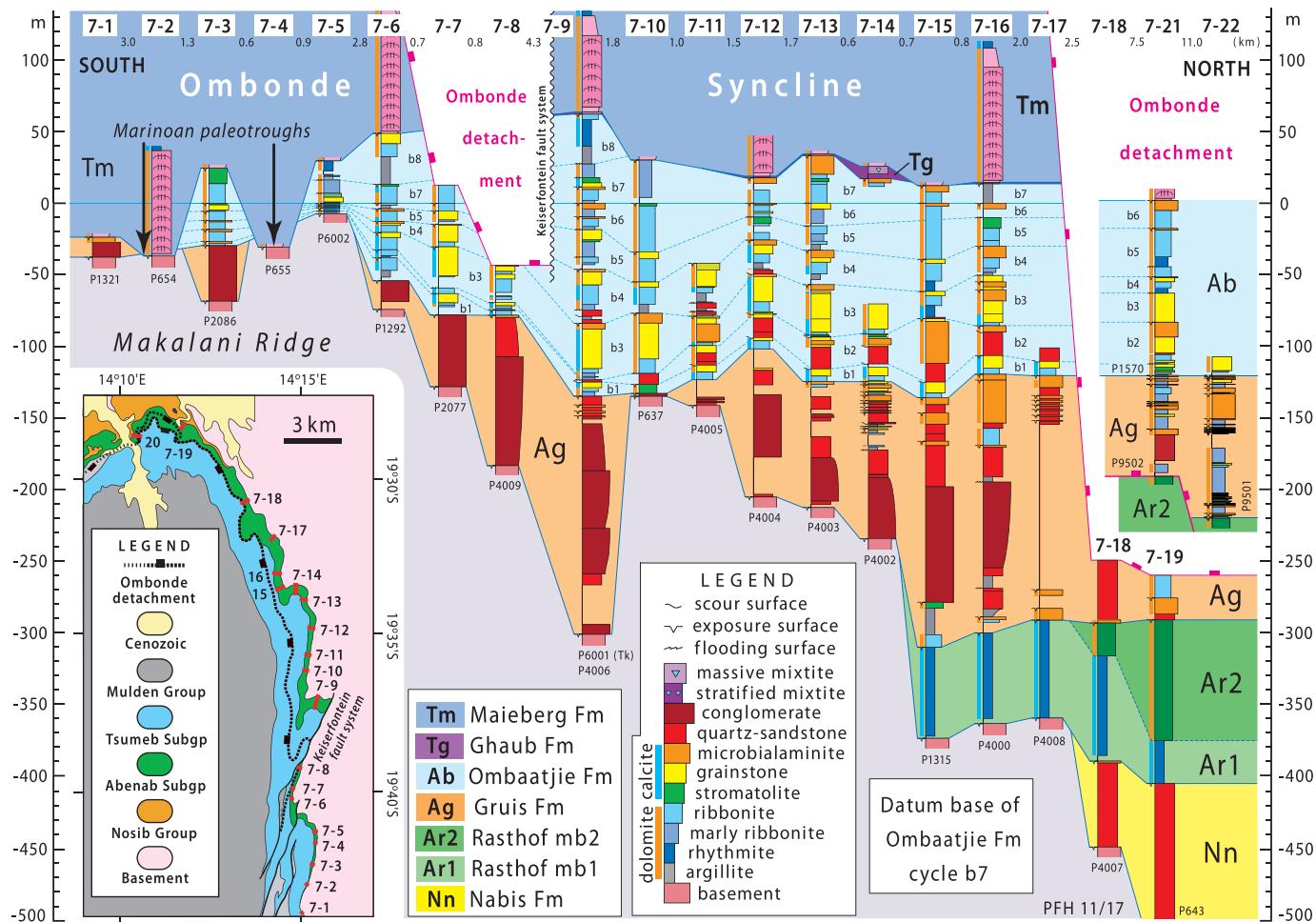


Fig. 88. Cryogenian and earliest Ediacaran columnar sections from Ombonde syncline (Tr7): see inset map for section locations 7–1–20, Fig. 89 for 7–21 and Fig. 96 for 7–22. Note offlaps of Nabis Fm (Nn) between 7 and 17–18, Rasthof Fm (Ar) between 7 and 14–15, and Gruis Fm (Ag) between 7 and 10–11 and 7–5–7. Offlaps are related to uplift, rotation (N-side-down) and erosion of Makalani dip-slope, an inferred pre-Ombaatjie Fm rift shoulder (Fig. 26). Truncation of Ombaatjie Fm (Ab) at 7–1, 2 and 4 is attributed to Marinoan glacial erosion. Missing strata related to Ombonde detachment are indicated at 7–7–8, 7–18–19 and 7–21–22. Proximal fanglomerate in Gruis Fm is analogous to 6–3 in Huab paleokarst (Figs. 71 & 86).

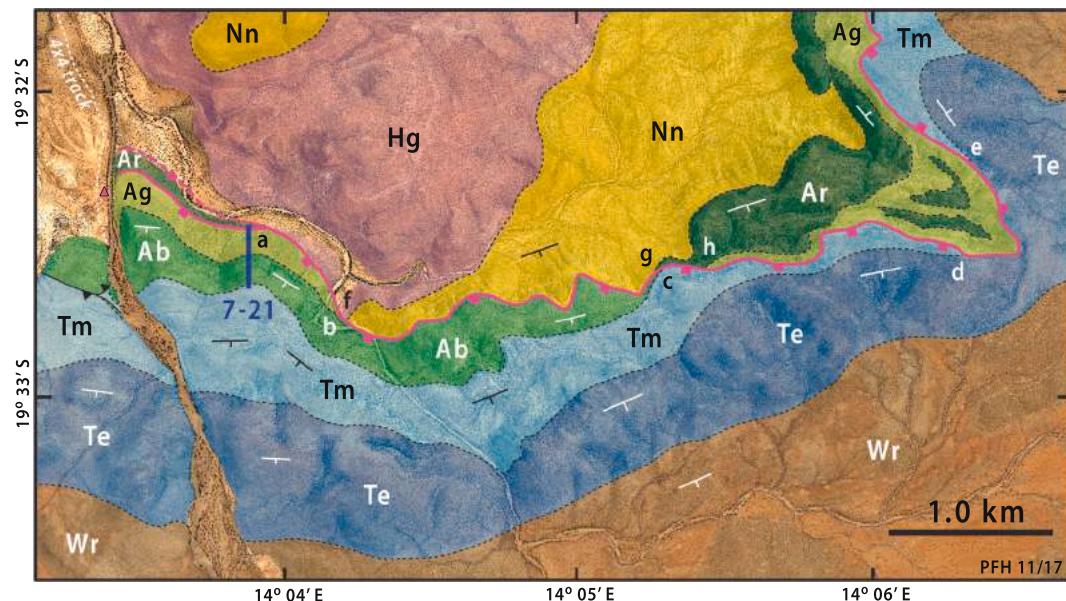


Fig. 89. Annotated satellite image of W Ombonde syncline (Tr7) (Fig. 87A). Rock units: Hg, Orosirian basement; Nn, Nabis Fm; Ar, Rasthof Fm; Ag, Gruis Fm; Ab, Ombaatjie Fm; Tm, Maieberg Fm; Te, Elandshoek Fm; Mr, Renosterberg Fm. Critical field relations: a, branch line of Rasthof horse; b, basal Ombaatjie Fm cut-off in detachment hangingwall; c, basal Maieberg Fm cut-off in detachment hangingwall; d and e, basal Elandshoek Fm cut-offs in detachment hangingwall; f, basal Nabis Fm cut-off in detachment footwall; g, basal Rasthof Fm cut-off in detachment footwall; h, basal Gruis Fm cut-off in detachment footwall. Close spacing of stratigraphic cut-offs reflects strike parallel to primary dip direction of detachment. For access to this segment see SOI S3.10.2. Google Earth: Image © 2020 Maxar Technologies.

stratigraphic cutoffs, is 20–22 km (Hoffman et al., 2016b). Values of 1.3° and 15–18 km (Hoffman and Hartz, 1999) are uncorrected for an estimated 25% W–E shortening by folding. Critically, paleovalleys filled by dolomite-chert-clast debris, conglomerate and terrigenous clastics of Mulden Group are incised cleanly across the fault surface in areas e and k

(Fig. 87A & B). They constrain the age of displacement as pre-basal Mulden Group, but post-terminal Otavi Group. This is identical to megakarst sculpting in Tr5 (Hoffman, 2021a), allowing for Mulden Group diachroneity as a cratonward younging foredeep.

The W-directed mass slide in Tr7, megakarst formation in Tr6, and

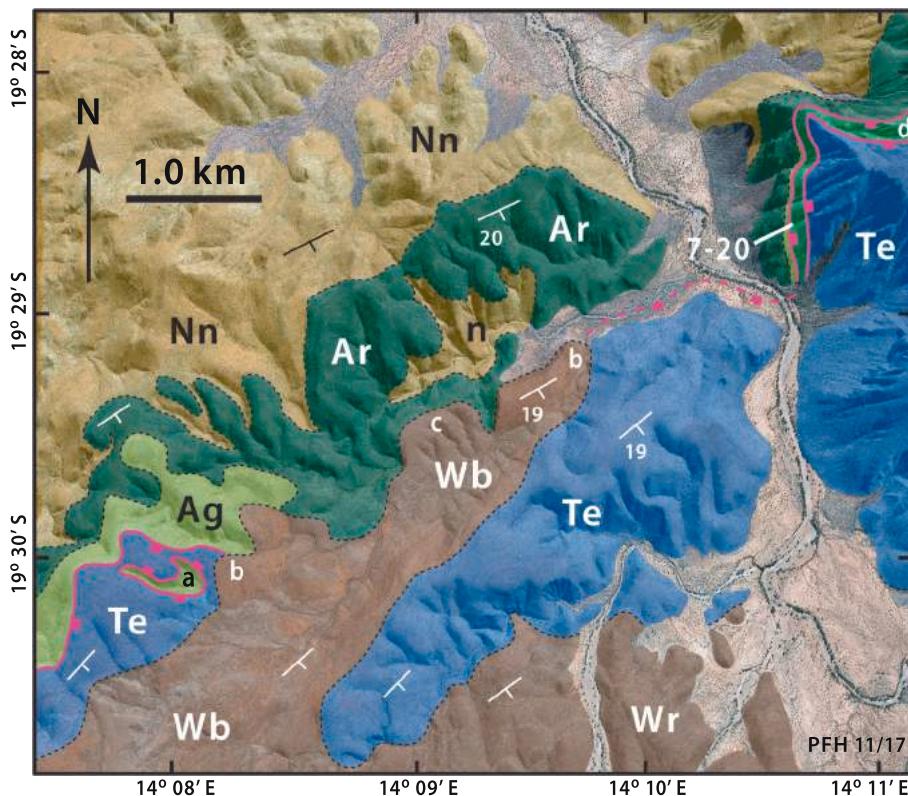


Fig. 90. Annotated satellite image of NW Ombonde syncline (Tr7) (Fig. 87A) where detachment (red lines with bars on hangingwall) is incised by sub-Mulden Group (Wb, Braklagte Fm) paleovalley, critically constraining the timing of detachment slip. See Fig. 89 caption for rock units. Critical field relations: a, erosional window in detachment exposing footwall Gruis Fm; b, detachment erosionally truncated on walls of sub-Renosterberg paleovalley (Fig. 87B); c, floor of sub-Renosterberg Fm paleovalley eroded down to lower Rasthof Fm; d, Ombaatjie Fm horse bounded by detachments that excise Gruis Fm (below) and Maieberg Fm (above). Google Earth: Image © 2020 Maxar Technologies.

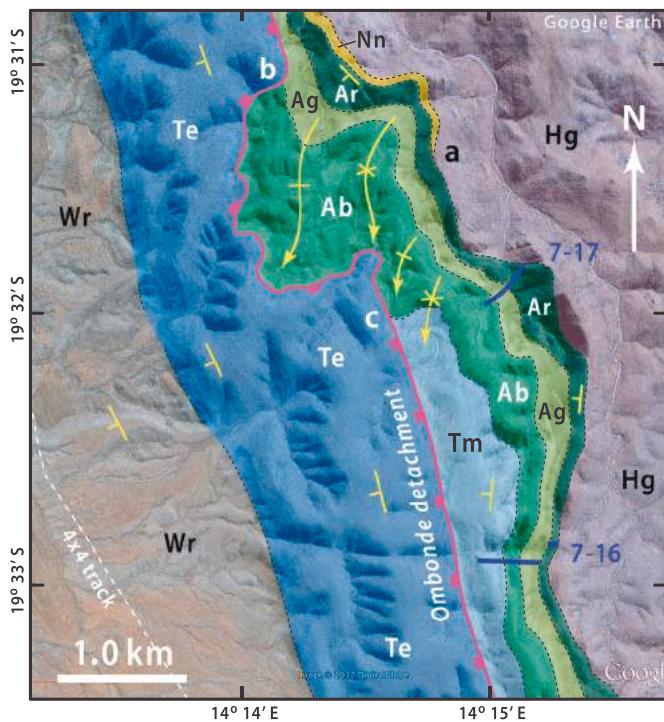


Fig. 91. Annotated satellite image of NE segment of Ombonde syncline (Tr7) (Fig. 87A) documenting footwall cut-offs of basal Ombaatjie and Maieberg formations (hangingwall cut-offs in Fig. 89). See Fig. 89 caption for rock units. Critical field relations: a, erosional truncation of basal Nabis Fm by Rasthof Fm; b, basal Ombaatjie Fm cut-off in detachment footwall; c, basal Maieberg Fm cut-off in detachment footwall. Footwall cut-offs at b and c are matched by hangingwall cut-offs b and c in Fig. 89. Google Earth: Image © 2020 Maxar Technologies.

SE-directed mass slides in Tr4 (Figs. 31 & 46), are viewed as different manifestations of forebulge uplift and plate-scale collapse into collisional foredeeps bordering Kaoko belt and Northern zone (Hoffman, 2021a). Forebulge uplift of ≥ 1.85 km relative to sea level in Tr6 (Hoffman, 2021a) greatly exceeds characteristic forebulge amplitudes of ca 0.5 km (Turcotte and Schubert, 1982; Tensi et al., 2006), and is attributed to a young weak plate (35–50 Myr old at 600 Ma) and the cusp geometry of Congo plate subduction where Kaoko belt and Northern zone meet at a right angle (Hoffman, 2021a, b). This interpretation assumes that subduction beneath Kaoko belt and Northern zone was contemporaneous, and that Congo craton was the subducting plate in both belts as discussed in 1.2..

Cryogenian offlaps and onlaps related to Makalani dip-slope (Fig. 87C) are best observed in the footwall of the detachment on the E-limb of Ombonde syncline (Figs. 87A & 88). Key stratigraphic cut-offs and facies changes are described below and documented in Figs. 89–92. A field guide to the area of sections 7–9 and 10 (Fig. 88) is given in SOI S3.10. and annotated satellite image Fig. S22.

2.7.1. Late Tonian of Tr7

Around the northern closure of Ombonde syncline, a S-tapered wedge of crossbedded, sub-feldspathic arenite appears between Otavi Group and basement (Fig. 87A). Nabis Fm of Nosib Group (Fig. 6D) forms a regionally extensive sheet of alluvial arenite and rudite deposited by southward-flowing drainages (Miller, 2008b, p. 13–14–16). It conformably underlies Beesvlakte Fm (Fig. 6D), the basal unit of Ombombo Subgroup in IPz (Fig. 5). The S limit of Beesvlakte Fm is near location a (Fig. 87A & C), while that of Nabis Fm is 5.5 km (3' of latitude) farther south at location g on the E limb of Ombonde syncline (Fig. 87A). Stratigraphic geometry implies that Nabis and Beesvlakte formations were tilted to NNW and erosionally beveled beneath Rasthof Fm

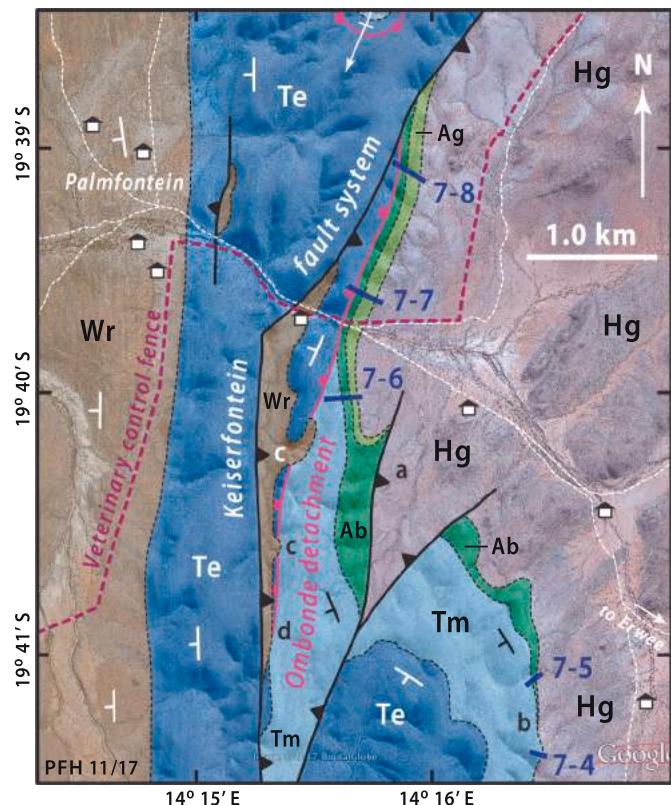


Fig. 92. Annotated satellite image of a SE segment of Ombonde syncline (Tr7) (Fig. 87A) where detachment reaches the top of Otavi Group. See Fig. 89 caption for rock units. Keiserfontein fault system is a relatively late, steeply dipping, flower structure resolving dextral transpression. Critical field relations: a, interpolated erosional cut-off of basal Gruis Fm by Ombaatjie Fm; b, erosional cut-off of basal Ombaatjie Fm by Maieberg Fm; c, small paleovalleys filled by Renosterberg Fm incised across Ombonde detachment; d, intersection of detachment with top of Elandshoek Fm in hangingwall, essentially the syn-detachment erosion surface. Google Earth: Image © 2020 Maxar Technologies.

(Fig. 87C). Structural rotation and erosion likely occurred during Sturtian glaciation, consistent with the absence of Chuos Fm in Tr7.

2.7.2. Cryogenian of Tr7

Rasthof Fm is erosionally truncated by Gruis Fm, which cuts progressively down section from N to S (Fig. 88). The Rasthof tip is at location i (Fig. 87A & C). Rasthof Fm itself is noteworthy for an expanded (≤ 70 m) lower member (Ar1), consisting of parallel-laminated dolomite rhythmite hosting calcitic turbidites (Fig. 93A–D). North of section 7–18, Ar1 is overlain by middle Rasthof (Ar2) lobate stromatolite (Fig. 69C) (Pruss et al., 2010). At 8–1 in Tr8, 20 km N of i, upper Rasthof grainstone (Ar3) signals a nearly complete Rasthof section. Estimating average Rasthof Fm thickness as 130 m yields an angular discordance of 0.4° between Rasthof and Gruis formations (Fig. 87C).

Gruis Fm directly overlies basement south of 7–14 and cobble conglomerate and pebbly feldspathic sandstone (Fig. 93E & F) of basement derivation are major components of Gruis Fm (Fig. 88) as far north as 7–16. Variation in Gruis Fm thickness indicates ≥ 165 m of local relief on the basement surface (Fig. 88). Within the coarse clastics are numerous horizons of sandy dolomite, characterized by tepees and locally by sand-filled mudcracks (Fig. 94A & B). North of Ombonde syncline, coarse clastics disappear and beds of tepee dolomite cap meter-scale coastal marine cycles containing dolomite ribbonite and marly ribbonite (7–22 in Fig. 88). The alluvial to paralic facies transition occurs over a S–N distance of 10 km.

Ombaatjie Fm is an aggradational stack of exclusively marine,

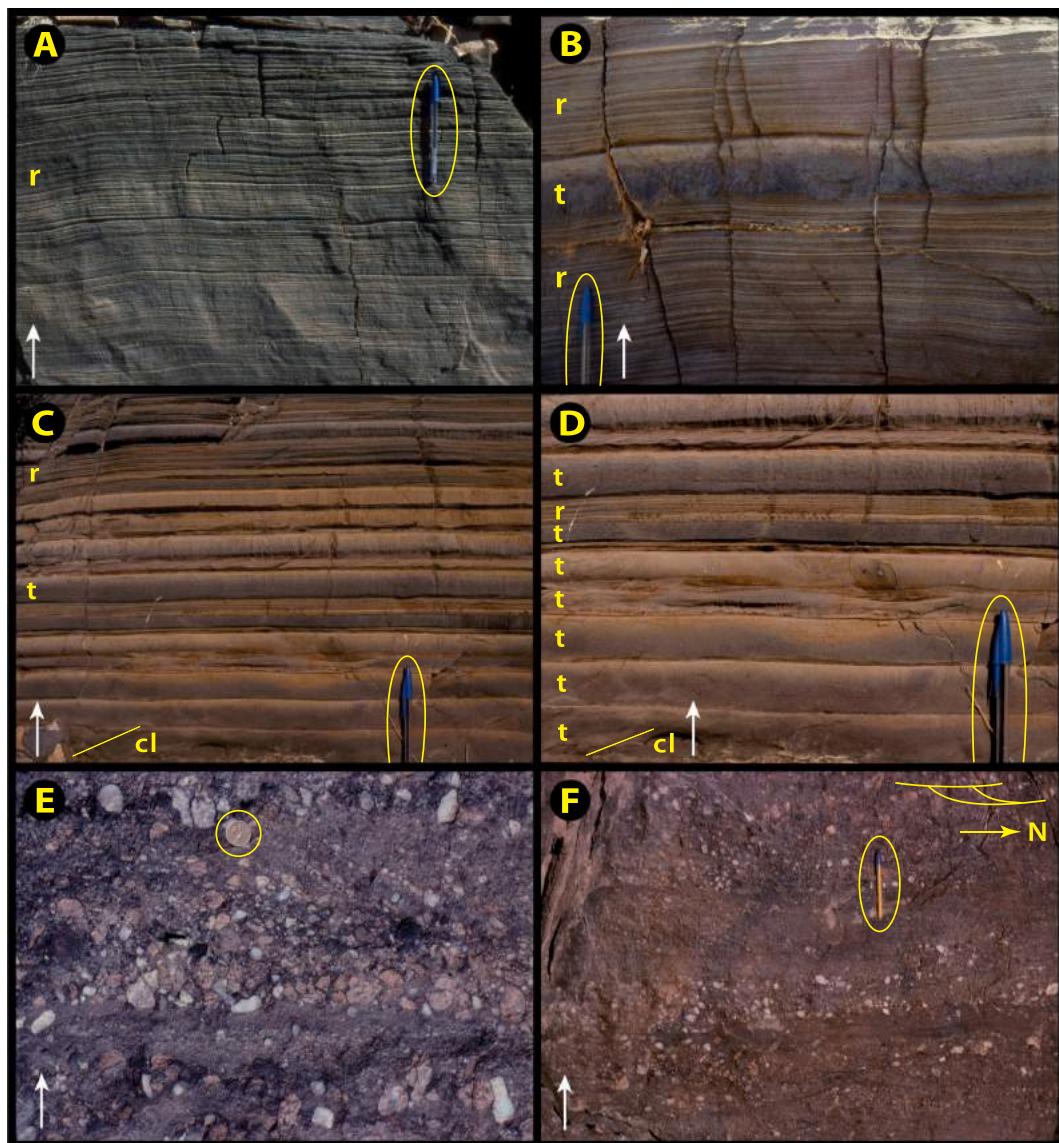


Fig. 93. Images of Rasthof and Gruis formations in Ombonde syncline (Tr7): white arrows indicate stratigraphic younging. (A–D) Parallel laminated abiotic rhythmite (r) and cm-scale turbidites (t) in lower Rasthof Fm (Ar1) cap-carbonate sequence in 7–19 (Fig. 88) at $-19.4704^{\circ}/14.1993^{\circ}$. Mb Ar1 thickness increases with turbidite fraction. Note partial dolomitization (pale buff) after calcite (dark grey), selective for finer-grained (formerly more organic-rich?) upper parts of graded turbidite units. Lateral variation in rhythmite lamina thickness is partly related to patchy dolomitization and consequent heterogeneous strain. Tectonic cleavage orientation indicated by inclined lines (cl). (E–F) Basement-derived feldspathic sandstone and conglomerate in middle Gruis Fm at $-19.6131^{\circ}/14.2734^{\circ}$ in 7–9 (Figs. 88 & S22). Note crossbedding (current bedding) indicating left-to-right (N-directed) paleocurrents (indicated schematically in F) in a high-gradient fluvial flow regime related to Gruis-age rotational uplift and erosion of Makalani ridge (Figs. 5 & 26).

decameter-scale parasequences, most of which are separated by non-karstic subaerial exposure surfaces (Fig. 88). The lower parasequences (b1–4) are richer in grainstone and limestone, while the upper ones are richer in ribbonite and dolomite (Fig. 88). In 7–9, as in Tr6, cycle b7 hosts the descending arm of Trezona CIE Cn5 (Fig. 10D) and cycle b8 the nadir (Fig. S23). In section 7–5, b1 directly overlies the basement and beds of well-sorted, even-textured, quartzarenite of marine origin are prominent in the lower parts of cycles b2 and b4 (Fig. 94C & D). The appearance of quartzarenite in the lower Ombaatjie Fm of Ombonde syncline suggests that basement remained emergent on Makalani ridge for a few Myr after the rift-to-shelf transition (Halverson et al., 2002). On the other hand, its specific occurrence in b2 and b4, if truly correlative (Fig. 88), raises the possibility of local structural reactivation at those times. However, direct evidence of reactivation in the form of intra-Ombaatjie Fm unconformities has not been observed.

Marinoan carbonate diamictite (Ghaub Fm) occurs in five sections

(7–9, 12–14, 16), but in only one is its thickness > 1.0 m (6.0 m in 7–14). Ghaub Fm invariably has a sharp erosive contact with underlying Ombaatjie Fm and is conformably draped by Keilberg Mb cap dolomite (Fig. 88). Ghaub diamictite is generally massive but 0.7 m of stratified diamictite occurs in 7–12. No diamictite occurs in sections 7–1–6, where the Marinoan disconformity variably overlies Gruis Fm (7–1), basement (7–2 and 4), or upper Ombaatjie Fm (7–3 and 5–6). The disconformity in those areas is a subglacial surface with ≤ 60 m of stratigraphic relief (Fig. 88).

2.7.3. Early Ediacaran of Tr7

Regionally, Keilberg cap dolomite thickness is inversely correlated with Ghaub diamictite thickness (Fig. 95) and Ombonde syncline is no exception. In Tr7, Keilberg thickness averages 78 m in sections 7–2, 6, 9 and 16 (Fig. 88). As in cozonial Tr5 and 6, Keilberg Mb is dominated by tubestome stromatolite (Fig. 94E & S23), with a basal 1–3-m-thick unit of

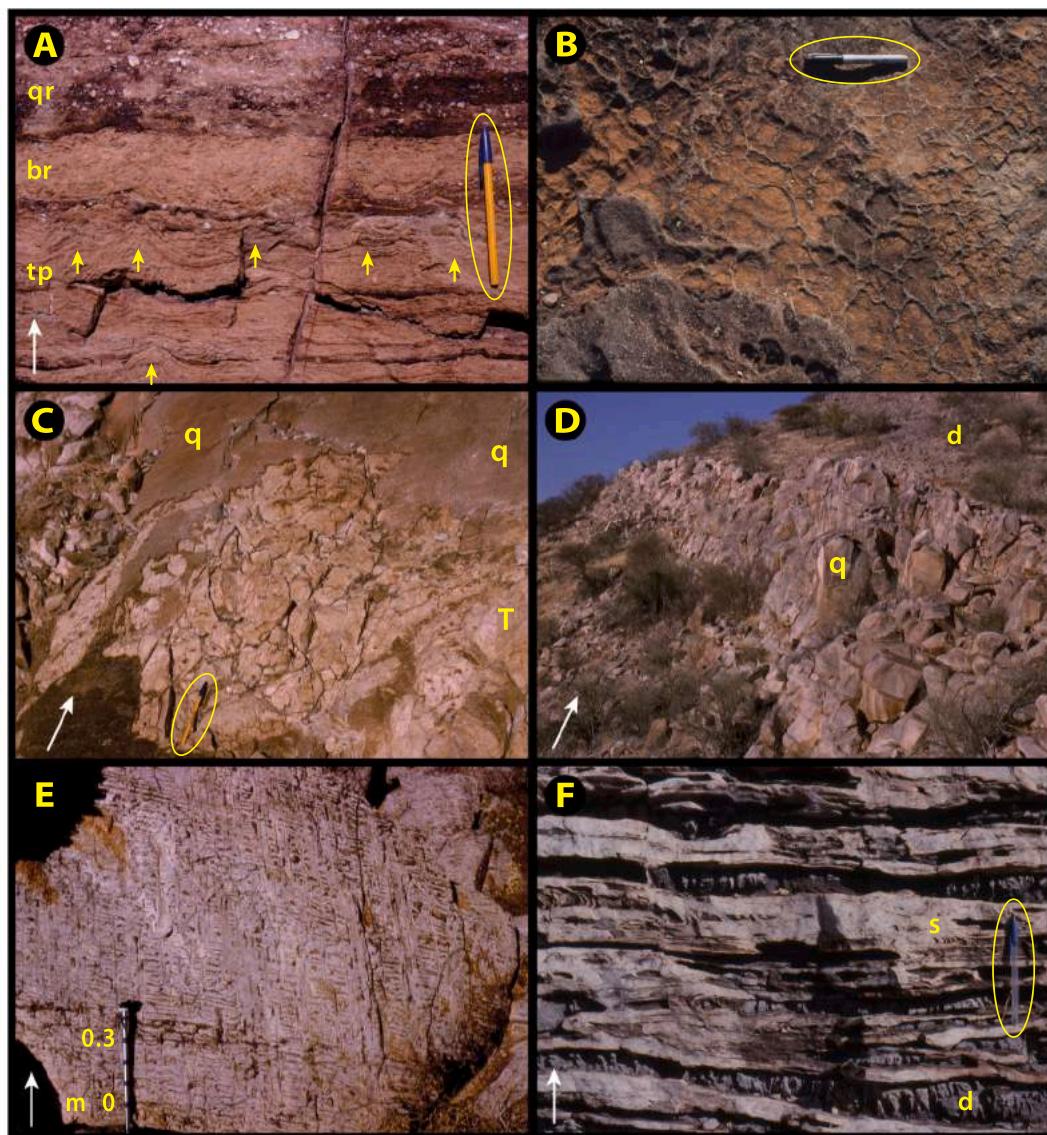


Fig. 94. Images of sedimentary features in Ombonde syncline (Tr7): white arrows indicate stratigraphic younging. (A-B) upper Gruis Fm at $-19.6134^{\circ}/14.2742^{\circ}$ in 7–9 (Fig. 88): (A) interstratified quartz-pebble conglomerate (qr), dolomite microbialaminite with polygonal tepee structures indicated by arrows (tp), and dolomite intraclast conglomerate composed of reworked tepee breccia clasts (br); (B) bedding surface of mudcracks in tan dolomicrite filled by quartz-arenite. (C-D) lower Ombaatjie Fm cycle b2 at 7–12–17 (Fig. 88): (C) *Tungussia*-type dolomite stromatolites (T) in marine quartz-arenite (q) at $-19.5588^{\circ}/14.2543^{\circ}$ in 7–15; (D) marine quartz-arenite (q) incursion into peritidal dolomite (d) at $-19.5584^{\circ}/14.2599^{\circ}$ in 7–14, suggesting reactivation of Makalani ridge or residual topography. (E) Geoplumb micritic tube structures (parallel to monopod) in dolomite microbialaminite of Keilberg Mb at $-19.6662^{\circ}/14.2594^{\circ}$ in 7–6 (Figs. 88 & 92); (F) Heavily-silicified dolomite ribbonite (d, dolomite; s, chert) in Elandshoek Fm (detachment hangingwall) near $-19.5691^{\circ}/14.2506^{\circ}$ in 7–15.

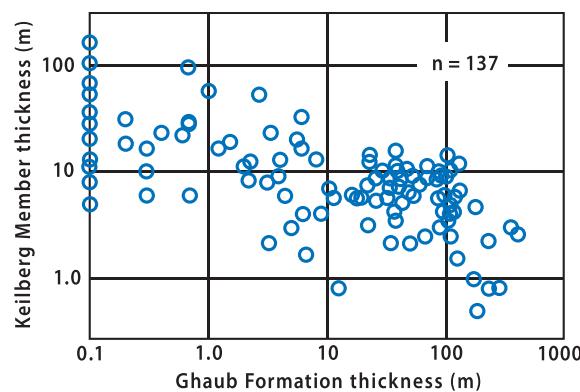


Fig. 95. Inverse correlation between thickness (note double log scales) of Marinoan glacial-periglacial Ghaub Fm and cap dolomite (Keilberg Mb) at 137 locations in all transects. Zero-thickness Ghaub sections are arbitrarily plotted at 0.1 m because zero is a non-existent value in a log scale. Proximal foreslope values are at lower right and outer platform values are at upper left.

low-angle cross-stratified dolopelarenite. The entire Maieberg Fm is 239 m thick in 7–2, where the normally calcitic middle member (Tm2) is dolomitized.

The sequence boundary at the top of the Maieberg Fm is overlain by an estimated 0.4–1.1 km of shallow-marine cyclic dolomite of early Ediacaran Elandschoek and Hüttenberg formations (Fig. 5). Authigenic chert (Fig. 94F) is prominent in these units, concentrated in but not limited to stromatolite and grainstone lithologies. South of latitude 19°39'S, where Tsumeb Subgroup is not attenuated by Ombonde detachment, erosion beneath the sub-Mulden Group disconformity appears to have removed much of Hüttenberg Fm. Consequently, we do not have a complete Tsumeb Subgroup section from Ombonde syncline.

Ombonde syncline provides our only transect of the Makalani dip-slope (Fig. 8B). Analogous stratigraphic relations may exist on the NE side of Kamanjab inlier (Hedberg, 1979), but extensive surficial calcrete seriously hinders stratigraphic investigation of that area.

2.7.4. Makalani dip-slope development

Makalani dip-slope (Fig. 88) was presumably non-existent when rivers that flowed towards it from the north deposited the Nabis Fm. It arose when Nabis Fm and conformably overlying Beesvlakte Fm were tilted northward and erosively beveled during Sturtian glaciation. Net glacial erosion is inferred from absent Sturtian glacial deposits. The beveled surface is the floor on which postglacial Rasthof Fm HST was deposited. Lack of terrigenous input implies rapid and deep postglacial marine flooding.

Renewed rotation of Makalani dip-slope produced a wedge of basement-derived alluvial fanglomerate and sandstone in middle Gruis Fm. This terrestrial wedge onlaps a rugged basement surface, and tapers northward into coastal marine marl and carbonate over a distance of 30 km. The narrow alluvial apron reflects the small drainage area of Makalani ridge, limited southward by an inferred S-side-down normal fault (Fig. 5). Makalani dip-slope records three offlap–onlap cycles (Fig. 88): Nabis–Rasthof, Rasthof–Gruis and Gruis–Ombaatjie. The first cycle was broadly coeval with antithetic Toekoms subbasin of Tr1 (Fig. 26). It was not evident in Tr6 (Fig. 71), where no pre-Sturtian cover is preserved.

Makalani ridge was less active after early Ombaatjie time. Broad regional subsidence accommodated shallow-marine carbonate accumulation, interrupted only by Marinoan glaciation until orogenic platform destruction. Southward taper of Ombaatjie Fm cycles b1–6 between 7 and 9 and 5 (Fig. 88) implies >125 m of differential subsidence over a distance of only 7 km. Southward of 7–9, marine quartzarenite beds occur in Ombaatjie cycles b2 and b4 (Fig. 88).

2.7.5. Ombonde detachment

This W-directed, low-angle, normal-sense, brittle fault is temporally associated with the Otavi–Mulden group transition and was inferentially triggered by foredeep flexure during incipient arc–continent collision in Kaoko orogen (Hoffman and Hartz, 1999; Hoffman et al., 2016b; Hoffman, 2021a). The structure predates all contractional deformation including the folding of Ombonde syncline, and is genetically distinct from normal-sense detachment structures associated with collapse of tectonically thickened crust (e.g., Wernicke, 1981; Burchfiel and Royden, 1985). The timing of Ombonde detachment and mechanical considerations (i.e., large normal stress on a low-angle fault plane) favour a gravitational origin as a (fast and/or slow) submarine mass–slide (e.g., Butler and Paton, 2010; Handwerger et al., 2016). Many such large low-angle detachments are observed in seismic profiles of modern continental margins (Masson et al., 2006), but few map-scale examples are known from ancient margins (Woodcock, 1979). Direct proof of a gravitational (i.e., non-rooted) origin for Ombonde detachment is precluded by down-slope Cretaceous cover (Fig. 8A).

Ombonde detachment was discovered in 1995 by Tony Prave and Dawn Sumner (Table 3), who observed a 400-m stratigraphic omission on the eastern limb of Ombonde syncline (Fig. 91). Even more illuminating are the sub-Mulden paleovalley (e in Figs. 87A–B & 90) that constrains the age of displacement, and the western ramp (Fig. 87A & 89) that parallels the inferred transport direction. A field guide to the western ramp is given in SOI S3.10, and an annotated satellite image is given in Fig. 89. In a 5-km-long stretch (along an elephant path), the detachment ramp cuts off basal Nabis, Rasthof and Gruis formations in its footwall (at f, g and h, respectively, Fig. 89), and topmost Gruis, Ombaatjie and Maieberg formations in its hangingwall (b, c and d, respectively, Fig. 89). Paired topmost Maieberg Fm cut-offs at d and e (Fig. 89) corroborate a W-dipping detachment surface relative of bedding (Hoffman and Hartz, 1999).

We interpret Rasthof Fm in the hangingwall W of a (Fig. 89) as a tectonic horse, bounded above and below by fault-splays. It is structurally analogous to the horse of Ombaatjie Fm in the axial plunge of Ombonde syncline (Fig. 87). If the Rasthof–Gruis contact at a (Fig. 89) is not a splay fault, then the distance between hangingwall and footwall cutoffs of basal Gruis Fm would be only 3 km (a to h, Fig. 89). This would be incompatible with all other matching cutoffs, which have horizontal displacements of 20–22 km (Fig. 87B) (Hoffman et al., 2016b). On the other hand, if the Rasthof–Gruis contact in section 7–21 is a splay fault of the detachment, then the true hangingwall cutoff of topmost Rasthof Fm lies farther W, compatible with displacements indicated from other matching cutoffs (Fig. 87B).

2.7.6. Highlights from Tr7

Chief highlights of Tr7 are: (1) three successive offlap–onlaps of Makalani dip-slope exposed in dip-section on the E limb of Ombonde syncline. They correspond to Nabis Fm offlap–Rasthof Fm onlap, Rasthof Fm offlap–Gruis Fm onlap, and Gruis Fm offlap–Ombaatjie Fm onlap (Figs. 87C & 88), and record late Tonian until late Cryogenian pulses of rift-shoulder uplift and erosion, related to N–S crustal stretching of OPz (Hoffman and Halverson, 2008); (2) the folded low-angle Ombonde detachment, which is exposed from the top of Otavi Group in its hangingwall to the base of Nosib Group in its footwall (Figs. 92, 89, 87A & B), and on which <2.0 km of coherent Neoproterozoic strata slid ≥20 km westward down the outer slope of a Kaoko collision-related foredeep (Hoffman, 2021a). Sliding occurred before the detachment was incised by basal Mulden Group (Braklaagte Fm) dolomite–chert clast conglomerate, which dips subparallel to and was broadly folded with the underlying Otavi Group (Fig. 90, 92, 87A & B).

2.8. Transect Tr8 – Omarumba paleovalley

Northward from Ombonde syncline (Tr7), a broad, flat-floored, steep-walled valley winds smoothly northward for 90 km before curving around the northern plunge of Kamanjab inlier and disappearing under Cenozoic cover (Kalahari Group) of the interior plateau (Figs. 8A & 96). The valley is 5 km wide on average and its eastern side exposes Orosirian basement and autochthonous conglomerate and feldspathic conglomeratic sandstone of Nabis Fm (Nosib Group). Its western side exposes gently W-dipping Otavi Group of IPz (Figs. 97 & 98A), broken here and there by high-angle faults and warped by open upright folds. Opposite the village of Ondevede (Fig. 96), the valley widens to accommodate a whaleback *inselberg* (monadnock) of westward-dipping Nabis clastics. Nearly 18 km long, the *inselberg* is smoothly rounded—blunt at the northern end and tapered at the downstream end. The western wall of the valley cuts smoothly across high-angle faults that would normally be physiographically expressed, and a side-valley at 8–6–8–7 (Omutirapo) resembles a glacial cirque

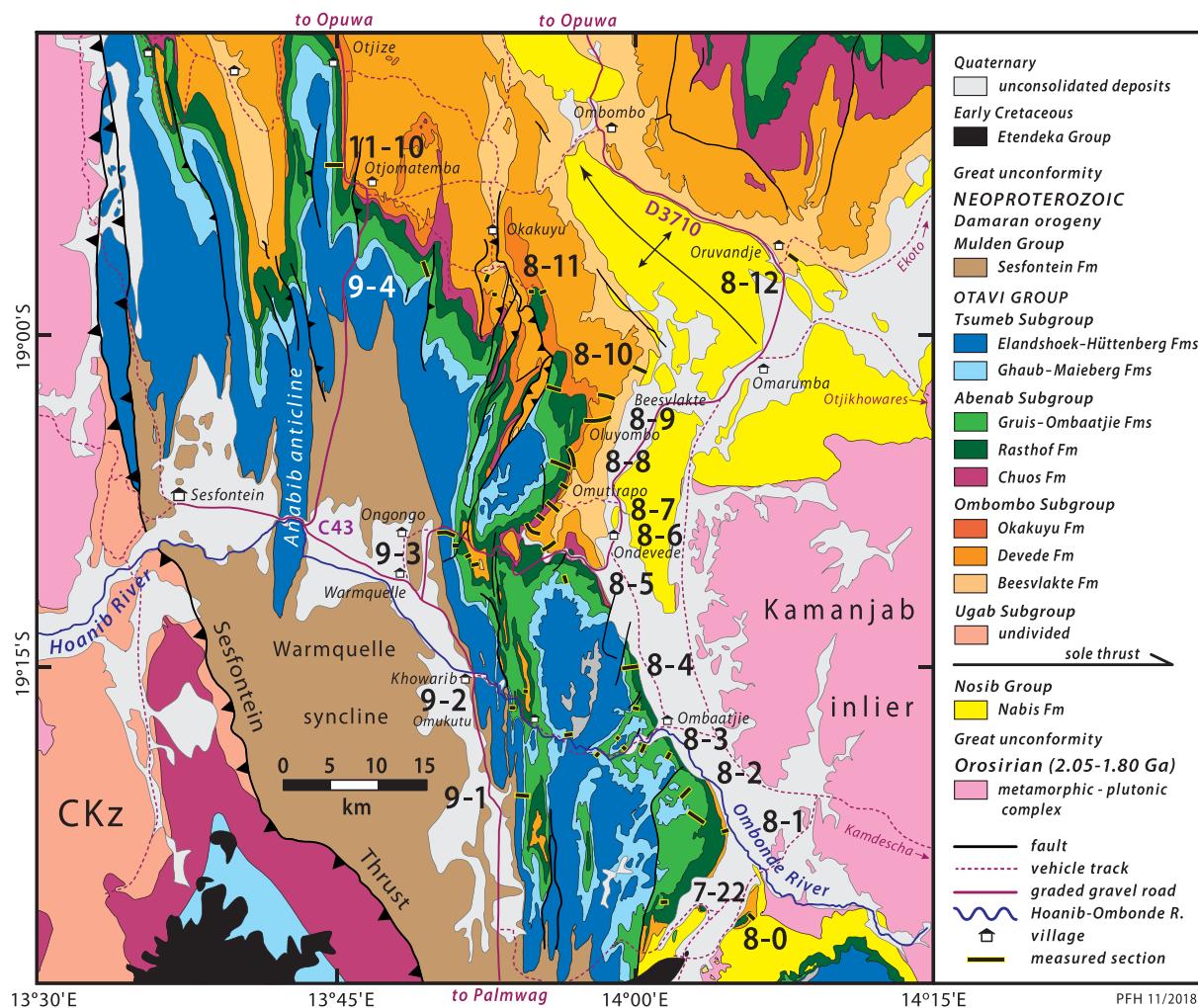


Fig. 96. Geological map of Omarumba paleovalley (Tr8) and Khowarib thrust-fold belt (Tr9) in southern EKz (Figs. 3 & 8A), N of Etendeka, E of Sesfontein thrust and W of Kamanjab inlier (modified after Guj, 1970; Hedberg, 1979; Killick et al., 1980). First-order structures are the NNW-plunging Kamanjab anticline and SSE-plunging Warmquelle syncline. Otavi and Mulden groups have been translated eastward, relative to basement and Nosib Group, on a folded thrust-duplex structure (Figs. 97 & 98B) within Beesvlakte Fm. Section locations shown for 7-22, 8-0-12, 9-1-4 and 11-10. Field guides for 8-3-4, 7-8 and 9-3 are in SOI S3.11-12.

(Figs. 97 & 98B). The landforms are familiar to anyone who grew up in terrain shaped by Pleistocene ice sheets. In fact, Omarumba valley is an exhumed paleovalley cut by a Carboniferous ice stream (Martin, 1961, 1968, 1981; Miller, 2008c).

To the W of Omarumba paleovalley is a 15–28-km-wide belt of doubly plunging Otavi Group folds (Fig. 96). In the W (Fig. S24B), the folds are tight with steeply dipping axial surfaces and thrust ramps, directed E or W without bias. Fold radii of curvature and absence of Nabis Fm (Fig. 96) imply a *décollement* between Nosib and Otavi groups. Tr9 follows the western belt of tight folds (Fig. 96). In the E (Fig. S24B), the folds are open and upright, with limb dips of $\leq 35^\circ$ (Fig. 98A & B). Tr8 follows the edge of the eastern belt of open folds (Fig. 96). It would be a mistake to infer that the eastern belt is autochthonous with respect to basement and Nosib Group, or that the *décollement* is limited to the western belt of tight folds. In fact, the *décollement* extends beneath the eastern belt and is exposed at the entrance to the paleo-cirque at Omutirapo (Ob2, Fig. 97) as an E-directed thrust-duplex (Fig. 98B) involving the middle dolomite member (Ob2, Fig. 99) of Beesvlakte Fm (Fig. 6D). The gently-dipping 2.0-km-thick Otavi Group succession above the Beesvlakte duplex (Fig. 98A) has been translated an unknown

distance eastward relative to Kamanjab inlier and its autochthonous Nosib Group cover (Fig. 96). Tr8 and 9 represent the southernmost IPz (Fig. 8B).

2.8.1. Late Tonian of Tr8

Km-thick late Tonian carbonates and clastics of Ombombo Subgroup (Fig. 98) set IPz apart from OPz (Fig. 5). Hoffman and Halverson (2008) divided Ombombo Subgroup into three formations (Fig. 99): (1) Beesvlakte Fm (Ob) in which the basal thrust duplex occurs, (2) carbonate-dominated Devede Fm (Od), which includes clastic tongues (Odq) derived from Makalani uplift in its lower part, and (3) Okakuyu Fm (Ok), a stack of coarsening-upward deltaic clastic cycles, the last capped by stromatolitic and oolitic dolomite preserved in Tr9 and 11 only.

In 8-12 (Fig. 96), Nabis subarkose is overlain by purplish siltstone of lower Beesvlakte Fm (Ob1, Fig. 99). The exact contact is covered, but a channel of pebbly subarkose resembling Nabis Fm occurs within the siltstone, suggesting depositional continuity between Nosib and Otavi groups. The siltstone has an early cleavage (C_1) that predates upright thick-skinned folds (F_2). The C_1 cleavage dips westward, relative to

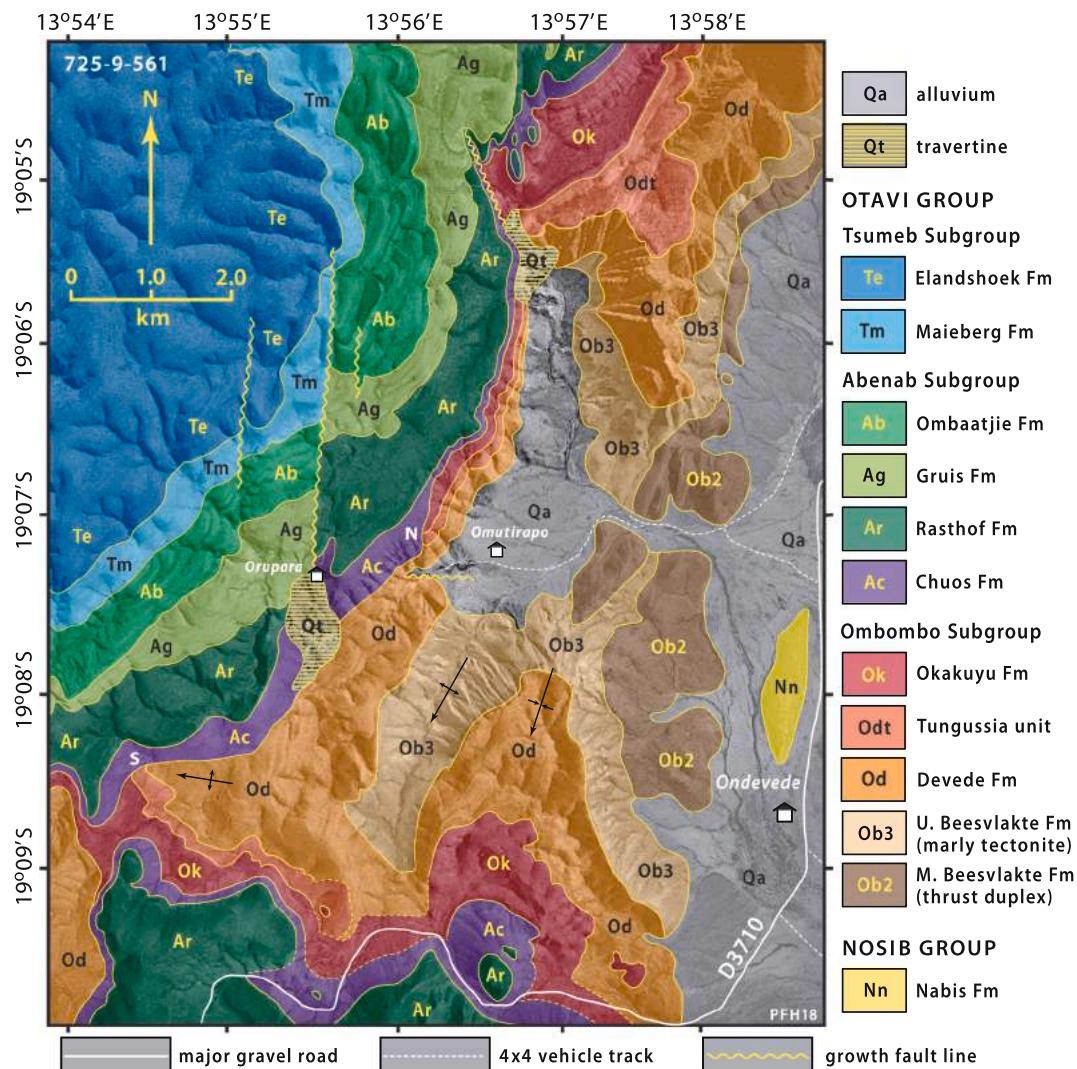


Fig. 97. Geological map of the Omutirapo area (8–6–8, Fig. 96), an inferred Carboniferous glacial cirque (Figs. 98 & 104) exposing a Sturtian glacial bedrock trough (Figs. 105–107) (Hoffman and Halverson, 2008; Le Heron et al., 2013a; Hoffman et al., 2017b) and Neoproterozoic growth faults that localize groundwater springs and associated travertine terraces. Geology superimposed on grey-tone Namibia air photo 725–9–561. Strata dip gently WNW overall, with open upright folds (Fig. 104), structurally underlain by an E-vergent thrust duplex (Figs. 98B & 100B) in Beesvlakte Fm and autochthonous Nosib Group feldspathic arenite. Nosib Group ‘whaleback’ ridge N of Ondedevede has the form of a Carboniferous *roche moutonnée*. Field guides for Omutirapo area (8–7 and 8) are in SOI S3.11.1.

bedding, with the result that it is subvertical on the W limb of the small F_2 anticline at 8–12 and subhorizontal on the E limb. Reduction spots are flattened in the C_1 plane and stretched (2–3:1) in a 080° azimuth, compatible with simple shear associated with ENE-directed thrusting. In the same area, the carbonate-rich middle Beesvlakte (Ob2, Fig. 99) is involved in a local thrust-duplex, forming a train of tight, ENE-facing, sub-thrust synclines spaced 0.15 km apart. These folds are 10× smaller than the equally tight *décollement* folds in the structurally overlying Devede Fm (Fig. 96). In 8–6–10, upper Beesvlakte (Ob3, Fig. 99) is a saprolitic marly calcite tectonite (Fig. 100B) with a 090° stretching lineation. Collectively, the above observations suggest that the *décollement* beneath the thin-skinned thrust-fold belt in these sections is not a plane but a zone encompassing Ob2 and Ob3 at a minimum, and that displacement vectors were approximately orthogonal to the fold belt.

The 0.5-km-thick Devede Fm is a cliff-forming assemblage of cyclic peritidal dolomite and minor clastics (Figs. 98, 99 & 100A).

Transgressive–regressive cycles in the lower 0.3 km average 8.5 m in thickness and terrigenous input, where present, occurs in the transgressive parts of cycles (Fig. 100C). Terrigenous sediment coarsens southward and includes rippled and mudcracked siltstone, crossbedded sandstone and pebble conglomerate derived from basement and Nabis sources (Fig. 100D–F). Regressive dolomite subcycles are capped by tepee breccia, intraclast or ooid grainstone (Fig. 101A & B), or columnar stromatolite (Fig. 101C & D). Authigenic components include gypsum pseudomorphs (Fig. 102A), fibrous dolomite void-filling cement (Fig. 102B) and cm-scale colloform nodules of chalcedonic silica, possibly pseudomorphic after anhydrite (Hood et al., 2015). The upper 0.2 km of the formation is dominated by cliff-forming biostromes (Fig. 101E) of *Tungussia*-type stromatolite (Figs. 69D & 101F) up to 70 m thick (Fig. 99). The biostromes are characteristically pale pinkish in colour and their subtle lamination defines columns with diverging branches that commonly propagate horizontally (Fig. 101F) (Hofmann, 1969; Grey et al., 2011). Although *Conophyton*-type columnar

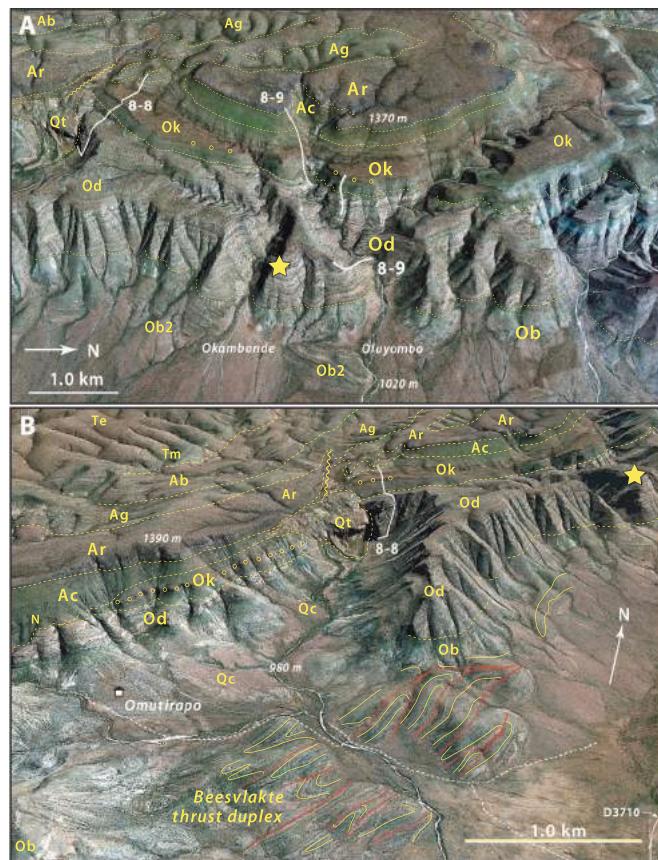


Fig. 98. Inclined satellite images of late Tonian Ombombo and Cryogenian Abenab subgroups exposed W of Omarumba paleovalley (Fig. 96), an exhumed Carboniferous glacial trough (Martin, 1961, 1968). Map unit symbols as in Fig. 97 (Table 5). Yellow stars are co-located in A (center) and B (upper right). (A) Ombombo Subgroup at Oluyombo (8-9) (Fig. 99), viewed looking obliquely westward. Pale band in upper Devede Fm (Od) is 60-m-thick *Tungussia*-type stromatolite biostrome (Fig. 101E). Small circles indicate conglomeratic marker in middle Okakuyu Fm (Fig. 99). Google Earth: Image © 2020 Maxar Technologies. (B) N half of Omurirapo area, looking obliquely NNW toward 8-8 at the head of the cirque (Fig. 100A & C). Swallows nest on the travertine face and rosy-faced lovebirds (*Agapornis roseicollis*) frequent the spring. Dotted magenta line marks traverse described in field guide SOI S3.11.1. Thrust duplex in Beesvlakte Fm (center foreground) accommodated eastward translation of Otavi and Mulden groups relative to autochthonous Nosib Group (Fig. 96). In the duplex, red and yellow lines trace faults and bedding, respectively. In upper left, small circles mark conglomerate bed in Okakuyu Fm (Ok), which is truncated by N-wall (N) of Chuos Fm (Ac) bedrock trough (far left). Local topographic relief of cirque wall is 410 m (elevations in italics wrt sea level). Omurirapo paleo-cirque is ideally suited for a geological field camp. In 1999, its tourist potential was under nascent development by residents of Ondevede (Fig. 97). Google Earth: Image © 2020 Maxar Technologies.

stromatolites also occur in Devede Fm (Fig. 101D), *Tungussia* (Grey et al., 2011) is by far the most common columnar stromatolite type in the late Tonian of Otavi Group, including Devede Fm. The *Tungussia*-dominated interval ends at a major flooding surface that is overlain by pink dolomite rhythmite with interbeds of purplish-grey argillite (Fig. 99). A sharp erosive contact separates the marly rhythmite from Okakuyu Fm.

The terrigenous Okakuyu Fm consists of sublittoral siltstone and coarsening-upward deltaic cycles (Fig. 102C) of reddish-brown weathering quartz-chert arenite (Fig. 102D) and dolomite-chert pebble conglomerate (Fig. 102E) derived from the underlying Devede Fm. Crossbedding and northward decrease in overall grain size imply that Devede Fm was eroded from the dip-slope of Makalani ridge, where Ombombo Subgroup no longer exists (Figs. 87 & 88). The youngest preserved conglomerate in 8-8 carries rounded pebbles of plagioclasephyric amygdaloidal lava (Fig. 102F), less strained and metamorphosed than Orosirian Khoabendus Group metavolcanic rocks in the basement complex (Porada, 1974). Lithologically, the volcanic pebbles resemble trachydacite lava of the 747 ± 2 Ma Upper Naauwpoort Fm in

Tr4 (Figs. 41, 42A & C), but no volcanics of that age are exposed in Tr7 where Makalani ridge is exposed.

2.8.2. Cryogenian of Tr8

Fig. 103 is a Cryogenian fence diagram for Tr8. Unlike OPz, IPz lacks rift-shoulder uplifts of Cryogenian age. Consequently, strata do not change greatly along the transect. The most significant changes are Chuos Fm thickening in 8-7, and Rasthof Fm thinning in 8-7–8 (Fig. 103).

Chuos Fm thickening is associated with a steep-walled paleovalley incised into Ombombo Subgroup (Figs. 104 & 105). The north wall of the paleovalley (N in Figs. 97 & 104–107) was documented by Hoffman and Halverson (2008) and Le Heron et al. (2013a); the south wall (S in Figs. 97 & 104) by Hoffman et al. (2017b). The paleovalley is 4.3 km wide in the SW–NE plane of section (Fig. 97) and the Chuos Fm is ≤ 0.52 km thick in its deepest part (P1626 and B1702, Fig. 105), 10× its average thickness (0.05 km) outside the paleovalley (Fig. 105). Chuos Fm is thin to S and SE as well (Fig. 97), suggesting a W–E trend for the paleovalley axis, roughly parallel to a growth fault striking 093° near the

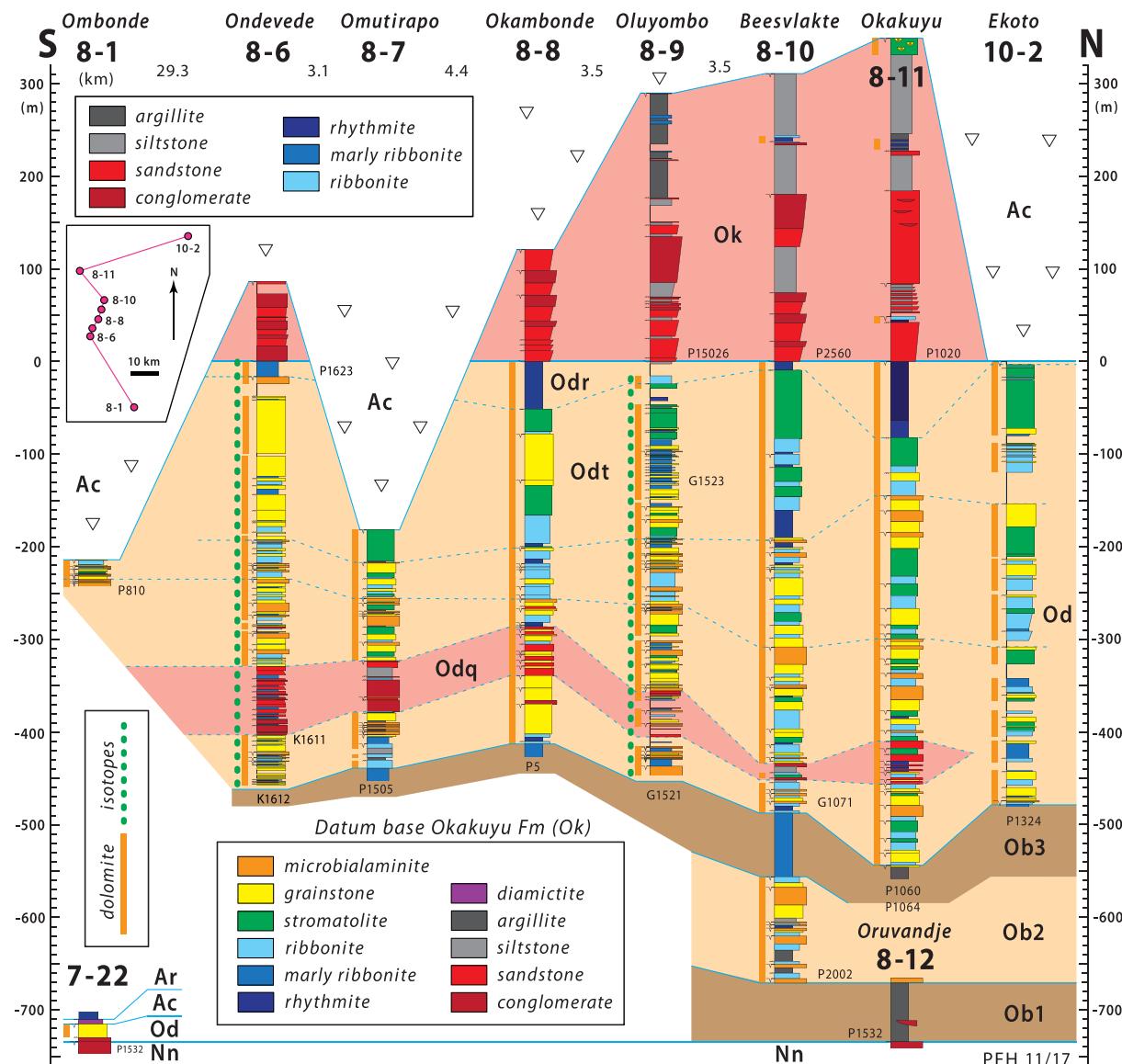


Fig. 99. Columnar sections of late Tonian Ombombo Subgroup W of Omarumba paleovalley (Tr8): section locations (upper left) in Fig. 96. Datum is base of Okakuyu Fm. Unit symbols (oldest to youngest): Nn, Nabis Fm (Nosib Group); Ob1, lower argillite member of Beesvlakte Fm; Ob2, middle dolomite member of Beesvlakte Fm; Ob3, upper marly calcite-marble tectonite member of Beesvlakte Fm; Od, Devede Fm; Odq, lower clastic tongue of Devede Fm; Odt, upper *Tungussia* member of Devede Fm; Odr, upper rhythmite member of Devede Fm; Ok, Okakuyu Fm; Ac, Chuos Fm. Note northward thinning and decrease in pebble/sand ratio in Odq and Ok, implicating Makalani ridge (Tr7) as the terrigenous source (Fig. 5).

north wall (Figs. 97, 104 & 106). The growth fault was previously inferred to have been active in pre-Sturtian time (Hoffman and Halverson, 2008; Hoffman et al., 2017b), but this was based on an erroneous assumption that the base of exposure N of the growth fault was close to the stratigraphic base of the Devede Fm and the calcrete pediment is on Beesvlakte Fm (Figs. 97 & 104). Additional sections measured in 2018 (Fig. 106) suggest instead that the first dolomite bluffs N of the fault are upper, not lower, Devede Fm, consistent with absence of lower Devede clastics (Odq, Fig. 105 & 107). The evidence for faulting is now reduced to a NW-plunging anticlinal flexure in Devede Fm directly S of the inferred fault trace (Fig. 104). Although there is an abrupt 0.2 km change in Chuos Fm thickness between sections B1702 and W1808 (Fig. 105) or W1807 (Fig. 107), the Devede-Chuos contact traces a smooth inflection (Fig. 106). If the fault was active while the paleovalley

was being eroded, glacial abrasion had the last word. If we assume that the paleovalley is oriented W–E, then its orthogonal rim-to-rim width is 3.0 km and its aspect ratio (0.52–0.05/3.0) is 0.16.

Outside the paleovalley, Chuos Fm consists almost exclusively of massive polymictic diamictite, in which subrounded clasts from the basement complex, Nabis Fm and Ombombo Subgroup float in an unsorted wackestone matrix. Within the paleovalley, especially near the valley walls, laterally discontinuous units of laminated argillite and siltstone, most with IRD (Fig. 108E), sorted sandstone and sandy conglomerate (Fig. 108C) are intercalated with diamictite (Figs. 105 & 107). In the deepest part of the paleovalley, the basal Chuos is a monomict breccia (Fig. 108A & B), derived from the directly underlying pale dolomite *Tungussia* type stromatolite. This basal breccia includes one or more boulder pavements (Fig. 108A). It is sharply overlain by a few

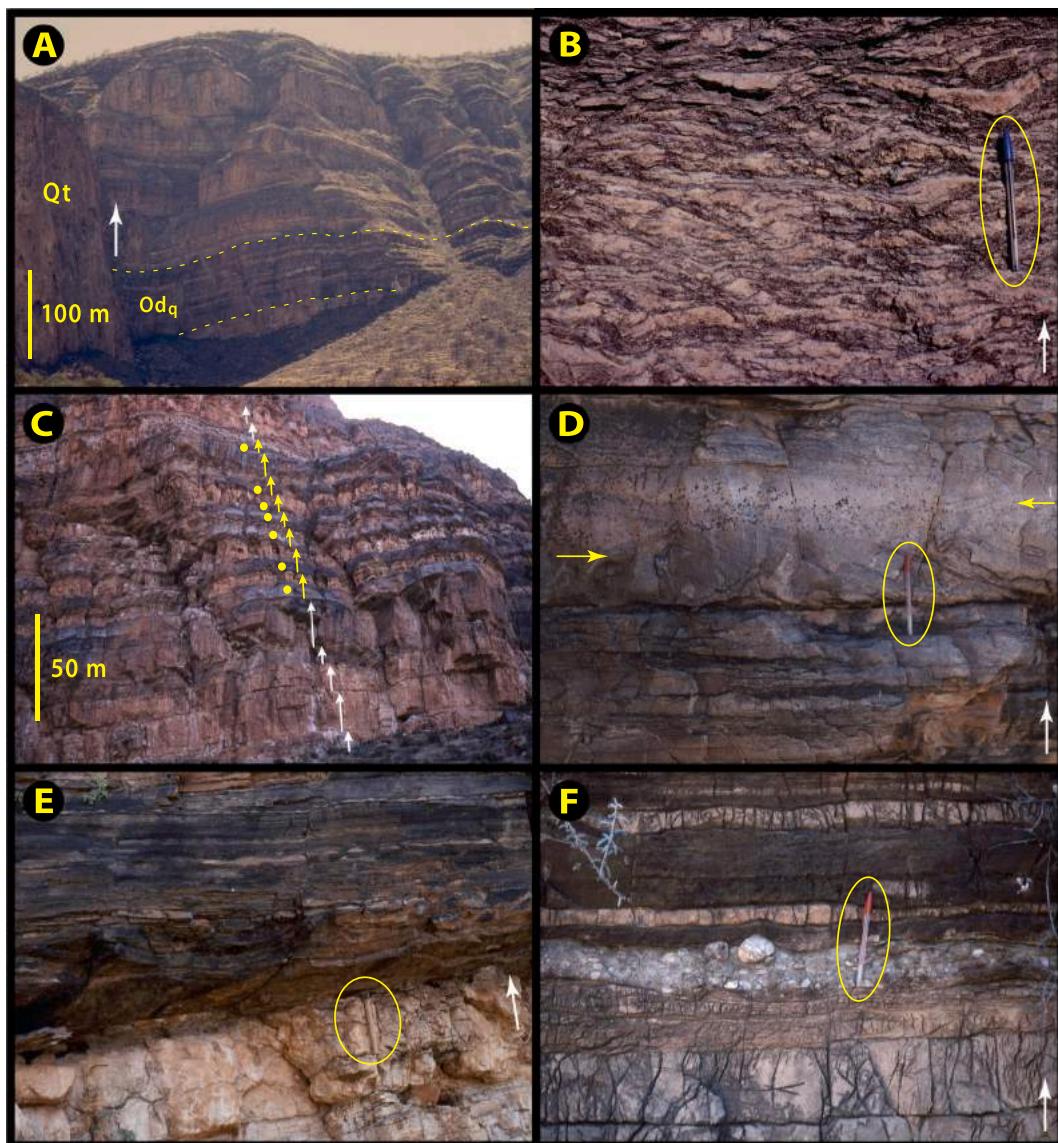


Fig. 100. Images from lower Ombombo Subgroup in Omutirapo paleo-cirque (Tr8): white arrows indicate stratigraphic younging. (A) Devede Fm type section (P5) at 8–8 (Figs. 97–99), $-19.0898^{\circ}/13.9522^{\circ}$, showing lower clastic-rich tongue (Odq) and upper cliffs of *Tungussia*-type stromatolite (Fig. 101C & F). 350 m of section is visible. Qt is a Quaternary travertine cliff populated by swallows. (B) Marly calcite-marble tectonite of upper Beesvlakte Fm at $-19.1327^{\circ}/13.9393^{\circ}$ in 8–7. Grain-scale fabric is annealed, but east–west stretching-lineation is preserved as are shear bands (S–C fabrics) indicating top-side-eastward (to the right) sense of shear. (C) Depositional cycles (arrows) in lower Devede Fm in same location as A. Tops of cycles are dolomite grainstone (Fig. 101A & B) or microbialaminite with evidence of subaerial exposure (tepees). Yellow dots indicate quartz-chert-arenite (see D) at bases of cycles. Yellow arrows indicate Odq clastic-rich tongue (see C). (D) Bidirectional crossbedding (arrows indicate apparent flow direction) in quartz-chert arenite of inferred shallow-marine origin in Odq tongue at $-19.0899^{\circ}/13.9532^{\circ}$ in 8–8. (E and F) Cycle boundaries in Odq tongue, where siliciclastic ribbonite (quartz-chert-arenite) sharply overlies dolomite cycle tops with tepee structure (E) and quartz-pebble lag (F) at boundary: same location as D.

meters of laminated IRD-bearing siltstone and sandstone (Fig. 108D & E). The first diamictite contains large rounded boulders of dolomite (Fig. 108F) and quartz-arenite (Fig. 109A), including clasts with faceted and striated surfaces (Fig. 109C & D). Within the paleovalley overall, diamictite matrices are variably argillaceous to sandy, and either massive (Fig. 109B), weakly bedded (Fig. 109E) or sheared (Fig. 109F). Argillite in the upper part of Chuos Fm host graded beds of detrital dolomite (Fig. 110E) and decameter-deep lenses of clast-supported polymictic conglomerate (Figs. 105 & 107).

Based on sedimentological comparison with Quaternary glacial deposits, Le Heron et al. (2013a) inferred that diamictites within and

around the Omutirapo paleovalley were deposited beneath a grounded ice sheet and its proximal floating extension. They further inferred that a 20–30-m-thick, IRD-free argillite (“shale”) unit ca 0.1 km below the top of Chuos Fm near the N wall of the paleovalley represents a complete ice withdrawal from the region associated with a global intra-Sturtian interglacial stage (Le Heron et al., 2013a). However, the intricate distribution of subaqueous argillite and siltstone (Figs. 105 & 107) is more easily explained if the paleovalley was an overdeepened bedrock trough, where the axial depth shallowed both upstream and downstream with respect to glacial flow. Such overdeeps (e.g., glacial fjords) are canonical glacial landforms (Penck, 1905; Sugden and John, 1976; Benn and

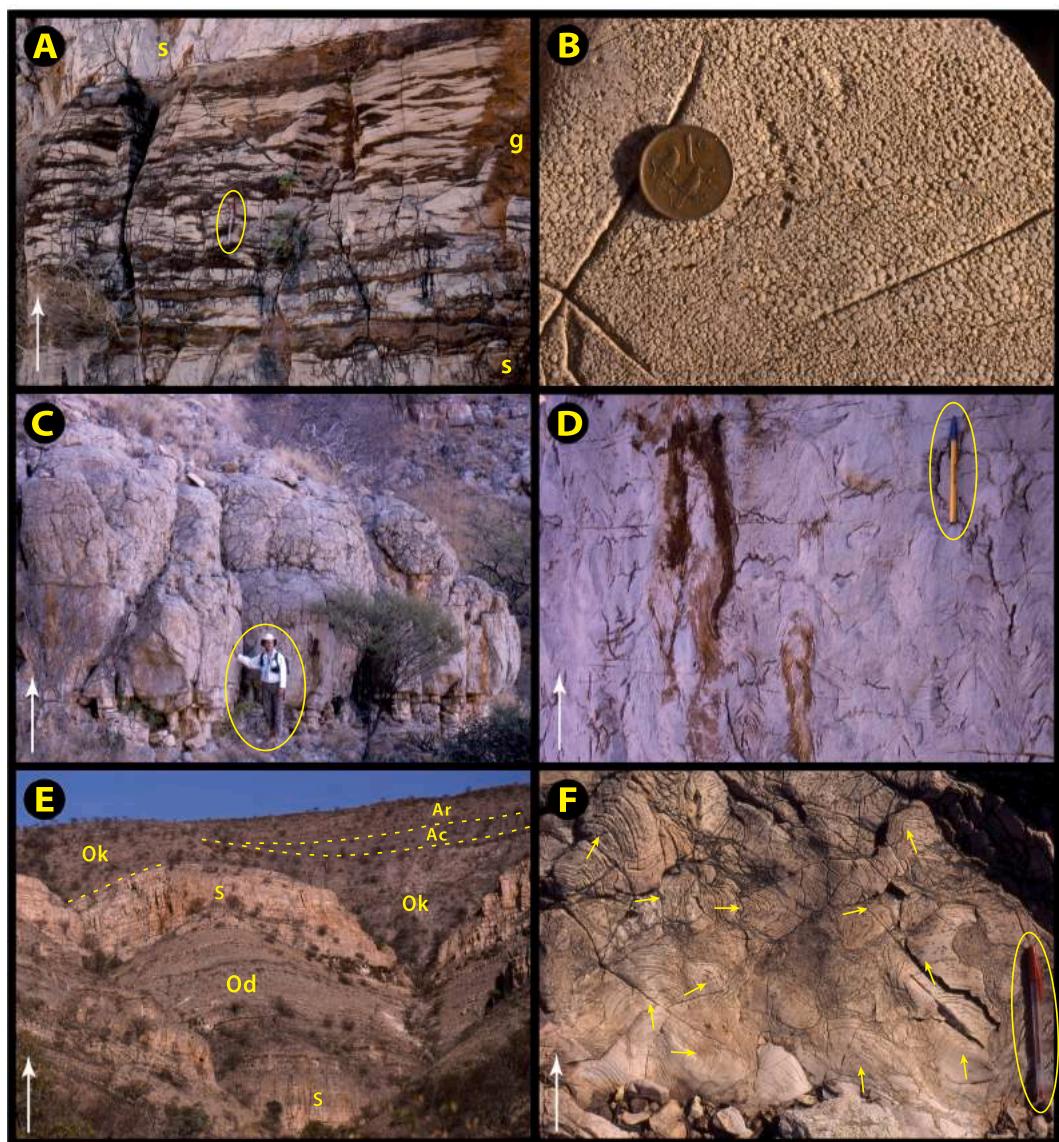


Fig. 101. Images of grainstones and stromatolites from late Tonian Devede Fm W of Omarumba paleovalley (Tr8): white arrows indicate stratigraphic younging. (A) Crossbedded dolomite grainstone (g) with authigenic chert, darkened by desert varnish, bounded by dolomite stromatolite beds (s) at $-19.0893^{\circ}/13.9531^{\circ}$ in 8–8. (B) Oolitic dolomite grainstone just below location A. 2-cm-diameter coin. (C) *Tungussia*-type dolomite stromatolite, underlain by ribbonite near $-19.0882^{\circ}/13.9530^{\circ}$ in 8–8. Pinkish tint is typical for this stromatolite type in Devede Fm. Note nodular, almost conglomerate-like, stromatolite presentation, which reflects subhorizontal growth of many stromatoid columns (see F). (D) *Conophyton*-type dolomite stromatolite with distinct apical cylinders near $-19.0887^{\circ}/13.9533^{\circ}$ in 8–8. Brown (desert varnish) indicates authigenic chert. (E) Pink *Tungussia*-type stromatolite biostromes (s) in upper Devede Fm (Od) at $-19.0410^{\circ}/13.9756^{\circ}$ between 8 and 9 and 8–10. Higher composite biostrome is 60 m thick. Ok, Okakuyu Fm; Ac, Chuos Fm; Ar, Rasthof Fm. (F) Detail of *Tungussia*-type stromatolite at $-19.0647^{\circ}/13.9649^{\circ}$ in 8–9 with arrows indicating growth directions of columnar elements. Elements lacking arrows grow into or out of outcrop surface, which is oriented normal to paleo-horizontal. *Tungussia*-type, defined by highly divergent branching, is the characteristic stromatolite type in late Tonian and middle Cryogenian of Otavi Group.

Evans, 1998). Subglacial meltwater tends to pond in overdeeps because, unlike river valleys, their axial depth does not deepen monotonically with distance downstream (Patton et al., 2016; Buechi et al., 2017). We suggest that poor drainage, not global deglaciation, better explains the distribution (and localization) of laminated silty argillite lenses in the Sturtian bedrock trough at Omutirapo (Fig. 105). Since overdeepening generally occurs at the equilibrium line altitude (ELA) of a glacier (Sugden and John, 1976; Anderson et al., 2006; Patton et al., 2016), where ice sliding velocity and hence erosive power are greatest (Hallet et al., 1996), we infer that a Sturtian ELA existed in the area of

Omutirapo at the time the bedrock trough was excavated. We further deduce that the ELA subsequently moved to higher elevations, consistent with CO₂ accumulation and snowball warming (Benn et al., 2015), allowing the trough to be filled to overflowing (Fig. 105) with debris released from the ablation zone of the same glacier or ice stream (Patton et al., 2016).

Rasthof Fm is well developed and exposed in Tr8 (Figs. 96–98, 103 & 104). It conformably overlies ferruginous Chuos diamictite with a knife-sharp contact (Fig. 110C & E). Fe enrichment in upper Chuos Fm is not correlated with lithology and appears to result from selective

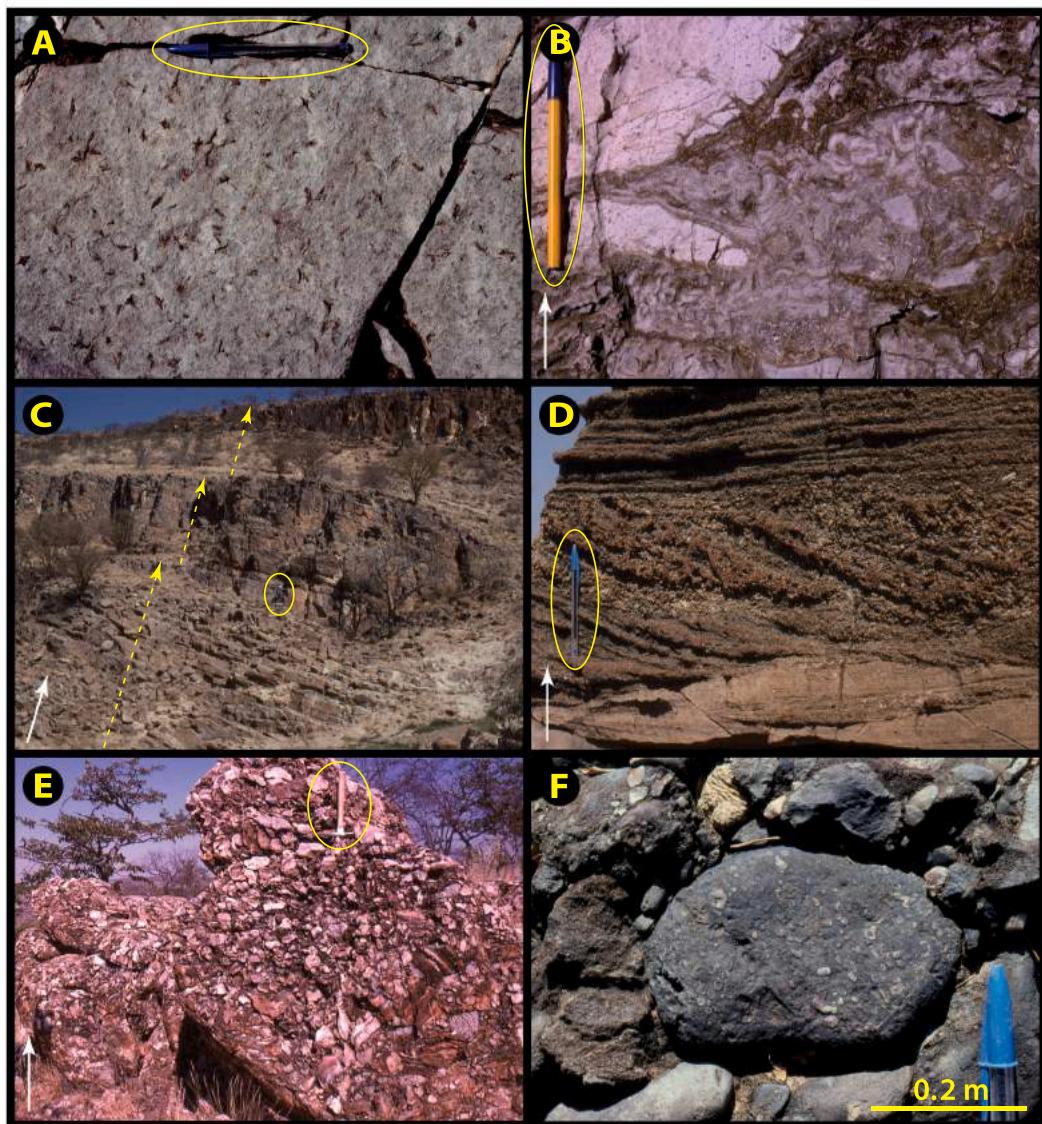


Fig. 102. Images from Devede and Okakuyu formations W of Omarumba paleovalley (Tr8): white arrows indicate stratigraphic younging. (A) Wedge-shaped pseudomorphs (dark) with ‘fishtail’ and ‘bow-tie’ twin habits characteristic of gypsum, on bedding surface of quartz-siltstone in lower Devede Fm clastic-rich tongue (Odq) at $-19.0898^\circ/13.9533^\circ$ in 8–8. (B) Fibrous isopachous dolomite cement encrusting ‘curled’ dolomitic intraclasts in lower Devede Fm near $-18.9591^\circ/13.8927^\circ$ in 8–11. Such fibrous cements are inferred to be of marine origin (Hood et al., 2015). (C) Upward-coarsening arenaceous cycles (arrows) in lower Okakuyu Fm at $-19.0704^\circ/13.9605^\circ$ near 8–9. Geologist (circled) gives scale. Cycles are inferred to represent prograded delta lobes. (D) Crossbedding in dolomite-chert granulestone in Okakuyu Fm cycle top at same location as C. (E) Dolomite-chert-clast conglomerate in lower Okakuyu Fm near $-19.0836^\circ/13.9506^\circ$ in 8–8. Clasts are presumably derived from Devede Fm eroded from Makalani ridge (Fig. 5). (F) Rounded cobble of amygdaloidal dacite (?) lava in upper Okakuyu Fm conglomerate at $-19.0820^\circ/13.9477^\circ$ in 8–8. Volcanic cobble superficially resembles lava of Upper Naauwpoort Fm in Tr4 (Figs. 41, 42A & C), which has a U–Pb zircon age of 747 ± 2 Ma (Hoffman et al., 1996). As a maximum age constraint for the upper Okakuyu Fm in 8–8, it would be compatible with 760 ± 1 Ma as a depositional age for upper Devede Fm in Tr9 (Fig. 123) (Halverson et al., 2005) given a hiatus between the two formations.

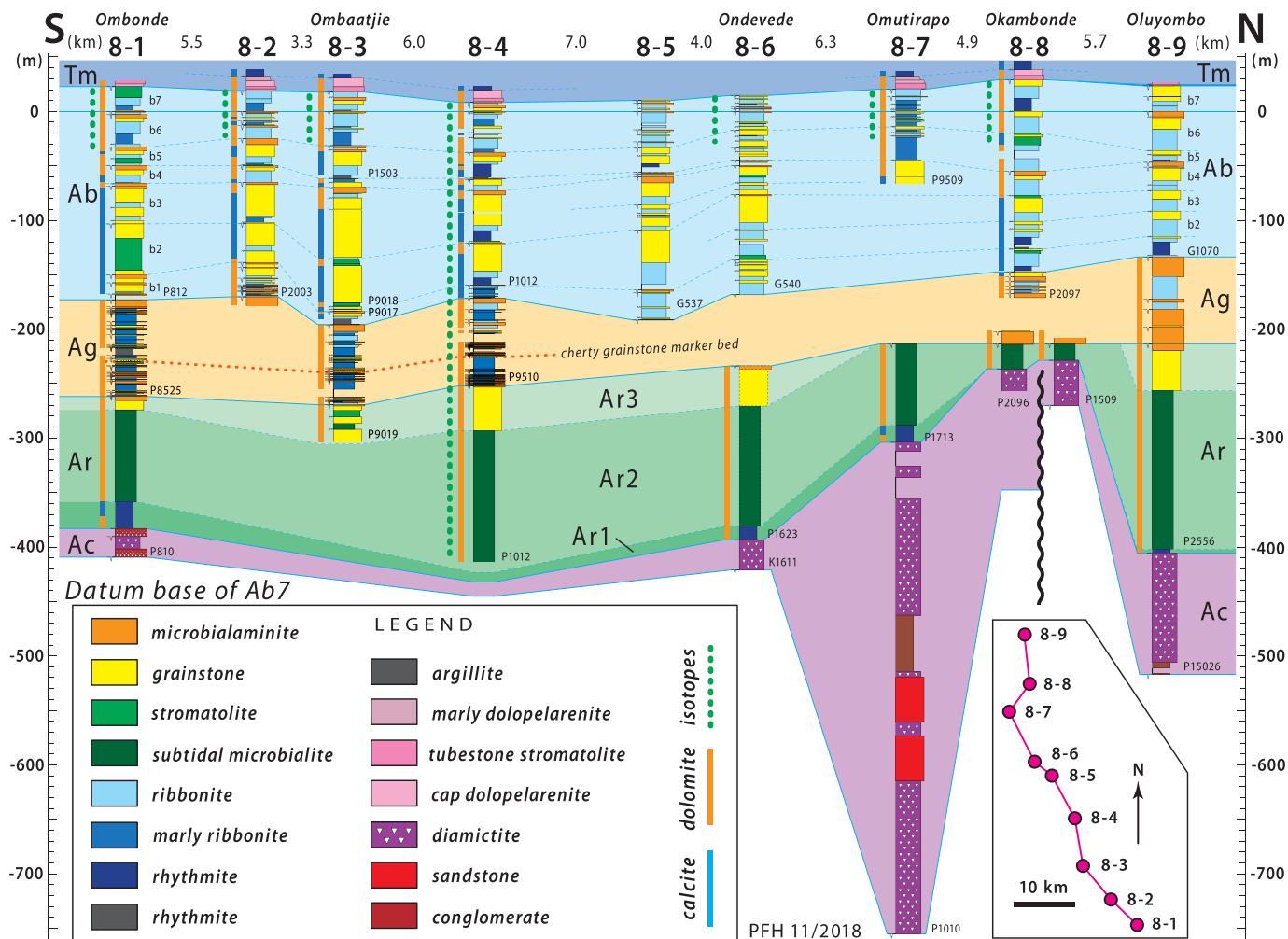


Fig. 103. Cryogenian and earliest Ediacaran columnar sections on the W side of Omarumba paleovalley (Tr8): section locations (lower right) in Fig. 96. Datum is base of cycle b7 in upper Ombaatjie Fm. Cycle b8 is missing due to Marinoan glacial erosion of Omarumba trough (Fig. 164), the floor of which has only 20 m of apparent relief over a distance of 45 km (8–1–9). Chuos Am thickening in 8–7 is accommodated by incision of Omutirapo bedrock trough (Figs. 99, 104 & 105). Rasthof Fm was structurally raised and erosional bevelled by Gruis Fm over an inferred growth fault (Hoffman and Halverson, 2008) at the N end of Omutirapo paleo-cirque (Figs. 97 & 98B).

sequestration of mobile Fe. Diffusion banding (*liesegang* rings) is common in Chuos Fm and Fe mineralization selectively follows cleavage planes and fracture networks. Rasthof Fm ranges from 120 to 190 m in thickness overall (Fig. 103), aside from top-truncated sections (8–7–8) related to post-Sturtian growth faults (Fig. 97). It divides naturally into three members (Ar1–3, Figs. 103 & 111): (Ar1) a basal rhythmite and turbidite member, (Ar2) a middle microbialite member and (Ar3) an upper grainstone member. Since Ar1 is the deepest-water facies and Ar3 the shallowest, ending at a subaerial exposure surface marked by tepees, Rasthof Fm as a whole represents a single HST of anomalous thickness (Hoffman et al., 1998a; Pruss et al., 2010; Wallace et al., 2014).

The Ar1 member is 5–26 m thick (Figs. 103 & 110D) and consists of parallel-laminated micrite hosting cm- to decimeter-thick turbidites and fine-grained intraclastic debrites (Yoshioka et al., 2003; Katsuta et al., 2007; Tojo et al., 2007). Ar1 is similar to but thinner than the same unit in Tr7 (Figs. 88 & 93A–D). The turbidites and debrites are typically calcitic, whereas the laminated micrite is dolomitic. This could indicate that dolomitization was favoured by slow sedimentation rate, presumably pointing to dolomitization on the seafloor. The calcite and dolomite

are dark and medium grey in colour, respectively, but even the darkest layers, almost black in colour, have very low organic contents (<0.4 wt % TOC). Fine-scale rheological layering made Ar1 particularly susceptible to kink-folding and small-scale thrust ramping during tectonic folding.

The Ar1–2 transition is abrupt but gradational over ≤1.0 m (Fig. 110D). Ar2 is 80–140 m thick overall and is divisible into three subunits (Fig. 111): (Ar2a) ‘lobate’ stromatolite (Fig. 69C), (Ar2b) roll-up microbial laminites, and (Ar2c) cryptic microbialite (Hoffman and Halverson, 2008; Pruss et al., 2010; Dalton et al., 2013; Le Ber et al., 2013; Wallace et al., 2014; Moore et al., 2017). From a distance, Ar2a appears tabular bedded at a m-scale, but in outcrop it is a poorly to non-bedded LLH-type stromatolite (Fig. 110A, B & E). Synoptic stromatolite morphology consists of two geometric types that can co-occur. The first and more common type propagates laterally (Fig. 110A). In section they bulge upward and outward above an inclined zone of disruption and void-filling cement (Figs. 69C & 110A). The lobes resemble anticlinal folds formed above thrust ramps. However, thrust-related folds form subparallel sets reflecting a common shortening direction. Ramp and

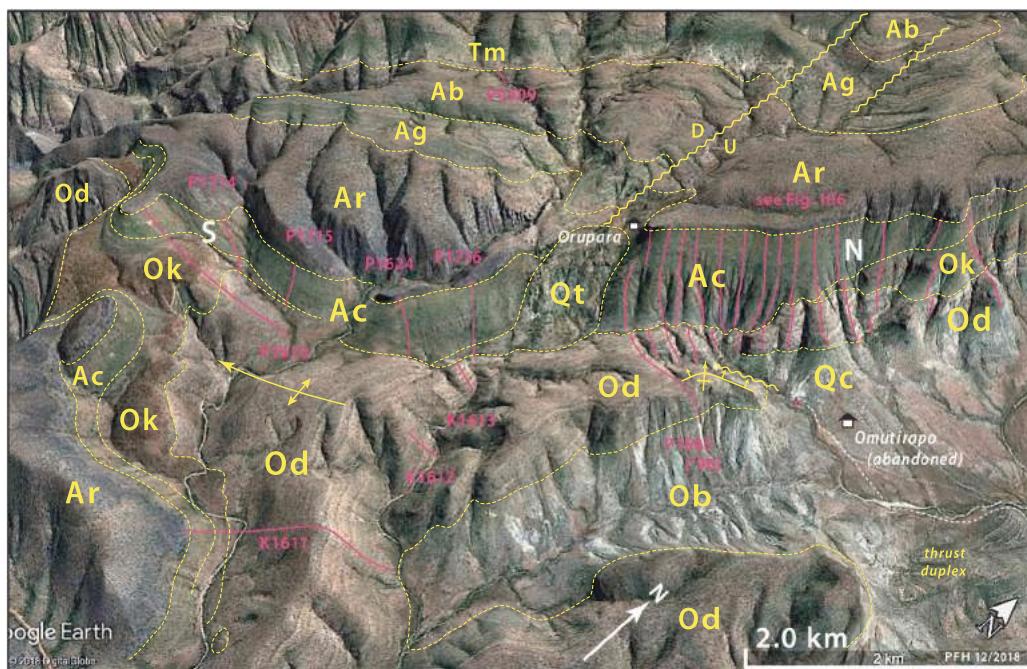


Fig. 104. Annotated satellite image looking obliquely NW toward Sturtian bedrock trough (Fig. 105) S of Omutirapo (Fig. 97). Trough was glacially incised 0.45 km deep into late Tonian Ombombo Subgroup and was ultimately overfilled by Sturtian subglacial deposits of Chuos Fm (Fig. 105). White letters S and N are rims of the Sturtian bedrock trough. Measured sections (Figs. 105 & 106) are in magenta. Yellow dashed lines are formation boundaries and wavy yellow lines are growth faults (D, down-side; U, up-side). Formations (oldest to youngerst): Ob, Beesvlakte Fm; Od, Devede Fm; Ok, Okakuyu Fm; Ar, Rasthof Fm; Ag, Gruis Fm; Ab, Omboaatje Fm; Tm, Maieberg Fm; Qt, Quaternary travertine. White dashed line is 4 × 4 vehicle track (Fig. 97) to campsite (small red triangle) near Omutirapo (abandoned). A field guide to Sturtian bedrock trough is provided in SOI S3.11.1. Google Earth: Image © 2020 Maxar Technologies.

lobe propagation directions in Ar2a are randomly oriented—cross-sections are self-similar regardless of orientation. This could be explained by isotropic expansion in the horizontal plane due to microbial growth, in effect accommodating lateral expansion close to the sediment–water interface by structural self-thickening (Hoffman et al., 1998a; Lokier et al., 2018). The second and less common stromatolite form are ridges (not pinnacles) at lobe crests (Fig. 110B). The crestal ridges are more-or-less pinched and accreted vertically upward (geoplumb). They are the only microbial forms in Ar2 suggestive of phototrophism. Lobate stromatolites in Ar2a were strictly subaqueous and uniformity through 30–80 m of vertical section suggests water depths potentially outside the euphotic zone. Delicate vuggy zones are uncompactated, however, implying rapid postdepositional lithification.

Subunit Ar2b sharply overlies Ar2a (Fig. 111). It is darker-grey in colour and more distinctly laminated in light-dark couplets on a mm-scale (Fig. 113A & B). The lamination is flat and parallel except where folded and refolded in characteristic roll-up structures (Fig. 113A & B), or cut by neptunian dykes packed with microbial intraclasts and void-filling cement. The roll-ups demonstrate that the laminated sediment was pliable but cohesive, presumably due to in situ growth of benthic microbial mat. Desiccation can be ruled out for want of evidence but the lack of granular sediment makes current action more difficult to exclude. As a roll-up generating mechanism, we prefer inflation and bursting of blisters of microbially evolved gases (CO_2 , CH_4 or O_2). Evidence linking Ar2b roll-ups to neptunian dykes (Pruss et al., 2010) will be described in Tr9 (2.9.2.).

Subunit Ar2b becomes paler in colour and less distinctly laminated upward and the transition to Ar2c is gradational (Fig. 111). Ar2c is unbedded and its microbial origin is cryptic. Decimeter scale ‘dish’

structure and complementary unbranched columnar microbialites are faintly developed. The transition to Ar3 grainstone is gradational on a scale of decameters. Pale grey-coloured dolomite grainstone of Ar3 is massive to crossbedded and up to 40 m thick (8–8, Fig. 103). The top of Ar3 is marked by littoral-type microbialaminite with intraclast lenses, small-scale disconformities and tepees indicating subaerial exposure (Figs. 103 & 111). The top of Rasthof Fm is defined by the first subaerial exposure surface, indicating that accommodation created by post-Sturtian marine flooding was finally filled at the given location. This surface is a mappable sequence boundary in IPz (Figs. 103, 111 & 112).

Low organic contents of Rasthof Fm (<0.4 wt% TOC) are probably not the result of low gross primary productivity. Both Ar2 and Ar3 are moderately rich in microfossils tentatively interpreted as agglutinated tests of unicellular heterotrophs (Bosak et al., 2011, 2012, 2013; Dalton et al., 2013; Moore et al., 2017). These were among the first putative eukaryotes recognized physically in Cryogenian carbonates. Biomarkers extracted from correlative post-Sturtian strata (Aralka Fm) in South Australia have high hopane to sterane ratios, indicating predominantly bacterial primary production, possibly due to intense post-snowball greenhouse warming, on the eve of the ‘rise of algae’ in the later, less heated, inter-snowball epoch (Brocks et al., 2017; Brocks, 2018).

Gruis Fm (Figs. 103 & 112) could hardly be more different from Rasthof Fm. Where Rasthof is grey-coloured, resistant, non-cyclic and strictly subaqueous, Gruis Fm is pinkish buff-coloured, recessive, and riddled with subaerial exposure surfaces bounding small-scale cycles. Exposure is indicated by tepee horizons (Fig. 113C & D), and 25–30 shoaling-upward cycles occur within the 76–90-m-thick formation (Fig. 103). Typical Gruis cycles begin with marly ribbonite on a basal flooding surface, and end with microbialaminite with tepees

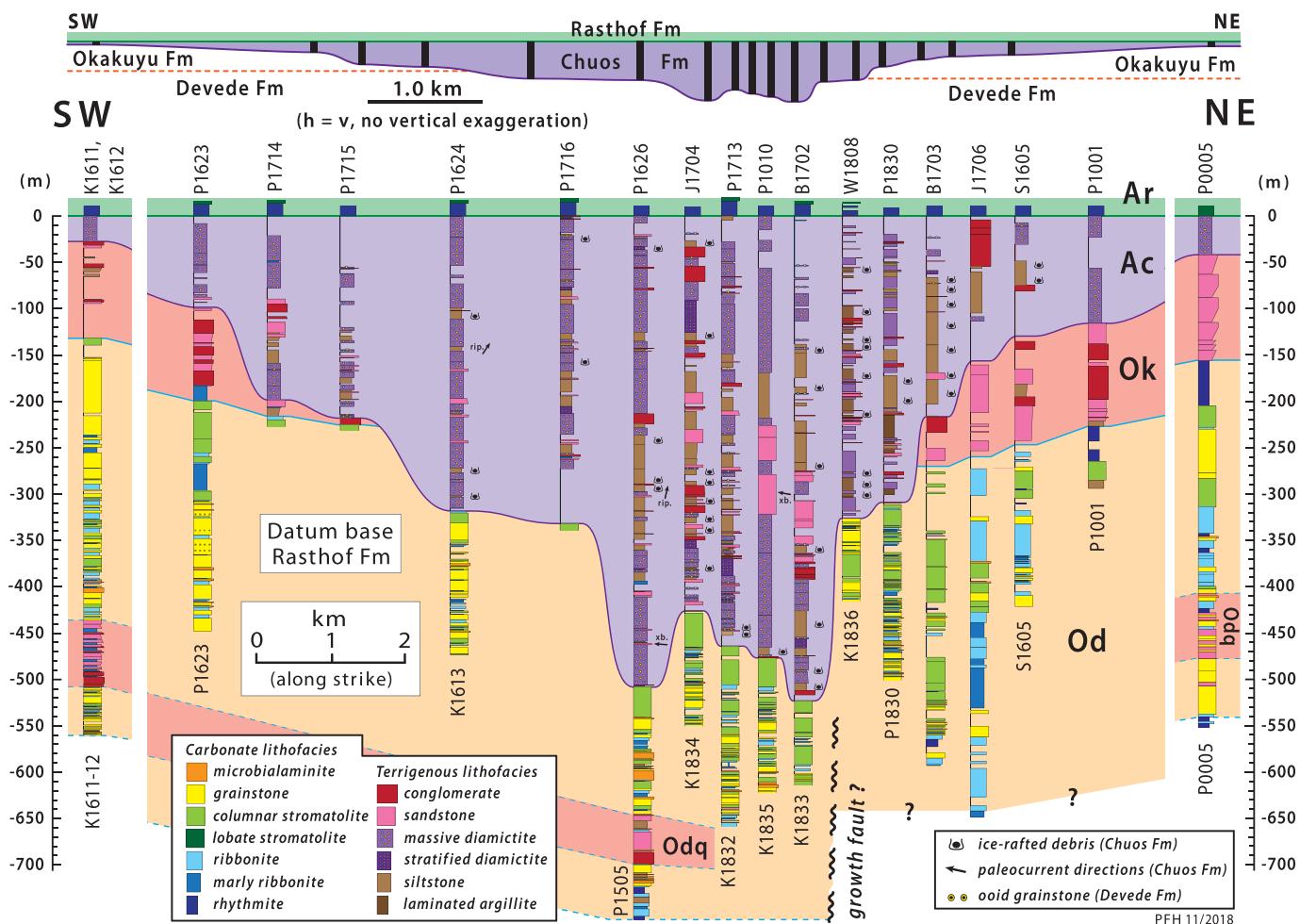


Fig. 105. Columnar sections of Sturtian bedrock trough at Omutirapo (Figs. 97 & 104), incised into Okakuyu (Ok) and Devede (Od) formations of Ombombo Subgroup, and filled by subglacial deposits of Chuos Fm (Ac). Datum is base of Rasthof Fm (Ar) postglacial cap-carbonate sequence: section locations in Figs. 104 & 106. Trough profile at top is without vertical exaggeration in the SW–NE plane of sections, which is presumably oblique to a trough axis of uncertain orientation. Abundant silt- and clay-size laminated deposits in Chuos Fm inside the trough (22% of total thickness and 2× thicker in aggregate than sandstone+conglomerate) suggest meltwater ponding (i.e., reverse gradient in down-stream direction). ‘Overdeepening’ is common in glacier-cut valleys and fjords, because glaciers are most erosive at their equilibrium lines, where sliding velocities are fastest, and because glaciers can flow uphill over bedrock topography. A pre-Okakuyu growth fault was previously inferred between B1702 and W1808 (Hoffman and Halverson, 2008; Hoffman et al., 2017b, 2018), but this stemmed from a questionable assumption that the base of exposed Devede Fm north of the fault trace was the top of Beesvlakte Fm. However, the absence of lower Devede clastic tongue (Odq) suggests instead that only upper Devede Fm is exposed N of the fault trace and that the base of exposure is merely the top of Quaternary calcrete (Qc, Fig. 104). This implies less throw on the inferred growth fault, the existence of which can now be inferred only from a sharp anticlinal flexure in lower Devede Fm (Fig. 104).

(Fig. 113C). Many tepee horizons are composite and may represent multiple cycles (Fig. 113D). Other cycles end at marine flooding surfaces, lacking tepees (Fig. 113E). A few cycles contain beds of coarse-grained ooid grainstone (Fig. 113F). Many cycles are marly, at least basally, and rift-shoulder uplifts in OPz were potential sources of wind-blown and aqueously suspended fine-grained terrigenous sediment. Rasthof and Gruis formations exemplify ‘catch-up’ and ‘keep-up’ modes, respectively, of carbonate accumulation (Sarg, 1988).

The transition from Gruis to Oombaattjie Fm is marked by an abrupt 5–6× increase in cycle thickness (Fig. 103) and appearance of dark-grey limestone cliffs (Fig. 114A & B). Earlier Oombaattjie cycles (b1–3) are mainly limestone; later ones (b4–7) are mostly dolomite (Figs. 103 & 114B). Earlier cycles are thicker and consist, in ascending order, of argillite, mottled and bedded ribbonite (Fig. 114C–E), mounded columnar stromatolites (Fig. 115A–C), and crossbedded grainstones (Fig. 114F) composed of intraclasts (Fig. 115D) and/or ooids (Fig. 115E

& F). Grainstone in some cycles is capped by supratidal microbialaminite with tepee breccia (Fig. 116B), while other cycles terminate at marine flooding surfaces (Fig. 116C). Locally, stromatolite occurs at the base of a cycle and represents a TST (Fig. 116D). In earlier cycles, dolomite is clearly secondary (Figs. 114C & 116E), but early enough to be reworked as intraclasts in grainstone (Figs. 115D & 116F). Preference of dolomite for thinner cycles (Fig. 103) could reflect inverse accumulation-rate dependence of dolomitization. Greater thickness of earlier cycles, prominence of grainstone facies and arrested dolomitization (Fig. 103) may relate to relatively rapid thermal subsidence in the wake of the rift-to-shelf transition (Halverson et al., 2002). Subaerial exposure surfaces between Oombaattjie Fm cycles have little evident karstic relief (≤ 2 m), suggesting that glacioeustatic changes were insignificant late in the Cryogenian inter-snowball epoch.

The top of the Oombaattjie Fm is a Marinoan glacial erosion surface (Fig. 117B), which is overlain either by the Keilberg cap dolomite

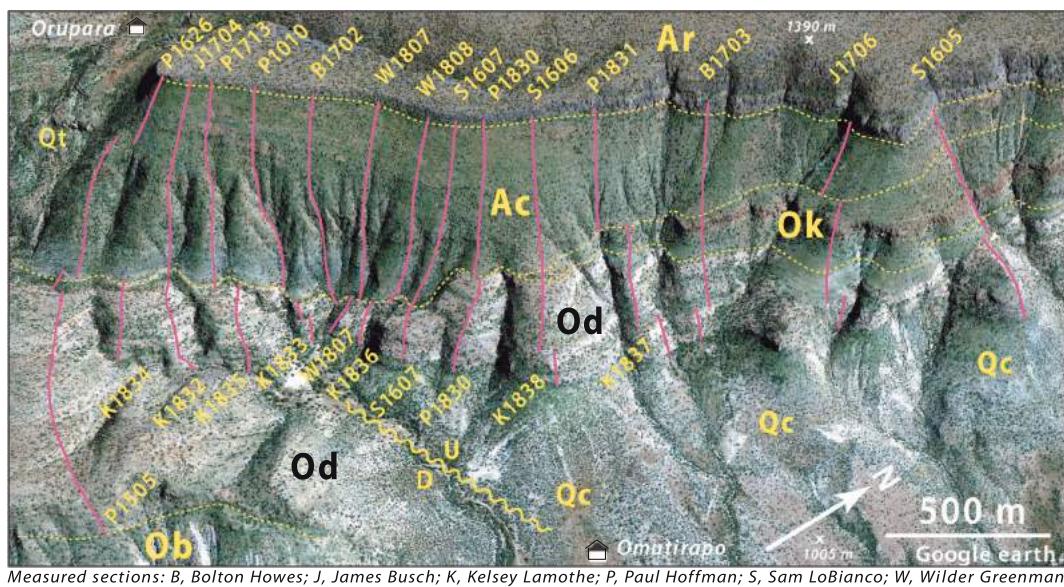


Fig. 106. Annotated satellite image, looking obliquely to NW, showing section locations (Fig. 107) on N side of Omurirapo bedrock trough (Fig. 104, 105). Sub-Chuos erosion surface cuts downward, relative to pre-Sturtian stratigraphy, from right (NE) to left (SW). Units: Ob, Beesvlakte Fm; Od, Devede Fm; Ok, Okakuyu Fm; Ac, Chuos Fm; Ar, Rasthof Fm; Qt, Quaternary travertine; Qc, Quaternary calcrete. Topographic relief is 390 m. Google Earth: Image © 2020 Maxar Technologies.

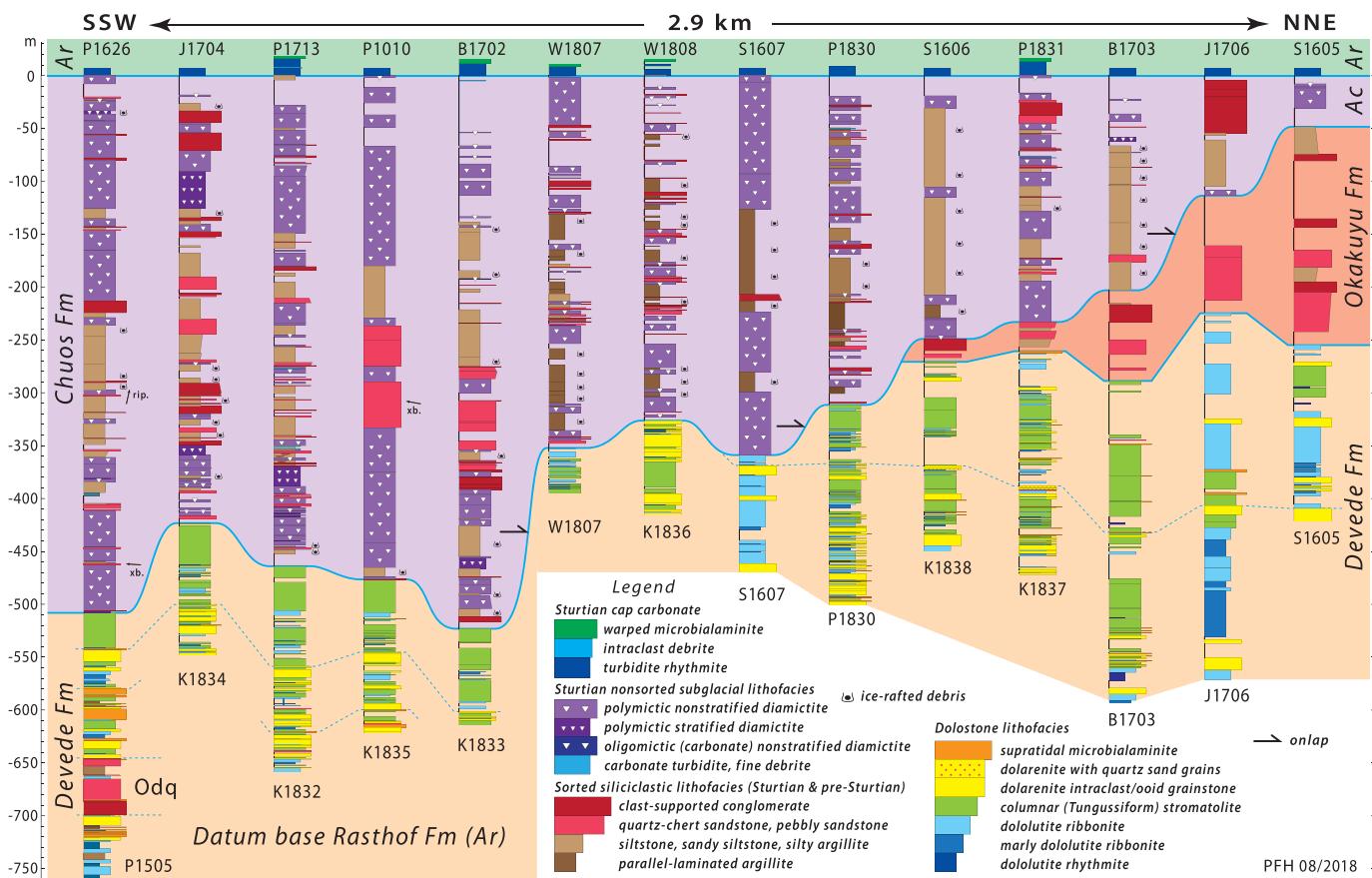


Fig. 107. Closely spaced columnar sections (Fig. 106) on N side of Sturtian bedrock trough at Omurirapo (8–7). Datum is base of Rasthof Fm cap-carbonate sequence. Units: Odq, clastic tongue in lower Devede Fm; Ac, Chuos Fm; Ar, Rasthof Fm. Abundance of parallel-laminated siltstone and argillite in Chuos Fm, relative to sorted sandstone and conglomerate, suggests ponding of subglacial meltwater in bedrock trough with reverse bed slope down stream (e.g., Buechi et al., 2017). Cross-bedding in sandstone indicates W-directed flow in P1626 and P1010.

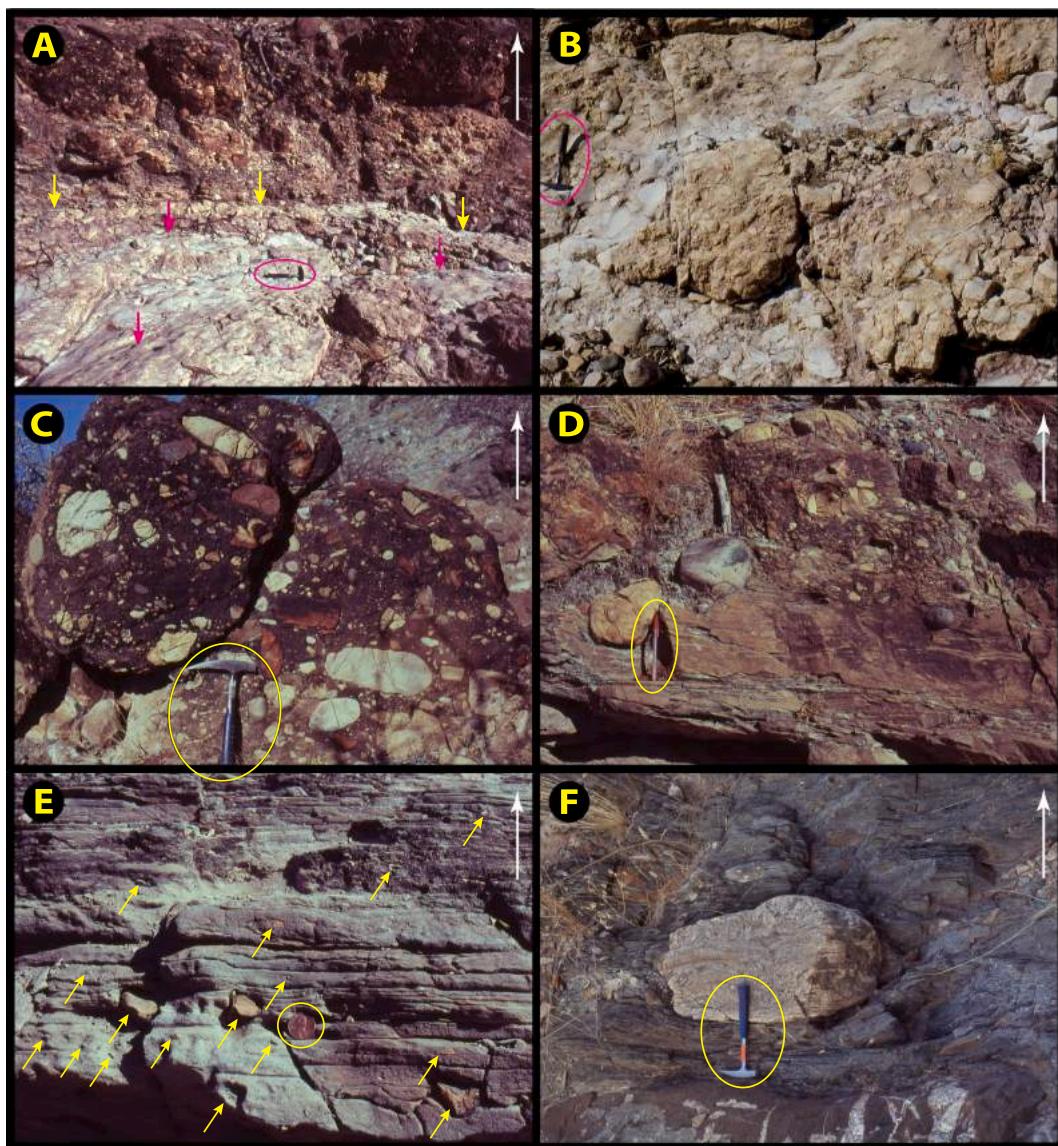


Fig. 108. Images of Chuos Fm near floor of Sturtian bedrock trough at Omutirapo (8–7): white arrows indicate stratigraphic younging. (A) Successive boulder pavements (magenta and yellow arrows) in basal Chuos Fm at $-19.1228^{\circ}/13.9355^{\circ}$ in 8–7 (base of P1010, [Figs. 106 & 107](#)). Pavements imply grounded ice and are composed of clasts exclusively derived from underlying Devede Fm *Tungussia*-type dolomite stromatolite. Pavements are overlain by pebble-rich sandstone as in C. (B) Plan view of oligomicitic boulder pavement at base of Chuos Fm at same location as A. (C) Sandstone crowded with rounded and subrounded dolomite and chert pebbles in lower Chuos Fm above basal boulder-pavement at same location as A. (D) Fine-grained sandstone with rounded dropstones grading into clast-rich diamictite in lower Chuos Fm at same location as A. (E) Swaley thin-bedded siltstone with dolomite dropstones (arrows) at same location as A. (F) Clast-poor diamictite with rounded boulder of dolomite ribbonite (Devede-derived), overlying sorted sandstone body (hammer head) in lower Chuos Fm near $-19.1237^{\circ}/13.9344^{\circ}$ in 8–7 (P1713, [Fig. 106](#)).

directly ([Fig. 118A & B](#)) or by thin Ghaub Fm dolomite diamictite ([Fig. 118C–E](#)). Compared with adjacent transects (7–9 & 10, 9–3 & 4, 10–2, 11–8 & 10), 50–80 m of upper Omboaatjie Fm are missing beneath the Marinoan erosion surface in Tr8, including most or all of cycle b8 ([Fig. 103](#)). The Ghaub Fm itself rarely exceeds 2.0 m in thickness and is discontinuous at the outcrop scale. It consists of massive to banded carbonate diamictite ([Fig. 118C](#)) with a strongly preferred 010° azimuthal orientation of elongate clasts ([Fig. 57](#)) in section 8–3. Given the known paleogeographic zonation, we infer from the clast fabric ([Dowdeswell et al., 1985](#)) that glacial flow was directed SSW (190°) in present coordinates, and that the thin and discontinuous Ghaub diamictite in Tr8 originated as melt-out and/or lodgement tills. Locally, as

in 8–5, large thin plates of Omboaatjie dolomite were lifted off intact and incorporated within Ghaub diamictite ([Fig. 118D](#)). Such plates appear to have undergone little lateral transport. They were possibly jacked up by grounded marine ice under the influence of surface ablation (i.e. sea-ice ‘elevator’ of [Goodman and Pierrehumbert, 2003](#); [Debenham, 1920](#)) and/or tides (e.g., [Dowdeswell et al., 2020](#)).

2.8.3. Early Ediacaran of Tr8

Since Tsumeb Subgroup changes little along the length of the transect, we focus here on well exposed and accessible sections in the upper Hoanib River gorge downstream from the village of Omboaatjie ([Fig. 96](#), see also SOI S3.11.3. and Fig. S25B). A composite section of Maieberg

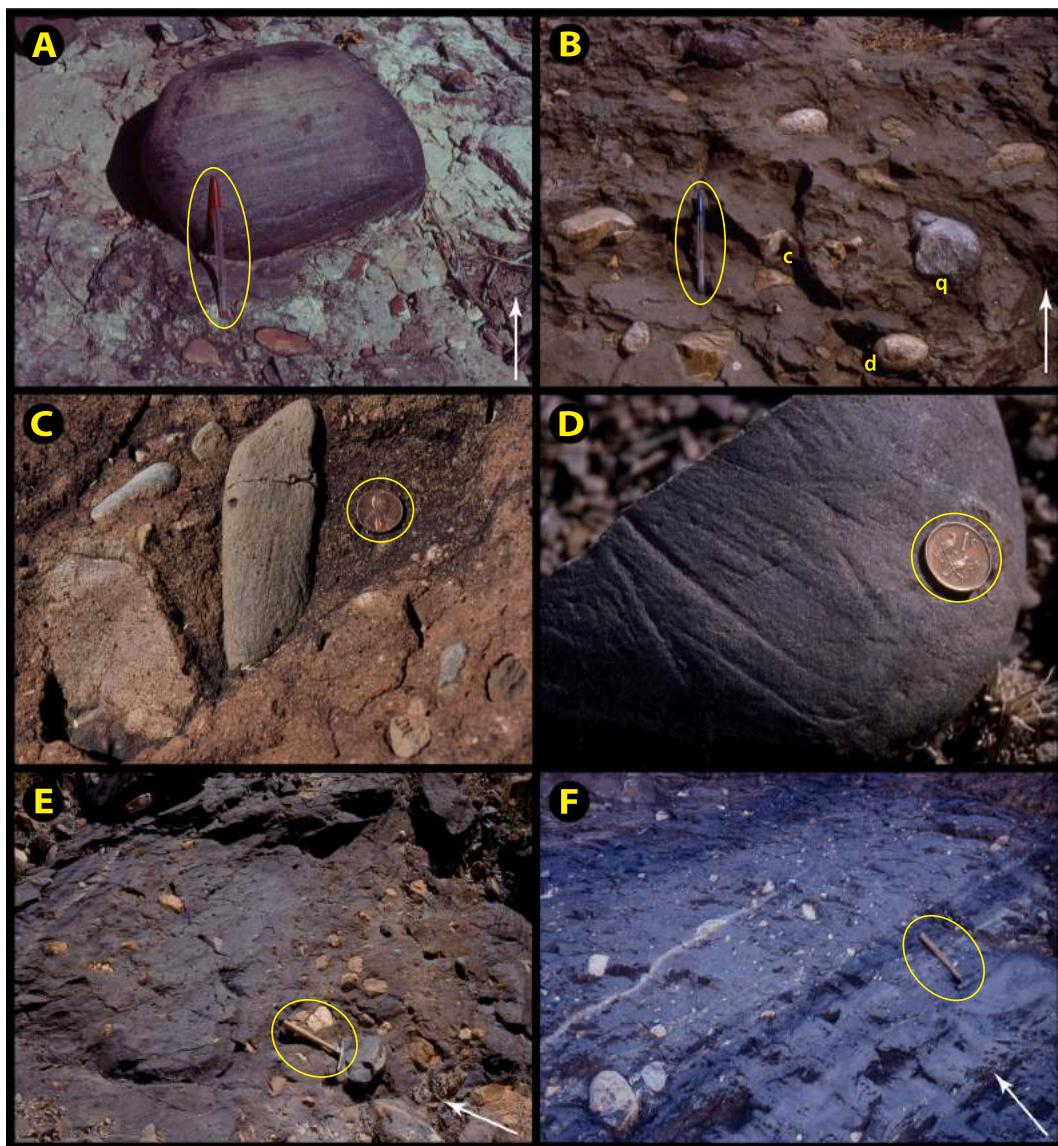


Fig. 109. Images of massive and stratified diamictites in Chuos Fm within bedrock trough at Omutirapo (8–7, Figs. 106 & 107): white arrows indicate stratigraphic younging. (A) Clast-poor diamictite near $-19.1230^{\circ}/13.9351^{\circ}$ in P1010 with argillaceous matrix holding a well-rounded boulder of crossbedded feldspathic quartzarenite derived from Nabis Fm. Rounding and polishing of boulders is characteristic of subglacial transport involving trituration and milling—it does not require aqueous transport. Crossbedding is internal to boulder, unlike superficial striations in C and D. (B) Massive diamictite at $-19.1221^{\circ}/13.9346^{\circ}$ in P1010 with silt-wackestone matrix and subrounded pebbles of dolomite (d), quartz-arenite (q) and chert (c). (C) Subrounded, bullet-shaped pebble of quartz-siltstone in massive sand-rich diamictite at $-19.1144^{\circ}/13.9404^{\circ}$ near P1831. Striations on siltstone pebble are superficial and inferred to be glaciogenic. (D) Multiple directions of crude superficial striations on siltstone pebble from diamictite at $-19.1219^{\circ}/13.9329^{\circ}$ in P1010 are also inferred to be glaciogenic (see also Le Heron et al., 2013a). (E) Crudely-stratified diamictite at same location as B with subrounded pebbles of dolomite and subordinate quartzarenite, grading to well stratified with dropstones in upper left. (F) Clast-rich shear-bands of possible glaciectonic origin in clast-poor diamictite with subrounded dolomite pebbles at $-19.1222^{\circ}/13.9349^{\circ}$ in P1010. Shear fabrics and associated glaciectonic features are stratigraphically confined and suggest SW-directed glacial flow (Le Heron et al., 2013a).

and Elandshoek formations is shown in Fig. 117A, along with an expanded section of Keilberg Mb (Fig. 117B). These sections may be compared with Ediacaran sections from the distal FSz (Fig. 19), proximal FSz (Fig. 44) and OPz (Fig. 82). As before, Maieberg Fm is divided into three members (Tm1–3), Tm1 is Keilberg Mb (Tk), which we subdivide into four units, Tk1–4 (Fig. 117B).

The base of Keilberg Mb is knife sharp (Fig. 118A–C) and subunit Tk1 consists of ≥ 1.0 m of dolopelarenite with ubiquitous low-angle swaley cross-stratification (Figs. 118B, 119A & B) and uncommon small-scale wave ripples (Fig. 119A). Tk1 is omnipresent, whether the

substrate is Ghaub diamictite (Figs. 118C, E & 119C) or Omibaatjie dolomite (Fig. 118A & B). Where the dolomites are in contact, the pale pinkish buff-weathering Keilberg Mb is distinct from the sombre grey-coloured Omibaatjie Fm (Fig. 118A–E).

Tubestone stromatolite (subunit Tk2) begins at nodes, spaced a few meters apart and ~ 1.0 m above the base of Tk1 (Figs. 69B, 117B, 118B, 119B & C, 120C & D). The nodes expand upward at the expense of mechanically stratified dolopelarenite. At ~ 2.2 m above the same datum, the stromatolite nodes coalesce to form a continuous biostrome (Figs. 118B, 119B & C). The top of the biostrome is undulating, with a

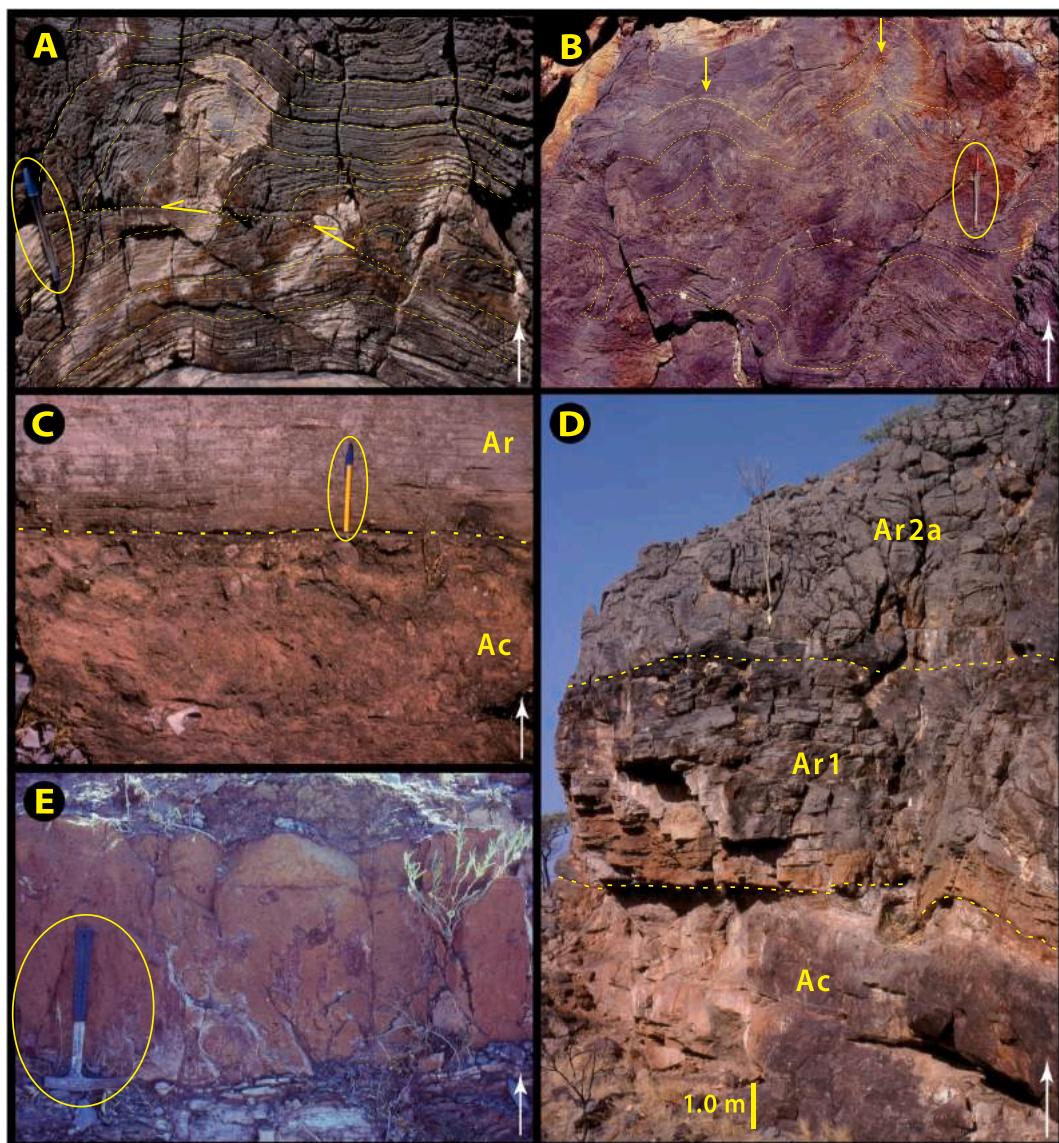


Fig. 110. Images of Sturtian glacial termination—upper Chuos and lower Rasthof formations—in Omarumba paleovalley (Tr8) N of Ondevede: white arrows indicate stratigraphic younging. (A–B) Lobate stromatolites in Ar2a member of Rasthof Fm (Fig. 111): $-19.1184^\circ/13.9286^\circ$ in 8–7 (Fig. 104). Lobes develop over inclined ramps (yellow arrows in A) but have no preferred azimuthal orientation, suggesting that isotropic expansion due to microbial growth was resolved by vertical thickening. Pinched lobe crests (yellow arrows) constitute the only potential evidence for phototropism in Ar2a lobate stromatolites. (C) Sharp flat contact (dashed line) at $-19.0805^\circ/13.9471^\circ$ in 8–8 between ferruginous Chuos Fm granule diamictite (Ac) and Rasthof Fm dolomite rhythmite (Ar1) (Fig. 111). (D) Contacts at $\sim 19.0332^\circ/13.9401^\circ$ in 8–9 between Chuos Fm (Ac) and Rasthof Fm basal rhythmite (Ar1) and lobate stromatolite (Ar2) members (Fig. 111). Lower contact is sharp; upper one gradational over ≤ 0.5 m. Basal Rasthof Fm dolomite is discoloured by Fe mobilized from Chuos Fm. (E) Dolomite turbidite unit rich in cm-scale clasts, in laminated silty argillite of upper Chuos Fm at $-19.1166^\circ/13.9370^\circ$ in 8–7. Dolomite turbidites occur sporadically in Chuos Fm stratified facies and are considered to be detrital in origin on textural grounds, but some are more ^{13}C -depleted than most pre-Sturtian sources (Figs. 158 & 10).

crest height of 4.2 m above the datum. In detail, the biostrome is composed of small, highly arched, vertically aggraded ‘stromatoids’ (Hofmann, 1969), ~2 cm in diameter (s in Figs. 69B, 119D & E). The stromatoids are separated by ‘tubes’ of laminated dolopelmicrite, curved concave-upward like a meniscus (t in Figs. 69B, 119D & E). The micrite-filled tubular structures are oriented paleovertically (geoplumb) and individual tubes persist for a meter or more vertically (Fig. 119B–D). Synoptic relief between arched stromatoids and intervening tube floors need not have exceeded 3 cm. In synoptic morphology, the stromatoids are shaped like an egg-carton and the tubes (where the eggs sit) are circular in plan view (Fig. 119F). In 8–1, Tk2 stromatoids form gutters,

oriented in a tilt-corrected azimuth of 023° (Fig. 57). Tk2 tubestone biostrome is laterally continuous for ≥ 70 km to the NE (Tr10) and NW (Tr11) of 8–1. Compared with OPz (Tr5–7), tubestone stromatolite in Tr8 is less-coarsely recrystallized and thinner as a fraction of the total Keilberg Mb (Fig. 117A). There is less void-filling cement within the tubes and cm-scale communal stromatoids replace the smoothly laminated decameter-scale domes in OPz (Fig. 69A).

Tk3 is the thickest subunit in Keilberg Mb (Fig. 117B) and is a mechanically deposited dolopelarenite characterized by ‘giant wave ripples’ (Allen and Hoffman, 2005a). These unusual bedforms occur in Marinoan cap dolomites in 12 basins on 7 paleocontinents (Hoffman and

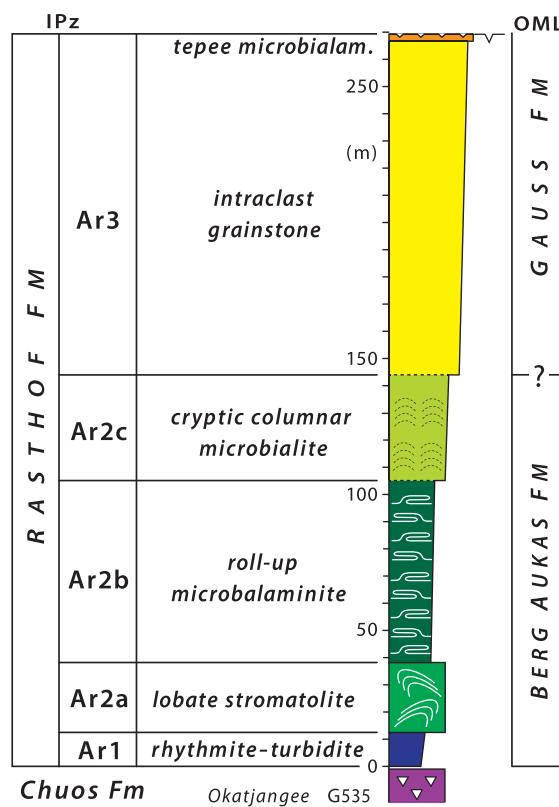


Fig. 111. Typical columnar section of Rasthof Fm in IPz (actually 10–5), showing informal members (Ar1–3) and lithologic correlation with Berg Aukas and lower Gauss formations in Otavi Mountainland (Wallace et al., 2014; Hoffman et al., 2018). Limited $\delta^{13}\text{C}$ data from Otavi Mountainland (Kaufman et al., 1991) are compatible with basal Gauss Fm lower wrt Rasthof Fm (Fig. 159) than indicated.

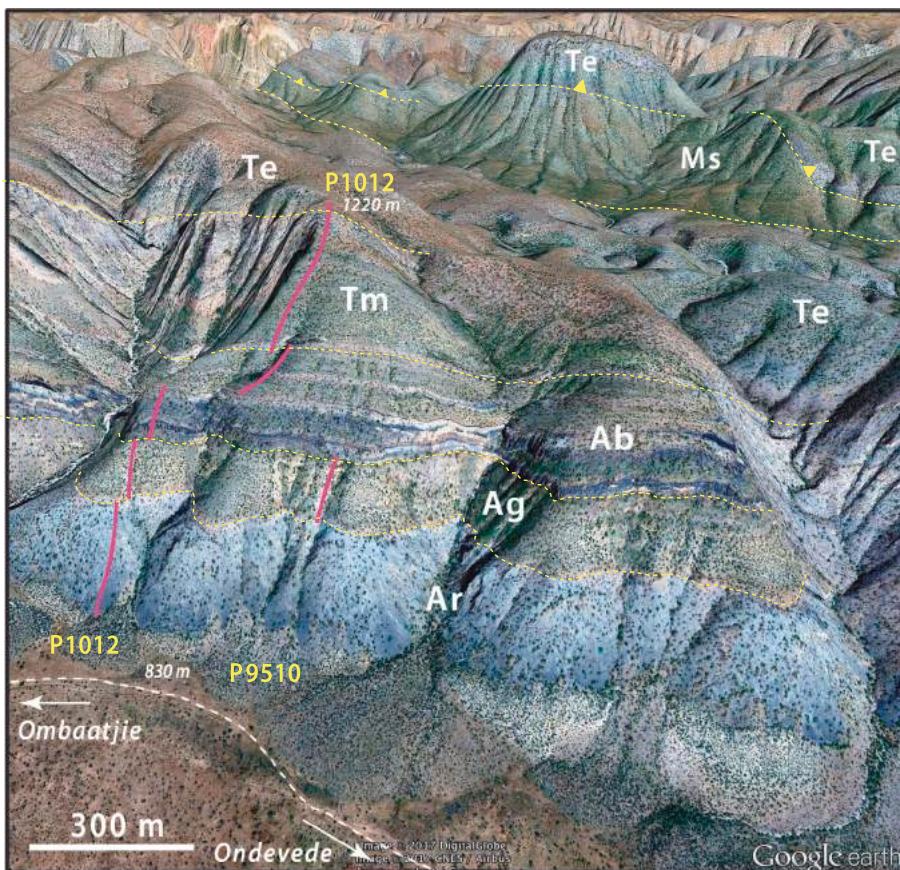


Fig. 112. Annotated satellite image of Middle Cryogenian and early Ediacaran formations in 8–4 N of Ombaatjie (Figs. 96, 103 & 117), looking obliquely WSW from Omarumba paleovalley (Tr8). Mappable formations (in stratigraphic order): Ar, Rasthof Fm; Ag, Gruis Fm; Ab, Ombaatjie Fm; Tm, Maieberg Fm; Te, Elandshoek Fm; Ms., Sesfontein Fm (Mulden Group). Base of Ar not exposed. Topographic relief from base to top of section P1012 is 390 m. Vehicle track (lower left) links villages of Ombaatjie and Ondevede (Fig. 96). Note contrast between non-cyclic Ar and cyclic Ab (Fig. 103). Lower Ab is mostly limestone (dark grey) and upper Ab is mostly dolomite (buff) (Fig. 103). In the distance, Te dolomite is thrust over Ms. schist in a pop-up structure. Field guide for section P1012 (8–4) is in SOI S3.11.2. Google Earth: Image © 2020 Maxar Technologies.

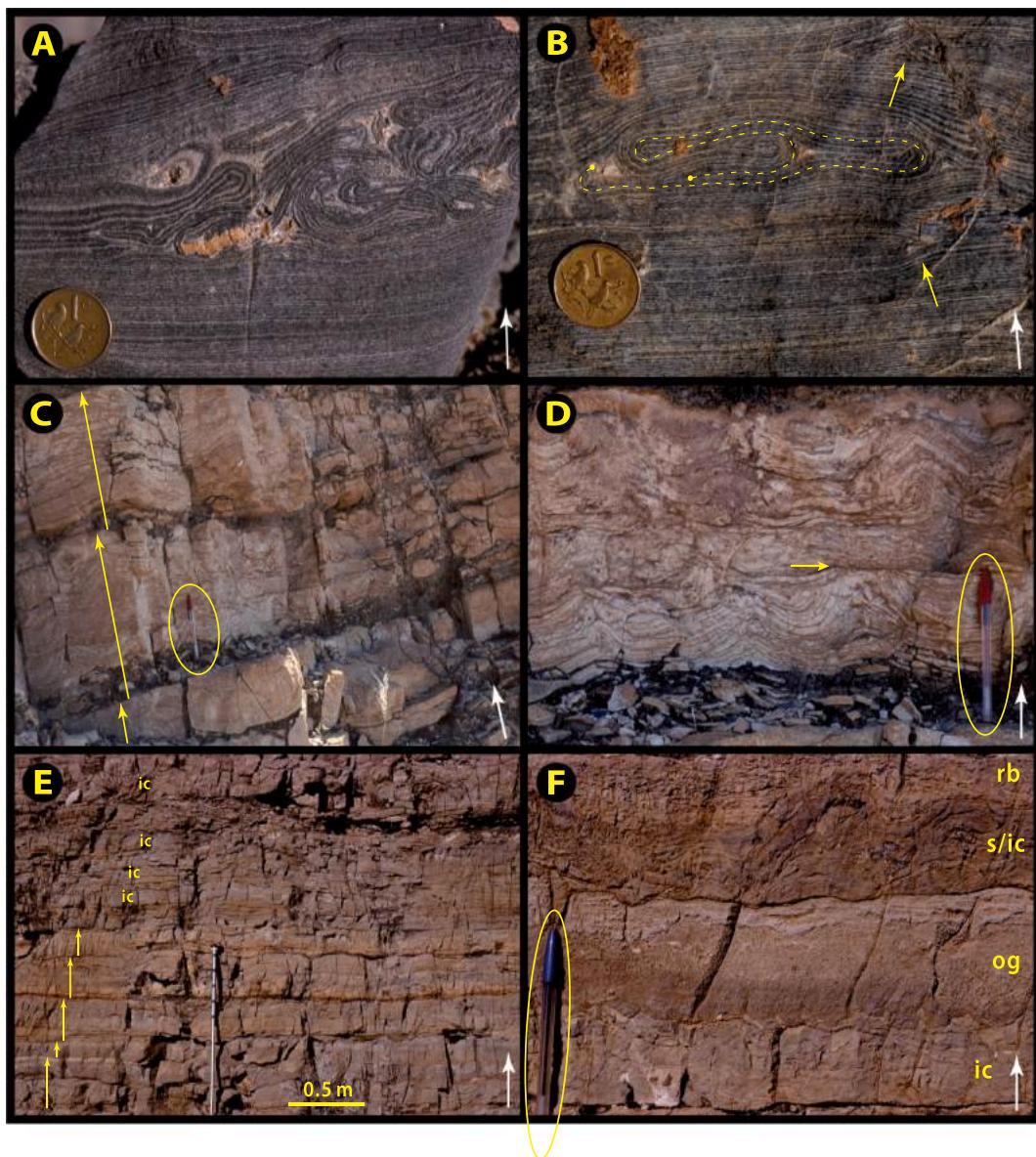


Fig. 113. Images of middle Cryogenian Rasthof and Gruis formations in Omarumba paleovalley (Tr8) north of Omibaatje (Figs. 96 & 103): white arrows indicate stratigraphic younging. (A–B) Rollups in Rasthof Fm microbiolaminite member Ar2b at $-19.2573^{\circ}/14.0040^{\circ}$ in 8–4 (P1012, Fig. 112), proving that dark laminae were pliable but cohesive, presumably bound by actively growing benthic filamentous microbes, not settled as pelagic organic ‘snow.’ Benthic microbes were apparently chemotrophic since sequence stratigraphic context (Fig. 111) suggests that Ar2b accumulated in water depths well below the euphotic zone. Not void-filling sparry cement in tangle of rollups in A. 2 cm diameter coin. Rollup in B dashed with dots at terminations. Arrows point to non-displaced terminations, where detached rollups like the doubly terminated dashed line could have originated. Cause of rollup detachment is conjectural but explosion of gas bubbles trapped beneath half-cm-thick surface layers is preferred in the absence of evidence for wave or current action, or slope instability. (C–D) Tepees (Kendall and Warren, 1987), indicating supratidal evaporative pumping, cap 30-cm-thick regressive cycles (arrows in C) of lower Gruis Fm at $-19.2584^{\circ}/14.0017^{\circ}$ in 8–4. Note truncated tepee (arrow) in D. Marly dolomite ribbonite forms thin recessive base of each cycle. (E–F) Small scale regressive ribbonite cycles (arrows in E), intraclast breccia beds (ic), ooid grainstone (og in F), stromatolite (s in F) and ribbonite (rb in F) in upper Gruis Formation at $-19.4365^{\circ}/14.0298^{\circ}$ in 8–0/7–22 (Figs. 96 & 88).

Li, 2009; Hoffman et al., 2011). They are trochoidal in cross-section with ≤ 0.35 cm of relief, trough to crest (Fig. 120A & B). Their crestlines are linear and parallel in a NW–SE azimuth (Fig. 57). Foreset laminae coarsen crestward and are bidirectional in the crestal area. Ripples and ripple trains aggrade for ≤ 1.4 m paleovertically, only migrating laterally near the base and top (Fig. 120A & B). The ripples develop from planar surfaces (Fig. 120B) and ultimately degrade or are erosionally truncated. The ripple flanks are typically oversteepened, $35\text{--}45^{\circ}$ with respect to

paleohorizontal, and their crestal orientations (Fig. 57) are subparallel to regional fold trends, suggesting that the ripple flanks were steepened during tectonic shortening. In section 8–3 (Fig. S25B), however, local fold axes strike 045° , nearly perpendicular to giant ripple crests.

Lamb et al. (2012) suggested that incipient lithification on the seafloor could account for giant wave ripple oversteepening. However, intraclasts (e.g., ‘grapestone’ composed of aggregated peloids), which are a common byproduct of early lithification, are notably absent in

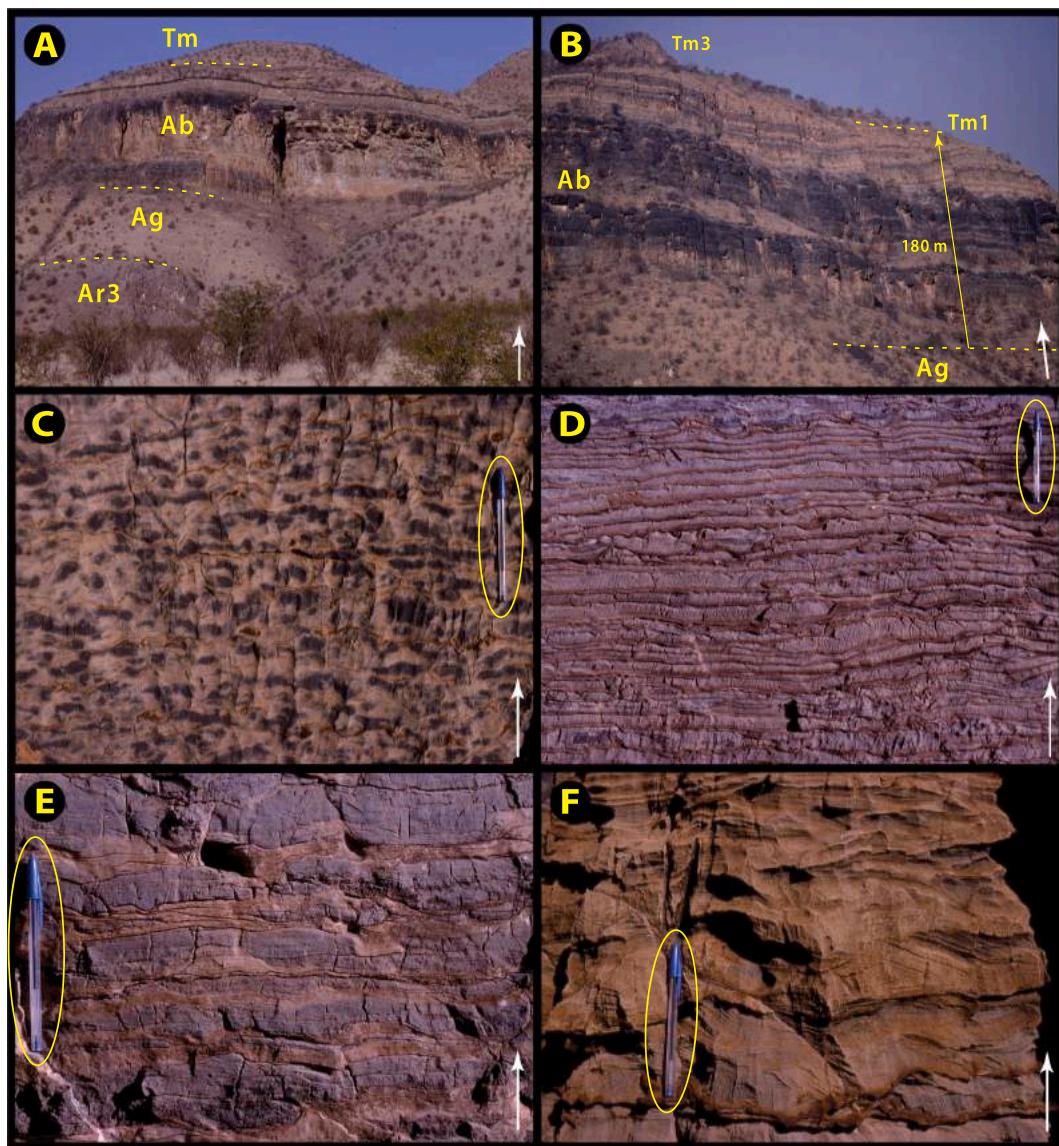


Fig. 114. Images of middle Cryogenian Ombaatjie Fm in Omarumba paleovalley (Tr8) between Ombaatjie and Ondedevede (Figs. 96 & 103): white arrows indicate stratigraphic younging. (A) Cliff-forming intraclast grainstone-dominated cycles of lower Ombaatjie Fm (Ab) at $-19.2886^{\circ}/14.0126^{\circ}$ between 8 and 3 and 4. Other units: Ar3, upper Rasthof Fm; Ag, Gruis Fm; Tm, lower Maieberg Fm. (B) Ombaatjie Fm section G540 at $-19.1815^{\circ}/13.9530$ in 8-5, showing cliff-forming, dark-grey, calcite-grainstone cycles b1-3, overlain by buff-coloured, dolomite-dominated, thinner cycles b4-7 (Fig. 103). (C) Partial dolomitization (buff colour) of calcite ribbonite (dark-grey) in lower Ombaatjie Fm at $-19.3227^{\circ}/14.0338^{\circ}$ in 8-2 (Fig. 103). (D-E) Marly-dolomite ribbonite in Ombaatjie Fm at $-19.2887^{\circ}/14.0047^{\circ}$: between 8 and 3 and 4. (F) Bidirectional crossbedding in lower Ombaatjie Fm intraclast grainstone at $-19.1840^{\circ}/13.9444^{\circ}$ in 8-5 (Fig. 103) composed of discrete dolomite (buff) and limestone (grey) grains, suggesting early dolomitization.

Keilberg Mb and other Marinoan cap dolomites with oversteepened giant wave ripples. Alternatively, we suggest that ripple flanks were steep because peloids had low specific gravity and mutual adhesion. We speculate that they were flocs and accretion balls of microscopic aragonite needles, held together by electrostatic forces and by mucilagenous organic matter (extracellular polymeric substances, or EPS) excreted by indwelling cyanobacteria. Accordingly, the peloids are essentially like modern Bahamian ooids, but non-laminated because they accreted continuously under the influence of perpetual trade winds, rather than episodically during tropical storms (Allen and Hoffman, 2005a, b).

Tk4 (Fig. 117B), is a fining-upward subunit of increasingly marly dolomite ribbonite and/or turbidite. It passes conformably into the middle member (Tm2) of Maieberg Fm at a horizon where calcite appears in marly rhythmite. We infer that water depth increased with stratigraphic height from Tk1 through lower Tm2 (Fig. 117B). This could account for upward disappearance of tubestome stromatolite as a function of light intensity for microbial mat, and downward disappearance of giant wave ripples as due to interference in shallower water by short-period waves. If sea-level rise was rapid, peloids might retain adhesive properties from EPS at depths where cyanobacteria were no longer productive. On the other hand, high surface temperatures in the

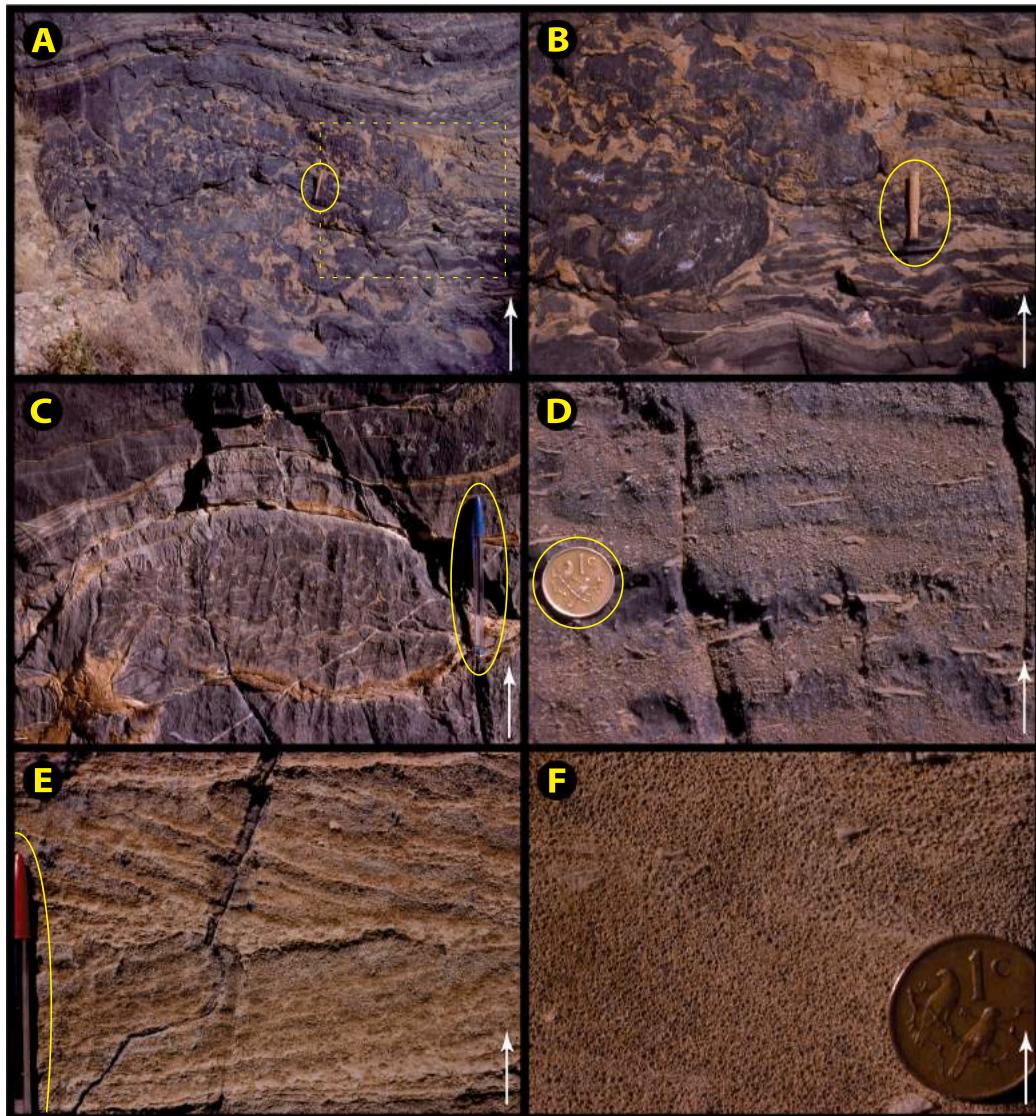


Fig. 115. Images of lower Ombaratjie Fm in Omarumba paleovalley (Tr8) between Ombaratjie and Ondedevede (Figs. 96 & 103): white arrows indicate stratigraphic younging. (A–C) Stromatolite bioherms in partially dolomitized ribbonite at $-19.3182^{\circ}/14.0126^{\circ}$ in 8–3 (Fig. 103). Dashed box in A, where ribbonite onlaps bioherm, shown in B. (D) Intraclast grainstone with mixed dolomite (buff) and calcite (grey) clasts in 8–6. (E–F) Ooid grainstone with bidirectional crossbeds at $-191.840^{\circ}/13.9442^{\circ}$ in 8–6 (E) and partially dolomitized ooids at $-19.2588^{\circ}/14.0005^{\circ}$ in 8–4 (F).

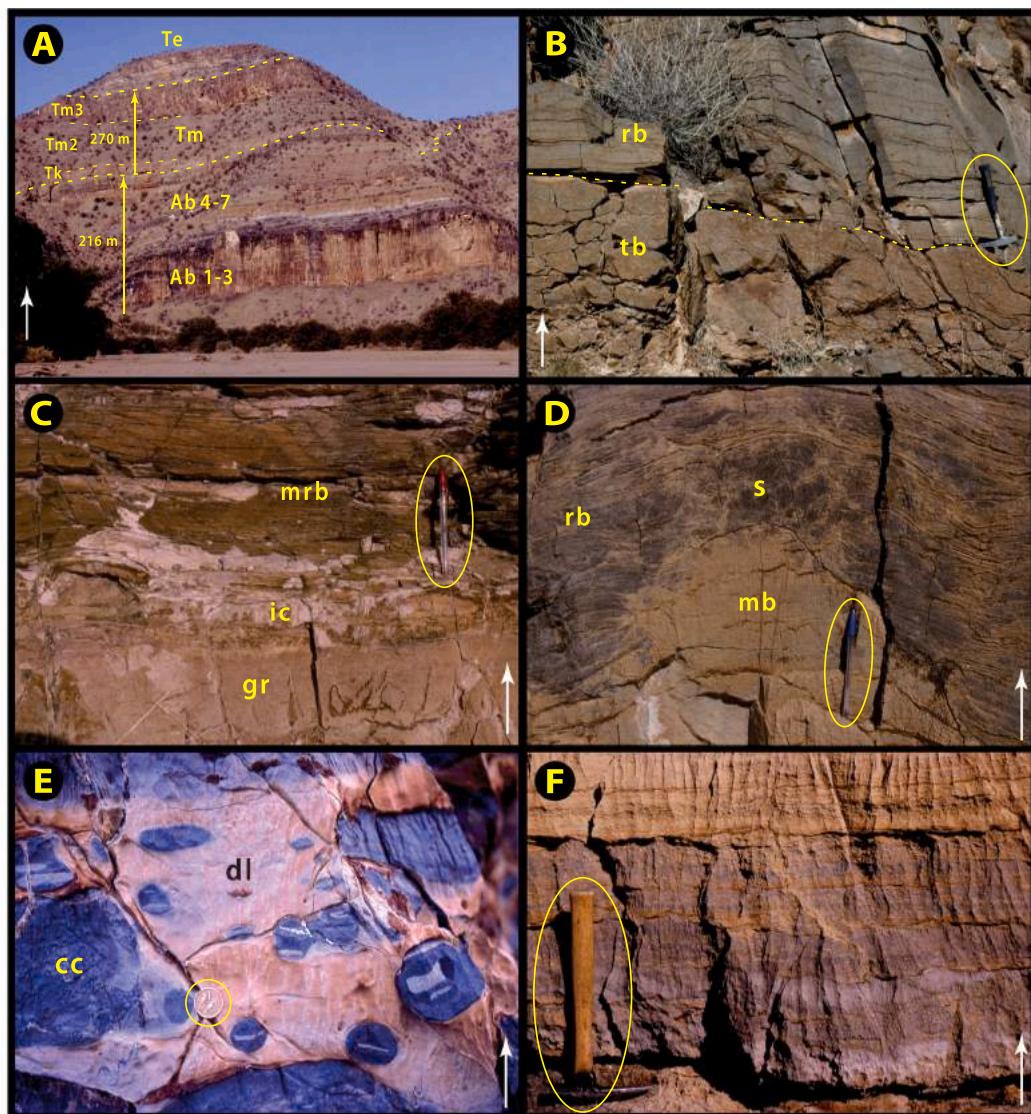


Fig. 116. Images of middle Cryogenian Ombaatjie Fm in Omarumba paleovalley (Tr8) near Ombaratjie (Figs. 96 & 103): white arrows indicate stratigraphic younging. (A) Ombaratjie, Maieberg and lower Elandshoek Fms at $-19.3160^{\circ}/14.0107^{\circ}$ in 8–3, on Hoanib River 2.8 km SW of Ombaratjie. (B) Dolomite ribbonite (rb) overlies tepee breccia (tb) at subaerial exposure surface (dashed line) in lower Ombaratjie Fm at $-19.3222^{\circ}/14.0340^{\circ}$ in 8–2. (C) Marly ribbonite (mrb) overlies dolomitic grainstone (gr) at marine flooding surface marked by transgressive intraclast lag (ic) in lower Ombaratjie Fm at same location as B. (D) Transgressive stromatolite (s), onlapped by ribbonite (rb), overlies disconformity surface above microbialaminite (mb) in lower Ombaratjie Fm near $-19.2588^{\circ}/14.0011^{\circ}$ in 8–4. (E) Calcite ribbonite (cc) partially replaced by dolomite (dl) in lower Ombaratjie Fm. (F) Intraclast grainstone with upward increase in dolomite/calcite clast ratio.

snowball aftermath would have likely favoured respiration over C fixation (e.g., Tait and Schiel, 2013), contributing to extraordinarily low organic contents in Marinoan cap dolomites globally.

There is no evidence in Tr8 for ‘early regression’ (Clark, 1976), as inferred in Tr5 (2.5.1.) from upward-shoaling basal turbidites and zones of sheet-crack cement (Hoffman and Macdonald, 2010). This is easily attributable to TST (cap dolomite) diachroneity as rising waters progressively inundated the foreslope and platform (Hoffman et al., 2007). ‘Early regression’ related to ice-sheet retreat was inferentially complete before IPz was flooded. We are not obligated to abandon cap-dolomite diachroneity, even if alternative ways of interpreting their $\delta^{13}\text{C}$ records prove to be true (Ahm et al., 2018). The argument for diachroneity from physical bedforms still stands—depth-dependent bedforms could not have formed simultaneously in vastly different water depths on the

distal foreslope and platform (Hoffman et al., 2007).

The maximum flooding stage (MFS) of Maieberg Fm is in the lower part of Tm2 (Fig. 117A). It is normally covered or poorly exposed (Fig. 121A). Section P4017 (Figs. 117A & S25B) was measured in an exceptional drainage chute, where Keilberg Mb (18.5 m) and Tm2 are continuously exposed in clean outcrop (see SOI S3.11.3.). The base of this section has geographical coordinates of $-19.30627^{\circ}/13.99227^{\circ}$, and the images in Fig. 118–120 are from within ~ 0.2 km of this location. In the drainage chute, Keilberg Mb Tk4 is conformably overlain by 57.5 m of nodular greenish- to pinkish-coloured marly calcite rhythmite, with spaced cm-scale turbidites of buff-weathering dolomite (Fig. 121B). Green metacrysts (chlorite?) are visible in the marly limestone with the aid of a hand lens. Within the marl, calcite is concentrated in sub-cm-scale blebs, which may have originated as clusters of microscopic

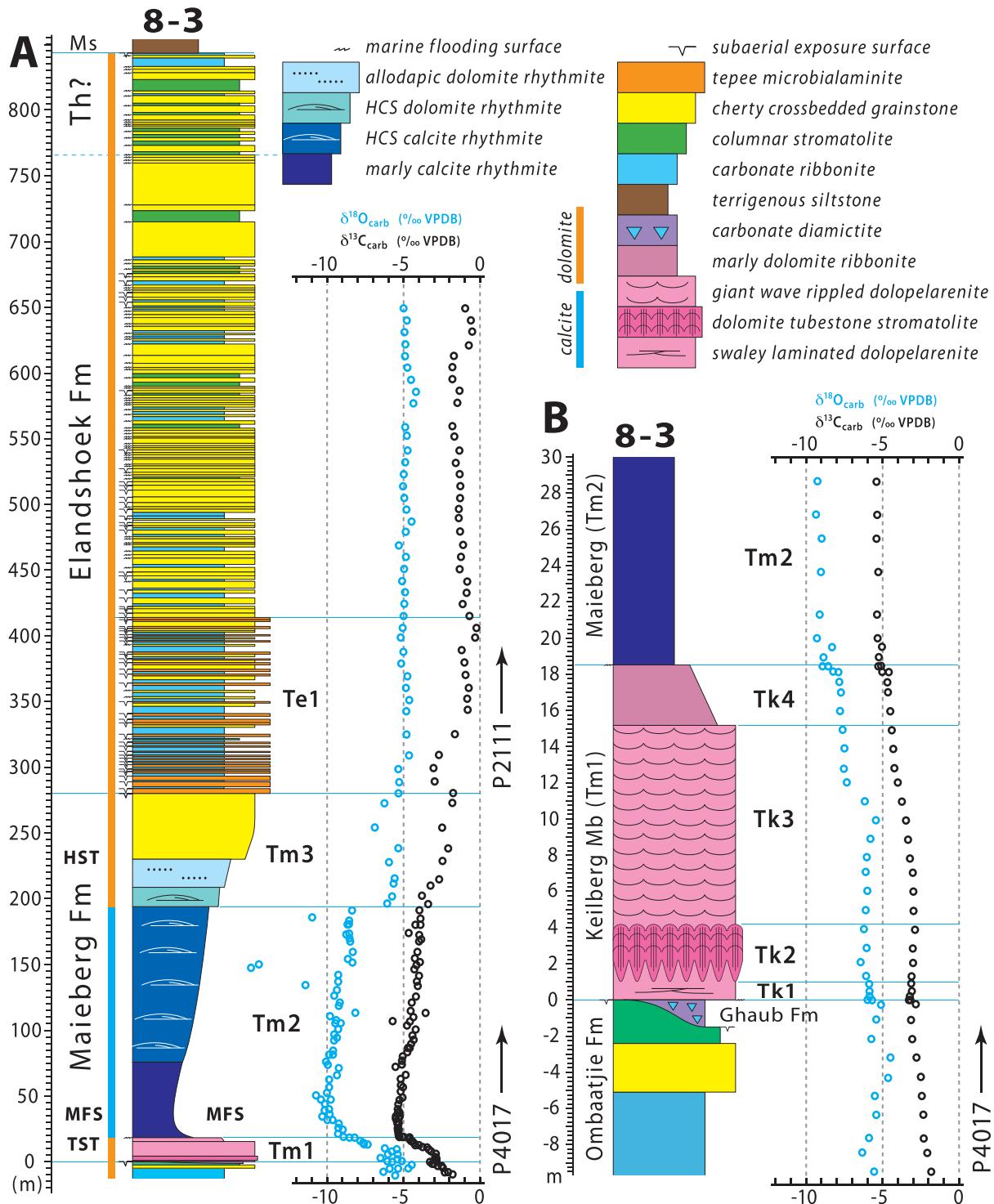


Fig. 117. (A) Composite columnar section of early Ediacaran Tsumeb Subgroup with $\delta^{18}\text{O}$ and $\delta^{13}\text{C}$ data from Hoanib River, 4.2 km (P4017) and 8.2 km (P2111) downstream from Oombaattjie. (B) Expanded section P4017 of Keilberg Mb cap dolomite with tubestone stromatolites, giant wave ripples, and paired $\delta^{18}\text{O}/\delta^{13}\text{C}$ data (images in Figs. 118–120).

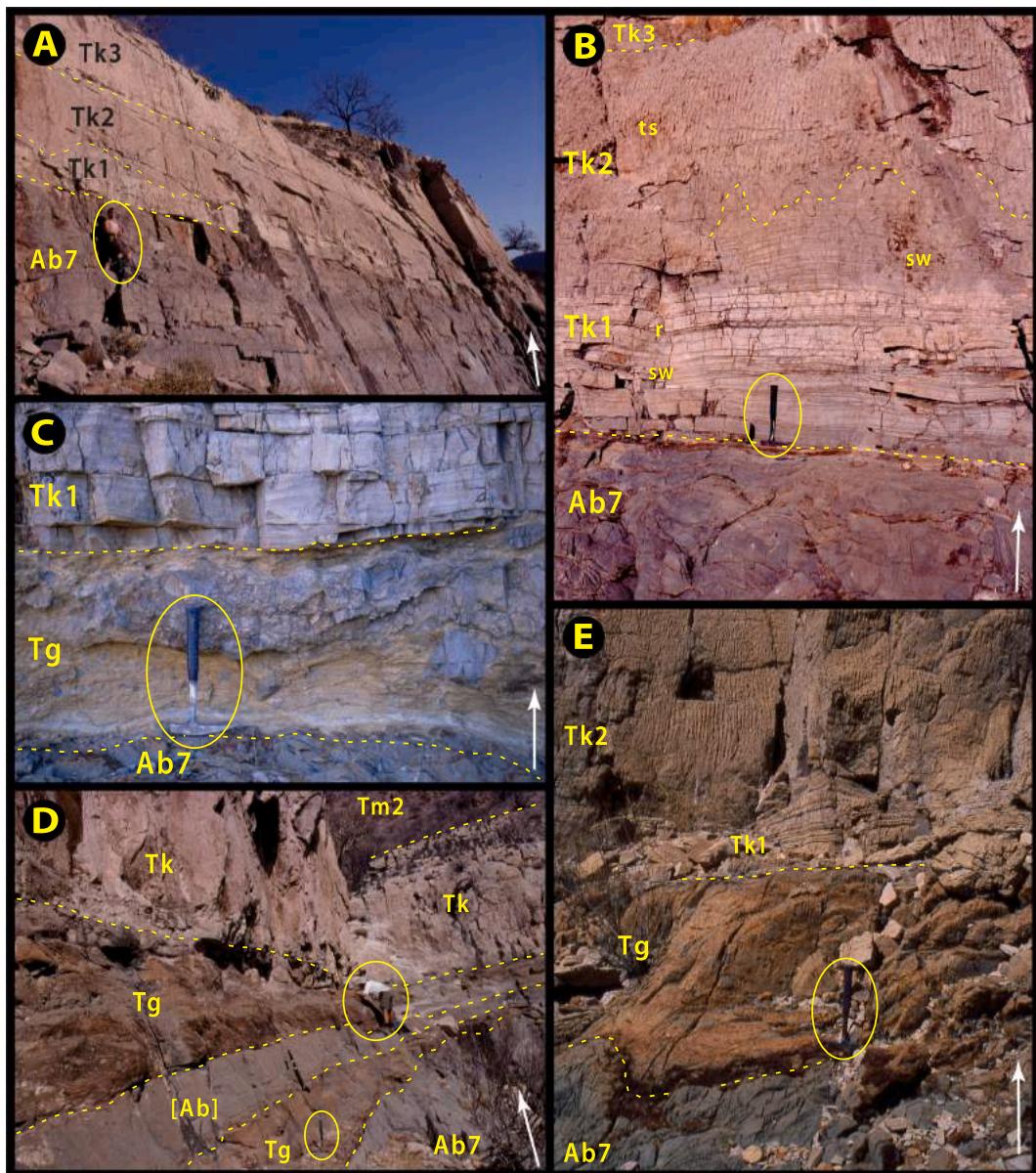


Fig. 118. Images of Ghaub Fm and Keilberg Mb cap dolomite in Marinoan Omarumba trough (Tr8) near Omaatjie (8–3, P4017) and Ondedevede (8–6) (Fig. 103): white arrows indicate stratigraphic younging. Omaatjie Fm cycle b8 is missing due to glacial erosion in Omarumba trough (Fig. 164). Keilberg Mb units: Tk1, swaley crossbedded dolopelarenite (Fig. 119A–B); Tk2, tubestone stromatolite (Figs. 119B–F & 120C–D); Tk3, dolopelarenite with giant wave ripples (Fig. 120A–B). (A–B) Disconformity between Omaatjie Fm cycle b7 (Ab7) and Keilberg Mb (Tk1–3) at $-19.3061^{\circ}/13.9925^{\circ}$ (A) and $-19.3055^{\circ}/13.9933^{\circ}$ (B) in P4017. Note absence of Omaatjie cycle b8 (eroded beneath glacial disconformity) and Ghaub Fm (no glacial recession deposits, implying rapid deglaciation). Geologist Samantha Evans for scale in A. In B, disconformity (hammer head) is coated by ‘microdiamictite’ ≤ 1.0 cm thick. Note spatially variable onset of tubestone stromatolite (ts) above swaley crossbedded grainstone (sw) with rare small-scale wave ripples (r). (C) Ghaub Fm carbonate lodgement tillite (Tg), 0.5 m thick, is sandwiched between Omaatjie cycle b7 (Ab7) and Keilberg cap dolomite (Tk1) at $-19.3177^{\circ}/13.9926^{\circ}$ in 8–3. Clasts in tillite with dimensional ratios $>2:1$ in bedding plane have a strongly preferred NNE–SSW azimuthal orientation (Fig. 57), consistent with glacial flow traction (Dowdeswell et al., 1985). (D) Thin plate of Omaatjie Fm dolomite ([Ab]) is detached and incorporated in Ghaub Fm carbonate diamictite (Tg) at $-19.1883^{\circ}/13.9370^{\circ}$ in 8–6. Plate is decameters in length but ≤ 0.7 m thick. Thin plate detachment of semi-lithified carbonate might result from basal freeze-on and vertical advection of sublimating ice grounded below sea level, aka ‘sea ice elevator’ (Goodman and Pierrehumbert, 2003). (E) Channel of Ghaub Fm diamictite (lodgement tillite?) cut into Ab7 and sharply overlain by Keilberg cap dolomite (Tk1–2) at $-19.3068^{\circ}/13.9907^{\circ}$ in P4017. Field guide for P4017 is SOI S3.11.3.

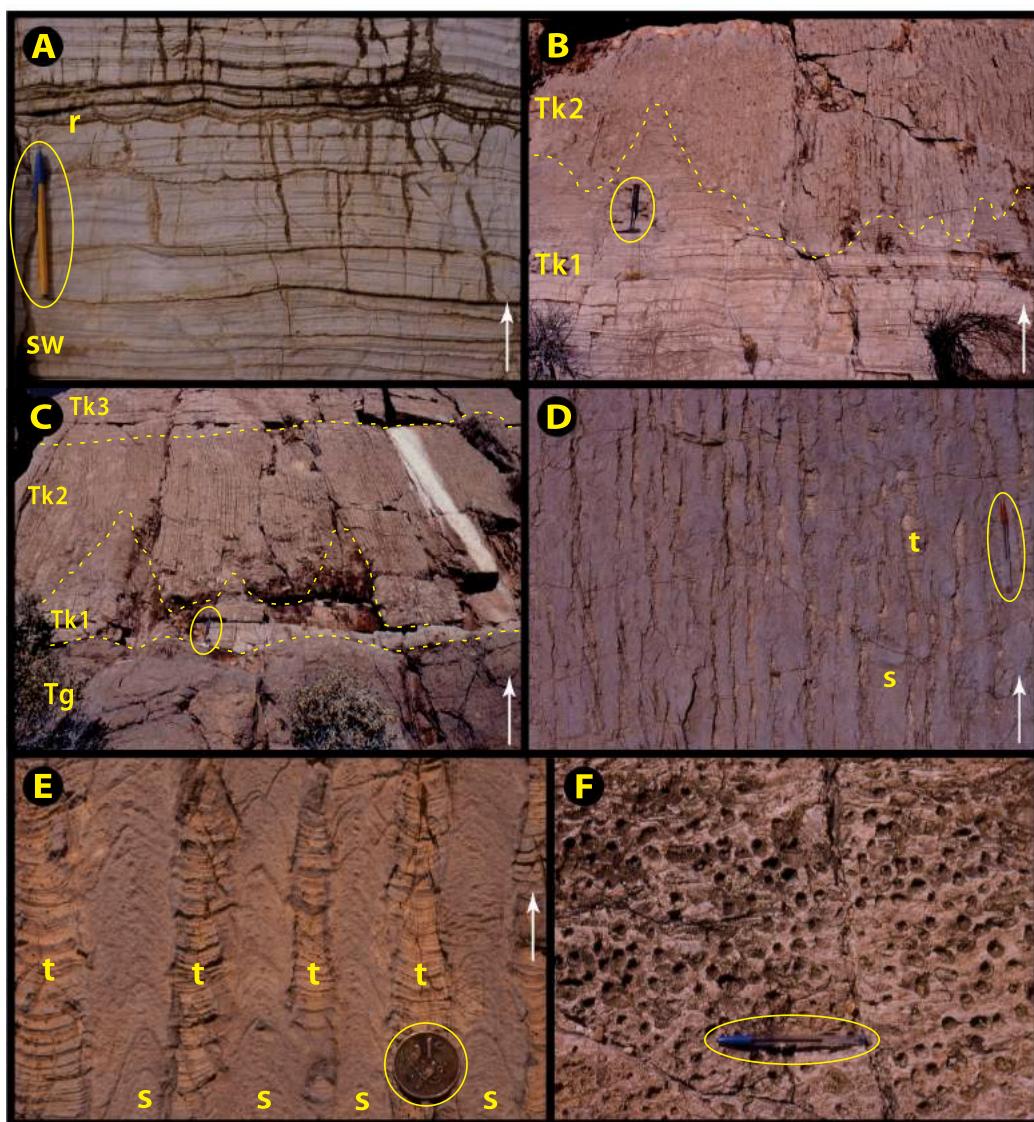


Fig. 119. Images of tubestome stromatolite of Keilberg Mb cap dolomite in Marinoan Omarumba trough (8–3) W of Ombaatjie in P4017 (Fig. 117 and SOI S3.11.3): white arrows indicate stratigraphic younging. Units are as in Fig. 118. (A) Tk1 peloid grainstone at $-19.3069^{\circ}/13.9905^{\circ}$ with low-angle swaley crossbedding (sw) and rare small-scale wave ripples (r). (B) Low-angle cross-stratified peloid grainstone (Tk1) at $-19.3055^{\circ}/13.9935^{\circ}$ overlain by tubestome stromatolite (Tk2) that begins at nodes (Fig. 120C–D) which expand upward and coalesce into a laterally continuous biostrome. (C) Tubestome stromatolite (Tk2) at $-19.3055^{\circ}/13.9932^{\circ}$ with characteristic non-uniform onset and uniform termination, bounded by mechanically bedded peloid grainstones (Tk1 and Tk3) and underlain by Ghaub Fm carbonate diamictite (Tg). (D–E) Tubestome stromatolite (Tk2) at $-19.3073^{\circ}/13.9902^{\circ}$ in bedding-normal section showing stromatoids (s) with highly arched microbial lamination and micrite-filled interspaces (t) with meniscus-like (concave-upward) abiotic laminae. In plan (F), micrite infills (t) are circular, forming vertical tube-like structures, while the stromatoids form a honeycomb-like structure encircling each tube-like depression. Note vertical continuity of structures. 2 cm coin in E. (F) Bedding plane surface of tubestome stromatolite (Tk2) at $-19.3224^{\circ}/13.9837^{\circ}$ (Hoanib River bank near parking area for walk to P4017) in which the micrite-filled tubular structures (t) form circular pits and raised areas are the microbial stromatoids (s). Field guide for P4017 is SOI S3.11.3.

ragonite needles of benthic origin. Macroscopic crystal fans were not observed. At a height of 76 m above the base of Keilberg Mb, calcite rhythmite replaces marly rhythmite and the greenish colour gives way to grey or pink. The stratification is defined by stylolites and m-scale swaley (Fig. 121C) and hummocky (Fig. 121D) cross-stratification are common over the next 130 m of section (Fig. 117A). Nearly 200 m above the datum, limestone is replaced by dolomite rhythmite, also with hummocky cross-stratification. Member Tm3 grades upward through intraclast debrite into upward-coarsening dolomite grainstone with high-angle crossbedding. A boxwork of chert extends downward from the distinct sequence boundary at the top of Tm3 (Fig. 117A). As a

whole, Maieberg Fm (including Keilberg Mb) represents a single 260-m-thick TST–HST depositional sequence without evident higher-order cycles (Figs. 117A & 121A) (Hoffman et al., 1998a).

In contrast, the overlying Elandsheek and Hüttenberg formations present a myriad of small-scale depositional cycles, averaging just 3.9 m thick over 563 m of section (Figs. 117A & 120E). At first, many cycles are capped by microbial laminites with tepees. Later cycles are capped by grainstone and end at exposure surfaces or marine flooding surfaces overlain by ribbonite or stromatolite (Fig. 117A). Grainstone and especially stromatolite units are selectively replaced by authigenic chert, on which ‘desert varnish’ accumulates producing dark bands visible on

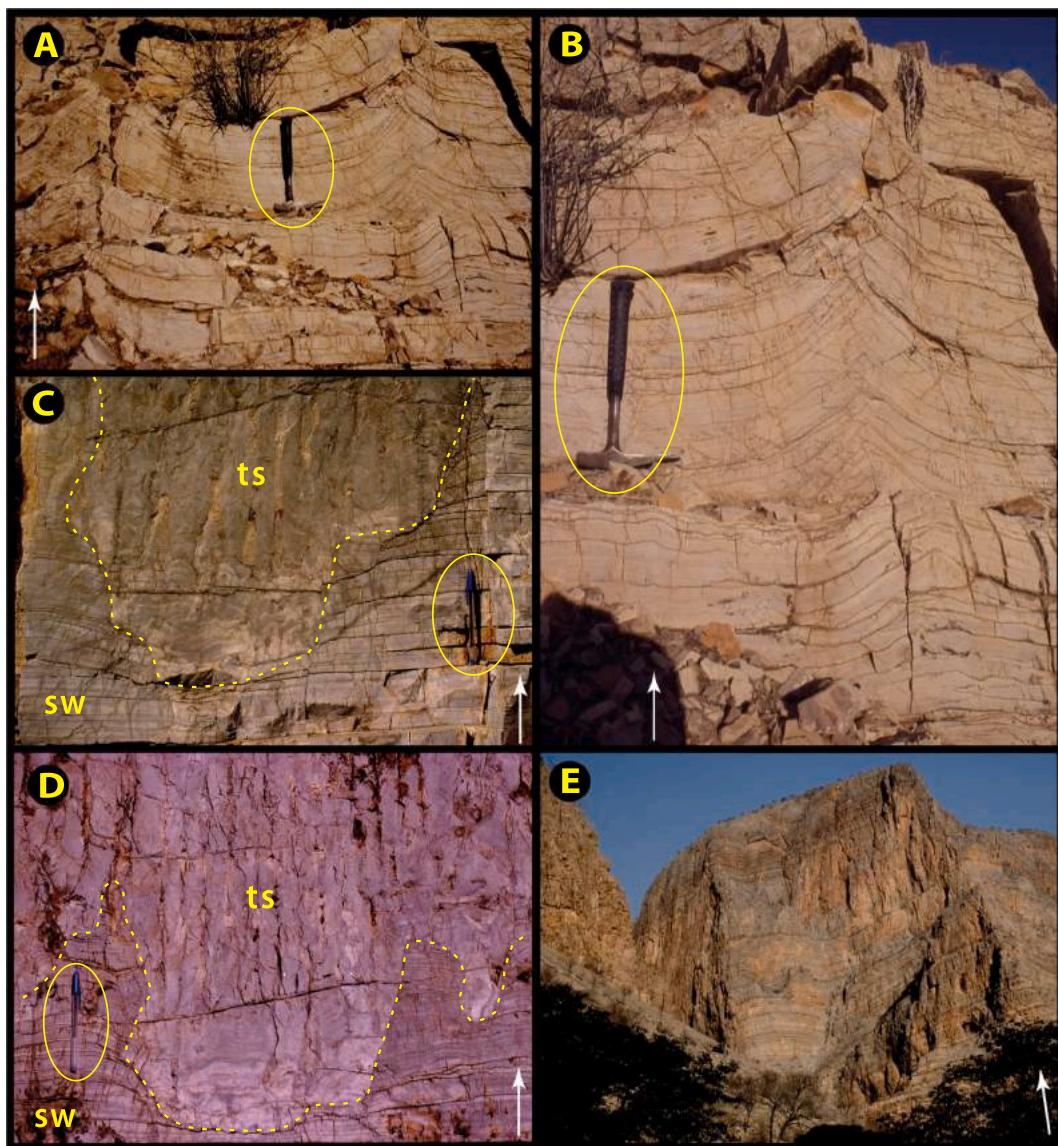


Fig. 120. Images of giant wave ripples and tubestone stromatolite starting nodes in Keilberg Mb cap dolomite of Omarumba trough (8–3) W of Omibaatjie in P4017 (Fig. 117): white arrows indicate stratigraphic younging. (A–B) Giant wave ripples (Allen and Hoffman, 2005a) in Tk3 member at $-19.3076^{\circ}/13.9900^{\circ}$ near section P4017. The ripples have bidirectional foresets, develop from planar beds and their crestlines are linear in plan view. They are thought to form in the deeper parts of the ocean mixed layer where only long-period waves ‘feel’ the bottom. Consistent azimuthal orientations (Fig. 57), oblique to tectonic strike, suggest that giant wave ripples are not products of hurricanes but of strong prevailing winds (e.g. trade winds) over large fetch (Allen and Hoffman, 2005b; Hoffman and Li, 2009). (C–D) Tubestone stromatolite (ts) initiates at nodes in swaley-bedded micropeloidal grainstone (sw) at $-19.3068^{\circ}/13.9906^{\circ}$ near P4017. Field guide for P4017 is SOI S3.11.3. (E) Repetitive peritidal dolomite cycles in Elandshoek and Hüttenberg Fms (Fig. 117) in Anabib anticline (Fig. 96). Darker layers are desert varnish on heavily silicified grainstone units. Cycles average ~ 3 m thick.

cliffs (Fig. 120E). Maieberg and Elandshoek formations represent post-Marinoan ‘catch-up’ and ‘keep-up’ accumulations, respectively, analogous to post-Sturtian Rasthof and Gruis formations (Fig. 103) (Hoffman et al., 1998a; Hoffman and Halverson, 2008).

It is not clear where to place the Elandshoek–Hüttenberg formation boundary in section 8–3 (Fig. 117). We tentatively place it such that the more prominent ‘tutu’ stromatolite beds are in the younger formation (King, 1994; Miller, 2008b). Hüttenberg Fm is disconformably overlain by terrigenous clastics (Sesfontein Fm) of lower Mulden Group. Sesfontein Fm (Fig. 6D) is made up mainly of semipelitic (quartz-sericite-chlorite) schist, but dolomite-chert debrite and conglomerate (Fig. 121E–F) derived from Tsumeb Subgroup are locally prominent basally and within Sesfontein Formation (Fig. 121E & F).

2.8.4. Highlights from Tr8

Chief highlights are: (1) Ombombo Subgroup and the evidence it provides for crustal stretching and rift-shoulder uplift in early Devede and Okakuyu Fm time, the former before 760 Ma and ≥ 100 Myr before the rift-to-shelf transition in OPz (Fig. 10A–C); (2) the Sturtian subglacial bedrock trough at *Omutirapo* (Fig. 105); (3) Rasthof Fm onlap and offlap beneath Gruis Fm, related to a growth fault, at 8–7–8 (Fig. 103); and (4) post-snowball ‘catch-up’ (Rasthof and Maieberg Fms) and ‘keep-up’ (Gruis and Elandshoek Fms) sequences (Sarg, 1988), dissimilar in lithofacies but alike in sequence-stratigraphic character and implications for Cryogenian glaciations—extreme durations and accumulated subsidences, undercompensated by synglacial sedimentation (Partin and Sadler, 2016).

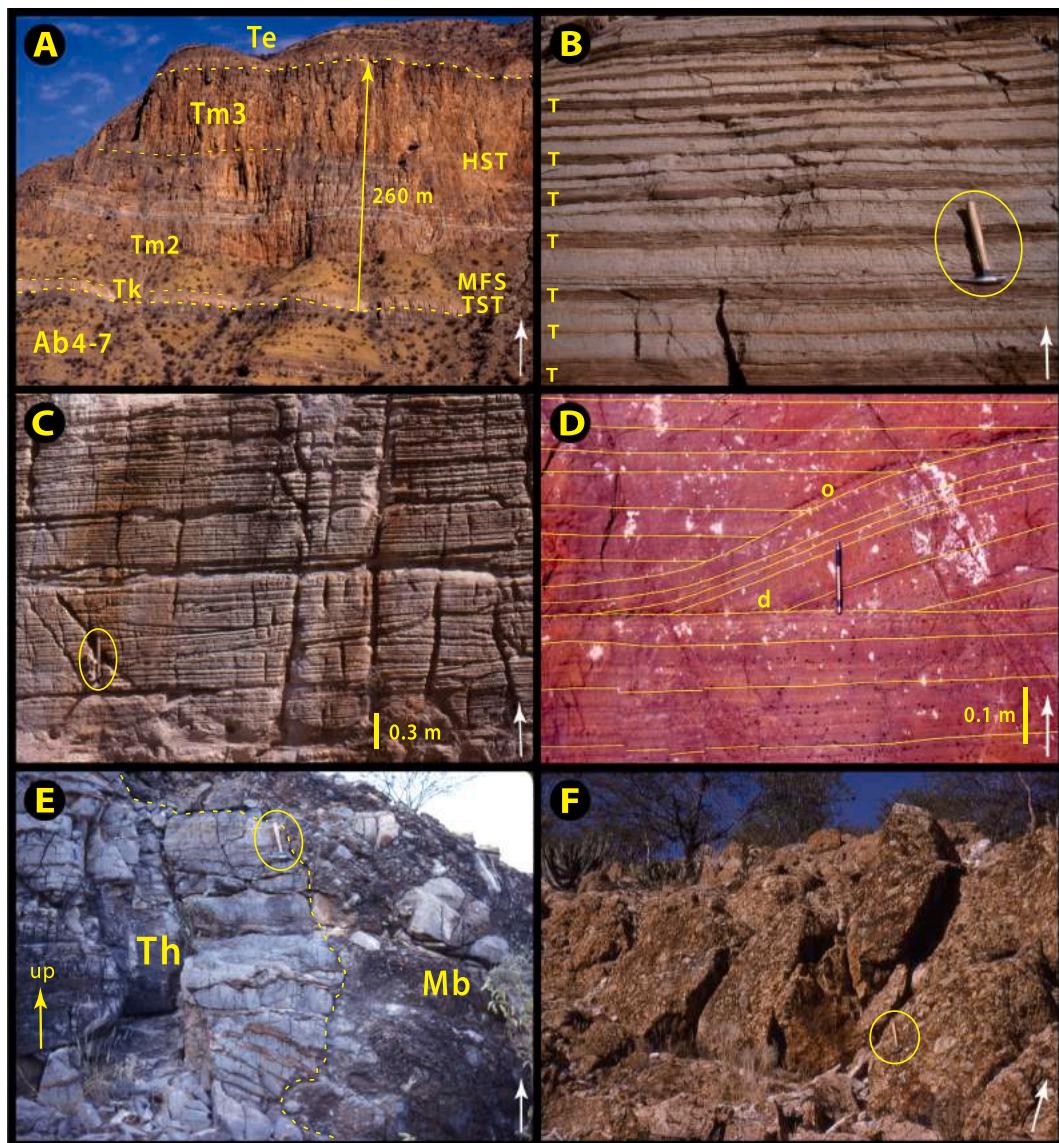


Fig. 121. Images of earliest Ediacaran Maieberg Fm and basal Mulden Group west of Omibaatje (8–3): white arrows indicate stratigraphic younging. (A) Complete Maieberg Fm in Hoanib River gorge at $-19.3107^{\circ}/13.9983^{\circ}$ (base of vertical arrow) between Omibaatje and P4017 (Fig. 117), which is directly behind the wall in view (Fig. S25B). Units: Ab4–7, Omibaatje Fm cycles b4–7; Tk, Keilberg Mb; Tm2, Maieberg Fm middle limestone member; Tm3, Maieberg Fm upper dolomite member; Te, lower Elandshoek Fm. Cap-carbonate sequence includes TST (=Tk), transgressive systems tract; MFS, maximum flooding stage; and HST, highstand systems tract. (B) Maieberg Fm MFS, normally covered (A), is 100% exposed in a clean gully at $-19.3063^{\circ}/13.9923^{\circ}$ in P4017 (Fig. 117A) and consists of nodular to thin-bedded calcite rhythmite with bundled marly dolomite turbidites (T). This association is representative of Tm2 MFS wherever it is exposed, with the addition of benthic crystal fans in areas of paleo-seafloor topography (Figs. 67B, 80A–F & 81A–B). (C) Low-angle swaley crossbedding in calcite ribbonite of upper Tm2 at $-19.2726^{\circ}/13.9292^{\circ}$ near 8–4. (D) Hummocky crossbedding in calcite ribbonite of upper Tm2 at $-19.3069^{\circ}/13.9929^{\circ}$ in P4017. Hummock with 0.3 m of synoptic relief is defined by downlap (d) and onlap (o) of inclined strata (yellow lines). Swaley and hummocky crossbedding are formed by highly oscillatory flows at depths approaching storm wave base (Cheel and Leckie, 1993; Dumas and Arnott, 2006). (E) Karstic unconformity between cherty dolomite grainstone of Hüttenberg Fm (Th) and derived dolomite-chert-clast conglomerate of Braklaagte Fm (Wb) at $-19.2659^{\circ}/13.9545^{\circ}$ (12 km E of Khowarib, Fig. 96). (F) Dolomite-chert-pebble conglomerate of basal Mulden Group (Braklaagte Fm) near location in E.

2.9. Transect Tr9 – Khowarib thrust-fold belt

Tr9 follows the belt of tight Otavi Group *décollement* folds and thrusts forming the E side of Warmquelle syncline (Fig. 96). It roughly parallels Tr8, ~20 km to the E on average, or ~30 km before W–E shortening. Together, Tr8 and 9 provide a sound basis for comparing S–N and W–E stratigraphic changes in IPz. We add sections from among 11–8–10 (Fig. 96) to Tr9 fence diagrams to extend their meridional range. Tr9 thrust-fold belt is named for the village of Khowarib, situated where the upper Hoanib River exits Otavi Group karst-mountains (≤ 600 m local relief) and enters the broad valley of Warmquelle syncline underlain by semi-pelitic schist of Sesfontein Fm (lower Mulden Group, Fig. 6D).

Section 9–3 (Fig. 122), on road D3710 E of Ongongo (Fig. 96), is an accessible, well exposed and virtually complete section of the entire Otavi Group. A field guide and annotated satellite images for this section are given in SOI S3.12., Fig. S28A & B.

2.9.1. Late Tonian of Tr9

Devede Fm shows no systematic change in thickness from S to N (Fig. 123), similar to Tr8 (Fig. 99). It is 8% thinner on average relative to Tr8, but the difference might not be significant given the small number of complete sections ($n = 5$ and 6). The carbonate lithofacies and their stacking patterns are similar in both transects as well, but *Tungussia* biostromes are less well developed in upper Devede Fm in Tr9. The

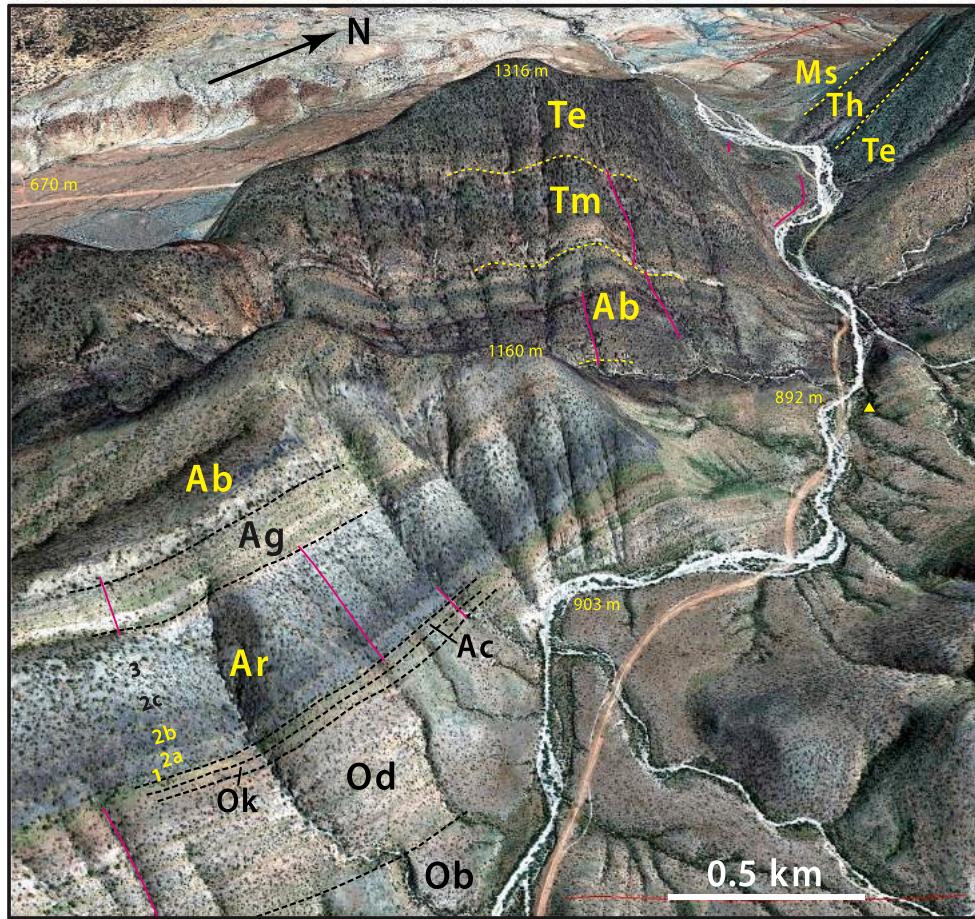


Fig. 122. Annotated satellite image looking obliquely NW toward Ongongo in Tr9 (Fig. 96). District road D3710 (center foreground) provides access to composite section 9–3 through entire Otavi Group (Figs. 123, 125, 129, 130, 133). Magenta lines indicate where composite section (Fig. 133) was measured. Elevations are in meters above sea level (430 m local relief). Formations (Fig. 6D) in stratigraphic order: Ob, Beesvlakte Fm; Od, Devede Fm; Ok, Okakuyu Fm; Ac, Chuos Fm; Ar, Rasthof Fm; Ag, Gruis Fm; Ab, Ombaatjie Fm; Tm, Maieberg Fm; Te, Elandshoek Fm; Th, Hüttenberg Fm; Ms., Sesfontein Fm. Rasthof Fm members (Fig. 125): 1, rhythmite-turbidite; 2a, lobate stromatolite; 2b, roll-up microbialaminite; 2c, cryptic microbialite; 3, highstand grainstone. Small yellow triangle (middle right) indicates a convenient off-road campsite (see field guide SOI S3.12. and annotated satellite images Fig. S28A & B). Google Earth: Image © 2020 Maxar Technologies.

major flooding surface above the last biostrome in Tr8 is potentially preserved in only one Tr9 section (9–3), suggesting deeper erosion beneath Okakuyu Fm in Tr9. Cannibalized clastics in the lower part of the Devede Fm (Fig. 124A) become thicker and coarser-grained southward (Odg, Fig. 123), just as they do in Tr8 (Fig. 99). This accords with derivation from Makalani dip-slope, where Tonian strata are absent (Figs. 87 & 88). Since lower Devede Fm clastics are older than 760 Ma (Fig. 123), we infer that Makalani dip-slope was tectonically active ≥ 100 Myr before its last reprise in Gruis Fm time (Fig. 88, 93E & F, 10A–C).

Okakuyu Fm varies erratically in thickness (Fig. 123), as it does in Tr8 (Fig. 99), due mainly to differential glacial erosion beneath Chuos Fm (Fig. 124B). Unlike lower Devede Fm clastics, there is no systematic meridional change in grain size in Okakuyu Fm—conglomerate occurs in even the most northerly sections (11–2 and 8). This implies that unidentified source areas north of Makalani dip-slope were active in Okakuyu time.

2.9.2. Cryogenian of Tr9

Cryogenian strata thicken northward by 70% between 9 and 1 and 11–10 (Fig. 125). Every formation thickens except Ghaub Fm, which is thin (≤ 2.4 m) and only occurs in 9–2 and 3. Thickening of Ombaatjie Fm is accompanied by loss of subaerial exposure surfaces and associated tepee microbialaminite. However, much Ombaatjie Fm thickening results from southward truncation of cycle b8 (Fig. 125). Likewise, truncation of b8 in Tr8 (Fig. 103) makes Ombaatjie Fm thinner in that transect compared with Tr9. If only cycles b1–6 are considered, only the northernmost Ombaatjie Fm sections (9–4 and 11–10, Figs. 96 & 125) are significantly thickened compared with other b8 and b9 sections.

Chuos Fm has a sharp erosive basal contact (Figs. 124B & 126C) with either the Okakuyu or Devede formation (Fig. 123). It includes polymictic conglomerate and laminated (non-varved) argillaceous siltstone with IRD (Fig. 124C), in addition to massive diamictite (Fig. 124D). The top of Chuos is enriched in Fe(III) (Fig. 124D), and the contact with Rasthof Fm is sharp and non-erosive (Figs. 124D & 126C).

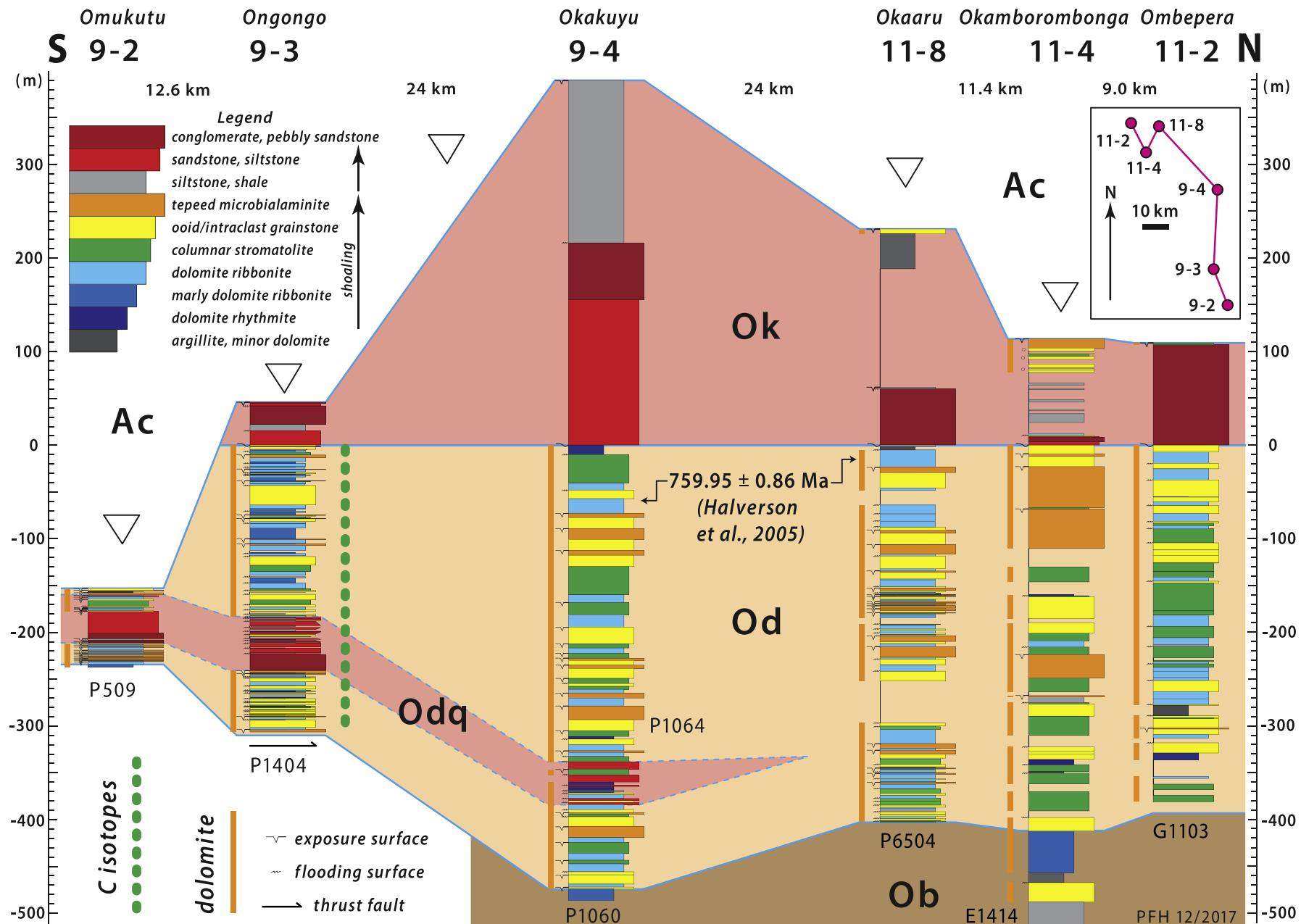


Fig. 123. Columnar sections of late Tonian Ombombo Subgroup in Tr9 and 11 (see Fig. 96 for section locations). Formations: Ob, Beesvlakte Fm; Od, Devede Fm; Ok, Okakuyu Fm; Ac, Chuos Fm. Compare with Fig. 99 (Tr8) and 196 (Tr10–11). Datum is base of Okakuyu Fm. Horizon inferred for an Upper Devede Fm bentonite (Fig. 142E), yielding zircons dated at 759.95 ± 0.86 Ma (Halverson et al., 2005), in a short section (not shown) 2.0 km ESE of Otjomatemba (Fig. 96).

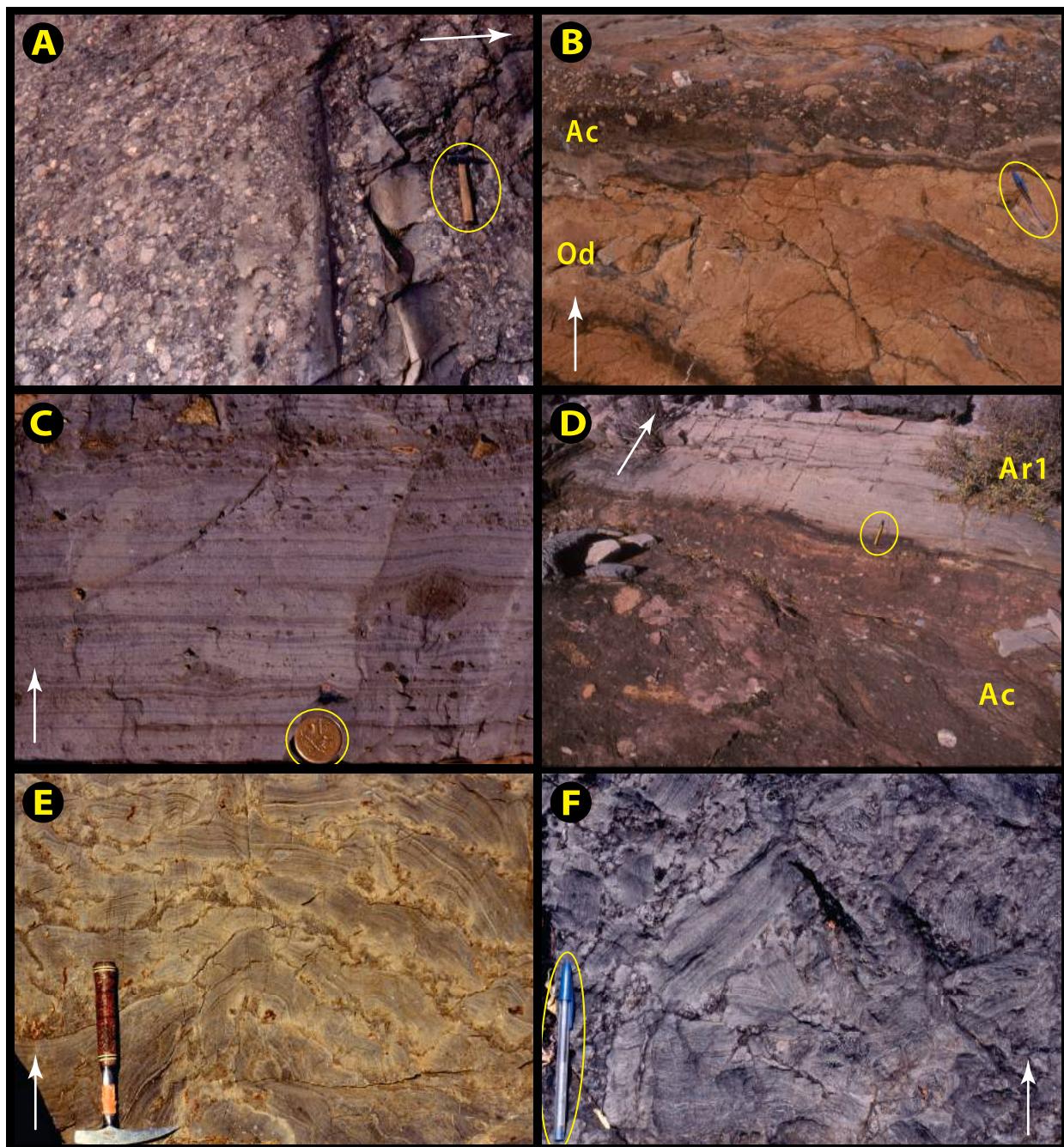
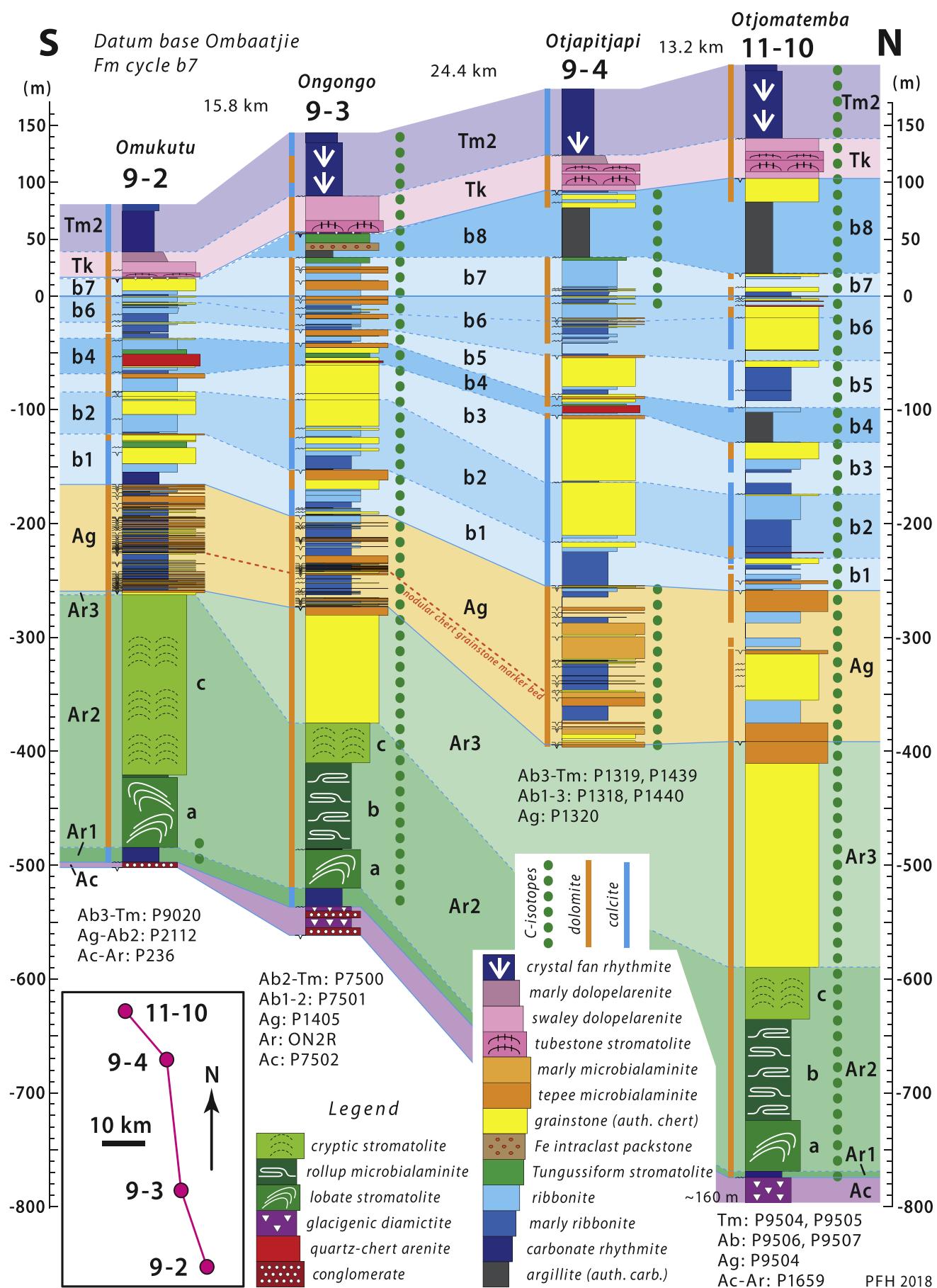


Fig. 124. Images of early Cryogenian (Sturtian) Chuos Fm and bounding dolomite units in Tr9 (Khowarib thrust-fold belt): white arrows indicate stratigraphic younging. (A) Pebble conglomerate with basement granitoid clasts in Devede Fm (Odq) at $-19.2685^{\circ}/13.9149^{\circ}$ in 9–2 (Fig. 123). (B) Disconformity between fractured dolomite of Devede Fm (Od) and Chuos Fm (Ac) diamictite and conglomerate at $-19.3907^{\circ}/13.9221^{\circ}$, 4.6 km SSE of 9–1 (Fig. 96). (C) Laminated siltstone in thin Chuos Fm with fine-grained ice-rafted debris (IRD) at $-19.2628^{\circ}/13.9170^{\circ}$, 3.2 km N of Omukutu near 9–2 (Fig. 125). IRD is concentrated in dark argillite layers and is rare in pale siltstone turbidites. (D) Sharp planar depositional contact (base of pen) between Chuos Fm (Ac) ferruginous diamictite and basal Rasthof Fm (Ar1) dolomite rhythmite at $-19.0266^{\circ}/13.9151^{\circ}$, WNW of 8–9 (Fig. 96). (E) Lobate stromatolite with void-filling dolomite cement (dark non-laminated) in middle Rasthof Fm (Ar2a) at $-19.1619^{\circ}/13.8631^{\circ}$ in 9–3 (Fig. 125). (F) Sedimentary breccia composed of rollup microbial laminites filling neptunian dyke in middle Rasthof Fm (Ar2b) near $-18.8398^{\circ}/13.7569^{\circ}$ in 11–10 (Figs. 125 & 137).

As in Tr8, Rasthof Fm is divided into 3 members (Ar1–3) and Ar2 into 3 subunits (Ar2a–c, Figs. 111 & 125). Ar1 is flat laminated and displays m-scale calcite–dolomite cycles (Fig. 126A–D), studied geochemically and isotopically in a continuous slab obtained at 9–2 (Yoshioka et al., 2003; Katsuta et al., 2007; Tojo et al., 2007). The change from flat-laminated non-microbial rhythmite (Ar1) to lobate stromatolite (Ar2a) is gradational but abrupt over 0.2 m (Fig. 126E). Rasthof Fm was studied in detail in section 9–3 (Fig. 122) (Pruss et al., 2010). Lobate

stromatolites (Ar2a) are intimately associated with vuggy zones rich in void-filling cement (Figs. 69C & 124E). Roll-up microbial laminites (Ar2b) contain neptunian dykes crowded with intraclasts (Fig. 124F). In some cases, microbial mats were repeatedly back-flipped bilaterally away from a neptunian dyke (Fig. 127A & B). Pruss et al. (2010) inferred that such dykes were conduits for escaping fluid or gas, which blistered and burst any microbial mat grown across the dyke orifice. Rasthof Fm thickens northward overall in Tr9, due to expansion of Ar3 grainstone



(caption on next page)

Fig. 125. Columnar sections of Cryogenian Abenab Subgroup and earliest Ediacaran lower Maieberg Fm in Khobarib thrust-fold belt (Tr9 & 11–10). Datum is base of Ombaratjie Fm cycle b7. Incision of cycle b8 toward 9–2 is attributed to Marinoan glacial erosion of Omarumba trough (Figs. 164 & 195C). Units: Ac, Chuos Fm; Ar1, lower Rasthof Fm rhythmite member; Ar2, middle Rasthof Fm microbialite member; Ar3, upper Rasthof Fm grainstone member; Ag, Gruis Fm; b1–8, Ombaratjie Fm cycles b1–8; Tk, Keilberg Mb; Tm2, middle Maieberg Fm rhythmite member, discordantly dolomitized (orange/blue bars). Terrigenous input identifies Ombaratjie Fm cycle b4 (Figs. 165 & 197).

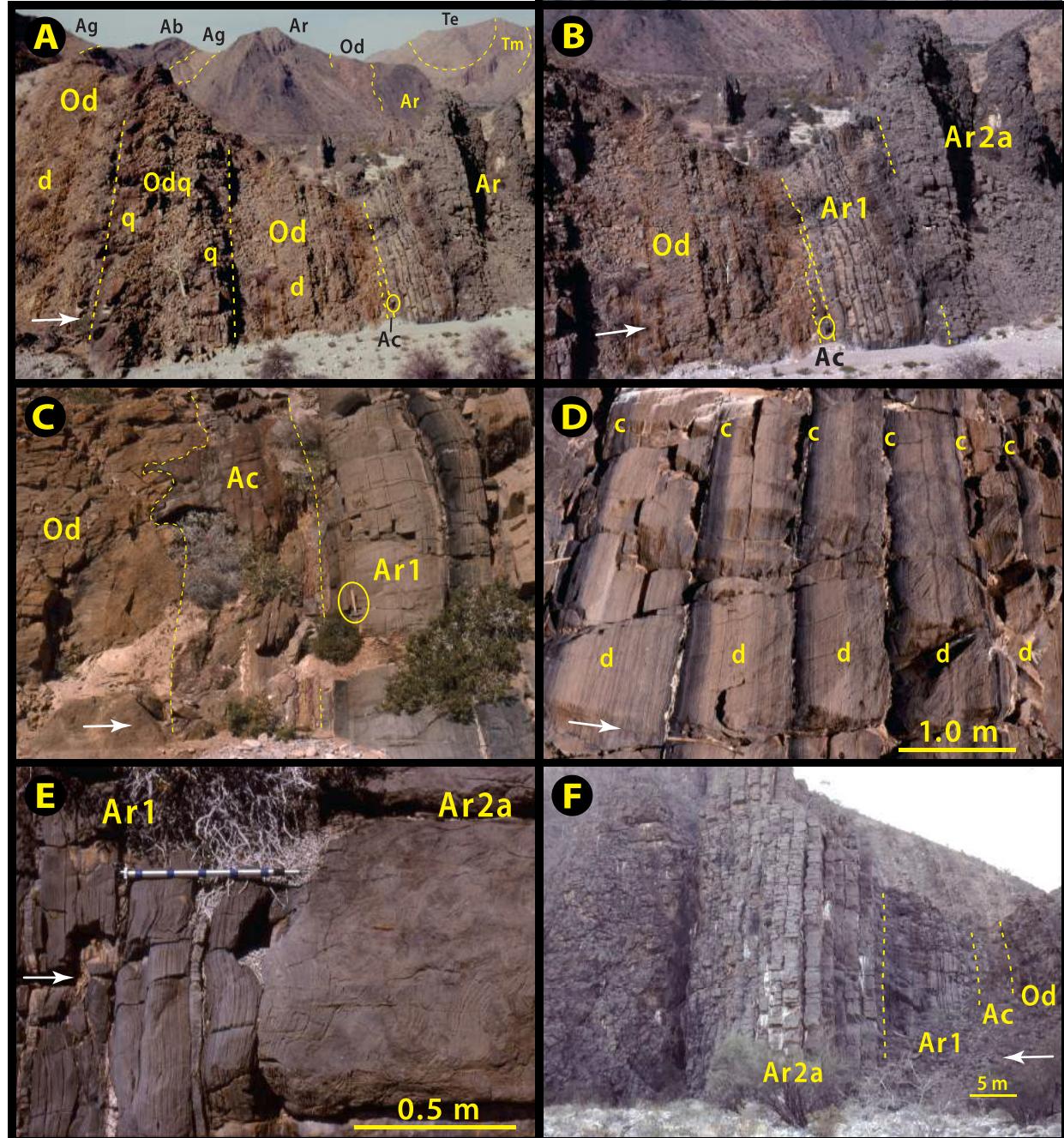


Fig. 126. Images of Sturtian glacial surface and lower Rasthof Fm cap carbonate at $-19.2690^{\circ}/13.9145^{\circ}$ (all images) in 9–2, 2.5 km NNW of Omukutu (Figs. 123 & 125); white arrows indicate stratigraphic younging. Lower Rasthof Fm (Ar1) geochemistry was studied here (Yoshioka et al., 2003; Tojo et al., 2007). (A–C) Looking southward at thin Chuos Fm (Ac), geologist circled for scale, disconformably underlain by lower Devede Fm (Fig. 123) and sharply but conformably overlain by Rasthof Fm (Ar1). Devede Fm clastic tongue Odq includes terrigenous sandstone and conglomerate (Fig. 124A) apparently derived from Makalani ridge (Fig. 5). Absence of Okakuyu and most of Devede formations indicates relatively deep (≥ 0.55 km) Sturtian erosion (Fig. 123), an average rate of only 0.1 m Myr $^{-1}$. (D) Calcite (c)/dolomite (d) cycles (Tojo et al., 2007) in basal Rasthof Fm rhythmite member (Ar1) in 9–2. (E) Abrupt but unbroken transition from basal rhythmite (Ar1) to middle lobate stromatolite member (Ar2a) of Rasthof Fm in 9–2 (Fig. 125). (F) Looking northward at same ridge section of Chuos and lower Rasthof Fm. Note characteristic meter-scale layering in lower Ar2a member (middle of image) corresponds to lobate stromatolite, not Ar1 rhythmite, and layering is nearly imperceptible on outcrop scale.

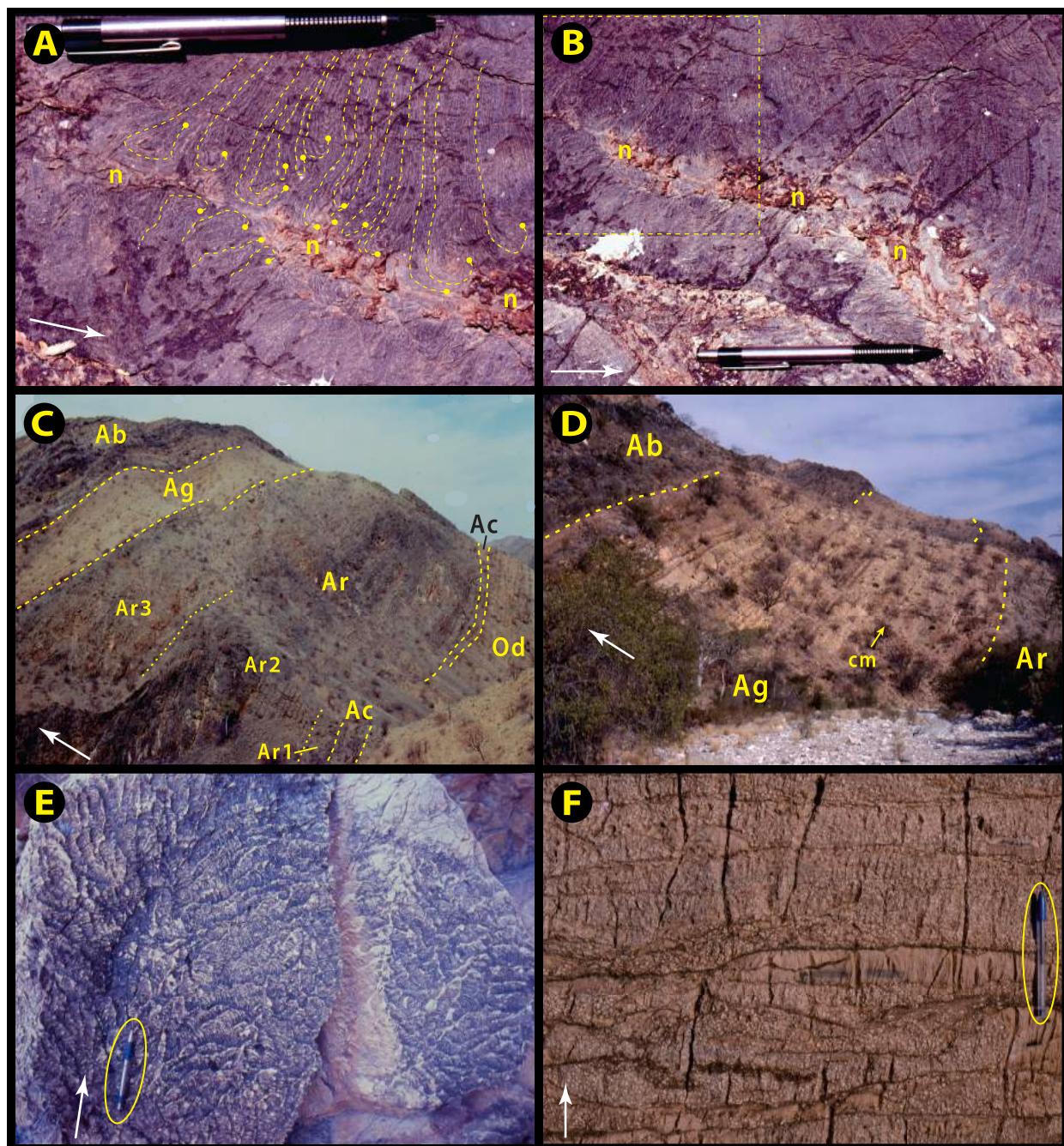


Fig. 127. Images of middle Cryogenian Abenab Subgroup in Khowarib thrust-fold belt (Tr9): white arrows indicate stratigraphic younging. (A-B) Neptunian dyke (n) bordered by successively back-flipped microbialaminite rollups (dashed lines with loose-ends dotted), middle Rasthof Fm Ar2b member near $-19.1636^{\circ}/13.8638^{\circ}$ in 9–3 (Figs. 122 & 125) (Pruss et al., 2010). Dashed box in B indicates area in A. (C) 240-m-thick Rasthof Fm HST (Ar1–3) at $-19.2677^{\circ}/13.9178^{\circ}$ near 9–2, N of Omukutu (Fig. 125). Formations: Od, Devede Fm; Ac, Chuos Fm; Ar, Rasthof Fm; Ag, Gruis Fm; Ab, Ombaatjie Fm. (D) Typical expression of meter-scale tepee-topped dolomite cycles in (unmeasured) 90-m-thick Gruis Fm at $-19.2612^{\circ}/13.9187^{\circ}$ near 9–2, N of Omukutu. Lower chert-marker grainstone bed (Figs. 125 & 162) labelled cm. Formations as in C. (E) *Tungussia*-type stromatolites with characteristic highly-divergent branching in Ombaatjie Fm at top of cycle b7 at $-19.1508^{\circ}/13.8533^{\circ}$ in 9–3 (P7500, Figs. 128, 129 & 165). (F) Fe-dolomite (ankerite?) intraclast packstone at $-19.1508^{\circ}/13.8531^{\circ}$ in Ombaatjie Fm cycle b8 in 9–3 (P7500, Fig. 129). Intraclasts are oligomictic and their Fe- and Mn-rich composition suggests an authigenic origin (cf. Tziperman et al., 2011). This unusual lithology is regionally widespread, wherever cycle b8 is preserved (Figs. 71 & 78F).

that more than compensates for northward thinning of Ar1 rhythmite (Fig. 125).

Northward thickening of Gruis Fm (Fig. 127C & D) is accompanied by declining frequency of subaerial exposure surfaces (Fig. 125). In Ombaatjie Fm, siliciclastic input to cycle b4 of becomes finer grained from S to N (Fig. 125), consistent with even thicker bodies of marine quartz-arenite in the same cycle (b4) in Tr7 (Fig. 88). Siliciclastic input

makes b4 a stratigraphic marker that we used to investigate lateral variability in cycle development and facies in closely spaced (≤ 1.0 km) parallel sections of upper Ombaatjie Fm cycles b4–8 in section 9–3 (Fig. 129). These sections exhibit subtle km-scale facies changes that persist for multiple cycles. Compound cycles b5–6, for example, are weighted toward sublittoral facies (marly ribbonite) in P1406 and 07, but toward littoral facies (microbialaminite) to the W and E (Figs. 128A

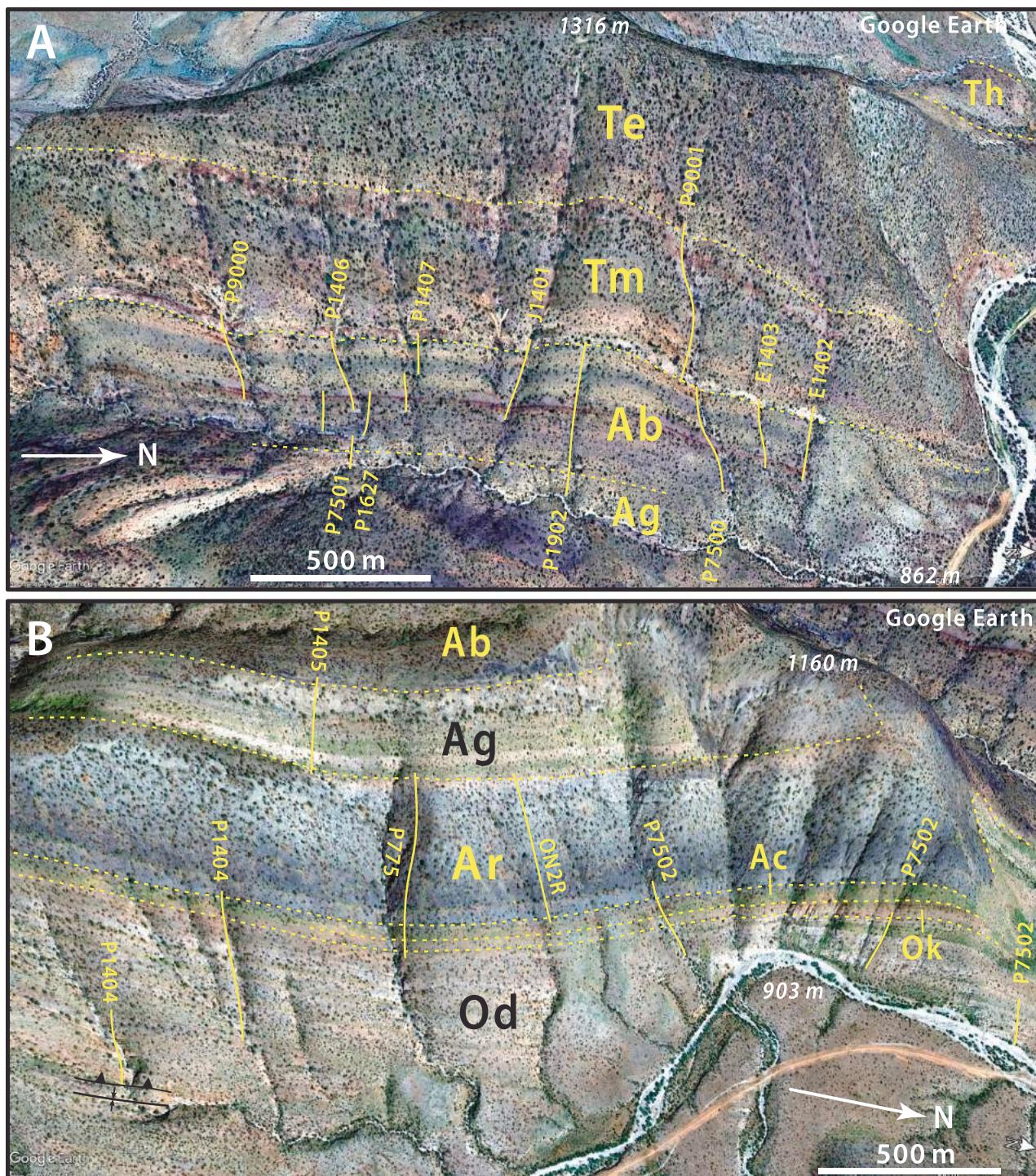


Fig. 128. Annotated satellite images looking obliquely toward W limb of doubly plunging anticline east of Ongongo (9–3, Figs. 96). Upper panel in A (passive-margin stage, Fig. 179) lies stratigraphically above (Fig. 122) lower panel in B (syn-rift stage, Fig. 133). The panels are separated by a short east dipping fold limb. Graded road D3710 (lower right in A & B,) links Warmquelle and Omarumba. Field guide (SOI S3.12.) describes what is arguably the most complete and accessible Otavi Group composite section in Kunene Region (Fig. 179). (A) Middle part of Ongongo (9–3) composite section combines P7501 (lower Omootjie Fm, Figs. 129 & 164), P7500 (upper Omootjie Fm, Figs. 129, 133 & 165) and P9001 (Maieberg Fm, Fig. 130). Chocolate-brown band in middle Omootjie Fm (behind Ab symbol) is quartz-arenite (desert varnish) in cycle b4 (Fig. 125), used as datum for closely spaced upper Omootjie Fm sections (Figs. 129 & 165) and platform wide (Fig. 164). P7500 has fine examples of *Tungussia*-type (Fig. 127E) stromatolite mounds and Fe-rich intraclast-packstone (Fig. 127F), both regionally associated with CIE Cn5 (Fig. 10D) in cycles b7 and 8 (Fig. 165). Continuing upward, lower P9001 has fine examples of dolomitized and undolomitized former-aragonite crystal fans (Fig. 132A–C) in lower Tm2 member of Maieberg Fm (Fig. 130). Google Earth: Image © 2020 Maxar Technologies. (B) Lower part of Ongongo (9–3) composite section combines P1404 (Devede Fm, Fig. 123), P7502 (Okakuyu and Chuos Fm, Figs. 123 & 125), ON2R (Rasthof Fm, Figs. 125, 133 & 159) and P1405 (Gruis Fm, Figs. 125, 161 & 162). Rasthof Fm microbial roll-ups (Ar2b, Fig. 111) are associated with neptunian dykes (Fig. 127A & B) in section ON2R (Pruss et al., 2010). Annotated satellite image of upper part of Ongongo composite section, including Elandshoek and Hüttenberg formations, is in Fig. S28B. Google Earth: Image © 2020 Maxar Technologies.

137

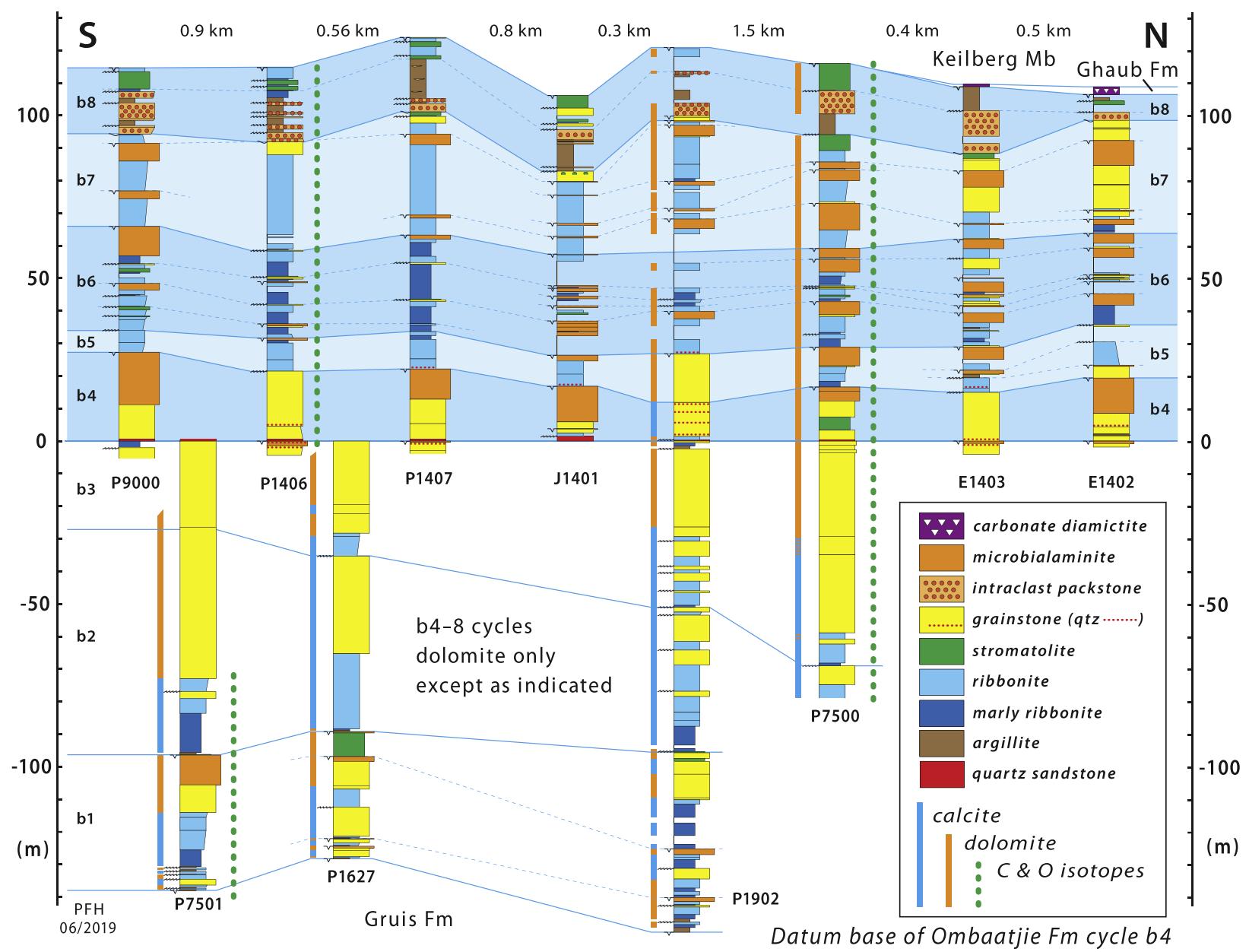


Fig. 129. Closely spaced upper Ombaatjie Fm columnar sections in 9–3 near Ongongo (see Fig. 128A for locations, Fig. 165 for $\delta^{13}\text{C}$ records). Datum is base of cycle b4, which is distinguished by quartz-sandstone incursions. Composite nature of numbered cycles (i.e., sub-cycles) and lateral facies variability are clearly evident. Closely spaced sectioning is possible along virtually the entire 90-km length of Tr9.

& 129). The compound nature of cycles b6 and b7 (Fig. 129) is readily apparent. The top of b6 was picked with the aid of $\delta^{13}\text{C}$ profiles, since b7 regionally hosts the CIE Cn5 descending arm (Fig. 10D) (see 3.3.4.).

Cycles b7–8 are also notable lithologically (Fig. 129). Mounded *Tungussia*-type stromatolites (Fig. 127E) are prominent in both cycles, as they are in Tr5 (Fig. 68), Tr6 (Fig. 71), Tr7 (Fig. 88) and Tr8 (Fig. 103). The association of stromatolites with CIE Cn5 was cited in support of enhanced anaerobic respiration in a geochemical model of the CIE (Tziperman et al., 2011). Anaerobic respiration is a pump for alkalinity

(e.g., $4\text{CH}_2\text{O} + 2\text{SO}_4^{2-} + \text{Fe}_2\text{O}_3 \rightarrow 4\text{HCO}_3^- + \text{FeS}_2 + \text{Fe}^{2+} + 2\text{OH}^- + \text{H}_2\text{O}$), favouring early lithification that provides stable substrate for colonization by microbial mats (Logan et al., 1974).

The nadir of CIE Cn5 corresponds with argillite in lower b8 (Fig. 125). In 9–3 (Fig. 129), the argillite is intimately associated with intraclast packstone (Fig. 127F), indistinguishable from that found in the same cycle (Fig. 78F) 134 km to SE (section 6–7, Fig. 71). The intraclasts are rounded, subequant, ~0.5 cm in diameter and of uniform ferroan dolomitic (ankerite?) composition. They are grain-supported

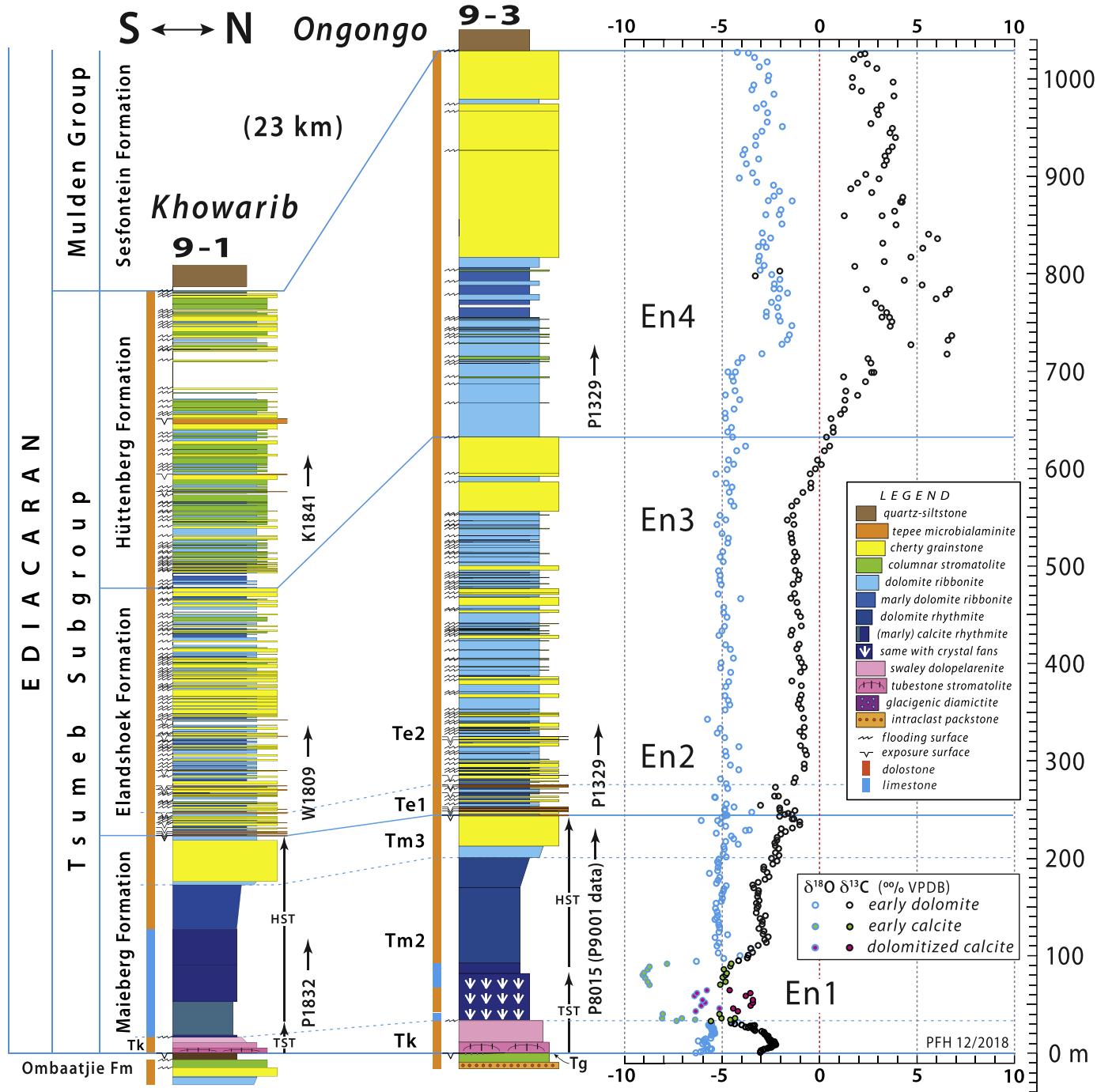


Fig. 130. Early Ediacaran Tsumeb Subgroup columnar sections 9-1 & 9-3 (locations in Fig. 96). Datum is base of Keilberg Mb (Tk). In Hüttenberg Fm, grainstone increases in abundance northward at the expense of stromatolite. In Elandshoek + Hüttenberg combined, 9-3 has 30% fewer cycles than 9-1 (95/136) despite 20% greater thickness (785/659 m), implying cycle amalgamation in thicker grainstone units in 9-3. $\delta^{13}\text{C}$ and $\delta^{18}\text{O}$ data are from 9 to 3 (CIEs 1–4 as in Fig. 10D). Pronounced isotopic effects associated with dolomitization are evident in Maieberg Fm Tm2. Base of Keilberg Mb in 9-1 (P1832) is at $-19.3510^\circ/13.9140^\circ$; base of Elandshoek Fm in 9-3 (P1329) is at $-19.1409^\circ/13.8482^\circ$.

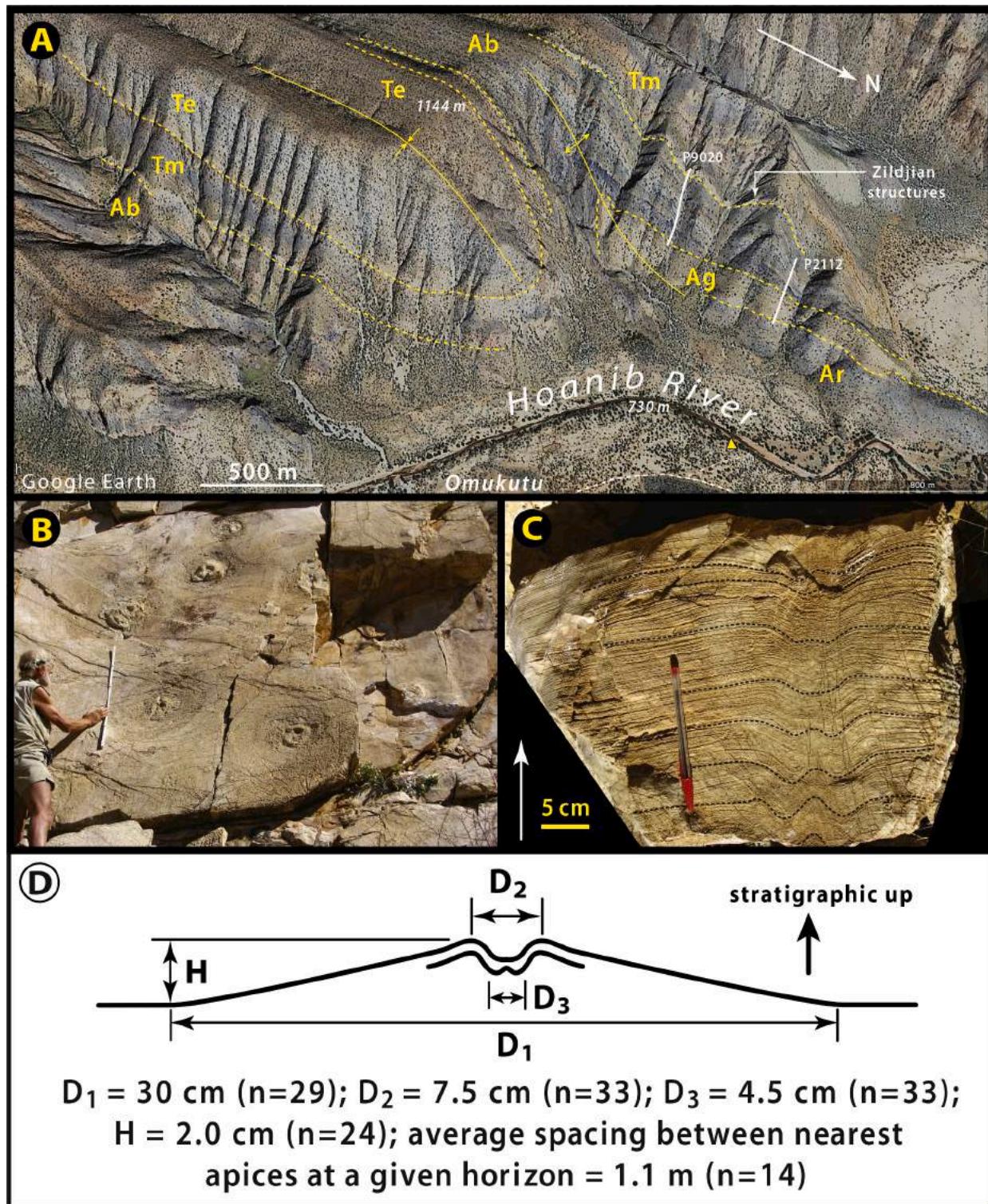


Fig. 131. Images of cymbal-shaped ('Zildjian') structures in earliest Ediacaran Keilberg Mb of Maieberg Fm in 9–2 (Fig. S24B), near Omukutu 6 km SE of Khowarib; white arrow in C indicates stratigraphic younging. (A) Tight folds of Abenab and Tsumeb subgroups in Khowarib thrust-fold belt breached by Hoanib River with surface flow (Khowarib Schlucht), 1 km downstream (W) from Omukutu. Zildjian structures (B–D) occur in steep E-dipping, W-facing Keilberg Mb as indicated. Elevations (white italics) are wrt sea level. Small yellow triangle is campsite. Google Earth: Image © 2020 Maxar Technologies. (B) Zildjian structures exposed in negative relief on undersides of steeply-dipping overthrust dolopelarenite in Keilberg Mb at $-19.2897^\circ/13.9017^\circ$. Note ring-shaped ridges around central depressions, corresponding in positive relief to ring-shaped apical troughs with central nipples. (C) Cross-section (loose block) of apical trough with central nipple indicated by dashed black lines. (D) Idealized profiles showing apical trough with and without a central nipple. Average dimensions (as defined) determined from 34 circular structures at heights of 8.2–13.5 m (most 8.2–9.1 m) stratigraphically above base of Keilberg Mb, over a strike length of 0.32 km. Structures are tentatively interpreted as peloidal sand volcanoes, not previously described from a post-Marinoan cap carbonate.

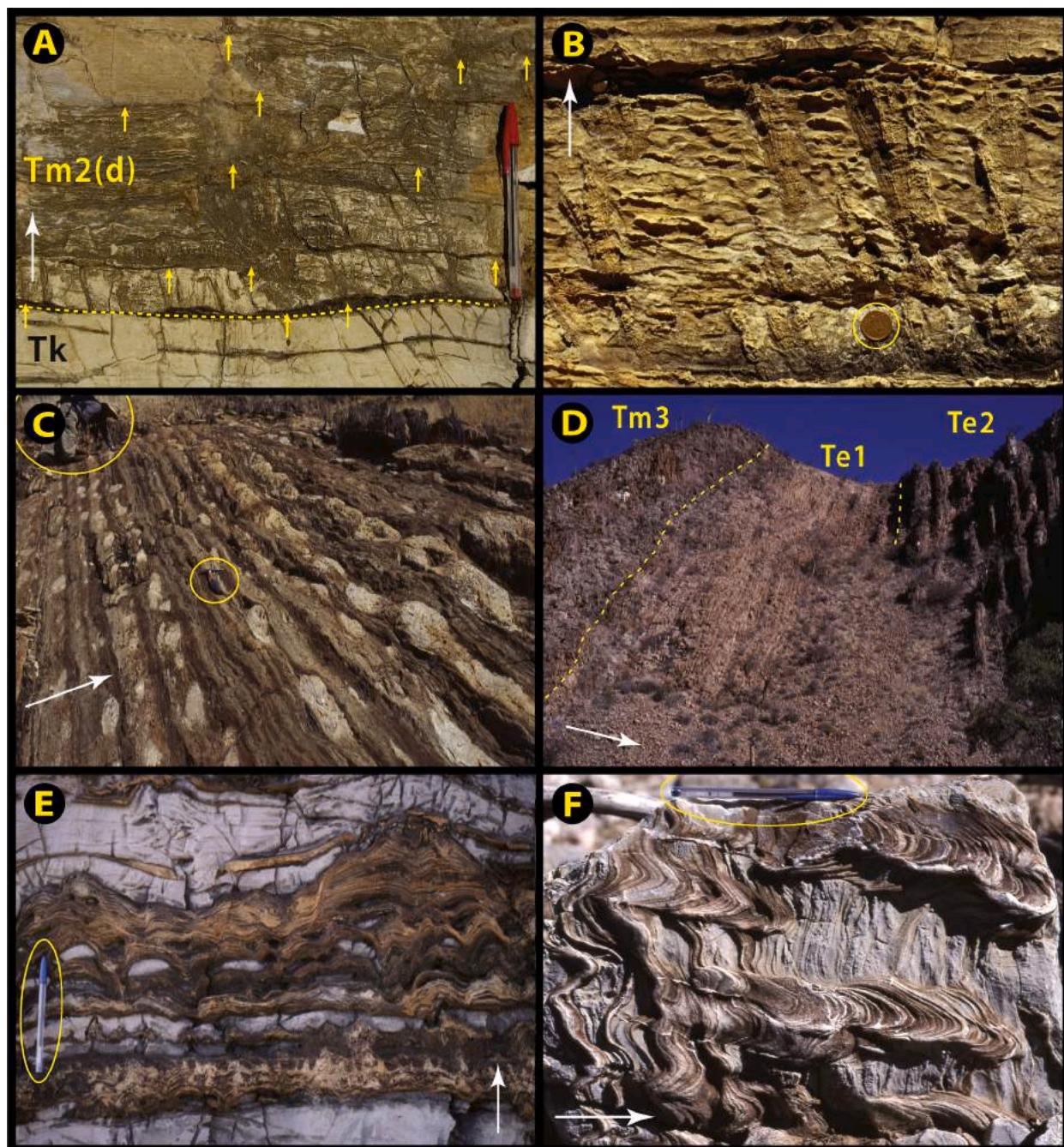


Fig. 132. Images of early Ediacaran Tsumeb Subgroup in Khowarib thrust-fold belt (Tr9): white arrows indicate stratigraphic younging. (A) Conformable contact between Keilberg Mb (Tk) peloid grainstone and dolomitized middle Maieberg Fm rhythmite (Tm2(d)) with former-aragonite crystal fans (yellow arrows) at $-19.1494^{\circ}/13.8531^{\circ}$ in 9-3 (E1403, Fig. 128A). Crystal fans begin at contact: none occur in Keilberg Mb. (B) Former aragonite crystal fans, 15 cm long, in dolomitized middle Maieberg Fm rhythmite at $-19.1509^{\circ}/13.8527^{\circ}$ in 9-3 (P8015 (Fig. 128). (C) Bundles of pale pinkish calcite, formerly sea-floor aragonite cement, in brownish-grey marly calcite rhythmite in lower Tm2 member of Maieberg Fm at $-19.1514^{\circ}/13.8524^{\circ}$ in 9-3 (P8015, Fig. 130). (D) Major sequence boundary (dashed line) separates upper Maieberg highstand grainstone (Tm3) from Elandschoek Fm tepee-capped (Te1) and grainstone-capped (Te2) cycles at $-19.2686^{\circ}/13.8883^{\circ}$ in 9-2, 2.3 km W of Khowarib (Fig. 130). (E–F) Typical selectively silicified stromatolites in Hüttenberg Fm dolomite at $-19.3501^{\circ}/13.9091^{\circ}$ in 9-1 (Fig. 130). Laterally linked stromatoids in E; intermittently-linked columnar forms in F (top to right).

and mechanically stratified, but the intergranular space is dolomicrite, not void-filling cement. Blebs of FeS₂ (oxidized) are common. The full story behind this peculiar lithology and its correlation with Cn5 has yet to be perceived, but we suspect the rock itself is a lag deposit of authigenic Fe(II)-rich carbonate, consistent with the anaerobic respiration reaction given above (Tziperman et al., 2011).

As in Tr8, Marinoan Ghaub Fm is absent (9-3–4) or limited to pockets of lodgement tillite (9-1–2) with a maximum observed

thickness of 2.4 m (E1402, Fig. 129).

2.9.3. Early Ediacaran of Tr9

Keilberg Member nearly doubles in thickness from 9 to 1 (16.2 m) to 9–4 (31.6 m), coincident with a nearly 7-fold increase in thickness of underlying b7 and 8 cycles combined (Fig. 125). Tubestone stromatolite occurs in the lower but not basal part of Keilberg Member (Fig. 125), but is poorly developed and lacks cm-scale, highly arched, inter-tube

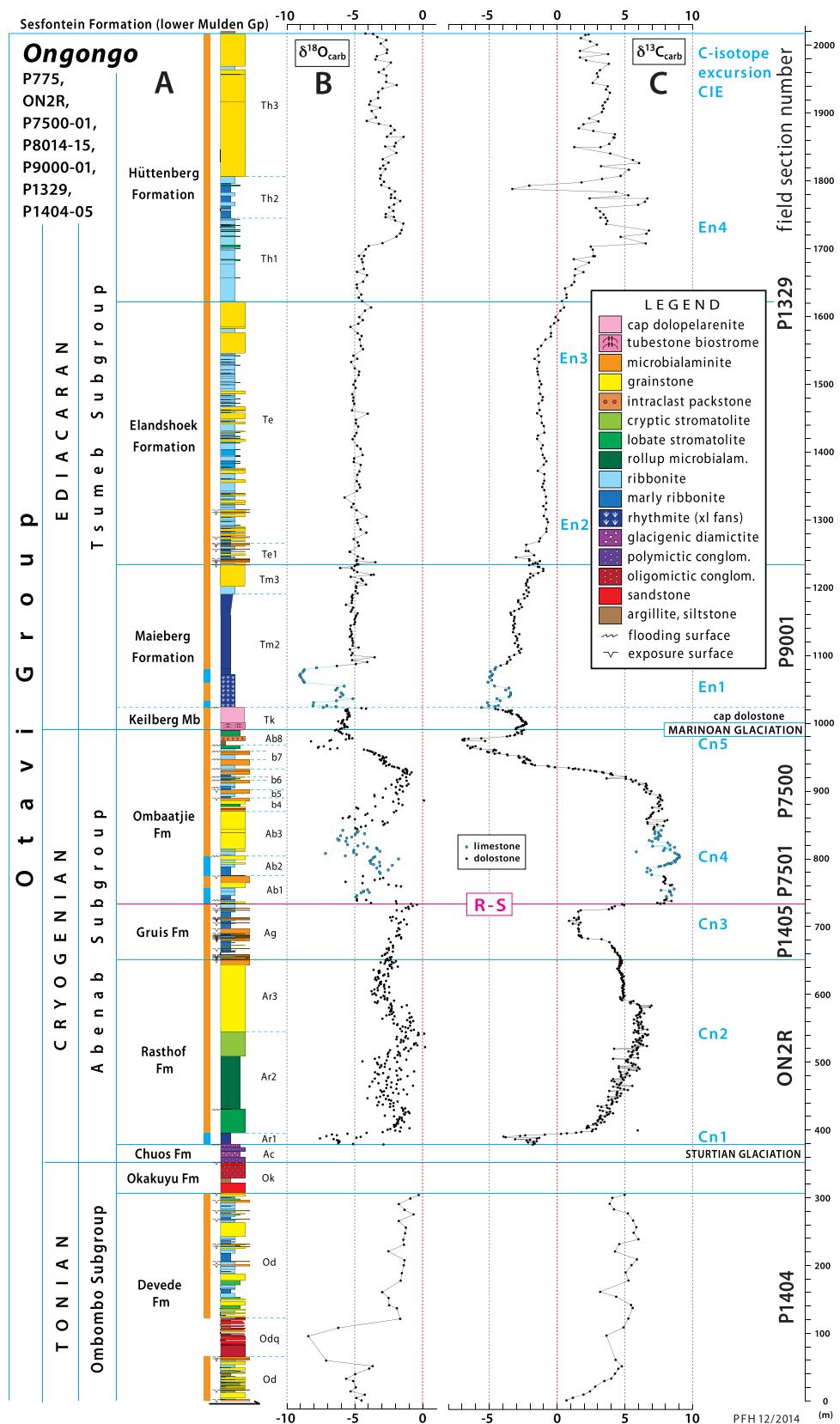


Fig. 133. Composite columnar section of (A) the entire Otavi Group in 9–3, east of Ongongo, showing (B) $\delta^{18}\text{O}$ and (C) $\delta^{13}\text{C}_{\text{carb}}$ records (Figs. 96, 122 & 128). Accessibility and completeness make this a valuable reference section for late Tonian (Fig. 123), Cryogenian (Figs. 125 & 129) and early Ediacaran (Fig. 130) strata of Otavi Group in IPz.

stromatoids like those in Tr8 (Fig. 119E). There are two tubestone stromatolite beds in 9–4 and 11–10 (Fig. 125), a lower one with domes but no tubes and an upper one with stubby tubes but no domes. Tubestone stromatolite is overlain by mechanically stratified dolopelarenite with swaley low-angle crossbedding, but no giant wave ripples.

In section 9–2 (Fig. 131B) at $-19.2896^{\circ}/13.9017^{\circ}$, near the village of Omukutu, circular structures with cymbal-shaped synoptic morphology (Fig. 131C–E) occur in mechanically-stratified dolopelarenite of Keilberg Mb over a 5.7 m stratigraphic interval, starting 1.3 m above the top of the tubestone stromatolite. The section dips steeply and is slightly overturned, so the structures are exposed in negative relief (Fig. 131C). In counterpart (positive) relief, they resembled sand or mud volcanoes, forming oblate cones with circular apical pits, some of which have a central nipple (Fig. 131D & E). Their average outer diameter (D_1 , Fig. 131E) is 30 cm ($n = 29$), rim diameter $D_2 = 7.5$ cm ($n = 33$), apical pit diameter $D_3 = 4.5$ cm ($n = 33$), vertical relief $H = 2.0$ cm ($n = 24$), and spacing between nearest apices at a given horizon = 1.1 m ($n = 14$). To our knowledge, such structures have not previously been described in a Marinoan cap dolomite. We have not seen them elsewhere in the region but, this could be because bedding planes are rarely exposed in Keilberg Mb, except where steep dips coincide with steep slopes, as in section 9–2 (Fig. 131B). Alluding to their shape and size, we describe the circular bedforms as ‘Zildjian’ structures after the Armenian-American maker of cymbals and other musical instruments (since 1623).

Keilberg Member is conformably overlain by deeper-water calcite rhythmite, locally dolomitized, of Maieberg Fm member Tm2 (Fig. 130). In 9–3–4 and 11–10 (Fig. 125), the lower part of Tm2 contains macroscopic pseudomorphs after benthic aragonite cement (Fig. 132A & B). In 9–3, spaced cm-scale crystal fans occur in the first 12 m of Tm2, starting on the contact surface with the underlying Keilberg Member (Fig. 132A). In the succeeding 27 m, the fans are congregated in discrete bundles, 10–15 cm in diameter (Fig. 132C). Their pale pinkish colour contrasts with the host greenish-grey marly rhythmite. Where crystal fans occur in limestone, they are flattened in the cleavage plane (Fig. 132C). In 9–3, where lower Tm2 rhythmite is partly dolomitized (Fig. 130), the crystal fans are nearly unstrained (Fig. 132B) due to greater stiffness of dolomite relative to calcite under middle greenschist-grade metamorphic conditions. Why do crystal fans occur in 9–3–4 and 11–10, but not in 9–2 (Fig. 125) or Tr8 (e.g., 8–3, Fig. 117)? By analogy with Tr5 and 6, we can relate their occurrence to seafloor topography, in this case a ~90-m sea-floor scarp between the area where Ombaatjie Fm cycle b8 was removed by Marinoan glacial erosion and where it was spared (Fig. 125). As will be discussed in 2.10.3., we relate its removal to a SSW–NNE glacial trough ≥ 30 km wide centered on Tr8. Accordingly, crystal-fan growth was localized at the sidewalls of this trough after it was flooded by Marinoan deglaciation (Creveling and Mitrovica, 2014; Yang et al., 2017).

Complete Tsumeb Subgroup (Fig. 6D) sections were measured in 9–1 and 3 (Fig. 130). They thicken northward by 31% overall, 784 to 1023 m, and by 6.3, 54 and 29% for Maieberg, Elandshoek and Hüttenberg formations, respectively. Maieberg Fm (Fig. 131A, compare with Fig. 121A) represents a single deposition sequence (TST + HST), without evident internal parasequences (cycles). In contrast, Elandshoek Fm presents 75 cycles (in both sections) with average thickness of 3.4 (9–1) or 5.1 (9–3) m (Fig. 130). In comparison, Ombaatjie Fm, representing the earliest stage of thermal subsidence (Halverson et al., 2002), has an average cycle thickness of 25 m in 9–3, counting 14 cycles including four each in b6 and 7 (P7500, Figs. 129 & 125). Anomalous accommodation space for the Maieberg Fm was created by thermal subsidence during the prolonged Marinoan glaciation, when the platform underwent net erosion (Hoffman et al., 1998a). The sequence boundary at the top of Maieberg Fm is marked by microbial laminitite with tepees, and a boxwork of chert propagates downward from the subaerial exposure surface into the underlying highstand grainstone (Fig. 132D).

In terms of W–E change, the total thickness of the three formations is exactly equal (844 m) in 9–1 and 8–3, if 60 m is added to the former to

compensate for its more southerly location (Fig. 96). The number of cycles in the combined Elandshoek and Hüttenberg formations is essentially identical (144) between the two sections as well, if we represent the covered interval in the upper Hüttenberg of 9–1 by 8 cycles (Fig. 130). On the other hand, grainstone is volumetrically more abundant in the east (Fig. 117), while ribbonite and stromatolite are better represented in the west (Fig. 130). This change in facies, at constant thickness and cycle frequency, is consistent with a marked westward decrease in the total number of subaerial exposure surfaces, from 57 (8–3) to 13 (9–1). The distinctive lower member of the Elandshoek Fm (Te1 in Fig. 132D), where tepee-capped cycles are concentrated, thins westward from 135 to 120 m between the same two sections, whose W–E separation is estimated to have been ~15 km before thin-skinned tectonic shortening. In both sections, heavily silicified stromatolites, both laterally linked (Fig. 132E) and columnar (Fig. 132F), are more numerous in the Hüttenberg compared with the Elandshoek Fm (Figs. 117 & 130).

The exact contact with the stratigraphically overlying Sesfontein Fm (lower Mulden Group) is generally covered, but the two units are structurally conformable. The westernmost Otavi Group panel on strike with the village of Khowarib (Fig. 96) is generally 10–25° overturned, westward facing but eastward dipping. Lower Sesfontein Fm consists of green phyllite with thin beds of fine-grained quartz-arenite and discontinuous thicker units of chert-dolomite-clast conglomerate, derived from the underlying Tsumeb Subgroup. The conglomerate implies that the Hüttenberg–Sesfontein contact is disconformable, consistent with Tr8 (Fig. 121E & F). Sesfontein Fm is stratigraphically and lithologically analogous to lower Kuiseb Fm in Tr2–3 (Fig. 6B & D), except that they overlie platformal Otavi Group and basinal Swakop Group, respectively.

When the district road D3710 linking Warmquelle and Ondevede (Fig. 96) was graded in the mid-2000s, section 9–3 in the pass (Figs. 122 & 128) due east of the travertine spring near Ongongo (Fig. 96) became an ideal reference section for the entire Otavi Group of the IPz (Fig. 133). Excluding Beesvlakte Fm, Otavi Group has a composite stratigraphic thickness of 2.02 km. A field guide and additional satellite images of this section are given in SOI S3.12., Fig. S28A & B.

2.9.4. Highlights from Tr9

Chief highlights are: (1) the spectacular Otavi Group reference section (9–3) east of Ongongo (Figs. 122, 128, 129 & 133); (2) northward not westward thickening of Abenab and Tsumeb subgroups in Tr9 as compared with Tr8 (Figs. 125 & 130); (3) return of Ombaatjie Fm cycle b8, missing in Tr8, along with the same enigmatic Fe-rich intraclast packstone observed in OPz Tr6 (Figs. 78F, 127F & 129); (4) *Tungussia*-type stromatolite bioherms (Figs. 69D & 127E) in Ombaatjie Fm cycles b8 and upper b7, similar to stromatolite proliferations coincident with CIE Cn5 in OPz Tr5–7 (Figs. 68, 71 & 88); (5) previously undescribed sand volcanoes (‘Zildjian’ structures) in cap dolopelarenite of Keilberg Mb in 9–2 near Omukutu (Fig. 131B–E); and (6) return of former aragonite sea-floor cement (crystal fans) in lower Maieberg Fm member Tm2 (Fig. 132A–C), temporally associated with the maximum post-glacial flooding stage (Fig. 130) and spatially with an inferred Marinoan glacial-trough margin (Fig. 125).

2.10. Transect Tr10 – Ekoto triangle zone

On the NE flank of Kamanjab inlier (Fig. 8A), Otavi Group can be mapped at the formation scale from satellite data, but on the ground recessive intervals are covered by calcrete or onlapping Cenozoic Kalahari Group (Miller, 2008c). To attempt sequence stratigraphy where recessive units are systematically covered is like doing seismic stratigraphy with reflectors removed.

An exception occurs where headwall erosion is removing Kalahari Group infill from Omarumba paleovalley at the northern plunge of Kamanjab inlier (Figs. 8A & 134). Here, Otavi Group is well exposed

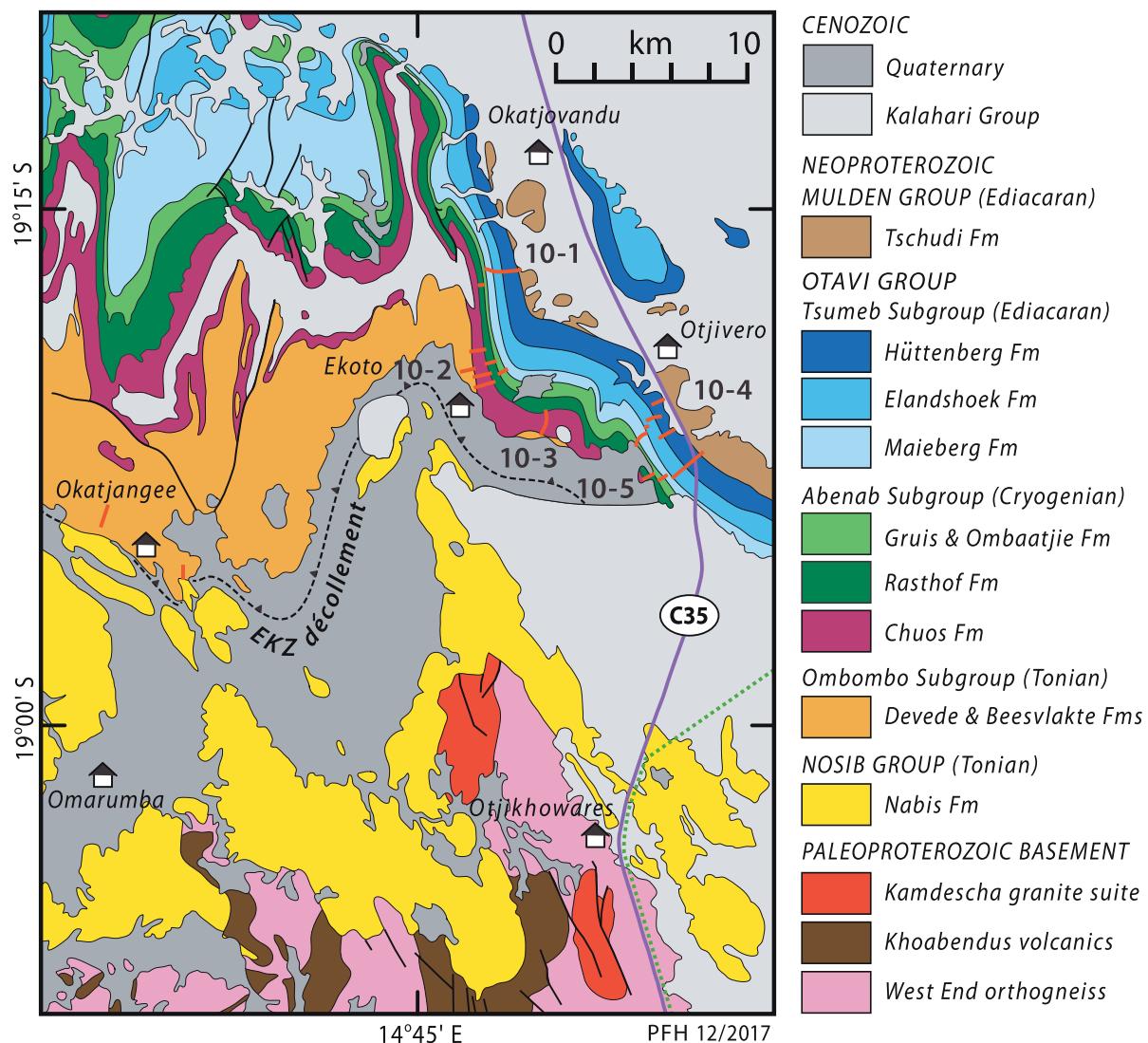


Fig. 134. Geologic map of Ekoto triangle structure (Tr10) showing locations of sections 10–1–5 (modified after Killick et al., 1980). Thin-skinned folds and thrusts involving Otavi Group were translated eastward relative to autochthonous Nosib Group and basement on a sole thrust (*décollement*) that was itself broadly folded around the northern anticlinal plunge of Kamanjab inlier (Fig. 8A). Apex of triangle zone is the plunging Chuos Fm anticline W of Okatjovandu.

around the village of Ekoto (Fig. 134) (Killick et al., 1980). The basal *décollement* of EKz wraps around a broad plunging anticline of Kamanjab basement and autochthonous Nosib Group cover (Fig. 134). Otavi Group above the *décollement* is severely shortened with tight 1-km-wavelength folds in Ombombo Subgroup and tight 9-km-wavelength folds in Abenab and Tsumeb subgroups. Northward-plunging *décollement* folds near Ekoto resemble ‘Type-1 (detachment-dominated) triangle zones’ (von Hagke and Malz, 2018), found at the front of many foreland thrust-fold belts.

We measured sections 10–1–5 (Fig. 134) in the forward (eastward) dipping limb of the triangle zone.

2.10.1. Late Tonian of Tr10

Devede Fm is similar in thickness (480 m in 10–2) to Tr8, with which it is graphically compared in Fig. 99. It has more offshore facies than Tr8—higher proportions of ribbonite and stromatolite relative to grainstone and microbialaminite—and it has far fewer subaerial exposure surfaces. The lower Devede clastic tongue pinches out south of 10–2, consistent with southerly derivation from Makalani dip-slope. The clastic-dominated Okakuyu Fm is absent in 10–2, but this is more likely related to erosion beneath Chuos Fm than to distance from Makalani

dip-slope, since no overall northward decrease in grain size is observed in Okakuyu Fm of Tr8 or 9 (Figs. 99 & 123).

2.10.2. Cryogenian of Tr10

Chuos Fm is anomalously thick, expanding southward from 661 to 1163 m between 10 and 2 and 3 (Fig. 135A). It is mostly composed of massive diamictite, carrying surrounded outsize clasts of dolomite, chert, subfeldspathic quartzite and crystalline rocks in varying proportions. There are decameter-scale units of greenish argillite and submeter-scale beds of sorted sandstone and pebbly sandstone, but they are subordinate. Stratified diamictite and ice-rafterd debris are uncommon. As a whole, the formation is 8.8–15.5× thicker than regional median Chuos Fm thickness (75 m, $n = 111$), but the origin of the Ekoto depocenter is not known. It is partly accommodated by erosion of Okakuyu Fm (Fig. 99), but the margins of the Sturtian depocenter have yet to be located and characterized.

Rasthof Fm is 35% (10–5) to 60% (10–1) thicker than in Tr8 (Fig. 103), consistent with Rasthof Fm taper in Tr9 (Fig. 125). In all three transects, Rasthof Fm thickening is accompanied by larger fractions of grainstone (Ar3), thinner basal rhythmite (Ar1), and little change in total microbialite (Ar2) thickness (Fig. 135B). Discrete non-branching

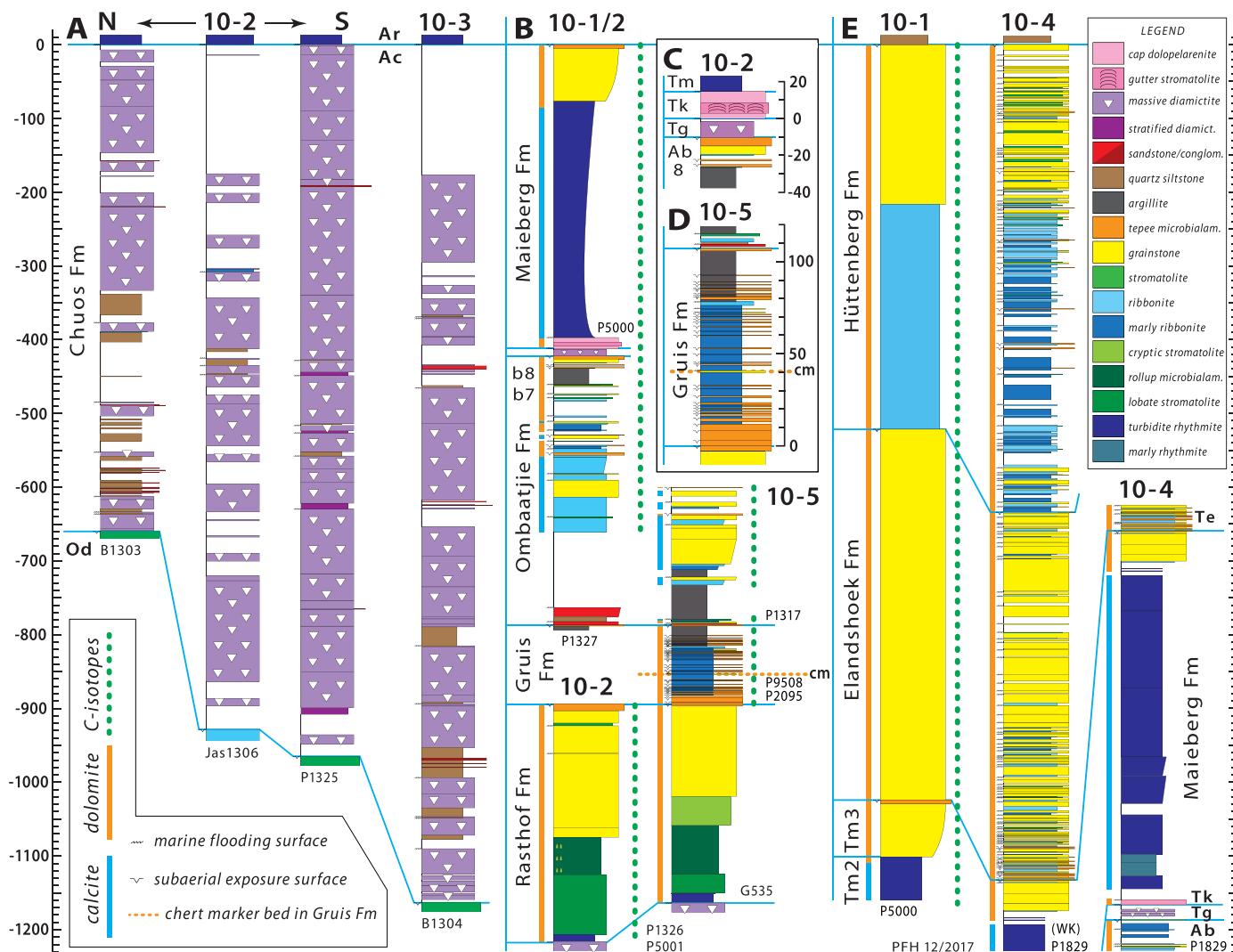


Fig. 135. Columnar sections from Tr10: locations shown in Fig. 134. (A) Chuos Fm at 10-2–3. Datum is base of Rasthof Fm. (B) Abenab Subgroup at 10-1–2 and 5. Datum at base and top of Gruis Fm. (C) Expanded Marinoan section at 10-2. Units: Ab, Oombaattjie Fm; Tg, Ghaub Fm; Tk, Keilberg Mb; Tm, middle Maieberg Fm. (D) Expanded Gruis Fm section at 10-5: cm, chert-marker grainstone bed. (E) Tsumeb Subgroup sections at 10-1 and 10-4. Datum is base of Mulden Group (Tschudi Fm sandstone).

columnar stromatolites (Fig. 136A) are relatively well defined in the ‘cryptic microbialite’ unit (Ar2c) and are enveloped by rinds of unlaminated microbialite as in the stromatolite form-genus *Boxonita* (Hoffmann, 1969). Tepees are well exposed on a dip-slope at the top of Rasthof Fm in 10-2 (Fig. 136B).

Gruis Fm is little changed from Tr8 and 9, although the upper 30 m are more argillaceous (Fig. 135D). There are 36 upward-shoaling cycles in section 10-5, with an average thickness of 3.0 m. The cherty grainstone marker bed appears on cue, 40 m above the base of the formation (Fig. 135D).

Oombaattjie Fm is 90% thicker (362 m) in 10-2 (Fig. 135B) than its average thickness in Tr8, and equal to the thickest section (9-4) in Tr9 (Fig. 125). This is consistent with northward and not westward thickening since 10-2 and 9-4 are at similar latitude but 58.5 km apart in the W–E (zonal) direction.

The Gruis–Oombaattjie transition is accompanied by an influx of clastics (Fig. 135B)—2.4 m of fine-grained quartz-chert arenite in 10-5 and 23.4 m in 10-2, where a lower fine-grained quartz-arenite of marine origin is separated by siltstone from an upward-coarsening feldspathic quartz-arenite. Above the arenites are 50 and 100 m of poorly exposed argillite in 10-5 and 2, respectively. A 1-m-thick bed of dark-grey calcite

microbialite (thrombolite) separates the quartz-chert arenite and argillite in 10-5.

Lower Oombaattjie Fm cycles in Tr10 are dominated by calcitic ooid-intraclast grainstone, with increasing proportions of calcite ribbonite northward (Fig. 135B), similar to Tr8 (Fig. 103) and Tr9 (Fig. 125). Upper Oombaattjie Fm cycles are poorly exposed, with thin dolomite caps on cycles dominated by argillite or marly ribbonite. Again, this is consistent with evidence in Tr8 and 9 for gradual northward deepening (Fig. 103, 125).

Up to 9 m of massive polymictic dolomite diamictite of Ghaub Fm disconformably overlie Oombaattjie Fm in 10-2 (Fig. 135C). Isotopic data from Oombaattjie Fm in 10-2 (3.3.4.) indicate that cycle b8 is fully present, similar to Tr9 (Fig. 125) but unlike Tr8 (Fig. 103). This implies that b8 absence is not a general feature of IPz, as previously inferred (Hoffmann, 2011a), but is related to glacial erosion of a Marinoan trough of limited (≤ 50 km) W–E extent. The trough evidently extends ≥ 60 km southward, to Tr7 (7–10–16, Fig. 88).

2.10.3. Early Ediacaran of Tr10

Keilberg Mb is 17 m thick in section 10-2 (Fig. 135C). The lower 3 m consist of mechanically stratified dolopelarenite with a 0.5 m thick zone

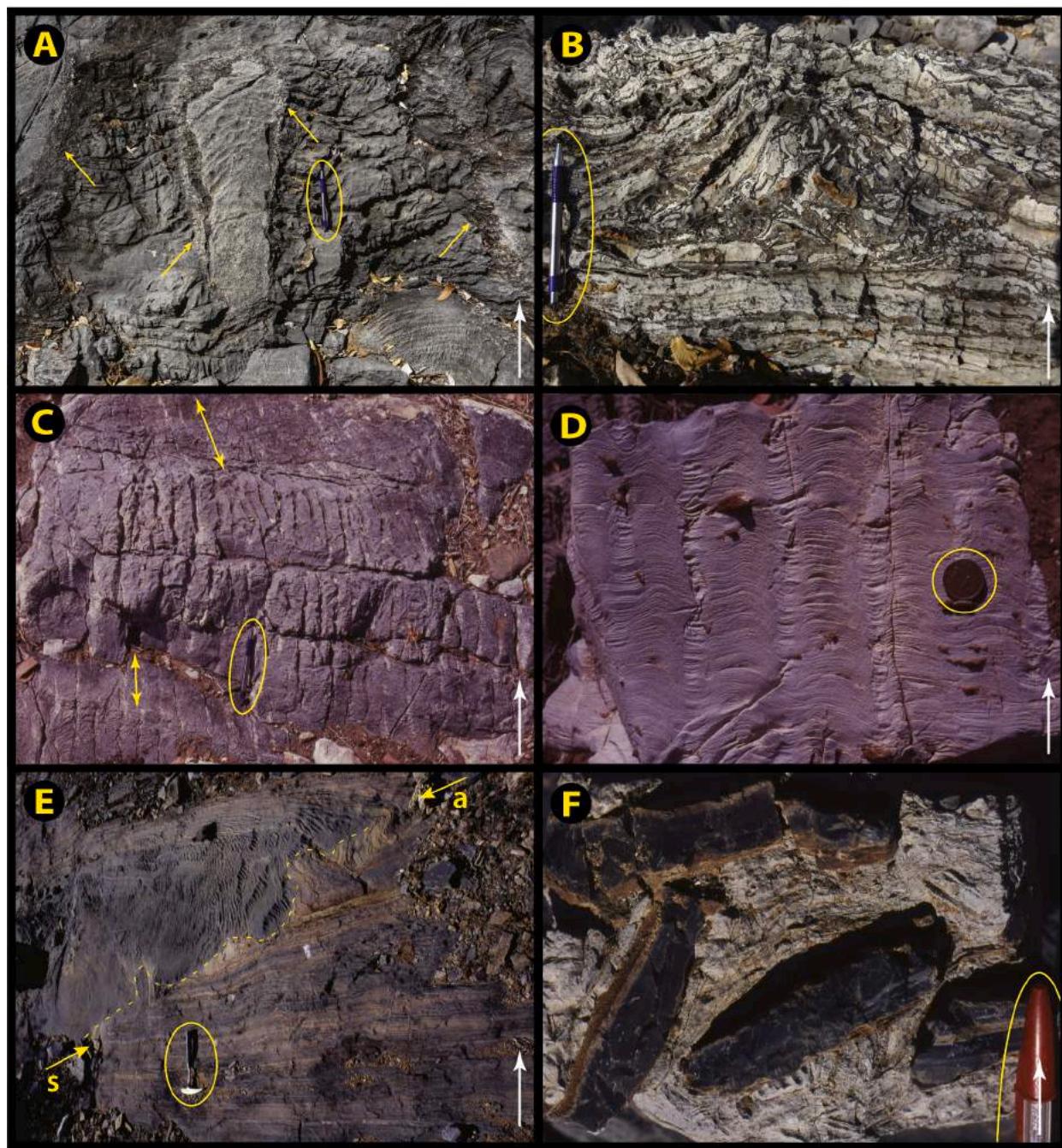


Fig. 136. Images of Rasthof and Maieberg cap-carbonate sequences in Tr10: white arrows indicate stratigraphic younging. (A) Discrete columnar stromatolites with unlaminated microbial ‘wall structure’ (yellow arrows) typical of form-genus *Boxonia*, middle Rasthof Fm member Ar2c (Fig. 111) at $-18.8308^{\circ}/14.2882^{\circ}$ in 10–2 (Fig. 135B). (B) Tepee structure and associated breccia indicating subaerial exposure at sequence boundary above Rasthof Fm at $-18.8297^{\circ}/14.2902^{\circ}$ in 10–2 (Fig. 135B). (C–D) Gutter stromatolites in Keilberg Mb at $-18.8261^{\circ}/14.2984^{\circ}$ in 10–2. On bedding planes (bidirectional arrows), gutters are oriented NNE–SSW, transverse to giant wave ripples in the same stratigraphic unit (Fig. 57). Cross-section in D, oriented normal to gutter direction and bedding, resembles tubestome stromatolite (Fig. 119E). (E) Soft-sediment thrust (dashed line) in calcite rhythmite near the top of middle Maieberg Fm Tm2 member at $-18.8585^{\circ}/14.3648^{\circ}$ in 10–4 (Fig. 135E). Yellow arrows point to axial surfaces of hangingwall anticline (a) and footwall syncline (s). Tip of thrust is in paired anticline-syncline in upper right. (F) Black chert clasts in debris of Maieberg Tm2 calcite rhythmite member. Same location as E. Black chert forms cm-thick layers and pods in calcite rhythmite. If chert is authigenic, it formed close to the sediment surface enabling involvement in debris flow.

of isopachous fibrous-dolomite sheet-crack cement near the base, which is covered. This is a rare occurrence of near-basal sheet-crack cement on the platform. A 3-m-thick stromatolite biostrome exhibits cm-scale stromatolites (Fig. 136D), as in Tr8 (Fig. 119D & E), but the micritic infills between the arched stromatoloids are not circular in plan view (Fig. 119F). Instead, they form parallel linear ‘gutters’ (Fig. 136C), like those in a Marinoan cap dolomite in NW Canada (James et al., 2001).

Tilt-corrected azimuthal orientation of the gutters is $020\text{--}200^{\circ}$, subparallel to Keilberg Mb gutter stromatolites in Tr8 and 9, and subnormal to crestlines of giant wave ripples in Tr5 and 8 (Fig. 57). This suggests that the gutters are a response to wave action. The gutters are also subparallel to Ghaub Fm diamictite clast fabric in Tr8 (Fig. 57) and groove marks on the sub-Ghaub glacial pavement in Tr5 (Domack and Hoffman, 2011). This implies that the vectors of ice movement and

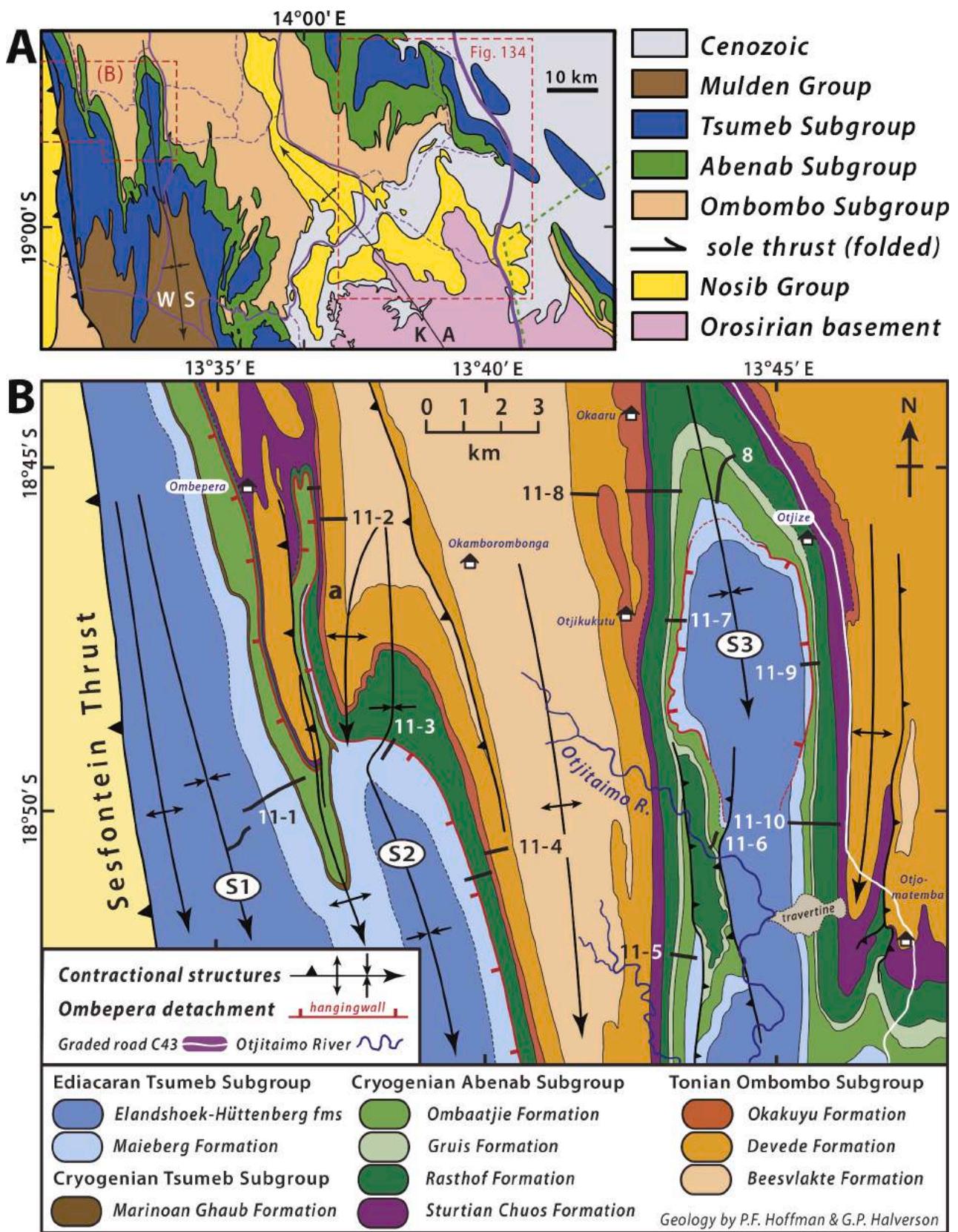


Fig. 137. Geological maps of Eastern Kaoko zone at latitudes of Tr10 and 11: (A) Damaran groups around the NW plunge of Kamanjab antiform (KA) and SSE plunge of Warmquelle synform (WS) (Fig. 8B). Dashed red boxes show areas of Fig. 134 (Tr10) and B (Tr11). (B) Geologic map of Tr11, showing three synclines (S1–3) and folded Ombepera detachment as solid red line. Ticks indicate hangingwall, which moved stratigraphically downward (i.e., normal-sense slip) and westward (Fig. 139), analogous to Omonde detachment in Tr7 (Fig. 87A & B). Also shown are locations of sections 11–1–10 (Figs. 139, 140 & 144).

postglacial long-period wave propagation were subparallel (Fig. 57), but presumably in opposite directions—the ice sheet flowing basinward (southward) and long-period wave trains (Allen and Hoffman, 2005a) in the glacial aftermath tracking landward.

The overall Ediacaran carbonate succession in 10–4 (Fig. 135E) is thicker, 1650 m, than in any previous transect. At 500 m, Maieberg Fm is 91 or 103% thicker than in 8–3 or 9.3 (Figs. 117 & 130), and Elandshoek and Hüttenberg formations are 28 and 62% thicker, respectively, than in 9–3 (Fig. 130). Northward thickening is therefore not simply a function of the depth of sub-Mulden Group erosion, which would be reflected by changes in Hüttenberg thickness alone. Tsumeb Subgroup was sampled for stable-isotopes in 10.1 (3.4.), but section 10–4 was subsequently measured in greater detail. 10–1 and 4 are 10 km apart but comparable in overall Tsumeb Subgroup thickness (Figs. 134 & 135E).

2.10.4. Highlights from Tr10

Chief highlights are: (1) a Chuos Fm depocenter, ≥ 1.16 km thick, of undetermined origin; (2) terrigenous inputs in lower (b1–2) and upper (b7) Ombaatjie Fm; (3) sheet-crack cements and gutter stromatolites in Keilberg Mb cap dolomite (10–2), and parallelism of such gutters (Tr8–10) with Marinoan glacial flow indicators (Fig. 57), and (4) northward thickening of all 4 non-glacial passive-margin formations.

2.11. Transect Tr11 – three synclines

From the north end of Tr9 (Fig. 8B), Abenab and Tsumeb subgroups wind their way westward around three southward plunging synclines (S1–3 in Fig. 137B) and intervening anticlines to Sesfontein Thrust, a crustal-scale structure that defines the Central/Eastern Kaoko zone boundary (CKz/EKz, Fig. 3). The larger of the two anticlines holds the

headwaters of Otjataimo River, which for reasons of impetuous headward development takes a wild excursion into the topographically imposing Otjize syncline (S3, Fig. 137B) on its way southward to Sesfontein valley, where it feeds into the upper Hoanib River (Fig. 46).

An overarching goal for investigating this transect was to find a western margin of the carbonate platform, or at least an indication that a margin was not far off. Reconnaissance of the western syncline (S1, Fig. 137B) revealed a more argillaceous upper Ombaatjie Fm (overlain by Ghaub diamictite) compared with the eastern syncline (S3), but no obvious change in Ediacaran carbonate facies. When Tr10, the most easterly transect, also revealed an argillaceous upper Ombaatjie Fm (Fig. 135B), the apparent Ombaatjie ‘shale-out’ in S1 became ambiguous. Was the shale-out a westward or northward trend?

2.11.1. Ombepera detachment

A more troubling result of early reconnaissance was a failure to find Keilberg Mb in syncline S2 (Fig. 137B). Keilberg Mb was recognized early on as a regionally extensive, laterally continuous and lithologically distinctive marker horizon (Hoffmann and Prave, 1996; Kennedy et al., 1998). Its relative stratigraphic position in S2 was predictable, but no Keilberg Mb could be found there.

Subsequently, Ombonde detachment (Fig. 87A & B) was discovered 100 km to the SE in 1995 (Hoffman and Hartz, 1999), but no similar structure was identified in EKz for the next 19 years. Not until S2 was revisited in the final week of the 2014 field season did the idea arise that an Ombonde-type (pre-folding) detachment fault might be responsible for the missing Keilberg Mb. A low-angle normal-sense detachment, ramping stratigraphically downward from E to W, should have an up-dip equivalent in S3 (Fig. 137B). The projected fault should be of equivalent magnitude but situated stratigraphically higher in both the footwall and

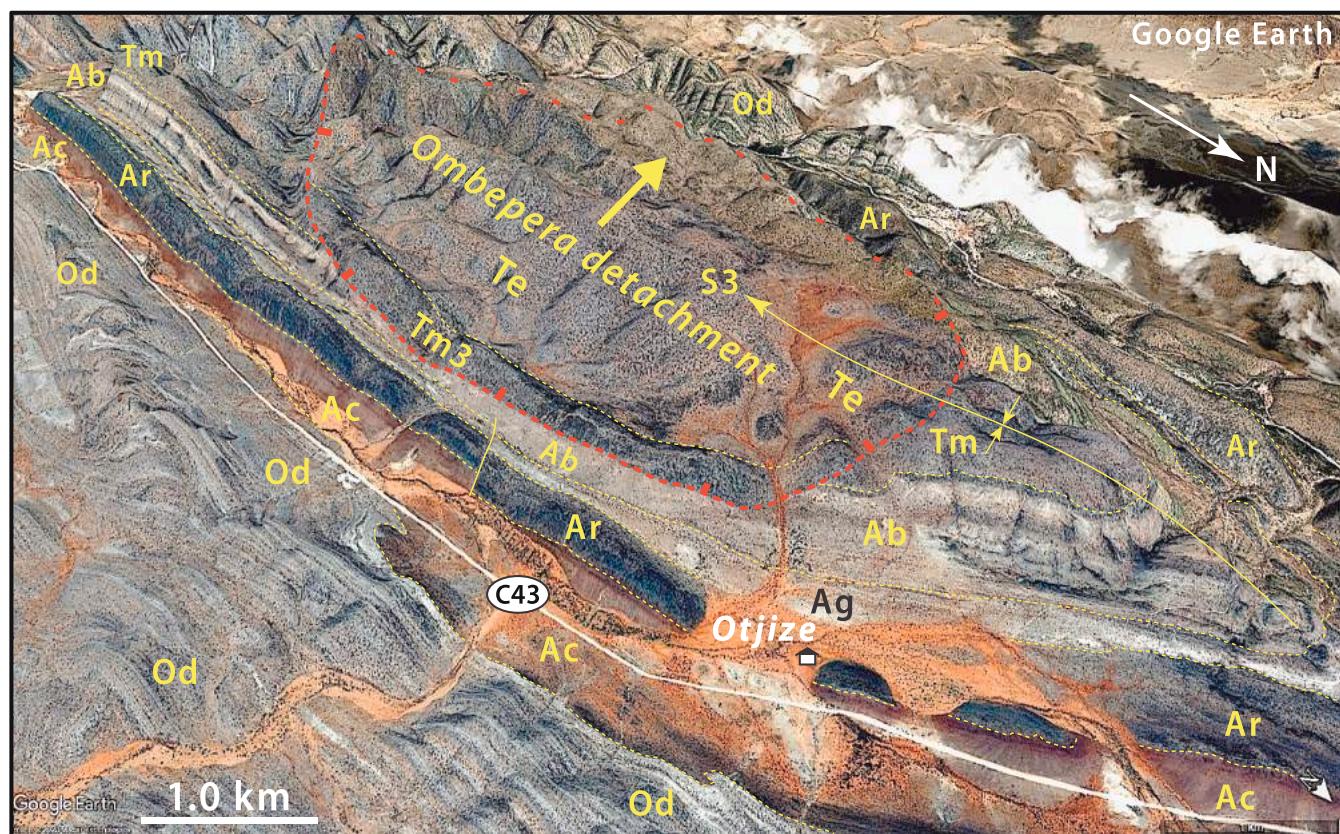


Fig. 138. Annotated satellite image of Otjize (Warmquelle) syncline (S3), looking obliquely SW to area of 11–8–10 (Figs. 137 & 140). Bold arrow indicates displacement direction of Ombepera detachment, indicated by dashed red line with bars on hangingwall. In footwall, Maieberg Fm (Tm) and upper Ombaatjie Fm (Ab) are truncated by lateral ramps spaced 5 km apart. 0.5 km of strata are excised across the detachment surface, which is folded by the S3 syncline. Ombepera detachment is exposed to the W at successively deeper stratigraphic levels in synclines S2 and S1 (Figs. 137 & 139). Google Earth: Image © 2020 Maxar Technologies.

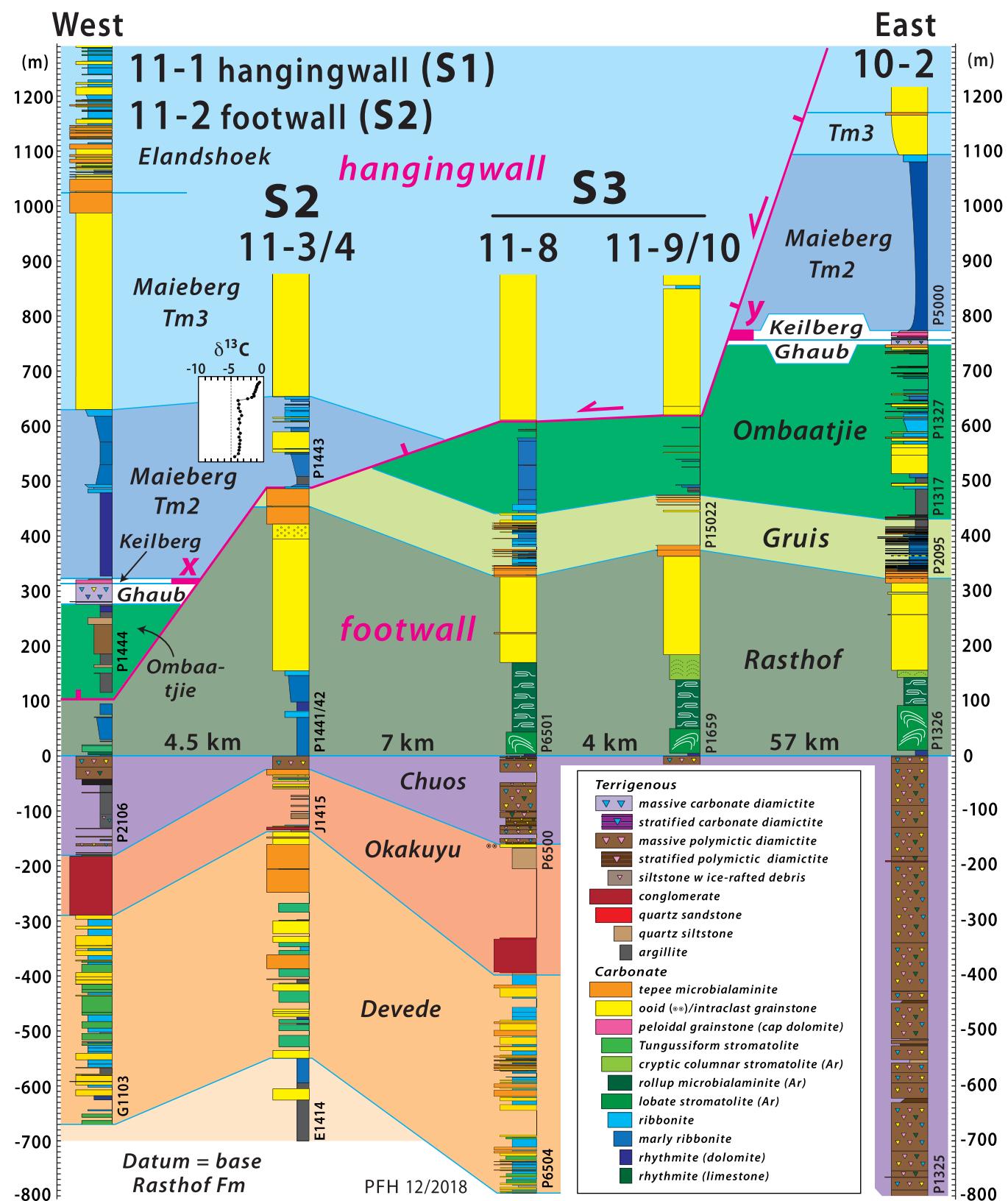


Fig. 139. Columnar sections from synclines S1–3 and section 10–2 projected onto W–E plane, showing stratigraphic descent of Ombepera detachment (red line) in hangingwall (red ticks) and footwall in the direction of inferred slip (red half-arrows). See Fig. 137B and Fig. 134 for section locations. Note matching cut-offs of Keilberg Mb in hangingwall at x and footwall at y. Accordingly, S1 hangingwall section 11–1 restores to an original (pre-detachment) location east of S3 section 11–9. Compare with Ombonde detachment (Fig. 87B). The riddle that led to discovery of Ombepera detachment (Hoffman et al., 2016b) was the absence of Keilberg Mb in S2.

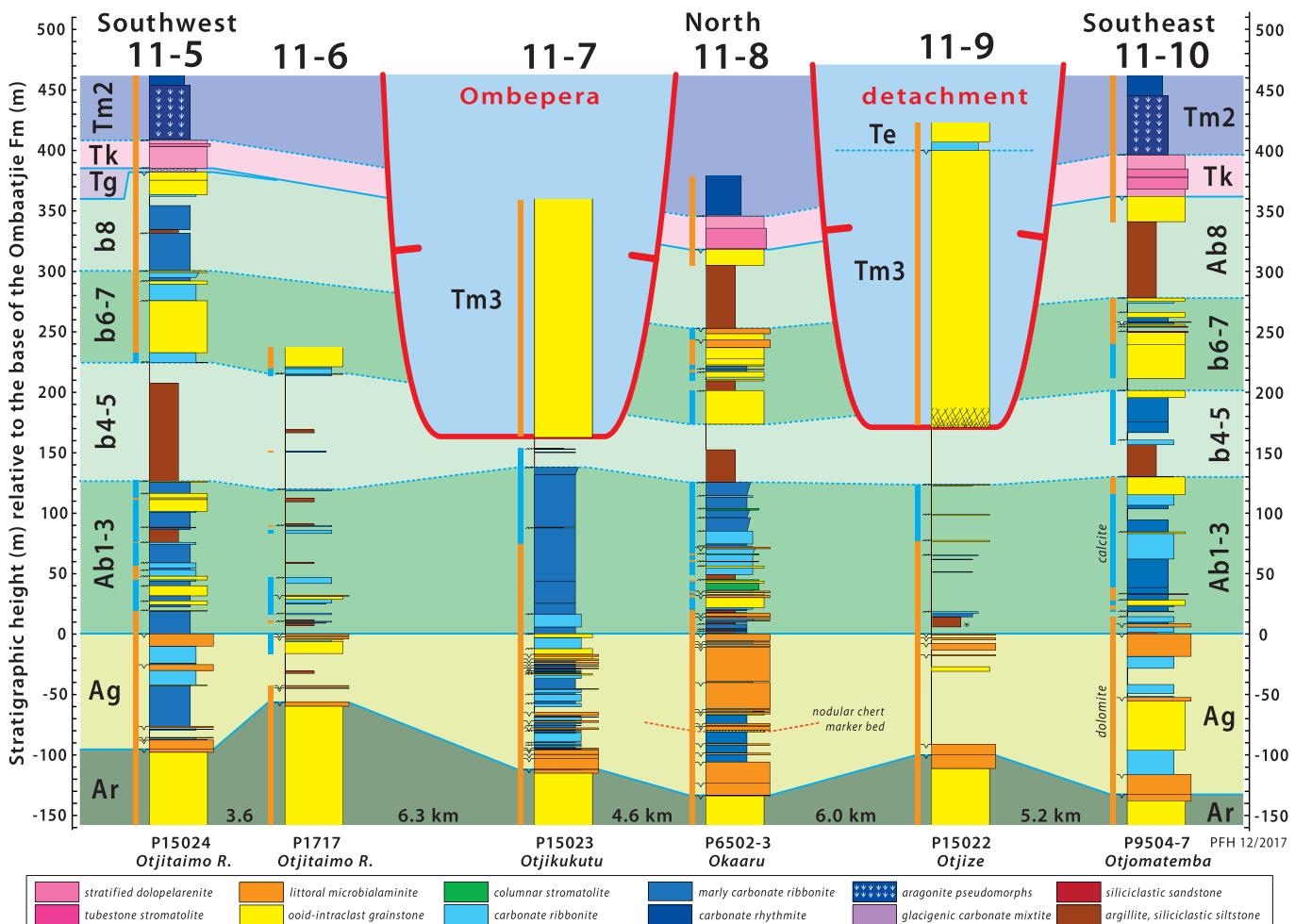


Fig. 140. Columnar sections from west (11–5–7) and east limb (11–8–10) of syncline S3: section locations are given in Fig. 137B. Datum is base of Ombaatjie Fm (Ab1–3). Sections 11–5–6 and 11–10 lie S of trough-shaped Ombepera detachment (Fig. 138), while 11–8 lies N of detachment. In 11–7 and 11–9, upper Maieberg Fm Tm3 grainstone is down-faulted onto Ombaatjie Fm cycles b4–5, excising 0.5-km-thick stratigraphic interval between Ombaatjie Fm cycle b6 and Maieberg Fm Tm2. Note brecciated Tm3 grainstone in detachment hangingwall in 11–9. Detachment is a brittle fault across which stratigraphic excision is the only evidence of its existence.

hangingwall. Conversely, the fault should appear in S1 at a lower stratigraphic level than in S2.

Each of these predictions proved to be true (Figs. 137B–140) (Hoffman et al., 2016b). In all three synclines, ~0.5 km of strata are missing across a brittle (cryptic) fault plane. In S1, middle Ombaatjie Fm is faulted down onto lower Rasthof Fm (11–1, Fig. 139). In S2, middle Maieberg Fm is faulted down onto lower Gruis Fm (11–4, Fig. 139). In S3, upper Maieberg Fm is faulted down onto middle Ombaatjie Fm (11–7 and 9, Figs. 138, 139 & 140). From east to west, the hangingwall ramps down 0.5 km stratigraphically from upper Maieberg to middle Ombaatjie Fm, while the footwall ramps down by the same amount from middle Ombaatjie to lower Rasthof Fm (Fig. 139). The fault is brittle with minor hangingwall brecciation in 11–9 (Fig. 140). The name ‘Ombepera detachment’ (Hoffman et al., 2016b) derives from the village of that name (Fig. 137B).

Since the hangingwall in S1 is at a roughly equivalent stratigraphic level (middle Ombaatjie Fm) as the footwall in S3, geometry requires that the former originated directly above the latter. Fault displacement is accordingly equal to the distance between S1 and S3, corrected for west–east shortening due to folding. The shortest east–west distance between the fault trace in the two synclines is 10 km (Fig. 137B) and the

shortening due to folding, given average limb dips of ~60° as observed, is about 50%. The minimum displacement on the detachment fault is therefore ~20 km, or four times its width (N–S) of 5 km in S3 (Figs. 137 & 138). Large ratios (≥ 1.0) of displacement to width are typical of large mass slides on continental margins (e.g., Martinez et al., 2005; Hjelstuen et al., 2007; Armandita et al., 2015; Brooks et al., 2017). This distinguishes them from normal faults of tectonic origin, for which displacement/length (‘width’) ratios are generally ≤ 0.02 (Dawers et al., 1993; Gudmundsson et al., 2013).

The age of displacement on Ombepera detachment is not as tightly constrained as Omponde detachment (Fig. 87A & B) because Mulden Group is not preserved in Tr11 (Fig. 137B). Ombepera detachment postdates lower Elandshoek Fm and predates décollement folding. We assume that the detachments were broadly contemporaneous on the basis of structural homology—both are brittle faults that ramp downward to the west and predate décollement folding. We relate both detachments to lithospheric flexure and abortive westward subduction during arc-continent collision in Kaoko orogen (Hoffman and Hartz, 1999; Hoffman et al., 2016b).

In comparing the sizes of mass slides imaged seismically on modern continental margins with ancient (Phanerozoic) analogs (Fig. 141),

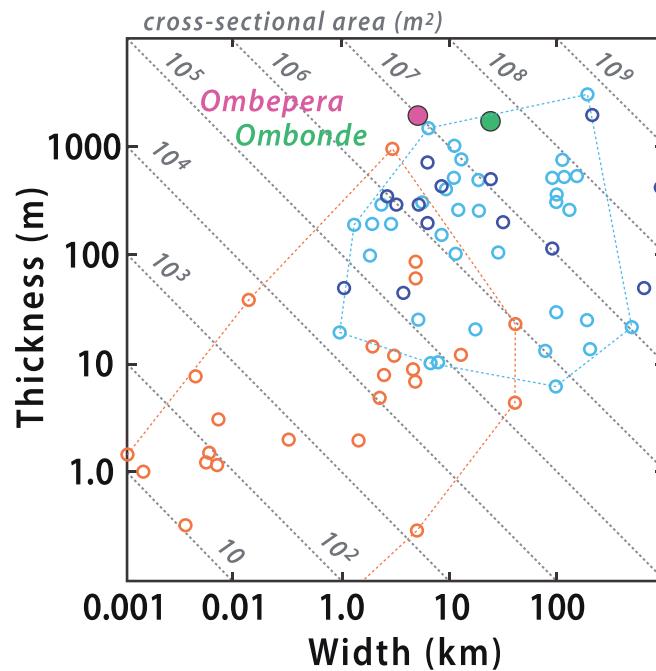


Fig. 141. Dimensions of submarine mass slides (blue circles) imaged seismically on modern continental margins and ancient (Phanerozoic) examples (orange circles) documented in outcrop studies (Woodcock, 1979). Smaller size of ancient examples was attributed to limitation of outcrop size (Woodcock, 1979). Ombonde and Ombepera detachments (Hoffman et al., 2016b), represented by red and green dots respectively, lie in the submarine field (blue), demonstrating that ancient mass slides as large as modern submarine examples can be observed when limitation of outcrop size is superceded by stratigraphic mapping (Figs. 87A & 137B).

Woodcock (1979) postulated that the smaller size of the latter might reflect the limited size of outcrops in which they could be observed. Ombonde and Ombepera detachments fall in the field of seismically-imaged examples (Fig. 141). Their extents were demonstrated by stratigraphic mapping not limited by outcrop size.

No lateral ramps like those observed in S3 (Figs. 137b, 138 & 140) are evident in S1. The argillaceous facies of Ombaatjie Fm continues northward along strike to latitude 18°26'S, where it is cut-off by Sesfontein Thrust. We postulate that the narrow slide mass in S3 is one of many that merge to form a laterally continuous structure in S1. S2 and 3 do not preserve Cryogenian–Ediacaran strata to the north of Tr11 because of their southward plunge. On the other hand, additional detachment structures may exist in the deeply incised and poorly-mapped terrain between Tr11 and Sesfontein valley (Fig. 96).

2.11.2. Footwall of Ombepera detachment

Footwall strata include pre-Sturtian Ombombo Subgroup and Chuos and Rasthof formations in S1 and S2 (Fig. 139), and the entire Otavi Group N and S of Ombonde detachment in S3 (Fig. 140). Devede Fm is similar in thickness, facies and cyclic character to Tr10 and the northern parts of Tr8 and 9 (Figs. 123 & 99). No E–W change is apparent and the absence of cannibalized clastics in lower Devede Fm is consistent with a southern source. At a location ($-18^{\circ}52.953'/13^{\circ}47.805'$) between sections 9–4 and 11–10 (Figs. 96 & 123), a ≤ 15 -cm-thick tuff (Fig. 142E) within dolomite ribbonite 16 m below the base of Okakuyu Fm yielded volcanic zircon with a weighted mean $^{207}\text{Pb}/^{206}\text{Pb}$ age of 759.95 ± 0.86 Ma (Halverson et al., 2005). This an important radiometric age constraint on Devede Fm, showing for example that it is >12 Myr older than lithologically similar Okotjize Fm (Ugab Subgroup) in Tr2–3, which postdates 746 ± 2 -Ma Lower Naauwpoort volcanics (Hoffman et al., 1996).

Okakuyu Fm consists of fine-grained clastics and thick wedges of alluvial conglomerate and associated sandstone (Figs. 139 & 123). The conglomerates are composed of well-rounded, self-supported clasts of dolomite and chert. They require unidentified local sources where

Devede Fm was faulted and tilted in late Tonian time. At the top of Okakuyu Fm in sections 11–4 and 8, biostromes of *Tungussia* type columnar stromatolitic dolomite and associated coarse-grained (<2 mm diameter) oolite (Fig. 142D) are preserved beneath the Sturtian glacial erosion surface.

Chuos Fm is best exposed around the northern closure of S3, where it is 160 m thick (P6500 in Fig. 139) and consists of massive polymictic diamictite bodies with greatly subordinate units of stratified diamictite, clast-supported conglomerate and green siltstone with polymictic debrites. Chuos Fm is increasingly enriched in ferric iron with stratigraphic height and diffusion bands (*liesegang* rings) (Fig. 142C) should not be mistaken for primary stratification. The Chuos–Rasthof contact is invariably sharp and unidirectional (Figs. 139 & 144).

Rasthof Fm (Fig. 139) is 15% thicker on average (345 m) in S3 compared with Tr10 (Fig. 136B), 60 km to the east, and nearly 30% thicker than in 9–3 (Fig. 125), 40 km to the south. It presents an over-thick HST in which the basal abiotic rhythmite (Ar1) is attenuated and dolomitic. Lobate stromatolite (Fig. 142A), roll-up microbial laminitic and cryptic columnar stromatolite (e.g., Fig. 136A) form a typical IPz succession within the microbial middle member (Ar2). The uppermost grainstone (Ar3) in 11–4 is coarsely oolitic (Fig. 139).

Between sections 11–2–3 (location a, Fig. 137B), Rasthof Fm thins northward from 345 to 95 m over a distance of just 1.5 km (Fig. 143). In S1 (Fig. 139), Rasthof does not exceed 70 m anywhere. Three explanations for this abrupt thinning have been offered. The first is a primary facies change involving northward deepening at a platform margin (Wallace et al., 2014), analogous to the Rasthof Fm facies change in eastern Tr6 (Fig. 76). A second is a lateral ramp in Ombepera detachment (Hoffman et al., 2016b), which hugs the top of the Rasthof Fm in S2 (Fig. 139). Accordingly, the missing Ar2–3 members were displaced westward and subsequently uplifted and eroded away on the hanging-wall of Sesfontein Thrust. The postulated northward-dipping lateral ramp at location a could bound a slide mass or lobe to the north of the mapped detachment in S3 (Fig. 137B). A third alternative combines the first two—a primary facies change that controlled the morphology of the

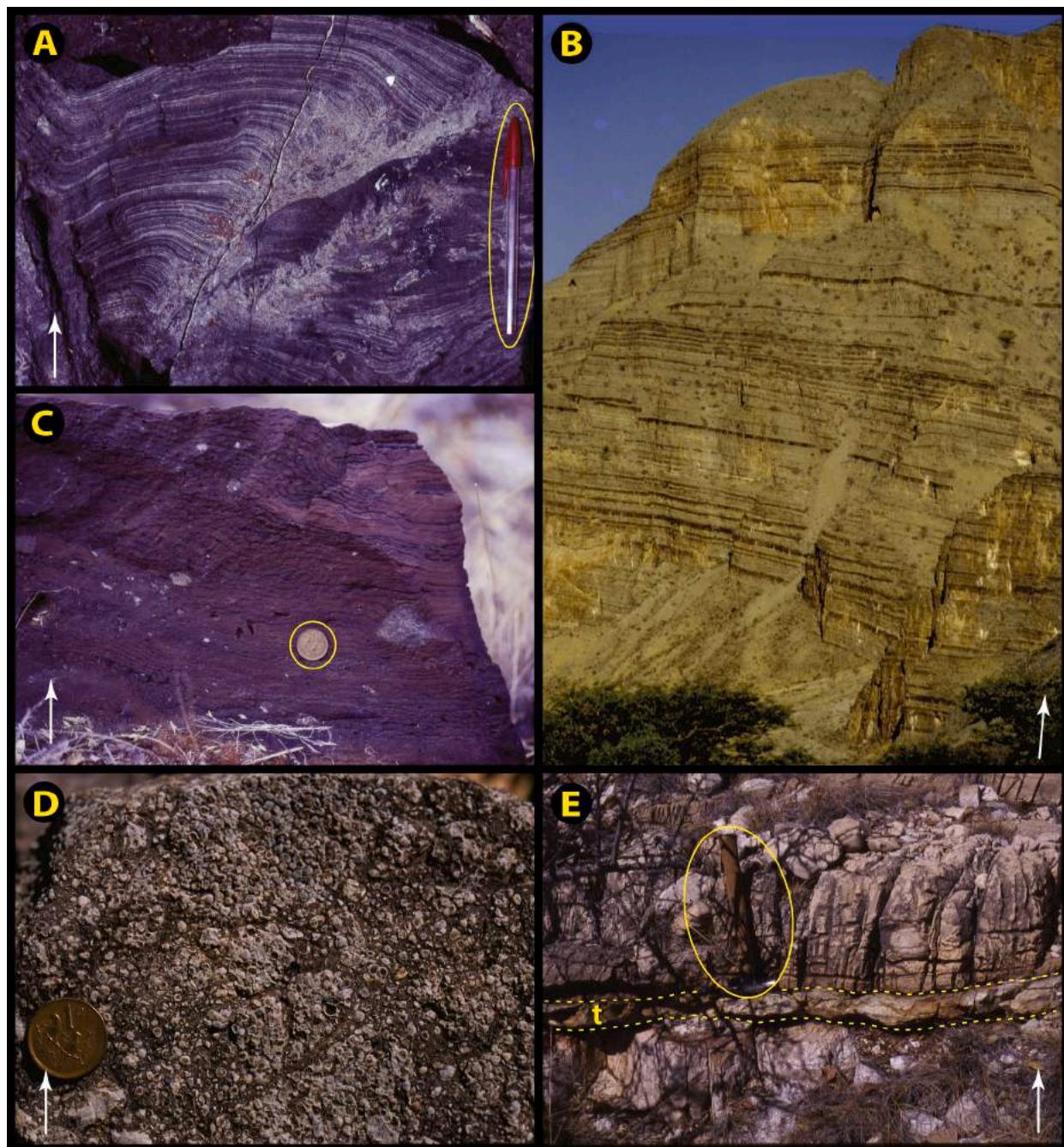


Fig. 142. Images in Tr11: white arrows indicate stratigraphic younging. (A) Lobate stromatolite (Fig. 69B) in Rasthof Fm Ar2a (Fig. 111) at $-18.8446^{\circ}/13.7190^{\circ}$ near 11–6 (Fig. 137B), showing characteristic sideways-climbing growth pattern, suggesting expansive growth in a laterally confined half-space (Lokier et al., 2018). (B) Dolomite ribbonite-grainstone cycles in early Ediacaran Elandschoek Fm exposed in axial zone of Anabib anticline (Guj, 1970) at $-19.1505^{\circ}/13.7092^{\circ}$, 10 km east of Sesfontein (Fig. 96). Dark bands are desert ‘varnish’ on authigenic chert in dolomite grainstone. Thickness of strata shown is ~ 240 m. (C) Clast-poor ferruginous diamictite in upper Chuos Fm at $-18.8447^{\circ}/13.7574^{\circ}$ near 11–10 (Fig. 139). Striping is related to secondary Fe diffusion (*liesegang* bands) and does not indicate depositional stratification, which is absent. *Liesegang* bands are common in upper Chuos Fm (Hedberg, 1979, p. 55) and may have been misinterpreted as microbial stromatolites (Le Heron et al., 2013b). (D) Coarse ooids (≤ 2.0 mm) in uppermost Okakuyu Fm dolomite grainstone directly beneath Chuos Fm diamictite at $-18.7029^{\circ}/13.7102^{\circ}$ in 11–8 (Fig. 139). (E) Volcanic tuff (t), or bentonite, in dolomite ribbonite of upper Devede Fm, 16.0 m stratigraphically below base of Okakuyu Fm (Fig. 123). It yielded zircon dated 759.95 ± 0.86 Ma (weighted-mean $^{207}\text{Pb}/^{206}\text{Pb}$ age) inferred as the depositional age (Halverson et al., 2005). Hammer (circled) is 33 cm long. A second (undated) tuff occurs 1.5 m stratigraphically higher in the same outcrop, which is located at $-18.8829^{\circ}/13.7973^{\circ}$, 2.2 km ESE of Otjomatembwa and 5.9 km SE of base of section 11–10 (Fig. 137B). The age is barely distinguishable from a Pb–Pb age of 756 ± 2 Ma (Hoffman et al., 1996) for peralkaline Oas quartz-syenite intrusion in Welwitschia Inlier (FSz, Fig. 8A), 190 km to the SSE, and indistinguishable from a U–Pb (SHRIMP) age of 757 ± 5 Ma (Nascimento et al., 2016) for a thick dacite ash-flow tuff in Austerlitz Fm of the Northern Damara zone (Figs. 6B & 15) at a similar distance.

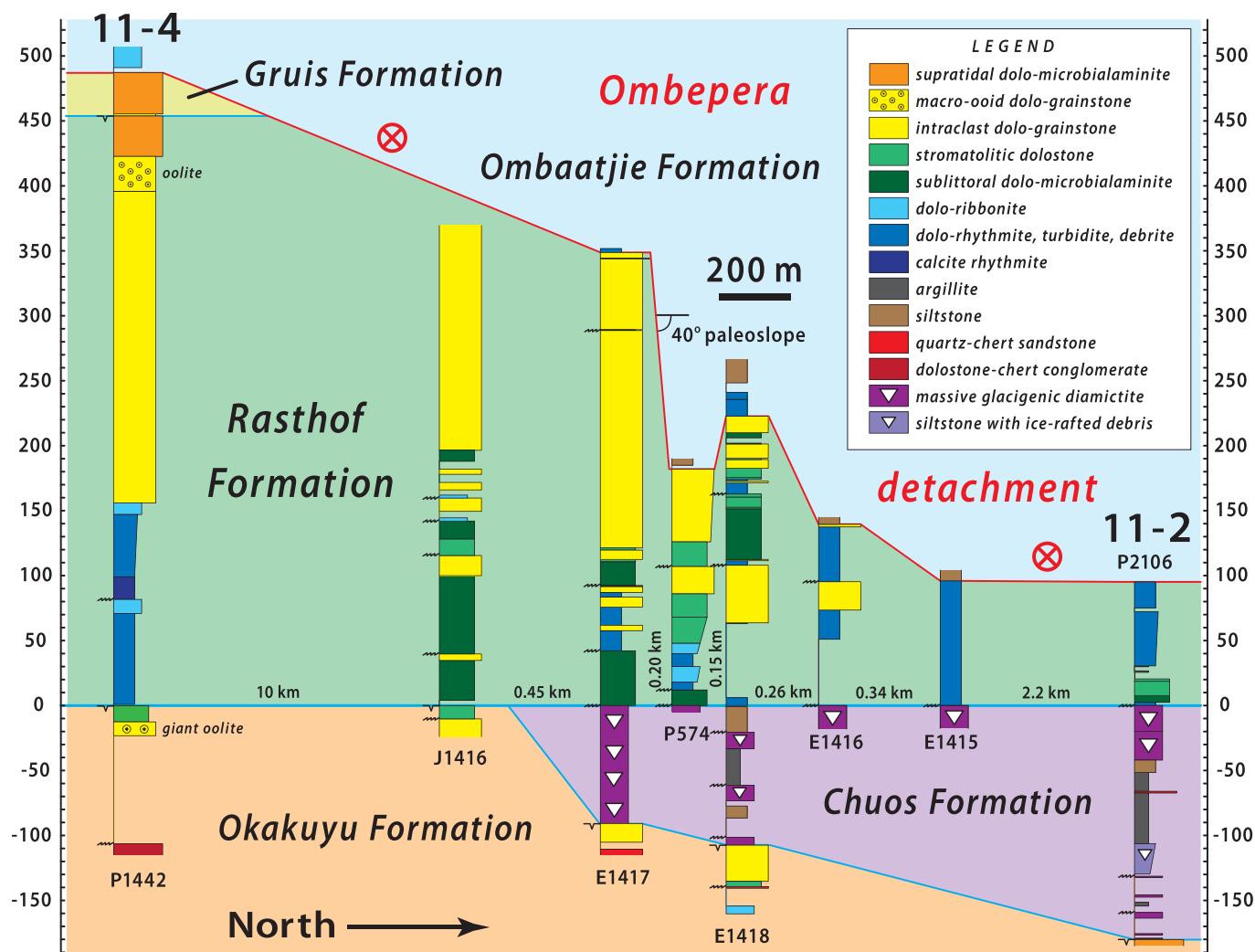


Fig. 143. Columnar sections of Cryogenian Chuos and Rasthof formations at location a (Fig. 137B), south of section 11-2. Datum is base of Rasthof Fm. Rapid northward attenuation of Rasthof Fm appears related to progressive truncation of higher stratigraphic units beneath lateral ramp of Ombepera detachment (red line), which slipped westward into the plane of section (Hoffman et al., 2016b). Alternatively, detachment tracks top of Rasthof Fm across a shelf-margin facies change (e.g., Wallace et al., 2014).

detachment surface (Hoffman et al., 2016b) (Fig. 143). Detailed facies mapping is required to adjudicate between these explanations. This should be feasible since the structural panel is steeply dipping (overturned) and well exposed.

Gruis Fm in S3 is not significantly changed from Tr9 or 10. The grainstone marker bed with nodular chert was identified in section 11-8 (Fig. 140), from which it extends southward ≥68 km to 8-2 (Fig. 125) and the same distance eastward to 10-5 (Fig. 135D).

Ombaatjie Fm cycles b1–3 are ribbonite-dominated like Tr10 to the E (Figs. 140 & 135B), and unlike their grainstone-dominated equivalents to the south in Tr8 and 9 (Figs. 103 & 125). S–N rather than W–E change is also implied by thick argillite in Ombaatjie Fm cycle b4 in S3 (Fig. 140), being a distal facies of quartzarenite in the same cycle in Tr9 (Fig. 125).

Marinoan Ghaub Fm was found in only one footwall section, 11-5 in S3 (Fig. 137B), where a dolomite-clast conglomerate, 3.3 m thick, disconformably overlies Ombaatjie cycle b8 grainstone and is conformably overlain by a 23- to 35-m-thick Keilberg cap dolomite (Fig. 140). The overlying middle member (Tm2) of Maienberg Fm is dolomitized. In sections 11-5 and 10 (Fig. 137B), preferentially silicified crystal fans, pseudomorphic after seafloor aragonite, occur throughout the lower 45–60 m of Tm2 dolomite rhythmite (Fig. 140). From structural

geometry, we estimate the total Tsumeb Subgroup in S3 to be ~1.6 km thick where it plunges beneath Sesfontein Fm (lower Mulden Group) (Fig. 137A), but we have not measured a detailed section to compare with the equivalent hangingwall section 11-1 (Fig. 144).

2.11.3. Hangingwall of Ombepera detachment

The most complete hangingwall section (11-1) is naturally the one farthest to the west (Figs. 139 & 144). As discussed earlier (2.11.1.), 11-1 originated in the area of S3, 10–14 km to the east (Fig. 144). The Cryogenian in 11-1 is therefore best compared with the footwall of sections (11-5, 7 and 10) in S3 (Fig. 140). Upper Ombaatjie Fm in 11-1 is dominated by argillite, quartz siltstone and fine-grained, tabular-bedded, quartz sandstone (Fig. 144). Carbonate, as turbidite beds in argillite, is exclusively limestone. These aspects are most similar to cycles b4 and 5 (Figs. 125 & 140). Cycle b8 is also rich in argillite but lacks sandstone and its carbonate is normally dolomite, not limestone. If the Ombaatjie Fm in 11-1 represents cycles b4–5, then the glaciogenic Ghaub Fm has eroded more deeply than in other platform sections. This would have created 0.2 km of additional accommodation for the moderately anomalous thickness (37.7 m) of the Ghaub Fm in 11-1, and the highly anomalous (0.70 km) Maienberg Fm (Fig. 144). To accommodate the Maienberg Fm in 11-1, the Ombaatjie would need to be eroded down to

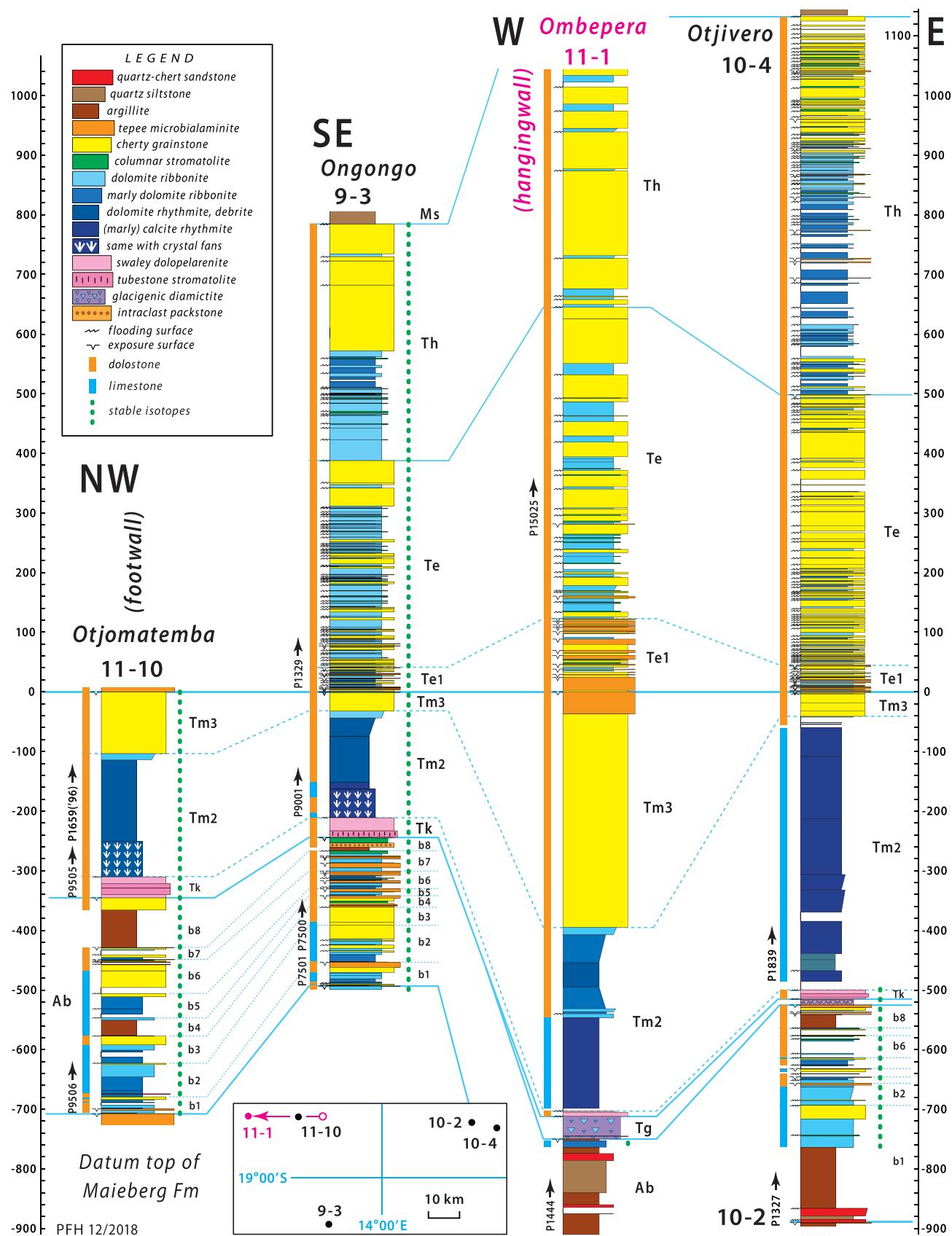
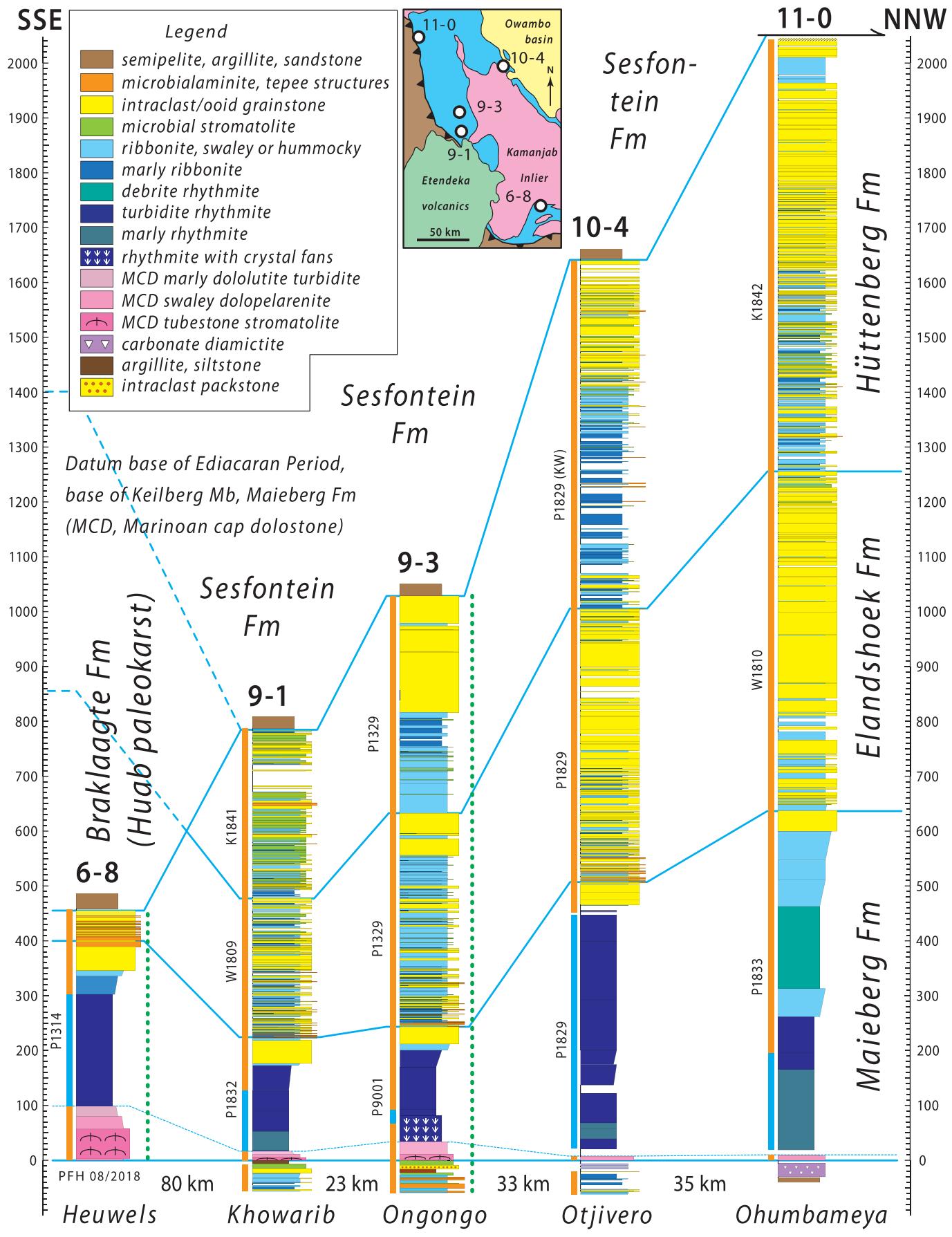


Fig. 144. Columnar sections of post-rift Omboaatjie Fm and Tsumeb Subgroup in Tr9–11, projected onto W–E plane. Units: Ab, Omboaatjie Fm (cycles b1–8); Tg, Ghaub Fm; Tk, Keilberg Mb; Tm2, middle Maieberg Fm; Tm3, upper Maieberg Fm; Te1, lower Elandshoek Fm; Te, Elandshoek Fm post-Te1; Th, Hüttenberg Fm; Ms., Sesfontein Fm (Mulden Group). Datum is base of Elandshoek Fm. Section 11–1 from hangingwall of Omboepera detachment has been restored E of footwall section 11–10, as required by matching cut-offs (Fig. 139). Position of section 9–2 relative to 11–1 is uncertain and its overall lesser thickness reflects its more southerly location relative to other sections (see inset map, lower left), given northward thickening of Omboaatjie Fm and Tsumeb Subgroup (Figs. 125 & 145).



(caption on next page)

Fig. 145. Columnar sections of early Ediacaran Tsumeb Subgroup in Tr6 and Tr9–11, projected onto SSE–NNW plane. Datum is base of Keilberg Mb (Maieberg Fm). Section 11–0 (Ohumbameya) is at $-18^{\circ}31.271'/13^{\circ}30.253'$, 34.2 km NNW of 11–1 (Hoffman et al., 2018). Note roughly proportional northward thickening of Maieberg, Elandshoek and Hüttenberg Fms from 9 to 1 to 11–0. Conversely, southward thickening of Maieberg Fm from 9 to 1 to 6–8 is accompanied by overall attenuation due to erosional downcutting of sub-Mulden Group disconformity surface (Huab paleokarst of Tr6). Assuming overall southward thickening (9–1 to 6–8) proportional to Maieberg Fm thickening yields an original thickness of 1400 m for the total Tsumeb Subgroup in Huab paleokarst outlier (Fig. 193). Marked northward thickening ($\times 2.63$) implies more-rapid thermal subsidence with distance from Congo cratonic promontory (Fig. 2 & 205). Thickness minimum at 9–1 suggests a flexural component in the lithospheric response to sedimentary and volcanic loads in the Northern Damara zone (Watts et al., 1982). We refer to this persistent minimum in early Ediacaran subsidence rate as Khobarib arch.

cycle b1, which in Tr10 is also rich in terrigenous sediment including quartz sandstone (Fig. 135B). We cannot rule out this possibility.

Ghaub Fm in 11–1 is composed of massive limestone- and dolomite-clast diamictite with a matrix of marly carbonate wackestone (Figs. 139 & 144). A solitary fining-upward unit of quartz-dolomite sandstone, 0.6 m thick, occurs near the base of the carbonate diamictite. Keilberg Member is 9.0 m thick and consists of low-angle cross-stratified dolopelarenite with reddish argillite interbeds in the upper 2.2 m. Tubestone stromatolite is absent in 11–1.

Maieberg Fm in 11–1 is 37% thicker (701 m) than in 10–4 (Fig. 144) and 71% thicker than in any other section. Unlike 10–3, the thickening is mostly in the upper grainstone member, Tm3 (Fig. 144). Since the grainstone is poorly stratified, we cannot rule out the possibility that Tm3 is structurally thickened in 11–1.

Elandshoek Fm is normal in thickness (370 m) and facies, including a well-developed basal member (Te1) with supratidal tepee-capped cycles (Fig. 144). However, placement of the Elandshoek–Hüttenberg contact (Fig. 144) is uncertain without chemostratigraphic data. Upper Tsumeb Subgroup is incomplete in 11–1 because of the S1 syncline (Fig. 137B). We therefore measured an auxiliary section, 28.7 km to the north-northwest of Ombepera in the same structural panel. Section 11–0 (Fig. 145) has its base at $-18.5258^{\circ}/13.5039^{\circ}$, near the village of Ohumbameya. It is also incomplete since its top is truncated by Sesfontein Thrust, but its total thickness of 2124 m—Ghaub Fm (32 m), Maieberg Fm (642 m), Elandshoek Fm (620 m) and Hüttenberg Fm (830 m)—demonstrates that northward thickening of Ediacaran carbonate formations continues for ≥ 90 km from section 9–1 (Fig. 145).

2.11.4. Highlights from Tr11

Chief highlights are: (1) Ombepera detachment (Figs. 137–141), a low-angle, W-side-down, normal-sense displacement surface that postdated Otavi Group yet predated décollement folding, and carried ≤ 2 km of carbonate strata ≥ 20 km down the dip of a brittle detachment bounded by lateral ramps only 5 km apart. It is manifested by 0.5 km of excised stratigraphy that descends 0.5 km in stratigraphic height from E to W in both its footwall and hangingwall within the confines of Tr11 (Hoffman et al., 2016b); (2) abrupt Rasthof Fm S-to-N thinning (Fig. 143) in the Ombepera detachment footwall (location a, Fig. 137), related to a facies change and/or top-down structural truncation; (3) northward but not westward thickening of Otavi Group post-rift strata, Ombaatjie Fm and Tsumeb Subgroup (Figs. 144 & 145); and (4) no hint of a W-facing carbonate shelf margin, in part because the farther W, the more of the section is of easterly derivation on the hangingwall of Ombepera detachment.

3. Depositional sequences and chemostratigraphy

In this section, we bring together stratigraphic data from all transects, formation by formation (3.1–5.). We synthesize stratigraphic development (3.6.) and compare $\delta^{13}\text{C}$ and $\delta^{18}\text{O}$ records within and between transects (3.7.), to test the reproducibility of base-line values, and positive and negative excursions. We examine their dependence on mineralogy (calcite vs dolomite), lithofacies, paleogeographic zonation and diagenetic setting. We introduce a few records from outside Kunene Region (e.g., Otavi Mountainland) for comparison. We compare a composite carbonate $\delta^{13}\text{C}$ record from Otavi/Swakop Group with correlative successions on other paleocontinents, period by period

(3.7.). Finally, we compile and compare other geochemical proxy records from Otavi/Swakop Group—B, N, Mg, S, Ca, Zn, Cr, Fe and Sr isotopes, trace elements and Fe-speciation (3.8.).

3.1. Nosib Group

Nabis Fm (SACS (South African Committee for Stratigraphy), 1980; Miller, 2008b) is a nonmarine assemblage of subarkosic sandstone and conglomerate that unconformably overlies Orosirian crystalline basement and underlies Otavi Group in IPz (Figs. 5, 6D & 8A). Its thickness is

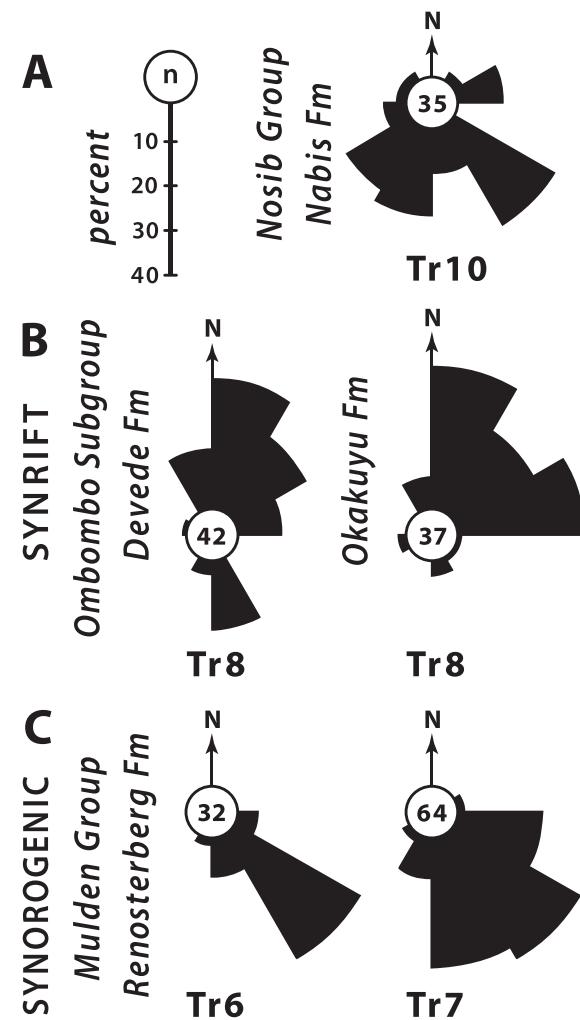


Fig. 146. Paleocurrent rose diagrams (circular histograms) based on tilt-corrected foreset dip directions from crossbedding in fluvial sandstones: (A) Nabis Fm WSW of Ekoto (Fig. 134) in Tr10; (B) Devede and Okakuyu Fms in 8–8–9 (Fig. 98); (C) Renosterberg Fm in 6–1 in Sout River (Fig. 83E–F & 84) and W of Palmfontein in Tr7 (Fig. 92). Synrift paleocurrents were N-directed off Makalani and Huab rift shoulders (Hoffman and Halverson, 2008). Synrogenic paleocurrents were SE-directed in response to orogenesis in Kaoko Belt (Stanistreet et al., 1991). Significance of S-directed paleocurrents in Nabis Fm, also observed in Tr7, is conjectural.

~1.25 km around the northern plunge of Kamanjab inlier (Miller, 2008b), but in Tr7 the formation is erosionally truncated by Abenab Subgroup on Makalani dip-slope (Figs. 87 & 88), and it is absent altogether in OPz. Basal clastics south of Kamanjab inlier in Tr1 and Tr4 (Austerlitz Fm of Hedberg, 1979) have been tentatively correlated with Nabis Fm (Miller, 2008b), but they may not be the same age as Nabis Fm in IPz. The latter must be substantially older than 760 ± 1 Ma (Halverson et al., 2005), the age of a tuff in the upper Devede Fm (Fig. 5), whereas a tuff in Austerlitz Fm on Austerlitz farm in Northern (Outjo) zone (Figs. 5 & 15) is 757 ± 5 Ma (Nascimento et al. 2016), implying that Austerlitz Fm is more nearly coeval with Devede Fm than with Nabis Fm (Fig. 6B & D).

Nabis Fm has long been viewed as a syn-rift assemblage related to early development of the southern and/or western margins of Congo craton. In Tr7 and 10, paleocurrent directions from crossbedding indicate southward transport for Nabis Fm (Fig. 146A). This direction is opposite to N-directed syn-rift clastics within lower Otavi Group (Fig. 146B), which are associated with uplift of Makalani and Huab dipslopes (Fig. 5). If Nabis Fm is rift-related, Makalani and Huab faults were not yet active at that time. Nabis Fm is possibly related to rifting of the western margin of Congo craton (Merdith et al., 2019).

3.2. Late Tonian in Otavi/Swakop Group

Pre-Sturtian Otavi/Swakop Group includes two spatially separate successions. Carbonate-dominated formations in each are distinctly different in age, despite shared lithofacies and stacking patterns. Ombombo Subgroup (Hoffmann and Prave, 1996; Hoffman and Halverson, 2008) is limited to IPz and the carbonate-dominated Devede Fm is mostly older than 760 ± 1 Ma (Fig. 123) (Halverson et al., 2005). Ugab Subgroup is limited to NDz and is younger than 747 ± 2 Ma (Hoffman et al., 1996). We start with the older succession.

3.2.1. Ombombo Subgroup

Representative columnar sections with carbonate $\delta^{13}\text{C}$ and $\delta^{18}\text{O}$ records are shown in Fig. 147. The subgroup is divided into 3 formations (Fig. 6D) (Hoffman and Halverson, 2008)—tectonized Beesvlakte Fm, carbonate-rich Devede Fm and clastic-rich Okakuyu Fm, in ascending order (Fig. 98A).

Beesvlakte Fm (Ob) has a lower argillite member, a middle member composed of peritidal dolomite cycles with supratidal tops, and an upper marly tectonite member (Fig. 147). Stretching lineation in the marble tectonite and long axes of reduction spots in strongly cleaved lower argillite are oriented approximately W/E, indicating a high degree of strain partitioning in the overall obliquely-convergent Kaoko orogen (Goscombe and Gray, 2008; Konopásek et al., 2005). The resistant middle member is intricately folded and imbricated (Fig. 98B), in response to *décollement* folding of overlying strata. Serious investigation of the mineralized Beesvlakte Fm would require 1:10 K-scale structural-stratigraphic mapping, which we did not attempt.

The 0.3–0.5-km-thick Devede Fm (Od) does not change much over the area of Tr7–10 (Fig. 147). It presents a stack of meter- and decameter-scale shoaling-upward peritidal dolomite cycles, with supratidal tops being most prevalent in the lower part of the formation. In some areas, upper Devede Fm contains decameter-thick biostromes of pale pinkish-coloured *Tungussia*-type stromatolite, forming cycles that are thicker than in non-stromatolitic parts of the formation. An incursion of cannibalized clastics spanning ten or more cycles occurs ~100 m above the base of the formation. Clastics form the TSTs of mixed cycles and dolomite the HSTs. The clastics coarsen southward, from siltstone to cobble conglomerate, consistent with N-directed paleocurrents derived from crossbedding (Fig. 146B). Lower Devede Fm clastics provide the oldest evidence for uplift and erosion of Makalani dip-slope.

Okakuyu Fm (Ok) records a major resumption of crustal stretching within the platform zone. Horizontal-axis rotations of crustal blocks created depocenters into which stacked fan-deltas were constructed of

debris eroded from uplifted dip slopes of Devede, Beesvlakte and Nabis formations, and locally basement rocks. The fan-deltas are upward-coarsening sandstone bodies culminating in cobble conglomerate. Makalani dip slope may have provided some of the debris, but cobble conglomerate up to 60 m thick (Fig. 147) in 11–2 and 8 indicates that unrecognized growth faults also existed within IPz. The youngest conglomerate in 8–8 contains rounded clasts of amygdaloidal dacite and rhyolite, lithologically resembling the 747-Ma Upper Naauwoort Fm in Tr4 (Fig. 41).

Okakuyu Fm is variably truncated by erosion beneath glacigenic Chuos Fm (Fig. 147). It was totally removed from the Sturtian paleovalley at Omutirapo springs (Fig. 105) and from a broader paleovalley in Tr10 whose margins have yet to be identified (Figs. 99 & 135A). In two of the thicker sections (8–10 and 11–8), Okakuyu Fm ends with a shoal-water dolomite unit in which mounds of columnar stromatolite are flanked by ooid grainstone with 5-mm-diameter ooids (Fig. 142D). Giant ooids preceded Sturtian glaciation also in California (Trower, 2020).

C- and O-isotope records from Devede Fm are broadly consistent between sections (Fig. 148). $\delta^{13}\text{C}$ gradually rises stratigraphically upward from +5‰ to +8‰ (VPDB), while $\delta^{18}\text{O}$ gradually rises from -5‰ to -2‰. The $\delta^{13}\text{C}$ peak in upper Devede Fm defines CIE Tn-2 (Fig. 10D), which is succeeded by lighter values, averaging 2.43‰ ($n = 5$), at the top of Okakuyu Fm (11–8, Fig. 147).

As observed in many ancient carbonate records, there is weak covariance between C- and O-isotope values (Fig. 149A). This is consistent with the expected inverse correlation between temperature-dependent respiration and fractional organic burial (Stanley, 2010; Finnegan et al., 2012). When temperature is lower and $\delta^{18}\text{O}$ consequently higher, respiration is less efficient and fractional organic burial is greater, resulting in more positive $\delta^{13}\text{C}$. The observed isotopic trends (Fig. 148) are therefore qualitatively consistent with a cooling trend over time. However, pelagic carbonate $\delta^{18}\text{O}$ varied by less than 2‰ in the late Pleistocene, when the additive effects of glacial-interglacial changes in seawater temperature and ice-sheet volume amplified isotopic variability. To account for a $\delta^{18}\text{O}_{\text{carb}}$ rise of 3‰ without ice sheets would require seawater to cool by between 9.5° and 13°C within the -2° to 25°C temperature range (Friedman and O'Neil, 1977). It seems unlikely that such a severe cooling could occur without ice-sheet development at high latitudes, for which evidence is lacking prior to Sturtian glaciation (Macdonald et al., 2010b).

The average $\delta^{13}\text{C}$ value of +5.1‰ (VPDB) for Ombombo Subgroup (Fig. 147) is consistent with coeval carbonate platforms globally (Fig. 1A), Akademikerbreen Supergroup in NE Svalbard and Tambien Group in N Ethiopia for example (Halverson et al., 2018b; Park et al., 2020). Such persistently enriched values present problems for isotopic mass balance. Assuming equilibrium fractionation and a C input composition of -5 ± 1‰ (Howell et al., 2020), an exorbitant fractional organic burial flux, $f_{\text{org}} \approx 0.4$ or twice modern, is required to maintain a steady state (Summons and Hayes, 1992). According to the reaction $\text{CO}_2 + \text{H}_2\text{O} \rightarrow \text{CH}_2\text{O} \downarrow + \text{O}_2 \uparrow$, however, the O_2 continuously generated by such a large f_{org} should have acted as a negative feedback limiting organic burial. One escape from this dilemma involves the formation and burial of authigenic carbonate, which inherited isotopically light C from organic matter that was respiration anaerobically within the sediment (Sun and Turchyn, 2014; Schrag et al., 2013). Burial of authigenic carbonate therefore complements organic burial in the isotopic mass balance, but without generating O_2 . Another way to bury 5‰ carbonate C while maintaining $f_{\text{org}} \approx 0.2$ is to raise the net $\delta^{13}\text{C}$ of the C sources to the ocean-atmosphere system. One means to accomplish this is to raise the carbonate weathering flux as a fraction of total C weathering (Kump and Arthur, 1999). We defer further discussion until we gain additional insight on the problem from Cryogenian and early Ediacaran parts of Otavi/Swakop Group.

The median $\delta^{18}\text{O}$ value for the Devede Fm (Fig. 150) of around -1.8‰ (VPDB) lies above the envelope of values for geon-7 (700–799 Ma) dolomites globally (Shields and Veizer, 2002). This could

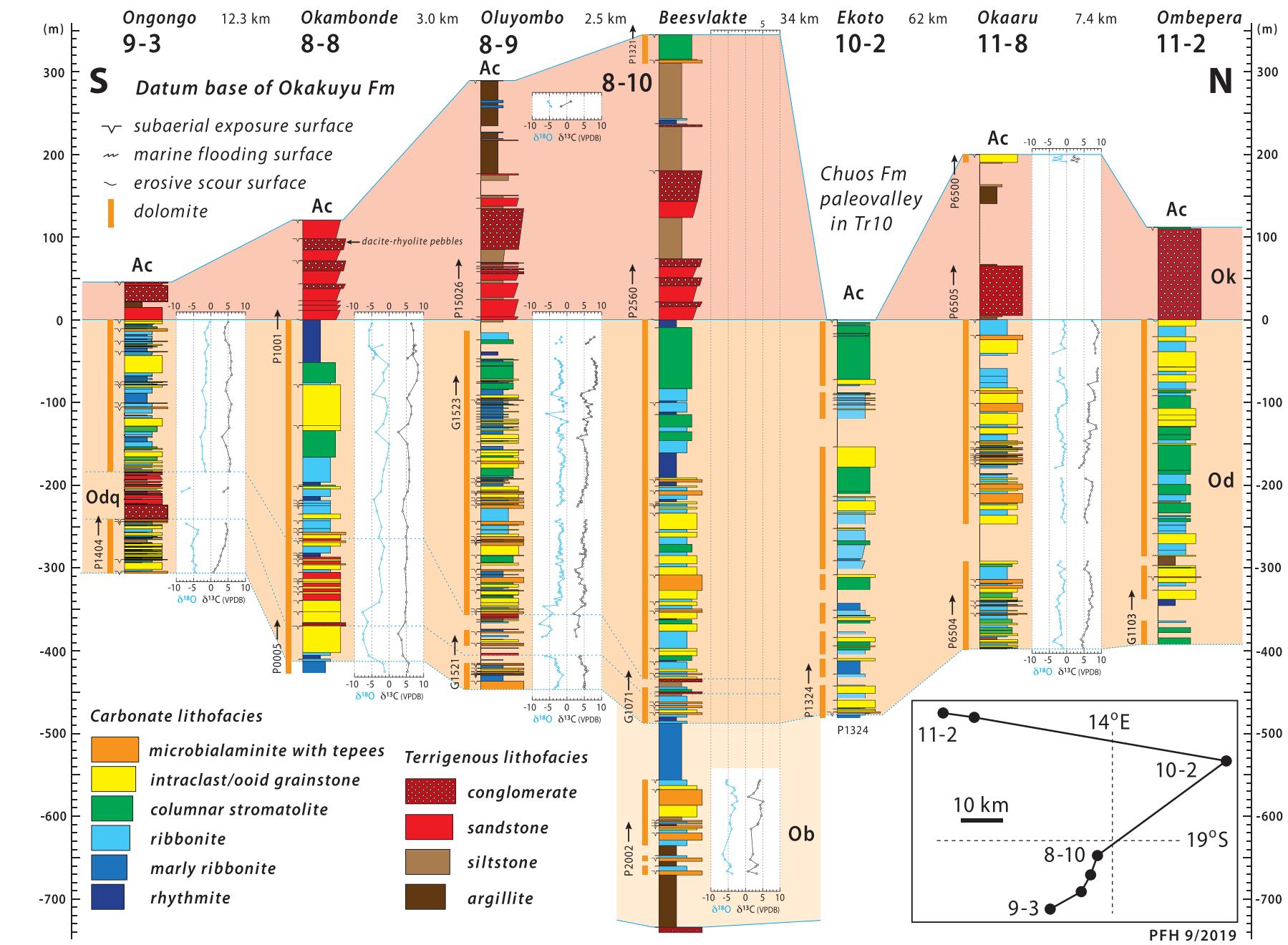


Fig. 147. Selected Ombombo Subgroup columnar sections with carbonate $\delta^{18}\text{O}$ and $\delta^{13}\text{C}$ records from IPz Tr8–11. Map of section locations shown inset lower right. Formations: Ob, Beesvlakte Fm; Od, Devede Fm; Odq, clastic tongue in lower Devede Fm; Ok, Okakuyu Fm; Ac, Chaos Fm. Datum is base of Okakuyu Fm.

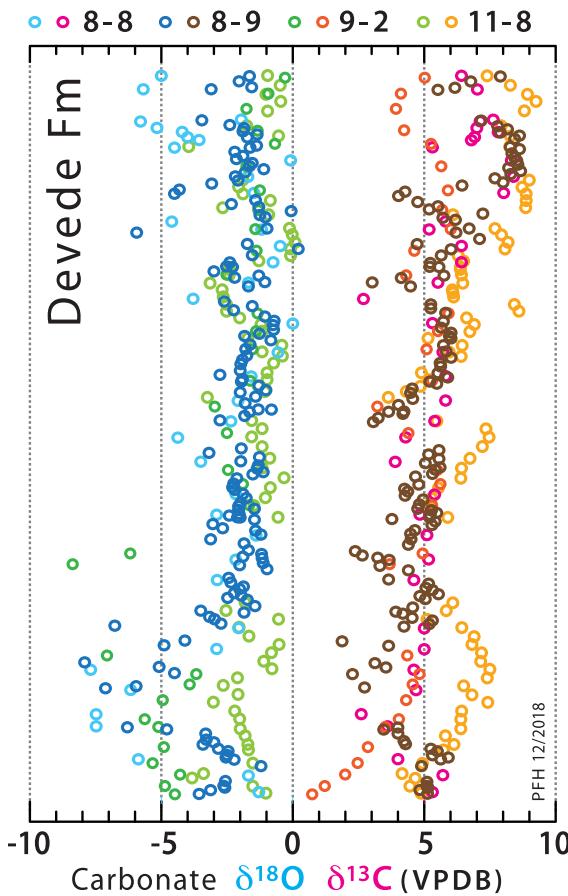


Fig. 148. Carbonate $\delta^{18}\text{O}$ and $\delta^{13}\text{C}$ records from Devede Fm, normalized to a common thickness and colour-coded by section (top row). See Fig. 149A for $\delta^{13}\text{C}/\delta^{18}\text{O}$ cross-plot.

reflect net evaporation in a semi-restricted subtropical marine setting (Hood et al., 2015). However, one might expect that such environments would be well represented in the global dolomite data-base (Shields and Veizer, 2002). Moreover, the Devede $\delta^{18}\text{O}$ values are not statistically distinct from those obtained from magnetite veins ($-1.33 \pm 0.98\text{‰}$ SMOW) precipitated from seawater-derived fluids in a black-smoker paleoenvironment of the 760-Ma Bou Azzer ophiolite in southern Morocco (Fig. 150) (Hodel et al., 2018).

3.2.2. Austerlitz Fm, Naauwpoort volcanic suites and Ugab Subgroup

Late Tonian Ugab Subgroup (Fig. 6B) (SACS (South African Committee for Stratigraphy), 1980) and associated Austerlitz and Naauwpoort formations (Hedberg, 1979) occur in transects Tr1 (Figs. 14 & 27), Tr2 (Fig. 30), Tr3 (Fig. 39) and Tr4 (Fig. 41). Regional mapping indicates that they are limited to the southern FSz and Bz (Frets, 1969; Guj, 1974; Hedberg, 1979; Miller, 1980; Clifford, 2008). Spatially, they are far removed from Nabis Fm and Ombombo Subgroup in IPz.

Austerlitz Fm (Ua) (Hedberg, 1979) unconformably overlies Orosirian basement orthogneiss and consists of locally derived oligomictic conglomerate, pebbly sandstone and laminated siltstone with calcareous bands. It is disconformably overlain by Berg Aukas Fm in western Tr1 (Fig. 27) and by glaciogenic Chuos Fm in eastern Tr1 (Fig. 22). It is overlain by Upper Naauwpoort Fm volcanics in Tr4 (Fig. 41) and around the southwestern plunge of Welwitschia inlier (Fig. 8A) (Frets, 1969). In NDz, it occurs in Austerlitz anticlinorium (Frets, 1969), south of eastern Tr1 (Fig. 15). The same unit was named “Kranzpoort Fm” by Guj (1974), following Clifford (1967), who introduced the name in a table of formations. It was not retained in his map of Neoproterozoic rocks between Tr3 and the town of Outjo (Fig. 4) (Clifford, 2008).

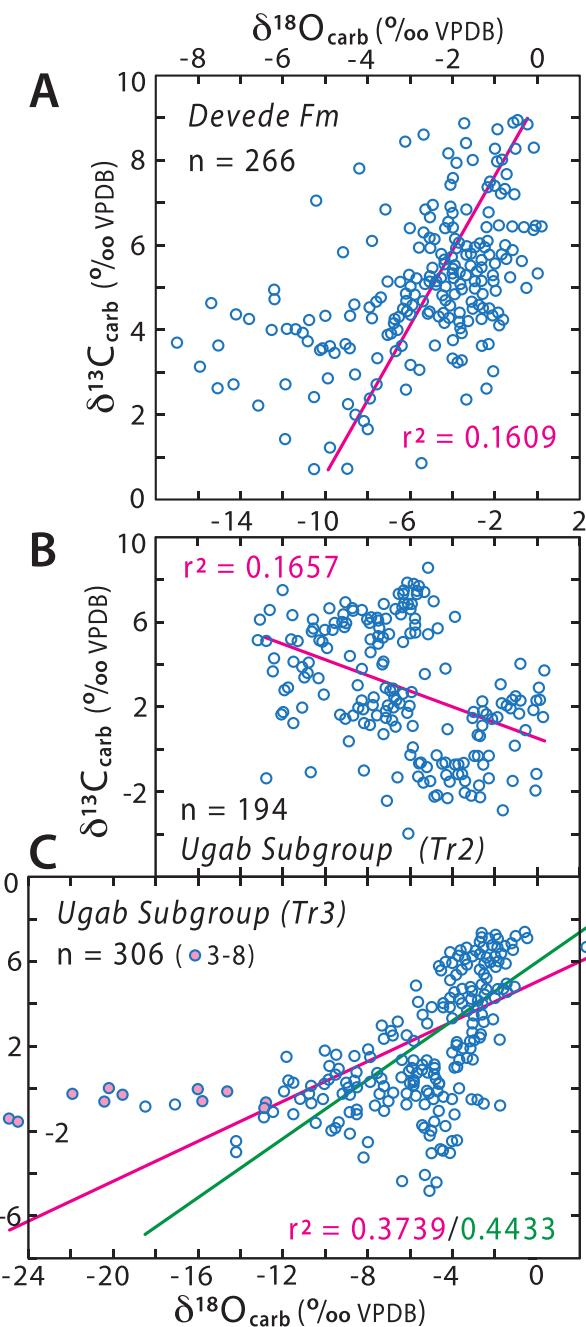


Fig. 149. Late Tonian carbonate $\delta^{13}\text{C}/\delta^{18}\text{O}$ cross-plots. (A) Total Devede Fm ($n = 266$) in IPz. (B) Ugab Subgroup from Tr2 (Vrede domes) in NDz ($n = 194$). (C) Ugab Subgroup from Tr3 (Summas dome) in NDz ($n = 306$). Correlation coefficients (r^2) given with (magenta) and without (green) data from section 3-8 (pink dots), which have anomalously light $\delta^{18}\text{O}$ possibly related to silicate-carbonate exchange. Note positive correlations in A and C, but negative correlation in B.

Historically, Austerlitz Fm has generally been included in Nosib Group (e.g., Guj, 1974; Hedberg, 1979; Miller and Grote, 1988; Schreiber, 2006; Miller, 2008b; Nascimento et al., 2016, 2017). In fact, all basement-onlapping and derived coarse-grained clastic units have tended to be identified with Nosib Group. The danger of this practice is most apparent in Tr7 (Fig. 88), where Cryogenian Gruis Fm would also be labelled Nosib Group according to the above criteria. In this case, Nosib Group would then both underlie and overlie Rasthof Fm in the same transect (Fig. 88), which is contradictory.

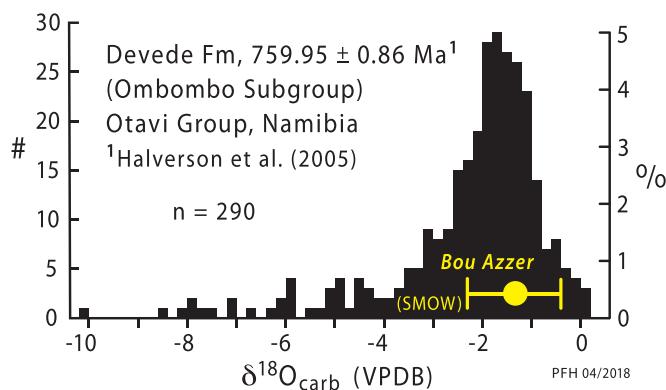


Fig. 150. Frequency histogram of $\delta^{18}\text{O}$ values for total Ombombo Subgroup ($n = 290$) in IPz (Fig. 147), compared with composition of coeval ocean deep-water estimated from pure magnetite veins in fossil black-smoker hydrothermal system associated with 760-Ma Bou Azzer ophiolite (Anti-Atlas, Morocco) (Hodel et al., 2018). Compare with Ugab Subgroup $\delta^{18}\text{O}$ histogram (Fig. 158B).

Miller (1974, 1980, 2008b) distinguished Lower and Upper Naauwpoort Fm volcanic assemblages in Tr3 and 4, respectively (Fig. 36). Lower Naauwpoort Fm (Nvl) includes ≥ 6.6 km of rhyolite ash-flow tuff and derived sediments with no base exposed (Miller, 1980), preserved in an 18-km-long elliptical structure that has been tectonically shortened to 10 km in a S–N direction (Miller, 1980, 2008b). Upper Naauwpoort Fm (Nvu) consists of ≤ 1.4 km of trachydacite and subordinate rhyolite lavas (Fig. 41) (Miller, 1980, 2008b). Nvl rhyolites occupy the ‘within-plate-granite’ field of a Nb/Y discrimination diagram (Miller, 1980), and the peralkaline (K-rich) character of Nvl and Nvu is consistent with continental rifting (Miller, 2008b). A swarm of dacite feeder dykes in Tr4 basement trend ENE to NNE.

ID-TIMS U–Pb zircon ages from the upper parts of Lower and Upper Naauwpoort Fm are indistinguishable at 746 ± 2 and 747 ± 2 Ma, respectively (Hoffman et al., 1996). The enormous thickness and extent ($> 150 \text{ km}^2$) of welded tuff in Tr3 is suggestive of a major cauldron-subsidence structure (Miller, 1980; Clough et al., 1909; Smith and Bailey, 1968). Upper Naauwpoort Fm in Tr4 could represent volcanic outflow. Miller (1980, Fig. 4.10) postulated that the outflow lavas were coeval with only the youngest intra-cauldron volcanics. Thus the U–Pb geochronology (Hoffman et al., 1996) does not contradict his model, pending determination of the duration of Lower Naauwpoort Fm volcanism.

In Tr4, outflow volcanics of Upper Naauwpoort Fm are disconformably overlain by Sturtian Chuos Fm diamictite (Fig. 41), but in Tr3 the two are separated by ≤ 0.7 km of mixed shallow-marine dolomite and siliciclastic rocks of Ugab Subgroup (Fig. 39). Miller (1974, 1980, 2008b) divided this succession into older dolomite-rich Okotjize Fm (Ut) (originally “Okatjise”) and younger siliciclastic-rich Orusewa Fm (Us) (Fig. 6B). Remarkably, this division appears to hold up in every section 3–5–15, despite a five-fold lateral variation in their aggregate thickness (Fig. 39). This implies that the thickness variations reflect subsidence rates, not variable completeness.

3.2.3. Composite chemostratigraphy of Ugab Subgroup

C-isotope profiles (Fig. 152) support the Okotjize–Orusewa division of Ugab Subgroup in Tr3 (Lamothe et al., 2019). $\delta^{13}\text{C}$ rises stratigraphically upward in Okotjize Fm from $\leq -1\text{\textperthousand}$ to $\geq +6\text{\textperthousand}$ (VPDB), before falling back toward 0\textperthousand in Orusewa Fm (Fig. 153B). A pair of negative anomalies ($\delta^{13}\text{C} \leq 0\text{\textperthousand}$) near the base of Okotjize Fm (Fig. 152) defines CIE Tn–3 (Fig. 10D), which is tentatively correlated (Lamothe et al., 2019) with Russøya (formerly Islay) CIE (Fig. 1A) (Halverson et al., 2018b). In Coates Lake and upper Fifteenmile groups in NW Canada, Russøya CIE is constrained between Re–Os isochron ages of 739.9 ± 6.5 and 732.2 ± 4.7 Ma, including decay-constant uncertainty (Rooney

et al., 2014, 2015; Strauss et al., 2014, 2015). The Lower Naauwpoort Fm age of 746 ± 2 Ma (Hoffman et al., 1996) from beneath Okotjize Fm (Fig. 36) is compatible with these constraints (Lamothe et al., 2019).

Rapid facies changes in Ugab Subgroup within Tr2 and 3 (Figs. 30, 39 & 152) make it unlikely that Okotjize and Orusewa formations could be correlated lithologically between transects 120 km apart (Fig. 8B). However, we obtained C isotope data from sections 2–1 and 6 (Fig. 153A) for comparison with the data from Tr3. The Tr2 data exhibit an overall $\delta^{13}\text{C}$ decline of $-8.5\text{\textperthousand}$ with stratigraphic height, which is more consistent with Orusewa than Okotjize Fm in Tr3 (Fig. 153B). The combined profiles satisfy a correlation in which time-equivalents of both formations occur in each transect, but Tr2 is mainly younger than Tr3, with ~ 200 m of stratigraphic overlap (Fig. 153B). In this correlation, the Tr2 record extends nearer in time to Sturtian onset and it is therefore reasonable to suggest (Lamothe et al., 2019) that the $\delta^{13}\text{C}$ nadir (CIE Tn–1, Fig. 10D) near the top of the profile (Fig. 153B) represents Garvellach (formerly Islay) CIE (Fig. 1A) (Fairchild et al., 2018), which is inferred as being continuous with glacial onset (Ali et al., 2018). If the Tr2 and 3 correlation (Fig. 153B) is valid, Ugab Subgroup would be the first place where Russøya (Tn–3) and Garvellach (Tn–1) CIEs were recognized in the same succession (Lamothe et al., 2019).

We do not favour an alternative relationship in which CIEs Tn–1 and –3 (Fig. 153B) are correlated, implying that Tonian strata in Tr2 are mostly older, not younger, than those in Tr3. This would significantly reduce stratigraphic overlap between Tr2 and 3. More importantly, it would correlate the youngest Tonian strata in Tr2 with Russøya CIE (Fig. 1A), which is ~ 20 Myr older than Sturtian glacial onset (Rooney et al., 2014, 2015; Macdonald et al., 2018). This would make the small stratigraphic relief (≤ 65 m) on the sub-Chuos Fm disconformity in Tr2 (Figs. 30 & 153A) implausibly fortuitous in an area where sedimentary facies (Fig. 30) imply active tectonics. If instead the CIEs were both correlated with Garvellach CIE (Fig. 1A), then 0.7 km of non-glacial Ugab Subgroup above the CIE in Tr3 would conflict with an unbroken Garvellach CIE–Sturtian glacial transition in the CIE’s type area (Ali et al., 2018).

Crossplots of $\delta^{13}\text{C}$ and $\delta^{18}\text{O}$ for Ugab Subgroup dolomite are plotted in Fig. 149. A surprising negative correlation in Tr2 (Fig. 149B) contrasts with more normal positive correlations in Tr3 (Fig. 149C) and Devede Fm (Fig. 149A). Negative correlation arises because $\delta^{18}\text{O}$ values decrease stratigraphically downward while $\delta^{13}\text{C}$ values rise in the same direction (Fig. 153A). Anomalous $\delta^{18}\text{O}$ does not appear to be related to the marble tectonite in the core of Vrede south dome (Fig. 29) because values in the lowest 40 m of 2–1, nearest the tectonite, are less depleted than those 40–180 m above the tectonite (Fig. 153A). Rather, persistent extreme $\delta^{18}\text{O}$ depletion appears to correlate with topographic elevation, or proximity to the horizontal Cretaceous paleosurface beneath Eten-deka Group aeolianite and flood basalt (Fig. 8A). We suspect, therefore, that $\delta^{18}\text{O}$ depletion in Tr2 is related to high-temperature groundwater circulation related to flood basalt emplacement. In Tr3, extreme $\delta^{18}\text{O}$ depletion occurs mainly in one section, 3–8 (Fig. 152), and the positive $\delta^{13}\text{C}/\delta^{18}\text{O}$ correlation coefficient is higher when data from this section are removed (Fig. 149C).

3.3. Cryogenian in Otavi/Swakop Group

The Cryogenian is divisible into three epochs (Table 1): (1) a 56-Myr Sturtian glaciation (717 to 661 Ma) represented by Chuos Fm; (2) a 10–20-Myr non-glacial middle Cryogenian (661–646 ± 5 Ma) represented by different formations in Otavi and Swakop groups (Table 5, Fig. 6B–D); and (3) a 6–16-Myr Marinoan glaciation (651–641 to 635 Ma) represented by Ghaub Fm.

The post-Sturtian Rasthof Fm (Otavi Group) is succeeded by Gruis and Omibaatjie formations (Fig. 6D). The latter are separated by a rift-to-shelf transition in Otavi Group. Assuming an average sediment accumulation rate of 65 m Myr^{-1} for Omibaatjie Fm (≤ 350 m), derived from a post-rift thermal subsidence model (Halverson et al., 2002), yields a rift-

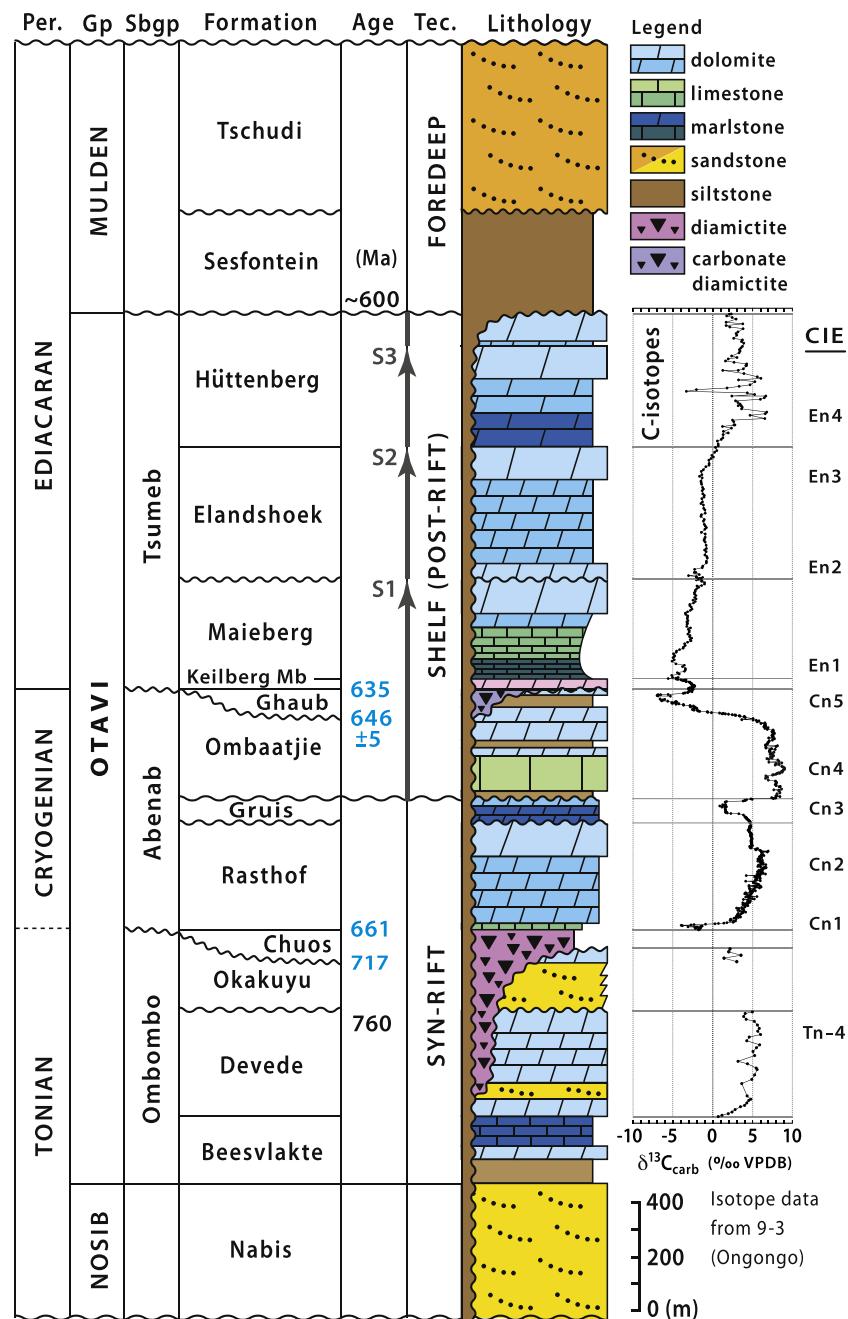


Fig. 151. Stratigraphic synthesis of Damara Supergroup in IPz. Abbreviations: Per., Periods; Gp, Group; Sbgr, Subgroup; Tec., tectonic basin type; CIE, carbon isotope excursion. S1–3 are postulated post-rift depositional sequences (see text). Radiometric ages in black from Otavi/Swakop Group and in blue from other areas.

to-shelf transition age ~ 5.4 Myr (350/65) before Marinoan onset.

The correlative post-Sturtian Berg Aukas Fm (Swakop Group) is succeeded by Okonguari, Narachaams and Franni-aus formations (Fig. 6B & C). Swakop Group experienced rift-related block rotation as young as late Cryogenian (Hoffman et al., 2018).

3.3.1. Sturtian Chuos Fm

The stratigraphic limits of Chuos Fm are unambiguous and sharply defined in most sections. This mirrors observations in other parts of Damara orogen (e.g., Central zone, Henry et al., 1986). Its base is an erosional unconformity above basement rocks, or disconformities above Ugab and Ombombo subgroups (Figs. 31D, 108A, 124B & 126C). In Toekoms subbasin of Tr1 (Fig. 22), the oldest diamictite body (base of Unit 2) sharply overlies conglomerate and associated arenite (Unit 1)

tentatively interpreted as pre-Sturtian (McGee et al., 2012; Hoffman et al., 2017b). However, lithologically similar conglomerate occurs within Chuos Fm (Units 2 and 3), so a synglacial age for Unit 1 cannot be ruled out. Arenite in Unit 1 appears to be fluvial in origin, whereas those in Units 2–4 were deposited in standing water. However, the change in facies could reflect rift-basin subsidence and deepening beneath a Sturtian ice sheet, subsequent to glacial onset. We could not confirm that Unit 1 conglomerate is intruded by pegmatite as earlier reported (McGee et al., 2012). We are inclined toward a pre-Sturtian age for Unit 1, but cannot demonstrate it. Elsewhere in Tr1, Chuos Fm overlies basement unconformably (Fig. 14).

The top of Chuos Fm is a knife-sharp contact with carbonate rhythmite of Berg Aukas (Figs. 31C & 47A), Okonguari (Fig. 25E & F) or Rasthof Fm (Figs. 110C-D, 124D & 126C). The contact with Rasthof Fm

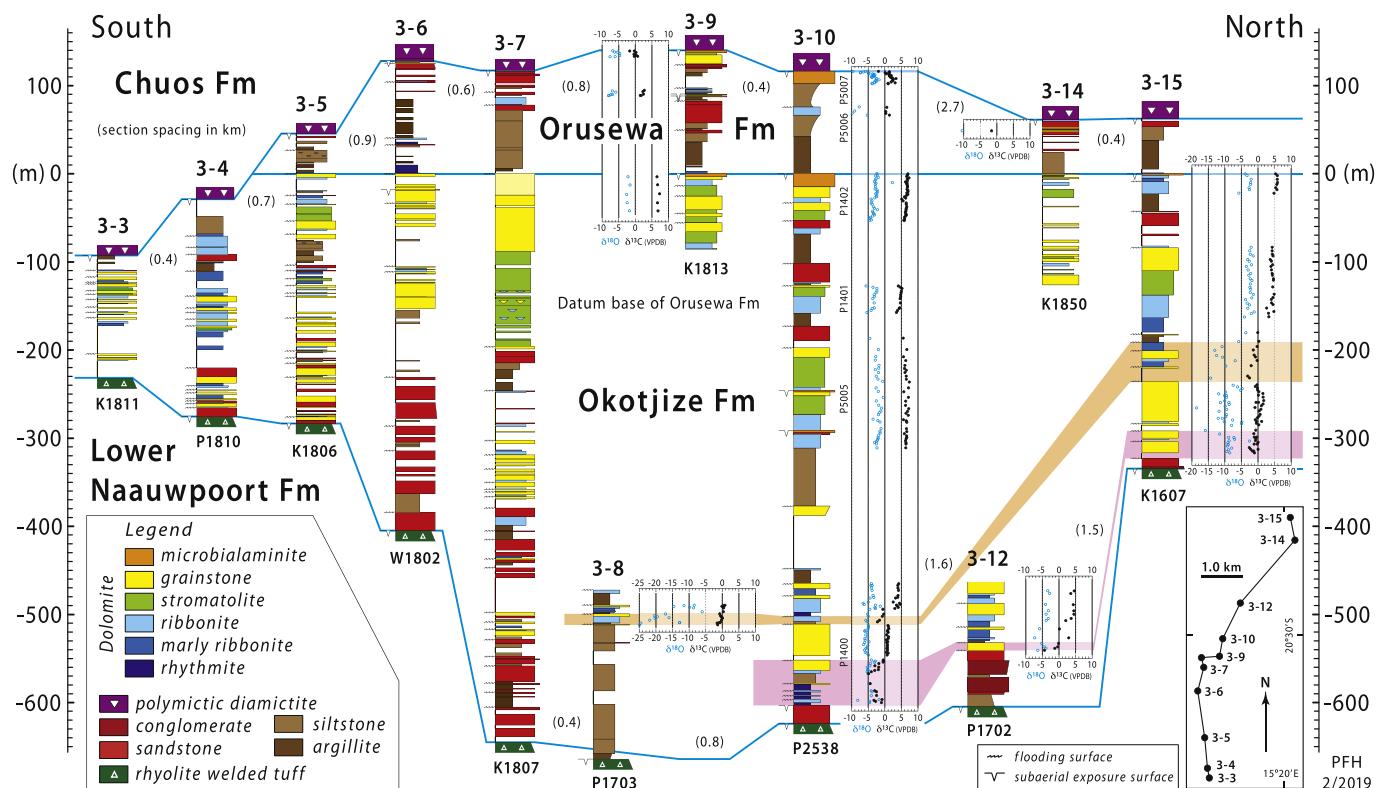


Fig. 152. Selected Ugab Subgroup columnar sections with carbonate $\delta^{18}\text{O}$ and $\delta^{13}\text{C}$ records from in Tr3 (Summas dome, see Fig. 37 for section locations). Double-pronged CIE Tn-3 (Lamothe et al., 2019), tentatively correlated with global Russøya CIE (Halverson et al., 2018b; MacLennan et al., 2018), is indicated by pink and orange bars. See Fig. 153 for proposed correlation with Ugab Subgroup in Tr2 (Vrede domes).

is complicated in 6–4 (P2509, Fig. 71) by synsedimentary slumping (Fig. 74C).

Chuos Fm occurs in all but one (Tr7) transect. Its thickness was measured in 110 complete sections and ranges from 0.3 to 1660 m (Fig. 154). A large difference between its median (76.0 m) and average (227.0 m) thickness indicates a skewed distribution toward thinner values. It is regionally thin, but locally thick (Hoffman et al., 2017b). Median and average accumulation rates (Table 6), averaged over the 56-Myr Sturtian epoch, are 1.36 and 4.05 m Myr⁻¹ (0.0014 and 0.0041 mm yr⁻¹). These rates are an order of magnitude slower than Holocene rates (range 0.02 to 0.04 mm yr⁻¹) under Larsen B (Antarctic Peninsula) ice shelf at sites far from the ice grounding line and with low biogenic input (Domack et al., 2005; Rebasco et al., 2014; Domack and Powell, 2018). However, Chuos Fm and Larsen B accumulation rates are comparable if the difference in averaging time is accounted for using the scaling relationship in Partin and Sadler (2016). But whereas the Chuos data include ice contact and ice-proximal deposits—massive diamictite makes up over half of total Chuos Fm (Fig. 155)—the Holocene data cited above exclude such deposits, which normally accumulate at far faster rates. Since Chuos glaciation occurred at much lower paleolatitude than Larsen B ice shelf (67°S), the logical reason for its low average accumulation rate is a weak hydrologic cycle in the cold dry atmosphere of a snowball Earth (Partin and Sadler, 2016; Pierrehumbert, 2005; Pierrehumbert et al., 2011; Abbot et al., 2013; Hoffman et al., 2017b).

Tectonic quiescence cannot explain the low sedimentation rates because the area was undergoing active crustal stretching and rift-shoulder uplift during the Sturtian epoch. Evidence for active tectonism includes the sub-Chuos/Rasthof unconformity, which bevels the three Tonian successions in their entirety on the Huab and Makalani dipslopes (Fig. 5). This is reflected in the polymictic nature of Chuos diamictites, which are typically composed of debris derived from basement,

Nosib Group and Tonian Otavi subgroups including the Naauwpoort volcanics (Figs. 24E, 31E & F, 38B–F, 42C, 47B, 74B, 109). The Toekoms synglacial half graben (Figs. 22 & 26) presents additional evidence for synglacial rift tectonics, creating what we infer was a subglacial rift-valley lake or fjord.

The regional tectonic setting may be compared with that of the Transantarctic Mountains, a Cenozoic rift-shoulder uplift (Wannamaker et al., 2018; Fielding, 2018) bordering the Ross Sea–Weddell Sea trough. Victoria Land Basin, the central segment of this trough, is underlain by a cratonward-dipping normal fault (Fielding, 2018), structurally analogous to Toekoms basin (Fig. 26) on a larger scale. The Transantarctic Mountains are 45% longer than the southern Congo craton margin, which stretched for 2400 km from NW Namibia to NE Zambia (Goscombe et al., 2020). For roughly half of its 40–55-Myr topographic existence (Goodge, 2020), the Transantarctic Mountains were abraded by the East Antarctic Ice Sheet (Zachos et al., 2001), which flows across the range from an ice divide deep in the interior of East Antarctica (Golledge et al., 2012).

What accounts for local thickenings of Chuos Fm, reflected in the steep tail of high values in the thickness distribution (Fig. 154A)? The tail consists of data from four depocenters in Swakop Group (Figs. 22, 32, 39 & 58), two in Otavi Group (Figs. 105 & 135), plus a single 1004-m-thick outlying section in northern Kunene Region (Steilrandberg, Fig. 4). Five can be classified according to their stratal geometric relation to under- and overlying sequences. The other two lack sufficient stratigraphic data. Three classes of repository can be distinguished (Fig. 156): (1) half grabens and rift valleys, (2) bedrock troughs, U-shaped valleys and fjords, and (3) positive topographic buildups like moraines, drumlins and eskers. Sturtian half grabens (Fig. 156A) occur in Tr1 (Fig. 22) (McGee et al., 2012; Hoffman et al., 2017b) and Tr5 (Fig. 58). Sturtian bedrock troughs (Fig. 156B) occur in Tr8 (Fig. 105) (Hoffman and Halverson, 2008; Le Heron et al., 2013a; Hoffman et al.,

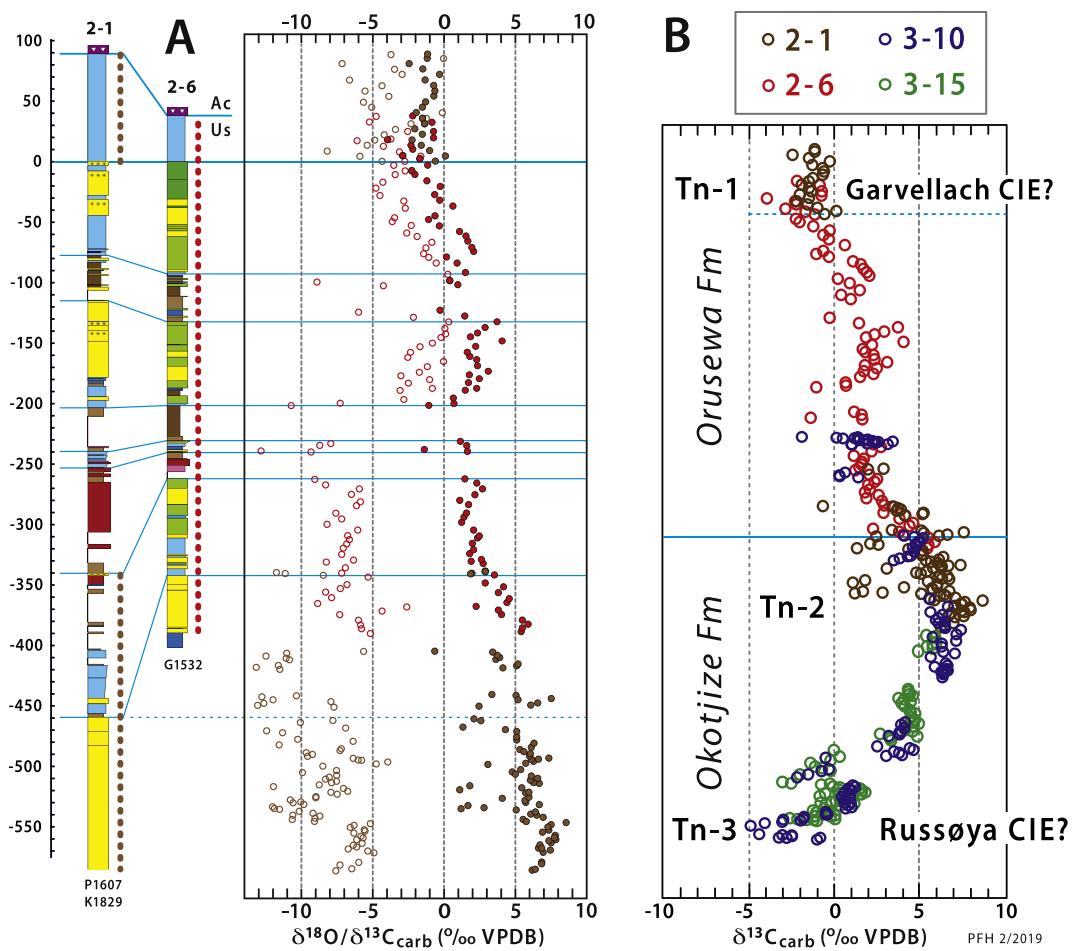


Fig. 153. Ugab Subgroup correlations between Tr2 (Vrede domes) and Tr3 (Summas dome). (A) Selected columnar sections (2-1, 2-6) and carbonate $\delta^{18}\text{O}$ and $\delta^{13}\text{C}$ records from Ugab Subgroup in Tr2 (see Fig. 29 for section locations). Data are colour-coded brown (2-1) or red (2-6). (B) Preferred correlation of $\delta^{13}\text{C}$ records between Tr2 (red and brown) and Tr3 (blue and green). CIE Tn-3 is tentatively correlated (Lamothe et al., 2019) with 739–735-Ma Russøya CIE (Halverson et al., 2018b; MacLennan et al., 2018), consistent with radiometric age constraints from 746-Ma Lower Nauwpoort volcanics (Hoffman et al., 1996) in Tr3 (Figs. 152 & 200). CIE Tn-1 is tentatively correlated (Lamothe et al., 2019) with post-720-Ma Garvellach CIE (Fairchild et al., 2018; MacLennan et al., 2018).

2017b) and probably Tr10 (Fig. 135A), based on the absence of underlying Okakuyu Fm (Fig. 99). Sturtian moraines (Fig. 156C), as positive paleotopographic entities composed of glacial diamictite and associated facies, whether constructional or erosional in origin, occur in Tr2 (Fig. 32) (Hoffman et al., 2016a, 2017b) and Tr3 (Fig. 39), based on evident non-incision of pre-Sturtian underlying strata (Figs. 30 & 39).

Chuos depocenters vary significantly in lithofacies makeup (Fig. 155). Massive diamictite (Figs. 31E, 47B, 74B, 109A & B) makes up 96, 97 and 87% of depocenters in Tr3, 5 and 10 (Fig. 155), but only 24% of Toekoms half graben in Tr1. Sandstone makes up 7% of Omutirapo trough (Tr8) as traction deposits and 13% of Toekoms half graben (Tr1) as turbidites (Fig. 24F), but $\leq 3\%$ of any other depocenter. Conglomerate (Figs. 25A & 108C) is most abundant (13%) by far in Toekoms half graben (excluding unit 1), a depocenter that stands out for its bimodal assemblage of intimately associated fine-grained (44%) and coarse-grained (41%) deposits (Fig. 155). In terms of massive diamictite as a fraction of total thickness, Toekoms half graben is an outlier (Fig. 157). Its dichotomous grain-size distribution (Fig. 24A–F), rarified limestones (Fig. 24C), and progressive Fe-enrichment contributed to the inference that it was a Sturtian subglacial rift-valley lake or fjord (Hoffman et al., 2017b).

A strictly terrestrial (including lacustrine) paleoenvironment for Chuos Fm is compatible with its gross lithofacies makeup. Massive and sheared diamictite (Fig. 109F) resembling ablation and meltout tills makes up 52% of all sections and 74% excluding the subaqueous

Toekoms half graben (Fig. 155). Conversely, only 2.8% consists of stratified diamictite (Figs. 38D, 108D & 124C) that is characteristic of proximal grounding-zone environments (McKay et al., 2009; Fielding et al., 2011; Passchier et al., 2011; Domack and Powell, 2018). Fine-grained subaqueous deposits, typically silt-laminated mudrock (argillite) with IRD (Figs. 24E, 25C, 108E & 124C) or without (Fig. 24C & D), makes up 28% of all sections, but only 15% of sections outside Toekoms half graben (Fig. 155). The bedrock trough in Tr8 contains 22% fine-grained subaqueous facies (Fig. 155), but the degree of lateral heterogeneity revealed by closely spaced sections is striking (Fig. 107). The patchy mix of ice-contact diamictite (Fig. 109F), sorted sandstone and conglomerate (Fig. 108C), and silty argillite bodies with and without IRD (Fig. 108E), suggest an evolving network of subglacial meltwater channels and ponds, as are revealed in the aptly-named Labyrinth (Lewis et al., 2006), due to retreat of Wright Upper Glacier in McMurdo Dry Valleys (Antarctica). Evidence for grounded ice in the Tr8 bedrock trough includes boulder pavements (Fig. 108A & B), striated clasts (Fig. 109C & D) and sheared diamictite (Fig. 109F) (Le Heron et al., 2013a), in addition to the incised trough itself (Fig. 105). Troughs excavated by glacial action are characteristically overdeepened at their equilibrium-line altitudes (Sugden and John, 1976; Anderson et al., 2006; Patton et al., 2016; Magrani et al., 2020), where ice-sliding velocities are fastest. Reverse bed-slopes downstream cause meltwater to pond, creating traps for suspended loads that glacial meltwaters have in abundance (Buechi et al., 2017). Such subglacial sediment traps are

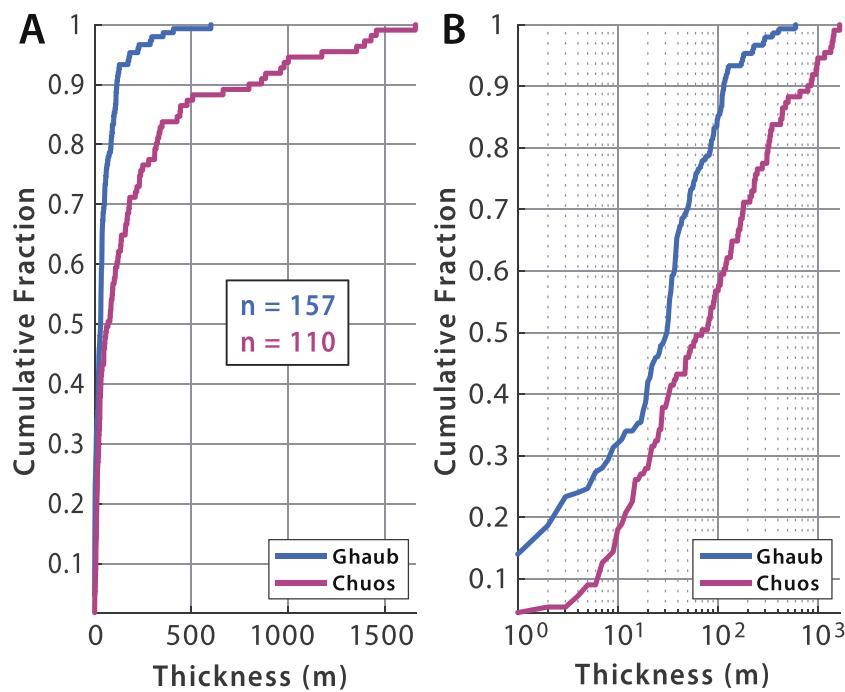


Fig. 154. Cumulative fractions of stratigraphic thickness variation in 110 Sturtian (Chuos Fm, red curves) and 157 Marinoan (Ghaub Fm, blue curves) measured sections, exclusive of incomplete and zero-thickness sections. (A) Linear thickness scale; (B) logarithmic thickness scale. Note nearly exponential thickness distributions in B.

widely distributed under the Antarctic Ice Sheet and most are overlain by 3–4 km of ice (Young et al., 2011; Wright and Siegert, 2012; Morighlem et al., 2020).

A glaciomarine origin for Chuos Fm has been inferred from its association with marine carbonates (Martin, 1964; Kröner and Rankama, 1972) and presence of Fe-rich facies (Hoffman, 2011b; Lechte and Wallace, 2016; Lechte et al., 2018, 2019). Neither argument is unambiguous. During a Snowball Earth, net sea-level falls of order –0.5 km are possible due to sequestering of water in terrestrial ice sheets, despite counteractive effects of glacio-isostatic loading and ice gravity (Liu and Peltier, 2013; Creveling and Mitrovica, 2014). Accordingly, neritic environments (i.e., ≤0.2 km below low tide) during non-glacial times would have been far above sea level during a Sturtian snowball. On the other hand, prolonged tectonic subsidence (Rooney et al., 2015, 2020a), combined with low rates of sediment accumulation (Partin and Sadler, 2016)—4.05 m Myr⁻¹ for the average Chuos Fm thickness of 227.0 m (Table 6)—could have lowered basins below sea level and even below ice grounding-line depths in areas of active subsidence. If Sturtian ice sheets contracted as CO₂ rose (Benn et al., 2015), global-mean sea level would slowly rise. However, the resultant flooding would be regionally counteracted by rising land surfaces and falling sea levels due to reduced ice loading and ice gravity, respectively (Creveling and Mitrovica, 2014).

Mid-ocean ridge hydrothermal activity is a viable source of dissolved Fe(II) in an anoxic subglacial ocean (Martin, 1964; Kirschvink, 1992; Klein and Beukes, 1993), especially since riverine sulfate input would be reduced (Canfield and Raiswell, 1999) as would hydrothermal vent S:Fe, due to lowered hydrostatic pressure (Kump and Seyfried Jr., 2005). This Fe would tend to be deposited at ice grounding lines if meltwater discharges were sources of dissolved O₂ (Hoffman, 2011b; Lechte and Wallace, 2016; Lechte et al., 2018, 2019). Conversely, subglacial meltwater beneath Taylor Glacier (McMurdo Dry Valleys, Antarctica) has 3.45 mM total dissolved Fe, 10⁶x more than modern seawater, and no detectable dissolved O₂ (Mikucki et al., 2009). Such a meltwater flux would constitute a source of dissolved Fe + Mn and a sink for O₂ if it

reached the ocean (Urban et al., 1992). The source of Fe in Taylor Glacier meltwater is presumably subglacial weathering of Ferrar Dolerite (Jurassic), but mafic rocks are less abundant in sub-Chuos Fm bedrock compared with that of Taylor Glacier.

Lechte et al. (2019) attempted to discriminate between these opposing scenarios by comparing Fe-isotope ($\delta^{56}\text{Fe}$) and Ce-anomaly (Ce/Ce*) data from Fe-rich synglacial deposits from ice-contact, ice-proximal and ice-distal settings, sedimentologically determined, in Chuos Fm and Sturtian formations in South Australia and California (USA). Their data indicate most oxygenated conditions in ice-contact facies and least oxygenated in ice-distal facies (Lechte et al., 2019), supporting a marine source of Fe(II) and a meltwater source of O₂.

The same inference was reached by Halverson et al. (2011) from $\delta^{56}\text{Fe}$ and Ce-anomaly data having the opposite facies relationships in a transgressive vertical sequence recording ice-grounding line advance into a salinity-stratified Sturtian marine basin in NW Canada. Here, the most ice-proximal facies were least oxygenated (i.e., higher $\delta^{56}\text{Fe}$ and Ce/Ce*) because water depth increased due to flexural loading by ice as the grounding line advanced basinward (Boulton, 1990). Consequently, the sediment-water interface in front of the advancing ice sheet subsided from more oxygenated meltwater-charged shallow water into deeper anoxic Fe-rich brine (Halverson et al., 2011). These data sets are not necessarily contradictory, but indicate that both spatial (Lechte et al., 2019) and sequential (Halverson et al., 2011) data may be required to properly interpret the sources of Fe and O₂ for any given synglacial iron formation.

Chuos Fm contains thin beds of yellowish-weathering impure dolomitic in Toekoms half graben (Fig. 22), Omurirapo trough (Fig. 107) and elsewhere. A laterally continuous bed of impure calcimicrite (≤ 1.5 m thick and ≥ 1.2 km in strike length) occurs 63 m above the base of Chuos Fm in Tr3 (3–5 to 6). Many such carbonate beds contain intraclasts and are grain-size or compositionally graded (Fig. 110E), suggesting emplacement as turbidity flows. Since carbonate debris (mostly dolomite) is common in Chuos Fm diamictites (Fig. 31E, 108F, 109B & E), it was assumed in the field that the carbonate turbidites are

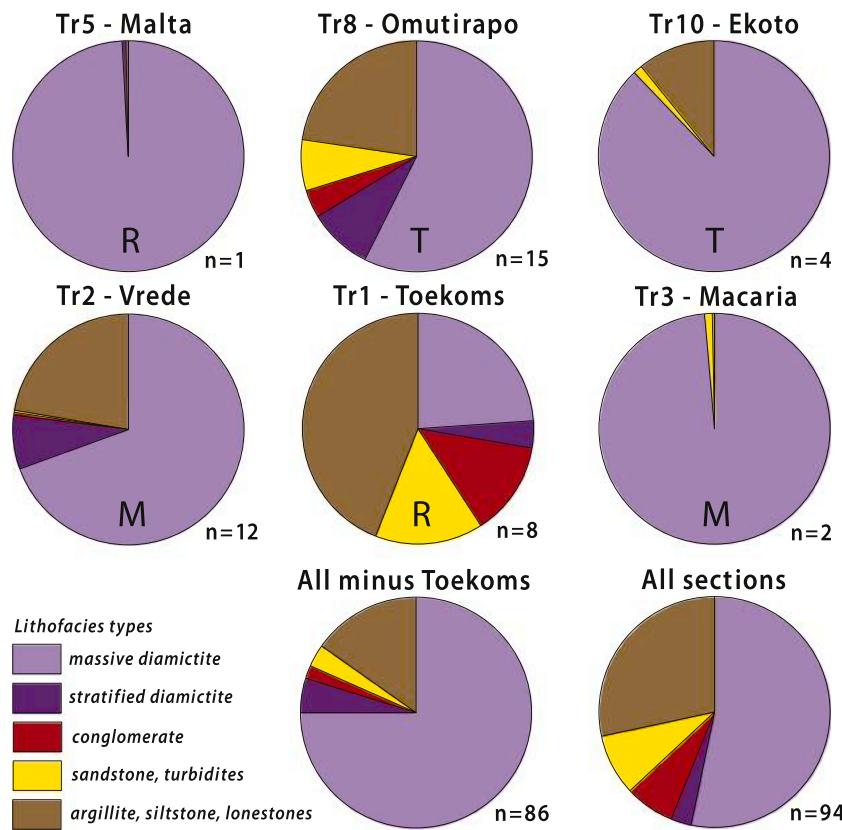


Fig. 155. Pie diagrams showing relative total thickness of different lithofacies types in major depocenters of Chuos Fm (M, morainal buildups; R, rift basins; T, bedrock troughs, Fig. 156). Note relatively large fraction of fine- and coarse-grained sorted facies in Toekoms half graben (Fig. 22), from which conglomeratic unit 1 was excluded on grounds of its putative pre-Sturtian age (McGee et al., 2012). Massive diamictite makes up 52% of all sections and 74% of sections excluding Toekoms half graben.

also of detrital origin. This is not borne out by their stable isotope compositions (Fig. 158).

$\delta^{13}\text{C}$ and $\delta^{18}\text{O}$ data from dolomitic turbidites of Unit 2 (1–31, P1612) and Unit 4 (1–33, P15009) in Toekoms half graben (Fig. 22), and the calcimicrite bed (3–5, K1810, P1811) in Tr3 (Fig. 39), are cross-plotted in Fig. 158A. All samples ($n = 13$) are isotopically light, with $\delta^{13}\text{C}$ ranging between -1.88 and $-9.25\text{\textperthousand}$, and $\delta^{18}\text{O}$ between -7.86 and $-14.69\text{\textperthousand}$ (both VPDB). For comparison, $\delta^{18}\text{O}$ and $\delta^{13}\text{C}$ frequency plots from Ugab Subgroup ($n = 500$), being the most probable pre-Sturtian source of carbonate detritus in Tr1–3, are given in Fig. 158B & C, respectively. Even assuming that the $\delta^{18}\text{O}$ values are altered, the question remains why Chuos Fm carbonate beds are systematically lighter, since their burial and metamorphic histories were not significantly different from Ugab Subgroup.

In a Quaternary-type ice age, seawater $\delta^{18}\text{O}$ becomes heavier because light meteoric water is sequestered into ice sheets. Subglacial meltwater is light for the same reason—it derives from basal ice that accumulated on the most elevated surface areas of an ice sheet and therefore experienced the most Rayleigh distillation during vapour transport. O-isotope dynamics on a snowball Earth have yet to be investigated in 2- or 3-D atmosphere-ice sheet-sea glacier-ocean models, but we expect seawater $\delta^{18}\text{O}$ to become lighter, rather than heavier, because of ice–water equilibrium fractionation. However, this fractionation is only $3.0 \pm 0.1\text{\textperthousand}$ (O’Neil, 1968), so if $1/3$ of the ocean were frozen (as a sea glacier and derived ice sheets), seawater $\delta^{18}\text{O}$ would fall by 1\textperthousand and ice would be 2\textperthousand heavier (than non-glacial seawater) on average. Meteoric ice in total on snowball Earth should be little fractionated relative to the ablative sea-glacier. Sublimation is nearly quantitative (i.e., little or no fractionation) due to slowness of diffusion in ice. Large fractionation ($\leq 15\text{\textperthousand}$) during snow formation in cold air (Uemura et al., 2005) should result in highly distilled (^{18}O -depleted) accumulation in the elevated interiors of large ice sheets. Since basal meltwater is largely derived from such ice, its preferential discharge into the snowball ocean should slowly magnify the isotopic contrast between

the snowball ocean (lower $\delta^{18}\text{O}$) and the global cryosphere (higher $\delta^{18}\text{O}$). However, a snowball Earth may be sufficiently prolonged that seawater $\delta^{18}\text{O}$ is reequilibrated by ambient high- and low-temperature seawater-silicate exchange reactions (Defliese, 2021). In this case, a long-lived positive $\delta^{18}\text{O}$ seawater anomaly is predicted for the snowball aftermath, caused by melting of an ^{18}O -enriched snowball cryosphere (Defliese, 2021).

Returning to the carbonate beds in Chuos Fm (Fig. 158A), their $\delta^{13}\text{C}$ values are even lower relative to Ugab Subgroup than their $\delta^{18}\text{O}$ values (Fig. 158C & B). Most samples are lighter than mantle C ($-5 \pm 1\text{\textperthousand}$, Howell et al., 2020), requiring an anomalous C source in addition to low organic burial. The light C source was presumably organic matter, either eroded from pre-glacial shelf sediments by glaciers or flushed from ambient cryoconite pans through moulin in the sea glacier (Hoffman, 2016; Hoffman et al., 2017a). Anaerobic respiration of such organic matter would supply alkalinity, apparently enabling rare local carbonate production despite secular pH lowering (CO_2 accumulation) and low respiration rates in frigid snowball brine. Alternative sites for snowball carbonate production are meromictic (salt-stratified) ice-covered lakes in coastal dry valleys, where salty bottom waters warm to $\leq 24^\circ\text{C}$ in present Antarctica (Hatherton, 1990).

3.3.2. Rasthof Fm

Rasthof Fm (Hedberg, 1979) is the Sturtian postglacial cap-carbonate sequence (Hoffmann and Prave, 1996; Hoffman et al., 1998a; Hoffman and Halverson, 2008; Pruss et al., 2010). It encompasses the first negative and positive Cryogenian CIEs, Cn1 and Cn2 (Fig. 151). It is broadly correlative with Berg Aukas plus lower Gauss formations in OML (Fig. 111) (Wallace et al., 2014; Hoffman et al., 2018). However, in the absence of chemostratigraphic data, we do not know where to place the top of Gauss Fm relative to Gruis or lower Omboaatjie formations (Fig. 6C & D).

Rasthof Fm is best developed in IPz (Fig. 159A & B), where it reaches 0.45 km in thickness. It begins at a knife-sharp contact above glaciogenic

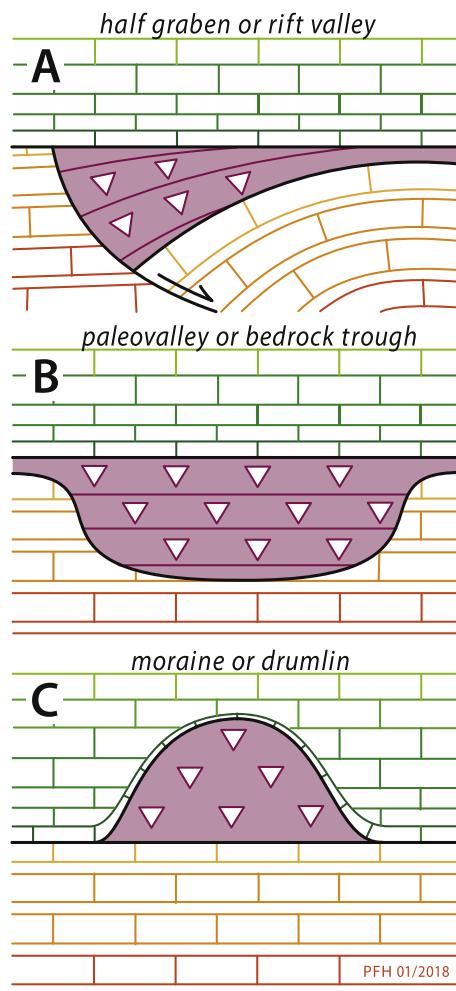


Fig. 156. Types of Chuos Fm depocenters inferred from geometric relation to older and younger strata (Hoffman et al., 2017b). (A) Half graben or rift valley (Figs. 22 & 58): Chuos Fm exhibits onlap and offlap relations to older and younger strata, respectively, and abuts against footwall strata at fault surface. (B) Paleovalley or bedrock trough (distinguished by unidirectional or bidirectional axial paleo-elevation gradients, respectively): Chuos Fm is incised into older strata but conformable with younger ones (Figs. 105, 135A & 147). (C) Moraine or erosional outlier (Figs. 29, 30 & 32): Chuos Fm is paraconformable with older strata but onlapped by younger ones.

diamictite of Chuos Fm (Figs. 25E & F, 31C, 47A, 110C & D, 124D & 126C). The deepest-water facies (Ar1) occur at the base—abiotic rhythmite (Figs. 93A–D, 110B & 126A–F) with turbidites and debrites (Figs. 47C–F & 74D–F). They are succeeded by a sequence of sublittoral microbialites (Ar2), massive to crossbedded grainstone (Ar3), ending with tepee-structured microbialaminite (Fig. 136B) indicating subaerial exposure (Figs. 103, 111, 125, 135, 139 & 159). The absence of either Chuos Fm reworking or a Rasthof Fm TST indicates deep net subsidence accumulation during Sturtian glaciation and rapid syndeglacial marine transgression. Deep net subsidence is consistent with the anomalously thick HST (Ar1–3), lacking meter- or decameter-scale cycles (Figs. 112 & 122). Subsidence was an inferred response to crustal stretching, manifest to Toekoms half graben in Tr1 (Fig. 26).

Diverse sublittoral microbialites of Ar2 are unique to Rasthof Fm in Otavi Group (Hoffman et al., 1998a; Hoffman and Halverson, 2008; Pruss et al., 2010; Le Ber et al., 2013; Wallace et al., 2014). The Ar1–2 boundary corresponds to the establishment of benthic microbial mat and is abruptly gradational over ≤ 1 m (Figs. 110B & 126E–F). It generally coincides with an increase in $\delta^{13}\text{C}$ by 4–5‰ (Figs. 159 &

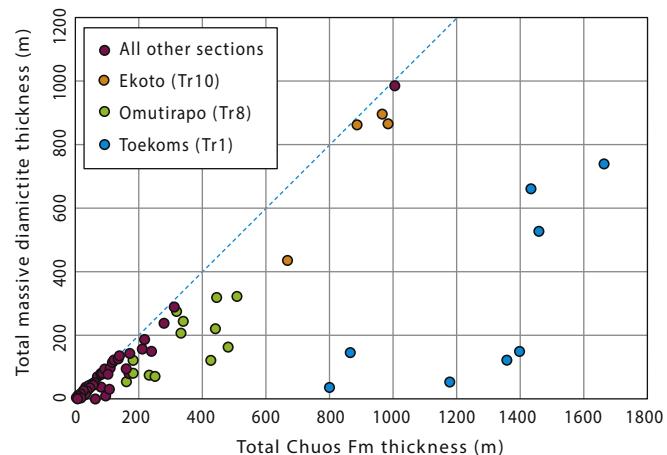


Fig. 157. Thickness of massive diamictite as a function of total Chuos Fm thickness in different transects. Massive diamictite dominates paleovalley in Tr10 (Fig. 135A), but is subordinate and variably abundant in Toekoms half graben (Fig. 22). Thickest massive diamictite section is located at $-17^{\circ}49.80'$ / $13^{\circ}31.46'$ in Steilrandberg, 42.0 km NW of Opuwa.

160A). Ar1 values are less depleted and the boundary increase in $\delta^{13}\text{C}$ less pronounced where Ar1 is dolomite rather than calcite (Fig. 160B). Ar2 microbialites lack evidence of wave action or subaerial exposure, and are not organized into small-scale peritidal cycles (Figs. 112, 122 & 138). They can generally be divided into three units (Fig. 111): (1) lobate stromatolite (Ar2a); (2) roll-up microbialaminite (Ar2b), and (3) cryptic columnar stromatolite (Ar2c) in ascending order. Lobate stromatolite (Figs. 69C, 75A–D, 110A & B, 124E, 126E & F, 142A) is a laterally linked form of stromatolite in which asymmetric swellings (lobes) develop above inclined zones of disrupted laminae and void-filling cement. The cements are characterized by ‘chambered structures’ (Wallace et al., 2014) described also in other Cryogenian and Ediacaran carbonates and inferred to be of microbial origin (Luo et al., 2017). These zones are inclined $\sim 30^{\circ}$ to the paleohorizontal, suggestive of horizontal compression, but the asymmetric lobes have no preferred azimuthal orientation. Cross-sections are self-similar in all orientations. Our tentative interpretation is that they manifest expansive microbial growth in a laterally confined half-space. This is analogous to the process proposed for microbial ‘polygons’ in permanently wet tidal ponds in coastal United Arab Emirates (Lokier et al., 2018).

Roll-up microbialaminite (Ar2b) is the darkest-coloured of the three microbial facies at the outcrop scale (Fig. 122), but it is the most distinctly laminated with an average thickness of 0.6 mm per dark–light couplet. Roll-ups refer to folded flaps, typically 5–10 laminations thick, of detached or semi-detached microbial mat (Figs. 33A, 113A & B). These flaps were coherent but pliable, presumably due to microbial binding. The mats were therefore benthic in origin, not merely accumulations of organic ‘snow’. Since the roll-ups formed on a regionally horizontal surface in the IPz and in the absence of evident current action, we surmise that the flaps were detached through inflation and bursting of gas or fluid pockets, within 0.5 cm of the mat surface. Zones of brecciated (lithified) mat (Fig. 124F) and neptunian dykes (Fig. 127B) containing rounded fragments of mat are not uncommon in this facies. Certain of the dykes have borders of recumbently folded mat (Fig. 127A & B), evidently resulting from successive back flipping of flap after flap, always directed away from the dyke (Pruss et al., 2010). Presumably these dykes served as conduits for fluid or gas expulsion that intermittently burst through any mat grown across their orifices. The breccia zones and lack of compaction-related strain imply rapid lithification. Ar2b sharply overlies Ar2a, with a few centimeters of silty marl between them in section 9–3 (Fig. 122). The top of Ar2b is gradational due to progressive fading of the dark laminae. The cause of the dark

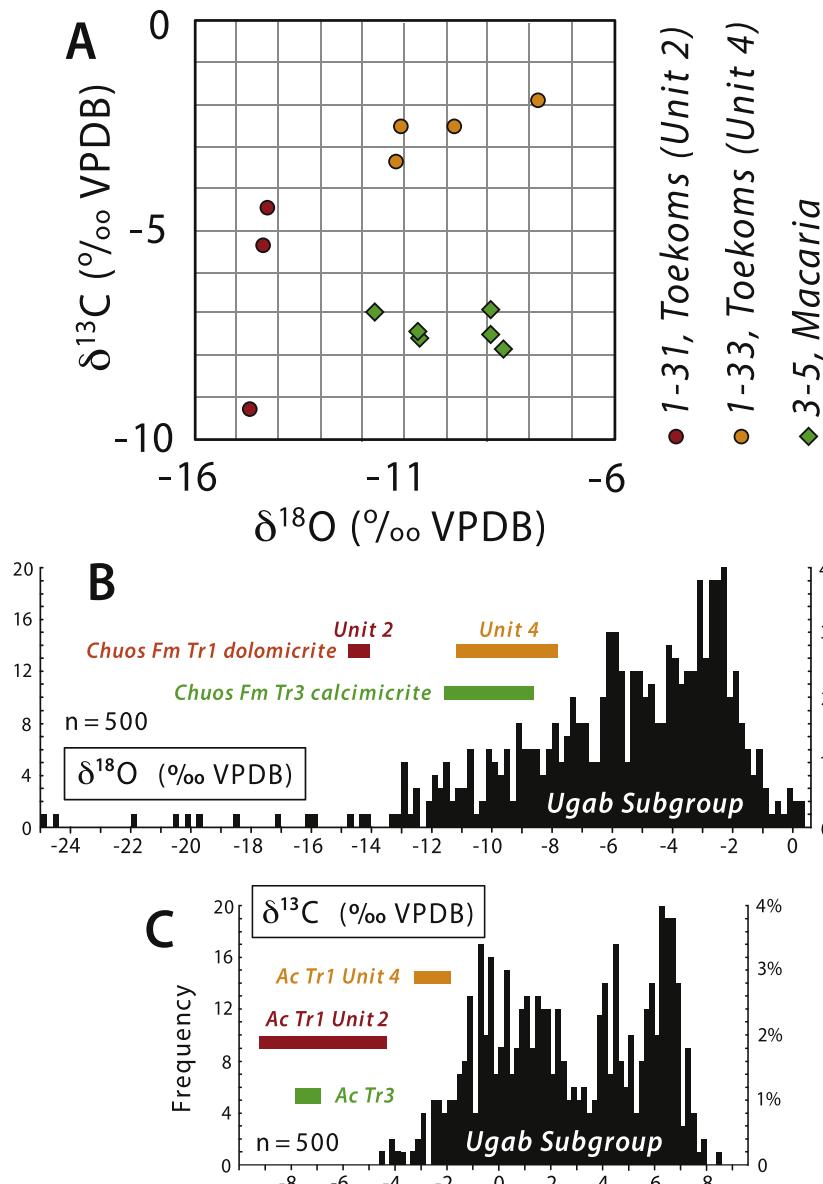


Fig. 158. (A) $\delta^{13}\text{C}$ vs $\delta^{18}\text{O}$ values for dolomite (circles) and limestone (diamonds) beds in Chuos Fm of Tr1 (Toekoms subbasin) and Tr3. Red and orange circles are from Unit 2 in section 1-31 and Unit 4 in 1-33, respectively (Fig. 22). Green diamonds are from a $\leq 1.5\text{-m-thick}$ limestone bed, $63 \pm 1\text{ m}$ above the base of Chuos Fm in sections 3-5 (K1810 and P1811) and 3-6 (Fig. 39). (B) Histogram of Ugab Subgroup $\delta^{18}\text{O}_{\text{Carb}}$ values ($n = 500$) with compositional ranges for dolomitic and calcimicrite beds in Chuos Fm in (A) shown at the same scale. Compare with $\delta^{18}\text{O}$ histogram for Devede Fm (Fig. 150). (C) Frequency bar diagram of Ugab Subgroup $\delta^{13}\text{C}_{\text{Carb}}$ values ($n = 500$) compared with compositional ranges (same scale) for dolomitic and calcimicrite beds in Chuos Fm in (A). Comparisons in (B) and (C) suggest that Chuos Fm micrite beds (A) are not composed of detrital carbonate derived from Ugab Subgroup or other known pre-Sturtian sources (Figs. 149A & 150).

colouration has not been investigated. The low organic content of the whole rock ($\leq 0.4\text{ wt\% TOC}$) suggests that sulfide or Mn-oxide may be responsible for the dark colour.

Unit Ar2c (cryptic microbialite) is gradational with Ar2b below and Ar3 grainstone above (Fig. 122). Its palimpsest microbial structure varies spatially from distinct to barely perceptible. In the former, discrete columnar stromatolites are embedded in intraclastic microbialaminite (Figs. 59B–E & 136A). The internal lamination of the columns is variably distinct (Fig. 59B & C, E) and the columns become lighter in colour up-section than the rounded microbialaminite intraclasts that occupy the space between columns (Fig. 59D). Evidence of wave or current action in the form of abraded intraclasts increases up-section between Ar2b and Ar2c (Fig. 111). The tallest discrete columnar stromatolites (Fig. 59E & F) occur in the Panorama salient of Tr5 (location 2 in Fig. 63). The columns are commonly enveloped by external crusts ('walls') $\leq 1\text{ cm}$ thick (Figs. 59B & 136A). This type of encrusted columnar stromatolite occurs in broadly coeval strata in north Asia, where it was described in paleontological literature under form-

genus *Boxonia* Korolyuk.

Nearly all Rasthof Fm facies contain agglutinated microfossils that most closely resemble the agglutinated tests of modern benthic protozoan heterotrophs (Bosak et al., 2011, 2012; Dalton et al., 2013; Moore et al., 2017). There are indications that different microfossil assemblages are facies specific, but phylogenetic assignment is uncertain due to likely morphological convergence and simplicity of forms.

There are a number of outstanding question regarding the benthic microbial facies of Ar2. What was the metabolic pathway for organic growth, since sequence stratigraphic context makes phototrophy unlikely for all but perhaps Ar2c? What process drove early lithification? What causes the dark colour, given low organic content? Microbial sulfate reduction respires organic matter and raises carbonate alkalinity, and seawater sulfate may have risen in response to post-Sturtian oxygenation (Lau et al., 2017). Extremely enriched sulfide and carbonate-associated sulfate S isotope values ($\delta^{34}\text{S}_{\text{Pyr}}$ up to +60‰ CDT) are observed in Rasthof Fm (Hurtgen et al., 2002) and other post-Sturtian deposits (Gorjan et al., 2000; Halverson et al., 2009, 2010;

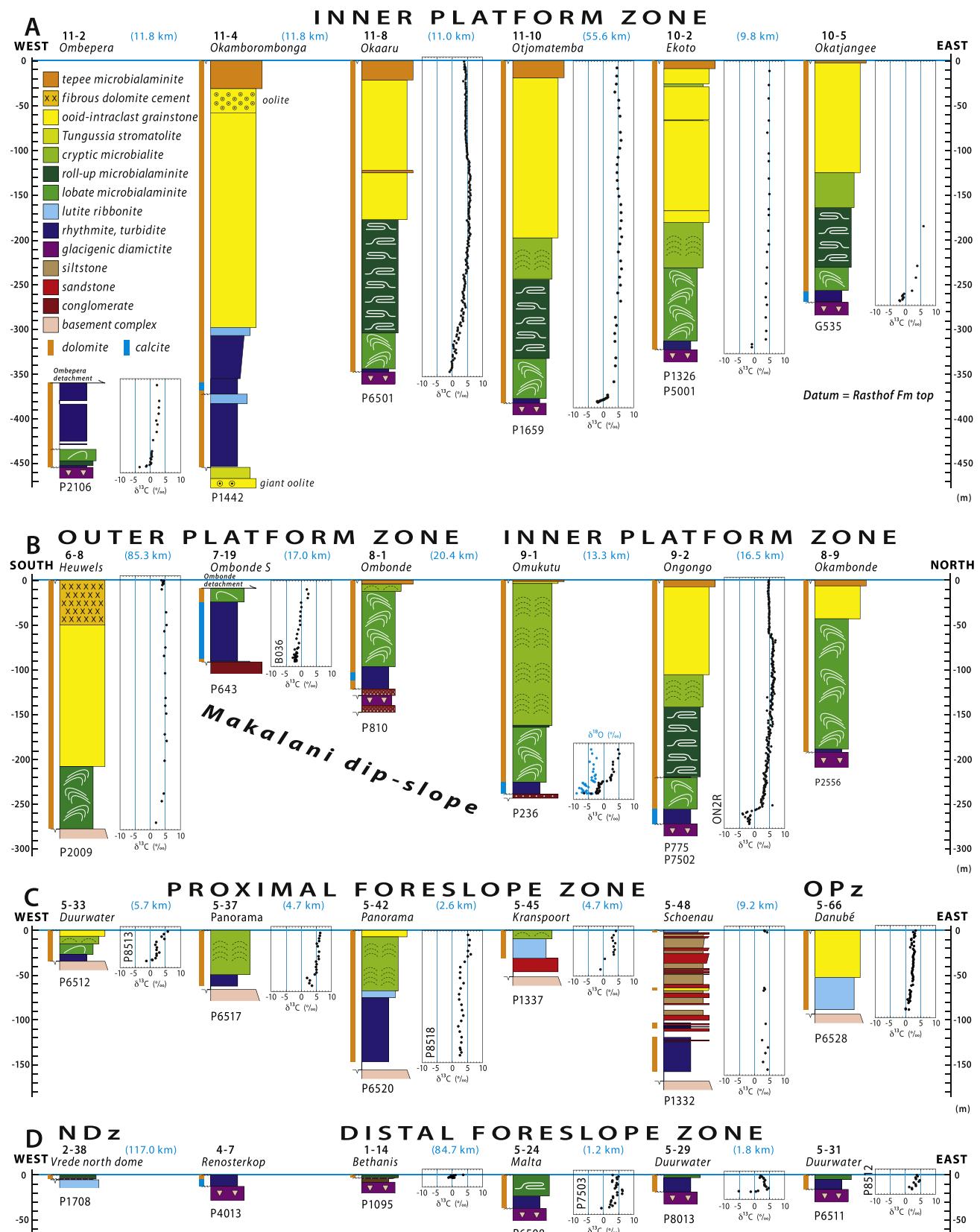


Fig. 159. Selected Rasthof/Berg Aukas Fm columnar sections with carbonate $\delta^{18}\text{O}$ and $\delta^{13}\text{C}$ records from all zones (Fig. 5). (A) W–E section in IPz Tr10–11 (see Figs. 134 & 137 for section locations). (B) S–N section of OPz Tr6–8 and IPz Tr9 (see Figs. 70, 87 & 96 for section locations). (C) W–E section of proximal FSz and outer OPz on Fransfontein Ridge, Tr5 (see Figs. 43, 63, 64 & 68 for section locations). (D) W–E section of NDz (Bz) Tr2 and distal FSz Tr1, 4, 5 (see Figs. 29, 43, 58 & 63 for section locations). Berg Aukas Fm in D is correlative with only lower Rasthof Fm in A and B (Fig. 111). Note CIE Cn1 in basal rhythmite member and its modification where dolomitized (e.g., Fig. 160).

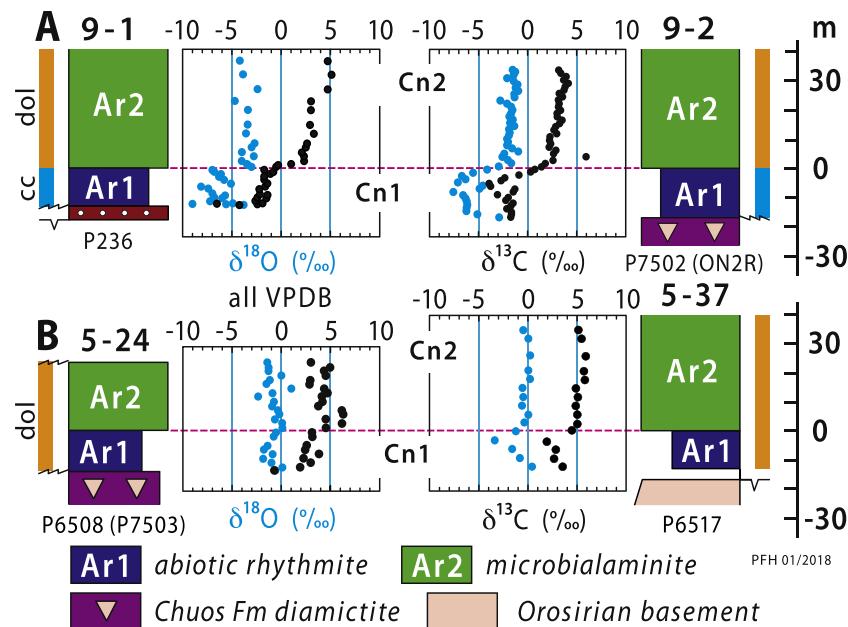


Fig. 160. Lower Rasthof Fm $\delta^{18}\text{O}$ and $\delta^{13}\text{C}$ records showing CIE Cn1 and effects of dolomitization. (A) Representative sections where Ar1 rhythmite member is calcitic (blue bars). $\delta^{18}\text{O}$ and $\delta^{13}\text{C}$ qualitatively covary and Cn1 termination correlates with calcite-dolomite and Ar1-2 transition. (B) Representative sections where Ar1 member is dolomitic (orange bars). Both $\delta^{18}\text{O}$ and $\delta^{13}\text{C}$ are altered to heavier values relative to A, but Cn1 is more altered than Cn2, lessening their distinctness.

Halverson and Shields-Zhou, 2011), pointing to quantitative reduction of available sulfate (Hurtgen et al., 2002; Parnell and Boyce, 2017). This should not be difficult to achieve in porewaters, but diffusion of sulfate must be sufficient to drive early lithification. In this respect, the closer to the sediment–water interface that sulfate reduction occurs, the better.

What is the significance of the sub-mm-scale lamination, so clearly developed in Ar2b (Fig. 113A & B)? Do the dark-coloured laminae represent pulses of organic growth, or absence of net carbonate production? Do the light-coloured laminae represent pulses of carbonate production? Was carbonate production planktonic or benthic (setting aside obviously-benthic void-filling cements)? In thin section, the darker laminae are seen as finer grained. The darker colour could simply be an optical effect of closer grain-boundary spacing, but the cause of grain-size variation would remain to be explained.

Why are aragonite crystal fans—prolific in Marinoan cap-carbonate sequences—totally absent from Rasthof and other Sturtian cap carbonates globally?

3.3.3. Gruis Fm

The recessive, thin-bedded and argillaceous Gruis Fm (Hedberg, 1979; Hoffmann and Prave, 1996; Hoffman and Halverson, 2008) contrasts with the cliff-forming, grainstone-dominated, upper Rasthof and lower Omibaatjie formations (Figs. 112, 114A, 122, 127C & D). Tidal flat and lagoonal carbonate facies in Gruis Fm of IPz grade laterally into basement-derived alluvial fan deposits on Makalani and Huab dip-slopes (Figs. 71 & 88), manifesting the last episode of crustal stretching and rift-shoulder uplift in the OPz. In the IPz, the Gruis Fm is a stack of meter-scale peritidal cycles composed of marly dolomite ribbonite (lagoonal facies) and buff-weathering pinkish dolomite microbialaminite (supratidal facies) with well-developed tepees (Fig. 113C–D). In section 9-1 (Fig. 161), for example, the formation is composed of 55 shoaling-upward cycles with an average thickness of

1.7 m, of which 82% are capped by supratidal facies. A laterally persistent meter-thick ‘marker’ bed of dolomite grainstone, characterized by authigenic chert nodules, occurs 30 to 40 m above the base of the formation (Figs. 127D, 161).

The Gruis Fm is host to Taishir (Cn3) CIE (Figs. 10D & 151)(Johnston et al., 2012; Bold et al., 2016). On average, $\delta^{13}\text{C}$ falls from a +4.5‰ plateau in basal Gruis Fm to a nadir of +1.5‰, before climbing to +7.5‰ at the top of the formation (Figs. 161 & 162). The CIE is highly reproducible (Fig. 162), considering inevitable stochastic variations in accumulation rate, compaction and tectonic strain. Consistent $\delta^{13}\text{C}$ values at the base and top suggest that Gruis Fm is isochronous (Fig. 162).

The grainstone marker bed (Figs. 103, 125, 127D, 135D & 140) with large chert nodules offers a test of $\delta^{13}\text{C}$ reproducibility (Fig. 162). It varies by 7.5‰ in relative stratigraphic height, which is not surprising given stochastic variation in accumulation rate and compaction. It coincides with the steepest part of the Cn3 decline (Fig. 162), but its composition (or interpolated composition) varies by <1.0‰ between six of the seven sections where it occurs. The outlier, section 7-22, is nearly 1‰ lighter than any other section. It is the section closest to Makalani dip-slope, and also to the Etendeka (Lower Cretaceous) volcanic plateau, although lava was likely erupted over the entire region. Its $\delta^{13}\text{C}$ composition is more scattered than other sections from the marker bed until high in the section (orange dots in Fig. 162). Aside from section 7-22, the $\delta^{13}\text{C}$ curve including the marker bed is remarkably reproducible for a formation riddled with subaerial surfaces.

Although Cn3 does not fall below 0‰ VPDB, the apparent correlative Taishir CIE in Zavkhan Basin of western Mongolia descends to mantle-like values ($-5 \pm 1\%$ VPDB) and exhibits quantitative covariance between organic and carbonate C in organic-rich limestone (Johnston et al., 2012; Bold et al., 2016). Since no conceivable diagenetic process could alter the reduced and oxidized pools of sedimentary C in parallel

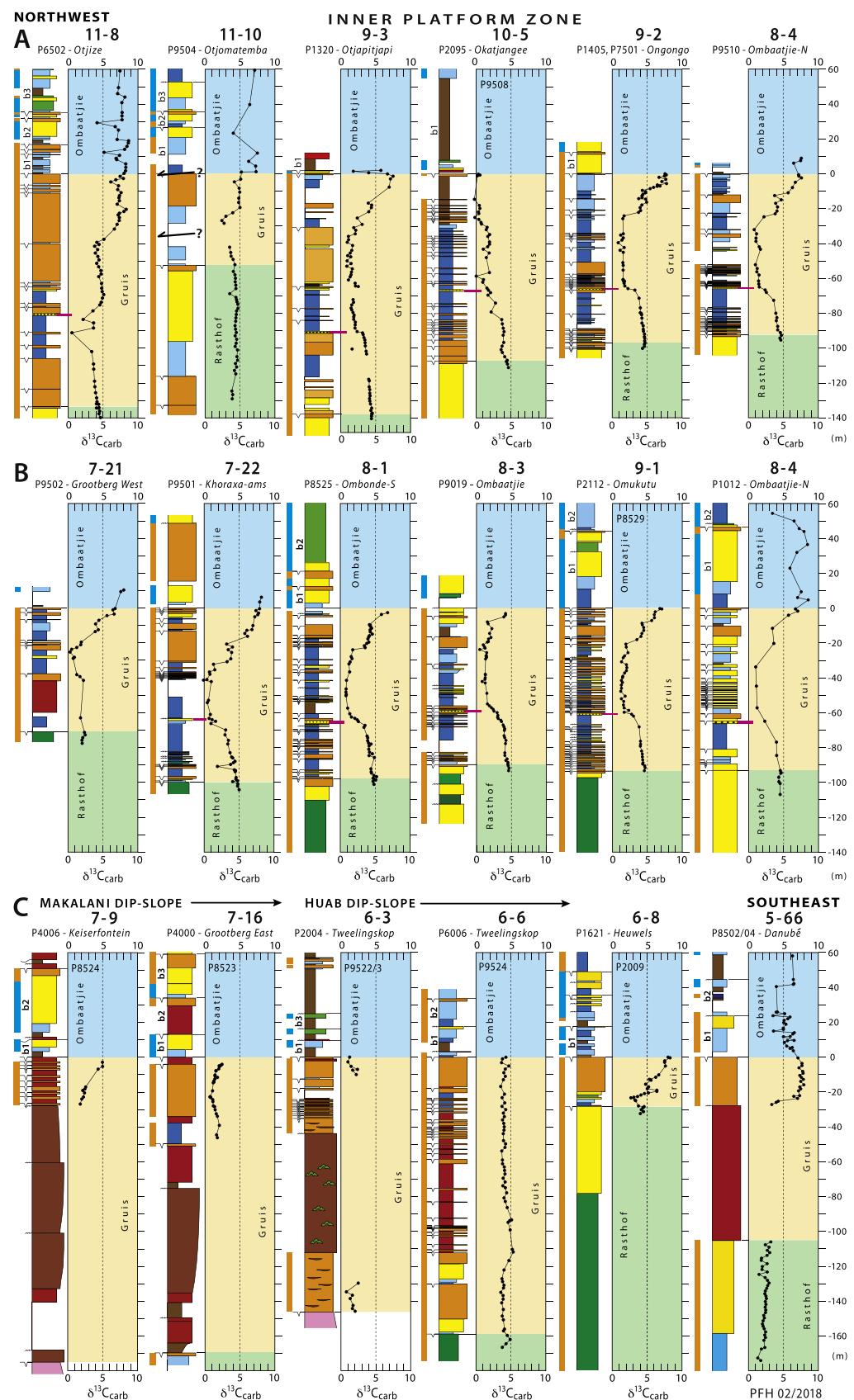


Fig. 161. Selected Gruis Fm columnar sections with carbonate $\delta^{13}\text{C}$ records, arranged roughly from NW (upper left) to SE (lower right) across (A-B) IPz and (C) OPz. CIE Cn3 is well expressed in IPz (Fig. 162), where chert-marker grainstone bed (Figs. 103, 125, 127D, 135 & 140) is shown as magenta bars. Cn3 is not well expressed in OPz, where terrigenous clastics were generated by erosion of Makalani and Huab dip-slopes (Figs. 5, 71, 86 & 88) during last episode of N–S crustal stretching.

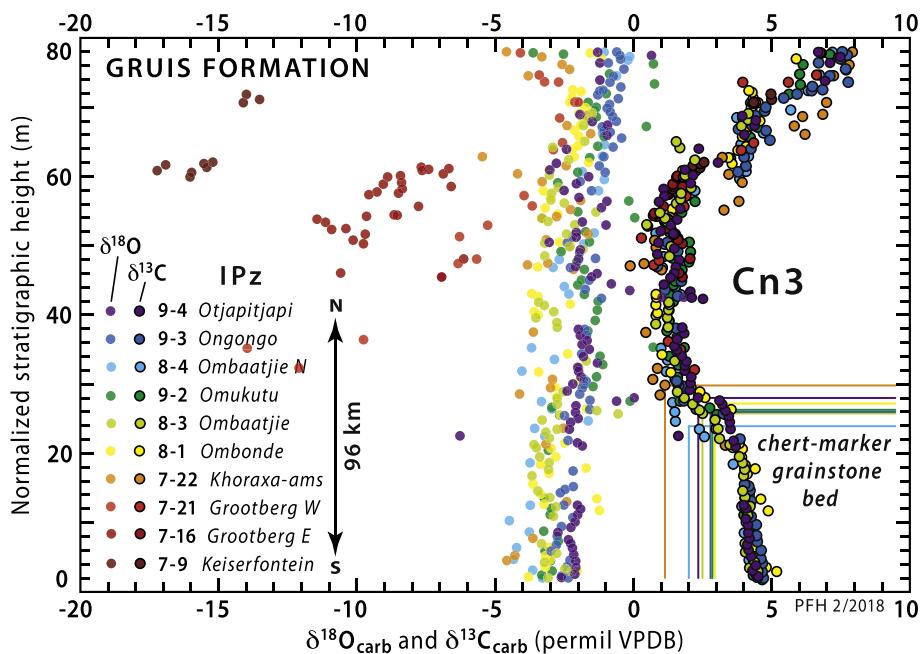


Fig. 162. 10 superimposed Gruis Fm $\delta^{18}\text{O}$ and $\delta^{13}\text{C}$ records from Inner Platform zone normalized to a common stratigraphic thickness. Data points are colour-coded by section as indicated, and span 96 km in a S–N direction across depositional strike. See Figs. 88, 89 & 96 for section locations. $\delta^{13}\text{C}$ values and normalized heights of chert-marker grainstone bed (Figs. 103, 125, 127D, 135 & 140) are shown as colour-coded lines. Consistent $\delta^{13}\text{C}$ values at base and top support isochronous boundaries, as is the integrity of CIE Cn3. Both $\delta^{18}\text{O}$ and $\delta^{13}\text{C}$ values rise overall from base to top but CIE Cn3 is not expressed in $\delta^{18}\text{O}$. Anomalously light $\delta^{18}\text{O}$ values in southernmost sections are associated with clastic input from Makalani dip slope (Figs. 88, 93E–F & 94A–B), and may be attributable to carbonate–silicate (clay mineral) exchange during middle greenschist-grade regional metamorphism.

by 10‰, the observed covariance strongly indicates that Taishir CIE is primary in origin (Johnston et al., 2012). In Gruis Fm, frequent subaerial exposure left the pale pinkish-coloured dolomite devoid of primary organic matter. Consequently, it is not possible to test Cn3 for covariance in Gruis Fm. The question remains why the nadir of Cn3 is ~7‰ heavier than Taishir CIE in Mongolia. Isotopic exchange associated with burial dolomitization seems unlikely, since Gruis Fm was likely dolomitized prior to burial, given preferential synsedimentary dolomitization of supratidal facies in the overlying lower Ombaatjie Fm (11–10, 7–22, 8–1, 8–4, 7–9 and 7–16, Fig. 161) and slow accumulation rate implied by cycle thickness. Seawater-buffered early diagenesis (Ahm et al., 2018; Higgins et al., 2018) seems to have operated in FSz and outer OPz, but not in IPz (Hoffman and Lamothe, 2019; see discussion in 3.7.2).

$\delta^{18}\text{O}$ data are more scattered than $\delta^{13}\text{C}$, but most sections rise steadily from an average of ~−3‰ at the base of Gruis Fm to ~−1‰ VPDB at the top (Fig. 162). Sections on Makalani dip-slope, rich in siliciclastic detritus (7–9, 16 and 21), are increasingly depleted southward (Fig. 162). The depletions are far too large, up to ~−15‰, to be accounted for by meteoric water diagenesis, since precipitation on tropical marine coasts is nearly unfractionated (e.g., Kendall and Coplen, 2001). Since isotopic depletion appears correlated with phyllosilicate content, we speculate that carbonate–silicate exchange reactions during regional greenschist-grade metamorphism (Faure, 1986) are responsible for the anomalously depleted $\delta^{18}\text{O}$ values observed in sections most proximal to onlapped basement of Makalani dip-slope (Figs. 87C & 88).

3.3.4. Ombaatjie Fm

Ombaatjie Fm records the initial phase of rapid thermal subsidence (Halverson et al., 2002) following the cessation of rifting in OPz (Figs. 151 & 163). We relate the end of rifting to passive-margin inception, because FSz and Bz subsided deeply in late Cryogenian and early Ediacaran time (Fig. 5). ‘Break-up’ unconformities are observed in Tr5 (Fig. 68), Tr6 (Figs. 71 & 86) and Tr7 (Fig. 88). In Tr5 and 7, Ombaatjie Fm oversteps older units including the basement.

A thermal subsidence model (Fig. 163A), although simple and conditional on certain assumptions (e.g., β), predicts an average accumulation rate of 65 m Myr^{−1} for Ombaatjie Fm, giving roughly 4 to 6 Myr for the formation as a whole. Assuming 10 Myr (661 to 551 Ma) for the inter-snowball interval in total (Rooney et al., 2015, 2020a; Bao et al., 2018), the age of the rift-to-drift transition was 657 to 655 Ma, assuming that the top of Ombaatjie Fm marks the Marinoan glacial onset at ~651 Ma (Bao et al., 2018). Ombaatjie Fm and its FSz correlatives provide sequence-stratigraphic and chemostratigraphic evidence that no major hiatus separates Abenab Subgroup from the Marinoan glacial onset.

Ombaatjie Fm is a weakly progradational stack of shoaling-upward carbonate cycles (Fig. 164). The cycles have an average thickness of 19.1 m and the average number of cycles per section is 9.4. The average cycle thickness is 11x greater than for the underlying syn-rift Gruis Fm (1.7 m). By early Ediacaran time, average cycle thickness in Elandsbaek Fm had fallen back to 4.2 m (3.4.3). Assuming that tectonic subsidence exerts the first-order control on cycle thickness, the observed history is consistent with an abrupt increase in subsidence rate at passive-margin inception, followed by exponential decay thereafter due to plate cooling (McKenzie, 1978). Slow average syn-rift subsidence is compatible with a modest stretching factor ($\beta \approx 1.5$, Fig. 163A) and prolonged stretching (>105 Myr, >760 to 655 Ma).

Accompanying the sharp increases in accumulation rate and cycle thickness is a marked drop in the dolomite/calcite ratio, from nearly 100% dolomite in Gruis Fm to <30% in lower Ombaatjie Fm (Figs. 103, 125, 135B, 140 & 164). Slow burial rates evidently favoured early dolomitization. HST grainstone is the facies least likely to be dolomitized, again pointing to accumulation rate as a critical factor in early dolomitization. Near-surface dolomitization is supported by dolomite intraclasts in undolomitized grainstone (Fig. 115D).

We provisionally divide Ombaatjie Fm into eight numbered cycles, b1 to b8 (Fig. 164). This number is somewhat arbitrary since composite cycles are common (e.g., Fig. 129). Lateral facies changes on a sub-kilometer scale (Fig. 165) make it unlikely that numbered cycles b1–6

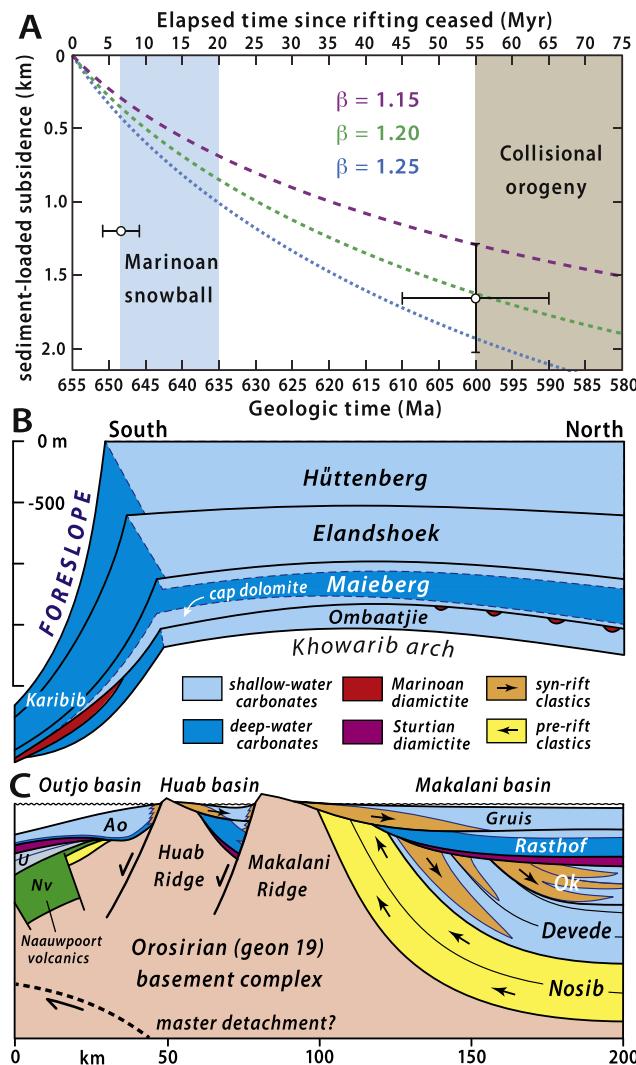


Fig. 163. (A) Thermal subsidence model for post-rift Otavi Group (Figs. 151 & 163B) with carbonate-sediment loading and different instantaneous stretching factors (β), modified after Halverson et al. (2002). Data point with uncertainties indicates collision age—destruction of Otavi platform by abortive subduction (Fig. 194)—and thickness of post-rift shelf succession (Ombaatjie Fm + Tsumeb Subgroup). (B) Stratigraphic restoration of post-rift succession, accommodated primarily by thermal subsidence (A). Lithospheric flexure (Watts et al., 1982) is indicated by stratigraphic thinnings (Fig. 145) of all units over Khowarib arch. Minor rift-fault reactivation may have occurred on the platform during Ombaatjie Fm time, and in Outjo basin during Marinoan glaciation (Macaria subbasin, Figs. 26 & 40). (C) Stratigraphic restoration during final rifting under Otavi Group platform at the end of Gruis/Okonguarri (Ao) Fm. Huab (Tr6) and Makalani (Tr7) rift-shoulder uplifts separate Outjo, Huab and Makalani rift basins. Outjo basin (Swakop Group) subsided deeply during and after Okonguarri Fm deposition, in response to continued crustal stretching in Northern (Outjo) zone (Fig. 26). Abbreviations: Ao, Okonguarri Fm; Nv, Naauwpoort Fm; U, Ugab Subgroup.

are exactly correlative between sections (Fig. 164). Cycles b7 and 8, on the other hand, are isotopically (Figs. 165 & 166) and lithologically (Figs. 78E & F, 79A, 127E & F) distinct. Cycle b7 corresponds to the CIE Cn5 downward trend (Figs. 165 & 166) and b8 to its nadir and partial recovery. Both cycles have exceptionally well-developed stromatolites (Figs. 79A & 127E) and b8 features enigmatic beds of Fe-rich intraclast packstone (Figs. 78F & 127F). Following Halverson et al. (2002), we

consider b7 and 8 to be correlative and broadly isochronous across the platform. However, b7 is commonly a composite cycle and its base in some sections might be different if $\delta^{13}\text{C}$ data were unavailable. Therefore, we use the base of cycle b4 as the datum for the platform-wide fence diagram (Fig. 164) because it can be identified on purely physical grounds independent of $\delta^{13}\text{C}$. It marks an injection of terrigenous clastics and changes in cycle thickness, lithofacies distribution and degree of dolomitization (Fig. 164). Lowering the datum from the 0%-crossover in b7 (Halverson et al., 2002; 2011a) to the base of b4 (Figs. 164 & 165) makes little difference in the reconstructed sub-Marinoan glacial surface to be discussed in 3.3.6..

Older cycles (b1–3) in IPz are thicker, less dolomitized and dominated by cliff-forming intraclast-oolith grainstone (Figs. 103, 112, 114A & B, 116A, 125 & 164). Younger cycles are thinner, more dolomitized and dominated by ribbonite and microbialaminite. On the outermost platform (Tr5 & 6), older cycles (b1–4) are thinner, ribbonite-dominated and terminate at flooding surfaces lacking evidence of subaerial exposure (Figs. 68, 71 & 88). The early Ombaratje shelf evidently deepened distally, but the outer shelf became a site of grainstone deposition in cycles b5–8 (Fig. 164).

Marine quartzarenite occurs sporadically in lower Ombaratje Fm—in cycle b1 in Tr10 (Fig. 135B), b2 and 3 in Tr7 (Figs. 88, 94C & D), and b4 in Tr7 and 9 (Fig. 125). The silica grains are quartz, not chert, and indicate relict rift-related topography and/or minor rift reactivation. Argillite and terrigenous siltstone locally mark the maximum flooding stage of cycles b1 through b6 in IPz (Fig. 164). Cycle b8 begins with argillite nearly everywhere the cycle is preserved (Fig. 164). The b8 argillite is commonly associated with enigmatic beds of intraclast packstone (Figs. 78F, 127F & 165) in which oligomictic intraclasts are composed of Fe-Mn-rich dolomite (ankerite). In many sections, cycles b7 and 8 have exceptionally well-developed columnar stromatolites of various types (Figs. 78E, 79A & 127E), supporting their chemostratigraphic correlation (Figs. 165 & 166).

C and O isotope profiles from 18 sections (Fig. 164) across the platform are combined in Fig. 166. Stratigraphic thicknesses are normalized for each of three intervals: cycles b1–6, cycle b7 and cycle b8. Cycles b1–6 are highly enriched (CIE Cn4, Fig. 151): $\delta^{13}\text{C}$ peaks between +8 and +9‰ (VPDB), with little secular change but considerable scatter toward lighter values. This scatter is most pronounced in OPz (Fig. 166). $\delta^{13}\text{C}$ begins to turn lighter below the base of b7, anti-correlated with $\delta^{18}\text{O}$, which turns heavier (Fig. 166). We correlate Cn4 with CIE Keele Peak in NW Canada and elsewhere (Kaufman et al., 1997; Halverson and Shields-Zhou, 2011).

Since interval b1–6 is only partially dolomitized and exhibits little secular change in isotopic composition (Fig. 166), we made a crossplot of $\delta^{13}\text{C}$ versus $\delta^{18}\text{O}$ for coexisting calcite and dolomite in that interval (Fig. 167). Although the calcite and dolomite fields overlap, dolomite is ~3.1‰ heavier in $\delta^{18}\text{O}$ on average, relative to calcite. This is close to the projected low-temperature equilibrium fractionation between dolomite and calcite (Fritz and Smith, 1970; Friedman and O'Neil, 1977). Dolomite is *lighter* in $\delta^{13}\text{C}$, relative to coexisting calcite, by 1.2‰ on average. This is contrary to expectation for equilibrium fractionation (Sheppard and Schwarcz, 1970; Friedman and O'Neil, 1977). The shift toward significantly heavier O and slightly lighter C is compatible with evaporative seepage-reflux dolomitization (Adams and Rhodes, 1960), as is the propagation of dolomite downward from tepee-structured supratidal horizons at the tops of cycles. However, there is no petrographic evidence that porewaters ever reached gypsum/anhydrite saturation in the Ombaatjie Fm. The shift in $\delta^{18}\text{O}$ is opposite of that predicted for lithification or diagenesis under the influence of meteoric or higher-temperature fluids (Knauth and Kennedy, 2009). Our preferred interpretation is near-surface dolomitization, equilibrated with marine platform-derived pore-fluids in which the DIC includes 14–18% remineralized organic C. Early marine dolomite and dolomitization with similar $\delta^{13}\text{C}/\delta^{18}\text{O}$ systematics (but shifted toward lighter $\delta^{18}\text{O}$) were documented petrographically in a middle Cryogenian reef complex in

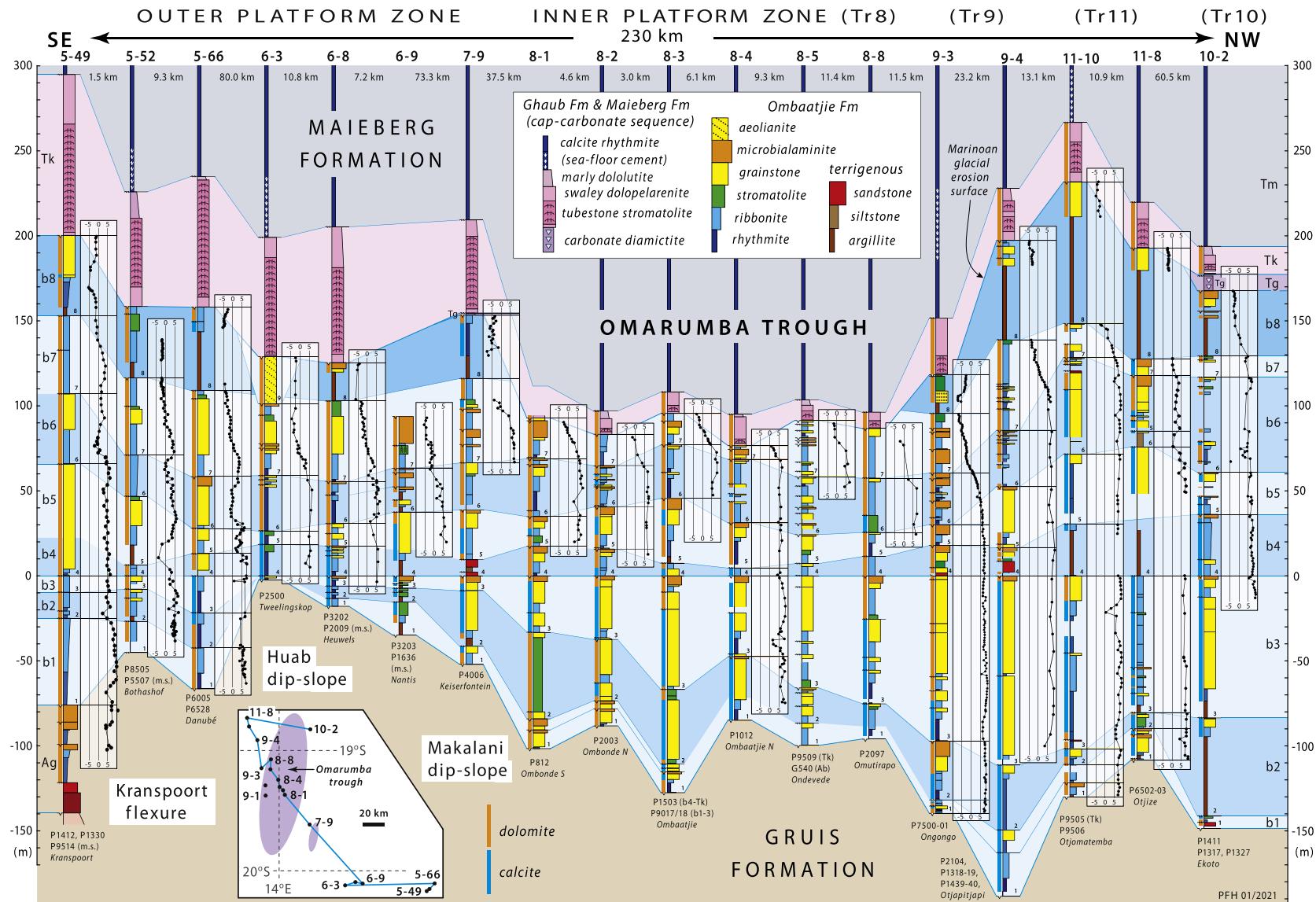


Fig. 164. Selected Omaatjie Fm sections with $\delta^{13}\text{C}$ records from Outer and Inner Platform zones. Inset map (lower left) shows relative section locations (see Figs. 43, 68, 70, 88, 96, 134 & 137 for section locations by transect). Datum (0.0 m) is the base of cycle b4, which is marked by input of clastic detritus (quartz sand and silt) and separates thick cycles dominated by limestone grainstone in cycles b1–3 from thinner more-dolomitized cycles in b4–7 (Fig. 114B). The same datum is used for closely spaced sections from 9 to 3 (Figs. 128A, 129 & 165). Clastic input is related to minor reactivation of Huab and Makalani rift shoulders. The descending arm of CIE Cn5 (Trezona excursion) occurs in cycle b7 in most sections, but in 10-2 it is recorded in thin dolomite beds within argillite of cycle b8. Omarumba trough is inferred to be a subglacial bedrock trough from which Omaatjie cycle b8 (dark blue background) and upper b7 were removed by Marinoan glacial erosion. Its known extent is limited to Tr8 and sections 9–1–2 (Figs. 125 & 145). Its trend, indicated by mauve ellipse on inset map of this figure, is assumed to parallel clast-fabric in Ghaub Fm lodgement tillite at section 8–3 (Fig. 57). As shown, Omarumba trough is broad and shallow (aspect ratio 0.002). Separate narrower Marinoan troughs of similar depth (ca 60 m) occur in OPz (7–1–4, Fig. 88). Unlike Sturtian Omurirapo trough in Tr8 (Fig. 105), Omarumba trough preserves little glacial debris (Figs. 103 & 118). Erosion of Omaatjie cycles b7–8 in IPz is an isotopically compatible source of clasts in Ghaub Fm glaciomarine diamictites in FSz (Fig. 173). Keilberg Mb is consistently thicker outside the trough than within the trough. Mutual consistency of above relations bolsters the Marinoan paleotopographic reconstruction and the aggradational b4–8 cycle structure. This implies an overall northward increase in subsidence rate. The locus of coarse-grained intraclast-oid grainstone accumulation (yellow) shifts seaward from the IPz in cycles b1–3 to OPz in b4–7. Previously sampled for pre-Marinoan geochemical proxy data, section 8–4 (Fig. 112) is the most top-truncated section in the axis of Omarumba trough.

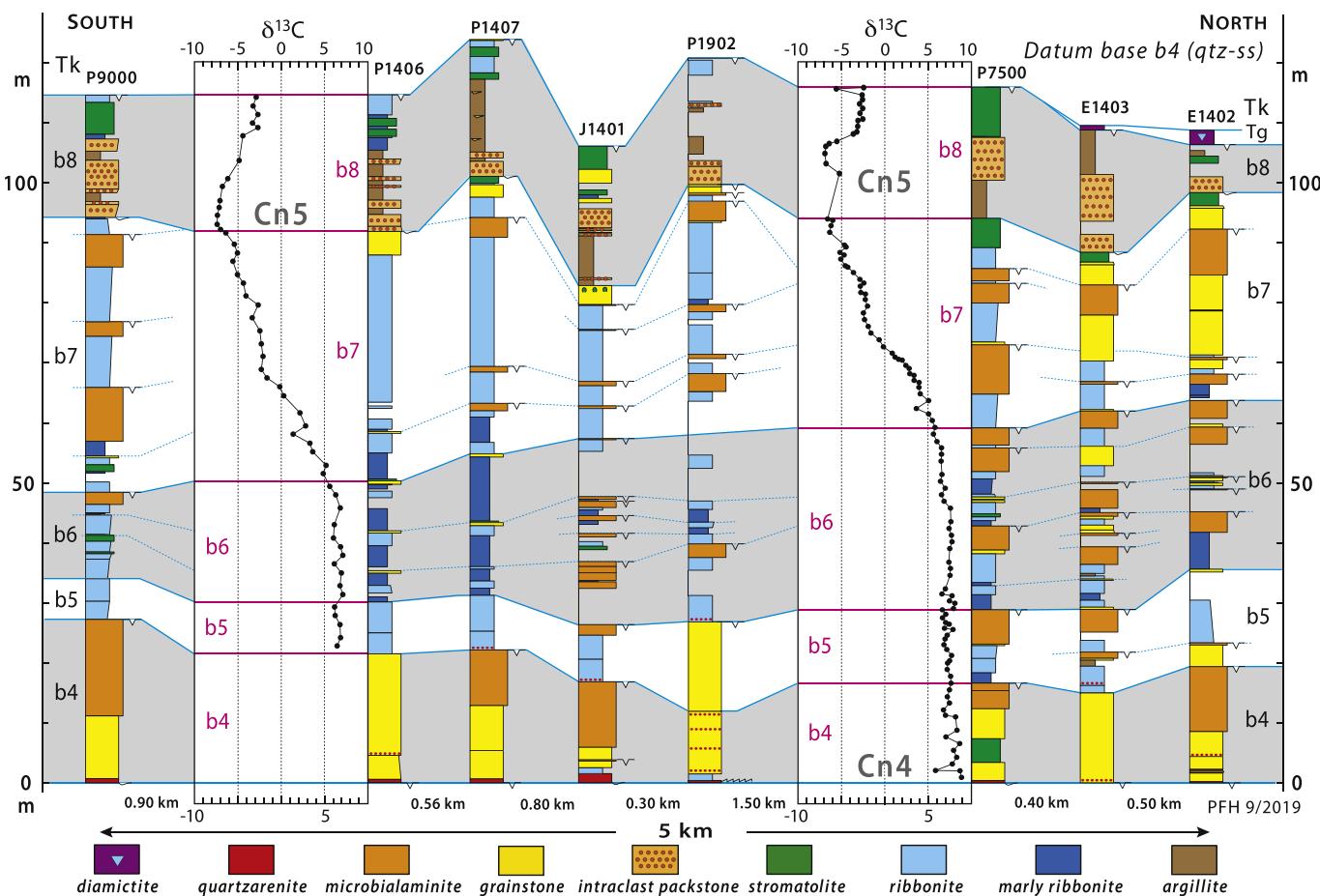


Fig. 165. Closely spaced upper Ombaatjie Fm columnar sections in 9-3, Ongongo (Figs. 128–129), with $\delta^{13}\text{C}$ records illustrating descent from Cn4 plateau (cycles b1–6) to Cn5 nadir in cycle b8 (Figs. 133 & 166). Datum is base of cycle b4, which is distinguished by incursions of quartz sand and arenite (dark-stained by desert varnish, Fig. 128). Sections P1406–P1902 are persistently of deeper-water lithofacies in b6–7 than in sections to N and S. Incidence of (*Tungussia*-type) stromatolites (Fig. 127E) is strongly associated with Cn5 (Tziperman et al., 2011). Oligomictic (siderite or ankerite) intraclast packstone (Fig. 127F) is uniquely associated with Cn5 nadir in lower b8, homologous to its occurrence at 6–7 (Figs. 71 & 78F), 132 km to the SE (Fig. 8B). Authigenic carbonate production is a predicted consequence of a biological origin for CIE Cn5 (Tziperman et al., 2011).

South Australia (Hood et al., 2011; Hood and Wallace, 2012, 2015). Early marine dolomite cementation with a pinch of organic C could explain those $\delta^{13}\text{C}$ records that are relatively insensitive to calcite or dolomite mineralogy.

Cycle b7 records the descending arm of CIE Cn5 (Fig. 151), which we correlate with Trezona CIE in South Australia and elsewhere (McKirdy et al., 2001; Rose et al., 2012). Cycle b8 records the nadir of Cn5 and its partial recovery (Fig. 166). Values for $\delta^{13}\text{C}$ and $\delta^{18}\text{O}$ covary in cycle b7, but not quantitatively—the decline in $\delta^{13}\text{C}$ is double that in $\delta^{18}\text{O}$. Data for both elements ‘fan’ stratigraphically upward in the normalized plot, with variance in $\delta^{13}\text{C}$ reaching 8% at the top of b7 (Fig. 166). Much of the fanning can be accounted for by differential erosion beneath cycle b8 and more importantly beneath the Marinoan glacial disconformity (Fig. 164). The more deeply b7 is eroded, the heavier its youngest isotopic composition. When $\delta^{13}\text{C}$ profiles for b7 are plotted against absolute rather than normalized stratigraphic height, IPz and OPz have statistically different slopes (Fig. 168). If we assume temporal change in $\delta^{13}\text{C}$, the difference in slope indicates 1.43x faster accumulation rates on average in IPz compared with OPz. The relative subsidence rate is the reverse of that observed in lower Ombaatjie Fm (discussed in paragraph 6 of this section). Alternatively, the difference in slope (Fig. 168) could reflect increasing intensity of seawater-buffered diagenesis with proximity to FSz (see 3.7.2.) (Hoffman and Lamothe, 2019).

The nadir of Cn5, $-7.5\text{\textperthousand}$ VPDB, is recorded in section 9-2 by intraclast packstone beds in the lower part of cycle b8 (Fig. 165). Values rise to a maximum of $-2\text{\textperthousand}$ at the top of the cycle, again with significant fanning due to differential Marinoan glacial erosion (Figs. 164 & 166). In South Australia, the first Marinoan ice-raftered debris (IRD) appears where $\delta^{13}\text{C}$ reaches $-2\text{\textperthousand}$ in its recovery from Trezona CIE Cn5 nadir (Rose et al., 2012). No IRD is known in Ombaatjie Fm. The first sign of Marinoan glaciation was a glacioeustatic fall that ended marine sedimentation on the platform (Hoffman, 1999, 2011b). Carbonate aeolianite, tentatively identified in section 6-3 (cycle b9) near the edge of the platform (Figs. 78B, 79B, 71 & 164), may also be a manifestation of glacioeustasy, as is the falling-stand wedge represented by Franni-aus Fm (3.3.5.). If the reversal in OPz-IPz subsidence rate in cycle b7 resulted from flexural isostasy associated with ice-sheet advance from the interior of the Congo craton, such flexural isostasy would contaminate or overwhelm the glacioeustatic record. We consider it more probable that ice-sheet growth at higher latitudes caused glacioeustasy to precede glacioisostasy on the Otavi platform.

The regional fence diagram (Fig. 164) reveals an apparent steep-walled, flat-floored, 0.05-km-deep trough on the Marinoan subglacial erosion surface. Here-named ‘Omarumba trough’, after the village of that name (Fig. 96), it is defined by complete removal of cycle b8 and partial to complete removal of b7 (Fig. 164). Hoffman and Halverson

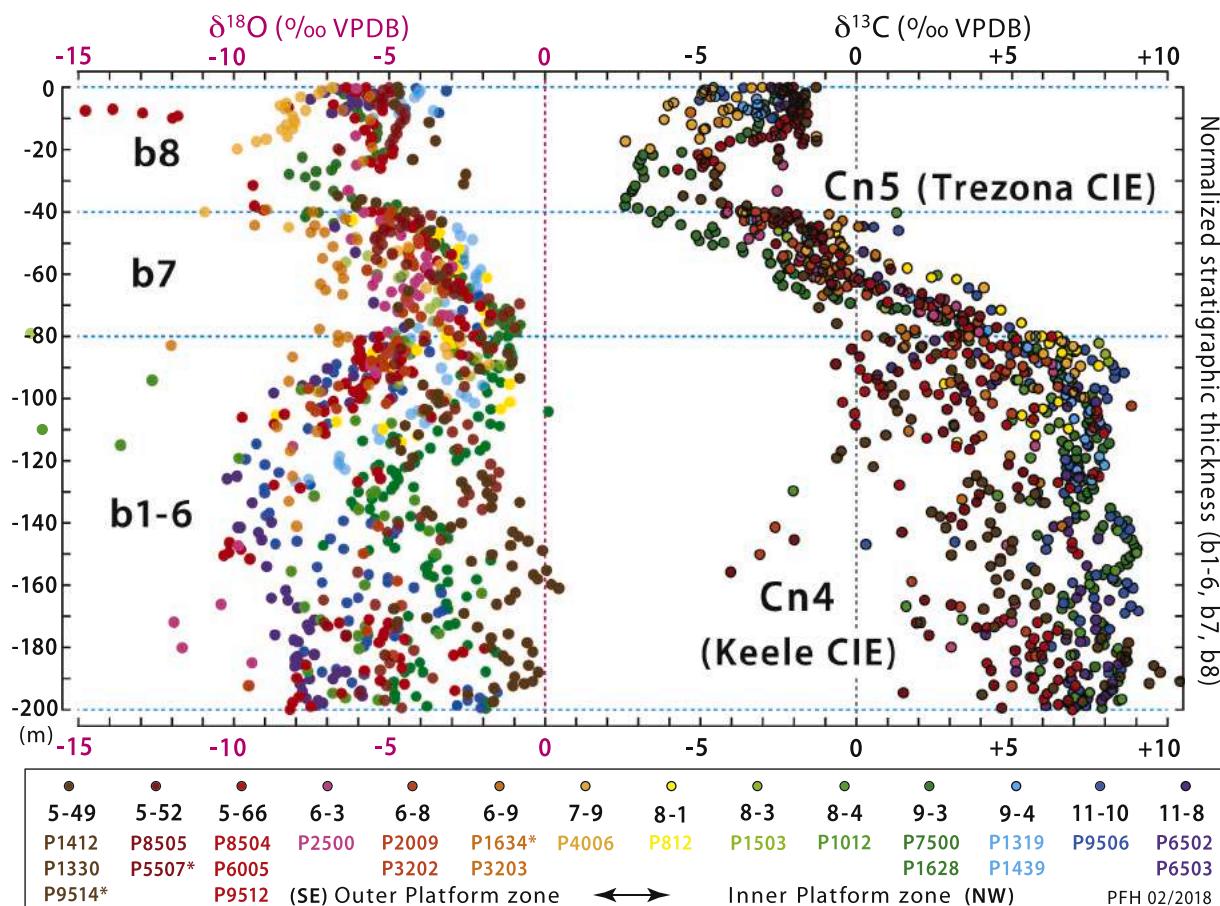


Fig. 166. Normalized Ombaatjie Fm $\delta^{18}\text{O}$ and $\delta^{13}\text{C}$ records from OPz (brown-red-pink-orange) and IPz (yellow-green-blue-violet). See Fig. 164 for section locations and columnar sections. Sections are thickness-normalized for each of 3 intervals: cycles b1–6, b7, and b8. Age-equivalent $\delta^{13}\text{C}$ values become lighter oceanward during Cn4, but heavier during Cn5. Both trends are consistent with diagenesis that was more strongly seawater-buffered oceanward, provided that Cryogenian $\delta^{13}\text{C}_{\text{DIC}}$ was persistently intermediate between Cn4 and Cn5 (Hoffman and Lamothe, 2019). Section numbers with asterisks are measured sections only—no isotope data. Data for other sections is in SOI S1 & S2.

(2008) took this erosion to be characteristic of IPz as opposed to OPz, but this is contradicted by the reappearance of those cycles in Tr9–11 (Fig. 164). We now postulate that Omarumba trough is elongate in a SSW–NNE orientation as shown in the inset location map (Fig. 164), an orientation derived from Ghaub Fm clast-fabric data from 8 to 3 (Fig. 57 & 118C), indicating the glacial flow direction (Dowdeswell et al., 1985).

3.3.5. Middle Cryogenian in Swakop Group: Berg Aukas, Okonguarri, Narachaams and Frannis-aus formations

The inter-snowball formations just described—Rasthof, Gruis and Ombaatjie formations—can be mapped and correlated without significant ambiguity for 200 km S–N across OPz and IPz (Figs. 5, 151, 159, 161, 162, 164 & 166). Major lithofacies change is limited to the syn-rift Gruis Fm (Fig. 86, 88, 161). The lateral continuity breaks down within 10 km across the OPz-to-FSz transition (5–44–65, Fig. 43). Most of the changes occur within 3 km across the depositional strike (5–44–49, Fig. 62–65). The overall time frame is not in doubt: the boundaries of the middle Cryogenian succession are mappable across the transition (Fig. 64). But the inter-snowball succession in Swakop Group (Table 5) demands a different stratigraphic nomenclature (Fig. 6B & C) from that in Otavi Group (Fig. 6D & E). The changed nomenclature reflects real difficulties in temporal correlation across the facies transition during this 10–20-Myr epoch (Table 1). These difficulties are compounded by different diagenetic regimes (e.g., seawater-buffered vs sediment-buffered) that compromise C-isotope chemostratigraphy between FSz and other zones (Ahm et al., 2018; Higgins et al., 2018; Hoffman and Lamothe, 2019).

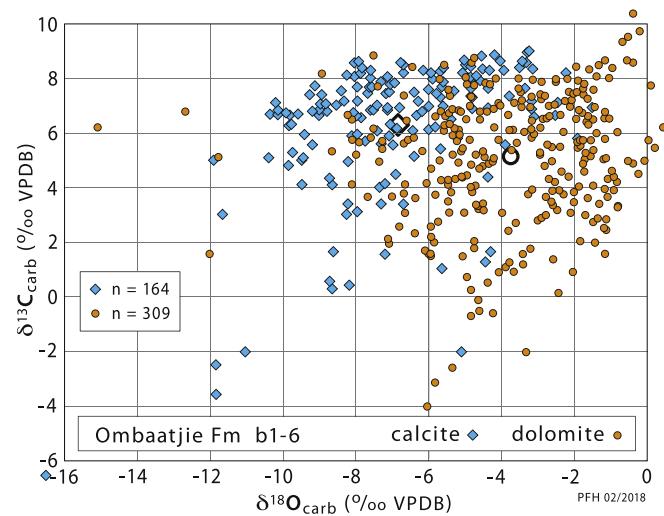


Fig. 167. $\delta^{13}\text{C}/\delta^{18}\text{O}$ crossplot for calcite (blue diamonds) and dolomite (orange circles) in partially dolomitized Ombaatjie Fm cycles b1–6 (Cn4) from all OPz and IPz sections (Fig. 166). Mean values indicated by black open symbols. On average, dolomite is 3.1‰ heavier in $\delta^{18}\text{O}$ and 1.2‰ lighter in $\delta^{13}\text{C}$ than calcite, broadly consistent with extrapolated low-temperature equilibrium fractionation for $\delta^{18}\text{O}$ but not $\delta^{13}\text{C}$ (C). This implies that dolomite and calcite are not in isotopic equilibrium wrt $\delta^{13}\text{C}$.

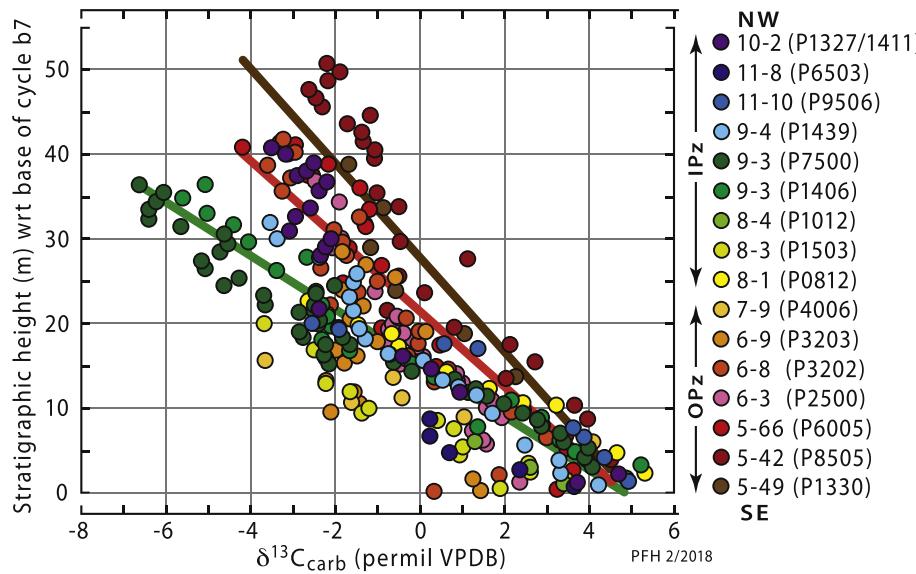


Fig. 168. $\delta^{13}\text{C}$ records for Ombaatjie Fm b7 in outer (OPz) and inner (IPz) platform zones (Fig. 166), plotted against stratigraphic height wrt datum 0 m at base of cycle b7 (Fig. 164). Linear trend lines shown for IPz (green), OPz (red) and outermost OPz (brown). Outermost (Tr5) sections are closest to shelf break (Figs. 43 & 68). Top of each section is Cn5 nadir for that section, so changes in slope are not attributable to different accumulation rates of variably incomplete sections. Slope changes reflect progressively heavier $\delta^{13}\text{C}$ values oceanward during Cn5 (Fig. 166), possibly reflecting more seawater-buffered conditions during early diagenesis (Hoffman and Lamothe, 2019). On the other hand, recovery from Cn5 nadir is observed in distal foreslope debrites of Frannis-aus Fm (Figs. 170, 172–173 & 202), inferred to have originated within the proximal foreslope, not in epi-platform waters.

Lower Rasthof-like rhythmite (Ar1) and microbialite (Ar2) sharply overlie Chuos Fm in FSz and Bz (Fig. 159B & C), as in Otavi Group (Fig. 111), but highstand grainstone (Ar3) is absent or poorly developed. This makes the post-Sturtian cap-carbonate sequence in Swakop Group more similar lithologically to Berg Aukas Fm of OML (Figs. 6E & 111) than to Rasthof Fm. It is therefore expedient to retain the name Berg Aukas Fm (Aa) for the Surtian cap-carbonate sequence in Swakop Group (Table 1, Fig. 6B & C). This acknowledges that the tops of Berg Aukas and Rasthof formations are not correlative. Stromatolites and related microbial structures are identifying features of Berg Aukas Fm in OML (SACS (South African Committee for Stratigraphy), 1980). They are present also in Swakop Group but are better developed in FSz (Figs. 59 & 62) than in Bz (Fig. 33A).

In Tr1 & 2 and the western half of Tr5 (5–1–25), Berg Aukas Fm is overlain by silty argillite interspersed with variably thick sets of mostly calcitic turbidites and debrites (Figs. 33B & 47C–F). We refer this deepwater carbonate-rich assemblage and its up-slope equivalents in Tr5 (5–25–50) to Okonguarri Fm (Ao). This formation was introduced, without elaboration, in a table of formations for part of Northern zone (Clifford, 1967), but later abandoned (Clifford, 2008). It was determined

to be middle Cryogenian in age in its eponymous area 30 km E of Tr3 by Hoffmann et al. (2004; see Miller, 2008b, p. 13–145–148). It has maximum thicknesses of 265 m (Soutput subbasin 1–22, Fig. 18) and 292 m (Toekoms subbasin 1–34, Fig. 22) in Tr1, 40 m in Tr2 (2–32, Fig. 32), 357 m in Tr3 (3–17), where it includes bundles of dolomite-cemented quartzarenite (Fig. 39), and 1260 m in Tr5 (5–40), where it consists mainly of dolomite grainstone with spaced bands of broad domal stromatolite (Figs. 43, 58, 62, 65 & 170). Its thick proximal ramp-like facies in Tr5 fills Kranspoort trough (Figs. 43 & 62), which we attribute to Sturtian glacial incision of Huab ridge basement, combined with crustal flexure at the tip of Huab ridge normal fault (Figs. 65B & 26) (Coleman et al., 2019). A syndepositional age for crustal flexure is supported by basement-derived sandstone with intraclast debrite in Berg Aukas Fm between sections 5–43 and –48 (Figs. 62, 65 & 66A–D).

The grainstone ramp of Okonguarri Fm has remarkably uniform $\delta^{13}\text{C}$ values of $3.95 \pm 1.02\text{‰}$ ($n = 426$, 5–31–45, Fig. 171B) that do not resemble the frequency distribution of any inter-snowball formation or combination of formations on the platform (Fig. 171A). Hoffman and Lamothe (2019) attribute its uniformity to early seawater-buffered dolomitization (Ahm et al., 2018; Higgins et al., 2018) and consequent

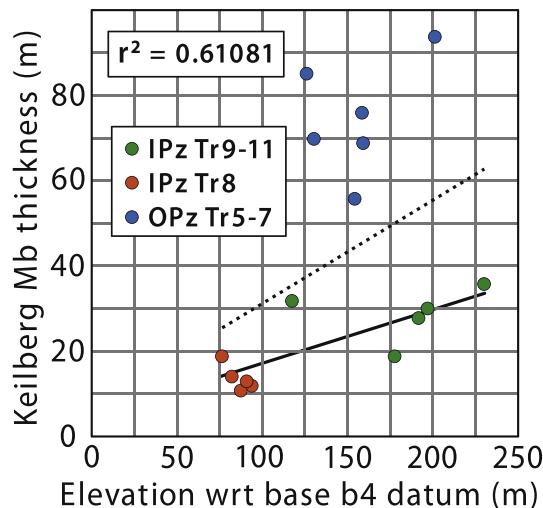


Fig. 169. Positive correlation between Keilberg Mb thickness and elevation of its base above the datum at the base of Ombaatjie Fm cycle b4, Fig. 164). Red dots are from Omarumba trough (Fig. 164), green dots are from IPz outside Omarumba trough, and blue dots are from OPz. Solid regression line is for IPz data ($r^2 = 0.61$) and dotted line for all data.

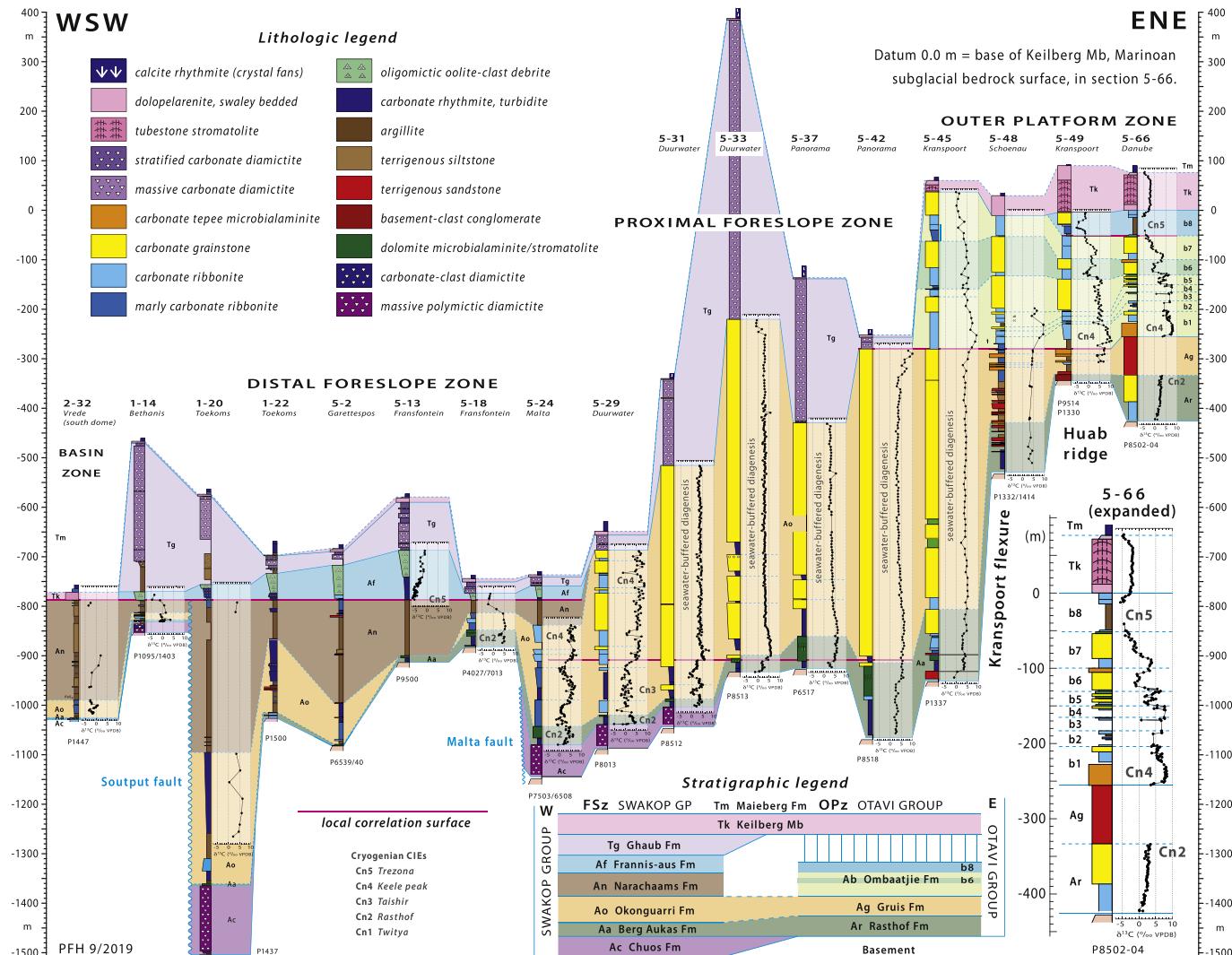


Fig. 170. Selected Cryogenian–earliest Ediacaran columnar sections with $\delta^{13}\text{C}$ records from FSz–OPz transition in Tr1 and Tr5 (see Figs. 15, 43, 58, 63, 64 & 68 for section locations). Permeable grainstone in proximal Okonguari Fm (sections 5–29–45) is inferred to have experienced seawater-buffered diagenesis during dolomitization (Hoffman and Lamothe, 2019), yielding uniform $\delta^{13}\text{C}$ values $\sim 3.65\text{‰ VPDB}$ (Fig. 171) that do not match modal Cryogenian values in IPz, distal FSz or Bz (Figs. 171 & 202). Seawater-buffered diagenesis is localized in proximal FSz by permeable lithology and geothermally driven porewater convection (Fig. 190) (Higgins et al., 2018; Ahm et al., 2018). Destruction of CIEs by seawater-buffered diagenesis impedes stratigraphic correlation across complex lithologic changes between OPz and FSz. Section 5–66 is tied to datum (0.0 m) at base of Keilberg Mb. All other sections aligned by local correlation surfaces (red lines), based on lithologic and/or isotopic criteria that are open to reinterpretation. Cryogenian $\delta^{13}\text{C}$ excursions (CIEs) identified by number Cn1–5 (Fig. 151).

destruction of CIEs Cn2–4 in permeable grainstone of the proximal FSz. These CIEs reappear in more distal and less permeable facies of Okonguari Fm in sections 5–18–31 of the distal FSz (Fig. 170). Accordingly, Okonguari Fm should be mainly coeval with Gruis Fm in Otavi Group (Fig. 170), consistent with basinward extension of lower Ombaatjie Fm above Okonguari Fm in 5–45–50 (Figs. 62, 64 & 65). Progradation of Okonguari Fm grainstone ramp at that time accords with limited accommodation on the platform, indicated by the myriad of closely spaced exposure surfaces in Gruis Fm (Fig. 161).

In Bz (Tr2 & 3) and distal FSz (Tr1, 4, 5–1–19 & 22–25), Okonguari Fm is overlain by greenish-grey argillite and silty argillite of Narachaams Fm (An) (Hoffman and Halverson, 2008). This recessive unit (Fig. 18–19, 27, 32, 39, 41, 43–44, 58 & 170) is 93 m thick on average ($n = 46$) and carries spaced tabular pods or beds of brown-weathering authigenic (?) dolomite. Pyrite cubes are locally abundant (e.g., 2–32). Where not deeply weathered, the unit is seen to be characterized by silt-argillite couples, 0.65 cm thick on average, that are remarkably parallel and laterally continuous (Figs. 33C & D, 42D) but for exceptional low-angle truncation surfaces (Fig. 33E). The base of Narachaams Fm is

generally sharp and could be a disconformity, since Okonguari Fm is missing in Tr4 (Fig. 41) and parts of Tr5 (5–7–16, Figs. 43 & 58). The top of Narachaams Fm is also sharp and normally overlain by Franni-aus Fm carbonate rhythmite (Fig. 43). Narachaams Fm tapers up-slope and does not extend beyond section 5–25a (Fig. 58), where it is erosional cut-off by the Marinoan Ghaub Fm. Narachaams Fm appears to be a basin-floor deposit equivalent to Ombaatjie Fm b1 through lower b8 in Otavi Group (Fig. 170). An alternative interpretation correlates Narachaams Fm with only the lower b8 siltstone of Ombaatjie Fm (e.g., 5–66 expanded, Fig. 170), but the CIE Cn5 downturn in the underlying cycle b7 (Figs. 164 & 165) is missing in Okonguari Fm (Fig. 170).

In the distal FSz (1–1–26, 5–1–19 & 23–25), Narachaams Fm is disconformably overlain by Franni-aus Fm (Figs. 18–19, 27, 43–44, 58 & 170), which is a coarsening-upward stack of calcite and/or dolomite rhythmites, turbidites and debrites (Fig. 172). Its interpretation as a falling-stand wedge (Fig. S10), signalling Marinoan glacial onset at higher paleolatitudes, is well-worn (Hoffman, 1999, 2005, Hoffman, 2011b). The base of Franni-aus Fm is sharp and locally erosive, and it ends at the sub-Ghaub Fm glacial disconformity (Figs. 20A, 48A, 49A &

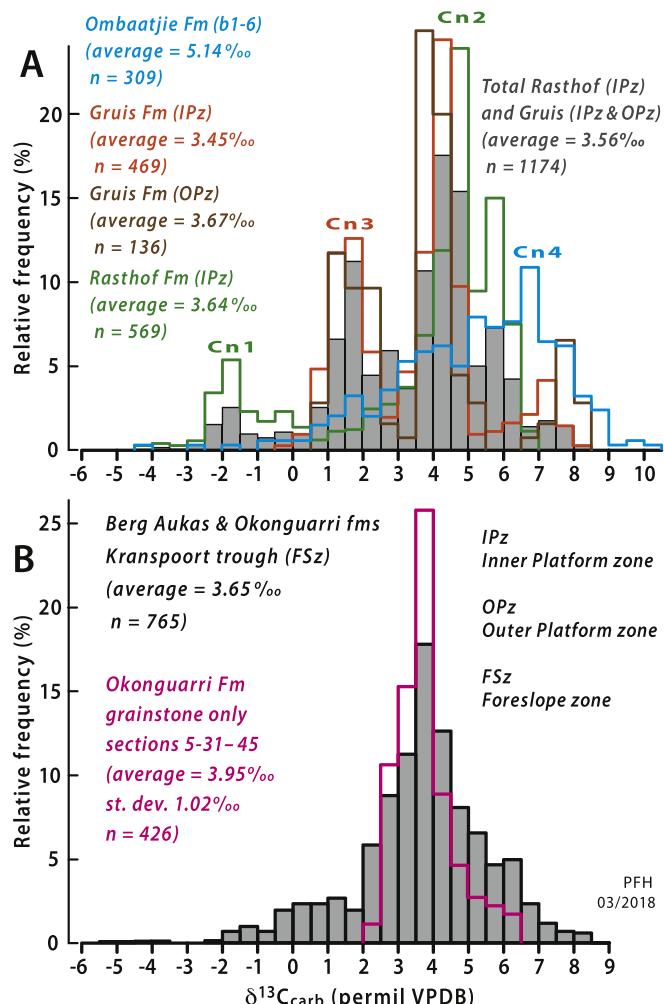


Fig. 171. Frequency histograms of $\delta^{13}\text{C}$ (VPDB) for Cryogenian formations in (A) IPz and OPz compared with (B) proximal FSz (Kranspoort trough, Fig. 43). Multimodal character of A (Cn1–5) is absent in B. Cn2 is defined in Rasthof Fm (Fig. 151); Gruis Fm peaks (brown and orange) near Cn2 are composites of Cn2 + Cn4 data in that formation (Figs. 151 & 162). Unimodal distributions in B are unlike any distribution in A and are attributed to early CIE-destructive seawater-buffered dolomitization of permeable grainstone on the upper FSz (Hoffman and Lamothe, 2019).

B) (Domack and Hoffman, 2011). The latter has ≤ 0.12 km of stratigraphic relief, with the result that Franni-aus Fm is locally cut out (e.g., 5–17, 20–22 & 26, Fig. 58), where paleogullies filled by stratified and massive diamictite (Figs. 60A–F & 61A–F) are floored by Narachaams or Okonguarri formations (Fig. 58). Coarse debrites in upper Franni-aus Fm contain tabular blocks and loose grains and grain-clusters of very coarse-grained and well-sorted oolite (Fig. 48E & F), heavily silicified where dolomitized. Individual ooid grains are ≤ 6 mm in diameter and no such coarse-grained oolite exists in Ombaatjie Fm of Otavi Group. The oolite is interpreted indigenously as having formed in the zone of breaking waves in FSz during glacioeustatic fall (Hoffman, 1999, 2005, Hoffman, 2011b; Hoffman and Halverson, 2008). Trower (2020) suggested that giant ooids occurring directly beneath Sturtian glacial deposits originated as low-density ikaite ($\text{CaCO}_3 \cdot 6\text{H}_2\text{O}$, specific gravity ~ 1.8), facilitating grain growth. Ikaite formation is favoured in cold waters with high dissolved phosphate content (Zhou et al., 2015). Runoff from newly emergent tropical shelves would have supplied phosphate during glacioeustatic falls. Continued sea-level fall caused emergence of ooid shoals, incipient lithification under meteoric

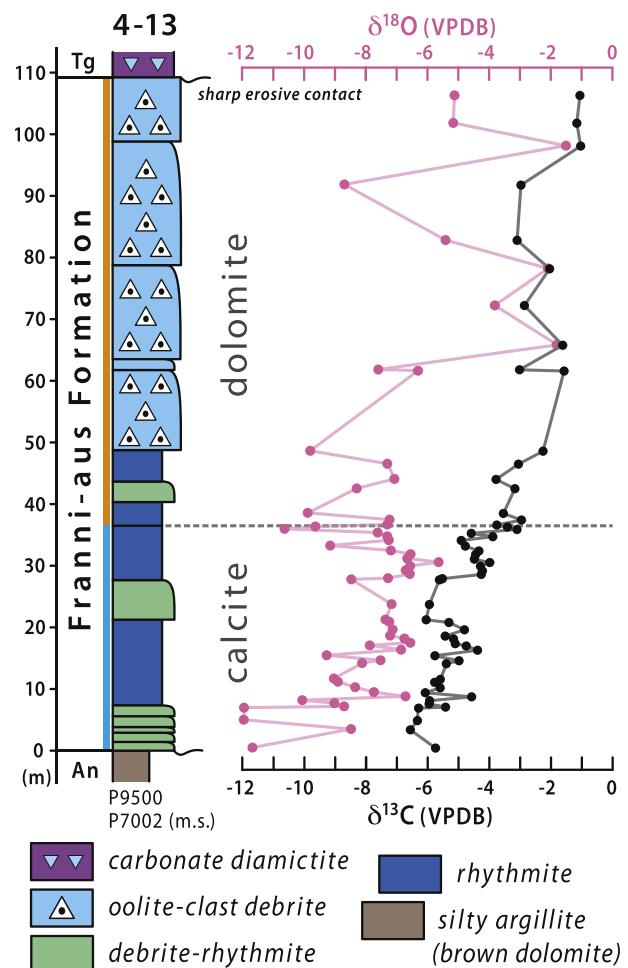


Fig. 172. Franni-aus Fm columnar section at 4-13 (Figs. 43, 44 & 170) with $\delta^{18}\text{O}$ and $\delta^{13}\text{C}$ records of recovery from CIE Cn5 (Fig. 151). Sequence-stratigraphic interpretation of Franni-aus Fm as a falling-stand wedge related to glacial onset (Hoffman, 2011a) connects Cn5 to Marinoan Snowball, consistent with first appearance in South Australia of ice-rafted debris at top of Trezona Fm and Trezona CIE recovery (Rose et al., 2012). Alternatively, coarser-grained and more-permeable upper Franni-aus Fm debrites (Fig. 48E & F) were selectively dolomitized under seawater-buffered conditions, whereas less-permeable micrite-rich lower Franni-aus Fm (Fig. 48C & D) is undolomitized. Oolite-clast debrite, inferred to have originated in proximal FSz and selectively dolomitized, is least ^{13}C -depleted.

conditions, and gravitational redeposition down-slope as oolite-clast debrites as observed (Fig. 48E & F). The coarsening-upward character of Franni-aus Fm debrites (Fig. 44) is also consistent with falling sea level. The Franni-aus Fm falling-stand wedge (Schlager and Warrlich, 2008) was glacially eroded and succeeded by Marinoan lowstand (LST) deposits of Ghaub Fm (Figs. 44 & S10). In this interpretation, Franni-aus Fm continued to accumulate in FSz for some time after the platform (i.e., Ombaatjie Fm b8) became emergent and marine sedimentation there ceased.

Franni-aus Fm records the ascending arm of CIE Cn5 (Fig. 172), as does Ombaatjie Fm cycle b8 (Figs. 165 & 166). The ascent rises to heavier values in Franni-aus compared with Ombaatjie Fm, consistent with earlier cessation of marine sedimentation on the platform relative to FSz. However, the difference in maximum $\delta^{13}\text{C}$ is small, $\geq 0.6\text{‰}$, implying that glacioeustatic fall was rapid relative to the rate of $\delta^{13}\text{C}$ change. In South Australia, the sub-Marinoan Trezona CIE recovery is linked to Marinoan glacial onset by the appearance of (ice-rafted?) extrabasinal debris at the top of the Trezona Fm (Rose et al., 2012,

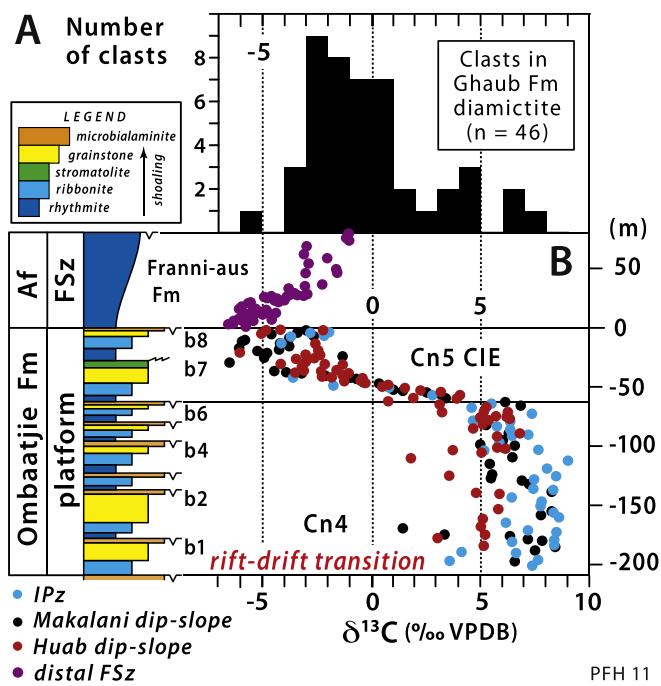


Fig. 173. $\delta^{13}\text{C}$ data for clasts in Ghaub Fm diamictites in Tr5 and their potential source rocks. (A) Frequency histogram of Ghaub-clast $\delta^{13}\text{C}$ ($n = 46$) from sections 5–6–15 (Fig. 46) (Fox et al., 2008). (B) Representative Ombaatjie Fm $\delta^{13}\text{C}$ profiles from inner (IPz) and outer (OPz) platform, and Frannis-aus Fm on distal foreslope (FSz). Ombaatjie and Frannis-aus formations are stacked for clarity of visual comparison with A. In reality, they occupy different zones and overlap in isotopic composition and age (Figs. 202 & 207). Ghaub clast data (A) are readily explained by derivation from b7–8 in IPz, where those cycles were glacially eroded to form Omarumba trough (Fig. 164), with additional contributions from Frannis-aus Fm of the proximal FSz, which is lithologically conspicuous among Ghaub Fm diamictite clasts (Fig. 50C–D). 3 clasts (6.5%) were evidently derived from Cn4 (cycle b6 and older), limiting >90% of Marinoan glacial erosion flux off Otavi platform to sources <100 m deep at glacial onset (Rose et al., 2012; Hoffman, 2011a).

2013). This supports coarse correlation of CIE Cn5 in Namibia and South Australia (Halverson et al., 2002, 2005), while permitting asynchronicity at fine scale since CIE recovery in Namibia accompanied extratropical ice-sheet growth whereas ice-rafting in South Australia occurred close to the paleoequator (Embleton and Williams, 1986; Evans and Raub, 2011).

3.3.6. Marinoan Ghaub Fm

High-latitude glaciations like those of the Late Paleozoic and Pleistocene are generally associated with relative sea-level rises in the vicinity of ice sheets (Visser, 1989; Boulton, 1990). This is because depression of the land surface under the load of an ice sheet (glaciostasy, GI) and rise of the sea surface in response to the gravitational attraction of the ice sheet (ice gravity, IG) combine to overwhelm the lowering of global mean sea level due to sequestering of seawater in ice sheets (glacio-eustasy, GE). Relative sea-level rise tends to increase over an orbitally-paced glacial cycle because glacial maxima are biased toward terminations, yielding ‘sawtooth’ $\delta^{18}\text{O}$ records of global ice volume and seawater temperature in deep-sea sediment cores (Imbrie et al., 2011). Snowball glaciations behave differently.

First, initial GE falls on a snowball Earth exceed the combined counteractive effects of GI and IG at continental margins because global ice-sheet volume is 2–3× larger than for high-latitude glaciations while average ice-sheet thickness is less due to slower accumulation and hence warmer ice (Rignot and Mouginot, 2012; Liu and Peltier, 2013; Creveling and Mitrovica, 2014; Benn et al., 2015). Second, marine ice shelves (aka sea glaciers) become progressively thinner during a snowball epoch in response to CO₂ rise and surface warming (Tziperman et al., 2012; Abbot et al., 2013). This causes ice grounding-lines to rise relative to sea level. Third, global ice-sheet volume shrinks in response to atmospheric CO₂ accumulation (Benn et al., 2015), causing net sea-level rise during a snowball epoch, opposite to late Quaternary glacial stages. Fourth, the longevity of snowball epochs (Rooney et al., 2015; Bao et al., 2018) and their paltry average rates of sediment accumulation (Partin and Sadler, 2016) favour the rise of relative to sea level due to tectonic subsidence accumulation (Fig. 163A). Accordingly, we should expect an early maximum in grounded glacial extent at a continental margin, followed by a long, slow and stepwise(?) grounding-line retreat. The early ice maximum would be accompanied by little sediment accumulation because of the weak meteoric ice flux at that time (Abbot et al., 2013). The slow retreat upslope should be accompanied by progressively rising rates of sediment accumulation due to an accelerating ice flux (Abbot et al., 2013; Benn et al., 2015). The snowball epoch ends with surface meltwater-driven perforation and disintegration of the tropical sea glacier starting at the paleoequator (Wu et al., 2021). Accelerated drainage and meltdown of grounded ice sheets follow, triggered by the loss of ice-shelf buttress and driven by ice-albedo, ice-elevation and sealevel feedbacks.

The extent of the sub-Marinoan unconformity and the zonal distribution of glacial-periglacial deposits (Ghaub Fm) appear to be broadly consistent with the snowball scenario just outlined. Ghaub Fm overlies a generally smooth and sharp erosion surface in virtually all sections in the distal FSz. Parallel grooves on this surface have a tilt-corrected azimuth of 210° in section 5–9 (Fig. 57), presumably indicating glacial flow (Domack and Hoffman, 2011). This erosion surface continues up the proximal foreslope, where it cut a notch that removed the seawardmost extent of Ombaatjie Fm (Fig. 164), and crosses OPz and IPz, where it carved the broad shallow Omarumba trough (Fig. 164). Ghaub Fm is typically absent in the most proximal FSz and OPz (Figs. 62, 64, 68 & 164), where the subglacial erosion surface is directly overlain by Keilberg Mb cap dolomite (Fig. 118A & B). Even in the Bz, where evidence for grounded ice is generally lacking, rises on the ancient seafloor were erosionally bevelled, presumably by the sea-glacier. This is documented for the relict Sturtian diamictite wedge in Tr2 (Figs. 32 & 35) and the structurally rotated pre-Marinoan panel (Macaria subbasin) in Tr3 (Figs. 26 & 39). The extent and paleo-depth range of the sub-Ghaub Fm erosion surface attests to an early Marinoan glacial maximum.

In Bz, Ghaub Fm consists exclusively of stratified deposits and is only 5.9 m thick on average ($n = 26$), or 10.2 m ($n = 15$) excluding zero-thickness sections. Ghaub Fm is thicker and coarser-grained in the distal FSz, averaging 50.5 m in Tr1 ($n = 26$) and 63.2 m in Tr5 (5–1–30, $n = 55$). Most distal FSz sections present alternations of massive and stratified diamictite (Figs. 45, 46 & 53), interpreted as grounding-line advances and retreats (King et al., 1991; Domack and Hoffman, 2011; Domack and Powell, 2018). Most sections have a terminal drape ≤ 16 -m-thick of chocolate-brown stratified diamictite (Bethanis Mb), choked with ice-rafter debris (Figs. 45, 46 & 54). Bethanis Mb is inferred to record the end-Marinoan deglaciation (Johnson et al., 2017). Ghaub Fm is thickest in the proximal FSz close to its upper limit, averaging 215 m ($n = 12$) in sections 5–31–42 (Fig. 62) constituting ‘Duurwater moraine’ (Fig. 43). These sections are composed mainly of massive diamictite

with discontinuous bodies of size-sorted carbonate-clast conglomerate. Ghaub Fm pinches out in the notch cut from Omibaatjie Fm (Figs. 62 & 64). The extent of massive diamictite tongues to the most distal FSz, combined with upslope thickening of Ghaub Fm as a whole, can be accounted for by overall grounding-line retreat (due to tectonic subsidence and ice-shelf thinning), accompanied by secular increase in ice flux and rates of sediment accumulation. Intertonguing of massive and stratified diamictites implies that grounding-line retreat was unsteady, with retreats and readvances perhaps paced by orbitally driven changes in ice sheet mass balance (Benn et al., 2015). Such grounding-line fluctuations would have been muted by the forward slope of the bed (Pollard and DeConto, 2007) and ultimately by the self-stabilizing effect of sediment accumulation (Duurwater moraine) itself (Alley et al., 2007).

The timescale of Ghaub grounding-zone wedge development is constrained by a U–Pb age for igneous zircon from one of the far-travelled volcanic ash layers in the middle Ghaub Fm immediately downslope from Duurwater moraine (5–28 and 30a, Figs. 58 & 43). A U–Pb (CA-IDTMS) age of 639.29 ± 0.26 Ma (Prave et al., 2016) was obtained from near 5–28 (K.-H. Hoffmann, pers. comm., 2018). The age is 3–4 Myr older than maximum age constraints on Marinoan termination from Central (Swakop) zone (Hoffmann et al., 2004) and Tasmania (Calver et al., 2013), and minimum constraints on its termination from different areas in South China (Condon et al., 2005; Zhou et al., 2019). Prave et al. (2016) assumed that discrete layers of non-local (airborne) volcanic ash could not have been deposited in the presence of an ice shelf. Hoffman et al. (2017a) counter-argued that for low paleolatitudes such ash layers were more likely to be deposited if a sea glacier was present. Ash that fell at any latitude on the sea glacier or an ice sheet feeding the sea glacier would be advected to the trans-equatorial ablation zone where, after collecting at the surface as ‘cryoconite’ (ice dust) it would be flushed through moulins to the sea-floor without dispersal by wave action. The estimated lag time between eruption and deposition would most often be within the uncertainty of U–Pb CA-IDTMS zircon dating (Hoffman et al., 2017a).

Ghaub Fm is almost entirely absent in OPz, appearing in only four sections (Fig. 88) overall ($n = 44$) and none in Tr5 (5–45–66, Fig. 68) or Tr6 (Fig. 71). In IPz, Ghaub Fm is thin and discontinuous (Fig. 118A–E), generally ≤ 2.0 m reaching 9.0 m in 10–3 (Fig. 135B & C). Where preserved, massive to sheared carbonate diamictite occupies depressions on a smooth and little-brecciated erosion surface (Fig. 118C) with up to a few meters of local relief. Ghaub Fm does not occur preferentially with respect to Omarumba trough (Fig. 164). Within the trough (8–3), azimuthal clast fabrics have strongly preferred SSW–NNE orientations (Fig. 57). Ghaub Fm in IPz is interpreted as lodgement tillite, deposited 80–150 km upstream from the grounding line in FSz. The contact in IPz between Ghaub Fm and Keilberg Mb is invariably sharp and without evident reworking (Figs. 118C & 119C), implying rapid synde-glacial marine inundation.

C-isotopic compositions of carbonate clasts ($n=46$) from Ghaub Fm in the distal FSz (5–6–15) were obtained (Fox et al., 2008) to constrain their sources (Fig. 173A). Most clasts have $\delta^{13}\text{C}$ between –4 and +1‰ (VPDB), consistent with derivation from the upper Frannis-aus Fm in FSz (Figs. 172 & 173B) and upper Omibaatjie Fm cycles b7 and 8 in IPz (Figs. 165 & 166). A Frannis-aus Fm source confirms lithologic fingerprints (coarse-grained oolite, Figs. 50C–D & 55C) and b7–8 clasts may have been eroded from Omarumba trough (Fig. 164). Above all, the clast $\delta^{13}\text{C}$ data (Fig. 173A) suggest that Frannis-aus Fm and cycles b7–8 were the youngest pre-Marinoan strata. Accordingly, the maximum depth of Marinoan erosion we observe on the platform is 150 m (Fig. 164) and over most of its area the depth of Marinoan erosion was ≤ 50 m.

Headwall erosion of Omibaatjie Fm upslope (5–44–45) from Duurwater moraine cuts Omibaatjie Fm cycles b1–6 that are ^{13}C -enriched (Fig. 170). It is therefore surprising that clasts with $\delta^{13}\text{C} \geq +5\text{\textperthousand}$ are so uncommon ($n = 3$, Fig. 173A). Perhaps it is because the headwall, being so steep (Fig. 43), had a small surface area to draw from compared with the top of the platform. A more testable explanation is that Omibaatjie Fm headwall erosion products occur in the more proximal Duurwater moraine (Fig. 62), which has yet to be sampled for detrital $\delta^{13}\text{C}$.

3.4. Ediacaran of Otavi/Swakop Group

3.4.1. Keilberg Mb

Keilberg Mb directly overlies Ghaub Fm or the associated Marinoan disconformity in all zones. It is everywhere composed of microcrystalline dolomite that is essentially devoid of organic matter. It is pale buff coloured where weathered and variably pinkish on fresh surfaces. It has a palimpsest peloidal texture lacking intraclasts or composite (grape-stone) grains (Figs. 67B & 131D). Keilberg Mb has a sharp basal contact (Fig. 55C) and a more gradational and marly top (Fig. 132A) overlain by deeper-water rhythmites and turbidites of middle Maieberg Fm member Tm2 (Figs. 44, 82 & 172). It was a product of a great marine transgression that accompanied Marinoan snowball deglaciation and whole-ocean warming (Yang et al., 2017). It belongs to a TST that began with Bethanis Mb and ended at a MFS in lower Tm2 member in Otavi Group (Fig. 82) and lower Karibib Fm in Swakop Group (Figs. 44). Keilberg Mb preceded and does not represent the MFS, as envisioned in alternative interpretations of post-Marinoan sequence stratigraphy (e.g., Kennedy and Christie-Blick, 2011; Nordsvan et al., 2019; Wallace et al., 2019). Its base marks the start of the Ediacaran Period (Knoll et al., 2006; Narbonne et al., 2012), which must therefore be diachronous on the time scale of the post-Marinoan marine transgression (Hoffman et al., 2007). This includes the millennial time scale for ice-sheet meltdown and the decamillennial time scales for whole-ocean warming (Yang et al., 2017) and GI adjustment (Creveling and Mitrovica, 2014).

The average thickness of Keilberg Mb in all zones is 16.9 m ($n = 140$) and 77.5 m ($n = 14$) in OPz. If 50 kyr is taken as a time frame for post-Marinoan sea-level rise (Yang et al., 2017), then average accumulation rates for Keilberg Mb must have exceeded 0.34 m kyr^{-1} overall and 1.55 m kyr^{-1} in OPz, since the transgression began before and continued after its deposition. These rates far exceed longer-term estimates of $0.04\text{--}0.05 \text{ m kyr}^{-1}$ for Tsumeb Subgroup (2000 m in 41–51 Myr). This is not surprising since TST accumulation is not limited by accommodation. Keilberg Mb is thickest in OPz (77.5 m) where Ghaub Fm is absent (Fig. 95), and thinnest on Duurwater moraine (average 1.65 m, $n = 10$) where Ghaub Fm is thickest (Figs. 43 & 62). The coarsest-grained peloids are found on Duurwater moraine (Fig. 67B), suggesting that winnowing might be responsible for Keilberg Mb attenuation there. Downslope from Duurwater moraine, Keilberg Mb averages 7.3 m ($n = 48$) in the distal FSz and 9.5 m ($n = 24$) in Bz. In IPz, Keilberg Mb is invariably thicker outside Omarumba trough than within the trough (Fig. 164), implying correlation between thickness and paleo-elevation (Fig. 169). However, Keilberg Mb is thicker in OPz (blue dots) than at equivalent or higher elevations in IPz (green dots, Fig. 169).

Keilberg Mb shares a distinctive set of sedimentary structures with basal Ediacaran cap dolomites elsewhere (Hoffman et al., 2011). In Keilberg Mb, their distribution is consistent with respect to vertical sequence and paleogeographic zone (Figs. 174 & 175). These structures include strata-bound sheet-crack cements (Figs. 34E & 55E–F), swaley low-angle cross-stratification (Figs. 67B & 119A–B), tubestone stromatolite (Figs. 67D–F, 119C–F & 120C–D), sedimentary volcanoes (Fig. 131C–E), and giant aggradational wave ripples (Figs. 56A–B &

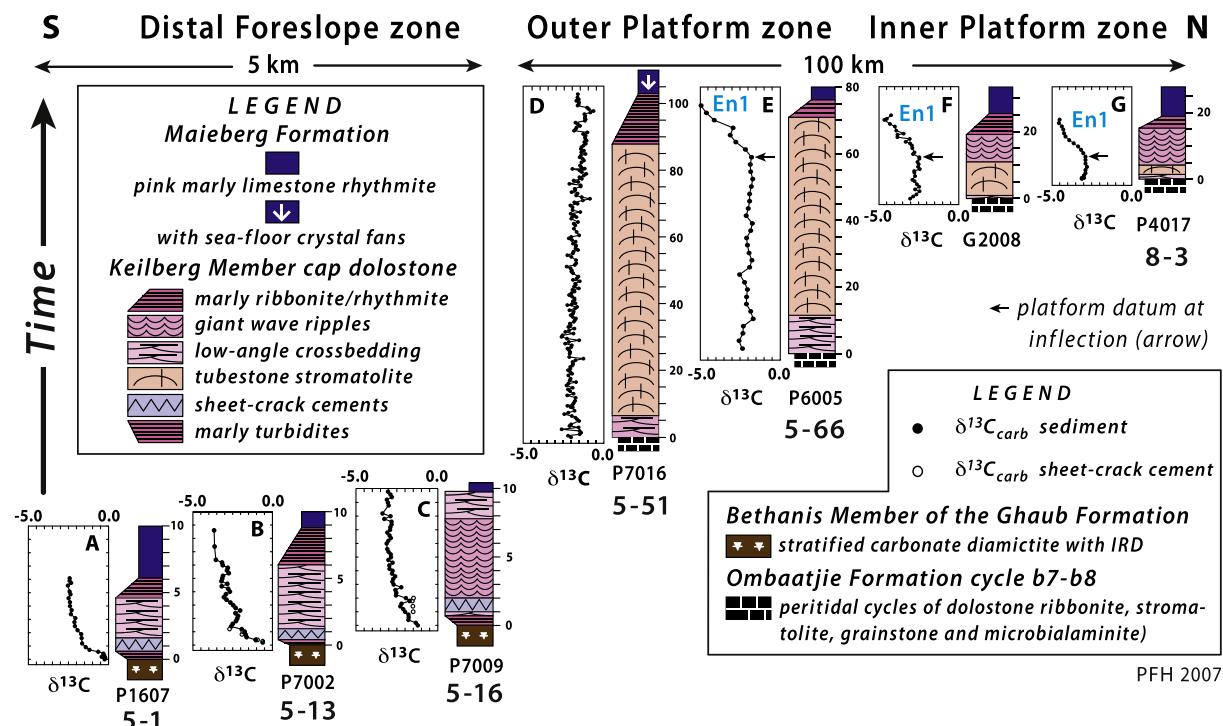


Fig. 174. Across-strike variation in Keilberg Mb lithofacies and $\delta^{13}\text{C}$ records from distal FSz at 5-1 (A) to IPz at 8-3 (G). G2008 (F) is from Arbeitsgenot (Fig. 4). Lateral variation in $\delta^{13}\text{C}$ records was related to diachronous deposition above wave-base and within euphotic zone during progressive marine inundation of FSz and platform as a result of Snowball deglaciation and whole-ocean warming (Hoffman et al., 2007; Creveling and Mitrovica, 2014; Yang et al., 2017). This implies an overall $\delta^{13}\text{C}$ change of -4‰ , from -0.5‰ at base of 5-1 to -4.5‰ at top of 8-3, on time scale of deglaciation and whole-ocean warming ($<20\text{--}100$ kyr, Yang et al., 2017). Seawater DIC could not be changed so rapidly, especially under the high $[\Sigma\text{CO}_2]$ condition necessary for Snowball deglaciation. In view of this, a secular decrease in temperature-dependent equilibrium fractionation between huge $\text{CO}_{2\text{gas}}$ and tiny CO_3^{2-} reservoirs (at low pH) was postulated (Hoffman et al., 2007), brought about by severe ocean warming (from 270 to ~ 325 K) accompanying global deglaciation (Yang et al., 2017). Fractionation reduction would shift carbonate $\delta^{13}\text{C}$ lighter, closer to $\delta^{13}\text{C}$ of $\text{CO}_{2\text{gas}}$. However, presence of Ombaatjie Fm cycle b8 beneath Keilberg Mb in 5-51 & 66 (D-E) (Fig. 68) means that absence of $\delta^{13}\text{C}$ inflection (arrows) in 5-51 cannot be attributed to lower elevation/older age, as previously inferred (Hoffman et al., 2007). Rather, CIE En1 may have been destroyed by seawater-buffered diagenesis at the shelf edge (e.g., 5-51) (Ahm et al., 2019). If the CIE was a (post-Marinoan) transient in open-ocean DIC, its destruction by seawater buffered diagenesis could simply reflect diagenetic reequilibration with seawater after the CIE's passing, provided that diagenesis was long-lived compared with DIC change. Sheet-crack cements are limited to the distal foreslope (A-C), contrary to an origin by permafrost-hydrate destabilization (Kennedy et al., 2001b), which predicts their preferred occurrence on the (emergent) upper foreslope and outer platform, but not the inner platform, which would have been insulated by thick ice (Fig. 178).

120A–B). The occurrence of giant wave ripples above tubestone stromatolite (Figs. 117, 174 & 175) would be consistent with increasing water-depth upward if stromatolite growth was limited by sunlight penetration and giant wave ripples to depths where only long-period waves touched the bottom (Allen and Hoffman, 2005a, b).

The vertical sequence of sedimentary structures in Keilberg Mb

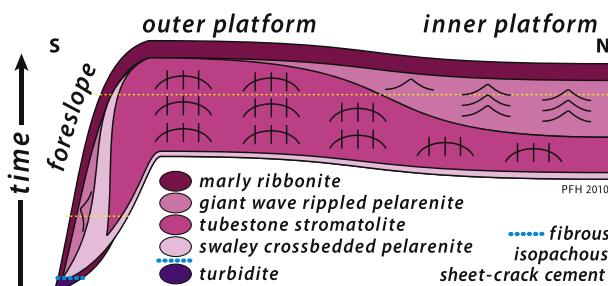


Fig. 175. Facies model for Keilberg Mb (post-Marinoan cap dolomite), based on representative columnar sections (e.g., Fig. 174). Vertical axis represents elapsed time, not stratigraphic thickness. Horizontal 'time' lines (e.g., dotted yellow lines) give synoptic facies distributions. Sheet-crack zone (Figs. 174, 34E, 55E & F) is taken to record early sea-level fall due to gravitational effect of regional ice-sheet meltdown (Clark, 1976; Hoffman and Macdonald, 2010; Creveling and Mitrovica, 2014).

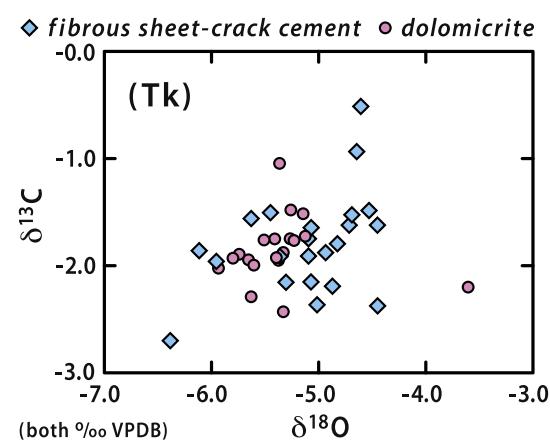


Fig. 176. $\delta^{13}\text{C}/\delta^{18}\text{O}$ crossplot for Keilberg Mb fibrous-isopachous sheet-crack dolomite cement (blue triangles) and coexisting dolomiticre (pink circles) in sections 5-1, 5-7, 5-13, 5-16 and 5-51 (Fig. 180B). Fibrous cement is not isotopically distinct from coexisting micrite, favouring cement production from sediment-buffered porewaters.

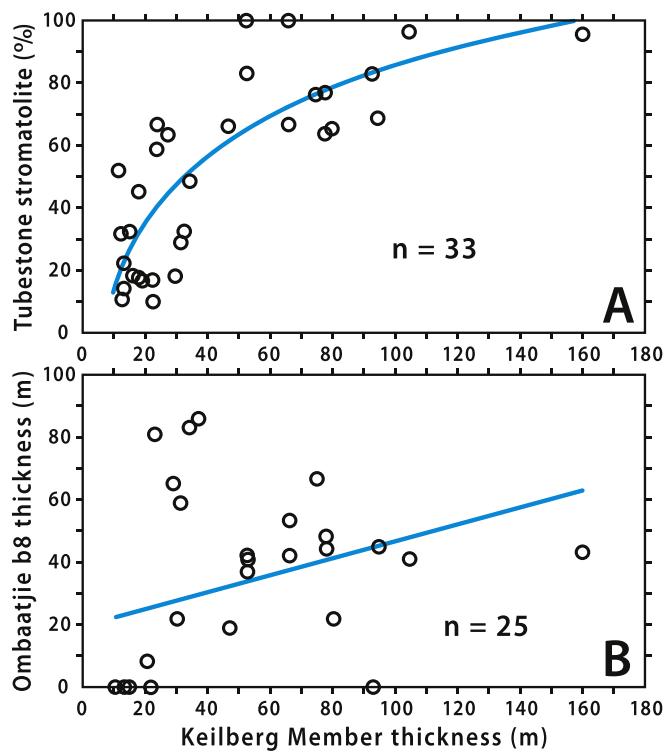


Fig. 177. Positive correlations between Keilberg Mb thickness and (A) percent tubestone stromatolite and (B) preserved thickness of underlying Ombaatjie Fm cycle b8 (Fig. 164). Since net accumulation equals deposition minus erosion, correlation in A could reflect less erosion of microbially bound (stromatolitic) versus loose sediment. Correlation in B could reflect more Keilberg erosion in Omarumba trough (Fig. 164), the orientation of which was parallel to wave propagation inferred from gutter stromatolite and giant wave-ripple orientations (Fig. 57). Although Omarumba trough originated through glacial erosion, its depth more than doubled as a result of non-uniform Keilberg accumulation (Fig. 164).

differs according to zone (Figs. 174 & 175). In distal FSz, a coarsening-upward set of dolomite turbidites occurs at the base (Figs. 55B & D, 174A–C). They culminate in a zone of buckled sheet-cracks filled by fibrous isopachous dolomite cement (Figs. 34E, 55E & F). The fibrous cement (FISC) is indistinguishable in isotopic composition from its peloidal dolomicrite host (Fig. 176). The fibrous structure suggests a repeated crack-seal process of formation, analogous to quartz fibres in tension cracks formed during low-grade metamorphism. Above the FISC zone, low-angle swaley crossbedding occurs with giant aggradational wave ripples in sections 5–21, 26b and 30 (Figs. 56A & B, 174A–C). If the wave ripples formed in water depths of 200–400 m (Allen and Hoffman, 2005a), the top of the platform may still have been emergent when Keilberg Mb was being deposited in the distal FSz (Hoffman et al., 2007). The top of Keilberg Mb in FSz is an increasingly marly and recessive ribbonite or rhythmite with turbidites (Fig. 174A & B). The initial regression below the FISC level could record regional sea level fall due to loss of IG as the local ice sheet retreats (Clark, 1976). Sheet cracks, which manifest vertical extension, might result from pore-fluid overpressure brought about by rapid sea-level fall and loss of hydrostatic head (Hoffman and Macdonald, 2010). This mechanism requires that the sediment be relatively impermeable, allowing pore-fluid overpressure to build up. Local ice-sheet retreat would have occurred early in the GE transgression (Fig. 175) because of its low-paleolatitude (Fig. 11).

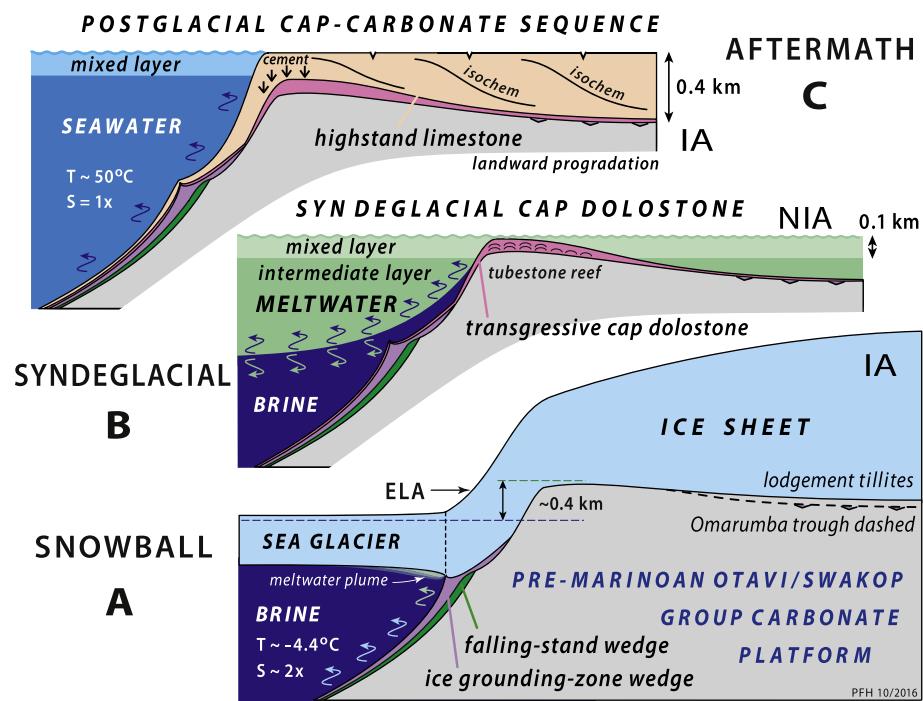
Progressing upslope, tubestone stromatolite (Figs. 69A & B, 175) first

appears in section 5–43 (Fig. 62). Its maximum development occurs in OPz, where Keilberg Mb as a whole is thickest (Figs. 174D & E, 175, 177A). Positive correlation between stromatolite abundance and total Keilberg Mb thickness (Fig. 177A) might reflect the stabilizing effect of a microbial mat, which increases net accumulation rate by simply reducing erosion. The average accumulation rate of 1.55 m kyr^{-1} (cited above) for OPz approaches the estimated limiting rate for cap-carbonate stromatolite accretion and lithification of 2.0 m kyr^{-1} (Bosak et al., 2013). Tubestone stromatolite is nowhere observed at the base of Keilberg Mb: it is everywhere preceded by physically stratified peloidal grainstone within which the stromatolites and genetically associated tube structures are nucleated (Figs. 118A & B, 118E, 119B & C, 120C & D). From this we infer that tube structure is not related to methane release from glacial-age (sub-Keilberg Mb) permafrost (Kennedy et al., 2001b). If the tubes originated by O_2 or CO_2 gas escape (Cloud et al., 1974; Hegenberger, 1987; Bosak et al., 2013), profligate development of such structures in basal Ediacaran cap dolomites (Corsetti and Grotzinger, 2005; Hoffman et al., 2011) may stem from rapid stromatolite growth rates, ultimately related to ocean warming, freshening and rapid GE rise during snowball deglaciation (Higgins and Schrag, 2003; Ridgwell et al., 2003; Shields, 2005; Pierrehumbert et al., 2011; Fabre et al., 2013; Creveling and Mitrovica, 2014; Yang et al., 2017; Hoffman et al., 2017a; Myrow et al., 2018). Models that attribute Marinoan cap dolomites to lack of detrital input (Kennedy and Christie-Blick, 2011; Nordsvan et al., 2019; Wallace et al., 2019) do not account for their idiosyncratic sedimentary structures.

In IPz, tubestone stromatolite thins more than Keilberg Mb as a whole, but maintains its position near but not at its base (Figs. 174F & G, 175). Giant wave ripples (Fig. 120A & B) occur above tubestone stromatolite in IPz (Figs. 174F & G, 175), implying that if long-period waves were responsible for their development (Allen and Hoffman, 2005a, b), they were capable of propagating 140 km across the drowned platform. Locally, the circular pits on the accreting surface that persist over time to make tube structures (Fig. 119E & F) become highly elongate in plan (Fig. 136C & D), forming 'gutter' stromatolites (James et al., 2001). The gutters are oriented SSW–NNE, nearly normal to giant wave ripple crestlines and parallel to preferred clast orientation in Ghaub Fm lodgement tillite (Fig. 57). The azimuthal data, although non-polar and limited in areal coverage, are compatible with SSW-directed ice movement and NNE-directed long-period wave propagation.

The presence of tubestone stromatolite and wave-generated bedforms in areas differing in paleoelevation by 0.25 and 0.8 km, respectively (Figs. 43, 58, 62, 174 & 175), implies that Keilberg Mb is diachronous (Hoffman et al., 2007). Neither the euphotic zone (stromatolite) nor the ocean mixed layer (wave ripples) could have spanned those depth ranges at any given sea level. Since Keilberg Mb is transgressive (i.e., deepening upward) overall and is associated with global ice-sheet meltdown, it is logical to assume that Keilberg Mb was deposited first in Bz and FSz, when the platform was emergent, and later in IPz and OPz when the platform was being flooded (Fig. 178B). Since Keilberg Mb hosts the descending limb of Ediacaran CIE, En1 (Fig. 179), its Bz and FSz records should fall earlier on the descending limb than the platform records. Keilberg Mb $\delta^{13}\text{C}$ records bear out this prediction (Hoffman et al., 2007): Bz + FSz records descend from 0 to $-3\text{\textperthousand}$ with concave-up trajectories (Figs. 174A–C & 180B), whereas OPz + IPz records descend from -2 to $-5\text{\textperthousand}$ with concave-down trajectories (Figs. 174E–G & 180A). The combined records define a sigmoidal trajectory with an overall decline of $-5\text{\textperthousand}$ (Fig. 180).

These data presented two immediate problems (Hoffman et al., 1998b; Higgins and Schrag, 2003; Hoffman et al., 2007). The first was to rationalize a $-5\text{\textperthousand}$ secular change on a time scale ($\leq 50 \text{ kyr}$) that was assumed to be significantly less than the residence time of C in the post-Marinoan meltwater lid (Fig. 178B). The second problem was the observed $1.5\text{\textperthousand}$ lateral increase in $\delta^{13}\text{C}$ in the seaward direction across the platform in isochronous sections (Fig. 180A). In an ocean–atmosphere with seawater $\text{pH} \leq 7.3$, the largest C pool is not HCO_3^- but $\text{CO}_{2\text{gas}}$



Omarumba trough (Fig. 164). Top of HST is a heavily silicified and dolomitized exposure surface atop regressive grainstone. HST accumulation is assumed to outlast meltwater lid, which is estimated to exist for 10^4 – 10^5 years (Yang et al., 2017). A and C are isostatically adjusted (IA); B is not adjusted (NIA) because deglaciation time scale is short (≤ 2 ka) relative to IA.

(Zeebe and Wolf-Gladrow, 2001). Consequently, there is a large equilibrium fractionation between CO_3^{2-} and the C pool because $\alpha = -6.3\%$ at 25°C for CO_3^{2-} with respect to $\text{CO}_{2\text{gas}}$. In contrast, $\alpha = -1.5\%$ with respect to HCO_3^- , the dominant C species at pH = 8.2 (pre-industrial seawater). Because of the large α at low pH, the temperature dependence of the equilibrium fractionation shifts the composition of the relatively tiny CO_3^{2-} reservoir significantly lighter (i.e., smaller fractionation) as temperature rises. A seawater temperature rise from 0 to 55°C (Yang et al., 2017) (Fig. 178C) is quantitatively sufficient to shift the $\delta^{13}\text{C}$ of CO_3^{2-} ~5‰ lighter (Zeebe and Wolf-Gladrow, 2001). Therefore, the secular change in $\delta^{13}\text{C}$ observed in Keilberg Mb could in principle be a record of surface ocean warming. Similarly, the gradient across the platform could record a synoptic temperature gradient, with colder water near the shelf break due to upwelling (Fig. 178B), and warmer water landward where cold deepwaters do not exist (Higgins and Schrag, 2003; Hoffman et al., 2007). The magnitude of the isotopic gradient can be satisfied with a temperature gradient of $0.1^\circ\text{C km}^{-1}$. Warm sea-surface temperatures are consistent with the virtual absence of organic matter in Keilberg Mb, despite evidence for benthic microbial mats (tubestone stromatolite), since respiration efficiency rises more with temperature than does organic production (Craine et al., 2010).

The acquisition of $\delta^{44}\text{Ca}$ and $\delta^{26}\text{Mg}$ data from Keilberg Mb and other Marinoan cap dolomites gave rise to an alternative explanation (Ahm et al., 2019) for the observed lateral $\delta^{13}\text{C}$ gradient across the platform (Fig. 180A). For independent reasons, Ca and Mg isotopes in tandem provide an effective means of distinguishing seawater-buffered from

Fig. 178. Idealized 3-stage model of post-Marinoan deglaciation and cap-carbonate sedimentation across Otavi/Swakop Group cratonic margin. Large vertical exaggeration is not uniformly scaled. Model assumes that deglaciation time scale was brief relative to isostatic adjustment (Creveling and Mitrovica, 2014) and ocean destratification (Yang et al., 2017). (A) Snowball state with lowered sea level (Creveling and Mitrovica, 2014), floating sea glacier (Goodman and Strom, 2013), grounded ice sheet (Benn et al., 2015), and eddy-rich deep-ocean brine (Jansen, 2016) with grounding-line meltwater plume (Hoffman et al., 2017a). Ice grounding-zone wedge (Ghaub Fm) consists of glacially advected debris (Domack and Hoffman, 2011) eroded from Omarumba trough and upslope extension of falling-stand wedge (Frannis-aus Fm) dating from glacial onset (Fig. S10). Lodgement tillites are preserved in Omarumba trough. (B) Transgressive cap dolomite (Keilberg Mb) was deposited diachronously in mixed layer of meltwater lid as platform was progressively flooded during deglaciation and subsequent whole-ocean thermal expansion (Yang et al., 2017). Thickest tubestone stromatolite is on outer platform. (C) Regressive 0.4–0.7-km-thick Maieberg Fm HST (Tm2-3) was diachronously deposited during landward progradation of ‘isochems’ (Hoffman, 2011a), defined as surfaces of uniform $\delta^{13}\text{C}$ (Fig. 183). Crystal fans, formerly aragonite sea-floor cement, formed during maximum flooding of HST and are localized at shelf break and over sea-floor topographic features like Duurwater moraine (Fig. 43) and sides of

sediment-buffered diagenesis (Higgins et al., 2018; Ahm et al., 2018). Fluid-buffered diagenesis is observed to occur on the flanks of carbonate platforms where seawater invades the sediment in response to geothermally driven porewater convection within the platform (Kohout, 1967; Wilson et al., 2001; Wilson, 2003, 2005; Higgins et al., 2018). Carbonate-buffered diagenesis prevails in platform interiors since porewaters progressively equilibrate with carbonate sediments along their advective pathways (Ahm et al., 2018).

Since Ca, Mg and C have broadly similar molar concentrations in carbonate sediments, carbonate $\delta^{13}\text{C}$ should also be susceptible to alteration during fluid-buffered diagenesis if the C-isotopic composition of seawater DIC differs from that of the original sediment (Higgins et al., 2018; Ahm et al., 2018). Accordingly, heavier $\delta^{13}\text{C}$ values in more seaward Keilberg Mb sections (Fig. 180A) might reflect a greater degree of seawater-buffered diagenesis. Lighter $\delta^{13}\text{C}$ values in the platform interior would not then reflect the composition of open-ocean (meltwater lid) DIC (Ahm et al., 2019; Hoffman and Lamothe, 2019; Crockford et al., 2021). Volumetrically small epi-platform ('bank-top') waters may have had a sufficiently short residence time to allow the large secular $\delta^{13}\text{C}$ changes recorded there (Fig. 180A). Conversely, the absence of an inflection to lighter values at the top of Keilberg Mb in 5–51 (Fig. 174D) could simply reflect more complete diagenetic equilibration in outermost OPz (Ahm et al., 2019), rather than an earlier Keilberg–Tm2 member transition as previously inferred (Hoffman et al., 2007). Along similar lines, preferential dolomitization of Keilberg Mb compared with Tm2 (Fig. 181) could simply reflect greater permeability

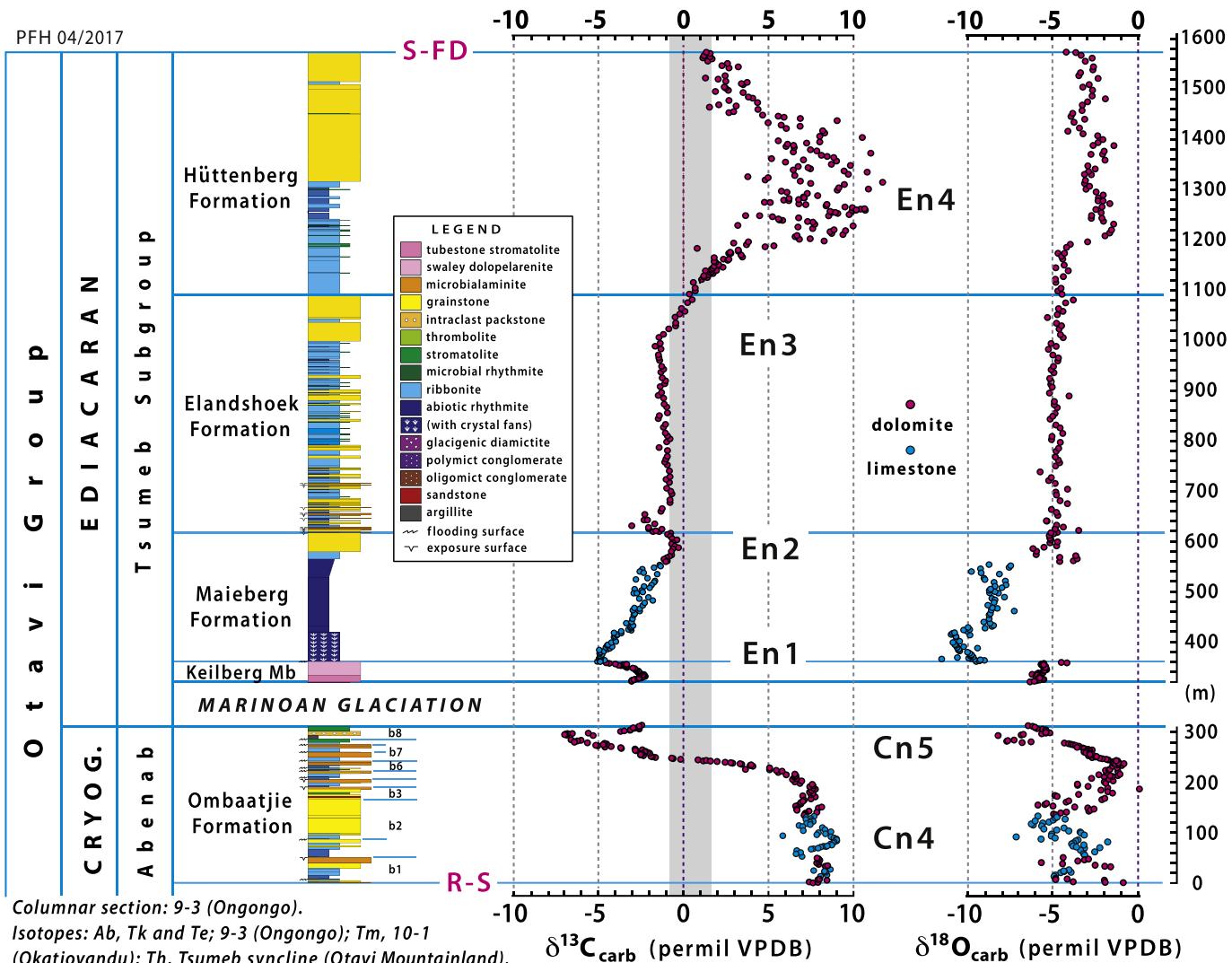


Fig. 179. Composite columnar section of post-rift Otavi Group (Ombaatjie Fm and Tsumeb Subgroup) with $\delta^{13}\text{C}$ and $\delta^{18}\text{O}$ records. Columnar section is from 9 to 3. Isotope records: Maieberg Fm, 10–1; Hüttenberg Fm, Tsumeb (OML); Keilberg Mb and all others, 9–3. Red dots are dolomite and blue dots calcite. CIEs numbered Cn4-5 and En1–4. Magenta R-S, rift-to-shelf transition; S-FD, shelf-to-foredeep transition.

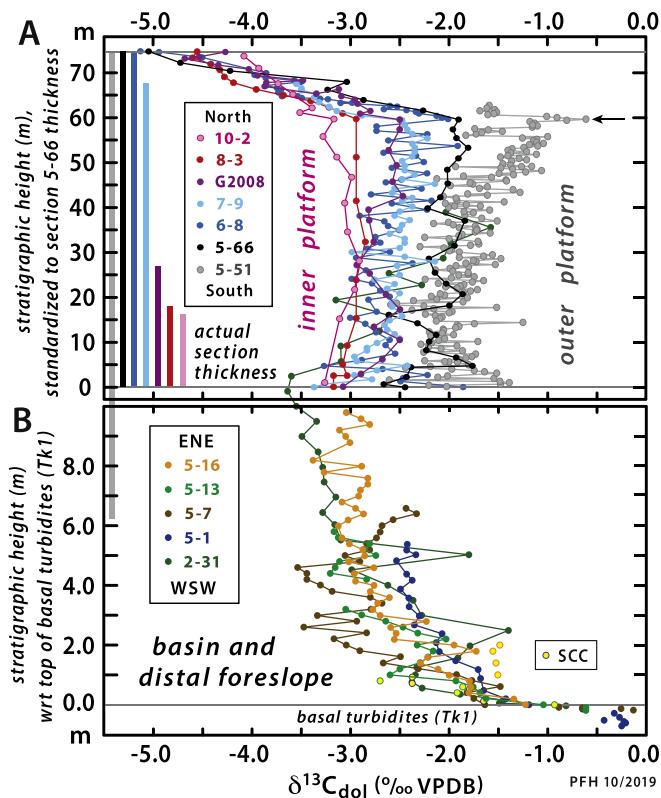


Fig. 180. Keilberg Mb $\delta^{13}\text{C}$ records from (A) IPz and OPz, and (B) FSz and Bz. Platform records in A are normalized to section 5–66 at deflection (black arrow at 60 m) and by total thickness. Actual thicknesses are shown as colour-coded vertical bars. Grey bar (section 5–51, 104 m) is hung from top. G2008 is from Arbeitsgenot (Fig. 4). Datum is base Keilberg Mb in A. In B, datum is top of basal turbidites (Tk1, Fig. 55B & D), or base of Keilberg Mb where basal turbidites are absent. Sections in B are scaled by actual thickness (normalized records in Fig. 186B). Note that section 2–31 at Vrede south dome (Fig. 32) is 16.5 m thick and continues upward in A (green dots) with no scale change. Yellow dots in colour-coded rings are from fibrous dolomite sheet-crack cement (SCC). The overall sigmoidal record (A + B) was interpreted in terms of diachronous deposition related to glacioeustatic rise, accompanied by severe mixed-layer warming responsible for large rapid $\delta^{13}\text{C}$ decline (Hoffman et al., 2007). In this interpretation, the observed N to S (IPz to OPz) $\delta^{13}\text{C}$ gradient in isochronous platform records (A) records a sea-surface temperature gradient ($0.1\text{ }^{\circ}\text{C km}^{-1}$), warming with distance from cold-water source at FSz (Hoffman et al., 2007). In contrast, Ahm et al. (2019) interpret the lateral $\delta^{13}\text{C}$ gradient in A to spatially variable early diagenesis, whereby IPz experienced sediment-buffered diagenesis (preserving sedimentary values) but seawater-buffered diagenesis (Fig. 190) was progressively more important seaward (southward), causing $\delta^{13}\text{C}$ to be shifted toward heavier values reflecting DIC in the evolving meltwater lid (Fig. 178B-C). Diagenetic interpretation may better account for seaward increase in point-to-point variability, but higher-resolution data are needed from condensed IPz sections for valid comparison.

and hence diagenetic alteration of peloidal grainstone compared with micritic rhythmite (Ahm et al., 2019). The notably more coarsely-recrystallized and silicified tubestone stromatolite in OPz (Figs. 67D–F, 79E & F, 94E), as compared with IPz (Figs. 119B–F, 136C & D, 175), is consistent with an early diagenetic interpretation (Ahm et al., 2019; Hoffman and Lamothe, 2019) of the lateral $\delta^{13}\text{C}$ gradient (Fig. 180A).

3.4.2. Maieberg Fm

Maieberg Fm (Otavi Group) is 0.23–0.72 km thick (Figs. 144 & 145)

and divisible into three members, Tm1–3 (Fig. 181). Tm1 is the Keilberg Mb (Hoffman et al., 1996). Tm2 consists of marly to pure calcite rhythmite with dolomite turbidites initially (Fig. 121B). Its lowest $\frac{1}{3}$ locally contains benthic former-aragonite cement (5–45 & 51, 6–5, 9–3 & 4, 11–5 & 10) (Figs. 80A–F, 81A & B, 132A–C). Its upper $\frac{2}{3}$ displays m-scale swaley and hummocky cross-stratification (Fig. 121C & D). Certain sections are entirely dolomitized (e.g., 7–1 & 11–10, Fig. 181). Tm2 encompasses the upper TST, MFS and lower HST of the post-Marinoan cap-carbonate depositional sequence (Hoffman and Schrag, 2002). In contrast to the bracketing Omaatjie and Elandshoek formations (Fig. 179), Maieberg Fm lacks evident higher-order cycles. In this regard, it is analogous to Rasthof Fm, both in relation to Sturtian glaciation and to its associated multicyclic Devede and Gruis formations (Fig. 133).

Historically, the anomalous sequence-stratigraphic character of Rasthof (0.19–0.45 km) and Maieberg (0.23–0.72 km) was the first indication that Cryogenian glaciations were long-lived (Hoffman et al., 1998a; Halverson et al., 2002). If short-lived, postglacial sea level would have returned to its preglacial level with little accumulated tectonic subsidence. Accommodation would disappear after GI adjustment. If short-lived, permanent accommodation would depend on net synglacial erosion, which was evidently limited (Table 6, Figs. 30 & 164). The impact of Rasthof and Maieberg sequence stratigraphy was reinforced by knowledge that analogous sequence-stratigraphic anomalies had been found (but not attributed to glacial duration) in South Australia (Tapley Hill and Brachina formations) and NW Canada (Twitya and Sheepbed formations) (Preiss and Forbes, 1981; Aitken, 1982; Eisbacher, 1985; Christie-Blick et al., 1995). More was learned about the nature of Cryogenian glaciations from cap-carbonate sequences than from glacial deposits.

The nadir of CIE En1 coincides with the MFS in lower Tm2 (Figs. 82, 117, 179 & 181), defined lithologically as the most marly and condensed interval (Figs. 121A & 131A). There is a conspicuous offset in $\delta^{18}\text{O}$ and less so in $\delta^{13}\text{C}$ (Fig. 182) between dolomite (Tm1 and 3) and calcite (Tm2). Dolomite–calcite isotopic discrimination in Maieberg Fm (Fig. 182) is distinct from that in Omaatjie Fm b1–6 (Fig. 167). In Maieberg Fm, calcite and dolomite fields are more discrete, and dolomite is 1.47 and 3.25‰ heavier in $\delta^{13}\text{C}$ and $\delta^{18}\text{O}$, respectively (Fig. 182). This is indistinguishable from extrapolated low-temperature dolomite–calcite equilibrium fractionation (Fritz and Smith, 1970; Sheppard and Schwarcz, 1970; Friedman and O’Neil, 1977), favouring a low-temperature marine origin for Maieberg Fm dolomite (Hoffman, 2011a), consistent with clumped-isotope ($\Delta^{13}\text{C}^{18}\text{O}^{16}\text{O}$) paleothermometry for Ediacaran early diagenetic dolomitization in South China (Chang et al., 2020).

Plotted against stratigraphic height, $\delta^{13}\text{C}$ trajectories through Tm2 vary systematically from S to N across the platform (Fig. 183). Although the variance is $\leq 1.0\text{‰}$ at MFS, it is 3.0 and 2.5‰ at the top of Tm2 and 3, respectively. The change with distance from the shelf break is opposite to that in Keilberg Mb (Fig. 183), with heavier values in more northerly Tm2 sections (10–1) and lightest values at the shelf break (5–66). Since the 0.2–0.4-km-thick HST was likely deposited over multiples of the ocean–atmosphere C residence time, the return to heavier values following En1 nadir could reflect a change in the composition of neritic DIC. If we assume strictly temporal variability in $\delta^{13}\text{C}$ of a spatially well-mixed DIC pool, then the upward fanning of $\delta^{13}\text{C}$ trajectories must reflect differences in accumulation rate. More rapid accumulation occurred at the shelf edge while $\delta^{13}\text{C}$ was still lighter. Slower accumulation occurred farther inboard, where accommodation was not filled until $\delta^{13}\text{C}$ returned to heavier values (Fig. 183). The resulting pattern of landward progradation from the shelf edge would produce a family of northward-dipping surfaces, or ‘isochems’ (Fig. 178C), of equal $\delta^{13}\text{C}$ composition. A testable prediction of the above interpretation is that the sequence boundary at the top of the Maieberg Fm represents a surface of non-deposition for a time interval during which $\delta^{13}\text{C}$ rose by 2.5‰. The test requires isotopic data from the Maieberg–Elandshoek Fm transition

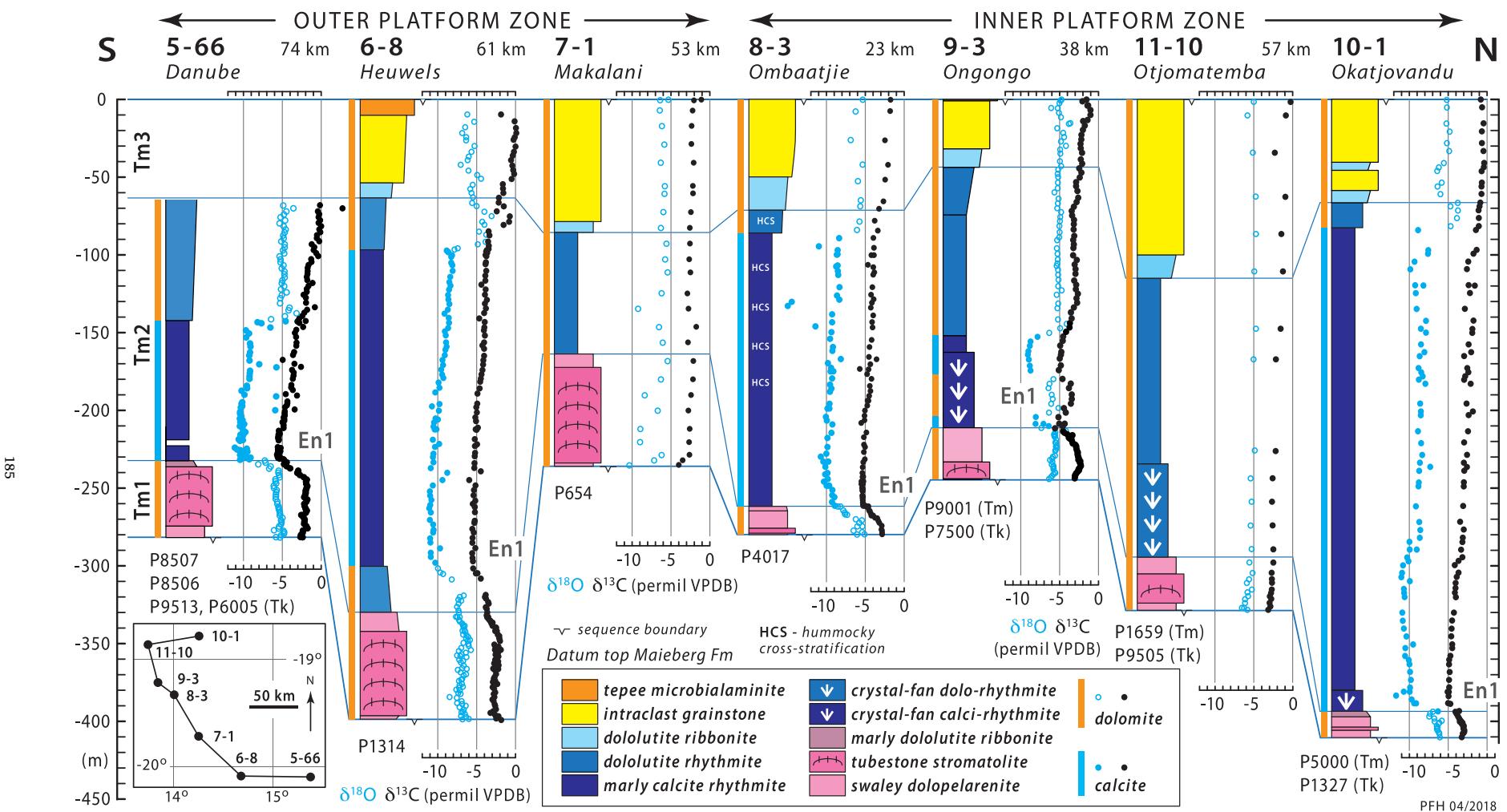


Fig. 181. Selected Maieberg Fm columnar sections with $\delta^{13}\text{C}$ (black) and $\delta^{18}\text{O}$ (blue) records from OPz and IPz. Datum is top of member Tm3, but arbitrary in 5-66 where Tm3 is not preserved due to folding. Maieberg Fm presents a single thick transgressive-regressive depositional sequence without higher-order parasequences. This reflects accommodation accumulated from tectonic subsidence and minor erosion during prolonged Marinoan glaciation with little compensatory sediment accumulation (Hoffman et al., 1998a). CIE En1 (Fig. 151) was destroyed in sections where middle Maieberg Tm2 member is completely dolomitized (7-1 and 11-10), and partially destroyed where Tm2 dolomitization is incomplete (9-3). See Fig. 182 for $\delta^{13}\text{C}/\delta^{18}\text{O}$ crossplot of these data.

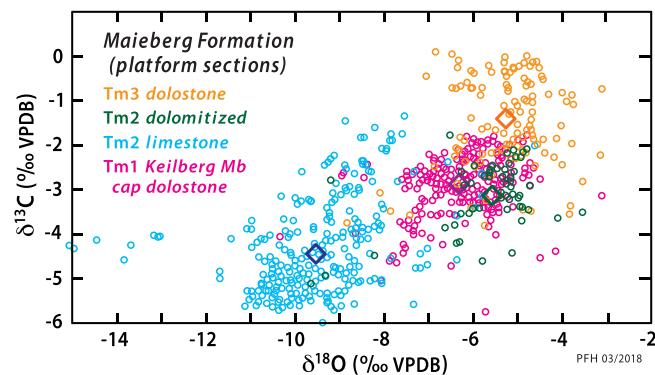


Fig. 182. $\delta^{13}\text{C}/\delta^{18}\text{O}$ cross plot of Maieberg Fm dolomite and limestone in Otvai Group (Fig. 181). Data are colour-coded as indicated: Tm1 (Keilberg Mb), magenta; Tm2 limestone, blue; Tm2 dolomite, green; Tm3 dolomite, orange. Average for each subset shown as large colour-coded diamonds. Unlike partially dolomitized Omibaatjie Fm (Fig. 167), Maieberg Fm $\delta^{13}\text{C}/\delta^{18}\text{O}$ values are consistent with equilibrium fractionation between dolomite and calcite extrapolated to low-temperature (Friedman and O'Neil, 1977), with dolomite 2–3× heavier than calcite in $\delta^{18}\text{O}$ compared with $\delta^{13}\text{C}$.

at the shelf edge, which so far has not been sampled (see 4.1.5.).

Tm2 is locally dolomitized (Fig. 181) and cation exchange was accompanied by $\leq 3.0\text{\textperthousand}$ relative enrichment of undolomitized sections (Figs. 184 & 182). The dolomite is fabric-retentive and volume-

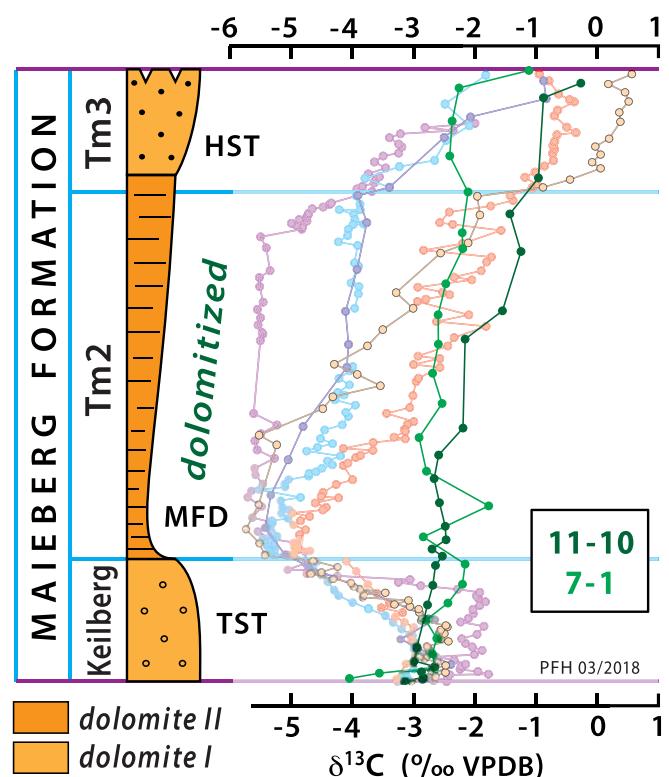


Fig. 184. Normalized Maieberg Fm $\delta^{13}\text{C}$ records from sections 7–1 and 11–10 (Fig. 181), where Tm2 is completely dolomitized ('dolomite II'), compared with faded sections where Keilberg Mb and Tm3 are dolomitized ('dolomite I') but Tm2 is largely calcitic (Fig. 183). $\delta^{13}\text{C}$ records of Tm2-dolomitized sections (green dots) follow mixing-lines between mid-Keilberg and Tm3 values. In Tm2, they are shifted $\leq 3.0\text{\textperthousand}$ heavier relative to undolomitized sections.

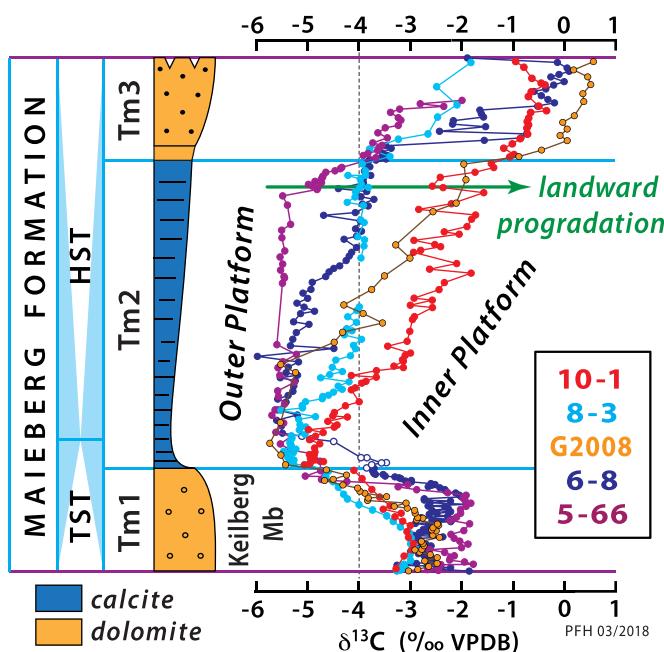


Fig. 183. Normalized $\delta^{13}\text{C}$ records from Maieberg Fm in OPz (5–66, 6–8) and IPz (G2008, 8–3, 10–1). G2008 is from Arbeitsgenot (Fig. 4). Normalization gives each member (Keilberg, Tm2, Tm3) the same relative thickness in all sections (see Fig. 181 for actual thicknesses). Open circles in lower Tm2 at 6–8 are dolomitized. Note reversal of IPz-OPz $\delta^{13}\text{C}$ gradient between Keilberg Mb (Fig. 180A) and Tm2–3. Divergent $\delta^{13}\text{C}$ records through Tm2 are attributed to diachronous filling of accommodation across platform from outer rim (5–66) northward (10–1) over time (Fig. 178C), assuming spatially uniform $\delta^{13}\text{C}$ values at all times (Hoffman, 2011a). For example, when $\delta^{13}\text{C}$ was $-4\text{\textperthousand}$ (dotted vertical line), section 5–66 was filled to Tm3 level, sections 6–8 and 8–3 were filled to upper Tm2, and 5–66 was filled to lower Tm2. Accordingly, 'isochores' (surfaces of uniform $\delta^{13}\text{C}$) dip northward (Fig. 178C) in direction of progradation. Asynchronous aggradation to sea level is indicated by variable $\delta^{13}\text{C}$ at top of Tm3.

conserved. Large $\delta^{13}\text{C}$ changes associated with dolomitization are found not only in IPz and OPz (Fig. 184), but also in FSz and Bz (see 3.4.4.). Where dolomitized, $\delta^{13}\text{C}$ values in Tm2 are shifted toward a mixing line between dolomites of lower Tm1 and 3 (Figs. 184). Upper Tm1, which normally trends to lighter values, is also shifted heavier where Tm2 is dolomitized (Fig. 184). This implies that isotopic alteration was not limited to strata normally preserved as calcite. We therefore caution that fabric-retentive, volume-conserving dolomitization of early Ediacaran age is not always isotopically benign.

3.4.3. Elandshoek and Hüttenberg formations

The sequence boundary at the top of Maieberg Fm (Figs. 178 & 179) signifies the filling of accommodation space created by tectonic subsidence and erosion during the Marinoan snowball. The overlying 0.5–1.4-km-thick stack of peritidal dolomite cycles, constituting Elandshoek and Hüttenberg formations (Figs. 145, 179 & 185), was accommodated by ongoing thermal subsidence (Fig. 163A) (Halverson et al., 2002). Relative to background subsidence, Maieberg Fm was a 'catch-up' stage and Elandshoek and Hüttenberg were 'keep-up' stages (Schlager, 1981). For the latter, we assume that rates of sediment accumulation, averaged over multiple cycles, decayed stratigraphically upward as a function of the square root of time (Fig. 163A).

In IPz, the base of Elandshoek Fm is a mappable sequence boundary (Fig. 132D) between silicified HST grainstone (Tm3) and tepee-capped peritidal ribbonite cycles of basal Elandshoek Fm (Te1) (Figs. 130, 144 & 145). The sequence boundary occurs close to the peak of CIE En2 (Figs. 179). Elandshoek and Hüttenberg formations are generally subequal in thickness (Fig. 145), aside from Tr6 (Huab cusp) where deep sub-Mulden Group erosion occurred (Hoffman, 2021a). The base of

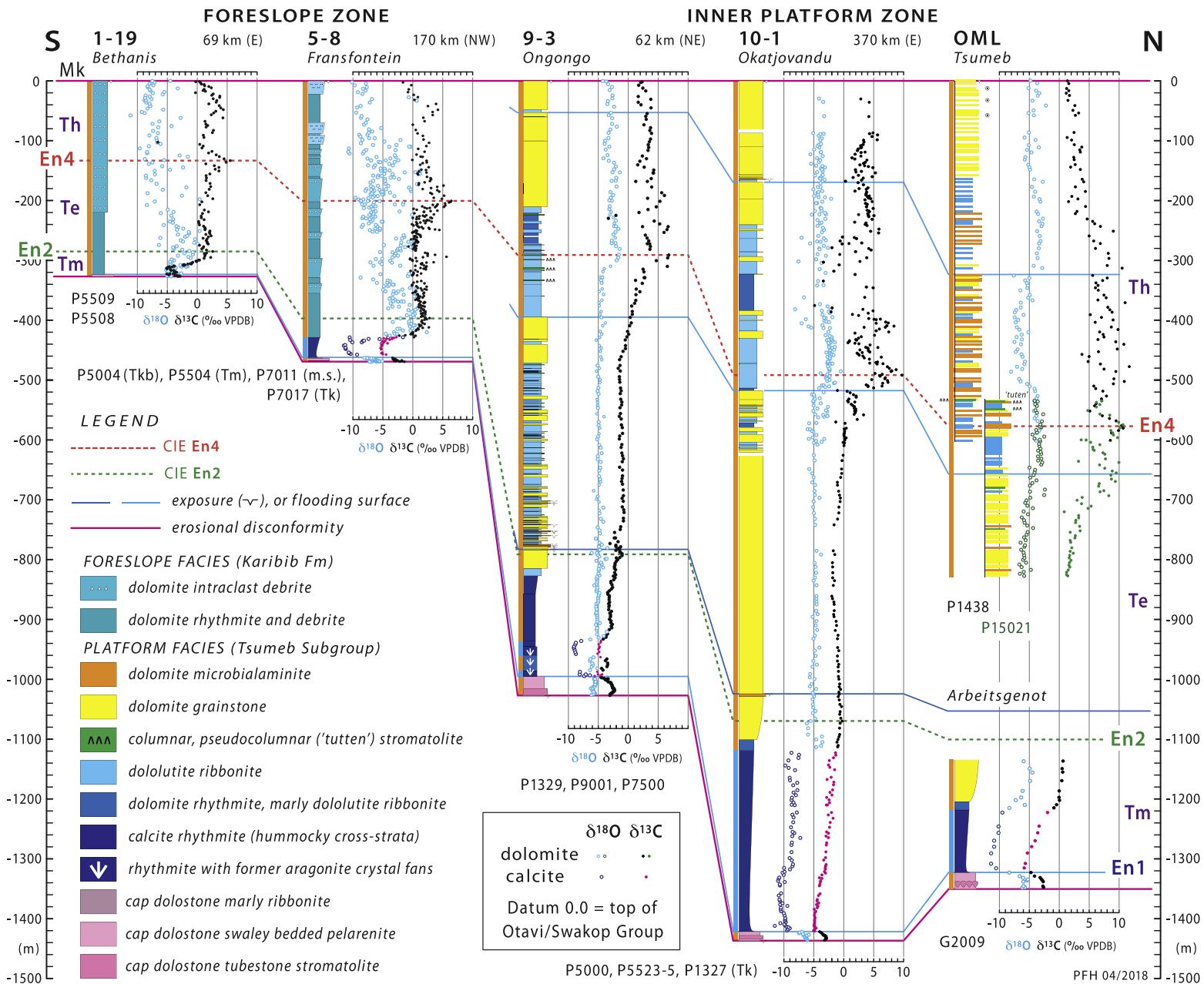


Fig. 185. Correlative early Ediacaran columnar sections with $\delta^{13}\text{C}$ and $\delta^{18}\text{O}$ records from FSz (Karibib Fm) and IPz (Tsumeb Subgroup). Extends Fig. 186 but at reduced scale to accommodate thicker IPz sections. G2009 (lower right) is from Arbeitsgenot (Fig. 4). CIEs En2 and En4 (dashed green and red lines), used for correlation between Tsumeb Subgroup (IPz and OPz) and Karibib Fm (FSz and Bz), approximate but do not exactly correspond to exposure or flooding surfaces (solid blue lines) used to divide Tsumeb Subgroup (shelf) into formations. $\delta^{18}\text{O}$ is strongly correlated with mineralogy in Maieberg Fm (Fig. 182). Correlation between closely adjacent overlapping sections (P1438 and P15021) at Tsumeb is based on pseudo-columnar stromatolite ("tutten") beds (Fig. 132F) as indicated. Base and top of combined section on south limb of Tsumeb anticline are at $-19^{\circ}14.23' / 17^{\circ}44.75'$ and $19^{\circ}14.92' / 17^{\circ}44.42'$, respectively.

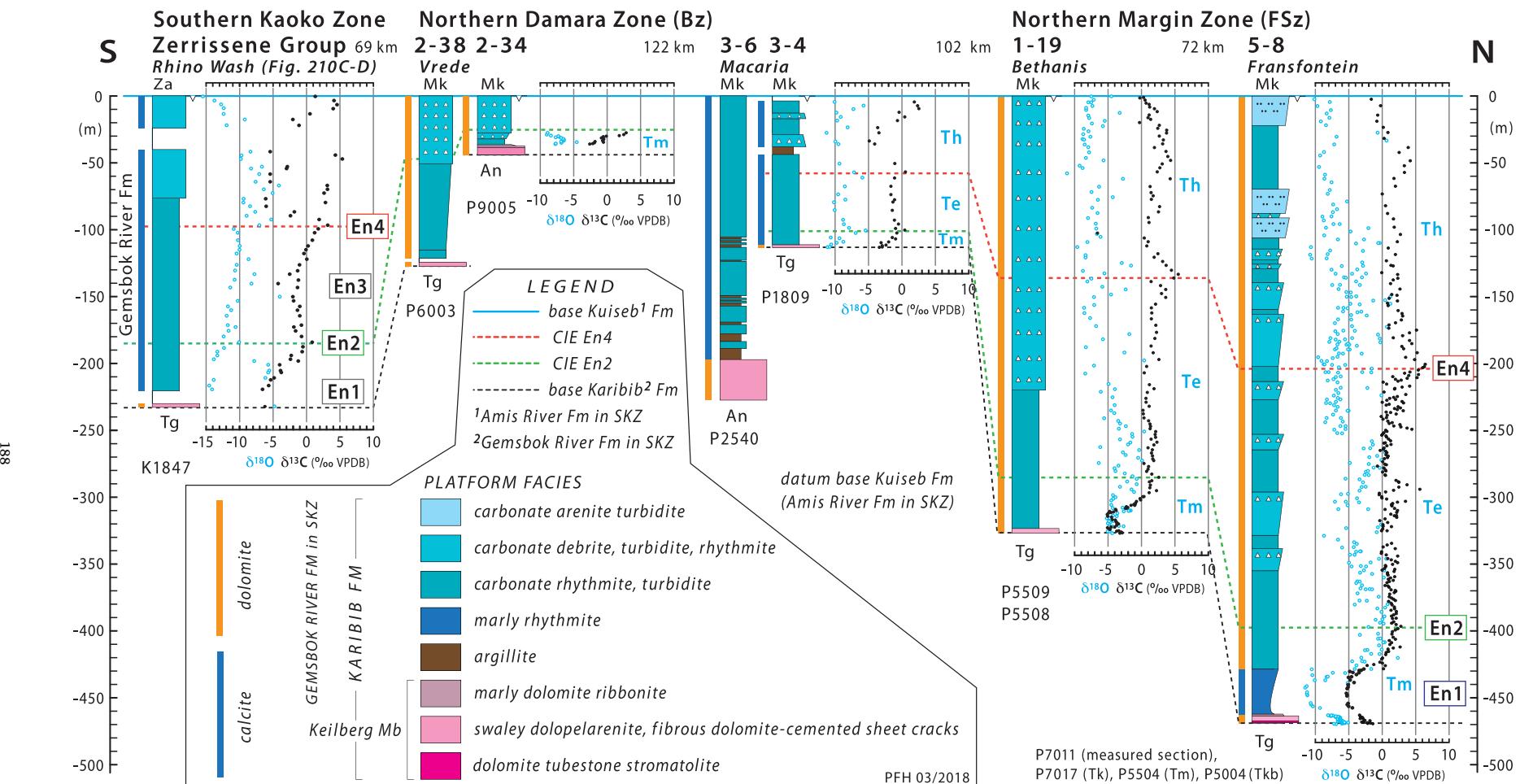


Fig. 186. Selected early Ediacaran columnar sections with $\delta^{13}\text{C}$ and $\delta^{18}\text{O}$ records from the FSz, Bz and SKZ. FSz and Bz sections are Karibib Fm (Swakop Group), the off-shelf continuation of Tsumeb Subgroup (Otavi Group). SKZ section near Rhino Wash (base at $-20^{\circ}59.140'/14^{\circ}02.010'$) is Gemsbok River Fm (Zg, Fig. 210C & D) of Zerrissene Group (Swart, 1992a, b; Nieminski et al., 2018). CIEs En1–4 enable correlation between these sections and with Tsumeb Subgroup (Halverson et al., 2005; Hoffman and Halverson 2008; Miller, 2008b; Hoffman and Lamothe, 2019). Chemostratigraphic equivalents of Maieberg (Tm), Elandshoek (Te) and Hüttenberg (Th) Fms indicated (blue letters). Keilberg Mb cap dolomite is recognizable in each section.

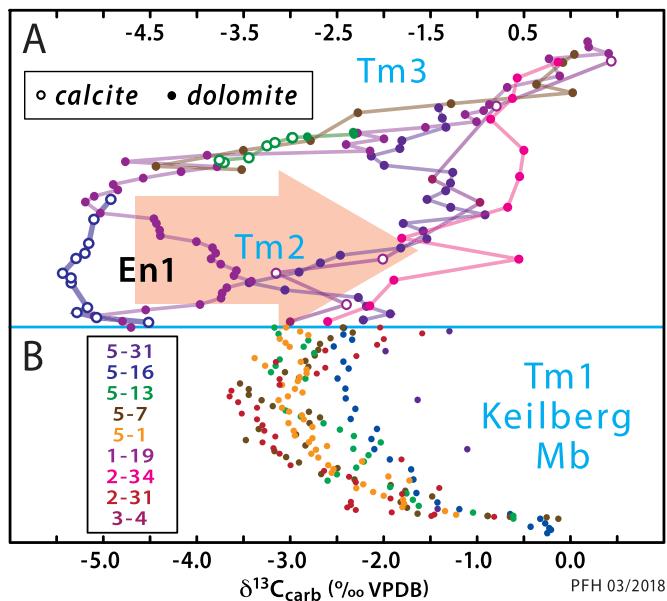


Fig. 187. (A) Progressive destruction of CIE En1 in FSz and Bz, where Tm2-equivalent lower Karibib Fm is variably dolomitized (solid circles) or undolomitized (open circles). Colours are coded by section (B). En1 as defined on platform (Fig. 183) is best preserved in limestone in 5-16 and 5-13. Complete En1 destruction in 2-34 yields a mixing line between Tm3-equivalent and upper Keilberg Mb (B), implying a shift (arrow) of $\leq 4.0\text{\textperthousand}$. 3-4 (*Macaria*) appears strongly altered despite being mostly undolomitized (Fig. 186). (B) Normalized Keilberg Mb $\delta^{13}\text{C}$ records from FSz and Bz (Fig. 180B). Records normalized from top of basal turbidites (Tk1), where present, to top of Keilberg Mb.

Hüttenberg Fm is placed at a mappable flooding surface (Figs. 145 & 185), consistent with its placement in OML (King, 1994, columnar sections in folder). This flooding surface lies stratigraphically between En3 and 4 (Figs. 179 & 185), which are useful for correlation with Karibib Fm of Swakop Group (Figs. 185 & 9B–D). In IPz and OML, both the sub-Hüttenberg Fm flooding surface and CIE En4 underlie a set of selectively-silicified, pseudo-*Conophyton* (LLH) stromatolite (Fig. 132F) biostromes, colloquially named ‘Tuten 1–3’ in OML (Krüger, 1969; Hedberg, 1979; Miller, 1980; King, 1994). A remarkable feature of Hüttenberg Fm, setting it apart from Elandshoek Fm, is CIE En4 (Figs. 179 & 185), which is characterized by highly enriched ($\leq +12\text{\textperthousand}$) $\delta^{13}\text{C}$ values with extreme point-to-point variability of $\leq 15\text{\textperthousand}$ (Halverson et al., 2005; Cui et al., 2018).

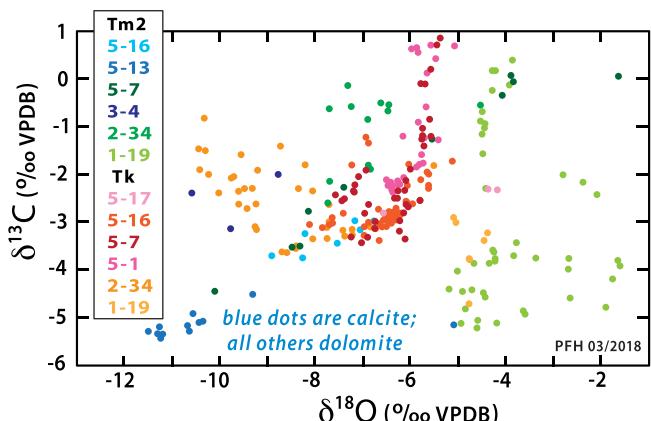


Fig. 188. $\delta^{13}\text{C}/\delta^{18}\text{O}$ crossplot for Keilberg Mb (Tk) and overlying lower Karibib Fm (Tm2) in FSz and Bz (Fig. 187). Blue dots (3-4, 5-13, 5-16) are calcite, all others dolomite.

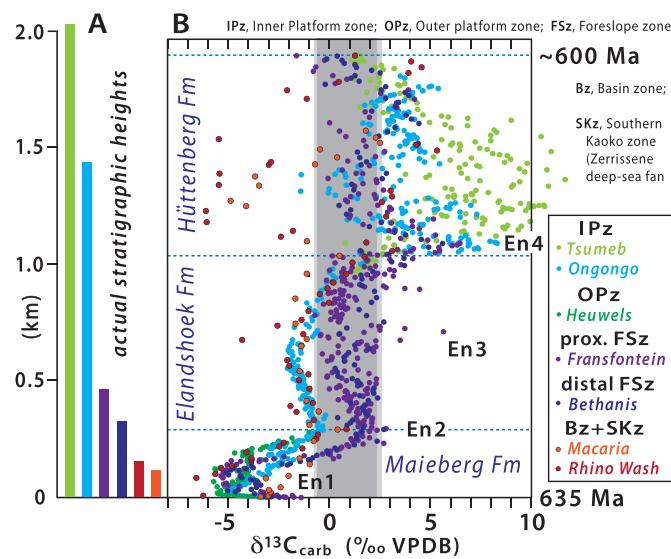


Fig. 189. Normalized early Ediacaran $\delta^{13}\text{C}$ records from Tsumeb Subgroup (IPz and OPz, Fig. 5) and Karibib Fm (FSz and Bz, Fig. 5). Sections are normalized to common thickness for each of three intervals, divided by dashed blue lines at En2 and at stepwise $\delta^{13}\text{C}$ rise below En4. CIEs En1 and En3 also indicated, as are formations of Tsumeb Subgroup. Actual stratigraphic thicknesses are shown as colour-coded vertical bars. Grey band gives $\delta^{13}\text{C}$ range of modern ocean DIC (Kroopnick, 1985). Hoffmann (2011a) inferred a ‘reverse’ seawater $\delta^{13}\text{C}_{\text{DIC}}$ depth gradient from offset En2-3 records. Hoffmann and Lamothe (2019) invoked seawater-buffered diagenesis, driven by geothermal porewater convection (Fig. 190), to account for proximal FSz values (blue dots), implying that early Ediacaran seawater DIC was compositionally similar to modern. If true, this would imply that IPz records, preserved through sediment-buffered diagenesis, are decoupled from open-ocean DIC. IPz records were also preserved in Bz, where platform-derived sediment carrying IPz $\delta^{13}\text{C}$ was advected onto basin-margin turbidite fans beyond the reach of seawater-buffered diagenesis (Hoffmann and Lamothe, 2019). Minimal destruction of CIE En1 in FSz may reflect rapid lithification due to anomalous carbonate oversaturation in post-snowball ocean (Hoffman et al., 2017a), attested by profligate production of benthic aragonite (Figs. 80A–F & 81A–B) during peak flooding stage of Maieberg Fm transgression (Fig. 178C).

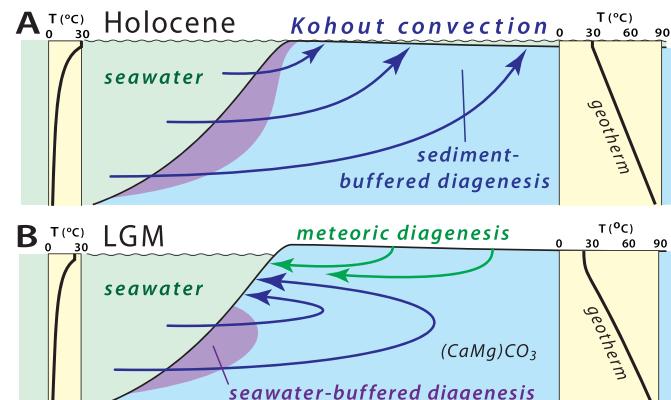


Fig. 190. (A) Idealized porewater convection (Kohout, 1967; Wilson et al., 2001; Wilson, 2003) during a sea-level highstand like the Holocene. Flow is driven by the horizontal temperature (density) gradient between seawater and porewater in the platform interior. Fluid-buffered diagenesis is predicted to occur on the foreslope, where seawater continually invades the sediment. Rock-buffered diagenesis occurs farther along the porewater pathway (Higgins et al., 2018; Ahm et al., 2018). (B) Same as A, but during a sea-level lowstand like the Last Glacial Maximum (LGM), when the platform top was emergent and therefore a recharge area for meteoric groundwater (Reilly and Goodman, 1985; Wilson, 2005) or brine reflux (Jones et al., 2002; Pal and Taberner, 2011).

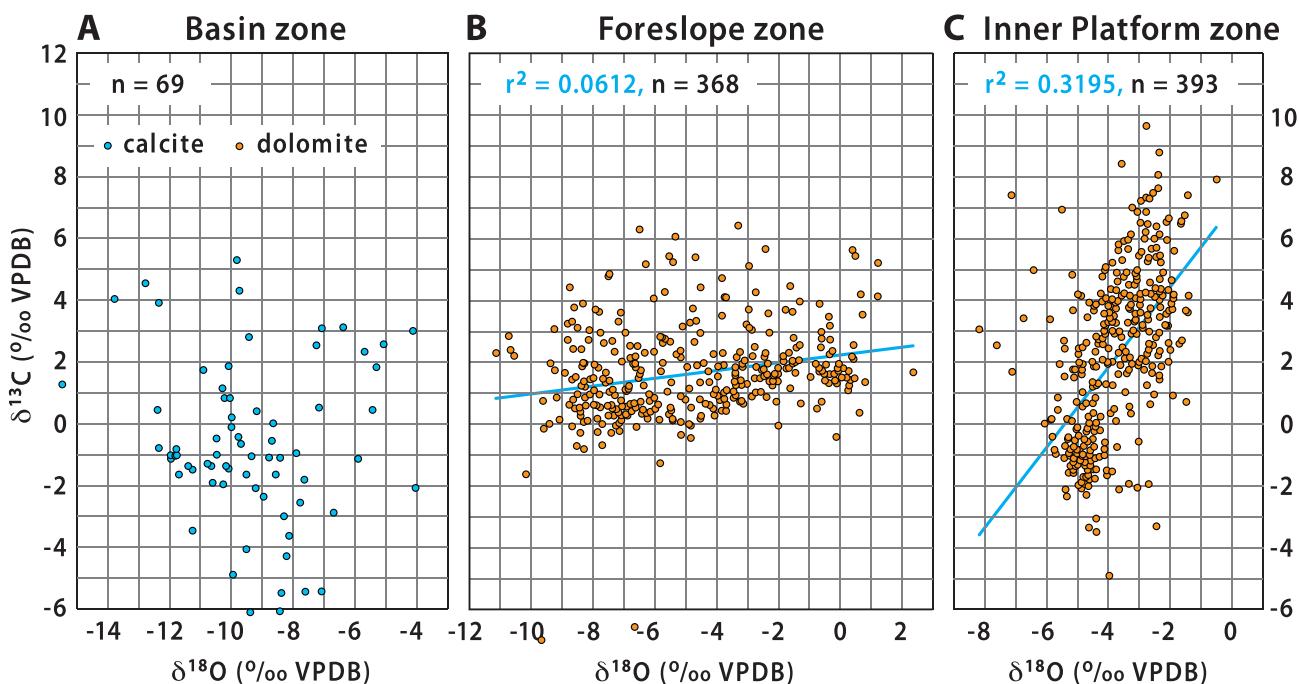


Fig. 191. $\delta^{13}\text{C}/\delta^{18}\text{O}$ crossplots from post-En1 records (Fig. 189) in (A) Bz, (B) FSz and (C) IPz, excluding Tsumeb because of stratigraphic incompleteness. Positive correlation in IPz dolomite is not preserved in FSz, where $\delta^{18}\text{O}$ has an expanded range. Bz calcite is depleted in $\delta^{13}\text{C}$ and $\delta^{18}\text{O}$ compared with dolomitized correlatives.

3.4.4. Karibib Fm of Swakop Group

Sequence boundaries at the base of Elandshoek and Hüttenberg formations disappear as down-slope conformities in Swakop Group. The three formations of Tsumeb Subgroup collectively become Karibib Fm in Swakop Group (Fig. 6B–E, Table 5). Peritidal cycles of the former pass laterally into a distally tapered wedge of carbonate rhythmite, turbidite and debrite (Figs. 185 & 186). The facies change between them remains to be investigated.

Calcite rhythmite of Tm2 can be distinguished lithologically in lower Karibib Fm in Tr5 (Fig. 56C & D), but the correlative MFS is dolomitized in Tr1 and 2 (Figs. 185 & 186). Isotopic changes accompanying dolomitization in lower Karibib Fm (Figs. 187 & 188) are similar but more extreme than those in Tm2 (Fig. 184). En1 shifts 4‰ heavier to a mixing line between the top of Keilberg Mb and base of Tm3 (Fig. 187). In Tr3 (also Gemsbok River Fm in SKz, Fig. 6A), nearly all Karibib Fm except Keilberg Mb is limestone (Fig. 186). CIE En1 is variably expressed in basal Karibib Fm in Tr1–3 (Figs. 189 & 186–187).

While the sequence boundaries defining Elandshoek and Hüttenberg formations disappear in Swakop Group, CIEs En2 and 4 that approximate them can be observed in Karibib Fm (Figs. 185 & 186) (Halverson et al., 2005; Hoffman and Halverson, 2008; Hoffman, 2011a). These chemostratigraphic correlations imply that Karibib Fm represents as much time (~35 Myr) as Tsumeb Subgroup in IPz (Fig. 151), despite Karibib Fm being thinner by factors of 2–20 (Figs. 145 & 186). This allows comparison of $\delta^{13}\text{C}$ profiles from Tsumeb Subgroup (IPz) and Karibib Fm (FSz and Bz), normalized at En2 and 4 (Fig. 189), assuming that these CIEs are isochronous on the time-scale of sediment transport off the platform and down the foreslope.

Comparison of $\delta^{13}\text{C}$ profiles, normalized by CIE (Fig. 189B) rather than by stratigraphic thickness (Fig. 189A), reveals striking differences

between zones (Hoffman and Lamothe, 2019). Bz and SKz profiles (orange and red dots) track IPz ones (light blue and green dots) through En2–4 (Fig. 189B), above which Bz and SKz exhibit large scatter toward lighter values rather than heavier ones as in IPz and OML (light green dots). The tracking suggests that rhythmite, turbidite and debrite of Karibib Fm in Bz represent sediment swept off the platform with its isotopic composition intact (Hoffman and Lamothe, 2019). In contrast, $\delta^{13}\text{C}$ profiles in FSz (purple and dark blue dots) parallel those in IPz and Bz, but are displaced toward values in the range of modern marine DIC (grey band, Fig. 189B, Kroopnick, 1985). FSz values are more enriched by 2.5‰ on average through En2 and 3, but are more depleted than IPz values between En4 and the top of Otavi/Swakop Group (Fig. 189B).

Hoffman and Lamothe (2019) postulated that FSz underwent early diagenesis (dolomitization) under seawater-buffered conditions (Fig. 190A), conditioned by seawater inflow driven by geothermal porewater convection (Kohout, 1967; Wilson et al., 2001; Wilson, 2003, 2005). Early seawater-buffered diagenesis has been documented on the flanks of Cenozoic carbonate platforms and modelled from its diagnostic effects on Ca and Mg isotopes (Higgins et al., 2018; Ahm et al., 2018). In contrast, the interiors of carbonate platforms and basin floors beyond the areas of seawater inflow undergo early diagenesis under sediment-buffered conditions (Fig. 190A) (Higgins et al., 2018; Ahm et al., 2018). Sediment-buffered diagenesis tends to preserve isotopic compositions inherited from epi-platform waters, where the sediment originated. Conversely, seawater-buffered diagenesis tends to drive isotopic re-equilibration with open-ocean thermocline water (Fig. 190). It follows from this interpretation that epi-platform and open-ocean waters were isotopically distinct after CIE En1, and that the latter were more stable after that time and isotopically similar to modern-ocean DIC (Hoffman and Lamothe, 2019).

Previously, the $\delta^{13}\text{C}$ offset between FSz and IPz records was attributed to a ‘reverse’ depth gradient (Hoffman, 2011a). This explanation was abandoned as inconsistent with the subsequently acquired Bz and SKz records (Fig. 189B).

Why was epi-platform carbonate isotopically depleted relative to open-ocean DIC in Elandshoek Fm time (Fig. 189B), and enriched (with large scatter) in Hüttenberg Fm time? Kinetic isotope effects can drive surface seawater isotopically lighter or heavier during rapid invasion or evasion of CO_2 gas, respectively (Lynch-Stieglitz et al., 1995). In restricted waters, CO_2 invasion drives DIC isotopically lighter in periods of intense photosynthesis (Lazar and Erez, 1990, 1992), and CO_2 expulsion drives DIC heavier during periods of intense evaporation (Stiller et al., 1985). The observed secular trend (Fig. 189B) is therefore consistent with drift of Otavi platform from equatorial to subtropical latitudes (Meert et al., 1995; Merdith et al., 2017a). Kinetic isotope effects operate on short time scales and could therefore contribute to the large point-to-point $\delta^{13}\text{C}$ variability observed in Hüttenberg Fm and derived strata (Fig. 189B).

In skeletal carbonate production, kinetic isotope effects drive linear correlation between carbonate $\delta^{13}\text{C}$ and $\delta^{18}\text{O}$ (McConaughey, 1989a, b; Adkins et al., 2003). In Elandshoek and Hüttenberg formations, $\delta^{13}\text{C}$ and $\delta^{18}\text{O}$ covariance is observed in IPz (Fig. 191C), but not in their FSz correlatives (Fig. 191B), consistent with kinetic disequilibria during epi-platform carbonate production, but not during fluid-buffered diagenesis. Carbonate $\delta^{18}\text{O}$ values are more uniform in IPz than in FSz or Bz (Fig. 191A–C). This suggests that diagenesis occurred more rapidly and over a smaller range of burial depths and temperatures in IPz, compared with FSz or Bz (Ahm et al., 2018).

3.5. Mulden Group

Otavi/Swakop Group is disconformably overlain by Mulden Group (Table 5, Figs. 4–6) (Hedberg, 1979; Miller, 1997, 2008b), a thick succession of terrigenous detrital foredeep deposits (Fig. 16), including subordinate locally derived coarse carbonate debris (Figs. 21C–F, 81D–F & 83A–F). Throughout most of Otavi fold belt (Fig. 4), Mulden Group (Tschudi Fm) overlies Hüttenberg Fm with ≤ 0.3 km of paleotopographic relief on their mutual disconformity surface (Hedberg, 1979). The situation is dramatically different in ‘Huab cusp’ (Hoffman, 2021a), where Kaoko and Northern Damara zones meet at the SW promontory of Congo craton (Figs. 2A, 3 & 192). The area is now dominated by Kamanjab basement inlier, a polygenetic structure with a history that includes Cryogenian rifting, early Ediacaran passive-margin subsidence, middle Ediacaran collisional subduction and late Ediacaran far-field (Southern Damara zone) crustal shortening (Porada, 1979; Stanistreet et al., 1991; Hoffman, 2021b; Goscombe et al., 2018). In Huab cusp, the sub-Mulden Group disconformity drops down onto the basement between Tr1 and 6, Tr6 and 5, and around most of Welwitschia inlier and its satellite (yellow stars in Figs. 4 & 192). Yet the Mulden and Otavi groups remain for the most part structurally concordant.

Expanding on previous observations (Frets, 1969; Guj, 1974; Hoffman and Halverson, 2008; Miller, 2008b), Hoffman (2021a) proposed that the sub-Mulden disconformity represents an Ediacaran megakarst landscape, where steep-walled karst mountains of flat-lying to gently-tilted, locally-faulted, Otavi/Swakop Group carbonate towered above broad valleys floored by Orosirian basement (Fig. 193). Paleotopographic relief is inferred to have at least equalled local Otavi Group stratigraphic thickness, estimated to have been 1.85 km (Hoffman, 2021a). The Ediacaran megakarst was filled in and buried by mainly

terrestrial Mulden Group foredeep clastics (Fig. 194B & C). Then the basement, Otavi/Swakop and Mulden groups were folded *en masse* to form doubly plunging map-scale folds that strike parallel to the respective orogenic belts (Fig. 192). Steeply inclined segments of the sub-Mulden Group disconformity define the western ends of both Tr5 (Fig. S14) and Tr6 (Figs. 84 & 85). The eastern end of Tr6 is a pre-Mulden Group fault (Figs. 70 & 73) and the NE end of Tr1 (Figs. 13) originated as a pre-Mulden Group flexure (Hoffman, 2021a). Each of these terminations is described in Hoffman (2021a) and need not be repeated.

In Achas Syncline (Fig. 192), Welkom Subgroup (Fig. 6C) of Mulden Group includes a lower siltstone-rich Braklaagte Fm of paralic or lacustrine origin, a middle arenaceous Renosterberg Fm deposited by SE-directed rivers (Figs. 146C, 83E & F), and an upper siltstone-rich Gaseneirob Fm. Braklaagte Fm is localized in paleotopographic depressions on the megakarst erosion surface (Figs. 85, 194, S12 & S19) and its contact with Renosterberg Fm is gradational. Mudcracks in Braklaagte Fm (Figs. 83C & 210A) imply that karstic topography was subaerial. Outside Huab cusp, sub-Mulden Group erosion was more subdued and Braklaagte Fm is thin or absent. Fluvial arenite (Tschudi Fm, Fig. 6D & E) directly overlies Hüttenberg Fm (Hedberg, 1979). In Northern (Outjo) zone and Warmquelle syncline (Fig. 96), deepwater clastics (Sesfontein and Kuiseb/Okaua formations, Fig. 6B & D) disconformably overlie Swakop or Otavi Group. In our model, they represent older and more external parts of the evolving Mulden Group foredeep (Fig. 194A–C). Upward and cratonward transitions from marine trench to terrestrial facies is an intrinsic property of collisional foredeeps (Fig. 16), exemplified by the *flysch* to *molasse* transition in the European Central Alps (e.g., Pfiffner, 1986).

In the foredeep (aka foreland basin) model (Figs. 16 & 194A–C), megakarst erosion is the expression of lithospheric forebulge migration, consistent with its pre-Mulden Group and post-Otavi/Swakop Group age. The problem is that characteristic forebulge amplitude is ca 0.5 km (Turcotte and Schubert, 1982; Tensi et al., 2006; Zhang et al., 2018), whereas uplift of Huab cusp is estimated to have been ≥ 1.85 km (Hoffman, 2021a), the inferred stratigraphic thickness of Otavi Group in that area. The thickest exposed section is 0.90 km, (6–8, Fig. 85), but most of Elandshoek Fm and all of Hüttenberg are missing, due to sub-Mulden Group erosion. Their original thickness can be estimated from Maieberg Fm thickness and its consistent fractional relationship to total thickness of Tsumeb Subgroup (Fig. 145). On this basis, total Tsumeb Subgroup in Huab cusp is estimated to have been 1.40 km (Fig. 145), to which is added 0.45 km of Abenab Subgroup (Fig. 85).

What could account for extreme forebulge uplift in Huab cusp? Two contributing factors stem from its location, where two orogenic belts meet at a right angle (Hoffman, 2021a). Each orogenic belt was a product of convergence and mass transfers (i.e., thrust sheets) from a subducting plate (Congo craton) to an overriding plate (the orogenic belt itself). If the orogenic belts were broadly contemporaneous, their respective forebulges would intersect in Huab cusp (Fig. 194D) and constructively interfere (Deplus and Dubois, 1989). The second factor is a space problem that results from the cuspatate slab geometry (Fig. 194D). It generates horizontal compressive stress (σ_1) in the slab oriented normal to the cusp axis. The result is failure or buckling of the slab that propagates cratonward with time due to plate convergence (Rogers, 1983a, b; Keen and Hyndman, 1979; Hoffman, 2021a). Both factors are contingent on outward-dipping slabs (wrt Congo craton) and broad contemporaneity of Kaoko and Northern Damara orogens. Kaoko belt structures (D2) postdated or outlasted Northern zone structures (D1) where they intersect (Coward, 1981; Hälbich and Freyer, 1985; Maloof,

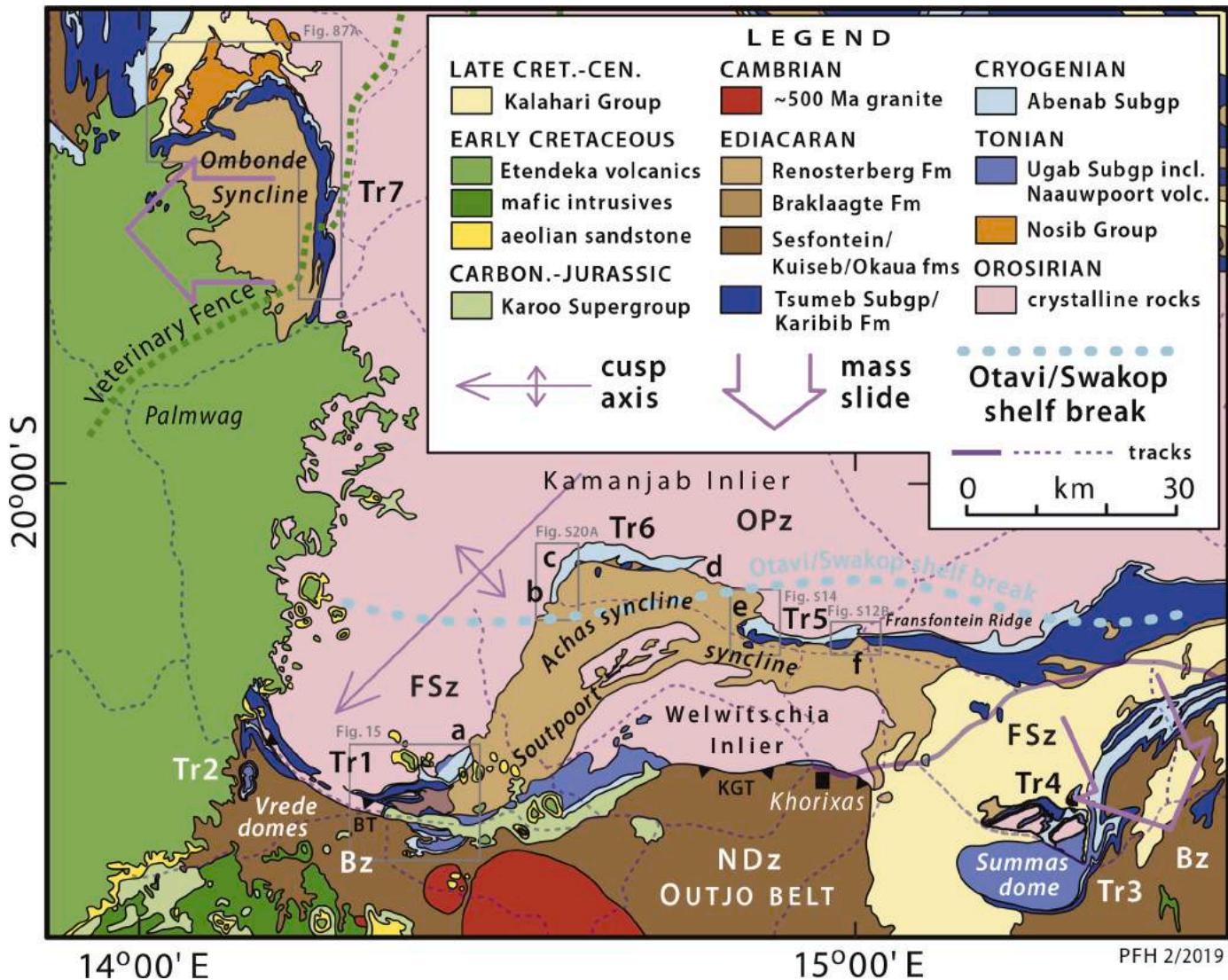


Fig. 192. Simplified geological map of the SW promontory of Kamanjab inlier (and Congo craton), which occupy a cusp at the junction of CKz and NDz accretionary belts (Figs. 2–4 & 8A). Cusp axis is indicated, as are locations and inferred transport directions of Ediacaran mass slides in NDz (Clifford, 1962, 2008) (Fig. 41) and EKz (Fig. 87). Otavi/Swakop shelf break divides OPz and FSz. Huab paleokarst evident from tilted paleovalleys between Tr1 & 6, and between Tr6 & 5, where sub-Mulden Group (brown colours) erosion removed Otavi Group, exposing crystalline basement over a wide area (Hoffman, 2021a). Otavi/Swakop Group cut-offs lettered a–f as in Fig. 193. Grey boxes are areas of (left to right) Figs. 87A, 15, S20A, S14 and S12B. BT, Bethanis thrust; KGT, Khorixas-Gaseneirob thrust (Miller, 2008b).

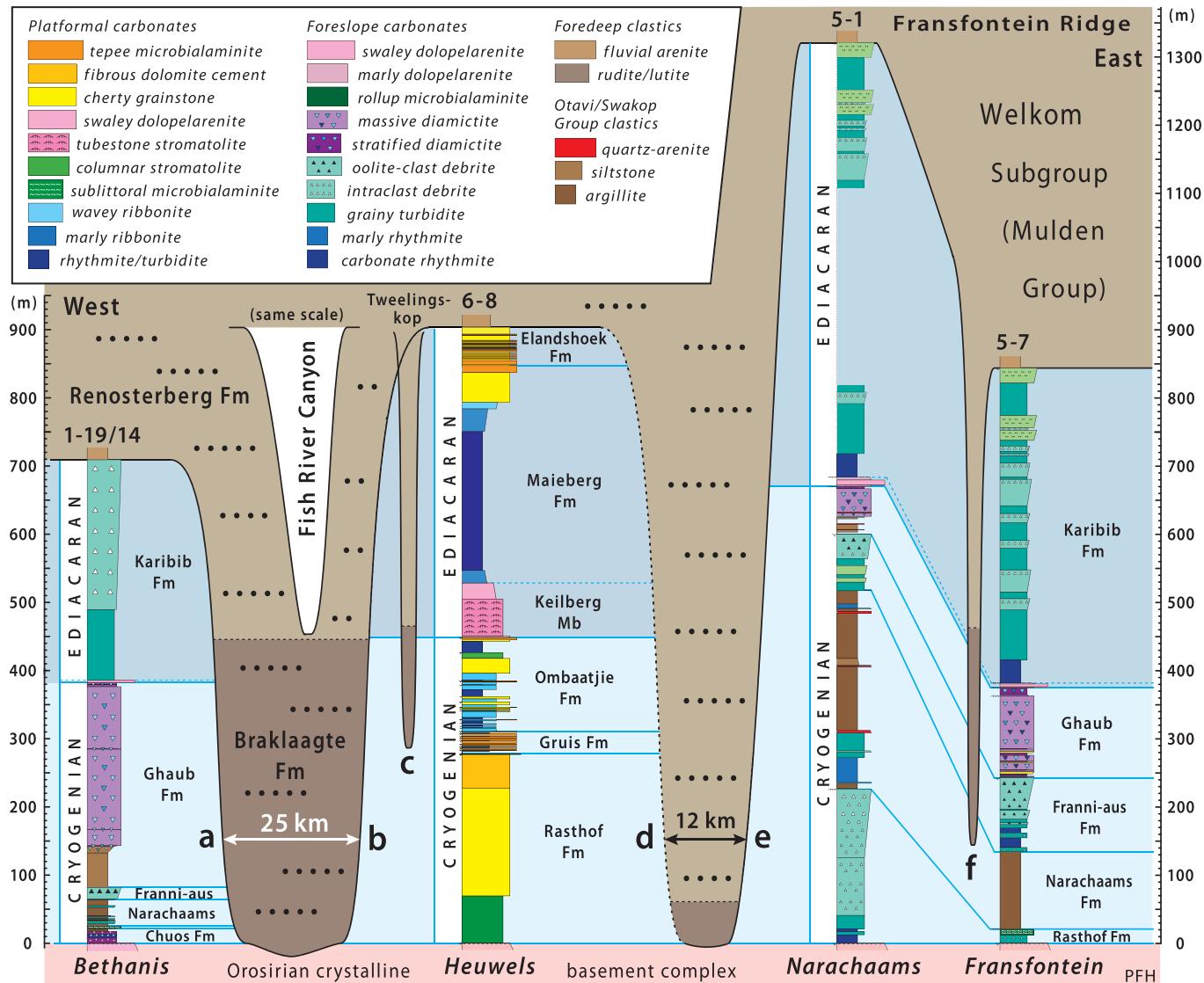


Fig. 193. Representative columnar sections of Swakop Group in Tr1 (left), Otavi Group in Tr6 (center) and Swakop Group in Tr5 (right), separated by broad paleovalleys (a–b and d–e) where foredeep clastics (Mulden Group) were deposited directly upon basement (Fig. 192). Narrow paleovalleys c and f are deeply incised into Otavi/Swakop Group. Datum is top of basement. Modern Fish River Canyon (southern Namibia) shown at the same scale for comparison. Paleoscarp a is described in Hoffman (2021a), b is in farm Welkom (Figs. 84 & 85, SOI S3.9.4.), d is Huab fault (Figs. 70 & 73), and e is W terminus of Transfontein Ridge (Fig. S14). Incision c is at 6–5 (Figs. 72 & 81F) and f is at 5–5–6 Transfontein (Fig. S12). Otavi/Swakop Group was faulted (e.g. Huab fault) and kinked locally, prior to and/or during paleokarst erosion (Hoffman, 2021a). Mulden and Otavi/Swakop groups were co-folded by Achas syncline (Fig. 192) and are structurally concordant on map scales. At outcrop scale, they are commonly discordant where in mutual contact, because of lithologic (semi-pelitic vs dolomite)/rheologic contrast in response to orthogonal thick-skinned foldings. In Welkom Subgroup, Braklaagte Fm is localized in paleovalleys. The entire paleokarst was buried under fluvial Renosterberg Fm (Fig. 146C), which is ≥ 3.0 km thick in Tr7 (Fig. 192). An estimated 945 m (Fig. 145) of Elandshoek and Hüttenberg formations were eroded from the top of Otavi Group in 6–8, implying ≥ 1.85 km depth of paleokarst erosion (Hoffman, 2021a).

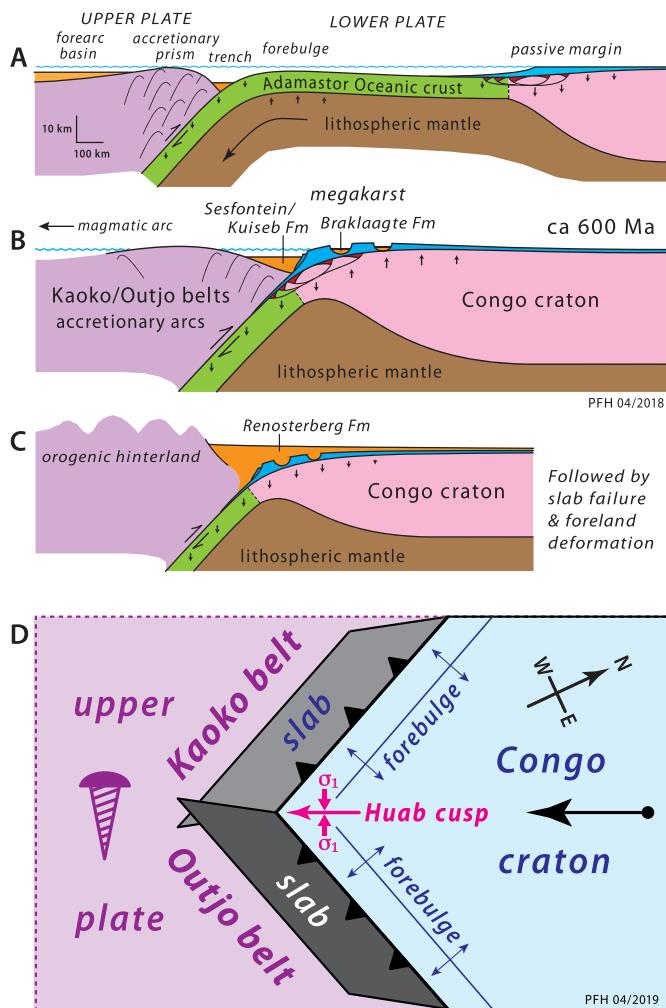


Fig. 194. Collisional foredeep model for transient (Myr) uplift of passive margin passing over forebulge, megakarst erosion and rapid burial by foredeep clastics (Mulden Group), immediately prior to onset of tectonic shortening, propagating cratonward due to plate convergence (Fig. 16). (A) Passively-subsiding rifted Congo margin (Fig. 26) converges with trenches bordering conjoined (?) Dom Feliciano (WKz) and Swakop (CDz) terranes (Fig. 3). Absence of remnant magmatic arc on either Congo margin indicates that passive margin did not originate as a back-arc (upper plate) basin. (B) Congo margin rides over flexural forebulge, resulting in megakarst landscape development (Fig. 193) and trenchward-directed mass slides (Figs. 87 & 192). (C) Megakarst landscape is rapidly buried by synorogenic foredeep clastics. Foredeep and underlying ACC margin subsequently underwent thin- and thick-skinned shortening (not shown) as accretionary deformation front prograded. (D) Two factors potentially contributed to forebulge amplification in Huab cusp: (1) constructive interference of two forebulges where they meet (Deplus and Dubois, 1989), and (2) slab constriction due to subduction geometry at a cusp (Rogers, 1983b; Keen and Hyndman, 1979; Bayly, 1982; Hoffman, 2021a). The latter is conditioned on concurrent subduction under CDz and NDz. The effect of cusp geometry can be seen by taking a leaf of note paper, slit at the cusp as shown, and bent along the trench lines (barbed) forming slabs that overlap down-dip from the cusp apex. In a coherent slab, constriction (overlap) would be manifest by slab buckling under horizontal compression normal to the cusp axis (σ_1). Deformation propagates NNE in Congo plate. Mass slides in Tr4 (Fig. 41) (Clifford, 2008), Tr7 (Fig. 87B) and Tr11 (Fig. 139) were triggered by plate flexure at trench outer slopes, including but not limited to Huab cusp.

2000, Passchier et al., 2002; Lehmann et al., 2015). Radiometric constraints on ages of dynamic metamorphism and anatexis support the same age sequence between belts, but with a sufficiently small age difference to allow for simultaneous subduction. D1-related phengite

growth in widely-spaced areas of Northern zone yielded $^{40}\text{Ar}/^{39}\text{Ar}$ laser-ablation age spectra of 598 ± 4 , 594 ± 7 and 584 ± 4 Ma (Lehmann et al., 2015), while zircon from a D2 anatetic granite in CKz gave consistent SHRIMP and evaporation $^{207}\text{Pb}/^{206}\text{Pb}$ dates of 580 ± 3 Ma (Seth et al., 1998).

Given forebulge uplift in Huab cusp of ≥ 1.85 km relative to sea level (Hoffman, 2021a), it is not surprising that map-scale mass slides are observed in Otavi/Swakop Group on its flanks, directed southward in Swakop Group (Clifford, 1962, 2008) and westward in Otavi Group of EKz (Hoffman and Hartz, 1999; Hoffman et al., 2016b). Omonde detachment in Tr7 (Fig. 87A–B, SOI S3.10.2.) is well constrained in terms of stratigraphic age and displacement (20 km). It postdates all of Otavi Group and predates local Mulden Group, similar megakarst erosion in Huab cusp, allowing for diachronous Mulden Group onlap (Fig. 16). Estimated fault displacement on the (subsequently) folded detachment surface is derived from matching cut-offs (Figs. 87B, 89 & 91), and displacement age from incised valleys cutting the fault surface filled by Mulden Group conglomerate (Figs. 87A–B, 90, 92 & 210B), later folded along with the incised Otavi Group.

Hoffman (2021a) identified a number of potentially analogous compressional uplifts of Cenozoic age, located in cusps where the Pacific, Juan de Fuca, Arabian and Indian plates are being subducted beneath the North American or Eurasian plates. Not discussed by Hoffman (2021a) is the Arica Bend (cusp) in the Peru–Chile Trench, where the Nazca plate is subducting beneath South America. Forebulge height along most of the trench system is ≤ 0.5 km, characteristic of trench outer rises globally (Zhang et al., 2018). In the Arica Bend, however, forebulge height increases to ≤ 1.5 km, which cannot be accounted for “if the 3–D trench curvature is not included in the modelling” (Manríquez et al., 2014).

3.6. Stratigraphic development: a synthesis

Our initial working hypothesis was that subsidence accommodating Otavi Group in the Eastern zone of Kaoko belt (EKz, Figs. 3 & 6D) was related to a W-facing continental margin, implied by Swakop-type facies in the Central zone of Kaoko belt (Guj, 1970; Henry et al., 1992/93; Stanistreet and Charlesworth, 1999). It was further assumed that the Nosib–Otavi group clastic-to-carbonate transition marked a secular change from active rifting to post-rift thermal subsidence (McKenzie, 1978). We found little support for the first assumption and the second was abandoned after Soffer’s study (Soffer, 1998) of Huab dip-slope in Tr6 (Fig. 86).

S – N changes in thickness and facies are more apparent than W – E changes in the Otavi Group of EKz. Paleocurrents in non-marine clastic units are either S – SE-directed (Nabis and Renosterberg formations) or N – NE-directed (Devede, Okakuyu and Gruis formations) (Fig. 146). S – N not W – E crustal stretching is implied by rift-shoulder offlap-onlap (Fig. 163C) geometries that project across Kamanjab inlier (Hoffman and Halverson, 2008). The observations are kinematically compatible with a rifted margin in Northern zone and a transform margin in Central Kaoko zone (Hoffman, 2021b). In Otavi Group, active rifting continued, at least intermittently, until middle Cryogenian (early Omboajtje Fm) time, >100 Myr after the Nosib–Otavi group transition (Fig. 151). Post-rift subsidence accounted for only $\sim 30\%$ of Otavi Group’s 170 Myr (0.77–0.60 Ga) duration.

3.6.1. Otavi Group (OPz and IPz)

Despite broad stratigraphic conformity in IPz, upper crustal faulting in response to lithospheric stretching is inferred from wedges of basement- and cover-derived conglomerate and sandstone in lower Devede and Okakuyu formations of Ombombo Subgroup (Figs. 99, 100A & C–D, 102C–F, 123, 139 & 147). Small growth faults, many flagged by Neogene travertine terraces, are common throughout IPz. A growth fault at 8–8, for example, involves stratigraphic onlap–offlap of Rasthof Fm and erosional beveling by Gruis Fm (Figs. 97 & 103). Growth faults

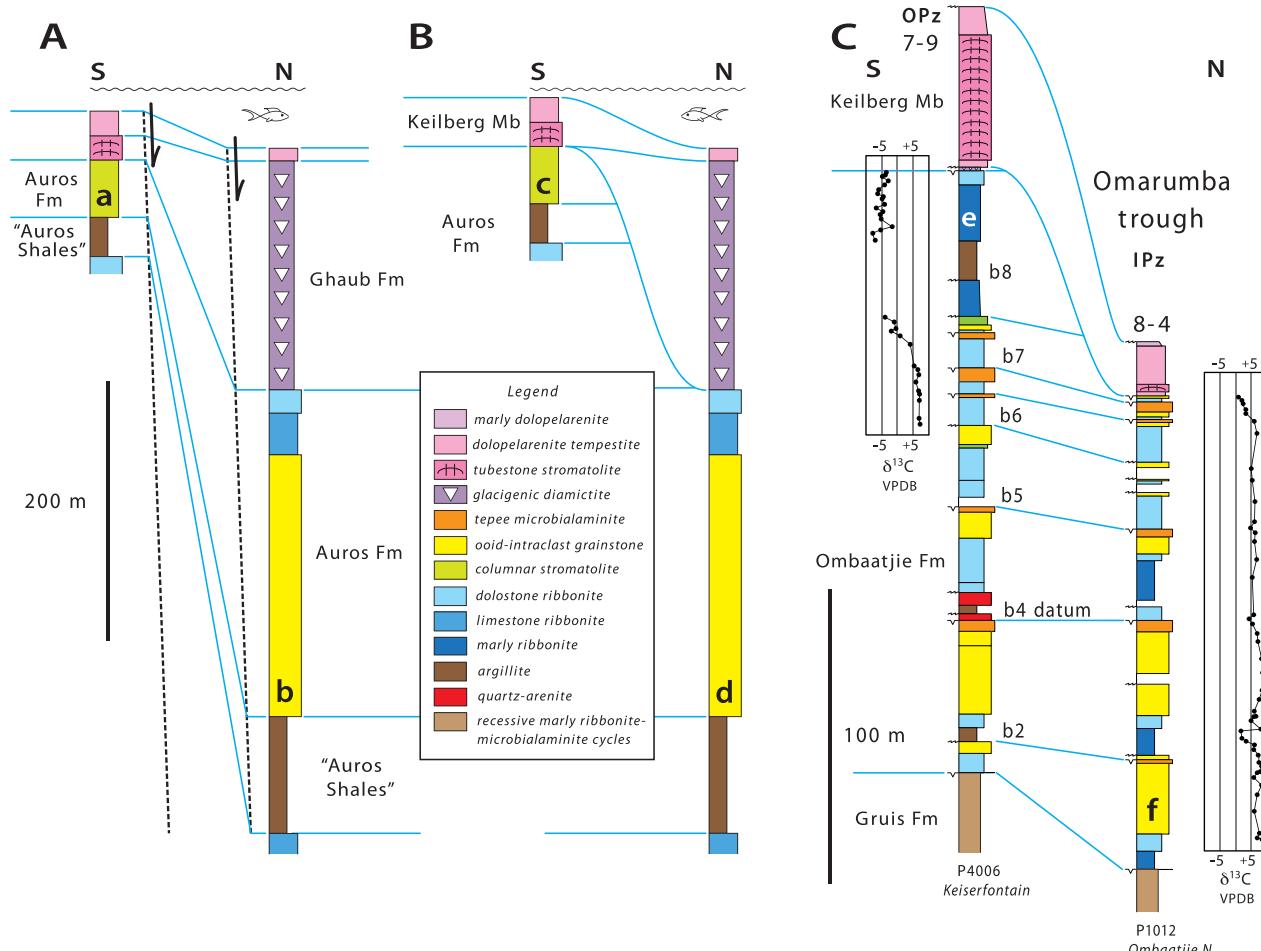


Fig. 195. Alternative interpretations of stratigraphic relations across Keilberg anticline in the Otavi Mountainland, according to (A) Bechstädt et al. (2018), and (B) by analogy with (C) Omarumba trough (Fig. 164). Glacial trough is debris-filled in B but nearly vacant in C. Blue lines are correlated surfaces, black dashed lines in A are growth faults or flexures, and dashed red line in C is 0‰ datum in CIE Cn5 (Fig. 151) descent (Halverson et al., 2002). Note that Bechstädt et al. (2018) include tubestone stromatolite (Cloud et al., 1974; Hegenberger, 1987; Corsetti and Grotzinger, 2005; Santos et al., 2021) in Ghaub Fm. In A, northward thickening and facies changes in Ghaub and Auros Fms are ascribed to N-side-down growth fault or flexure, inferred to have persisted throughout Otavi time (Bechstädt et al., 2018). This interpretation is critically dependent on correlation of “Auros shales.” If dolomites a and b are correlative, they should have similar $\delta^{13}\text{C}$ but data are lacking (Bechstädt et al., 2018). In B, Ghaub Fm diamictite is accommodated by a paleovalley eroded during synglacial sea-level lowstand. Dolomites c and d are not correlative and the argillite stratigraphically below c is correlated with cycle b8 argillite below dolomite e in C. Dolomite e records Cn5, the global Trezona CIE (Halverson and Shields-Zhou, 2011) and is isotopically depleted ($\delta^{13}\text{C} \approx -5\text{‰}$ VPDB), whereas dolomite f (analogous to d) records Cn4 (Keeler peak CIE) and is isotopically enriched ($\delta^{13}\text{C} \approx +6\text{‰}$ VPDB). No local tectonics of Marinoan age are required in B or C. Note different scale bars. Scale bar in A is approximate, since sections were constructed from ‘mapping’ (Bechstädt et al., 2018). Sections are 3–4 km apart and located in south-central Otavi Mountainland 30 km south of Tsumeb (Fig. 4). Mapping (Bechstädt et al., 2018) did not include the E-plunging anticlinal fold-hinge, where the growth faults/flexures inferred in A should project in outcrop.

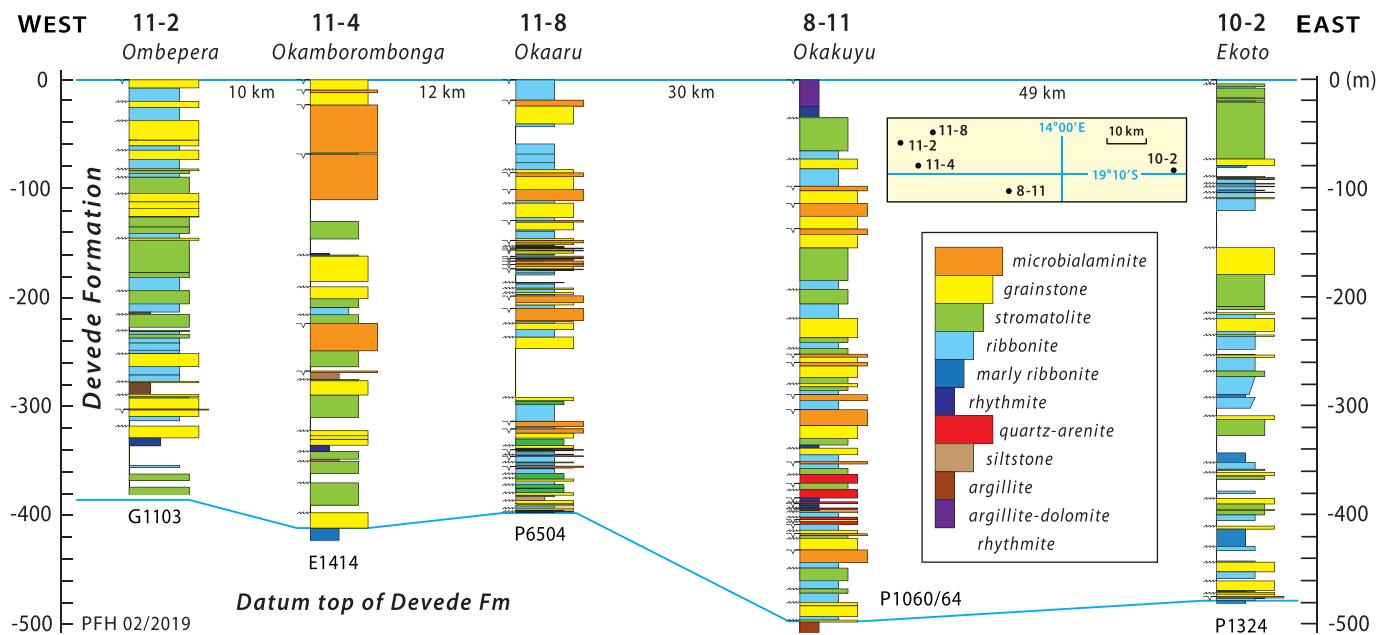


Fig. 196. Selected Devede Fm columnar sections from a 70-km-long W–E corridor across EKz encompassing Tr10-11 (Fig. 8B). Section locations are shown on inset map and Figs. 96, 134 & 137. There is little change in thickness or lithofacies, aside from possible westward shoaling in lower half of section.

within the thin-skinned thrust-fold belt (Tr9 & 11) were rotated during folding.

In OPz, where Tonian strata are absent, basement offlap unconformities and associated fanglomerate–sandstone wedges record dip-slope rotation and uplift of Huab (Tr6) and Makalani (Tr7) rift shoulders (Figs. 5, 86, 71, 77A–F, 87C & 88). South-dipping normal faults inferentially responsible for those uplifts are covered by Mulden Group or Cretaceous onlaps (Fig. 8A), but the rift shoulders shed detritus into IPz in late Tonian (Devede and Okakuyu formations) and middle Cryogenian (Gruis Fm) time (Fig. 86A). Huab and Makalani dip-slopes are bevelled and onlapped by Ombaatjie Fm (Figs. 71, 86B & 88). However, incursions of texturally-mature (marine) quartzarenite in Ombaatjie Fm cycles b1 (Figs. 71, 78D & 85), b2 and b4 (Figs. 88, 94C–D, 125 & 164) imply that relict basement topography or minor fault reactivation persisted into Ombaatjie Fm time. Terrigenous input in Ombaatjie Fm cycle b8 (Figs. 164 & 165) could also be rift-related, since structural rotation of late Cryogenian age is documented in Northern zone (Tr3, Fig. 40) and implied by reconnaissance observations in Epupa inlier 120 km NW of Opuwa (Fig. 4), described in 4.1.3.

Bechstdt et al. (2018) investigated Cryogenian strata in south-central OML, specifically in E-plunging Keilberg anticline (Hedberg, 1979; King, 1994) on farm Jakkal–Omuramba (formerly Maieberg 790 and Keilberg 743). Bechstdt et al. (2018) did not measure stratigraphic sections but constructed “idealized” sections of the N and S limbs of the fold based on mapping. Their sections and correlations are reproduced in modified form (e.g., conventional W-facing orientation) in Fig. 195A. They describe major differences between the fold limbs, which they ascribe to active N-side-down growth faulting or flexuring. They suggest that the inferred faulting accommodated Marinoan Ghaub Fm in its type area (Le Roex, 1941; Hoffmann and Prave, 1996) and accounts for stratigraphic thickening and facies changes in the underlying Auros Fm (Bechstdt et al., 2018). They note that “*This inference contrasts strongly with the assumption [sic] of a tectonically quiet Transfontein depositional*

area by e.g. Domack and Hoffman (2011) and Hoffman et al. (2014).” There is, of course, no *a priori* reason for rifting to have ended synchronously in areas 350 km apart.

Their interpretation (Fig. 195A) is predicated on correlation of “Auros shales” across the anticline. These shales “*do not outcrop well*” (Bechstdt et al., 2018) and little information is given about the underlying “Gauss Fm.” If the “Auros shales” are not correlative, other interpretations are possible. In Fig. 195B, an alternative interpretation of the same sections requires no growth fault and closely resembles stratigraphic relations observed in Kunene Region (Fig. 195C) across the margin of Omarumba trough (Fig. 164). In Fig. 195B, the “Auros shales” on the S limb of Keilberg anticline are equivalent to the thick argillite of Ombaatjie Fm cycle b8 (Figs. 125, 140 & 164). On the N limb, the “Auros shales” represent recessive Gruis Fm (Fig. 127C & D). This interpretation (Fig. 195B) is testable with C isotopes. It predicts that dolomite directly above “Auros shales” are isotopically depleted (CIE Cn5) on the S limb, but enriched (CIE Cn4) on the N limb (see Fig. 195C). In contrast, Bechstdt et al.’s (2018) interpretation (Fig. 195A) predicts that their $\delta^{13}\text{C}$ compositions are the same. Bechstdt et al. (2018), provide no isotopic data from Keilberg anticline. Nor did they map around the nose of the plunging anticline where their postulated fault zone or flexure (Fig. 195A) should be exposed.

After rifting ceased, thermally driven subsidence accompanying lithospheric thickening would have decayed as a function of the square root of time (McKenzie, 1978). Amplified by sediment loading, thermal subsidence would have endured for ~ 55 Myr, from ~ 655 until ~ 600 Ma when the passive margin was destroyed by collision (Fig. 194A–C). The amount of subsidence at any elapsed time would depend on the lithospheric stretching factor $\beta(L_{\text{final}}/L_{\text{initial}})$ and flexural effects of loading. For example, total passive-margin thickness (i.e., Ombaatjie Fm + Tsu-meb Subgroup) is 1.28 km in Tr9 (Fig. 133) and 2.02 km in Tr10 (Fig. 135B & E). Isostatically corrected for sediment loading, these thicknesses correspond to stretching factors (β) of 1.14 and 1.24,

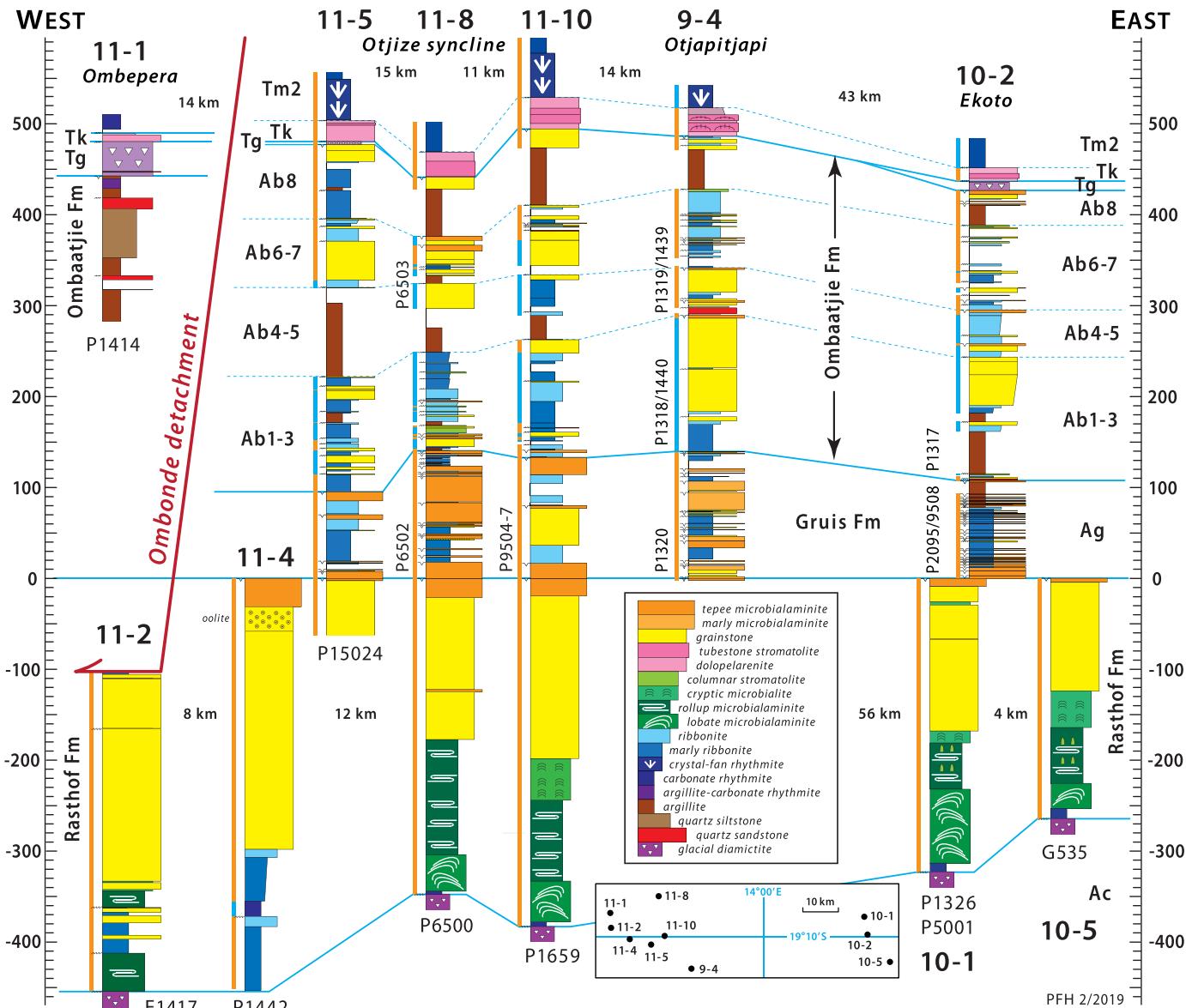


Fig. 197. Selected middle and late Cryogenian and earliest Ediacaran (cap to cap) columnar sections from an 80-km-long corridor across EKz, encompassing Tr10-11 and northernmost Tr-9 (Fig. 8B). Section locations are shown on inset map and Figs. 96, 134 & 137. Section 11-1 is situated on hangingwall of Omboonde detachment (Fig. 139) and accordingly originated E of 11-10, possibly E of 9-4. W–E changes are subtle. Rasthof Fm thickens modestly westward. In Ombaatjie Fm, grainstone is biased eastward in cycles b1–3 but westward in b6–8. A similar pattern is observed meridionally (Fig. 164): grainstone bias shifted from N to S over time. Ghaub Fm diamictite appears only in E (10-2 & 11-1 restored). Fig. 144 shows early Ediacaran (Tsumeb Subgroup) changes in same corridor (11-1 & 10-4).

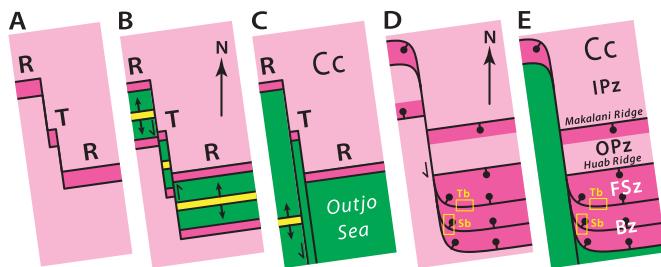


Fig. 198. Simplified rift–transform models for opening the SW cape of Congo craton (Hoffman, 2021b). Colour code: pink, non-stretched continental crust; red, modestly stretched ($\beta \leq 0.3$) continental crust; green, oceanic and/or highly stretched continental crust. (A–C) NNW–SSE plate divergence produces SSE-facing rifted (R) and WSW-facing transform (T) margins. A single rhombochasm is shown on the transform margin. Rifted margin undergoes syn- and post-rift subsidence (Figs. 26 & 163). There is little change in subsidence normal to the transform margin aside from weak thermal effects of spreading-ridge passage (B), accounting for weak W–E thickness or facies change (Figs. 196, 197 & 144). (D–E) Same as A & C but with antithetic normal faults in OPz and FSz (Fig. 26)—ball ornaments on hangingwalls—and curved splay faults (Tibaldi et al., 2016) linking normal faults on rifted margin with strike-slip faults on transform margin. Tb and Sb indicate fault orientations consistent with restored Toekoms and Soutput subbasins respectively (Fig. 17). Other abbreviations: Cc, Congo craton; Bz, basin zone; FSz, foreslope zone; IPz, inner platform zone; OPz, outer platform zone. Subduction of areas in green led to orogenic foreshortening of Congo margin in Northern Damara and Kaoko belts.

respectively (Fig. 163A). The simplified thermal subsidence model (McKenzie, 1978) assumes stretching was instantaneous, whereas it actually occurred over >110 Myr (Fig. 151). Therefore, stretching factors (β) must have been somewhat larger, to compensate for lithospheric cooling as stretching progressed.

Although the age of rift-to-shelf transition in OML remains uncertain, Tsumeb Subgroup alone is 2.15 km thick in Tsumeb syncline (King, 1994) and the Omboaatjie Fm-equivalent part of Auros Fm (Fig. 6E) is 0.15 km thick in nearby Nosib anticline (Hoffman et al., 2018), giving a potential passive-margin thickness of 2.30 km in northern OML. Northward thickening of Tsumeb Subgroup in EKz (Fig. 145) and eastward thickening toward OML implies a minimum rate of passive-margin subsidence at the SW cape of Congo craton (Fig. 2).

3.6.2. Swakop Group (FSz and Bz)

In FSz, growth faults of early and middle Cryogenian age border the 2.35-km-deep Toekoms and 0.74-km-deep Soutput subbasins (Tr1), respectively (Figs. 14, 18 & 22). Tilt correction restores the Toekoms border fault to a cratonward-dipping orientation (Fig. 26), striking parallel to Damara orogen (pTF_(o), Fig. 17). Landward-dipping normal faults occur on many rifted continental margins, including both volcanic and non-volcanic present Atlantic passive margins (McDermott et al., 2015; Clerc et al., 2018; Chauvet et al., 2021).

In Tr5, a small pre-Rasthof growth fault borders a 0.17-km-deep subbasin under Malta trough (Figs. 43 & 58), but no post-Rasthof growth faults were found. In their absence, a down-to-the-south crustal flexure of middle Cryogenian age is inferred to have partly accommodated the 1.5-km-deep Kranspoort trough, containing the distally tapered Okonguari Fm carbonate ramp (Figs. 43, 62, 65A & 68). We relate this flexure to the tip of the buried Huab ridge normal fault (Figs. 26 & 65B). Omboaatjie Fm shelf aggraded above the flexure, but its seaward edge was removed by glacial erosion during the Marinoan sea-level lowstand (Figs. 43, 62, 68 & 86).

The sequence-stratigraphic record of Marinoan glaciation is clearest in the FSz of Tr1 and 5 (Figs. 19, 43 & S10). The record (Fig. 44) includes a FST (Frannis-aus Fm), a LST (main Ghaub Fm including Duurwater moraine) and a TST (Bethanis Mb, Keilberg Mb and lowermost Karibib Fm). The Marinoan ice sheet eroded ≤ 120 m of lithified Omboaatjie Fm

cycles b7 and 8 from troughs (e.g., Omarumba trough) in IPz (Fig. 164), headwall erosion from the entire 328-m-thickness of outermost Omboaatjie Fm in OPz (Figs. 43 & 62), and Frannis-aus Fm from the more proximal FSz (Figs. 43, 50C & 55C). Debris was deposited in Duurwater moraine (Figs. 43 & 62) and a grounding-zone wedge at the foot of the moraine (Figs. 43–46 & 173) (Domack and Hoffman, 2011; Hoffman, 2011a). Some fraction of fine-grained carbonate debris must have dissolved in buffering the slow acidification of Marinoan seawater (Higgins and Schrag, 2003; Le Hir et al., 2008). This dissolved fraction would have reprecipitated as new carbonate in the Marinoan aftermath (Ridgwell et al., 2003; Higgins and Schrag, 2003), when snowball brine and meltwaters mixed and warmed (Shields, 2005; Fabre et al., 2013; Yang et al., 2017), continental shelves were flooded (Berger, 1982), and pH eventually rose (Le Hir et al., 2009; Fabre et al., 2011; Mills et al., 2011; Fabre and Berger, 2012).

Facies relations and stratigraphic architecture between FSz and OPz in early Ediacaran time have yet to be investigated. In Tr6, these strata were mostly removed by sub-Mulden Group erosion (Fig. 193). In the NE segment (OPz) of Tr5 (Fig. 68B), Tsumeb Subgroup presents a train of km-scale upright folds. Stratigraphic markers would be needed to construct a composite section there. The nearest homoclinal section close to the Otavi–Swakop transition is on farm Neuland 217 (NL, Fig. 4), 57 km east of 5–66 and 23.5 km west of Outjo.

In Bz (Northern zone), late Tonian faulting is suggested by steep depositional gradients in Ugab Subgroup of Tr2, where alluvial fan-ganglular changes to neritic carbonate laterally within a palinspastic distance of ≤ 10 km from S to N (Fig. 30). Peralkaline–alkaline igneous rocks were emplaced in FSz at 756 ± 2 and 747 ± 2 Ma (Hoffman et al., 1996), and in Bz at 757.7 ± 5.4 Ma (Nascimento et al., 2016) and 746 ± 2 Ma (Hoffman et al., 1996). In Tr3, rift-related structural rotation (around a subhorizontal axis) tilted late Tonian through middle Cryogenian strata during Marinoan glaciation (Figs. 37, 39 & 40), implying that crustal stretching continued in Bz for 5–20 Myr after it ceased in OPz (Hoffman et al., 2018). Comparable seaward-younging break-up fault sequences are inferred from thermo-mechanical modelling and 3D seismic data from North and South Atlantic margins (e.g., Brune et al., 2014; Lymer et al., 2019). The time interval between rift cessation (655–635 Ma) and collisional onset (≥ 600 Ma) was brief (35–55 Myr) compared with a 157-Myr average duration of passive margins globally since 1.0 Ga (Bradley, 2008).

3.6.3. Glacial paleotopography

It was recently proposed that the global average depth of Cryogenian glacial erosion on the continents was 3–5 km, and that the accommodation thus created explains a stepwise increase across the Ediacaran–Cambrian boundary, 95 Myr later, in preserved (North American) sediment volume as a function of age (Keller et al., 2019). Low global rates of Sturtian and Marinoan sediment accumulation (Partin and Sadler, 2016), consistent with our data (Table 5), were attributed to high rates of sediment subduction (Keller et al., 2019). Stratigraphic context in Otavi/Swakop Group provides constraints independent of sediment accumulation rates on the depths of glacial erosion and resulting paleotopographic relief. The Marinoan glaciation is the more informative because local structural rotations were largely absent (Fig. 5) and the paleobathymetric range on the bathyal foreslope was large (Fig. 163B & C), spanning ice equilibrium-line elevations (ELA, Fig. 178A) where the ice flux and hence erosion rates would have peaked (Hallet et al., 1996). We caution that, unlike Partin and Sadler (2016), our observations on glacial erosion pertain to a small region, a region that on account of its location at a continental promontory might have had lower than average glacial fluxes (e.g., Golledge et al., 2012), depending on spatial and temporal variations in ice-sheet mass balance (Benn et al., 2015). Proximity to sources of water vapour (sea glacier ablation), for example, might raise the glacial flux off a low-latitude continental promontory, by analogy with Quaternary West Antarctic Peninsula (Golledge et al., 2012).

We assume that CIE Cn5 in Ombaatjie Fm cycles b7–8 (Figs. 151 & 166) is correlative with Trezona CIE in South Australia (Halverson et al., 2005; Halverson and Shields-Zhou, 2011). In South Australia, Trezona CIE recovers to -1% VPDB (Fig. 166) in uppermost Trezona Fm, which is temporally linked to Marinoan glacial onset by the first appearance of extrabasinal (granitoid) ice-raftered debris (Rose et al., 2012). In Namibia, the same $\delta^{13}\text{C}$ value (-1%) is reached at the top of the Frannis-aus Fm (Figs. 172 & 173), the incipient Marinoan falling-stand wedge, and is closely approached (-1.3%) in the outermost section 5–49 of Ombaatjie Fm cycle b8 (Figs. 164 & 166, SOI S2). We therefore infer that b8 was the last marine carbonate cycle deposited on the Otavi platform before Marinoan glaciation. The original top of b8 would be the best neutral surface below which to estimate depths of Marinoan erosion, exclusive of any eroded aeolianite that accumulated upon that surface before glaciation.

Table 7 lists estimates of average Marinoan erosion for each transect on the platform, as well as the average depths of erosion in all transects, -49.4 m ($n = 62$), and sections outside and inside Omarumba trough (Fig. 164), -37.4 m ($n = 46$) and -83.0 m ($n = 16$). Paleo-relief (i.e., minimum minus maximum erosion depths) are also listed (Table 7). The estimates are based on assumed original thicknesses of cycle b8 ranging from 65 m in OPz to 85 m in Tr10–11 (Table 7). Northward increase in b8 thickness reflects northward thickening of the lower argillite-siltstone (Fig. 164). Justifications for the prescribed original b8 thicknesses are best done transect by transect.

In the platform segment of Tr5 (5–49–66, Figs. 43 & 68), cycle b8 is preserved in every section ($n = 18$) and its thickness ranges from 36.5 to 64.0 m, averaging 45.0 m. Much of the thickness variation is in the argillite-siltstone (Fig. 68) and could be structural in origin. A Marinoan erosion surface of modest relief ($\leq 27.5\text{ m}$ in 10 km SW–NE) is indicated. In terms of cycle-scale lithofacies sequence (Fig. 12), several sections preserve relatively complete highstand sub-cycles (5–49, 50, 51, 53, 57 & 63) and they average 47.6 m thick (Fig. 68). The original thickness cannot have been less than the thickest preserved section (5–60, 64.0 m), although this section may have been structurally thickened (Fig. 68). With these considerations in mind, we settled on 65 m as the original b8 thickness in Tr5, yielding an average depth of Marinoan erosion of -20.4 m (Table 7).

In Tr6, cycle b8 is again preserved in all sections ($n = 7$), ranging from 7.0 to 49.5 m and averaging 28.4 m including the incised aeolianite (?) in 6–3 (Fig. 71). Since Tr6 is cozonial with NE–Tr5 (Fig. 8B), we again take 65 m as the original b8 thickness, yielding an average Marinoan erosion depth of -36.6 m (Table 7). Tr7 is more deeply eroded than Tr5 or 6, and b8 is preserved in only 3 of 13 sections (Fig. 88). So we averaged the elevations of the Marinoan erosion surface relative to the base of cycle b7 (Fig. 88) and added 20 m of erosion for the average thickness of b7 (7–5, 6 & 9) and 65 m for erosion of b8 as before. The

resulting average depth of erosion in Tr7 is 72.2 m (Table 7). Paleo-relief on the glacial erosion surface in Tr7 is 98.0 m, the largest of any transect (Table 7). Quartz-sandstone tongues (b2 & 4) and stratigraphic thinning (b1–7) over Makalani ridge (Fig. 88) imply a lower average Ombaatjie subsidence rate over the buried rift-shoulder. If this continued into the late Cryogenian, a bedrock ridge would have grown beneath the Marinoan ice sheet, resulting in accelerated flow across the obstruction. Such flow acceleration might explain the $\geq 50\text{-m}$ -deep glacial troughs floored by basement in sections 7–2 and 4 (Fig. 88).

Tr8 is the most deeply eroded transect (Fig. 164), where cycle b8 is missing in every section (Fig. 103). The original b8 thickness is assumed to have been 75 m and the original b7 thickness can be estimated from the average thickness of 36 m ($n = 9$) for complete b7 sections in cozonial Tr9 (Figs. 125 & 129). Accordingly, the average depth of Marinoan erosion in Tr8 is -92.6 m (Table 7), which is taken to represent the floor of Omarumba trough (Fig. 194). It has the lowest paleo-relief of any transect (Table 7), only 21.0 m ($n = 9$) in 55 km (Fig. 103). Tr9 parallels Tr8 (Fig. 96) but only sections 9–1 and 2 occur within Omarumba trough (Fig. 164) where b8 was completely eroded (Figs. 125 & 145). In 9–3 and 4 (Figs. 125 & 129), cycle b7 is complete and averages 36 m ($n = 9$), which we take as its thickness in 9–1 and 2, same as Tr8. Assuming an original b8 thickness of 75 m, same as Tr8, yields an average Marinoan erosion depth in Tr9 of -54.8 m (Table 7).

Cycle b8 is preserved in Tr10 (Fig. 135) and in three footwall sections beneath Ombepera detachment in Tr11 (Fig. 140). Assuming an original b8 thickness of 85 m yields an average Marinoan erosion depth of only -17.6 m for Tr10 and 11 (Table 7), reflecting the average preserved b8 thickness of 67.4 m (Figs. 140 & 164).

Considering all transects, the average Marinoan erosion depth within Omarumba trough is 45.6 m deeper than outside the trough (Table 7). The overall average erosion depth of -49.4 m ($n = 62$) is 60–100 times lower than the global estimate of 3–5 km (Keller et al., 2019), but is similar to the average thickness of Marinoan glacial deposits (Ghaub Fm) of 52.9 m (Table 6), not counting zero-thickness sections. We do not expect glacial erosion and glacial deposits to balance exactly where carbonate is involved, because a fraction of the eroded carbonate would have dissolved to buffer the progressive acidification of the snowball ocean (Hoffman et al., 1998a; Higgins and Schrag, 2003; Le Hir et al., 2008).

Neither the average (-49.4 m) nor maximum (-122 m in 7–2) depths of Marinoan erosion is sufficient to provide accommodation for Maieberg Fm, the post-Marinoan cap-carbonate sequence, which has an average thickness of 383 m ($n = 11$) on the platform (Figs. 144, 145 & 181). Accommodation for Maieberg Fm must instead have been created by ongoing late Cryogenian tectonic subsidence (Fig. 163A) (Hoffman et al., 1998a, b; Halverson et al., 2002). Long before the accumulation step at the Ediacaran–Cambrian boundary (540 Ma) identified by Keller et al. (2019), Marinoan accommodation was filled by Maieberg Fm in Namibia and by Brachina Fm (2.75 km thick) in South Australia (Preiss and Forbes, 1981). Similarly, Sturtian accommodation was filled by Rasthof Fm in Namibia (Figs. 151 & 159) and by Tapley Hill Fm (1.55 km thick) in South Australia (Preiss and Forbes, 1981). Post-snowball steps in preserved sediment volume per unit age are possibly evident in Laurentia's Macrostrat database (Keller et al., 2019), but they predate the Ediacaran-Cambrian boundary step, which must therefore have had a different origin.

Maximum depths of Marinoan erosion occurred on the proximal foreslope, where 318 m of Ombaatjie Fm were removed by headwall erosion at a shelf-edge paleoscarp between sections 5–44 and 45 (Figs. 62 & 170). The Frannis-aus Fm is 80 m thick at its preservational limit in 5–25 (Figs. 43 & 58), upslope from which it was completely removed by glacial erosion. We know that Frannis-aus Fm originally extended farther upslope because its coarse-grained oolite (Fig. 48F) occurs as debris in Ghaub Fm diamictite in 5–31 (Figs. 43 & 170). Maxima in Marinoan erosion and accumulation were cozonial, with the crest of Duurwater moraine (5–33) situated only 5 km downslope from

Table 7

Estimated depths of Marinoan glacial erosion relative to the top of Ombaatjie Fm cycle b8, assuming original (uneroded) b8 thickness of 65 m (OPz) and 75–85 m (IPz), as described in text 3.6.3.

Transect	n	Uneroded cycle 8	Average erosion depth wrt top b8	Paleo-relief	Figures
Tr5 (49–66)	19	65 m	-20.4 m	27.0 m	68
Tr6	7	65 m	-36.6 m	42.5 m	71
Tr7	13	65 m	-72.2 m	98.0 m	88
Tr8	9	75 m	-92.6 m	21.0 m	103
Tr9	10	75 m	-54.8 m	76.0 m	125 & 129
Tr10 & 11	4	85 m	-17.6 m	44.2 m	135 & 140
Total OPz–IPz	62	65–85 m	-49.4 m	121.0 m	164
Outside trough	46	65–85 m	-37.4 m	121.0 m	164
Inside trough	16	75 m	-83.0 m	49.0 m	164

the subglacial headwall scarp in Ombaatjie Fm between 5 and 44 and 45 (Figs. 62–64 & 170). The locus of Marinoan erosion in the proximal FSz may reflect accelerated glacial flow due to the sloping bed itself and its likely proximity to the equilibrium line altitude (ELA, Fig. 178A).

Depths of Sturtian glacial erosion are more difficult to quantify because of active crustal stretching and resultant structural rotations. Clear evidence of Sturtian glacial incision (Fig. 156B) of 0.45 km depth exists in Tr8 (Omutirapo trough, Fig. 105). Sturtian incisions possibly exist in Tr5 (Kranspoort trough, Fig. 43) and Tr10 (Fig. 136). Thick Chuos Fm depocenters in Tr1 (Toekoms subbasin, Fig. 22) and Tr5 (Fig. 58) were accommodated by rift faulting (Fig. 156A), rather than by glacial erosion. Other depocenters in Tr2 (Figs. 32 & 35) and Tr3 (Fig. 39) were neither incised nor accommodated by faulting, and were evidently moraine-like positive paleotopographic features (Fig. 156C). Although Chuos Fm is 4.3 times thicker than Ghaub Fm on average (Table 6), its accumulation rate was faster only if Marinoan glaciation lasted ≥ 13.3 Myr. Apparently, enhanced Sturtian bedrock topography did not result in a significantly faster average rate of glacial erosion (Table 6).

3.6.4. The elusive western margin

We expected to see evidence for a west-facing Neoproterozoic continental margin in EKz (Fig. 3), but we have yet to find it. The Nabis Fm (Nosib Group) is a southward-tapered sheet of alluvial braid-plain deposits (crossbedded pebbly feldspathic arenite) extending from SW Angola to Kamanjab inlier and OML (Figs. 5 & 6D–E) (Kröner and Correia, 1980). It underlies Beesvlakte Fm with apparent conformity at the northern plunge of Kamanjab inlier (section 8–12, Figs. 96 & 99), but its maximum age is poorly constrained in the absence of detrital-zircon geochronology (Fig. 9). If Nabis Fm was related to western-margin development, we would expect eastward-directed paleoflow due to rift-shoulder topography, and/or younger westward-directed paleoflow due to post-rift thermal subsidence. Paleocurrent data, although limited, indicate instead southward-directed paleoflow (Fig. 146A). This is opposite in direction to synrift clastics shed from Makalani rift-shoulder (Figs. 147B & 5), from which we infer that Nabis Fm predated active rifting on the southern cratonic margin. Southward-directed flow could be explained as a trunk drainage fed by eastward-flowing tributaries draining the dip-slope of a western rift-shoulder. This would be analogous to the modern Nile River, which flows northward for >2400 km subparallel to the Red Sea Rift. We consider an intra-rift origin for Nabis Fm as unlikely because of its sheet-like geometry (Kröner and Correia, 1980) and absence of typical terrestrial rift-basin deposits like organic-rich shale, lacustrine carbonate or evaporite.

A rifted western margin predicts that westward thickening should be observed in post-rift passive-margin strata. This should be evident in the Otavi Group between Tr10 and 11, including the north ends of Tr8 and 9, which collectively span 80 km in a W–E direction (Fig. 8B). In fact, there is little evidence for systematic W–E change in Devede Fm (Fig. 196) or in the middle Cryogenian Abenab Subgroup (Fig. 197). Okakuyu and Chuos formations are omitted because they undergo rapid local changes in thickness related to paleo-relief on the sub-Chuos disconformity (Figs. 99, 105, 123, 139 & 143). The occurrence of quartz-chert sandstone beds in Devede Fm at 8–11 (Fig. 196) is consistent with its more southerly location relative to the other sections, given the observed southward increase in thickness and grain size of terrigenous input in both Tr8 and 9 (Figs. 99 & 123). Subaerial exposure surfaces are more numerous in the three middle sections (11–8 and 8–11, Fig. 196) than in the westernmost (11–2) or easternmost (10–2) sections. If this was a manifestation of lithospheric flexure in response to loading at a continental margin (Watts et al., 1982), the margin must have been located tens of kilometers (flexural half-wavelength) to the west prior to tectonic shortening.

Rasthof, Gruis and Ombaatjie formations thicken westward by 37, 28 and 21%, respectively (Fig. 197). In comparison, the same formations thicken northward in Tr9 by 61, 38 and 100%, respectively, over a 21%

shorter distance (Fig. 125). While the siliciclastic-rich Ombaatjie Fm of section 11–1 (and northward) were formerly assumed to indicate a westward ‘shale-out,’ its structural position in the hangingwall of Ombepera detachment (Hoffman et al., 2016b) implies a paleo-location east of Otjize syncline (11–10, Figs. 197 & 139). Considering only the detachment footwall, the only systematic change in lithofacies from E to W in any Cryogenian formation is an increased thickness of agillite in Ombaatjie Fm cycle b4 (Fig. 197).

Maieberg Fm thickens westward by 40% between sections 10–4 and 11–1, after first thinning by 33% in palinspastic intermediate section 11–10 (Fig. 144). It is possible that the top of 11–10 is truncated by Omboonde detachment (Fig. 137), however stratigraphic thinning is indicated by member Tm2 alone, which is 33 or 53% thinner in 11–10 than in 11–1 or 10–4, respectively (Fig. 144).

We are unable to properly constrain W–E changes in Elandshoek or Hüttenberg formations because section 11–1 is incomplete due to folding (S1 in Fig. 137). It also lacks $\delta^{13}\text{C}$ data to locate CIE En4 in lower Hüttenberg Fm (Fig. 185), the base of which is not obvious lithologically (Fig. 144). There is no doubt that both formations thicken northward, since they are thickest in the easternmost (10–4) and westernmost (11–0) sections in EKz (Fig. 145). Nor is there any doubt that cyclic peritidal lithofacies prevail in both formations as far west as the footwall of Sesfontein thrust (11–1, Figs. 144 & 137D; 11–0, Fig. 145).

Why is there little evidence in EKz of a rifted western Congo margin, when rift-related Swakop Group lithofacies occur in the hangingwall of Sesfontein thrust in CKz (Guj, 1970; Henry et al., 1992/93; Stanistreet and Charlesworth, 1999)? One explanation is a narrow marginal zone that was excised by Sesfontein thrust. Another explanation is a transform margin (Hoffman, 2021b), kinematically compatible with orthogonal rifting on the southern cratonic margin (Fig. 198A–C). A transform margin might undergo little stretching or post-rift thermal subsidence, consistent with uniform W–E thicknesses across EKz (Figs. 196 & 197). It would experience a transient heating event related to passage of a spreading ridge (Fig. 198B), but this might be too short-lived to create significant subsidence by thermally driven erosion (Sleep, 1971). In a transform scenario, rift-like Swakop Group basins in CKz (Stanistreet and Charlesworth, 1999) could represent rhombochasm (Carey, 1958), aka ‘pull-apart’ basins (Fig. 198A–C).

As discussed 2.1.3., the NNW-striking Soutput fault in Tr1 (Figs. 14, 15, 17B & 18) can be interpreted as a splay fault at a rift–transform junction (e.g., Tibaldi et al., 2016). As such, it could connect a NNW-dipping normal fault in Northern zone (e.g., Toekoms border fault) with a left-lateral NNW strike-slip fault in Kaoko belt (Fig. 198D & E). From the perspective of Otavi/Swakop Group, the early Ediacaran SW cape of Congo craton is reasonably inferred to have originated as a rift–transform junction (Hoffman, 2021b).

A transform western margin and rifted southern margin are also consistent with a near absence of rift-related igneous rocks in CKz and West Congo belt (Schermerhorn, 1961; Guj, 1970; Henry et al., 1992/93; Stanistreet and Charlesworth, 1999; Miller, 2008b), but many large rift-related igneous centres in Swakop Group of Northern (Outjo) zone (Smit, 1962; Frets, 1969; Miller, 1974, 1980, 2008b; SACS (South African Committee for Stratigraphy), 1980; Hoffman et al., 1996; Nascimento et al., 2016). The observed magmatic asymmetry alone is suggestive of a rift–transform junction. A transform margin is not easily reconciled with a western sea (Adamaster ocean of Hartnady et al., 1985) that was underlain exclusively by highly-extended continental crust (Konopásek et al., 2020; Percival et al., 2021).

3.7. Carbon isotope variability: a synthesis

Carbon isotope records obtained from Neoproterozoic marine carbonate successions (Fig. 1) exhibit positive and negative CIEs that are larger in amplitude and duration than Phanerozoic counterparts (Boyle et al., 2018). Many CIEs appear to be inter-regionally correlative, allowing them to be calibrated by radiometric ages and other seawater

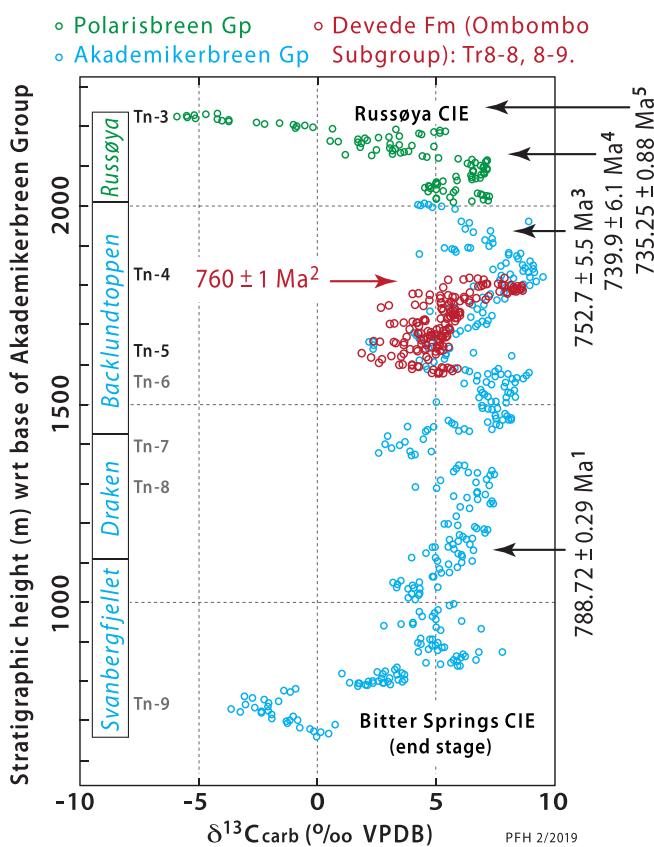


Fig. 199. Devede Fm $\delta^{13}\text{C}$ records from 8 to 8 and 8–9 (Figs. 147 & 148) shown as red circles, superimposed on records from Akademikerbreen (blue circles) and Russøya groups in NE Svalbard (Halverson et al., 2018b). Vertical axis is stratigraphic thickness in Svalbard. Devede record is reduced to 53.5% of its actual thickness (i.e., Devede subsidence rate was nearly double that of middle Backlundtoppen Fm in Svalbard). Chronostratigraphic pegs on $\delta^{13}\text{C}$ record: ¹CA-IDTIMS U–Pb age for zircon from tuff in upper Tsedia Fm, Tambien Group, Ethiopia (Swanson-Hysell et al., 2015b); ²IDTIMS Pb–Pb age for zircon from tuff in upper Devede Fm (Halverson et al., 2005); ³Re–Os isochron from organic-rich shale at base of Callison Lake Fm, Mount Harper Group, NW Canada (Rooney et al., 2015); ⁴Re–Os isochron from organic-rich shale at top of Callison Lake Fm (Strauss et al., 2014); ⁵CA-IDTIMS U–Pb zircon age from tuff close to base of Matheos Fm, Tambien Group (MacLennan et al., 2018).

proxy data (e.g., $^{87}\text{Sr}/^{86}\text{Sr}$) where available (Halverson et al., 2005, 2007, 2018b; Swanson-Hysell et al., 2015b; MacLennan et al., 2018; Canfield et al., 2020; Rooney et al., 2020b). The origins and significance of the CIEs remain controversial, however, and their very existence, regardless of origin, presents challenges in accounting for isotope mass balance and electron charge balance (Rothman et al., 2003; Bristow and Kennedy, 2008; Swart, 2008; Derry, 2010a, b; Bjerrum and Canfield, 2011; Swart and Kennedy, 2012; Schrag et al., 2013; Bachan et al., 2017; Boyle et al., 2018; Miyazaki et al., 2018; Shields, 2018; Shields et al., 2019). The longer lived the CIE, the bigger the challenge.

New $\delta^{13}\text{C}$ records from Tonian, Cryogenian and Ediacaran parts of Otavi/Swakop Group contribute in different ways to the ongoing discussion. The late Tonian record (Lamothe et al., 2019) is a consistency test for existing reference curves (Halverson et al., 2018b; Fairchild et al., 2018; MacLennan et al., 2018). Cryogenian global composite curves are heavily based on Otavi Group data, so our expanded database is most useful in examining intra-regional variability, including variability in diagenetic history (Hoffman and Lamothe, 2019). The early Ediacaran global composite curve is not well defined because key regions are either stratigraphically condensed (South China), carbonate-poor (South Australia), or isotopically dichotomous (Liljestrand et al., 2020).

3.7.1. Late Tonian $\delta^{13}\text{C}$ record

The late Tonian global composite curve features prolonged periods of heavily enriched values ($\geq +4\text{‰ VPDB}$), punctuated by three negative CIEs, the youngest of which directly preceded the Sturtian glaciation (Fig. 1). The oldest (Bitter Springs CIE) occurred between 811 and 789 Ma (Swanson-Hysell et al., 2015b) and is not represented in Otavi/Swakop Group. The younger two were formerly thought to be one and the same. The name ‘Islay CIE’ was used, referring to an island in the W of Scotland where the CIE was first documented (Brasier and Shields, 2000). More recently, the age of ‘Islay CIE’ was radiometrically constrained in NW Canada and Ethiopia between 0.74 and 0.73 Ga (Rooney et al., 2014; Strauss et al., 2015; MacLennan et al., 2018), strongly suggesting that it is not the same excursion as the one in Scotland, which appears to be gradational with Sturtian glacial deposits and accordingly much closer in age to the glacial onset at 717 Ma (Fairchild et al., 2018; Ali et al., 2018; Macdonald et al., 2018). To avoid confusion, we follow (Fig. 1) a recent proposal that the older (0.74–0.73 Ga) excursion be renamed ‘Russøya CIE’ (Halverson et al., 2018b), after islands in Svalbard where it was first described (Halverson et al., 2004). The name ‘Garvellach CIE’ (Fairchild et al., 2018) was proposed for the younger excursion, after islands in the west of Scotland where its relation to Sturtian glacial deposits (Port Askaig Fm) is best observed (Ali et al., 2018).

There are two carbonate-rich intervals in the Tonian of Otavi/Swakop Group. Devede Fm (Ombombo Subgroup) of IPz has a U–Pb zircon age of $759 \pm 1\text{ Ma}$ (Halverson et al., 2005) from a tuff near its top. Accordingly, it was deposited between Bitter Springs and Russøya CIEs (Fig. 199). Ugab Subgroup in NDz (Tr2 and 3) is underlain by Lower Naaupoort Fm volcanics, dated at $746 \pm 2\text{ Ma}$ (Hoffman et al., 1996). It might therefore record Russøya CIE and the interval between it and Garvellach CIE (Fig. 200). Devede and Ugab $\delta^{13}\text{C}$ records can be compared with age-calibrated, high-resolution records from Svalbard (Fig. 199) (Halverson et al., 2005, 2018a, b) and Ethiopia (Fig. 200) (MacLennan et al., 2018; Park et al., 2020), respectively.

Thick carbonate-dominated successions accumulated between the Bitter Springs (0.81–0.80 Ga) and Russøya (0.74–0.73) CIEs on the (present) northeastern and northwestern margins of Laurentia, which then lay in the deep tropics (Li et al., 2008; Merdith et al., 2017b). These successions are notably well exposed in NE Svalbard (Hecla Hoek Supergroup), East Greenland (Eleonore Bay Group), and Northwest Territories (Little Dal Group) and Yukon (Fifteenmile Group) in Canada. In Svalbard, a chronometric age-biostratigraphically-calibrated, high-resolution, $\delta^{13}\text{C}$ record for this interval was recently constructed (Fig. 199) (Halverson et al., 2018b). In Devede Fm, significant differences exist between the records from different sections (Fig. 148), despite their rather uniform thickness and a seemingly correlative tongue of siliciclastic-rich cycles in the lower part of the formation (Fig. 147). We therefore used only the two most consistent records (8–8 and 9) for comparison with the Svalbard record (Fig. 199). The best fit, consistent with chronometric constraints, implies that Devede Fm is broadly correlative with middle Backlundtoppen Fm of Akademikerbreen Group (Fig. 199). It lies within the biozone of testate amoebae (Halverson et al., 2018b; Porter and Knoll, 2000; Porter et al., 2003; Strauss et al., 2014). Devede Fm accumulated during an enigmatic 60-Myr interval, 0.80–0.74 Ga, when carbonate $\delta^{13}\text{C}$ was persistently enriched (+3–9‰ VPDB) yet the average organic content of shales was anomalously low (Woltz et al., 2021), and when phosphate was not a limiting nutrient (Cohen et al., 2017; Riedman et al., 2021) yet marine primary production was predominantly bacterial in origin (Brocks et al., 2017; Zumberge et al., 2020).

High-resolution $\delta^{13}\text{C}$ records have been acquired from the Tambien Group in northern Ethiopia (MacLennan et al., 2018; Park et al., 2020). These late Tonian strata are comparable to the Ugab Subgroup in thickness, but the data (Fig. 200) are plotted not against stratigraphic height but against geologic time, in an age model calibrated by CA-IDTIMS zircon U–Pb ages of 735.25 ± 0.88 and $719.68 \pm 0.94\text{ Ma}$

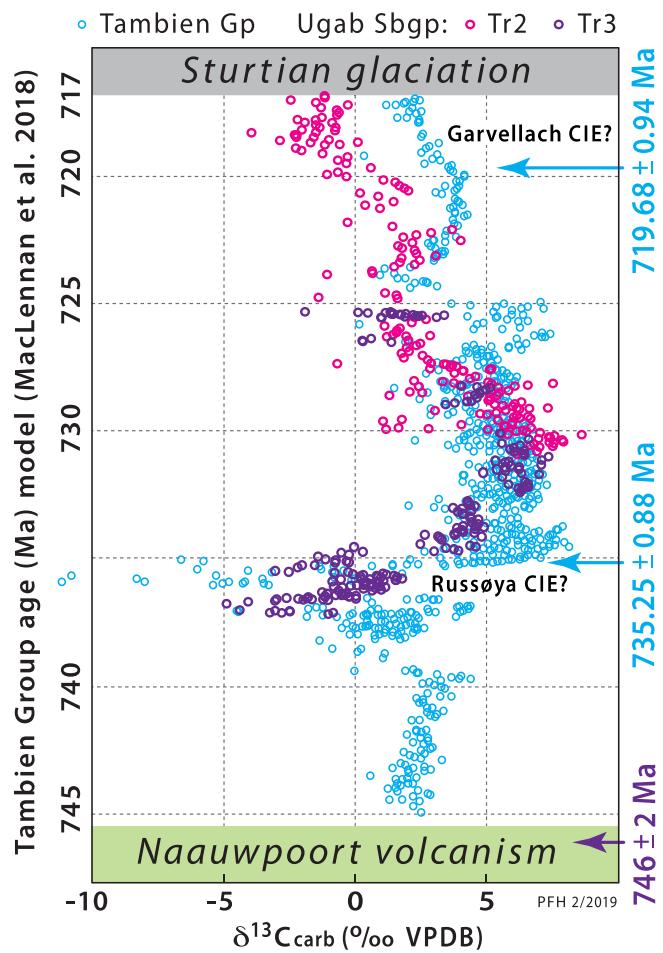


Fig. 200. $\delta^{13}\text{C}$ records for Ugab Subgroup (Figs. 152 & 153) from Tr2 (magenta) and Tr3 (purple), superimposed on an age model (elapsed time, not stratigraphic thickness, on y-axis) for a composite $\delta^{13}\text{C}$ record from Tambien Group in northern Ethiopia (MacLennan et al., 2018; Park et al., 2020). CA-IDTIMS U–Pb zircon ages from tuffs in basal Matheos and upper Mariam Bohkahko Fms in same succession (MacLennan et al., 2018).

obtained for tuffs in Tambien Group (MacLennan et al., 2018). The older age constrains the end of Russøya CIE and the younger one predates Sturtian onset by ≤ 3 Myr (Fig. 200). The composite Ugab $\delta^{13}\text{C}$ curve from Tr2 and 3 (Fig. 153B), fitted to the Tambien record at Russøya CIE and Sturtian onset, follows a broadly similar trajectory (Fig. 200). The match is promising considering that the Ugab records were neither decompacted nor adjusted for incompleteness or unsteady accumulation, or by ‘fitting’ the curves. The most prominent mismatches are the double-pronged Russøya CIE in the Ugab records (sections 3–10 and 15, Fig. 152) and more depleted values directly beneath Chuos Fm in Namibia compared with Ethiopia (Fig. 200). Values in Namibia are less depleted than the type Garvellach CIE in Scotland (Fairchild, et al., 2018; Ali et al., 2018). Either the CIE is less depleted in Garvellach-age strata in Tambien Group, or else those strata were removed or never deposited in Ethiopia. If the latter, Ugab Subgroup preserves the more complete preglacial record despite an erosive contact with Chuos Fm (Figs. 31D & 30). Ugab Subgroup is the first-known succession in which Russøya and Garvellach CIEs are both preserved (Lamothe et al., 2019).

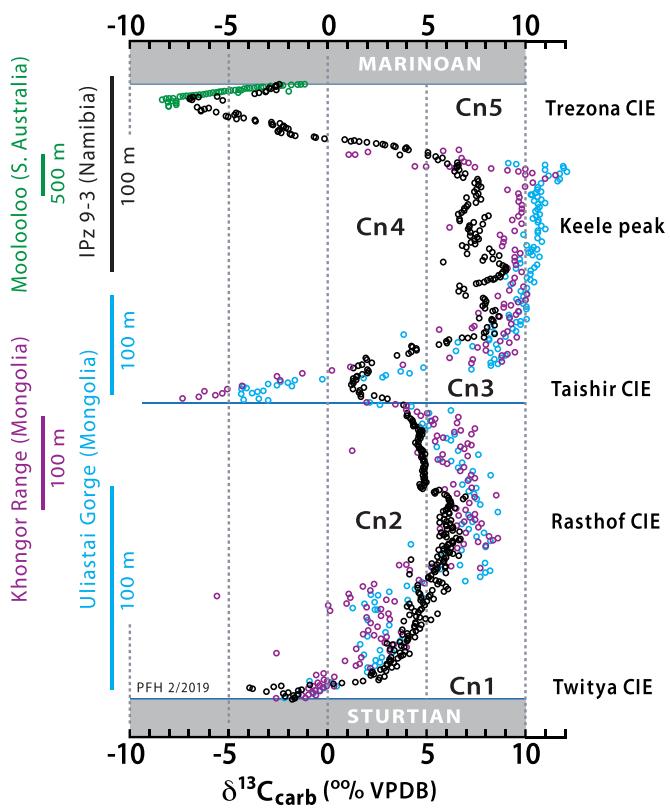


Fig. 201. Normalized Cryogenian inter-Snowball $\delta^{13}\text{C}$ records: Zavkhan Basin, Mongolia (purple and blue circles) from Bold et al. (2016); Abenab Subgroup (black circles) from section 9–3 (Fig. 133); Trezona Fm, South Australia (green circles) from Rose et al. (2012). Sections normalized at base of CIE Cn3: actual thicknesses indicated by colour-coded scale bars (shorter blue bar above base Cn3). Compared with calcitic Mongolian records, dolomitic Namibian ones are less ^{13}C -enriched in Cn2 and Cn4, and less depleted in Cn3. Cn5 is absent in Mongolia, possibly due to Marinoan glacial erosion. Cn5 is less depleted in Namibia (dolomite) than in South Australia (calcite).

3.7.2. Cryogenian $\delta^{13}\text{C}$ record

The global composite carbonate $\delta^{13}\text{C}$ record for the middle Cryogenian (Halverson et al., 2005, 2010; Halverson and Shields-Zhou, 2011) was founded on Otavi/Swakop Group records, critically augmented by data from Trezona CIE Cn5 recovery in South Australia (McKirky et al., 2001; Rose et al., 2012) and Taishir CIE Cn3 in western Mongolia (Johnston et al., 2012; Bold et al., 2016). Otavi/Swakop Group data previously used can be improved with the high-resolution record from IPz section 9–3 (Figs. 201, 122, 133 & 165). The record features two broad positive anomalies (Cn2 and 4), bracketed by three sharp negative excursions, Cn1 (Twitya CIE), Cn3 (Tayshir CIE) and Cn5 (Trezona CIE) (Fig. 201). Cn3 in Gruis Fm is shallower and blunter than in Mongolia, where the nadir hovers near -7.5‰ (VPDB) and $\delta^{13}\text{C}$ of bulk organic matter (0.05–0.20 wt% TOC in limestone) closely tracks the CIE in coexisting carbonate (Johnston et al., 2012). The younger and more extreme of the positive anomalies (Cn4) was named ‘Keele peak’ (Kaufman et al., 1997) after the youngest pre-Marinoan formation in the Mackenzie Mountains (NW Canada). In Oombaattjie Fm (Fig. 201), Cn5 looks less like a peak than a tepui (plateau), where base level is raised to $+8\text{‰}$ in Otavi Group and $+10\text{‰}$ in Mongolia (Johnston et al., 2012).

Hoffman and Lamothe (2019) drew attention to middle Cryogenian records in Swakop Group (Fig. 170). In Fig. 202, $\delta^{13}\text{C}$ profiles from 5 to

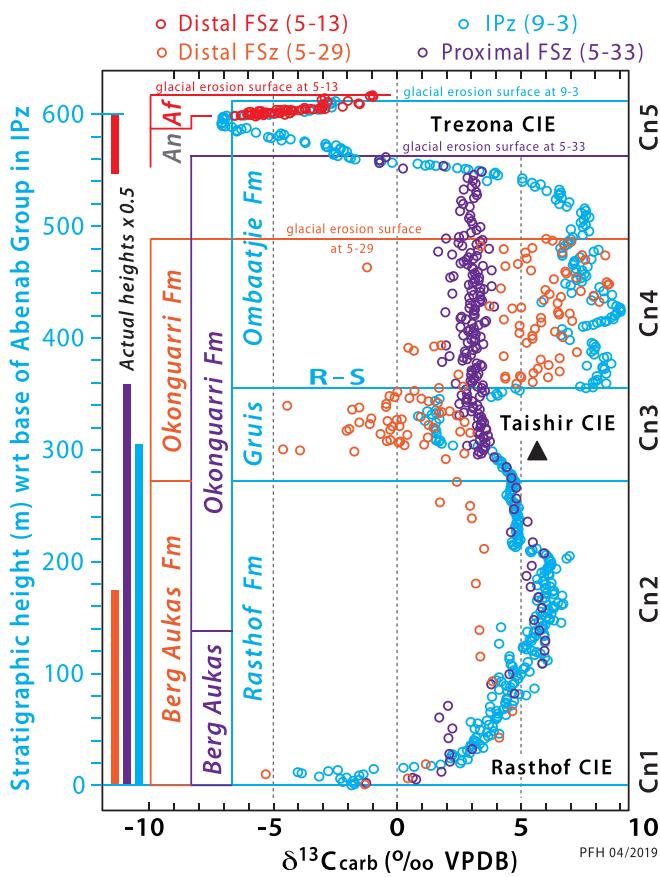


Fig. 202. Thickness-normalized middle Cryogenian $\delta^{13}\text{C}$ records of Otavi/Swakop Group from different zones (Hoffman and Lamothe, 2019). IPz (blue) is represented by composite 9–3 (Figs. 125 & 133), proximal FSz (purple) by 5–33 (Figs. 43, 62 & 170), and distal FSz (orange) by 5–29 (Figs. 43, 58, 62 & 170) and (red) 5–13 (Figs. 43–44, 170 & 172). Formations defined lithologically on columnar sections are colour-coded to $\delta^{13}\text{C}$ records on left. Numbered CIEs on right. R–S is rift-to-shelf transition at base of Ombaatjie Fm on platform. Distal FSz $\delta^{13}\text{C}$ record (orange) is normalized to IPz record at base of Rasthof Fm and at abrupt secular shift to heavier values between Cn3 and 4, which corresponds to R–S in IPz. Proximal FSz record (purple) is normalized to IPz record at base of Rasthof Fm and at top of Cn2, corresponding to lower-middle Gruis Fm in IPz (black triangle). Bars on left indicate relative actual thickness. Cn1 and 2 are observed in all zones. Cn3–5 are expressed in IPz and distal FSz, but are not observed in proximal FSz, where $\delta^{13}\text{C}$ persists $\sim +3\text{\textperthousand}$ (VPDB), an uncommon value in other zones (Fig. 208). Hoffman and Lamothe (2019) speculate that CIE Cn 3–4 were destroyed by seawater-buffered diagenesis and dolomitization (Fig. 190) in permeable Okonguarri Fm grainstone of proximal FSz (Kranspoort trough, Fig. 43), and Cn5 was removed by Marinoan glacial erosion that was focussed in proximal FSz (Figs. 43, 170, 173 & 178A).

29 and 33 represent distal (orange) and proximal (purple) FSz, respectively. Section 5–13 (red) represents Franni-aus Fm. All profiles are normalized to IPz section 9–3 (blue). Berg Aukas–Okonguarri Fm profiles are divided into two segments, each normalized independently to the onset of CIE Cn3 in IPz (black triangle, Fig. 202). The older segments of both profiles are normalized to the base of Rasthof Fm in IPz. The top of the younger segment in proximal FSz (purple) is fitted to the descending leg of Cn5 in IPz (Fig. 202). The younger segment in distal FSz (orange) is scaled such that the shift from less to more depleted values corresponds to the Gruis–Ombaatjie Fm contact in IPz (Fig. 202). The scaling determines the top of Okonguarri Fm in distal FSz, which is truncated at the sub-Ghaub Fm glacial disconformity (Figs. 58 & 170).

The third FSz segment is Franni-Aus Fm (Af), which is represented by distal FSz section 5–13. It was scaled to fit the ascending limb of Cn5 in IPz (Figs. 170, 172 & 202). Franni-aus Fm reaches 1.5‰ heavier values

than are preserved in uppermost Ombaatjie Fm, consistent with earlier cessation of the IPz record due to glacioeustatic emergence.

Proximal FSz and IPz profiles are well matched in the first segment (below the triangle), but the middle and upper Okonguarri Fm profile is completely incompatible with IPz (Fig. 202). The former is nearly invariant around $+3.0\text{--}3.5\text{\textperthousand}$ (VPDB), values that are intersected but never maintained in the IPz profile (Fig. 202). Cn3 is absent in proximal FSz, as is Cn4 (Fig. 170). No amount of fitting can reconcile the FSz and IPz profiles through Cn3 and 4 (Fig. 202). The simplest explanation is that proximal FSz carbonate $\delta^{13}\text{C}$ was post-depositionally altered to uniform values that slowly declined from $+3.5\text{\textperthousand}$ to $3.0\text{\textperthousand}$, irrespective of more depleted (Cn3) or enriched (Cn4) starting compositions (Hoffman and Lamothe, 2019).

Interestingly, the more distal FSz profile (5–29) is a better match for IPz than the proximal one (Fig. 202). Both Cn3 and 4 are expressed, each with large point-to-point variability (Fig. 202). Cn3 is *more* depleted in distal FSz than in IPz (Fig. 202), but less so than its nominal correlative in Mongolia (Fig. 201).

The spatial pattern just described—broad positive and sharp negative CIEs in IPz, distal FSz and Bz, replaced in coeval proximal FSz by uniform values close to those of modern seawater (Fig. 202)—is familiar. The same pattern was described and discussed earlier (3.4.4.) in reference to CIEs En2–4 (Fig. 189). Hoffman and Lamothe (2019) postulated that early seawater-buffered diagenesis/dolomitization (Higgins et al., 2018; Ahm et al., 2019; Bold et al., 2020), driven by porewater convection (Fig. 190), isotopically altered permeable (proximal) FSz lithologies, whereas IPz carbonates underwent sediment-buffered diagenesis that preserved their isotopic compositions inherited from semi-restricted epi-platform waters. These compositions were retained in sediment swept off the shelf and deposited distally, beyond the zone of seawater-buffered diagenesis (Fig. 190). Accordingly, uniform values in proximal FSz (Fig. 122) should reflect more reliably the composition of Cryogenian open-ocean DIC (Fig. 190). This postulate (Hoffman and Lamothe, 2019) invites criticism because it removes the well-mixed ocean as the rationale for putatively correlative CIEs, Cn3–4 (Fig. 201) and En2–4 (Fig. 203). The postulate is not that open-ocean DIC did not change, but that it hovered at $+3.0\text{--}3.5\text{\textperthousand}$ in Cn3–4 time (Fig. 202) and $+0.9 \pm 1.5\text{\textperthousand}$ in En2–3 time (Fig. 189).

The preferred normalization of FSz profiles with IPz (Fig. 202) implies that the onset of seawater-buffered diagenesis in proximal FSz was coeval with middle Gruis Fm in IPz (black triangle, Fig. 202). This is stratigraphically *below* the rift-to-shelf (R–S) transition, when no discrete FSz yet existed (Fig. 26). Hoffman and Lamothe (2019) note that diagenesis occurs in subsurface, altering sediment that was deposited earlier. When the foreslope first developed, sediment that was diagenetically altered by seawater invasion (Fig. 190) had been deposited before the foreslope existed. The depth of the black triangle below the R–S transition is the same in both FSz profiles, 0.10 km in stratigraphic thickness (Fig. 170). Considering all the FSz profiles (Fig. 170), homogeneously altered $\delta^{13}\text{C}$ profiles are clearly correlated with permeable grainstone, which served as preferred pathways for pore-fluid migration.

What about CIEs Cn5 and En1 in proximal FSz? Cn5 is problematic because Marinoan glacial erosion was most aggressive in the proximal FSz (Figs. 43, 170 & 178A). In Tr5, Okonguarri Fm is glacially truncated in every section upslope from 5 to 25 (Fig. 58), which is also the last section in which Franni-aus Fm is preserved. A short tail of declining $\delta^{13}\text{C}$ values ($n = 5$) at the top of Okonguarri Fm in 5–33 is the only surviving record of Cn5 downturn in FSz (Figs. 170 & 202). Hoffman and Lamothe (2019) point out that seawater-buffered diagenesis of youngest inter-snowball deposits would have ended prematurely because of Marinoan sea-level fall, enhancing the prospects for survival of Cn5 if not glacially removed. On the other hand, seaward increase in seawater-buffered diagenesis (Fig. 190) could explain the difference in slope between OPz and IPz of the $\delta^{13}\text{C}$ downturn toward Cn5 nadir (Fig. 168).

Regarding En1, sporadic dolomitization and associated isotopic

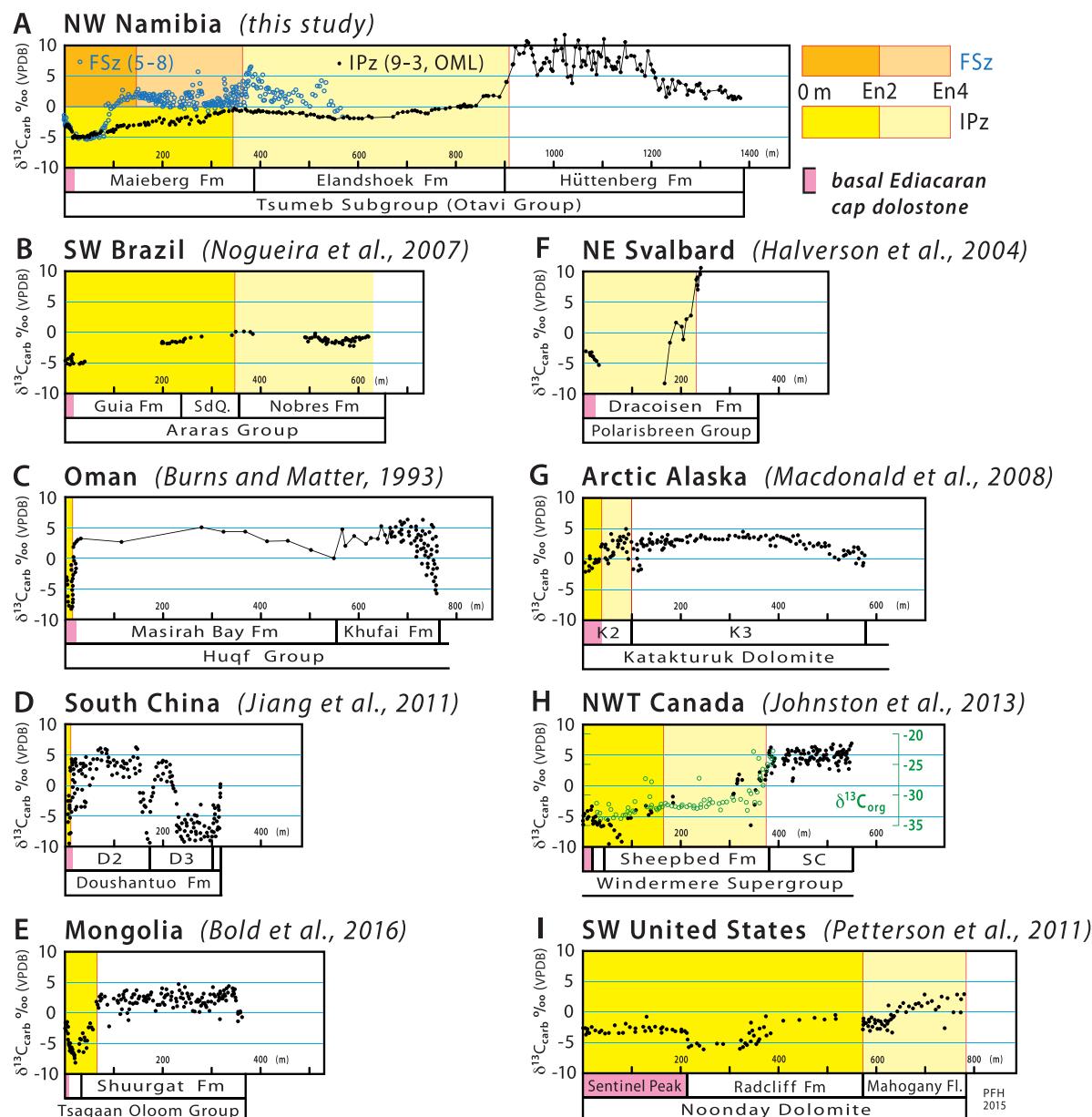


Fig. 203. Comparison of early Ediacaran $\delta^{13}\text{C}$ records normalized by stratigraphic thickness on the x-axis. Basal Ediacaran cap dolomite (*sensu stricto*) is indicated by pink bar. Bold and pale yellow/orange bands indicate stratigraphic heights of CIEs En2 and En4, respectively, in IPz/FSz. (A) NW Namibia (this study): FSz (5–6) blue; IPz (9–3 and Tsumeb, Fig. 188) black. (B) SW Brazil, Amazonia craton (Nogueira et al., 2007). (C) Oman (Burns and Matter, 1993). (D) South China (Jiang et al., 2011). (E) Mongolia, Zavkhan Basin (Bold et al., 2016). (F) NE Svalbard, NE Laurentia craton (Halverson et al., 2004). (G) Arctic Alaska, NW Laurentia craton (Macdonald et al., 2008). (H) Mackenzie Mountains, NW Canada, NW Laurentia (Johnston et al., 2013). Green circles are $\delta^{13}\text{C}_{\text{org}}$ data from organic-rich black shale, scaled as $\delta^{13}\text{C}_{\text{org}} = \delta^{13}\text{C}_{\text{carb}} - 28\text{‰}$. (I) Death Valley area, SW USA, Laurentia (Petterson et al., 2011). Based on chemostratigraphic correlations (yellow bands), Tsumeb Subgroup (A) is more expanded (i.e., higher apparent average accumulation rate) than early Ediacaran successions other than SW Brazil (B) and SW United States.

alteration of Maieberg Fm Tm2 or its Swakop Group equivalent is documented in all zones (Figs. 184, 182, 187 & 188). We cannot say if alteration was more pervasive in proximal FSz because we have no En1 profiles from that area. In OPz, Ca- and Mg-isotope data (Ahm et al., 2019) strongly suggest that seawater-buffered diagenesis accounts for the lateral $\delta^{13}\text{C}$ gradient observed in isochronous profiles of Keilberg Mb, which increase seaward from -3.0 to -1.0‰ across the OPz (Fig. 180A). Pervasive dolomitization of Keilberg Mb may have been favoured by its permeable peloidal grainstone texture (Ahm et al., 2019; Bold et al., 2020), which contrasts with impermeable micritic and marly rhythmite of Tm2 that is typically undolomitized or only partially dolomitized (Fig. 181). Rapid carbonate accumulation rates resulting

from anomalous carbonate oversaturation in the Marinoan aftermath would have shortened the time available for early diagenesis, if limited to shallow depth of burial (Hoffman and Lamothe, 2019).

Are the correlations of proximal (purple) and distal (orange) FSz profiles (Fig. 202) mutually compatible? It might appear that a fatal mismatch exists between the basal Okonguarri Fm in those sections (Fig. 202). This is not necessarily the case. If Okonguarri Fm accumulated as a prograding stack of down-lapping clinoforms, basal Okonguarri Fm should become younger in the seaward direction. The observed upward and landward coarsening and shoaling of lithofacies across Kranstoort trough (Figs. 43 & 62) are consistent with a progradational mode of accretion.

3.7.3. Early Ediacaran $\delta^{13}\text{C}$ record

Fig. 203 shows representative $\delta^{13}\text{C}$ records from carbonate-rich marine successions on six different paleocontinents, with Laurentia represented by four different margins (Fig. 203F–I). CIE En1 occurs in all, but is highly condensed in Oman (Fig. 203C) and South China (Fig. 203D), and expanded in Congo (Fig. 203A), Amazonia (Fig. 203B), and in Arctic (Fig. 203F) and Pacific Laurentia (Fig. 203H–I). Accumulation rate exerts the main control on these differences in stratigraphic expression.

In Fig. 203A, we show in black a composite Tsumeb Subgroup record from the IPz ($\text{Tm} + \text{Te}$ from 9 to 3, Th from OML, Fig. 185), and in blue a FSz record (5–8) that is normalized to the IPz record as indicated in Fig. 189. Might the sharp rise to high values (lower Hüttenberg Fm) in the IPz record be useful for inter-regional correlation? A sharp rise of similar magnitude (but lower absolute values) is seen in unit SC (“Sheepbed carbonate” of Macdonald et al., 2013b) in NW Canada (Fig. 203H). Conversely, the absence of such a rise might be used to infer that the Nobres Fm in Amazonia (Fig. 103B) is pre-Hüttenberg in age. However, chemostratigraphic correlation is made more complicated by the weak expression of the same $\delta^{13}\text{C}$ rise in the Namibian FSz (Fig. 203A). Might fluid-buffered diagenesis, as inferred for the FSz (Fig. 190), also account for the rather featureless record from Arctic Alaska (Fig. 203G), which has little in common with early Ediacaran records from other Laurentian margins (Fig. 203F, H, I) (Strauss et al., 2013)?

The late Tonian and Cryogenian breakup of the paleo-tropical supercontinent Rodinia (e.g., Li et al., 2013; Merdith et al., 2017a, 2019) must have created many new carbonate shelves and platforms. As the sea floors adjacent to these neritic carbonate factories slowly subsided, the evolving bathyal slopes should have become increasingly prone to seawater invasion in response to porewater convection (Fig. 190). Paired Ca- and Mg-isotope records from these margins are increasingly documenting the elemental and isotopic effects of localized seawater-buffered diagenesis (Ahm et al., 2019; Bold et al., 2020; Crockford et al., 2021).

3.8. Other paleoenvironmental proxy records

A number of paleoenvironmental proxy records besides $\delta^{13}\text{C}$ and $\delta^{18}\text{O}$ have been obtained from parts of Otavi/Swakop Group. We briefly review and discuss these findings in light of our stratigraphic work and current understanding of the Neoproterozoic Earth system. We treat each proxy in historical order of publication.

3.8.1. Sulfur isotopes

The S-isotope composition ($\delta^{34}\text{S}$) of seawater-dissolved sulfate has undergone large secular variation since the Archean eon (Canfield and Raiswell, 1999; Havig et al., 2017; Crockford et al., 2019). The biogeochemical cycle of sulfur is complex, involving redox-dependent chemical reactions, multiple valence states of sulfur, and large biologically mediated isotope fractionations. The $\delta^{34}\text{S}$ of seawater sulfate reflects the compositions of S sources and sinks, in which the dominant fractionation mechanism is discrimination against the heavier isotope(s) during sulfate reduction by anaerobic bacteria. Additional fractionation can occur during microbial sulfide re-oxidation, through anaerobic disproportionation of elemental sulfur. Accordingly, if the proportion of microbially reduced S in the sediment flux (e.g., as FeS_2) were to rise, all else unchanged, so too would the $\delta^{34}\text{S}$ of seawater sulfate. Such a change could reflect increased ocean anoxia (more pyrite burial) or decreased sulfate evaporite deposition. If rivers, the primary source of marine sulfate, were to be seriously curtailed, as during a snowball epoch, drawdown of dissolved sulfate would be accompanied by progressively more extreme isotopic enrichment of both sulfide and residual dissolved sulfate through Rayleigh distillation, accompanied by gradual loss of fractionation between them. In diagenesis, microbial sulfate reduction and authigenic pyrite formation drive isotopic enrichment in residual

dissolved porewater sulfate, wherever accumulation rates outpace diffusive equilibration with overlying seawater. Consequently, pyrite $\delta^{34}\text{S}$ records from rapidly accumulated nearshore sediments are decoupled from seawater and from seawater-buffered pyrite $\delta^{34}\text{S}$ records in slowly-accumulated deeper-water sediments (Pasquier et al., 2021).

Deep oxidative weathering of the Southern African Plateau in the Cenozoic (Roberts and White, 2010) and Upper Cretaceous (Guillocheau et al., 2012; Braun et al., 2014) means that sulfide $\delta^{34}\text{S}$ studies must utilize drillcore, which is limited to the OML (Kaufman et al., 1991; Cui et al., 2018). Seawater sulfate, on the other hand, is captured in trace amounts in marine carbonate. This carbonate-associated sulfate (CAS) has been shown to preserve generally reliable records of seawater sulfate $\delta^{34}\text{S}$ variation over geologic time, with potential exceptions associated with burial dolomitization as indicated below.

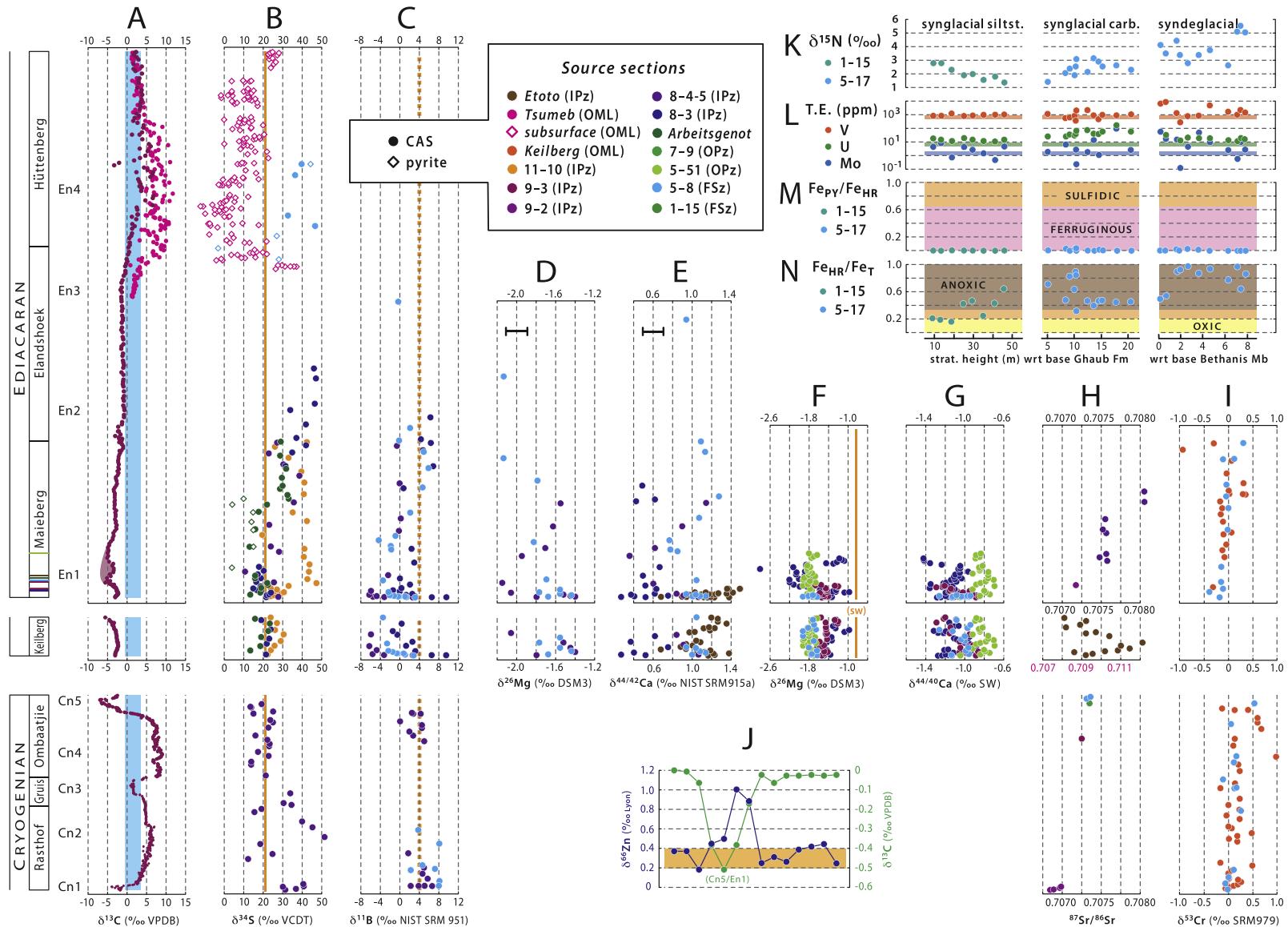
In Fig. 204B, published $\delta^{34}\text{S}$ data for CAS (closed circles) and pyrite (open diamonds) from the Otavi/Swakop Group are plotted (Hurtgen et al., 2002, 2006; Halverson and Hurtgen, 2007; Cui et al., 2018). Five of the sections from which data were obtained can be identified with our sections as indicated (Fig. 204B). Pyrite data from the Hüttenberg Fm were obtained from a deep drillcore in Tsumeb syncline (Cui et al., 2018), and both pyrite and CAS data from Maieberg Fm (Hurtgen et al., 2006) were obtained from a surface section on farm Arbeitsgenot (Fig. 4), ~90 km WSW of Tsumeb. The data are normalized to a common stratigraphic profile (Fig. 204B). Data from Elandshoek (8–3) and Karibib (5–8) formations are from Halverson and Hurtgen (2007). Karibib Fm pyrite and CAS data are from FSz and correspond to uppermost Elandshoek and lower Hüttenberg formations, based on sample heights and chemostratigraphic correlation (Figs. 185 & 204B). Accordingly, they can be compared with the pyrite data from Tsumeb (Cui et al., 2018). We are unaware of any Tonian $\delta^{34}\text{S}$ data from the Otavi/Swakop Group.

The CAS data (Fig. 204B) exhibit large departures from the $\delta^{34}\text{S}$ of modern seawater sulfate of 21‰ (VCDT). The basal calcite rhythmite member of Rasthof Fm is strongly enriched (30–41‰) and even more extreme enrichment is observed in the upper part of the microbialite-dominated middle Rasthof Fm Ar2 member. In Omabaatje Fm, average $\delta^{34}\text{S}$ is close to modern (orange bar, Fig. 204B), but fluctuations of $\leq 12\text{‰}$ on timescales of ≤ 1.0 Myr (Fig. 163A) imply a small seawater sulfate reservoir (Hurtgen et al., 2002). Only the descending leg of (Trezena) CIE Cn5 is preserved in section 8–4–5 (Fig. 164), so the response of $\delta^{34}\text{S}$ to Cn5 is not captured in the existing data (Fig. 204B).

Keilberg Mb cap dolomite has average $\delta^{34}\text{S}$ only slightly above modern, but the observed variability of $\leq 17\text{‰}$ on a timescale of ≤ 50 kyr (Yang et al., 2017; Crockford et al., 2018) again implies a small sulfate reservoir in the transient meltwater lid of the post-Snowball ocean, consistent with other geochemical evidence (Crockford et al., 2016). In the middle Maieberg Fm, there is little difference between coexisting pyrite and CAS $\delta^{34}\text{S}$ (diamonds and circles, respectively, in Fig. 204B), consistent with low seawater sulfate content (Hurtgen et al., 2002), and both are somewhat depleted relative to modern seawater sulfate.

Section 11–10 is an outlier, being extremely ^{34}S -enriched in middle Maieberg Fm Tm2 member (Fig. 204B). Tm2 is anomalously dolomitized in this section and $\delta^{13}\text{C}$ is altered by $\leq 4\text{‰}$ (Figs. 184 & 182). Hurtgen et al. (2006) attributed these changes to restricted circulation, but we subsequently found similar $\delta^{13}\text{C}$ shifts associated with dolomitization in FSz and Bz (Figs. 187 & 188), where restriction should not apply. Since 11–10 is far from FSz, we are inclined to exclude its Tm2 data as proxies for Ediacaran seawater.

On the other hand, undolomitized sections 8–3 and Arbeitsgenot exhibit a remarkable rise in CAS $\delta^{34}\text{S}$ between Tm2 and lower Elandshoek Fm (Fig. 204B). Highly enriched values, averaging nearly 40‰ with large variability, may have been sustained through lower Hüttenberg time, based on limited FSz data from 5 to 8, but by this time the difference between coexisting pyrite and CAS $\delta^{34}\text{S}$ had widened (one data-point excepted) to $\sim 25\text{‰}$, the equilibrium fractionation associated with microbial sulfate reduction when seawater sulfate is abundant



206

Fig. 204. Multiple proxy records, normalized by formation, from Cryogenian and Ediacaran sections of Otavi/Swakop Group in NW Namibia. Data points are colour-coded by section location, identified in box upper centre. Keilberg Mb thickness indicated by colour-coded lines within Maieberg Fm box. Normalized Keilberg Mb repeated at expanded scale below Ediacaran box. Significance of records is discussed in text sections 3.7. and 3.8. (A) $\delta^{13}\text{C}_{\text{carb}}$ (VPDB) from IPz sections 9–3 and Tsumeb (this study). Pale blue band gives range of Cenozoic benthic foraminiferal $\delta^{13}\text{C}$ (Zachos et al., 2001). (B) $\delta^{34}\text{S}$ (VCDT) from carbonate-associated sulfate (closed circles) and FeS_2 (open diamonds) (Hurgen et al., 2002, 2006; Halverson and Hurgen, 2007; Cui et al., 2018). Orange line is $\delta^{34}\text{S}$ of dissolved sulfate in modern seawater. (C) $\delta^{11}\text{B}_{\text{carb}}$ (NIST SRM 951), a proxy for relative pH, with dashed orange line indicating composition assumed to best represent “Neoproterozoic climatic normalcy” (Kasemann et al., 2005, 2010). (D) $\delta^{26}\text{Mg}$ (DSM3) (Kasemann et al., 2005, 2014). (E) $\delta^{44}/^{42}\text{Ca}$ (NIST SRM 915a) (Kasemann et al., 2005, 2014; Wei et al., 2019). (F) $\delta^{26}\text{Mg}$ (DSM3) (Ahm et al., 2019). (G) $\delta^{44}/^{42}\text{Ca}$ (modern seawater) (Ahm et al., 2019). (H) $^{87}\text{Sr}/^{86}\text{Sr}$ (Yoshioka et al., 2003; Halverson et al., 2007; Rodler et al., 2017; Wei et al., 2019). (I) $\delta^{53}\text{Cr}$ (Rodler et al., 2016, 2017). (J) $\delta^{65}\text{Zn}$ (Thiemens et al., 2012). (K) $\delta^{15}\text{N}$, (L) redox-sensitive trace-element (V, U, Mo) abundance, (M) $\text{Fe}_{\text{PY}}/\text{Fe}_{\text{HR}}$, and (N) $\text{Fe}_{\text{HR}}/\text{Fe}_{\text{T}}$ from (left column) basal siltstone member of Ghaub Fm at 1–15 (Figs. 18–20A), (center column) stratified carbonate diamictite from main Ghaub Fm at 5–17 (Figs. 43, 58, 60 & 61), and (right column) stratified carbonate diamictite from terminal Bethanis Mb of Ghaub Fm, also at 5–17 (Johnson et al., 2017). Fe_{PY} is pyrite Fe, Fe_{HR} is highly reactive (i.e., diothionite-extractable) and Fe_{T} is total Fe.

(more than a few mM). The observed simultaneous rise in CAS $\delta^{34}\text{S}$ and $\Delta^{34}\text{S}$ (i.e., $\delta^{34}\text{S}_{\text{CAS}}$ minus $\delta^{34}\text{S}_{\text{pyrite}}$) was attributed to growth of the seawater sulfate reservoir in response to an early Ediacaran rise in atmospheric oxygen, preceding the Shuram CIE (Halverson and Hurtgen, 2007). An oxygenation pulse during the Hüttenberg Fm is inferred from anticorrelated negative $\delta^{34}\text{S}_{\text{pyrite}}$ and positive $\delta^{13}\text{C}_{\text{org}}$ anomalies in the Tsumeb drillcore (Cui et al., 2018). Additional CAS and pyrite $\delta^{34}\text{S}$ data from the Elandschoek and Hüttenberg formations would be worth acquiring.

Otavi/Swakop Group was not the first succession in which super-heavy CAS and pyrite follow Cryogenian glaciations. In addition to Rasthof Fm (Fig. 204B), they occur following Sturtian glaciation in central and South Australia (Aralka and Tapley Hill formations), western Canada (Twitya Fm), South China (Datangpo Fm) and Kalahari craton (Gobabis Mb of Court Fm) in central Namibia (Gorjan et al., 2000, Goscombe et al., 2003a; Hurtgen et al., 2002, 2005). Following Marinoan glaciation, superheavy CAS and pyrite most similar to upper Maieberg and younger formations of Otavi/Swakop Group (Fig. 204B) are found in the homologous Araras Group (SW Brazil) in Amazonia (Sansjofre et al., 2016). In addition to $\delta^{34}\text{S}$ of CAS and pyrite, Sansjofre et al. (2016) measured deviations from mass-dependence of multiple isotopes, $\Delta^{33}\text{S}$ and $\Delta^{36}\text{S}$, in CAS. They found that as both CAS and pyrite $\delta^{34}\text{S}$ systematically rise ($\sim 20\text{\textperthousand}$) with stratigraphic height, there is a positively correlated rise in $\Delta^{33}\text{S}$ (+0.1%) and a negatively correlated decline in $\Delta^{36}\text{S}$ (-0.4%). According to Sansjofre et al. (2016), these relations cannot be reconciled with steady state (S in = S out) over the time period represented by ~ 250 m of platformal strata. They are most easily accounted for by assuming a profound drawdown of the marine sulfate reservoir, presumably by microbial reduction (MSR) and burial as pyrite (Sansjofre et al., 2016). The magnitude of pyrite burial implies a significant addition of O_2 to the atmosphere, assuming the pyrite was not reoxidized, but this O_2 must have first arisen earlier, in order to generate the marine sulfate reservoir to begin with (Sansjofre et al., 2016). Early Ediacaran oxygenation is consistent with the rise at that time of bacterial sulfur disproportionation, which is strongly indicated by a globally observed secular change in multiple S isotope ($\Delta^{33}\text{S}/\delta^{34}\text{S}$) arrays (Kunzmann et al., 2017).

3.8.2. Boron isotopes

Boron isotopes are widely used in Cenozoic paleoceanography as a proxy for seawater pH and therefore for paleo-atmospheric $p\text{CO}_2$ (Foster and Rae, 2016). There are two boron species in seawater, boric acid, B (OH_3), and borate ion, $\text{B}(\text{OH})_4^-$, the latter being exclusively incorporated into carbonate. There is a large (26%) equilibrium fractionation in $\delta^{11}\text{B}$ between the species (Klochko et al., 2006; Nir et al., 2015), most of which occurs over the pH range of 7.5 to 9.5. Consequently, the $\delta^{11}\text{B}$ of carbonate precipitated from modern seawater would range from just over 20‰ to just under 40‰ (wrt SRM 951 boric acid standards), respectively, over the same pH range. In other words, the $\delta^{11}\text{B}$ of carbonate rises with increasing pH. Modern marine carbonates fall within the range 20–24‰, consistent with seawater pH = 8.1 (Zeebe and Wolf-Gladrow, 2001).

Kasemann et al. (2005, 2010, see also Ohnemueller et al., 2014) measured boron isotopes in Otavi Group carbonates (Fig. 204C) in order to test a prediction of the Snowball Earth hypothesis that Cryogenian deglaciations could only occur under extremely elevated $p\text{CO}_2$, hence low seawater pH. Strong greenhouse radiative forcing is a necessary condition for snowball deglaciation due to high planetary albedo. There are three difficulties with this approach. The first is that, depending on the pH of non-glacial Neoproterozoic seawater, much of the pH change accompanying a snowball epoch might fall outside the range ($\text{pH} < 7$) of boron isotope sensitivity. The second is that the boron isotopic composition of Neoproterozoic seawater is unknown, meaning that absolute pH cannot be inferred, only pH relative to an arbitrary or inferred baseline. Kasemann et al. (2005) argue that seawater (ΣB) $\delta^{11}\text{B}$ could only have increased over the course of a snowball epoch, due primarily

to diminished continental runoff, opposite to the effect on borate $\delta^{11}\text{B}$ of pH lowering. Therefore, they measured $\delta^{11}\text{B}$ in upper Omibaatje Fm (Fig. 204C) to establish a non-glacial Cryogenian carbonate baseline. Since little new carbonate was produced during Sturtian or Marinoan epochs, they measured $\delta^{11}\text{B}$ in Rasthof and Maieberg cap-carbonate sequences in IPz and FSz (Fig. 204C). This introduces the third difficulty, which is that cap-carbonate sequences represent mixing zones between glacial meltwater and snowball-evolved brine (Shields, 2005; Stewart et al., 2015; Yang et al., 2017; Ahm et al., 2019; Wei et al., 2019).

$\delta^{11}\text{B}$ values for Rasthof Fm ($n = 23$) average 4.54‰ (NIST SRM 251), differing by 1.0‰ between the IPz and FSz (Kasemann et al., 2005, 2010). The Rasthof Fm average is just 1.2‰ heavier than the upper Omibaatje Fm average ($n = 9$) of 2.87‰ (Fig. 204C). Kasemann et al. (2010) take the average value of 4.07‰ for Rasthof and Omibaatje data combined as best representing “Neoproterozoic climatic normalcy.” This implicitly assumes that the Rasthof preserves no Sturtian glacial signal. Alternatively, Rasthof data might reflect counteractive effects of reduced Sturtian runoff (higher $\delta^{11}\text{B}$) and elevated $p\text{CO}_2$ (lower $\delta^{11}\text{B}$), in which case the small (1.2‰) difference between Rasthof and Omibaatje values would be fortuitous.

Maieberg Fm $\delta^{11}\text{B}$ records are quite distinct from Rasthof Fm (Fig. 204C). All three Maieberg sections (5–8, 8–3–4) decline precipitously over the basal 1.6 m of Keilberg Mb, by -5.6, -8.0 and -8.2‰, respectively. They then gradually recover over the full thickness of Maieberg Fm (132, 260 and 240 m, respectively). Section 8–2 begins nearly 7‰ heavier (+9.7‰) than the other sections, and all three sections bottom out at different values, -3.5, -1.2 and -6.2‰, respectively (Fig. 204C). Not surprisingly, attention was drawn to the steep decline in values at the base of Keilberg Mb (Kasemann et al., 2005, 2010), a pattern replicated in Marinoan cap dolomites in Kazakhstan and South China (Ohnemueller et al., 2014).

Kasemann et al. (2005, 2010) and Ohnemueller et al. (2014) interpret the initial steep $\delta^{11}\text{B}$ decline strictly in terms of pH change. They postulate that seawater pH changed little during the Marinoan snowball because seawater was shielded from the increasingly CO_2 -rich atmosphere by marine ice cover. When ice cover collapsed at snowball termination, atmospheric CO_2 invaded the ocean, causing abrupt acidification. The pH declines are estimated between -1.2 and -1.5 pH units, assuming a uniform minimum pH of just under 7.0 (Kasemann et al., 2010), or between -0.7 and -1.6 pH units assuming non-uniform pH minimums of 7.7 (5–8), 8.0 (8–3) and 6.7 (8–4) (Ohnemueller et al., 2014; see also Kasemann et al., 2005). Ocean deacidification is inferred on the timescale of middle and upper Maieberg Fm (Kasemann et al., 2005, 2010; Ohnemueller et al., 2014).

There are problems with the foregoing interpretation and glacial scenario. The first is that the subglacial seawater would not likely have maintained a high (neutral) pH because mid-ocean ridge volcanism would have outgassed CO_2 directly into the snowball ocean. Seafloor weathering could not likely have consumed the outgassed CO_2 entirely, because seafloor-weathering rate is retarded by low temperature at high pH (Brady and Gislason, 1997; Gislason and Oelkers, 2003; Le Hir et al., 2008; Coogan and Gillis, 2013; Coogan and Dosso, 2015). A second problem is that on a timescale of ≤ 14 Myr, the ocean and atmosphere could have equilibrated wrt CO_2 by air-sea gas exchange through moulins and crack systems in the sea glacier (Higgins and Schrag, 2003; Le Hir et al., 2008; Hoffman et al., 2017a).

A third problem is that if a large pH fall were to occur suddenly, carbonate saturation would fall as well. Carbonate would dissolve, rather than precipitate. If an abrupt severe acidification had occurred, no cap carbonate would have been produced to record it. Cap carbonates are remarkable because the extent of carbonate production expanded (Hoffman and Li, 2009), implying an unusual degree of carbonate oversaturation, which is normally limited by carbonate production. Conversely, if ocean acidification occurred slowly, during prolonged glaciation, it would have been buffered by dissolution of detrital

carbonate delivered by glaciation action (Hoffman et al., 1998b; Hoffman and Schrag, 2002). Carbonate saturation could be maintained, alkalinity greatly enlarged, and evolved subglacial waters primed for carbonate production very soon after snowball termination (Higgins and Schrag, 2003; Fabre and Berger, 2012; Fabre et al., 2013). Profligate seafloor cement in the MFS of the cap-carbonate sequence (Figs. 67C, 80A–F, 81A–B & 132A–C) is a manifestation of carbonate oversaturation of formerly subglacial deepwater, actively mixing with overlying meltwater (Fig. 178B).

How, then, should the steep (but quantitatively non-uniform) declines in $\delta^{11}\text{B}$ observed consistently at the base of Marinoan (but not Sturtian) cap dolomites be interpreted? The $\delta^{11}\text{B}$ of dissolved boron in 25 large rivers distributed globally is highly variable, -6 to $+43\text{‰}$ (SRM 951), but the composition of the total flux is 10% (Lemarchand et al., 2000; Mao et al., 2019), or 20% lighter than seawater dissolved ΣB , which is quite uniform in the open ocean because of its long residence time of ~ 14 Myr. Similarly, boron in glacial meltwater streams and ponds of the McMurdo Dry Valleys (Antarctica) ranges from 12 to 33% (Leslie et al., 2014), substantially lighter than seawater (39.5% at present), which is driven heavy through preferential removal of ^{10}B by adsorption on clay minerals, incorporation in (biogenic) carbonate, and exchange reactions with oceanic crust (Zeebe and Wolf-Gladrow, 2001). Ice-covered brine lakes in the Dry Valleys have B-rich deepwaters that are derived from and are isotopically enriched wrt seawater, but their hypolimnions are derived from meltwater runoff that is isotopically depleted (Leslie et al., 2014). During the Marinoan snowball, porewater in the Otavi/Swakop Group carbonate platform would have been dominated by subglacial meltwater with low $\delta^{11}\text{B}$, recharged by the SW lobe of the Congo ice sheet. The subglacial ocean would have been a B-rich brine with $\delta^{11}\text{B}$ (ΣB) above $+40\text{‰}$ (Kasemann et al., 2005). At the glacial termination, rapid melting of the sea-glacier and continental ice sheets would have created stable density-stratified oceans that would mix and destratify slowly over 10s of kyr (Shields, 2005; Hoffman, 2011a; Yang et al., 2017). Initial mixing between ^{11}B -enriched glacial-evolved seawater and a growing supply of ^{11}B -depleted meltwater runoff could explain the rapid isotopic shifts observed at the base of the Keilberg cap dolomite (Fig. 204C). The mixing zone could either be in the water column, during cap carbonate precursor (aragonite?) production, or in groundwater mixing zones during early diagenesis and dolomitization (Stewart et al., 2015; Ahm et al., 2019; Wei et al., 2019).

Two observations (Kasemann et al., 2010; Ohnemueller et al., 2014) may be more consistent with a diagenetic rather than a primary origin for the $\delta^{11}\text{B}$ records in the Keilberg Member (Fig. 204C). If primary, the fact that the steep $\delta^{11}\text{B}$ falls occur invariably at the base of the cap dolomite would be difficult to reconcile with diachronous deposition of water-depth specific sedimentary facies during progressive flooding of a continental margin (Hoffman et al., 2007). Conversely, if the sorted peloidal grainstone constituting all but the base and top of the Keilberg Member served as an aquifer for meteoric groundwater of glacial origin, actively displaced by the invasion of denser seawater (Ahm et al., 2019; Wilson, 2005), then its basal interface with relatively impermeable (lithified) preglacial carbonate or “tight” (unsorted) glacial diamictite would be exactly where a steep isotopic gradient of diagenetic origin should occur (Stewart et al., 2015; Ahm et al., 2019). The second observation is spatial heterogeneity in the absolute range of the initial $\delta^{11}\text{B}$ decline (Fig. 204C). The heaviest range occurs not in the most seaward section (5–8), but in section 8–3, just 5.2 km south of the section (8–4) with the lightest range values in the steep initial decline. Such spatial heterogeneity in $\delta^{11}\text{B}$ is perhaps more consistent with heterogeneous glacial sources of groundwater (Leslie et al., 2014) than with a coastal mixing zone in the water column. The Maieberg Fm $\delta^{11}\text{B}$ data (Kasemann et al., 2005, 2010) are no less valuable in our interpretation.

If the $\delta^{11}\text{B}$ excursion in the Keilberg (and other Marinoan cap dolomites) is related to meteoric diagenesis in a paleo-aquifer (peloidal grainstone), then the absence of a negative excursion in the Rasthof cap carbonate could be explained petrographically. The basal Rasthof Fm

Ar1 member is composed of impermeable calcimicrite rhythmite and cm-thick wackestone turbidites (Fig. 93A–D), and would have acted as an aquoclade.

3.8.3. Calcium and magnesium isotopes

Stable isotopes of Ca and Mg were measured in Maieberg Fm (Fig. 204D–G) as a means of tracking paleoceanographic (Kasemann et al., 2005, 2014; Wei et al., 2019) or diagenetic (Ahm et al., 2019) changes in the aftermath of Marinoan glaciation. The isotopic composition of seawater dissolved Ca is enriched (higher $\delta^{44}\text{Ca}$) relative to sources and sinks, due to mineralogy-dependent equilibrium fractionation when calcite or aragonite are precipitated, aragonite having a larger fractionation factor. Therefore, the composition of dissolved Ca and consequently carbonate production can change should there be a sustained imbalance between Ca input and output. For example, carbonate production (Ca output) might cease during a snowball chron as observed, due to ocean acidification, but carbonate dissolution (Ca input) would continue in response to CO_2 rise (Higgins and Schrag, 2003; Le Hir et al., 2008). As a result, $\delta^{44}\text{Ca}$ of dissolved Ca would asymptote toward the input composition (i.e., preglacial carbonate being glacially eroded) over a few Ca residence times. This pool of isotopically depleted Ca might conceivably be expressed in carbonate sediment when subglacial deepwater mixed with surface meltwater following deglaciation (Yang et al., 2017; Ahm et al., 2019; Wei et al., 2019). Conversely, extreme seawater warming (roughly 50 K in 50 kyr, Yang et al., 2017) would result in Ca output exceeding input, driving $\delta^{44}\text{Ca}$ higher, but this effect would be counteracted by reduced fractionation at higher temperature. Kasemann et al. (2005, 2014) sought a signal of intense weathering and associated pH rise in the glacial aftermath. Intense carbonate weathering during deglaciation, before carbonate shelves and platforms were flooded by rising sea level, would raise carbonate saturation and lower $\delta^{44}\text{Ca}$, whereas silicate-dominated weathering after sea-level rise would drive pH and $\delta^{44}\text{Ca}$ higher (Kasemann et al., 2014).

A different approach is taken by Ahm et al. (2019), based on the observation in long sediment cores and surface sediments from the Cenozoic Great Bahama Bank and northwestern Australia shelf that diagenesis including dolomitization under fluid-buffered (i.e., seawater invasive) conditions drives $\delta^{44}\text{Ca}$ higher, toward the composition of seawater, while diagenesis under sediment-buffered conditions drives $\delta^{26}\text{Mg}$ higher, due to distillation in the porewater as Mg is taken up by dolomitization (Higgins et al., 2018; Ahm et al., 2018). Accordingly, Ca and Mg isotopes in tandem offer a powerful means of diagnosing fluid-buffered diagenesis, which is predicted to occur on the flanks of carbonate platforms where geothermal porewater convection (Kohout convection) drives seawater invasion (Fig. 190) (Wilson et al., 2001). Since C and Ca + Mg are of equal molar abundance in carbonate rocks, $\delta^{13}\text{C}$ evidence for fluid-buffered diagenesis in FSz (Figs. 189, 191 & 202) suggests that $\delta^{44}\text{Ca}$ and $\delta^{26}\text{Mg}$ may also have been diagenetically altered in that zone. Indeed, $\delta^{44}\text{Ca}$ in Keilberg Mb is significantly heavier at the shelf edge (5–51) than in IPz (Fig. 204G), and $\delta^{26}\text{Mg}$ is lighter at the shelf edge and distal FSz (5–8) than in IPz (Fig. 204F) (Ahm et al., 2019). In middle Maieberg Fm Tm2 member, negative excursions are observed in both $\delta^{44}\text{Ca}$ and $\delta^{26}\text{Mg}$ (Fig. 204D–E), but the nadirs of both are significantly deeper in IPz than in distal FSz (Kasemann et al., 2014).

3.8.4. Strontium isotopes

$^{87}\text{Sr}/^{86}\text{Sr}$ of seawater has fluctuated over geologic time in response to changes in the leading sources of Sr: radiogenic (high $^{87}\text{Sr}/^{86}\text{Sr}$) Sr in runoff from weathering of old continental crust, non-radiogenic Sr (low $^{87}\text{Sr}/^{86}\text{Sr}$) from seawater–basalt exchange reactions at mid-ocean ridges, and isotopically conservative Sr from carbonate diagenesis (e.g., aragonite \rightarrow calcite). Due to the long oceanic residence time of Sr, seawater $^{87}\text{Sr}/^{86}\text{Sr}$ is highly uniform and, where unaltered, its record in carbonate sediment provides an effective means of inter-regional correlation over the last 150 Myr, when $^{87}\text{Sr}/^{86}\text{Sr}$ rose from 0.7067 to

0.7092 at present (Burke et al., 1982). A comparable rise occurred between 880 and 540 Ma, when $^{87}\text{Sr}/^{86}\text{Sr}$ rose from 0.7058 to 0.7085 (Fig. 1A) (Halverson et al., 2007; Halverson and Shields-Zhou, 2011). Part of the older rise can be seen in select data from Otavi/Swakop Group (Fig. 204H) (Yoshioka et al., 2003; Halverson et al., 2007; Rodler et al., 2017).

Carbonate $^{87}\text{Sr}/^{86}\text{Sr}$ is susceptible to alteration from external and internal sources of radiogenic Sr. During diagenesis, porewater may introduce radiogenic Sr acquired from detrital Rb-bearing phases encountered along the fluid pathway. Ancient carbonates may have slowly accumulated radiogenic Sr ingrown from Rb decay in clay-mineral impurities. Consequently, the least altered (i.e., least radiogenic) samples are those with high Sr contents (≥ 400 ppm) and low Rb/Sr ratios. Unfortunately, this eliminates dolomite, which normally contains ≤ 50 ppm Sr. However, contamination by ingrown radiogenic Sr can be minimized by separating carbonate for analysis in multiple dissolution steps using very weak acids (Liu et al., 2014). This method was used by Wei et al. (2019), who measured paired $^{87}\text{Sr}/^{86}\text{Sr}$ and $\delta^{44}\text{Ca}$ ($\delta^{44/42}\text{Ca}$) in closely-spaced samples from a 10-m-thick Keilberg cap dolomite at Etoto (Fig. 204E & H), 150 km N of the northern plunge of Kamanjab inlier (Fig. 4), southwest of Ruacana. They found the two were strongly anti-correlated, with ^{44}Ca falling and $^{87}\text{Sr}/^{86}\text{Sr}$ rising toward the stratigraphic middle of the unit (Wei et al., 2019). They attributed this to the growth and decline of a coastal meltwater-dominated wedge with high $^{87}\text{Sr}/^{86}\text{Sr}$ and low $\delta^{44}\text{Ca}$ relative to ambient seawater. However, coastal meltwater on an undeformed carbonate platform might instead have neutral $^{87}\text{Sr}/^{86}\text{Sr}$, reflecting the composition of pre-Marinoan seawater (Fig. 1A) when bedrock carbonate was deposited. Anticorrelation between ^{44}Ca and $^{87}\text{Sr}/^{86}\text{Sr}$ might also be consistent with a diagenetic origin involving focussed meteoric (subglacial) groundwater flow in a Keilberg paleo-aquifer (permeable peloid grainstone), with entrained seawater-derived porewater providing Mg for dolomitization (Ahm et al., 2019).

Existing data provide little support for a large decline in seawater $^{87}\text{Sr}/^{86}\text{Sr}$ during Marinoan glaciation, as initially predicted for a snowball chron in which the continental Sr flux was greatly reduced relative to seawater–basalt exchange (Jacobsen and Kaufman, 1999). A larger flux of isotopically conservative Sr from carbonate dissolution in response to snowball ocean acidification would have damped the predicted $^{87}\text{Sr}/^{86}\text{Sr}$ decline (Higgins and Schrag, 2003), but a more basic problem is that there are no data representing the snowball ocean because of the absence of synglacial marine carbonate. Marine cement described as indigenous to Ghaub Fm (Kennedy et al., 2001a) is quite likely to be preglacial in origin, since dilatant breccias with fibrous dolomite cement directly underlie Ghaub Fm where the reported cements (Kennedy et al., 2001a) occur in Tr5 (Figs. 62, 65, 66E & F). These cements occur as clasts in Ghaub Fm diamictite (Fig. 56F) and match the $\delta^{13}\text{C}$ composition purported to represent Marinoan seawater (Kennedy et al., 2001a). Keilberg Mb and other basal Ediacaran cap dolomites cannot be used as proxies for glacial seawater because their $^{87}\text{Sr}/^{86}\text{Sr}$, whether primary or diagenetic, was heavily influenced by continental meltwater (Hoffman, 1999; Shields, 2005; Ahm et al., 2019; Wei et al., 2019). It seems unlikely that Marinoan deepwater could have risen and produced carbonate without contamination by meltwater bearing more radiogenic Sr derived from continental silicate and/or carbonate bedrock (Yang et al., 2017).

3.8.5. Zinc isotopes

Zn is an essential micronutrient and oceanographic studies indicate that organic production in surface waters preferentially takes up the lighter isotope (^{64}Zn), which is released at depth by respiration creating an isotopic depth gradient that dynamically steepens or shallows according to export productivity (Maréchal et al., 2000). Thiemens et al. (2012) measured paired $\delta^{66}\text{Zn}$ and $\delta^{13}\text{C}$ in 14 samples collected from strata above and below the Ghaub Fm in Tr5 (5–1, 7) and Tr8 (8–3, 5). The data (Fig. 204J) are not presented (Thiemens et al., 2012) in an

inferred stratigraphic sequence, nor are pre- and post-glacial samples distinguished. Nevertheless, four samples are strongly depleted in ^{13}C and presumably represent the Cn5 and/or En1 CIEs that bracket Ghaub Fm in both transects (Figs. 204A & 44). $\delta^{66}\text{Zn}$ and $\delta^{13}\text{C}$ are strongly anti-correlated (Fig. 204J), opposite to expectation if they were both governed by the biological pump (export production and respiration at depth). Similar $\delta^{66}\text{Zn}$ and $\delta^{13}\text{C}$ anti-correlation is observed in the upper half of Nuccaleena Fm, the Marinoan cap dolomite in South Australia (Kunzmann et al., 2013; John et al., 2017). The rise in $\delta^{66}\text{Zn}$ is attributed to enhanced weathering and export production in the snowball aftermath, while the lack of a parallel response in $\delta^{13}\text{C}$ is attributed to ocean acidification and consequent growth of the DIC reservoir (Higgins and Schrag, 2003; Le Hir et al., 2008), making it insensitive to the biological pump (Kunzmann et al., 2013). Despite higher organic productivity, cap carbonate production may have pushed fractional organic burial (f_{org}) and hence $\delta^{13}\text{C}$ of DIC lower (Hoffman and Schrag, 1999).

3.8.6. Chromium isotopes

Cr isotopes ($\delta^{53}\text{Cr}$) have been used to track oxygenation of the Proterozoic atmosphere (e.g., Frei et al., 2009; Planavsky et al., 2014) on the assumption that the composition of seawater dissolved Cr is controlled primarily by oxidative weathering of continental crust, which mobilizes isotopically-enriched (high $\delta^{53}\text{Cr}$) Cr(VI) at the expense of isotopically-depleted Cr(III). However, the $\delta^{53}\text{Cr}$ of dissolved Cr in the modern ocean is quite variable ($\pm 0.5\text{\textperthousand}$) and exhibits nutrient-like behaviour in which export of light Cr with sinking organic matter raises $\delta^{53}\text{Cr}$ in surface waters and lowers it in intermediate waters, where respiration occurs (Scheiderich et al., 2015; Janssen et al., 2020). Rodler et al. (2016, 2017) measured $\delta^{53}\text{Cr}$ in Otavi/Swakop Group carbonate from sections in the distal FSz (5–7) and OML (farm Keilberg, now Jackal Omuramba). The samples are moderately enriched on average, except for those from lower Maieberg Fm, which are depleted ($\delta^{53}\text{Cr} \geq -0.4\text{\textperthousand}$ SRM979) relative to bulk silicate Earth (Fig. 204I). The low- $\delta^{53}\text{Cr}$ anomaly, if interpreted in terms of a less oxygenated weathering regime, are jarring in view of the majority pink to red colour of Maieberg Fm Tm2 limestones, unlike the grey to black colours of most other limestones in Otavi/Swakop. Rodler et al. (2016, 2017) suggest that the observed postglacial ^{53}Cr depletion might be a product of Cr cycling in a redox-stratified water column, or alternatively of biological fractionation during microbially-mediated dolomitization. Alternatively, syndeglacial sea-level rise (Creveling and Mitrovica, 2014; Yang et al., 2017; Myrow et al., 2018) would have flooded the platform with ^{53}Cr -depleted intermediate waters, at a time when the isotopic depth gradient was large because of weathering-enhanced export productivity (Kunzmann et al., 2013; Thiemens et al., 2012). However, the existence of a $\delta^{53}\text{Cr}$ depth gradient predicts that samples from the distal FSz (5–8, blue dots in Fig. 204I) should be more depleted on average than their correlative in the IPz (scarlet dots). No such difference between the zones is observed (Fig. 204I).

3.8.7. Osmium and helium isotopes

Bodiselitch et al. (2005) reported spikes in iridium (Ir) concentration at or near the contacts between Sturtian and Marinoan diamictites with their respective cap carbonates in drillcore from the Lufilian Arc (Katanga Supergroup, DR Congo and Zambia), about 1000 km northeast of Kunene Region (Fig. 2). Assuming the Ir is cosmogenic and had accumulated in ice sheets and sea-glacier ice over the respective glacial epochs, Bodiselitch et al. (2005) inferred that glacial durations were “at least 3 million, and most likely 12 million, years” depending on the Ir flux and assuming globally uniform Ir dispersal upon deglaciation. As a test of the assumed extra-terrestrial origin of the Ir spike, Peucker-Ehrenbrink et al. (2016) measured osmium ($^{187}\text{Os}/^{188}\text{Os}$) and helium ($^{3}\text{He}/^{4}\text{He}$) isotopes in 4.5-m-long continuous rock slabs transecting the Ghaub diamictite–Keilberg cap dolomite contact in FSz (5–7) and IPz (8–3). Extraterrestrial and mantle-derived He and Os, a platinum-group element (PGE) like Ir, should be distinctly less radiogenic (lower

$^3\text{He}/^4\text{He}$ and $^{187}\text{Os}/^{188}\text{Os}$) than He and Os derived from average continental crust in Neoproterozoic time. Peucker-Ehrenbrink et al. (2016) found PGE spikes at the Ghaub–Keilberg smaller than those reported from Central Africa (Bodiselitch et al., 2005). More importantly, their He and Os isotopes are indistinguishable from background values and imply derivation largely from continental crust, ruling out an extraterrestrial origin (Peucker-Ehrenbrink et al., 2016).

3.8.8. Nitrogen isotopes

Redox-sensitive microbial N cycling (along with lightning strikes) is the major source of nutrient N in forms accessible to the biosphere. Although microbial N-fixation ($\text{N}_2 \rightarrow \text{NO}_3^-$) involves little isotopic fractionation, denitrification ($\text{NO}_3^- \rightarrow \text{N}_2$) is accompanied by a large fractionation ($\sim -25\%$) that drives residual NO_3^- (nitrate) heavier (higher $\delta^{15}\text{N}$) so long as denitrification is incomplete. The modern ocean $\delta^{15}\text{N}$ is enriched by 5–7‰ relative to atmospheric N_2 , reflecting a balance between fixation (nitrification) and limited denitrification. Most N in sediments derives from postdepositional breakdown of organic matter and substitution of NH_4^+ for K^+ in clay minerals. This involves little net isotopic fractionation with the result that sedimentary $\delta^{15}\text{N}$ should be broadly reflective of water column $\Sigma \delta^{15}\text{N}$.

Johnson et al. (2017) measured $\delta^{15}\text{N}$, TOC, Al content (clay proxy), Fe speciation ($\text{Fe}_{\text{HT}}/\text{Fe}_{\text{T}}$ and $\text{Fe}_{\text{PY}}/\text{Fe}_{\text{HR}}$) and redox-sensitive trace elements (U, Mo, V) in three sample sets from Ghaub Fm in FSz. Two sample sets (Fig. 204K–L) are synglacial in age and the third (Fig. 204 M) is syndeglacial (Bethanis Mb). The synglacial sample sets have distinct lithological compositions. The first (Fig. 204 K) is from the basal quartz-siltstone rhythmite (Tg_q) member of Ghaub Fm in 1–15 (Figs. 19 & 20A). This unit contains dropstones toward the top and is otherwise parallel-laminated, consistent with an overlying ice shelf. Sample set 2 (Fig. 204 L) was collected from stratified carbonate diamictite, underlying and interleaved with massive carbonate diamictite, in lower Ghaub Fm in 5–17 (Figs. 43, 58, 60 & 61). Sample set 3 is from Bethanis Mb (Fig. 54A & B) in same section (5–17) and is inferred to postdate tropical sea-glacier collapse, with IRD delivery by free-floating icebergs rather than by an ice shelf (Hoffman and Halverson, 2008; Domack and Hoffman, 2011; Hoffman, 2011a).

Trace-element data (Johnson et al., 2017) imply a well-oxygenated surface environment, while Fe speciation data indicate suboxic to anoxic ferruginous (not sulfidic) bottom waters for all samples (Fig. 204K–M). The two synglacial sample sets share a common $\delta^{15}\text{N}$ range of +1–3‰, significantly less enriched than the modern ocean, but not 0‰. This implies that aerobic N fixation persisted during Marinoan chron, and that denitrification was neither absent nor complete, either of which would have resulted in $\delta^{15}\text{N}_{\text{sed}}$ close to 0‰ (Johnson et al., 2017). $\delta^{15}\text{N}$ declines overall in sample set 1, contrary to sample set 2. Both come from lower Ghaub Fm in their respective sections, but synchronicity is not assumed. The syndeglacial sample set 3 is significantly more enriched in ^{15}N , rising to near modern values directly beneath the Keilberg cap dolomite (Fig. 204 M). This indicates incomplete denitrification and survival of enriched NO_3^- in the water column at this time (Johnson et al., 2017). Those authors conclude that oxygenated surface waters and a redoxcline at depth were persistent features of the Marinoan ocean, implying that marine ice cover was incomplete or intermittent, inconsistent with a snowball Earth (Johnson et al., 2017).

The implication regarding Snowball Earth may be premature, however, since a continuous ice cover would itself constitute a hard but leaky redoxcline. Microbial N cycling occurs in a variety of modern polar meltwater-based ecosystems (Vincent, 1988; Hawes et al., 2008; Cameron et al., 2012; Vincent and Quesada, 2012), suggesting that Marinoan primary production and N-fixation by cyanobacteria was sustained in well-oxygenated and illuminated supraglacial meltwater ponds and streams in the vast ($6 \times 10^7 \text{ km}^2$) equatorial marine ablation zone (Vincent and Howard-Williams, 2000; Vincent et al., 2000, 2004; Hawes et al., 2018). Surface accumulation of solar energy-absorbing mineral dust, infused with darkly-pigmented cyanobacteria, causes

melting to occur in the ablation zone even where surface air temperature is continuously below freezing (McIntyre, 1984; Wharton Jr et al., 1985; Vincent et al., 2000; Takeuchi, 2002; Hoffman, 2016; Musilova et al., 2016). ‘Cryoconite’ (i.e., detrital dust+volcanic ash+indigenous organic matter, mainly extracellular polymeric substances copiously produced by cyanobacteria) would have been regularly flushed through moulins into the cold anoxic subglacial ocean (Goodman and Strom, 2013), where it would accumulate as sediment (Hoffman, 2016; Hoffman et al., 2017a). Burial of cryoconite organic matter must have provided the O_2 flux required to offset consumption by volcanic outgassing of reduced gaseous species (H_2S , SO_2 , etc.). Absent organic burial, atmospheric O_2 would have been drawn down and Marinoan trace-element contents (Fig. 204K–M) would consequently be quite different. When the tropical sea glacier finally collapsed, the nature of the redoxcline changed. The hard but leaky sea glacier was replaced by a dynamic water column, characterized by extreme density (salinity and temperature) stratification (Yang et al., 2017) and enhanced (bacterial) primary production (Brocks, 2018; Bobrovskiy et al., 2020; Liljestrand et al., 2020). Data from Johnson et al. (2017) are valuable in that they represent the specific interval between Marinoan snowball termination and cap-carbonate onset.

3.8.9. Iron isotopes

Fe isotopes ($\delta^{57}\text{Fe}$ or $\delta^{56}\text{Fe}$) of Sturtian synglacial Fe-rich sediments (hematite-jaspilite and hematite-argillite), in conjunction with Ce-anomaly (Ce/Ce^*) data, have been employed as redox proxies for their depositional environments (Halverson et al., 2011), which must have involved an anoxic medium to transport soluble Fe^{2+} and an electron acceptor (e.g., O_2) that localizes Fe^{3+} precipitation. Lechte et al. (2019) obtained $\delta^{56}\text{Fe}$ and Ce-anomaly data from iron-formation and Fe-rich diamictite in Chuos Fm from 4 locations, 1 in IPz (Okavare) and 3 in NDz (farms Landeck, Tr3–Löwenfontein, and Orusewa). On lithofacies criteria (Lechte et al., 2018, 2019), they characterize the NDz samples as “ice contact” deposits and the IPz samples as “ice proximal.” They found the NDz (ice-contact) samples to have lighter $\delta^{56}\text{Fe}$ on average ($-0.57\text{\textperthousand}$, $n=14$) than the IPz ones ($+0.95\text{\textperthousand}$, $n=5$). The observed correlation parallels their data (Lechte et al., 2019) from Sturtian glaciogenic iron-formations and associated Fe-rich sediments in South Australia (Holowilena Ironstone) and SW USA (Kingston Peak Fm, Death Valley area, CA). The data imply more oxygenated conditions in the areas dominated by ice-contact deposits (e.g., NDz) and progressively greater anoxia in ice-proximal and ice-distal environments (Lechte et al., 2019). They support scenarios in which the snowball ocean is anoxic-ferruginous and Fe^{3+} is titrated at marine ice grounding lines where oxygenated subglacial meltwater is discharged (Halverson et al., 2011; Hoffman et al., 2011; Lechte and Wallace, 2016; Lechte et al., 2018). Lechte et al. (2019) go on to speculate that micro-aerophilic Fe-oxidizing bacteria provided organic substrate for eukaryotic, possibly multicellular, heterotrophs at such well oxygenated but aphotic subglacial discharge sites. It must be borne in mind, however, that energy obtainable from Fe-oxidation is small (Nealson and Conrad, 1999).

4. Conclusions and recommendations for future studies

Otavi Group is a long-lived (0.77–0.60 Ga), 1.5–3.5-km-thick, neritic carbonate platform covering SW Congo craton. Swakop Group (minus Kuiseb Fm) is its S-facing, distally tapered, bathyal foreslope (Fig. 5). Two stages of subsidence accommodated Otavi Group: (1) intermittent S–N crustal stretching from ~ 770 until ~ 656 – 651 Ma, and (2) post-rift thermal subsidence and associated flexure until collisional destruction of the platform at ~ 600 Ma (Figs. 151, 163A-B, 179 & 205). Rifting lasted until late Cryogenian in Swakop Group. Crustal stretching in Otavi Group is manifested by S-dipping rift faults with N-sloping rift-shoulders, and by N- and S-dipping rift faults in Swakop Group (Fig. 26). Rift-related alkaline-peralkaline magmatism occurred in Swakop Group between 760 and 746 Ma, but preferentially on the

southern margin of Congo craton (Northern Damara zone) compared to the western margin (Central Kaoko and West Congo belts).

Post-rift Otavi/Swakop Group is divisible into five facies zones: (1) inner platform, (2) outer platform, (3) proximal foreslope, (4) distal foreslope and (5) basin. Zones 1–4 are autochthonous with respect to Congo craton. Basin zone is coextensive with Northern zone (Outjo belt) of Damara orogen (Fig. 4). Stratigraphic evidence (e.g., rift-shoulder uplift) for a western rift margin is lacking in Otavi Group (Figs. 196 & 197). This and the magmatic asymmetry suggest that the western cratonic margin (Central Kaoko zone, Fig. 3) was a transform margin, kinematically consistent with S–N plate divergence (Fig. 198).

Discrete early and late Cryogenian glaciations are evident in all zones. Stratigraphic records of both glaciations start and end abruptly, enabling unambiguous division of those records into five epochs, the boundaries of which can be chronometrically calibrated according to widely accepted inter-cratonic correlations: (1) late Tonian, 770–717 Ma (Macdonald et al., 2018); (2) early Cryogenian (Sturtian snowball), 717–661 Ma (Rooney et al., 2020a); (3) middle Cryogenian (inter-snowball), 661–646 ± 5 Ma (Prave et al., 2016; Bao et al., 2018; Nelson et al., 2020); (4) late Cryogenian (Marinoan snowball), 646 ± 5–635 Ma (Zhou et al., 2019); and (5) early Ediacaran, 635–600 Ma (Lehmann et al., 2015). There is no evidence for local or remote glaciation (e.g., glacioeustatic evidence) during odd-numbered epochs.

Sturtian glaciation occurred during active rifting, reflected in subglacial angular unconformities (Fig. 5) and polymictic glacial diamicrites derived from all older units including crystalline basement. Marinoan glaciation occurred during early post-rift subsidence on the platform and final rifting in the basin. The bathyal foreslope preserves a marine ice-grounding zone wedge, including a proximal 600-m-high grounding-line moraine (Figs. 43, 62, 206A & 207A). Marinoan glacial debris was mainly derived from a shallow (<70 m) trough on the inner platform (Fig. 164) and a bench on the proximal foreslope ≥300 m below the top of the glaciated platform (Figs. 206A & 207A). No marine grounding-zone wedge is evident in Sturtian depocenters (Fig. 154), which include subglacial rift basins (Figs. 22 & 58), overdeepened bedrock troughs (Fig. 105), and moraine-like buildups (Figs. 32, 39 & 156) (Hoffman et al., 2017b). Limitation of glaciomarine sedimentation to late Cryogenian, after ocean-basin opening, may have been conditioned by large net sea-level falls, whereby glacioeustasy exceeded glacioisostasy plus ice gravity in most areas (Liu and Peltier, 2013; Creveling and Mitrovica, 2014; Benn et al., 2015). We infer that the early Cryogenian rift zone remained above the Sturtian marine ice grounding-line elevation.

Averaged over glacial durations of 56 Myr (Sturtian) and 6–16 Myr (Marinoan), sediment accumulation rates were extremely low, 4.0 and 3.3–8.8 m Myr⁻¹ respectively (Table 6), reflecting the weak hydrologic cycle of a snowball climate (Abbot et al., 2013; Abbot, 2014). Estimated average Marinoan erosion rates across the platform (Table 7) were of the same magnitude (3.1–8.2 m Myr⁻¹). Average accumulation rates for each snowball were remarkably similar, implying that tectonic enhancement of Sturtian erosion rates barely compensated for an otherwise lower average rate due to its longer duration (Sadler, 1981; Partin and Sadler, 2016). Ghaub Fm, the Marinoan lowstand grounding-zone wedge, overlies an apparent glacial erosion surface extending far down the distal foreslope (Figs. 206A & 207B). Net secular grounding-line retreat before terminal deglaciation (Figs. 206B & 207A) manifests the combined effect of sea-glacier thinning (Abbot et al., 2013), glacioeustatic rise (Benn et al., 2015) and ongoing tectonic subsidence (Figs. 163A & 207A). Together, they evidently overcame the counteractive effects of ice-sheet mass loss on isostatic adjustment and gravitational forces. Despite its 3.5–9.3× longer duration, total Sturtian tectonic subsidence was 37% less than Marinoan, based on average thicknesses of 0.32 and 0.44 km for their respective postglacial depositional sequences ($n = 8$ for each) in Otavi Group (Figs. 159, 178 & 181). Therefore, Sturtian condensation and Marinoan expansion of the

transgressive stage of their respective cap-carbonate sequences cannot be attributed to deeper Sturtian subsidence.

The Marinoan transgressive cap dolomite (Keilberg Mb) has a regional average thickness of 17 m ($n = 140$), 50 m on ($n = 32$) and 7 m off ($n = 108$) the platform (Figs. 95 & 206A). A peloidal grainstone, it is virtually devoid of organic matter, possibly due to complete respiration in extremely warm surface waters (50–60 °C, Pierrehumbert, 2002; Pierrehumbert et al., 2011). Particular sedimentary features—dilatant sheet-crack marine cements, tubestone stromatolite bioherms, giant aggradational wave ripples and reef-size constructs of former-aragonite crystal fans—occur sequentially in Maieberg Fm (Figs. 175 & 206A), the Marinoan cap-carbonate sequence. Such features point to anomalous carbonate oversaturation and/or saturation gradients in the Marinoan aftermath. The Sturtian cap-carbonate sequence (Rasthof/Berg Aukas Fm) lacks these features, but has its own distinctive ones—lobate and roll-up microbialaminites, encrusted columnar stromatolites, and agglutinating protistan microfauna (Pruss et al., 2010; Dalton et al., 2013; Moore et al., 2017).

Late Tonian shallow-neritic $\delta^{13}\text{C}_{\text{carb}}$ records were obtained from 0.4-km-thick Devede Fm in Otavi Group and 0.7-km-thick Ugab Subgroup in Swakop Group. Devede Fm is isotopically heavy, rising from +4 to +8‰ VPDB at the top (Figs. 148 & 199), which is dated at 760 Ma (Halverson et al., 2005). Ugab Subgroup postdates 746 Ma volcanics and displays two negative $\delta^{13}\text{C}$ excursions bridged by heavy values (Figs. 153B & 200). The negative excursions are tentatively correlated with Russøya and Garvellach CIEs in NE Laurentia (Lamothe et al., 2019).

Middle Cryogenian neritic $\delta^{13}\text{C}$ records (Fig. 201) from the inner platform feature two heavy plateaus bracketed by three negative excursions correlated with Twitya (NW Canada), Taishir (Mongolia) and Trezona (South Australia) CIEs. The same pattern is observed in carbonate turbidites in distal Swakop Group, where the sub-Marinoan falling-stand wedge hosts the Trezona CIE recovery (Fig. 202). Proximal Swakop Group strata equivalent to Taishir CIE and its subsequent heavy plateau are shifted bidirectionally to intermediate values between

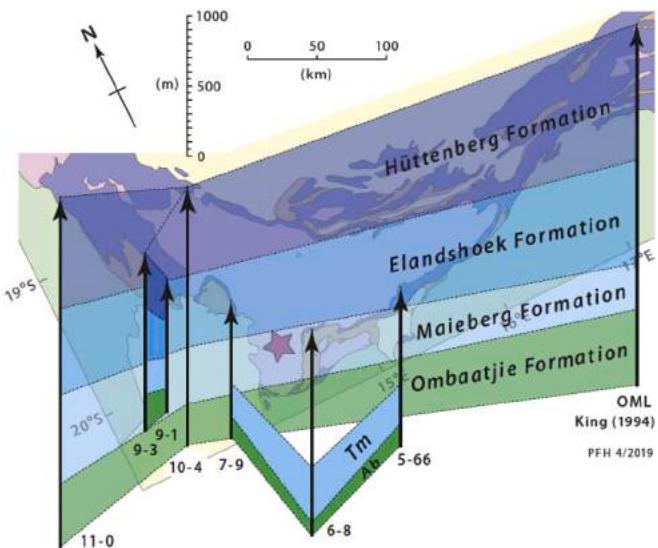
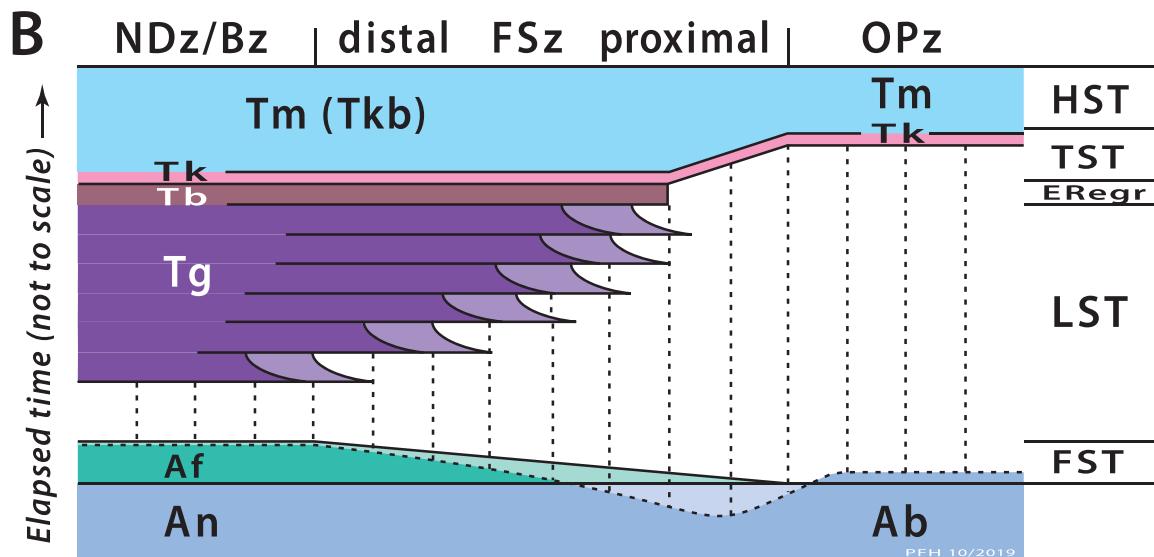
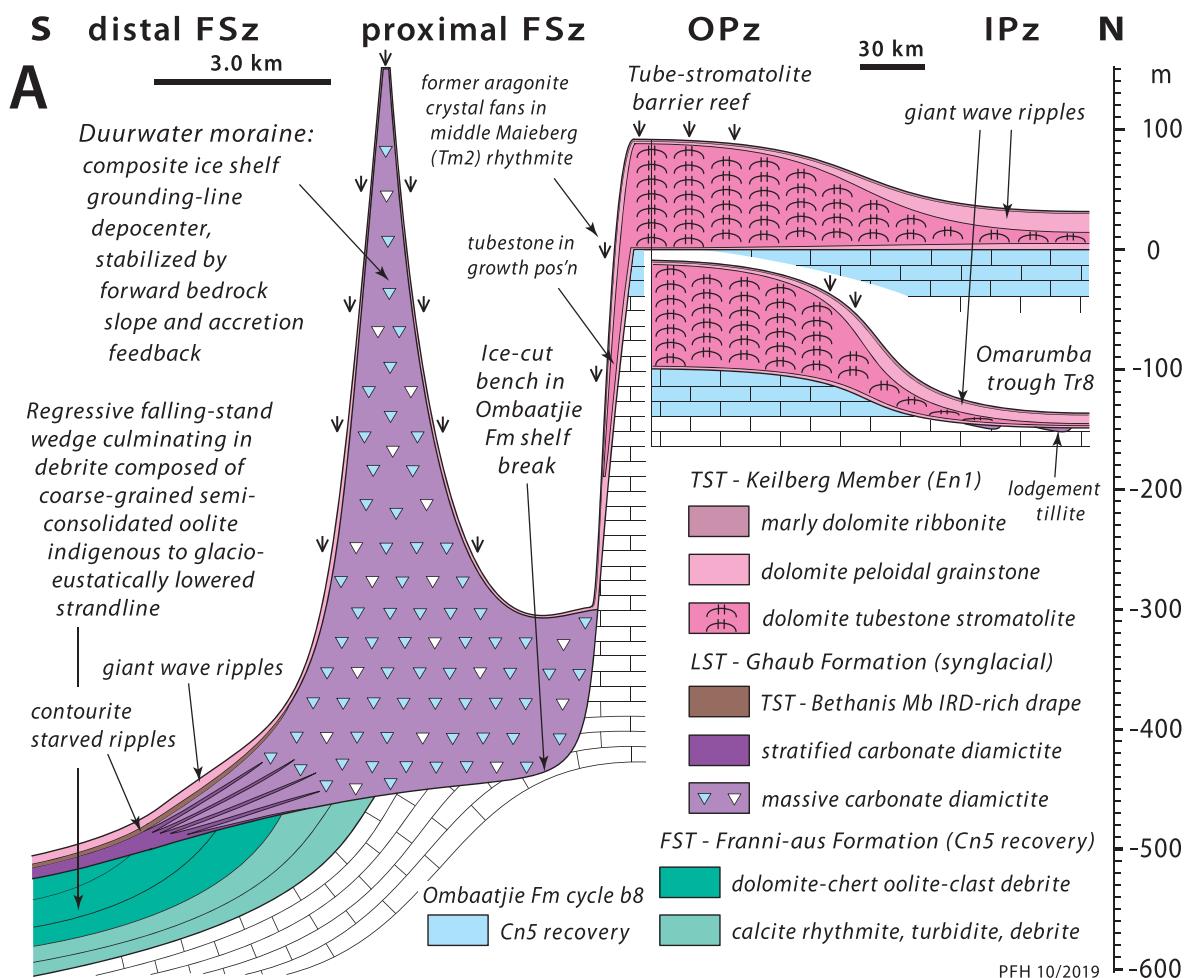


Fig. 205. Fence-diagram showing thickness variations in post-rift formations (Figs. 151, 163B & 179) of Otavi Group. Tips of vertical arrows indicate section locations on geologic map (Fig. 4). Note inclined N-arrow for map. Thickest formations are in sections (11–0, 10–4, OML) farthest from cratonic promontory, indicated on map by magenta star. From N to S, all formations thin to minima at 9–1 (Fig. 145), after which Maieberg Formation thickens southward to 6–8. Thickness minimum (9–1) ca 100 km inboard from the shelf edge suggests a component of flexure in passive-margin basin formation (Watts et al., 1982). The thickness minima (paleo-arch) extend eastward to the southern Otavi Mountainland (Hedberg, 1979), favouring an origin related to the Northern Damara zone not the cratonic promontory.



(caption on next page)

Fig. 206. (A) Schematic summary of Swakop/Otavi Group stratigraphic and facies relations resulting from Marinoan glaciation in Kunene Region. Note 26× difference in horizontal scale between foreslope and platform. Pink colours are Keilberg Mb, mauve colours are Ghaub Fm, blue is CIE Cn5 recovery leg on platform (Ombaatjie Fm cycle b8) and aqua is the same in FSz (Frannis-aus Fm). Glacial erosion includes removal of cycle b8 in shallow (≤ 60 m deep) Omarumba-like troughs in IPz, headwall erosion of Ombaatjie Fm shelf edge, and notching of pre-Marinoan foreslope strata beneath Ghaub Fm. Ghaub Fm records retreat and aggradation of ice-shelf grounding-line moraine in response to progressive ice-shelf thinning (Abbot et al., 2013) and ongoing passive-margin subsidence (Fig. 163A). Extreme height of Duurwater moraine (0.60 km) reflects grounding-line stabilization by forward-dipping bedrock slope (Pollard and DeConto, 2007), sediment accumulation feedback (Alley et al., 2007) and sea-level fall accompanying ice sheet retreat (Gomez et al., 2010). Diachronous deposition of Keilberg Mb is indicated by occurrence of giant wave ripples in distal FSz and IPz (Figs. 56A-B & 120A-B) (Hoffman et al., 2007). Keilberg Mb is thinnest over Duurwater moraine, where macropeloids (Fig. 67B) suggest winnowing, and thickest in OPz where tubestone stromatolite is most abundant (Fig. 177A). Crystal fans in lower Tm2 member of Maieberg Fm are localized over Duurwater moraine (Fig. 62), tubestone stromatolite shelf-rim (Figs. 68 & 71) and lip of Omarumba trough (Fig. 164). (B) Sequence stratigraphic chart of Marinoan glaciation. Zones: Bz, basin zone; FSz, foreslope zone (distal and proximal); OPz, outer platform zone. Sequences: FST, falling-stand wedge; LST, lowstand wedge; ERegr, early regression (ice gravity effect, Clark, 1976); TST, transgressive systems tract; HST, highstand systems tract. Stratigraphic units: An, Narachaams Fm; Ab, Ombaatjie Fm; Af, Frannis-aus Fm; Tg, Ghaub Fm; Tb, Bethanis Mb; Tk, Keilberg Mb; Tm, Maieberg Fm; Tm (Tkb), Maieberg Fm equivalent in lower Karibib Fm of Swakop Group (Figs. 184, 188 & 189). Vertical dashed lines indicate stratigraphic hiatus. Dashed line within units Af and Ab indicates Marinoan subglacial erosion. In Ghaub Fm, purple and pale mauve colours indicate massive and stratified diamictite, respectively. Y-axis is elapsed time (not to scale), not stratigraphic thickness.

+3.0 and +3.5‰ (Fig. 208) (Hoffman and Lamothe, 2019).

Early Ediacaran neritic $\delta^{13}\text{C}$ records (Fig. 179) from the inner platform display a deep negative excursion, coincident with the post-Marinoan depositional sequence, and heavy values ($\leq +11\text{\textperthousand}$) with extreme point-to-point variability ($\leq 10\text{\textperthousand}$) in the youngest Otavi Group Hüttenberg Fm. Distal Swakop Group mimics older parts of the early Ediacaran inner platform $\delta^{13}\text{C}$ records (Fig. 189), but proximal Swakop Group values are shifted bidirectionally to $+0.9 \pm 1.5\text{\textperthousand}$ after the post-Marinoan negative excursion (Figs. 189 & 208) (Hoffman and Lamothe, 2019).

Destruction of positive and negative CIEs in proximal Swakop Group (Fig. 208) is attributed to early seawater-buffered diagenesis (dolomitization), driven by geothermal porewater convection that sucked seawater into the proximal foreslope of the platform (Fig. 190) (Higgins et al., 2018; Ahm et al., 2018; Hoffman and Lamothe, 2019). This hypothesis provocatively implies that CIEs originating in epi-platform waters and shed far downslope as turbidites were decoupled from open-ocean DIC, which is recorded by the altered proximal Swakop Group values closer to those of Cenozoic seawater (Zachos et al., 2001). Inter-regional correlation of middle Cryogenian–early Ediacaran CIEs will take on a new face if the seawater-buffered diagenetic interpretation of proximal Swakop Group $\delta^{13}\text{C}$ records (purple, Fig. 208) is supported by Ca- and Mg-isotope data still to be acquired.

Carbonate accumulation ceased when the cratonic margins were abortively subducted beneath the Northern Damara and Kaoko orogens at 0.60–0.58 Ga (Fig. 194). A forebulge unconformity separates Otavi/Swakop Group from overlying foredeep clastics. In Huab cusp (Figs. 192, 194B & 209), where the orogens meet at a right angle, the forebulge unconformity had an astounding ≥ 1.85 km of megakarstic relief (Figs. 193, 145 & 205), and km-thick mass slides (Figs. 41 & 87B) were simultaneously displaced gravitationally toward both trenches (Fig. 209A). Forebulge amplification is attributed to slab constriction imposed by the cuspatate geometry, assuming that southward and westward subduction was contemporaneous (Fig. 209A–C). The paleo-megakarst and mass slides were preserved geologically because of immediate burial by foredeep clastics (Figs. 194, 210A & B). Continued orogenic shortening produced the thick-skinned fold belt rimming the craton (Fig. 4), in which the mass slides, the paleo-megakarst, and the Otavi/Swakop Group are exposed.

4.1. Future studies

Our work left many questions unanswered which can be tackled with new field and laboratory studies. The following list is by no means exhaustive and omits creative and new approaches we didn't consider.

4.1.1. C-isotope chemostratigraphy in Otavi Mountainland

Aside from Hüttenberg Fm (Cui et al., 2018), there have been no new

$\delta^{13}\text{C}$ data from the Otavi Group type area since a profile based on 40 samples from drillcore was published 30 years ago (Kaufman et al., 1991). That reconnaissance profile aligns perfectly with our results, but the middle Cryogenian (Abenab Subgroup) data are too sparse ($n = 6$) to resolve uncertainty in correlation between Berg Aukas-Gauss-Auros formations in OML and Rasthof-Gruis-Ombaatjie formations in Kunene Region (Fig. 6D & E). Whatever the outcome of our inferences regarding seawater-buffered diagenesis in the FSz and the $\delta^{13}\text{C}$ composition of Cryogenian seawater (section 3.7.2., Hoffman and Lamothe, 2019; Bold et al., 2020), CIE Cn3 is highly reproducible in the IPz of our study area (Fig. 162).

4.1.2. Potential OPz–FSz transition in Otavi Valley syncline

Tr5 is a key transect in our study because it alone intersects the foreslope-platform transition (Fig. 43). An eastward extension of this transition is most likely to be exposed between the S and N limbs of the E-plunging Otavi Valley syncline in southern OML (Smit, 1962; Hedberg, 1979; Miller, 2008b). A detailed stratigraphic investigation of this structure may be highly rewarding for a geologist undaunted by the prospect of gaining access from many land-owners. Satellite imagery suggests that farm Nordland 510 on the S limb would be a good place to start.

4.1.3. W–E versus S–N changes in Otavi Group N of 18°S

N of Opuwa (Fig. 4), Otavi fold belt bends to a W–E trend and then to SE–NW approaching Kunene River and the Angola border. Otavi Group is preserved in large E-plunging synclines with tight keels (Ombazu and Ehomboberg synclines of Hedberg, 1979). It is not known if the sinuous structural trend reflects changes in depositional strike. Reconnaissance of Ombazu syncline revealed a condensed middle Cryogenian (0.42 km) section and expanded late Tonian (1.44 km), early Cryogenian (1.00 km), late Cryogenian (115 m) and early Ediacaran sections of Otavi Group. Tantalizingly, at $-17.3179^\circ/12.9382^\circ$, 20 km NW of Etengwa and 30 km SW of Kunene River at Otjimborombonga, basal Maieberg Fm directly overlies metamorphic basement, suggesting that a major buried basement uplift (rift shoulder?) of Marinoan age exists in that area.

4.1.4. A transform margin in CKz?

Absence of W–E changes in Otavi Group thickness and lithofacies, and lack of stratal offlap-onlap relations in that direction, suggest that the western margin of Congo craton in Namibia was a transform margin, consistent with S–N plate divergence (Fig. 198E). No margin occurs in EKz, yet the existence of Kaoko orogen implies that a W-facing margin was created. S-directed paleocurrents in fluvial Nabis Fm (Fig. 146A) provide little support for western margin opening in Nosib Group time. Recent work sheds little light on this question, except that a western sea (Adamastor ocean of Hartnady et al., 1985) underlain exclusively by

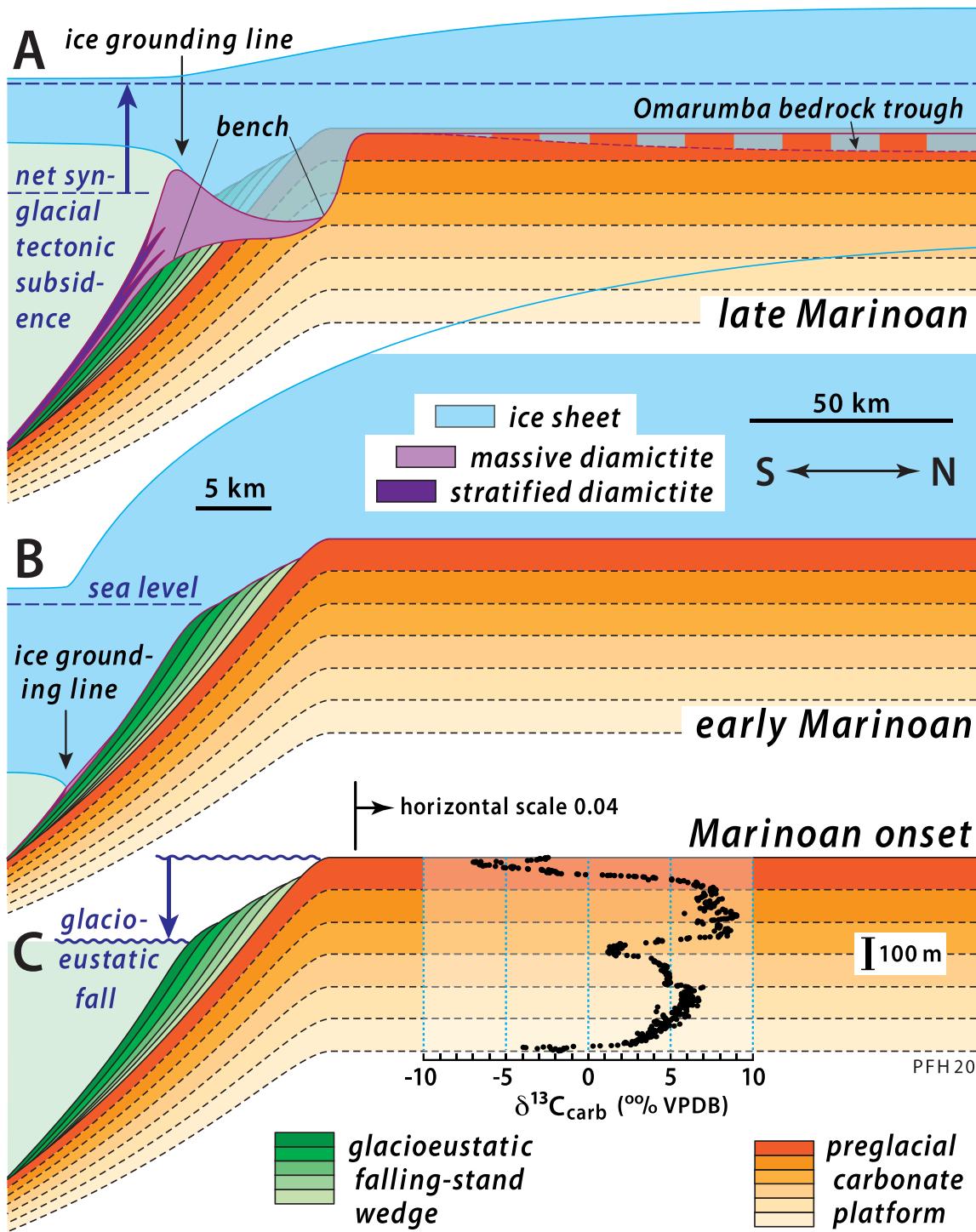


Fig. 207. Schematic sections of Otavi/Swakop Group platform, foreslope and ice sheet at (A) the glacial minimum near the end of the Marinoan snowball and (B) the glacial maximum near the start of the Marinoan snowball. (C) Glacioeustatic fall due to high-latitude ice-sheet growth during incipient Marinoan glaciation. Note change in horizontal scale between foreslope and platform. Aggraded middle Cryogenian Abenab Subgroup is shown in shades of orange, before any high-latitude ice sheets existed. Representative $\delta^{13}\text{C}$ record is from 9 to 3 (Figs. 122 & 133). Green shades depict the falling-stand wedge (Frannis-aus Fm.). Downward-pointing arrow in C indicates magnitude of glacioeustatic fall prior to ice-sheet buildup on paleotropical platforms. Sea level in B reflects additional glacioeustatic fall due to tropical ice sheet growth, countered by glacioisostatic depression of the platform and ice-sheet gravitational effect on local sea level. Lowered sea level and thick ice shelf cause ice grounding-line advance to the distal foreslope in B, producing the basal Marinoan erosion surface on which Ghaub Fm was deposited. Low atmospheric $p\text{CO}_2$ in B results in large ice volume but low ice velocities and sediment accumulation rates (Benn et al., 2015). High $p\text{CO}_2$ in A results in lower ice volume but higher ice velocities and sediment accumulation rates. Net sea level rise (upward arrow) and larger upward migration of ice grounding line from B to A was driven by ongoing tectonic subsidence (Fig. 163A) and shelf-ice thinning. Loci of glacial erosion were Omarumba trough on the inner platform and a bench on the proximal foreslope. Locus of accumulation was Duurwater moraine, seated at the edge of the ice-cut bench (Figs. 43, 62, 63 & 206A). Most glacial debris was quarried locally (Fig. 173, see also 4.1.8.). Perforation of the equatorial sea glacier by meltwater triggered snowball deglaciation subsequent to A (Wu et al., 2021), resulting in a post-snowball scenario depicted in Fig. 178B & C.

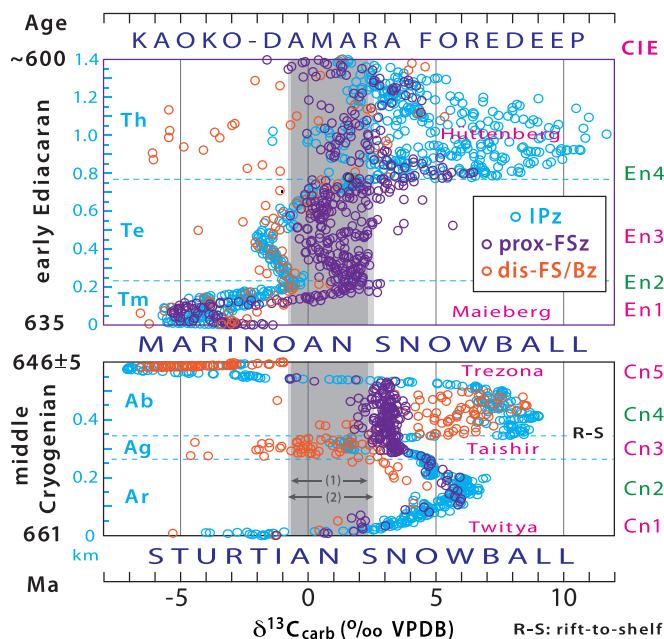


Fig. 208. Representative $\delta^{13}\text{C}$ records for Abenab (Cryogenian) and Tsumeb (early Ediacaran) subgroups colour-coded according to paleobathymetric zone: IPz, inner platform zone; prox-FSz, proximal foreslope zone; dis-FS/Bz, distal foreslope (Cryogenian) and basin (Ediacaran) zones (Hoffman and Lamothe, 2019). CIEs Cn1–5 and En1–4 (CIE names in magenta) were used to normalize the records (see Figs. 189 & 202 for actual stratigraphic thicknesses). Formations: Ar, Rasthof Fm; Ag, Gruis Fm; Ab, Ombaatjie Fm; Tm, Maieberg Fm; Te, Elandshoek Fm; Th, Hüttenberg Fm. Vertical grey bands give $\delta^{13}\text{C}$ ranges for (1) modern marine DIC (Kroopnick, 1985) and (2) Cenozoic benthic foraminiferal aragonite (Zachos et al., 2001). IPz and dis-FS/Bz records are broadly similar below En4, consistent with advection of platform-derived carbonate sediment onto foreslope and basin-margin turbidite fans (Hoffman and Lamothe, 2019). prox-FSz record tracks IPz only during Cn1–2, before FSz development. After R-S, middle Cryogenian prox-FSz record stabilizes ~ + 3‰, and its early Ediacaran record falls within the grey bands except at En1 and 4 (prox-FSz record of Cn5 was removed by Marinoan glacial erosion, Figs. 202 & 207). Hoffman and Lamothe (2019) postulate that CIEs Cn3–4 and En2–3 were destroyed in prox-FSz by seawater-buffered diagenesis (Fig. 190), implying that CIEs were decoupled from open-ocean DIC.

stretched continental crust (Konopásek et al., 2020; Percival et al., 2021) analogous to westernmost Tethys antecedent to the European Alps (e.g., Helwig, 1976), is not easily reconciled with a transform-type western Congo margin. Excellent mapping by Guj (1970) implies that the Otavi–Swakop lithofacies boundary is occluded by Sesfontein thrust, which defines the CKz–EKz boundary (Fig. 3). However, Guj's (1970) mapping did not extend S of 19°30'S latitude. Stanistreet and Charlesworth (1999) interpreted Sesfontein thrust as an inverted normal fault, with Tsonguari syncline (W of Tr11) as an infolded remnant of the original hangingwall rift basin. Alternatively, the pre-Ediacaran of Swakop Group in CKz could represent rhombochasms ('pull-apart' basins) in a transform fault system (Fig. 198A–C). Despite penetrative strain and limited vehicle access, CKz offers nearly continuous exposure. Stratigraphy can be mapped, but not measured. A sedimentary perspective on the Damaran succession preserved in S-plunging Khankhaib and Mudorib synclinoria (Hedberg, 1979) between Hoanib River and the Etendeka (plateau) is needed. Such a study should also seek evidence for back-arc volcanism, as predicted in back-arc rift models for the western Congo margin (Goscombe and Grey, 2008, 2018; Konopásek et al., 2014, 2018, 2020).

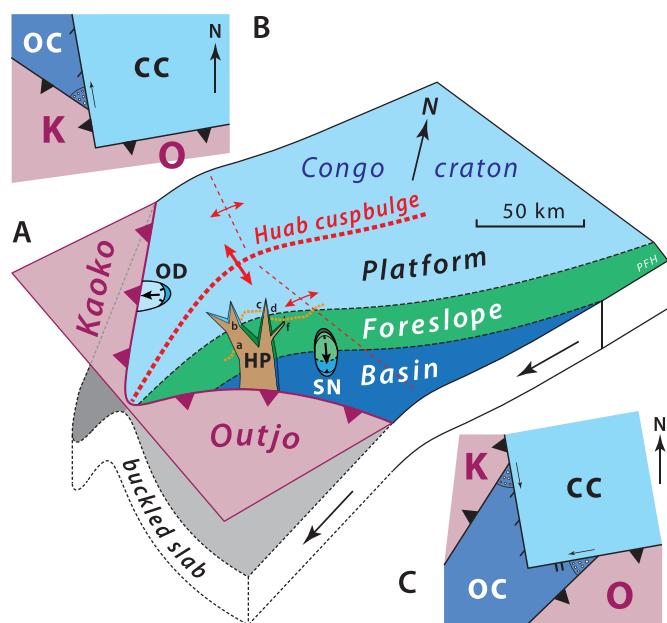


Fig. 209. (A) Schematic block diagram of Huab cusp ca. 0.60 Ga. Congo plate, including the SSE-facing Otavi Group platform margin, is being subducted beneath Kaoko and Outjo belt accretionary prisms. Foredeep sediments and upper-plate topography are not shown. Lateral constriction of subducting plate due to the cusp geometry (Fig. 194D) causes buckling of the slab and amplified forebulge uplift in the cusp axis. Resulting features, described in the text include: HP, Huab palaeokarst (Frets, 1969; Guj, 1974; Miller, 2008b; Hoffman, 2021a); OD, Odmonde detachment (Hoffman & Hartz, 1999; 2016b); SN, Saturn nappe (Clifford, 1962, 2008). Dotted orange lines are the present Otavi Group monoclines on the S flank of Kamanjab inlier (Figs. 8 & 9). Huab paleoescarpments a–f as indicated in Figs. 192 & 193. Diachronous basin closure from NW toward SE is inferred from SE-directed fluvial transport of Mulden Group foredeep clastics (Fig. 146C). Implied younger age of Outjo belt contraction relative to Kaoko belt is opposite to that inferred from structure (Maloof, 2000; Lehmann et al., 2015). (B) Alternative model similar to (A) except that basin (oc) closes diachronously from SE toward NW, implying older contraction in Outjo relative to Kaoko belt, consistent with structural relations (Maloof, 2000; Lehmann et al., 2015). (C) Third model in which Outjo belt (O) and Kaoko belt (K) converged on Congo craton (cc) independently by subduction of oceanic lithosphere (oc). Both collisions progressed (small arrows) toward cratonic promontory, accounting for (1) the unlikely location of a large-scale deep-sea fan (Zerrissene Group, Fig. 210C & D) at a cape, (2) junction (Fig. 3) of offshore magnetic anomalies (Corner, 2000, 2008; Corner and Durrheim, 2018) suggestive that Swakop and Dom Feliciano magmatic arcs conjoin southward face-to-face, and (3) dynamic support for Huab cuspbulge from mantle upwelling driven by slab convergence (Holt et al., 2017). There is no subduction cusp in this model and therefore no compressive stress related to cusp geometry (Hoffman, 2021a). Upper plates indicated by teeth, transform margin by oblique ticks and rifted margin by double ticks.

4.1.5. Otavi–Swakop (OPz–FSz) group transition after CIE En1

Because of sub-Mulden Group erosion in Tr6 and a long fold train in NE-Tr5 of thick strata lacking reliable stratigraphic markers, we were unable to document the Otavi–Swakop (shelf–foreslope) transition in post-Maieberg Fm time (Fig. 5). Our southernmost complete section of Tsumeb Subgroup (9–1, Fig. 145) is 90 km N of Fransfontein Ridge (Tr5). However, 58 km E of Tr5 (5–66), Fransfontein Ridge once again presents a simple steep S-dipping autochthonous monocline, exposing complete Cryogenian and early Ediacaran Otavi Group sections. The best-exposed and accessible sections are at longitudes 15°56'E on farm

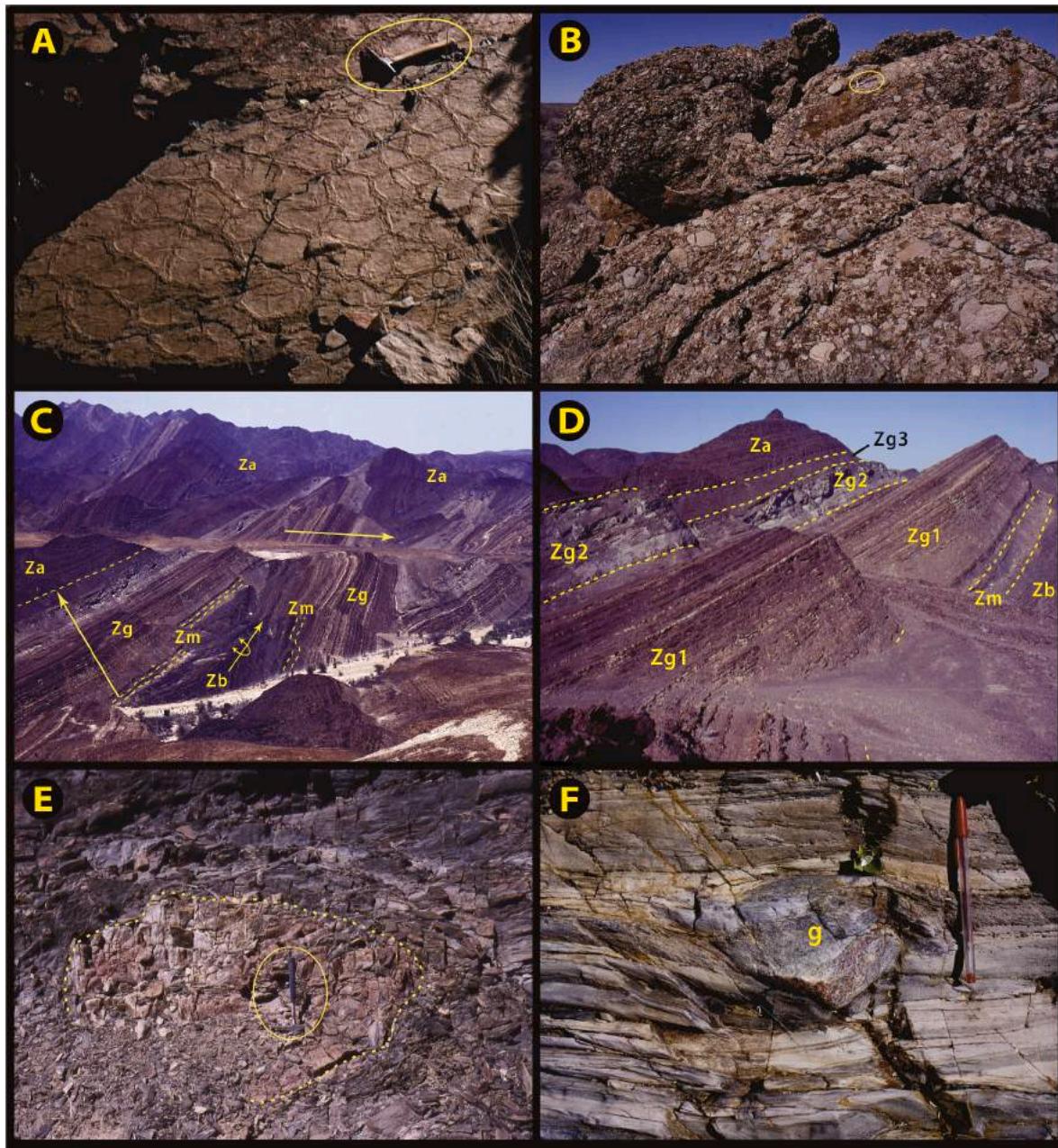


Fig. 210. Images of foredeep clastics (Mulden Group) and SKz deep-sea fan (Zerrissene Group). (A) Desiccation cracks in basal Mulden Group argillaceous siltstone at $-19.2912^{\circ}/13.9652^{\circ}$, 6–2 km WNW of Omibaatjie (8–3). Mulden Group lies disconformably on lower Hüttenberg Fm at this location. (B) Dolomite- and chert-clast conglomerate of lower Mulden Group (Braklaagte Fm) filling paleovalley incised across Ombonde detachment at $-19.3194^{\circ}/14.1603^{\circ}$ on NW limb of Ombonde syncline (Figs. 87A-B & 90). Incision demonstrates that slip on Ombonde detachment, which cuts entire Otavi Group (Fig. 87), predated the oldest local foredeep deposits. (C) Folded deep-sea turbidites of upper Zerrissene Group (Fig. 6A) in SKz (Miller et al., 1983; Swart, 1990, 1992a, b; Paciullo et al., 2007; Miller, 2008b; Nieminski et al., 2018), viewed looking southward across Lower Ugab River (foreground) from Jeppe's lookout at $-20.9652^{\circ}/14.0377^{\circ}$ off Rhino Wash. Units: Zb, Brak River Fm (middle Cryogenian), terrigenous turbidites; Zm, 'Ghaub Fm' (Miller et al., 1983; Miller, 2008b) (late Cryogenian), laminated siltstone with rare extrabasinal limestones of metasedimentary and granitoid lithologies (E-F), presumably sea-glacier rafted; Zg, Gemsbok River Fm (early Ediacaran), mixed carbonate and terrigenous turbidites, broadly coeval with Karibib Fm in Swakop Group; Za, Amis River Fm (middle Ediacaran), terrigenous turbidites, broadly coeval with Kuiseb Fm and Mulden Group (Fig. 6A–C). Original location and sediment source of deep-sea fan is disputed, but detrital zircon age spectra (Nieminski et al., 2018) have more in common with Kalahari craton and CDz than with Congo craton (Fig. 9). Zerrissene Group is exposed in a 100-km-wide belt of chevron-type folds that are overturned westward and plunge N or S as a result of late-stage belt-parallel shortening (Passchier et al., 2002). (D) Three divisions (Zg1–3) of early Ediacaran Gemsbok River Fm, viewed looking southward from point at $-20.9811^{\circ}/14.0303^{\circ}$, between Brakpütz and Rhino Wash. Zg1, mixed greywacke and carbonate turbidites; Zg2, limestone turbidites; Zg3, mica schist with subordinate carbonate turbidites. Za, Zm and Zb as in C. Gemsbok River Fm $\delta^{13}\text{C}$ record (dark green dots SKz in Fig. 189) are from a nearby section SSW of Rhino Wash–Ugab River junction (base at $-20.9856^{\circ}/14.0332^{\circ}$; top at $-20.9849^{\circ}/14.0311^{\circ}$). (E) Granite linstone (outlined by dashed yellow line) 1.75 m in diameter in unit Zm on Sesob River tributary at $-21.0817^{\circ}/13.9394^{\circ}$ (Miller et al., 1983; Swart, 1992a). (F) Fine-grained granodiorite linstone (g), apparently puncturing underlying layers, in laminated siltstone of unit Zm at $-20.9856^{\circ}/14.0337^{\circ}$, 1.47 km SSW of Rhino Wash–Ugab River junction. Similar limestones are exposed in same unit on Ugab River bank at $-20.9762^{\circ}/14.0381^{\circ}$, 0.35 km SSW of Rhino Wash, but ice rafting was rejected by Paciullo et al. (2007).

Neuland 541, 16°02'E on farm Belina 132, and 16°13'E on farm Mountbatten. These sections should be well situated to test the extent of seawater-buffered, sediment-buffered and/or meteoric diagenesis (Figs. 189–191B & C).

4.1.6. W–E facies changes in Rasthof Fm of Tr6

A major eastward-deepening facies change occurs in Rasthof Fm (0.28–0.36 km thick) in Tr6 (Fig. 71). Argillaceous carbonate turbidites pass laterally in <1.0 km into a stromatolite-intraclastic barrier complex (Figs. 76 & 73). Lower Rasthof Fm stromatolites (Fig. 75A–D) on farm Aub 683 (Fig. 70) have been examined by M.W. Wallace (University of Melbourne), but the 20-km-long transect westward to Huab River (Fig. 70) has only 1 measured section (6–8). Since the significance of W–E facies change is unknown, and the nature and history of Huab fault incomplete, a systematic study of Rasthof Fm in Tr6 would be a worthwhile undertaking.

4.1.7. Cyclostratigraphy of middle Cryogenian Narachaams Fm (Swakop Group)

The duration of the Cryogenian inter-snowball epoch was estimated to be 9.8 Myr from cyclostratigraphic analysis of a drillcore through Datangpo Fm in South China (Bao et al., 2018). Datangpo Fm is a laminated silty argillite that is lithologically similar to its age-equivalents in Swakop Group (Okonguarri + Narachaams Fm) of Tr2 (Fig. 32). Relatively well-exposed on the E sides of Vrede N and S domes (Fig. 29), both formations are dominated by flat-laminated siltstone-argillite couplets with 0.6-cm average but variable couplet thickness (Fig. 33C & D). Okonguarri Fm has added cm-scale calcimicrite turbidites (Fig. 33B). The only evident stratigraphic breaks are synsedimentary slips (Fig. 33E). Lateral changes in stratigraphic thickness between adjacent sections (Fig. 32) may be structural in origin, accommodating disharmonic folding of stiff bracketing dolomites (Orusewa and Karibib formations). The nature of such structural accommodation, distributed or discretized, would need to be ascertained through bed-scale mapping.

4.1.8. $\delta^{13}\text{C}$ clast test for source rocks of Marinoan Duurwater moraine

Frequency distribution of $\delta^{13}\text{C}$ values for carbonate clasts of Ghaub Fm diamictite in sections 5–6–15 (Figs. 173A, 43 & 46) indicate derivation predominantly from Ombaatjie Fm cycles b7–8 and not b1–6 (Figs. 173B & 166) (Fox et al., 2008). This implies derivation mainly from 2 sources: (1) the upslope extension of Franni-aus Fm (Figs. 43, 172 & 173), which is supported lithologically (Fig. 50C & D), and (2) the top 80 m of Ombaatjie Fm platform (e.g., Omarumba trough, Figs. 164 & 166). This raises the question: why is there not a more evident contribution of isotopically-heavy (CIE Cn4) debris derived from headwall erosion of Ombaatjie Fm b1–6 in the ice-cut bench seaward of section 5–49 (Figs. 43, 206A & 207A)? Might this debris exist in Duurwater moraine (5–31–42), which has not been sampled? Access is shown (Fig. 63) to the most appropriate sections of Duurwater Moraine to sample, numbered 9 (5–37) and 11 (5–33). The internal structure of Duurwater moraine remains to be resolved, as does the geometry and paleo-environmental significance of sorted carbonate-clast conglomerate bodies within the moraine (Fig. 62).

4.1.9. Depositional cycles in Ombaatjie Fm

Shoaling-upward depositional cycles are clearly developed in Ombaatjie Fm, with an average thickness of 19.1 m per cycle, 9.4 cycles per section, and a reasonable estimate of 3.8 Myr for the formation as a whole if each cycle is assumed to be paced by the long eccentricity (ca 404 kyr) orbital period. Yet, despite 56 complete measured sections (Figs. 68, 71, 88, 103, 125, 129, 135 & 140), including 18 with $\delta^{13}\text{C}$ profiles (Fig. 164), correlation of cycles below b8 remains uncertain from section to section. It cannot even be claimed with confidence that the $\delta^{13}\text{C}$ inflection between CIE Cn4 plateau and Cn5 decline occurs in the same cycle (i.e., base of b7) from section to section. Even where

sections are closely spaced (Fig. 165), the base of b7 may have been correlated differently if $\delta^{13}\text{C}$ data were not available. Since the number of complete sections suitable for measurement is far from exhausted, Ombaatjie Fm is ripe for cyclostratigraphic investigation with more advanced analytical procedures and concepts than we employed (e.g., Kominz and Bond, 1990; Drummond and Wilkinson, 1993; Sadler, 1994; Petersen et al., 2010; Hinnov, 2013; Purkis et al., 2015; Dyer et al., 2018; Geyman et al., 2021). To this end, copies of our stratigraphic logs are available on request from author PFH.

4.1.10. Detrital zircon age spectra of sediment sourced from Congo craton

Despite contrary claims (Foster et al., 2015), only four detrital age spectra (Fig. 9G–J) known to us have been published for sediments in Namibia sourced from Congo craton (Nascimento et al., 2017, 2018; Hoffman and Halverson, 2018; see also Frimmel et al., 2006, for data from equatorial West Congo belt). Three are from Tr1 and have similar, near-unimodal, early Stratherian (1.74–1.77 Ga) peaks: N14-3-13 (Fig. 9H) from basal Chuos Fm (Unit 2) and N14-3-15 (Fig. 9G) from upper Chuos Fm (Unit 4), both near 1–33 in Toekoms subbasin (Fig. 22); and N14-1-3 (Fig. 9I) from Ugab Subgroup or Chuos Fm between 1 and 6 and 7 on farm Opdraend (Fig. 27). The fourth, N14-1-6 (Fig. 9J), is allochthonous (Northern zone) and has bimodal late Orosirian (1.87 Ga) and Ectasian (1.23–1.29 Ga) peaks. It is from lower Ugab Subgroup near 2–10 in Vrede north dome (Figs. 29 & 30). Pre-orogenic sandstones derived from Congo craton from which detrital zircons have yet to be dated include Nabis Fm of Nosib Group (Figs. 5 & 8A), Devede and Okakuyu formations of Ombombo Subgroup (Figs. 99, 123 & 147), Gruis and Ombaatjie formations of Abenab Subgroup (Fig. 68, 71, 88 & 125), Berg Aukas and Okonguarri formations of Swakop Group (Fig. 65), and the basal quartz-siltstone member of Ghaub Fm in Bethanis subbasin (Fig. 18–20A). Many of these units were sampled by one of us (KGL) and hopefully results will be forthcoming after the 2020–2021 pandemic is over. They will provide a firmer basis for comparison with detrital zircon age spectra from middle Cryogenian–early Ediacaran turbidites of the Zerrissene Group deep-sea fan in SKz (Figs. 3, 9A–F & 210C–F), all of which have highest-probability peaks of Stenian (1.2–1.0 Ga) age (Nieminski et al., 2018), as does epicratonic West Congo belt (Frimmel et al., 2006).

Meanwhile, we observe that the existing Congo-sourced age spectra from Namibia (Fig. 9G–J) (Nascimento et al., 2017), bear little resemblance to age spectra from Central Damara zone (Foster et al., 2015), whether from Tonian (Fig. 9L & M) or middle Cryogenian–early Ediacaran (Fig. 9K) deposits, consistent with our contention that Central zone (Fig. 3) is not simply an extension of Congo craton (Fig. 194) (Hoffman, 2021a). Detrital age spectra from Central zone (Fig. 9K–M) have more in common with Zerrissene Group (Fig. 9A–F) than with Congo craton (Fig. 9G–J). On the other hand, Congo craton-derived Tonian and Cryogenian clastics in equatorial West Congo belt (Frimmel et al., 2006) have age spectra (Fig. 9N) that do closely resemble those of Zerrissene Group and Central zone, suggesting the possibility of southward tectonic translation those terranes during sinistral transform development of the western Congo margin (Fig. 198).

4.1.11. Mulden Group

The collisional foredeep model (Fig. 16) for post-Otavi/Swakop Group clastics (Kuiseb Fm and Mulden Group) is attractive because it accounts for terminal emergence and karstic erosion of the carbonate platform by migrating forebulge uplift, followed by drowning and rapid burial by thick terrigenous clastics that shoal upward and cratonward from flysch-type (Kuiseb and Sesfontein Fm) to molasse-type (Renosterberg and Tschudi Fm) facies, coincident with crustal thickening outboard. A comprehensive structural, stratigraphic, sedimentological and geochronological study of Kuiseb Fm and Mulden Group is needed to test this model and better constrain the age of platform destruction.

4.1.12. Duration of the inter-snowball epoch

The middle Cryogenian (Table 1) is remarkable as a short-lived (≤ 20 Myr) Precambrian epoch that can be stratigraphically correlated by virtue of bracketing glacial deposits between no fewer than eleven paleocontinents—Amazonia, Australia, Baltica, Congo, Kalahari, Laurentia, Oman, Siberia, South China, Tarim and Zavkhan (Arnaud et al., 2011). The epoch began with a snowball termination and ended with a snowball inception. Before it ended, green algae became the first major eukaryotic contributors to marine primary production, according to molecular fossil evidence (Brocks et al., 2017; Hoshino et al., 2017; Brocks, 2018). There has yet to be a global synthesis of the epoch and so far it remains unnamed. In the absence of tight radiometric constraints on the age of Marinoan onset (Table 1), the best current estimate of its duration is 9.8 Myr from astrochronologic analysis of magnetic susceptibility data from a drillcore of fine-grained siliciclastic lithology (Datangpo Fm) from the distal foreslope of Nanhua Basin in South China (Bao et al., 2018). The recovered drillcore begins near the top of the Sturtian glacial diamictite (Tiesi'ao Fm) and includes a complete 302-m-thick section of Datangpo Fm consisting of three units: a basal 10-m-thick Mn-rich calcareous shale (cap carbonate), 32 m of organic-rich black shale (postglacial flooding) and 260 m of parallel-laminated muddy siltstone with thin interbeds of shale and fine-grained sandstone. A 3-m-thick transition into the overlying Marinoan glaciomarine Nantuo Fm appears to be unbroken and is marked by decreasing magnetic susceptibility and the first appearance of ice-raftered debris, increasing upward toward the first massive diamictite (basal Nantuo Fm). Orbital parameters (Bao et al., 2018) were constrained by Marinoan (Elatina Fm) tidal rhythmite data from South Australia (Williams, 2000) and theoretical predictions (Berger and Loutre, 1994; Waltham, 2015). The 9.8-Myr estimate for Datangpo Fm (Bao et al., 2018) implies a Marinoan onset ~ 651 Ma (Table 1), a Marinoan duration of ~ 16 Myr, and average rates of Marinoan sediment accumulation and platform erosion in NW Namibia of 3.3 and 3.1 m Myr $^{-1}$ (Tables 6 & 7). This low accumulation rate is consistent with global average Marinoan rates, which are closer to average Sturtian rates if Marinoan duration was ~ 16 Myr (Partin and Sadler, 2016). The expanded stratigraphic record in NW Namibia (Figs. 151 & 163) does not conflict with a 9.8-Myr duration for the middle Cryogenian (Bao et al., 2018). Nevertheless, independent radiometric constraints on the age of Marinoan onset have high priority, since well-tested chronologies underpin all estimates involving geologic rates.

Funding

Research in Namibia was funded by the Natural Science and Engineering Research Council (NSERC) of Canada (1993–94), National Science Foundation (NSF) of USA (Tectonics EAR–95-06769, Earth System History EAR–95-10339 & 96-30928, Paleoclimate EAR–99-05495, Sedimentary & Paleoenvironmental Geology EAR–04-17422), U.S. National Aeronautics & Space Administration (NASA) Astrobiology Institute (1999), Harvard University (1994–2008), and the Canadian Institute for Advanced Research (CIFAR) Earth System Evolution program (2010–15). Support from the Geological Survey of Namibia, McGill University, Princeton University, Dartmouth College and University of Victoria is also gratefully acknowledged.

Sample availability

Sample sets from 1993 to 2014 are stored at Harvard University (Department of Earth and Planetary Sciences) and aliquots may be obtained through curator Dr. Raquel Alonso Perez <ralonzo@fas.harvard.edu>. Sample sets from 2015 to 19 are at McGill University (Department of Earth and Planetary Sciences), where requests should be addressed to Galen Halverson <galen.halverson@mcgill.ca>.

Declaration of Competing Interest

The authors declare no conflict of interest.

Acknowledgments

We thank Tim Horscroft for inviting the paper and Chris Fielding for Editorship. We are indebted to Reviewers Ganqing Jiang, Tony Prave and Malcolm Wallace for prompt, detailed, thoughtful and positive comments and editing, which distinctly improved the final product. This project grew from a suggestion by John Grotzinger and encouragement from the Geological Survey of Namibia. We benefited immeasurably from discussions with Namibian geologists Eckhart Freyer, Albrecht Giesecke, Wolf. Hegenberger, Karl-Heinz Hoffmann, Louis Krüger, Roy Miller, Ute Schreiber and Roger Swart. Field work was facilitated by Directors and staff of the Geological Survey of Namibia, particularly Jane Eiseb, Brian Goal, Estelle Grobler, Kombada Mhopjeni, Anna Nguno, Gabi Schneider, Ute Schreiber, Gloria Simubali and Batseba Tjizoo, in addition to those named earlier. We benefited from observations made by field excursion participants in 1994 (International Conference on Proterozoic Crustal & Metallogenetic Evolution), 1997 (Geological Society of Namibia), 1999 (self-organized), 2002 (International Sedimentological Conference) and 2008 (self-organized), as well as by many others who contributed to field work over the years (Table 3). Our work benefited from comments, suggestions and information freely provided by Phil Allen, Yoshihiro Asahara, Doug Benn, Nic Beukes, Sam Bowring, Clive Calver, Farid Chemale, Gary Clarke, Tom Clifford, Dan Condon, Carol Dehler, Lou Derry, David Evans, Ian Fairchild, Eric Font, Ben Goscombe, Peter Gresse, Michael Hambrey, Brian Harland, Chris Hartnady, Ebbe Hartz, John Hayes, George Henry, Ash Hood, Matt Hurtgen, Peter Huybers, Ganqing Jiang, Stephen Johnston, Fred Kamona, Jay Kaufman, Shin-ichi Kawakami, Joe Kirschvink, Alfred Kröner, Lee Kump, Marcus Kunzmann, Guillaume Le Hir, Adam Maloof, Shawn Marshall, Mike McElroy, Jerry Mitrovica, Ben Mapane, Afonso Nogueira, Cees Passchier, Bernhard Peucker-Ehrenbrink, Ray Pierrehumbert, Susannah Porter, Tony Prave, Judy Pu, Catherine Rose, Pierre Sansjofre, Gad Soffer, Justin Strauss, Bunji Tojo, Ricardo Trindade, Sasha Turchyn, Jan Veizer, Jim Walker, Malcolm Wallace, Steve Warren, Marek Wendorff, Don Winston, Shuhai Xiao, Hideyoshi Yoshioka, Shihong Zhang, Chuanming Zhou and others inadvertently omitted. We are grateful to Edila Köhler and other landowners and residents in Kunene Region for access to their land.

Appendix A. Supplementary data

Supplementary data to this article can be found online at <https://doi.org/10.1016/j.earscirev.2021.103616>.

References

- Abbot, D.S., 2014. Resolved Snowball Earth clouds. *J. Clim.* 27 (12), 4391–4402.
- Abbot, D.S., Voigt, A., Li, D.W., Le Hir, G., Pierrehumbert, R.T., Branson, M., Pollard, D., Koll, D.B.B., 2013. Robust elements of Snowball Earth atmospheric circulation and oases for life. *J. Geophys. Res.-Atmos.* 118, 6017–6027. <https://doi.org/10.1002/jgrd.50540>.
- Abraevitch, A., Van der Voo, R., 2010. Incompatible Ediacaran paleomagnetic directions suggest an equatorial geomagnetic dipole hypothesis. *Earth Planet. Sci. Lett.* 293, 164–170.
- Ackouala Mfere, A.P., Delpomidor, F., Proust, J.-N., Boudzoumou, F., Callec, Y., Préat, A., 2020. Facies and architecture of the SCIC formation (Schisto-Calcaire Group), Republic of the Congo, in the Niari-Nyanga and Comba subbasins of the neoproterozoic west Congo basin after the marinoan glaciation event. *J. Afr. Earth Sci.* 166, 103776.
- Adams, J.E., Rhodes, M.L., 1960. Dolomitization by seepage refluxion. *Bull. Am. Ass. Petrol. Geol.* 44, 1912–1920.
- Adkins, J.F., Boyle, E.A., Curry, W.B., Lutringer, A., 2003. Stable isotopes in deep-sea corals and new mechanism for “vital effects.”. *Geochim. Cosmochim. Acta* 67, 1129–1143.
- Affaton, P., Kalsbeek, F., Boudzoumou, F., Trompette, R., Thrane, K., Frei, R., 2016. The Pan-African West Congo belt in the Republic of Congo (Congo Brazzaville):

- stratigraphy of the Mayombe and West Congo Supergroups studied by detrital zircon geochronology. *Precambrian Res.* 272, 185–202.
- Ahm, A.-S.C., Bjerrum, C.J., Blättler, C.L., Swart, P.K., Higgins, J.A., 2018. Quantifying early marine diagenesis in shallow-water carbonate sediments. *Geochim. Cosmochim. Acta* 236, 140–159.
- Ahm, A.-S.C., Maloof, A.C., Macdonald, F.A., Hoffman, P.F., Bjerrum, C.J., Bold, U., Rose, C.V., Strauss, J.V., Higgins, J.A., 2019. An early diagenetic deglacial origin for basal Ediacaran “cap dolostones”. *Earth Planet. Sci. Lett.* 506, 292–307.
- Aitken, J.D., 1967. Classification and environmental significance of cystalgal limestones and dolomites, with illustrations from the Cambrian and Ordovician of southwestern Alberta. *J. Sediment. Petrol.* 37, 1163–1178.
- Atkin, J.D., 1982. Precambrian of the Mackenzie fold belt—a stratigraphic and tectonic overview. In: Hutchison, R.W., Spence, C.D., Franklin, J.M. (Eds.), *Precambrian Sulfide Deposits*, H.S. Robinson Memorial Volume, Geological Association of Canada, St. John's, NF, Sp. Pap. 25, pp. 149–161.
- Ali, D.O., Spencer, A.M., Fairchild, I.J., Chew, K.J., Anderton, R., Levell, B.K., Hambrey, M.J., Dove, D., Le Heron, D.P., 2018. Indicators of relative completeness of the glacial record of the Port Askaig Formation, Garvellach Islands, Scotland. *Precambrian Res.* 319, 65–78.
- Allen, P.A., Hoffman, P.F., 2005a. Extreme winds and waves in the aftermath of a Neoproterozoic glaciation. *Nature* 433, 123–127.
- Allen, P.A., Hoffman, P.F., 2005b. Reply to: Jerolmack, D. J. & Mohrig, D. *Nature* 436, E1–E2. <https://doi.org/10.1038/nature04026>.
- Alley, R.B., Anandakrishnan, S., Dupont, T.K., Parizek, B.R., Pollard, D., 2007. Effect of sedimentation on ice-sheet grounding-line stability. *Science* 315, 1838–1841.
- Alves, A., Janasi, V.A., Neto, M.C.C., Heaman, L., Simonetti, A., 2013. U–Pb geochronology of the granite magmatism in the Embu Terrane: Implications for the evolution of the Central Ribeira Belt, SE Brazil. *Precambrian Res.* 230, 1–12.
- Anderson, J.B., 1999. *Antarctic Marine Geology*. Cambridge University Press, Cambridge, UK, 289 p.
- Anderson, R.S., Molnar, P., Kessler, M.A., 2006. Features of glacial valley profiles simply explained. *J. Geophys. Res.* 111, F01004 <https://doi.org/10.1029/2005JF000344>.
- Armandita, C., Morley, C.K., Rowell, P., 2015. Origin, structural geometry, and development of a giant coherent slide: the South Makassar Strait mass transport complex. *Geosphere* 11, 376–403.
- Arnaud, E., Halverson, G.P., Shields-Zhou, G. (Eds.), 2011. *The Geological Record of Neoproterozoic Glaciations*. Geological Society, London, Mem. 36, 735 p.
- Ashkenazy, Y., Tziperman, E., 2016. Variability, instabilities, and eddies in a Snowball Ocean. *J. Clim.* 29, 869–888.
- Ashkenazy, Y., Gildor, H., Losch, M., Macdonald, F.A., Schrag, D.P., Tziperman, E., 2013. Dynamics of a Snowball Earth ocean. *Nature* 495, 90–95.
- Ashkenazy, Y., Gildor, H., Losch, M., Tziperman, E., 2014. Ocean circulation under globally glaciated Snowball Earth conditions: steady-state solutions. *J. Phys. Oceanogr.* 44, 24–43.
- Ashwal, L.D., Twiss, D., 1994. The Kunene complex, Angola/Namibia: a composite massif-type anorthositic complex. *Geol. Mag.* 131, 579–591.
- Bachan, A., Lau, K.V., Saltzman, M.R., Thomas, E., Kump, L.R., Payne, J.L., 2017. A model for the decrease in amplitude of carbon isotope excursions across the Phanerozoic. *Am. J. Sci.* 317, 641–676.
- Bandeira, J., McGee, B., Nogueira, A.C.R., Collins, A.S., Trindade, R., 2012. Sedimentological and provenance response to Cambrian closure of the Clymene ocean: the upper Alto Paraguay Group, Paraguay belt, Brazil. *Gondwana Res.* 21, 323–340.
- Bankfield, L.A., Anderson, J.B., 1997. Grounding zone and associated proglacial seismic facies from Bransfield Basin, Antarctica. In: Davies, T.A., Bell, T., Cooper, A.K., Josenhaus, H., Polyak, L., Solheim, A., Stoker, M.S., Stravers, J.A. (Eds.), *Glaciated Continental Margins: An Atlas of Acoustic Images*. Chapman & Hall, London, pp. 100–103.
- Bao, H.M., Lyons, J.R., Zhou, C., 2008. Triple oxygen isotope evidence for elevated CO₂ levels after a Neoproterozoic glaciation. *Nature* 452, 504–506.
- Bao, H.M., Fairchild, I.J., Wynn, P.M., Spötl, C., 2009. Stretching the envelope of past surface environments: Neoproterozoic glacial lakes from Svalbard. *Science* 323, 119–122.
- Bao, X.J., Zhang, S.H., Jiang, G.Q., Wu, H.C., Li, H.Y., Wang, X.Q., An, Z.Z., Yang, T.S., 2018. Cyclostratigraphic constraints on the duration of the Datangpo Formation and the onset age of the Nantuo (Marinoan) glaciation in South China. *Earth Planet. Sci. Lett.* 483, 52–63.
- Barnes, S.-J., 1983. Pan-African serpentinites in central South West Africa/Namibia and the chemical classification of serpentinites. Miller, R.McG. (Ed.), In: *Evolution of the Damara Orogen of South West Africa/Namibia*. Geological Society of South Africa, Johannesburg, Sp. Publ. 11, pp. 147–155.
- Barnes, S.-J., Sawyer, E.W., 1980. An alternative model for the Damara mobile belt: ocean crust subduction and continental convergence. *Precambrian Res.* 13, 297–336.
- Basei, M.A.S., Frimmel, D.E., Neto, M.C.C., Araujo, C.E.G., Castro, N.A., Passarelli, C.R., 2018. The tectonic history of the southern Adamastor ocean based on a correlation of the Kaoko and Dom Feliciano belts. In: Siegesmund, S., Basei, M.A.S., Ohyantçabal, P., Oriolo, S. (Eds.), *Geology of Southwest Gondwana*. Springer International, Berlin, pp. 63–85.
- Bayly, B., 1982. Geometry of subducted plates and island arcs viewed as a buckling problem. *Geology* 10, 629–632.
- Bechstädter, T., Jäger, H., Spence, G., Werner, G., 2009. Late Cryogenian (Neoproterozoic) glacial and post-glacial successions at the southern margin of the Congo craton, northern Namibia: facies, palaeogeography and hydrocarbon perspective. In: Graig, J., Thurow, J., Thusu, B., Thitham, A., Abutarroma, Y. (Eds.), *Global Neoproterozoic Petroleum Systems: The Emerging Potential in North Africa*. Geological Society, London, Sp. Publ. 326, pp. 255–287.
- Bechstädter, T., Jäger, H., Rittersbacher, A., Schweisfurth, B., Spence, G., Werner, G., Boni, M., 2018. The cryogenian ghaub formation of Namibia – new insights into Neoproterozoic glaciations. *Earth-Sci. Rev.* 177, 678–714.
- Benn, D.I., Evans, D.J.A., 1998. *Glaciers and Glaciation*. Arnold, London, 734 p.
- Benn, D.I., Le Hir, G., Bao, H.M., Donnadieu, Y., Dumas, C., Fleming, E.J., Hambrey, M.J., McMillan, E.A., Petronis, M.S., Ramstein, G., Stevenson, C.T.E., Wynn, P.M., Fairchild, I.J., 2015. Orbitally forced ice sheet fluctuations during the Marinoan Snowball Earth glaciation. *Nat. Geosci.* 8, 704–708.
- Bercovici, D., Schubert, G., Ricard, Y., 2015. Abrupt tectonics and rapid slab detachment with grain damage. *Proc. Natl. Acad. Sci. U. S. A.* 112, 1287–1291.
- Berger, W.H., 1982. Increase of carbon dioxide in the atmosphere during deglaciation: the coral reef hypothesis. *Naturwissenschaften* 69, 87–88.
- Berger, A., Loutre, M.F., 1994. Astronomical forcing through geological time. In: De Boer, P.L., Smith, D.G. (Eds.), *Orbital Forcing and Cyclic Sequences*, 19. Blackwell, Oxford, pp. 15–24.
- Bjerrum, C.J., Canfield, D.E., 2011. Towards a quantitative understanding of the late Neoproterozoic carbon cycle. *Proc. Natl. Acad. Sci. U. S. A.* 108 (14), 5542–5547.
- Bjørlykke, K.O., 1973. Glacial conglomerates of late Precambrian age from the Bunyoro Series, W. Uganda. *Geol. Rundsch.* 62, 938–947.
- Blanco, G., Rajesh, H.M., Germs, G.J.B., Zimmermann, U., 2009. Chemical composition and tectonic setting of chromian spinels from the Ediacaran-Early Paleozoic Nama Group, Namibia. *J. Geol.* 117, 325–341.
- Blanco, G., Germs, G.J.B., Rajesh, H.M., Chamale Jr., F., Dussin, I.A., Justino, D., 2011. Provenance and paleogeography of the Nama Group (Ediacaran to early Paleozoic, Namibia): petrography, geochemistry and U–Pb detrital zircon geochronology. *Precambrian Res.* 187, 15–32.
- Bobrovskiy, I., Hope, J.M., Ivantsev, A., Nettersheim, B.J., Hallmann, C., Brocks, J.J., 2018. Ancient steroids establish the Ediacaran fossil Dickinsonia as one of the earliest animals. *Science* 361, 1246–1249.
- Bobrovskiy, I., Hope, J.M., Golubkova, E., Brocks, J.J., 2020. Food sources for the Ediacara biota communities. *Nat. Commun.* <https://doi.org/10.1038/s41467-020-15063-9>.
- Bodiselitch, B., Koeberl, C., Master, S., Reimold, W.U., 2005. Estimating duration and intensity of Neoproterozoic Snowball glaciations from Ir anomalies. *Science* 308, 239–242.
- Bold, U., Smith, E.F., Rooney, A.D., Bowring, S.A., Buchwaldt, R., Dudás, F.Ö., Ramezani, J., Crowley, J.L., Schrag, D.P., Macdonald, F.A., 2016. Neoproterozoic stratigraphy of the Zavkhan terrane of Mongolia: the backbone for Cryogenian and early Ediacaran chemostratigraphic records. *Am. J. Sci.* 316, 1–63.
- Bold, U., Crüger Ahn, A.-S., Schrag, D.P., Higgins, J.A., Jamsran, E., Macdonald, F.A., 2020. Effect of dolomitization on isotopic records from Neoproterozoic carbonates in southwestern Mongolia. *Precambrian Res.* 350 (105902), 1–19.
- Bosak, T., Lahr, D.J.G., Pruss, S.B., Macdonald, F.A., Dalton, L., Matys, E., 2011. Agglutinated tests in post-Sturtian cap carbonates of Namibia and Mongolia. *Earth Planet. Sci. Lett.* 308, 29–40.
- Bosak, T., Lahr, D.J.G., Pruss, S.B., Macdonald, F.A., Gooday, A.J., Dalton, L., Matys, E.D., 2012. Possible early foraminiferans in post-Sturtian (716–635 Ma) cap carbonates. *Geology* 40, 67–70.
- Bosak, T., Mariotti, G., Macdonald, F.A., Perron, J.T., Pruss, S.B., 2013. Microbial sedimentology in Neoproterozoic cap carbonates. In: Bush, A.M., Pruss, S.B., Payne, J.L. (Eds.), *Ecosystem Paleobiology and Geobiology, Paleontological Society Papers*, 19, pp. 1–25.
- Boulton, G.S., 1990. Sedimentary and sea level changes during glacial cycles and their control on glacimarine facies architecture. In: Dowdeswell, J.A., Scourse, J.D. (Eds.), *Glacimarine Environments: Processes and Sediments*. Geological Society, London, Sp. Publ. 53, pp. 15–52.
- Boyle, R.A., Dahl, T.W., Bjerrum, C.J., Canfield, D.E., 2018. Bioturbation and directionality in Earth's carbon isotope record across the Neoproterozoic–Cambrian transition. *Geobiology* 16, 252–278.
- Bradley, D.C., 2008. Passive margins through earth history. *Earth-Sci. Rev.* 91, 1–26.
- Brady, P.V., Gislason, S.R., 1997. Seafloor weathering controls on atmospheric CO₂ and global climate. *Geochim. Cosmochim. Acta* 61, 965–973.
- Brain, C.K., Prave, A.R., Hoffmann, K.-H., Fallick, A.E., Botha, A., Herd, D.A., Sturrock, C., Young, I., Condon, D.J., Allison, S.G., 2012. The first animals: ca 760-million-year-old sponge-like fossils from Namibia. *S. Afr. J. Sci.* 108 (1/2) <https://doi.org/10.4102/sajs.v108i1.2658>. Art. #658.
- Bramlette, M.N., 1946. The Monterey Formation of California and the origin of its siliceous rocks. United States Geological Survey, Prof. Pap. 212, 57 p.
- Brasier, M.D., Shields, G., 2000. Neoproterozoic chemostratigraphy and correlation of the Port Askaig glaciation, Dalradian Supergroup of Scotland. *J. Geol. Soc. Lond.* 157, 909–914.
- Braun, J., Guillocheau, F., Robin, C., Baby, G., Jelsma, H., 2014. Rapid erosion of the Southern African Plateau as it climbs over a mantle superswell. *J. Geophys. Res.* 119, 6093–6112.
- Bristow, C., Kennedy, M.J., 2008. Carbon isotope excursions and the oxidant budget of the Ediacaran atmosphere and ocean. *Geology* 36, 863–866.
- Brocks, J.J., 2018. The transition from a cyanobacterial to algal world and the emergence of animals. *Emerg. Top. Life Sci.* <https://doi.org/10.1042/ETLS20180039>.
- Brocks, J.J., Jarrett, A.J.M., Siranteone, E., Hallmann, C., Hoshino, Y., Liyanage, T., 2017. The rise of algae in Cryogenian oceans and the emergence of animals. *Nature* 548, 578–581.
- Brooks, H.L., Hodgson, D.M., Brunt, R.L., Peakall, J., Flint, S.S., 2017. Exhumed lateral margins and increasing flow confinement of a submarine landslide complex. *Sedimentology* 65, 1067–1096.

- Brune, S., Heine, C., Pérez-Gussinyé, M., Sobolev, S.V., 2014. Rift migration explains continental margin asymmetry and crustal hyper-extension. *Nature Comms.* 5, 4014. <https://doi.org/10.1038/ncomms5014>.
- Budyko, M.I., 1968. On the origin of the glacial epochs. *Meteorol. Hydrol.* 11, 3–12.
- Budyko, M.I., 1969. The effect of solar radiation variations on the climate of the Earth. *Tellus* 21, 611–619.
- Buechi, M.W., Frank, S.M., Graf, H.R., Menzies, J., Anselmetti, F.S., 2017. Subglacial emplacement of till and meltwater deposits at the base of overdeepened bedrock troughs. *Sedimentology* 64, 658–685.
- Burchfiel, B.C., Royden, L.H., 1985. North–South extension under the convergent Himalayan regime. *Geology* 13, 679–682.
- Burke, W.H., Denison, R.E., Heatherington, E.A., Koepnick, R.B., Nelson, H.F., Otto, J.B., 1982. Variation of seawater $^{87}\text{Sr}/^{86}\text{Sr}$ through Phanerozoic time. *Geology* 10, 516–519.
- Burns, S.J., Matter, A., 1993. Carbon isotopic record of the latest Proterozoic from Oman. *Eclog. Geol. Helvet.* 86, 595–607.
- Busfield, M.E., Le Heron, D.P., 2013. Glacitectonic deformation in the Chuos Formation of northern Namibia: implications for Neoproterozoic ice dynamics. *Proc. Geol. Assoc.* 124, 778–789.
- Busfield, M.E., Le Heron, D.P., 2018. Snowball Earth under the microscope. *J. Sediment. Res.* 88, 659–677.
- Butler, R.W.H., Paton, D.A., 2010. Evaluating lateral compaction in deepwater fold and thrust belts: How much are we missing from “nature’s sandbox”? *GSA Today* 20 (3). <https://doi.org/10.1130/GSATG77A.1>.
- Cahen, L., 1950. Le calcaire de Sekelolo le Complexe tillitique et la Dolomite rose CI dans l’Anticinal de Congo dia Kati (Bas-Congo). *Annal. Mus. Belg. Congo, Tervuren. Sci. Geol.* 7, 10–55.
- Cahen, L., 1963. Glaçiations anciennes et dérive des continents [Ancient glaciations and continental drift]. *Ann. Soc. Géol. Belg.* 86 (B), 19–84.
- Cahen, L., 1978. La stratigraphie et la tectonique du Supergroupe Ouest-Congolien dans les zones médiane et externe de l’orogène Ouest-Congolien (Pan-Africain) au Bas-Zaire et dans les régions voisines. *Annal. Roy. Mus. C. Afr., Tervuren. Sci. Geol.* 83, 1–150.
- Cahen, L., Lerpersonne, J., 1967. The Precambrian of the Congo, Rwanda, and Burundi. In: Rankama, K. (Ed.), *The Precambrian*, Vol. 3. Interscience, New York, pp. 143–290.
- Cahen, L., Lerpersonne, J., 1981. Proterozoic diamictites of Lower Zaire. In: Hambrey, M. J., Harland, W.B. (Eds.), *Earth’s Pre-Pleistocene Glacial Record*. Cambridge Univ. Press, Cambridge, UK, pp. 153–157.
- Cailleteaux, J.L.H., De Putter, T., 2019. The Neoproterozoic Katanga Supergroup (D. R. Congo): State-of-the-art and revisions of the lithostratigraphy, sedimentary basin and geodynamic evolution. *J. Afr. Earth Sci.* 150, 522–531.
- Cairncross, B., 1997. The Otavi Mountain Land Cu-Pb-Zn-V deposits. *Mineral. Rec.* 28, 109–130.
- Calver, C.R., Crowley, J.L., Wingate, M.T.D., Evans, D.A.D., Raub, T.D., Schmitz, M.D., 2013. Globally synchronous Marinoan deglaciation indicated by U–Pb geochronology of the Cottons Breccia, Tasmania, Australia. *Geology* 41, 1127–1130.
- Cameron, K.A., Hodson, A.J., Osborn, A.M., 2012. Carbon and nitrogen biogeochemical cycling potentials of supraglacial cryoconite communities. *Polar Biol.* 35, 1375–1393.
- Canfield, D.E., Raiswell, R., 1999. The evolution of the sulfur cycle. *Am. J. Sci.* 299, 697–723.
- Canfield, D.E., Knoll, A.H., Poulton, S.W., Narbonne, G.M., Dunning, G.R., 2020. Carbon isotopes in clastic rocks and the Neoproterozoic carbon cycle. *Am. J. Sci.* 320, 97–124.
- Cao, X.B., Bao, H.M., 2013. Dynamic model constraints on oxygen-17 depletion in atmospheric O_2 after a snowball Earth. *Proc. Natl. Acad. Sci. U. S. A.* 110 (36), 14,546–14,550.
- Carey, S.W., 1958. The tectonic approach to continental drift. In: Carey, S.W. (Ed.), *Continental Drift: A Symposium*. University of Tasmania, Hobart, Geology Department, pp. 177–363.
- Chang, B., Li, C., Liu, D., Foster, I., Tripathi, A., Lloyd, M.K., Maradiaga, I., Luo, G.M., An, Z.H., She, Z.B., Xie, S.C., Tong, J.N., Huang, J.H., Algeo, T.J., Lyons, T.W., Immenhauser, A., 2020. Massive formation of early diagenetic dolomite in the Ediacaran ocean: Constraints on the “dolomite problem”. *Proc. Natl. Acad. Sci. U. S. A.* 117 (14), 005–14,014.
- Chauvet, F., Sapin, F., Geoffrey, L., Ringenbach, C.-C., Ferry, J.-N., 2021. Conjugate volcanic passive margins in the austral segment of the South Atlantic – architecture and development. *Earth-Sci. Rev.* 212 (103461), 1–34.
- Cheek, R.J., Leckie, D.A., 1993. Hummocky cross-stratification. *Sedimentol. Rev.* 1, 103–122.
- Chemale Jr., F., Mallmann, G., de Bitencourt, M.F., Kawashita, K., 2012. Time constraints on magmatism along the Major Gercino Shear Zone, southern Brazil: Implications for West Gondwana reconstruction. *Gondwana Res.* 22, 184–199.
- Christie-Blick, N., Dyson, I.A., von der Boch, C.C., 1995. Sequence stratigraphy and the interpretation of Neoproterozoic earth history. *Precambrian Res.* 73, 3–26.
- Clark, J.A., 1976. Greenland’s rapid postglacial emergence: A result of ice-water gravitational attraction. *Geology* 4, 310–312.
- Clerc, C., Ringenbach, J.-C., Jolivet, L., Ballard, J.-F., 2018. Rifted margins: Ductile deformation, boudinage, continentward-dipping normal faults and the role of the weak lower crust. *Gondwana Res.* 53, 20–40.
- Clifford, T.N., 1962. Notes on nappes in the Otavi facies of northern South-West Africa. 6th Ann. Rep. Res. Inst. Afr. Geol. University of Leeds, pp. 44–45.
- Clifford, T.N., 1967. The Damaran episode in the Upper Proterozoic – Lower Paleozoic structural history of southern Africa. Geological Society of America, New York, Sp. Pap. 92, 100 p.
- Clifford, T.N., 2008. The geology of the Neoproterozoic Swakop–Otavi transition zone in the Outjo District, northern Damara Orogen, Namibia. *S. Afr. J. Geol.* 111, 117–140, 3 maps scale 1:40,000.
- Cloetingh, S.A.P.L., Wortel, M.J.R., Vlaar, N.J., 1982. Evolution of passive continental margins and initiation of subduction zones. *Nature* 297, 139–142.
- Cloud, P., Wright, L.A., Williams, E.G., Diehl, P., Walter, M.R., 1974. Giant stromatolites and associated vertical tubes from the upper Proterozoic Noonday Dolomite, Death Valley region, eastern California. *Geol. Soc. Am. Bull.* 85, 1869–1882.
- Clough, C.T., Maufe, H.B., Bailey, E.B., 1909. The cauldron subsidence of Glencoe and the associated igneous phenomena. *Quart. J. Geol. Soc., London* 65, 611–674.
- Cohen, P.A., Knoll, A.W., 2012. Scale microfossils from the mid-Neoproterozoic Fifteenmile Group, Yukon Territory. *J. Paleontol.* 86, 775–800.
- Cohen, P.A., Knoll, A.H., Kodner, R.B., 2009. Large spinose microfossils in Ediacaran rocks as resting stages of early animals. *Proc. Natl. Acad. Sci. U. S. A.* 106, 6519–6524.
- Cohen, P.A., Strauss, J.V., Rooney, A.D., Sharma, M., Tosca, N., 2017. Controlled hydroxyapatite biomineralization in an ~810 million-year-old unicellular eukaryote. *Sci. Adv.* 3, e1700095.
- Cohen, P.A., Vizcaíno, M., Anderson, R.P., 2020. Oldest fossil ciliates from the Cryogenian glacial interlude reinterpreted as possible red algal spores. *Palaeontology* 63, 941–950.
- Coleman, A.J., Duffy, O.B., Jackson, C.A.-L., 2019. Growth faults above propagating normal faults. *Earth-Sci. Rev.* 196 (102885), 1–31.
- Collier, J.S., McDermott, C., Warner, G., Gyori, N., Schnabel, M., McDermott, K., Horn, B. W., 2017. New constraints on the age and style of continental breakup in the South Atlantic from magnetic anomaly data. *Earth Planet. Sci. Lett.* 477, 27–40.
- Collom, C.J., Johnston, P.A., Powell, W.G., 2009. Reinterpretation of ‘Middle’ Cambrian stratigraphy of the rifted western Laurentian margin: Burgess Shale Formation and continuous units (Sauk II megasequence), Rocky Mountains, Canada. *Palaeogeogr. Palaeoclimatol. Palaeoecol.* 277, 63–85.
- Condon, D.J., Prave, A.R., Benn, D.I., 2002. Neoproterozoic glacial-rainout intervals: observations and implications. *Geology* 30, 35–38.
- Condon, D., Zhu, M.Y., Bowring, S.A., Wang, W., Yang, A.H., Jin, Y.G., 2005. U–Pb ages from the Neoproterozoic Doushantuo Formation, China. *Science* 308, 95–98.
- Conor, C.H.H., Preiss, W.V., 2020. Cryogenian glaciomarine megaclasts of the McDonald Corridor, Bimbawrie Conservation Park, Olary Region, South Australia. *Austral. J. Earth Sci.* doi: <https://doi.org/10.1080/08120099.2018.1553206>.
- Coogan, L.A., Dosso, S.E., 2015. Alteration of ocean crust provides a strong temperature dependent feedback on the geological carbon cycle and is a primary driver of the Sr-isotopic composition of seawater. *Earth Planet. Sci. Lett.* 415, 38–46.
- Coogan, L.A., Gillis, K.M., 2013. Evidence that low-temperature oceanic hydrothermal systems play an important role in the silicate–carbonate weathering cycle and long-term climate regulation. *Geochem. Geophys. Geosyst.* 14 <https://doi.org/10.1002/ggge.20113>.
- Corner, B., 2000. Crustal framework of Namibia derived from magnetic and gravity data. *Communis Geol. Surv. Namibia* 12, 13–19, 6 maps scale 1:5M.
- Corner, B., 2008. Crustal framework of Namibia derived from an integrated interpretation of geophysical and geological data. In: Miller, RMcG (Ed.), *The Geology of Namibia*, Vol. 1. Geological Survey of Namibia, Windhoek, 2–1–2–19 and 5 figs.
- Corner, B., Durrheim, R.J., 2018. An integrated geophysical and geological interpretation of the Southern African lithosphere. In: Siegesmund, S., Basei, M., Oyhantçabal, P., Oriolo, S. (Eds.), *Geology of Southwest Gondwana*. Springer International, Berlin, pp. 19–61.
- Corsetti, F.A., Grotzinger, J.P., 2005. Origin and significance of tube structure in Neoproterozoic post-glacial cap carbonates: example from the Noonday Dolomite, Death Valley, Unites States. *Palaeos* 20, 348–362.
- Cowan, E.A., Zellers, S.D., Müller, J., Walczak, M.H., Worthington, L.L., Caissie, B.E., Clary, W.A., Jager, J.M., Gulick, S.P., Pratt, J.W., Mix, A.C., Fallon, S.J., 2020. Sediment controls dynamis behaviors of a Cordilleran ice stream at the Last Glacial Maximum. *Nat. Comms* 11, 1826. <https://doi.org/10.1038/s41467-020-15679-0>.
- Coward, M.P., 1981. The junction between Pan-African mobile belts in Namibia: its structural history. *Tectonophysics* 76, 59–73.
- Coward, M.P., 1983. The tectonic history of the Damaran belt. In: Miller, RMcG (Ed.), *Evolution of the Damara Orogen of South West Africa/Namibia*. Geological Society of South Africa, Sp. Publ. 11, pp. 409–421.
- Cox, G.M., Strauss, J.V., Halverson, G.P., Schmitz, M.D., McClelland, W.C., Stevenson, R. S., Macdonald, F.A., 2015. Kikiktitav volcanics of Arctic Alaska—Melting of harzburgitic mantle associated with the Franklin large igneous province. *Lithosphere* 7, 275–295.
- Cox, G.M., Isakson, V., Hoffman, P.F., Geron, T.M., Schmitz, M.D., Shahin, S., Collins, A. S., Preiss, W., Blades, M.L., Mitchell, R.N., Nordvan, A., 2018. South Australian U–Pb zircon (CA-ID-TIMS) age supports globally synchronous Sturtian deglaciation. *Precambrian Res.* 315, 257–263.
- Craine, J.M., Fierer, N., McLauchlan, K.K., 2010. Widespread coupling between rate and temperature sensitivity of organic matter decay. *Nat. Geosci.* 3, 854–857.
- Creveling, J.R., Mitrovica, J.X., 2014. The sea-level fingerprint of a Snowball Earth glaciation. *Earth Planet. Sci. Lett.* 399, 74–85.
- Crevello, P.D., Wilson, J.L., Sarg, J.F., Read, J.F. (Eds.), 1989. Controls on Carbonate Platform and Basin Development. Sp. Pub. 44. SEPM Society for Sedimentary Geology, Tulsa, OK, 405 p.
- Crockford, P.W., Cowie, B.R., Johnston, D.T., Hoffman, P.F., Sugiyama, I., Pellerin, A., Bui, T.H., Hayles, J., Halverson, G.P., Macdonald, F.A., Wing, B.A., 2016. Triple oxygen and multiple sulfur isotope constraints on the evolution of the post-Marinoan sulfur cycle. *Earth Planet. Sci. Lett.* 435, 74–83.

- Crockford, P.W., Hodgskiss, M.S.W., Uhlein, G.J., Caxito, F., Hayles, J.A., Halverson, G.P., 2018. Linking paleocontinents through triple oxygen isotope anomalies. *Geology* 46, 179–182.
- Crockford, P.W., Kunzmann, M., Bekker, A., Hayles, J., Bao, H.M., Halverson, G.P., Peng, Y.B., Bui, T.H., Cox, G.M., Gibson, T.M., Wörndl, S., Rainbird, R., Lepland, A., Swanson-Hysell, N.L., Master, S., Sreenivas, B., Kuznetsov, A., Krupenik, V., Wing, B.A., 2019. Claypool continued: extending the isotopic record of sedimentary sulfate. *Chem. Geol.* 513, 200–225.
- Crockford, P.W., Kunzmann, M., Blättler, C.L., Kalderon-Asael, B., Murphy, J.G., Ahm, A.-S., Shiloni, S., Halverson, G.P., Planavsky, N.J., Halevy, I., Higgins, J.A., 2021. Reconstructing Neoproterozoic seawater chemistry from diagenetic dolomite. *Geology* 49. <https://doi.org/10.1130/G48213.1>.
- Cui, H., Kaufman, A.J., Peng, Y.B., Liu, X.M., Plummer, R.E., 2018. The Neoproterozoic Hüttenberg $\delta^{13}\text{C}$ anomaly: genesis and global implications. *Precambrian Res.* 313, 242–262.
- Dalton, L.A., Bosak, T., Macdonald, F.A., Lahr, D.J.G., Pruss, S.B., 2013. Preservational and morphological variability of assemblages of agglutinated eukaryotes in Cryogenian cap carbonates of northern Namibia. *Palaios* 28, 67–79.
- Dawers, N.H., Anders, M.H., Scholz, C.H., 1993. Growth of normal faults: displacement-length scaling. *Geology* 21, 1107–1110.
- De Angelis, H., Skvarca, P., 2003. Glacier surge after ice shelf collapse. *Science* 299, 1560–1562.
- de Charpentier, J., 1841. *Essai sur les Glaciers et sur le Terrain Erratique du Bassin du Rhône*. Ducloux, Lausanne, 363 p.
- de Cock, G.S., 2000. A reappraisal of the Namibian Damara stratigraphy in part of the Southern Swakop Terrane and its implications to basin evolution. *S. Afr. J. Geol.* 104, 115–136.
- de Cock, G.S., Eglington, B., Armstrong, R.A., Harmer, R.E., Walraven, F., 2000. U–Pb and Pb–Pb ages of the Nauwpoort rhyolite, Kawakeup leptite and Okongava diorite: implications for the onset of rifting and of orogenesis in the Damara belt, Namibia. *Communs. Geol. Surv. Namibia* 12, 81–88.
- de Cock, M.O., Ernst, R., Söderlund, U., Jourdan, F., Hofmann, A., Le Gall, B., Bertrand, H., Chisonga, B.C., Beukes, N., Rajesh, H.M., Moseki, L.M., Fuchs, R., 2014. Dykes of the 1.1 Ga Umkondo LIP, Southern Africa: Clues to a complex plumbing system. *Precambrian Res.* 249, 129–143.
- de Wit, M.J., Stankiewicz, J., Reeves, C., 2008. Restoring Pan-African–Brasiliano connections: more Gondwana control, less Trans-Atlantic corruption. In: Pankhurst, R.J., Trouw, R.A.J., Brito Neves, B.B., de Wit, M.J. (Eds.), West Gondwana: Pre-Cenozoic Correlations Across the South Atlantic Region. Geological Society, London, Sp. Publ. 294, pp. 399–412.
- Debenham, F., 1920. A new mode of transportation by ice: the raised muds of South Victoria Land (Antarctica). *Quart. J. Geol. Soc. Lond.* 75, 51–76.
- Defliese, W.F., 2021. The impact of Snowball Earth glaciation on ocean water $\delta^{18}\text{O}$ values. *Earth Planet. Sci. Lett.* 554, 116661.
- Delpomdor, F., Préat, A., 2013. Early and Late Neoproterozoic C, O and Sr isotope geochemistry in the carbonates of West Congo and Mbuj-Mayi supergroups: a preserved marine signature? *Palaeogeogr. Palaeoclimatol. Palaeoecol.* 389, 35–47.
- Delpomdor, F., Schröder, S., Préat, A., Lapointe, P., Blanpied, C., 2018. Sedimentology and geochemistry of the late Neoproterozoic carbonate ramp sequences of the Hüttenberg Formation (northwestern Namibia) and the C5 Formation (western central Democratic Republic of Congo): Record of the late post-Marinoan marine transgression on the margin of the Congo Craton. *S. Afr. J. Geol.* 121, 23–42.
- Denysyn, S.W., Halls, H.C., Davis, D.W., Evans, D.A.D., 2009. Paleomagnetism and U–Pb geochronology of Franklin dykes in High Arctic Canada and Greenland: a revised age and paleomagnetic pole constraining block rotations in the Nares Strait region. *Can. J. Earth Sci.* 46, 689–705.
- Deplus, C., Dubois, J., 1989. Flexural response of the oceanic lithosphere at an arc–arc junction: implication for the subduction of aseismic ridges. *Tectonophysics* 160, 63–73.
- Derry, L.A., 2010a. A burial diagenesis origin for the Ediacaran Shuram–Wonoka carbon isotope anomaly. *Earth Planet. Sci. Lett.* 294, 152–162.
- Derry, L.A., 2010b. On the significance of $\delta^{13}\text{C}$ correlations in ancient sediments. *Earth Planet. Sci. Lett.* 296, 497–501.
- Dill, R.F., Shinn, E.A., Jones, A.T., Kelly, K., Steinen, R.P., 1986. Giant subtidal stromatolites forming in normal salinity water. *Nature* 324, 55–58.
- Dodd, S.C., Mac Niocaill, C., Muxworthy, A.R., 2015. Long duration (>4 Ma) and steady-state volcanic activity in the early Cretaceous Paraná–Etendeka Large Igneous Province: New paleomagnetic data from Namibia. *Earth Planet. Sci. Lett.* 414, 16–29.
- Domack, E.W., Hoffman, P.F., 2011. An ice grounding-line wedge from the Ghauβ glaciation (635 Ma) on the distal foreslope of the Otavi carbonate platform, Namibia, and its bearing on the Snowball Earth hypothesis. *Geol. Soc. Am. Bull.* 123, 1448–1477.
- Domack, E., Powell, R., 2018. Modern glaciomarine environments: an Antarctic perspective. In: Menzies, J., van der Meer, J.J.M. (Eds.), Past Glacial Environments, 2nd ed. Elsevier, Amsterdam, pp. 181–272.
- Domack, E.W., Duran, D., Leventer, A., Ishman, S.E., Doane, S., McCallum, S., Ring, J., Gilbert, R., Prentice, M., 2005. Stability of the Larsen B ice shelf on the Antarctic Peninsula during the Holocene epoch. *Nature* 436, 681–685.
- Donnadieu, Y., Fluteau, F., Ramstein, G., Ritz, C., Besse, J., 2003. Is there a conflict between the Neoproterozoic glacial deposits and the snowball Earth interpretation: an improved understanding with numerical modeling. *Earth Planet. Sci. Lett.* 208, 101–112.
- Dowdeswell, J.A., Fugelli, E.M.G., 2012. The seismic architecture and geometry of grounding-zone wedges formed at the marine margins of past ice sheets. *Geol. Soc. Am. Bull.* 124, 1750–1761.
- Dowdeswell, J.A., Hambrey, M.J., Wu, R.T., 1985. A comparison of clast fabric and shape in Late Precambrian and modern glaciogenic sediments. *J. Sediment. Petrol.* 55, 691–704.
- Dowdeswell, J.A., Hogan, K.A., Arnold, N.S., Mugford, R.I., Wells, M., Hirst, P.P., Decalf, C., 2015. Sediment-rich meltwater plumes and ice-proximal fans at the margins of modern and ancient tidewater glaciers: Observations and modelling. *Sedimentology* 62, 1665–1692.
- Dowdeswell, J.A., Batchelor, C.L., Montelli, A., Ottesen, D., Christie, F.D.W., Dowdeswell, E.K., Evans, J., 2020. Delicate seafloor landforms reveal past Antarctic grounding-line retreat of kilometers per year. *Science* 368, 1020–1024.
- Driscoll, N.W., Hogg, J.R., Christie-Blick, N., Karner, G.D., 1995. Extensional tectonics in the Jeanne d'Arc Basin, offshore Newfoundland: implications for the timing of breakup between Grand Banks and Iberia. In: Scrutton, R.A., Stoker, M.S., Shimmield, G.B., Tudhope, A.W. (Eds.), The Tectonics, Sedimentation and Palaeoceanography of the North Atlantic Region. Geological Society, London, Sp. Publ. 90, pp. 1–28.
- Drummond, C.N., Wilkinson, B.H., 1993. Carbonate cycle stacking patterns and hierarchies of orbitally forced eustatic sealevel change. *J. Sediment. Petrol.* 63, 369–377.
- Drüppel, K., Littmann, S., Romer, R.L., Okrusch, M., 2007. Petrology and isotope geochemistry of the Mesoproterozoic anorthosite and related rocks of the Kunene Intrusive Complex, NW Namibia. *Precambrian Res.* 156, 1–31.
- Du Toit, A.L., 1937. Our Wandering Continents. Hafner, New York, 366.
- Dumas, S., Arnott, R.W.C., 2006. Origin of hummocky and swaley cross-stratification—the controlling influence of unidirectional current strength and aggradation rate. *Geology* 34, 1073–1076.
- Dunham, R.J., 1962. Classification of carbonate rocks according to depositional textures. In: Ham, W.E. (Ed.), Classification of Carbonate Rocks – a Symposium. Mem. 1. American Association of Petroleum Geologists, Tulsa, OK, pp. 108–121.
- Dunn, P.R., Thompson, B.P., Rankama, K., 1971. Late Pre-Cambrian glaciation in Australia as a stratigraphic boundary. *Nature* 231, 498–602.
- Dürr, S.B., Dingeldey, D.P., 1996. The Kaoko belt (Namibia): part of a late Neoproterozoic continental-scale strike-slip system. *Geology* 24, 503–506.
- Dyer, B., Maloof, A.C., Purkis, S.J., Harris, P.M., 2018. Quantifying the relationship between water depth and carbonate facies. *Sediment. Geol.* 373, 1–10.
- Eberli, G.P., Ginsburg, R.N., 1987. Segmentation and coalescence of Cenozoic carbonate platforms, northwestern Great Bahama Bank. *Geology* 15, 75–79.
- Eberli, G.P., Anselmetti, F.S., Kent, J.A.M., McNeill, D.F., Melim, L.A., 2001. Calibration of seismic sequence stratigraphy with cores and logs. In: Ginsburg, R.N. (Ed.), Subsurface Geology of a Prograding Carbonate Platform Margin, Great Bahama Bank: Results of the Bahamas Drilling Project. SEPM (Society for Sedimentary Geology), Tulsa, Oklahoma, Sp. Publ. 70, pp. 241–265.
- Eisbacher, G.H., 1985. Late Proterozoic rifting, glacial sedimentation, and sedimentary cycles in the light of Windermere deposition, western Canada. *Palaeogeogr. Palaeoclimatol. Palaeoecol.* 51, 231–254.
- Embleton, B.J.J., Williams, G.E., 1986. Low latitude of deposition for late Precambrian periglacial varvites in South Australia: implications for palaeoclimatology. *Earth Planet. Sci. Lett.* 79, 419–430.
- Eriksson, E., 1968. Air-ocean-icecap interactions in relation to climatic fluctuations and glaciation cycles. *Meteorol. Monogr.* 8, 68–92.
- Ernst, R.E., Pereira, E., Hamilton, M.A., Pisarevsky, S.A., Rodriguez, J., Tassinari, C.C.G., Texeira, W., Van-Dunem, V., 2013. Mesoproterozoic intraplate magmatic ‘bar code’ record of the Angola portion of the Congo craton: Newly dated magmatic events at 1505 and 1110 Ma and implications for Nuna (Columbia) supercontinent reconstructions. *Precambrian Res.* 230, 103–118.
- Erwin, D.H., Laflamme, M., Tweedt, S.M., Sperling, E.A., Pisani, D., Peterson, K.J., 2011. The Cambrian conundrum: Early divergence and later ecological success in the early history of animals. *Science* 334, 1091–1097.
- Evans, D.A.D., 2000. Stratigraphic, geochronological, and paleomagnetic constraints upon the Neoproterozoic climatic paradox. *Am. J. Sci.* 300, 347–433.
- Evans, D.A.D., Raub, T.D., 2011. Neoproterozoic glacial palaeolatitudes: a global update. In: Arnaud, E., Halverson, G.P., Shields-Zhou, G. (Eds.), The Geological Record of Neoproterozoic Glaciations. Geological Society, London, Mem. 36, pp. 93–112.
- Ewing, R.C., Eisenman, I., Lamb, M.P., Poppick, L., Maloof, A.C., Fischer, W.W., 2014. New constraint on equatorial temperatures during a Late Neoproterozoic snowball Earth glaciation. *Earth Planet. Sci. Lett.* 406, 110–122.
- Eyles, N., Januszczak, N., 2007. Syntectonic subaqueous mass flows of the Neoproterozoic Otavi Group, Namibia: Where is the evidence of global glaciation? *Basin Res.* 19, 179–198.
- Eyster, A.E., Fu, R.F., Strauss, J.V., Weiss, B.P., Roots, C.F., Halverson, G.P., Evans, D.A., Macdonald, F.A., 2017. Paleomagnetic evidence for large rotation of the Yukon block relative to Laurentia: implications for a low-latitude Sturtian glaciation and the break-up of Rodinia. *Geol. Soc. Am. Bull.* 129, 38–58.
- Eyster, A., Weiss, B.P., Karlstrom, K., Macdonald, F.A., 2020. Paleomagnetism of the Chuar Group and evaluation of the late Tonian Laurentian apparent polar wander path with implications for the makeup of breakup of Rodinia. *Geol. Soc. Am. Bull.* 132, 710–738.
- Fabre, S., Berger, G., 2012. How tillite weathering during the snowball Earth aftermath induced cap carbonate deposition. *Geology* 40, 1027–1030.
- Fabre, S., Berger, G., Nédélec, A., 2011. Modeling of continental weathering under high-CO₂ atmospheres during Precambrian times. *Geochem. Geophys. Geosyst.* 12, Q10001. <https://doi.org/10.1029/2010GC003444>.
- Fabre, S., Berger, G., Chavagnac, V., Besson, P., 2013. Origin of cap carbonates: an experimental approach. *Palaeogeogr. Palaeoclimatol. Palaeoecol.* 392, 524–533.

- Fairbridge, R.W., 1964. The importance of limestone and its Ca/Mg content to palaeoclimatology. In: Nairn, A.E.M. (Ed.), *Problems in Palaeoclimatology*. Wiley Interscience, London, pp. 431–478.
- Fairchild, I.J., 1993. Balmby shores and ice wastes: the paradox of carbonates associated with glacial deposits in Neoproterozoic times. *Sedimentol. Rev.* 1, 1–16.
- Fairchild, I.J., Bonnand, P., Davies, T., Fleming, E., Grassineau, N., Halverson, G.P., Hambrey, M.J., McMillan, E.M., McKay, E., Parkinson, I.J., Stevenson, C.T.E., 2016. The late Cryogenian warm interval, NE Svalbard: chemostratigraphy and genesis. *Precambrian Res.* 281, 128–154.
- Fairchild, I.J., Spencer, A.M., Ali, D.O., Anderson, R.P., Anderton, R., Boomer, I., Dove, D., Evans, J.D., Hambrey, M.J., Howe, J., Sawaki, Y., Shields, G.A., Skelton, A., Tucker, M.E., Wang, Z.R., Zhou, Y., 2018. Tonian–Cryogenian boundary sections of Argyll, Scotland. *Precam. Res.* 319, 37–64.
- Faleiros, F.M., Campanha, G.A.C., Martins, L., Vlach, S.R.F., Vasconcelos, P.M., 2011. Ediacaran high-pressure collisional metamorphism and tectonics of the southern Ribeira Belt (SE Brazil): Evidence for terrane accretion and dispersion during Gondwana assembly. *Precambrian Res.* 189, 263–291.
- Faure, G., 1986. *Principles of Isotope Geology*, 2nd ed. John Wiley & Sons, New York. 589 p.
- Fielding, C.R., 2018. Stratigraphic architecture of the Cenozoic succession in the McMurdo Sound region, Antarctica: An archive of polar palaeoenvironmental change in a failed rift setting. *Sedimentology* 65, 1–61.
- Fielding, C.R., Browne, G.H., Field, B., Florindo, F., Harwood, D.M., Krissek, L.A., Levy, R.H., Panter, K.S., Passchier, S., Pekar, S.F., 2011. Sequence stratigraphy of the ANDRILL AND-2A drillcore, Antarctica: a long-term ice-proximal record of Early to Mid-Miocene climate, sea-level and glacial dynamism. *Palaeogeogr. Palaeoclimatol. Palaeoecol.* 305, 337–351.
- Finnegan, S., Fike, D.A., Jones, D., Fischer, W.W., 2012. A temperature dependent positive feedback on the magnitude of carbon isotope excursions. *Geosci. Can.* 39, 122–131.
- Fischer, W.W., Knoll, A.H., 2009. An iron shuttle for deepwater silica in Late Archean and early Paleoproterozoic iron formation. *Geol. Soc. Am. Bull.* 121, 222–235.
- Folk, R.L., 1959. Practical petrographic classification of limestones. *Bull. Am. Assoc. Pet. Geol.* 43, 1–38.
- Foster, D.A., Goscombe, B.D., 2013. Continental growth and recycling in convergent orogens with large turbidite fans on oceanic crust. *Geosciences* 3, 354–388.
- Foster, G.L., Rae, J.W.B., 2016. Reconstructing ocean pH with boron isotopes in foraminifera. *Annu. Rev. Earth Planet. Sci.* 44, 207–237.
- Foster, D.A., Goscombe, B.D., Newstead, B., Mapani, B., Mueller, P.A., Gregory, L.C., Muvanga, E., 2015. U–Pb and Lu–Hf isotopic data of detrital zircons from the Neoproterozoic Damara Sequence: Implications for Congo and Kalahari before Gondwana. *Gondwana Res.* 28, 179–190.
- Fox, T.J., Domack, E.W., Hoffman, P.F., 2008. Clast provenance and geochemistry of the Ghaub Formation, northern Namibia. *Geol. Soc. Am. Abstr. Programs* 40 (2), 2 abs. 8–3.
- Frei, R., Gaucher, C., Poulton, S.W., Canfield, D.E., 2009. Fluctuations in Precambrian atmospheric oxygenation recorded by chromium isotopes. *Nature* 461, 250–253.
- Frets, D.C., 1969. Geology and structure of the Huab–Welwitschia area, South West Africa. University of Cape Town, Precambrian Research Unit, Bull 5, 255 p. and 1 map-sheet, scale 1:150,000.
- Freund, R., 1970. Rotation of strike-slip faults in Sistan, southeast Iran. *J. Geol.* 78, 188–200.
- Freund, R., 1974. Kinematics of transform and transcurrent faults. *Tectonophysics* 21, 93–134.
- Friedman, I., O’Neil, J.R., 1977. Chapter KK. Compilation of stable isotope fractionation factors of geochemical interest. In: Fleischer, M. (Ed.), *Data of Geochemistry*, 6th Ed. United States Geological Survey, Prof. Pap. 44-KK, Washington, DC.
- Frimmel, H.E., Tack, L., Basei, M.S., Nutman, A.P., Boven, A., 2006. Provenance and chemostratigraphy of the Neoproterozoic West Congolian Group in the Democratic Republic of Congo. *J. Afr. Earth Sci.* 46, 221–239.
- Fritz, P., Smith, D.C.W., 1970. The isotopic composition of secondary dolomites. *Geochim. Cosmochim. Acta* 34, 1161–1173.
- Fuck, R.A., Brito Neves, B.B., Schobbenhaus, C., 2008. Rodinia descendants in South America. *Precambrian Res.* 160, 108–126.
- Garrels, R.M., Mackenzie, F.T., 1971. Evolution of Sedimentary Rocks. W.W. Norton & Co., New York, 397 p.
- Gee, Z.Y., Warsitzka, M., Rosenau, M., Gawthorpe, R.L., 2019. Progressive tilting of salt-bearing continental margins controls thin-skinned deformation. *Geology* 47, 1122–1126.
- Gee, J.S., Kent, D.V., 2007. Source of oceanic magnetic anomalies and the geomagnetic polarity time scale. In: Kono, M. (Ed.), *Treatise on Geophysics, Geomagnetism*, Vol. 5. Elsevier, Amsterdam, pp. 455–507.
- Germs, G.J.B., Gresse, P.G., 1991. The foreland basin of the Damara and Gariep orogens in Namaqualand and southern Namibia: stratigraphic correlations and basin dynamics. *S. Afr. J. Geol.* 94, 159–169.
- Gevers, T.W., 1931. An ancient tillite in South-West Africa. *Trans. Geol. Soc. S. Afr.* 34, 1–17.
- Geyman, E.C., Maloof, A.C., 2019. A diurnal carbon engine explains ^{13}C -enriched carbonates without increasing the global production of oxygen. *Proc. Natl. Acad. Sci. U. S. A.* 116 (24), 433–24,439.
- Geyman, E.C., Maloof, A.C., Dyer, B., 2021. How is sea level change encoded in carbonate stratigraphy? *Earth Planet. Sci. Lett.* 560, 116790.
- Giddings, J.A., Wallace, W.W., 2009. Facies-dependent $\delta^{13}\text{C}$ variation from a Cryogenian platform margin, South Australia: evidence for stratified Neoproterozoic oceans? *Palaeogeogr. Palaeoclimatol. Palaeoecol.* 271, 196–214.
- Giddings, J.A., Wallace, M.W., Woon, E.M.S., 2009. Interglacial carbonates of the Cryogenian Umberata Group, northern Flinders Ranges, South Australia. *Austral. J. Earth Sci.* 56, 907–925.
- Gilleadeau, G.J., Kah, L.C., 2013. Carbon isotope records in a Mesoproterozoic epicratonic sea: Carbon cycling in a low oxygen world. *Precambrian Res.* 228, 85–101.
- Ginsburg, R.N., James, N.P., 1976. Submarine botryoidal aragonite in Holocene reef limestones, Belize. *Geology* 4, 431–436.
- Giribet, G., Edgecombe, G.D., 2019. The phylogeny and evolutionary history of arthropods. *Curr. Biol.* 29, 592–602.
- Gislason, S.R., Oelkers, E.H., 2003. Mechanism, rates, and consequences of basaltic glass as a function of pH and temperature. *Geochim. Cosmochim. Acta* 67, 3817–3822.
- Goddéris, Y., Le Hir, G., Donnadieu, Y., 2011. Modelling the snowball Earth. In: Arnaud, E., Halverson, G.P., Shields-Zhou, G. (Eds.), *The Geological Record of Neoproterozoic Glaciations*. Geological Society, London, Mem. 36, pp. 151–161.
- Golledge, N.R., Fogwill, C.J., Mackintosh, A.N., Buckley, K.M., 2012. Dynamics of the last glacial maximum Antarctic ice-sheet and its response to ocean forcing. *Proc. Natl. Acad. Sci. U. S. A.* 109 (16), 051–16,056.
- Gomez, N., Mitrovica, J.X., Huybers, P., Clark, P.U., 2010. Sea level as a stabilizing factor for marine-ice-sheet grounding lines. *Nat. Geosci.* 3, 850–853.
- Gomez, N., Pollard, D., Mitrovica, J.X., Huybers, P., Clark, P.U., 2012. Evolution of a coupled marine ice sheet–sea level model. *J. Geophys. Res.* 117, F01013 <https://doi.org/10.1029/2011JF002128>.
- Goodge, J.W., 2020. Geologic and tectonic evolution of the Transantarctic Mountains, from ancient craton to recent enigma. *Gondwana Res.* 80, 50–122.
- Goodman, J., Pierrehumbert, R.T., 2003. Glacial flow of floating marine ice in “Snowball Earth”. *J. Geophys. Res.* 108 (C10), 3308. <https://doi.org/10.1029/2002JC001471>.
- Goodman, J.C., Strom, D.C., 2013. Feedbacks in a coupled ice-atmosphere-dust model of the glacial Neoproterozoic “Mudball Earth”. *J. Geophys. Res.* 118, 1–12. <https://doi.org/10.1002/jgrd.50849>.
- Gorjan, P., Veevers, M.R., Walter, M.R., 2000. Neoproterozoic sulfur-isotope variation in Australia and global implications. *Precambrian Res.* 100, 151–179.
- Goscombe, B., Gray, D.R., 2007. The Coastal Terrane of the Kaoko Belt, Namibia: outboard arc-terrane and tectonic significance. *Precambrian Res.* 155, 139–158.
- Goscombe, B., Gray, D., 2008. Structure and strain variation at mid-crustal levels in a transpressional orogen: a review of Kaoko Belt structure and the character of West Gondwana amalgamation and dispersal. *Gondwana Res.* 13, 45–85.
- Goscombe, B., Hand, M., Gray, D., 2003a. Structure of the Kaoko Belt, Namibia: progressive evolution of a classic transpressional orogen. *J. Struct. Geol.* 25, 1049–1081.
- Goscombe, B., Hand, M., Gray, D., Mawby, J., 2003b. The metamorphic architecture of a transpressional orogen: the Kaoko Belt, Namibia. *J. Petrol.* 44, 679–711.
- Goscombe, B., Gray, D., Armstrong, R., Foster, D.A., Vogl, J., 2005. Event geochronology of the Pan-African Kaoko Belt, Namibia. *Precambrian Res.* 140, 103.e1–e41.
- Goscombe, B., Foster, D.A., Gray, D., Wade, B., Marsellos, A., Titus, J., 2017. Deformation correlations, stress field switches and evolution of an orogenic intersection: the Pan-African Kaoko–Damara orogenic junction, Namibia. *Geosci. Front.* 8, 1187–1232.
- Goscombe, B., Foster, D.A., Gray, D., Wade, B., 2018. The evolution of the Damara orogenic system: a record of West Gondwana assembly and crustal response. In: Siegesmund, S., Basei, M.A.S., Oyhantçabal, P., Oriolo, S. (Eds.), *Geology of Southwest Gondwana*. Springer International, Berlin, pp. 303–352.
- Goscombe, B., Foster, D.A., Gray, D., Wade, B., 2020. Assembly of central Gondwana along the Zambezi Belt: metamorphic response and basement reactivation during the Kuunga Orogeny. *Gondwana Res.* 80, 410–465.
- Gray, D.R., Foster, D.A., Meert, J.G., Goscombe, B.D., Armstrong, R., Trouw, R.A.J., Passchier, C.W., 2008. A Damara orogen perspective on the assembly of southwestern Gondwana. In: Pankhurst, R.J., Trouw, R.A.J., Brito-Neves, B.B., de Wit, M.J. (Eds.), *West Gondwana: Pre-Cenozoic Correlations Across the South Atlantic Region*. Geological Society, London, Sp. Publ. 294, pp. 257–278.
- Gresse, P.G., Germs, G.J.B., 1993. The Nama foreland basin: sedimentation, major unconformity bounded sequences and multisided active margin advance. *Precambrian Res.* 63, 247–272.
- Grey, K., Hill, A.C., Calver, C., 2011. Biostratigraphy and stratigraphic subdivision of Cryogenian successions of Australia in a global context. In: Arnaud, E., Halverson, G.P., Shjelds-Zhou, G. (Eds.), *The Geological Record of Neoproterozoic Glaciations*. Geological Society, London, Mem. 36, pp. 113–134.
- Grotzinger, J.P., 1986a. Cyclicity and paleoenvironmental dynamics, Rocknest platform, northwest Canada. *Geol. Soc. Am. Bull.* 97, 1208–1231.
- Grotzinger, J.P., 1986b. Evolution of early Proterozoic passive-margin carbonate platform, Rocknest Formation, Wopmay orogen, Northwest Territories, Canada. *J. Sed. Petrol.* 56, 831–847.
- Grotzinger, J.P., 1989. Facies and evolution of Precambrian carbonate depositional systems: emergence of the modern platform archetype. In: Crevello, P.D., Wilson, J.L., Sarg, J.F., Read, J.F. (Eds.), *Controls on Carbonate Platform and Basin Development*. SEPM (Society for Sedimentary Geology), Tulsa, OK, Sp. Publ. 44, pp. 79–106.
- Grotzinger, J.P., 1990. Geochemical model for Proterozoic stromatolite decline. *Am. J. Sci.* 290–A, 80–103.
- Grotzinger, J.P., James, N.P., 2000. Precambrian carbonates: evolution of understanding. In: Grotzinger, J.P., James, N.P. (Eds.), *Carbonate Sedimentation and Diagenesis in the Evolving Precambrian World*. SEPM (Society for Sedimentary Geology), pp. 3–20. Tulsa, Oklahoma, Sp. Publ. 67.
- Grotzinger, J.P., Miller, R.McG., 2008. The Geology of Namibia. In: Miller, R.McG. (Ed.), *Neoproterozoic to Lower Palaeozoic, 2. Geological Survey of Namibia*, Windhoek, pp. 13-229–13-272.

- Grotzinger, J.P., Bowring, S.A., Saylor, B.Z., Kaufman, A.J., 1995. Biostratigraphic and geochronologic constraints on early animal evolution. *Science* 270, 598–604.
- Grotzinger, J.P., Adams, E., Schröder, S., 2005. Microbial-metazoan reefs of the terminal Proterozoic Nama Group (ca 550–543 Ma), Namibia. *Geol. Mag.* 142, 499–517.
- Grotzinger, J.P., Fike, D.A., Fischer, W.W., 2011. Enigmatic origin of the largest-known carbon isotope excursion in Earth's history. *Nat. Geosci.* 4, 285–292.
- Gudmundsson, A., De Guido, G., Scudero, S., 2013. Length-displacement scaling and fault growth. *Tectonophysics* 608, 1298–1309.
- Guillocheau, F., Rouby, D., Robin, C., Helm, C., Rolland, N., Le Charlier de Veslud, C., Braun, J., 2012. "Quantification and causes of the terrigenous sediment budget at the scale of a continental margin" a new method applied to the Namibia–South Africa margin. *Basin Res.* 24, 3–30.
- Guj, P., 1970. The Damara Belt in the south-western Kaokoveld, South West Africa. University of Cape Town, Precam. Res. Unit Bull. 8, 168 p., 4 map sheets (scale 1: 125,000) and cross-sections.
- Guj, P., 1974. A revision of the Damara stratigraphy along the southern margin of the Kamanjab inlier, South West Africa. In: Kröner, A. (Ed.), Contributions to the Precambrian Geology of Southern Africa: A Volume in Honour of John de Villiers, pp. 167–176. Univ. Cape Town, Precam. Res. Unit Bull. 15.
- Hagen, J.O., 2008. Glacier surge in Svalbard with examples from Usherbreen. *Nor. Geogr. Tidsskr.* 42, 208–213.
- Hälbich, I.W., Freyer, E.E., 1985. Structure and metamorphism of Damaran rocks in the Ugab profile. *Communs. Geol. Surv. S. W. Afr./Namibia* 1, 97.
- Hallet, B., Hunter, L., Bogen, J., 1996. Rates of erosion and sediment evacuation by glaciers: a review of field data and their implications. *Glob. Planet. Chang.* 12, 213–235.
- Halls, H.C., Lovette, A., Hamilton, M., Söderlund, U., 2015. A paleomagnetic and U–Pb geochronology study of the western end of the Grenville dyke swarm: Rapid changes in paleomagnetic field direction at ca. 585 Ma related to polarity reversals? *Precambrian Res.* 257, 137–166.
- Halverson, G.P., Hurtgen, M.T., 2007. Ediacaran growth of the marine sulfate reservoir. *Earth Planet. Sci. Lett.* 263, 32–44.
- Halverson, G.P., Shields-Zhou, G., 2011. Chemostratigraphy and the Neoproterozoic glaciations. In: Arnaud, E., Halverson, G.P., Shields-Zhou, G. (Eds.), *The Geological Record of Neoproterozoic Glaciations*. Geological Society, London, Mem. 36, pp. 51–66.
- Halverson, G.P., Hoffman, P.F., Schrag, D.P., Kaufman, A.J., 2002. A major perturbation of the carbon cycle before the Ghaub glaciation (Neoproterozoic) in Namibia: Prelude to snowball Earth? *Geochem. Geophys. Geosyst.* 3 <https://doi.org/10.1029/2001GC000244>.
- Halverson, G.P., Maloof, A.C., Hoffman, P.F., 2004. The Marinoan glaciation (Neoproterozoic) in northeast Svalbard. *Basin Res.* 16, 297–324.
- Halverson, G.P., Hoffman, P.F., Schrag, D.P., Maloof, A.C., Rice, A.H., 2005. Toward a Neoproterozoic composite carbon-isotope record. *Geol. Soc. Am. Bull.* 117, 1081–1207.
- Halverson, G.P., Dudás, F.Ó., Maloof, A.C., Bowring, S.A., 2007. Evolution of the $^{87}\text{Sr}/^{86}\text{Sr}$ composition of Neoproterozoic seawater. *Palaeogeogr. Palaeoclimatol. Palaeoecol.* 256, 103–129.
- Halverson, G.P., Hurtgen, M.T., Porter, S.M., Collins, A.S., 2009. Neoproterozoic–Cambrian biogeochemical evolution. In: Gaucher, C., Sial, A.N., Halverson, G.P., Frimmel, H.E. (Eds.), *Neoproterozoic–Cambrian Tectonics, Global Change and Evolution: a focus on southwestern Gondwana*. Dev. Precam. Geol. 16. Elsevier, Amsterdam, pp. 351–365.
- Halverson, G.P., Wade, B.P., Hurtgen, M.T., Barovich, K.M., 2010. Neoproterozoic chemostratigraphy. *Precambrian Res.* 182, 337–350.
- Halverson, G.P., Poitrasson, F., Hoffman, P.F., Nédélec, A., Montel, J.-M., Kirby, J., 2011. Fe isotope and trace element geochemistry of the Neoproterozoic syn-glacial Rapitan iron formation. *Earth Planet. Sci. Lett.* 309, 100–112.
- Halverson, G.P., Kunzmann, M., Strauss, J.V., Maloof, A.C., 2018a. The Tonian–Cryogenian transition in Northeastern Svalbard. *Precambrian Res.* 319, 79–95.
- Halverson, G.P., Porter, S.M., Gibson, T.M., 2018b. Dating the late Proterozoic stratigraphic record. *Emerg. Top. Life Sci.* <https://doi.org/10.1042/ETLS20170167>.
- Hambrey, M.J., Harland, W.B., 1981. *Earth's Pre-Pleistocene Glacial Record*. Cambridge University Press, Cambridge, UK, 1004 p.
- Handwerger, A.L., Rempel, A.W., Skarbek, R.M., Roering, J.J., Hiley, G.E., 2016. Rate-weakening friction characterizes both slow sliding and catastrophic failure of landslides. *Proc. Natl. Acad. Sci. U. S. A.* 113 (37), 10,281–10,286.
- Harland, W.B., 1964. Evidence of late Precambrian glaciation and its significance. In: Nairn, A.E.M. (Ed.), *Problems in Palaeoclimatology*. Interscience, London, pp. 119–149.
- Harland, W.B., Herod, K.N., 1975. Glaciations through time. In: Wright, A.E., Mosely, F. (Eds.), *Ice Ages: Ancient and Modern*. Steel House Press, Liverpool, pp. 189–216.
- Hartnady, C.J., Joubert, P., Stowe, C., 1985. Proterozoic crustal evolution in southwestern Africa. *Episodes* 8 (4), 236–244.
- Hatherton, T., 1990. Antarctica: the Ross Sea Region. DSIR, Wellington, NZ, 287 p.
- Havig, J.R., Hamilton, T.L., Bachan, A., Kump, L.R., 2017. Sulfur and carbon isotopic evidence for metabolic pathway evolution and a four-stepped Earth system progression across the Archean and Paleoproterozoic. *Earth-Sci. Rev.* 174, 1–21.
- Hawes, I., Howard-Williams, C., Fountain, A.G., 2008. Ice-based freshwater ecosystems. In: Vincent, W.F., Laybourn-Parry, J. (Eds.), *Polar Lakes and Rivers: Limnology of Arctic and Antarctic Aquatic Ecosystems*. Oxford University Press, Oxford, U.K., pp. 103–118.
- Hawes, I., Jungblut, A.D., Matys, E.D., Summons, R.E., 2018. The "dirty ice" of the McMurdo Ice Shelf: analogues for biological oases during the Cryogenian. *Geobiology* 16, 369–377.
- Hawkins, A.D., Xiao, S.H., Jiang, G.J., Wang, X.Q., Shi, X.Y., 2017. New biostratigraphic and chemostratigraphic data from the Ediacaran Doushantuo Formation in intra-shelf and upper slope facies of the Yangtze platform: implications for biozonation of acanthomorphic actinarians in South China. *Precambrian Res.* 300, 28–39.
- Hedberg, R.M., 1979. Stratigraphy of the Ovamboland Basin, South West Africa. University of Cape Town, Precam. Res. Unit Bull 24, 325 p. and 6 map sheets (scale 1:250,000).
- Hegenberger, W., 1987. Gas escape structures in Precambrian peritidal carbonate rocks. *Communs. Geol. Surv. Namibia* 3, 49–55.
- Hegenberger, W., 1993. Stratigraphy and sedimentology of the Late Precambrian Witvlei and Nama groups, east of Windhoek. *Geological Survey of Namibia, Windhoek*, Mem. 17, 82 p.
- Heilbron, M., Valeriano, C.M., Tassinari, C.C.G., Almeida, J.C.H., Tupinambá, M., Siga, O., Trouw, R.A.J., 2008. Correlation of Neoproterozoic terranes between the Ribeira Belt, SE Brazil and its African counterpart: comparative tectonic evolution and open questions. In: Pankhurst, R.J., Trouw, R.A.J., de Brito Neves, B.B., de Wit, M.J. (Eds.), *West Gondwanan Pre-Cenozoic Correlations Across the South Atlantic Region*. Geological Society, London, Sp. Publ. 294, pp. 211–237.
- Heilbron, M., Tupinambá, M., Valeriano, C.M., Armstrong, R., Silva, L.G.E., Melo, R.S., Simonet, A., Soares, A.C.P., Machado, N., 2013. The Serra da Bolivia complex: the record of a new arc-related unit at Ribeira belt. *Precambrian Res.* 238, 158–175.
- Helwig, J., 1976. Shortening of continental crust in orogenic belts and plate tectonics. *Nature* 260, 768–770.
- Henry, G., Stanistreet, I.G., Maiden, K.J., 1986. Preliminary results of a sedimentological study of the Chuos Formation in the Central Zone of the Damara Orogen: Evidence for mass flow processes and glacial activity. *Communs. Geol. Surv. S.W. Africa/Namibia* 2, 75–92.
- Henry, G., Clendenin, C.W., Stanistreet, I.G., Maiden, K.J., 1990. Multiple detachment model for the early rifting stage of the Late Proterozoic Damara orogen in Namibia. *Geology* 18, 67–71.
- Henry, G., Osborne, M.A., Schmerold, R.K., 1992/93. Note: proposed lithostratigraphic subdivision of the Ugab Subgroup (Damara Sequence) in Kaokoland, Namibia. *Communs. Geol. Surv. Namibia* 8, 143–145.
- Higgins, J.A., Schrag, D.P., 2003. Aftermath of a snowball Earth. *Geochem. Geophys. Geosyst.* 4 <https://doi.org/10.1029/2002GC000403>.
- Higgins, J.A., Fischer, W.W., Schrag, D.P., 2009. Oxygenation of the ocean and sediments: Consequences for the seafloor carbonate factory. *Earth Planet. Sci. Lett.* 284, 25–33.
- Higgins, J.A., Blättler, C.L., Lundstrom, E.A., Santiago-Ramos, D.P., Akhtar, A.A., Crüger Ahm, A.-S., Bialik, O., Holmden, C., Bradbury, H., Murray, S.T., Swart, P.K., 2018. Mineralogy, early marine diagenesis, and the chemistry of shallow-water carbonate sediments. *Geochim. Cosmochim. Acta* 220, 512–534.
- Hinnov, L.A., 2013. Cyclostratigraphy and its revolutionizing applications in the earth and planetary sciences. *Geol. Soc. Am. Bull.* 125, 1703–1734.
- Hjelstuen, B.O., Eldholm, O., Faleide, J.I., 2007. Recurrent Pleistocene mega-failures on the SW Barents Sea margin. *Earth Planet. Sci. Lett.* 258, 605–618.
- Hodel, F., Macouin, M., Trindade, R.I.F., Triantafyllou, A., Ganne, J., Chavagnac, V., Berger, J., Rospabé, M., Destrigneveille, C., Carlut, J., Ennih, N., Agrinier, P., 2018. Fossil black smoker yields oxygen isotopic composition of Neoproterozoic seawater. *Nat. Commun.* 9, 1453. <https://doi.org/10.1038/s41467-018-03890-w>.
- Hodgskiss, M.S.W., Frost, J.L., Dagnaud, O.M.J., Schmitz, M.D., Halverson, G.P., Sperling, E.A., 2019. New insights on the Orosirian carbon cycle, early Cyanobacteria, and the assembly of Laurentia from the Belcher Group. *Earth Planet. Sci. Lett.* 520, 141–152.
- Hoernerle, K., Rohde, J., Hauff, F., Garbe-Schönberg, D., Homrighausen, S., Werner, R., Morgan, J.P., 2015. How and when plume zonation appeared during the 132 Myr evolution of the Tristan Hotspot. *Nat. Commun.* 6, 7799. <https://doi.org/10.1038/ncomms8799>.
- Hoffman, P.F., 1976. Environmental diversity of Middle Precambrian stromatolites. In: Walter, M.R. (Ed.), *Stromatolites*. Elsevier, Amsterdam, pp. 599–611.
- Hoffman, P.F., 1987. Proterozoic foredeeps, foredeep magmatism, and Superior-type iron-formation in the Canadian shield. In: Kröner, A. (Ed.), *Proterozoic Lithospheric Evolution*. American Geophysical Union, Geodynamics Series 17, pp. 85–97. Washington, D.C.
- Hoffman, P.F., 1999. The break-up of Rodinia, birth of Gondwana, true polar wander and the snowball Earth. *J. Afr. Earth Sci.* 28, 17–33.
- Hoffman, P.F., 2005. 28th DeBeers Alex. Du Toit Memorial Lecture: On Cryogenian (Neoproterozoic) ice-sheet dynamics and the limitations of the glacial sedimentary record. *S. Afr. J. Geol.* 108, 557–576.
- Hoffman, P.F., 2011a. Strange bedfellows: glacial diamictite and cap carbonate from the Marinoan (635 Ma) glaciation in Namibia. *Sedimentology* 58, 57–119.
- Hoffman, P.F., 2011b. Glaciogenic and associated strata of the Otavi carbonate platform and foreslope, northern Namibia: evidence for large base-level and glacioeustatic changes. In: Arnaud, E., Halverson, G.P., Shields-Zhou, G. (Eds.), *The Geological Record of Neoproterozoic Glaciations*. Geological Society, London, Mem. 36, pp. 195–209.
- Hoffman, P.F., 2016. Cryoconite pans on Snowball Earth: supraglacial oases for Cryogenian eukaryotes? *Geobiology* 14, 531–542.
- Hoffman, P.F., 2021a. Cusp tectonics: an Ediacaran megakarst landscape and bidirectional mass slides in a Pan-African syntaxis (NW Namibia). In: Murphy, J.B., Strachan, R.A., Quesada, C. (Eds.), *Pannotia to Pangaea: Neoproterozoic and Palaeozoic Orogenic Cycles in the Circum-Atlantic Region*. Geological Society, London, Spec. Publ. 503, pp. 105–142.
- Hoffman, P.F., 2021b. On the kinematics and timing of Rodinia breakup: a possible Cryogenian rift-transform junction at the SW cape of Congo Craton, NW Namibia. *S. Afr. J. Geol.* (accepted).

- Hoffman, P.F., Halverson, G.P., 2008. Otavi Group of the western Northern Platform, the eastern Kaoko Zone and the western Northern Margin Zone. In: Miller, R.M.C.G. (Ed.), *The Geology of Namibia, Vol. 2. Geological Survey of Namibia*, Windhoek, 13–69–136.
- Hoffman, P.F., Halverson, G.P., 2018. Discussion of “Depositional ages and provenance of the Neoproterozoic Damara Supergroup (northwest Namibia): Implications for the Angola–Congo and Kalahari cratons connection” by D. B. Nascimento, R. S. Schmitt, A. Ribeiro, R. A. J. Trouw, C. W. Passchier, and M. A. S. Basei. *Gondwana Res.* 58, 235–238.
- Hoffman, P.F., Hartz, E.H., 1999. Large, coherent, submarine landslide associated with Pan-African foreland flexure. *Geology* 27, 687–690.
- Hoffman, P.F., Lamothe, K.G., 2019. Seawater-buffered diagenesis, destruction of carbon isotope excursions, and the composition of DIC in Neoproterozoic oceans. *Proc. Natl. Acad. Sci. U. S. A.* 116 (18), 874–18,879.
- Hoffman, P.F., Li, Z.X., 2009. A palaeogeographic context for Neoproterozoic glaciation. *Palaeogeogr., Palaeoclimatol., Palaeoecol.* 277, 158–172.
- Hoffman, P.F., Macdonald, F.A., 2010. Sheet-crack cements and early regression in Marinoan (635 Ma) cap dolostones: Regional benchmarks of vanishing ice-sheets? *Earth Planet. Sci. Lett.* 300, 374–384.
- Hoffman, P.F., Schrag, D.P., 1999. Response: considering a Neoproterozoic snowball Earth. *Science* 284 online. <http://www.sciencemag.org/cgi/content/full/284/5417/1087a>.
- Hoffman, P.F., Schrag, D.P., 2002. The snowball Earth hypothesis: testing the limits of global change. *Terra Nova* 14, 129–155.
- Hoffman, P.F., Hawkins, D.P., Isachsen, C.E., Bowring, S.A., 1996. Precise U–Pb zircon ages for early Damaran magmatism in the Summas Mountains and Welwitschia Inlier, northern Damara Belt, Namibia. *Communs. Geol. Surv. Namibia* 11, 47–52.
- Hoffman, P.F., Kaufman, J.A., Halverson, G.P., 1998a. Comings and goings of global glaciations on a Neoproterozoic carbonate platform in Namibia. *GSA Today* 8, 1–9.
- Hoffman, P.F., Kaufman, A.J., Halverson, G.P., Schrag, D.P., 1998b. A Neoproterozoic snowball Earth. *Science* 281, 1342–1346.
- Hoffman, P.F., Halverson, G.P., Grotzinger, J.P., 2002. Comment: Are Proterozoic cap carbonates and isotopic excursions a record of gas hydrate destabilization following Earth's coldest intervals? *Geology* 30, 286–287.
- Hoffmann, K.-H., Condon, D.J., Bowring, S.A., Crowley, J.L., 2004. U–Pb zircon date from the Neoproterozoic Ghaub Formation, Namibia: Constraints on Marinoan glaciation. *Geology* 32, 817–820.
- Hoffman, P.F., Halverson, G.P., Domack, E.W., Husson, J.M., Higgins, J.A., Schrag, D.P., 2007. Are basal Ediacaran (635 Ma) post-glacial “cap dolostones” diachronous? *Earth Planet. Sci. Lett.* 258, 114–131.
- Hoffman, P.F., Macdonald, F.A., Halverson, G.P., 2011. Chemical sediments associated with Neoproterozoic glaciation: iron formation, cap carbonate, barite and phosphorite. In: Arnaud, E., Halverson, G.P., Shields-Zhou, G. (Eds.), *The Geological Record of Neoproterozoic Glaciations*. Geological Society, London, Mem. 36, pp. 67–80.
- Hoffman, P.F., Bellefroid, E., Hodgkin, E.B., Johnson, B.W., Kunzmann, M., Sansjofre, P., Strauss, J.V., Schrag, D.P., 2014. A cryogenian–early Ediacaran carbonate shelf break dominated by glacial paleotopography, Fransfontein Ridge, Kunene Region, Namibia. *Geol. Soc. Am., Ann. Mtg. Vancouver* 2014, 130–132. Session T196, Poster Pap. <https://gsa.confex.com/gsa/2014AM/webprogram/Paper246872.html>.
- Hoffman, P.F., Bellefroid, E.J., Crockford, P.W., de Moor, A., Halverson, G.P., Hodgkin, E.B., Hodgskiss, M.S.W., Holtzman, B.K., Jasechko, G.R., Johnson, B.W., Lamothe, K.G., 2016a. A misfit Cryogenian diamictite in the Vredefontein domes, Northern Damara Zone, Namibia: Chuos (Sturtian) or Ghaub (Marinoan) formation? Moraine or paleovalley? *Communs. Geol. Surv. Namibia* 17, 1–16.
- Hoffman, P.F., Bellefroid, E., Johnson, B.W., Hodgskiss, M.W., Schrag, D.P., 2016b. Early extensional detachments in a contractional orogen: coherent, map-scale, submarine slides (mass transport complexes) on the outer slope of an Ediacaran collisional foredeep, eastern Kaoko belt, Namibia. *Can. J. Earth Sci.* 53, 1177–1189.
- Hoffman, P.F., Abbot, D.S., Ashkenazy, Y., Benn, D.I., Brocks, J.J., Cohen, P.A., Cox, G.M., Creveling, J.R., Donnadieu, Y., Erwin, D.H., Fairchild, I.J., Ferreira, D., Goodman, J.C., Halverson, G.P., Jansen, M.F., Le Hir, G., Love, G.D., Macdonald, F.A., Maloof, A.C., Partin, C.A., Ramstein, G., Rose, B.E.J., Rose, C.V., Sadler, P.M., Tziperman, E., Voigt, A., Warren, S.G., 2017a. Snowball Earth climate dynamics and Cryogenian geology–geobiology. *Sci. Adv.* 3 (e1600983), 1–43.
- Hoffman, P.F., Lamothe, K.G., Lo Bianco, S.J.C., Hodgskiss, M.S.W., Bellefroid, E.J., Johnson, B.W., Hodgkin, E.B., Halverson, G.P., 2017b. Sedimentary depocenters on Snowball Earth: Case studies from the Sturtian Chuos Formation in northern Namibia. *Geosphere* 13 (i. 3), 811–837.
- Hoffman, P.F., Lamothe, K.G., Greenman, J.W., 2018. Report: Stratigraphic investigations of the Neoproterozoic Otavi/Swakop Group in the southern Kunene Region. *Communs. Geol. Surv. Namibia* 20, 100–113.
- Hoffmann, K.-H., 1989. New aspects of lithostratigraphic subdivision and correlation of late Proterozoic to early Cambrian rocks of the southern Damara Belt and their correlation with the central and northern Damara Belt and the Gariep Belt. *Communs. Geol. Surv. Namibia* 5, 59–67.
- Hoffmann, K.-H., 1991. Stratigraphic analysis of eustatic and tectonic effects on subsidence and deposition during convergent margin sedimentation in the Damara Belt and adjacent cratonic foreland basins. *Terra Nova*, Abs. Suppl. 3, 15–16.
- Hoffmann, K.-H., 1994. New constraints on the timing of continental breakup and collision in the Damara Belt. Abstracts, Proterozoic Crustal and Metallogenic Evolution, Geological Survey of Namibia, Windhoek, p. 30.
- Hoffmann, K.-H., Prave, A.R., 1996. A preliminary note on a revised subdivision and regional correlation of the Otavi Group based on glaciogenic diamictites and associated cap dolomites. *Communs. Geol. Surv. Namibia* 11, 77–82.
- Hofmann, H.J., 1969. Attributes of stromatolites. *Geological Survey of Canada, Ottawa, Pap.* 69–139.
- Holland, H.D., 1978. *The Chemistry of the Atmosphere and Oceans*. Wiley-Interscience, New York, 351 p.
- Holland, H.D., 1984. *The Chemical Evolution of the Atmosphere and Oceans*. Princeton University Press, Princeton, NJ, 582 p.
- Hood, A.V.S., Wallace, M.W., 2012. Synsedimentary diagenesis in a Cryogenian reef complex: Ubiquitous marine dolomite precipitation. *Sediment. Geol.* 255–256, 56–71.
- Hood, A.V.S., Wallace, M.W., 2015. Extreme ocean anoxia during the Late Cryogenian recorded in reef carbonates of Southern Australia. *Precambrian Res.* 261, 96–111.
- Hood, A.V.S., Wallace, M.W., Drysdale, R.N., 2011. Neoproterozoic aragonite–dolomite seas? Widespread marine dolomite precipitation in Cryogenian reef complexes. *Geology* 39, 871–874.
- Hood, A.V.S., Wallace, M.W., Reed, C.P., Hoffmann, K.-H., Freyer, E.E., 2015. Enigmatic carbonates of the Ombombo Subgroup, Otavi Fold Belt, Namibia: A prelude to extreme Cryogenian anoxia? *Sediment. Geol.* 324, 12–31.
- Hood, A.V.S., Planavsky, N.J., Wallace, M.W., Xiangli, Wang, Bellefroid, E.J., Gueguen, B., Cole, D.B., 2016. Integrated geochemical–petrographic insights from component-selective $\delta^{238}\text{U}$ of Cryogenian marine carbonates. *Geology* 44, 935–938.
- Hoshino, Y., Posibayeva, A., Meredith, W., Snape, C., Posibayev, V., Versteegh, G.J.M., Kuznetsov, N., Leider, A., van Maldegem, L., Neumann, M., Naehler, S., Moczydlowska, M., Brocks, J.J., Jarrett, A.J.M., Tang, Q., Xiao, S., McKirdy, D., Das, S.K., Alvaro, J.J., Sansjofre, P., Hallmann, C., 2017. Cryogenian evolution of stigmatoroid biosynthesis. *Sci. Adv.* 3 (e1700887), 1–7.
- Howell, D., Stachel, T., Stern, R.A., Pearson, D.G., Nestola, F., Hardman, M.F., Harris, J.W., Jaques, A.L., Shirey, S.B., Cartigny, P., Smit, K.V., Aulbach, S., Brenker, F.E., Jacob, D.E., Thomassot, E., Walter, M.J., Navon, O., 2020. Deep carbon through time: Earth's diamond record and its implications for carbon cycling and fluid speciation in the mantle. *Geochim. Cosmochim. Acta* 275, 99–120.
- Hueck, B., Oyhantçabal, P., Philipp, R.P., Basei, M.A.S., Siegesmund, S., 2018. In: Siegesmund, S., Basei, M.A.S., Oyhantçabal, P., Oriolo, S. (Eds.), *The Dom Feliciano Belt in southern Brazil and Uruguay. Geology of Southwest Gondwana*, Springer Nature, pp. 267–302.
- Hurtgen, M.T., Arthur, M.A., Suits, N.S., Kaufman, A.J., 2002. The sulfur isotopic composition of Neoproterozoic seawater sulfate: implications for a snowball Earth? *Earth Planet. Sci. Lett.* 203, 413–429.
- Hurtgen, M.T., Arthur, M.A., Halverson, G.P., 2005. Neoproterozoic sulfur isotopes, the evolution of microbial sulfur species, and the burial efficiency of sulfide as sedimentary pyrite. *Geology* 33, 41–44.
- Hurtgen, M.T., Halverson, G.P., Arthur, M.A., Hoffman, P.F., 2006. Sulfur cycling in the aftermath of a 635-Ma snowball glaciation: Evidence for a syn-glacial sulfidic deep ocean. *Earth Planet. Sci. Lett.* 245, 551–570.
- Imbrie, J.Z., Imbrie-Moore, A., Lisicki, L.E., 2011. A phase-space model for Pleistocene ice volume. *Earth Planet. Sci. Lett.* 307, 94–102.
- Isson, T.T., Planavsky, N.J., 2018. Reverse weathering as a long-term stabilizer of marine pH and planetary climate. *Nature* 560, 471–475.
- Jackson, M.P.A., Warin, O.N., Woad, G.M., Hudec, M.R., 2003. Neoproterozoic allochthonous salt tectonics during Lufilian orogeny in the Katangan Copperbelt, central Africa. *Geol. Soc. Am. Bull.* 115, 314–330.
- Jacob, R.E., Moore, J.M., Armstrong, R.A., 2000. Zircon and titanite age determinations from igneous rocks in the Karibib District, Namibia: implications for Navachab vein-style gold mineralization. *Communs. Geol. Surv. Namibia* 12, 157–166.
- Jacobsen, S.B., Kaufman, A.J., 1999. The Sr, C and O isotopic evolution of Neoproterozoic seawater. *Chem. Geol.* 161, 37–57.
- James, N.P., Narbonne, G.M., Kyser, T.K., 2001. Late Neoproterozoic cap carbonates: Mackenzie Mountains, northwestern Canada: precipitation and global glacial meltdown. *Can. J. Earth Sci.* 38, 1229–1262.
- Jansen, M.F., 2016. The turbulent circulation of a Snowball Earth Ocean. *J. Phys. Oceanogr.* 46, 1917–1933.
- Jansen, D.J., Rickli, J., Quay, P.D., White, A.E., Nasemann, P., Jaccard, S.L., 2020. Biological control of chromium redox and stable isotope composition in the surface ocean. *Glob. Biogeochem. Cycles* 34 e2019GB006397.
- Jerolmack, D.J., Mohrig, D., 2005. Formation of Precambrian sediment ripples. Arising from: P. A. Allen & P. F. Hoffman, *Nature* 433, (2005).123–127 *Nature* 436, E1, doi: <https://doi.org/10.1038/nature04015>.
- Jerram, D., Mountney, N., Holzförster, F., Stollhofen, H., 1999. Internal stratigraphic relationships in the Etendeka Group in the Huab Basin, NW Namibia: understanding the onset of flood volcanism. *J. Geodyn.* 28, 393–418.
- Jerram, D.A., Mountney, N., Howell, J., Stollhofen, H., 2000a. The Fossilized Desert: recent developments in our understanding of the Lower Cretaceous deposits in the Huab Basin, NW Namibia. *Communs. Geol. Surv. Namibia* 12, 303–313.
- Jerram, D.A., Mountney, N.P., Howell, J.A., Long, D., Stollhofen, H., 2000b. Death of a sand sea: an active aeolian erg systematically buried by the Etendeka flood basalts of NW Namibia. *J. Geol. Soc. Lond.* 157, 513–517.
- Jiang, G.Q., Shi, X., Zhang, S., Wang, Y., Xiao, S.H., 2011. Stratigraphy and paleogeography of the Ediacaran Doushantuo Formation (ca. 635–551 Ma) in South China. *Gondwana Res.* 10, 831–849.
- Jiang, L., Planavsky, N., Zhao, M.Y., Liu, W., Wang, X.L., 2019. Authigenic origin for a massive negative carbon isotope excursion. *Geology* 47, 115–118.
- John, S.G., Kunzmann, M., Townsend, E.J., Rosenberg, A.D., 2017. Zinc and cadmium stable isotopes in the geologic record: a case study from the post-snowball Earth Nuccaleena cap dolostone. *Palaeogeogr. Palaeoclimatol. Palaeoecol.* 466, 202–208.
- Johnson, S.D., Poujol, M., Kisters, A.F.M., 2006. Constraining the timing and migration of collisional tectonics in the Damara Belt, Namibia: U–Pb zircon ages for the syntectonic Salem-type Stinkbank granite. *S. Afr. J. Geol.* 109, 611–624.

- Johnson, B.W., Poulton, S.W., Goldblatt, C., 2017. Marine oxygen production and open water supported an active nitrogen cycle during the Marinoan Snowball Earth. *Nat. Geosci.* 8 (1316), 1–10.
- Johnston, D.T., Macdonald, F.A., Gill, B.C., Hoffman, P.F., Schrag, D.P., 2012. Uncovering the Neoproterozoic carbon cycle. *Nature* 483, 320–323.
- Johnston, D.T., Poulton, S.W., Tosca, N.J., O'Brien, T., Halverson, G.P., Schrag, D.P., Macdonald, F.A., 2013. Searching for an oxygenation event in the fossiliferous Ediacaran of northwestern Canada. *Chem. Geol.* 362, 273–286.
- Jones, G.D., Whitaker, F.F., Smart, P.L., Sanford, W.E., 2002. Fate of reflux brines in carbonate platforms. *Geology* 30, 371–374.
- Jung, S., Brandt, S., Nebel, O., Hellebrand, E., Seth, B., Jung, C., 2014a. The P-T-t paths of high-grade gneisses, Kaoko Belt, Namibia: Constraints from mineral data, U-Pb allanite and monazite and Sm-Nd/Lu-Hf garnet ages and garnet ion probe data. *Gondwana Res.* 25, 775–796.
- Jung, G., Prange, M., Schulz, M., 2014b. Uplift of Africa as a potential cause for Neogene intensification of the Benguela upwelling system. *Nat. Geosci.* 7, 741–747.
- Kadima, E., Delvaux, D., Sebaggenzi, S.N., Tack, L., Kabeya, S.M., 2011. Structure and geological history of the Congo Basin: an integrated interpretation of gravity, magnetic and reflection seismic data. *Basin Res.* 23, 499–527.
- Kalkowski, E., 1908. Oolith und Stromatolith im norddeutschen Buntsandstein. *Z. Deut. Geol. Ges.* 60, 68–125.
- Kamguia Kamani, M.S., Wang, W., Tchouankoue, J.-P., Huang, S.F., Yomeun, B., Xue, E. K., Lu, G.M., 2021. Neoproterozoic syn-collision magmatism in the Nkondjock region at the northern border of Congo craton in Cameroon: Geodynamic implications for the Central African orogenic belt. *Precambrian Res.* 353, 106015.
- Kamona, A.F., Günzel, A., 2007. Stratigraphy and base metal mineralization in the Otavi Mountain Land, Northern Namibia—a review and regional interpretation. *Gondwana Res.* 11, 396–413.
- Karig, D.E., 1974. Evolution of arc systems in the western Pacific. *Annu. Rev. Earth Planet. Sci.* 2, 51–75.
- Kasch, K.W., 1983a. Folding and thrust tectonics in the south-eastern portion of the Damara orogen around Ommita, Namibia. In: Miller, R.M.C.G. (Ed.), *Evolution of the Damara Orogen*. Geological Society of South Africa, Johannesburg, Sp. Pub. 11, pp. 175–184.
- Kasch, K.W., 1983b. Continental collision, suture progradation and thermal relaxation: a plate tectonic model for the Damara Orogen. In: Miller, R.M.C.G. (Ed.), *Evolution of the Damara Orogen*. Geological Society of South Africa, Johannesburg, Sp. Pub. 11, pp. 423–429.
- Kasemann, S.A., Hawkesworth, C.J., Prave, A.R., Fallick, A.E., Pearson, P.N., 2005. Boron and calcium isotope composition in Neoproterozoic carbonate rocks from Namibia: evidence for extreme environmental change. *Earth Planet. Sci. Lett.* 231, 73–86.
- Kasemann, S.A., Prave, A.R., Fallick, A.E., Hawkesworth, C.J., Hoffmann, K.-H., 2010. Neoproterozoic ice ages, boron isotopes, and ocean acidification: Implications for a snowball Earth. *Geology* 38, 775–778.
- Kasemann, S.A., Pogge von Strandmann, P.A.E., Prave, A.R., Fallick, A.E., Elliott, T., Hoffmann, K.-H., 2014. Continental weathering following a Cryogenian glaciation: evidence from calcium and magnesium isotopes. *Earth Planet. Sci. Lett.* 396, 66–77.
- Katsuta, N., Tojo, B., Takano, M., Yoshioka, H., Kawakami, S., Ohno, T., Kumazawa, M., 2007. Non-destructive method to detect the cycle of lamination in sedimentary rocks: rhythmic sequence in Neoproterozoic cap carbonates. In: Vickers-Rich, P., Komarower, P. (Eds.), *The Rise and Fall of the Ediacaran Biota*. Geological Society, London, Sp. Publ. 286, pp. 27–34.
- Kaufman, A.J., Hayes, J.M., Knoll, A.H., Germs, G.J.B., 1991. Isotopic compositions of carbonates and organic carbon from upper Proterozoic successions in Namibia: stratigraphic variation and the effects of diagenesis and metamorphism. *Precambrian Res.* 49, 301–327.
- Kaufman, A.J., Knoll, A.H., Narbonne, G.M., 1997. Isotopes, ice ages, and terminal Proterozoic earth history. *Proc. Natl. Acad. Sci. U. S. A.* 94, 6600–6605.
- Keen, C.E., Hyndman, R.D., 1979. Geophysical review of the continental margins of eastern and western Canada. *Can. J. Earth Sci.* 16, 712–747.
- Keller, C.B., Husson, J.M., Mitchell, R.N., Bottke, W.F., Geron, T.M., Boehnke, P., Bell, E.A., Swanson-Hysell, N.L., Peters, S.E., 2019. Neoproterozoic glacial origin of the Great Unconformity. *Proc. Natl. Acad. Sci. U. S. A.* 116, 1136–1145.
- Kendall, C., Coplen, T.B., 2001. Distribution of oxygen-18 and deuterium in river waters across the United States. *Hydrocl. Process.* 15, 1363–1393.
- Kendall, G.S.C., Warren, J., 1987. A review of the origin and setting of tepees and their associated fabrics. *Sedimentology* 34, 1007–1027.
- Kendall, B., Creaser, R.A., Selby, D., 2006. Re-Os geochronology of postglacial black shales in Australia: Constraints on the timing of “Sturtian” glaciation. *Geology* 34, 729–732.
- Kennedy, M.J., 1996. Stratigraphy, sedimentology, and isotopic geochemistry of Australian Neoproterozoic postglacial cap dolostones: deglaciation, $\delta^{13}\text{C}$ excursions, and carbonate precipitation. *J. Sediment. Res.* 66, 1050–1064.
- Kennedy, M.J., Christie-Blick, N., 2011. Condensation origin for Neoproterozoic cap carbonates during deglaciation. *Geology* 39, 319–322.
- Kennedy, M.J., Runnegar, B., Prave, A.R., Hoffmann, K.-H., Arthur, M.A., 1998. Two or four Neoproterozoic glaciations? *Geology* 26, 1059–1063.
- Kennedy, M.J., Christie-Blick, N., Prave, A.R., 2001a. Carbon isotopic composition of Neoproterozoic glacial carbonates as a test of paleoceanographic models for snowball Earth phenomena. *Geology* 29, 1135–1138.
- Kennedy, M.J., Christie-Blick, N., Sohl, L.E., 2001b. Are Proterozoic cap carbonates and isotopic excursions a record of gas hydrate destabilization following Earth's coldest intervals? *Geology* 29, 443–446.
- Khoza, T.D., Jones, A.G., Muller, M.R., Evans, R.L., Miensopust, M.P., Webb, S.J., 2013. Lithospheric structure of an Archean craton and adjacent mobile belt revealed from 2-D and 3-D inversion of magnetotelluric data: Example from southern Congo craton in northern Namibia. *J. Geophys. Res. Solid Earth* 118. <https://doi.org/10.1002/jgrb.50258>.
- Killick, A.M., Lombard, H., Marsh, A.M., Parsons, C.F., Proctor, W.D.E., 1980. *Geology, Kaokoland/Owambo Block. CDM Mineral Surveys*, Windhoek, map scale 1, p. 250,000.
- King, L.C., 1962. The Morphology of the Earth. Oliver and Boyd, Edinburgh, 699 p.
- King, C.H.M., 1994. Carbonates and mineral deposits of the Otavi Mountainland. *Geological Survey of Namibia*, Windhoek. In: *Intl. Conf. Proterozoic Crustal & Metallagenic Evol., Excursion* 4, 40 p.
- King, L.H., Rokoengen, K., Fader, G.B.J., Gunleksrud, T., 1991. Till-tongue stratigraphy. *Geol. Soc. Am. Bull.* 103, 637–659.
- Kirschvink, J.L., 1992. Late Proterozoic low-latitude glaciation: the snowball Earth. In: Schopf, J.W., Klein, C. (Eds.), *The Proterozoic Biosphere*. Cambridge University Press, Cambridge, UK, pp. 51–52.
- Klein, C., Beukes, N.J., 1993. Sedimentology and geochemistry of the glaciogenic Late Proterozoic Rapitan iron-formation in Canada. *Econ. Geol.* 88, 542–565.
- Klochko, K., Kaufman, A.J., Yao, W.S., Byrne, R.H., Tossell, J.A., 2006. Experimental measurement of boron isotope fractionation in seawater. *Earth Planet. Sci. Lett.* 248, 276–285.
- Knauth, L.P., Kennedy, M.J., 2009. The late Precambrian greening of the Earth. *Nature* 460, 728–732.
- Knoll, A.H., Walter, M.R., Narbonne, G.M., Christie-Blick, N., 2006. The Ediacaran Period: a new addition to the geologic time scale. *Lethaia* 39, 13–30.
- Kohout, F.A., 1967. Ground-water flow and the geothermal regime of the Floridian Plateau. *Gulf Coast Assoc. Geol. Soc. Trans.* 17, 339–354.
- Kominz, M.A., Bond, G.C., 1990. A new method of testing periodicity in cyclic sediments: application to the Newark Supergroup. *Earth Planet. Sci. Lett.* 98, 233–244.
- Konopásek, J., Kröner, S., Kitt, S.L., Passchier, C.W., Kröner, A., 2005. Oblique collision and evolution of large-scale transcurrent shear zones in the Kaoko belt, NW Namibia. *Precambrian Res.* 136, 139–157.
- Konopásek, J., Košler, J., Tajčmanová, L., Ulrich, S., Kitt, S., 2008. Neoproterozoic igneous complex emplaced along major tectonic boundary in the Kaoko Belt (NW Namibia): ion probe and LA-ICP-MS dating of magmatic and metamorphic zircons. *J. Geol. Soc. Lond.* 165, 153–165.
- Konopásek, J., Košler, J., Sláma, J., Janousek, V., 2014. Timing and sources of pre-collisional Neoproterozoic sedimentation along the SW margin of the Congo Craton (Kaoko Belt, NW Namibia). *Gondwana Res.* 26, 386–401.
- Konopásek, J., Sláma, J., Košler, J., 2016. Linking the basement geology along the Africa-South America coasts in the South Atlantic. *Precambrian Res.* 280, 221–230.
- Konopásek, J., Hoffmann, K.-H., Sláma, J., Košler, J., 2017. The onset of flysch sedimentation in the Kaoko Belt (NW Namibia) – implications for the pre-collisional evolution of the Kaoko-Dom Feliciano-Gariep orogen. *Precambrian Res.* 298, 220–234.
- Konopásek, J., Janoušek, V., Oyhantçabal, P., Sláma, J., Ulrich, S., 2018. Did the circum-Rodinia subduction trigger the Neoproterozoic rifting along the Congo-Kalahari Craton margin? *Int. J. Earth Sci.* 107, 1859–1894.
- Konopásek, J., Cavalcante, C., Fossen, H., Janoušek, V., 2020. Adamastor – an ocean that never existed? *Earth Sci. Rev.* <https://doi.org/10.1016/j.earscirev.2020.103201>.
- Köppen, W., Wegener, A., 2015. The climates of the geological past. In: Thiede, J., Loche, K., Dummermuth, A. (Eds.), *The Climates of the Geological Past/Die Klimate der geologischen Vorzeit* (Facsimile German and English translation by B. Oelkers of the original 1924 edition). Borntraeger, Stuttgart, pp. 343–657.
- Kouchinsky, A., Bengtson, S., Runnegar, B., Skovsted, C., Steiner, M., Vendrasco, M., 2012. Chronology of early Cambrian biomineralization. *Geol. Mag.* 149, 221–251.
- Krissansen-Totton, J., Buick, R., Catling, D.C., 2015. A statistical analysis of the carbon isotope record from the Archean to Phanerozoic and implications for the rise of oxygen. *Am. J. Sci.* 315, 275–316.
- Kröner, A., Correia, H., 1973. Further evidence for glaciogenic origin of Late Precambrian mixites in Angola. *Nature* 246, 115–117.
- Kröner, A., Correia, H., 1980. Continuation of the Pan-African Damara belt into Angola: a proposed correlation of the Chela Group in southern Angola with the Nosib Group in northern Namibia/SWA. *Trans. Geol. Soc. Afr.* 83, 5–16.
- Kröner, A., Rankama, K., 1972. Late Precambrian glaciogenic sedimentary rocks in southern Africa: A compilation with definitions and corrections. *University of Cape Town. Precam. Res. Unit Bull.* 11, 1–37.
- Kröner, A., Rojas-Agramonte, Y., 2017. Mesoproterozoic (Grenville-age) granitoids and supracrustal rocks in Kaokoland, northwestern Namibia. *Precambrian Res.* 298, 572–592.
- Kröner, A., Retief, E.A., Compston, W., Jacob, R.E., Burger, A.J., 1991. Single-grain and conventional zircon dating of remobilized basement gneisses in the central Damara belt of Namibia. *S. Afr. J. Geol.* 94, 379–387.
- Kröner, A., Rojas-Agramonte, Y., Hegner, E., Hoffmann, K.-H., Wingate, M.T.D., 2010. SHRIMP zircon dating and Nd isotopic systematics of Palaeoproterozoic migmatitic orthogneisses in the Epupa Complex of northwestern Namibia. *Precambrian Res.* 183, 50–69.
- Kröner, A., Rojas-Agramonte, Y., Wong, J., Wilde, S.A., 2015. Zircon reconnaissance dating of Proterozoic gneisses along the Kunene River of northwestern Namibia. *Tectonophysics* 662, 125–139.
- Kroopnick, P.M., 1985. The distribution of ^{13}C of ΣCO_2 in the world oceans. *Deep-Sea Res.* 32, 57–84.
- Krüger, L., 1969. Stromatolites and oncrites in the Otavi Series, South West Africa. *J. Sediment. Petrol.* 39, 1046–1056.
- Kukla, P.A., 1992. Tectonics and sedimentation of a Late Proterozoic Damaran convergent continental margin, Khomas Hochland, central Namibia. *Geological Survey of Namibia*, Windhoek, Mem. 12, 95 p.

- Kukla, P.A., Stanistreet, I.G., 1991. Record of the Damaran Khomas Hochland accretionary prism in central Namibia: Refutation of an "ensialic" origin of a Late Proterozoic orogenic belt. *Geology* 19, 473–476.
- Kump, L.R., Arthur, M.A., 1999. Interpreting carbon-isotopic excursions: carbonates and organic matter. *Chem. Geol.* 161, 181–198.
- Kump, L.R., Seyfried Jr., W.E., 2005. Hydrothermal Fe fluxes during the Precambrian: effect of low oceanic sulfate concentrations and low hydrostatic pressure on the composition of black smokers. *Earth Planet. Sci. Lett.* 235, 654–662.
- Kunzmann, M., Halverson, G.P., Sossi, P.A., Raub, T.D., Payne, J.L., Kirby, J., 2013. Zn isotope evidence for immediate resumption of primary productivity after snowball Earth. *Geology* 41, 27–30.
- Kunzmann, M., Thi-Hao, Bui, Croxford, P.W., Halverson, G.P., Scott, C., Lyons, T.W., Wing, B.A., 2017. Bacterial sulfur disproportionation constrains timing of Neoproterozoic oxygenation. *Geology* 45, 207–210.
- Lahr, D.J.G., Kosakyan, A., Lara, E., Mitchell, E.A.D., Morais, L., Porfirio-Sousa, A.L., Ribeiro, G., Tice, A.K., Pánek, T., Kang, S., 2019. Phylogenomics and morphological reconstruction of Arcellinida testate amoebae highlight diversity of microbial eukaryotes in the Neoproterozoic. *Curr. Biol.* 29, 991–1001.
- Lamb, M.P., Fischer, W.W., Raub, T.D., Perron, J.T., Myrow, P.M., 2012. Origin of giant wave ripples in snowball Earth cap carbonate. *Geology* 40, 827–830.
- Lamothe, K.G., Hoffman, P.F., Greenman, J.W., Halverson, G.P., 2019. Stratigraphy and isotope geochemistry of the pre-Sturtian Ubag Subgroup, Otavi/Swakop Group, northwestern Namibia. *Precambrian Res.* 332, 105387.
- Lan, Z.W., Li, X.H., Zhu, M.Y., Chen, Z.Q., Zhang, Q.R., Li, Q.L., Lu, D.B., Liu, Y., Tang, G.Q., 2014. A rapid and synchronous initiation of the wide spread Cryogenian glaciations. *Precambrian Res.* 255, 401–411.
- Lan, Z.W., Huyskens, M.H., Lu, K., Li, X.H., Zhang, G.Y., Lu, D.B., Yin, Q.Z., 2020. Toward refining the onset age of Sturtian glaciation in South China. *Precambrian Res.* 338 (105555), 1–8.
- Lasaga, A., 1998. Kinetic Theory in the Earth Sciences. Princeton University Press, NJ.
- Lau, K.V., Macdonald, F.A., Maher, K., Payne, J.L., 2017. Uranium isotope evidence for temporary ocean oxygenation in the aftermath of the Sturtian Snowball Earth. *Earth Planet. Sci. Lett.* 458, 282–292.
- Lazar, B., Erez, J., 1990. Extreme ^{13}C depletions in seawater-derived brines and their implications for the past geochemical carbon cycle. *Geology* 18, 1191–1194.
- Lazar, B., Erez, J., 1992. Carbon geochemistry of marine-derived brines: I. ^{13}C depletions due to intense photosynthesis. *Geochim. Cosmochim. Acta* 56, 335–345.
- Le Ber, E., Le Heron, D.P., Winterleitner, G., Bosence, D., Vining, B.A., 2013. Microbialite recovery in the aftermath of the Sturtian glaciation: Insights from the Rasthof Formation, Namibia. *Sed. Geol.* 294, 1–12.
- Le Heron, D.P., Busfield, M.E., Kamona, F., 2013a. An interglacial on snowball Earth? Dynamic ice behaviour revealed in the Chuos Formation, Namibia. *Sedimentology* 60, 411–427.
- Le Heron, D.P., Busfield, M.E., LeBer, E., Kamona, A.F., 2013b. Neoproterozoic ironstones in northern Namibia: Biogenic precipitation and Cryogenian glaciation. *Palaeogeogr. Palaeoclimatol. Palaeoecol.* 369, 48–57.
- Le Heron, D.P., Busfield, M.E., Kettler, C., 2020. Ice rafted dropstones in "postglacial" Cryogenian cap carbonates. *Geology*. <https://doi.org/10.1130/G48208.1>.
- Le Hir, G., Ramstein, G., Donnadieu, Y., Goddériss, Y., 2008. Scenario for the evolution of atmospheric pCO_2 during a snowball Earth. *Geology* 36, 47–50.
- Le Hir, G., Donnadieu, Y., Goddériss, Y., Pierrehumbert, R.T., Halverson, G.P., Macouin, M., Nédélic, A., Ramstein, G., 2009. The snowball Earth aftermath: Exploring the limits of continental weathering processes. *Earth Planet. Sci. Lett.* 277, 453–463.
- Le Roex, H.D., 1941. A tillite in the Otavi Mountains, S.W.A. *Trans. Geol. Soc. S. Afr.* 44, 207–218.
- Lechte, M., Wallace, M., 2016. Sub-ice shelf ironstone deposition during the Neoproterozoic Sturtian glaciation. *Geology* 44, 891–894.
- Lechte, M.A., Wallace, M.W., Hoffmann, K.-H., 2018. Glacio-marine iron formation deposition in a c. 700 Ma glaciated margin: insights from the Chuos Formation, Namibia. In: Le Heron, D.P., Hogan, K.A., Phillips, E.R., Huuse, M., Busfield, M.E., Graham, A.G.C. (Eds.), *Glaciated Margins: The Sedimentary and Geophysical Archive*. Geological Society, London, Sp. Publ. 475, pp. 9–34.
- Lechte, M.A., Wallace, M.W., van Smeerdijk Hood, A., Li, W.Q., Jiang, G.Q., Halverson, G.P., Asael, D., McColl, S.L., Planavsky, N.J., 2019. Subglacial meltwater supported aerobic marine habitats during Snowball Earth. *Proc. Natl. Acad. Sci. U. S. A.* 116 (25), 478–483.
- Ledwell, J.R., Montgomery, E.T., Polzin, K.L., St Laurent, L.C., Schmitt, R.W., Toole, J.M., 2000. Evidence for enhanced mixing over rough topography in the abyssal ocean. *Nature* 403, 179–182.
- Lehmann, J., Saalmann, K., Naydenov, K.V., Milani, L., Belyanin, G.A., Zwingmann, H., Charlesworth, G., Kinnaird, J.A., 2015. Structural and geochronological constraints on the Pan-African tectonic evolution of the northern Damara Belt, Namibia. *Tectonics* 34. <https://doi.org/10.1002/2015TC003899>.
- Lehmann, J., Bybee, G.M., Hayes, B., Owen-Smith, T.M., Belyanin, G., 2020. Emplacement of the giant Kunene AMCG complex into a contractile ductile shear zone and implications for the Mesoproterozoic tectonic evolution of SW Angola. *Int. J. Earth Sci.* 109, 1463–1485.
- Lehtonen, M.I., Manninen, T.E.T., Schreiber, U.M., 1996. Report: lithostratigraphy of the area between the Swakop, Khan and lower Omaruru Rivers, Namib Desert. *Communs Geol. Surv. Namibia* 11, 65–75.
- Lemarchand, D., Gaillardet, J., Lewin, É., Allègre, C.J., 2000. The influence of rivers on marine boron isotopes and implications for reconstructing past ocean pH. *Nature* 408, 951–954.
- Leslie, D., Lyons, W.B., Warner, N., Vengosh, A., Olesik, J., Welch, K., Deuerling, K., 2014. Boron isotopic geochemistry of the McMurdo Dry Valley lakes, Antarctica. *Chem. Geol.* 386, 152–164.
- Lewis, A.R., Marchant, D.R., Kowalewski, D.E., Baldwin, S.L., Webb, L.E., 2006. The age and origin of the Labyrinth, western Dry Valleys, Antarctica: Evidence for extensive middle Miocene subglacial floods and freshwater discharges to the South Ocean. *Geology* 34, 513–516.
- Li, D.W., Pierrehumbert, R.T., 2011. Sea glacier flow and dust transport on Snowball Earth. *Geophys. Res. Lett.* 38, L17501. <https://doi.org/10.1029/2011GL048991>.
- Li, Z.X., Bogdanova, S.V., Collins, A.S., Davidson, A., De Waele, B., Ernst, R.E., Fitzsimons, I.C.W., Fuck, R.A., Gladkochub, D.P., Jacobs, J., Karlstrom, K.E., Lu, S., Natapov, L.M., Pease, V., Pisarevsky, S.A., Thrane, K., Vernikovsky, V., 2008. Assembly, configuration, and break-up history of Rodinia: a synthesis. *Precambrian Res.* 160, 179–210.
- Li, Z.X., Evans, D.A.D., Halverson, G.P., 2013. Neoproterozoic glaciations in a revised global palaeogeography from the breakup of Rodinia to the assembly of Gondwanaland. *Sediment. Geol.* 294, 219–232.
- Liljestrand, F.L., Laakso, T.A., Macdonald, F.A., Schrag, D.P., Johnston, D.T., 2020. Isotopically anomalous organic carbon in the aftermath of the Marinoan snowball Earth. *Geobiology* 18, 476–485.
- Liu, Y.G., Peltier, W.R., 2013. Sea level variations during snowball Earth formation: 1. A preliminary analysis. *J. Geophys. Res. Solid Earth* 118, 4410–4424.
- Liu, C., Wang, Z.R., Raub, T.D., Macdonald, F.A., 2014. Neoproterozoic cap-dolostone deposition in a stratified glacial meltwater plume. *Earth Planet. Sci. Lett.* 404, 22–32.
- Liu, P.J., Li, X.H., Chen, S.M., Lan, Z.W., Yang, B., Shang, X.D., Yin, C.Y., 2015. New SIMS U–Pb zircon age and its constraint on the beginning of the Nantuo glaciation. *Sci. Bull.* 60, 958–963.
- Liu, Y.G., Yang, J., Bao, H.M., Shen, B., Hu, Y.Y., 2020. Large equatorial seasonal cycle during Marinoan snowball Earth. *Sci. Adv.* 6, 1–10 eaay2471.
- Logan, B.W., Hoffman, P.F., Gebelein, C.D., 1974. Algal mats, cryptalgal fabrics and structures, Hamelin Pool, Western Australia. In: Logan, B.W. (Ed.), *Evolution and Diagenesis of Quaternary Sequences, Shark Bay, Western Australia*. AAPG, Tulsa, OK, USA, Am. Assoc. Petrol. Geol. Mem. 22, pp. 140–194.
- Lokier, S.W., Andrade, L.L., Court, W.M., Dutton, K.E., Head, I.M., van der Land, C., Paul, A., Sherry, A., 2018. A new model for the formation of microbial polygons in a coastal sabkha setting. *Depos. Rec.* 3 (2), 201–208.
- Lombaard, A.F., Günzel, A., Innes, J., Krüger, T.L., 1986. The Tsumeb lead-copper-zinc-silver deposit, South West Africa/Namibia. In: Anhaeusser, C.R., Maske, S. (Eds.), *Mineral Deposits of Southern Africa, Vol. 2. Geological society of south africa, johannesburg*, pp. 1761–1787.
- Luo, C., Pan, B., Reitner, J., 2017. Chambered structures from the Ediacaran Dengying Formation, Yunnan, China: comparison with the Cryogenian analogues and their microbial interpretation. *Geol. Mag.* 154, 1269–1284.
- Lyell, C., 1840. The Boulder Formation, or Drift, and associated freshwater deposits composing the mud cliffs of eastern Norfolk. *Proc. Geol. Soc. Lond.* 3, 171–179.
- Lymer, G., Cresswell, D.J.F., Reston, T.J., Bull, J.M., Sawyer, D.S., Morgan, J.K., Stevenson, C., Causer, A., Minshull, T.A., 2019. 3D development of detachment faulting during continental breakup. *Earth Planet. Sci. Lett.* 515, 90–99.
- Lynch-Stieglitz, J., Stocker, T.F., Broecker, W.S., Fairbanks, R.G., 1995. The influence of air-sea gas exchange on the isotopic composition of oceanic carbon: observations and modeling. *Glob. Biogeochem. Cycles* 9, 653–665.
- Mabbatt, J.A., 1950. The evolution of the middle Ubag Valley, Damaraland, South West Africa. *Trans. Roy. Soc. S. Afr.* 33, 333–365.
- Macdonald, F.A., McClelland, W.C., Schrag, D.P., Macdonald, W.P., 2009. Neoproterozoic glaciation on a carbonate platform margin in Arctic Alaska and the origin of the North Slope subterrane. *Geol. Soc. Am. Bull.* 121, 448–473.
- Macdonald, F.A., Schmitz, M.D., Crowley, J.L., Roots, C.F., Jones, D.S., Maloof, A.C., Strauss, J.V., Cohen, P.A., Johnston, D.T., Schrag, D.P., 2010a. Calibrating the Cryogenian. *Science* 327, 1241–1243.
- Macdonald, F.A., Strauss, J.V., Rose, C.V., Dudás, F.Ó., Schrag, D.P., 2010b. Stratigraphy of the Port Nolloth Group of Namibia and South Africa and implications for the age of Neoproterozoic iron formations. *Am. J. Sci.* 310, 862–888.
- Macdonald, F.A., Prave, A.R., Petterson, R., Smith, E.F., Pruss, S.B., Oates, K., Waechter, F., Trotzuk, D., Fallick, A.E., 2013a. The Laurentian record of Neoproterozoic glaciation, tectonism, and eukaryotic evolution in Death Valley, California. *Geol. Soc. Am. Bull.* 125, 1203–1223.
- Macdonald, F.A., Strauss, J.V., Sperling, E.A., Halverson, G.P., Narbonne, G.M., Johnston, D.T., Kunzmann, M., Schrag, D.P., Higgins, J.A., 2013b. The stratigraphic relationship between the Shuram carbon isotope excursion, the oxygenation of Neoproterozoic oceans, and the first appearance of the Ediacara biota and bilaterian trace fossils in northwestern Canada. *Chem. Geol.* 362, 250–272.
- Macdonald, F.A., Schmitz, M.D., Strauss, J.V., Halverson, G.P., Gibson, T.M., Eyster, A., Cox, G., Mamroo, P., Crowley, J.L., 2018. Cryogenian of Yukon. *Precambrian Res.* 319, 114–143.
- MacLennan, S., Park, Y., Swanson-Hysell, N., Maloof, A., Schoene, B., Gebreslassie, M., Antilla, E., Tesema, T., Alene, M., Haileab, B., 2018. The arc of the Snowball: U–Pb dates constrain the Islay anomaly and the initiation of the Sturtian glaciation. *Geology* 46, 539–542.
- Magrani, F., Valla, P.C., Gribenski, N., Serra, E., 2020. Glacial overdeepenings in the Swiss Alps and foreland: Spatial distribution and morphometrics. *Quat. Sci. Rev.* 243, 106483.
- Maier, W.D., Rasmussen, B., Fletcher, I.R., Li, C., Barnes, S.-J., Huhma, H., 2013. The Kunene anorthosite complex, Namibia, and its satellite intrusions: geochemistry, geochronology, and economic potential. *Econ. Geol.* 108, 953–986.

- Maloof, A.C., 2000. Superposed folding at the junction of the inland and coastal belts, Damara Orogen, NW Namibia. *Communs. Geol. Surv. Namibia* 12, 89–98.
- Manríquez, P., Contreras-Reyes, E., Osses, A., 2014. Lithospheric 3–D flexure modelling of the oceanic plate seaward of the trench using variable elastic thickness. *Geophys. J. Int.* 196, 681–693.
- Mao, H.R., Liu, C.Q., Zhao, Z.Q., 2019. Source and evolution of dissolved boron in rivers: Insights from boron isotope signatures of end-members and model of boron isotopes during weathering processes. *Earth-Sci. Rev.* 190, 439–459.
- Maréchal, C.N., Nicolas, E., Doucet, C., Albarède, F., 2000. Abundance of zinc isotopes as a marine biogeochemical tracer. *Geochem. Geophys. Geosyst.* 1, 1015. <https://doi.org/10.1029/1999GC00029>.
- Marsh, J.S., Ewart, A., Milner, S.C., Duncan, A.R., Miller, R.McG., 2001. The Etendeka Igneous Province: magma types and their stratigraphic distribution with implications for the evolution of the Paraná–Etendeka flood basalt province. *Bull. Volcanol.* 62, 464–486.
- Martin, H., 1961. The hypothesis of continental drift in the light of recent advances of geological knowledge in Brazil and in South West Africa. Geological Society of South Africa, Johannesburg. Alex. L. Du Toit Mem. Lect. 7. Annex. v. 64, 47 p.
- Martin, H., 1964. Beobachten zum Problem der Jung-Präkambrischen Glazialen Ablagerungen in Südwestafrika. *Geol. Rundsch.* 54, 115–127.
- Martin, H., 1965. The Precambrian Geology of South West Africa and Namaqualand. University of Cape Town, Precam. Res. Unit, 159 p., map scale 1:5M.
- Martin, H., 1968. Paläomorphologische Formelemente in den Landschaften Südwest-Afrikas. *Geol. Rundsch.* 58, 121–128.
- Martin, H., 1981. The Late Paleozoic Dwyka Group of the South Kalahari Basin in Namibia and Botswana and the subglacial valleys of the Kaokoveld in Namibia. In: Hambrey, M.B., Harland, W.B. (Eds.), *Earth's Pre-Pleistocene Glacial Record*. Cambridge Univ. Press, Cambridge, UK, pp. 61–66.
- Martin, H., 1983. Overview of the geosynclinal, structural and metamorphic development of the intracontinental branch of the Damara orogen. In: Martin, H., Eder, F.W. (Eds.), *Intracontinental Fold Belts*. Springer-Verlag, Berlin, pp. 473–502.
- Martin, H., Porada, H., Wittig, R., 1983. Where lies the root zone of the Naukluft nappe complex? In: Miller, R.M.C.G. (Ed.), *Evolution of the Damara Orogen of South West Africa/Namibia*. Geological Society of South Africa, Johannesburg, Spec. Publ. 11, pp. 199–207.
- Martin, H., Porada, H., Walliser, O.H., 1985. Mixtite deposits of the Damara sequence, Namibia, problems of interpretation. *Palaeogeogr. Palaeoclimatol. Palaeoecol.* 51, 159–196.
- Martinez, J.F., Cartwright, J., Hall, B., 2005. 3D seismic interpretation of slump complexes: examples from the continental margin of Israel. *Basin Res.* 17, 83–108.
- Mashayek, A., Ferrari, R., Merrifield, S., Ledwell, J.R., St Laurent, L., Garabato, N., 2017. Topographic enhancement of vertical turbulent mixing in the Southern Ocean. *Nat. Commun.* 8, 14197. <https://doi.org/10.1038/ncomms14197>.
- Masson, D.G., Harbitz, C.B., Wynn, R.B., Pedersen, G., Løvholt, F., 2006. Submarine landslides: processes, triggers and hazard prediction. *Phil. Trans. R. Soc. Lond. Ser. A* 364, 1009–2039.
- Master, S., Wendoff, M., 2011. Neoproterozoic glaciogenic diamictites of the Katanga Supergroup, Central Africa. In: Arnaud, E., Halverson, G.P., Shields-Zhou, G. (Eds.), *The Geological Record of Neoproterozoic Glaciations*. Geological Society, London, Mem. 36, pp. 173–184.
- Mayer, A., Hofmann, A.W., Singoi, S., Morais, E., 2004. Mesoproterozoic Sm–Nd and U–Pb ages for the Kunene Anorthosite Complex of SW Angola. *Precambrian Res.* 133, 187–206.
- Mbede, E.I., Kampunzu, A.B., Armstrong, R.A., 2004. Neoproterozoic inheritance during Cainozoic rifting in the western and southern branches of the East African rift system: Evidence from carbonatite and alkaline intrusions. *Conference abstract, The East African Rift System: Development, Evolution and Resources*, Addis Ababa, Ethiopia, June 20–24, 2004.
- McConaughey, T., 1989a. ^{13}C and ^{18}O isotopic disequilibrium in biological carbonates: I. Patterns. *Geochim. Cosmochim. Acta* 53, 151–162.
- McConaughey, T., 1989b. ^{13}C and ^{18}O isotopic disequilibrium in biological carbonates: II. In vitro simulation of kinetic isotope effects. *Geochim. Cosmochim. Acta* 53, 163–171.
- McCourt, S., Armstrong, R.A., Jelsma, H., Mapeo, R.B.M., 2013. New U–Pb SHRIMP ages from the Lubango region, SW Angola: insights into the Palaeoproterozoic evolution of the Angolan Shield, southern Congo Craton, Africa. *J. Geol. Soc. Lond.* 170, 353–363.
- McDermott, K., Gillbard, E., Clarke, N., 2015. From basalt to skeletons – the 200 million-year history of the Namibian margin uncovered by new seismic data. *First Break* 33, 77–85.
- McGee, B., Halverson, G.P., Collins, A.S., 2012. Cryogenian rift-related magmatism and sedimentation: South-western Congo Craton, Namibia. *J. Afr. Earth Sci.* 76, 34–49.
- McGee, B., Collins, A.S., Trindade, R.I.F., Jourdan, F., 2015a. Investigating mid-Ediacaran glaciation and final Gondwana amalgamation using coupled sedimentology and $^{40}\text{Ar}/^{39}\text{Ar}$ detrital muscovite provenance from the Paraguay Belt, Brazil. *Sedimentology* 62, 130–154.
- McGee, B., Collins, A.S., Trindade, R.I.F., Payne, J., 2015b. Age and provenance of the Cryogenian to Cambrian passive margin to foreland basin sequence of the northern Paraguay Belt, Brazil. *Geol. Soc. Am. Bull.* 127, 76–86.
- McIntyre, N.F., 1984. Cryonite hole thermodynamics. *Can. J. Earth Sci.* 21, 152–156.
- McKay, R., Browne, G., Carter, L., Cowan, E., Dunbar, G., Krissek, L., Naish, T., Powell, R., Reed, J., Talarico, F., Wilch, T., 2009. The stratigraphic signature of the late Cenozoic Antarctic Ice Sheets in the Ross Embayment. *Geol. Soc. Am. Bull.* 121, 1537–1561.
- McKenzie, D.P., 1969. Speculations on the consequences and causes of plate motions. *Geophys. J. R. Astron. Soc.* 18, 1–32.
- McKenzie, D., 1978. Some remarks on the development of sedimentary basins. *Earth Planet. Sci. Lett.* 40, 25–32.
- McKirdy, D.M., Burgess, J.M., Lemon, N.M., Xu, X., Cooper, A.M., Gostin, V.A., Jenkins, R.J.F., 2001. A chronostratigraphic overview of the late Cryogenian interglacial sequence in the Adelaide fold-thrust belt, South Australia. *Precambrian Res.* 106, 149–186.
- Meert, J.G., van der Voo, R., Ayub, S., 1995. Paleomagnetic investigations of the Neoproterozoic Gagwe lavas and Mbozi complex, Tanzania and the assembly of Gondwana. *Precambrian Res.* 74, 225–244.
- Mendelsohn, J., Jarvis, A., Roberts, C., Robertson, T., 2002. *Atlas of Namibia: A Portrait of the Land and its People*. David Philip, Cape Town, 200 p.
- Meneghini, F., Kisters, A., Buick, I., Fagereng, Å., 2014. Fingerprints of late Neoproterozoic ridge subduction in the Pan-African Damara belt, Namibia. *Geology* 42, 903–906.
- Merdith, A.S., Collins, A.S., Williams, S.E., Pisarevsky, S., Foden, J.D., Archibald, D.B., Blades, M.L., Alessio, B.L., Armistead, S., Plavsa, D., Clark, C., Müller, R.D., 2017a. A full-plate global reconstruction of the Neoproterozoic. *Gondwana Res.* 50, 84–134.
- Merdith, A.S., Williams, S.E., Müller, R.D., Collins, A.S., 2017b. Kinematic constraints on the Rodinia to Gondwana transition. *Precambrian Res.* 299, 132–150.
- Merdith, A.S., Williams, S.E., Brune, S., Collins, A.S., Müller, R.D., 2019. Rift and plate boundary evolution across two supercontinent cycles. *Glob. Planet. Chang.* 173, 1–14.
- Michel, J., Lauglé, M., Pohl, A., Lantgeaume, C., Masse, J.-P., Donnadieu, Y., Borgoman, J., 2019. Marine carbonate factories: a global model of carbonate platform distribution. *Int. J. Earth Sci.* 108, 1773–1792.
- Mickala, O.-R., Vidal, L., Boudzoumou, F., Affaton, P., Vandamme, D., Borschneck, D., Mounguengui, M.M., Fournier, F., Nganga, D.M.M., Miche, H., 2014. Geochemical characterization of the Marinoan “Cap Carbonate” of the Niari–Nyanga Basin (Central Africa). *Precambrian Res.* 255, 367–380.
- Mikucki, J.A., Pearson, A., Johnston, J.T., Turchyn, A.V., Farquhar, J., Schrag, D.P., Anbar, A.D., Priscu, J.C., Lee, P.A., 2009. A contemporary microbially maintained subglacial ferrous “ocean”. *Science* 324, 397–400.
- Miles, W., Oneschuk, D., 2016. Magnetic Anomaly Map of Canada. Geological Survey of Canada, Open File 7799, 1 sheet scale 7.5 M. <https://doi.org/10.4095/297337> (open access).
- Miller, R.McG., 1974. The stratigraphic significance of the Nauwpoort Formation of east central Damaraland, South West Africa. *Trans. Geol. Soc. S. Afr.* 77, 636–637.
- Miller, R.McG., 1980. Geology of a Portion of Central Damaraland, South West Africa/Namibia. Geological Survey of South Africa, Pretoria, S. W. Afr. Ser. 6, 78 p.
- Miller, R.McG., 1983. Evolution of the Damara Orogen of South West Africa/Namibia. Geological Society of South Africa, Johannesburg, Sp. Publ. 11, 515 p.
- Miller, R.McG., 1997. The Owambo Basin of northern Namibia. In: Selley, R.C. (Ed.), *African Basins*, 3. Elsevier, Amsterdam, pp. 237–268. *Sedimentary Basins of the World*.
- Miller, R.McG., 2008a. The Geology of Namibia. In: Vol.1, *Archaean to Mesoproterozoic Geological Survey of Namibia*, Windhoek.
- Miller, R.McG., 2008b. The Geology of Namibia. In: Vol. 2, *Neoproterozoic to Lower Palaeozoic Geological Survey of Namibia*, Windhoek.
- Miller, R.McG., 2008c. The Geology of Namibia. In: Vol. 3, *Palaeozoic to Cenozoic Geological Survey of Namibia*, Windhoek.
- Miller, R.McG., 2013. Comparative stratigraphic and geochronological evolution of the Northern Damara Supergroup in Namibia and the Katanga Supergroup in the Lufilian Arc of Central Africa. *Geosci. Can.* 40 <https://doi.org/10.12789/geocan.2013.40.007>.
- Miller, R.McG., Grote, W., 1988. *Geological map of the Damara Orogen, South West Africa / Namibia*, scale 1:500K. Geological Survey of Namibia, Windhoek.
- Miller, R.McG., Schalk, K.E.L., 1980. *Geological Map of Namibia*, scale 1:1M. Geological Survey of Namibia, Windhoek.
- Miller, R.McG., Freyer, E.E., Hälbich, I.W., 1983. A turbidite succession equivalent to the entire Swakop Group. In: Miller, R.McG. (Ed.), *Evolution of the Damara Orogen of South West Africa/Namibia*. Geological Society of South Africa, Johannesburg, II, pp. 65–71. Sp. Publ. 11.
- Miller, R.McG., Pickford, M., Senut, B., 2010. The geology, palaeontology and evolution of the Etosha Pan, Namibia: implications for terminal Kalahari deposition. *S. Afr. J. Geol.* 113, 307–334.
- Millero, F.J., 1979. The thermodynamics of the carbonate system in seawater. *Geochim. Cosmochim. Acta* 43, 1651–1661.
- Mills, B., Watson, A.J., Goldblatt, C., Boyle, R., Lenton, T.M., 2011. Timing of Neoproterozoic glaciations linked to transport-limited global weathering. *Nat. Geosci.* 4, 861–864.
- Mitrovica, J.X., Gomez, N., Clark, P.U., 2009. The sea-level fingerprint of West Antarctic collapse. *Science* 323, 753.
- Miyazaki, Y., Planavsky, N.J., Bolton, E.W., Reinhard, C.T., 2018. Making sense of massive carbon isotope excursions with an inverse carbon cycle model. *J. Geophys. Res. Biogeosci.* 123, 2485–2496.
- Moore, K.R., Bosak, T., Macdonald, F.A., Lahr, D.J.G., Newman, S., Settens, C., Pruss, S. B., 2017. Biologically-agglutinated eukaryotic microfossil from Cryogenian cap carbonates. *Geobiology* 15, 499–515.
- Morlighem, M., Rignot, E., Binder, T., Blankenship, D., Drews, R., Eagles, G., Ferraccioli, F., Forsberg, R., Fretwell, P., Goel, V., Greenbaum, J.S., Gudmundsson, H., Guo, J.X., Helm, V., Hofstede, C., Howat, I., Humbert, A., Jakob, W., Karlsson, N.B., Lee, W.S., Matsuoka, K., Millan, R., Mourginot, J., Paden, J., Pattyn, F., Roberts, J., Rosier, S., Ruppel, A., Seroussi, H., Smith, E.C., Steinbäck, D., Sun, B., van den Broeke, M.R., van Ommen, T.D., van Wessem, M., Young, D.A., 2020. Deep glacial troughs and stabilizing ridges unveiled beneath the margins of the Antarctic Ice Sheet. *Nat. Geosci.* 13, 132–137.

- Musilova, M., Tranter, M., Bamber, J.L., Takeuchi, N., Anesio, A.M., 2016. Experimental evidence that microbial activity lowers the albedo of glaciers. *Geochim. Persp. Lett.* 2, 106–116.
- Myrow, P.M., Lamb, M.P., Ewing, R.C., 2018. Rapid sea level rise in the aftermath of a Neoproterozoic snowball Earth. *Science* 360, 649–651.
- Narbonne, G.M., 2005. The Ediacara biota: Neoproterozoic origin of animals and their ecosystems. *Annu. Rev. Earth Planet. Sci.* 33, 421–442.
- Narbonne, G.M., Xiao, S.H., Shields, G.A., 2012. The Ediacaran period. In: Gradstein, F.M., Ogg, J.G., Schmitz, M.D., Ogg, G.M. (Eds.), *The Geologic Time Scale 2012*. Elsevier, Amsterdam, pp. 413–435.
- Nascimento, D.B., Ribeiro, A., Trouw, R.A.J., Schmitt, R.S., Passchier, C.W., 2016. Stratigraphy of the Neoproterozoic Damara Sequence in northwest Namibia: Slope to basin sub-marine mass-transport deposits andolistolith fields. *Precambrian Res.* 278, 108–125.
- Nascimento, D.B., Schmitt, R.S., Ribeiro, A., Trouw, R.A.J., Passchier, C.W., Basei, M.A.S., 2017. Depositional ages and provenance of the Neoproterozoic Damara Supergroup (northwest Namibia): implications for the Angola–Congo and Kalahari cratons connection. *Gondwana Res.* 52, 153–171.
- Nascimento, D.B., Ribeiro, A., Trouw, R.A.J., Schmitt, R.S., Passchier, C.W., 2018. Reply to discussion by Hoffman and Halverson (2018) on the article: "Depositional ages and provenance of the Neoproterozoic Damara Supergroup (northwest Namibia): Implications for the Angola–Congo and Kalahari cratons connection" by Nascimento et al. (2017). *Gondwana Res.* 58, 153–171.
- Nealson, K.H., Conrad, P.G., 1999. Life: past, present and future. *Philos. Trans. R. Soc. Lond. B* 354, 1923–1939.
- Nelson, L.L., Smith, E.F., Hodgkin, E.B., Crowley, J.L., Schmitz, M.D., Macdonald, F.A., 2020. Geochronological constraints on Neoproterozoic rifting and onset of the Marinoan glaciation from the Kingston Peak Formation in Death Valley, California. *Geology*. <https://doi.org.ezp-prod1.hul.harvard.edu/10.1130/G47668.1>.
- Nieminski, N.M., Grove, M., Lowe, D.R., 2018. Provenance of the Neoproterozoic deep-water Zerrissene Group of the Damara Orogen, Namibia, and paleogeographic implications for the closing of the Adamastor Ocean and assembly of the Gondwana supercontinent. *Geol. Soc. Am. Bull.* 131, 355–371.
- Nir, O., Vengosh, A., Harkness, J.S., Dwyer, G.S., Lahav, O., 2015. Direct measurement of the boron isotope fractionation factor: reducing the uncertainty in reconstructing ocean paleo-pH. *Earth Planet. Sci. Lett.* 414, 1–5.
- Nogueira, A.C.R., Riccomini, C., Sial, A.N., Moura, C.A.V., Trindade, R.I.F., Fairchild, T.R., 2007. Carbon and strontium isotope fluctuations and paleoceanographic changes in the late Neoproterozoic Araras carbonate platform, southern Amazon craton, Brazil. *Chem. Geol.* 237, 168–190.
- Nordsvan, A.R., Barham, M., Cox, G., Kirscher, U., Mitchell, R.N., 2019. Major shoreline retreat and sediment starvation following Snowball Earth. *Terra Nova* 21, 495–502.
- Norin, E., 1937. Geology of western Quruq Tagh, eastern Tien Shan. In: Hedin, S. (Ed.), Reports from the Scientific Expedition to the North-Western Provinces of China under Leadership of Dr Sven Hedin, the Sino-Swedish Expedition. Aktiebolaget Thule, Stockholm, 191 p., 43 plates, 2 geological maps scale 1:100K and sections.
- O'Neil, J.R., 1968. Hydrogen and oxygen isotope fractionation between ice and water. *J. Phys. Chem.* 72, 3683–3684.
- Ogg, J.G., Hinnov, L.A., Huang, C., 2012. Cretaceous. In: Gradstein, F.M., Ogg, J.G., Schmitz, M.D., Ogg, G.M. (Eds.), *The Geologic Time Scale 2012*, Vol. 2. Elsevier, Amsterdam, pp. 793–853.
- Ohnemueller, F., Prave, A.R., Fallick, A.E., Kasemann, S.A., 2014. Ocean acidification in the aftermath of the Marinoan glaciation. *Geology* 42, 1103–1106.
- Oyhançabal, P., Siegesmund, S., Wemmer, K., Presnyakov, S., Layer, P., 2009. Geochronological constraints on the evolution of the southern Dom Feliciano Belt (Uruguay). *J. Geol. Soc. Lond.* 166, 1075–1084.
- Oyhançabal, P., Siegesmund, S., Wemmer, K., Passchier, C.W., 2011. The transpressional connection between Dom Feliciano and Kaoko belts at 580–550 Ma. *Int. J. Earth Sci.* 100, 379–390.
- Paciullo, F.V.P., Ribeiro, A., Trouw, R.A.J., Passchier, C.W., 2007. Facies and facies association of the siliciclastic Brak River and carbonate Gemsbok formations in the Lower Ugab River valley, Namibia, W. Africa. *J. Afr. Earth Sci.* 47, 121–134.
- Pal, M., Taberner, C., 2011. Simulation of brine reflux and geothermal circulation in large carbonate platforms. *Proc. 2011 COMSOL Conf.* Stuttgart 1–11.
- Park, Y., Swanson-Hysell, N.L., MacLennan, S.A., Maloof, A.C., Gebreslassie, M., Tremblay, M.M., Schoene, B., Alene, M., Anttila, E.S.C., Tesema, T., Haileab, B., 2020. The lead-up to the Sturtian Snowball Earth: Neoproterozoic chronostratigraphy time-calibrated by the Tambien Group of Ethiopia. *Geol. Soc. Am. Bull.* 132, 1119–1149.
- Parnell, J., Boyce, A.J., 2017. Microbial sulphate reduction during Neoproterozoic glaciation, Port Askaig Formation, UK. *J. Geol. Soc. Lond.* 174, 850–854.
- Parsons, B., Molnar, P., 1976. Research note: The origin of outer topographic rises associated with trenches. *Geophys. J. R. Astron. Soc.* 45, 707–712.
- Partin, C.A., Sadler, P.M., 2016. Slow net sediment accumulation sets snowball Earth apart from all younger glacial episodes. *Geology* 44, 1019–1022.
- Pasquier, V., Bryant, R.N., Fike, D.A., Halevy, I., 2021. Strong local, not global, controls on marine pyrite sulfur isotopes. *Sci. Adv.* 7 eabb7403.
- Passchier, C.W., Trouw, R.A.J., Ribeiro, A., Paciullo, F.V.P., 2002. Tectonic evolution of the southern Kaoko belt, Namibia. *J. Afr. Earth Sci.* 35, 61–75.
- Passchier, S., Browne, G., Field, B., Fielding, C.R., Krissek, L.A., Panter, K., Pekar, S.F., ANDRILL–SMS Science Team, 2011. Early and middle Miocene Antarctic glacial history from the sedimentary facies distribution in the AND-2A drill hole, Ross Sea. *Antarctica. Geol. Soc. Am. Bull.* 123, 2352–2365.
- Passchier, C., Trouw, R., da Silva Schmitt, R., 2016. How to make a transverse triple junction—New evidence for the assemblage of Gondwana along the Kaoko–Damara belts, Namibia. *Geology* 44, 843–846.
- Patton, H., Swift, D.A., Clark, C.D., Livingstone, S.J., Cook, S.J., 2016. Distribution and characteristics of overdeepening beneath the Greenland and Antarctic ice sheets: implications for overdeepening origin and evolution. *Quat. Sci. Rev.* 148, 128–145.
- Peate, D.W., 1997. The Paraná–Etendeka Province. In: Mahoney, J.J., Coffin, M.F. (Eds.), *Large Igneous Provinces*. American Geophysical Union, Washington, DC, Geophys. Monogr. 100, pp. 217–245.
- Penck, A., 1905. Glacial features in the surface of the Alps. *J. Geol.* 13, 1–19.
- Peng, S., Babcock, L.E., Cooper, R.A., 2012. The Cambrian period. In: Gradstein, F.M., Ogg, J.G., Schmitz, M.D., Ogg, G.M. (Eds.), *The Geologic Time Scale 2012* Vol. 2. Elsevier, Amsterdam, pp. 437–488.
- Peng, X., Zhu, X.K., Shi, F.Q., Yan, B., Zhang, F.F., Zhao, N.N., Peng, P.G., Li, J., Wang, D., Shields, G.A., 2019. A deep marine organic carbon reservoir in the non-glacial Cryogenian ocean (Nanhua Basin, South China) revealed by organic carbon isotopes. *Precambrian Res.* 321, 212–220.
- Percival, J.J., Konopásek, J., Eiesland, R., Sláma, J., de Campos, R.S., Battisti, M.A., de Bitencourt, M.F., 2021. Pre-orogenic connection of the foreland domains of the Kaoko–Dom Feliciano–Gariep orogenic system. *Precambrian Res.* 354 (106060), 1–20.
- Peters, E.S., Husson, J.M., Wilcots, J., 2017. The rise and fall of stromatolites in shallow marine environments. *Geology* 45, 487–490.
- Petersen, K.D., Nielsen, S.B., Clausen, O.R., Stephenson, R., Gerya, T., 2010. Small-scale mantle convection produces stratigraphic sequences in sedimentary basins. *Science* 329, 827–830.
- Petrie, S.H., Brown, J.R., Granger, P.J., Lovell, J.P.B., 1989. Mesozoic history of the Celtic Sea basins. In: Tankard, A.J., Balkwill, H.R. (Eds.), *Extensional Tectonics of the North Atlantic Margins*. American Association of Petroleum Geologists, Mem. 46, pp. 433–444.
- Petterson, R., Prave, A.R., Wernicke, B.P., Fallick, A.E., 2011. The Neoproterozoic Noonday Formation, Death Valley region California. *Geol. Soc. Am. Bull.* 123, 1317–1336.
- Peucker-Ehrenbrink, B., Waters, C.A., Kurz, M.D., Hoffman, P.F., 2016. No evidence of extraterrestrial noble metal and helium anomalies at Marinoan glacial termination. *Earth Planet. Sci. Lett.* 437, 76–88.
- Pfiffner, O.A., 1986. Evolution of the north Alpine foreland basin in the Central Alps. In: Allen, P.A., Homewood, P. (Eds.), *Foreland Basins*. International Association of Sedimentologists/Blackwell, Sp. Publ. 8, pp. 219–228.
- Pierrehumbert, R.T., 2002. The hydrologic cycle in deep-time climate problems. *Nature* 419, 191–198.
- Pierrehumbert, R.T., 2005. Climate dynamics of a hard snowball Earth. *J. Geophys. Res.* 110, D01111 <https://doi.org/10.1029/2004JD005162>.
- Pierrehumbert, R.T., Abbott, D.S., Voigt, A., Koll, D., 2011. Climate of the Neoproterozoic. *Annu. Rev. Earth Planet. Sci.* 39, 417–460.
- Pisarevsky, S.A., Murphy, J.B., Cawood, P.A., Collins, A.S., 2008. Late Neoproterozoic and Early Cambrian paleogeography: models and problems. In: Pakhurst, R.J., Trouw, R.A.J., de Brito Neves, B.B., de Wit, M.J. (Eds.), *West Gondwana: Pre-Cenozoic Correlations Across the South Atlantic Region*. Geological Society, London, pp. 9–31. Sp. Publ. 294.
- Planavsky, N.J., Reinhard, C.T., Wang, X.L., Thomson, D., McGoldrick, P., Rainbird, R.H., Johnson, T., Fischer, W.W., Lyons, T.W., 2014. Low mid-Proterozoic atmospheric oxygen levels and the delayed rise of animals. *Science* 346, 635–638.
- Playford, P.E., Cockbain, A.E., Berry, P.F., Roberts, A.P., Haines, P.W., Brooke, B.P., 2013. The Geology of Shark Bay. *Geological Survey of Western Australia, Bull.* 146, 281 p.
- Playton, T.E., Kerans, C., 2015a. Late Devonian carbonate margins and foreslopes of the Lennard Shelf, Canning Basin, Western Australia, Part A: Development during backstepping and the aggradation-to-progradation transition. *J. Sediment. Res.* 85, 1334–1361.
- Playton, T.E., Kerans, C., 2015b. Late Devonian carbonate margins and foreslopes of the Lennard Shelf, Canning Basin, Western Australia, Part B: Development during progradation and across the Frasnian–Fammenian biotic crisis. *J. Sediment. Res.* 85, 1362–1392.
- Playton, T.E., Janson, X., Kerans, C., 2010. Carbonates slopes. In: James, N.P., Dalrymple, R.W. (Eds.), *Facies Models 4*. Geological Association of Canada, pp. 449–476.
- Poidevin, J.-L., 2007. Stratigraphie isotopique du strontium et datation des formations carbonées et glaciogéniques néoproterozoïques du Nord et de l'Ouest du craton du Congo. *Compt. Rendus Geosci.* 339, 259–273.
- Pollard, D., DeConto, R.M., 2007. A coupled ice-sheet/ice-shelf/sediment model applied to a marine-margin flowline: forced and unforced variations. In: Hambrey, M.J., Christoffersen, P., Glasser, N.F., Hubbard, B. (Eds.), *Glacial Sedimentary Processes and Products*. Blackwell, Malden, MA, USA, pp. 37–52. Int. Assoc. Sedimentol., Sp. Publ. 39.
- Pollard, D., Kasting, J.F., 2004. Climate-ice sheet simulations of Neoproterozoic glaciation before and after collapse to Snowball Earth. In: Jenkins, G.S., McMenamin, M.A.S., McKay, C.P., Sohl, L. (Eds.), *The Extreme Proterozoic: Geology, Geochemistry, and Climate*. American Geophysical Union, Washington, DC, pp. 91–105. Geophys. Monogr. 146.
- Porada, H.R., 1974. The Khoabendum Formation in the Area Northwest of Kamanjab and in the Southeastern Kaokoveld, South West Africa. *Geological Survey of South Africa, Pretoria, South West Africa Ser.* 4, 23 p.
- Porada, H., 1979. The Damara–Ribeira orogen of the Pan-African–Brasiliano cycle in Namibia (Southwest Africa) and Brazil as interpreted in terms of continental collision. *Tectonophysics* 57, 237–265.
- Porada, H., 1989. Pan-African rifting and orogenesis in southern to equatorial Africa and eastern Brazil. *Precambrian Res.* 44, 103–136.

- Porada, H., Ahrendt, H., Behr, H.-J., Weber, K., 1983. The join of the coastal and intracontinental branches of the Damara Orogen, Namibia, South West Africa. In: Martin, H., Eder, F.W. (Eds.), *Intracontinental Fold Belts*. Springer-Verlag, Berlin, pp. 901–912.
- Porter, S.M., Knoll, A.H., 2000. Testate amoebae in the Neoproterozoic Era: evidence from vase-shaped microfossils in the Chuar Group, Grand Canyon. *Paleobiology* 26, 360–385.
- Porter, S.M., Meisterfeld, R., Knoll, A.H., 2003. Vase-shaped microfossils from the Neoproterozoic Chuar Group, Grand Canyon: a classification guided by modern testate amoebae. *J. Paleontol.* 77, 409–429.
- Powell, R.D., 1990. Glacimarine processes at grounding-line fans and their growth to ice-contact deltas. In: Dowdeswell, J.A., Scourse, J.D. (Eds.), *Glacimarine Environments: Processes and Sediments*. Geological Society, London, Sp. Publ. 53, pp. 53–73.
- Prave, A.R., 1996. Tale of three cratons: Tectonostratigraphic anatomy of the Damara orogen in northwestern Namibia and the assembly of Gondwana. *Geology* 24, 1115–1118.
- Prave, A.R., Condon, D.J., Hoffmann, K.-H., Tapster, S., Fallackson, A.E., 2016. Duration and nature of the end-Cryogenian (Marinoan) glaciation. *Geology* 44, 631–634.
- Preiss, W.V., Forbes, B.G., 1981. Stratigraphy, correlation and sedimentary history of Adelaidean (Late Proterozoic) basins in Australia. *Precambrian Res.* 15, 255–304.
- Pruss, S.B., Bosak, T., Macdonald, F.A., McLane, M., Hoffman, P.F., 2010. Microbial facies in a Sturtian cap carbonate, the Rasthof Formation, Otavi Group, northern Namibia. *Precambrian Res.* 181, 187–198.
- Pu, J.P., Bowring, S.A., Ramezani, J., Myrow, P., Raub, T.D., Landing, E., Mills, A., Macdonald, F.A., 2016. Dodging snowballs: Geochronology of the Gaskiers glaciation and the first appearance of the Ediacara biota. *Geology* 44, 955–958.
- Purkis, S.J., Rowlands, G.P., Kerr, J.M., 2015. Unravelling the influence of water depth and wave energy on the facies diversity of shelf carbonates. *Sedimentology* 62, 541–565.
- Purser, B.H., Bosence, D.W.J. (Eds.), 1998. *Sedimentation and Tectonics in Rift Basins: Red Sea – Gulf of Aden*. Chapman & Hall, London, 663 p.
- Ramsay, J.G., Huber, M.I., 1987. *The Techniques of Modern Structural Geology Vol. 2: Folds and Fractures*. Academic Press, London, 700 p.
- Rebesco, M., Domack, E., Zgur, F., Lavoie, C., Leventer, A., Brachfield, S., Willmot, Halverson, G.V., Truffer, M., Scambos, T., Smith, J., Petit, E., 2014. Boundary condition of grounding lines prior to collapse, Larsen-B Ice Shelf, Antarctica. *Science* 345, 1354–1358.
- Reid, R.P., Macintyre, I.G., Browne, K.M., Steneck, R.S., Miller, T., 1995. Modern marine stromatolites in the Exuma Cays, Bahamas: Uncommonly common. *Facies* 33, 1–18.
- Reilly, T.E., Goodman, A.S., 1985. Quantitative analysis of saltwater–freshwater relationships in groundwater systems – a historical perspective. *J. Hydrol.* 80, 125–160.
- Ridgwell, A.J., Kennedy, M.J., Caldeira, K., 2003. Carbonate deposition, climate stability, and Neoproterozoic ice ages. *Science* 302, 859–862.
- Riedman, L.A., Porter, S.M., Czaja, A.D., 2021. Phosphatic scales in vase-shaped microfossil assemblages from Death Valley, Grand Canyon, Tasmania, and Svalbard. *Geobiology* 20, 10/111/gbi.12439.
- Rignot, E., Mouginot, J., 2012. Ice flow in Greenland for the International Polar Year 2008–2009. *Geophys. Res. Lett.* 39, L11501 <https://doi.org/10.1029/2012GL051634>.
- Rivers, T., Culshaw, N., Hynes, A., Indares, A., Jamieson, R., Martignole, J., 2012. The Grenville Orogen – a post-LITHOPROBE perspective. In: Percival, J.A., Cook, F.A., Clowes, R.M. (Eds.), *Tectonic Styles in Canada: The LITHOPROBE Perspective*. Geological Association of Canada, Spec. Pap. 49, pp. 97–236.
- Roberts, G.G., White, N., 2010. Estimating uplift rate histories from river profiles using African examples. *J. Geophys. Res.* 115, B02406 <https://doi.org/10.1029/2009JB006692>.
- Robinson, P., Dowdeswell, J.A., 2011. Submarine landforms and the behaviour of a surging ice cap since the last glacial maximum: the open-marine setting of eastern Austfonna, Svalbard. *Marine Geol.* 286, 82–94.
- Rodgers, J., 1957. The distribution of marine carbonate sediments: a review. In: Le Blanc, R.J., Breeding, J.G. (Eds.), *Regional Aspects of Carbonate Deposition*. Society of Economic Paleontologists and Mineralogists, Sp. Publ. 5, Tulsa, OK, pp. 2–14.
- Rodler, A.S., Frei, R., Gaucher, C., Germs, G.J.B., 2016. Chromium isotope, REE and redox-sensitive trace element chemostratigraphy across the late Neoproterozoic Ghaub glaciation, Otavi Group, Namibia. *Precambrian Res.* 286, 234–249.
- Rodler, A.S., Frei, R., Gaucher, C., Korte, C., Rosing, S.A., Germs, G.J.B., 2017. Multiproxy isotope constraints on ocean compositional changes across the late Neoproterozoic Ghaub glaciation, Otavi Group, Namibia. *Precambrian Res.* 298, 306–324.
- Rogers, G.C., 1983a. Seismotectonics of British Columbia. Ph.D. thesis. University of British Columbia, Vancouver, 227 p.
- Rogers, G.C., 1983b. Some comments on the seismicity of northern Puget Sound – southern Vancouver Island region. U. S. Geol. Surv. Open-File Rept 83, 19–39.
- Rohde, J., Hoernle, K., Hauff, F., Werner, R., O'Connor, J., Class, C., Garbe-Schönberg, D., Jokat, W., 2013. 70 Ma chemical zonation of the Tristan–Gough hotspot track. *Geology* 41, 335–338.
- Rooney, A.D., Macdonald, F.A., Strauss, J.V., Dudás, F.Ö., Hallmann, C., Selby, D., 2014. Re–Os geochronology and coupled Os–Sr isotope constraints on the Sturtian snowball Earth. *Proc. Natl. Acad. Sci. U. S. A.* 111 (1), 51–56.
- Rooney, A.D., Strauss, J.V., Brandon, A.D., Macdonald, F.A., 2015. A Cryogenian chronology: two long-lasting synchronous Neoproterozoic glaciations. *Geology* 43, 459–462.
- Rooney, A.D., Yang, C.A., Condon, D.J., Zhu, M.Y., Macdonald, F.A., 2020a. U–Pb and Re–Os geochronology tracks stratigraphic condensation in the Sturtian snowball Earth aftermath. *Geology* 48, 625–629.
- Rooney, A.D., Cantine, M.D., Bergmann, K.D., Gómez-Pérez, I., Al Baloushi, B., Boag, T. H., Busch, J.F., Sperling, E.A., Strauss, J.V., 2020b. Calibrating the co-evolution of Ediacaran life and environment. *Proc. Natl. Acad. Sci. U. S. A.* 117 (16), 824–16,830.
- Rose, C.V., Swanson-Hysell, N.L., Husson, J.M., Poppick, L.N., Cottle, J.M., Schoene, B., Maloof, A.C., 2012. Constraints on the origin and relative timing of the Trezona $\delta^{13}\text{C}$ anomaly below the end-Cryogenian glaciation. *Earth Planet. Sci. Lett.* 319–320, 241–250.
- Rose, C.V., Maloof, A.C., Schoene, B., Ewing, R.C., Linnemann, U., Hofmann, M., Cottle, J.M., 2013. The end-Cryogenian glaciation of South Australia. *Geosci. Can.* 40 <https://doi.org/10.12789/geocanj.2013.40.019>.
- Rothman, D.H., Hayes, J.M., Summons, R.E., 2003. Dynamics of the Neoproterozoic carbon cycle. *Proc. Natl. Acad. Sci. U. S. A.* 100, 8124–8129.
- SACS (South African Committee for Stratigraphy), 1980. Damara sequence. In: Kent, L.E. (Ed.), *Stratigraphy of South Africa Part 1: Lithostratigraphy of the Republic of South Africa, South West Africa/Namibia and the Republics of Bophuthatswana, Transkei and Venda*, Geological Survey of South Africa, Pretoria, Handbook, 8, pp. 415–438.
- Sadler, P.M., 1981. Sediment accumulation rates and the completeness of stratigraphic sections. *J. Geol.* 89, 569–584.
- Sadler, P.M., 1994. The expected duration of upward-shoaling peritidal carbonate cycles and their terminal hiatuses. *Geol. Soc. Am. Bull.* 106, 791–802.
- Salminen, J., Hanson, R., Evans, D.A.D., Gong, Z., Larson, T., Walker, O., Gumsley, A., Söderlund, U., Ernst, R., 2018. Direct Mesoproterozoic connection of the Congo and Kalahari cratons in proto-Africa: strange attractors across supercontinental cycles. *Geology* 46, 1011–1014.
- Saltzman, M.R., Thomas, E., 2012. Carbon isotope stratigraphy. In: Gradstein, F., Ogg, J. G., Schmitz, M., Ogg, G. (Eds.), *The Geologic Time Scale 2012*, Vol. 1. Elsevier, Amsterdam, pp. 207–232.
- Sansofre, P., Cartigny, P., Trindade, R.I.F., Nogueira, A.C.R., Agrinier, P., Ader, M., 2016. Multiple sulfur isotope evidence for massive oceanic sulfate depletion in the aftermath of Snowball Earth. *Nat. Comms.* 7, 12192. <https://doi.org/10.1038/ncomms12192>.
- Santos, R.F., Nogueira, A.C.R., Romero, G.R., Soares, J.L., Bandeira Junior, J., 2021. Life in the aftermath of Marinoan glaciation: the giant stromatolite evolution in the Puga cap carbonate, southern Amazon Craton, Brazil. *Precambrian Res.* 354 (106059), 1–13.
- Sarg, J.R., 1988. Carbonate sequence stratigraphy. In: Wilgus, C.K., Posamentier, H., Ross, C.A., Kendall, GGStC (Eds.), *Sea-Level Changes: An Integrated Approach*. SEPM (Society for Sedimentary Research), Tulsa, OK, pp. 155–181.
- Saylor, B.Z., Kaufman, A.J., Grotzinger, J.P., Urban, F., 1998. A composite reference section for terminal Proterozoic strata of southern Namibia. *J. Sediment. Res.* 68, 1223–1235.
- Scheiderich, K., Amini, M., Holmden, C., François, R., 2015. Global variability of chromium isotopes in seawater demonstrated by Pacific, Atlantic, and Arctic Ocean samples. *Earth Planet. Sci. Lett.* 423, 87–97.
- Schermerhorn, L.J.G., 1961. Sedimentary cycles in the West Congo Geosyncline of Northwest Angola. *Bol. Serv. Geol. Minas (Luanda, Angola)* 3, 47–62.
- Schermerhorn, L.J.G., 1974. Late Precambrian mixtites: glacial and/or non-glacial? *Am. J. Sci.* 274, 673–824.
- Schermerhorn, L.J.G., 1975. Tectonic framework of Late Precambrian supposed glacials. In: Wright, A.E., Moseley (Eds.), *Ice Ages: Ancient and Modern*. Seel House Press, Liverpool, pp. 241–274.
- Schermerhorn, L.J.G., 1976. Reply: Late Precambrian mixtites: glacial and/or nonglacial? Dealing especially with the mixtites of West Africa. *Am. J. Sci.* 276, 1315–1324.
- Schermerhorn, L.J.G., Stanton, W.I., 1963. Tilloids in the West Congo geosyncline. *Quart. J. Geol. Soc., Lond* 119, 201–241.
- Schlager, W., 1981. The paradox of drowned reefs and carbonate platforms. *Geol. Soc. Am. Bull.* 92, 197–211.
- Schlager, W., 2005. *Carbonate Sedimentology and Sequence Stratigraphy*. SEPM (Society for Sedimentary Geology), Tulsa, OK. Concepts Sediment. Paleontol. 8, 200 p.
- Schlager, W., Warrlich, G., 2008. Record of sea-level fall in tropical carbonates. *Basin Res.* 20, 1–16. <https://doi.org/10.1111/j.1365-2117.2008.00383.x>.
- Schmidt, P.W., Williams, G.E., Embleton, B.J.J., 1991. Low palaeolatitude of Late Proterozoic glaciation: early timing of remanence in haematite of the Elatina Formation, South Australia. *Earth Planet. Sci. Lett.* 105, 355–367.
- Schmitt, R.S., Trouw, R.A.J., Vn Schmus, W.R., Passchier, C.W., 2008. Cambrian orogeny in the Ribeira Belt (SE Brazil) and correlations within West Gondwana: ties that bind underwater. In: Pankhurst, R.J., Trouw, R.A.J., Brito Neves, B.B., de Wit, M.J. (Eds.), *West Gondwana: Pre-Cenozoic Correlations Across the South Atlantic Region*, pp. 279–296. Geological Society, London, Sp. Publ. 294.
- Schmitt, R.S., Trouw, R.A.J., Passchier, C.W., Medeiros, S.R., Armstrong, R., 2012. 530 Ma syntectonic syenites and granites in NW Namibia – Their relation with collision along the junction of the Damara and Kaoko belts. *Gondwana Res.* 21, 362–377.
- Schneiderhöhn, H., 1920. Beiträge zur Kenntnis der erzlagerstätten und der geologischen Verhältnisse des Otavi-Berglandes, Deutsch-Südwestafrika. *Senckenbergische Naturforschende Gesellschaft*, 318 p.
- Schneiderhöhn, H., 1929. Das Otavi-Bergland und seine Erzlagerstätten. *Z. Prakt. Geol.* 37, 85–116.
- Schrag, D.P., Berner, R.A., Hoffman, P.F., Halverson, G.P., 2002. On the initiation of a snowball Earth. *Geophys., Geochem., Geosyst.* 3. <https://doi.org/10.1029/2001GC000219>.
- Schrag, D.P., Higgins, J.A., Macdonald, F.A., Johnston, D.T., 2013. Authigenic carbonate and the history of the global carbon cycle. *Science* 339, 540–543.
- Schreiber, U.M., 2006. Sheet 2014 – Fransfontein (Provisional). Geological Survey of Namibia, Windhoek, Geol. Map Nam., 1:250,000 scale Geol. Ser.

- Sellers, W.D., 1969. A global climatic model based on the energy balance of the Earth-atmosphere system. *J. Appl. Meteorol.* 8, 392–400.
- Sengör, A.M., 1984. The Cimmeride Orogenic System and the Tectonics of Eurasia. Geological Society of America, Sp. Pap. 195, Boulder, CO, 82 p.
- Sengör, A.M., Lom, N., Zabci, C., Sunal, G., Öner, T., 2020. Reconstructing orogens without biostratigraphy: The Saharides and continental growth during the final assembly of Gondwana-Land. *Proc. Natl. Acad. Sci. U. S. A.* 117 (51), 32,278–32,284.
- Seth, B., Kröner, A., Mezger, K., Nemchin, A.A., Pidgeon, R.T., Okrusch, M., 1998. Archaean to Neoproterozoic magmatic events in the Kaoko belt of NW Namibia and their geodynamic significance. *Precambrian Res.* 92, 341–363.
- Seth, B., Okrusch, M., Wilde, M., Hoffmann, K.-H., 2000. The Voetspoor Intrusion, Southern Kaoko Zone, Namibia: mineralogical, geochemical and isotopic constraints for the origin of a syenitic magma. *Communs. Geol. Surv. Namibia* 12, 125–137.
- Sheppard, S.M.F., Schwarzbach, H.P., 1970. Fractionation of carbon and oxygen isotopes and magnesium between metamorphic calcite and dolomite. *Contrib. Mineral. Petrol.* 26, 161–198.
- Shields, G.A., 2005. Neoproterozoic cap carbonates: a critical appraisal of existing models and the plume-world hypothesis. *Terra Nova* 17, 299–310.
- Shields, G.A., 2018. Carbon and carbon isotope mass balance in the Neoproterozoic Earth system. *Emerg. Top. Life Sci.* <https://doi.org/10.1042/ETLS20170170>.
- Shields, G.A., Veizer, J., 2002. Precambrian marine carbonate isotope database: Version 1.1. *Geochim. Geophys. Geosyst.* 3 <https://doi.org/10.1029/2001GC000266>.
- Shields, G.A., Mills, B.J.W., Zhu, M.Y., Raub, T.D., Daines, S.J., Lenton, T.M., 2019. Unique Neoproterozoic carbon isotope excursions sustained by coupled evaporite dissolution and pyrite burial. *Nat. Geosci.* 12, 823–827.
- Shields-Zhou, G.A., Porter, S., Halverson, G.P., 2015. A new rock-based definition for the Cryogenian Period (circa 720 – 635 Ma). *Episodes* 39, 1–8.
- Siegesmund, S., Basei, M.A.S., Öyhantçabal, P., Oriolo, S. (Eds.), 2018. *Geology of Southwest Gondwana*. Springer International, Berlin, 688 p.
- Sleep, N.H., 1971. Thermal effects of the formation of Atlantic continental margins by continental break up. *Geophys. J. R. Astron. Soc.* 24, 325–350.
- Smit, J.M., 1962. Stratigraphy and metamorphism of the Otavi Series south-east of Otavi, South West Africa. *Trans. Geol. Soc. S. Afr.* 65, 63–78.
- Smith, J., 1839. On the last changes in the relative levels of the land and sea in the British Islands. *Wernerian Natural History Society, Edinburgh, Mem.* 8, 49–88.
- Smith, R.L., Bailey, R.A., 1968. Resurgent cauldrons. In: Coats, R.R., Hay, R.L., Anderson, C.A. (Eds.), *Studies in Volcanology*. Geological Society of America, Mem. 116, pp. 613–662. <https://doi.org/10.1130/MEM116-p613>.
- Soffer, G., 1998. Evolution of a Neoproterozoic continental margin subject to tropical glaciation. B.A. thesis. Harvard College, Cambridge, MA, USA, 59 p.
- Sohl, L.E., Christie-Blick, N., Kent, D.V., 1999. Paleomagnetic polarity reversals in Marinoan (ca 600 Ma) glacial deposits of Australia: implications for the duration of low-latitude glaciation in Neoproterozoic time. *Geol. Soc. Am. Bull.* 111, 1120–1139.
- Söhne, P.G., 1957. Revision of the geology of the Otavi Mountainland, South West Africa (with 1958 amended stratigraphic table). Unpubl. Rep., Tsumeb Corp. Ltd, Tsumeb.
- Söhne, P.G., 1964. The geology of the Tsumeb mine. In: Haughton, S.H. (Ed.), *The Geology of Some Ore Deposits in Southern Africa*. Geological Society of South Africa, Johannesburg, Spec. Publ. 2, pp. 367–382.
- Söhne, P.G., 1967. Tsumeb – a historical sketch. South West Africa Scientific Society, Windhoek, Sci. Res. S. W. Afr., Ser. 5, 92 p.
- Song, G.Y., Wang, X.Q., Shi, X.Y., Jiang, G.Q., 2017. New U–Pb age constraints on the upper Banxi Group and synchrony of the Sturtian glaciation in South China. *Geosci. Front.* 8, 1161–1173.
- Stanistreet, I.G., Charlesworth, E.G., 1999. Damaran basement-cored fold nappes incorporating pre-collisional basins, Kaoko belt, Namibia, and controls on Mesozoic supercontinental breakup. University of Witwatersrand, Johannesburg. Econ. Geol. Res. Unit Information Circ 332, 14 p.
- Stanistreet, I.G., Kukla, P.A., Henry, G., 1991. Sedimentary basinal responses to a Late Precambrian Wilson Cycle: the Damara Orogen and Nama Foreland, Namibia. *J. Afr. Earth Sci.* 13 (1), 141–156.
- Stanley, S.M., 2010. Relation of Phanerozoic stable isotope excursions to climate, bacterial metabolism, and major extinctions. *Proc. Natl. Acad. Sci. U. S. A.* 107 (19), 185–19189.
- Stanton, W.I., Schermerhorn, L.J.G., Korpershoek, H.R., 1963. The West Congo System. *Bol. Serv. Geol. Minas (Luanda, Angola)* 8, 69–78.
- Stewart, J.A., Gutjahr, M., Pearce, F., Swart, P.K., Foster, G.L., 2015. Boron during meteoric diagenesis and its potential implications for Marinoan snowball Earth $\delta^{11}\text{B}$ –pH excursions. *Geology* 43, 627–630.
- Stiller, M., Rounick, J.S., Shasha, S., 1985. Extreme carbon-isotope enrichments in evaporating brines. *Nature* 316, 434–435.
- Strauss, J.V., Tosca, N.J., 2020. Mineralogical constraints on Neoproterozoic $p\text{CO}_2$ and marine carbonate chemistry. *Geology* 48, 599–603.
- Strauss, J.V., Macdonald, F.A., Taylor, J.F., Repetski, J.E., McClelland, W.C., 2013. Laurentian origin for the North Slope of Alaska: Implications for the tectonic evolution of the Arctic. *Lithosphere*. <https://doi.org/10.1130/L284.1>.
- Strauss, J.V., Rooney, A.D., Macdonald, F.A., Brandon, A.D., Knoll, A.H., 2014. 740 Ma vase-shaped microfossils from Yukon, Canada: Implications for Neoproterozoic chronology and biostratigraphy. *Geology* 42, 659–662.
- Strauss, J.V., Macdonald, F.A., Halverson, G.P., Tosca, N.J., Schrag, D.P., Knoll, A.H., 2015. Stratigraphic evolution of the Neoproterozoic Callison Lake Formation: linking the break-up of Rodinia to the Islay carbon isotope excursion. *Am. J. Sci.* 315, 881–944.
- Stump, E., 2011. *The Roof at the Bottom of the World: Discovering the Transantarctic Mountains*. Yale University Press, 254 p.
- Sugden, D.E., John, B.S., 1976. *Glaciers and Landscape*. Edward Arnold, London, 376 p.
- Summons, R.E., Hayes, J.M., 1992. Principles of molecular and isotopic biogeochemistry. In: Schopf, J.W., Klein, C. (Eds.), *The Proterozoic Biosphere*. Cambridge University Press, Cambridge, UK, pp. 83–93.
- Sun, X.L., Turchyn, A.V., 2014. Significant contribution of authigenic carbonate to marine carbonate burial. *Nat. Geosci.* 7, 201–204.
- Suppe, J., 1981. Mechanics of mountain building and metamorphism in Taiwan. *Mem. Geol. Soc. China* 4, 67–89.
- Suppe, J., 1984. Kinematics of arc-continent collision, flipping of subduction, and back-arc spreading near Taiwan. *Mem. Geol. Soc. China* 6, 21–33.
- Swanson-Hysell, N.L., Kilian, T.M., Hanson, R.E., 2015a. A new grand mean palaeomagnetic pole for the 1.11 Ga Umkondo large igneous province with implications for palaeogeography and the geomagnetic field. *Geophys. J. Int'l* 203, 2237–2247.
- Swanson-Hysell, N.L., Maloof, A.C., Condon, D.J., Jenkin, G.R.T., Aleene, M., Tremblay, M.M., Tesema, T., Rooney, A.D., Haileab, B., 2015b. Stratigraphy and geochronology of the Tambien Group, Ethiopia: Evidence for globally synchronous carbon isotope change in the Neoproterozoic. *Geology* 43, 323–326.
- Swart, R., 1990. The late Proterozoic Amis River Formation of Namibia—a turbidite system developed by vertical accretion. *Sediment. Geol.* 67, 101–113.
- Swart, R., 1992a. The sedimentology of the Zerrissen turbidite system, Damara Orogen, Namibia. *Geological Survey of Namibia, Windhoek, Mem.* 13, 54 p.
- Swart, R., 1992b. Facies analysis of late Proterozoic carbonate turbidites in the Zerrissen Basin, Damara Orogen, Namibia. *J. Afr. Earth Sci.* 14, 283–294.
- Swart, P.K., 2008. Global synchronous changes in the carbon isotopic composition of carbonate sediments unrelated to changes in the global carbon cycle. *Proc. Natl. Acad. Sci. U. S. A.* 105 (13), 741–13,745.
- Swart, P.K., Eberli, G., 2005. The nature of the $\delta^{13}\text{C}$ of periplatform sediments: Implications for stratigraphy and the global carbon cycle. *Sediment. Geol.* 175, 115–129.
- Swart, P.K., Kennedy, M.J., 2012. Does the global stratigraphic reproducibility of $\delta^{13}\text{C}$ in Neoproterozoic carbonates require a marine origin? A Pliocene–Pleistocene comparison. *Geology* 40, 87–90.
- Tait, L.W., Schiel, D.R., 2013. Impacts of temperature on primary productivity and respiration in naturally structured macroalgal assemblages. *PLoS One* 8 (e74413), 1–10.
- Tait, J., Delpomdor, F., Prétat, A., Tack, L., Straathof, G., Nkula, V.K., 2011. Neoproterozoic sequences of the West Congo and Lindi/Ubangi supergroups in the Congo craton, central Africa. In: Arnaud, E., Halverson, G.P., Shields-Zhou (Eds.), *The Geological Record of Neoproterozoic Glaciations*. Geological Society, London, Mem. 36, pp. 185–194.
- Takeuchi, N., 2002. Optical characteristics of cryoconite (surface dust) on glaciers: the relationship between light absorbancy and the property of organic matter contained in the cryoconite. *Ann. Glaciol.* 34, 409–414.
- Tegtmeyer, A., Kröner, A., 1985. U–Pb zircon ages fro granitoid gneisses in northern Namibia and their significance for Proterozoic crustal evolution of southwestern Africa. *Precambrian Res.* 28, 311–326.
- Tensi, J., Mouthereau, F., Lacombe, O., 2006. Lithospheric bulge in the West Taiwan Basin. *Basin Res.* 18, 277–299.
- Thiede, D.S., Vasconcelos, P.M., 2010. Paraná flood basalts: Rapid extrusion hypothesis confirmed by new $^{40}\text{Ar}/^{39}\text{Ar}$ results. *Geology* 38, 747–750.
- Thiemens, M.M., Moynier, F., Thiemens, M.H., Shaheen, R., Chong, K., Koeberl, C., Popp, F., Gyallai, I., 2012. Zn and C isotopic variations associated with Neoproterozoic ice ages. *43rd Lunar Planet. Sci. Conf.* (2012), 2499.
- Tibaldi, A., Bonali, F.L., Pasquare Mariotti, F.A., 2016. Interaction between transform faults and rift systems: a combined field and experimental approach. *Front. Earth Sci.* 4 (33), 1–18. <https://doi.org/10.3389/feart.2016.00033>.
- Tojo, B., Katsuta, N., Takano, M., Kawakami, S., Ohno, T., 2007. Calcite-dolomite cycles in the Neoproterozoic Cap carbonates, Otavi Group, Namibia. In: Vickers-Rich, P., Komarower, P. (Eds.), *The Rise and Fall of the Ediacaran Biota*. Geological Society, London, Sp. Publ. 286, pp. 103–113.
- Trindade, R.I.F., Macouin, M., 2007. Paleolatitude of glacial deposits and paleogeography of Neoproterozoic ice ages. *Compt. Rendus Geosci.* 339, 200–211.
- Trompette, R., 1994. Geology of Western Gondwana (2000–500 Ma): Pan-African – Brasiliano Aggregation of South America and Africa (Carozzi, A.V., transl.). A. A. Balkema, Rotterdam, 350 p.
- Trower, E.J., 2020. The enigma of Neoproterozoic giant ooids—Fingerprints of extreme climate? *Geophys. Res. Lett.* 47, 1–10 e2019GL086146.
- Tucker, M.E., Wilson, J.L., Crevello, P.D., Sarg, J.R., Read, J.F., 1990. Carbonate Platforms: Facies, Sequences and Evolution. Blackwell Scientific, Oxford, UK, Sp. Publ. 9, 328 p.
- Tupinambá, M., Heilbron, M., Valeriano, C., Júnior, R.P., Dios, F.B., Machado, N., 2012. Juvenile contribution of the Neoproterozoic Rio Negro magmatic arc (Ribeira Belt, Brazil): Implications for Western Gondwana amalgamation. *Gondwana Res.* 21, 422–438.
- Turcotte, D.L., Schubert, G., 1982. *Geodynamics: Applications of Continuum Physics to Geological Problems*. John Wiley & Sons, New York, 450 p.
- Tziperman, E., Halevy, I., Johnston, D.T., Knoll, A.H., Schrag, D.P., 2011. Biologically induced initiation of Neoproterozoic snowball-Earth events. *Proc. Natl. Acad. Sci. U. S. A.* 108 (37), 15,091–15,096.
- Tziperman, E., Abbot, D.S., Ashkenazy, Y., Gildor, H., Pollard, D., Schoof, C.G., Schrag, D.P., 2012. Continental constriction and oceanic ice-cover thickness in a Snowball-Earth scenario. *J. Geophys. Res.* 117 (C05016), 1–12.

- Uemura, R., Matsui, Y., Yoshida, N., Abe, O., Mochizuki, S., 2005. Isotopic fractionation of water during snow formation: Experimental evidence of kinetic effect. *Polar Meteorol. Glaciol.* 19, 1–14.
- Urban, H., Stribny, B., Lippolt, H.J., 1992. Iron and manganese deposits of the Urucum District, Mato Grosso do Sul, Brazil. *Econ. Geol.* 87, 1375–1392.
- Verbeek, T., 1970. Géologie et lithostratigraphie du Lindien (Précambrien supérieur du nord de la République Démocratique du Congo). *Annal. Mus. Roy. Afr. Centr.*, ser. 8, 66, 1–309.
- Vincent, W.F., 1988. Microbial Ecosystems of Antarctica. Cambridge University Press, Cambridge, U.K., 304 p.
- Vincent, W.F., Howard-Williams, C., 2000. Life on Snowball Earth. *Science* 287, 2421.
- Vincent, W.F., Quesada, A., 2012. Cyanobacteria in high latitude lakes, rivers and seas. In: Whitton, B.A. (Ed.), Ecology of Cyanobacteria II: Their Diversity in Space and Time. Springer Science+Business Media B.V, pp. 371–385. https://doi.org/10.1007/978-94-007-3855-3_13.
- Vincent, W.F., Gibson, J.A.E., Pienitz, R., Villeneuve, V., Broady, P.A., Hamilton, P.B., Howard-Williams, C., 2000. Ice shelf microbial ecosystems in the High Arctic and implications for life on snowball Earth. *Naturwissenschaften* 87, 137–141.
- Vincent, W.F., Mueller, D., Van Hove, P., Howard-Williams, C., 2004. Glacial periods on early Earth and implications for the evolution of life. In: Seckbach, J. (Ed.), Origins: Genesis, Evolution and Diversity of Life. Kluwer, Dordrecht, pp. 481–499.
- Visser, J.N.J., 1989. The Permo-Carboniferous Dwyka Formation of southern Africa: deposition by a predominantly subpolar marine ice sheet. *Palaeogeog. Paleoclimatol. Palaeoecol.* 70, 377–391.
- Voigt, A., Abbot, D.S., Pierrehumbert, R.T., Marotzke, J., 2011. Initiation of a Marinoan Snowball Earth in a state-of-the-art atmosphere-ocean general circulation model. *Clim. Past* 7, 1–15.
- von Hagke, C., Malz, A., 2018. Triangle zones – Geometry, kinematic, and the need for appreciation of uncertainties. *Earth-Sci. Rev.* 177, 24–42.
- Walker, J.C.G., Hays, P.B., Kasting, J.F., 1981. A negative feedback mechanism for the long-term stabilization of Earth's surface temperature. *J. Geophys. Res.* 86 (C10), 9776–9782.
- Wallace, M.W., Hood, A.V.S., Woon, E.M.S., Hoffmann, K.-H., Reed, C.P., 2014. Enigmatic chambered structures in Cryogenian reefs: the oldest sponge-grade organisms? *Precambrian Res.* 255, 109–123.
- Wallace, M.W., Hood, A.V.S., Fayle, J., Hordern, E.S., O'Hare, T.F., 2019. Neoproterozoic marine dolomite hardgrounds and their relationship to cap dolomites. *Precambrian Res.* 328, 269–286.
- Waltham, D., 2015. Milankovitch period uncertainties and their impact on cyclostratigraphy. *J. Sediment. Res.* 122, 990–998.
- Wannamaker, P., Hill, G., Stodt, J., Maris, V., Ogawa, Y., Selway, K., Boren, G., Bertrand, D., Ayling, B., Green, A.M., Feucht, D., 2018. Uplift of the central Transantarctic Mountains. *Nature Comms.* 18, 1588. <https://doi.org/10.1038/s41467-017-01577-2>.
- Warren, S.G., Brandt, R.E., Grenfell, T.C., McKay, C.P., 2002. Snowball Earth: Ice thickness on the tropical ocean. *J. Geophys. Res.* 107 (C10), 3167. <https://doi.org/10.1029/2001JC001123>.
- Watts, A.B., Karner, G.D., Steckler, M.S., 1982. Lithospheric flexure and the evolution of sedimentary basins. *Phil. Trans. R. Soc. Ser. A* 305 (1489), 249–281.
- Wei, G.Y., Hood, A.V.S., Chen, X., Li, D., Wei, W., Wen, B., Gong, Z., Yang, T., Zhang, Z. F., Ling, H.F., 2019. Ca and Sr isotope constraints on the formation of the Marinoan cap dolostones. *Earth Planet. Sci. Lett.* 511, 202–212.
- Wernicke, B., 1981. Low-angle normal faults in the Basin and Range Province: nappe tectonics in an extending orogen. *Nature* 291, 645–648.
- Whalen, J.B., Hildebrand, R.S., 2019. Trace element discrimination of arc, slab failure, and A-type granitic rocks. *Lithos* 348–349 (105179), 1–19.
- Wharton Jr., R.A., McKay, C.P., Simmons Jr., G.M., Parker, B.C., 1985. Cryoconite holes on glaciers. *BioScience* 35, 499–503.
- Will, T.M., Okrusch, M., Gruner, B.B., 2004. Barrovian and Buchan type metamorphism in the Pan-African Kaoko belt, Namibia: implications for its geotectonic position with the framework of Western Gondwana. *S. Afr. J. Geol.* 107, 431–454.
- Williams, G.E.G., 1979. Sedimentology, stable-isotope geochemistry and paleoenvironment of dolostones capping late Precambrian glacial sequences in Australia. *J. Geol. Soc. Aust.* 26, 377–386.
- Williams, G.E., 2000. Geological constraints on the Precambrian history of Earth's rotation and the Moon's orbit. *Rev. Geophys.* 38, 37–59.
- Wilson, J.L., 1975. Carbonate Facies in Geologic History. Springer Verlag, New York. https://doi.org/10.1007/978-1-4612-6383-8_471 p.
- Wilson, W.E., 1977. Tsumeb – the world's greatest mineral locality. *Mineral. Rec.* 8, 1–128.
- Wilson, A., 2003. The occurrence and chemical implications of geothermal convection of seawater in continental shelves. *Geophys. Res. Lett.* 30, 2127. <https://doi.org/10.1029/2003GL018499>.
- Wilson, A., 2005. Fresh and saline groundwater discharge to the ocean: a regional perspective. *Water Resour. Res.* 41, W01016 <https://doi.org/10.1029/2004WR003399>.
- Wilson, A.M., Sanford, W., Whitakker, F., Smart, P., 2001. Spatial patterns of diagenesis during geothermal circulation in carbonate platforms. *Am. J. Sci.* 301, 727–752.
- Witus, A.E., Branecky, C.M., Anderson, J.B., Szczuciński, W., Schroeder, D.M., Blankenship, D.D., Jakobsson, M., 2014. Meltwater intensive glacial retreat in polar environments and investigation of associated sediments: example from Pine Island Bay, West Antarctica. *Quat. Sci. Rev.* 85, 99–118.
- Woltz, C.R., Porter, S.M., Agić, H., Dehler, C.M., Junium, C.K., Riedman, L.A., Hodgeskiss, M.S.W., Wörndl, S., Halverson, G.P., 2021. Total organic carbon and the preservation of organic microfossils in Precambrian shale. *Geology* 49. <https://doi.org/10.1130/G48116.1>.
- Wood, R.A., 2011. Paleoecology of the earliest skeletal metazoan communities: implications for early biomineralization. *Earth Sci. Rev.* 106, 184–190.
- Woodcock, N.H., 1979. Sizes of submarine slides and their significance. *J. Struct. Geol.* 1, 137–142.
- Wright, A., Siegert, M., 2012. A fourth inventory of Antarctic subglacial lakes. *Antarct. Sci.* 24, 659–664.
- Wu, J.C., Liu, Y.G., Zhao, Z.Q., 2021. How should snowball Earth deglaciation start. *J. Geophys. Res.* 126 e2020JD033833.
- Wunsch, C., 1970. On oceanic boundary mixing. *Deep-Sea Res.* 17, 293–301.
- Wunsch, M., Betzler, C., Lindhorst, S., Lüdemann, T., Eberli, G., 2017. Sedimentary dynamics along carbonate slopes (Bahamas archipelago). *Sedimentology* 64, 631–657.
- Xiao, S.H., Laflamme, M., 2008. On the eve of animal radiation: phylogeny, ecology and evolution of the Ediacara biota. *Trends Ecol. Evol.* 24, 31–40.
- Xiao, S.H., Muscente, A.D., Chen, L., Zhou, C.M., Schiffbauer, J.D., Wood, A.D., Polys, N. F., Yuan, X.L., 2014. The Weng'an biota and the Ediacaran radiation of multicellular eukaryotes. *Natl. Sci. Rev.* 1, 498–520.
- Yang, J., Jansen, M.F., Macdonald, F.A., Abbot, D.S., 2017. Persistence of a surface freshwater ocean after a Snowball Earth. *Geology* 45, 615–618.
- Yin, C.Y., Liu, P.J., Awramik, S.M., Chen, S.M., Tang, F., Gao, L.Z., Wang, Z.Q., Riedman, L.A., 2011. Acanthomorph biostratigraphic succession of the Ediacaran Doushantuo Formation in the east Yangtze Gorges, South China. *Acta Geol. Sin.* 85, 283–295.
- Yoshioka, H., Asahara, Y., Tojo, B., Kawakami, S., 2003. Systematic variations in C, O, and Sr isotopes and elemental concentrations in Neoproterozoic carbonates in Namibia: implications for a glacial to interglacial transition. *Precambrian Res.* 124, 69–85.
- Young, D.A., Wright, A.P., Roberts, J.I., Warner, R.C., Young, N.W., Greenbaum, J.S., Schroeder, D.M., Holt, J.W., Sugden, D.E., Blankenship, D.D., van Ommen, T.D., Siegert, M.J., 2011. A dynamic early East Antarctic Ice Sheet suggested by ice-covered fjord landscapes. *Nature* 474, 72–75.
- Zachos, J., Pagani, M., Thomas, E., Billups, K., 2001. Trends, rhythms, and abberations in global climate 65 Ma to present. *Science* 292, 686–693.
- Zeebe, R.E., Wolf-Gladrow, D., 2001. CO₂ in Seawater: Equilibrium, Kinetics, Isotopes. Elsevier, Amsterdam, 346 p.
- Zhang, S.H., Jiang, G.Q., Han, Y.G., 2008. The age of the Nantuo Formation and Nantuo glaciation in South China. *Terra Nova* 20, 289–294.
- Zhang, S.H., Evans, D.A.D., Li, H.Y., Wu, H.C., Jiang, G.Q., Dong, J., Zhao, Q.L., Raub, T. D., Yang, T.S., 2013. Paleomagnetism of the late Cryogenian Nantuo Formation and paleogeographic implications for the South China Block. *J. Asian Earth Sci.* 72, 164–177.
- Zhang, F., Lin, J., Zhou, Z.Y., Yang, H.F., Zhan, W.H., 2018. Intra- and intertrench variations in flexural bending of the Manila, Marianas and global trenches: implications on plate weakening in controlling trench dynamics. *Geophys. J. Int.* 212, 1429–1449.
- Zhou, X.L., Lu, Z.L., Rickaby, R.E.M., Domack, E.W., Wellner, J.S., Kennedy, H.A., 2015. Ikaite abundance controlled by porewater phosphorus level: potential links to dust and productivity. *J. Geol.* 123, 269–281.
- Zhou, C.M., Huyskens, M.H., Lang, X.G., Xiao, S.H., Yin, Q.Z., 2019. Calibrating the terminations of Cryogenian global glaciations. *Geology* 47, 251–254.
- Zhou, Y., Pogge von Strandmann, P.A.E., Zhu, M.Y., Ling, H.F., Manning, C., Li, D., He, T. C., Shields, G.A., 2020. Reconstructing Tonian seawater ⁸⁷Sr/⁸⁶Sr using calcite microspar. *Geology* 48. <https://doi.org/10.1130/G48756.1>.
- Zumberge, J.A., Rocher, D., Love, G.D., 2020. Free and kerogen-bound biomarkers from late Tonian sedimentary rocks record abundant eukaryotes in mid-Neoproterozoic marine communities. *Geobiology* 18, 326–347.